Jie-Zhi Wu
Hui-Yang Ma
Ming-De Zhou

# Vorticity

# Vortex D

# Vorticity and Vortex Dynamics

J.-Z. Wu H.-Y. Ma M.-D. Zhou

# Vorticity and Vortex Dynamics

With 291 Figures

Springer

Professor Jie-Zhi Wu
State Key Laboratory for Turbulence and Complex System, Peking University
Beijing 100871, China
University of Tennessee Space Institute
Tullahoma, TN 37388, USA

Professor Hui-Yang Ma
Graduate University of The Chinese Academy of Sciences
Beijing 100049, China

Professor Ming-De Zhou
The University of Arizona, Tucson, AZ 85721, USA
State Key Laboratory for Turbulence and Complex System, Peking University
Beijing, 100871, China
Nanjing University of Aeronautics and Astronautics
Nanjing, 210016, China

Library of Congress Control Number: 2005938844

ISBN-10 3-540-29027-3 Springer Berlin Heidelberg New York
ISBN-13 978-3-540-29027-8 Springer Berlin Heidelberg New York

This work is subject to copyright. All rights are reserved, whether the whole or part of the material is concerned, specifically the rights of translation, reprinting, reuse of illustrations, recitation, broadcasting, reproduction on microfilm or in any other way, and storage in data banks. Duplication of this publication or parts thereof is permitted only under the provisions of the German Copyright Law of September 9, 1965, in its current version, and permission for use must always be obtained from Springer. Violations are liable to prosecution under the German Copyright Law.

Springer is a part of Springer Science+Business Media.

springer.com

© Springer-Verlag Berlin Heidelberg 2006
Printed in Germany

The use of general descriptive names, registered names, trademarks, etc. in this publication does not imply, even in the absence of a specific statement, that such names are exempt from the relevant protective laws and regulations and therefore free for general use.

Typesetting by the Authors and SPI Publisher Services using a Springer TEX macro package
Cover design: eStudio Calamar Steinen

Printed on acid-free paper SPIN 10818730 61/3141/SPI 5 4 3 2 1 0

# Preface

The importance of vorticity and vortex dynamics has now been well recognized at both fundamental and applied levels of fluid dynamics, as already anticipated by Truesdell half century ago when he wrote the first monograph on the subject, *The Kinematics of Vorticity* (1954); and as also evidenced by the appearance of several books on this field in 1990s. The present book is characterized by the following features:

1. *A basic physical guide throughout the book.* The material is directed by a basic observation on the splitting and coupling of two fundamental processes in fluid motion, i.e., shearing (unique to fluid) and compressing/expanding. The vorticity plays a key role in the former, and a vortex is nothing but a fluid body with high concentration of vorticity compared to its surrounding fluid. Thus, the vorticity and vortex dynamics is accordingly defined as the theory of shearing process and its coupling with compressing/expanding process.
2. *A description of the vortex evolution following its entire life.* This begins from the generation of vorticity to the formation of thin vortex layers and their rolling-up into vortices, from the vortex-core structure, vortex motion and interaction, to the burst of vortex layer and vortex into small-scale coherent structures which leads to the transition to turbulence, and finally to the dissipation of the smallest structures into heat.
3. *Wide range of topics.* In addition to fundamental theories relevant to the above subjects, their most important applications are also presented. This includes vortical structures in transitional and turbulent flows, vortical aerodynamics, and vorticity and vortices in geophysical flows. The last topic was suggested to be added by Late Sir James Lighthill, who read carefully an early draft of the planned table of contents of the book in 1994 and expressed that he likes "all the material" that we proposed there.

These basic features of the present book are a continuation and development of the spirit and logical structure of a Chinese monograph by the same authors, *Introduction to Vorticity and Vortex Dynamics*, Higher

Education Press, Beijing, 1993, but the material has been completely rewritten and updated. The book may fit various needs of fluid dynamics scientists, educators, engineers, as well as applied mathematicians. Its selected chapters can also be used as textbook for graduate students and senior undergraduates. The reader should have knowledge of undergraduate fluid mechanics and/or aerodynamics courses.

Many friends and colleagues have made significant contributions to improve the quality of the book, to whom we are extremely grateful. Professor Xuesong Wu read carefully the most part of Chaps. 2 through 6 of the manuscript and provided valuable comments. Professor George F. Carnevale's detailed comments have led to a considerable improvement of the presentation of entire Chap. 12. Professors Boye Ahlhorn, Chien Cheng Chang, Sergei I. Chernyshenko, George Haller, Michael S. Howe, Yu-Ning Huang, Tsutomu Kambe, Shigeo Kida, Shi-Kuo Liu, Shi-Jun Luo, Bernd R. Noack, Rick Salmon, Yi-Peng Shi, De-Jun Sun, Shi-Xiao Wang, Susan Wu, Au-Kui Xiong, and Li-Xian Zhuang reviewed sections relevant to their works and made very helpful suggestions for the revision. We have been greatly benefited from the inspiring discussions with these friends and colleagues, which sometimes evolved to very warm interactions and even led to several new results reflected in the book. However, needless to say, any mistakes and errors belong to our own.

Our own research results contained in the book were the product of our enjoyable long-term cooperations and in-depth discussions with Professors Jain-Ming Wu, Bing-Gang Tong, James C. Wu, Israel Wygnanski, Chui-Jie Wu, Xie-Yuan Yin, and Xi-Yun Lu, to whom we truly appreciate. We also thank Misses Linda Engels and Feng-Rong Zhu for their excellent work in preparing many figures, and Misters Yan-Tao Yang and Ri-Kui Zhang for their great help in the final preparation and proof reading of the manuscript.

Finally, we thank the University of Tennessee Space Institute, Peking University, and Tianjin University, without their hospitality and support the completion of the book would have to be greatly delayed. The highly professional work of the editors of Springer Verlag is also acknowledged.

Beijing-Tennessee-Arizona
October 2005

*Jie-Zhi Wu*
*Hui-Yang Ma*
*Ming-de Zhou*

# Contents

## Part II Vortex Dynamics

# 1

# Introduction

Vortices are a special existence form of fluid motion with origin in the rotation of fluid elements. The most intuitive pictures of these organized structures range from spiral galaxies in universe to red spots of the Jupiter, from hurricanes to tornadoes, from airplane trailing vortices to swirling flows in turbines and various industrial facilities, and from vortex rings in the mushroom cloud of a nuclear explosion or at the exit of a pipe to coherent structures in turbulence. The physical quantity characterizing the rotation of fluid elements is the *vorticity* $\boldsymbol{\omega} = \nabla \times \boldsymbol{u}$ with $\boldsymbol{u}$ being the fluid velocity; thus, qualitatively one may say that *a vortex is a connected fluid region with high concentration of vorticity compared with its surrounding.*[1]

Once formed, various vortices occupy only very small portion in a flow but play a key role in organizing the flow, as *"the sinews and muscles of the fluid motion"* (Küchemann 1965) and *"the sinews of turbulence"* (Moffatt et al. 1994). Vortices are also *"the voice of fluid motion"* (Müller and Obermeier 1988) because at low Mach numbers they are the only source of aeroacoustic sound and noise. These identifications imply the crucial importance of the vorticity and vortices in the entire fluid mechanics. The generation, motion, evolution, instability, and decay of vorticity and vortices, as well as the interactions between vortices and solid bodies, between several vortices, and between vortices and other forms of fluid motion, are all the subject of *vorticity and vortex dynamics*.[2]

The aim of this book is to present systematically the physical theory of vorticity and vortex dynamics. In this introductory chapter we first locate the position of vorticity and vortex dynamics in fluid mechanics, then briefly review its development. These physical and historical discussions naturally lead to an identification of the scope of vorticity and vortex dynamics, and

[1] This definition is a generalization of that given by Saffman and Baker (1979) for inviscid flow.

[2] In Chinese, the words "vorticity" and "vortex" can be combined into one character sounds like "vor," so one has created a single word "*vordynamics*".

thereby determine what a book like this one should cover. An outline of every chapter concludes this chapter.

## 1.1 Fundamental Processes in Fluid Dynamics and Their Coupling

A very basic fact in fluid mechanics is the coexistence and interaction of two fundamental dynamic processes: the *compressing/expanding process* ("*compressing process*" for short) and the *shearing process*, of which a rational definition will be given later. In broader physical context these are called *longitudinal* and *transverse* processes, respectively (e.g., Morse and Feshbach 1953). They behave very differently, represented by different physical quantities governed by different equations, with different dimensionless parameters (the Mach number for compressing and the Reynolds number for shearing). These two fundamental processes and their interactions or couplings stand at the center of the entire fluid mechanics.

If we further compare a fluid with a solid, we see at once that their compressing properties have some aspects in common, e.g., both can support longitudinal waves including shock waves, but cannot be indefinitely compressed. What really makes a fluid essentially differ from a solid is their response to a shear stress. While a solid can remain in equilibrium with finite deformation under such a stress, a fluid at rest cannot stand any shear stress. For an ideal fluid with strictly zero shear viscosity, a shearing simply causes one fluid layer to "slide" over another without any resistance, and across the "slip surface" the velocity has a tangent discontinuity. But all fluids have more or less a nonzero shear viscosity, and a shear stress always puts fluid elements into spinning motion, forming *rotational* or *vortical* flow. A solid never has those beautiful vortices which are sometimes useful but sometimes harmful, nor turbulence. It is this basic feature of yielding to shear stress that makes the fluid motion extremely rich, colorful, and complicated.

Having realized this basic difference between fluid and solid, one cannot but highly admire a very insightful assertion of late Prof. Shi-Jia Lu (1911–1986), the only female student of Ludwig Prandtl, made around 1980 (private communication):

*The essence of fluid is vortices. A fluid cannot stand rubbing; once you rub it there appear vortices.*

For example, if a viscous flow has a stationary solid boundary, a strong "rubbing" must occur there since the fluid ceases to move on the boundary. A boundary layer is thereby formed, whose separation from the solid boundary is the source of various free shear layers that roll into concentrated vortices which evolve, interact, become unstable and break to turbulence, and finally dissipate into heat.

Of the two fundamental processes and their coupling in fluid, two key physical mechanisms deserve most attention. First, in the interior of a flow,

the so-called *Lamb vector* $\boldsymbol{\omega} \times \boldsymbol{u}$ not only leads to the richest phenomena of shearing process via its curl, such as vortex stretching and tilting as well as turbulent coherent structures formed thereby,[3] but also serves as the crossroad of the two processes. Through the Lamb vector, shearing process can be a byproduct of strong compressing process, for example vorticity produced by a curved shock wave; or vice versa, for example sound or noise produced by vortices. Second, on flow boundaries the two processes are also coupled, but due to the viscosity and the adherence condition. In particular, a tangent pressure gradient (a compressing process) on a solid surface always produces new vorticity, which alters the existing vorticity distributed in the boundary layer and has significant effect on its later development.

The presentation of the entire material in this book will be guided by the earlier concept of two fundamental processes and their coupling.

## 1.2 Historical Development

Although vortices have been noticed by the mankind ever since very ancient time, rational theories were first developed for the relatively simpler compressing process, from fluid statics to the Bernoulli theorem and to ideal fluid dynamics based on the Euler equation. The theory of *rotational flow* of ideal fluid was founded by the three vorticity theorems of Helmholtz (1858, English translation 1867), who named such flows as "*vortex motions*." His work opened a brand new field, which was enriched by, among others, Kelvin's (1869) circulation theorem. But the inviscid fluid model on which these theorems are based cannot explain the generation of the vortices and their interaction with solid bodies. Most theoretical studies were still confined to potential flow, leaving the famous *D'Alembert's paradox* that a uniformly translating body through the fluid would experience no drag. The situation at that time was as Sir Hinshelwood has observed, *"... fluid dynamicists were divided into hydraulic engineers who observed what could not be explained, and mathematicians who explained things that could not be observed"*. (Lighthill 1956). The theoretical achievements by then has been summarized in the classic monograph of Lamb (1932, first edition: 1879), in which the inviscid, incompressible, and irrotational flow occupies the central position and vortex motion is only a small part. Thus, *"Sydney Goldstein has observed that one can read all of Lamb without realizing that water is wet!"* (Birkhoff 1960).

A golden age of vorticity and vortex dynamics appeared during 1894–1910s as the birth of *aerodynamics* associated with the realization of human power

[3] Here lies one of the hardest unsolved mathematic problems, on the finite-time existence, uniqueness, and regularity of the solutions of the Navier–Stokes equations. To quote Doering and Gibbon 1995: *"It turns out that the nonlinear terms that can't be controlled mathematically are precisely those describing what is presumed to be the basic physical mechanism for the generation of turbulence, namely vortex stretching"*.

flight.[4] Owing to the astonishing achievements of those prominent figures such as Lanchester, Joukowski, Kutta, and Prandtl, one realized that a wing can fly with sustaining lift and relatively much smaller drag due solely to the vortex system it produces.

More specifically, in today's terminology, the *Kutta–Joukowski theorem* (1902–1906) proves that the lift on an airfoil is proportional to its flight speed and surrounding velocity circulation, which is determined by the *Kutta condition* that the flow must be regular at the sharp trailing edge of the airfoil. The physical root of such a vortex system lies in the viscous shearing process in the thin *boundary layer* adjacent to the wing surface, as revealed by Prandtl (1904). The wing circulation is nothing but the net vorticity contained in the asymmetric boundary layers at upper and lower surfaces of the wing, and the Kutta condition imposed for inviscid flow is simply a synthetic consequence of these boundary layers at the trailing edge.

The wing vortex system has yet another side. The boundary layers that provide the lift also generate a *friction drag*. Moreover, as the direct consequence of the theorems of Helmholtz and Kelvin, these layers have to leave the wing trailing edge to become free vortex layers that roll into strong trailing vortices in the wake (already conceived by Lanchester in 1894), which cause an *induced drag*.

All these great discoveries made in such a short period formed the classic low-speed aerodynamics theory. Therefore, at a low Mach number all aspects of the wing-flow problem (actually any flow problems) may essentially amount to vorticity and vortex dynamics. The rapid development of aeronautical techniques in the first half of the twentieth century represented the greatest practice in the human history of utilization and control of vortices, as summarized in the six- and two-volume monographs edited by Durand (1934–1935) and Goldstein (1938), respectively.

Then, the seek for high flight speed turned aerodynamicists' attention back to compressing process. High-speed aerodynamics is essentially a combination of compressing dynamics and boundary-layer theory (cf. Liepmann and Roshko 1957). But soon after that another golden age of vorticity and vortex dynamics appeared owing to the important finding of vortical structures of various scales in transitional and turbulent flows. In fact, the key role of vortex dynamics in turbulence had long been speculated since 1920–1930s, a concept that attracted leading scientists like Taylor and Thomson, and reflected vividly in the famous verse by Richardson (1922):

*Big whirls have little whorls,*
*Which feed on their velocity.*
*And little whorls have lesser whorls,*
*And so on to viscosity.*

[4] For a detailed historical account of the times from Helmholtz to this exciting period with full references, see Giacomelli and Pistolesi (1934).

This concept was confirmed and made more precise by the discovery of turbulent coherent structures, which immediately motivated extensive studies of vortex dynamics in turbulence. The intimate link between aerodynamic vortices and turbulence has since been widely appreciated (e.g., Lilley 1983). In fact, this second golden age also received impetus from the continuous development of aerodynamics, such as the utilization of stable separated vortices from the leading edges of a slender wing at large angles of attack, the prevention of the hazardous effect of trailing vortices on a following aircraft, and the concern about vortex instability and breakdown. Meanwhile, the importance and applications of vorticity and vortex dynamics in ocean engineering, wind engineering, chemical engineering, and various fluid machineries became well recognized. On the other hand, the formation and evolution of large-scale vortices in atmosphere and ocean had long been a crucial part of geophysical fluid dynamics.

The second golden age of vorticity and vortex dynamics has been anticipated in the writings of Truesdell (1954), Lighthill (1963), and Batchelor (1967), among others. Truesdell (1954) made the first systematic exposition of vorticity kinematics. In the introduction to his book, Batchelor (1967) claimed that *"I regard flow of an incompressible viscous fluid as being at the center of fluid dynamics by virtue of its fundamental nature and its practical importance. ... most of the basic dynamic ideas are revealed clearly in a study of rotational flow of a fluid with internal friction; and for applications in geophysics, chemical engineering, hydraulics, mechanical and aeronautical engineering, this is still the key branch of fluid dynamics"*. It is this emphasis on viscous shearing process, in our view, that has made Batchelor's book a representative of the second generation of textbooks of fluid mechanics after Lamb (1932). In particular, the article of Lighthill (1963) sets an example of using vorticity to interpret a boundary layer and its separation, indicating that *"although momentum considerations suffice to explain the local behavior in a boundary layer, vorticity considerations are needed to place the boundary layer correctly in the flow as a whole. It will also be shown (surprisingly, perhaps) that they illuminate the detailed development of the boundary layer ... just as clear as do momentum considerations..."*. Therefore, Lighthill has placed the entire boundary layer theory (including flow separation) correctly in the realm of vorticity dynamics as a whole.

So far the second golden age is still in rapid progress. The achievements during the second half of the twentieth century have been reflected not only by innumerable research papers but also by quite a few comprehensive monographs and graduate textbooks appeared within a very short period of 1990s, e.g., Saffman (1992), Wu et al. (1993), Tong et al. (1994), Green (1995), and Lugt (1996), along with books and collected articles on special topics of this field, e.g., Tong et al. (1993), Voropayev and Afanasyev (1994), and Hunt and Vassilicos (2000). Yet not included in but relevant to this list are books on steady and unsteady flow separation, on the stability of shear flow and vortices, etc. In addition to these, very far-reaching new directions has also

emerged, such as applications to external and internal biofluiddynamics and biomimetics, and vortex control that in broad sense stands at the center of the entire field of flow control (cf. Gad-el-Hak 2000). The current fruitful progress of vortex dynamics and control in so many branches will have a very bright future.

## 1.3 The Contents of the Book

Based on the preceding physical and historical discussions, especially following Lu's assertion, we consider the vorticity and vortex dynamics a branch of fluid dynamics that treats *the theory of shearing process and its interaction with compressing process*. This identification enables one to study as a whole the full aspects and entire life of a vortex, from its kinematics to kinetics, and from the generation of vorticity to the dissipation of vortices. But this identification also posed to ourselves a task almost impossible, since it implies that the range of the topics that should be included is too wide to be put into a single volume. Thus, certain selection has to be made based on the authors' personal background and experience. Even so, the content of the book is still one of the widest of all relevant books.

A few words about the terminology is in order here. By the qualitative definition of a vortex given at the beginning of this section, a vortex can be identified when a vorticity concentration of arbitrary shape occurs in one or two spatial dimensions, having a layer-like or axial structure, respectively. The latter is the strongest form permissible by the solenoidal nature of vorticity, and as said before is often formed from the rolling up of the former as a further concentration of vorticity. But, conventionally layer-like structures have their special names such as boundary layer (attached vortex layer) and free shear layer or mixing layer (free vortex layer). Only axial structures are simply called vortices, which can be subdivided into *disk-like vortices* with diameter much larger than axial scale such as a hurricane, and *columnar vortices* with diameter much smaller than axial length such as a tornado Lugt (1983). While we shall follow this convention, it should be borne in mind that the layer-like and axial structures are often closely related as different temporal evolution stages and/or spatial portions of a single vortical structure.

Having said these, we now outline the organization of the book, which is divided into four parts.

Part I concerns vorticity dynamics and consists of five chapters. Chapter 2 is an overall introduction of two fundamental dynamic processes in fluid motion. After highlighting the basis of fluid kinematics and dynamics, this chapter introduces the mathematic tools for decomposing a vector field into a longitudinal part and a transverse part. This decomposition is then applied to the momentum equation, leading to an identification of each process and their coupling.

Chapter 3 gives a systematic presentation of vorticity kinematics, from spatial properties to temporal evolution, both locally and globally. The word "kinematics" is used here in the same spirit of Truesdell (1954); namely, without involving specific kinetics that identifies the cause and effect. Therefore, the results remain universal.[5] The last section of Chap. 3 is devoted to the somewhat idealized *circulation-preserving flow*, in which the kinetics enters the longitudinal (compressing) process but keeps away from the transverse (shearing) process. Rich theoretical consequences follow from this situation.

Chapter 4 sets a foundation of vorticity dynamics. First, the physical mechanisms that make the shearing process no longer purely kinematic are addressed and exemplified, with emphasis on the role of viscosity. Second, the characteristic behaviors of a vorticity field at small and large Reynolds' numbers are discussed, including a section on vortex sheet dynamics as an asymptotic model when the viscosity approaches zero (but not strictly zero). Finally, formulations of viscous flow problems in terms of vorticity and velocity are discussed, which provides a theoretical basis for developing relevant numerical methods.[6]

Chapter 5 presents theories of *flow separation* (more specifically and importantly, boundary-layer separation at large Reynolds' numbers). Due to separation, a boundary layer bifurcates to a free shear layer, which naturally rolls up into a concentrated vortex. Thus, typically though not always, a vortex originates from flow separation. Therefore, this chapter may serve as a transition from vorticity dynamics to vortex dynamics.

The next three chapters constituent Part II as fundamentals of vortex dynamics. In Chap. 6 we present typical vortex solutions, including both exact solutions of the Navier–Stokes and Euler equations (often not fully realistic) and asymptotic solutions that are closer to reality. The last section of the chapter discusses an open issue on how to *quantitatively* identify a vortex. According to the evolution order of a vortex in its whole life, this chapter should appear after Chap. 7; but it seems better to introduce the vortex solutions as early as possible although this arrangement makes the logical chain of the book somewhat interrupted.

The global *separated flow* addressed in Chap. 7 usually has vortices as sinews and muscles, which evolve from the local flow separation processes (Chap. 5). After introducing a general topological theory as a powerful qualitative tool in analyzing separated flow, we discuss steady and unsteady separated flows. The former has two basic types: *separated bubble flow* and *free vortex-layer separated flow*, each of which can be described by an asymptotic theory as the viscosity approaches zero. In contrast, unsteady separated flow is much more complicated and no general theory is available. We thus confine ourselves to the most common situation, the unsteady separated flow behind

[5] For many authors, any time evolution of a system is considered falling into the category of dynamics.

[6] The methods themselves are beyond the scope of the book.

a bluff body, and focus on its phenomena and some qualitative physical interpretations.

To describe different stages of the entire life of a vortex, various approximate theories have been developed to capture the dominant dynamic mechanisms. These are discussed in Chap. 8, including vortex-core dynamics, three-dimensional vortex filaments, two-dimensional point-vortex systems, and vortex patches, etc. The chapter also discusses typical interactions of a vortex with a solid wall and a free surface.

The vorticity plays a crucial role as flow becomes unstable, and rich patterns of vortex motion appear during the transition to turbulent flow and in fully developed turbulence. The relevant complicated mechanisms are discussed in Part III as a more advanced part of vorticity and vortex dynamics. Chapter 9 presents selected hydrodynamic stability theories for vortex layers and vortices. In addition to interpreting the basic concepts and classic results of shear-flow instability in terms of vorticity dynamics, some later developments of vortical-flow stability will be addressed. The chapter also introduces recent progresses in the study of vortex breakdown, which is a highly nonlinear process and has been a long-standing difficult issue.

Chapter 10 discusses the vortical structures in transitional and turbulent flows, starting with the concept of coherent structure and a discussion on coexistence of vortices and waves in turbulence fields. The main contents focus on the physical and qualitative understanding of the formation, evolution, and decay of coherent structures using mixing layer and boundary layer as examples, which are then extended to vortical structures in other shear flows. The understanding of coherent structure dynamics is guided by the examination of two opposite physical processes, i.e., the instability, coherence production, self-organization or negative entropy generation (the first process) and the coherent-random transfer, cascade, dissipation or entropy generation (the second process). The energy flow chart along the two processes and its impact on the philosophy of turbulent flow control is briefly discussed. Based on the earlier knowledge, typical applications of vorticity equations in studying coherent structures are shown. The relation between the vortical structures and the statistical description of turbulence field are also discussed, which may lead to some expectation on the future studies.

The topics of Part IV, including Chaps. 11 and 12, are somewhat more special. As an application of vorticity and vortex dynamics to external-flow aerodynamics, Chap. 11 presents systematically two types of theories, the *projection theory* and *derivative-moment theory*, both having the ability to reveal the local shearing process and flow structures that are responsible for the total force and moment but absent in conventional force–moment formulas. The classic aerodynamics theory will be rederived with new insight. This subject is of great interest for understanding the physical sources of the force and moment, for their diagnosis, configuration design, and effective flow control.

Chapter 12 is an introduction to vorticity and vortical structures in geophysical flow, which expands the application of vorticity and vortex dynamics

to large geophysical scales. The most important concept in the determination of large-scale atmospheric and oceanic vortical motion is the *potential vorticity*. The dynamics of vorticity also gains some new characters due to the Earth's rotation and density stratification.

Throughout the book, we put the physical understanding at the first place. Whenever possible, we shall keep the generality of the theory; but it is often necessary to be confined to as simple flow models as possible, provided the models are not oversimplified to distort the subject. Particularly, incompressible flow will be our major model for studying shearing process, due to its relative simplicity, maturity, and purity as a test bed of the theory. Obviously, to enter the full coupling of shearing and compressing processes, at least a weakly compressible flow is necessary.

The reader is assumed to be familiar with general fluid dynamics or aerodynamics at least at undergraduate level but better graduate level of major in mechanics, aerospace, and mechanical engineering. To make the book self-contained, a detailed appendix is included on vectors, tensors, and their various operations used in this book.

# Part I

# Vorticity Dynamics

# 2

# Fundamental Processes in Fluid Motion

## 2.1 Basic Kinematics

For later reference, in this section we summarize the basic principles of fluid *kinematics*, which deals with the fluid deformation and motion in its most general continuum form, without any concern of the causes of these deformation and motion. We shall be freely using tensor notations and operations, of which a detailed introduction is given in Appendix.

### 2.1.1 Descriptions and Visualizations of Fluid Motion

As is well known, the fluid motion in space and time can be described in two ways. The first description follows every fluid particle, exactly the same as in the particle mechanics. Assume a fluid body $\mathcal{V}$ moves arbitrarily in the space, where a fixed Cartesian coordinate system is introduced. Let a fluid particle in $\mathcal{V}$ locate at $\boldsymbol{X} = (X_1, X_2, X_3)$ at an initial time $\tau = 0$, then $\boldsymbol{X}$ is the *label* of this particle at any time.[1] This implies that

$$\frac{\partial \boldsymbol{X}}{\partial \tau} = \boldsymbol{0}. \tag{2.1}$$

Assume at a later time $\tau$ the fluid particle moves smoothly to $\boldsymbol{x} = (x_1, x_2, x_3)$. Then all $\boldsymbol{x}$ in $\mathcal{V}$ can be considered as differentiable functions of $\boldsymbol{X}$ and $\tau$:

$$\boldsymbol{x} = \boldsymbol{\phi}(\boldsymbol{X}, \tau), \tag{2.2}$$

where $\boldsymbol{\phi}(\boldsymbol{X}, 0) = \boldsymbol{X}$. For fixed $\boldsymbol{X}$ and varying $\tau$, (2.2) gives the path of the particle labeled $\boldsymbol{X}$; while for fixed $\tau$ and varying $\boldsymbol{X}$, it determines the spatial region $\mathcal{V}(\tau)$ of the whole fluid body at that moment. This description is called *material description* or *Lagrangian description*, and $(\boldsymbol{X}, \tau)$ are material or Lagrangian variables.

[1] More generally, the label of a fluid particle can be any set of three numbers which are one-to-one mappings of the particle's initial coordinates.

Equation (2.2) is a continuous mapping of the physical space onto itself with parameter $\tau$. But functionally the spaces spanned by $\boldsymbol{X}$ and $\boldsymbol{x}$ are different. We call the former *reference space* or simply the $\boldsymbol{X}$-space. In this space, differenting (2.2) with respect to $\boldsymbol{X}$, gives a tensor of rank 2 called the *deformation gradient tensor*:

$$\mathbf{F} = \nabla_X \boldsymbol{x} \quad \text{or} \quad F_{\alpha i} = x_{i,\alpha}, \tag{2.3}$$

which describes the displacement of all particles initially neighboring to the particle $\boldsymbol{X}$. Hereafter we use Greek letters for the indices of the tensor components in the reference space, and Latin letters for those in the physical space. The gradient with respect to $\boldsymbol{X}$ is denoted by $\nabla_X$, while the gradient with no suffix is with respect to $\boldsymbol{x}$. $(\cdot)_{,\alpha}$ is a simplified notation of $\partial(\cdot)/\partial X_\alpha$.

The deformation gradient tensor $\mathbf{F}$ defines an infinitesimal transformation from the reference space to physical space. Indeed, assume that at $\tau = 0$ a fluid element occupies a cubic volume $\mathrm{d}V$, and at some $\tau$ it moves to the neighborhood of $\boldsymbol{x}$, occupying a volume $\mathrm{d}v$. Then according to the theory of multivariable functions and the algebra of mixing product of vectors, we see that

$$\mathrm{d}v = J\mathrm{d}V, \tag{2.4}$$

where the Jacobian

$$J \equiv \frac{\partial(x_1, x_2, x_3)}{\partial(X_1, X_2, X_3)} = \det \mathbf{F} \tag{2.5}$$

represents the expansion or compression of an infinitesimal volume element during the motion. Moreover, keeping the labels of particles, any variation of $J$ can only be caused by that of $\boldsymbol{x}$. By using (2.4), an infinitesimal change of $J$ is given by (for an explicit proof see Appendix, A.4.1)

$$\delta J = J\nabla \cdot \delta \boldsymbol{x}. \tag{2.6}$$

Initially separated particles cannot merge to a single point at later time, even though they may be tightly squeezed together; meanwhile, a single particle initially having one label cannot be split into several different ones. Thus we can always trace back to the particle's initial position from its position $\boldsymbol{x}$ at any $\tau > 0$. This means the mapping (2.2) is one-to-one and has inverse

$$\boldsymbol{X} = \boldsymbol{\Phi}(\boldsymbol{x}, t). \tag{2.7}$$

Here $t = \tau$ is the same time variable but used along with $\boldsymbol{x}$. Functions $\boldsymbol{\Phi}$ and $\boldsymbol{\phi}$ are assumed to have derivatives of sufficiently many orders. Since (2.2) is invertible, $J$ must be regular, i.e.,

$$0 < J < \infty. \tag{2.8}$$

In the Lagrangian description $\boldsymbol{X}$ and $\tau$ are both independent variables, so the particle's velocity and acceleration are

$$\boldsymbol{u} = \frac{\partial \boldsymbol{x}}{\partial \tau}, \quad \boldsymbol{a} = \frac{\partial^2 \boldsymbol{x}}{\partial \tau^2} = \frac{\partial \boldsymbol{u}}{\partial \tau},$$

respectively. Therefore, the study of fluid motion in this description amounts to solving a dynamic system of infinitely many degrees of freedom. Unlike solids which can only have relatively small deformation gradient, a fluid cannot stand shearing and hence $\mathbf{F}$ may have very complicated behavior. Thus, the Largangian approach is generally inconvenient. However, it finds some important applications in both theoretical and computational vorticity dynamics. Special topics of Lagrangian description useful in some later chapters are given in Appendix A.4.

Instead of following the motion of each particle, we may concentrate on the spatial distribution of physical quantities and their temporal variation at every point $\boldsymbol{x}$. This leads to the *field description* or *Eulerian description*. By (2.2) and (2.7), any field quantity $F(\boldsymbol{x}, t)$ can be expressed as

$$F(\boldsymbol{x}, t) = F(\boldsymbol{\phi}(\boldsymbol{X}, \tau), \tau),$$

which is also a function of $(\boldsymbol{X}, \tau)$, and vice versa. Now there is

$$\frac{\partial F}{\partial \tau} = \frac{\partial F}{\partial t} + \frac{\partial x_i}{\partial \tau} \frac{\partial F}{\partial x_i},$$

thus

$$\frac{\partial}{\partial \tau} = \frac{\partial}{\partial t} + \boldsymbol{u} \cdot \nabla \equiv \frac{\mathrm{D}}{\mathrm{D}t} \tag{2.9}$$

is the operator of *material derivative* (i.e., the rate of change following the same particles) in the field description. Here $\partial/\partial t$ implies the local rate of change at fixed $\boldsymbol{x}$, while $\boldsymbol{u} \cdot \nabla$ is the rate of change due to advection. Clearly, $\partial/\partial \tau$ for fixed $\boldsymbol{X}$ and $\partial/\partial t$ for fixed $\boldsymbol{x}$ are different operations. Thus, (2.1) and $\boldsymbol{a} = \partial \boldsymbol{u}/\partial \tau$ in the Eulerian description become, respectively,

$$\frac{\mathrm{D}\boldsymbol{X}}{\mathrm{D}t} = \boldsymbol{0}, \tag{2.10}$$

$$\boldsymbol{a} = \frac{\mathrm{D}\boldsymbol{u}}{\mathrm{D}t} = \frac{\partial \boldsymbol{u}}{\partial t} + \boldsymbol{u} \cdot \nabla \boldsymbol{u}. \tag{2.11}$$

Moreover, from (2.6) and (2.9) follows the classic *Euler formula* for the rate of change of $J$:

$$\frac{\mathrm{D}J}{\mathrm{D}t} = J \nabla \cdot \boldsymbol{u}. \tag{2.12}$$

As a field theory, Eulerian description does not care which fluid particle occupies a position $\boldsymbol{x}$ at time $t$. As long as two flow fields have the same velocity distribution in space and time, they will be considered kinematically identical, no matter if their individual particles experience the same motion. In other words, fluid particles are allowed to be *relabeled* during the motion

in the Eulerian description. This is the case in most applications. Hence, the information in the Eulerian description is less than that in the Lagrangian description.

Some developments of fluid mechanics, however, are based on taking (2.11) as a nonlinear system and thus require tracing individual particles. This requirement happens in the study of, e.g., chaos and mixing, as well in variational approaches of vortical flows. In these situations one has to keep the particle labels $\boldsymbol{X}$ unchanged. This is simply done by adding to the Eulerian description condition (2.10), known as *Lin's constraint* (cf. Serrin 1959). Then the two descriptions become fully equivalent (for more discussion see Sect. 3.6).

It is appropriate here to distinct three different types of curves in a flow field, defined based on the earlier two descriptions. First, as noted earlier, a *pathline* is the curve created by the motion of a particle $\boldsymbol{X}$ as time goes on, described by (2.2), where $\boldsymbol{X}$ is fixed and $0 < \tau < \infty$. Equation (2.2) is the solution curve of the ordinary differential equation

$$\frac{\mathrm{d}x_i}{\mathrm{d}t} = u_i(\boldsymbol{x}, t) \tag{2.13}$$

under the initial condition $\boldsymbol{x}(0) = \boldsymbol{X}$.

Next, a curve tangent to the velocity $\boldsymbol{u}(\boldsymbol{x}, t)$ everywhere at a time $t$ is a *streamline* at this time. Its equation follows from eliminating $\mathrm{d}t$ in (2.13):

$$\frac{\mathrm{d}x_1}{u_1(\boldsymbol{x}, t)} = \frac{\mathrm{d}x_2}{u_2(\boldsymbol{x}, t)} = \frac{\mathrm{d}x_3}{u_3(\boldsymbol{x}, t)}, \tag{2.14}$$

of which the solution curve $f_1(\boldsymbol{x}, t) = 0, \quad f_2(\boldsymbol{x}, t) = 0$ passing a given $\boldsymbol{x}$ at a given $t$ is the required streamline.

Then, consider all the fluid particles which have passed a point $\boldsymbol{x}_0$ at any $t < t_0$ and continue to move ahead. The set of their spatial positions at $t_0$ constitute a curve passing $\boldsymbol{x}_0$, called a *streakline* passing $(\boldsymbol{x}_0, t_0)$. By (2.7), the labels of these particles are $\boldsymbol{\Phi}(\boldsymbol{x}_0, t), \quad -\infty < t \le t_0$, where $t$ becomes a parameter for identifying different particles. The positions of these particles at $t_0$ follow from (2.2):

$$\boldsymbol{x}(\boldsymbol{x}_0, t_0, t) = \boldsymbol{\phi}(\boldsymbol{\Phi}(\boldsymbol{x}_0, t), t_0), \quad -\infty < t \le t_0. \tag{2.15}$$

It is easily seen that at a given $t_0$, the streamline passing $\boldsymbol{x}_0$, the pathline of a particle locating at $\boldsymbol{x}_0$ and the streakline passing $\boldsymbol{x}_0$ have a common tangent vector at $\boldsymbol{x}_0$. When the flow is steady, i.e., in (2.13) $\boldsymbol{u}$ is independent of $t$, the three curves coincide. But even in this case the streamlines may not necessarily be well-ordered; in Sect. 3.2.3 we shall see a famous counter-example. For more general unsteady flows, then, the three curves are entirely different. The behavior of streamlines and pathlines vary drastically as the observer changes from a fixed frame of reference to a moving one, but the streaklines will remain the same (Taneda 1985). Figure. 2.1 sketches the unsteady streamlines and streaklines due to the instability traveling waves in a flat-plate boundary

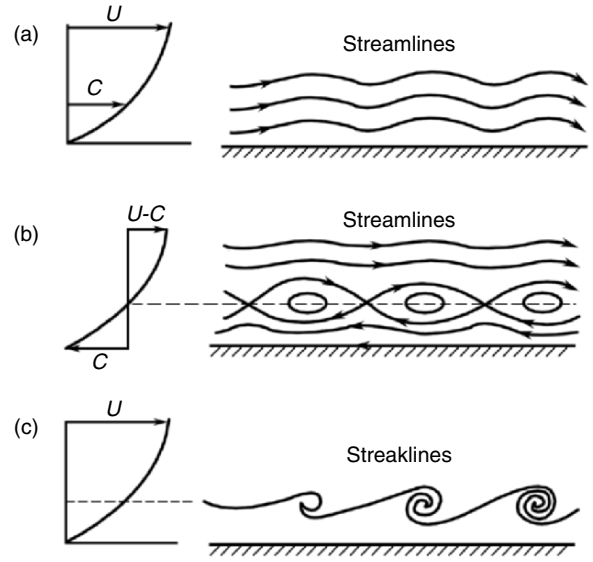


**Fig. 2.1.** Schematic streamlines (viewed in different frames) and streaklines in a boundary layer with traveling instability waves. $C$ is the wave speed. Reproduced from Taneda (1985)

layer, viewed from different frames of reference. Note that the streamlines in the frame moving with the wave exhibit some vortex-like structure (so-called "cat-eyes"), but whether or not these cat-eyes can be classified as vortices should be judged by the concentration of vorticity rather than merely by the frame-dependent streamlines. A discussion on vortex definition will be made in Sect. 6.6.

Flow visualization is a powerful and intuitive means in understanding various vortical flows (see Van Dyke 1982), of which the foundation is a clear distinction of the earlier three types of curves. If one introduces a tracer particle into the fluid and photographs its motion with a long time exposure, he/she obtains a pathline. If one spreads the tracer particles and takes photo with very short time exposure, then he/she sees a set of short line segments, of which a smooth connection can represent a family of instant streamlines. If one introduces some dyed fluid continuously at a fixed point $\boldsymbol{x}_0$ and takes a fast photograph at a later time $t_0$, then he/she obtains the streakline consisting of all particles passing $\boldsymbol{x}_0$ at any $t \leq t_0$.

A pathline or a streakline can intersect itself, but a streamline cannot. Most visualization experiments with vortical flows give at least streaklines. But their interpretation needs great care, since vortical flows are inherently more or less unsteady. Ignoring the difference of these three types of lines in an unsteady flow may lead to serious misunderstanding. Figure. 2.2 shows both streamlines and streaklines due to the unsteady vortex shedding from a

**Fig. 2.2.** Streamlines and streaklines in unsteady vortex shedding from a circular cylinder. From Taneda (1985)

circular cylinder, where their difference is obvious. However, while streaklines can tell where the vorticity resides in a flow, it tells very little about the surrounding fluid and the entrainment process. In this regard instantaneous streamlines in an unsteady flow are still useful; and it can be shown that over a very short time interval streaklines, pathlines, and instantaneous streamlines are identical (Perry et al. 1982).

Finally, if one inserts a straight metal wire across a moving fluid (say, water) and introduces pulsating current with fixed frequency $\omega$ through it, then the wire will electrolyze the water and release hydrogen bubbles periodically, which are advected by local flow velocity. Hence the pulsating appearance of bubbles will form a velocity profile along the wire (Fig. 2.3). These pulsating lines are called *time-lines*. Referring to Fig. 2.3 and assume the metal line is located along the $y$-axis. Then at time $t$, the time line released from all points $\boldsymbol{x}_0 = (0, y)$ at initial time $t_0 < t$ is given by

$$\boldsymbol{x}(\boldsymbol{x}_0, t_0, t; \omega) = \boldsymbol{\phi}(\boldsymbol{\Phi}(0, y, t_0), t; \omega) \quad \text{for all} \quad y, t > t_0. \tag{2.16}$$

### 2.1.2 Deformation Kinematics. Vorticity and Dilatation

The central issue of fluid kinematics concerns the deformation rate of a material fluid line, surface, and volume element. We first consider the rate of change of a material line element $\mathrm{d}\boldsymbol{x}$. By using (2.2), since $\boldsymbol{X}$ is fixed, there is

$$\frac{\mathrm{D}}{\mathrm{D}t}(\mathrm{d}x_i) = \frac{\mathrm{D}}{\mathrm{D}t}(x_{i,\alpha}\,\mathrm{d}X_\alpha) = u_{i,\alpha}\,\mathrm{d}X_\alpha = u_{i,\alpha}X_{\alpha,j}\,\mathrm{d}x_j = u_{i,j}\,\mathrm{d}x_j,$$

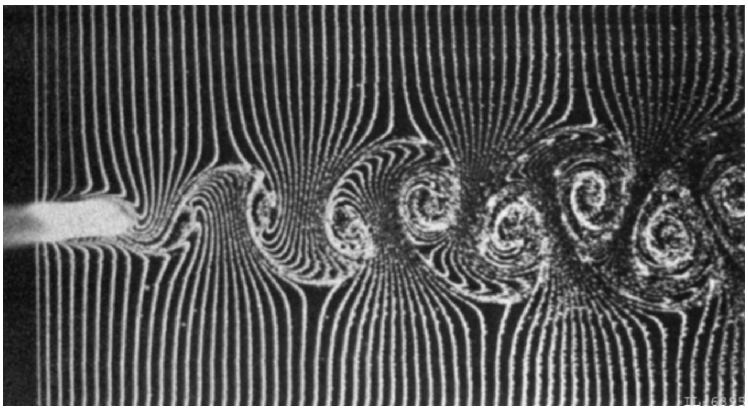

**Fig. 2.3.** Time lines behind a circular cylinder at Reynolds number 152. From Taneda (1985)

thus

$$\frac{\mathrm{D}}{\mathrm{D}t}(\mathrm{d}\boldsymbol{x}) = \mathrm{d}\boldsymbol{x} \cdot \nabla \boldsymbol{u} = \mathrm{d}\boldsymbol{u}. \tag{2.17}$$

Therefore, the rate of change of a material line element results in the velocity difference $\mathrm{d}\boldsymbol{u}$ at the two ends of the element. This rate of change includes both magnitude and direction, which should be analyzed separately. But the more fundamental quantity in (2.17) is the velocity gradient $\nabla \boldsymbol{u}$, the *deformation-rate tensor* (not to be confused with the deformation gradient tensor $\mathbf{F}$ defined by (2.3)), which is independent of the choice of specific line element. The intrinsic decomposition of $\nabla \boldsymbol{u}$ into symmetric and antisymmetric parts gives

$$\nabla \boldsymbol{u} = \mathbf{D} + \boldsymbol{\Omega}, \tag{2.18}$$

where $\mathbf{D}$ and $\boldsymbol{\Omega}$ are the *strain-rate tensor* and *vorticity tensor* (or spin tensor), defined by

$$\mathbf{D} = \frac{1}{2}[\nabla \boldsymbol{u} + (\nabla \boldsymbol{u})^{\mathrm{T}}], \quad \text{with} \quad D_{ii} = \vartheta, \tag{2.19a}$$

$$\boldsymbol{\Omega} = \frac{1}{2}[\nabla \boldsymbol{u} - (\nabla \boldsymbol{u})^{\mathrm{T}}], \quad \text{with} \quad \epsilon_{ijk}\Omega_{jk} = \omega_i, \tag{2.19b}$$

respectively, with the superscript T denoting transpose. Here,

$$\vartheta = \nabla \cdot \boldsymbol{u}, \quad \boldsymbol{\omega} = \nabla \times \boldsymbol{u} \tag{2.20}$$

are the *dilatation* and *vorticity*, respectively, which are the central concepts of this book and serve as the *kinematic representations* of the compressing and shearing processes.[2]

[2] In a shearing process the vorticity usually coexists with the rate of strain, see the example of simple shear flow discussed later and a general triple decomposition

By (A.12), (2.17) gives

$$\frac{\mathrm{D}}{\mathrm{D}t}(\mathrm{d}\boldsymbol{x}) = \mathrm{d}\boldsymbol{x}\cdot\mathbf{D} + \frac{1}{2}\boldsymbol{\omega}\times\mathrm{d}\boldsymbol{x}. \tag{2.21}$$

Thus, the point $\boldsymbol{x}+\mathrm{d}\boldsymbol{x}$ rotates around $\boldsymbol{x}$ with angular velocity $\boldsymbol{\omega}/2$, which changes the direction of $\mathrm{d}\boldsymbol{x}$. This is a primary interpretation of the meaning of vorticity. However, the concept of angular velocity is taken from the rotation of a rigid vector, and how to extend it to a fluid element still needs to be clarified. We return to this issue in Sect. 3.1.

Then, the inner product of $\mathrm{d}\boldsymbol{x}$ and (2.21) yields the rate of change of the length of the line element:

$$\frac{\mathrm{D}}{\mathrm{D}t}(\mathrm{d}s^2) = 2\frac{\mathrm{D}}{\mathrm{D}t}(\mathrm{d}\boldsymbol{x})\cdot\mathrm{d}\boldsymbol{x} = 2\,\mathrm{d}\boldsymbol{x}\cdot\mathbf{D}\cdot\mathrm{d}\boldsymbol{x}. \tag{2.22}$$

Therefore, $\mathbf{D}$ measures the change of the magnitude but not that of the direction of $\mathrm{d}\boldsymbol{x}$. For rigid bodies $\mathrm{d}s^2$ is invariant, so $\mathbf{D}$ is identically zero. If $\mathbf{D}$ is isotropic, i.e., $\mathbf{D}=\vartheta\mathbf{I}$ with $\mathbf{I}$ being the unit tensor, then the right-hand side of (2.22) is $2\vartheta\,\mathrm{d}s^2$ which implies an isotropic expansion or contraction. This is a primary interpretation of dilatation. The nonisotropic part of $\mathbf{D}$,

$$\mathbf{D}' = \mathbf{D} - \frac{1}{3}\vartheta\mathbf{I} \quad \text{with } \mathrm{tr}\ \mathbf{D}' = 0, \tag{2.23}$$

is called the *deviator* of $\mathbf{D}$.

Now, let $\boldsymbol{t}$ be a given unit vector, onto which the projection of $\mathbf{D}$ is a vector $A_i = D_{ij}t_j$. Then $\boldsymbol{t}$ and $\boldsymbol{A}$ will be parallel if $A_i = \lambda t_i$, or

$$(D_{ij} - \lambda\delta_{ij})t_j = 0,$$

which has no trivial solution since $|\boldsymbol{t}| = 1$ and thus implies a third-order equation for eigenvalues:

$$\lambda^3 - \mathrm{I}\lambda^2 + \mathrm{II}\lambda - \mathrm{III} = 0,$$

where I,II,III are three basic invariants of $\mathbf{D}$. Since $\mathbf{D}$ is symmetric, the eigenvalues $(\lambda_1, \lambda_2, \lambda_3)$ are all real, associated with three orthogonal principal directions $(\boldsymbol{p}_1, \boldsymbol{p}_2, \boldsymbol{p}_3)$. Thus we can introduce a local Cartesian system at

---

of the strain-rate tensor (Sect. 2.4). But the most essential property of shearing is fluid particle spinning, thus one cannot take the rate of strain that also exists in an irrotational flow to characterize the shearing process. On the other hand, in some very special equilibrium state of the evolution of a shearing process, the spin may disappear while the vorticity is still nonzero, such as a solid-like rotation (e.g., near the axis of a nonstretched vortex or in a circular cylindric container rotating about its axis), or the vorticity vanishes but spin still exists (e.g., outside a point vortex). These exception happen because in a curved flow the vorticity contains not only spinning but also trajectory rotation of fluid particles (Sect. 3.1).

each $(\boldsymbol{x}, t)$, called the *principal-axis system*, with its axes along the principal directions. By their derivation, the principal axes are not bending during infinitesimal deformation, but only subjected to stretching or shrinking. They are instantaneously rigid.

Moreover, consider a small spherical fluid element centered at $\boldsymbol{x}$ with specified $\mathbf{D}$. By (2.22), we may define a quadratic form of $\boldsymbol{r} = \boldsymbol{x}' - \boldsymbol{x}$ with $|\boldsymbol{r}| \ll 1$:

$$2\varphi \equiv \boldsymbol{r} \cdot \mathbf{D} \cdot \boldsymbol{r} = \text{const.},$$

which represents a family of quadratic surfaces, the *deformation ellipsoids*. The gradient of the above equation is

$$\nabla\varphi = \boldsymbol{r} \cdot \mathbf{D}.$$

Thus, the strain-rate tensor "induces" a potential velocity field in the neighborhood of the point under consideration, with direction normal to the deformation ellipsoid.

In summary, the velocity at $\boldsymbol{x}' = \boldsymbol{x} + \boldsymbol{r}$ is

$$\boldsymbol{u}(\boldsymbol{x}') = \boldsymbol{u}(\boldsymbol{x}) + \nabla\varphi + \frac{1}{2}\boldsymbol{\omega} \times \boldsymbol{r}. \tag{2.24}$$

This result is known as the **fundamental theorem of deformation kinematics**: *The instantaneous state of the fluid motion at every point is the superposition of a uniform translation, an irrotational stretching or shrinking along three orthogonal principal axes, and a rigid rotation around an axis.* Figure. 2.4 illustrates this theorem schematically.

A typical example illustrating the earlier theorem is the simple unidirectional shear flow $\boldsymbol{u} = (kx_2, 0, 0)$ with constant shearing rate $k$. Its vorticity

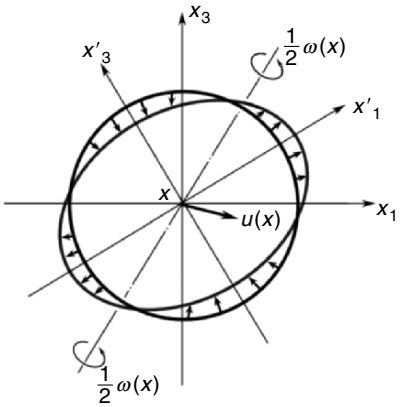


**Fig. 2.4.** The deformation of small fluid sphere. Only the pattern on the $(x_1, x_3)$ plane is shown

and strain rate are $\boldsymbol{\omega} = (0, 0, -k)$ and

$$D_{ij} = \begin{pmatrix} 0 & k/2 & 0 \\ k/2 & 0 & 0 \\ 0 & 0 & 0 \end{pmatrix},$$

respectively, both being characterized by $k$. Moreover, it follows from this $D_{ij}$ that the direction of principal axes of $\mathbf{D}$ is the $(x_1, x_2)$ axes rotating counter-clockwise by $\pi/4$, and in this principal system $D_{ij}$ has only two nonzero components (the principal values) $\pm\, k/2$. In this example $\vartheta = 0$, thus $\mathbf{D}$ is a pure deformation. A small sphere of radius $\epsilon$ will deform to an ellipsoid during a time interval $\mathrm{d}t$, with the length of its semiaxes being $\epsilon(1 + k\,\mathrm{d}t/2), \epsilon,$ and $\epsilon(1 - k\,\mathrm{d}t/2)$. However, the rotation around the $x_2$ axis has a tendency of turning the principal axes back to their original directions in order to maintain the shear flow pattern. For instance, after a $\mathrm{d}t$ time the actual angle between the first principal axis and the $x_1$ axis is $\pi/4 - k\,\mathrm{d}t/2$ (Lighthill 1986b).

### 2.1.3 The Rate of Change of Material Integrals

The rate of change of a material volume element $\mathrm{d}v$ directly follows from (2.4) and the Euler formula (2.12):

$$\frac{\mathrm{D}}{\mathrm{D}t}(\mathrm{d}v) = \vartheta\,\mathrm{d}v, \tag{2.25}$$

where $\vartheta = \nabla \cdot \boldsymbol{u}$ is again the dilatation.

The rate of change of a directional material surface element $\mathrm{d}\boldsymbol{S} = \boldsymbol{n}\,\mathrm{d}S$, where $\boldsymbol{n}$ is its unit normal vector, can be derived from that of line and volume elements. Take a line element $\mathrm{d}\boldsymbol{x}$ not tangent to the surface element, such that $\mathrm{d}\boldsymbol{x} \cdot \mathrm{d}\boldsymbol{S}$ constitutes a volume element $\mathrm{d}v$. Then

$$\frac{\mathrm{D}}{\mathrm{D}t}(\mathrm{d}v) = \frac{\mathrm{D}}{\mathrm{D}t}(\mathrm{d}\boldsymbol{x}) \cdot \mathrm{d}\boldsymbol{S} + \mathrm{d}\boldsymbol{x} \cdot \frac{\mathrm{D}}{\mathrm{D}t}(\mathrm{d}\boldsymbol{S}),$$

thus by (2.17) and (2.25),

$$\vartheta\,\mathrm{d}\boldsymbol{x} \cdot \mathrm{d}\boldsymbol{S} = \mathrm{d}\boldsymbol{x} \cdot \nabla\boldsymbol{u} \cdot \mathrm{d}\boldsymbol{S} + \mathrm{d}\boldsymbol{x} \cdot \frac{\mathrm{D}}{\mathrm{D}t}(\mathrm{d}\boldsymbol{S}).$$

Since $\mathrm{d}\boldsymbol{x}$ was chosen arbitrarily, there must be

$$\frac{\mathrm{D}}{\mathrm{D}t}(\mathrm{d}\boldsymbol{S}) = \mathrm{d}\boldsymbol{S} \cdot \mathbf{B} \quad \text{or} \quad \frac{1}{\mathrm{d}S}\frac{\mathrm{D}}{\mathrm{D}t}(\mathrm{d}\boldsymbol{S}) = \boldsymbol{n} \cdot \mathbf{B}, \tag{2.26}$$

where, denoting the unit tensor by $\mathbf{I}$,

$$\mathbf{B} \equiv \vartheta\mathbf{I} - (\nabla\boldsymbol{u})^{\mathrm{T}} \tag{2.27}$$

is the *surface deformation-rate tensor*. The vector $\boldsymbol{n}\cdot\mathbf{B}$ represents the strain-rate of a surface element of unit area. From a vector identity

$$(\boldsymbol{a}\times\nabla)\times\boldsymbol{b}=\boldsymbol{a}\cdot\{(\nabla\boldsymbol{b})^{\mathrm{T}}-(\nabla\cdot\boldsymbol{b})\mathbf{I}\},\tag{2.28}$$

it follows that

$$\frac{1}{\mathrm{d}S}\frac{\mathrm{D}}{\mathrm{D}t}(\mathrm{d}\boldsymbol{S})=\boldsymbol{n}\cdot\mathbf{B}=-(\boldsymbol{n}\times\nabla)\times\boldsymbol{u}.\tag{2.29}$$

Since $(\boldsymbol{n}\times\nabla)$ is a tangent derivative operator, we see that the surface deformation is determined by the velocity distribution on the surface only, independent of any flow field away from it. In other words, like the surface tension, this is a *surface process* rather than a volumetric process.

The knowledge of the rate of change of $\mathrm{d}\boldsymbol{x}$, $\mathrm{d}v$, and $\mathrm{d}\boldsymbol{S}$ enables us to obtain the rate of change of integrations of any physical quantity $\mathcal{F}$ (which can be a tensor of arbitrary rank) over a finite material line, surface or volume. This is the basis of deriving fundamental fluid dynamic equations. Since a material line, surface or volume consists of the same set of particles, the operator $\mathrm{d}/\mathrm{d}t$ in front of a material integral should be $\partial/\partial\tau$ and can directly enter the integrals to become $\mathrm{D}/\mathrm{D}t$ therein.

First, denote any meaningful tensor product by $\circ$, for a material curve $\mathcal{C}$ there is

$$\frac{\mathrm{d}}{\mathrm{d}t}\int_{\mathcal{C}}\mathrm{d}\boldsymbol{x}\circ\mathcal{F}=\int_{\mathcal{C}}\left\{\frac{\mathrm{D}}{\mathrm{D}t}(\mathrm{d}\boldsymbol{x})\circ\mathcal{F}+\mathrm{d}\boldsymbol{x}\circ\frac{\mathrm{D}\mathcal{F}}{\mathrm{D}t}\right\},$$

thus by (2.17),

$$\frac{\mathrm{d}}{\mathrm{d}t}\int_{\mathcal{C}}\mathrm{d}\boldsymbol{x}\circ\mathcal{F}=\int_{\mathcal{C}}\left(\mathrm{d}\boldsymbol{x}\circ\frac{\mathrm{D}\mathcal{F}}{\mathrm{D}t}+\mathrm{d}\boldsymbol{x}\cdot\nabla\boldsymbol{u}\circ\mathcal{F}\right).\tag{2.30}$$

The most important example of line integral is the *circulation* defined by

$$\Gamma_{\mathcal{C}}=\oint_{\mathcal{C}}\boldsymbol{u}\cdot\mathrm{d}\boldsymbol{x}=\int_{\mathcal{S}}\boldsymbol{\omega}\cdot\boldsymbol{n}\,\mathrm{d}S,\tag{2.31}$$

where $\mathcal{S}$ is any surface with $\mathcal{C}$ as its boundary and $\boldsymbol{\omega}$ the vorticity. Denote $q=|\boldsymbol{u}|$, since $\mathrm{d}\boldsymbol{u}\cdot\boldsymbol{u}=\mathrm{d}(q^2/2)$, (2.30) gives

$$\frac{\mathrm{d}}{\mathrm{d}t}\int_{\mathcal{C}}\boldsymbol{u}\cdot\mathrm{d}\boldsymbol{x}=\int_{\mathcal{C}}\boldsymbol{a}\cdot\mathrm{d}\boldsymbol{x}+\frac{q^2}{2}\bigg|_1^2$$

over an open material curve, where $\boldsymbol{a}=\mathrm{D}\boldsymbol{u}/\mathrm{D}t$ is acceleration and 1,2 indicate the end points of the curve. Thus, we immediately obtain the *Kelvin circulation formula*

$$\frac{\mathrm{d}\Gamma_{\mathcal{C}}}{\mathrm{d}t}=\frac{\mathrm{d}}{\mathrm{d}t}\int_{\mathcal{S}}\boldsymbol{\omega}\cdot\boldsymbol{n}\,\mathrm{d}S=\oint_{\mathcal{C}}\boldsymbol{a}\cdot\mathrm{d}\boldsymbol{x}\tag{2.32}$$

for any closed *material* curve $\mathcal{C}$.

Similarly, for any material surface $\mathcal{S}$, by (2.26) we have

$$\frac{\mathrm{d}}{\mathrm{d}t}\int_{\mathcal{S}} \mathrm{d}\boldsymbol{S}\circ\mathcal{F}=\int_{\mathcal{S}}\left[\mathrm{d}\boldsymbol{S}\circ\frac{\mathrm{D}\mathcal{F}}{\mathrm{D}t}+(\mathrm{d}\boldsymbol{S}\cdot\mathbf{B})\circ\mathcal{F}\right]. \tag{2.33}$$

As a trivial example, let $S$ be a closed surface and set $\mathcal{F}=1$. Then by using the generalized Gauss theorem (A.15) there is

$$\int_{\mathcal{S}}\boldsymbol{n}\cdot\mathbf{B}\,\mathrm{d}S=\mathbf{0}, \tag{2.34a}$$

which also implies

$$\nabla\cdot\mathbf{B}=\mathbf{0}, \tag{2.34b}$$

as can be directly verified by (2.27).

Finally, for any material volume $\mathcal{V}$, by (2.25) there is

$$\frac{\mathrm{d}}{\mathrm{d}t}\int_{\mathcal{V}}\mathcal{F}\mathrm{d}v=\int_{\mathcal{V}}\left(\frac{\mathrm{D}\mathcal{F}}{\mathrm{D}t}+\vartheta\mathcal{F}\right)\mathrm{d}v. \tag{2.35a}$$

$$=\int_{V}\frac{\partial\mathcal{F}}{\partial t}\mathrm{d}V+\int_{\partial V}\mathcal{F}\boldsymbol{u}\cdot\boldsymbol{n}\,\mathrm{d}S, \tag{2.35b}$$

where $V$ is a fixed *control volume* coinciding with $\mathcal{V}$ instantaneously. It is clear that the second terms in (2.30), (2.33), and (2.35a) are the contribution of the motion and deformation of $\mathcal{C}$, $\mathcal{S}$ and $\mathcal{V}$, respectively.

Note that (2.35b) is a special case of the more general **Reynolds transport theorem**:

$$\frac{\mathrm{d}}{\mathrm{d}t}\int_{V(t)}\mathcal{F}\mathrm{d}V=\int_{V(t)}\frac{\partial\mathcal{F}}{\partial t}\mathrm{d}V+\int_{\partial V(t)}\mathcal{F}\boldsymbol{v}\cdot\boldsymbol{n}\,\mathrm{d}S \tag{2.36}$$

for any time-dependent control volume $V(t)$ with velocity $\boldsymbol{v}$ at $\partial V(t)$, which could be, e.g., a body-fitted grid with time-dependent shape and boundary. We may continue $\boldsymbol{v}(\boldsymbol{x},t)$ smoothly into the interior of $V(t)$, so that

$$\int_{\partial V(t)}\mathcal{F}\boldsymbol{v}\cdot\boldsymbol{n}\,\mathrm{d}S=\int_{V(t)}\nabla\cdot(\boldsymbol{v}\mathcal{F})\mathrm{d}V=\int_{V(t)}\nabla\cdot[\boldsymbol{u}\mathcal{F}-(\boldsymbol{u}-\boldsymbol{v})\mathcal{F}]\mathrm{d}V,$$

where $\boldsymbol{u}$ is the fluid velocity. Thus (2.36) can be cast to

$$\frac{\mathrm{d}}{\mathrm{d}t}\int_{V(t)}\mathcal{F}\,\mathrm{d}V=\int_{V(t)}\left(\frac{\mathrm{D}\mathcal{F}}{\mathrm{D}t}+\vartheta\mathcal{F}\right)\mathrm{d}V-\int_{\partial V(t)}(u_n-v_n)\mathcal{F}\,\mathrm{d}S. \tag{2.37}$$

If $V(t)$ is a material volume $\mathcal{F}$ with $\boldsymbol{v}=\boldsymbol{u}$, then we return to (2.35a).

## 2.2 Fundamental Equations of Newtonian Fluid Motion

Fluid *kinetics* involves constitutive structures relating internal forces and deformation of a fluid. This book considers Newtonian fluid only, characterized by the linearity of its constitutive equation. The balances of mass,[3] momentum, and energy, which govern the global and local rate of change of flow quantities, follow from the combination of kinematics, kinetics, and general physical laws, which establish the fundamental equations of fluid *dynamics*. In this section we first list the main dynamic and thermodynamic theorems with necessary remarks. The integrated theorems are all referred to a material volume $\mathcal{V}$, which are used to derive corresponding differential equations.

### 2.2.1 Mass Conservation

Without any internal source or sink, the fluid mass is conserved:

$$\frac{\mathrm{d}}{\mathrm{d}t}\int_{\mathcal{V}} \rho \,\mathrm{d}v = 0, \tag{2.38}$$

where $\rho$ is the density. From (2.38) and (2.35) follows the *continuity equation*:

$$\frac{\mathrm{D}\rho}{\mathrm{D}t} + \rho\vartheta = 0, \quad \vartheta = \nabla\cdot\boldsymbol{u}, \tag{2.39a}$$

or

$$\frac{\partial\rho}{\partial t} + \nabla\cdot(\rho\boldsymbol{u}) = 0. \tag{2.39b}$$

By (2.12) and (2.39a) we can express the dilatation in terms of the Jacobian or density:

$$\vartheta = \frac{1}{J}\frac{\mathrm{D}J}{\mathrm{D}t} = -\frac{1}{\rho}\frac{\mathrm{D}\rho}{\mathrm{D}t}, \quad \text{so} \quad \rho J = \rho_0. \tag{2.40}$$

For any tensor $\mathcal{F}$, upon substituting (2.40) into (2.35a) and setting $\mathcal{F} = \rho\widehat{\mathcal{F}}$ ($\widehat{\mathcal{F}}$ is defined for per unit mass), we obtain a convenient general formula

$$\frac{\mathrm{d}}{\mathrm{d}t}\int_{\mathcal{V}} \rho\widehat{\mathcal{F}}\,\mathrm{d}v = \int_{\mathcal{V}} \rho\frac{\mathrm{D}\widehat{\mathcal{F}}}{\mathrm{D}t}\mathrm{d}v, \tag{2.41}$$

which is used below in deriving all dynamic equations from integral to differential form.

[3] The mass conservation is independent of constitutive structure and sometimes treated as a kinematical condition, especially for incompressible flow.

### 2.2.2 Balance of Momentum and Angular Momentum

Let $\boldsymbol{f}$ be the body force of unit mass and $\boldsymbol{t}(\boldsymbol{x}, \boldsymbol{n})$ be the surface force per unit area, where $\boldsymbol{n}$ is the unit normal vector. The surface force is caused by internal interaction. Then the *momentum balance* reads

$$\frac{\mathrm{d}}{\mathrm{d}t}\int_{\mathcal{V}} \rho \boldsymbol{u}\,\mathrm{d}v = \int_{\mathcal{V}} \rho \boldsymbol{f}\,\mathrm{d}v + \int_{\partial\mathcal{V}} \boldsymbol{t}\,\mathrm{d}S. \tag{2.42}$$

From (2.42) we have the following results. First, let $l$ be the length scale of $\mathcal{V}$ so that $\mathcal{V} \sim l^3$ and $\partial\mathcal{V} \sim l^2$. Dividing both sides of (2.42) by $l^2$ and let $l \to 0$, since volume integrals yields terms of $O(l)$, we obtain

$$\lim_{l\to 0}\left(\frac{1}{l^2}\int_{\partial\mathcal{V}} \boldsymbol{t}(\boldsymbol{x}, \boldsymbol{n})\mathrm{d}S\right) = \boldsymbol{0},$$

indicating that *the surface force is locally self-balanced*. This is a theorem due to Cauchy.

Second, observe that $\boldsymbol{t}\,\mathrm{d}S$ is a vector proportional to $\mathrm{d}S$, while a surface element is always directional with a normal $\boldsymbol{n}$, i.e., $\mathrm{d}\boldsymbol{S} = \boldsymbol{n}\,\mathrm{d}S$ is also a vector. The two vectors $\boldsymbol{t}$ and $\boldsymbol{n}$ must then be linearly related, or the $j$th component of $\boldsymbol{t}$ must be a linear form of the $i$th component of $\boldsymbol{n}$: $t_j = T_{ij}n_i$, where $T_{ij}$ are the coefficients independent of $\boldsymbol{n}$. Now, to ensure this vector equality the coefficients $T_{ij}$ have to be the components of a tensor $\mathbf{T}$ of rank 2, called the *stress tensor*. Namely, we have

$$\boldsymbol{t}(\boldsymbol{x}, \boldsymbol{n}) = \boldsymbol{n} \cdot \mathbf{T}(\boldsymbol{x}). \tag{2.43}$$

The existence of the stress tensor is known as the *Cauchy stress theorem*. The classic proof of the theorem (e.g., Lamb 1932; Serrin 1959; Batchelor 1967) appeals to the application of the earlier local self-balance of the surface force to the boundary of a small cubic or tetrahedral fluid element; but here it directly follows from the vector property of $\boldsymbol{t}$, $\boldsymbol{n}$, and their linear relation.

Having obtained (2.43), from (2.42) and the Gauss theorem we obtain the *Cauchy motion equation*

$$\rho\frac{\mathrm{D}\boldsymbol{u}}{\mathrm{D}t} = \rho\boldsymbol{f} + \nabla \cdot \mathbf{T}. \tag{2.44}$$

For Newtonian fluid, $\mathbf{T}$ is related to the pressure $p$, the strain rate $\mathbf{D}$, and its trace $\vartheta$ *linearly*, given by the *Cauchy–Poisson constitutive equation*

$$\mathbf{T} = (-p + \lambda\vartheta)\mathbf{I} + 2\mu\mathbf{D}, \tag{2.45}$$

with $\mu$ and $\lambda$ being the first (shear) and second viscosity coefficients. Thus, by (2.43) the surface force reads

$$\boldsymbol{t}(\boldsymbol{x}, \boldsymbol{n}) = (-p + \lambda\vartheta)\boldsymbol{n} + 2\mu\boldsymbol{n} \cdot \mathbf{D}. \tag{2.46}$$

Substituting (2.46) into (2.42) or (2.45) into (2.44), we obtain the *Navier–Stokes equation*

$$\rho\frac{\mathrm{D}\boldsymbol{u}}{\mathrm{D}t} = \rho\boldsymbol{f} - \nabla(p - \lambda\vartheta) + \nabla\cdot(2\mu\mathbf{D}). \tag{2.47}$$

**Remarks:**

1. Only a part of the stress tensor $\mathbf{T}$,

$$\mathbf{V} \equiv \mathbf{T} + p\mathbf{I} = \lambda\vartheta\mathbf{I} + 2\mu\mathbf{D} \tag{2.48}$$

   is related to fluid deformation rate through viscosities. The constitutive equation (2.45) can be expressed in terms of $\mathbf{V}$ and the deviator of $\mathbf{D}$, see (2.23):

$$\mathbf{V} = 2\mu\mathbf{D}' + \zeta\vartheta\mathbf{I}, \tag{2.49}$$

   where $\zeta = \lambda + 2\mu/3$ is the *bulk viscosity*.
2. The mean normal force with sign reversed is

$$\overline{p} \equiv -\frac{1}{3}T_{ii} = p - \zeta\vartheta, \tag{2.50}$$

   which differs from the pressure for compressible flow when $\zeta \neq 0$. Some authors assume $\zeta = 0$ so that $\overline{p} = p$ as first did by Stokes. In this case $\mathbf{V}$ is the deviator of $\mathbf{T}$. But generally $\zeta$ does not vanish and turns out to be frequency-dependent so that it exhibits dispersion (Landau and Lifshitz 1987).

Now, let $\boldsymbol{x}_0$ be a fixed point in space and $\boldsymbol{r} = \boldsymbol{x} - \boldsymbol{x}_0$. The vector product of $\boldsymbol{r}$ and the general Cauchy motion equation (2.44) yields

$$\rho\frac{\mathrm{D}}{\mathrm{D}t}(\boldsymbol{r}\times\boldsymbol{u}) = \rho\boldsymbol{r}\times\boldsymbol{f} + \boldsymbol{r}\times(\nabla\cdot\mathbf{T}),$$

where $\rho(\boldsymbol{r}\times\boldsymbol{u})$ is the *angular momentum* (or *moment of momentum*) per unit volume about the point $\boldsymbol{x}_0$. Since for a Newtonian fluid

$$\epsilon_{ijk}r_jT_{lk,l} = (\epsilon_{ijk}r_jT_{lk})_{,l} - \epsilon_{ijk}T_{jk} = (\epsilon_{ijk}r_jT_{lk})_{,l}$$

due to $T_{jk} = T_{kj}$ implied by (2.45), integrating the earlier moment equation gives the balance of *angular momentum* about the point $x_0$:

$$\frac{\mathrm{d}}{\mathrm{d}t}\int_{\mathcal{V}}\rho\boldsymbol{r}\times\boldsymbol{u}\,\mathrm{d}v = \int_{\mathcal{V}}\rho\boldsymbol{r}\times\boldsymbol{f}\,\mathrm{d}v + \int_{\partial\mathcal{V}}\boldsymbol{r}\times\boldsymbol{t}\,\mathrm{d}S. \tag{2.51}$$

If one assumes (2.51) as the basis of angular momentum balance, then reversing the earlier procedure will show that the stress tensor $\mathbf{T}$ must be symmetric. Therefore, for Newtonian fluid the angular momentum balance does not lead to an independent equation. Nevertheless, the concept of angular momentum is useful, and the rate of change of the fluid angular momentum is of direct relevance to the total moment acted to a body moving in the fluid; see Sect. 2.2.4.

### 2.2.3 Energy Balance, Dissipation, and Entropy

From the inner product of the momentum balance (2.44) with $\boldsymbol{u}$, one obtains the *balance of kinetic energy*:

$$\frac{\mathrm{d}}{\mathrm{d}t}\int_{\mathcal{V}}\frac{1}{2}\rho q^2\,\mathrm{d}v=\int_{\mathcal{V}}(\rho\boldsymbol{f}\cdot\boldsymbol{u}+p\vartheta-\Phi)\mathrm{d}v+\int_{\partial\mathcal{V}}\boldsymbol{t}\cdot\boldsymbol{u}\,\mathrm{d}S, \tag{2.52}$$

$$\rho\frac{\mathrm{D}}{\mathrm{D}t}\left(\frac{1}{2}q^2\right)=\rho\boldsymbol{f}\cdot\boldsymbol{u}+p\vartheta+\nabla\cdot(\mathbf{T}\cdot\boldsymbol{u})-\Phi, \tag{2.53}$$

where $q=|\boldsymbol{u}|$ and, by (2.45) and using double dots to denote twice contraction,

$$\Phi\equiv\mathbf{D}:\mathbf{V}=\lambda\vartheta^2+2\mu\mathbf{D}:\mathbf{D} \tag{2.54}$$

is the *dissipation rate* of the Newtonian fluid, the rate at which the mechanical work is transferred into heat.

**Remark**: For a volume element $\delta V$ the resultant rate of work done by $\boldsymbol{t}$ *per unit volume* must be

$$\lim_{\delta V\to 0}\left(\frac{1}{\delta V}\int_{\partial\delta V}\boldsymbol{t}\cdot\boldsymbol{u}\,\mathrm{d}S\right)=\nabla\cdot(\mathbf{T}\cdot\boldsymbol{u}) \tag{2.55}$$

due to the Gauss theorem, as appearing in (2.53). It would be incorrect to consider $\nabla\cdot\mathbf{T}$ as a body force and simply take $(\nabla\cdot\mathbf{T})\cdot\boldsymbol{u}$ as the corresponding rate of work. It is this difference between the body force $\rho\boldsymbol{f}$ and resultant surface force that leads to the dissipation $\Phi$ as well as the pressure work $p\vartheta$.

The appearance of $\Phi$ in the balance of kinetic energy implies the involvement of thermodynamics. Let $e$ be the specific *internal energy*, $T$ the temperature, and $\kappa$ the heat conductivity. Then by the *Fourier law*

$$\boldsymbol{q}=-\kappa\nabla T \tag{2.56}$$

is the heat flux through the boundary of a fluid body ($-\boldsymbol{q}\cdot\boldsymbol{n}=\kappa\partial T/\partial n$ is the heat entering the fluid per unit area per unit time). An application of the first law (energy conservation) and second law of thermodynamics[4] leads to, respectively, the *total energy equation*[5]

$$\frac{\mathrm{d}}{\mathrm{d}t}\int_{\mathcal{V}}\rho\left(e+\frac{1}{2}q^2\right)\mathrm{d}v=\int_{\mathcal{V}}\rho\boldsymbol{f}\cdot\boldsymbol{u}\,\mathrm{d}v+\int_{\partial\mathcal{V}}(\boldsymbol{t}\cdot\boldsymbol{u}-\boldsymbol{q}\cdot\boldsymbol{n})\mathrm{d}S \tag{2.57}$$

[4] The rigorous approach to the first law and second law of thermodynamics and their form in continuous mechanics is still a subject of research; see, e.g., Serrin (1986).

[5] We neglect the heating by radiation.

and *Clausius–Duham inequality*

$$\frac{\mathrm{d}}{\mathrm{d}t}\int_{\mathcal{V}}\rho s\,\mathrm{d}v \geq -\int_{\partial\mathcal{V}}\frac{\boldsymbol{q}\cdot\boldsymbol{n}}{T}\mathrm{d}S, \tag{2.58}$$

where $s$ is the specific *entropy* which relates to $e$ by

$$\mathrm{d}e = c_v\,\mathrm{d}T = T\,\mathrm{d}s - p\mathrm{d}\left(\frac{1}{\rho}\right), \tag{2.59}$$

where $c_\mathrm{v}$ is the *specific heat at constant volume*. Subtracting (2.52) from (2.57) yields the *internal energy equation*, of which the local form reads

$$\rho\frac{\mathrm{D}e}{\mathrm{D}t} = \mathbf{T}:\mathbf{D} - \nabla\cdot\boldsymbol{q}. \tag{2.60}$$

From this equation and using (2.59) and (2.54), an elegant equation follows:

$$\rho T\frac{\mathrm{D}s}{\mathrm{D}t} = \Phi - \nabla\cdot\boldsymbol{q}. \tag{2.61}$$

Dividing (2.61) by $T$ and integrating over a fluid body, we obtain

$$\frac{\mathrm{d}}{\mathrm{d}t}\int_{\mathcal{V}}\rho s\,\mathrm{d}v = \int_{\mathcal{V}}\left(\frac{\Phi}{T} - \frac{\boldsymbol{q}\cdot\nabla T}{T^2}\right)\mathrm{d}v - \int_{\partial\mathcal{V}}\frac{\boldsymbol{q}\cdot\boldsymbol{n}}{T}\mathrm{d}S. \tag{2.62}$$

Compare this with (2.58), we see that the second law of thermodynamics is ensured if

$$\Phi \geq 0, \quad \boldsymbol{q}\cdot\nabla T \leq 0,$$

which by (2.54) and (2.56) requires

$$\lambda + 2\mu \geq 0, \quad \mu \geq 0, \quad \kappa \geq 0.$$

It is often convenient to replace the internal energy by *enthalpy* $h$ and to replace the total energy by total enthalpy $H$, defined by

$$h = c_\mathrm{p}T = e + \frac{p}{\rho}, \quad H = h + \frac{1}{2}q^2, \tag{2.63}$$

respectively, where $c_\mathrm{p}$ the *specific heat at constant pressure*. From the first relation and (2.59) there is

$$\mathrm{d}h = T\,\mathrm{d}s + \frac{1}{\rho}\mathrm{d}p. \tag{2.64}$$

Thus, replacing $d$-operation by $\mathrm{D}/\mathrm{D}t$, from (2.61) and (2.54) it follows that

$$\rho\frac{\mathrm{D}h}{\mathrm{D}t} = \mathbf{D}:\mathbf{V} - \nabla\cdot\boldsymbol{q} + \frac{\partial p}{\partial t} + \boldsymbol{u}\cdot\nabla p.$$

But by (2.46), after neglecting the body force $\boldsymbol{f}$ there is

$$\boldsymbol{u}\cdot\nabla p=\nabla\cdot(\boldsymbol{u}\cdot\mathbf{V})-\mathbf{D}:\mathbf{V}-\rho\frac{\mathrm{D}}{\mathrm{D}t}\left(\frac{1}{2}q^2\right).$$

Therefore, we obtain the *total enthalpy equation*

$$\rho\frac{\mathrm{D}H}{\mathrm{D}t}=\frac{\partial p}{\partial t}+\nabla\cdot(\boldsymbol{u}\cdot\mathbf{V}-\boldsymbol{q}), \tag{2.65}$$

where the dissipation term is canceled.

### 2.2.4 Boundary Conditions. Fluid-Dynamic Force and Moment

Boundary conditions are necessary in solving the fluid dynamic equations for various specific problems. We denote a *material boundary* of a viscous flow by $\mathcal{B}$, which can be either a rigid or flexible wall, or an immiscible interface of two different fluids. When there is a need for distinguishing a solid wall and an interface, we set $\mathcal{B}=\partial B$ for the former and $\mathcal{B}=S$ for the latter. Let us agree that the unit normal vector $\boldsymbol{n}$ points *out of* the flow domain on $\partial B$ and from fluid 1 to fluid 2 on $S$.

A material boundary can be defined by an equation of surface

$$\mathcal{B}: F(\boldsymbol{x},t)=0. \tag{2.66a}$$

Since $\mathcal{B}$ remains to be a material surface during the fluid motion, it immediately follows that there must be

$$\frac{\mathrm{D}F}{\mathrm{D}t}=\frac{\partial F}{\partial t}+\boldsymbol{u}\cdot\nabla F=0\ \text{ on }\mathcal{B} \tag{2.66b}$$

as a *kinematic boundary condition*. For viscous flows some further conditions on $\mathcal{B}$ have to be satisfied, which can be stated in a unified way. Let $[\![\mathcal{F}]\!]$ denote the jump of any quantity $\mathcal{F}$ right across $\mathcal{B}$, so that on a solid boundary $[\![\boldsymbol{u}]\!]=\boldsymbol{u}-\boldsymbol{b}$, where $\boldsymbol{b}$ is the solid velocity, while on an interface between fluid 1 and fluid 2, say, $[\![\boldsymbol{u}]\!]=\boldsymbol{u}_1-\boldsymbol{u}_2$. Then, the boundary conditions should ensure the continuity of velocity and that of surface force with allowance of surface tension (Wehausen and Laitone (1960); Batchelor (1967)). The velocity continuity implies $[\![\boldsymbol{u}]\!]=\mathbf{0}$ on $\mathcal{B}$, or, in decomposed form, the *no-through condition* and *no-slip condition*:

$$\boldsymbol{n}\cdot[\![\boldsymbol{u}]\!]=0, \tag{2.67a}$$

$$\boldsymbol{n}\times[\![\boldsymbol{u}]\!]=\mathbf{0}. \tag{2.67b}$$

Similarly, let $T$ be the surface tension which vanishes on $\mathcal{B}$, then the surface-force continuity across $\mathcal{B}$ implies

$$\boldsymbol{n}\cdot[\![\boldsymbol{t}]\!]+T\kappa=0, \tag{2.68a}$$

$$\boldsymbol{n}\times[\![\boldsymbol{t}]\!]=\mathbf{0}, \tag{2.68b}$$

where $\kappa$ is the mean curvature of $\mathcal{B}$. Note that, with surface tension $T = 0$, (2.68) applies equally well to any material surface *inside* a viscous flow as well as on solid boundary $\partial B$. For the latter case it simply tells that the forces experienced by the solid wall equal that by the fluid but with opposite sign (Newton's third law).

For vorticity dynamics, in addition to the earlier primary boundary conditions we also need some derived boundary conditions, which are corollaries of (2.67). First, (2.67b) directly implies the *continuity of normal vorticity*:

$$\boldsymbol{n} \cdot [\![\boldsymbol{\omega}]\!] = (\boldsymbol{n} \times \nabla) \cdot [\![\boldsymbol{u}]\!] = 0 \quad \text{on } \mathcal{B}. \tag{2.69}$$

Thus, on a nonrotating $\mathcal{B}$ there must be $\boldsymbol{n}\cdot\boldsymbol{\omega} = 0$. In contrast, since the tangent vorticity involves normal gradient of the tangent velocity, it is generically *discontinuous* across $\mathcal{B}$. For example, assume a solid body in the fluid rotates with angular velocity $\boldsymbol{W}$ and consider a boundary point $\boldsymbol{x}$ on $\partial B$ with $\boldsymbol{n}\cdot\boldsymbol{W} \neq 0$. The fluid vorticity at $\boldsymbol{x}$ is decomposed to a normal vector $\boldsymbol{\omega}_{\rm n}$ and a tangent vector $\boldsymbol{\omega}_\pi$, see Fig. 2.5. Then $\boldsymbol{\omega}_{\rm n}$ must go through $\partial B$ to continuously connect to the normal component $2\boldsymbol{W}_{\rm n}$ of the body vorticity, but $\boldsymbol{\omega}_\pi \neq 2\boldsymbol{W}_\pi$. We may conveniently define a *relative vorticity* $\boldsymbol{\omega}_{\rm r} \equiv \boldsymbol{\omega} - 2\boldsymbol{W}$, which by (2.69) only has tangent components at $\mathcal{B}$ that have to stay in the fluid and go around the body. It is this discontinuity of $\boldsymbol{\omega}_\pi$ across $\mathcal{B}$ that is responsible for the skin friction (Sect. 2.4.2) and the very important mechanism of *tangent-vorticity creation at boundaries* to be addressed in Sect. 4.1.3.

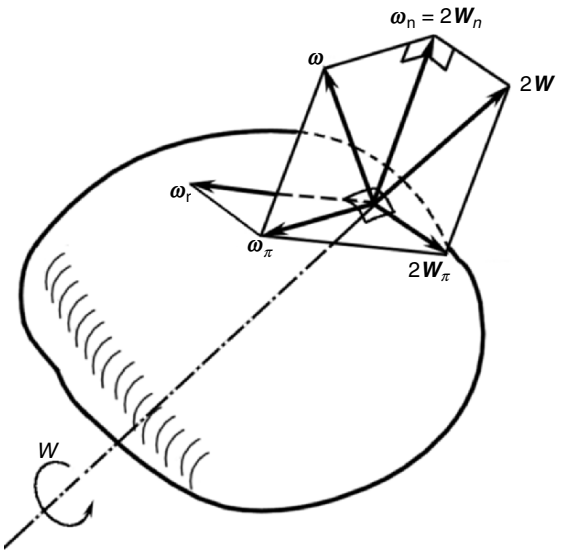


**Fig. 2.5.** The continuation of normal vorticity and discontinuation of tangent vorticity on a rotating body surface. The relative vorticity $\boldsymbol{\omega}_{\rm r} = \boldsymbol{\omega} - 2\boldsymbol{W}$ has only tangent components

Second, if at an initial time $t = 0$ a fluid particle sticks to a point of a solid wall, or a particle of fluid 1 sticks to a particle of fluid 2 at an interface, by (2.67) the stickiness will continue as time goes on. Thus, there must be the *continuity of acceleration*:

$$\boldsymbol{n} \cdot [\![\boldsymbol{a}]\!] = 0, \tag{2.70a}$$

$$\boldsymbol{n} \times [\![\boldsymbol{a}]\!] = \boldsymbol{0}. \tag{2.70b}$$

Conversely, (2.70) plus the initial velocity adherence ensures (2.67).

Having stated the boundary conditions for a viscous fluid, it is straightforward to obtain the total force and moment acting on boundary by the fluid. Consider a solid body $B$ moving in an otherwise unbounded fluid, so that $\partial\mathcal{V} = \partial B$ in these equations. Then, since the unit normal out of the body is $\widehat{\boldsymbol{u}} = -\boldsymbol{n}$, by (2.68) the forces acting on the body surface must be $-\boldsymbol{t} = \widehat{\boldsymbol{n}} \cdot \mathbf{T}$ on $\partial B$. Hence, along with (2.42) and (2.51), the total force $\boldsymbol{F}$ acted to the body and the total moment $\boldsymbol{M}$ about $\boldsymbol{x}_0 = \boldsymbol{0}$ are given by

$$\boldsymbol{F} = -\int_{\partial B} \boldsymbol{t}\, \mathrm{d}S = -\frac{\mathrm{d}}{\mathrm{d}t}\int_{\mathcal{V}} \rho\boldsymbol{u}\, \mathrm{d}v + \int_{\mathcal{V}} \rho\boldsymbol{f}\, \mathrm{d}v, \tag{2.71}$$

$$\boldsymbol{M} = -\int_{\partial B} \boldsymbol{x} \times \boldsymbol{t}\, \mathrm{d}S = -\frac{\mathrm{d}}{\mathrm{d}t}\int_{\mathcal{V}} \rho\boldsymbol{x} \times \boldsymbol{u}\, \mathrm{d}v + \int_{\mathcal{V}} \rho\boldsymbol{x} \times \boldsymbol{f}\, \mathrm{d}v. \tag{2.72}$$

The total force can also be expressed by using a *control volume* $V$ fixed in the space, bounded internally by the body surface $\partial B$ and externally by a *control surface* $\Sigma$. Then applying the Reynolds transfer theorem (2.36) to (2.42), and using the first equality of (2.71), we obtain

$$\boldsymbol{F} = \int_V \left(-\frac{\partial(\rho\boldsymbol{u})}{\partial t} + \rho\boldsymbol{f}\right) \mathrm{d}V + \int_\Sigma (\boldsymbol{t} - \rho\boldsymbol{u}\boldsymbol{u} \cdot \boldsymbol{n}) \mathrm{d}S. \tag{2.73}$$

For the total moment $\boldsymbol{M}$ a similar formula exists.

In particular, for steady flow without body force in $V$, the control-volume approach finds important application in studying an externally unbounded flow past a body with uniform upstream velocity $\boldsymbol{U}$. In this case the control surface $\Sigma$ can be chosen large enough such that the viscous stress thereon can be neglected. Then (2.73) is reduced to

$$\boldsymbol{F} = -\int_\Sigma (p\boldsymbol{n} + \rho\boldsymbol{u}\boldsymbol{u} \cdot \boldsymbol{n}) \mathrm{d}S. \tag{2.74}$$

Another formula for the *rate of work done by a rigid body* for maintaining its motion can be derived from the kinetic-energy balance (2.52). The general motion of a rigid body is given by

$$\boldsymbol{u}_{\mathrm{B}} = \boldsymbol{U}(t) + \boldsymbol{W}(t) \times \boldsymbol{x}, \tag{2.75}$$

where $\boldsymbol{W}$ is the angular velocity of the body and like (2.72) we locate the origin of $\boldsymbol{x}$ at the instantaneous rotating center. Assume the fluid is externally

unbounded and at rest at infinity. Then we have

$$\int_{\partial B} \boldsymbol{t} \cdot \boldsymbol{u}_{\mathrm{B}} \, \mathrm{d}S = -\boldsymbol{U} \cdot \boldsymbol{F}_{\mathrm{B}} - \boldsymbol{W} \cdot \boldsymbol{M}_{\mathrm{B}} = UD + WM,$$

where $D$ and $M$ are the drag and resistance torque, respectively. Hence, by (2.52) we simply have

$$UD + WM = \frac{\mathrm{d}}{\mathrm{d}t} \int_{\mathcal{V}} \frac{1}{2} \rho q^2 \, \mathrm{d}v + \int_{\mathcal{V}} \Phi \, \mathrm{d}v - \int_{\mathcal{V}} (\rho \boldsymbol{f} \cdot \boldsymbol{u} + p\vartheta) \mathrm{d}v. \tag{2.76}$$

Thus, the rate of work done by the moving body, including translation and rotation, is consumed to change the fluid kinetic energy, to overcome the rate of work done by the body force and pressure force to the fluid, and to cause the dissipation. More discussions on the total force and moment will be made in Chap. 11.

### 2.2.5 Effectively Inviscid Flow and Surface of Discontinuity

So far our fundamental equations and boundary conditions have been formulated for viscous fluids, since all fluids are viscous no matter how small the viscosity could be. Inspecting the Navier–Stokes equation (2.47), especially its natural Helmholtz-decomposition form (2.134) later, we see that the viscous effect always coexists with vorticity and dilatation (more precisely, their gradient or the second-order derivatives of velocity). This effect can compete the inertial force only if

$$\mu \|\nabla \boldsymbol{\omega}\| = O(1), \quad (\mu + 2\lambda)|\nabla \vartheta| = O(1).$$

As the shear viscosity $\mu$ decreases or the Reynolds number $Re = \rho UL/\mu$ increases, the strong viscous effect occurs only in some progressively thinner layers with very high peaks of $\|\nabla \boldsymbol{\omega}\| = O(Re^{-1})$, for example the strong shear layer (*boundary layer*) adjacent to a solid wall where the no-slip condition (2.67b) holds (Sect. 4.3 below) or in very thin but strong compressing layers in supersonic flow (*shock layer*). In the large remaining regions a mild vorticity or dilatation is insufficient to reach an $O(1)$ viscous effect, and hence the flow there can be treated as *effectively inviscid* (Batchelor 1967), with the Navier–Stokes equation degenerating to the *Euler equation*[6]

$$\rho \frac{\mathrm{D}\boldsymbol{u}}{\mathrm{D}t} = \rho \boldsymbol{f} - \nabla p. \tag{2.77}$$

We may further talk about the asymptotic state of the flow as $\mu \to 0$ or $Re \to \infty$, for which the region covered by (2.77) becomes almost the entire

[6] It should be noticed that even at an arbitrary Reynolds number there can still be viscous but irrotational flow. A typical example is the asymptotic steady state of the flow outside a rotating circular cylinder (e.g., Lagerstrom 1964).

flow domain except vanishingly thin shear layers and shock layers. Across these layers the flow velocity varies abruptly, associated with infinitely large peaks of $\boldsymbol{\omega}$ and/or $\vartheta$. Following Lagerstrom (1977), we call this asymptotic state the *Euler limit*, which should not be confused with the completely inviscid flow of an ideal fluid.

Having said these, in what follows we highlight some issues of inviscid-flow theory. First, because the *Prandtl number* $Pr = \mu c_\mathrm{p}/\kappa$ is of $O(1)$, the heat conductivity $\kappa$ in (2.56) should be neglected wherever so is $\mu$; hence when (2.77) applies the entropy equation (2.61) is reduced to the *isentropic condition*

$$\frac{\mathrm{D}s}{\mathrm{D}t} = 0, \tag{2.78}$$

while the total-enthalpy equation (2.65) is reduced to

$$\rho\frac{\mathrm{D}H}{\mathrm{D}t} = \frac{\partial p}{\partial t}, \tag{2.79}$$

indicating that if the flow is steady then the total enthalpy is *conservative*.

In the Euler limit, the mathematic models of infinitely thin shock layers and shear layers are *surfaces of normal and tangential discontinuity*, respectively, which are permitted by the Euler equation (2.77) and across which the differential form of the fundamental equations are no longer applicable. To describe surfaces of discontinuity in accordance with using (2.77) to (2.79), we need to extend the integral form of the fundamental theorems. Let $\boldsymbol{u}_\mathrm{d}$ be the velocity of a surface of discontinuity $S_\mathrm{dis}$, $V_\mathrm{n} = \boldsymbol{n}\cdot(\boldsymbol{u}-\boldsymbol{u}_\mathrm{d})$ be the normal velocity of the fluid relative to the moving $S_\mathrm{dis}$. Then using the preceding jump notation and generalized Reynolds transport equation (2.37), there is

$$\frac{\mathrm{d}}{\mathrm{d}t}\int_\mathcal{V}\mathcal{F}\,\mathrm{d}v = \int_\mathcal{V}\left(\frac{\mathrm{D}\mathcal{F}}{\mathrm{D}t}+\vartheta\mathcal{F}\right)\mathrm{d}V + \int_{S_\mathrm{dis}}[\![\mathcal{F}V_\mathrm{n}]\!]\mathrm{d}S. \tag{2.80}$$

Setting $\mathcal{F}$ as $\rho$, $\rho\boldsymbol{u}$, $\rho(e+q^2/2)$, and $\rho s$ in turn, we obtain the general *jump conditions* imposed by dynamics and thermodynamics:

$$[\![\rho V_\mathrm{n}]\!] = 0, \tag{2.81a}$$

$$[\![\rho V_\mathrm{n}\boldsymbol{u}+p\boldsymbol{n}]\!] = \boldsymbol{0}, \tag{2.81b}$$

$$[\![\rho V_\mathrm{n}(q^2/2+e)+p\boldsymbol{u}\cdot\boldsymbol{n}]\!] = 0, \tag{2.81c}$$

$$[\![\rho V_\mathrm{n}s]\!] \geq 0. \tag{2.81d}$$

When (2.81b) is applied to an interface or free surface, the surface tension should be added. In these relations there are jumps of some products, say $[\![fg]\!]$, which can be treated by using a pair of identities:

$$[\![fg]\!] = \overline{f}[\![g]\!] + [\![f]\!]\overline{g}, \tag{2.82a}$$

$$\overline{fg} = \overline{f}\,\overline{g} + \frac{1}{4}[\![f]\!][\![g]\!]. \tag{2.82b}$$

In (2.81a), $\rho_1 V_{\mathrm{n}1} = \rho_2 V_{\mathrm{n}2} = m$ is the *mass flux* across $S_{\mathrm{dis}}$. If $m = 0$ we call $S_{\mathrm{dis}}$ a *contact discontinuity*, across which some tangent components are discontinuous. If $m \neq 0$ we call $S_{\mathrm{dis}}$ a *shock*, across which some normal components are discontinuous. For each of these two kinds, (2.81) can be accordingly simplified. We exemplify this by the jump conditions across a stationary shock. Denote the tangent component of a vector by suffix $\pi$ and assume on both sides of the shock $V_{\mathrm{n}} > 0$. The tangent component of (2.81b) is $[\![\rho V_{\mathrm{n}} \boldsymbol{u}_\pi]\!] = 0$, which by (2.81a) implies $[\![\boldsymbol{u}_\pi]\!] = 0$. Thus, a shock can only have normal velocity discontinuity. Using this condition and (2.82), (2.81) is cast to the classic *Rankine–Hugoniot shock relations*

$$[\![\rho V_{\mathrm{n}}]\!] = [\![m]\!] = 0, \tag{2.83a}$$

$$[\![\rho V_{\mathrm{n}}^2 + p]\!] = 0, \quad [\![\boldsymbol{u}_\pi]\!] = \boldsymbol{0}, \tag{2.83b}$$

$$[\![H]\!] = 0, \quad H = \frac{1}{2} V_{\mathrm{n}}^2 + h, \tag{2.83c}$$

$$[\![s]\!] \geq 0. \tag{2.83d}$$

Note that *across a stationary shock the total enthalpy is preserved.*

The basic properties and dynamics of a surface of contact discontinuity are also derived from (2.81) with zero mass flux, as will be fully addressed in Sect. 4.4. But a few words is in order here. In an ideal fluid with $\mu \equiv 0$, on a surface of contact discontinuity the fluid particles of both sides just slide over each other as schematically shown in Fig. 2.6a. This happens especially on a boundary $\mathcal{B}$ since there one can only impose normal conditions (2.67a) and (2.68a). In contrast, in the Euler limit of viscous flow this surface is actually a thin vortex layer with singular vorticity distribution, across which the integral of $\boldsymbol{\omega}$ remains finite. Such a surface is known as a *vortex sheet* consisting of material fluid elements, which has extremely strong shearing as sketched in Fig. 2.6b. Vortex sheets and shocks are the idealized asymptotic states of shearing and compressing processes in a viscous flow, respectively.

It is known that in a flow domain with no-through boundary condition the Euler solution is not unique; for example, for a uniform oncoming flow over a circular cylinder the solution of (2.77) can either be fully attached or separate from the cylinder surface at any point (cf. Sect. 5.3.3). Of these possible Euler

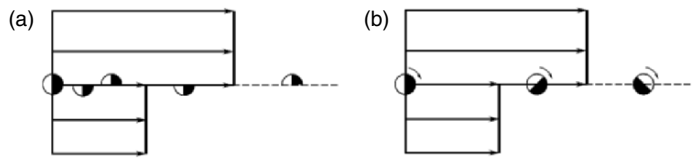


**Fig. 2.6.** (**a**) Tangent discontinuity in strictly inviscid flow. (**b**) Vortex sheet

solutions only one is qualified to be the Euler limit of the viscous solution,[7] which is referred to as the *relevant Euler solution* (Lagerstrom, 1977).

Once a relevant Euler solution is known, at least in principle one can reversely perturb either a shock or a vortex sheet to construct an approximate Navier–Stokes solution with $\mu \ll 1$. A perturbation to the Rankine–Hugoniot relations (2.83) means to replace a shock by a viscous *shock layer* of thickness $\delta \ll 1$, inside which the differential dynamic equations still apply. If the coordinate normal to the shock layer, say $x$, is rescaled by $x = \delta X$ so that $X = O(1)$, then it can be proved (Serrin 1959) that a smooth shock-layer can exist only if it matches (2.83) as $\delta \to 0$ and $X \to \pm\infty$. Conversely, with (2.83) as boundary conditions at $X \to \pm\infty$ the shock-layer solution can be obtained. An important observation is that the Reynolds number based on $\delta$ must be of $O(1)$, and hence the ratio of $\delta$ to the global length scale $L$ must be $O(Re^{-1})$. In air, if the Mach number ahead of the shock layer is 2.0, one finds $\delta \sim 2.5 \times 10^{-6}$ cm, the same order of molecular free path.

In contrast, a perturbation to a vortex sheet attached to a wall leads to the boundary layer theory to be discussed in Sect. 4.3, which shows that the layer's thickness is of $O(Re^{-1/2})$, much thicker than shock layers. Therefore, for compressing process one can well assume the flow is inviscid (unless the internal structure of shock layers is the concern), and the governing parameter is the Mach number; while for shearing process the viscosity is of fundamental importance, and the governing parameter is the Reynolds number.

## 2.3 Intrinsic Decompositions of Vector Fields

As defined in Chap. 1, the vorticity dynamics is the theory of shearing (transverse) process and its interaction with compressing (longitudinal) process. We thus need to examine how a fluid motion is split into these distinct processes and what their respective characters are. In the standard form of kinematic relations and dynamic equations as appeared in the preceding sections, however, only quite limited relevant clues can be found. A more systematic mathematic approach is necessary, which is the classic Helmholtz decomposition and its modern sharpenings to be introduced in this section. While the theory applies to any vector field, we use vector fields in fluid mechanics as illustration.

### 2.3.1 Functionally Orthogonal Decomposition

In the discussion of boundary conditions of a flow field, we have applied the familiar geometrically orthogonal decomposition of a vector to the component along a given direction, say $\boldsymbol{n}$, and the components perpendicular to it,

[7] Here we assume the solution of a well-posed Navier–Stokes problem exists and is unique, and do not consider chaos and turbulence.

e.g., (2.67) and (2.68). From these component vectors one recovers the original vector, say velocity $\boldsymbol{u}$, by the well-known identity:

$$\boldsymbol{u} = \boldsymbol{n}(\boldsymbol{n}\cdot\boldsymbol{u}) - \boldsymbol{n}\times(\boldsymbol{n}\times\boldsymbol{u}) \equiv \boldsymbol{u}_{\parallel} + \boldsymbol{u}_{\perp}, \tag{2.84}$$

where $\parallel$ and $\perp$ denote the component vectors parallel and perpendicular to $\boldsymbol{n}$, respectively. This decomposition is intrinsic with respect to the specified direction $\boldsymbol{n}$. More generally, if we have two vectors such as velocity $\boldsymbol{u}$ and vorticity $\boldsymbol{\omega}$, then the geometrically orthogonal decomposition of $\boldsymbol{\omega}$ with respect to $\boldsymbol{u}$, and that of $\boldsymbol{u}$ with respect to $\boldsymbol{\omega}$, are[8]

$$|\boldsymbol{u}|^2\boldsymbol{\omega} = \boldsymbol{u}(\boldsymbol{\omega}\cdot\boldsymbol{u}) - \boldsymbol{u}\times(\boldsymbol{u}\times\boldsymbol{\omega}), \tag{2.85a}$$

$$|\boldsymbol{\omega}|^2\boldsymbol{u} = \boldsymbol{\omega}(\boldsymbol{\omega}\cdot\boldsymbol{u}) - \boldsymbol{\omega}\times(\boldsymbol{\omega}\times\boldsymbol{u}). \tag{2.85b}$$

It is worth mentioning that in (2.85) there appears two quantities of crucial importance in vorticity dynamics: scalar $\boldsymbol{\omega}\cdot\boldsymbol{u}$, known as the *helicity density*, and vector $\boldsymbol{\omega}\times\boldsymbol{u}$, the *Lamb vector*. Their roles as well as the implication of (2.85a) will be fully discussed later.

Splitting a vector into parallel and perpendicular parts as in (2.85) is the prototype of a more advanced orthogonal decomposition of vectors, which can be conveniently observed by replacing $\boldsymbol{\omega}$ by $\nabla$ in (2.85b), yielding a differential identity

$$\begin{aligned}\nabla^2\boldsymbol{u} &= \nabla(\nabla\cdot\boldsymbol{u}) - \nabla\times(\nabla\times\boldsymbol{u})\\ &= \nabla\vartheta - \nabla\times\boldsymbol{\omega}.\end{aligned} \tag{2.86}$$

This is an example of the well-known *Helmholtz decomposition*, characterized by the fact that the first part is curl-free (irrotational) while the second part is divergence-free (solenoidal).

In fluid mechanics, the Helmholtz decomposition is most often used to decompose the velocity field:

$$\boldsymbol{u} = \nabla\phi + \nabla\times\boldsymbol{\psi}, \tag{2.87}$$

where $\phi$ and $\boldsymbol{\psi}$ are the *scalar* and *vector potentials* of velocity, respectively. Of the three independent components of $\boldsymbol{u}$, $\phi$ represents one of them, so we always choose $\boldsymbol{\psi}$ to have only two independent components by imposing a constraint or *gauge condition*

$$\nabla\cdot\boldsymbol{\psi} = 0, \tag{2.88}$$

which in (2.86) is automatically satisfied. Then, taking divergence and curl of (2.87) and using (2.88) yield

[8] The geometrically orthogonal decomposition (2.84) and (2.85) can be generalized to any tensor of higher rank.

$$\nabla^2\phi = \vartheta, \tag{2.89a}$$

$$\nabla^2\boldsymbol{\psi} = -\boldsymbol{\omega}, \tag{2.89b}$$

which can be solved for $\phi$ and $\boldsymbol{\psi}$ for given $\vartheta$ and $\boldsymbol{\omega}$, respectively, under proper boundary conditions to be discussed later. Thus, velocity potentials carry the same physical information as dilatation and vorticity. This along with (2.87) confirms our statement following (2.20) on the role of $\vartheta$ and $\boldsymbol{\omega}$.

Now, as a generalization of geometric orthogonality, the vector fields $\nabla\phi$ and $\nabla\times\boldsymbol{\psi}$ in (2.87) defined on a domain $V$ are said *functionally orthogonal* in the inner-product integral sense, if and only if they are square-integrable and

$$\int_V \nabla\phi\cdot(\nabla\times\boldsymbol{\psi})\mathrm{d}V = 0. \tag{2.90}$$

For simplicity assume $V$ is *simply-connected*. Condition (2.90) implies that the curl-free and solenoidal parts of (2.87) will behave quite independently, or are decoupled. When (2.90) holds, we use the same notation $\parallel$ and $\perp$ to denote

$$\boldsymbol{u}_\parallel = \nabla\phi, \quad \boldsymbol{u}_\perp = \nabla\times\boldsymbol{\psi}, \tag{2.91}$$

and specifically call $\boldsymbol{u}_\parallel$ and $\boldsymbol{u}_\perp$ the *longitudinal* and *transverse* parts, respectively.

If $V$ is an unbounded domain where the potentials decay sufficiently fast as approaching infinity (see Sect. 2.3.2 later), or a cubic box with periodic boundary condition, such that the Fourier analysis applies, then the Helmholtz decomposition (2.87) plus (2.88) is unique and the decomposed parts are functionally orthogonal. In this case, the decomposition is best expressed in the Fourier space spanned by wave vector $\boldsymbol{k} = (k_1, k_2, k_3)$:

$$F\{\boldsymbol{u}(\boldsymbol{x})\} = \widehat{\boldsymbol{u}}(\boldsymbol{k}) = \frac{1}{(2\pi)^3}\int \boldsymbol{u}(\boldsymbol{x})\mathrm{e}^{-\mathrm{i}\boldsymbol{k}\cdot\boldsymbol{x}}\mathrm{d}^3x, \quad \mathrm{d}^3x \equiv \mathrm{d}x_1\,\mathrm{d}x_2\,\mathrm{d}x_3, \tag{2.92}$$

where $F\{\cdot\}$ denotes the Fourier transform operator. It then follows that

$$F\{\nabla\cdot\boldsymbol{u}\} = \mathrm{i}\boldsymbol{k}\cdot\widehat{\boldsymbol{u}}, \tag{2.93a}$$

$$F\{\nabla\times\boldsymbol{u}\} = \mathrm{i}\boldsymbol{k}\times\widehat{\boldsymbol{u}}. \tag{2.93b}$$

Hence, the functional orthogonality in physical space degenerates to the geometric one in spectral space. Equation (2.93) clearly reveals that *a dilatation wave is a longitudinal wave*, *and a vorticity wave is a transverse wave*. Their oscillating directions are geometrically along and perpendicular to the direction of wave vector $\boldsymbol{k}$, respectively.[9]

[9] This explains the name of our two fundamental processes. We shall use these terms in a broader sense than that implied by (2.93). If in a bounded domain the Fourier expansion is not feasible, the simple geometric relations between wave oscillating directions and $\boldsymbol{k}$ no longer exists, while (2.91) still defines the longitudinal and transverse parts of a vector.

Moreover, the Fourier transform of (2.87) and (2.88) is

$$\widehat{\boldsymbol{u}} = \mathrm{i}(\boldsymbol{k}\widehat{\phi} + \boldsymbol{k} \times \widehat{\boldsymbol{\psi}}), \tag{2.94}$$

$$\mathrm{i}\boldsymbol{k} \cdot \widehat{\boldsymbol{\psi}} = 0, \tag{2.95}$$

which decomposes $\widehat{\boldsymbol{u}}$ into components along and normal to $\boldsymbol{k}$; while the Fourier transform of (2.86) is

$$k^2\widehat{\boldsymbol{u}} = \boldsymbol{k}(\boldsymbol{k} \cdot \widehat{\boldsymbol{u}}) - \boldsymbol{k} \times (\boldsymbol{k} \times \widehat{\boldsymbol{u}}), \tag{2.96}$$

the same form as (2.85). Thus, to obtain the transverse part of $\widehat{\boldsymbol{u}}$, one simply has

$$\widehat{u}_{\perp i} = P_{ij}\widehat{u}_j, \quad P_{ij} \equiv \delta_{ij} - \frac{k_i k_j}{k^2}, \tag{2.97}$$

where $P_{ij}$ is a projection operator.

In contrast to the earlier decomposition in the spectral space, in an arbitrary bounded domain $V$ the Helmholtz potentials in (2.87) are not unique, since $\boldsymbol{\psi} + \nabla\eta$ for an arbitrary scalar $\eta$ is also a vector potential due to $\nabla \times \nabla\eta = 0$. This arbitrariness cannot be completely removed by (2.88), which only implies $\nabla^2\eta = 0$. The uniqueness and orthogonality of $\nabla\phi$ and $\nabla \times \boldsymbol{\psi}$ in a bounded $V$ depend on their boundary conditions. By $\nabla \cdot \boldsymbol{u}_\perp = 0$ and the Gauss theorem, there is

$$\int_V \nabla\phi \cdot \boldsymbol{u}_\perp \,\mathrm{d}V = \int_V \nabla \cdot (\phi\boldsymbol{u}_\perp)\mathrm{d}V = \int_{\partial V} \phi\boldsymbol{n} \cdot \boldsymbol{u}_\perp \,\mathrm{d}S.$$

Therefore, the orthogonality condition (2.90) holds if

$$\boldsymbol{n} \cdot \boldsymbol{u}_\perp = 0 \quad \text{on} \quad \partial V, \tag{2.98a}$$

i.e., $\boldsymbol{u}_\perp$ is parallel to $\partial V$. This implies that the normal component of $\boldsymbol{u}$ on $\partial V$ comes entirely from $\boldsymbol{u}_\parallel$; hence a scalar equivalence of (2.98a) is

$$\frac{\partial\phi}{\partial n} = \boldsymbol{n} \cdot \boldsymbol{u} \quad \text{on} \quad \partial V. \tag{2.98b}$$

Condition (2.98) ensures not only the orthogonality but also the uniqueness and existence of the decomposition. Suppose $\boldsymbol{u}$ has two different splittings $\boldsymbol{u} = \nabla\phi_1 + \boldsymbol{u}_{\perp 1} = \nabla\phi_2 + \boldsymbol{u}_{\perp 2}$, both satisfying (2.98). Then

$$\boldsymbol{0} = \boldsymbol{u}_{\perp 1} - \boldsymbol{u}_{\perp 2} + \nabla(\phi_1 - \phi_2).$$

Taking the inner product with $\boldsymbol{u}_{\perp 1} - \boldsymbol{u}_{\perp 2}$ and integrating, we have

$$\begin{aligned} 0 &= \int_V \{|\boldsymbol{u}_{\perp 1} - \boldsymbol{u}_{\perp 2}|^2 + (\boldsymbol{u}_{\perp 1} - \boldsymbol{u}_{\perp 2}) \cdot \nabla(\phi_1 - \phi_2)\}\mathrm{d}V \\ &= \int_V |\boldsymbol{u}_{\perp 1} - \boldsymbol{u}_{\perp 2}|^2 \mathrm{d}V \end{aligned}$$

due to the Gauss theorem and (2.98a). Thus, there must be $\boldsymbol{u}_{\perp 1} = \boldsymbol{u}_{\perp 2}$ and hence $\nabla\phi_1 = \nabla\phi_2$. This guarantees the uniqueness of the decomposition and excludes any scalar potentials from $\boldsymbol{u}_\perp$. Moreover, (2.89a) and (2.98b) form a well-posed Neumann problem for $\phi$, of which the solution exists and is unique up to an additive constant. Hence so does $\boldsymbol{u}_\perp = \boldsymbol{u} - \nabla\phi$. Collecting the earlier results, we have (Chorin and Marsden 1992)

**Helmholtz–Hodge Decomposition Theorem.** *A vector field $\boldsymbol{u}$ on $V$ can be uniquely and orthogonally decomposed in the form $\boldsymbol{u} = \nabla\phi + \boldsymbol{u}_\perp$, where $\boldsymbol{u}_\perp$ has zero divergence and is parallel to $\partial V$.*

This result sharpens the Helmholtz decomposition (2.87) and is called *Helmholtz–Hodge decomposition*. It is one of the key mathematic tools in examining the physical nature of various fluid-dynamics processes.

Note that from scalar $\phi$ one can further separate a harmonic function $\psi$ with $\nabla^2\psi = 0$, such that $\nabla\psi$ is also orthogonal to both $\nabla(\phi - \psi)$ and $\boldsymbol{u}_\perp$. Thus, strictly, $\boldsymbol{u}$ has a triple orthogonal decomposition. The harmonic part belongs to neither compressing nor shearing processes, but is necessary for $\phi$ and $\boldsymbol{\psi}$ to satisfy the orthogonality boundary conditions and thereby influences both. For example, if a vorticity field $\boldsymbol{\omega}$ has zero normal component on boundary so that $\boldsymbol{\omega} = \boldsymbol{\omega}_\perp$, there can be $\nabla \times \boldsymbol{\omega} \neq (\nabla \times \boldsymbol{\omega})_\perp$ if the former is not tangent to the boundary. In this case we introduce a harmonic function $\chi$, say, and write

$$\nabla \times \boldsymbol{\omega} = (\nabla \times \boldsymbol{\omega})_\perp + \nabla\chi, \tag{2.99}$$

where

$$\nabla^2\chi = 0 \quad \text{in} \quad V, \tag{2.100a}$$

$$\frac{\partial\chi}{\partial n} = \boldsymbol{n} \cdot (\nabla \times \boldsymbol{\omega}) = (\boldsymbol{n} \times \nabla) \cdot \boldsymbol{\omega} \quad \text{on} \quad \partial V. \tag{2.100b}$$

The second equality of (2.100b) implies that $\chi$ is not trivial once $\boldsymbol{\omega}$ varies along $\partial V$, of which the significant consequence will be analyzed in Sect. 2.4.3.

### 2.3.2 Integral Expression of Decomposed Vector Fields

In the special case where the Fourier transform applies, we have obtained the explicit expressions of $\boldsymbol{u}_\parallel$ and $\boldsymbol{u}_\perp$ in terms of a given $\boldsymbol{u}$ as seen from (2.96). This local relation in the spectral space must be *nonlocal* in the physical space after the inverse transform is performed. Indeed, comparing (2.87) with identity (2.86), it is evident that if we set $\boldsymbol{u} = -\nabla^2\boldsymbol{F}$ then the Helmholtz potentials in (2.87) are simply given by $\phi = -\nabla\cdot\boldsymbol{F}$ and $\boldsymbol{\psi} = \nabla\times\boldsymbol{F}$. Computing these potentials for given $\boldsymbol{u}$ amounts to solving Poisson equations, and the result must be nonlocal.

Without repeatedly mentioning, in what follows use will be frequently made of the generalized Gauss theorem given in Appendix A.2.1. Let $G(\boldsymbol{x})$ be the fundamental solution of Poisson equation

$$\nabla^2 G(\boldsymbol{x}) = \delta(\boldsymbol{x}) \tag{2.101}$$

in free space, which in $n$-dimensional space, $n = 2, 3$, is known as

$$G(\boldsymbol{x}) = \begin{cases} \dfrac{1}{2\pi} \log |\boldsymbol{x}|, & \text{if } n = 2, \\ -\dfrac{1}{4\pi|\boldsymbol{x}|}, & \text{if } n = 3. \end{cases} \tag{2.102}$$

The gradient of $G$ will be often used:

$$\nabla G = \frac{\boldsymbol{x}}{2(n-1)\pi|\boldsymbol{x}|^n}. \tag{2.103}$$

Now assume $\boldsymbol{u}$ is given in a domain $V$ and $\boldsymbol{u} = \boldsymbol{0}$ outside $V$. We define a vector $\boldsymbol{F}$ by

$$\boldsymbol{F}(\boldsymbol{x}) = -\int_V G(\boldsymbol{x} - \boldsymbol{x}')\boldsymbol{u}(\boldsymbol{x}')\,\mathrm{d}V',$$

where $\mathrm{d}V' = \mathrm{d}V(\boldsymbol{x}')$. On both sides we consider the Laplacian, which does not act to functions of $\boldsymbol{x}'$ but to $G(\boldsymbol{x} - \boldsymbol{x}')$ only. By (2.101) we have

$$-\nabla^2 \boldsymbol{F} = \int_V \delta(\boldsymbol{x} - \boldsymbol{x}')\boldsymbol{u}(\boldsymbol{x}')\mathrm{d}V' = \begin{cases} \boldsymbol{u} \text{ if } \boldsymbol{x} \in V, \\ \boldsymbol{0} \text{ if } \boldsymbol{x} \notin V. \end{cases}$$

Thus, replacing $\boldsymbol{u}$ in identities (2.86) and (2.87) by $\boldsymbol{F}$, and denoting the gradient operator with respect to the integration variable $\boldsymbol{x}'$ by $\nabla'$ so that $\nabla G = -\nabla' G$ and $\nabla^2 G = \nabla'^2 G$, we obtain, when $\boldsymbol{x}$ is in $V$,

$$\begin{aligned} \phi = -\nabla \cdot \boldsymbol{F} &= -\int \nabla' G \cdot \boldsymbol{u}\,\mathrm{d}V' \\ &= \int_V G\vartheta\,\mathrm{d}V' - \int_{\partial V} G\boldsymbol{n} \cdot \boldsymbol{u}\,\mathrm{d}S', \qquad (2.104a) \\ \boldsymbol{\psi} = \nabla \times \boldsymbol{F} &= \int \nabla' G \times \boldsymbol{u}\,\mathrm{d}V' \\ &= -\int_V G\boldsymbol{\omega}\,\mathrm{d}V + \int_{\partial V} G\boldsymbol{n} \times \boldsymbol{u}\,\mathrm{d}S', \qquad (2.104b) \end{aligned}$$

where the second-line expressions were obtained by integration by parts. When $\boldsymbol{x}$ is outside $V$, these integrals vanish. Therefore, we have constructed a Helmholtz decomposition of $\boldsymbol{u}$:

$$\begin{aligned} \boldsymbol{u} &= \nabla\phi + \nabla \times \boldsymbol{\psi} \quad \text{for } \boldsymbol{x} \in V, \\ \boldsymbol{0} &= \nabla\phi + \nabla \times \boldsymbol{\psi} \quad \text{for } \boldsymbol{x} \notin V. \end{aligned}$$

For unbounded domain, the Helmholtz decomposition is still valid provided that the integrals in (2.104) converge. This is the case if $(\boldsymbol{\omega}, \vartheta)$ vanish outside

some finite region or decay sufficiently fast (Phillips 1933; Serrin 1959).[10] Therefore, (2.104) provides a constructive proof of the global existence of the Helmholtz decomposition for any differentiable vector field. Moreover, (2.104) indicates that the split vectors $\nabla\phi$ and $\nabla\times\boldsymbol{\psi}$ can be expressed in terms of dilatation and vorticity, respectively:

$$\nabla\phi = \int_V \vartheta\nabla G\,\mathrm{d}V' - \int_{\partial V}(\boldsymbol{n}\cdot\boldsymbol{u})\nabla G\,\mathrm{d}S', \tag{2.105a}$$

$$\nabla\times\boldsymbol{\psi} = \int_V \boldsymbol{\omega}\times\nabla G\,\mathrm{d}V' - \int_{\partial V}(\boldsymbol{n}\times\boldsymbol{u})\times\nabla G\,\mathrm{d}S'. \tag{2.105b}$$

This result is the *generalized Biot–Savart formulas* to be discussed in detail in Chap. 3. The formulas not only show the nonlocal nature of the decomposition but also, via (2.103), tells how fast the influence of $\boldsymbol{\omega}$ and $\vartheta$ at $\boldsymbol{x}'$ on the field point $\boldsymbol{x}$ decays as $|\boldsymbol{x}-\boldsymbol{x}'|$ increases.

It should be stressed that for bounded domain the earlier results only provide *one of all possible pairs* of Helmholtz decomposition of $\boldsymbol{u}$. It does not care any boundary condition for $\nabla\phi$ and $\nabla\times\boldsymbol{\psi}$. In order to obtain the unique Helmholtz–Hodge decomposition, the simplest way is to solve the scalar boundary-value problem (2.89a) and (2.98b). To see the structure of the solution, we use Green's identity

$$\int_V (G\nabla^2\phi - \phi\nabla^2 G)\mathrm{d}V = \int_{\partial V}\left(G\frac{\partial\phi}{\partial n} - \phi\frac{\partial G}{\partial n}\right)\mathrm{d}S$$

along with (2.98b) to obtain

$$\phi = \int_V G\vartheta\,\mathrm{d}V - \int_{\partial V}\left(G\boldsymbol{n}\cdot\boldsymbol{u} + \phi\frac{\partial G}{\partial n}\right)\mathrm{d}S. \tag{2.106}$$

Compared with (2.104a), we now have an additional surface integral with unknown boundary value of $\phi$. To remove this term we have to use a boundary-geometry dependent Green's function $\widehat{G}$ instead of $G$, which is the solution of the problem

$$\nabla^2\widehat{G}(\boldsymbol{x}) = \delta(\boldsymbol{x}), \quad \frac{\partial\widehat{G}}{\partial n} = 0 \ \text{ on } \ \partial V. \tag{2.107}$$

This gives a unique

$$\nabla\widehat{\phi} = \int_V \vartheta\nabla\widehat{G}\,\mathrm{d}V - \int_{\partial V}\boldsymbol{n}\cdot\boldsymbol{u}\nabla\widehat{G}\,\mathrm{d}S, \tag{2.108}$$

and hence $\boldsymbol{u}_\perp = \boldsymbol{u} - \nabla\widehat{\phi}$ is the unique transverse vector.

The Helmholtz–Hodge decomposition is also a powerful and rational tool for analyzing numerically obtained vector fields, provided that effective methods able to extend operators gradient, curl, and divergence from differential formulation to discrete data can be developed. For recent progress see, e.g., Tong et al. (2003).

[10] For the asymptotic behavior of velocity field in unbounded domain see Sect. 3.2.3.

### 2.3.3 Monge–Clebsch decomposition

So far we have been able to decompose a vector field into longitudinal and transverse parts. It is desirable to seek a further intrinsic decomposition of the transverse part into its two independent components. A classic approach is to represent the solenoidal part of a vector, say $\boldsymbol{v} \equiv \boldsymbol{u} - \nabla\phi = \nabla \times \boldsymbol{\psi}$, by two scalars explicitly, at least locally:

$$\boldsymbol{v} = \nabla\psi \times \nabla\chi. \tag{2.109}$$

The variables $\phi$, $\psi$, and $\chi$ are known as *Monge potentials* (Truesdell 1954) or *Clebsch variables* (Lamb 1932). For the proof of the *local existence* of $\psi$ and $\chi$, the reader is referred to Phillips (1933). Then, since $\nabla \times (\psi\nabla\chi) = \nabla\psi \times \nabla\chi$, for the Helmholtz vector potential of $\boldsymbol{u}$ we may set (Phillips 1933; Lagerstrom 1964)

$$\boldsymbol{\psi} = \psi\nabla\chi, \tag{2.110}$$

or more symmetrically (Keller 1996),

$$\boldsymbol{\psi} = \frac{1}{2}(\psi\nabla\chi - \chi\nabla\psi). \tag{2.111}$$

Both ways cast the Helmholtz decomposition (2.87) to a special form

$$\boldsymbol{u} = \nabla\phi + \nabla\psi \times \nabla\chi, \tag{2.112}$$

where the vector stream function $\boldsymbol{\psi}$ is replaced by two scalar stream functions $\psi$ and $\chi$. Accordingly, the vorticity is given by

$$\begin{aligned}\boldsymbol{\omega} &= \nabla \times (\nabla\psi \times \nabla\chi) \\ &= \nabla^2\chi\nabla\psi - \nabla^2\psi\nabla\chi + (\nabla\chi \cdot \nabla)\psi - (\nabla\psi \cdot \nabla)\chi.\end{aligned} \tag{2.113}$$

The Monge–Clebsch decomposition has proven useful in solving some vortical flow problems (Keller 1998, 1999), but it is not as powerful as the Helmholtz–Hodge decomposition since unlike the latter it may not exist globally. Thus, if one wishes $\psi$ and $\chi$ satisfy boundary condition (2.98a) or

$$\boldsymbol{n} \cdot (\nabla\psi \times \nabla\chi) = 0 \quad \text{on} \quad \partial V \tag{2.114}$$

and thereby produce a Helmholtz–Hodge decomposition, the problem may not be solvable. Also note that neither (2.110) nor (2.111) satisfies the gauge condition (2.88) although both contain only two independent variables.

Instead of the solenoidal part of $\boldsymbol{u}$, one can also represent the vorticity $\boldsymbol{\omega}$ in the form of (2.109). In this case we set

$$\boldsymbol{u} = \nabla\phi + \boldsymbol{v}, \quad \boldsymbol{v} = \lambda\nabla\mu, \tag{2.115}$$

so that $\boldsymbol{\omega} = \nabla\lambda \times \nabla\mu$ and $\nabla \times (\boldsymbol{u} - \lambda\nabla\mu) = \boldsymbol{0}$. This is the original form of the *Monge decomposition*, also called the *Clebsch transformation* (Lamb 1932; Serrin 1959). But in general $\lambda\nabla\mu$ is not a solenoidal vector and (2.115) does not represent any Helmholtz decomposition.

### 2.3.4 Helical–Wave Decomposition

An entirely different approach to intrinsically decompose a transverse vector and giving its two independent components clear physical meaning, free from the mathematical limitation of Clebsch variables, can be inspired by observing light waves. A light wave is a transverse wave and can be intrinsically split into right- and left-polarized (helical) waves.[11] Mathematically, making this splitting amounts to finding a complete set of intrinsic basis vectors, which are mutually orthogonal in the sense of (2.90), and by which any transverse vector can be orthogonally decomposed.

Recalling that the curl operator retains only the solenoidal part of a vector, and observe that the sign of its eigenvalues may determine the right- and left-polarity or handedness. We thus expect that the desired basis vectors should be found from the eigenvectors of the curl. Indeed, denote the curl-eigenvalues by $\lambda k$, where $\lambda = \pm 1$ marks the polarity and $k = |\boldsymbol{k}| > 0$ is the wave number with $\boldsymbol{k}$ the wave vector. Then there is

**Yoshida–Giga Theorem** (Yoshida and Giga 1990). *In a singly-connected domain $\mathcal{D}$, the solutions of the eigenvalue problem*

$$\begin{aligned} \nabla \times \boldsymbol{\phi}_\lambda(\boldsymbol{k},\boldsymbol{x}) &= \lambda k \boldsymbol{\phi}_\lambda(\boldsymbol{k},\boldsymbol{x}) \ \text{ in } \mathcal{D}, \\ \boldsymbol{n}\cdot\boldsymbol{\phi}_\lambda(\boldsymbol{k},\boldsymbol{x}) &= 0 \ \text{ on } \partial\mathcal{D}, \end{aligned} \qquad \lambda = \pm 1, \tag{2.116}$$

*exist and form a complete orthogonal set $\{\boldsymbol{\phi}_\lambda(\boldsymbol{k},\boldsymbol{x})\}$ to expand any transverse vector field $\boldsymbol{u}_\perp$ parallel to $\partial\mathcal{D}$.*[12]

These $\boldsymbol{\phi}_\lambda$s can only be found in complex vector space. Their orthogonality (normalized) is expressed by

$$\langle \boldsymbol{\phi}_\lambda(\boldsymbol{k},\boldsymbol{x}), \boldsymbol{\phi}^*_\mu(\boldsymbol{k}',\boldsymbol{x})\rangle = \delta_{\lambda\mu}\delta(\boldsymbol{k}-\boldsymbol{k}'), \quad \lambda,\mu = \pm 1, \tag{2.117a}$$

$$\sum_{\boldsymbol{k}} \phi_{\lambda i}(\boldsymbol{k},\boldsymbol{x})\phi_{\lambda j}(\boldsymbol{k},\boldsymbol{x}') = \delta_{ij}\delta(\boldsymbol{x}-\boldsymbol{x}'), \quad \lambda = \pm 1, \tag{2.117b}$$

where the asterisk means complex conjugate and repeated indices imply summation. Using this basis to decompose a transverse vector is called the *helical-wave decomposition* (HWD). For neatness we use $\langle\cdot,\cdot\rangle$ to denote the inner-product integral over the physical space, then the HWD of $\boldsymbol{F}_\perp$ reads

---

[11] A transverse vector, which can be constructed by vector product or curl operation, is an *axial vector* or *pseudovector*. It is always associated with an antisymmetric tensor (see Appendix A.1) and changes sign under a mirror reflection. And, like polarized light, an axial vector is associated with certain *polarity* or *handedness*. A *true* vector, also called *polar vector*, does not change sign by mirror reflection and has no polarity. In an $n$-dimensional space the number of independent components of a true vector must be $n$, but that of an axial vector is the number of the independent components in its associated antisymmetric tensor, which is $m = n(n-1)/2$. Thus, only in three-dimensional space there is $m{=}n$, but in two-dimensional space an axial vector has only one independent variable (e.g., Lugt 1996).

[12] Additional condition is necessary in a multiple-connected domain.

$$\boldsymbol{F}_\perp(\boldsymbol{x},t)=\sum_{\boldsymbol{k}}F^\lambda(\boldsymbol{k},t)\boldsymbol{\phi}_\lambda(\boldsymbol{k},\boldsymbol{x}), \tag{2.118a}$$

$$F^\lambda(\boldsymbol{k},t)=\langle\boldsymbol{F}(\boldsymbol{x},t),\boldsymbol{\phi}^*_\lambda(\boldsymbol{k},\boldsymbol{x})\rangle. \tag{2.118b}$$

Note that $\langle\boldsymbol{F}-\boldsymbol{F}_\perp,\boldsymbol{\phi}_\lambda\rangle=0$.

For example, for an incompressible flow with $u_\mathrm{n}=\omega_\mathrm{n}=0$ on $\partial\mathcal{D}$, one can expand

$$\boldsymbol{u}(\boldsymbol{x},t)=\sum_{\boldsymbol{k},\lambda}u^\lambda(\boldsymbol{k},t)\boldsymbol{\phi}_\lambda(\boldsymbol{k},\boldsymbol{x}),\quad \boldsymbol{\omega}(\boldsymbol{x},t)=\sum_{\boldsymbol{k},\lambda}\lambda u^\lambda(\boldsymbol{k},t)\boldsymbol{\phi}_\lambda(\boldsymbol{k},\boldsymbol{x}). \tag{2.119}$$

Here the term-by-term curl operation on the infinite series converges. However, as seen from (2.99) and (2.100), although $\nabla\times\boldsymbol{\omega}$ is solenoidal, only $(\nabla\times\boldsymbol{\omega})_\perp$ can have HWD expansion on which the term-by-term curl operation converges. Therefore, the result is

$$\nabla\times\boldsymbol{\omega}=\sum_{\boldsymbol{k},\lambda}\lambda^2u^\lambda\boldsymbol{\phi}_\lambda+\nabla\chi, \tag{2.120}$$

where $\chi$ is determined by (2.100).

The specific form of HWD basis depends solely on the domain shape. In a periodic box (2.116) is simplified to

$$\mathrm{i}\boldsymbol{k}\times\boldsymbol{\phi}_\lambda(\boldsymbol{k},\boldsymbol{x})=\lambda k\boldsymbol{\phi}_\lambda(\boldsymbol{k},\boldsymbol{x}),$$

from which the normalized HWD eigenvectors can be easily found (Moses 1971, Lesieur 1990):

$$\begin{aligned}\boldsymbol{\phi}_\lambda(\boldsymbol{k},\boldsymbol{x})&=\boldsymbol{h}_\lambda(\boldsymbol{k})\mathrm{e}^{\mathrm{i}\boldsymbol{k}\cdot\boldsymbol{x}},\\ \boldsymbol{h}_\lambda(\boldsymbol{k})&=\frac{1}{\sqrt{2}}[\boldsymbol{e}_1(\boldsymbol{k})+\mathrm{i}\lambda\boldsymbol{e}_2(\boldsymbol{k})],\end{aligned} \tag{2.121}$$

where $\lambda=\pm1$, and $\boldsymbol{e}_1(\boldsymbol{k})$, $\boldsymbol{e}_2(\boldsymbol{k})$, and $\boldsymbol{k}/k$ form a right-hand Cartesian triad. In this case (2.117a) is simplified to

$$\boldsymbol{h}_\lambda(\boldsymbol{k})\cdot\boldsymbol{h}^*_\mu(\boldsymbol{k})=\delta_{\lambda\mu}. \tag{2.122}$$

If the Cartesian triad is so chosen such that $\boldsymbol{k}=k\boldsymbol{e}_z$, then

$$\phi_{\lambda x}(\boldsymbol{k},\boldsymbol{x})=\frac{1}{\sqrt{2}}\cos kz,\quad \phi_{\lambda y}(\boldsymbol{k},\boldsymbol{x})=-\frac{\lambda}{\sqrt{2}}\sin kz,\quad \phi_{\lambda z}(\boldsymbol{k},\boldsymbol{x})=0. \tag{2.123}$$

Therefore, as we move along the $z$-axis, the locus of the tip of $\boldsymbol{\phi}_\lambda(\boldsymbol{k},\boldsymbol{x})$ will be a left-handed (or right-handed) helix if $\lambda=1$ (or $-1$), having a pitch equal to wavelength $2\pi/k$, see Fig. 2.7. In other words, each eigenmode with nonzero eigenvalue is a helical wave. This explains the name HWD. A combined use of the Helmholtz–Hodge and HWD decompositions permits splitting a vector intrinsically to its finest building blocks.

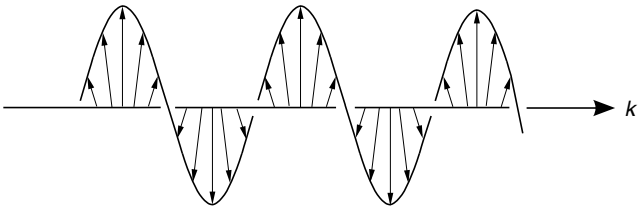


**Fig. 2.7.** A helical wave

The simple Fourier HWD basis cannot be applied to domains other than periodic boxes. To go beyond this limitation, we notice that the curl of (2.116) along with itself leads to a vector *Helmholtz equation*

$$\nabla^2 \boldsymbol{\phi}_\lambda + k^2 \boldsymbol{\phi}_\lambda = \mathbf{0}. \tag{2.124}$$

Unlike (2.116), now the three component equations are decoupled, each representing a Sturm–Liouville problem. Then in principle one can use the Helmholtz vectors to construct the HWD bases. Since a transverse vector field depends on only two scalar fields, say $\psi$ and $\chi$, a simplification may occur if both scalars are solutions of the *scalar* Helmholtz equation

$$\nabla^2 \psi + k^2 \psi = 0. \tag{2.125}$$

Morse and Feshbach (1953, pp. 1764–1766) have shown that this can indeed be realized in and only in Cartesian, cylindrical, spherical, and conical coordinates. Specifically, a transverse solutions (not normalized) of (2.124) can be written as

$$\boldsymbol{a}_\perp = \boldsymbol{M} + \boldsymbol{N}, \quad \boldsymbol{M} = \nabla \times (\boldsymbol{e} w \psi), \quad \boldsymbol{N} = \frac{1}{k} \nabla \times \nabla \times (\boldsymbol{e} w \chi),$$

where $\boldsymbol{e}$ can be three Cartesian unit vectors, the unit vector along the axis in cylindrical coordinates, or that along the radial direction in spherical and conical coordinates, but none other. the scalar $w$ in the first two cases is 1, while in the others is the radius $r$. In particular, when $\psi = \chi$ there is

$$\nabla \times (\boldsymbol{M} + \lambda \boldsymbol{N}) = \lambda k (\boldsymbol{M} + \lambda \boldsymbol{N});$$

thus, one can write down the HWD basic vector (not normalized)

$$\boldsymbol{\phi}_\lambda = \nabla \times (\boldsymbol{e} w \psi) + \frac{\lambda}{k} \nabla \times \nabla \times (\boldsymbol{e} w \psi). \tag{2.126}$$

Chandrasekhar and Kendal (1957) have given the HWD basis in terms of spherical coordinates. For vorticity dynamics the basis in terms of cylindrical coordinates $(r, \theta, z)$ is of interest. Assume that along the $z$-axis we can impose periodic boundary condition. Then a scalar Helmholtz solution that is regular

at $r = 0$ is

$$\psi = J_m(\beta r)\mathrm{e}^{\mathrm{i}(m\theta + k_z z)}, \quad k_z = \frac{\pi n}{L},$$
$$\beta^2 = k^2 - k_z^2, \quad m = 0, 1, 2, \ldots, \quad n = \pm 1, \pm 2, \ldots,$$

where $J_m(\beta r)$ are Bessel functions of the first kind. Substituting this $\psi$ into (2.126) and multiplying the result by a constant $\mathrm{i}\alpha^\lambda(\lambda, n) \equiv \mathrm{i}\lambda k/k_z$, we obtain

$$\begin{aligned}
\phi_r^\lambda &= \left[J_{m+1}(\beta r) - \frac{m}{\beta r}(1 + \alpha^\lambda)J_m(\beta r)\right]\mathrm{e}^{\mathrm{i}(m\theta + k_z z)}, \\
\phi_\theta^\lambda &= \mathrm{i}\left[\alpha^\lambda J_{m+1}(\beta r) - \frac{\lambda m}{\beta r}(1 + \alpha^\lambda)J_m(\beta r)\right]\mathrm{e}^{\mathrm{i}(m\theta + k_z z)}, \\
\phi_z^\lambda &= \mathrm{i}\frac{\beta}{k_z}J_m(\beta r)\mathrm{e}^{\mathrm{i}(m\theta + k_z z)}.
\end{aligned} \tag{2.127}$$

This result has been applied to vortex-core dynamics, see Sect. 8.1.4. The HWD has also found important applications in the analysis of turbulent cascade process; e.g., Waleffe (1992, 1993); Chen et al. (2003), and references therein. For a bounded domain of arbitrary shape, finding the curl-eigenvectors is not an easy task and requires special numerical algorithms (e.g., Boulmezaoud and Amari 2000).

### 2.3.5 Tensor Potentials

Before closing this section we take a further look at the Helmholtz potentials. Return to the Cauchy motion equation (2.44) and denote

$$\boldsymbol{f}_\mathrm{s} \equiv \nabla \cdot \mathbf{T} = \lim_{V \to 0}\left(\frac{1}{V}\int_{\partial V} \boldsymbol{t}\,\mathrm{d}S\right), \tag{2.128}$$

which is the resultant surface force per unit volume and contains most of the kinetic properties of flows. Assume we have decomposed $\boldsymbol{f}_\mathrm{s}$ to

$$\boldsymbol{f}_\mathrm{s} = -\nabla\Phi + \nabla \times \boldsymbol{\Psi}, \quad \nabla \cdot \boldsymbol{\Psi} = 0. \tag{2.129}$$

Observe that

$$-\Phi_{,i} + \epsilon_{ijk}\Psi_{k,j} = -(\Phi\delta_{ji} + \epsilon_{jik}\Psi_k)_{,j},$$

where

$$\epsilon_{jik}\Psi_k \equiv \Psi_{ji} = -\Psi_{ij} \tag{2.130}$$

is an antisymmetric tensor. Thus, (2.129) can be written as

$$\boldsymbol{f}_\mathrm{s} = \nabla \cdot \widehat{\mathbf{T}}, \quad \widehat{T}_{ij} \equiv -(\Phi\delta_{ij} + \Psi_{ij}). \tag{2.131}$$

As a generalization of the concept of scalar and vector potentials $\phi$ and $\boldsymbol{\psi}$ in (2.87), we may view the stress tensor $\mathbf{T}$ and the tensor $\widehat{\mathbf{T}}$ as *tensor potentials*

of $\boldsymbol{f}_\mathrm{s}$. Obviously there must be $\nabla\cdot(\mathbf{T}-\widehat{\mathbf{T}})=\mathbf{0}$. Any other tensor, say $\mathbf{T}'$, can also be a tensor potential of $\boldsymbol{f}_\mathrm{s}$ provided that $\mathbf{T}-\mathbf{T}'$ is divergenceless. Thus, while for Newtonian fluid the stress tensor $\mathbf{T}$ is uniquely given by (2.45), $\boldsymbol{f}_\mathrm{s}$ has infinitely many tensor potentials, among which the above $\widehat{\mathbf{T}}$ with only three independent components is the simplest one. We call it the *Helmholtz tensor potential* of $\boldsymbol{f}_\mathrm{s}$.

The value of introducing the Helmholtz potential lies in the fact that in (2.44) the six-component $\mathbf{T}$ plays a role only through its divergence. Therefore, once the expression of $\widehat{\mathbf{T}}$ (or the Helmholtz potentials $\Phi$ and $\boldsymbol{\Psi}$) is known, in the local momentum balance $\mathbf{T}$ can well be replaced by the simpler $\widehat{\mathbf{T}}$. Thus we call $\widehat{\mathbf{T}}$ the *reduced stress tensor*. However, on any *open* surface $\widehat{\mathbf{T}}$ produces a *reduced surface force*

$$\widehat{\boldsymbol{t}}(\boldsymbol{x},\boldsymbol{n})=\boldsymbol{n}\cdot\widehat{\mathbf{T}}(\boldsymbol{x})=-\Phi\boldsymbol{n}+\boldsymbol{n}\times\boldsymbol{\Psi}, \tag{2.132}$$

which is generically different from the full surface force $\boldsymbol{t}$ given by (2.43). It is here that the extra part of $\mathbf{T}$ cannot be ignored. Nevertheless, the replacement of $\boldsymbol{t}$ by $\widehat{\boldsymbol{t}}$ is feasible when one considers the volume integral of $\boldsymbol{f}_\mathrm{s}$:

$$\int_V \boldsymbol{f}_\mathrm{s}\,\mathrm{d}V=\int_{\partial V}\boldsymbol{t}\,\mathrm{d}S=\int_{\partial V}\widehat{\boldsymbol{t}}\,\mathrm{d}S \tag{2.133}$$

due to the Gauss theorem.

**Remarks**:

1. We know the divergence of any differentiable tensor of rank 2 is a vector. Now since for any vector field one can always find its Helmholtz potentials as proven by the Helmholtz–Hodge theorem, we see the inverse is also true.
2. Because the Helmholtz decomposition is a global operation, in applications the replacement of $(\mathbf{T},\boldsymbol{t})$ by $(\widehat{\mathbf{T}},\widehat{\boldsymbol{t}})$ is convenient only when $\boldsymbol{f}_\mathrm{s}$ has a *natural Helmholtz decomposition*, as in the kinematic case of (2.86). This important situation also occurs in dynamics as will be seen in the Sect. 2.4.
3. The body force $\rho\boldsymbol{f}$ in (2.44) can also be expressed as the divergence of a tensor potential. But this in no ways means that one may cast any body force to a resultant surface force. Whether a force is a body force or surface force should be judged by physics rather than mathematics; a surface force is caused by internal contact interaction of the fluid.

## 2.4 Splitting and Coupling of Fundamental Processes

Having reviewed the basic principles of Newtonian fluid dynamics and introduced the intrinsic decomposition of vector fields, we can now gain a deeper insight into the roles of compressing and shearing processes in the kinematics and dynamics of a Newtonian fluid. Our main concern is the splitting and coupling of the two processes in the Navier–Stokes equation (2.47). As just

remarked, the splitting will be convenient when a *natural Helmholtz decomposition* manifests itself from (2.47). Remarkably, this is the case as long as $\mu$ is constant. By using (2.86) we have

$$2\nabla \cdot \mathbf{D} = \nabla\vartheta + \nabla^2 \boldsymbol{u} = 2\nabla\vartheta - \nabla \times \boldsymbol{\omega},$$

so (2.47) immediately yields a natural Helmholtz decomposition of the total body force (inertial plus external) as pointed out by Truesdell (1954):

$$\rho\frac{\mathrm{D}\boldsymbol{u}}{\mathrm{D}t} - \rho\boldsymbol{f} = -\nabla\Pi - \nabla \times (\mu\boldsymbol{\omega}), \tag{2.134}$$

where

$$\Pi \equiv p - (\lambda + 2\mu)\vartheta \tag{2.135}$$

consists of the pressure and a viscous contribution of dilatation. The appearance of pressure changes the *dynamic measure* of the compressing process to the *isotropic part of* $\mathbf{T}$ (per unit volume), which is $\Pi$; and the dynamic measure of the shearing process remains to be the vorticity $\boldsymbol{\omega}$ (multiplied by the shear viscosity).[13]

The elegance of (2.134) lies in the fact that $\Pi$ and $\boldsymbol{\omega}$ have only three independent components, and three more independent components in the strain-rate tensor $\mathbf{D}$ do not appear. This fact deserves a systematic examination of its physical root and consequences, which is the topics of this section.

### 2.4.1 Triple Decomposition of Strain Rate and Velocity Gradient

According to our discussion on tensor potentials of a vector in Sect. 2.3.5 and the Cauchy motion equation (2.44), the natural Helmholtz decomposition in (2.134) implies that there must be a natural *algebraic* decomposition of the stress tensor $\mathbf{T}$ for Newtonian fluid, able to explicitly reveal the Helmholtz tensor-potential part of $\mathbf{T}$. This, by the Cauchy–Poisson equation (2.45), in turn implies that the desired algebraic decomposition must exist in the strain-rate tensor $\mathbf{D}$. Therefore, we return to kinematics. Unlike the classic symmetric-antisymmetric decomposition (2.18), we now consider the intrinsic constituents of $\mathbf{D}$ in terms of fundamental processes. The result is simple, but has much more consequences than merely for rederiving (2.134).

Since $\mathbf{D}^{\mathrm{T}} = \mathbf{D}$ but $\boldsymbol{\Omega}^{\mathrm{T}} = -\boldsymbol{\Omega}$, we may write

$$(\nabla\boldsymbol{u})^{\mathrm{T}} = \mathbf{D} - \boldsymbol{\Omega} + \vartheta\mathbf{I} - \vartheta\mathbf{I},$$

[13] The dynamic measure of compressing process *per unit mass* may switch to other scalars, see later.

so that by (2.27) there is an *intrinsic triple decomposition* of $\mathbf{D}$ and $\nabla \boldsymbol{u}$ (Wu and Wu 1996):

$$\mathbf{D} = \vartheta \mathbf{I} + \boldsymbol{\Omega} - \mathbf{B}, \tag{2.136a}$$

$$\nabla \boldsymbol{u} = \vartheta \mathbf{I} + 2\boldsymbol{\Omega} - \mathbf{B}. \tag{2.136b}$$

Thus, *the velocity gradient and rate of strain consist of a uniform expansion/compression, a rotation, and a surface deformation.* Here, $\mathbf{B}$ has most complicated structure among the three tensors on the right-hand side, and needs a further examination.

As seen from (2.26) and (2.29), the primary appearance of $\mathbf{B}$ is in the form of $\boldsymbol{n} \cdot \mathbf{B}$ for the rate of change of a surface element $\mathrm{d}\boldsymbol{S} = \boldsymbol{n}\,\mathrm{d}S$, which involves the kinematics on the surface only. Denoting the tangent components of any vector by suffix $\pi$, it can then be shown that (Appendix A.3.2)

$$\boldsymbol{n} \cdot \mathbf{B} = (\nabla_\pi \cdot \boldsymbol{u})\boldsymbol{n} - (\nabla_\pi u_\mathrm{n} + \boldsymbol{u} \cdot \mathbf{K}), \tag{2.137}$$

where

$$\mathbf{K} \equiv -\nabla_\pi \boldsymbol{n} \tag{2.138}$$

is the symmetric curvature tensor of $\mathrm{d}\boldsymbol{S}$ consisting of three independent tangent components. Then (2.137) can be written as

$$\boldsymbol{n} \cdot \mathbf{B} = \frac{\boldsymbol{n}}{\mathrm{d}S}\frac{\mathrm{D}}{\mathrm{D}t}\mathrm{d}S + \frac{\mathrm{D}\boldsymbol{n}}{\mathrm{D}t} = \boldsymbol{n} r_\mathrm{s} + \boldsymbol{W} \times \boldsymbol{n}, \tag{2.139}$$

where $r_\mathrm{s}$ is the rate of change of the surface area and $\boldsymbol{W}(\boldsymbol{x}, t)$ is the angular velocity of $\boldsymbol{n}$, expressed solely in terms of the velocity and geometry of the surface (the normal component of $\boldsymbol{W}$ is simply $W_\mathrm{n} = \omega_\mathrm{n}/2$):

$$r_\mathrm{s} = \nabla_\pi \cdot \boldsymbol{u} = \vartheta - u_{n,n} \tag{2.140a}$$

$$\boldsymbol{W}_\pi = -\boldsymbol{n} \times (\nabla_\pi u_\mathrm{n} + \boldsymbol{u} \cdot \mathbf{K}). \tag{2.140b}$$

Return now to the triple decomposition (2.136). As a special case and a fundamental application, we consider its form on an arbitrary material boundary $\mathcal{B}$ with unit normal $\boldsymbol{n}$ and velocity $\boldsymbol{u} = \boldsymbol{b}$. The resulting kinematic knowledge (Wu et al. 2005c) is indispensible in studying any fluid-boundary interactions. Due to the adherence, we may write

$$\nabla \boldsymbol{u} = \boldsymbol{n}(\boldsymbol{n} \cdot \nabla \boldsymbol{u}) + \nabla_\pi \boldsymbol{u} = \boldsymbol{n}(\boldsymbol{n} \cdot \nabla \boldsymbol{u}) + \nabla_\pi \boldsymbol{b} \quad \text{on} \quad \mathcal{B}.$$

Since (2.136b) gives

$$\boldsymbol{n} \cdot \nabla \boldsymbol{u} = \boldsymbol{n}\vartheta + \boldsymbol{\omega} \times \boldsymbol{n} - \boldsymbol{n} \cdot \mathbf{B},$$

we obtain

$$\nabla \boldsymbol{u} = \boldsymbol{n}\boldsymbol{n}\vartheta + \boldsymbol{n}(\boldsymbol{\omega} \times \boldsymbol{n}) - \boldsymbol{n}(\boldsymbol{n} \cdot \mathbf{B}) + \nabla_\pi \boldsymbol{b} \quad \text{on} \quad \mathcal{B}. \tag{2.141}$$

Here, the tensor $\nabla_\pi \boldsymbol{b}$ depends solely on the motion and deformation of $\mathcal{B}$ but independent of the flow. To see the implication of (2.141), we first assume $\mathcal{B}$ is rigid to which our frame of reference can be attached, so the last two terms vanish:

$$\nabla \boldsymbol{u} = \boldsymbol{n}\boldsymbol{n}\vartheta + \boldsymbol{n}(\boldsymbol{\omega} \times \boldsymbol{n}).$$

Then, taking the symmetric part immediately yields the *Caswell formula* (Caswell 1967):

$$2\mathbf{D} = 2\boldsymbol{n}\boldsymbol{n}\vartheta + \boldsymbol{n}(\boldsymbol{\omega} \times \boldsymbol{n}) + (\boldsymbol{\omega} \times \boldsymbol{n})\boldsymbol{n}, \tag{2.142}$$

where by (2.140a) $\vartheta$ can be replaced by $u_{n,n}$ since $r_\mathrm{s} = 0$.

We now extend (2.142) to an arbitrary deformable surface $\mathcal{B}$ (to which no frame of reference can be attached). For this purpose we only need to treat the tensor $\nabla_\pi \boldsymbol{b}$ in (2.141). In general, it consists of a tangent–tangent tensor $(\nabla_\pi \boldsymbol{b})_\pi$ and a tangent–normal tensor

$$(\nabla_\pi \boldsymbol{b} \cdot \boldsymbol{n})\boldsymbol{n} = (\nabla_\pi b_\mathrm{n} - \boldsymbol{b} \cdot \nabla_\pi \boldsymbol{n})\boldsymbol{n} = -(\boldsymbol{W} \times \boldsymbol{n})\boldsymbol{n}$$

due to (2.138) and (2.140b). Substituting these into (2.141) and using (2.139) to express $\boldsymbol{n} \cdot \mathbf{B}$, we obtain a general kinematic formula:

$$\nabla \boldsymbol{u} = \boldsymbol{n}\boldsymbol{n}u_{n,n} + \boldsymbol{n}(\boldsymbol{\omega} \times \boldsymbol{n}) - [\boldsymbol{n}(\boldsymbol{W} \times \boldsymbol{n}) + (\boldsymbol{W} \times \boldsymbol{n})\boldsymbol{n}] + (\nabla_\pi \boldsymbol{b})_\pi. \tag{2.143}$$

Note that $r_\mathrm{s}$ in the normal–normal component is canceled. Then, let $\mathbf{S}$ and $\mathbf{A}$ be the symmetric and antisymmetric parts of $(\nabla_\pi \boldsymbol{b})_\pi$, from (2.143) it follows that

$$2\mathbf{D} = 2\boldsymbol{n}\boldsymbol{n}u_{n,n} + \boldsymbol{n}(\boldsymbol{\omega}_\mathrm{r} \times \boldsymbol{n}) + (\boldsymbol{\omega}_\mathrm{r} \times \boldsymbol{n})\boldsymbol{n} + 2\mathbf{S}, \tag{2.144}$$

$$2\boldsymbol{\Omega} = \boldsymbol{n}(\boldsymbol{\omega} \times \boldsymbol{n}) - (\boldsymbol{\omega} \times \boldsymbol{n})\boldsymbol{n} + 2\mathbf{A}, \tag{2.145}$$

where $\boldsymbol{\omega}_\mathrm{r} \equiv \boldsymbol{\omega} - 2\boldsymbol{W}$ is the *relative vorticity* with $\boldsymbol{n} \cdot \boldsymbol{\omega}_\mathrm{r} = 0$, see (2.69). Tensor $\mathbf{S}$ has three independent components and can be called *surface-stretching tensor*. In contrast, $\mathbf{A}$ has only one independent component, which must be $\omega_\mathrm{n}$. Note that on a rigid boundary (2.144) reduces to (2.142), but viewed in a frame of reference fixed in the space.

The *generalized Caswell formula* (2.144) contains the key kinematics on an arbitrary boundary $\mathcal{B}$. It represents an intrinsic decomposition of $\mathbf{D}$ with respect to one normal (N) and two tangent (T) directions, along with their respective physical causes. Namely: the N–N component caused by the normal gradient of normal velocity; the N–T and T–N components caused by the relative vorticity; and the T–T components caused by the surface flexibility. With known $\boldsymbol{b}(\boldsymbol{x}, t)$-distribution and surface geometry, (2.143) and (2.144) express a basic fact that the motion and deformation of a fluid element neighboring $\mathcal{B}$ are described by only three independent components of velocity derivatives.

The form of (2.144) suggests a convenient curvilinear orthonormal basis $(\boldsymbol{e}_1, \boldsymbol{e}_2, \widehat{\boldsymbol{n}})$ on $\mathcal{B}$. Let $\boldsymbol{e}_2$ be along $\boldsymbol{\omega}_\mathrm{r}$, $\widehat{\boldsymbol{n}} = -\boldsymbol{n}$ (towards fluid), and hence $\boldsymbol{e}_1$ is

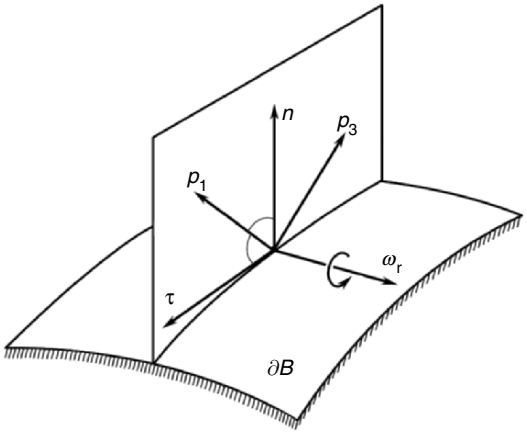


**Fig. 2.8.** Principal directions of the strain-rate tensor on a rigid boundary

along $\boldsymbol{\omega}_\mathrm{r} \times \widehat{\boldsymbol{n}}$. It will be seen below (Sect. 2.4.2) that for Newtonian fluid $\boldsymbol{e}_1$ is the direction of shear stress $\boldsymbol{\tau}$; thus we call this frame the $\boldsymbol{\tau}$-*frame*. Then (2.144) reads

$$\{D_{ij}\} = \begin{bmatrix} S_{11} & S_{12} & \omega_\mathrm{r}/2 \\ S_{12} & r_\mathrm{s} - S_{11} & 0 \\ \omega_\mathrm{r}/2 & 0 & u_{n,n} \end{bmatrix}. \tag{2.146}$$

We have seen in Sect. 2.1.2 that the first and third eigenvalues $\lambda_{1,3}$ and associated principal directions of $\mathbf{D}$ reflect the maximum stretching/shrinking rates and directions, respectively. On a boundary $\mathcal{B}$ they have dominant effect on the near-boundary flow structures and their stability. Let $\theta_{1,3}$ be the angles between the stretching/shrinking principal axes and $\boldsymbol{e}_1$ of the $\boldsymbol{\tau}$-frame. If $\mathcal{B}$ is rigid with $\mathbf{S} = \mathbf{0}$ and if the flow is incompressible, from (2.146) it follows at once that $\lambda_{1,3} = \pm\,\omega_\mathrm{r}/2$, $\lambda_2 = 0$, and $\theta_{1,3} = \pm\,45^\circ$, as sketched in Fig. 2.8. But the situation can be very different if $\mathcal{B}$ is deformable, as demonstrated by Wu et al. (2005c).

### 2.4.2 Triple Decomposition of Stress Tensor and Dissipation

We move on to dynamics. Substituting (2.136a) into (2.45) immediately leads to a *triple decomposition of the stress tensor*

$$\mathbf{T} = -\Pi\mathbf{I} + 2\mu\boldsymbol{\Omega} - 2\mu\mathbf{B}, \tag{2.147}$$

where $\Pi$ is defined by (2.135). Then since by (2.34b) $\mu\mathbf{B}$ is a trace-free tensor, the first two terms on the right-hand side of (2.147) form the natural Helmholtz tensor potential of the surface force. In other words, *for flow with constant $\mu$, the surface deformation process does not affect the local*

*momentum balance* (Wu and Wu 1993). This explains the origin of (2.134) and permits introducing the *reduced stress tensor* and *reduced surface stress* solely in terms of compressing and shearing processes:

$$\widehat{\mathbf{T}} = -\Pi\mathbf{I} + 2\mu\boldsymbol{\Omega}, \tag{2.148}$$

$$\widehat{\boldsymbol{t}} = \boldsymbol{n}\cdot\widehat{\mathbf{T}} = -\Pi\boldsymbol{n} + \mu\boldsymbol{\omega}\times\boldsymbol{n}. \tag{2.149}$$

The conceptual simplification brought by $\widehat{\mathbf{T}}$ can also lead to significant computational benefit. For example, Eraslan et al. (1983) have developed a Navier–Stokes solver where some components of $\mathbf{T}$ were found never useful and hence simply dropped. Consequently, for incompressible flow the solver reached a big saving of CPU in stress computation.

Evidently, although for constant $\mu$ the surface-deformation stress does not contribute to the differential momentum equation nor integrated surface force over a closed boundary, it must show up in more general circumstances. Here we consider two simple examples; in Sect. 4.3.2 we shall see the crucial role of the surface-deformation stress in free-surface flow.

First, on any surface element of unit area in the fluid or at its boundary, we have a triple decomposition of the surface force:

$$\boldsymbol{t} = \widehat{\boldsymbol{t}} + \boldsymbol{t}_\mathrm{s}, \quad \boldsymbol{t}_\mathrm{s} = -2\mu\boldsymbol{n}\cdot\mathbf{B} = -2\mu(\boldsymbol{n}r_\mathrm{s} + \boldsymbol{W}\times\boldsymbol{n}), \tag{2.150}$$

where $\boldsymbol{t}_\mathrm{s}$ is the *viscous resistance of the fluid surface to its motion and deformation*, which has both normal and tangent components. Thus, denote the orthogonal decomposition of the stress by $\boldsymbol{t} = -\widetilde{\Pi}\boldsymbol{n} + \boldsymbol{\tau}$, by (2.135) the general normal and tangent components are

$$\widetilde{\Pi} = \Pi + 2\mu r_\mathrm{s} = p - \lambda\vartheta - 2\mu u_{n,n}, \tag{2.151a}$$

$$\boldsymbol{\tau} = \mu\boldsymbol{\omega}_\mathrm{r}\times\boldsymbol{n}, \quad \boldsymbol{\omega}_\mathrm{r} = \boldsymbol{\omega} - 2\boldsymbol{W}. \tag{2.151b}$$

On a solid wall $\boldsymbol{\tau}_\mathrm{w} = -\boldsymbol{\tau}$ is the skin-friction stress, always determined by the relative vorticity. Note that $\boldsymbol{t}_\mathrm{s} = \mathbf{0}$ only if the surface performs uniform translation; even a rigid rotation will cause a nonzero $\boldsymbol{t}_\mathrm{s}$ due to the viscous resistance to the variation of $\boldsymbol{n}$.

Second, using the generalized Stokes theorem (A.17) and its corollary (A.26), from (2.150) and (2.29) we find the general formulas for integrated force and moment due to $\boldsymbol{t}_\mathrm{s}$ on an open surface $S$ with boundary loop $C$:

$$\int_S \boldsymbol{t}_\mathrm{s}\,\mathrm{d}S = 2\mu\oint_C \mathrm{d}\boldsymbol{x}\times\boldsymbol{u}, \tag{2.152a}$$

$$\int_S \boldsymbol{x}\times\boldsymbol{t}_\mathrm{s}\,\mathrm{d}S = 2\mu\oint_C \boldsymbol{x}\times(\mathrm{d}\boldsymbol{x}\times\boldsymbol{u}) - 2\mu\int_S \boldsymbol{n}\times\boldsymbol{u}\,\mathrm{d}S. \tag{2.152b}$$

In particular, on a closed boundary $\partial V$ of a fluid volume $V$, by the generalized Gauss theorem (A.14), the total moment due to $\boldsymbol{t}_\mathrm{s}$ is proportional to the total

vorticity in $V$ (Wu and Wu 1993):

$$\int_{\partial V} \boldsymbol{x} \times \boldsymbol{t}_{\mathrm{s}}\,\mathrm{d}S = -2\mu \int_{\partial V} \boldsymbol{n} \times \boldsymbol{u}\,\mathrm{d}S = -2\mu \int_{V} \boldsymbol{\omega}\,\mathrm{d}V. \tag{2.153}$$

Corresponding to (2.147), a triple decomposition can also be made for the dissipation $\Phi$, which brings some simplification too. We start from a kinematic identity (cf. Truesdell 1954)

$$\mathbf{D} : \mathbf{D} = \vartheta^2 + \frac{1}{2}\omega^2 - \nabla \cdot (\mathbf{B} \cdot \boldsymbol{u}), \tag{2.154}$$

where $\omega^2 \equiv |\boldsymbol{\omega}|^2$ is called the *enstrophy*. Thus, for constant $\mu$, (2.54) yields the *triple decomposition of dissipation rate*:

$$\Phi = (\lambda + 2\mu)\vartheta^2 + \mu\omega^2 - \nabla \cdot (2\mu\mathbf{B} \cdot \boldsymbol{u}). \tag{2.155}$$

Once again, the role of the three viscous constituents of stress tensor is explicitly revealed. Note that the $\mathbf{B}$-part of $\Phi$ can be either positive or negative. More interestingly, we have

$$\boldsymbol{t} \cdot \boldsymbol{u} = -\Pi \boldsymbol{n} \cdot \boldsymbol{u} + \mu\boldsymbol{\omega} \cdot (\boldsymbol{n} \times \boldsymbol{u}) - \boldsymbol{n} \cdot (2\mu\mathbf{B} \cdot \boldsymbol{u});$$

substituting this and (2.155) into (2.52), we see that the $\mathbf{B}$-part of $\Phi$ and that of $\boldsymbol{t} \cdot \boldsymbol{u}$ are canceled. Explicitly, at each point the work rate per unit volume done by $\boldsymbol{t}_{\mathrm{s}}$ is

$$w_{\mathrm{s}} \equiv \lim_{\mathcal{V} \to 0} \frac{1}{\mathcal{V}} \int_{\partial \mathcal{V}} \boldsymbol{t}_{\mathrm{s}} \cdot \boldsymbol{u}\,\mathrm{d}S = -\nabla \cdot (2\mu\mathbf{B} \cdot \boldsymbol{u}),$$

precisely the last term of (2.155), say $\Phi_s$. Therefore, the work done by $\boldsymbol{t}_{\mathrm{s}}$ does not influence the change of kinetic energy but always directly dissipated into heat (Wu et al. 1999a). Hence, instead of (2.52) and (2.53) we can simply write

$$\frac{\mathrm{d}}{\mathrm{d}t} \int_{\mathcal{V}} \rho \left(\frac{1}{2}q^2\right) \mathrm{d}v = \int_{\mathcal{V}} (\rho \boldsymbol{f} \cdot \boldsymbol{u} + p\vartheta - \widehat{\Phi}) \mathrm{d}v + \int_{\partial \mathcal{V}} \widehat{\boldsymbol{t}} \cdot \boldsymbol{u}\,\mathrm{d}S, \tag{2.156a}$$

$$\rho \frac{\mathrm{D}}{\mathrm{D}t} \left(\frac{1}{2}q^2\right) = \rho \boldsymbol{f} \cdot \boldsymbol{u} + p\vartheta + \nabla \cdot (\widehat{\mathbf{T}} \cdot \boldsymbol{u}) - \widehat{\Phi}, \tag{2.156b}$$

where $\widehat{\mathbf{T}}$ and $\widehat{\boldsymbol{t}}$ are given by (2.148) and (2.149), and

$$\widehat{\Phi} \equiv \Phi - \Phi_{\mathrm{s}} = (\lambda + 2\mu)\vartheta^2 + \mu\omega^2 \geq 0 \tag{2.157}$$

is the *reduced dissipation*, again due only to compressing and shearing processes. Wu et al. (1999a) notice that the characteristic distribution of scalars $\vartheta^2$, $\omega^2$, and $\Phi_{\mathrm{s}}$ in (2.157) may serve as good indicators for identifying different structures in a complex high Reynolds-number flow. However, it should be warned

that it is the full dissipation $\Phi$ rather than $\widehat{\Phi}$ that causes the entropy production in (2.61). Otherwise a fluid making a solid-like rotation would have a dissipation $\mu\omega^2$, which is of course incorrect.

Finally, for constant $\mu$, from (2.155) the total dissipation over a volume $V$ is

$$\int_V \Phi \,\mathrm{d}V = \int_V [(\lambda + 2\mu)\vartheta^2 + \mu\omega^2]\mathrm{d}V + \int_{\partial V} \boldsymbol{t}_s \cdot \boldsymbol{u} \,\mathrm{d}S. \tag{2.158}$$

This result generalizes the *Bobyleff–Forsythe formula* (Serrin 1959) for incompressible flow:

$$\int_V \Phi \,\mathrm{d}V = \mu \int_V \omega^2 \,\mathrm{d}V + 2\mu \int_{\partial V} \boldsymbol{u} \cdot \nabla \boldsymbol{u} \cdot \boldsymbol{n} \,\mathrm{d}S. \tag{2.159}$$

If $\partial V$ extends to infinity where the fluid is at rest, then only the reduced dissipation $\widehat{\Phi}$ contributes to the total full dissipation.

So far we have assumed a constant $\mu$. More generally, with $\mu = \mu(T)$ the natural Helmholtz decomposition of the momentum equation (2.134) no longer exactly holds. Rather, there will be (Wu and Wu 1998)

$$\rho \frac{\mathrm{D}\boldsymbol{u}}{\mathrm{D}t} - \rho \boldsymbol{f} = -\nabla \Pi - \nabla \times (\mu \boldsymbol{\omega}) - 2\nabla\mu \cdot \mathbf{B}, \tag{2.160a}$$

where $\mathbf{B}$ is the surface strain rate tensor. Here, the viscosity gradient can be cast to

$$-\nabla\mu = \frac{S_\mu Pr}{h}\boldsymbol{q} \quad \text{with} \quad S_\mu \equiv \frac{\mathrm{d}\,\log\mu}{\mathrm{d}\,\log T}, \tag{2.160b}$$

where $h = c_\mathrm{p}T$ is the enthalpy and $\boldsymbol{q} = -\kappa\nabla T$ the heat flux. Both the Prandtl number $Pr = \mu c_\mathrm{p}/\kappa$ and $S_\mu$ are of $O(1)$. Because $\boldsymbol{q}$ is along the normal of isothermal surfaces, the extra term in (2.160a) is proportional to the *viscous resistance of isothermal surfaces to their deformation.* In most cases this effect is small.

### 2.4.3 Internal and Boundary Coupling of Fundamental Processes

For vorticity dynamics (and sometimes "compressing dynamics" as well), the Navier–Stokes equation expressed for unit mass is more useful than that for unit volume. But, once the fluid density is a variable, such an equation with constant $\mu$,

$$\frac{\mathrm{D}\boldsymbol{u}}{\mathrm{D}t} = \boldsymbol{f} - \frac{1}{\rho}\nabla\Pi - \nu\nabla \times \boldsymbol{\omega}, \tag{2.161}$$

where $\nu = \mu/\rho$ is the kinematic viscosity, is no longer a natural Helmholtz decomposition. To discover the underlying physics of the two fundamental processes and their coupling most clearly, we need a different decomposition to *maximally reveal the natural potential and solenoidal parts.*

First, on the left-hand side of (2.161) it is the nonlinear advective acceleration $\boldsymbol{u}\cdot\nabla\boldsymbol{u}$ that causes all kinematic complexity of fluid motion, never encountered in solid mechanics. Thus we decompose it first. Write

$$\nabla\boldsymbol{u}=\nabla\boldsymbol{u}-(\nabla\boldsymbol{u})^{\mathrm{T}}+(\nabla\boldsymbol{u})^{\mathrm{T}}=2\boldsymbol{\Omega}+(\nabla\boldsymbol{u})^{\mathrm{T}},$$

such that

$$2\boldsymbol{u}\cdot\boldsymbol{\Omega}=\boldsymbol{\omega}\times\boldsymbol{u},\quad \boldsymbol{u}\cdot(\nabla\boldsymbol{u})^{\mathrm{T}}=\nabla\boldsymbol{u}\cdot\boldsymbol{u}.$$

Then (2.11) is cast to the *vorticity form*, very important in vorticity and vortex dynamics:

$$\frac{\mathrm{D}\boldsymbol{u}}{\mathrm{D}t}=\frac{\partial\boldsymbol{u}}{\partial t}+\boldsymbol{\omega}\times\boldsymbol{u}+\nabla\left(\frac{1}{2}q^2\right),\quad q\equiv|\boldsymbol{u}|. \tag{2.162}$$

Therefore, the advective acceleration consists of two parts. One is the gradient of kinetic energy, evidently a longitudinal process, implying that the acceleration increases as fluid particles move toward higher kinetic-energy region. The other is the *Lamb vector* $\boldsymbol{\omega}\times\boldsymbol{u}$ already encountered in (2.85), which is analogous to the Coriolis force observed in a rotating frame of reference (see Sect. 12.1.1) and drives the particles move around the vorticity direction. Generically $\boldsymbol{\omega}\times\boldsymbol{u}$ is neither solenoidal nor irrotational, and hence appears in the evolution of both longitudinal and transverse processes.

Next, on the right-hand side of (2.161) there is an inviscid term $-\nabla p/\rho$, which by (2.64) equals $-\nabla h+T\nabla s$, where $\nabla h$ is also a natural longitudinal process. Thus, (2.161) can be cast to the *Crocco–Vazsonyi equation* (its inviscid version is the *Crocco equation*):

$$\frac{\partial\boldsymbol{u}}{\partial t}+\boldsymbol{\omega}\times\boldsymbol{u}-T\nabla s=\boldsymbol{f}-\nabla H+\boldsymbol{\eta}, \tag{2.163}$$

where $H$ is the total enthalpy defined in (2.63), and

$$\boldsymbol{\eta}\equiv\frac{1}{\rho}\nabla\cdot\mathbf{V}=\frac{1}{\rho}\nabla[(\lambda+2\mu)\vartheta]-\nu\nabla\times\boldsymbol{\omega}+\frac{2}{\rho}\nabla\mu\cdot\mathbf{D} \tag{2.164}$$

collects all viscous forces including variable $\mu$. We may introduce a constant averaged kinematic shear viscosity $\nu_0$ and write $\boldsymbol{\eta}=\boldsymbol{\eta}'-\nu_0\nabla\times\boldsymbol{\omega}$ to separate a basic viscous force due to vorticity diffusion, so that on the right-hand side of (2.163) an explicit Helmholtz decomposition is recovered. The extra term $\boldsymbol{\eta}'$ originates from compressibility and thermodynamics, which in most cases is negligible. Therefore, the main complexity of (2.163) lies in its inviscid nonlinear term called *generalized Lamb vector*:

$$\boldsymbol{L}\equiv\boldsymbol{\omega}\times\boldsymbol{u}-T\nabla s, \tag{2.165}$$

which is usually dominated by the Lamb vector $\boldsymbol{\omega}\times\boldsymbol{u}$.

Now, in order to examine to what degree the two fundamental processes can be split and how they are coupled, we assume the external body force

does not exist (to be discussed in Sects. 3.6.2, 4.1.1, and Chap. 12), and take the curl and divergence of (2.163). Since $\nu_0 \nabla \times \boldsymbol{\omega}$ is divergence-free, this yields

$$\frac{\partial \boldsymbol{\omega}}{\partial t} - \nu_0 \nabla^2 \boldsymbol{\omega} = -\nabla \times (\boldsymbol{L} - \boldsymbol{\eta}'), \tag{2.166}$$

$$\frac{\partial \vartheta}{\partial t} + \nabla^2 H = -\nabla \cdot (\boldsymbol{L} - \boldsymbol{\eta}'). \tag{2.167}$$

While (2.166) represents the general *vorticity transport equation* which characterizes all transverse interactions, (2.167) characterizes all longitudinal interactions and suggests that the viscous effect is much weaker than that in (2.166). Because the Helmholtz decomposition is a linear operation, the nonlinearity in $\boldsymbol{L} - \boldsymbol{\eta}'$ in both equations makes the coupling of both processes inevitable. It is their *intersection*.

For weakly compressible flow the entropy gradient can be neglected and $\nu$ is nearly constant. Then (2.166) is reduced to the classic *Helmholtz equation* for the vorticity to be studied in depth in this book:

$$\frac{\partial \boldsymbol{\omega}}{\partial t} + \nabla \times (\boldsymbol{\omega} \times \boldsymbol{u}) - \nu \nabla^2 \boldsymbol{\omega} = \boldsymbol{0}, \tag{2.168}$$

where the solenoidal part of the Lamb vector $\boldsymbol{\omega} \times \boldsymbol{u}$ is the only nonlinear term. Meanwhile, under the same condition, (2.167) is reduced to

$$\frac{\partial \vartheta}{\partial t} + \nabla^2 H + \nabla \cdot (\boldsymbol{\omega} \times \boldsymbol{u}) = 0, \tag{2.169}$$

where the potential part of the Lamb vector $\boldsymbol{\omega} \times \boldsymbol{u}$ appears. As a scalar equation, the spatial structure of (2.169) is simpler than (2.168); but we have to express one of the two scalars $\vartheta$ and $H$ by the other, which complicates the final form of (2.169). The result is an *advective wave equation* for the total enthalpy $H$ obtained by Howe (1975, 1998, 2003), with the Lamb vector and entropy variation being the source of the wave. We illustrate the *Howe equation* for inviscid homentropic flow. Multiplying the inviscid version of (2.163) by $\rho$ and taking divergence, we have

$$\nabla \cdot \left( \rho \frac{\partial \boldsymbol{u}}{\partial t} \right) + \nabla \cdot (\rho \nabla H) = -\nabla \cdot (\rho \boldsymbol{\omega} \times \boldsymbol{u}).$$

Here, using (2.40) and the inviscid version of (2.65), there is

$$\begin{aligned} \nabla \cdot \left( \rho \frac{\partial \boldsymbol{u}}{\partial t} \right) &= \nabla \rho \cdot \frac{\partial \boldsymbol{u}}{\partial t} - \rho \frac{\partial}{\partial t} \frac{\mathrm{D} \ln \rho}{\mathrm{D}t} = -\rho \frac{\mathrm{D}}{\mathrm{D}t} \frac{\partial \ln \rho}{\partial t} \\ &= -\rho \frac{\mathrm{D}}{\mathrm{D}t} \left( \frac{1}{\rho c^2} \frac{\partial p}{\partial t} \right) = -\rho \frac{\mathrm{D}}{\mathrm{D}t} \left( \frac{1}{c^2} \frac{\mathrm{D}H}{\mathrm{D}t} \right), \end{aligned}$$

where $c = (\mathrm{d}p/\mathrm{d}\rho)_\mathrm{s}^{1/2}$ is the speed of sound. Therefore, it follows that (Howe, 2003)

$$\left[\frac{\mathrm{D}}{\mathrm{D}t}\left(\frac{1}{c^2}\frac{\mathrm{D}}{\mathrm{D}t}\right) - \frac{1}{\rho}\nabla\cdot(\rho\nabla)\right] H = \frac{1}{\rho}\nabla\cdot(\rho\boldsymbol{\omega}\times\boldsymbol{u}). \tag{2.170}$$

In its most general form (Howe 1998), the Howe equation governs almost all compressing processes and could be solved jointly with the vorticity transport equation (2.166). But its main application is on the sound generated by unsteady vorticity field, known as *vortex sound* named by Powell (1961, 1964), who studied this topic extensively under far-field approximation (see the review of Powell (1995)). By using singular perturbation to match the far-field and near-field solutions, Crow (1970a) was the first to prove rigorously that the principal source of sound at low Mach numbers is the divergence of the Lamb vector. In aeroacoustics, the variable describing the sound field in a flow can be the fluctuating part of $p$, $\rho$, etc. but it has been found that the most appropriate one is the disturbance total enthalpy $H$ (Howe 1975; Doak 1998). Hence, (2.170) reveals that *in a homentropic flow the moving vorticity is the only source of sound*, or sound is a byproduct of vortex motion.

In particular, at low Mach numbers with $|\boldsymbol{u}|/c \ll 1$, $c$ and $\rho$ in (2.170) can be replaced by their constant mean values $c_0$ and $\rho_0$, so that the equation is reduced to the classic linear wave equation and can be solved by using the Green's function method. In this case the sound-wave length $\lambda$ is generically much larger than the scale of the moving vortices, so that to an observer at a far-field point $\boldsymbol{x}$ the emission-time difference at different points $\boldsymbol{y}$ in the source region is negligible: one has $r = |\boldsymbol{x}-\boldsymbol{y}| \simeq |\boldsymbol{x}|$. Then a general result of interest is that *the far-field acoustic pressure $p'$ depends linearly on the unsteady vorticity alone* (Möhring 1978, Kambe et al. 1993, Powell 1994):

$$p'(\boldsymbol{x},t) = \frac{\rho_0\beta_i\beta_j}{4\pi c_0^2 x}\frac{\partial^3}{\partial t^3}\int \frac{1}{3}y_i(\boldsymbol{y}\times\boldsymbol{\omega})_j(t-x/c_0)\mathrm{d}^3y, \tag{2.171}$$

where $x = |\boldsymbol{x}|$, $\beta_i = x_i/x$ is the directional cosine of $\boldsymbol{x}$ in the observation direction, and the integrand is estimated at an earlier time $t - x/c_0$.

The earlier coupling between the two processes dominated by the nonlinear Lamb vector is inviscid in nature. It no longer exists on a solid boundary $\partial B$ with known motion or at rest. Due to the acceleration adherence (2.70), the left-hand side of (2.161) is known, or simply vanishes in the frame of reference fixed to the solid boundary. However, there appears a different type of *viscous boundary coupling* of which the effect may also reach the interior of the flow field. To illustrate the situation in its simplest circumstance, assume the flow is incompressible and the solid wall is at rest. Then the momentum balance implies

$$\nabla p + \mu\nabla\times\boldsymbol{\omega} = \mathbf{0} \quad \text{on} \quad \partial B,$$

so that

$$\boldsymbol{n} \times \nabla p = -\mu \boldsymbol{n} \times (\nabla \times \boldsymbol{\omega}), \tag{2.172a}$$

$$\boldsymbol{n} \cdot \nabla p = -\mu (\boldsymbol{n} \times \nabla) \cdot \boldsymbol{\omega}. \tag{2.172b}$$

This pair of equations, especially (2.172a), contain rich physical and mathematical information relevant to vorticity dynamics and will be fully explored later. The absence of advection makes the coupling *linear* and hence a series of formally analytical results are possible.

From the preceding analysis we may also summarize the involvement of thermodynamics in dynamic processes, which can be both inviscid and viscous. The viscous involvement of thermodynamics has been encountered in (2.160). Inviscidly, it appears in the generalized Lamb vector (2.165). If the flow is *baroclinic*, i.e., with more than one independent thermodynamic variables, thermodynamics enters both compressing and shearing processes through $(p, \rho)$ in (2.161), or through $(T, s)$ in (2.163). Two independent variables determine a surface with a normal direction; and in a baroclinic flow this normal is $\nabla\rho \times \nabla p$ or $\nabla T \times \nabla s$. In contrast, if the flow is *barotropic*, i.e., with only one independent thermodynamic variables so that $\nabla T \times \nabla s = 0$, the inviscid coupling of thermodynamics and dynamics occurs only in compressing process. For more discussion see Sects. 3.6.2 and 4.1.2 later.

### 2.4.4 Incompressible Potential Flow

In the context of Helmholtz–Hodge decomposition we have seen that a scalar function $\chi$ with $\nabla^2\chi = 0$ is necessary, and in general at large $Re$ a big portion of a viscous flow field can be irrotational. It is appropriate here to briefly review some basic issues of incompressible potential flow.

Consider an externally unbounded fluid domain $V_\mathrm{f}$ which is at rest at infinity and in which a moving body $B$ causes a single-valued or *acyclic* (or noncirculatory) velocity potential $\phi$,[14] which is solved from the kinematic problem

$$\nabla^2 \phi = 0 \quad \text{in} \quad V_\mathrm{f}, \tag{2.173a}$$

$$\frac{\partial \phi}{\partial n} = \boldsymbol{n} \cdot \boldsymbol{b} \quad \text{on} \quad \partial B, \quad \phi \to 0 \quad \text{as} \quad |\boldsymbol{x}| = r \to \infty, \tag{2.173b}$$

where $\boldsymbol{b}$ is the velocity of $\partial B$. It is known that the far-field asymptotic behavior of such a $\phi$ and $\boldsymbol{u}$ is

$$\phi = -\frac{\boldsymbol{A} \cdot \boldsymbol{n}}{r^{n-1}} + ..., \quad \boldsymbol{u} = \nabla\phi = \frac{n(\boldsymbol{A} \cdot \boldsymbol{n})\boldsymbol{n} - \boldsymbol{A}}{r^n} + ... \,, \tag{2.174a,b}$$

[14] A single-valued potential cannot have discontinuity, and hence excludes any vortex sheet, across which a loop going once will have nonzero circulation, see (4.128) and Fig. 4.19 of Sect. 4.4.

where $n = 2, 3$ is the space dimensions, $\boldsymbol{n} = \boldsymbol{x}/r$, and $\boldsymbol{A}$ depends on the body shape and velocity.

First, by (2.173), the total kinetic energy of the flow is

$$K = \frac{\rho}{2}\int_{V_\mathrm{f}} \nabla\phi\cdot\nabla\phi\,\mathrm{d}V = \frac{\rho}{2}\int_{V_\mathrm{f}} \nabla\cdot(\phi\nabla\phi)\mathrm{d}V = \frac{\rho}{2}\int_{\partial B}\phi\boldsymbol{n}\cdot\boldsymbol{b}\,\mathrm{d}S. \tag{2.175}$$

Thus, the flow has no memory on its history but completely depends on the current motion of boundary. Since $K = 0$ implies $\nabla\phi = \boldsymbol{0}$ everywhere, if $\partial V_\mathrm{f}$ is suddenly brought to rest then the entire flow stops instantaneously, which is evidently unrealistic. *In reality a fluid flow without moving boundary must be vortical and/or compressible.*

If one adds any disturbance $\boldsymbol{u}'$ to the velocity field with kinetic energy $K' > 0$, such that $\boldsymbol{u}_1 = \nabla\phi + \boldsymbol{u}'$, and if $\boldsymbol{u}'\cdot\boldsymbol{n} = 0$ on $\partial V_\mathrm{f}$, then

$$\begin{aligned} K_1 &= \frac{\rho}{2}\int_{V_\mathrm{f}} (\nabla\phi+\boldsymbol{u}')\cdot(\nabla\phi+\boldsymbol{u}')\mathrm{d}V \\ &= K + K' + \rho\int_{\partial V_\mathrm{f}} \boldsymbol{n}\cdot\boldsymbol{u}'\phi\,\mathrm{d}S = K + K' > K. \end{aligned} \tag{2.176}$$

This is the famous **Kelvin's minimum kinetic energy theorem**: *Among all incompressible flows satisfying the same normal velocity boundary condition, the potential flow has minimum kinetic energy.*

Next, the total force and moment acting to $V_\mathrm{f}$ come only from the pressure on $\partial B$. The Crocco–Vazsonyi equation (2.163) can then be integrated once to yield the well-known *Bernoulli equation*

$$\frac{\partial\phi}{\partial t} + \frac{p}{\rho} + \frac{1}{2}q^2 = C(t), \tag{2.177}$$

where $C(t)$ can be absorbed into $\phi$ without affecting $\boldsymbol{u} = \nabla\phi$. Therefore, once $\phi$ is known by solving (2.173), one can obtain the total force and moment acting on $V_\mathrm{f}$ via the first equality of (2.71) and (2.72), respectively. But in force and moment analysis it is often convenient to employ the concept of *hydrodynamic impulse* and *angular impulse* (Lamb 1932; Batchelor 1967; Saffman 1992). These are the hypothetical impulsive force and moment that bring the fluid from rest to the current motion instantaneously. Suppose at $t = 0^+$ there is a finite velocity field $\boldsymbol{u}(\boldsymbol{x}, 0^+)$, which is imagined to be suddenly generated from the fluid at rest everywhere at $t = 0^-$ by an impulsive external force density $\boldsymbol{F} = \boldsymbol{i}(\boldsymbol{x})\delta(t)$ distributed in a *finite* region. We integrate the incompressible Navier–Stokes equation (say (2.161) with $\Pi = p$ and constant $\nu$) over a small time interval $[0^-, \delta t]$. Since all finite terms in the equation including advection and diffusion can only have a variation of $O(\delta t)$, $\boldsymbol{u}(\boldsymbol{x}, 0^+)$ must be solely generated by the infinitely large $\boldsymbol{F}$ at $t = 0$, which also causes a pressure impulse:

$$P(\boldsymbol{x}) = \frac{1}{\rho}\int_{0^-}^{\delta t} p(\boldsymbol{x}, t)\,\mathrm{d}t.$$

Hence, the momentum balance implies

$$\boldsymbol{u}(\boldsymbol{x}, 0^+) = -\nabla P + \boldsymbol{i}(\boldsymbol{x}). \tag{2.178}$$

From (2.178) it follows that $\nabla^2 P = \nabla \cdot \boldsymbol{i}$ and $\boldsymbol{\omega} = \nabla \times \boldsymbol{i}$. While the integral of $\boldsymbol{i}$ leads to so-called *vortical impulse* to be addressed in Sect. 3.4.1, in a potential flow one simply has $P = -\phi$. The integrals of $-\boldsymbol{n}P$ and $-\boldsymbol{x} \times \boldsymbol{n}P$ over $\partial V_\mathrm{f} = \partial B + \partial V_\infty$ are known as the *potential impulse* and *angular impulse* of the fluid, respectively, denoted by $\boldsymbol{I}_\phi$ and $\boldsymbol{L}_\phi$:

$$\boldsymbol{I}_\phi \equiv -\int_{\partial V_\mathrm{f}} \boldsymbol{n}P \,\mathrm{d}S = \int_{\partial V_\mathrm{f}} \boldsymbol{n}\phi \,\mathrm{d}S, \tag{2.179}$$

$$\boldsymbol{L}_\phi \equiv -\int_{\partial V_\mathrm{f}} \boldsymbol{x} \times \boldsymbol{n}P \,\mathrm{d}S = \int_{\partial V_\mathrm{f}} \boldsymbol{x} \times \boldsymbol{n}\phi \,\mathrm{d}S. \tag{2.180}$$

Note that by (2.174) the integrals of $\boldsymbol{n}\phi$ and $\boldsymbol{x} \times \boldsymbol{n}\phi$ over $\partial V_\infty$ have poor convergence property; but our concern here is the rate of change of these impulses, which is definitely finite. In fact, since $\partial V_\mathrm{f}$ consists of material surfaces, there is

$$\frac{\mathrm{d}}{\mathrm{d}t}\int_{\partial V_\mathrm{f}} \phi\boldsymbol{n} \,\mathrm{d}S = \int_{\partial V_\mathrm{f}} \frac{\mathrm{D}}{\mathrm{D}t}(\phi\boldsymbol{n} \,\mathrm{d}S), \quad \frac{\mathrm{d}}{\mathrm{d}t}\int_{\partial V_\mathrm{f}} \boldsymbol{x} \times \phi\boldsymbol{n} \,\mathrm{d}S = \int_{\partial V_\mathrm{f}} \frac{\mathrm{D}}{\mathrm{D}t}(\boldsymbol{x} \times \phi\boldsymbol{n} \,\mathrm{d}S).$$

Here, since now (2.26) is reduced to

$$\frac{\mathrm{D}}{\mathrm{D}t}(n_i \,\mathrm{d}S) = -\phi_{,ij} n_j \,\mathrm{d}S,$$

we have

$$\frac{\mathrm{D}}{\mathrm{D}t}(\phi n_i \,\mathrm{d}S) = [(\phi_{,t} + \phi_{,j}\phi_{,j})n_i - \phi\phi_{,ij}n_j] \,\mathrm{d}S,$$

where by using (2.173a) the last term integrates to

$$-\int_{\partial V_\mathrm{f}} \phi\phi_{,ij}n_j \,\mathrm{d}S = -\frac{1}{2}\int_{\partial V_\mathrm{f}} (\phi_{,j}\phi_{,j})n_i \,\mathrm{d}S.$$

Hence, by using (2.177), it follows that

$$\frac{\mathrm{d}}{\mathrm{d}t}\int_{\partial V_\mathrm{f}} \phi\boldsymbol{n} \,\mathrm{d}S = \int_{\partial V_\mathrm{f}} \left(\frac{\partial\phi}{\partial t} + \frac{1}{2}q^2\right)\boldsymbol{n} \,\mathrm{d}S = -\frac{1}{\rho}\int_{\partial B} p\boldsymbol{n} \,\mathrm{d}S, \tag{2.181}$$

where the integral over $\partial V_\infty$ with constant $p = p_\infty$ vanishes.

Similarly, for computing $\mathrm{d}\boldsymbol{L}_\phi/\mathrm{d}t$ there is

$$\frac{\mathrm{D}}{\mathrm{D}t}(\epsilon_{ijk}x_j\phi n_k \,\mathrm{d}S) = \epsilon_{ijk}[x_j(\phi_{,t} + \phi_{,l}\phi_{,l})n_k + \phi\phi_{,j}n_k - x_j\phi\phi_{,kl}n_l]\mathrm{d}S.$$

By casting the last two terms on the right to a volume integral over $B$ and simplifying the result, the volume integral can be transformed back to surface

integral and yields

$$\frac{\mathrm{d}}{\mathrm{d}t}\int_{\partial V_\mathrm{f}} \boldsymbol{x}\times\phi\boldsymbol{n}\,\mathrm{d}S = \int_{\partial V_\mathrm{f}} \boldsymbol{x}\times\left(\frac{\partial\phi}{\partial t}+\frac{1}{2}q^2\right)\boldsymbol{n}\,\mathrm{d}S = -\frac{1}{\rho}\int_{\partial B}\boldsymbol{x}\times p\boldsymbol{n}\,\mathrm{d}S. \quad (2.182)$$

Therefore, the force and moment acting to $\partial V_\mathrm{f}$ are

$$\boldsymbol{F} = -\int_{\partial B} p\boldsymbol{n}\,\mathrm{d}S = \rho\frac{\mathrm{d}\boldsymbol{I}_\phi}{\mathrm{d}t}, \quad (2.183)$$

$$\boldsymbol{M} = -\int_{\partial B} \boldsymbol{x}\times p\boldsymbol{n}\,\mathrm{d}S = \rho\frac{\mathrm{d}\boldsymbol{L}_\phi}{\mathrm{d}t}. \quad (2.184)$$

Specifically, assume $B$ moves with uniform velocity $\boldsymbol{b}=\boldsymbol{U}(t)$. In this case, since both (2.173a) and (2.173b) are linear, there must be $\phi = U_j\widehat{\phi}_j$, where $\widehat{\phi}_j$ is the potential caused by the same rigid body moving with *unit velocity along the $j$-direction*. Namely, $\widehat{\phi}_j$ satisfies (2.173a), while if $\boldsymbol{e}_j$ ($j=1,2,3$) are the Cartesian basis vectors, (2.173b) becomes

$$\boldsymbol{n}\cdot\nabla\widehat{\phi}_j = \boldsymbol{n}\cdot\boldsymbol{e}_j = n_j \ \text{ at } \ \partial B, \quad (2.185a)$$

$$\boldsymbol{n}\cdot\nabla\widehat{\phi}_j = 0 \ \text{ at infinity}. \quad (2.185b)$$

Therefore, we can define a tensor solely determined by the body's geometry:[15]

$$M_{ij} = \rho\int_{\partial B}\widehat{\phi}_i n_j\,\mathrm{d}S, \quad (2.186)$$

which is symmetric (Batchelor 1967). Once $M_{ij}$ is calculated for a given body, the potential flow caused by any translational motion of the body can be known at once.

Now, substituting $\phi = U_j\widehat{\phi}_j$ into (2.183) and noticing the integral over $\partial V_\infty$ plays no role, we obtain

$$\boldsymbol{F} = \mathbf{M}\cdot\dot{\boldsymbol{U}}, \quad (2.187)$$

where $\dot{\boldsymbol{U}} = \mathrm{d}\boldsymbol{U}/\mathrm{d}t$. Hence, the total force experienced by the body of mass $m_\mathrm{B}$ is

$$\boldsymbol{F}_\mathrm{B} = -(\mathbf{M}+m_\mathrm{B}\mathbf{I})\cdot\dot{\boldsymbol{U}}, \quad (2.188)$$

implying that $M_{ij}$ acts as a *virtual mass* (or apparent or added mass) as one calls it. Thus, in an acyclic potential flow a rigid body performing constant translation experiences no force. This is the classic *D'Alembert paradox* which will be revisited later in different contexts. Likewise, (2.175) is

[15] The approach can be generalized to rigid-body rotation, e.g., Batchelor (1967), but not to deformable body.

simplified to

$$K = \frac{\rho}{2} U_i \int_{\partial B} n_i \phi \, \mathrm{d}S = \frac{1}{2} U_i M_{ij} U_j, \tag{2.189}$$

so by (2.76),

$$\frac{\mathrm{d}K}{\mathrm{d}t} = UD = \dot{\boldsymbol{U}} \cdot \mathbf{M} \cdot \boldsymbol{U}, \tag{2.190}$$

where $D$ is the drag. Note that without the assumed acyclic feature of $\phi$ we cannot derive (2.183) and (2.184), and hence neither (2.187); but (2.189) is not affected. In this case the D'Alembert paradox can be said for drag only, and a finite lateral force perpendicular to $\boldsymbol{U}$ is not excluded, say a lift (see Sect. 4.4 and Chap. 11).

It should be stressed again that the result of this subsection can approximately represent a real viscous flow only in a portion of the flow domain and in the sense of effectively inviscid flow. There is no such thing like ideal fluid, and a globally effective potential flow is an oversimplified model. To quote Saffman (1981):

*"if $\boldsymbol{\omega} = \mathbf{0}$ everywhere in an incompressible fluid, then the fluid really ceases to be a fluid; it losses its infinite number of degrees of freedom, which makes possible the infinite variety of fluid motion, and becomes a flexible extension of the bodies whose movement generates the flow; bring the walls to rest and the fluid stops immediately."*

## Summary

1. The vorticity and vortex dynamics for Newtonian fluid is based on the general principles of fluid dynamics, especially the Navier–Skokes equations with small viscosity. The tangent continuity of velocity and surface forces across boundaries is of crucial importance for the vorticity generation from boundaries, which accordingly excludes any globally ideal fluid model in the study of vorticity dynamics. But at large Reynolds numbers a big portion of the flow can be treated effectively inviscid, to which the Euler equation applies. The viscous effect is significant only in thin layers with extremely high concentration of vorticity or dilatation. In the asymptotic limit of infinite Reynolds number (the Euler limit), these layers are treated as surfaces of tangent and normal discontinuities in an effectively inviscid flow.
2. The mathematic tool for understanding the decomposition and coupling of the fundamental kinematic and dynamic processes in a flow field is the Helmholtz decomposition and its modern development. The Helmholtz decomposition allows splitting a vector field into solenoidal and potential parts. It is sharpened by the Helmholtz–Hodge decomposition that ensures the uniqueness and functional orthogonality of the split parts, i.e., transverse and longitudinal vectors, respectively. A transverse vector is

always an axial or pseudovector with two independent components, which can be expressed explicitly (and at least locally) by two Clebsch variables. The helical-wave decomposition further splits the transverse part into two intrinsic polarity states, and any transverse vector can be expanded by a complete orthonormal set of curl-eigenvectors.

3. The fundamental processes in volumetric fluid motion are longitudinal compressing and transverse shearing, with governing dimensionless parameter being the Mach number and Reynolds number, respectively. The latter is more complicated since it is a vector process. There is yet a surface process due to fluid surface deformation. The explicit coexistence of these processes in the strain rate tensor, velocity gradient tensor, stress tensor, surface stress, and the dissipation roots in the very fundamental and simple triple decomposition (2.136). The coupling and decoupling of the two volumetric processes and a surface process in the governing dynamic equations and boundary conditions can then be examined systematically.
4. The representative variable for shearing process is always the vorticity vector $\boldsymbol{\omega}$, governed by vorticity transport equation. The representative variable for compressing process varies in different situations and formulations. Kinematically it is the dilatation $\vartheta$. Dynamically the choice of compressing variable is not unique. It can be the normal force $\Pi$, pressure or density as in classic acoustics, or the total enthalpy as in vortex-sound theory. It can also be the velocity potential $\phi$ as in classic high-speed aerodynamics. The process is governed by the Howe equation.
5. For a Newtonian fluid with constant shear viscosity $\mu$, the compressing variable $\Pi$ and the shearing variable $\mu\boldsymbol{\omega}$ form a reduced stress tensor $\widehat{\mathbf{T}}$, having three independent components. It is the Helmholtz tensor potential of the resultant surface force per unit volume. $\widehat{\mathbf{T}}$ can replace the full stress tensor $\mathbf{T}$ in the Cauchy motion equation and the kinetic-energy balance without affecting any result. The remaining part of $\mathbf{T}$ comes from surface deformation rate tensor $\mathbf{B}$. This $\mathbf{B}$-part enters the angular momentum balance, its rate of work is always directly and locally transferred to heat and thereby affects the internal-energy increase only.
6. The two fundamental volumetric processes are generically coupled through two mechanisms. In the interior of the flows the coupling is caused by the nonlinearity in advection (mainly the Lamb vector) and the nonlinear involvement of thermodynamics especially in baroclinic flows. At a solid boundary a linear viscous coupling is caused by the momentum balance, which occurs whenever the longitudinal and transverse variables are not uniformly distributed on the boundary. But the role of one process in the evolution of another is not equally important. In certain situations the shearing process is dominant and the compressing process is a byproduct, e.g., vortex sound; while in some other situations their relative importance is opposite (cf. Sect. 4.1.2).
7. In some purified situations the two fundamental processes are decoupled. In a viscous incompressible flow there only exists shearing process and

all waves are transverse. In contrast, in an irrotational compressible flow there only exists compressing process and all waves are longitudinal. However, these two extreme situations are not of equal importance. While the viscous incompressible flow is a good approximation of a big class of real flows, No real flow can be completely irrotational in its full domain. Finally, incompressible potential flow belongs to neither compressing process nor shearing process, but is an inevitable constituent for satisfying boundary conditions and coupled with other constituents.

# 3

# Vorticity Kinematics

Compared with general fluid kinematics reviewed in Sect. 2.1, the content of vorticity kinematics is much more abundant (Truesdell 1954; Truesdell and Toupin 1960). It covers even a major part of vorticity and vortex dynamics, and makes this chapter very heavy. We begin with the physical interpretation of vorticity (Sect. 3.1), and then consider the spatial properties of a vorticity field (Sects. 3.2–3.4), followed by the temporal evolution of vorticity and other related quantities (Sect. 3.5). With a few exceptions, no kinetics will be introduced to the shearing process, and hence the results possess general validity. This chapter concludes with a general theory of circulation-preserving flows (Sect. 3.6), where the kinetics never appears in shearing process.

While most of the materials are presented in terms of Eulerian description, we shall gain some unique insight by using Lagrangian description with relevant mathematical details given in Appendix A.4.

## 3.1 Physical Interpretation of Vorticity

As seen in Chap. 1, the concept of vortices is very intuitive but the rigorous definition of a vortex is difficult, see Sect. 6.6. Lugt (1983, 1996) observed that the situation for the vorticity is opposite: its physical interpretation is not as self-evident as its mathematical definition. Before developing the general theory of vorticity kinematics, therefore, it is necessary to gain a good understanding of this key vector.

In Sect. 2.1.2, the vorticity is roughly interpreted as twice of the angular velocity of a fluid element. This interpretation needs elaboration and refinement. First of all, the concept "angular velocity " itself, originally defined for rigid motion, needs be extended when applied to a deformable fluid. Consider a small circular disk $\mathcal{A}$ of radius $\epsilon$ centered at $\boldsymbol{x}$, with unit normal $\boldsymbol{n}$ (Fig. 3.1). If $\mathcal{A}$ is rigid, its angular velocity around $\boldsymbol{n}$ (the projection of angular velocity vector $\boldsymbol{W}$ onto $\boldsymbol{n}$) is simply the tangent velocity along $\partial\mathcal{A}$ divided by $\epsilon$. But for a fluid disk the tangential velocity is variable and an average must be

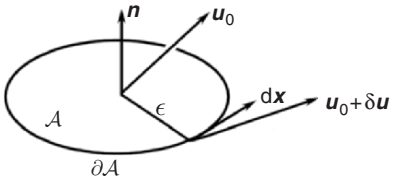


**Fig. 3.1.** A fluid disk for defining angular velocity

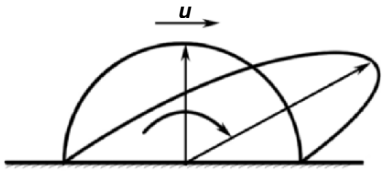


**Fig. 3.2.** Vorticity on a boundary

used. Thus a natural extension of the concept of angular velocity around $\boldsymbol{n}$ is (Batchelor 1967)

$$\begin{aligned}\boldsymbol{W}\cdot\boldsymbol{n} &= \epsilon^{-1}\,(\text{averaged tangential velocity along } \partial\mathcal{A})\\ &= \frac{1}{2\pi\epsilon^2}\oint_{\partial\mathcal{A}}\boldsymbol{u}\cdot\mathrm{d}\boldsymbol{x} = \frac{1}{2\pi\epsilon^2}\int_{\mathcal{A}}\boldsymbol{\omega}\cdot\boldsymbol{n}\,\mathrm{d}S,\end{aligned}\tag{3.1}$$

which approaches $\boldsymbol{\omega}\cdot\boldsymbol{n}/2$ as $\epsilon\to 0$. Since $\boldsymbol{n}$ is arbitrary, $\boldsymbol{\omega}(\boldsymbol{x})/2$ can be interpreted as the angular velocity of the fluid element centered at $\boldsymbol{x}$. However, this interpretation cannot be applied to the vorticity right on a boundary $\mathcal{B}$, although the boundary vorticity is certainly meaningful and important as can be seen from (2.142) and (2.151b). The situation for the latter is sketched in Fig. 3.2, where neither the hemispheric element can rotate as a whole, nor can there be a fluid disk centered at $\mathcal{B}$ with normal vector tangent to it.

A unified interpretation of vorticity requires something which rotates as a rigid body, at least locally and instantaneously, both inside the fluid and on boundaries. In Sect. 2.1.2 we have seen that the principal axes of the strain-rate tensor have this property. Thus, it is more precise to interpret the vorticity $\boldsymbol{\omega}(\boldsymbol{x})$ as *twice the angular velocity of the instantaneous principal axes of the strain-rate tensor of an fluid element centered at* $\boldsymbol{x}$.[1]

Interpreting the vorticity in terms of angular velocity, however, by no means implies that the angular velocity is a more fundamental concept than vorticity. On the contrary, as indicated by (3.1), the latter is an extension of the former. To see this more clearly, we express the vorticity in an *intrinsic coordinate system* moving along a streamline $C$. At each point on $C$ there is an orthonormal triad consisting of the tangent vector $\boldsymbol{t}$, the principal normal $\boldsymbol{n}$ (toward the center of curvature), and the binormal $\boldsymbol{b}=\boldsymbol{t}\times\boldsymbol{n}$ (see A.3.1).

[1] According to Truesdell (1954), this interpretation is attributed to Boussinesq.

In this frame the velocity is $\boldsymbol{u} = q\boldsymbol{t}$ with $q = |\boldsymbol{u}|$, thus

$$\boldsymbol{\omega} = \nabla \times (q\boldsymbol{t}) = \nabla q \times \boldsymbol{t} + q\nabla \times \boldsymbol{t},$$

which as shown in Sect. A.3.1 yields

$$\boldsymbol{\omega} = \xi q\boldsymbol{t} + \frac{\partial q}{\partial b}\boldsymbol{n} + \left(\kappa q - \frac{\partial q}{\partial n}\right)\boldsymbol{b}, \tag{3.2}$$

where $\kappa$ is the curvature of $C$ and

$$\xi \equiv \boldsymbol{t} \cdot (\nabla \times \boldsymbol{t}) = \boldsymbol{b} \cdot \frac{\partial \boldsymbol{t}}{\partial n} - \boldsymbol{n} \cdot \frac{\partial \boldsymbol{t}}{\partial b} \tag{3.3}$$

is called the *torsion of neighboring vector lines* (Truesdell 1954). Equation (3.2) reveals the inherent complication of a full physical understanding of the vorticity. Note that a kink of the streamline with $\kappa \to \infty$ must have $q = 0$, for otherwise there would be $|\boldsymbol{\omega}| \to \infty$ there.

A special case is two-dimensional flow, where the only nonzero component of $\boldsymbol{\omega}$ is along the $\boldsymbol{b} = \boldsymbol{e}_3$ direction and (3.2) is reduced to

$$\boldsymbol{\omega} = \omega\boldsymbol{e}_3 = \left(\frac{q}{r} + \frac{\partial q}{\partial r}\right)\boldsymbol{e}_3 = \frac{1}{r}\frac{\partial (rq)}{\partial r}\boldsymbol{e}_3 \tag{3.4}$$

in which $r = \kappa^{-1}$ is the radius of curvature and $\mathrm{d}r = -\mathrm{d}n$. An axisymmetric rectilinear vortex is a further special case of (3.4). The two terms, $q/r$ and $\partial q/\partial r$, represent *trajectory rotation* and *spin* of a fluid element, respectively, see Fig. 3.3. Only for uniform vorticity $\omega = 2W$, say (so the vorticity on $C$ is

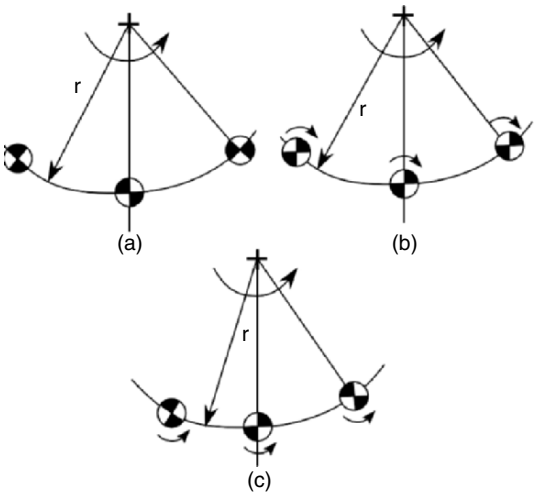


**Fig. 3.3.** Trajectory rotation and spin of a fluid element. (**a**) Rigidly rotating flow; (**b**) irrotational flow; and (**c**) generic rotational flow

the same as that at the curvature center), we will have $q/r = \partial q/\partial r = W$ and the flow behaves as a rigid rotation with angular velocity $W$. In contrast, if in a flow both $q/r$ and $\partial q/\partial r$ exist but $q/r = -\partial q/\partial r$ and hence $q = C/r$, then the flow is irrotational with a singularity at $r = 0$. In more general case each point has its own $\boldsymbol{\omega}$ as the angular velocity $2\boldsymbol{W}$ of the principal axes of strain-rate tensor. Moreover, as $r \to \infty$, a rigid (or global) rotation is impossible but a local spin of fluid elements may still exist if there is a shearing.

In a three-dimensional flow the situation is more complicated, where the vorticity may also have components along the $\boldsymbol{t}$ and $\boldsymbol{n}$ directions. An $\omega_n$ will appear if $q$ depends on $b$, and $\omega_t$ will appear if the torsion of neighboring streamlines does not vanish.

In literature the vorticity has sometimes been interpreted as the angular momentum $\boldsymbol{M}$ of a fluid element. This is easily misleading and special care is necessary, because although both describe fluid rotation they do in different ways. By definition, the vorticity is a local quantity but the angular momentum given in (2.51) is an integrated quantity depending on one's choice of a common origin $\boldsymbol{x}_0$ about which the moment is taken. Assume a constant density $\rho$, we may further compare a vorticity integral with the angular momentum per unit mass

$$\frac{\boldsymbol{M}}{\rho} = \int_V \boldsymbol{r} \times \boldsymbol{u} \mathrm{d}V, \quad \boldsymbol{r} = \boldsymbol{x} - \boldsymbol{x}_0. \tag{3.5}$$

The dimension of $\boldsymbol{\omega}$ and (3.5) suggests that $\boldsymbol{M}/\rho$ should be related to an integrated second-order vector moment of the vorticity, which may take three forms as appearing in and related by the identity

$$\boldsymbol{r} \times (\boldsymbol{r} \times \boldsymbol{\omega}) = \boldsymbol{r}(\boldsymbol{r} \cdot \boldsymbol{\omega}) - r^2 \boldsymbol{\omega}. \tag{3.6}$$

Each of these vorticity moments is related to $\boldsymbol{M}/\rho$ by an identity, see Appendix A.2.2. One of these reads, for example,

$$\int_V \boldsymbol{r} \times \boldsymbol{u} \, \mathrm{d}V = -\frac{1}{2} \int_V r^2 \boldsymbol{\omega} \, \mathrm{d}V + \frac{1}{2} \int_{\partial V} r^2 \boldsymbol{n} \times \boldsymbol{u} \, \mathrm{d}S. \tag{3.7}$$

Thus, $\boldsymbol{M}/\rho$ can be viewed as any one of the three second-order vorticity moments plus boundary contribution. To interpret $\boldsymbol{\omega}$ by $\boldsymbol{M}/\rho$, therefore, we need some further specifications.

First, let $\boldsymbol{u}(\boldsymbol{x}) = \boldsymbol{u}_0 + \boldsymbol{\delta u}$ where $\boldsymbol{u}_0 = \boldsymbol{u}(\boldsymbol{x}_0)$, it is easily seen that $\boldsymbol{u}_0$ will have no contribution to the boundary integral in (3.7) if $\partial V$ has *spherical symmetry*. Then, let $\boldsymbol{x}_0$ be the mass center of a sphere of radius $\epsilon$, such that $\boldsymbol{r} = \epsilon \boldsymbol{n}$ on $\partial V$. In this case (3.7) is reduced to

$$\int_V \boldsymbol{r} \times \boldsymbol{u} \, \mathrm{d}V = \frac{1}{2} \int_V (\epsilon^2 - r^2) \boldsymbol{\omega} \, \mathrm{d}V, \tag{3.8}$$

so $\boldsymbol{M}/\rho$ is solely related to vorticity moments.

Next, let $\epsilon$ be sufficiently small such that inside the sphere $\boldsymbol{\omega}(\boldsymbol{x}) = \boldsymbol{\omega}(\boldsymbol{x}_0)$ is constant. Then by (2.24) we may replace $\delta\boldsymbol{u}$ by $\boldsymbol{\omega} \times \boldsymbol{r}/2$. Substituting this into the left-hand side of (3.8) then yields

$$\boldsymbol{M} = \frac{1}{2}\boldsymbol{\omega} \cdot \mathbf{J}, \tag{3.9}$$

where

$$\mathbf{J} = \rho \int_V (r^2\mathbf{I} - \boldsymbol{r}\boldsymbol{r})\,\mathrm{d}V \quad \text{or} \quad J_{ij} = \rho \int_V (r^2\delta_{ij} - r_i r_j)\,\mathrm{d}V \tag{3.10}$$

is the symmetric tensor of *moment of inertia* of the fluid in $V$ (e.g., Landau and Lifshitz 1976). For a sphere of mass $m = \rho V$ there is $\mathbf{J} = 2m\epsilon^2\mathbf{I}/5$, hence the angular momentum of the sphere of unit volume with respect to its mass center is

$$\frac{\boldsymbol{M}}{V} = \frac{1}{5}\rho\epsilon^2\boldsymbol{\omega},$$

indicating that for such a spherical element the vorticity is proportional to the angular momentum (Lighthill 1986b; Saffman 1992). As $V$ further shrinks to a point, however, the vorticity remains a finite vector but the angular momentum vanishes as $\epsilon^5$. An infinitesimal fluid element has an angular velocity but no angular momentum. Nevertheless, since $\boldsymbol{\omega}$ is a quantity defined on a fluid element per unit mass, it is fairer to compare it with the angular momentum per unit moment of inertia that remains finite too as $\epsilon \to 0$.

The above analysis indicates that the vorticity may be interpreted by angular momentum only under very restrictive conditions. Alternatively, one might be tempted to consider the angular momentum of a fluid element as $\nabla \times (\rho\boldsymbol{u}) = \rho\boldsymbol{\omega} + \nabla\rho \times \boldsymbol{u}$, which is, however, not Galilean invariant. Thus the vorticity, with kinematic dimension, is the unique measure of the rotation status of a fluid element. This is why vorticity transport equations are always written in terms of unit mass rather than unit volume.

## 3.2 Vorticity Integrals and Far-Field Asymptotics

With a single exception on the far-field vorticity in Sect. 3.2.1 where dynamics has to enter, in this and the following two sections we consider the spatial properties of the vorticity field at a fixed time $t$. These properties are based on the definition of vorticity $\boldsymbol{\omega} = \nabla \times \boldsymbol{u}$ and its direct consequence $\nabla \cdot \boldsymbol{\omega} = 0$, and are therefore universally true. Unless stated otherwise, we always consider viscous fluid so that the no-slip condition (2.67b) holds at boundary.

### 3.2.1 Integral Theorems

All the spatial integral properties of vorticity field are based on its divergence-free feature, which can be derived by various methods (Truesdell 1954; Howard

1957). We start from a single identity. Let $\mathcal{F}$ be any tensor and $\boldsymbol{f} = \nabla \times \boldsymbol{A}$ be any solenoidal vector field, such that $\boldsymbol{f} \cdot \nabla \mathcal{F} = \nabla \cdot (\boldsymbol{f}\mathcal{F})$. Then by the generalized Gauss theorem there is

$$\int_V \boldsymbol{f} \cdot \nabla \mathcal{F} \, \mathrm{d}V = \int_{\partial V} (\boldsymbol{n} \cdot \boldsymbol{f}) \mathcal{F} \, \mathrm{d}S. \tag{3.11a}$$

Namely, The volume integral of $\boldsymbol{f} \cdot \nabla \mathcal{F}$ is completely determined by the value of $\mathcal{F}$ and normal component of $\boldsymbol{f}$ on the boundary. In particular, if $\boldsymbol{f}_\perp$ is a transverse vector satisfying boundary condition (2.98a), then

$$\int_V \boldsymbol{f}_\perp \cdot \nabla \mathcal{F} \, \mathrm{d}V = 0. \tag{3.11b}$$

Now, setting $\boldsymbol{f} = \boldsymbol{\omega}$ yields a general *vorticity integral identity*

$$\int_V \boldsymbol{\omega} \cdot \nabla \mathcal{F} \, \mathrm{d}V = \int_{\partial V} (\boldsymbol{n} \cdot \boldsymbol{\omega}) \mathcal{F} \, \mathrm{d}S. \tag{3.12}$$

If $\partial V$ is nonrotating such that by (2.69) there is $\boldsymbol{\omega} \cdot \boldsymbol{n} = 0$ on $\partial V$, or if $\partial V$ extends to infinity with vorticity decaying sufficiently fast, then $\boldsymbol{\omega} = \boldsymbol{\omega}_\perp$ and (3.11b) applies. Obviously, by assigning $\mathcal{F}$ as different quantities, we may obtain infinitely many conserved vorticity integrals. Among these the following ones are most useful, where the vorticity appears as the only physical quantity.

The simplest application of (3.12) results from setting $\mathcal{F} = 1$, implying

$$\int_{\partial V} \boldsymbol{\omega} \cdot \boldsymbol{n} \, \mathrm{d}S = 0, \tag{3.13}$$

which is evidently the direct consequence of $\nabla \cdot \boldsymbol{\omega} = 0$. Now, a curve in a flow field tangent to the vorticity $\boldsymbol{\omega}$ at every point is called a *vorticity line*. A tube-like surface formed by all vorticity lines passing through a closed curve, which itself is not a vorticity line and can shrink to a point inside the fluid, is called a *vorticity tube* ("*vortex tube*" in most publications).[2] Let two sectional surfaces $S_\alpha$ with boundary loops $C_\alpha$ ($\alpha = 1, 2$) cut the tube to form a volume $V$, with $S_3$ being its side boundary, see Fig. 3.4. Then it is well known that, along with (2.31), (3.13) implies

$$\int_{S_1} \boldsymbol{\omega} \cdot \boldsymbol{n} \, \mathrm{d}S = \int_{S_2} \boldsymbol{\omega} \cdot \boldsymbol{n} \, \mathrm{d}S \quad \text{or} \quad \oint_{C_1} \boldsymbol{u} \cdot \mathrm{d}\boldsymbol{x} = \oint_{C_2} \boldsymbol{u} \cdot \mathrm{d}\boldsymbol{x}.$$

Therefore, we arrive at a fundamental theorem of Helmholtz (1858).

[2] The popular name "vortex tube" is imprecise, because the rigorous definition of a vortex is still a controversial issue, see Sect. 6.6. This name is also easily misleading, since in general the side boundary of a vortex (as qualitatively identified in the beginning of Chap. 1 or rationally defined in Sect. 6.6) is not a vorticity surface.

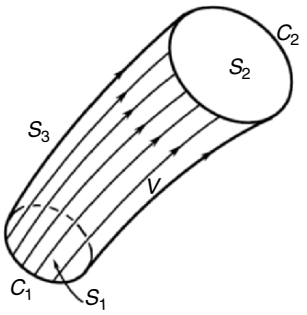


**Fig. 3.4.** A vorticity tube

**The First Helmholtz Vorticity Theorem.** *The integrated vorticity flux over a cross surface of a vorticity tube or the circulation of the tube is constant, independent of the shape and location of the cross surface or its boundary over which the integrals are estimated.*

Owing to this theorem, the integrated vorticity flux or circulation is a proper measure of the *strength* of a vorticity tube. If a cross surface of a vorticity tube shrinks to a point, then the vorticity there must be infinity, which is impossible. Therefore, *vorticity tubes cannot terminate inside a fluid*; they must form closed loops or extend through an interface to another fluid. Note that due to (2.69) these tubes cannot terminate at a nonrotating solid boundary either, on which the no-slip condition holds.[3] Rather, as a vorticity tube approaches such a boundary, (2.69) forces the sectional area of the vorticity tube to increase infinitely like a horn, in order to keep its constant strength.

This situation is illustrated in Fig. 3.5a, where a *tornado-like vortex* hits a nonrotating wall. The figure also shows that a single vorticity line rather than a vorticity tube can terminate at the wall (unlike vorticity tubes, the vorticity can vary along a vorticity line and becomes zero when the line hits the boundary). Thus, if one creates a vortex in a cup of water with a spoon, its vorticity tubes must turn to the direction along the bottom and climb up along the side wall, forming a boundary layer with vorticity of the sign opposite to that of the main vortex, as in Fig. 3.5b. Fig. 3.5c is another familiar example, where a pair of vortices shed from the wing tips of an aircraft, known as *trailing vortices* or *wing-tip vortices*. This vortex pair must also form a closed loop: its upstream segment consists of the boundary layers of upper and lower surfaces of the wing and is the source of the lift and drag (Chap. 11), while its downstream segment is called the *starting vortex*

[3] This point had been ignored until it was first clarified by Kellogg (1929). See also Serrin (1959) and Lighthill (1963). The vorticity-tube termination on a nonrotating wall would be allowable if the fluid is ideal and only impermeable condition (2.67a) is imposed. This is, however, unrealistic, since then the main source of vortices would be lost.

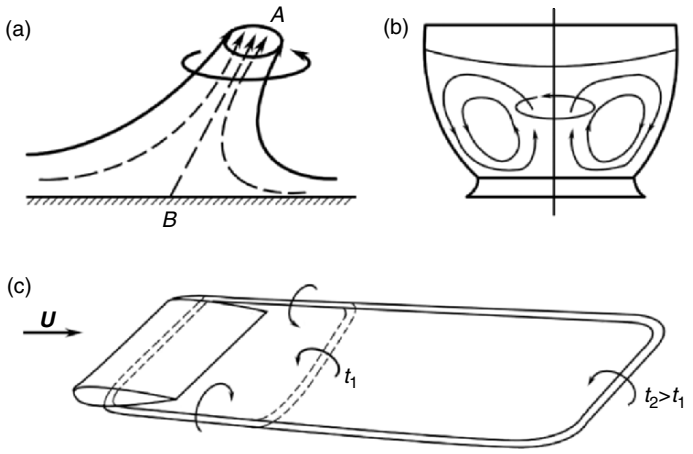


**Fig. 3.5.** (**a**) Vorticity lines in a tornado-like vortex. (**b**) Vorticity lines in a cup of rotating water. (**c**) Vortex system associated with a flying wing

*system* which is about at rest relative to the surrounding air. But the vortex loop in this figure is merely a highly simplified sketch. The trailing vortices are actually unstable and will break into vortex rings (Sect. 9.4; Fig. 9.25). Thus, rather than all the way connecting with the starting vortices, the real downstream end of the wing vortex system is at the location where the first vortex ring is formed.

If a flow field has a material boundary $\mathcal{B}$, either solid wall or an interface with another fluid, the velocity adherence (2.67) on $\mathcal{B}$ allows us to conveniently consider the fluid plus solid or another fluid as a single *unbounded continuous system* in which the velocity is everywhere continuous, and across $\mathcal{B}$ the *normal component* of vorticity is also continuous. The first Helmholtz theorem still applies to this unbounded system where all vorticity tubes remain to be closed loops. But, due to the discontinuity of tangent vorticity at $\mathcal{B}$ (see Fig. 2.5), when a fluid vorticity tube reaches a rotating $\mathcal{B}$ it must be split into a normal tube and a tangent tube. The former goes across $\mathcal{B}$ with the solid or another fluid as a continuation of the tube, while the latter has to go around $\mathcal{B}$.

Next to (3.13), we now let $\mathcal{F}$ in (3.12) be the position vector $\boldsymbol{x}$. Then since $x_{i,j} = \delta_{ij}$, we obtain at once a general formula for total vorticity:

$$\int_V \boldsymbol{\omega}\,\mathrm{d}V = \int_{\partial V} (\boldsymbol{n}\cdot\boldsymbol{\omega})\boldsymbol{x}\,\mathrm{d}S. \tag{3.14}$$

In particular, for nonrotating boundary or if $V$ is unbounded with $|\boldsymbol{\omega}| \sim |\boldsymbol{x}|^{-k}$ and $k > 3$ as $|\boldsymbol{x}| \to \infty$, (3.14) is reduced to the *Föppl theorem of total vorticity conservation* (Föppl 1897)

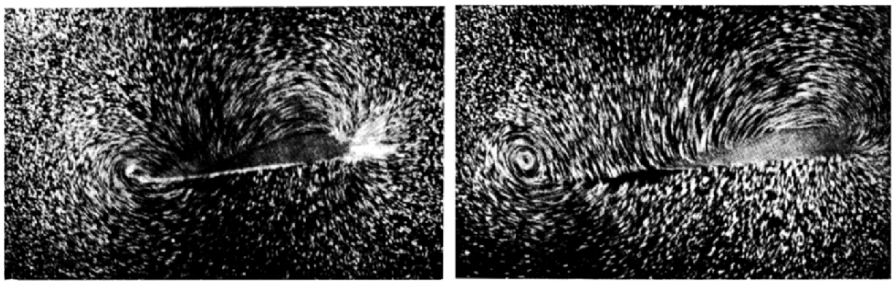

**Fig. 3.6.** The streamlines showing the formation of starting vortex and lifting vortex as an airfoil begins to move (from *left* to *right*). (**a**) Soon after the airfoil has begun to move, (**b**) after the airfoil has moved steadily through about one chord length. From Prandtl and Tietjens (1934)

$$\int_V \boldsymbol{\omega}\, \mathrm{d}V = \mathbf{0} \tag{3.15}$$

as a special case of a general integral property (3.11b) of a pure transverse vector in $V$. This theorem implies that the contribution of one piece of a vorticity tube to the total vorticity must be cancelled by another piece with vorticity of opposite sign, which is possible only if all vorticity tubes are closed. Therefore, Helmholtz's first theorem and Föppl's theorem reflect the same solenoidal nature of the vorticity field from different aspects. Equation (3.15) also applies to the abovementioned continuous system of fluid plus solid.

In two-dimensional flows on the $(x, y)$-plane, $\boldsymbol{\omega} = \omega \boldsymbol{e}_z$ and the integral of $\boldsymbol{\omega}$ over $V$ becomes the total circulation along the boundary line of the flow domain. In this case (3.14) does not apply,[4] because the vorticity lines do not form closed loops. But another general kinematic result holds, known as the **total circulation conservation theorem**: *For an externally unbounded fluid at rest at infinity, there is*

$$\frac{\mathrm{d}\Gamma_\infty}{\mathrm{d}t} = 0. \tag{3.16}$$

The proof is deferred to the beginning of Sect. 3.5.2. Thus, if initially there is $\Gamma_\infty = 0$, it will be always so. This is true for any fluid motion starting from rest. A nonzero $\Gamma_\infty$ implies that the velocity decays as slowly as $|\boldsymbol{x}|^{-1}$, which must imply unrealistically an infinite total kinetic energy and angular momentum.[5] Therefore, one may simply set $\Gamma_\infty = 0$. The appearance of $\Gamma_\infty$ in some of our later formulas is merely for completeness and illustrating its role.

As a famous demonstration of (3.16), Fig. 3.6 shows a flow visualization photo taken from Prandtl and Tietjens (1934), where an airfoil moves (from

[4] This fact can be verified by considering a deck-like volume on the flow plane with unit thickness. Applying (3.14) to the deck would lead to trivial result $0 = 0$.

[5] This can be most easily verified for the potential flow induced by a single line vortex given by (3.33).

left to right) in an undisturbed fluid a short time after start. The picture can be viewed as the mid-span portion of Fig. 3.5c. The vorticity shed from the airfoil forms a concentrated vortex, which is the two-dimensional version of the *starting vortex* with a circulation $\Gamma_{\text{start}} < 0$. Thus by (3.16) there must be a circulation around the airfoil with circulation $\Gamma_{\text{airfoil}} = -\Gamma_{\text{start}}$, which is the root of the lift (Chap. 11).

More generally, again start from (3.12) but assign $\mathcal{F}$ as a tensor of rank $n$ generated by the product of $n$ position vectors:

$$\mathcal{F} = \boldsymbol{x}^{(n)} \equiv \boldsymbol{x}\boldsymbol{x}\ldots\boldsymbol{x}.$$

Then on the left-hand side of (3.12) we have

$$\begin{aligned}\omega_l(x_i x_j \ldots x_k)_{,l} &= \omega_l(\delta_{il}x_j \ldots x_k + x_i\delta_{jl}x_k + \cdots + x_i x_j \ldots \delta_{kl}) \\ &= \omega_i x_j \ldots x_k + x_i\omega_j \ldots x_k + \cdots + x_i x_j \ldots \omega_k,\end{aligned}$$

where the last expression defines a *symmetric vorticity moment* of order $m = n - 1$, denoted by

$$\{\boldsymbol{x}^{(m)}\boldsymbol{\omega}\} \equiv \boldsymbol{x}^{(m)}\boldsymbol{\omega} + \boldsymbol{x}^{(m-1)}\boldsymbol{\omega}\boldsymbol{x} + \ldots + \boldsymbol{\omega}\boldsymbol{x}^{(m)}. \tag{3.17a}$$

Thus (3.12) now yields the *vorticity moment theorem* (Truesdell 1954)

$$\int_V \{\boldsymbol{x}^{(m)}\boldsymbol{\omega}\}\mathrm{d}V = \int_{\partial V} (\boldsymbol{n}\cdot\boldsymbol{\omega})\boldsymbol{x}^{(m+1)}\mathrm{d}S, \tag{3.17b}$$

showing that *the integrated effect of the nth symmetric vorticity moment depends solely on the boundary distribution of normal vorticity.* Equations (3.13) and (3.14) are the simplest cases of (3.17) with $n = 0$ and 1 respectively. Once again this theorem applies only to three-dimensional flows.

In an unbounded fluid as we often encounter, whether (3.17b) is meaningful depends on the convergence of the surface integral. This (and many other surface integrals involving vorticity to be studied later) requires a general estimate of the vorticity decay rate at far field. Here we state the result, leaving its proof and some discussion to the end of this section.

**Theorem.** *Let an externally unbounded incompressible fluid start to be in motion from rest at $t = 0$, and assume the vorticity of the flow is initially confined in a finite region. Then at any finite $t < \infty$, the vorticity at far field decays exponentially:*

$$|\boldsymbol{\omega}| \sim \mathrm{O}(e^{-ax}), \quad a > 0, \quad x \equiv |\boldsymbol{x}| \to \infty. \tag{3.18}$$

Under the condition of the theorem, for externally unbounded flow the outer boundary integral in (3.17) for any $m$ can be dropped. Thus, denote $\langle\mathcal{F}\rangle \equiv \int \mathcal{F}\mathrm{d}V$ for neatness, there is $\langle\{\boldsymbol{x}^{(m)}\boldsymbol{\omega}\}\rangle = \boldsymbol{0}$, or in component form

$$\langle x_i x_j \ldots \omega_k\rangle + \cdots + \langle x_i\omega_j \ldots x_k\rangle + \langle\omega_i x_j \ldots x_k\rangle = 0. \tag{3.19}$$

Integral relations like (3.19) are known as *consistency conditions*, which are necessary for a vorticity field to be divergence-free. These conditions can be used to determine the far field asymptotic behavior of velocity, see Sect. 3.2.3, and to control numerical error in computations where an unbounded domain is always approximated by a bounded one. To understand what is meant by (3.19), we first note that for $m = 1$ there is $\langle \boldsymbol{x}\boldsymbol{\omega} + \boldsymbol{\omega}\boldsymbol{x} \rangle = \mathbf{0}$, indicating that the tensor $\langle \boldsymbol{x}\boldsymbol{\omega} \rangle$ is anti-symmetric with only three independent components:

$$\langle x_i \omega_j \rangle = \frac{1}{2} \langle x_i \omega_j - \omega_i x_j \rangle. \tag{3.20a}$$

Similarly, for $m = 2$, by taking $i = j$, $j = k$, and $k = l$ in turn, and letting all of them be different, respectively, we obtain 10 constraint equations

$$\left.\begin{aligned} \langle x_i^2 \omega_i \rangle = 0, \quad & i, j = 1, 2, 3 \quad \text{(no summation)} \\ \langle x_i^2 \omega_j \rangle + 2\langle x_i \omega_i x_j \rangle = 0, \quad & i, j = 1, 2, 3, \ i \neq j \\ \langle x_1 x_2 \omega_3 \rangle + \langle x_2 x_3 \omega_1 \rangle + \langle x_3 x_1 \omega_2 \rangle = 0 & \end{aligned}\right\} \tag{3.20b}$$

Because $x_i x_j = x_j x_i$, there are 18 second-order moments, thus only 8 linear combinations of the second moments are independent (Ting 1983). In general, the number of $m$th moment is $3(m+2)(m+1)/2$, and the number of constraint equations obtained from (3.19) is $(m + 3)(m + 2)/2$. Thus the number of independent combinations of the moments, say $N(m)$, is

$$N(m) = \frac{3}{2}(m + 2)(m + 1) - \frac{1}{2}(m + 3)(m + 2) = m(m + 2). \tag{3.21}$$

There remains the proof of (3.18). Following Wu (1982), we cast the incompressible vorticity transport equation (2.168) to an inhomogeneous diffusion equation:

$$\left( \frac{\partial}{\partial t} - \nu_0 \nabla^2 \right) \boldsymbol{\omega} = \boldsymbol{F}, \quad \boldsymbol{F} \equiv -\nabla \times (\boldsymbol{\omega} \times \boldsymbol{u})$$

of which the solution structure can be qualitatively analyzed by its fundamental solution

$$G^*(\boldsymbol{r}, \tau) = \frac{H(\tau)}{(4\pi\nu\tau)^{n/2}} \exp\left( -\frac{|\boldsymbol{r}|^2}{4\nu\tau} \right), \quad \boldsymbol{r} = \boldsymbol{x} - \boldsymbol{x}', \quad \tau = t - t', \tag{3.22}$$

where $H$ is the Heaviside step function and $n = 2, 3$ is the spatial dimension. Thus, for arbitrary volume $V$ there is

$$\begin{aligned} \boldsymbol{\omega}(\boldsymbol{x}, t) = & \int_V (G^* \boldsymbol{\omega}')|_{t'=0} \, \mathrm{d}V' + \int_0^t \mathrm{d}t' \int_V G^* \boldsymbol{F}' \, \mathrm{d}V' \\ & + \int_0^t \mathrm{d}t' \int_{\partial V} \nu \left( G^* \frac{\partial \boldsymbol{\omega}'}{\partial n} - \boldsymbol{\omega}' \frac{\partial G^*}{\partial n} \right) \mathrm{d}S', \end{aligned} \tag{3.23}$$

where the prime means taking the value at $(\boldsymbol{x}', t')$. Now, without really solving for $\boldsymbol{\omega}$, it can be seen that as long as $t < \infty$ the vorticity field must be confined

to a finite region since it is so initially. Then, on the righthand side of (3.23) the vorticity appears homogeneously, so the integration variable $\boldsymbol{x}'$ is bounded. But the field point $\boldsymbol{x}$ can be arbitrarily far away from the body, permitting $|\boldsymbol{r}| \to \infty$. Because $G^*$ also appears homogeneously, from (3.22) we obtain (3.18) at once.

An inspection of the above proof indicates that the validity of (3.18) can be extended to a vorticity field governed by the general transport equation (2.166). In fact, the only additional condition is that $\nabla \times (T\nabla s + \boldsymbol{\eta}')$ must be confined in a finite region in the entire time interval $[0, t]$. This is possible because any long-range propagation of disturbance caused by $T\nabla s + \boldsymbol{\eta}'$ will take the form of sound wave, which is eliminated by the curl.

It should be stressed that the far-field behavior of the vorticity field in a strictly steady and externally unbounded flow can be very different from (3.18), see Sect. 4.2.3. However, such a flow does not exist in reality and the steadiness is always an approximate concept. If a body has been in uniform translational motion for $t \gg 1$ after start but still $t < \infty$, the influence of its far-wake unsteady evolution on the flow around the body can be neglected, let alone the influence of the starting vortex system. Then in the frame of reference fixed to the body the near-field flow can well be considered steady, which holds at a large but finite distance from the body. This is all what the concept of steadiness is about. Therefore, assuming $t < \infty$ and including the starting vortex system in the flow domain does not conflict the near-field steadiness at all.

### 3.2.2 Biot–Savart Formula

An important kinematic aspect of the vorticity and dilatation is the relations of their distribution to the velocity field, in which the time evolution is not involved. For a given velocity field $\boldsymbol{u}$ these relations are nothing but the definition (2.20) of $\vartheta$ and $\boldsymbol{\omega}$. Our interest here is the inverse problem, the determination of $\boldsymbol{u}$ from an $(\boldsymbol{\omega}, \vartheta)$ field *specified* in a flow domain $V$. Then (2.20) becomes a pair of differential equations for $\boldsymbol{u}$:

$$\nabla \cdot \boldsymbol{u} = \vartheta, \quad \nabla \times \boldsymbol{u} = \boldsymbol{\omega} \tag{3.24a,b}$$

of which the solvability is ensured by the compatibility conditions

$$\int_V \vartheta \, \mathrm{d}V = \oint_{\partial V} u_n \, \mathrm{d}S, \quad \nabla \cdot \boldsymbol{\omega} = 0, \tag{3.25a,b}$$

and proper boundary condition of $\boldsymbol{u}$ on $\partial V$. This problem can be solved by either differential or integral approach, which is a necessary kinematic part in developing vorticity-based numerical schemes.

We first seek the boundary condition under which the solution of (3.24) is *unique*. Suppose that $u_n$ is given at $\partial V$ and assume $\boldsymbol{u}_1$ and $\boldsymbol{u}_2$ are two solutions of (3.24), so that $\boldsymbol{v} = \boldsymbol{u}_1 - \boldsymbol{u}_2$ must be both solenoidal and irrotational, i.e.,

$\boldsymbol{v} = \nabla\phi$ for some harmonic $\phi$. Then by assumption there must be $\partial\phi/\partial n = 0$ on $\partial V$ and hence $\phi$ can only be a constant. Therefore, there can be at most only one solution. Alternatively, suppose $\boldsymbol{n} \times \boldsymbol{u}$ is given at $\partial V$. Then there must be $\boldsymbol{n} \times \nabla\phi = \boldsymbol{0}$ for the same $\phi$ over the entire $\partial V$, again leading to the same conclusion.

The existence of a velocity field with given $(\boldsymbol{\omega}, \vartheta)$ and $u_n$ or $\boldsymbol{n} \times \boldsymbol{u}$ on $\partial V$ is somewhat more difficult. Within the range of *kinematics*, the above uniqueness argument implies that the existence consideration should be made with either $\boldsymbol{n}\cdot\boldsymbol{u}$ or $\boldsymbol{n}\times\boldsymbol{u}$ given at the boundary, but not both. A well-posedness theorem for the differential approach to (3.24), where the boundary conditions are both sufficient and necessary, will be given in Sect. 4.5. Here we focus on the integral approach, for which two alternative formulations can be made.

The first formulation is based on the potentials

$$\phi = \int_V G\vartheta \, \mathrm{d}V', \quad \boldsymbol{\psi} = -\int_V G\boldsymbol{\omega} \, \mathrm{d}V',$$

where $G$ is given by (2.102). We may then construct $\boldsymbol{v} = \nabla\phi + \nabla \times \boldsymbol{\psi}$, so that

$$\nabla \cdot \boldsymbol{v} = \nabla^2\phi = 0, \quad \nabla \times \boldsymbol{v} = \nabla(\nabla \cdot \boldsymbol{\psi}) - \nabla^2\boldsymbol{\psi} = \boldsymbol{\omega}$$

if the gauge condition (2.88) holds. To check this construction, we note that

$$\nabla \cdot \boldsymbol{\psi} = -\int_V \nabla G \cdot \boldsymbol{\omega} \, \mathrm{d}V' = \int_V \nabla' \cdot (G\boldsymbol{\omega}) \, \mathrm{d}V' = \int_{\partial V} G\boldsymbol{n} \cdot \boldsymbol{\omega} \, \mathrm{d}S.$$

Therefore, $\boldsymbol{v}$ has the desired feature if $\boldsymbol{n} \cdot \boldsymbol{\omega} = 0$. This condition is satisfied by (3.18) for an externally unbounded fluid, as well as for a viscous flow in the exterior or interior of any nonrotating body surface $\partial B$. If $\boldsymbol{\omega} \cdot \boldsymbol{n} \neq 0$ on $\partial B$, then, one may continue $\boldsymbol{\omega}$ through $\partial B$ to a new virtual boundary outside $V$ with $\boldsymbol{\omega} \cdot \boldsymbol{n} = 0$ there, while keeping $\boldsymbol{\omega} \cdot \boldsymbol{n}$ continuous across $\partial B$, namely letting vorticity lines going through the boundary. This continuation is not unique; for example, one may choose $\boldsymbol{\omega} = \nabla\eta$ with $\partial\eta/\partial n = \boldsymbol{\omega} \cdot \boldsymbol{n}$ on $\partial B$ and $\nabla^2\eta = 0$ in the virtual domain (Serrin 1959; Batchelor 1967). Note that the velocity so constructed may not satisfy the specified $\boldsymbol{n} \cdot \boldsymbol{u}$ or $\boldsymbol{n} \times \boldsymbol{u}$ on $\partial V$; which is taken care of by a harmonic component $\nabla\chi$ as remarked at the end of Sect. 2.3.1. Therefore, we now have

$$\begin{aligned} \boldsymbol{u} &= \textstyle\int_V (\vartheta\nabla' G + \boldsymbol{\omega} \times \nabla' G)\mathrm{d}V' + \nabla\chi, \\ \nabla^2\chi = 0, &\quad \boldsymbol{\omega} \cdot \boldsymbol{n} = 0 \text{ on } \partial V \text{ or extended boundary.} \end{aligned} \tag{3.26}$$

The second formulation directly follows from the already constructed velocity (2.105). A substitution of (2.103) then yields (Phillips 1933; Serrin 1959)

$$\boldsymbol{u} = \frac{1}{2(n-1)\pi} \left( \int_V \frac{\vartheta\boldsymbol{r} + \boldsymbol{\omega} \times \boldsymbol{r}}{r^n} \mathrm{d}V + \boldsymbol{B} \right), \tag{3.27}$$

where $n = 2, 3$ is the spatial dimension and

$$\boldsymbol{B} = -\int_{\partial V} [(\boldsymbol{n}\cdot\boldsymbol{u})\boldsymbol{r} + (\boldsymbol{n}\times\boldsymbol{u})\times\boldsymbol{r}]\frac{\mathrm{d}S}{r^n}$$
$$= -\int_{\partial V} [(\boldsymbol{n}\cdot\boldsymbol{r})\boldsymbol{u} + (\boldsymbol{n}\times\boldsymbol{r})\times\boldsymbol{u}]\frac{\mathrm{d}S}{r^n} \tag{3.28}$$

is a boundary integral. Equation (3.26) or (3.27) is known as the *generalized Biot–Savart formula*, which are actually equivalent to each other because one can directly verify $\boldsymbol{B} = \nabla\chi$ and $\nabla^2\chi = 0$.

It should be emphasized that, in general, a specified distribution of $\boldsymbol{\omega}$ and $\vartheta$ and their "induced" velocity field via the Biot–Savart formula may not represent any physically realistic flow. The preceding uniqueness analysis clearly indicates that, if the full adherence condition is imposed to fix the boundary velocity $\boldsymbol{u}$ in (3.28), then generically no continuous velocity field obtained from (3.27) can fit this boundary velocity.[6] Usually, to ensure the kinematic existence one imposes the nonpermeable condition (2.67a) only; the simple example in Sect. 2.3.2 has shown that (2.107) and (2.108) with known $u_n$ do ensure a unique solution. However, only if the flow is strictly inviscid, can (3.27) yield a $\boldsymbol{u}$ field with *any* given $\boldsymbol{\omega}$ distribution in $V$ and given $u_n$ on $\partial V$. But this simply implies that for inviscid flow the vorticity field is indeterminate, which is not the reality.

It is precisely the impossibility of imposing the full adherence condition to the velocity field derived from a given $(\boldsymbol{\omega}, \vartheta)$ distribution, plus a harmonic part, that has a deep physical reason: for viscous fluid the $\boldsymbol{\omega}$ field cannot be arbitrarily given in a bounded fluid domain $V$, say bounded internally by a solid surface $\partial B$. If the no-through condition has been satisfied, adding a given $\boldsymbol{n}\times\boldsymbol{u}$ on $\partial B$ must create a vortex sheet thereon due to the no-slip condition. This is the mechanism of vorticity generation at $\partial B$ and must alter the originally specified vorticity field. The vorticity creation at boundary and the methods of solving the vorticity field for viscous flow (with (3.24) and (3.25) as the kinematic part of the problem) will be addressed in Sects. 4.1 and 4.5, respectively. Only after such an $(\boldsymbol{\omega}, \boldsymbol{u})$ field has been *dynamically* solved, can the full adherence condition be satisfied on $\partial B$. In this case, then, (3.28) clearly indicates that the boundary integral can be removed by continuing the velocity field into $B$ to form an unbounded continuous system $V+B$, for which (3.26) and (3.27) can be applied without ambiguity. In the following kinematic discussions, therefore, we always assume the real flow has been solved and hence the domain can be treated as unbounded, with the understanding that whenever necessary the system can consist of both fluid and solid or more than one fluids.

The incompressible version of (3.27) is our major interest, which reads:

$$\boldsymbol{u}(\boldsymbol{x}) = \frac{1}{2(n-1)\pi}\int_V \frac{\boldsymbol{\omega}\times\boldsymbol{r}}{r^n}\,\mathrm{d}V. \tag{3.29}$$

[6] This happens because $G$ is the free-space Green's function.

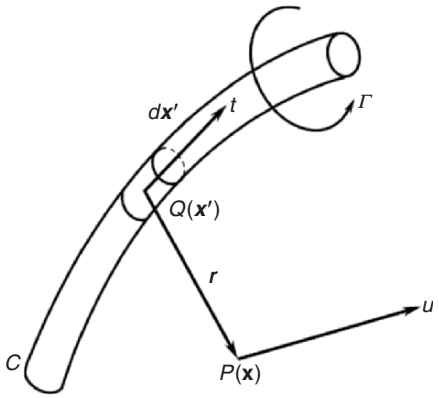


**Fig. 3.7.** The velocity at point $P(\mathbf{x})$ induced by a vortex filament of circulation $\Gamma$

If moreover $\boldsymbol{\omega}$ is confined in a thin vortex sheet $S$ of thickness $\delta \to 0$, with a finite strength

$$\boldsymbol{\gamma} = \lim_{\delta \to 0} \int_0^\delta \boldsymbol{\omega} \, \mathrm{d}n, \tag{3.30}$$

then we have $\boldsymbol{\omega} \, \mathrm{d}V = \boldsymbol{\gamma} \, \mathrm{d}S$ and

$$\boldsymbol{u}(\boldsymbol{x}) = \frac{1}{2(n-1)\pi} \int_S \frac{\boldsymbol{\gamma} \times \boldsymbol{r}}{r^n} \, \mathrm{d}S, \tag{3.31}$$

which is a basis of vortex-sheet kinematics. On the other hand, if $\boldsymbol{\omega}$ is confined in a very thin closed vorticity tube $C$, called *vortex filament* (Fig. 3.7), then by the first Helmholtz theorem the tube has a single strength or circulation $\Gamma$. Thus, let $\mathrm{d}\boldsymbol{x}' = \boldsymbol{t} \, \mathrm{d}s$ be a line element of $C$, there is $\boldsymbol{\omega} \, \mathrm{d}V = \Gamma \boldsymbol{t} \, \mathrm{d}s$ and (3.29) is reduced to

$$\boldsymbol{u}(\boldsymbol{x}) = \frac{\Gamma}{2(n-1)\pi} \oint_C \frac{\boldsymbol{t} \times \boldsymbol{r}}{r^n} \, \mathrm{d}s, \tag{3.32}$$

which is a basis of vortex-filament kinematics. In the limit as the filament diameter approaches zero, the vortex filament is called a *line vortex* in which the vorticity is singular.[7]

The simplest form of (3.32) is the velocity "induced" by a single straight line vortex of circulation $\Gamma$, located at the center of a cylindrical coordinate system $(r, \theta, z)$. We only need to consider a "*point vortex*" in the two-dimensional flow on a cross plane; with $\boldsymbol{u} = (u_r, u_\theta)$ and $n = 2$ in (3.32), the

[7] The name of the generalized Biot–Savart law came from the analogy between (3.32) and the Biot–Savart law for the static magnetic field induced by a line current. But in fluid mechanics "induction" is a misnomer, since in the kinematic relations between the vorticity, dilatation, and velocity no causality can be identified. With this reservation in mind, the word "induction" will still be used for simplicity.

familiar elementary result follows:

$$u_r = 0, \quad u_\theta = \frac{\Gamma}{2\pi r}. \tag{3.33}$$

Since in Cartesian coordinates $(x_1, x_2)$ there is $u = -u_\theta \sin\theta$ and $v = u_\theta \cos\theta$, in terms of complex variable

$$Z = x_1 + \mathrm{i}x_2, \quad \frac{\mathrm{d}Z}{\mathrm{d}t} = u + \mathrm{i}v,$$

equation (3.32) can be cast to $\mathrm{d}Z^*/\mathrm{d}t = \Gamma/(2\pi \mathrm{i} Z)$, where $*$ denotes the complex conjugate. Therefore, for $N$ point vortices with circulation $\Gamma_k$ located at $Z_k$ $(k = 1, \ldots, N)$, there is

$$\frac{\mathrm{d}Z^*}{\mathrm{d}t} = \frac{1}{2\pi i} \sum_{k=1}^{N} \frac{\Gamma_k}{Z - Z_k}, \tag{3.34}$$

which is the basis of *point-vortex system dynamics* to be explored in Chap. 8. Finally, if all point vortices line up along a curve, with $N \to \infty$ and $\Gamma_k$ being replaced by a continuous distribution $\gamma(s)\mathrm{d}s$ ($\mathrm{d}s$ is the arclength of the curve), then (3.34) is changed to the velocity "induced" by a two-dimensional vortex sheet

$$\frac{\mathrm{d}Z^*}{\mathrm{d}t} = \frac{1}{2\pi i} \int \frac{\gamma(s)\mathrm{d}s}{Z - Z(s)}, \tag{3.35}$$

which is merely the complex form of (3.31) with $n = 2$.

Before closing this subsection, we remark that from the generalized Biot–Savart formula one can further derive the strain-rate tensor associated with a given vorticity and dilatation. Assume the flow is unbounded with $\nabla\chi = \mathbf{0}$ in (3.26), then in component form there is

$$2D_{ij} = \int [\vartheta(G_{,ij} + G_{,ji}) + \omega_k(\epsilon_{ikl}G_{,lj} + \epsilon_{jkl}G_{,li})]\,\mathrm{d}V.$$

Here, $G_{,ij} = G_{,ji}$, and from (2.103) it follows that

$$G_{,ij}(\boldsymbol{r}) = \frac{\delta_{ij} - n e_i e_j}{2(n-1)\pi r^n}, \quad \boldsymbol{e} = \frac{\boldsymbol{r}}{r}. \tag{3.36}$$

Therefore, we obtain

$$\mathbf{D} = \frac{1}{4(n-1)\pi} \int \{2(\mathbf{I} - n\boldsymbol{e}\boldsymbol{e})\vartheta + n[\boldsymbol{e}(\boldsymbol{\omega} \times \boldsymbol{e}) + (\boldsymbol{\omega} \times \boldsymbol{e})\boldsymbol{e}]\} \frac{\mathrm{d}V}{r^n} \tag{3.37}$$

of which the incompressible version for $n = 3$ was derived by Constantin (1994) and will be used later in the study of vorticity-tube stretching.

We have seen the local relation between $\mathbf{D}$ and $\boldsymbol{\omega}$ for the special case of simple shear flow in Sect. 2.1.2, and general local relation (2.136) between

$\mathbf{D}$, $\vartheta$, and $\boldsymbol{\Omega}$, but with the surface-deformation rate tensor $\mathbf{B}$ involved. The $\mathbf{B}$-tensor is now removed from (3.37) with the expense that the relation must be global. Remarkably, (3.37) bears some resemblance to the Caswell formula (2.142), where the $\mathbf{B}$ tensor disappears on any stationary wall. The unit normal $\boldsymbol{n}$ in (2.142) is now replaced by the unit vector $\boldsymbol{e}$ along the $\boldsymbol{r}$ direction.

### 3.2.3 Far-Field Velocity Asymptotics

The vorticity moment theorem and the Biot–Savart formula obtained in the preceding sections allow us to analyze the asymptotic behavior of the velocity field in an unbounded domain. Again assume the flow is incompressible, with vorticity decaying exponentially, see (3.18).[8] Let $\boldsymbol{x}$ be the field point with $|\boldsymbol{x}| = x$ and $\boldsymbol{x}'$ be the moving point inside the finite vortical region with $|\boldsymbol{x}'| = x'$, such that at far field $x \gg x'$. This implies that in the free-space Green's function $G(\boldsymbol{x} - \boldsymbol{x}')$ defined by (2.102) there is $r = |\boldsymbol{x} - \boldsymbol{x}'| \simeq x$. More precisely, denote the values of $G$ and its derivatives at $\boldsymbol{x}' = \mathbf{0}$ by suffix 0 and recalling that $\nabla = -\nabla'$, we have the Taylor expansion with respect to $\boldsymbol{x}'$:

$$G(\boldsymbol{x} - \boldsymbol{x}') = G_0 - x_i'(G_{,i})_0 + \frac{1}{2}x_i'x_j'(G_{,ij})_0 + \cdots,$$

where $G_0$ is given by (2.102) for spatial dimensionality $n = 2, 3$, while from (2.103) and (3.36) there is

$$\begin{aligned}(G_{,i})_0 &= \frac{1}{2(n-1)\boldsymbol{\pi}}\frac{x_i}{x^n},\\ (G_{,ij})_0 &= \frac{1}{2(n-1)\boldsymbol{\pi}}\left(\frac{\delta_{ij}}{x^n} - \frac{nx_ix_j}{x^{n+2}}\right) + \mathrm{O}(x^{-m}), \quad m \geq 4.\end{aligned}$$

This expansion converges as long as $x > x'$. In general, a scalar

$$\mathcal{F} = \frac{\partial^n F_{ijk\ldots}}{\partial x_i \partial x_j \partial x_k \ldots} \tag{3.38}$$

is called a *multipole of order* $2^n$. Hence, the terms in the above expansion are recognized as monopole, dipole, quadrupole, etc. at $\boldsymbol{x} = \mathbf{0}$. Then the substitution of this $G$-expansion into (2.104b) yields

$$\boldsymbol{\psi} = -G_0\langle\boldsymbol{\omega}\rangle + \frac{1}{2(n-1)\boldsymbol{\pi}}\sum_{m=1}^{\infty}\boldsymbol{\psi}^{(m)} \tag{3.39}$$

with

$$\begin{aligned}\psi_k^{(1)} &= \frac{x_i}{x^n}\langle x_i'\omega_k\rangle,\\ \psi_k^{(2)} &= \frac{1}{2x^n}\left(\frac{nx_ix_j}{x^2} - \delta_{ij}\right)\langle x_i'x_j'\omega_k\rangle, \quad \text{etc.}\end{aligned} \tag{3.40}$$

[8] The far-field asymptotic behavior of the velocity associated with a given dilatation distribution is fully discussed in Batchelor (1967).

Here, the same simplified notation is used for integrals as in Sect. 3.2.1, and the consistency conditions (3.19) can be used for estimating any $\boldsymbol{\psi}^{(m)}$.

We can now consider the far-field behavior of $\boldsymbol{u} = \nabla \times \boldsymbol{\psi}$, for which two- and three-dimensional flows should be analyzed separately. In three dimensions, the Föppl theorem (3.15) immediately implies $\boldsymbol{\psi}^{(0)} = \boldsymbol{0}$. Then (3.20a) gives

$$\boldsymbol{\psi}^{(1)} = \frac{1}{2x^3}\boldsymbol{x} \cdot \langle \boldsymbol{x}'\boldsymbol{\omega} - \boldsymbol{\omega}\boldsymbol{x}' \rangle = -\frac{1}{2x^3}\boldsymbol{x} \times \langle \boldsymbol{x}' \times \boldsymbol{\omega} \rangle = \nabla\left(\frac{1}{x}\right) \times \boldsymbol{I}, \tag{3.41}$$

where

$$\boldsymbol{I} \equiv \frac{1}{2}\int \boldsymbol{x} \times \boldsymbol{\omega}\, \mathrm{d}V \tag{3.42}$$

is the *vortical impulse*, which in unbounded domain must be finite as ensured by (3.18) and will be shown a motion invariant. Thus, since $\boldsymbol{I}$ is independent of $\boldsymbol{x}$ and $\nabla^2(1/x) = 0$ for $x \neq 0$, by (3.41) the leading term of the velocity expansion is

$$\begin{aligned} \boldsymbol{u} &\sim \frac{1}{4\pi}\nabla \times \left[\nabla\left(\frac{1}{x}\right) \times \boldsymbol{I}\right] = \frac{1}{4\pi}\nabla\left[\nabla\left(\frac{1}{x}\right) \cdot \boldsymbol{I}\right] \\ &= \frac{1}{4\pi}\boldsymbol{I} \cdot \nabla\nabla\left(\frac{1}{x}\right) = \frac{1}{4\pi x^3}\left(3\boldsymbol{I} \cdot \frac{\boldsymbol{x}\boldsymbol{x}}{x^2} - \boldsymbol{I}\right), \end{aligned} \tag{3.43}$$

which behaves as the *potential flow* induced by a dipole of strength $\boldsymbol{I}$ at the origin. The omitted terms are of $\mathrm{O}(x^{-m})$, $m \geq 4$. In particular, on a large sphere of radius $R \to \infty$, since $\boldsymbol{x} = R\boldsymbol{n}$, (3.43) yields

$$\boldsymbol{u} = \frac{1}{4\pi}\nabla\left(\frac{\boldsymbol{n}}{R^2}\right) \cdot \boldsymbol{I} = \frac{1}{4\pi R^3}(3\boldsymbol{n}\boldsymbol{n} \cdot \boldsymbol{I} - \boldsymbol{I}). \tag{3.44}$$

For two-dimensional flows, we have $\boldsymbol{\psi} = (0, 0, \psi)$, $\boldsymbol{\omega} = (0, 0, \omega)$, and $\langle \omega \rangle = \mathit{\Gamma}_\infty$. The first vorticity moment has two components $\langle x\omega \rangle$ and $\langle y\omega \rangle$, which form a vector

$$\boldsymbol{I} \equiv \int \omega\boldsymbol{x} \times \boldsymbol{e}_z\, \mathrm{d}V \tag{3.45}$$

as the two-dimensional vortical impulse. It differs from (3.42) by a factor $1/2$ due to the geometrical reason (Sect. 3.4.1). Similar to the preceding procedure, the two-dimensional counterpart of (3.41) and (3.43) reads:

$$\boldsymbol{\psi} = -\frac{1}{2\pi}(\mathit{\Gamma}_\infty \boldsymbol{e}_z \ln x + \nabla \ln x \times \boldsymbol{I}) + \mathrm{O}(x^{-m}), \quad m \geq 2, \tag{3.46}$$

$$\begin{aligned} \boldsymbol{u} &= -\frac{1}{2\pi}[\mathit{\Gamma}_\infty \nabla \ln x \times \boldsymbol{e}_z + \nabla(\nabla \ln x \cdot \boldsymbol{I})] + \mathrm{O}(x^{-m}) \\ &= \frac{1}{2\pi x^2}\left(\mathit{\Gamma}_\infty \boldsymbol{e}_z \times \boldsymbol{x} + 2\boldsymbol{I} \cdot \frac{\boldsymbol{x}\boldsymbol{x}}{x^2} - \boldsymbol{I}\right) + \mathrm{O}(x^{-m}), \quad m \geq 3. \end{aligned} \tag{3.47}$$

The two terms correspond to the flows induced by a rectilinear vortex (point vortex) of circulation $\Gamma_\infty$ and a dipole of strength $\boldsymbol{I}$, respectively, both at the origin. To see this clearly, take a large circle $C$ of radius $R$ that contains all the vorticity and let $\boldsymbol{t}$ be the unit vector tangent to $C$ such that $(\boldsymbol{n}, \boldsymbol{t}, \boldsymbol{e}_z)$ form a local orthogonal triad. Then (3.47) gives a flow irrotational at $x \neq 0$

$$\boldsymbol{u} = \frac{\Gamma_\infty}{2\pi R}\boldsymbol{t} + \frac{2\boldsymbol{n}\boldsymbol{n}\cdot\boldsymbol{I} - \boldsymbol{I}}{2\pi R^2} + \mathrm{O}(R^{-3}). \tag{3.48}$$

In two dimensions with $\boldsymbol{\omega}\cdot\boldsymbol{x} \equiv 0$, of the three second-order vorticity moments related by (3.6) only one is independent. Later, it will be shown that the second-order vorticity moments of an unbounded domain are also time invariant. Because the multipoles depend on $\boldsymbol{x}$ only but not the distributed vorticity field, they can be easily obtained. Only their strengths need to be computed, but the invariants can be obtained once and for all.

For later use, we list some asymptotic behaviors of the potential-flow at a large spherical surface $\partial V_R$ for $n = 3$ and a large circle $C_R$ for $n = 2$ in terms of $\boldsymbol{I}$ (different from (2.174) in form), with radius $R \to \infty$ and $\boldsymbol{x} = R\boldsymbol{n}$. First, from (3.44) and (3.47), the velocity potential $\phi$ behaves as (we retain $\Gamma_\infty$ for seeing its role)

$$n = 3: \ \phi = -\frac{1}{4\pi R^2}\boldsymbol{n}\cdot\boldsymbol{I}, \tag{3.49a}$$

$$n = 2: \ \phi = -\frac{1}{2\pi}\left(\Gamma_\infty \ln R + \frac{1}{R}\boldsymbol{n}\cdot\boldsymbol{I}\right), \tag{3.49b}$$

where we recall $\boldsymbol{I}$ differs by a factor $1/2$ for $n = 2$ and 3. Then, the tangent velocity $\boldsymbol{n}\times\boldsymbol{u}$ is given by

$$n = 3: \ \boldsymbol{n}\times\boldsymbol{u} = -\frac{\boldsymbol{n}\times\boldsymbol{I}}{4\pi R^3}, \tag{3.50a}$$

$$n = 2: \ \boldsymbol{n}\times\boldsymbol{u} = \frac{\Gamma_\infty}{2\pi R}\boldsymbol{e}_z - \frac{\boldsymbol{n}\times\boldsymbol{I}}{2\pi R^2}. \tag{3.50b}$$

## 3.3 Lamb Vector and Helicity

The local geometrically orthogonal decomposition (2.85) introduces two quantities, the Lamb vector $\boldsymbol{\omega}\times\boldsymbol{u}$ and the helicity density $\boldsymbol{\omega}\cdot\boldsymbol{u}$. This decomposition implies a triangle relation:

$$q^2\omega^2 = |\boldsymbol{\omega}\cdot\boldsymbol{u}|^2 + |\boldsymbol{\omega}\times\boldsymbol{u}|^2, \quad q = |\boldsymbol{u}|. \tag{3.51}$$

In terms of the intrinsic orthonormal basis vectors moving along a streamline, the vorticity components are given by (3.2), where appears the torsion of neighboring streamlines $\xi$. Thus (3.51) is reduced to

$$\omega^2 = \xi^2 q^2 + |\boldsymbol{\omega}\times\boldsymbol{t}|^2, \tag{3.52}$$

and the helicity density is given by

$$\boldsymbol{\omega} \cdot \boldsymbol{u} = \xi q^2. \tag{3.53}$$

Thus, for given $q$ and $|\boldsymbol{\omega}|$, *whenever there is a high helicity density the Lamb vector must be small, and vise versa*. The key role of the Lamb vector have been made clear in Sect. 2.4.3, and more will be seen later. We now discuss some kinematic aspects of these pair of quantities.

### 3.3.1 Complex Lamellar, Beltrami, and Generalized Beltrami Flows

Based on (3.51), two extreme flow types with both $\boldsymbol{\omega} \neq \mathbf{0}$ and $\boldsymbol{u} \neq \mathbf{0}$ are of special interest: $\boldsymbol{\omega} \cdot \boldsymbol{u} = 0$ and $\boldsymbol{\omega} \times \boldsymbol{u} = \mathbf{0}$. We discuss these flows separately.

First, if the helicity density $\boldsymbol{\omega} \cdot \boldsymbol{u} = 0$ everywhere, i.e., the streamlines are orthogonal to vorticity lines, the flow is called *complex lamellar flow*.[9] Such a flow exists if and only if (Truesdell 1954)

$$\boldsymbol{u} = \lambda \nabla \mu, \tag{3.54}$$

which is the second term of the Monge decomposition (2.115). In this flow, there exists a set of equi-potential surfaces $\mu = \text{const.}$ orthogonal to streamlines everywhere, and potential flow is the special case with $\lambda = 1$. Since $\boldsymbol{\omega} = \nabla\lambda \times \nabla\mu$ we indeed have $\boldsymbol{\omega} \cdot \boldsymbol{u} = 0$.

It can be easily seen that both two-dimensional flow and rotationally symmetric flow are complex lamellar flow.[10] Both allow for introducing a scalar stream function $\psi$, which is the only nonzero component of the vectorial potential $\boldsymbol{\psi}$ of the velocity. In two-dimensional flow $\psi(x, y)$ is the third component of $\boldsymbol{\psi}$ or stream function, which satisfies $\boldsymbol{u} = \nabla\psi \times \boldsymbol{e}_z$ or

$$u = \frac{\partial \psi}{\partial y}, \quad v = -\frac{\partial \psi}{\partial x}. \tag{3.55}$$

In this case (2.89b) is reduced to a scalar Poisson equation

$$\nabla^2 \psi = -\omega. \tag{3.56}$$

In rotationally symmetric flow observed in cylindrical coordinates $(r, \theta, z)$ there is $\boldsymbol{\psi} = (0, \psi_\theta, 0)$, so

$$\nabla \times \boldsymbol{\psi} = \frac{\boldsymbol{e}_z}{r} \frac{\partial (r\psi_\theta)}{\partial r} - \frac{\boldsymbol{e}_r}{r} \frac{\partial (z\psi_\theta)}{\partial z}.$$

[9] This name came from some similarity with potential flow, which used to be called lamellar flow.

[10] A rotationally symmetric flow is generated by a flow on the meridian plane rotating around the $z$-axis. It is a subclass of axisymmetric flow with zero circumferential velocity.

Thus, let $\psi(r,z) = r\psi_\theta$ be the *Stokes stream function*, for $\boldsymbol{u} = (u, 0, w)$ there is

$$u = -\frac{1}{r}\frac{\partial \psi}{\partial z}, \quad w = \frac{1}{r}\frac{\partial \psi}{\partial r}. \tag{3.57}$$

Correspondingly, the vorticity is $\boldsymbol{\omega} = (0, \omega_\theta, 0)$, having only one component as well; and (2.89b) is reduced to

$$\frac{\partial}{\partial r}\left(\frac{1}{r}\frac{\partial \psi}{\partial r}\right) + \frac{1}{r}\frac{\partial^2 \psi}{\partial z^2} = -\omega_\theta. \tag{3.58}$$

These scalar stream functions automatically ensure the incompressibility $\nabla \cdot \boldsymbol{u} = 0$ and can fully describe the velocity and vorticity field. Note that the use of scalar stream functions can be somewhat extended. First, for *steady incompressible flow* the continuity equation reduces to $\nabla \cdot (\rho \boldsymbol{u}) = 0$, and hence $(u, v)$ and $(u, w)$ in (3.55) and (3.57) can be replaced by $(\rho u, \rho v)$ and $(\rho u, \rho w)$, respectively. Second, if in a three-dimensional flow the third velocity component $w$ is independent of $z$, then it does not appear in the continuity equation and (3.55) still holds. The same is true for a nonzero circumferential velocity $v$ in an axisymmetric flow, and (3.57) still holds. But in these extended cases a single $\psi$ cannot fully describe the flow field.

We digress to make an observation. Assume the Lamb vector $\boldsymbol{\omega} \times \boldsymbol{u}$ is also a complex lamellar field, i.e., it can be written as $\boldsymbol{\omega} \times \boldsymbol{u} = g \nabla h$, say, such that

$$(\boldsymbol{\omega} \times \boldsymbol{u}) \cdot [\nabla \times (\boldsymbol{\omega} \times \boldsymbol{u})] = 0, \quad \boldsymbol{\omega} \times \boldsymbol{u} \neq \boldsymbol{0}. \tag{3.59}$$

Then there exists a set of surfaces $h = \text{const.}$, known as the *Lamb surfaces*, which are orthogonal to the Lamb vector everywhere. Since both $\boldsymbol{u}$ and $\boldsymbol{\omega}$ are tangent to these surfaces, a Lamb surface is both stream surface and vorticity surface (Fig. 3.8). Sposito (1997) has made a comprehensive study of Lamb surfaces for steady flows.

The existence of Lamb surfaces is important regarding the *integrability* and *chaos* of the flow. For a system, if under a given initial condition of finite accuracy its motion in subsequent times can be determined with finite accuracy, then the system is said to be *integrable*. Otherwise, the system is *nonintegrable*, extremely sensible to the initial condition. An uncertainty of the initial condition will cause the system's motion indeterminate or impossible to determine, and the motion will exhibit chaos. It can be shown that the pathline equations for a steady flow on a two-dimensional surface is always integrable; thus, *steady flow with Lamb surfaces can in no way be chaotic.*

The other extreme situation, i.e., $\boldsymbol{\omega} \times \boldsymbol{u} = \boldsymbol{0}$ and $\boldsymbol{\omega} \cdot \boldsymbol{u} \neq 0$, implies that the streamlines are always parallel to vorticity lines, i.e., $\boldsymbol{\omega} = \xi \boldsymbol{u}$. This type of flow is called *Beltrami flow* or *helical flow*. Then, the vorticity form of the acceleration formula (2.162) is reduced to

$$\frac{\mathrm{D}\boldsymbol{u}}{\mathrm{D}t} = \frac{\partial \boldsymbol{u}}{\partial t} + \nabla\left(\frac{1}{2}q^2\right), \tag{3.60}$$

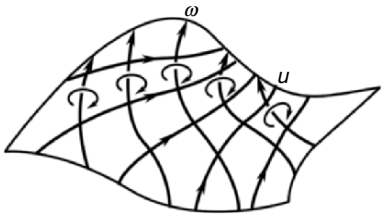


**Fig. 3.8.** A Lamb surface

the same as for potential flow. Moreover, for steady compressible Beltrami flow or any incompressible Beltrami flow, there is

$$\nabla \cdot (\rho \boldsymbol{u}) = \nabla \cdot \left( \frac{\rho \boldsymbol{\omega}}{\xi} \right) = \nabla \left( \frac{\rho}{\xi} \right) \cdot \boldsymbol{\omega} = 0$$

due to the continuity. Thus, by using (3.53), the surfaces

$$\frac{\xi}{\rho} = \frac{\boldsymbol{\omega} \cdot \boldsymbol{u}}{\rho q^2} = \frac{\omega}{\rho q} = \text{const.} \tag{3.61}$$

are both vorticity surfaces and stream surfaces.

The above discussion shows that each of the complex-lamellar flow and helical flow shares some of the properties of potential flow (Truesdell 1954). However, these two extrema are not of equal importance or simplicity. As seen in Sect. 2.4.3, the Lamb vector is the major source of the flow nonlinearity. Once it vanishes as in any Beltrami flow, the Helmholtz equation (2.168) is linearized, while (2.169) indicates that the coupling of shearing and compressing processes disappears inside the flow field.[11] Later in Sect. 3.4.2 we will see that the total kinetic energy of incompressible flow can be expressed in terms of an integrated scalar moment of the Lamb vector, indicating that an unbounded flow can by no means be entirely Beltramian, let alone having a solid body moving through it. Therefore, a local flow region may be Beltramian in a real flow field, but this region is inactive and quite passively driven by the surrounding non-Beltramian motion.

On the other hand, because the governing equation of a Beltrami flow is often directly solvable, some thorough analysis becomes possible. In particular, $\nabla \times \boldsymbol{u} = \xi \boldsymbol{u}$ implies that $\boldsymbol{u}$ is an eigenvector of the curl operator associated with eigenvalue $\xi$. If $\xi$ is constant, the flow is specifically called a *Trkalian flow* (Aris 1962). Recall the discussion on helical wave decomposition (HWD) in Sect. 2.3.4, we recognize that each Trkalian flow is a basis vector of HWD.

A nontrivial example of Trkalian flow was proposed by Arnold (1965a), whose intention was to seek the possibility of chaos in steady inviscid flows. As mentioned before, for searching chaos, steady flows having Lamb surfaces must

[11] But the vorticity-induced velocity is involved in the total enthalpy $H$.

be excluded. Thus the desired flow, if exists, must be Beltramian. Moreover, if in (3.61) $\nabla\xi \neq 0$, the velocity will be on the surfaces with $\nabla\xi$ as normal, and is still integrable. Therefore, the only possibility of incompressible chaotic steady flow should be that with $\nabla\xi \equiv 0$, i.e., a Trkalian flow. Without loss of generality, we take $\xi = 1$ such that $\boldsymbol{\omega} = \boldsymbol{u}$ in the whole flow field. We confine our attention to a periodic box $0 \leq (x, y, z) \leq 2\pi$ so that the Fourier transform of the Trkalian flow is one of the Fourier HWD basis vectors (2.121) with $k = 1$ and $\lambda = +1$, not normalized

$$\boldsymbol{u}^+(\boldsymbol{x}) = \sum_{|\boldsymbol{k}|=1} u^+(\boldsymbol{k})(\boldsymbol{e}_1 + \mathrm{i}\boldsymbol{e}_2)\mathrm{e}^{\mathrm{i}\boldsymbol{k}\cdot\boldsymbol{x}}, \quad |\boldsymbol{k}| = 1,$$

where $(\boldsymbol{e}_1, \boldsymbol{e}_2, \boldsymbol{k})$ form a Cartesian triad. By letting $\boldsymbol{e}_1$ be along the plus or minus direction of three Cartesian bases $(\boldsymbol{e}_x, \boldsymbol{e}_y, \boldsymbol{e}_z)$ in turn and enforcing the reality condition $u^{+*}(\boldsymbol{k}) = u^+(-\boldsymbol{k})$ to $\boldsymbol{u}$, due to the arbitrariness of translation along the Cartesian axes, we find that the number of independent coefficients $u^+(\boldsymbol{k})$ determining the flow is only 3. Denoting these by $A, B$, and $C$, we obtain

$$u^+ = A\sin z + C\cos y, \quad v^+ = B\sin x + A\cos z, \quad w^+ = C\sin y + B\cos x. \tag{3.62}$$

By (3.60), this flow is a solution of the incompressible steady Euler equation with $p = -q^2/2$. After Arnold, this Beltrami flow was analyzed by Childress (1970) and is therefore called the "*ABC flow*". Careful studies have shown that it indeed exhibits chaotic streamlines for certain range of the values of $A, B$, and $C$ (Dombre et al. 1986). Note that if we add $\lambda = -1$ modes to (3.62), then the interaction between the two modes will make the flow no longer Beltramian.

While the Beltrami flow represents an extreme class of three-dimensional vortical flows, a much wider class of vortical flows can be found if we relax the condition of $\boldsymbol{\omega} \times \boldsymbol{u} = \boldsymbol{0}$ to

$$\nabla \times (\boldsymbol{\omega} \times \boldsymbol{u}) = \boldsymbol{0} \quad \text{or} \quad \boldsymbol{\omega} \times \boldsymbol{u} = \nabla\chi. \tag{3.63}$$

A flow satisfying (3.63) is called a *generalized Beltrami flow* (Wang 1990, 1991). It has some nice properties. First, (3.59) is ensured, so any generalized Beltrami flow, steady or unsteady, must have Lamb surfaces. Second, (3.63) makes the incompressible Helmholtz equation (2.168) linearized, and thus opens a door to many analytically obtainable exact vortex flow solutions, some are very useful and will be given in Chap. 6.

Third, the complex lamellar flow and generalized Beltrami flow have an interesting intersection set, when a single scalar stream function $\psi$ can fully describe the velocity and vorticity, see (3.55)–(3.58). Denote the single nonzero vorticity component in both (3.56) and (3.58) by $\omega$, for two-dimensional flow we have $\boldsymbol{\omega} \times \boldsymbol{u} = \omega\nabla\psi$ and

$$\nabla \times (\boldsymbol{\omega} \times \boldsymbol{u}) = \boldsymbol{e}_z \left[ \frac{\partial}{\partial x}\left(\omega\frac{\partial\psi}{\partial y}\right) - \frac{\partial}{\partial y}\left(\frac{\partial\psi}{\partial x}\right)\right],$$

while for rotationally symmetric flow there is $\boldsymbol{\omega}\times\boldsymbol{u}=(\omega/r)\nabla\psi$ and

$$\nabla\times(\boldsymbol{\omega}\times\boldsymbol{u})=\boldsymbol{e}_\theta\left[\frac{\partial}{\partial z}\left(\frac{\omega}{r}\frac{\partial\psi}{\partial r}\right)-\frac{\partial}{\partial r}\left(\frac{\omega}{r}\frac{\partial\psi}{\partial z}\right)\right].$$

In both cases the square brackets is a Jacobian, which vanishes if and only if $\omega$ and $\psi$ or $\omega/r$ and $\psi$ depend solely on each other (this does not exclude their dependence on $t$). Therefore, *two-dimensional flow and rotationally symmetric flow are generalized Beltramian if and only if* (Wang 1990,1991)

$$\omega=\begin{cases} f(\psi,t) & \text{for two-dimensional flow,}\\ rf(\psi,t) & \text{for rotationally symmetric flow.}\end{cases}\tag{3.64}$$

This condition reduces (3.56) and (3.58) to

$$\nabla^2\psi=-f(\psi,t),\tag{3.65}$$

$$\frac{\partial}{\partial r}\left(\frac{1}{r}\frac{\partial\psi}{\partial r}\right)+\frac{1}{r}\frac{\partial^2\psi}{\partial z^2}=-rf(\psi,t),\tag{3.66}$$

respectively. In both cases it can be easily verified that

$$\boldsymbol{\omega}\times\boldsymbol{u}=\omega\nabla\psi=f(\psi,t)\nabla\psi=\nabla\int f(\psi,t)\,\mathrm{d}\psi,\tag{3.67}$$

which explicitly gives the scalar potential $\chi$ in (3.63).

As will be demonstrated in Sect. 6.4.3, however, for a viscous flow, while it is easy to solve a linearized vorticity equation, it may not be so to satisfy the kinematic constraint (3.65) or (3.66) necessary for the linearization, especially when $f(\psi)$ is a nonlinear function.

### 3.3.2 Lamb Vector Integrals, Helicity, and Vortex Filament Topology

We now look at the volume integrals of the Lamb vector and helicity density. First, by using (2.162) and noticing

$$\boldsymbol{u}\cdot\nabla\boldsymbol{u}=\nabla\cdot(\boldsymbol{u}\boldsymbol{u})-\boldsymbol{u}\vartheta,$$

where $\vartheta$ is the dilatation, we have identity

$$\boldsymbol{\omega}\times\boldsymbol{u}+\vartheta\boldsymbol{u}=\nabla\cdot\left(\boldsymbol{u}\boldsymbol{u}-\frac{1}{2}q^2\mathbf{I}\right).\tag{3.68}$$

Indicating that the tensor in the bracket on the right is a natural tensor potential of $\boldsymbol{\omega}\times\boldsymbol{u}+\vartheta\boldsymbol{u}$. Thus, using direct integration and integration by parts, one easily obtains (again $n=2,3$ is the spatial dimensionality)

$$\int_V (\boldsymbol{\omega} \times \boldsymbol{u} + \vartheta \boldsymbol{u})\, \mathrm{d}V = \int_{\partial V} \left( \boldsymbol{n} \cdot \boldsymbol{u}\boldsymbol{u} - \frac{1}{2} q^2 \boldsymbol{n} \right) \mathrm{d}S, \tag{3.69}$$

$$\int_V \boldsymbol{x} \times (\boldsymbol{\omega} \times \boldsymbol{u} + \vartheta \boldsymbol{u})\, \mathrm{d}V = \int_{\partial V} \boldsymbol{x} \times \left( \boldsymbol{n} \cdot \boldsymbol{u}\boldsymbol{u} - \frac{1}{2} q^2 \boldsymbol{n} \right) \mathrm{d}S. \tag{3.70}$$

$$\int_V \boldsymbol{x} \cdot (\boldsymbol{\omega} \times \boldsymbol{u} + \vartheta \boldsymbol{u})\, \mathrm{d}V = \int_{\partial V} \boldsymbol{x} \cdot \left( \boldsymbol{n} \cdot \boldsymbol{u}\boldsymbol{u} - \frac{1}{2} q^2 \boldsymbol{n} \right) \mathrm{d}S + \frac{1}{2}(n-2) \int_V q^2 \mathrm{d}V, \quad q = |\boldsymbol{u}|. \tag{3.71}$$

The $n = 3$ case of (3.71) is evidently relevant to the total kinetic energy of incompressible flows with uniform density (Sect. 3.4.2); while (3.69) and (3.70) are relevant to the evolution of vortical impulse and angular impulse (Sect. 3.5.2). In particular, in an unbounded incompressible fluid at rest at infinity, the surface integrals in these identities can be taken over the surface at infinity where $\boldsymbol{u} = \nabla \phi$, which must vanish by (3.49). Therefore, it follows that:

$$\int_{V_\infty} \boldsymbol{\omega} \times \boldsymbol{u}\, \mathrm{d}V = \boldsymbol{0}, \tag{3.72}$$

$$\int_{V_\infty} \boldsymbol{x} \times (\boldsymbol{\omega} \times \boldsymbol{u})\, \mathrm{d}V = \boldsymbol{0}, \tag{3.73}$$

$$\int_{V_\infty} \boldsymbol{x} \cdot (\boldsymbol{\omega} \times \boldsymbol{u})\, \mathrm{d}V = \frac{1}{2}(n-2) \int_{V_\infty} q^2\, \mathrm{d}V. \tag{3.74}$$

If the fluid has internal boundary, say a solid surface $\partial B$, to use (3.69) to (3.74) one may either employ the velocity adherence to cast the surface integrals over $\partial B$ to volume integrals over $B$, or continue the Lamb vector into $B$. Both ways form a single continuous medium although locally $\boldsymbol{\omega}$ is discontinuous across $\partial B$.

The integral of helicity density $\boldsymbol{\omega} \cdot \boldsymbol{u}$ is called the *helicity*. Moffatt (1969) finds that this integral is a measure of the state of "knotness" or "tangledness" of vorticity lines. We demonstrate this feature for thin vortex filaments (thin vorticity tubes). Assume that in a domain $V$ with $\boldsymbol{n} \cdot \boldsymbol{\omega} = 0$ on $\partial V$ there are two thin vortex filaments $C_1$ and $C_2$, with strengths (circulation) $\kappa_1$ and $\kappa_2$ respectively, away from which the flow is irrotational. $C_1$ and $C_2$ must be both closed loops. Suppose $C_1$ is not self-knotted, such that it spans a piece of surface $S_1$ without intersecting itself, and that the circulation *along* $C_1$ is

$$\Gamma_1 = \oint_{C_1} \boldsymbol{u} \cdot \mathrm{d}\boldsymbol{x} = \int_{S_1} \boldsymbol{\omega} \cdot \boldsymbol{n}\, \mathrm{d}S.$$

In the present situation, $\Gamma_1$ can only come from the contribution of the filament $C_2$. Therefore, if $C_1$ and $C_2$ are not tangled (Fig. 3.9a) then $\Gamma_1 = 0$; but if $C_2$ goes through $C_1$ once (Fig. 3.9b) then $\Gamma_1 = \pm\kappa_2$, with the sign depending on the relative direction of the vorticity in $C_1$ and $C_2$. More generally, $C_2$

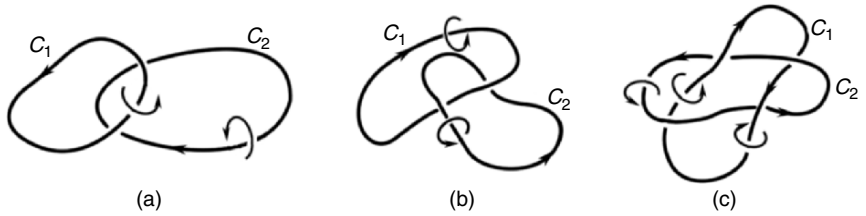


**Fig. 3.9.** The winding number of closed vortex filaments $C_1$ and $C_2$. (**a**) $\alpha_{12} = 0$, (**b**) $\alpha_{12} = -1$ , (**c**) $\alpha_{12} = 2$

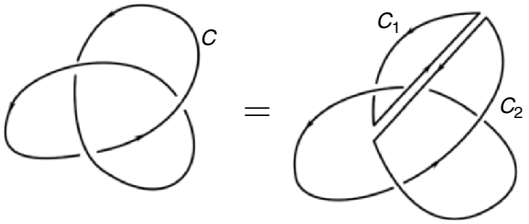


**Fig. 3.10.** Decomposition of a knotted vortex filament

can go through $C_1$ an integer number of times (Fig. 3.9c), so that $\Gamma_1 = \alpha_{12}\kappa_2$, where $\alpha_{12} = \alpha_{21}$ is a positive or negative integer called the *winding number* of $C_1$ and $C_2$.

By inserting one or more pair of filaments of opposite circulations, a self-knotted vortex filament can always be decomposed into two or more filaments which go through each other but are not self-knotted. Figure. 3.10 shows the decomposition of a triple knot, for which we have

$$\oint_C \boldsymbol{u} \cdot \mathrm{d}\boldsymbol{x} = \oint_{C_1} \boldsymbol{u} \cdot \mathrm{d}\boldsymbol{x} + \oint_{C_2} \boldsymbol{u} \cdot \mathrm{d}\boldsymbol{x} = 2\kappa.$$

In general, if there are $n$ unkotted vortex filaments, then the circulation along the $i$th closed filament is

$$\Gamma_i = \oint_{C_i} \boldsymbol{u} \cdot \mathrm{d}\boldsymbol{x} = \sum_{j=1}^{n} \alpha_{ij}\kappa_j,$$

where $\alpha_{ij}$ is the winding number of $C_i$ and $C_j$. Multiplying both sides by $\kappa_i$, we get (repeated indices imply summation)

$$\kappa_i\Gamma_i = \oint_{C_i} \kappa_i\boldsymbol{u} \cdot \mathrm{d}\boldsymbol{x} = \alpha_{ij}\kappa_i\kappa_j.$$

Now, observe that since the filaments are sufficiently thin, $\kappa_i\,\mathrm{d}\boldsymbol{x}$ is nothing but $\boldsymbol{\omega}dV$ for the $i$th vortex filament; thus

$$\alpha_{ij}\kappa_i\kappa_j = \int_V \boldsymbol{\omega} \cdot \boldsymbol{u}\,\mathrm{d}V, \tag{3.75}$$

which is precisely the helicity. Therefore, *the helicity measures the strengths of vortex filaments and their winding numbers.*

A remark is in order here. If we express the velocity by the Monge decomposition (2.115), there is

$$\boldsymbol{\omega} \cdot \boldsymbol{u} = \epsilon_{ijk}(\phi\lambda_{,j}\mu_{,k})_{,i} - \epsilon_{ijk}(\phi\lambda_{,j}\mu_{,ik}),$$

where the second term vanishes. Hence

$$\int_V \boldsymbol{\omega} \cdot \boldsymbol{u}\, \mathrm{d}V = \int_{\partial V} \boldsymbol{n} \cdot \boldsymbol{\omega}\phi\, \mathrm{d}S, \tag{3.76}$$

which is zero by assumption, conflicting (3.75) if the filaments are knotted. This apparent paradox comes from the local effectiveness of (2.115). Bretherton (1970) has pointed out that for knotted filaments the potential $\phi$ cannot be single-valued and hence the argument leading to (2.115) (Phillips 1933) does not hold.

The knotness or tangledness, characterized by the winding number, is known as the *topological property* of a curve. A topological property of a geometric configuration remains invariant under any continuous deformation. Thus, configurations in Fig. 3.11a have the same topological property. To retain the continuity during the deformation process, no tearing or reconnection is allowed; thus the patterns in Fig. 3.11a are topologically different from those in Fig. 3.11b. The former is simply connected, but the latter is doubly connected (connectivity is also a topological property).

A flow also has its topological structure. When a flow structure is a material curve like a vortex filament, the state of its knotness or tangledness is its topological property. Some new progress in the study of this property has

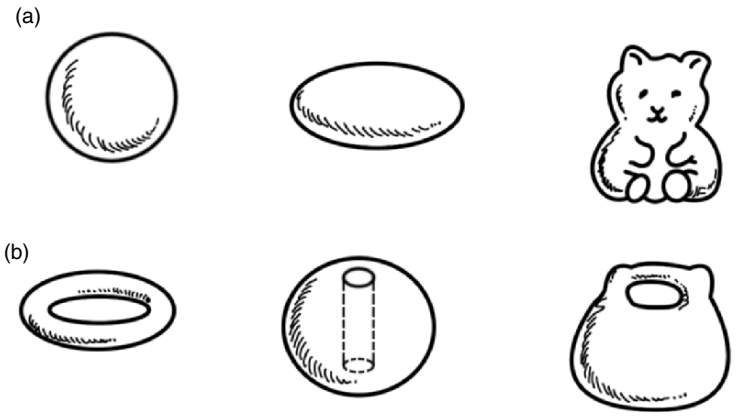


**Fig. 3.11.** Topological property of geometric configurations. Topologically, the configurations in (**a**) are the same as a sphere, and those in (**b**) are the same as a torus

been reviewed by Ricca and Berger (1996). Later in Sect. 7.1 we shall meet the topological structure of a vector field, which is a powerful tool in studying separated vortical flows. For fluid mechanics these topological properties are of qualitative value; in fact, just because quantitative details are beyond its concern, the topological analysis is generally valid.

## 3.4 Vortical Impulse and Kinetic Energy

This section establishes direct relations between vorticity integrals and two fundamental integrated dynamic quantities: the total momentum and kinetic energy of incompressible flows with uniform density $\rho = 1$. The results suggest that almost the entire incompressible fluid dynamics falls into vorticity and vortex dynamics (complemented by the potential-flow theory of Sect. 2.4.4).

### 3.4.1 Vortical Impulse and Angular Impulse

It has long been known that the total momentum and angular momentum of an unbounded fluid, which is at rest at infinity, are not well defined since relevant integrals are merely conditionally convergent. To avoid this difficulty, one appeals to the concept of *hydrodynamic impulse* (impulse for short) and *angular impulse*. The *potential impulse* has been introduced in Sect. 2.4.4, and we now consider the impulse and angular impulse associated with vortical flow, i.e., the vector field $\boldsymbol{i}(\boldsymbol{x})$ in (2.178), which is nonzero in a *finite* region. Since $\boldsymbol{\omega} = \nabla \times \boldsymbol{i}$, integrating $\boldsymbol{i}$ and using the derivative-moment identity (A.23) in $n$-dimensional space, we obtain

$$\int_V \boldsymbol{i}\,\mathrm{d}V = \frac{1}{n-1}\int_V \boldsymbol{x}\times\boldsymbol{\omega}\,\mathrm{d}V - \frac{1}{n-1}\int_{\partial V} \boldsymbol{x}\times(\boldsymbol{n}\times\boldsymbol{i})\,\mathrm{d}S, \quad n = 2, 3. \tag{3.77}$$

As $\partial V$ encloses the entire vector field $\boldsymbol{i}(\boldsymbol{x})$, the surface integral vanishes since $\boldsymbol{i} = \boldsymbol{0}$ there by assumption. This proves that

$$\int_V \boldsymbol{i}\,\mathrm{d}V = \boldsymbol{I} \equiv \frac{1}{n-1}\int_V \boldsymbol{x}\times\boldsymbol{\omega}\,\mathrm{dV}, \tag{3.78}$$

which defines the total *vortical impulse* $\boldsymbol{I}$, already introduced by (3.42) for $n = 3$ and (3.45) for $n = 2$. Evidently, due to (3.18), $\boldsymbol{I}$ is well defined and finite. A similar argument on the instantaneous angular momentum balance, using (A.24a), shows that

$$\int_V \boldsymbol{x}\times\boldsymbol{i}\,\mathrm{d}V = \boldsymbol{L} \equiv -\frac{1}{2}\int_V x^2\boldsymbol{\omega}\,\mathrm{d}V \tag{3.79}$$

which defines the total *vortical angular impulse*.

Now, by applying the same identities to the integral of $\boldsymbol{u}$ and $\boldsymbol{x}\times\boldsymbol{u}$, we immediately obtain (Thomson 1883)

$$\int_V \boldsymbol{u}\,\mathrm{d}V = \boldsymbol{I} - \frac{1}{n-1}\int_{\partial V} \boldsymbol{x}\times(\boldsymbol{n}\times\boldsymbol{u})\,\mathrm{d}S, \tag{3.80}$$

$$\int_V \boldsymbol{x}\times\boldsymbol{u}\,\mathrm{d}V = \boldsymbol{L} + \frac{1}{2}\int_{\partial V} x^2\boldsymbol{n}\times\boldsymbol{u}\,\mathrm{d}S, \tag{3.81a}$$

$$= \boldsymbol{L}' - \frac{1}{3}\int_{\partial V} \boldsymbol{x}\times[\boldsymbol{x}\times(\boldsymbol{n}\times\boldsymbol{u})]\,\mathrm{d}S, \tag{3.81b}$$

where

$$\boldsymbol{L}' \equiv \frac{1}{3}\int_V \boldsymbol{x}\times(\boldsymbol{x}\times\boldsymbol{\omega})\,\mathrm{d}V \tag{3.82}$$

is an alternative definition of the angular impulse, see (3.6). Comparing (3.81a) and (3.81b), for $n = 3$ there is

$$\begin{aligned}\boldsymbol{L}' - \boldsymbol{L} &= \frac{1}{6}\int_{\partial V}(2\boldsymbol{x}\boldsymbol{x} + x^2\mathbf{I})\cdot(\boldsymbol{n}\times\boldsymbol{u})\mathrm{d}S \\ &= \frac{1}{6}\int_V (2\boldsymbol{x}\boldsymbol{x} + x^2\mathbf{I})\cdot\boldsymbol{\omega}\,\mathrm{d}V = \frac{1}{6}\int_{\partial V} x^2\boldsymbol{x}(\boldsymbol{n}\cdot\boldsymbol{\omega})\mathrm{d}S,\end{aligned} \tag{3.83}$$

so $\boldsymbol{L}' = \boldsymbol{L}$ if $\boldsymbol{n}\cdot\boldsymbol{\omega} = 0$ on $\partial V$. Each of these vortical impulses differs from the total momentum and angular momentum only by a surface integral.

While identities (3.80) and (3.81) hold for any volume $V$, an important situation is that $V$ contains all vorticity so that on $\partial V$ the flow has *acyclic potential* $\phi$ (see Sect. 2.4.4). Then we can replace $\boldsymbol{u}$ by $\nabla\phi$ in the above surface integrals, which can then be simplified owing to the *derivative-moment transformation* (A.25) and (A.28a,c):[12]

$$-\frac{1}{n-1}\int_{\partial V}\boldsymbol{x}\times(\boldsymbol{n}\times\boldsymbol{u})\,\mathrm{d}S = \int_{\partial V}\phi\boldsymbol{n}\,\mathrm{d}S, \tag{3.84}$$

$$\begin{aligned}\frac{1}{2}\int_{\partial V} x^2\boldsymbol{n}\times\boldsymbol{u}\,\mathrm{d}S &= -\frac{1}{3}\int_{\partial V}\boldsymbol{x}\times[\boldsymbol{x}\times(\boldsymbol{n}\times\boldsymbol{u})]\,\mathrm{d}S \\ &= \int_{\partial V}\boldsymbol{x}\times\phi\boldsymbol{n}\,\mathrm{d}S.\end{aligned} \tag{3.85}$$

Recall the definition of potential impulse and angular impulse $\boldsymbol{I}_\phi$ and $\boldsymbol{L}_\phi$ given by (2.179) and (2.180), we see that the total momentum and angular momentum in $V$ with $\rho = 1$ are reduced to $\boldsymbol{I} + \boldsymbol{I}_\phi$ and $\boldsymbol{L} + \boldsymbol{L}_\phi$, respectively.

As observed in Sect. 2.4.4, if $V$ extends to infinity as in the case of externally unbounded flow, by (3.49) (with $\Gamma_\infty = 0$ when $n = 2$) the convergence

[12] The derivative-moment transformation is a set of integral identities in two- and three-dimensional spaces, which express the integral of a vectorial function to that of the moment of its derivatives, plus a boundary term. The details are given in Appendix A.2.

property of $\boldsymbol{I}_\phi$ and $\boldsymbol{L}_\phi$ are poor. This unpleasant feature is evidently given to the volume integrals of $\boldsymbol{u}$ and $\boldsymbol{x}\times\boldsymbol{u}$ (e.g., Batchelor 1967; Saffman 1992; Wu 1981). Take the far-field boundary shape as a large sphere ($n=3$) or circle ($n=2$) of radius $R\to\infty$. We can then estimate the surface integral in (3.84) by using (3.49). This yields (for $n=2$, $\Gamma_\infty$ has no contribution to the integral)

$$\int_{\partial V_R}\phi\boldsymbol{n}\,\mathrm{d}S=-\frac{1}{n}\boldsymbol{I}. \tag{3.86}$$

Thus, no matter how large $R$ could be, there is always $\boldsymbol{I}/n$ being communicated to the potential flow outside the sphere or circle. This apparent paradox, that a potential flow can carry a part of vortical impulse, is explained by Landau and Lifshitz (1976) as due to the assumption of incompressibility. Once a slight compressibility with constant speed of sound $c$ is introduced, then at time $t$ the momentum inside the sphere $R=ct$ is $(n-1)\boldsymbol{I}/n$ and the "lost" momentum $\boldsymbol{I}/n$ is transmitted by a spherical pressure wave front $R=ct$.

In contrast, the surface integral in (3.85) is simple when $n=3$ or $n=2$ with $\Gamma_\infty=0$, since over the sphere or circle $\boldsymbol{x}\times\phi\boldsymbol{n}=R\phi\boldsymbol{n}\times\boldsymbol{n}=\boldsymbol{0}$. But for $n=2$ with $\Gamma_\infty\neq 0$, $\phi$ is not single-valued and it is better to apply (3.50b) to the surface integral of (3.81a). This yields an $R^2$-divergence:

$$\oint_C x^2\boldsymbol{n}\times\boldsymbol{u}\,\mathrm{d}s=\frac{R^2}{2}\Gamma_R\boldsymbol{e}_z.$$

However, these discussions are of mainly academic interest. What enters dynamics is only the rate of change of these integrals, for which the divergence issue does not appear at all (Sects. 2.4.4 and 3.5.2; Chap. 11).

In two dimensions, the simplest vortex system with finite total momentum and angular momentum is a vortex couple of circulation $\mp\Gamma\boldsymbol{e}_z$ ($\Gamma<0$) located at $x=\pm r/2$, respectively, see Fig. 3.12. Then by (3.78) there is

$$\boldsymbol{I}=\boldsymbol{e}_y\Gamma r. \tag{3.87}$$

The fluid in between is pushed downward by the vortex couple.

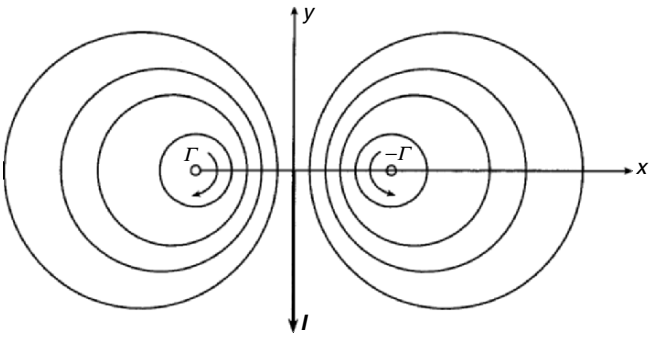


**Fig. 3.12.** The impulse produced by a vortex couple with $\Gamma<0$ in two dimensions

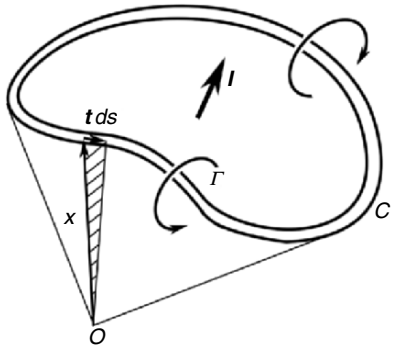


**Fig. 3.13.** The impulse produced by a vortex loop in three dimensions

In three dimensions, the simplest vortex system is a closed loop $C$ of thin vortex filament of circulation $\Gamma$, see Fig. 3.13. In this case (3.78) is reduced to, owing to (A.19)

$$\boldsymbol{I} = \frac{\Gamma}{2}\oint_C \boldsymbol{x}\times\boldsymbol{t}\,\mathrm{d}s = \Gamma\int_S \mathrm{d}\boldsymbol{S} = \Gamma\boldsymbol{S}, \tag{3.88}$$

where $\mathrm{d}\boldsymbol{S} = \boldsymbol{x}\times\boldsymbol{t}\,\mathrm{d}s/2$ is the vector surface element spanned by the triangle formed by $\boldsymbol{x}$ and $\mathrm{d}\boldsymbol{x} = \boldsymbol{t}\,\mathrm{d}s$, and $\boldsymbol{S}$ is the vector surface spanned by $C$. Note that $|\boldsymbol{S}|$ is the area of the *minimum surface* spanned by the loop, just like the area of a soap film spanned by a metal frame. It is very different from the area $S$ of a cone with apex at the origin of $\boldsymbol{x}$ that depends on the arbitrarily chosen origin. Similarly, if the vortex loop is isolated, by (3.82) and (3.83) we have

$$\boldsymbol{L} = \frac{\Gamma}{3}\oint_C \boldsymbol{x}\times(\boldsymbol{x}\times\boldsymbol{t})\mathrm{d}s = \frac{2\Gamma}{3}\int_S \boldsymbol{x}\times\mathrm{d}\boldsymbol{S}. \tag{3.89}$$

### 3.4.2 Hydrodynamic Kinetic Energy

Lamb (1932) gives two famous formulas for the total kinetic energy in a domain $V$,

$$K = \int_V \frac{1}{2}q^2\,\mathrm{d}V, \quad q = |\boldsymbol{u}|, \tag{3.90}$$

in terms of vorticity. Here the flow is assumed incompressible with $\rho = 1$. The first formula is based on the identity

$$q^2 = \boldsymbol{u}\cdot(\nabla\phi + \nabla\times\boldsymbol{\psi}) = \nabla\cdot(\boldsymbol{u}\phi + \boldsymbol{\psi}\times\boldsymbol{u}) + \boldsymbol{\omega}\cdot\boldsymbol{\psi}, \tag{3.91}$$

where $\phi$ and $\boldsymbol{\psi}$ are the Helmholtz potentials given by (2.104) with $\vartheta = 0$ now. The second formula is the direct consequence of (3.74) for three-dimensional

flow only. Thus, *Lamb's first and second formulas for kinetic energy* read, respectively,

$$K = \frac{1}{2}\int_V \boldsymbol{\omega}\cdot\boldsymbol{\psi}\,\mathrm{d}V + \frac{1}{2}\int_{\partial V} \boldsymbol{u}\cdot(\boldsymbol{n}\phi + \boldsymbol{n}\times\boldsymbol{\psi})\mathrm{d}S, \quad n = 2, 3, \tag{3.92}$$

$$K = \int_V (\boldsymbol{\omega}\times\boldsymbol{u})\cdot\boldsymbol{x}\,\mathrm{d}V + \int_{\partial V} \boldsymbol{x}\cdot\left(\frac{1}{2}q^2\boldsymbol{n} - \boldsymbol{u}\boldsymbol{u}\cdot\boldsymbol{n}\right)\mathrm{d}S, \quad n = 3. \tag{3.93}$$

If there is $\boldsymbol{u} = \nabla\phi$ on $\partial V$, the surface integrals in both formulas are reduced to the potential-flow kinetic energy $K_\phi$ given by (2.175). More specifically, as $x = |\boldsymbol{x}| \to \infty$, for $n = 3$ the surface integrals in both formulas decay as $\mathrm{O}(x^{-3})$. For $n = 2$, by (3.46) and (3.47), if $\Gamma_\infty = 0$, then the surface integral in (3.92) decays as $\mathrm{O}(x^{-2})$. However, if $\Gamma_\infty \neq 0$, there will be

$$|\boldsymbol{u}\phi| \sim \|\boldsymbol{u}\boldsymbol{\psi}\| = \mathrm{O}(x^{-1}\ln x)$$

and the surface integral is infinity. Therefore, for unbounded two-dimensional flows Lamb's first formula can be applied only if $\Gamma_\infty = 0$. We will be confined to this case. By taking a large sphere or circle, the preceding argument in dealing with impulse and angular impulse indicates that for unbounded flow (3.92) can be written as a double volume integral

$$K = \frac{1}{2\pi}\int\int G\boldsymbol{\omega}\cdot\boldsymbol{\omega}'\mathrm{d}V\mathrm{d}V', \tag{3.94}$$

where $G$ is given by (2.102). Hence, in three dimensions there is

$$K = -\frac{1}{8\pi}\int\int \frac{\boldsymbol{\omega}\cdot\boldsymbol{\omega}'}{|\boldsymbol{x}-\boldsymbol{x}'|}\mathrm{d}V'\mathrm{d}V \tag{3.95a}$$

$$= \int \boldsymbol{x}\cdot(\boldsymbol{\omega}\times\boldsymbol{u})\,\mathrm{d}V. \tag{3.95b}$$

Some general comparisons of the two formulas for any domain $V$ can be made. They both consist of a volume integral and a boundary integral, which can be symbolically expressed by

$$K = K_V^{(\alpha)} + K_S^{(\alpha)}, \tag{3.96}$$

with $\alpha = 1, 2$ denoting which of the two formulas is referred to. Then:

1. Since both formulas are obtained by integration by parts, the integrand of the volume integrals in (3.92) and (3.93),

$$k_V^{(1)}(\boldsymbol{x}) \equiv \frac{1}{2}\boldsymbol{\omega}\cdot\boldsymbol{\psi}, \tag{3.97a}$$

$$k_V^{(2)}(\boldsymbol{x}) \equiv (\boldsymbol{\omega}\times\boldsymbol{u})\cdot\boldsymbol{x} = (\boldsymbol{x}\times\boldsymbol{\omega})\cdot\boldsymbol{u}, \tag{3.97b}$$

do not represent the local kinetic energy density $q^2/2$. They are even not positively definite. However, like in many other formulas from integration by parts, only $k_V^{(\alpha)}$, $\alpha = 1, 2$, have net volumetric contribution (positive or negative) to $K$, with more localized support but containing more information on flow structures than $q^2/2$. In this sense, $k_V^{(\alpha)}$ can be viewed as the *net kinetic-energy carriers* (per unit mass). As illustration, Fig. 3.14 compares the instantaneous distribution of $q^2/2$ and $\omega\psi/2$ for a two-dimensional homogeneous and isotropic turbulence obtained by direct numerical simulation. We see that while $\omega\psi/2$ has high peaks in vortex cores and hence clearly shows the vortical structures, $q^2/2$ distributes more evenly with larger values *in between* neighboring vortices of opposite signs due to the strong induced velocity there.

2. While $k_V^{(1)}$ directly reflects the vortical structures of the flow, $k_V^{(2)}$ depends on the choice of the origin of $\boldsymbol{x}$. Thus, when the flow domain is a periodic box, the surface integral $K_S^{(1)}$ vanishes; but the appearance of $\boldsymbol{x}$ in $K_S^{(2)}$ makes the boundary contribution to $K$ from opposite sides of the box *doubled*. In a sense, by integration by parts, (3.93) shifts more net kinetic-energy carrier from the interior of the flow to boundary.
3. Despite the above inconvenience of Lamb's second formula, it has some unique significance. As seen in Sect. 2.4.3, the Lamb vector $\boldsymbol{\omega} \times \boldsymbol{u}$ is at the intersection point of two fundamental processes. Moreover, (3.97b) indicates that $k_V^{(2)}$ may be interpreted as an "effective rate of work" done by the "impulse density" $\boldsymbol{x} \times \boldsymbol{\omega}$. In particular, if we consider the rate of change of the local kinetic energy $q^2/2$ by taking inner product of (2.162) and $\boldsymbol{u}$, then evidently the Lamb vector has no contribution. But now it dominates the total kinetic energy as a net kinetic-energy carrier. This fact is a reflection of the nonlinearity in vortical flow advection.

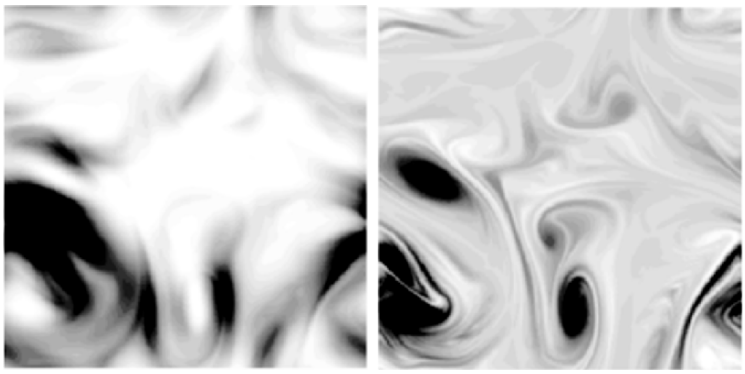


**Fig. 3.14.** Instantaneous distribution of (**a**) $q^2/2$ and (**b**) $\omega\psi/2$ in a two-dimensional homogeneous and isotropic turbulence, based on direct numerical simulation. Courtesy of Xiong

It is of interest to observe that, if we use (2.162) to compute the rate of change of the kinetic energy, then since $(\boldsymbol{\omega} \times \boldsymbol{u}) \cdot \boldsymbol{u} = 0$ the vorticity will have no local nor global inviscid contribution, see (2.52) and (2.53). Now, for incompressible flow Lamb's second formula asserts that the vorticity does affect the total kinetic energy, but indirectly. In fact, through the Lamb vector, the vorticity as an analogue of the Coriolis force must induce a change of not only direction but also magnitude of $\boldsymbol{u}$, and hence of $q^2/2$. It is this mechanism that is explicitly reflected by Lamb's first formula. For a similar mechanism involved in the total disturbance kinetic energy and its relation to flow stability see Sect. 9.1.3.

## 3.5 Vorticity Evolution

We now examine the temporal evolution of vorticity and related quantities, including the rate of change of circulation, total vorticity and its moments, helicity, vortical impulse, and total enstrophy. In the evolution of all these quantities there appears a key vector $\nabla \times \boldsymbol{a}$, where $\boldsymbol{a} = \mathrm{D}\boldsymbol{u}/\mathrm{D}t$ is the fluid acceleration which bridges kinematics to kinetics. Following Truesdell (1954), to keep the results universal we shall often stay with $\nabla \times \boldsymbol{a}$ in its general form. But it should be kept in mind that behind $\nabla \times \boldsymbol{a}$ is the *shearing kinetics*, which will be addressed in Sect. 4.1.

### 3.5.1 Vorticity Evolution in Physical and Reference Spaces

The time-evolution of vorticity in physical space comes from the curl of the vorticity form of the material acceleration, (2.162), and the result can be expressed in a few equivalent forms:

$$\nabla \times \boldsymbol{a} = \frac{\partial \boldsymbol{\omega}}{\partial t} + \nabla \times (\boldsymbol{\omega} \times \boldsymbol{u}) \tag{3.98a}$$

$$= \frac{\partial \boldsymbol{\omega}}{\partial t} + \nabla \cdot (\boldsymbol{u}\boldsymbol{\omega} - \boldsymbol{\omega}\boldsymbol{u}) \tag{3.98b}$$

$$= \frac{\mathrm{D}\boldsymbol{\omega}}{\mathrm{D}t} - \boldsymbol{\omega} \cdot \nabla \boldsymbol{u} + \vartheta \boldsymbol{\omega}. \tag{3.98c}$$

Introducing the continuity equation (2.39) into (3.98c) brings a slight simplification, known as the *Beltrami equation*:

$$\frac{\mathrm{D}}{\mathrm{D}t}\left(\frac{\boldsymbol{\omega}}{\rho}\right) = \frac{\boldsymbol{\omega}}{\rho} \cdot \nabla \boldsymbol{u} + \frac{1}{\rho} \nabla \times \boldsymbol{a}. \tag{3.99}$$

Moreover, since $\nabla \boldsymbol{u} = \mathbf{D} + \boldsymbol{\Omega}$ and $\boldsymbol{\omega} \cdot \boldsymbol{\Omega} = \boldsymbol{\omega} \times \boldsymbol{\omega}/2 = 0$, there is

$$\boldsymbol{\omega} \cdot \nabla \boldsymbol{u} = \boldsymbol{\omega} \cdot \mathbf{D} = \mathbf{D} \cdot \boldsymbol{\omega} = \boldsymbol{\omega} \cdot (\nabla \boldsymbol{u}^{\mathrm{T}}), \tag{3.100}$$

where the first two equalities imply that this term is a *coupling of strain-rate tensor and vorticity tensor*, while the last equality implies that $\boldsymbol{\omega}\cdot\nabla\boldsymbol{u}-\vartheta\boldsymbol{\omega}=-\boldsymbol{\omega}\cdot\mathbf{B}$ with $\mathbf{B}=\vartheta\mathbf{I}-(\nabla\boldsymbol{u})^{\mathrm{T}}$ being the surface deformation tensor, see the context of (2.27). This leads to another compact form of (3.98c):

$$\frac{\mathrm{D}\boldsymbol{\omega}}{\mathrm{D}t}+\boldsymbol{\omega}\cdot\mathbf{B}=\nabla\times\boldsymbol{a}. \tag{3.101}$$

The unique kinematic property of vorticity evolution in three-dimensional flows is reflected by the key term $\boldsymbol{\omega}\cdot\mathbf{B}$. Let $\mathrm{d}\boldsymbol{S}=\boldsymbol{n}\,\mathrm{d}S$ be a cross surface element of a thin vorticity tube so that $\boldsymbol{\omega}=\omega\boldsymbol{n}$. Then

$$\boldsymbol{\omega}\cdot\mathbf{B}=\frac{\omega}{\mathrm{d}S}\frac{\mathrm{D}}{\mathrm{D}t}(\boldsymbol{n}\,\mathrm{d}S)=\omega\left[\frac{\mathrm{D}\boldsymbol{n}}{\mathrm{D}t}+\frac{\boldsymbol{n}}{\mathrm{d}S}\frac{\mathrm{D}}{\mathrm{D}t}(\mathrm{d}S)\right], \tag{3.102}$$

where the two terms represents the *tilting* and *stretching* or *shrinking* of a material vorticity tube, measured by the rate of change of $\boldsymbol{n}$ and cross area $\mathrm{d}S$ of the tube, respectively. These mechanisms do not create vorticity from an irrotational flow but alter the existing vorticity distribution, leading to very far-reaching results (Sect. 3.5.3, Chap. 9 and 10). In two-dimensional flow $\boldsymbol{\omega}\cdot\mathbf{B}=\boldsymbol{\omega}\vartheta$, only the compressibility may change the cross area of a vorticity tube.

Associated with the tilting and stretching of vorticity tube, a vorticity line is also subjected to tilting and stretching. To see this, we assume $\nabla\times\boldsymbol{a}=\mathbf{0}$, so (3.99) indicates that the equation for $\boldsymbol{\omega}/\rho$ has exactly the same form as the rate of change of a material line element $\boldsymbol{\delta x}$ given by (2.17). Suppose $\boldsymbol{\delta x}$ is a segment of a vorticity line and at $t=0$, $\boldsymbol{\delta x}=\epsilon\boldsymbol{\omega}/\rho$. Then there is

$$\frac{\mathrm{D}}{\mathrm{D}t}\left(\boldsymbol{\delta x}-\epsilon\frac{\boldsymbol{\omega}}{\rho}\right)=\left(\boldsymbol{\delta x}-\epsilon\frac{\boldsymbol{\omega}}{\rho}\right)\cdot\nabla\boldsymbol{u}, \tag{3.103}$$

which forms a set of ordinary differential equations in terms of Lagrangian variables. If $\nabla\boldsymbol{u}$ is bounded (and integrable), then the existence and uniqueness theory for the initial-value problem of these equations ensures $\boldsymbol{\delta x}=\epsilon\boldsymbol{\omega}/\rho$ for all later $t$ (e.g., Whitham 1963). Therefore, once $\nabla\times\boldsymbol{a}=\mathbf{0}$ each line of $\boldsymbol{\omega}/\rho$ remains the same material line at any time. This is the *second Helmholtz vorticity theorem* to be discussed later.

We now take the inner product of (3.99) and the gradient of an arbitrary tensor $\mathbf{S}$ (we use a tensor of rank 2 in the algebra but the result holds for any rank). Since

$$\begin{aligned}\frac{\mathrm{D}}{\mathrm{D}t}\left(\frac{\omega_i}{\rho}S_{kl,i}\right)&=\frac{\partial}{\partial t}\left(\frac{\omega_i}{\rho}\right)S_{kl,i}+\frac{\omega_i}{\rho}\left(\frac{\partial S_{kl}}{\partial t}\right)_{,i}+u_j\left(\frac{\omega_i}{\rho}\right)_{,j}S_{kl,i}+\frac{\omega_i}{\rho}u_jS_{kl,ij}\\&=\frac{\mathrm{D}}{\mathrm{D}t}\left(\frac{\omega_i}{\rho}\right)S_{kl,i}+\frac{\omega_i}{\rho}\left[\left(\frac{\mathrm{D}S_{kl}}{\mathrm{D}t}\right)_{,i}-u_{j,i}S_{kl,j}\right],\end{aligned}$$

by (3.99) we obtain a *generalized vorticity formula* (Truesdell 1954)

$$\frac{\mathrm{D}}{\mathrm{D}t}\left(\frac{\boldsymbol{\omega}}{\rho}\cdot\nabla\mathbf{S}\right)=\frac{\boldsymbol{\omega}}{\rho}\cdot\nabla\left(\frac{\mathrm{D}\mathbf{S}}{\mathrm{D}t}\right)+\frac{1}{\rho}(\nabla\times\boldsymbol{a})\cdot\nabla\mathbf{S}. \tag{3.104}$$

Assigning $\mathbf{S}$ with different quantities may lead to a variety of results. Taking $\mathbf{S}=\boldsymbol{x}$ simply returns to (3.99). The major applications of (3.104) is when $\mathbf{S}$ is Lagrangian invariant:

$$\frac{\mathrm{D}\mathbf{S}}{\mathrm{D}t}=\mathbf{0}. \tag{3.105a}$$

Then there is

$$\frac{\mathrm{D}}{\mathrm{D}t}\left(\frac{\boldsymbol{\omega}}{\rho}\cdot\nabla\mathbf{S}\right)=\frac{1}{\rho}(\nabla\times\boldsymbol{a})\cdot\nabla\mathbf{S}. \tag{3.105b}$$

A special case of (3.105) is that $\mathbf{S}$ is a conservative scalar $\phi$. The scalar $(\boldsymbol{\omega}/\rho)\cdot\nabla\phi$ is known as the *potential vorticity* introduced by Rossby (1936, 1940) and Ertel (1942), governed by (the name will be explained in Sect. 3.6.1)

$$\frac{\mathrm{D}}{\mathrm{D}t}\left(\frac{\boldsymbol{\omega}}{\rho}\cdot\nabla\phi\right)=\frac{1}{\rho}(\nabla\times\boldsymbol{a})\cdot\nabla\phi,\quad\frac{\mathrm{D}\phi}{\mathrm{D}t}=0. \tag{3.106}$$

Because (3.106) is the simplest form of (3.105), we call the tensor $(\boldsymbol{\omega}/\rho)\cdot\nabla\mathbf{S}$, with $\mathbf{S}$ being a Lagrangian invariant, the *generalized potential vorticity*.

Moreover, since by (2.1) or (2.10) the fluid–particle label $\boldsymbol{X}$ is also Lagrangian invariant, an important example of generalized potential vorticity is obtained by setting $\mathbf{S}=\boldsymbol{X}$ in (3.105b):

$$\frac{\mathrm{D}}{\mathrm{D}t}\left(\frac{\boldsymbol{\omega}}{\rho}\cdot\nabla\boldsymbol{X}\right)=\frac{1}{\rho}(\nabla\times\boldsymbol{a})\cdot\nabla\boldsymbol{X}, \tag{3.107}$$

where $\nabla\boldsymbol{X}=\mathbf{F}^{-1}$ is the inverse of the deformation gradient tensor $\mathbf{F}=\nabla_X\boldsymbol{x}$ defined by (2.3). The vectors in (3.107) are defined in the reference space spanned by $\boldsymbol{X}$, indicating that we have obtained *the vorticity transport equation in reference space*. Then, since in the Lagrangian description $\mathrm{D}\,/\,\mathrm{D}t=\partial/\partial\tau$, where $\tau=t$ is the time variable, (3.107) can be integrated once. Set $\boldsymbol{x}=\boldsymbol{X}$ and $\nabla\boldsymbol{X}=\mathbf{I}$ at $t=0$, we obtain

$$\frac{\boldsymbol{\omega}}{\rho}\cdot\mathbf{F}^{-1}=\frac{\boldsymbol{\omega}_0}{\rho_0}+\int_0^\tau\frac{1}{\rho}(\nabla\times\boldsymbol{a})\cdot\mathbf{F}^{-1}\,\mathrm{d}\tau. \tag{3.108}$$

A detailed explanation of this formula and its physical meaning is given in Appendix. A.4, where a different derivation of (3.108) can be inferred. Taking the inner product of both sides with $\mathbf{F}$ from the right, (3.108) is transformed back to the physical space:

$$\frac{\boldsymbol{\omega}}{\rho}=\left(\frac{\boldsymbol{\omega}_0}{\rho_0}+\int_0^\tau\frac{1}{\rho}(\nabla\times\boldsymbol{a})\cdot\mathbf{F}^{-1}\,\mathrm{d}\tau\right)\cdot\mathbf{F}. \tag{3.109}$$

Truesdell (1954) calls (3.109) the *fundamental vorticity formula*. Its two terms have distinct physical sources and behavior. Recall that $\mathbf{F}$ measures

the relative displacement of fluid particles that were in the neighborhood of $\boldsymbol{X}$ at $t = 0$. At any $t$, $\mathbf{F}$ depends only on the displacement of the particles from their initial position but *independent of* the history of their motion. Hence, so is the first term of (3.109). The evolution represented by this term is *purely kinematic*. In contrast, since the kinetics of shearing process is fully reflected by $\nabla \times \boldsymbol{a}$, we now see that through the time integral in (3.109) the shearing kinetics yields an *accumulated* effect on the vorticity at all points through which a fluid particle $\boldsymbol{X}$ goes. This makes the final state of vorticity of the fluid particles inherently rely on their history, which is precisely the characteristics of kinetics. Following Truesdell (1954) but adding an adjective, we call $\nabla \times \boldsymbol{a}$ the *vorticity diffusion vector* and $\rho^{-1}(\nabla \times \boldsymbol{a}) \cdot \mathbf{F}^{-1}$ the *material vorticity diffusion vector*, to which the study of vorticity kinetics is thereby attributed: what causes the vorticity to diffuse and how much the diffusion will be. This is the topic of Sect. 4.1.

### 3.5.2 Evolution of Vorticity Integrals

Let $\mathcal{V}$ be a material volume and $V$ a fixed control volume. The integral form of (3.98)is obvious:

$$\frac{\mathrm{d}}{\mathrm{d}t}\int_{\mathcal{V}} \boldsymbol{\omega}\,\mathrm{d}v = \int_{\partial\mathcal{V}} (\boldsymbol{\omega}\cdot\boldsymbol{n})\boldsymbol{u}\,\mathrm{d}S + \int_{\partial\mathcal{V}} \boldsymbol{n}\times\boldsymbol{a}\,\mathrm{d}S, \tag{3.110}$$

$$\int_{V} \frac{\partial\boldsymbol{\omega}}{\partial t}\mathrm{d}V = \int_{\partial V} \boldsymbol{n}\cdot(\boldsymbol{\omega}\boldsymbol{u} - \boldsymbol{u}\boldsymbol{\omega})\mathrm{d}S + \int_{\partial V} \boldsymbol{n}\times\boldsymbol{a}\,\mathrm{d}S, \tag{3.111}$$

where $\boldsymbol{n}\cdot(\boldsymbol{\omega}\boldsymbol{u}-\boldsymbol{u}\boldsymbol{\omega}) = -\boldsymbol{n}\times(\boldsymbol{\omega}\times\boldsymbol{u})$. Applying these integrals to an unbounded fluid at rest at infinity, by (3.18) there is

$$\frac{\mathrm{d}}{\mathrm{d}t}\int_{V_\infty} \boldsymbol{\omega}\,\mathrm{d}V = \mathbf{0}. \tag{3.112}$$

This result is consistent with the Föppl theorem (3.15) for three-dimensional flow, and provides a proof of the total-circulation conservation theorem (3.16) for two-dimensional flow.

We proceed to consider the rate of change of some vorticity-related integrals. First, (3.110) is a special case of the time-evolution of a general $n$th-order moment (3.17b), of which the derivation is longer but straightforward; the result reads:

$$\frac{\mathrm{d}}{\mathrm{d}t}\int_{\mathcal{V}} \{\boldsymbol{\omega}\boldsymbol{x}^{(n)}\}\mathrm{d}v = \int_{\partial\mathcal{V}} \boldsymbol{\omega}\cdot\boldsymbol{n}\{\boldsymbol{x}^{(n)}\boldsymbol{u}\}\mathrm{d}S + \int_{\partial\mathcal{V}} \{\boldsymbol{x}^{(n)}(\boldsymbol{n}\times\boldsymbol{a})\}\mathrm{d}S. \tag{3.113}$$

Second, let $\mathcal{S}$ be any material surface bounded by $\mathcal{C}$. As the classic example of the Stokes theorem (A.17), we have obtained the *Kelvin circulation formula* (2.32). Noticing that the circulation of the potential part of $\boldsymbol{a}$, say $-\nabla\phi^*$, must vanish if $\phi^*$ is single-valued. Thus, denoting the rotational part of $\boldsymbol{a}$ by $\boldsymbol{a}_r$,

(2.32) can be written

$$\frac{\mathrm{d}\Gamma_{\mathcal{C}}}{\mathrm{d}t} = \oint_{\mathcal{C}} \boldsymbol{a}_r \cdot \mathrm{d}\boldsymbol{x} = \int_{\mathcal{S}} (\nabla \times \boldsymbol{a}) \cdot \boldsymbol{n}\, \mathrm{d}S, \tag{3.114}$$

which also implies (3.16). Compared with (3.98), (3.99), or (3.101), the evolution of circulation is independent of the effect of vorticity stretching and tilting. This simplicity is achieved at the expense of less information. As a scalar, $\Gamma$ only reflects the strength of a vortex tube but not its orientation, nor the vorticity magnitude at a point.

Next, consider the evolution of *helicity* defined as the material volume integral of helicity density. Its rate of change can be derived from (3.99) by using (2.41):

$$\begin{aligned}\frac{\mathrm{d}}{\mathrm{d}t}\int_{\mathcal{V}} \boldsymbol{\omega}\cdot\boldsymbol{u}\,\mathrm{d}v &= \frac{\mathrm{d}}{\mathrm{d}t}\int_{\mathcal{V}} \rho\left(\frac{\boldsymbol{\omega}}{\rho}\cdot\boldsymbol{u}\right)\mathrm{d}v = \int_{\mathcal{V}} \rho\frac{\mathrm{D}}{\mathrm{D}t}\left(\frac{\boldsymbol{\omega}}{\rho}\cdot\boldsymbol{u}\right)\mathrm{d}v \\ &= \int_{\mathcal{V}} [\boldsymbol{\omega}\cdot\nabla\boldsymbol{u}\cdot\boldsymbol{u} + (\nabla\times\boldsymbol{a})\cdot\boldsymbol{u} + \boldsymbol{\omega}\cdot\boldsymbol{a}]\mathrm{d}v.\end{aligned}$$

Then since

$$\boldsymbol{\omega}\cdot\nabla\boldsymbol{u}\cdot\boldsymbol{u} = \nabla\cdot\left(\frac{1}{2}q^2\boldsymbol{\omega}\right), \quad \boldsymbol{\omega}\cdot\boldsymbol{a} = \nabla\cdot(\boldsymbol{u}\times\boldsymbol{a}) + (\nabla\times\boldsymbol{a})\cdot\boldsymbol{u},$$

we obtain

$$\frac{\mathrm{d}}{\mathrm{d}t}\int_{\mathcal{V}} \boldsymbol{\omega}\cdot\boldsymbol{u}\,\mathrm{d}v = 2\int_{\mathcal{V}} (\nabla\times\boldsymbol{a})\cdot\boldsymbol{u}\,\mathrm{d}v + \int_{\partial\mathcal{V}}\left(\frac{1}{2}q^2\boldsymbol{\omega} + \boldsymbol{u}\times\boldsymbol{a}\right)\cdot\boldsymbol{n}\,\mathrm{d}S. \tag{3.115}$$

In particular, for an unbounded fluid at rest at infinity, there is

$$\frac{\mathrm{d}}{\mathrm{d}t}\int_{\mathcal{V}} \boldsymbol{\omega}\cdot\boldsymbol{u}\,\mathrm{d}v = 2\int_{\mathcal{V}} (\nabla\times\boldsymbol{a})\cdot\boldsymbol{u}\,\mathrm{d}v. \tag{3.116}$$

Finally, the rate of change of vortical impulse $\boldsymbol{I}$ and angular impulse $\boldsymbol{L}$ defined by (3.78) and (3.79), respectively, are closely related to the integrals of the Lamb vector $\boldsymbol{l} \equiv \boldsymbol{\omega}\times\boldsymbol{u}$ and its moment. Instead of directly calculating the time derivative of $\boldsymbol{I}$ and $\boldsymbol{L}$, we start from making the *derivative-moment transformation* of acceleration $\boldsymbol{a}$ by using (A.23) for any fluid domain $\mathcal{D}$:

$$\int_{\mathcal{D}} \boldsymbol{a}\,\mathrm{d}V = \frac{1}{k}\int_{\mathcal{D}} \boldsymbol{x}\times(\nabla\times\boldsymbol{a})\mathrm{d}V - \frac{1}{k}\int_{\partial\mathcal{D}} \boldsymbol{x}\times(\boldsymbol{n}\times\boldsymbol{a})\mathrm{d}S, \tag{3.117a}$$

where $k = n-1$ and $n = 2, 3$ is the spatial dimensionality, and $\nabla\times\boldsymbol{a}$ is expressed by (3.98a). We than use (A.23) again to transform the integral of $\nabla\times\boldsymbol{l}$ ($\boldsymbol{l} = \boldsymbol{\omega}\times\boldsymbol{u}$ denotes that Lamb vector) back to the integral of $\boldsymbol{l}$, obtaining

$$\int_{\mathcal{D}} \boldsymbol{a}\,\mathrm{d}V = \int_{\mathcal{D}}\left(\frac{1}{k}\boldsymbol{x}\times\boldsymbol{\omega}_{,t} + \boldsymbol{l}\right)\mathrm{d}V - \frac{1}{k}\int_{\partial\mathcal{D}} \boldsymbol{x}\times[\boldsymbol{n}\times(\boldsymbol{a}-\boldsymbol{l})]\mathrm{d}S. \tag{3.117b}$$

Hence, if the flow is incompressible and $\mathcal{D}$ is a material volume $\mathcal{V}$, by (2.35b), comparing (3.117a) and (3.117b) yields

$$\frac{\mathrm{d}\boldsymbol{I}_{\mathcal{V}}}{\mathrm{d}t}+\int_{\mathcal{V}}\boldsymbol{l}\,\mathrm{d}v-\frac{1}{k}\int_{\partial\mathcal{V}}\boldsymbol{x}\times\boldsymbol{u}\omega_n\,\mathrm{d}S=\frac{1}{k}\int_{\mathcal{V}}\boldsymbol{x}\times(\nabla\times\boldsymbol{a})\mathrm{d}v. \tag{3.118}$$

A similar approach to the integral of $\boldsymbol{x}\times\boldsymbol{a}$ by using (A.24a) yields

$$\frac{\mathrm{d}\boldsymbol{L}_{\mathcal{V}}}{\mathrm{d}t}+\int_{\mathcal{V}}\boldsymbol{x}\times\boldsymbol{l}\,\mathrm{d}v+\frac{1}{2}\int_{\partial\mathcal{V}}x^2\boldsymbol{u}\omega_n\,\mathrm{d}S=-\frac{1}{2}\int_{\mathcal{V}}x^2\nabla\times\boldsymbol{a}\,\mathrm{d}v. \tag{3.119}$$

In particular, if the fluid is unbounded both internally and externally, and at rest at infinity, then since by (3.72) and (3.73) the integrals of the Lamb vector and its moment vanish, we simply have

$$\frac{\mathrm{d}\boldsymbol{I}_{\infty}}{\mathrm{d}t}=\frac{1}{k}\int_{V_\infty}\boldsymbol{x}\times(\nabla\times\boldsymbol{a})\,\mathrm{d}V, \tag{3.120}$$

$$\frac{\mathrm{d}\boldsymbol{L}_{\infty}}{\mathrm{d}t}=-\frac{1}{2}\int_{V_\infty}x^2\nabla\times\boldsymbol{a}\,\mathrm{d}V. \tag{3.121}$$

Moreover, since $\nabla\times\boldsymbol{a}=\nabla\times\boldsymbol{a}_{\mathrm{r}}$ where $\boldsymbol{a}_{\mathrm{r}}=\nabla\times\boldsymbol{\psi}^*$ is the rotational part of $\boldsymbol{a}$, we may apply (3.117a) to $\boldsymbol{a}_{\mathrm{r}}$ only, so that the second term of (3.120) is cast to surface integrals of $\boldsymbol{\psi}^*$ and $\boldsymbol{a}_{\mathrm{r}}$, which vanish as $|\boldsymbol{x}|\to\infty$ (e.g., for viscous incompressible flow $\boldsymbol{\psi}^*=-\nu\boldsymbol{\omega}$). The same can be similarly done for the right-hand side of (3.121). Hence, *the vortical impulse and angular impulse of an unbounded fluid is time invariant.*

### 3.5.3 Enstrophy and Vorticity Line Stretching

Owing to the Föppl theorem (3.15), the integral of vorticity vector $\boldsymbol{\omega}$ cannot tell the total amount of shearing in a flow domain. Similar to the kinetic energy, we use the *enstrophy* $\omega^2/2$ for such a measurement and now examine its time evolution.

The inner product of $\boldsymbol{\omega}$ with (3.101) yields

$$\frac{\mathrm{D}}{\mathrm{D}t}\left(\frac{1}{2}\omega^2\right)=-\boldsymbol{\omega}\cdot\mathbf{B}\cdot\boldsymbol{\omega}+\boldsymbol{\omega}\cdot(\nabla\times\boldsymbol{a}). \tag{3.122}$$

Unlike circulation, in (3.122) the stretching effect is retained but tilting effect is removed. Write $\boldsymbol{\omega}=\boldsymbol{t}\omega$, we have

$$-\boldsymbol{\omega}\cdot\mathbf{B}\cdot\boldsymbol{\omega}=\alpha\omega^2,\quad \alpha\equiv-\boldsymbol{t}\cdot\mathbf{B}\cdot\boldsymbol{t}=\boldsymbol{t}\cdot\mathbf{D}\cdot\boldsymbol{t}-\vartheta. \tag{3.123}$$

The scalar $\alpha$ is the *stretching rate* of an infinitely thin vorticity tube or a single vorticity line. Namely, there is

$$\frac{\mathrm{D}}{\mathrm{D}t}\left(\frac{1}{2}\omega^2\right)=\alpha\omega^2+\boldsymbol{\omega}\cdot(\nabla\times\boldsymbol{a}), \tag{3.124}$$

$$\frac{\mathrm{D}\omega}{\mathrm{D}t}=\alpha\omega+\boldsymbol{t}\cdot(\nabla\times\boldsymbol{a}), \tag{3.125}$$

showing that the magnitude of vorticity will be intensified by a positive stretching.

In Lagrangian description (3.124) or (3.125) can be integrated with respect to time. Again let $\tau$ be the Lagrangian time and denote

$$A(\tau) = \int_0^\tau \alpha \mathrm{d}\eta, \tag{3.126a}$$

there is

$$\omega(\tau) = \omega(0)\mathrm{e}^{A(\tau)} + \int_0^\tau \boldsymbol{t} \cdot (\nabla \times \boldsymbol{a})\mathrm{e}^{A(\tau-\eta)}\mathrm{d}\eta. \tag{3.126b}$$

While the effect of $\nabla \times \boldsymbol{a}$ on the variation of $\omega$ is formally linear, that of stretching is *exponential*.

Figure. 3.15 shows a numerical example due to Siggia (1985), who computed the evolution of a vorticity loop which is initially elliptic on the $(y, z)$-plane. Let $L$ be its total length and $\sigma$ be the cross-sectional radius, and assume that $\sigma^2 L$ is time-invariant. At time $t = 0$, $\sigma_0$, and $L_0$ were taken as 0.2 and $\sim$10, respectively, and the ratio of the axes of the initial elliptical ring was 4:1. The self-induction is nonuniform, as can be inferred from (3.32). This induction causes the vortex ring to deform quickly and the filament to stretch nonuniformly. Figure. 3.15a shows a sequence of the vorticity-loop shapes and Fig. 3.15b shows the growth of $L$ in time, where the last three points imply an exponential growing.

As a nonlinear effect, vortex stretching is a crucial kinematic mechanism in the entire theory of shearing process. This mechanism and vortex tilting, as well as the cut and reconnect of vortices due to viscosity (Sect. 8.3.3), are the key to understanding many complex vortical flows. In particular, stretching is responsible for the *cascade* process in turbulence, by which large-scale vortices become smaller and smaller ones with increasingly stronger enstrophy (Chap. 10). In fact, turbulence may be briefly defined as *randomly stretched vortices* (Bradshaw, private communication, 1992). The strain rate $\mathbf{D}$ that causes stretching can be either a background field induced by other vortices, or induced locally by the vortex itself. The strongest stretching and shrinking occur if $\boldsymbol{\omega}$ is aligned to the stretching and shrinking principal axes of $\mathbf{D}$, respectively. Then the stretching rate $\alpha$ is the maximum eigenvalue of $\mathbf{D}$.

Generically, $\boldsymbol{\omega}$ is not aligned to any principal axis of $\mathbf{D}$, and it is desired to analyze the mechanisms responsible for $\alpha$. We now give two general formulas for incompressible flow. The first formula is local. Similar to the intrinsic streamline triad used before, we introduce an intrinsic triad along a vorticity line, with $(\boldsymbol{t}, \boldsymbol{n}, \boldsymbol{b})$ being the unit tangent, normal, and bi-normal vectors, respectively. Let $\kappa$ and $\tau$ be the curvature and torsion of the $\boldsymbol{\omega}$-line, and $\boldsymbol{u} = (u_s, u_n, u_b)$. Then by the Frenet–Serret formulas (A.39) there is

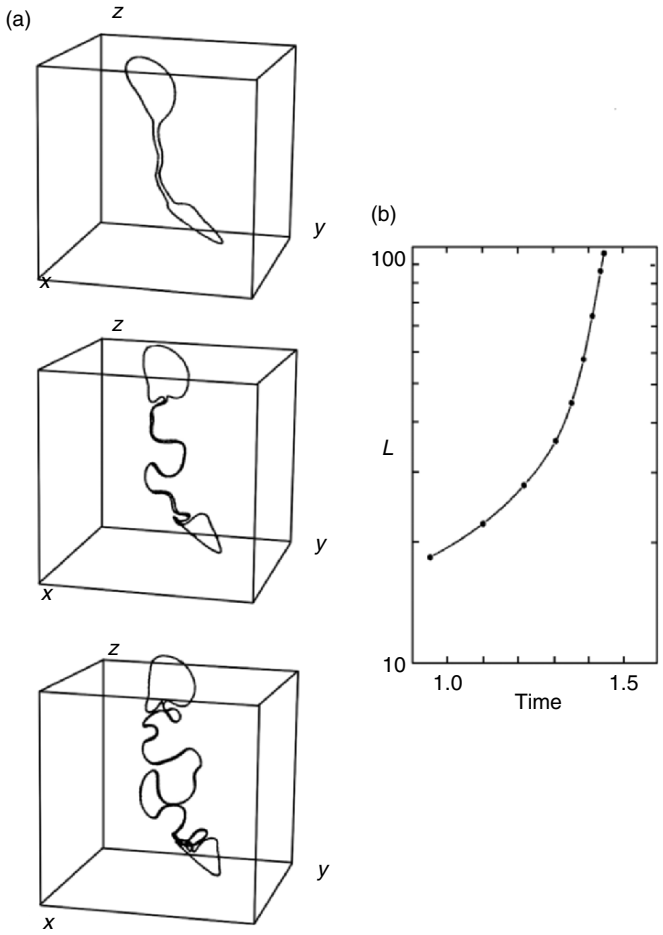


**Fig. 3.15.** The self-induced stretching of a vorticity loop, starting from an elliptical vortex ring on the $(y, z)$ plane. (**a**) The shape evolution of the loop, (**b**) the growth of the length $L$ of the loop. From Siggia (1985)

$$\boldsymbol{t}\cdot\nabla\boldsymbol{u}=\left(\frac{\partial u_s}{\partial s}-u_n\kappa\right)\boldsymbol{t}+\left(\frac{\partial u_n}{\partial s}+u_s\kappa-u_b\tau\right)\boldsymbol{n}+\left(\frac{\partial u_b}{\partial s}+u_n\tau\right)\boldsymbol{b}. \tag{3.127}$$

The component of $\boldsymbol{t}\cdot\nabla\boldsymbol{u}$ along $\boldsymbol{t}$ makes the $\boldsymbol{\omega}$-line stretched or contracted, and those along $\boldsymbol{n}$ and $\boldsymbol{b}$ make it tilted. Thus

$$\alpha=\frac{\partial u_s}{\partial s}-u_n\kappa. \tag{3.128}$$

For small $\kappa$ and $\tau$, the $\boldsymbol{\omega}$-line stretching (or contracting) and tilting are dominated by the increments of $u_s$ and $(u_n, u_b)$ along $s$, respectively (Batchelor 1967). However, a strong stretching may occur at a point of a vortex filament even if $\partial u_s/\partial s = 0$, as long as $\kappa \gg 1$ and $u_n < 0$ (outward from the curvature center). Inversely, if $u_n > 0$ (toward the curvature center) then the vortex filament will be significantly compressed and becomes much thicker. Note that this curvature effect cannot be explained solely by the strain-rate tensor of a background flow; the local self-induced velocity has to be included.

The second formula is global, which expresses the stretching rate caused by a distributed vorticity field rather than a thin vortex filament. Assume the incompressible flow is unbounded and at rest at infinity. The strain rate tensor $\mathbf{D}$ has been expressed by vorticity integral in (3.37). Making inner product at its both sides with the unit vector $\boldsymbol{t}(\boldsymbol{x})$ along $\boldsymbol{\omega}(\boldsymbol{x})$, and writing $\boldsymbol{\omega}(\boldsymbol{x}') = \boldsymbol{t}'\omega'$, the desired formula follows (Constantin (1994)):

$$\alpha(\boldsymbol{x}) = \frac{3}{4\pi}\int (\boldsymbol{e}\cdot\boldsymbol{t})[\boldsymbol{t}'\cdot(\boldsymbol{t}\times\boldsymbol{e})]\omega'\frac{\mathrm{d}V'}{r^3}. \tag{3.129}$$

To see the implication of this result, assume the distribution of $|\boldsymbol{\omega}(\boldsymbol{x})| = \omega(\boldsymbol{x})$ is given. Then $\alpha(\boldsymbol{x})$ solely depends on the orientation of the three unit vectors $\boldsymbol{e}$, $\boldsymbol{t}'$, and $\boldsymbol{t}$. Here, $|\boldsymbol{e}\cdot\boldsymbol{t}| \le 1$ and the scalar in square brackets is the volume of the prism formed by these three unit vectors. This volume crucially depends on the orientation of $\boldsymbol{t}'$ and $\boldsymbol{t}$. The local vorticity $\boldsymbol{\omega}(\boldsymbol{x}')$ will have a strongest contribution to the stretching rate $\alpha(\boldsymbol{x})$ if $\boldsymbol{\omega}(\boldsymbol{x})$ and $\boldsymbol{\omega}(\boldsymbol{x}')$ are *perpendicular*, and if $\boldsymbol{\omega}$ and $\boldsymbol{r}$ is neither parallel nor perpendicular. Denote $\boldsymbol{t}\cdot\boldsymbol{t}' = \cos\phi$, then

$$|(\boldsymbol{e}\cdot\boldsymbol{t})(\boldsymbol{t}'\times\boldsymbol{t})\cdot\boldsymbol{e}| \le |\sin\phi|.$$

It should be stressed that, as seen from Fig. 3.15, when the vortex ring is stretched it is also tilted. A straight vortex cannot be stretched unboundedly: Chorin (1994) points out that by (3.95a) this would increases the induced kinetic energy $K$ unboundedly, but the total kinetic energy is conserved (or decreasing due to dissipation) if in (2.52) no external force is imposed and the fluid is unbounded. To offset the increase of kinetic energy due to stretching, therefore, there must be vortex tilting, see the first term of (3.102), which may cause a partial cancellation of part of $\mathbf{D}$. Note that, contrary to the stretching, (3.95a) indicates that the main contribution to $K$ is from those vortex segments that are *parallel* to each other.

The vortex stretching also plays a key role in the mathematical aspects of the Navier–Stokes equation. It is especially relevant to a long-standing unsolved problem on whether a three-dimensional Navier–Stokes solution with smooth initial condition can spontaneously develop a singularity at a finite time $t^*$ (and hence for $t > t^*$ the solution no longer exists). Beale et al. (1984) have proved that only if the maximum of $|\boldsymbol{\omega}|$ diverges as $t \to t^*$, can the three-dimensional Euler solution blow up. In other words, vortex stretching dominates the regularity of flows (see also Majda 1986; Doering and Gibbon 1995; Majda and Bertozzi 2002). But the final answer remains unknown.

Finally, we mention that in two-dimensional flow without vorticity-tube stretching and tilting, the vorticity field may also evolve to some structures and the transition to turbulence may still happen. The underlying physical mechanism is quite different, though, and will be addressed in Chap. 12.

## 3.6 Circulation-Preserving Flows

Since the shearing kinetics is solely reflected by the specific content of the vorticity diffusion vector $\nabla \times \boldsymbol{a}$, a great simplification can be achieved if any one of the following three equivalent conditions holds:

$$\nabla \times \boldsymbol{a} = \boldsymbol{0}, \tag{3.130a}$$

$$\boldsymbol{a} + \nabla \phi^* = \boldsymbol{0}, \tag{3.130b}$$

$$\frac{\mathrm{d}}{\mathrm{d}t} \oint_{\mathcal{C}} \boldsymbol{u} \cdot \mathrm{d}\boldsymbol{x} = 0, \tag{3.130c}$$

where $\mathcal{C}$ is any material loop. Equation (3.130c) comes from (3.114) and is the well-known **Kelvin circulation theorem**: *If and only if the acceleration is curl-free, the circulation along any material loop is time invariant.* Conditions in (3.130) define a special class of flows of significant interest, known as *circulation-preserving flows* (Truesdell 1954).

In terms of the two fundamental processes, an overall physical understanding can be gained for the very nature of circulation-preserving flows. Because $\boldsymbol{a}$ and $\nabla \times \boldsymbol{a}$ are the bridges of kinematics and kinetics in the momentum equation and the vorticity transport equation, respectively, we see at once that (3.130a) implies that *in a circulation-preserving flow the evolution of shearing process is purely kinematic.* Consequently, a series of important Lagrangian invariant quantities or conservation theorems for the shearing process exist, which we present first. On the other hand, (3.130b) implies that the kinetics only enters the compressing process through the acceleration potential $\phi^*$, which suggests a possibility for the momentum equation be integrated once to yield Bernoulli integrals. This is our second topic. Then, since the vorticity conservation and Bernoulli integral appear as the two sides of a coin, a combination of both may lead to a deeper understanding of this class of flows and some further important theoretical results. These can be best revealed in the Hamiltonian formalism and is our third topic. The study of this section naturally paves a way to vorticity dynamics, which starts from Chap. 4.

### 3.6.1 Local and Integral Conservation Theorems

Almost all the results of this subsection come solely from (3.130a). The central local conservation theorem is a direct consequence of (3.130) and (3.105).

**The Generalized Potential Vorticity Conservation Theorem.** *Let* $\mathbf{S}$ *be any conservative tensor with* $\mathrm{D}\mathbf{S}/\mathrm{D}t = \boldsymbol{0}$ *and assume* $(\nabla \times \boldsymbol{a}) \cdot \nabla \mathbf{S} = \boldsymbol{0}$.

*Then the generalized potential vorticity* $(\boldsymbol{\omega}/\rho)\cdot\nabla\mathbf{S}$ *of each fluid particle is preserved.* Namely,

$$\frac{\mathrm{D}}{\mathrm{D}t}\left(\frac{\boldsymbol{\omega}}{\rho}\cdot\nabla\mathbf{S}\right)=\mathbf{0}, \tag{3.131a}$$

or

$$\frac{\boldsymbol{\omega}}{\rho}\cdot\nabla\mathbf{S}=\frac{\boldsymbol{\omega}_0}{\rho_0}\cdot\nabla\mathbf{S}_0 \quad \text{following particles.} \tag{3.131b}$$

For steady flow this theorem implies that the generalized potential vorticity is constant along a streamline. On the other hand, under the same conditions any tensor function $\mathcal{F}$ of the generalized vorticity must also be a conserved quantity, and so is the material-volume integral of $\rho\mathcal{F}$ owing to (2.41)

$$\int_{\mathcal{V}}\rho\mathcal{F}\left(\frac{\boldsymbol{\omega}}{\rho}\cdot\nabla\mathbf{S}\right)\mathrm{d}v=\text{const.} \tag{3.132}$$

This theorem has two important corollaries. First, setting $\mathbf{S}=\boldsymbol{X}$ in (3.131) and define

$$\boldsymbol{\Omega}(\boldsymbol{X},\tau)\equiv\frac{\boldsymbol{\omega}}{\rho}\cdot\mathbf{F}^{-1} \tag{3.133a}$$

as the *Lagrangian vorticity*, which is the image of the physical vorticity in the reference space (see Appendix A.4 and a comprehensive study of Casey and Naghdi 1991). Then by (2.1), (3.107), and (3.109), we have

$$\frac{\partial\boldsymbol{\Omega}}{\partial\tau}=\mathbf{0} \quad \text{or} \quad \frac{\boldsymbol{\omega}}{\rho}=\frac{\boldsymbol{\omega}_0}{\rho_0}\cdot\mathbf{F}, \tag{3.133b}$$

known as the *Cauchy vorticity formula*. Thus, the Lagrangian vorticity is *stationary* in the reference space, always equal to its initial distribution. In physical space, of course $\boldsymbol{\omega}$ keeps evolving, but is solely driven by the deformation gradient tensor $\mathbf{F}$ and independent of the history. Evidently, any $\mathcal{F}(\boldsymbol{\Omega})$ is also conserved, and in reference space we have

$$\frac{\partial}{\partial\tau}\int_{\mathcal{V}}\mathcal{F}(\boldsymbol{\Omega})\rho_0\,\mathrm{d}^3X=0. \tag{3.134}$$

Moreover, as a special case of (3.133b) we have *Cauchy potential-flow theorem*: *every initially irrotational fluid element will always be irrotational if and only if the flow is circulation-preserving.*

Second, taking $\mathbf{S}=\phi$ as a conserved scalar, from (3.131) follows that, if

$$\frac{\mathrm{D}\phi}{\mathrm{D}t}=0, \quad \text{for any } \phi \text{ and} \quad P\equiv\frac{\boldsymbol{\omega}}{\rho}\cdot\nabla\phi, \tag{3.135}$$

then

$$\frac{\mathrm{D}P}{\mathrm{D}t}=0. \tag{3.136}$$

This is the famous **Ertel's potential-vorticity theorem** (Ertel 1942): *The potential vorticity defined in (3.106) is Lagrangian invariant if and only if either the flow is circulation-preserving or* $\nabla\phi$ *is perpendicular to the vorticity diffusion vector.*

The dimension of $P$ may not be the same as that of the vorticity. The name "potential vorticity" came from the fact that, if the distance between two neighboring iso-$\phi$ surfaces increases such that $|\nabla\phi|$ is reduced, then by (3.136) the component of $\boldsymbol{\omega}/\rho$ parallel to $\nabla\phi$ must be enhanced. If $\rho$ varies very weakly, what is changing must be the vorticity, and the stretching of the distance between iso-$\phi$ surfaces has an effect similar to the vorticity-tube stretching.

The Ertel theorem has found most comprehensive applications in geophysical fluid dynamics to be examplified in Chap. 12. As an easy application of the Ertel theorem, take $\phi = z$ in two-dimensional flow. Since $\mathrm{D}z/\mathrm{D}t = w = 0$, $\nabla z = \boldsymbol{e}_z$, and $\boldsymbol{\omega} \cdot \boldsymbol{e}_z = \omega$ is the only nonzero vorticity component, for two-dimensional circulation-preserving flows there is

$$\frac{\mathrm{D}}{\mathrm{D}t}\left(\frac{\omega}{\rho}\right) = 0, \tag{3.137}$$

which also follows directly from the Beltrami equation (3.99). Similarly, for rotationally symmetric flow, take $\phi$ as the polar angle $\theta$ in a cylindrical coordinates. Then since $r\mathrm{D}\theta/\mathrm{D}t = u_\theta = 0$ and $\nabla\theta = \boldsymbol{e}_\theta/r$, we get

$$\frac{\mathrm{D}}{\mathrm{D}t}\left(\frac{\omega_\theta}{\rho r}\right) = 0. \tag{3.138}$$

In addition to these local conservation theorems, there are various integral conservation theorems of which the central one is the Kelvin circulation theorem (3.130c). Except its extensive practical applications, this powerful theorem has been used to prove other conservation theorems, including the Cauchy potential flow theorem and the following theorem.

**The Second and Third Helmholtz Vorticity Theorems** (Helmholtz 1858). *If and only if the flow is circulation-preserving, a material vorticity tube will move with the fluid* (the second theorem) *and its strength is time-invariant* (the third theorem).

**Remark.** The first Helmholtz theorem (Sect. 3.2.1) is universally true, since it only relies on the spatial property $\nabla\cdot\boldsymbol{\omega} \equiv 0$. The second and third Helmholtz theorems are *conditional* since they involve dynamic assumptions.

The proof of the second and third theorems can be found in standard textbooks. We just recall that a proof of the second theorem has already appeared following (3.103), where the same circulation-preserving condition was used but applies to *any single vorticity line*, more general than the second Helmholtz theorem. Actually, the sufficient and necessary condition for a vorticity line to remain a material line, and hence for the second Helmholtz

theorem to hold, can be relaxed to (Truesdell 1954)[13]

$$\boldsymbol{\omega} \times (\nabla \times \boldsymbol{a}) = \boldsymbol{0}, \tag{3.139}$$

i.e., $\nabla \times \boldsymbol{a}$ is aligned to $\boldsymbol{\omega}$. To prove this, consider a material line $\boldsymbol{x} = \boldsymbol{x}(s,t)$ with $s$ being the parameter defining the line. At a time $t$ this line coincides with a vorticity line if and only if

$$\frac{\partial \boldsymbol{x}}{\partial s} \times \boldsymbol{\omega} = \boldsymbol{0} \quad \text{or} \quad \frac{\partial \boldsymbol{x}}{\partial s} = f\boldsymbol{\omega}, \tag{3.140a,b}$$

where $f \neq 0$ is a scalar. If the vorticity line is still tangent to this material line at $t + \mathrm{d}t$, there must be

$$\frac{\mathrm{D}}{\mathrm{D}t}\left(\frac{\partial \boldsymbol{x}}{\partial s} \times \boldsymbol{\omega}\right) = \left(\frac{\partial \boldsymbol{x}}{\partial s} \cdot \nabla \boldsymbol{u}\right) \times \boldsymbol{\omega} + \frac{\partial \boldsymbol{x}}{\partial s} \times \frac{\mathrm{D}\boldsymbol{\omega}}{\mathrm{D}t} = \boldsymbol{0},$$

where by (3.140a,b) the right-hand side reads:

$$f\boldsymbol{\omega} \times \left(\frac{\mathrm{D}\boldsymbol{\omega}}{\mathrm{D}t} - \boldsymbol{\omega} \cdot \nabla \boldsymbol{u}\right) = f\boldsymbol{\omega} \times (\nabla \times \boldsymbol{a})$$

due to (3.98c). Thus, (3.139) is a necessary condition. Conversely, if (3.139) holds and if at $t = 0$ we have (3.140a,b), then $(\partial \boldsymbol{x}/\partial s) \times \boldsymbol{\omega}$ will vanish at $t = 0$ and have a vanishing material derivative; hence it must always be zero. Thus (3.139) is also sufficient.

Note that by (3.98a), for steady flow (3.139) implies the alignment of $\nabla \times (\boldsymbol{\omega} \times \boldsymbol{u})$ and $\boldsymbol{\omega}$, which by (3.59) ensures the existence of Lamb surfaces (Sposito 1997). Thus, the material surfaces forming any vorticity tubes are Lamb surfaces.

Next, by (3.115) we have the **helicity conservation theorem** (Moffatt 1969): *The helicity of circulation-preserving flow in a domain is time-invariant if* $\boldsymbol{\omega} \cdot \boldsymbol{n} = 0$ *and* $\boldsymbol{n} \times \boldsymbol{a} = \boldsymbol{0}$ *on the boundary*:

$$\frac{\mathrm{d}}{\mathrm{d}t}\int_{\mathcal{V}} \boldsymbol{\omega} \cdot \boldsymbol{u}\, \mathrm{d}v = 0. \tag{3.141}$$

Due to (3.75) and (3.130c), the theorem implies that *the topology of vortex filaments is invariant for circulation-preserving flow* under the aforementioned boundary condition. Note that although a wall-bounded *viscous* flow may satisfy this boundary condition, it cannot be circulation preserving near the wall.

Finally, it is worth emphasizing again that, as shown in Sect. 3.5.2, the vortical impulse and angular impulse are invariant even for viscous flow if *it is incompressible, unbounded, and at rest at infinity* (e.g. Saffman 1992).

[13] This argument is invalid for two-dimensional flow, since there (3.140a,b) is impossible.

### 3.6.2 Bernoulli Integrals

We now turn to the consequence of (3.130b) to seek *Bernoulli integrals*, first in terms of the Eulerian description and then Lagrangian description. We stay with the *acceleration potential* $\phi^*$ in its general form until the most general Bernoulli integral of circulation-preserving flows is found. The kinetic content of $\phi^*$ will then be identified.

Substituting (3.130b) into (2.162) yields

$$\frac{\partial \boldsymbol{u}}{\partial t} + \boldsymbol{\omega} \times \boldsymbol{u} + \nabla \left( \frac{1}{2} q^2 + \phi^* \right) = \boldsymbol{0}. \tag{3.142}$$

Evidently, if in a region the flow is irrotational such that $\boldsymbol{u} = \nabla \varphi$, then (3.142) can be integrated once to yield the most commonly encountered Bernoulli integral, with (2.177) being a special case:

$$\frac{\partial \varphi}{\partial t} + \frac{1}{2} q^2 + \phi^* = 0, \tag{3.143}$$

where the integration "constant" $C(t)$ has been absorbed into $\varphi$. However, our main interest is Bernoulli integrals for *rotational flow*. In this case, if on a line, a surface or in a volume the first two terms of (3.142) can be reduced to a gradient of a scalar, then (3.142) can be integrated once on that line, surface or volume, yielding a corresponding Bernoulli integral.

In the Eulerian description, when (3.130b) holds, the weakest condition for the existence of a Bernoulli integral is that the flow is rotational but *the vorticity is steady*:

$$\frac{\partial \boldsymbol{\omega}}{\partial t} = \nabla \times \left( \frac{\partial \boldsymbol{u}}{\partial t} \right) = \boldsymbol{0}.$$

Then the local acceleration $\partial \boldsymbol{u}/\partial t$ has a potential, say

$$\frac{\partial \boldsymbol{u}}{\partial t} = \nabla \beta,$$

and hence

$$\boldsymbol{u}(\boldsymbol{x}, t) = \nabla \left( \int \beta(\boldsymbol{x}, t) \mathrm{d}t \right) + \boldsymbol{v}(\boldsymbol{x}) = \nabla \varphi + \boldsymbol{v}.$$

This situation occurs, for instance, when an acoustic wave hits a steady vorticity field. Then (3.142) becomes

$$\boldsymbol{\omega} \times \boldsymbol{u} + \nabla \left( \frac{\partial \varphi}{\partial t} + \frac{1}{2} q^2 + \phi^* \right) = \boldsymbol{0}. \tag{3.144}$$

But this implies at once that (3.63) is satisfied, i.e., the flow is generalized Beltramian. If the potential $\chi$ of $\boldsymbol{\omega} \times \boldsymbol{u}$ is known, say (3.67) for two-dimensional or rotationally symmetric flow, then a *volume Bernoulli integral* exists:

$$\frac{\partial \varphi}{\partial t} + \frac{1}{2}q^2 + \phi^* + \chi = C(t). \tag{3.145}$$

Alternatively, since (3.63) implies (3.59), there must exist a set of Lamb surfaces which are orthogonal to the Lamb vector everywhere. Denoting these surfaces by $\mathcal{S}_\mathrm{L}$ and integrating (3.144) along such a surface, we obtain a *surface Bernoulli integral*

$$\frac{\partial \varphi}{\partial t} + \frac{1}{2}q^2 + \phi^* = C(\mathcal{S}_\mathrm{L}, t), \tag{3.146}$$

where $C(\mathcal{S}_\mathrm{L}, t)$ is the integration "constant" which varies with $\mathcal{S}_\mathrm{L}$ and $t$. Note that the kinetic energy $q^2/2$ may contain the contribution of the velocity induced by a vorticity field, which and the Lamb surfaces are the place where the coupling with shearing process (see Sect. 2.4.3) enters the Bernoulli integral.

The Bernoulli integrals appearing in most books represent various applications and simplifications of (3.145) or (3.146). But since the circulation preserving is a Lagrangian property, the most general form of the Bernoulli integral should be best revealed in the Lagrangian description, where the troublesome nonlinear Lamb vector in (3.142) is absent. This integral follows from inspecting the $\boldsymbol{X}$-space image of the acceleration, which reads (for derivation see Appendix. A.4)

$$\frac{\partial \boldsymbol{U}}{\partial \tau} = \boldsymbol{A} + \nabla_X \left(\frac{1}{2}q^2\right), \tag{3.147}$$

where

$$U_\alpha \equiv x_{i,\alpha} u_i \quad \text{or} \quad \boldsymbol{U} = \mathbf{F} \cdot \boldsymbol{u}, \tag{3.148}$$

$$A_\alpha \equiv x_{i,\alpha} a_i \quad \text{or} \quad \boldsymbol{A} = \mathbf{F} \cdot \boldsymbol{a} \tag{3.149}$$

are the *images of velocity and acceleration in the reference space*, respectively. Then by (3.130b) there is

$$A_\alpha = -\phi^*_{,i} x_{i,\alpha} = -\phi^*_{,\alpha}, \tag{3.150}$$

hence (3.147) is reduced to

$$\frac{\partial \boldsymbol{U}}{\partial \tau} = \nabla_X \left(\frac{1}{2}q^2 - \phi^*\right), \tag{3.151}$$

which can be integrated once:

$$\boldsymbol{U} = \boldsymbol{u}_0 + \nabla_X \Psi, \quad \Psi = \int_0^\tau \left(\frac{1}{2}q^2 - \phi^*\right) \mathrm{d}\tau. \tag{3.152}$$

This equation for compressing process can be compared with the Cauchy vorticity formula (3.133) for the transverse process. Unlike the latter, the velocity evolution depends on the history of fluid particles, and hence cannot

be attributed to pure kinematics even if the flow is circulation-preserving. This is what we asserted in the beginning of the section.

We now need to map (3.152) from the reference space to physical space. First, we make a Monge decomposition of $\boldsymbol{u}_0$ at $\tau = 0$ (see (2.115)):

$$\boldsymbol{u}_0 = \nabla_X \phi_0 + g \nabla_X h, \tag{3.153}$$

where $\phi_0$, $g$, and $h$ are functions of $\boldsymbol{X}$ only. Substitute this into (3.152), and set

$$\Phi(\boldsymbol{X}, \tau) = \phi_0(\boldsymbol{X}) + \Psi(\boldsymbol{X}, \tau),$$

we have

$$\boldsymbol{U} = \nabla_X \Phi + g \nabla_X h.$$

Taking inner product of both sides with $\nabla \boldsymbol{X}$ then gives the counterpart of (3.152) in physical space at any time:

$$\boldsymbol{u} = \nabla \Phi + g \nabla h, \quad \frac{\mathrm{D}g}{\mathrm{D}t} = \frac{\mathrm{D}h}{\mathrm{D}t} = 0. \tag{3.154a,b}$$

The special feature of this Monge–Clebsch decomposition is that the circulation-preserving condition ensures the existence of two Lagrangian invariant potentials $g$ and $h$. Physically, we have $\boldsymbol{\omega} = \nabla g \times \nabla h$, so that surfaces $g =$ constant and $h =$ constant are material vorticity surfaces, in consistency with the Helmholtz second vorticity theorem. Note that as remarked following (2.115), $\Phi$ is *not* the full velocity potential and depends on history.

Finally, substituting (3.154a) into the acceleration formula (2.11), i.e., $\boldsymbol{a} = \partial \boldsymbol{u}/\partial t + \boldsymbol{u} \cdot \nabla \boldsymbol{u}$, and using (3.154b), we obtain

$$a_i = \frac{\partial}{\partial t}(\Phi_{,i} + g h_{,i}) + u_j (\Phi_{,i} + g h_{,i})_{,j} = \left( \frac{\mathrm{D}\Phi}{\mathrm{D}t} - \frac{1}{2} q^2 \right)_{,i}$$

where by (3.154a)

$$\frac{\mathrm{D}\Phi}{\mathrm{D}t} = \frac{\partial \Phi}{\partial t} + u_i (u_i - g h_{,i}) = \frac{\partial \Phi}{\partial t} + q^2 + g \frac{\partial h}{\partial t}.$$

Thus, a comparison with (3.130b) yields the most general Bernoulli integral, written in terms of Lagrangian and Eulerian descriptions, respectively (Serrin 1959),

$$\frac{\partial \Phi}{\partial \tau} - \frac{1}{2} q^2 + \phi^* = 0, \tag{3.155a}$$

$$\frac{\partial \Phi}{\partial t} + \frac{1}{2} q^2 + g \frac{\partial h}{\partial t} + \phi^* = 0, \quad \frac{\mathrm{D}g}{\mathrm{D}t} = \frac{\mathrm{D}h}{\mathrm{D}t} = 0, \tag{3.155b}$$

where again the arbitrary integration constant has been absorbed into one of the potentials. Therefore, we have proved the following theorem.

**Theorem .** *For any circulation-preserving flow there exists a Bernoulli integral (3.155) following each fluid particle.*

Equation (3.155a) has been used in the Lagrangian approach of some flow problems (e.g., Baker et al. 1982), but in practice (3.155b) is of little value. It requires solving seven first-order equations for $(u_i, \phi^*, \Phi, g, h)$ and, in general, even for steady flow there will still be $g\,\partial h/\partial t \neq 0$ (Serrin 1959). Nevertheless, we may easily see the connection of (3.155b) and preceding Bernoulli integrals. Assume the vorticity is steady and $\partial \boldsymbol{u}/\partial t = \nabla(\partial\varphi/\partial t)$ as before. Comparing (3.144) and (3.155b) yields

$$\boldsymbol{\omega} \times \boldsymbol{u} = \nabla\left(\frac{\partial \Phi}{\partial t} - \frac{\partial \varphi}{\partial t} + g\frac{\partial h}{\partial t}\right),$$

indicating the existence of a set of Lamb surfaces. Thus we return to (3.146).

Note that in (3.155a) the sign in front of $q^2/2$ is negative; we shall soon see that for effectively inviscid flow satisfying (3.130), $q^2/2 - \phi^*$ is nothing but the Lagrangian density which integrates to the *Lagrangian action*, while the total energy $q^2/2 + \phi^*$ appeared in the Bernoulli integrals in the Eulerian description is the *Hamiltonian density*.

It is in order now to identify the dynamic and thermodynamic content as well as the physical meaning of $\phi^*$. By (2.44) and (2.163), the momentum equation can be rewritten

$$\boldsymbol{a} = \boldsymbol{f} - \frac{1}{\rho}\nabla p + \boldsymbol{\eta} = \boldsymbol{f} - \nabla h + T\nabla s + \boldsymbol{\eta}, \tag{3.156}$$

where $\boldsymbol{\eta}$ is the viscous force given by (2.164). Thus, the vorticity diffusion vector reads

$$\nabla \times \boldsymbol{a} = \nabla \times \boldsymbol{f} + \frac{1}{\rho^2}\nabla\rho \times \nabla p + \nabla \times \boldsymbol{\eta} \tag{3.157a}$$

$$= \nabla \times \boldsymbol{f} + \nabla T \times \nabla s + \nabla \times \boldsymbol{\eta}. \tag{3.157b}$$

Evidently, a flow will be circulation-preserving if and only if all terms on the right-hand side disappear.

First, $\nabla \times \boldsymbol{f} = \boldsymbol{0}$ if and only if $\boldsymbol{f} = -\nabla\zeta$, say. In many applications the existence of $\zeta$ is not a problem. For a gas motion $\boldsymbol{f}$ is negligible, and for liquid the gravitational force has a potential $\zeta = gz$, with $z$ being the vertical distance from a reference level.

Next, the second term of (3.157a) disappears if $\nabla\rho$ and $\nabla p$ are parallel. This is so for incompressible flow without density stratification. For a compressible flow $\nabla\rho \times \nabla p = 0$ *if and only if the flow is barotropic*, i.e., in the flow only one thermodynamic variable is independent (a flow with two or more independent thermodynamic variables is called *baroclinic*). The proof of "if" is evident, since then there must be $p = f(\rho)$, say, so $\nabla p = f'(\rho)\nabla\rho$ which is parallel to $\nabla\rho$. To prove the "only if," observe that the condition

$$\boldsymbol{0} = \nabla p \times \nabla\rho = \nabla \times (p\nabla\rho)$$

implies either $p = f(\rho)$ and hence the flow is barotropic, or $p\nabla\rho = \nabla\lambda$ has a potential. But in the latter case $\lambda$ can be taken as the unique independent thermodynamic variable; thus the proof is completed. Consequently, we have $\nabla p/\rho = \nabla(\int \mathrm{d}p/\rho)$. Similarly one can prove $\nabla T \times \nabla s = \mathbf{0}$ in (3.157b).

Finally, the third term of (3.157) disappears if and only if there exists a potential, say $\sigma$, such that

$$\boldsymbol{\eta} = -\nabla\sigma, \tag{3.158}$$

which is trivially satisfied for effectively inviscid flows but holds only for a special class of viscous flows. Note that an inviscid flow is a nondissipative system but viscous flow contains irreversible process due to friction. While the isentropic condition $\mathrm{D}s/\mathrm{D}t = 0$ applies only to the former, a flow having a Bernoulli integral is not necessarily inviscid. In any case, when all the preceding three conditions are satisfied, the acceleration potential $\phi^*$ exists and is given by

$$\phi^* = \zeta + \int \frac{\mathrm{d}p}{\rho} + \sigma, \tag{3.159}$$

showing that Bernoulli integrals are *energy integrals* governing the transfer of one kind of energy to another.

Finally, we remark that the circulation preserving is sufficient but not necessary for having a Bernoulli integral. For example, one may use (3.142) to construct a Bernoulli integral along a line perpendicular to both $\partial\boldsymbol{u}/\partial t$ and $\boldsymbol{\omega}\times\boldsymbol{u}$ (Truesdell 1954). However, this kind of integrals are not practically useful.

### 3.6.3 Hamiltonian Formalism

Having examined the implication of (3.130) to the shearing and compressing processes separately, We now seek a combination of both sides. For nondissipative systems with $\boldsymbol{\eta} = \mathbf{0}$, this is best done in terms of the Hamiltonian formalism, see, e.g., Lanczos (1970) for a basic knowledge of *variational calculation* as well as *Lagrangian and Hamiltonian mechanics*. A comprehensive presentation of Hamiltonian fluid dynamics is given by Salmon (1998). Viscous circulation-preserving flows will be addressed in Sect. 3.6.5.

In fluid mechanics, the direct counterpart of finite-number discrete particles is the infinitely many Lagrangian labels $\boldsymbol{X}$, while the counterpart of generalized coordinates and generalized velocity are the position vector $\boldsymbol{x}(\boldsymbol{X},\tau)$ and velocity $\dot{\boldsymbol{x}}(\boldsymbol{X},\tau) = \partial\boldsymbol{x}/\partial\tau$ of particle $\boldsymbol{X}$ at time $\tau$. The summation over the particle number is replaced by integration over the $\boldsymbol{X}$-space. Therefore, for the *Lagrangian* $L$ we have

$$L = \int_{\mathcal{V}} \rho_0 \mathcal{L}\, \mathrm{d}^3X, \tag{3.160}$$

where $\mathcal{L}$ is the *Lagrangian density*. The mass conservation requires that $\rho_0 \mathrm{d}^3X = \rho\,\mathrm{d}v$ is invariant during variation. The *Hamilton's principle* reads:

$$\int_{t_1}^{t_2} \mathrm{d}\tau \int_{\mathcal{V}} \rho_0 \delta\mathcal{L}\, \mathrm{d}^3 X = 0 \tag{3.161}$$

from which follows the *Euler–Lagrange equation* for $\mathcal{L}$:

$$\frac{\partial \mathcal{L}}{\partial x_i} - \frac{\partial}{\partial \tau}\left(\frac{\partial \mathcal{L}}{\partial \dot{x}_i}\right) = 0. \tag{3.162}$$

In carrying out variations in the $\boldsymbol{X}$-space, all Lagrangian variables are to be kept fixed and Eulerian variables are to be varied (and vise versa if we work in the physical space).

The choice of Lagrangian density is not unique. Let $k = q^2/2 = \dot{\boldsymbol{x}} \cdot \dot{\boldsymbol{x}}/2$ be the kinetic energy per unit mass, the motion equation of a physical field can be written

$$\frac{\partial}{\partial \tau}\frac{\partial k}{\partial \dot{x}_i} = -\frac{\partial \mathcal{U}}{\partial x_i}, \tag{3.163}$$

where $\mathcal{U}(\boldsymbol{x}, t)$ collects other kinds of energy which do not explicitly depend on $\dot{\boldsymbol{x}}$. Then one can set $\mathcal{L} = k - \mathcal{U}$ such that (3.163) leads to (3.162). Specifically, one may choose $\mathcal{U} = \zeta + e$ as the sum of potential and internal energies, so that

$$\widehat{\mathcal{L}} = \frac{1}{2}\dot{\boldsymbol{x}} \cdot \dot{\boldsymbol{x}} - (\zeta + e). \tag{3.164}$$

By using the continuity equation (2.40) and isentropic condition (2.78), it can be shown that this choice casts (3.161) to (Salmon (1998))

$$\int_{t_1}^{t_2} \mathrm{d}\tau \int_{\mathcal{V}} \rho \left[\left(\nabla\zeta + \frac{1}{\rho}\nabla p\right) \cdot \delta\boldsymbol{x}\right] \mathrm{d}^3 x = 0,$$

from which and (3.162) follows the Euler motion equation for effectively inviscid and barotropic flow with conservative body force:

$$\frac{\partial^2 \boldsymbol{x}}{\partial \tau^2} = -\nabla\zeta - \frac{1}{\rho}\nabla p, \quad p = f(\rho). \tag{3.165}$$

Alternative to (3.164), since (3.130b) is nothing but the general momentum equation of circulation-preserving flow, comparing it with (3.163) suggests that we may simply set $\mathcal{U} = \phi^*$ if the flow is effectively inviscid. In fact, since in (3.159) with $\sigma = 0$ there is $\zeta = \zeta(\boldsymbol{x}, t)$, $p = p(\rho)$, $\rho = \rho(J)$ by (2.40) while $J = J(\boldsymbol{x})$ for fixed $\boldsymbol{X}$, $\phi^*(\boldsymbol{x}, t)$ indeed does not explicitly depend on $k$. Thus, we now have

$$\mathcal{L} = \frac{1}{2}q^2 - \phi^* = \frac{1}{2}\dot{\boldsymbol{x}} \cdot \dot{\boldsymbol{x}} - \zeta - \int \frac{\mathrm{d}p}{\rho}. \tag{3.166}$$

Note that this identification gives (3.151) a deeper implication

$$\frac{\partial \boldsymbol{U}}{\partial \tau} = \nabla_X \mathcal{L}, \tag{3.167}$$

which is an $\boldsymbol{X}$-space image of the circulation-preserving acceleration formula (3.130b). Correspondingly, the Bernoulli integral (3.155a) now simply reads.

$$\frac{\mathrm{D}\Phi}{\mathrm{D}t} = \mathcal{L}. \tag{3.168}$$

Then, since the $\delta$-operation and $\partial/\partial\tau = \mathrm{D}/\mathrm{D}t$ operation are permutable, we have identity

$$\frac{\partial}{\partial\tau}(\boldsymbol{u}\cdot\delta\boldsymbol{x}) = \boldsymbol{a}\cdot\delta\boldsymbol{x} + \boldsymbol{u}\cdot\delta\frac{\partial\boldsymbol{x}}{\partial\tau} = \boldsymbol{a}\cdot\delta\boldsymbol{x} + \delta\left(\frac{1}{2}q^2\right), \tag{3.169}$$

and hence from (3.166) there is

$$\delta\mathcal{L} = \delta\left(\frac{1}{2}q^2\right) - \nabla\phi^*\cdot\delta\boldsymbol{x} = \frac{\partial}{\partial\tau}(\boldsymbol{u}\cdot\delta\boldsymbol{x}) - (\boldsymbol{a}+\nabla\phi^*)\cdot\delta\boldsymbol{x}.$$

Substituting this into (3.161) and note that the first term integrates to zero for fixed $t_1$ and $t_2$, from the arbitrariness of $\delta\boldsymbol{x}$ we return to the "momentum equation" (3.130b). This confirms our choice (3.166) for $\mathcal{L}$. More explicitly, by (3.166), for fixed $\boldsymbol{X}$ we have

$$\frac{\partial\mathcal{L}}{\partial x_i} = -\zeta_{,i} - \frac{1}{\rho}p_{,i}, \quad \frac{\partial\mathcal{L}}{\partial\dot{x}_i} = \dot{x}_i$$

so from (3.162) we re-obtain (3.165).

Moreover, similar to particle mechanics, there is

$$\frac{\mathrm{D}}{\mathrm{D}t}\left(\frac{1}{2}q^2 + \phi^*\right) = -\frac{\partial\mathcal{L}}{\partial t}. \tag{3.170}$$

Hence, the total energy is conserved if $\mathcal{L}$ is independent of time. Then, since

$$\frac{\mathrm{D}}{\mathrm{D}t}\left(\frac{1}{2}q^2\right) = \boldsymbol{u}\cdot\boldsymbol{a} = -\boldsymbol{u}\cdot\nabla\phi^*,$$

we also have

$$\frac{\partial\mathcal{L}}{\partial t} = -\frac{\partial\phi^*}{\partial t}. \tag{3.171}$$

We may also obtain the Hamiltonian of circulation-preserving flow, but the partial derivatives with respect to generalized coordinates and generalized momentum for particle system (e.g., Lanczos 1970) need to be replaced by corresponding variational derivatives. Thus, now the generalized momentum is

$$p_i = \frac{\delta}{\delta u_i}\int_{\mathcal{V}}\left(\frac{1}{2}q^2 - \phi^*\right)\mathrm{d}^3X = u_i = \dot{x}_i.$$

Therefore, the Hamiltonian is simply given by

$$H = \int_{\mathcal{V}} \mathcal{H}\, \mathrm{d}^3 X, \quad \mathcal{H} \equiv \frac{1}{2} q^2 + \phi^*, \tag{3.172a,b}$$

where the *Hamiltonian density* $\mathcal{H}$ satisfies the canonical equations:

$$\dot{u}_i = -\frac{\delta \mathcal{H}}{\delta x_i}, \quad \dot{x}_i = \frac{\delta \mathcal{H}}{\delta u_i}. \tag{3.173a,b}$$

Here, (3.173a) is nothing but $\boldsymbol{a} = -\nabla \phi^*$ and (3.173b) comes from (3.172b). We also have

$$\frac{\mathrm{D}\mathcal{H}}{\mathrm{D}t} = -\frac{\partial \mathcal{L}}{\partial t} = \frac{\partial \phi^*}{\partial t}. \tag{3.173c}$$

due to (3.171).

The Hamilton's principle (3.161) is formulated in the reference space. The derivation of momentum equation for such flows in Eulerian description is more complicated, where the key is keeping the full equivalence of the two descriptions (but, see some different findings below), which is ensured by Lin's constraint (2.10). For effectively inviscid flows, in terms of the Eulerian variables the Lagrangian density was chosen as $\widehat{\mathcal{L}}$ defined by (3.164), of which the variation is subjected to three constraints: the mass conservation $\mathrm{D}\rho/\mathrm{D}t = -\rho\vartheta$, the energy conservation $\mathrm{D}s/\mathrm{D}t = 0$, and Lin's constraint $\mathrm{D}\boldsymbol{X}/\mathrm{D}t = \boldsymbol{0}$. Then the Euler equation follows. This formulation is called *Herrivel–Lin variational principle*, see Serrin (1959), who also proved that conversely every Euler flow is an extremal under those three constraints. For further discussions see Bretherton (1970) and Salmon (1988).

### 3.6.4 Relabeling Symmetry and Energy Extremum

At this place we observe that, as a close analogy with particle mechanics, the Hamiltonian formalism so far developed for circulation-preserving flow concentrates only on energy consideration, where both the Lagrangian density $\mathcal{L}$ and the Hamiltonian density $\mathcal{H}$ belong to the longitudinal part only. This is natural because particle mechanics does not have any transverse interaction. Actually, the self-closure of *compressing dynamics* makes this direct analogy possible. It is then clear that in the Hamiltonian formalism there must still be a room to add the information on shearing process, which is now a purely kinematic matter. Therefore, the Hamiltonian structure of circulation-preserving flows is more abundant than its particle-mechanics counterpart, and *any results derived from a transverse variable must be unique to continuum mechanics* (Salmon 1988).

First, recall that the Hamiltonian principle for circulation-preserving flow is formulated in the $\boldsymbol{X}$-space, in which the Lagrangian vorticity $\boldsymbol{\Omega}(\boldsymbol{X})$ defined by (3.133a) is time-independent (Lagrangian invariant). A virtual change $\delta\boldsymbol{X}$ of the particle label $\boldsymbol{X}(\boldsymbol{x}, t)$ during variation implies a *relabeling* of the fluid

particles; while the observation following (3.165) has indicated that the $\boldsymbol{X}$ enters the Lagrangian (3.164) or (3.166) only through the density $\rho = J^{-1}\rho_0$. Thus, the dynamics of circulation-preserving flow will be unaffected provided $\delta J^{-1} = 0$, which imposes a constraint to the possible relabeling. In fact, due to the symmetry between the mappings $\boldsymbol{x} = \boldsymbol{\phi}(\boldsymbol{X}, \tau)$ and $\boldsymbol{X} = \boldsymbol{\Phi}(\boldsymbol{x}, t)$, the reverse of (2.6) must be

$$\delta J^{-1} = J^{-1}\nabla_X \cdot \delta \boldsymbol{X}. \tag{3.174}$$

Hence, $\delta J^{-1} = 0$ if and only if

$$\delta \boldsymbol{X} = \nabla_X \times \boldsymbol{c} \tag{3.175}$$

for some vector $\boldsymbol{c}$. Namely, in a circulation-preserving flow a solenoidal relabeling $\delta \boldsymbol{X}$ does not alter any fluid motion. A variation that leaves $\mathcal{L}$ unchanged implies a symmetry; so we now have a *relabeling symmetry*.

Conversely, by the *Noether theorem* (e.g., Lanczos 1970), the invariance of $\mathcal{L}$ under certain transformation must imply a conservation law. To see what this law is in the present case, we use (3.175) for any vector $\boldsymbol{c}$ to compute $\delta\mathcal{L}$ defined by (3.166):

$$\begin{aligned}
\delta\mathcal{L} &= u_i \delta\left(\frac{\partial x_i}{\partial \tau}\right) - \phi^*_{,\alpha}\delta X_\alpha = u_i x_{i,\alpha}\frac{\partial}{\partial\tau}(\delta X_\alpha) - \phi^*_{,\alpha}\delta X_\alpha \\
&= \epsilon_{\alpha\beta\gamma}\left(U_\alpha \frac{\partial c_{\gamma,\beta}}{\partial\tau} - \phi^*_{,\alpha}c_{\gamma,\beta}\right) \\
&= \epsilon_{\alpha\beta\gamma}\left[\frac{\partial}{\partial\tau}(U_\alpha c_{\gamma,\beta}) - (\phi^*_{,\alpha}c_\gamma)_{,\beta} - \frac{\partial U_{\alpha,\beta}}{\partial\tau}c_\gamma\right],
\end{aligned}$$

where $U_\alpha$ is defined by (3.148a). Substituting this into (3.161), since the first two terms integrate to zero, it follows that:

$$\delta\int_{t_1}^{t_2}\mathrm{d}\tau\int_{\mathcal{V}}\mathcal{L}\rho_0\mathrm{d}^3X = \int_{t_1}^{t_2}\mathrm{d}\tau\int_{\mathcal{V}}\boldsymbol{c}\cdot\frac{\partial\boldsymbol{\Omega}}{\partial\tau}\rho_0\mathrm{d}^3X = 0,$$

where $\boldsymbol{\Omega}$ is the Largangian vorticity defined by (3.133a). Therefore, due to the arbitrariness of $\boldsymbol{c}$, we return to (3.134), which is equivalent to (3.130). Thus, we arrive at the remarkable conclusion as given below.

**Relabeling Symmetry Theorem.** *The fluid particle-relabeling symmetry and circulation preserving are equivalent.*

This theorem was discovered and formulated in different ways by a number of authors during 1960s–1980s (for brief reviews of its history see, Salmon 1988 and Padhye and Morrison 1996). It implies that for circulation-preserving flow, Lin's constraint $\mathrm{D}\boldsymbol{X}/\mathrm{D}t = \boldsymbol{0}$, which was considered necessary for deriving the Euler equation for isentropic vortical flow in physical space but is inconvenient

in applications, can be relaxed to solenoidal exchange of particle labels without altering the flow field.

In fact, a recent work of Kambe (2003, 2004) based on the *gauge field theory* has shown that even the entire issue of particle labeling can be avoided. Assuming the flow is inviscid and isentropic, Kambe first shows that the Eulerian variation of the Lagrangian of the free field of fluid flows implies the potential-flow equation, which is, however, not invariant under a local rotational gauge transformation. He then shows that the vorticity is the *gauge field* of the flow required by the local rotational gauge invariance, just like the electromagnetic field is the gauge field of charged particles. In this approach Lin's constraint is not needed at all. Kambe (private communication) conjectured that the principle of local rotational gauge invariance is equivalent to chasing particle motion.

Owing to these progresses, it can be said that *for circulation-preserving flow the Eulerian description alone is complete (closed).* The underlying physics can be easily understood in terms of fundamental processes. Circulation preserving makes the transverse part retreat within kinematics and has no direct influence on the Lagrangian. Conversely, since the Lagrangian (3.166) comes from the direct analogy with particle mechanics that contains only longitudinal part of the motion, if this part is self-closed, then the transverse part must not enter dynamics and the flow must be circulation preserving.

The relabeling symmetry has not yet fully explored the joint properties of compressing dynamics and shearing kinematics. By the *Lyapunov stability theory* (see Chap. 9), if for a flow one can find a scalar function which takes extremum (maximum or minimum) among all flows of the same kind satisfying the same boundary conditions, then this flow will be stable. Therefore, finding extrema for certain flows is of great interest in fluid-dynamic stability analysis, which is, however, difficult in general cases. But, for certain circulation-preserving flow several extremum theorems have been found.

For incompressible potential flow we have Kelvin's minimum kinetic-energy theorem (Sect. 2.4.4), of which the condition is unfortunately too limited. It is natural to attempt its generalization to circulation-preserving flow. Kelvin (1887) himself conjectured that "The condition for steady motion of an incompressible inviscid fluid filling a finite fixed portion of space... is that, with a given vorticity, the energy is a thorough maximum, or a thorough minimum, or a minimax." This conjecture was first proven by Arnold (1965b,c) for incompressible circulation-preserving flow. We restate the first part of his results as follows.

**Arnold's Energy Theorem .** *Of all possible circulation-preserving flows having the same Lagrangian vorticity and satisfying the same boundary condition, the total energy of steady flow takes stationary value.*

The basic idea behind this theorem can be interpreted as follows. To find a stationary value (necessary for being extremum) of a functional by the variational method, a common choice of the functional is conservative quantities.

As indicated by (3.172) and (3.173c), the total energy $H$ is such a functional when the flow is steady. However, to cover the rotational flow one has to add a new conservative scalar

$$C = \int_{\partial\mathcal{V}} c(\boldsymbol{\Omega})\rho_0 \mathrm{d}^3X \quad \text{with} \quad \frac{\partial C}{\partial \tau} = 0. \tag{3.176}$$

Therefore, instead of $\delta H = 0$ alone that leads to the steady momentum equation, we should consider the conditional variation of $H$ under the constraint of the Lagrangian constancy of $C$ and to seek for the result of

$$\delta(H + C) = \delta \int_{\mathcal{V}} [\mathcal{H} + c(\boldsymbol{\Omega})]\rho_0 \mathrm{d}^3X = 0. \tag{3.177}$$

No Lagrangian multiplier is needed due to the arbitrariness of $c(\boldsymbol{\Omega})$. We then expect that (3.177) should lead to steady circulation-preserving vortical flow. This can be proven by different ways; one of which starting from (3.177) is given by Holm (1986). Here, we cite a neater approach for incompressible flow given by Vladimirov and Ilin (1988), quite close to Arnold's original approach.

Consider an inviscid and incompressible circulation-preserving flow with $\boldsymbol{a} = -\nabla\phi^*$ in a singly connected fixed domain $\mathcal{D}$, so by (3.130a) there is (subscripts denote partial derivatives),

$$\boldsymbol{u}_t + \boldsymbol{\omega} \times \boldsymbol{u} + \nabla\left(\frac{1}{2}q^2 + \phi^*\right) = \boldsymbol{0}, \quad \boldsymbol{n} \cdot \boldsymbol{u} = 0 \ \text{ on } \partial\mathcal{D}. \tag{3.178}$$

We perform the variation of $\boldsymbol{u}$ in a way to preserve the circulation along any material loop. To this end, Arnold introduces a set of transformations $g^\epsilon : \boldsymbol{x} \Longrightarrow \tilde{\boldsymbol{x}}(\boldsymbol{x}, \epsilon)$ of the domain $\mathcal{D}$ to itself, defined by

$$\frac{\mathrm{d}\tilde{\boldsymbol{x}}}{\mathrm{d}\epsilon} = \boldsymbol{\xi}(\boldsymbol{x}, \epsilon), \tag{3.179a}$$

where $\boldsymbol{\xi}$ satisfies

$$\nabla \cdot \boldsymbol{\xi} = 0 \ \text{ in } \mathcal{D}, \quad \boldsymbol{n} \cdot \boldsymbol{\xi} = 0 \ \text{ on } \partial\mathcal{D}. \tag{3.179b}$$

Namely, $g^\epsilon$ can be interpreted as a "virtual incompressible motion" of the fluid away from the real flow field, with $\epsilon$, $\tilde{\boldsymbol{x}}$, and $\boldsymbol{\xi}$ being the "virtual time," "virtual position" of fluid particle whose position at $\epsilon = 0$ was $\boldsymbol{x}$, and the "virtual velocity," respectively. This virtual motion creates a vector field $\tilde{\boldsymbol{u}}(\tilde{\boldsymbol{x}}, \epsilon)$ such that $\tilde{\boldsymbol{u}}(\tilde{\boldsymbol{x}}, \epsilon)|_{\epsilon=0} = \boldsymbol{u}(\boldsymbol{x})$ is the real velocity, and for any $\epsilon$ there is $\boldsymbol{n} \cdot \tilde{\boldsymbol{u}} = 0$ on $\partial\mathcal{D}$. Thus, we may define operator $\mathrm{D}/\mathrm{D}\epsilon$ such that

$$\frac{\mathrm{D}\tilde{\boldsymbol{u}}}{\mathrm{D}\epsilon} = \tilde{\boldsymbol{u}}_\epsilon + \boldsymbol{\xi} \cdot \tilde{\nabla}\tilde{\boldsymbol{u}}, \quad \frac{\mathrm{D}}{\mathrm{D}\epsilon}\mathrm{d}\tilde{\boldsymbol{x}} = \mathrm{d}\tilde{\boldsymbol{x}} \cdot \tilde{\nabla}\boldsymbol{\xi} \tag{3.180}$$

as we did for real flow, see (2.11) and (2.17). Then, assuming $\epsilon$ is small, we can use Taylor expansion to write

$$\delta \boldsymbol{u} \equiv \tilde{\boldsymbol{u}}_\epsilon\big|_{\epsilon=0}, \quad \delta^2 \boldsymbol{u} \equiv \frac{1}{2}\tilde{\boldsymbol{u}}_{\epsilon\epsilon}\big|_{\epsilon=0}. \tag{3.181}$$

Now, to ensure $g^\epsilon$ is circulation-preserving, for any material loop $C(t)$ which is transformed to $g^\epsilon C(t)$, there should be

$$\oint_{g^\epsilon C} \tilde{\boldsymbol{u}} \cdot \mathrm{d}\tilde{\boldsymbol{x}} - \oint_C \boldsymbol{u} \cdot \mathrm{d}\boldsymbol{x} = \epsilon \frac{\mathrm{d}\tilde{\Gamma}}{\mathrm{d}\epsilon}\Big|_{\epsilon=0} + \frac{1}{2}\epsilon^2 \frac{\mathrm{d}^2\tilde{\Gamma}}{\mathrm{d}\epsilon^2}\Big|_{\epsilon=0} + \mathrm{O}(\epsilon^2) = 0. \tag{3.182}$$

Here, by (3.180) and using identities

$$\boldsymbol{a} \cdot \nabla \boldsymbol{b} + \nabla \boldsymbol{a} \cdot \boldsymbol{b} = \nabla(\boldsymbol{a} \cdot \boldsymbol{b}) - \boldsymbol{a} \times (\nabla \times \boldsymbol{b}), \tag{3.183a}$$

$$\oint \mathrm{d}\boldsymbol{x} \cdot \nabla \chi = 0 \quad \text{for any } \chi, \tag{3.183b}$$

there is

$$\begin{aligned} \frac{\mathrm{d}}{\mathrm{d}\epsilon} \oint_{g^\epsilon C} \tilde{\boldsymbol{u}} \cdot \mathrm{d}\tilde{\boldsymbol{x}} &= \oint_{g^\epsilon C} \left\{ \mathrm{d}\tilde{\boldsymbol{x}} \cdot \frac{\mathrm{D}\tilde{\boldsymbol{u}}}{\mathrm{D}\epsilon} + \frac{\mathrm{D}}{\mathrm{D}\epsilon}(\mathrm{d}\tilde{\boldsymbol{x}}) \cdot \tilde{\boldsymbol{u}} \right\} \\ &= \oint_{g^\epsilon C} \mathrm{d}\tilde{\boldsymbol{x}} \cdot (\tilde{\boldsymbol{u}}_\epsilon + \boldsymbol{\xi} \cdot \tilde{\nabla}\tilde{\boldsymbol{u}} + \tilde{\nabla}\boldsymbol{\xi} \cdot \tilde{\boldsymbol{u}}) = \oint_{g^\epsilon C} (\tilde{\boldsymbol{u}}_\epsilon + \tilde{\boldsymbol{\omega}} \times \boldsymbol{\xi}) \cdot \mathrm{d}\tilde{\boldsymbol{x}}. \end{aligned}$$

Thus, the $\mathrm{O}(\epsilon)$ term in (3.182) yields

$$\delta \boldsymbol{u} = \boldsymbol{\xi} \times \boldsymbol{\omega} - \nabla\alpha \quad \text{and hence} \quad \delta\boldsymbol{\omega} = \nabla \times (\boldsymbol{\xi} \times \boldsymbol{\omega}), \tag{3.184}$$

where $\alpha$ is a scalar function. Therefore, by using (3.184), (3.178), and (3.179b), the first energy variation for steady flow under the circulation-preserving condition is given by

$$\delta K = \int_{\mathcal{D}} \boldsymbol{u} \cdot \delta\boldsymbol{u}\, \mathrm{d}V = \int_{\mathcal{D}} \boldsymbol{\xi} \cdot (\boldsymbol{\omega} \times \boldsymbol{u}) \mathrm{d}V = -\int_{\mathcal{D}} \boldsymbol{\xi} \cdot \nabla \left( \frac{1}{2}q^2 + \phi^* \right) \mathrm{d}V = 0, \tag{3.185}$$

which proves the theorem.

For later use in stability analysis (Chap.9), let us proceed to derive the second energy variation. Similar to the derivation of $\delta\boldsymbol{u}$, by using (3.183) and (3.184) we find

$$\frac{\mathrm{d}^2}{\mathrm{d}\epsilon^2} \oint_{g^\epsilon C} \tilde{\boldsymbol{u}} \cdot \mathrm{d}\tilde{\boldsymbol{x}} = \oint_{g^\epsilon C} \{\tilde{\boldsymbol{u}}_{\epsilon\epsilon} + \boldsymbol{\xi} \times [\tilde{\nabla} \times (\tilde{\boldsymbol{\omega}} \times \boldsymbol{\xi}) + \tilde{\boldsymbol{\omega}} \times \boldsymbol{\xi}_\epsilon]\} \cdot \mathrm{d}\tilde{\boldsymbol{x}}.$$

Thus, the $\mathrm{O}(\epsilon^2)$ term in (3.182) yields

$$\delta^2 \boldsymbol{u} = \boldsymbol{\xi} \times \delta\boldsymbol{\omega} + \boldsymbol{\psi} \times \boldsymbol{\omega} - \nabla\beta, \quad \boldsymbol{\psi} \equiv \boldsymbol{\xi}_\epsilon\big|_{\epsilon=0}. \tag{3.186}$$

Then, we have

$$\delta^2 K = \int_{\mathcal{D}} \left\{ \frac{1}{2}(\delta\boldsymbol{u})^2 + \boldsymbol{u} \cdot \delta^2\boldsymbol{u} \right\} \mathrm{d}V,$$

where, by (3.186) and (3.178) there is

$$\boldsymbol{u}\cdot(\boldsymbol{\psi}\times\boldsymbol{\omega})=(\boldsymbol{\omega}\times\boldsymbol{u})\cdot\boldsymbol{\psi}=-\nabla\cdot\left[\boldsymbol{\psi}\left(\frac{1}{2}q^2+\phi^*\right)\right]$$

since $\nabla\cdot\boldsymbol{\psi}=0$. Therefore, it follows that:

$$\delta^2K=\frac{1}{2}\int_{\mathcal{D}}\{(\delta\boldsymbol{u})^2+\delta\boldsymbol{\omega}\cdot(\boldsymbol{u}\times\boldsymbol{\xi})\}\mathrm{d}V. \tag{3.187}$$

### 3.6.5 Viscous Circulation-Preserving Flow

We close this lengthy section by viscous circulation-preserving flows satisfying (3.158). In contrast to other terms in (3.156), although $\sigma$ also has dimension of energy per unit mass, since now the process is irreversible, a nonzero $\sigma$ is a function of that process rather than a function of equilibrium thermodynamic state. Only a few special viscous flows can satisfy (3.158). Consider incompressible flow with $\boldsymbol{\eta}=-\nu\nabla\times\boldsymbol{\omega}$, (3.158) requires

$$\nu\nabla\times\boldsymbol{\omega}=\nabla\sigma,\quad\nabla^2\sigma=0, \tag{3.188a}$$

or

$$\nabla^2\boldsymbol{\omega}=\boldsymbol{0}. \tag{3.188b}$$

This will be satisfied if the vorticity is a linear function of $\boldsymbol{x}$:

$$\omega_i=C_{ij}x_j+\mathrm{D}_i. \tag{3.189}$$

Then there is

$$\sigma=-\nu\epsilon_{ijk}C_{ij}x_k, \tag{3.190}$$

which vanishes if $C_{ij}=C_{ji}$. The viscous Poiseuille flow ($\mathrm{D}_i=0$) and Couette flow ($C_{ij}=0$) between parallel plates are of this type. For the simple shear flow exemplified in Sect. 2.1.2, we may write $\omega=C_{32}x_2$ and hence $\sigma=\nu C_{32}x_1$. Actually, for any viscous unidirectional flow there is $\boldsymbol{u}\cdot\nabla\boldsymbol{u}=\boldsymbol{0}$ (see Sect. 4.1.4 below), so if the flow is steady there is

$$\nu\nabla\times\boldsymbol{\omega}=-\frac{1}{\rho}\nabla p.$$

Thus, we simply have $\sigma=-p/\rho$, implying that the pressure work is completely spent on compensating the viscous dissipation.

Note that for a *steady* incompressible viscous flow the Helmholtz equation (2.168) indicates that (3.188) holds if and only if so is (3.63), i.e., the flow is generalized Beltramian.

A viscous circulation-preserving flow also has some unique features. First, for the total enstrophy, there is (Wu et al. 1993):

**Minimum Enstrophy Theorem .** *Among all viscous incompressible flows satisfying the same adherence boundary condition, the circulation-preserving flow has minimum total enstrophy.*

The proof is similar to that of Kelvin's minimum kinetic-energy theorem (Sect. 2.4.4). Denote the total enstrophy by $E$, and assume a circulation-preserving flow $\boldsymbol{u}$ is disturbed to $\boldsymbol{u}_1 = \boldsymbol{u} + \boldsymbol{u}'$ with $\boldsymbol{u}' = \boldsymbol{0}$ on the boundary so that

$$E_1 = \frac{1}{2}\int_V (\boldsymbol{\omega} + \boldsymbol{\omega}') \cdot (\boldsymbol{\omega} + \boldsymbol{\omega}')\mathrm{d}V = E + E' + \int_V \boldsymbol{\omega} \cdot \boldsymbol{\omega}'\mathrm{d}V.$$

To handle the integral, we use the identity

$$\nabla \cdot (\boldsymbol{u}' \times \boldsymbol{\omega}) = \boldsymbol{\omega} \cdot (\nabla \times \boldsymbol{u}') - \boldsymbol{u}' \cdot (\nabla \times \boldsymbol{\omega}).$$

Hence, since $\boldsymbol{\eta} = -\nu\nabla \times \boldsymbol{\omega} = -\nabla\sigma$ by (3.158) and $\boldsymbol{u}' \cdot \nabla\sigma = \nabla \cdot (\boldsymbol{u}'\sigma)$, we obtain

$$\int_V \boldsymbol{\omega} \cdot \boldsymbol{\omega}' \,\mathrm{d}V = \int_{\partial V} \boldsymbol{n} \cdot \left(\boldsymbol{u}' \times \boldsymbol{\omega} - \frac{1}{\nu}\boldsymbol{u}'\sigma\right) \mathrm{d}V = 0$$

due to $\boldsymbol{u}' = 0$ on $\partial V$. Thus, we have $E_1 = E + E' \geq E$.

It will be shown in Sect. 4.1 that the creation of vorticity and enstrophy at boundary is inevitable for viscous flows, which is in general a noncirculation-preserving process. Therefore, on a bounded viscous circulation-preserving flow such as the Poiseuille flow, the continuously produced new enstrophy must be immediately dissipated to ensure no enstrophy accumulation. The minimum enstrophy theorem is precisely a quantitative reflection of this physics.

As a corollary, we recall the generalized Bobyleff–Forsythe formula (2.158) links the total enstrophy to dissipation, where in the last term the surface deformation stress $\boldsymbol{t}_s$ is fixed for given boundary. Hence, for the disturbed flow we simply have $\boldsymbol{t}_{s1} \cdot \boldsymbol{u}_1 = \boldsymbol{t}_s \cdot \boldsymbol{u}$. Therefore, when the flow is incompressible,

$$\int_V \Phi_1 \,\mathrm{d}V = \int_V \Phi \,\mathrm{d}V + 2\mu E' \geq \int_V \Phi \,\mathrm{d}V,$$

which is the classic **Helmholtz–Rayleigh minimum dissipation theorem**[14] stated exactly in the same way as the minimum enstrophy theorem. Moreover, from this theorem and entropy equation (2.61), when the heat flux $\boldsymbol{q}$ can be neglected and hence the flow is isothermal, we arrive at one more similar theorem of *minimum entropy production* for circulation-preserving *isothermal* flow.

The proofs of the above theorems crucially depends on the incompressibility condition. Variational calculation is necessary once we enter compressible

[14] Its direct proof is simpler than that for the minimum enstrophy theorem, see Serrin (1959), p. 258.

flow. Consider the total dissipation for general circulating-preserving flow. Assume the flow is *steady*, so the continuity equation is $\nabla\cdot(\rho\boldsymbol{u})=0$, which serves as a constraint to the variational problem of total dissipation. Thus, we write

$$\delta\int_V[\Phi-\lambda\nabla\cdot(\rho\boldsymbol{u})]\mathrm{d}V=0,$$

where $\Phi=D_{ij}V_{ij}$ is the full dissipation rate defined by (2.54) and $\lambda$ is a Lagrangian multiplier. An integration by parts gives

$$\delta\int_{\mathcal{V}}\widetilde{\Phi}\mathrm{d}V=0,\quad \widetilde{\Phi}=\Phi-\rho\boldsymbol{u}\cdot\nabla\lambda.$$

Since $\Phi=\mathbf{V}:\mathbf{D}$ does not explicitly depend on velocity, we have

$$\frac{\partial\widetilde{\Phi}}{\partial u_i}=-\rho\lambda_{,i},$$
$$\frac{\partial\widetilde{\Phi}}{\partial u_{i,j}}=\frac{1}{2}V_{lk}\frac{\partial}{\partial u_{i,j}}(u_{k,l}+u_{l,k})=\frac{1}{2}V_{lk}(\delta_{ik}\delta_{jl}+\delta_{il}\delta_{jk})=V_{ji}.$$

Thus, from the Euler–Lagrangian equation, it follows that there must be

$$\boldsymbol{\eta}\equiv\frac{1}{\rho}\nabla\cdot\mathbf{V}=\nabla\lambda,$$

which is simply (3.158). Therefore, *among all compressible viscous flows satisfying the same adherence boundary condition*, *the total dissipation of steady circulation-preserving flow takes stationary value.* It has been explicitly shown by He et al. (1988) that this is true for Newtonian fluid, and moreover such a steady flow satisfies the necessary condition of having minimum total dissipation.

## Summary

Vorticity kinematics studies the behavior of a vorticity field and relevant quantities in space and time without introducing the constitutive structure of the fluid, and hence is most widely valid. The content of vorticity kinematics is far more abundant than general fluid kinematics due solely to taking the curl of the latter. It constitutes an important part of the entire vorticity dynamics.

1. The concept of vorticity itself needs careful physical interpretation. Either inside the fluid or on boundaries, the vorticity at a point equals twice of the angular velocity of the principal exes of the strain-rate tensor at the point. But the vorticity should be viewed as a generalization of the concept of the angular velocity in an infinitely deformable medium. It differs from the concept of angular momentum per unit mass. Only for a small and finite spherical element of unit mass the vorticity is proportional to the angular momentum about the center of the sphere.

2. The basic spatial properties of a vorticity field are the first Helmholtz theorem and vorticity moment theorem. Along with the no-slip condition, the first Helmholtz theorem excludes the possibility of a vorticity tube (not a single vorticity line) terminating at a nonrotating wall. The vorticity moment theorem establishes infinitely many kinematic constraints on the asymptotic behavior of the velocity field that extends to infinity. The spatial properties also include the generalized Boit–Savart formula that determines the velocity field associated with ("induced by") a given vorticity and dilatation field. All these results are solely from the solenoidal feature of the vorticity and its mathematic definition, and hence are universally true.

   Special care is necessary for the vorticity kinematics in two-dimensional flow.
3. The geometric relation between the vorticity and velocity at a point reveals different key roles of the Lamb vector and the helicity density. The complex-lamellar flow with zero helicity density and helical (Beltrami) flow with zero Lamb vector represent a pair of exclusive extrema of vortical flows, each of which shares some feature of potential flow. By relaxing the condition of Beltrami flow one gets the generalized Beltrami flow, in which the Lamb vector has only longitudinal part and hence the key kinematic nonlinearity in the shearing process disappears. Moreover, the helicity (integral of helicity density) represents the topological structure of thin vortex filament loops.
4. For incompressible flows the total momentum and angular momentum can be expressed by the first- and second-order vorticity moments or vortical impulse and angular impulse, respectively. Similarly, the total kinetic energy can be expressed by double vorticity integrals or scalar moment of the Lamb vector. These hydrodynamic integrals enable replacing a widely distributed (even not unconditionally convergent) integrand by a much more compact vorticity-related integrand. This is not only a matter of convenience but also an indication that physically vortices are the *"sinews and muscles of the fluid motion"* (Küchemann 1965).
5. The entire temporal evolution of the vorticity field is most neatly described by the Lagrangian vorticity equation in the reference space. The temporal properties of a vorticity field can be reflected from the evolution of many relevant quantities, such as the vorticity itself and total vorticity, circulation, potential vorticity, helicity, and enstrophy, as well as vortical impulses. The rate of change of these quantities contains two types of mechanisms. The first type is purely kinematics, among which the vorticity stretching and tilting are most remarkable, which lie at the root of the complexity of turbulence. The second type has its root at the curl of acceleration (the vorticity diffusion vector), behind which is the kinetics.
6. Among various vortical flows the simplest class is circulation-preserving flows, where the vorticity diffusion vector vanishes or the acceleration has a potential. In these flows the shearing appears as only a kinematic process.

This class of flows permits many conservation theorems, in particular the Cauchy vorticity formula, the Kelvin circulation theorem, the second and third Helmholtz vorticity theorems, and the conservation of vortex-filament topology, etc. As the other side of the coin, the kinetics enters the compressing process, but the momentum equation can be integrated once to yield various Bernoulli integrals. For effectively inviscid flows, both sides can be put into the Hamiltonian formalism, where the kinetic energy and acceleration potential constitute the Lagrangian density and Hamiltonian for the longitudinal part, and there exist the fluid–particle relabeling symmetry and kinetic-energy extremum theorem. Then, a viscous circulation-preserving flow has minimum dissipation, which when the flow is incompressible is equivalent to minimum enstrophy.

# 4

# Fundamentals of Vorticity Dynamics

This chapter enters vorticity dynamics. The comprehensive discussions of vorticity kinematics in Chap. 3 enables us to focus on the situations with nonzero vorticity diffusion vector $\nabla \times \boldsymbol{a}$, of which the physical sources will be addressed first. We then examine the dependence of the behavior of the shearing process on its governing dimensionless parameter, the Reynolds number. Finally we present a couple of general formulations of viscous incompressible flow problems in terms of vorticity, which may serve as a theoretical foundation of vorticity-based numerical methods. Further materials of vorticity dynamics will appear in later chapters.

## 4.1 Vorticity Diffusion Vector

For clarity, each of the three effects of the vorticity diffusion vector seen in (3.157):

$$\nabla \times \boldsymbol{a} = \nabla \times \boldsymbol{f} + \frac{1}{\rho^2} \nabla \rho \times \nabla p + \nabla \times \boldsymbol{\eta}, \tag{3.157a}$$

$$= \nabla \times \boldsymbol{f} + \nabla T \times \nabla s + \nabla \times \boldsymbol{\eta}, \tag{3.157b}$$

namely, nonconservative body force, baroclinicity, and viscosity, will be examined in an isolated circumstance where the others are assumed not to occur. We first discuss the two inviscid effects, followed by various aspects of the viscous effect that has universal existence and fundamental importance.

### 4.1.1 Nonconservative Body Force in Magnetohydrodynamics

Consider an incompressible flow with uniform density $\rho$, not bounded by a free surface. Then the role of pressure is merely to ensure the incompressibility.[1]

[1] As implied by (2.68a), on a free surface the pressure must appear in the dynamic boundary condition.

Since any conservative body force can be absorbed into a modified pressure gradient, these forces do not alter the flow field at all because one can well solve the flow from the vorticity transport equation and proper boundary conditions (see Sect. 4.5). This observation underscores the sole role of a nonconservative body force in affecting the flow development through its interaction with the vorticity field.

The most familiar nonconservative body force is the Coriolis force observed in a rotating frame of reference, which serves as an internal source of the *relative* vorticity viewed in that frame. This effect is important in geophysical vorticity dynamics to be addressed in Chap. 12. Here we consider a true nonconservative body force that has a variety of significant effects on the vorticity, namely the rotational part of the *Lorentz force* in an electrically conducting and nonmagnetic fluid, which is a major concern of *magnetohydrodynamics* (MHD) encountered in many engineering problems as well as geophysics and astrophysics. For introductory books on this field see, e.g., Shercliff (1965) and Davidson (2001).

It is well known that a particle of charge $q$ moving through an electric field $\boldsymbol{E}$ and a magnetic field $\boldsymbol{B}$ will experience an electrostatic force and a Lorentz force, of which the sum is $q(\boldsymbol{E}+\boldsymbol{u}\times\boldsymbol{B})$. In a continuous medium with charge density $\rho_e$, this force becomes $\rho_e\boldsymbol{E}+\boldsymbol{J}\times\boldsymbol{B}$ per unit volume, where $\boldsymbol{J}=\rho_e\boldsymbol{u}$ is the current density. In MHD the forces on individual charges are unimportant compared to those on the bulk of the fluid; so the force is simply $\boldsymbol{J}\times\boldsymbol{B}$. Therefore, the Navier–Stokes equation reads

$$\frac{\mathrm{D}\boldsymbol{u}}{\mathrm{D}t}=-\frac{1}{\rho}\nabla p-\nu\nabla\times\boldsymbol{\omega}+\frac{1}{\rho}\boldsymbol{J}\times\boldsymbol{B}, \tag{4.1}$$

while the vorticity transport equation becomes

$$\frac{\partial\boldsymbol{\omega}}{\partial t}+\nabla\times(\boldsymbol{\omega}\times\boldsymbol{u})=\nu\nabla^2\boldsymbol{\omega}+\frac{1}{\rho}\nabla\times(\boldsymbol{J}\times\boldsymbol{B}). \tag{4.2}$$

Such a flow problem has to be solved in couple with electrodynamic equations which relate $\boldsymbol{J}$, $\boldsymbol{B}$, and $\boldsymbol{E}$. Since in MHD the displacement currents are negligible compared to $\boldsymbol{J}$, it suffices to use pre-Maxwellian equations, namely *Ohm's law*, *Ampère's law* plus charge conservation, and *Faraday's law* plus the solenoidal condition of the magnetic field. These equations read, respectively,

$$\boldsymbol{J}=\sigma(\boldsymbol{E}+\boldsymbol{u}\times\boldsymbol{B}), \tag{4.3a}$$

$$\nabla\times\boldsymbol{B}=\mu_{\mathrm{m}}\boldsymbol{J},\quad \nabla\cdot\boldsymbol{J}=0, \tag{4.3b}$$

$$\nabla\times\boldsymbol{E}=-\frac{\partial\boldsymbol{B}}{\partial t},\quad \nabla\cdot\boldsymbol{B}=0, \tag{4.3c}$$

where $\sigma$ and $\mu_{\mathrm{m}}$ are the electrical conductivity and magnetic permeability, respectively. Now, by (4.3b) the Lorentz force can be cast to

$$\boldsymbol{J}\times\boldsymbol{B}=\frac{1}{\mu_{\mathrm{m}}}\left(\boldsymbol{B}\cdot\nabla\boldsymbol{B}-\frac{1}{2}\nabla|\boldsymbol{B}|^2\right)=\frac{1}{\mu_{\mathrm{m}}}\left[\nabla\cdot(\boldsymbol{B}\boldsymbol{B})-\frac{1}{2}\nabla|\boldsymbol{B}|^2\right],$$

which is in exact analogy with the Lamb vector in the flow convection as the *vortex force* per unit volume, see (2.162):

$$\rho(\boldsymbol{\omega}\times\boldsymbol{u})=\rho\left(\boldsymbol{u}\cdot\nabla\boldsymbol{u}-\frac{1}{2}\nabla|\boldsymbol{u}|^2\right)=\rho\left[\nabla\cdot(\boldsymbol{u}\boldsymbol{u})-\frac{1}{2}\nabla|\boldsymbol{u}|^2\right].$$

The rotational part of the Lorentz force forms a true internal vorticity source:

$$\nabla\times(\boldsymbol{J}\times\boldsymbol{B})=\frac{1}{\mu_{\mathrm{m}}}\nabla\times[\nabla\cdot(\boldsymbol{B}\boldsymbol{B})]. \tag{4.4}$$

Moreover, by combining (4.3a–c) we find the magnetic field satisfies exactly the same transport equation as the vorticity field:

$$\frac{\partial\boldsymbol{B}}{\partial t}+\nabla\times(\boldsymbol{B}\times\boldsymbol{u})=\lambda\nabla^2\boldsymbol{B},\quad \lambda=(\mu_{\mathrm{m}}\sigma)^{-1}. \tag{4.5}$$

The constant $\lambda$ is called the magnetic diffusivity which, along with the characteristic velocity $U$ and length scale $L$, defines a *magnetic Reynolds number*

$$R_{\mathrm{m}}=\frac{UL}{\lambda}=UL\mu_{\mathrm{m}}\sigma. \tag{4.6}$$

If $R_{\mathrm{m}}\ll 1$, the reaction of the current (carried by the electrically conducting flow) to an imposed magnetic field, say $\boldsymbol{B}_0$, can be neglected and one only needs to study the effect of $\boldsymbol{B}_0$ on the fluid motion. Note in passing that there are some further analogies between vorticity dynamics and MHD, of course one being the original Biot–Savart law as the inversion of (4.3b),

$$\boldsymbol{B}=\frac{\mu_{\mathrm{m}}}{2(n-1)\pi}\int\frac{\boldsymbol{J}\times\boldsymbol{r}}{r^n}\mathrm{dV}, \tag{4.7}$$

from which (3.27) gained its name.

The earlier-cited books contain many examples in nature and technology on how the rotational part of the Lorentz force creates, suppresses, and propagates a vorticity field. This important role of the Lorentz force has also made it a potential means in vortical-flow control, especially near-wall turbulence control, of a conducting fluid (e.g., Du and Karniadakis (2000); Gad-el-Hak (2000)). Here, we follow Davidson (2001) to consider a linearized MHD flow in an imposed uniform magnetic field $\boldsymbol{B}_0$. The flow carries a weak current $\boldsymbol{j}$ which induces a small disturbance magnetic field $\boldsymbol{b}$ by (4.3b), governed by

$$\frac{\partial\boldsymbol{b}}{\partial t}=\nabla\times(\boldsymbol{u}\times\boldsymbol{B}_0)+\lambda\nabla^2\boldsymbol{b}=\boldsymbol{B}_0\cdot\nabla\boldsymbol{u}+\lambda\nabla^2\boldsymbol{b},$$

of which the curl is

$$\frac{\partial\boldsymbol{j}}{\partial t}=\frac{1}{\mu_{\mathrm{m}}}\boldsymbol{B}_0\cdot\nabla\boldsymbol{\omega}+\lambda\nabla^2\boldsymbol{j}.$$

Comparing this with the linearized version of (4.2),

$$\frac{\partial \boldsymbol{\omega}}{\partial t} = \frac{1}{\rho}\boldsymbol{B}_0 \cdot \nabla \boldsymbol{j} + \nu \nabla^2 \boldsymbol{\omega},$$

we eliminate $\boldsymbol{j}$ to obtain a linear wave equation for the MHD vorticity:

$$\frac{\partial^2 \boldsymbol{\omega}}{\partial t^2} = \frac{1}{\rho \mu_\mathrm{m}} (\boldsymbol{B}_0 \cdot \nabla)^2 \boldsymbol{\omega} + (\nu + \lambda)\nabla^2 \left( \frac{\partial \boldsymbol{\omega}}{\partial t} \right) - \lambda \nu \nabla^4 \boldsymbol{\omega}, \tag{4.8}$$

which permits a traveling vorticity wave $\boldsymbol{\omega} \sim \boldsymbol{\omega}_0 \, \mathrm{e}^{\mathrm{i}(\boldsymbol{k}\cdot\boldsymbol{x} - nt)}$ with $n$ being the circular frequency. Substituting this wave into (4.8) yields the dispersion relation

$$n = -\frac{\mathrm{i}}{2}(\nu + \lambda)k^2 \pm \sqrt{\frac{B_0^2 k_\parallel^2}{\rho \mu_\mathrm{m}} - \frac{1}{4}(\nu - \lambda)^2 k^4}, \tag{4.9a}$$

where $k_\parallel$ is the component of the wave vector $\boldsymbol{k}$ parallel to $\boldsymbol{B}_0$. A negative imaginary part of $n$ implies a damping. For inviscid flow (4.9a) is reduced to

$$n = -\frac{\mathrm{i}}{2}\lambda k^2 \left( 1 \mp \sqrt{1 - \frac{4 B_0^2 k_\parallel^2}{\rho \mu_\mathrm{m} \lambda^2 k^4}} \right). \tag{4.9b}$$

From (4.9) some simple solutions can be deduced. First, if both $\nu = 0$ and $\lambda = 0$ or $R_\mathrm{m} \to \infty$ by (4.6), (4.9a) gives the classic *Alfvén wave* with frequency $n = \pm v_\mathrm{a} k_\parallel$ and phase velocity $v_\mathrm{a} = B_0/(\rho\mu_\mathrm{m})^{1/2}$. This solution represents the propagation of transverse (vorticity) inertial waves, an important phenomenon in astrophysics. Then, if $\nu = 0$ and $\lambda$ is small but finite, (4.9b) gives a damped Alfvén wave due to Ohmic dissipation (Fig. 4.1a):

$$n = -\frac{\mathrm{i}}{2}\lambda k^2 \pm v_\mathrm{a} k_\parallel.$$

Finally, if $\lambda \to \infty$ ($R_\mathrm{m} \to 0$) as in typical liquid-metal MHD, by (4.9b) one has

$$n = -\mathrm{i}\lambda k^2 \quad \text{or} \quad n = -\frac{\mathrm{i} k_\parallel^2}{\tau k^2},$$

where $\tau = (\sigma B_0^2/\rho)^{-1}$ is the magnetic damping time. While the former is simply a rapid-dissipated disturbance, the latter is a nonoscillating disturbance that decays slowly on a time scale of $\tau$ (Fig. 4.1b).

### 4.1.2 Baroclinicity

Consider now the baroclinic effect in (3.157) due to nonzero $\nabla T \times \nabla s$ or $\nabla \rho \times \nabla p$. To isolate this effect, assume the external body force and viscosity are both zero. Then the Kelvin circulation formula (2.32) implies

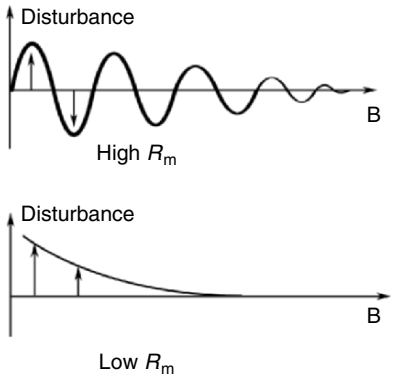


**Fig. 4.1.** Damped Alfvén waves at high and low $R_m$.

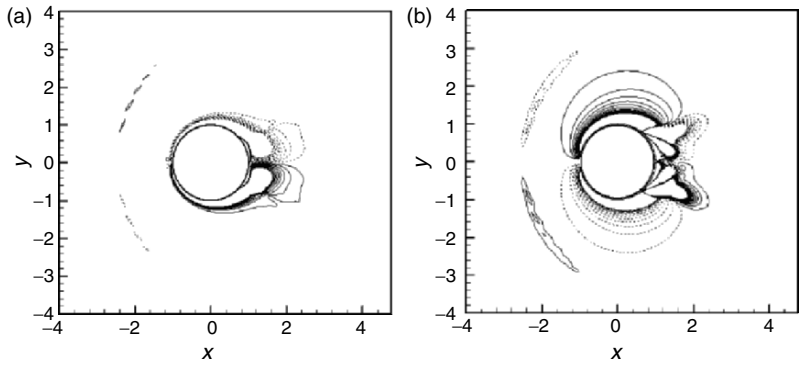


**Fig. 4.2.** A numerical Navier–Stokes solution of the steady flow past a circular cylinder at $M = 0.8$ and $Re = 500$ (based on cylinder's diameter). **(a)** Vorticity contours, and **(b)** baroclinicity as the vorticity source. From Luo (2004)

$$\frac{\mathrm{d}\Gamma_{\mathcal{C}}}{\mathrm{d}t} = -\oint_{\mathcal{C}} \frac{1}{\rho}\mathrm{d}p = \int_{\mathcal{S}} \frac{1}{\rho^2}\boldsymbol{n}\cdot(\nabla\rho\times\nabla p)\mathrm{d}S, \tag{4.10a}$$

$$= \oint_{\mathcal{C}} T\,\mathrm{d}s \quad = \int_{\mathcal{S}} \boldsymbol{n}\cdot(\nabla T\times\nabla s)\mathrm{d}S. \tag{4.10b}$$

A typical baroclinic flow to which (4.10a) applies is the *density stratification* in atmosphere and sea water due to gravity (Chap. 12). Here we note that the viscosity plays a key implicit role behind the apparently inviscid formula (4.10b) via the dissipation-caused entropy increase, see (2.61).

As a demonstration, Fig. 4.2a shows the vorticity contours for a two-dimensional steady viscous flow past a circular cylinder at freestream Mach number 0.8. One sees a weak bow-shape vortex layer in front of the cylinder, which can only be a baroclinic effect. In fact, at the location of the vortex layer both density and pressure, as well as the local Mach number, have quite

strong gradients. In terms of the intrinsic streamline coordinates $(s, n, z)$ with $\boldsymbol{u} = (q, 0, 0)$, from the two-dimensional inviscid and steady vorticity transport equation one finds that, along a streamline starting from a point $s_0$ in upstream irrotational region, the vorticity at $s$ is an accumulated effect of the baroclinicity:

$$\omega(s) = \int_{s_0}^{s} \frac{1}{q\rho^2} \frac{\partial(\rho, p)}{\partial(s, n)} \mathrm{d}s.$$

The distribution of this Jacobian divided by $\rho^2$ is shown in Fig. 4.2b, which also reveals some stronger baroclinic sources of vorticity in the boundary layers and wake vortices.

In fact, in the transonic regime, a bow-shape shock wave appears at about the same location as the bow baroclinic zone. In the Euler limit this layer becomes a normal discontinuity which hides the baroclinic mechanism. Nevertheless, the newly produced vorticity *behind* the shock can be analytically obtained from the inviscid theory and Rankine–Hugoniot shock relations (2.83), and the result is consistent with the corresponding viscous solution. The creation of vorticity across a curved shock, across which the entropy increase is not uniform, is sketched in Fig. 4.3. This inviscid theory has been developed by Lighthill (1957) and Hayes (1957), which we present later.

Assume the flow is steady and let the shock have normal $\boldsymbol{n}$. As explained in the context of (2.83), the normal velocity $u_\mathrm{n} = \boldsymbol{u} \cdot \boldsymbol{n}$ as well as $p$ and $\rho$ will experience a jump as the flow goes through the shock, but the tangential velocity $\boldsymbol{u}_\pi \equiv \boldsymbol{n} \times (\boldsymbol{u} \times \boldsymbol{n})$ remains continuous. Thus, no new normal vorticity is created across the shock. In contrast, a tangent vorticity will appear behind an oblique curved shock. In the Euler equation the vorticity appears explicitly only through the Lamb vector $\boldsymbol{\omega} \times \boldsymbol{u}$, which must experience a discontinuity. Thus, we take the jump of the tangential component of the steady Euler equation:

$$\boldsymbol{n} \times [\![\rho(\boldsymbol{\omega} \times \boldsymbol{u} + q\nabla q)]\!] = -\boldsymbol{n} \times \nabla [\![p]\!], \quad q^2 = |\boldsymbol{u}|^2 = u_\pi^2 + u_\mathrm{n}^2, \tag{4.11}$$

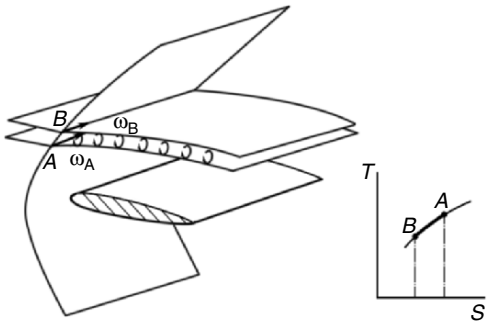


**Fig. 4.3.** Vortex layer behind a curved shock wave. Reproduced from Kármán (1954)

where $[\![\cdot]\!] = (\cdot)_1 - (\cdot)_0$, with subscripts 0 and 1 referring to quantities ahead of and behind the shock, respectively. Then by using (2.82a) and (2.83a,b) it can be shown

$$\begin{aligned} -\boldsymbol{n}\times\nabla[\![p]\!] &= m\boldsymbol{n}\times\nabla[\![u_{\rm n}]\!] + [\![u_{\rm n}]\!]\boldsymbol{n}\times\nabla m,\\ \boldsymbol{n}\times[\![\rho\boldsymbol{\omega}\times\boldsymbol{u}]\!] &= m[\![\boldsymbol{\omega}]\!] - (m\boldsymbol{n} + [\![\rho]\!]\boldsymbol{u}_\pi)\omega_{\rm n},\\ \boldsymbol{n}\times[\![\rho q\nabla q]\!] &= [\![\rho]\!]u_\pi\boldsymbol{n}\times\nabla u_\pi + m\boldsymbol{n}\times\nabla[\![u_{\rm n}]\!]. \end{aligned}$$

Thus, from (4.11) we obtain a general formula for the vorticity jump behind a curved shock in steady flow (Hayes (1957), who also addresses the unsteady effect):

$$[\![\boldsymbol{\omega}]\!] = [\![\boldsymbol{\omega}_\pi]\!] = \left(\boldsymbol{n} + \frac{[\![\rho]\!]}{m}\boldsymbol{u}_\pi\right)\omega_{0\rm n} + \frac{[\![u_{\rm n}]\!]}{m}\boldsymbol{n}\times\nabla m - \frac{[\![\rho]\!]}{m}u_\pi\boldsymbol{n}\times\nabla u_\pi. \quad (4.12)$$

Specifically, if $\rho_0$ and $\boldsymbol{u}_0 = \boldsymbol{U}$ are constant, there is $m = \rho_0 U_{\rm n} = \rho_1 u_{1\rm n}$ and $\omega_{0\rm n} = 0$, and since $\boldsymbol{n}\times\nabla U^2 = \boldsymbol{0}$ we have $\boldsymbol{n}\times\nabla U_\pi^2 = -\boldsymbol{n}\times\nabla U_{\rm n}^2$, so (4.12) is simplified to

$$\boldsymbol{\omega}_1 = \boldsymbol{\omega}_{1\pi} = \frac{1}{m}(\rho_0[\![u_{\rm n}]\!] + U_{\rm n}[\![\rho]\!])\boldsymbol{n}\times\nabla U_{\rm n},$$

where

$$\frac{\rho_0[\![u_{\rm n}]\!]}{m} = \frac{u_{1\rm n}\rho_0}{u_{1\rm n}\rho_1} - \frac{U_{\rm n}\rho_0}{U_{\rm n}\rho_0} = -\frac{[\![\rho]\!]}{\rho_1}, \quad \frac{U_{\rm n}[\![\rho]\!]}{m} = \frac{[\![\rho]\!]}{\rho_0}.$$

Thus,

$$\boldsymbol{\omega}_{1\pi} = \frac{(1-\epsilon)^2}{\epsilon}\boldsymbol{n}\times\nabla U_{\rm n}, \quad \epsilon \equiv \frac{\rho_0}{\rho_1} \le 1. \quad (4.13)$$

Finally, let $\mathbf{K} \equiv -\nabla_\pi\boldsymbol{n}$ be the curvature tensor of the shock surface, since

$$\nabla_\pi(\boldsymbol{U}\cdot\boldsymbol{n}) = \nabla_\pi\boldsymbol{U}\cdot\boldsymbol{n} + \boldsymbol{U}\cdot\nabla_\pi\boldsymbol{n} = -\boldsymbol{U}\cdot\mathbf{K}$$

due to $\nabla_\pi\boldsymbol{U} = \boldsymbol{0}$, (4.13) can also be written as (Hayes 1957; Lighthill 1957)

$$\boldsymbol{\omega}_{1\pi} = -\frac{(1-\epsilon)^2}{\epsilon}\boldsymbol{n}\times(\boldsymbol{U}\cdot\mathbf{K}). \quad (4.14)$$

Remarkably, the newly produced tangent vorticity $\boldsymbol{\omega}_{1\pi}$ depends only on the velocity in front of the shock and shock curvature as well as the density ratio across it, but completely independent of the theromodynamic process inside the shock layer. Note that while the entropy increase across a shock is of $O([\![\rho]\!]^3)$ (e.g., Serrin 1959), now (4.13) or (4.14) indicates that the vorticity generated by a curved shock is of $O([\![\rho]\!]^2)$.

A shock is a strong compressing process. The vorticity generation across a curved shock is a byproduct of the nonuniform density jump $[\![\rho]\!]$, which is a good example of the nonlinear coupling of the two fundamental processes through the Lamb vector as discussed in Sect. 2.4.3.

Another interesting strong baroclinic effect occurs when a highly concentrated energy is suddenly deposited into a narrow channel of the fluid, say by laser and electric discharges in ambient air. Any asymmetry of the energy deposition will cause a nonzero $\nabla\rho \times \nabla p$ and create vortices, which significantly accelerate the mixing of the air. Consequently, following expansion to pressure equilibrium, the hot channel cools down at a rate which is several orders of magnitude faster than that due to thermal conduction (Picone and Boris 1983). This phenomenon has been used to explain, for instance, the fast production of atmospheric nitrogen oxides by lightning (Picone et al. 1981; Kurzweil et al. 2002).

### 4.1.3 Viscosity Diffusion, Dissipation, and Creation at Boundaries

The viscosity has *multiple effects* in vorticity dynamics, each deserving an in-depth analysis. For incompressible flow without nonconservative body force, (3.157) is reduced to

$$\nabla \times \boldsymbol{a} = \nu \nabla^2 \boldsymbol{\omega}. \tag{4.15}$$

The first effect of viscosity is causing the *vorticity diffusion*. The Kelvin circulation formula (2.32) now gives

$$\frac{\mathrm{d}\Gamma}{\mathrm{d}t} = -\nu \oint (\nabla \times \boldsymbol{\omega}) \cdot \mathrm{d}\boldsymbol{x}. \tag{4.16}$$

To understand how the right-hand side changes the circulation, we generalize an argument of Lamb (1932) to examine the vorticity diffusion across the side surface $S$ of a sufficiently thin vorticity tube with outward unit normal $\boldsymbol{n}$, in which the vorticity lines are all parallel. At a point $\boldsymbol{x}$ on $S$, let $\boldsymbol{e}_2 = \boldsymbol{\omega}/\omega$ be the unit vector along the vorticity line through $\boldsymbol{x}$ such that $\boldsymbol{e}_1 = \boldsymbol{e}_2 \times \boldsymbol{n}$ defines a unit vector tangent to $S$. Based on the triple decomposition of Sect. 2.4.2, $\boldsymbol{e}_1$ is actually along the direction of shear force $\boldsymbol{\tau} = \mu\boldsymbol{\omega} \times \boldsymbol{n}$. Let $\boldsymbol{x}$ move along the $\boldsymbol{e}_1$-direction around the tube once to form a closed line $C$; see the sketch of Fig. 4.4.

We now apply (4.16) to loop $C$. For this thin tube, the curvature of $S$ along the tube direction $\boldsymbol{e}_2$, i.e., $\boldsymbol{e}_2 \cdot \mathbf{K} \cdot \boldsymbol{e}_2$, is negligible. The variation of the orthonormal triad $(\boldsymbol{e}_1, \boldsymbol{e}_2, \boldsymbol{n})$ as $\boldsymbol{x}$ moves over $S$ is given by the Frenet–Serret formula (A.39a,b,c). It can then be shown that

$$(\nabla \times \boldsymbol{\omega}) \cdot \mathrm{d}\boldsymbol{x} = -\boldsymbol{e}_2 \cdot \frac{\partial \boldsymbol{\omega}}{\partial n} \mathrm{d}s,$$

and hence (4.16) yields

$$\frac{\mathrm{d}\Gamma}{\mathrm{d}t} = \oint_C \boldsymbol{\sigma} \cdot \boldsymbol{e}_2 \, \mathrm{d}s,$$

where

$$\boldsymbol{\sigma} \equiv \nu \boldsymbol{n} \cdot \nabla \boldsymbol{\omega} = \nu \frac{\partial \boldsymbol{\omega}}{\partial n} \tag{4.17}$$

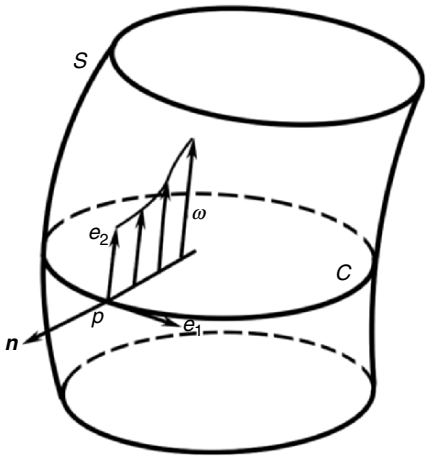


**Fig. 4.4.** Intrinsic frame $\boldsymbol{e}_1, \boldsymbol{e}_1, \boldsymbol{n}$ on the side surface $S$ of a vorticity tube

defines the vectorial *vorticity diffusion flux* (similar to the scalar heat flux across a surface) through the side surface of the tube, which measures how much vorticity is diffused in or out of $S$ per unit area and unit time. If $\boldsymbol{\omega}$ increases along the $\boldsymbol{n}$ direction, vorticity will be diffused from outside into the tube to enhance its circulation, and vice versa. A very important effect of vorticity diffusion occurs when two pieces of thin vortex filaments are sufficiently close, which causes the cut and reconnection of the filaments and hence alter their topology (Sect. 8.3.3).

The relation between $\boldsymbol{\sigma}$ and the more intrinsic *vorticity diffusive-flux tensor* $\nu\nabla\boldsymbol{\omega}$ is the same as that between the surface stress $\boldsymbol{t}$ and stress tensor $\mathbf{T}$, and $\nu\nabla\boldsymbol{\omega}$ is a tensor potential of $\nabla \times \boldsymbol{a} = \nu\nabla^2\boldsymbol{\omega}$ (Sect. 2.3.5). An observation similar to this has led Hornung (1989, 1990)) to develop a general tensor formulation of vorticity sources applicable to any continuum (see Wu and Wu (1998) and Kolár (2003) for further discussion). We just mention that for incompressible flow the Helmholtz equation (2.168) can be written

$$\frac{\mathrm{D}\boldsymbol{\omega}}{\mathrm{D}t} = \nabla \cdot \mathbf{J}, \quad \mathbf{J} \equiv \boldsymbol{\omega}\boldsymbol{u} + \nu\nabla\boldsymbol{\omega}, \tag{4.18}$$

so $\mathbf{J}$ is the tensor potential of the material rate of change of vorticity. In two dimensions $\nabla\boldsymbol{\omega}$ degenerates to the vorticity gradient vector $\nabla\omega$ to be discussed in Chap. 12.

While diffusion simply transfers vorticity from a point to another, the vorticity is also dissipated by viscosity. This can be understood by examining the change of total enstrophy $E$ (Sect. 3.5.3). By (4.15) and since

$$\omega_i\omega_{i,jj} = (\omega_i\omega_{i,j})_{,j} - \omega_{i,j}\omega_{i,j},$$

integrating (3.124) over a material volume $\mathcal{V}$ leads to the rate of change of total enstrophy $E$ in $\mathcal{V}$:

$$\frac{\mathrm{d}E}{\mathrm{d}t} = 2\overline{\alpha}(t)E + \int_{\partial\mathcal{V}} \eta \,\mathrm{d}S - \int_{\mathcal{V}} \Phi_\omega \,\mathrm{d}v, \tag{4.19}$$

where $\overline{\alpha}(t)$ is a mean value of the vorticity stretching rate $\alpha$ in $\mathcal{V}$,

$$\eta \equiv \nu \frac{\partial}{\partial n}\left(\frac{1}{2}\omega^2\right) = \boldsymbol{\omega}\cdot\boldsymbol{\sigma} \tag{4.20}$$

is the *enstrophy diffusion flux*, and

$$\Phi_\omega \equiv \mu \nabla\boldsymbol{\omega} : \nabla\boldsymbol{\omega} \geq 0 \tag{4.21}$$

is the *enstrophy dissipation rate* analogous to the kinetic-energy dissipation rate (2.54). In particular, for a two-dimensional unbounded viscous flow which is uniform at infinity, $E$ must monotonically decrease until $\Phi_\omega = 0$ everywhere. This state will be arrived when either the vorticity distribution becomes uniform, while the kinetic-energy dissipation continues with a constant rate, see (2.155); or the flow becomes irrotational so that the initial vorticity is entirely dissipated.

The defining equations (4.17) for $\boldsymbol{\sigma}$ and (4.20) for $\eta$ do not tell the relative importance of vorticity diffusion and dissipation in a flow region under consideration, compared to the advection. To know this we observe that, like $\nu\nabla\times\boldsymbol{\omega}$, the form of (4.17) suggests that $\boldsymbol{\sigma}$ must join the momentum balance on any surface $S$, making it *expressible by other dynamic quantities* thereon. This enables identifying various physical mechanisms that affect $\boldsymbol{\sigma}$ (and $\eta$) on any surface $S$. Thus, consider the tangent components of the incompressible version of (2.134) on $S$. By combining vector identities (the first is (2.28))

$$(\boldsymbol{b}\times\nabla)\times\boldsymbol{c} = (\nabla\boldsymbol{c})\cdot\boldsymbol{b} - \boldsymbol{b}(\nabla\cdot\boldsymbol{c}),$$
$$\boldsymbol{b}\times(\nabla\times\boldsymbol{c}) = (\nabla\boldsymbol{c})\cdot\boldsymbol{b} - \boldsymbol{b}\cdot\nabla\boldsymbol{c},$$

we obtain

$$(\boldsymbol{b}\times\nabla)\times\boldsymbol{c} - \boldsymbol{b}\times(\nabla\times\boldsymbol{c}) = \boldsymbol{b}\cdot\nabla\boldsymbol{c} - \boldsymbol{b}(\nabla\cdot\boldsymbol{c}),$$

so there is

$$-\nu\boldsymbol{n}\times(\nabla\times\boldsymbol{\omega}) = \nu\boldsymbol{n}\cdot\nabla\boldsymbol{\omega} - \nu(\boldsymbol{n}\times\nabla)\times\boldsymbol{\omega}. \tag{4.22}$$

Therefore, we arrive at a general expression for $\boldsymbol{\sigma}$ (Wu 1986a; Wu and Wu 1993):

$$\begin{aligned}\boldsymbol{\sigma} &= \boldsymbol{n}\times\left(\boldsymbol{a} - \boldsymbol{f} + \frac{1}{\rho}\nabla p\right) + \nu(\boldsymbol{n}\times\nabla)\times\boldsymbol{\omega}\\ &= \boldsymbol{\sigma}_\mathrm{a} + \boldsymbol{\sigma}_\mathrm{f} + \boldsymbol{\sigma}_\mathrm{p} + \boldsymbol{\sigma}_\mathrm{vis},\end{aligned} \tag{4.23}$$

where

$$\boldsymbol{\sigma}_\mathrm{a} = \boldsymbol{n}\times\boldsymbol{a}_\mathrm{B}, \qquad \boldsymbol{\sigma}_f = -\boldsymbol{n}\times\boldsymbol{f}, \tag{4.24a}$$

$$\boldsymbol{\sigma}_\mathrm{p} = \frac{1}{\rho}\boldsymbol{n}\times\nabla p, \quad \boldsymbol{\sigma}_\mathrm{vis} = \nu(\boldsymbol{n}\times\nabla)\times\boldsymbol{\omega} \tag{4.24b}$$

are the diffusive fluxes caused by the tangent components of the fluid acceleration $\boldsymbol{a}$, the external body force, the pressure gradient, and a viscous vortical effect, respectively. Note that $\boldsymbol{\sigma}_{\rm vis} \equiv \mathbf{0}$ in two dimensions. In three dimensional flow, like (2.137), $\boldsymbol{\sigma}_{\rm vis}$ can be expanded by identity (A.69):

$$\boldsymbol{\sigma}_{\rm vis} = \nu(\nabla_\pi \omega_n + \boldsymbol{\omega}_\pi \cdot \mathbf{K} - \boldsymbol{n}\nabla_\pi \cdot \boldsymbol{\omega}), \tag{4.25}$$

where $\mathbf{K}$ is the curvature tensor of $S$. Therefore, the tangent and normal components of $\boldsymbol{\sigma}$ are given by:

$$\boldsymbol{\sigma}_\pi = \boldsymbol{\sigma}_{\rm a} + \boldsymbol{\sigma}_{\rm f} + \boldsymbol{a}_{\rm p} + \nu\boldsymbol{\omega}_\pi \cdot \mathbf{K} + \nu\nabla_\pi \omega_{\rm n}, \tag{4.26a}$$

$$\sigma_{\rm n} = -\nu\nabla_\pi \cdot \boldsymbol{\omega}. \tag{4.26b}$$

Note that (4.23)–(4.26) *express normal derivatives by tangent ones*: on their right-hand side all quantities take values on $S$. Evidently, $\sigma_{\rm n}$ is a *purely kinematic effect* of $\nabla \cdot \boldsymbol{\omega} = 0$; if the tangent vorticity $\boldsymbol{\omega}_\pi$ has a two-dimensional source or sink on $S$ then a normal vorticity flux will be formed. Moreover, by (2.134), for compressible flow with constant dynamic viscosity $\mu$, the only change of the earlier formulas is to replace $\boldsymbol{\sigma}_{\rm p}$ by (Wu et al. 1988a)

$$\boldsymbol{\sigma}_{\Pi} = \frac{1}{\rho}\boldsymbol{n} \times \nabla\Pi, \quad \Pi = p - (\lambda + 2\mu)\vartheta. \tag{4.27}$$

The preceding analysis indicates that the relative importance of $\boldsymbol{\sigma}$ and $\eta$ depends on the Reynolds number $Re$ and the location of surface $S$. They are weak when $Re \gg 1$ and $S$ is in the interior of the fluid, because to the leading order the inviscid terms (the three terms in the bracket on the right-hand side of (4.23)) are self-balanced via the Euler equation. But when $Re \ll 1$ the diffusion and dissipation are crucial. On the other hand, if $S = \partial B$ is a solid-body surface, since the fluid elements sticking to it cannot freely respond the pressure gradient, the on-wall momentum balance is mainly established between the pressure gradient and $\boldsymbol{\sigma}$, implying $|\boldsymbol{\sigma}| = O(1)$ generically *at any Re*. This coupling was already observed at the end of Sect. 2.4.3 and will be further explored later.

In the interior of a homogeneous fluid the viscosity never produces new vorticity but only diffuses and dissipates it. However, across a *material boundary* $\mathcal{B}$ the vorticity diffusion flux $\boldsymbol{\sigma}$ is generically discontinuous, implying that there must be a mechanism to create *new* vorticity at $\mathcal{B}$. This is the third effect of the viscosity, unique to vorticity. The vorticity creation is the most active event that occurs at material boundaries of all viscous flows and has profound influence to the entire flow evolution.

The on-wall mechanism of vorticity creation is the no-slip condition. It creates only new *tangent* vorticity at $\mathcal{B}$, which is then diffused into the fluid by $\boldsymbol{\sigma}$. Therefore, $\boldsymbol{\sigma}$ gains a new important physical implication: it measures the rate at which the vorticity is created at the boundary and diffused into the fluid per unit area and time. Thus, on a boundary, we specifically call $\boldsymbol{\sigma}$ the

*boundary vorticity flux*. Equations (4.22)–(4.27) still hold, applicable to any deformable solid wall or interface of two fluids including free surface. Since $\boldsymbol{a}$ and $\omega_{\rm n}$ are continuous across $\mathcal{B}$ (Sect. 2.2.4), if the wall is *rigid* and has angular velocity $\boldsymbol{W}(t)$, in (4.17) we may replace $\boldsymbol{\omega}$ by the relative vorticity $\boldsymbol{\omega}_{\rm r} = \boldsymbol{\omega} - 2\boldsymbol{W}$ with $\boldsymbol{n}\cdot\boldsymbol{\omega}_{\rm r} \equiv 0$. Meanwhile, by (4.26a), the tangent component of $\boldsymbol{\sigma}_{\rm vis}$ is reduced to the sole contribution of wall skin-friction $\boldsymbol{\tau}_w = \mu\boldsymbol{n}\times\boldsymbol{\omega}_{\rm r}$ via curvature:

$$\boldsymbol{\sigma}_{\pi{\rm vis}} = \nu\boldsymbol{\omega}_{\rm r}\cdot\mathbf{K} = \frac{1}{\rho}(\boldsymbol{\tau}_w\times\boldsymbol{n})\cdot\mathbf{K}, \tag{4.28}$$

where $\boldsymbol{\tau}$ or $\boldsymbol{\omega}_{\rm r}$ is in turn a *temporal-spatial accumulated effect* of the entire $\boldsymbol{\sigma}$ as will be demonstrated in Sects. 4.1.4 and 4.2.3.

On a boundary $\mathcal{B}$, $\sigma_{\rm n}$ represents a kinematic tilting of the vorticity lines on $\mathcal{B}$ toward the normal direction. This mechanism can be very significant at a solid wall as seen in tornado-like vortices (Fig. 3.5a), and is an ingredient of three-dimensional flow separation (Chap. 5). Figure 4.5 shows a pair of $\sigma_{\rm n}$-peaks with opposite signs on a channel wall and a *hairpin vortex* above the wall in the sublayer of a turbulent flow, indicating the correlation between the $\sigma_{\rm n}$-pair and hairpin vortex.

For a flow with given wall acceleration and external body force, $\boldsymbol{\sigma}_{\rm a}$ and $\boldsymbol{\sigma}_{\rm f}$ in (4.24) are known. As the measure of vorticity generation rate, these two boundary vorticity-flux constituents can be viewed as the *roots* of the vorticity field in the flow. In contrast, the *stress-related* constituents $\boldsymbol{\sigma}_{\rm p}$ and $\boldsymbol{\sigma}_{\rm vis}$ are the result or *footprints* of the entire flow and boundary condition. But once they are established through the momentum balance, they become

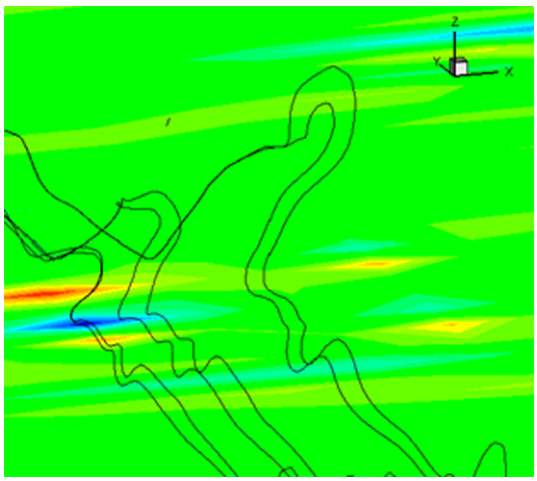


**Fig. 4.5.** A local plot of instantaneous $\sigma_{\rm n}$ (contours) on the wall and vorticity lines right above the wall in a turbulent channel flow. The two dark spots on the wall are a pair of $\sigma_{\rm n}$ peaks of opposite signs. From a direct numerical simulation of Zhao et al. (2004)

the root of the vorticity field. Distinguishing $\boldsymbol{\sigma}_{\mathrm{a}}$ and $\boldsymbol{\sigma}_{\mathrm{f}}$ from $\boldsymbol{\sigma}_{\mathrm{p}}$ and $\boldsymbol{\sigma}_{\mathrm{vis}}$ is very important for understanding the force and moment acting to the wall (Chap. 11) and for near-wall flow control (Zhu 2000; Zhao et al. 2004). For example, if in a conducting fluid an imposed near-wall electromagnetic field can effectively control the vorticity generation through a Lorentz force $\boldsymbol{f}$ (Du and Karniadakis 2000), then by (4.23) the on-wall effect of $\boldsymbol{f}$ can in principle be replaced by an equivalent wall tangent acceleration so that the control could be applied to nonconducting fluid (Zhao et al. 2004). But it will be hard (if not impossible) to impose a distributed $\boldsymbol{\sigma}_{\mathrm{p}}$ as control means.

The relative magnitudes of the four constituents of the boundary vorticity flux vary from one specific problem to another. For an incompressible flow over a three-dimensional stationary body without body force, only $\boldsymbol{\sigma}_{\mathrm{p}}$ and $\boldsymbol{\sigma}_{\mathrm{vis}}$ exist. Naturally and as will be seen in the following sections, they are of the same order when $Re \ll 1$, but $\boldsymbol{\sigma}_{\mathrm{p}}$ becomes much stronger and the most fundamental mechanism of vorticity creation when $Re \gg 1$. In particular, for a two-dimensional flow in the $(x, y)$-plane over a stationary wall with $\boldsymbol{\sigma} = \sigma_{\mathrm{p}} \boldsymbol{e}_z$, (4.24b) and (2.172b) form a pair of Cauchy-Riemann relations:

$$\mu \frac{\partial \omega}{\partial n} = -\frac{\partial p}{\partial s}, \quad \frac{\partial p}{\partial n} = \mu \frac{\partial \omega}{\partial s}. \tag{4.29a,b}$$

Lighthill (1963) was the first to interpret (4.29a) as the measure of vorticity creation and emphasize the role of tangent pressure gradient. His pioneer insight was followed by many workers who added other constituents and extended the theory to two-fluid interface, see the review of Wu and Wu (1996). The physical implication of (4.29a) can be easily understood from Fig. 4.6. Replacing the pressure gradient by a wall acceleration from right to left or a body force from left to right, the mechanisms of $\boldsymbol{\sigma}_{\mathrm{a}}$ and $\boldsymbol{\sigma}_{\mathrm{f}}$ can also be easily understood. Notice the difference of Figs. 4.6 and 3.2. The mechanism of vorticity creation should not be confused with that of boundary vorticity $\boldsymbol{\omega}_{\mathrm{B}}$.

We stress that although (4.23) is derived for viscous flow with acceleration adherence, the form of (4.29a) shows that the amount of $\sigma$ is *independent* of viscosity. Thus, as $\mu \to 0$ there must be $\partial\omega/\partial n \to \infty$ to ensure the momentum

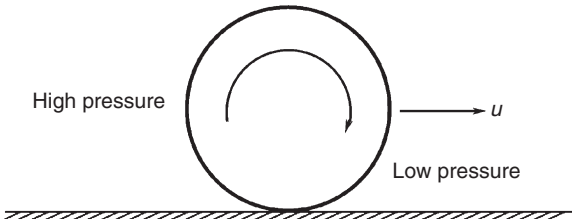


**Fig. 4.6.** Schematic illustration of vorticity generation by pressure gradient and no-slip condition

balance and no-slip condition. At this asymptotic limit the newly created vorticity forms a vortex sheet adjacent to the wall.

Corresponding to the boundary vorticity flux, we also have *boundary enstrophy flux* $\eta$ defined by (4.20). In terms of this scalar flux the flow boundary $\mathcal{B}$ can be divided into three different parts: $\mathcal{B}_0$, where $\eta = 0$ due to the absence of boundary vorticity and/or its flux; $\mathcal{B}_+$, where $\eta > 0$; and $\mathcal{B}_-$, where $\eta < 0$. Thus

$$\int_{\mathcal{B}} \eta \, \mathrm{d}S = \int_{\mathcal{B}_+} |\eta| \, \mathrm{d}S - \int_{\mathcal{B}_-} |\eta| \, \mathrm{d}S. \tag{4.30}$$

It can then be said that $\mathcal{B}_+$ (or $\mathcal{B}_-$) is a *vorticity source* (or *sink*), where the existing vorticity is strengthened (or weakened) by the newly created one.

### 4.1.4 Unidirectional and Quasiparallel Shear Flows

In this subsection we illustrate the basic physics of vorticity diffusion and generation from boundaries by some simple unidirectional and quasiparallel viscous shear flows.

#### Unidirectional Flow Driven by Pressure Gradient and Wall Acceleration

Consider a flow on the half plane $y > 0$ with $\rho = 1$ and

$$\boldsymbol{u} = (u(y,t), 0, 0), \quad \boldsymbol{\omega} = (0, 0, \omega(y,t)), \quad \omega(y,t) = -\frac{\partial u}{\partial y}. \tag{4.31}$$

The fluid and boundary are assumed at rest for $t < 0$, and at $t = 0$ let there appear a tangent motion of the boundary with speed $b(t)$, and a uniform, time-dependent pressure gradient $\partial p/\partial x = P(t)$. In this case, the Navier–Stokes equation and vorticity transport equation are linearized:

$$\frac{\partial u}{\partial t} = -P(t) - \nu \frac{\partial \omega}{\partial y} = -P(t) + \nu \frac{\partial^2 u}{\partial y^2}, \tag{4.32}$$

$$\frac{\partial \omega}{\partial t} = \nu \frac{\partial^2 \omega}{\partial y^2}. \tag{4.33}$$

Applying (4.32) to the wall gives

$$\sigma = \frac{\mathrm{d}b}{\mathrm{d}t} + P(t) \quad \text{at} \quad y = 0, \tag{4.34}$$

which is evidently independent of viscosity. Equation (4.33) under the Newmann condition (4.34) has solution

$$\omega(y,t) = \int_{0^-}^{t} \frac{\sigma(t')}{\sqrt{\pi\nu(t-t')}} \exp\left[-\frac{y^2}{4\nu(t-t')}\right] \mathrm{d}t'. \tag{4.35}$$

The flux $\sigma$ can be regular or singular. If at $t = 0$ there is an impulsive $P(t)$ and $\mathrm{d}b/\mathrm{d}t$, they will cause a suddenly appeared uniform fluid velocity $\boldsymbol{U} = (U, 0, 0)$ and wall velocity $b_0$, respectively. This yields

$$\sigma(t) = -(U - b_0)\delta(t) = \gamma_0\delta(t) \quad \text{for} \quad 0^- \le t \le 0^+, \tag{4.36}$$

where $\gamma_0 = -(U - b_0)$ is the initial vortex-sheet strength. Separating this singular part from (4.35) yields

$$\omega(y,t) = \frac{\gamma_0}{\sqrt{\pi\nu t}} \exp\left(-\frac{y^2}{4\nu t}\right) + \int_{0^+}^{t} \frac{\sigma(t')}{\sqrt{\pi\nu(t-t')}} \exp\left[-\frac{y^2}{4\nu(t-t')}\right] \mathrm{d}t'. \tag{4.37}$$

With a finite $\nu$, the initially singular vorticity in the sheet $\gamma_0$ is soon diffused into the fluid as reflected by the first term of (4.37). This problem is referred to as the *generalized Stokes problem*. Setting $y = 0$ in (4.37) gives

$$\omega_{\mathrm{B}}(t) = \frac{\gamma_0}{\sqrt{\pi\nu t}} + \frac{1}{\sqrt{\pi\nu}} \int_{0^+}^{t} \frac{\sigma(t')}{\sqrt{t-t'}} \mathrm{d}t', \tag{4.38}$$

indicating clearly that in this example $\omega_{\mathrm{B}}$ is a temporal accumulated effect of $\sigma$. On the other hand, by (4.37) one may verify that the rate of change of total vorticity is

$$\frac{\mathrm{d}}{\mathrm{d}t} \int_0^\infty \omega(y,t)\mathrm{d}y = \sigma(t), \tag{4.39}$$

which confirms the physical meaning of $\sigma$.

Two special cases of (4.37) were first studied by Stokes. The *Stokes first problem* or *Rayleigh problem* is that the flow is entirely caused by an impulsive start of the wall from rest, with $P = 0$ for all $t$ and $\sigma = 0$ for $t \ge 0^+$. Hence

$$\omega(y,t) = \frac{b_0}{\sqrt{\pi\nu t}} \exp\left(-\frac{y^2}{4\nu t}\right). \tag{4.40}$$

The *Stokes second problem* is that the wall makes a sinusoidal oscillation, say $b = b_0 \cos nt$ (or $b_0 \sin nt$, the difference being that the former contains an impulsive start). The full solution has been studied by Panton (1968). If only the transient boundary vorticity is considered, with $b = b_0 \cos nt$ the integral in (4.38) can be carried out analytically:

$$\omega_{\mathrm{B}}(t) = \frac{\gamma_0}{(\pi\nu t)^{1/2}} + b_0 \left(\frac{2n}{\nu}\right)^{1/2} \left[S(\sqrt{nt}) \cos nt - C(\sqrt{nt}) \sin nt\right], \tag{4.41}$$

where $S(x)$ and $C(x)$ are Fresnel's integrals (e.g., Abramowitz and Stegun 1972). As $t \to \infty$ this solution degenerates to a stationary oscillating state

$$\omega_{\mathrm{B}}(t) = b_0 \left(\frac{n}{\nu}\right)^{1/2} \cos\left(nt + \frac{\pi}{4}\right). \tag{4.42}$$

At this stage, inside the fluid the vorticity field also has a stationary oscillation, which is a *viscous transverse wave* propagating along the $y$-direction:

$$\omega(y,t) = b_0 \left(\frac{n}{\nu}\right)^{1/2} \mathrm{e}^{-y/\delta} \cos\left(\frac{y}{\delta} - nt - \frac{\pi}{4}\right), \quad \delta = k_\mathrm{r}^{-1} = \left(\frac{2\nu}{n}\right)^{1/2}. \tag{4.43}$$

The length scale $\delta = k_\mathrm{r}^{-1}$, with $k_\mathrm{r}$ being the real part of the complex wave number, characterizes the *diffusion distance* of the wave or the thickness of a shear layer in which the flow has significant transverse wave. This layer is known as the *Stokes layer*. The phase speed $c$ and group speed $c_\mathrm{g}$ of the transverse wave are

$$c = \frac{n}{k_\mathrm{r}} = \sqrt{2\nu n}, \quad c_\mathrm{g} = \frac{\mathrm{d}n}{\mathrm{d}k_\mathrm{r}} = 2\sqrt{2\nu n} > c, \tag{4.44}$$

which are frequency-dependent, so the wave is *dispersive*.

### Unidirectional Interfacial Flow

As an extension of the Stokes first problem, we now insert a flat interface $S$ at $y = 1$ into the preceding unidirectional flow at $y > 0$ (Wu 1995). A flat interface of water and air may occur when the gravitational force is much larger than inertial force. Both flow 1 (e.g., the water) at $y \in [0, 1]$ and flow 2 (e.g., the air) at $y = (1, \infty)$ are governed by the same equations as (4.32) with $P = 0$ and (4.33), and the matching condition of two flows is velocity adherence and surface-force continuity (2.68), which yields an integral equation for the unknown interface velocity $u_1 = u_2 = v$ at $y = 1$. The only surface force on $S$ is the shear stress $\mu\boldsymbol{\omega} \times \boldsymbol{n}$, which by (2.68) implies a vorticity jump $\omega_1/\omega_2 = \mu_2/\mu_1$. Thus, the impulsively started bottom wall drives flow 1, which drives flow 2 that in turn reacts to flow 1.

The velocity profiles in water and air at different times are shown in Fig. 4.7a. The interface vorticity is initially zero, then increases to a positive peak due to the diffusion of $\omega_1 > 0$ (entirely generated at $t = 0$) to $S$, and then decreases to zero as it diffuses into fluid 2, see Fig. 4.7b. In addition to the singular generation of $\omega_1$ at the wall, at $S$ there also appears a boundary vorticity flux on both sides:

$$\sigma_1 = \nu_1 \frac{\partial \omega_1}{\partial y} = -\frac{\mathrm{d}v}{\mathrm{d}t} = -\sigma_2 = \nu_2 \frac{\partial \omega_2}{\partial y} \quad \text{at} \quad y = 1. \tag{4.45}$$

Initially there is $\sigma_1 = 0$. When $\omega_1 > 0$ is diffused to $S$ to induce a tangent interface acceleration $\mathrm{d}v/\mathrm{d}t$, $\sigma_1$ starts to become negative, reaching a peak value and then returns to zero, see Fig. 4.7c. $\sigma_2$ follows a similar trend but with opposite sign and different magnitude (not shown).

Since $\rho_2/\rho_1 \ll 1$, the effect of the air motion on the water can be ignored and the interface problem can be simplified to a *free-surface problem*. Then the interface vorticity will be identically zero and flow 1 alone can be solved. A remarkable difference of this free-surface model and interface flow is that,

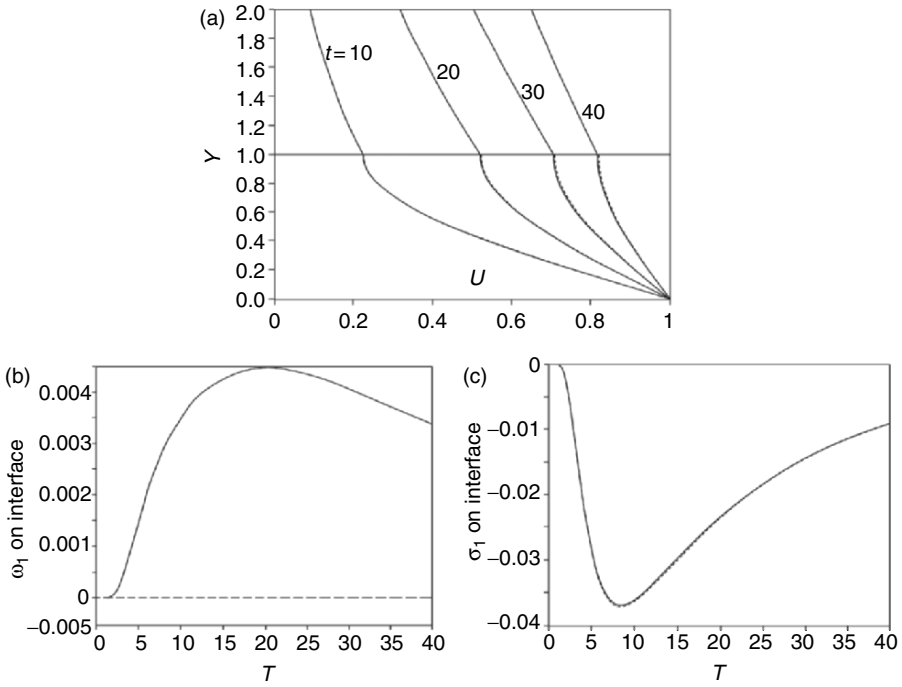


**Fig. 4.7.** Generalized Stokes' first problem for interacting water–air system. (**a**) Velocity profiles at different times. (**b**) Time variation of water vorticity on the interface. (**c**) Time variation of vorticity flux at the interface. Solid lines are water–air coupled solution and dash lines are obtained by free-surface approximation. Quantities are made dimensionless by the bottom-plate initial velocity, the water depth, and water density. Reproduced from Wu (1995)

for the former the boundary enstrophy flux $\eta$ defined by (4.20) is zero both at $y = 0$ for $t > 0$ due to $\sigma = 0$, and at $y = 1$ due to $\omega = 0$, respectively. Consequently, the enstrophy of the water cannot "escape" out of the free surface at all, although it eventually decays to zero. This can only be explained by a $\sigma \leq 0$ at $S$ found in both interface and free-surface flows, which generates opposite vorticity that diffuses downward to cancel that generated at the wall. Despite the difference of interface vorticity (Fig. 4.7b), the prediction of free-surface model on the velocity profile of flow 1 and its boundary vorticity flux on $S$ agree very well with that of the interface.

### Acoustically Created Vorticity Wave from Flat Plate

As an extension of Stokes' second problem, we replace $P(t)$ in (4.32) by a harmonic traveling pressure wave (a sound wave):

$$p = A\mathrm{e}^{\mathrm{i}k(x-ct)}, \quad A = \rho u_0 c, \quad c = \frac{n}{k}, \tag{4.46}$$

where $u_0$ and $\rho$ are constant. Then instead of (4.34) there is

$$\sigma = \frac{1}{\rho}\frac{\partial p}{\partial x} = Re\left\{\mathrm{i}nu_0\,\mathrm{e}^{\mathrm{i}k(x-ct)}\right\} = -nu_0\sin(kx-nt), \tag{4.47}$$

which excites a Stokes layer of thickness $\delta$ defined in (4.43). Let $\zeta = y/\delta$ be the rescaled normal distance. Then the velocity field inside the layer is

$$u = u_0\left\{1-\mathrm{e}^{(\mathrm{i}-1)\zeta}\right\}\mathrm{e}^{\mathrm{i}k(x-ct)}, \tag{4.48a}$$

$$v = ku_0\delta\left\{-\mathrm{i}\zeta + \frac{1-\mathrm{i}}{2}\left(\mathrm{e}^{(\mathrm{i}-1)\zeta}-1\right)\right\}\mathrm{e}^{\mathrm{i}k(x-ct)}, \tag{4.48b}$$

indicating that the flow is no longer unidirectional when $k \neq 0$. The $\omega$-wave produced by the $p$-wave is

$$\omega = (\mathrm{i}-1)\frac{u_0}{\delta}\mathrm{e}^{-\zeta}\,\mathrm{e}^{\mathrm{i}(kx-nt+\zeta)} + O(k^2\delta), \tag{4.49}$$

where the contribution of $\partial v/\partial x$ is ignored. The associated boundary enstrophy flux is

$$\eta = \left(\frac{n}{2}\right)^{3/2}\frac{u_0^2}{\sqrt{\nu}}\left\{1+\sqrt{2}\sin\left[2(kx-nt)-\frac{\pi}{4}\right]\right\}, \tag{4.50}$$

which has a *positive average*.

Lin (1957) has shown that for any external flow (even turbulent), if the frequency is so high that $\delta$ is much smaller than the boundary-layer thickness, then inside the Stokes layer the linear approximation (4.48) and (4.49) still holds. A direct numerical simulation of channel-turbulence control by flexible wall traveling wave confirmed Lin's assertion (Yang 2004).

### Sound-Vortex Interaction in a Duct

According to the vortex-sound theory outlined in Sect. 2.4.3, the sound-generated vorticity in the earlier example 3 will in turn produce sound, which may have strong effect when the sound wave is confined in a duct. Thus, consider a weakly compressible flow with disturbance velocity $\boldsymbol{u} = (u, v)$ and dilatation $\vartheta = \nabla\cdot\boldsymbol{u}$ in a two-dimensional duct, bounded by parallel plates at $y = 0$ and 2. Assume the mean flow has unidirectional velocity $U(y)$ that satisfies the no-slip condition. Due to the nonuniformity of $U$, a sound wave having a plane front at $x = 0$, say, must be refracted towards the walls, and only a part of modes can reach far downstream. This is a closed-loop coupling between shearing and compressing processes as well as sound propagation by $U(y)$ in the duct. Both processes should be solved simultaneously, governed by a pair of linear equations derived from (2.168) and (2.169):

$$(D_0 - \nu\nabla^2)\omega = U''v + U'\vartheta, \tag{4.51a}$$

$$D_0\vartheta + \nabla^2 p = -2U'\frac{\partial v}{\partial x}, \tag{4.51b}$$

under boundary conditions (4.29). Here, $D_0 \equiv \partial_t + U\partial_x$ and $(\cdot)' = \mathrm{d}(\cdot)/\mathrm{d}y$. In example 3 the pressure wave is specified and only (4.51a) was used; while the inviscid problem (4.51b) alone with homogeneous boundary conditions (an eigenvalue problem) has also been well studied (e.g., Pridmore-Brown 1958; Shankar 1971). But now the fully coupled problem is nonlinear. A simplified approach was given by Wu et al. (1994a), who split this closed-loop interaction into two subprocesses and solved them sequentially. First, an inviscid refracted pressure field was computed by (4.51b) as an eigenvalue problem, which then produces a vorticity wave by (4.51a) and (4.29a). Second, (4.51b) was cast to a linearized vortex-sound equation in terms of the total enthalpy $H$ as a special case of (2.170). With the mean-flow Mach number $M = U/c$, the dimensionless $H$-equation reads

$$\nabla^2 H - (D_0^2 H + MM'D_0 v) = M''u - 2M'\omega - M\frac{\partial \omega}{\partial y}, \tag{4.52}$$

from which the $p$-field due to the acoustically created $\omega$-wave can be calculated and added to the initial inviscid $p$-wave solution. In solving (4.52) a *viscous* boundary condition derived from (4.29b) has to be imposed even though the equation is inviscid.

For a parabolic mean flow $M(y) = M_\infty(2y - y^2)$, the amplitude of vorticity wave produced by the refracted $p$-wave obtained by this sequential approach is shown in Fig. 4.8a, and the wall sound pressure level (SPL) at different wave number $k$ and Reynolds number $Re$ is shown in Fig. 4.8b. Note that Fig. 4.8b shows that the effect of viscosity may be nonmonotonic. When a

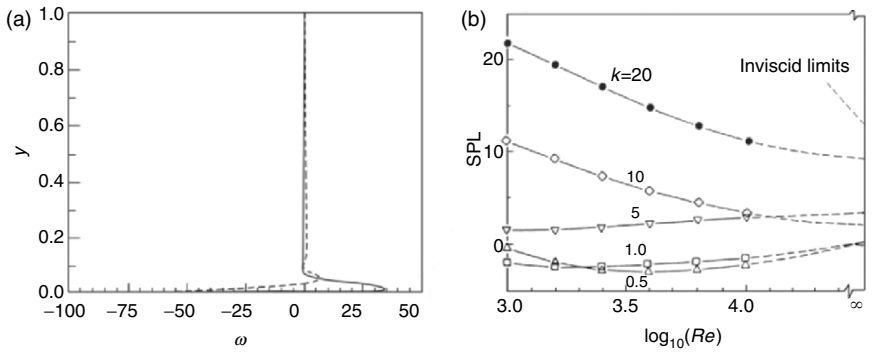


**Fig. 4.8.** Sound–vortex interaction in a duct at $M = 0.3$. (**a**) The amplitude of sound-generated vorticity wave at $x = 20$, $k = 5$, and $Re = 1{,}000$ (real part: solid line; imaginary part: dash line). (**b**) The wall SPL at $x = 20$ and different $k$ and $Re$. From Wu et al. (1994a)

$p$-wave excites an $\omega$-wave through the no-slip condition, it loses some kinetic energy; but, (4.51a) indicates that there is an interior unsteady source $U''v$ for disturbance vorticity, which makes the acoustically created $\omega$-wave able to absorb enstrophy from the mean flow and becomes a self-enhanced source of sound.

## 4.2 Vorticity Field at Small Reynolds Numbers

It has been asserted in Chap. 2 that the dominating parameter of the shearing process is the Reynolds number. The effect of this parameter on vortical flows is very complicated, as demonstrated by the well-known photographs of flow over a circular cylinder of diameter $D$ at different $R_{\rm D} = UD/\nu$ (Van Dyke 1982; see also Fig. 10.42). If $R_{\rm D} = O(1)$, we have the full Navier–Stokes equation and no simplification can be made. But both $R_{\rm D} \ll 1$ and $R_{\rm D} \gg 1$ provide a small parameter, and the *matched asymptotic expansion* (e.g., Van Dyke 1975) can lead to approximate solutions. We take this convenience to discuss the behavior of incompressible vorticity field at small Reynolds numbers in this section, and at large Reynolds numbers in the next two sections.

Small Reynolds-number flows are called *Stokes flows*. The viscous length scale of a flow is $\nu/U$, where $U$ is the oncoming velocity. Compared to the body length scale $D$, $R_{\rm D} \ll 1$ implies that

$$\frac{\text{Viscous length scale}}{\text{Body length scale}} \gg 1.$$

This occurs if either (a) $U \ll 1$, or (b) $D \ll 1$. To the leading order, case (a) implies that the inertial force can be ignored, while case (b) implies that the flow is almost uniform. These two views led to different approximate solutions studied by Stokes (1851) and Oseen (1910), respectively. They had not been unified until 1950s, when Kaplun (1957) realized that the Stokes solution is effective only near the body surface while the Oseen solution is effective for far field, and they should be matched to form a uniformly effective solution.

We illustrate the situation by a steady incompressible flow $U\boldsymbol{e}_x$ over a sphere of radius $a$, examined in the spherical coordinates $(R, \theta, \phi)$ shown in Fig. 4.9. This problem has extensive applications in many fields of science and technology, such as artificial raining, air dust removing, boiling heat transfer, powder transportation, measurements of fluid viscosity and charge of electron, and the motion of blood cells, etc. From now on we use $a$ to define the Reynolds number $Re = aU/\nu$. When $Re = \epsilon \ll 1$, the steady governing equations read

$$\epsilon \boldsymbol{u} \cdot \nabla \boldsymbol{u} = -\epsilon \nabla p - \nabla \times \boldsymbol{\omega}. \tag{4.53}$$

### 4.2.1 Stokes Approximation of Flow Over Sphere

We first follow Stokes' approach to simply set $\epsilon = 0$, which leads to four component equations from $\nabla \times \boldsymbol{\omega} = \boldsymbol{0}$ and condition $\nabla \cdot \boldsymbol{u} = 0$ for three

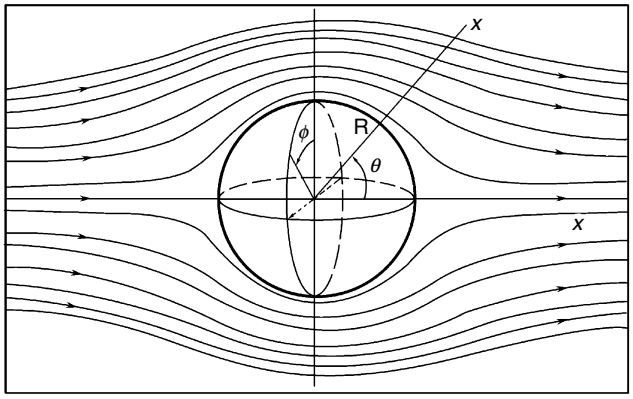


**Fig. 4.9.** Flow over a sphere at small Reynolds number

unknown variables. To make the problem solvable we retain the pressure term by setting $P \equiv \epsilon(p - p_\infty)$. Then by (4.53), the lowest-order approximation (the *Stokes approximation*) is

$$\nabla P + \nabla \times \boldsymbol{\omega} = \mathbf{0}. \tag{4.54}$$

Hence, both $P$ and $\boldsymbol{\omega}$ are harmonic:

$$\nabla^2 P = 0, \quad \nabla^2 \boldsymbol{\omega} = \mathbf{0}, \tag{4.55a,b}$$

which and (4.29) indicate that in two-dimensional flow $P + \mathrm{i}\omega$ is a complex analytic function. Although the inviscid coupling of shearing and compressing processes via nonlinearity inside the flow field is absent, *the viscous linear coupling is strong* on the body surface via the adherence condition (Sect. 2.4.3).

In the spherical coordinates, after scaled by $a$ and $U$, the boundary conditions read

$$\boldsymbol{u} = \boldsymbol{e}_x, \quad P = 0, \quad R \to \infty, \tag{4.56a}$$

$$\boldsymbol{u} = \mathbf{0} \quad \text{at} \quad R = 1. \tag{4.56b}$$

The flow occurs on the $(R, \theta)$ plane and is rotationally symmetric. As argued by Batchelor (1967), because the form of (4.55) is independent of the choice of coordinates, by inspecting the form of (4.56) one finds that $P$ and $\boldsymbol{\omega}$ can only depends on $\boldsymbol{x}$, $\boldsymbol{e}_x$, and $R$. $P$ must take on the form $\boldsymbol{x} \cdot \boldsymbol{e}_x F(R)$, while $\boldsymbol{\omega}$ must be along the $\boldsymbol{e}_\phi$-direction and only depends on $\boldsymbol{e}_x \times \boldsymbol{x} F(R)$. Then since $1/R$ is a fundamental solution of Laplace equations (the origin is singular but outside the flow field), the proper $P$ should be found in the series solution (cf. Sect. 3.2.3)

$$P = \sum_{n=0}^{\infty} C_n \left(\frac{\partial}{\partial x}\right)^n \left(\frac{1}{R}\right).$$

In fact, only the term $n = 1$ in this series fits (4.56), so we have

$$P = \frac{C}{R^2}\cos\theta, \quad \boldsymbol{\omega} = \boldsymbol{e}_\phi \frac{C}{R^2}\sin\theta.$$

Both $P$ and $\boldsymbol{\omega}$ have full fore-and-aft symmetry, and have the same constant $C$ due to (4.54).

There remains using (4.56b) to fix a scalar constant $C$. To this end we only need to apply the Biot–Savart formula to a single convenient point, say the origin where $\boldsymbol{u} = \boldsymbol{0}$. Since $\boldsymbol{\omega} \neq \boldsymbol{0}$ for $R \geq 1$, it follows that

$$\boldsymbol{e}_x = -\frac{C}{4\pi}\int_0^\pi \mathrm{d}\theta \int_1^\infty \frac{\boldsymbol{e}_R \times \boldsymbol{e}_\phi}{R^2}\sin^2\theta\,\mathrm{d}R = -\frac{2}{3}C\boldsymbol{e}_x,$$

which gives $C = -3/2$. This simple approach is possible because of the symmetry of the flow. Return to the dimensional form with density $\rho$, the desired solution is

$$\boldsymbol{\omega} = -\frac{3}{2}aU\frac{\sin\theta}{R^2}\boldsymbol{e}_\phi, \tag{4.57a}$$

$$p - p_\infty = -\frac{3}{2}\mu aU\frac{\cos\theta}{R^2}. \tag{4.57b}$$

From (4.57a) we obtain the velocity $\boldsymbol{u} = (u_r, u_\theta, 0)$, where

$$u_r = \frac{3}{4}\left(2R - 3 + \frac{1}{R}\right)\sin\theta\cos\theta, \tag{4.58a}$$

$$u_\theta = -\frac{3}{2}(R-1)\sin^2\theta. \tag{4.58b}$$

Therefore, the entire flow is fore-and-aft symmetric or *wake-free*, of which the streamlines are plotted in Fig. 4.9. The vorticity created from the sphere surface spreads to the flow field solely by diffusion. But the dissipation makes the total drag nonzero. The pressure drag and skin-friction drag can be easily obtained by applying (4.57a) and (4.57b) to $r = a$ and integration. This gives the *Stokes drag law*, which agrees with experiments up to $Re \sim 1$:

$$D = 6\pi\mu Ua \quad \text{or} \quad C_\mathrm{D} = \frac{D}{\frac{1}{2}\rho U^2\pi a^2} = \frac{12}{Re}. \tag{4.59}$$

Another way of deriving the drag with more flavor of vorticity dynamics is combining (2.76) and (2.159). Because in this wake-free steady flow the kinetic energy is completely dissipated in the near field, the total kinetic energy $K$ is time-invariant and $-\mathbf{B}\cdot\boldsymbol{u} = \boldsymbol{u}\cdot\nabla\boldsymbol{u} = \boldsymbol{0}$ at infinity. Thus, we simply have

$$D = \frac{1}{U}\int \Phi\,\mathrm{d}V = \frac{\mu}{U}\int \omega^2\,\mathrm{d}V = \frac{2\pi\mu}{U}\int_0^\pi \mathrm{d}\theta\int_a^\infty \omega^2 R^2\sin\theta\,\mathrm{d}R,$$

which by (4.57a) returns (4.59).[2]

[2] More methods of calculating force and moment will be given in Chap. 11.

Finally, from (4.57a) the boundary vorticity flux $\boldsymbol{\sigma}_\pi = \sigma \boldsymbol{e}_\phi$ defined by (4.26a) can be easily obtained. Since the curvature of unit sphere is $\mathbf{K} = \boldsymbol{e}_\theta \boldsymbol{e}_\theta + \boldsymbol{e}_\phi \boldsymbol{e}_\phi$, we have $\boldsymbol{\sigma}_{\rm vis} = \epsilon^{-1} \omega_{\rm B} \boldsymbol{e}_\phi$ and $\boldsymbol{\sigma}_{\rm p} = \boldsymbol{\sigma} - \boldsymbol{\sigma}_{\rm vis}$. It then turns out that the pressure gradient and boundary vorticity have exactly the same contribution to $\boldsymbol{\sigma}$:

$$\boldsymbol{\sigma}_{\rm p} = \boldsymbol{\sigma}_{\rm vis} = \frac{1}{2}\boldsymbol{\sigma} = -\frac{3\nu U}{2a^2} \sin\theta \, \boldsymbol{e}_\phi \quad \text{on sphere.} \tag{4.60a}$$

Moreover, the boundary enstrophy flux defined by (4.20) is, by (4.60a) and (4.57a),

$$\eta = \frac{9\nu U^2}{2a^3} \sin^2\theta. \tag{4.60b}$$

One may check that the surface integral of $\eta$ over the sphere equals exactly the total dissipation, which is possible only when the flow is wake-free. Note that $\boldsymbol{\sigma}$ and $\eta$ are of $O(\epsilon^{-1}) \gg 1$ although $|\boldsymbol{\omega}| = O(1)$. This is in contrast to the flow at large Reynolds numbers dominated by advection (Sect. 4.3 below), which has $|\boldsymbol{\sigma}| = O(1)$ and $\eta = O(Re^{1/2})$.

### 4.2.2 Oseen Approximation of Flow Over Sphere

In the earlier Stokes solution the entire inertial force $\boldsymbol{u} \cdot \nabla \boldsymbol{u} = \boldsymbol{\omega} \times \boldsymbol{u} + \nabla q^2/2$ was ignored. While $\nabla q^2/2$ can be absorbed by $P$, for fixed $Re \ll 1$ we have a very slow decay of $\boldsymbol{\omega} \times \boldsymbol{u}$ as $R \to \infty$, which is the main source of far-field inertial force. Because at far field $|\boldsymbol{u}| = O(1)$, from (4.57a) we find that the inertial force is of $O(R^{-3})$. On the other hand, the viscous force is $\epsilon^{-1} \nabla \times \boldsymbol{\omega} = O(\epsilon^{-1} R^{-2})$. Thus,

$$\frac{\text{Inertial force}}{\text{Viscous force}} = O(\epsilon R/a) \quad \text{for} \quad R \to \infty, \quad \epsilon = Re = \frac{Ua}{\nu}.$$

Therefore, the error of the Stokes approximation is $O(\epsilon)$ when $R/a = O(1)$, but becomes $O(1)$ when $R/a = O(\epsilon^{-1})$. One is just lucky to get (4.56a) satisfied.[3] To describe the far-field behavior, we need a different approximation and match the two solutions somewhere between near and far fields.

A far-field observer will see a sphere of very small radius, so the flow is almost uniform. This is the view (b) mentioned in the beginning of the section, which led to the *Oseen Approximation*. Thus, set $\boldsymbol{u} = U\boldsymbol{e}_x + \boldsymbol{u}'$ with $|\boldsymbol{u}'| \ll U$ for $R = O(\epsilon^{-1} a)$. Then the dimensional form of (4.53) with $\rho = 1$ is linearized to

$$U \frac{\partial \boldsymbol{u}'}{\partial x} = -\nabla p - \nu \nabla \times \boldsymbol{\omega}, \tag{4.61}$$

from which follows $\nabla^2 p = 0$ as in (4.55a), but instead of (4.55b) there is

[3] It will be not so lucky if one considers the Stokes approximation of a flow over a circular cylinder (e.g., Van Dyke 1975).

$$\left(\nabla^2 - 2k\frac{\partial}{\partial x}\right)\boldsymbol{\omega} = \mathbf{0}, \quad k = \frac{U}{2\nu} = \frac{\epsilon}{2a}, \tag{4.62}$$

of which the solution has been well known (Lamb 1932; Milne-Thomson 1968):

$$\omega = A(1+kR)\frac{\sin\theta}{R^2}\mathrm{e}^{-kR(1-\cos\theta)}. \tag{4.63}$$

This is an *outer solution* effective for $R \gg a$. To fix the constant $A$ we match (4.63) and the *inner solution* (4.57a) at $R = O(a)$. To this end we notice that at $R = O(\epsilon^{-1})$ (4.63) suggests a natural rescaling $\rho = 2kR$, such that the outer and inner solutions read

$$\omega_{\mathrm{out}}(\rho,\theta) = \epsilon^2 A\left(1+\frac{1}{2}\rho\right)\frac{\sin\theta}{\rho^2}\mathrm{e}^{-(1/2)\rho(1-\cos\theta)},$$
$$\omega_{\mathrm{in}}(\rho,\theta) = -\frac{3}{2}\epsilon^2\frac{\sin\theta}{\rho^2}.$$

Then the *asymptotic matching principle* requires the two solution to connect smoothly at $R = O(1)$ or $\rho = O(\epsilon)$ in the limit $\epsilon \to 0$:

$$\lim_{\rho\to 0}\omega_{\mathrm{out}}(\rho,\theta) = \lim_{\rho\to\infty}\omega_{\mathrm{in}}(\rho,\theta), \quad \rho = O(\epsilon), \tag{4.64}$$

yielding $A = -3/2$. Hence, the far-field solution becomes

$$\omega = -\frac{3}{2}\frac{\sin\theta}{R^2}\left(1+\frac{\epsilon}{2}R\right)\mathrm{e}^{-kR(1-\cos\theta)}, \quad R \gg 1. \tag{4.65}$$

If we expand this solution to $O(\epsilon)$ at $R + O(1)$, there is

$$\omega = -\frac{3}{2}\frac{\sin\theta}{R^2}\left(1+\frac{\epsilon}{2}R\right) + O(\epsilon^2), \quad R = O(1), \tag{4.66}$$

indicating an $O(\epsilon)$ error. Although on the sphere this solution does not exactly satisfy the boundary condition (4.56b) but the Stokes solution does, the latter still has an error of $O(\epsilon)$ at $R = 1$, no better than the former. Therefore, after matching with the Stokes solution the Oseen solution is the lowest-order *uniformly effective solution*.

The disturbance velocity $\boldsymbol{u}'$ can be solved from $\nabla\times\boldsymbol{u}' = \boldsymbol{\omega}$, which consists of both potential and vortical parts.[4] Then the pressure is obtained from (4.61), and the drag can be computed by considering the normal and shear stresses on the sphere (e.g., Milne-Thomson 1968). The result is

$$D = 6\rho U^2\pi a\left(1+\frac{3}{8}Re\right), \quad \text{or} \quad C_{\mathrm{D}} = \frac{12}{Re}\left(1+\frac{3}{8}Re\right), \tag{4.67}$$

which will be compared with (4.59) in Fig. 4.14 below. For more discussions see Proudman and Pearson (1957) and Chester (1962).

[4] This decomposition can be explicitly written because (4.61) is linear. For the unsteady version of (4.61), then, the potential and rotational parts of the disturbance velocity represent longitudinal and transverse waves, respectively (Lagerstrom 1964).

### 4.2.3 Separated Vortex and Vortical Wake

From the point of view of vorticity dynamics, a remarkable feature of the Oseen approximation is that its solution permits a standing vortical bubble (a vortex ring) behind the sphere. The two-term singular perturbation solution of Proudman and Pearson (1957) gives the Stokes stream function in the vicinity of the sphere of unit radius, satisfying the adherence condition:

$$\begin{aligned}\psi &= \psi^{(0)} + \epsilon\psi^{(1)} \\ &= \frac{1}{4}(R-1)^2 \sin^2\theta \left[\left(1+\frac{3\epsilon}{8}\right)\left(2+\frac{1}{R}\right) - \frac{3\epsilon}{8}\left(2+\frac{1}{R}+\frac{1}{R^2}\right)\cos\theta\right].\end{aligned} \tag{4.68}$$

One sees that $\psi = 0$ not only on the sphere but also along the revolutionary surface

$$\cos\theta = \left(\frac{8}{3\,Re}+1\right)\frac{2R^2+R}{2R^2+R+1}, \tag{4.69}$$

which may enclose a ring-like separated vortex bubble. The downstream end of the bubble is at

$$l = \frac{1}{4}(\sqrt{1+3\,Re}-1). \tag{4.70}$$

A real bubble exists when $l > 1$ or $Re > 8$. The bubble shape is shown in Fig. 4.10, and its length vs. $Re$ is shown in Fig. 4.11. Surprisingly, the agreement with experiments persists up to $Re = 60$, far beyond the assumed effective range of (4.61).

For incompressible flow, the vorticity is solely created at the body surface (Sect. 4.1.3), always with a precise rate as needed for the satisfaction of the no-slip condition. But once generated and diffused into the flow, except a part that diffuses to the front of the body, more vorticity is advected downstream as well as diffusion, and hence accumulated in the rear part. The flow can

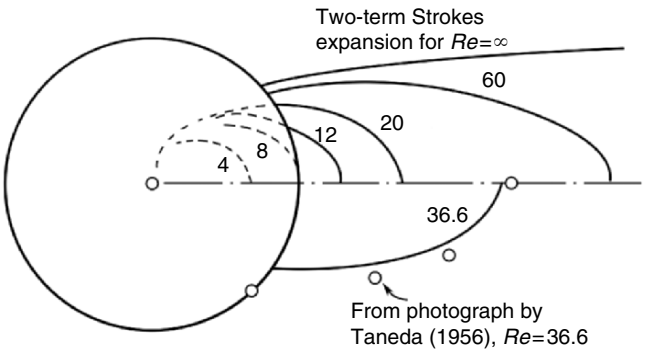


**Fig. 4.10.** Separation bubble for small Reynolds-number flow over sphere. Reproduced from Van Dyke (1975)

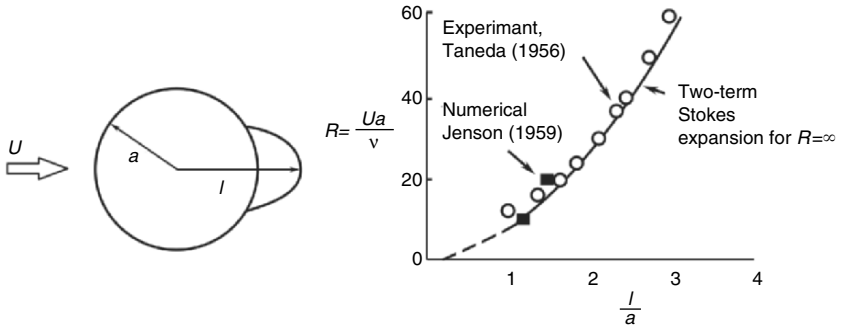


**Fig. 4.11.** Bubble length vs. $Re$ for sphere flow. Reproduced from Van Dyke (1975)

no longer be completely attached as the accumulated vorticity reaches a saturation level at a critical Reynolds number; then a vortex bubble starts to appear at the rear stagnation point and grows as $Re$ increases. The formation of the bubble represents a *bifurcation* of the Navier–Stokes solution from *attached flow* to *separated flow*. This bifurcation process is known as *flow separation* and will be extensively studied in Chap. 5; but as the first quantitative prototype, the present example deserves a further analysis.

The basic physics of flow separation can be made clear in terms of the boundary vorticity $\boldsymbol{\omega}_{\rm B} = \omega_{\rm B}\boldsymbol{e}_\phi$ and boundary vorticity flux $\boldsymbol{\sigma} = \sigma\boldsymbol{e}_\phi = \boldsymbol{\sigma}_p + \boldsymbol{\sigma}_{\rm vis}$. From $\boldsymbol{\omega} = -\nabla^2\boldsymbol{\psi}$ with $\boldsymbol{\psi} = (0, \psi_\theta, 0)$ there is

$$-\omega = \frac{1}{R^2}\frac{\partial}{\partial R}\left(R^2\frac{\partial\psi_\theta}{\partial R}\right) + \frac{1}{R^2\sin\theta}\frac{\partial}{\partial\theta}\left(\sin\theta\frac{\partial\psi_\theta}{\partial\theta}\right),$$

where $\psi_\theta = \psi/R$. Then from (4.68) it follows that, in dimensionless form,

$$\omega_{\rm B} = -\frac{3}{2}\sin^2\theta\left[1 + \frac{3\epsilon}{8}\left(1 - \frac{4}{3}\cos\theta\right)\right], \tag{4.71a}$$

$$\sigma = -\frac{3}{\epsilon}\sin^2\theta\left[1 + \frac{3\epsilon}{8}\left(1 - \frac{13}{2}\cos\theta\right)\right], \tag{4.71b}$$

$$\sigma_{\rm p} = -\frac{3}{2\epsilon}\sin^2\theta\left[1 + \frac{3\epsilon}{8}(1 - 3\cos\theta)\right]. \tag{4.71c}$$

Thus, $\omega_{\rm B}$, $\sigma$, and $\sigma_{\rm p}$ change sign at

$$\cos\theta_1 = \frac{3}{4}\left(1 + \frac{8}{3\,Re}\right), \quad \cos\theta_2 = \frac{6}{13}\left(1 + \frac{8}{3\,Re}\right), \quad \cos\theta_3 = \frac{1}{3}\left(1 + \frac{8}{3\,Re}\right), \tag{4.72}$$

respectively. While $\theta_1 > 0$ exists for $Re > 8$ as said before, $\theta_2$ and $\theta_3$ appear for $Re \geq 16/7$ and $4/3$, respectively. These critical angles move upstream as $Re$ increases.

Unlike the Stokes approximation, now $\sigma_{\rm p}$ is slightly stronger than $\sigma_\tau$, implying that the advection driven by pressure gradient cannot be completely

balanced by diffusion. Since $\theta_1 < \theta_2 < \theta_3$, as one moves from the front stagnation point ($\theta = \pi$) to the rear stagnation point ($\theta = 0$), the tangent pressure gradient becomes adverse first at $\theta_3$ and then overcomes an opposite $\sigma_\tau$ at $\theta_2$ such that the vorticity of opposite sign starts to be created. This vorticity weakens the existing boundary vorticity, and its continuous generation eventually forces $\omega_B$ to vanish, where separation occurs, and then take opposite sign in the separation bubble. In contrast, the Stokes approximation (4.60a) indicates that no flow separation can occur.

The above order of $\theta_1$, $\theta_2$, and $\theta_3$ can be observed in many other situations. For two-dimensional viscous flow over a flat plate along the $x$-direction, the same order $x_1 > x_2 > x_3$ for the sign change of $\sigma_p$, $\sigma$, and $\omega_B$ holds as the pressure gradient changes from favorable to adverse. Figure. 4.12 shows schematically the velocity and vorticity profiles, and the $x$-variation of $\sigma$ and enstrophy flux $\eta$, for such a flow before and after separation. The sign change of boundary vorticity $\omega_B$ signifies the separation point, while the appearance of vorticity sink ($\eta < 0$) warns that the separation may soon happen.

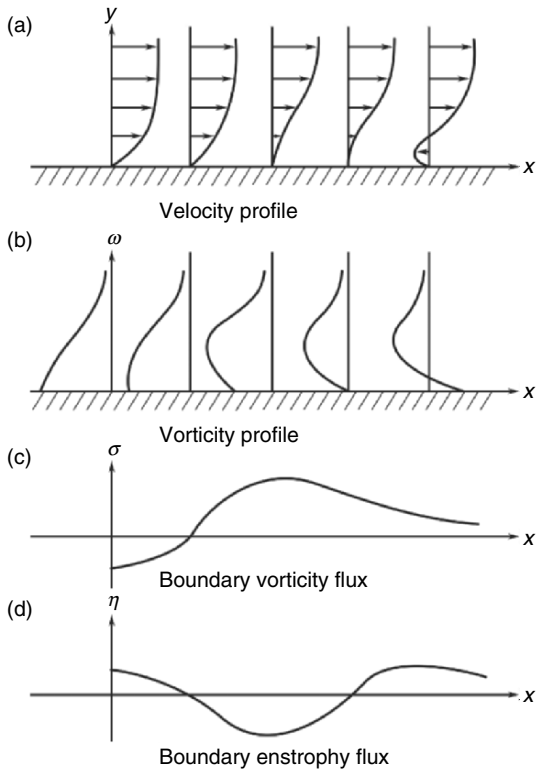


**Fig. 4.12.** Sketch of the profiles of velocity (**a**) and vorticity (**b**), and the variations of the fluxes of vorticity (**c**) and enstrophy (**d**) on the wall, for a flat-plate flow in a pressure gradient changing from favorable to adverse

It is conceptually useful to divide the vorticity field created by a moving body into two parts. One part is dragged along by or *attaches* to the body, and the other *detaches* and shed into the wake. Of course the attached part does not consist of the same set of fluid particles; it is a dynamic balance between the continuous creation, diffusion, and downstream advection.[5] Due to the no-slip condition, the attached part is inevitable and sometimes useful; the aerodynamic lift (Chap. 11) is a typical example. The detached part can be very favorable (e.g., additional vortex lift on a slender wing or mixing enhancement in a combustion chamber) or useless and even hazardous, and once detached the vortices can hardly be controled. How to design a body shape such that its motion can create exactly the desired attached or detached vorticity field for one's purpose, and how to further control it under wider working conditions and to minimize its unfavorable effect, have been a major challenge to applied fluid dynamics.

Now, for an observer located at $|\boldsymbol{x}| \gg 1$, the body is very small and only causes a small disturbance to the uniform flow, independent of the Reynolds number based on body size. Consequently, *the Oseen approximation describes the far-field asymptotic behavior of an incompressible viscous flow at any Reynolds number*. The larger the $Re$ is, the narrower is the wake, see Fig. 5.4.1 of Batchelor (1967). This being the case, let us revisit the issue of the far-field vorticity in steady flow over a body. As explained in Sect. 3.2.1, the steadiness may hold at most to a finite downstream distance of the body, and so do various estimates of steady far-field vorticity decaying rate. Further far downstream the flow is inherently unsteady and (3.18) still holds. The following discussions should all be understood in this sense.

It can be shown that (e.g., Serrin (1959), Sect. 77) for any three-dimensional viscous and steady incompressible flow at any Reynolds number, there is

$$|\boldsymbol{\omega}(\boldsymbol{x})| = O(|\boldsymbol{x}|^{-n}) \quad \text{as} \quad |\boldsymbol{x}| \to \infty, \quad n \leq 3.$$

This estimate is quite conservative because it does not take into consideration of the fore-and-aft asymmetry of the vorticity field. The Stokes solution (4.57) just corresponds to the case $n = 2$, but it is not effective for large $|\boldsymbol{x}|$. The Oseen solution (4.65) improves this estimate, indicating that only inside the wake region there is $|\boldsymbol{\omega}| = O(|\boldsymbol{x}|^{-2})$, otherwise it decays exponentially. Then, for a body experiencing only a drag, the velocity behavior in a far wake can also be easily analyzed based on the Oseen approximation (4.61),[6] e.g., Crabtree et al. (1963) and Batchelor (1967). In this far wake the direct effect of the moving body disappears, and the vorticity is diffused laterally; but the pressure has recovered approximately uniform as that outside the wake. Consequently, in the Cartesian coordinate system with $x$ along the freestream direction, one has $u = U + u'$ with $|u'| \ll U$, so the acceleration in the

[5] This vorticity balance for both steady and unsteady separated flows, either laminar or turbulent, will be revisited in Sect. 10.6.3.

[6] The wake associated with lift will be addressed in Chap. 11.

$x$-direction is approximately $U\partial u/\partial x$. Hence, in dimensional form, (4.61) is reduced to a diffusion equation for $u$:

$$U\frac{\partial u}{\partial x} = \nu\left(\frac{\partial^2 u}{\partial y^2} + \frac{\partial^2 u}{\partial z^2}\right). \tag{4.73}$$

It will be seen in Sect. 4.3.1 that (4.73) is a linearized boundary-layer equation. In other words, *the boundary layer theory at large Re may also serve as the far-wake theory at small Re*. Now, under the boundary condition $u \to U$ as $\sqrt{y^2+z^2} \to \infty$, the solution of (4.73) is

$$U - u = \frac{QU}{4\pi\nu x}\exp\left\{-\frac{U(x^2+y^2)}{4\nu x}\right\}, \quad Q = \int_W (U-u)\,\mathrm{d}S, \tag{4.74}$$

where $W$ is a *wake plane* perpendicular to the $x$-axis, which cuts through the wake and extends to arbitrarily large distance in $y, z$ directions. The form of $Q$ suggests that it must be related to the drag of the body, and hence is independent of the $x$ location of $W$. Indeed, since at far downstream the pressure recovers to $p_\infty$ outside the wake, to the leading order (2.74) is reduced to

$$D = \rho U\int_W (U-u)\mathrm{d}S = \rho U Q > 0. \tag{4.75}$$

Thus, in the wake there must be a *velocity deficit*, i.e., $u' = u - U < 0$, which is balanced by an entrainment of fluid into the wake. A more accurate near-wake theory will be introduced in Chap. 11.

### 4.2.4 Regular Perturbation

It is worth digressing from vorticity dynamics to some observation on the perturbation methods for small-*Re* flow. Compared with (4.59), (4.67) does not improve the agreement with experiments, see Fig. 4.14 below. Several higher-order approximations have been obtained with more complicated expansions, but still unable to significantly improve the drag prediction. Van Dyke (1975, p. 234) points out that the basic reason for the very limited success of these efforts lies in the use of singular perturbation method. *Regular perturbations* may lead to agreement with experiments at Reynolds numbers considerably larger than unity.

A significant progress on regular-perturbation solution for flow over sphere has been made by Chen (1975), who seeks the analytical solutions of the successive approximation of the Navier–Stokes equations

$$\boldsymbol{u}_{m-1}\cdot\nabla\boldsymbol{u}_{m-1} + U\frac{\partial \boldsymbol{u}_m}{\partial x} = -\frac{1}{\rho}\nabla p_m + \nu\nabla^2\boldsymbol{u}_m, \quad m = 1, 2, \ldots, \tag{4.76}$$

with $\nabla\cdot\boldsymbol{u}_m = 0$ and $\boldsymbol{u}_0 = \boldsymbol{0}$. Thus, $m = 1$ is the Oseen solution, which is solved by separation of variables. The solutions for $m > 1$ can in principle be

obtained recursively *without* small-$Re$ expansion. After very lengthy algebra, for $m = 2$ Chen obtains a new formula for the drag coefficient of the sphere:

$$C_{\mathrm{D1}} = \frac{12}{Re}\frac{4 - Re^2 - (2+Re)^2\mathrm{e}^{-Re}}{1 - \frac{1}{2}Re^2 - (1+Re)\mathrm{e}^{-Re}}, \tag{4.77}$$

which for $Re \ll 1$ is reduced to

$$C_{\mathrm{D1}} = \frac{12}{Re}\left(1 + \frac{3}{8}Re - \frac{19}{320}Re^2\right) + O(Re^2), \tag{4.78}$$

the same as that obtained by Lamb (1911) up to $O(Re)$ (in bracket) and that by Goldstein (1929) up to $O(Re^2)$, who calculated six terms of a series. Chen (1975) has gone further to $m = 3$ by very tedious algebra (by hand), which predicts

$$C_{\mathrm{D}} = C_{\mathrm{D1}}F(Re) + \frac{41}{160}Re^2\,\mathrm{e}^{-Re}, \tag{4.79a}$$

$$F(Re) = 1 + \frac{3}{40}Re^2\left[5E_i(-2\,Re) - 2E_i(-Re) - \frac{319}{60}\mathrm{e}^{-Re}\right] + \frac{27}{320}Re^3[2E_i(-2Re) + E_i(Re)], \tag{4.79b}$$

where $C_{\mathrm{D1}}$ is given by (4.77) and

$$E_i(-Re) = \int_{\infty}^{Re}\frac{\mathrm{e}^{-r}}{r}\mathrm{d}r, \quad E_i(-2\,Re) = \int_{\infty}^{Re}\frac{\mathrm{e}^{-2r}}{r}\mathrm{d}r.$$

A comparison of this formula with experimental data shows excellent agreement up to $Re \simeq 6$ (or $R_{\mathrm{D}} = 12$), see Fig. 4.13.

For small $Re$, (4.79) is reduced to

$$C_{\mathrm{D}} = \frac{12}{Re}\left\{1 + \frac{3}{8}Re + \frac{9}{40}Re^2\left(\ln\,Re + \gamma + \frac{5}{3}\ln\,2 - \frac{323}{360}\right) + \frac{27}{80}Re^3\,\ln Re + \cdots\right\}, \tag{4.80}$$

where $\gamma = 0.5772...$ is the Euler constant, exactly the same as the prediction of Chester and Breach (1969) by using the matched asymptotic method.

Chen (1983, 1989) has extended his successive approximation to small-$Re$ flow over circular and elliptic cylinders, respectively. The result for the former agrees with experiment up to $Re \simeq 5$, and an extremal case of the latter yields the flat-plate solution.

In addition to the unified effectiveness in the flow domain, regular perturbation also permits using computer to expand a series to very high orders. Van Dyke (1970) extends Gold's (1929) series to $Re^{23}$. A systematic

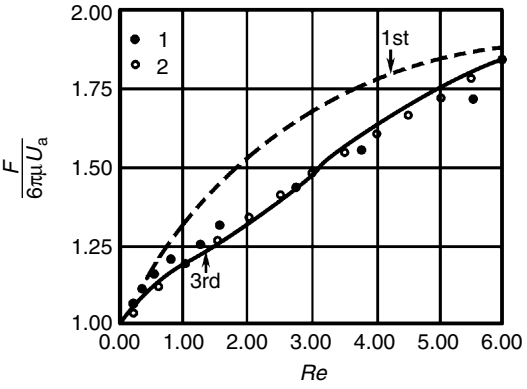


**Fig. 4.13.** Drag coefficient of a sphere derived from (4.76) for $m = 1$ (*dashed line*) and $m = 3$ (*solid line*), compared with the experiments of Maxworthy (1965, dots) and Pruppacher and Steinberger (1968, circles). Reproduced from Chen (1975); also Yan (2002)

"*homotopy analysis method*" (HAM) for obtaining the analytical solutions of a class of nonlinear partial differential equations without small parameter, by computer-aided series expansion, has been developed by Liao (1997, 1999a,b). The basic idea is to cast the original nonlinear problem to an infinite sequence of linear subproblems of which the analytical solutions can be found. Using this method, Liao (2002) has obtained the tenth-order analytical approximation of the Navier–Stokes solution for flow over sphere at small $Re$. The drag curve is shown in Fig. 4.14 for a few choices of an adjustable control parameter $h$, compared with experiments and previous perturbation solutions. The agreement is excellent for $R_{\rm D} = 2\,Re < 30$.

## 4.3 Vorticity Dynamics in Boundary Layers

Opposite to the Stokes and Oseen approximations, at large Reynolds numbers the small parameter becomes $\epsilon = Re^{-1} \ll 1$. The dimensionless incompressible Navier–Stokes equation now reads

$$\frac{\partial \boldsymbol{u}}{\partial t} + \boldsymbol{u} \cdot \nabla \boldsymbol{u} = -\nabla p - \epsilon \nabla \times \boldsymbol{\omega}. \tag{4.81}$$

To the leading order we ignore the viscous force and obtain the Euler equation, just like in the Stokes approximation we ignored the inertial force, so that a large portion of the flow is effectively inviscid. But in regions near boundaries, in particular near a solid wall, the no-slip condition implies that the viscous force must be comparable to the inertial force and strong shearing process must occur.

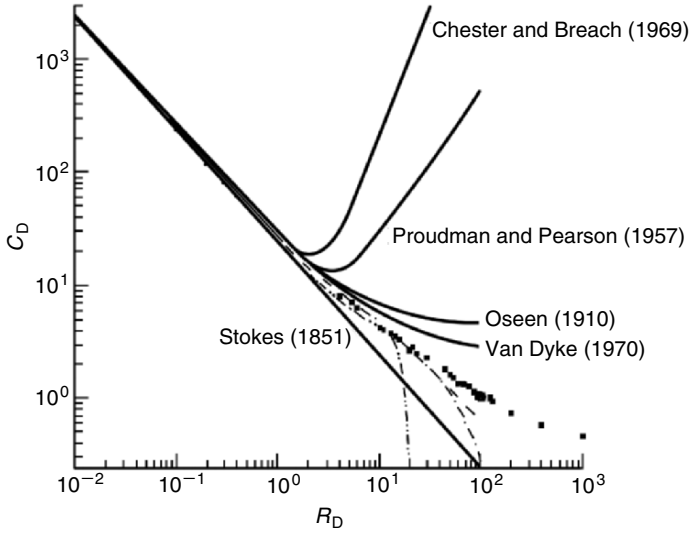


**Fig. 4.14.** Comparison of the tenth-order HAM drag formulas for $h = -1/3$ (*dash-dot-dot line*), $-1/3 \exp(-R_D/30)$ (*dash-dot line*), and $-(1 + R_D/4)^{-1}$ (*dash line*) with previous theoretical results (*solid lines*) and experimental data (*black squares*). $R_D$ is the Reynolds number based on diameter. From Liao (2002)

Effectively inviscid flow can well be vortical and highly unsteady with very complicated patterns as will be exemplified in Sect. 7.4. In this introductory section we consider only the simplest cases in which the flow is *fully attached*, such that a one-to-one correspondence between Euler solution ($\epsilon = 0$) and viscous solution ($\epsilon \ll 1$) exists, and the vorticity is confined in a thin layer adjacent to the wall. Namely, we come to the *boundary layer theory* established by Prandtl (1904) in his seminal paper. As the most successful and typical approximate theory at large Reynolds numbers, the boundary layer theory on a solid wall, both two- and three-dimensional, steady or unsteady, has been well documented in all books on viscous flows (e.g., Schlichting 1978; Rosenhead 1963). Our focus here is the behavior of the vorticity field in a boundary layer, illustrated by a two-dimensional wall boundary layer and the less familiar free-surface boundary layer.

### 4.3.1 Vorticity and Lamb Vector in Solid-Wall Boundary Layer

Consider a two-dimensional steady incompressible flow $\boldsymbol{u}$ over a semiinfinite solid wall located at $y = 0$, $x \geq 0$, where $x$ is the coordinate along the wall and $y$ along the normal. For $y \geq 0$ the dimensionless component form of (4.81) and continuity equation reads

$$u\frac{\partial u}{\partial x}+v\frac{\partial u}{\partial y}=-\frac{\partial p}{\partial x}+\epsilon\left(\frac{\partial^2 u}{\partial x^2}+\frac{\partial^2 u}{\partial y^2}\right), \tag{4.82a}$$

$$u\frac{\partial v}{\partial x}+v\frac{\partial v}{\partial y}=-\frac{\partial p}{\partial y}+\epsilon\left(\frac{\partial^2 v}{\partial x^2}+\frac{\partial^2 v}{\partial y^2}\right), \tag{4.82b}$$

$$\frac{\partial u}{\partial x}+\frac{\partial v}{\partial y}=0. \tag{4.82c}$$

We first briefly review the derivation of boundary-layer equations.

The Euler solution (denoted by suffix $e$) by setting $\epsilon = 0$ is simply a potential flow $\boldsymbol{u}_\mathrm{e}$, having a Bernoulli integral. At $y = 0$ the integral reads

$$p_\mathrm{e}(x)+\frac{1}{2}u_\mathrm{e}^2(x)=p_\infty+\frac{1}{2}q_\infty^2, \tag{4.83}$$

where $u_\mathrm{e}(x)$ is the slip velocity as only an outer solution. Once again we need to match it with an inner solution, which by nature must be viscous and form a smooth transition from $u = 0$ on the wall to $u_\mathrm{e}$ within a thin layer of thickness $O(\delta) = O(\delta(\epsilon)) \ll 1$. Inside the layer the $y$-variation of the flow must be much stronger than its $x$-variation. In order to estimate the order of magnitude of each term in (4.82) so that all retained terms are of $O(1)$, we rescale the inner independent variables as $(X, Y) = (x, y/\delta(\epsilon))$, such that $\lim_{\epsilon\to 0}\delta(\epsilon) = 0$ and $X, Y = O(1)$. Then (4.82c) becomes

$$\frac{\partial u}{\partial X}+\delta^{-1}\frac{\partial v}{\partial Y}=0,$$

which requires rescaling $(U, V) = (u, \delta^{-1}v) = O(1)$. On the other hand, from (4.82a) the balance of inertial and viscous terms requires

$$\delta=\epsilon^{1/2}, \tag{4.84}$$

i.e., the boundary-layer thickness is of $O(Re^{-1/2})$. If the wall curvature radius is much larger than $\delta$, the rescaled boundary-layer equations follow:

$$U\frac{\partial U}{\partial X}+V\frac{\partial U}{\partial Y}=-\frac{\partial p}{\partial X}+\frac{\partial^2 U}{\partial Y^2}+O(\epsilon), \tag{4.85a}$$

$$\frac{\partial p}{\partial Y}=O(\epsilon), \tag{4.85b}$$

$$\frac{\partial U}{\partial X}+\frac{\partial V}{\partial Y}=0. \tag{4.85c}$$

While the continuity equation is exactly satisfied as it always should, the momentum equation is greatly simplified. First, (4.85b) implies $p = p_\mathrm{e}(X)$ across the layer, so that in (4.85a) one can replace $\partial p/\partial X$ by the known $\mathrm{d}p_\mathrm{e}/\mathrm{d}X = -u_\mathrm{e}(x)u_\mathrm{e}'(x)$ at the outer edge of the layer. Second, (4.85a) degenerates from an elliptic equation to a parabolic one, which is the only equation to be solved.

Many exact or approximate solutions of (4.85a) have been investigated. The simplest one has $\boldsymbol{u}_\mathrm{e} = U\boldsymbol{e}_x$ and $\mathrm{d}p_\mathrm{e}/\mathrm{d}X = 0$. As is well known, in terms of similarity variable $\eta = Y/\sqrt{X}, \quad 0 \le \eta < \infty$, this boundary layer can be solved for the stream function $\psi(X, Y) = \sqrt{X} f(\eta)$, which casts (4.85a) to the nonlinear *Blasius equation* for $f$:

$$f''' + \frac{1}{2} f f'' = 0, \tag{4.86a}$$

which should be solved under boundary conditions

$$f(0) = f'(0) = 0, \quad f(\infty) = 1, \tag{4.86b}$$

but there is no closed-form solution. Blasius (1908) presented a series solution

$$f(\eta) = \sum_{k=0}^{\infty} \left(-\frac{1}{2}\right)^k \frac{A_k \sigma^{k+1}}{(3k+2)!} \eta^{3k+2}, \tag{4.87}$$

where $A_0 = A_1 = 1$ and $A_2, \ldots$ can be found recursively; but unfortunately $\sigma \equiv f''(0)$ cannot be determined by the series, which measures the skin friction. Besides, the convergence range of (4.87) is restricted to $\eta < 5.69$. Hence, numerical method has to be used, and the computed velocity and vorticity profiles are shown in Fig. 4.15.

Here again, Liao's homology analysis method (Sect. 4.2.4) has led to an explicit and totally analytic series solution (Liao 1999a,b). What he obtained is a modification of (4.87):

$$f(\eta) = \lim_{m \to \infty} \sum_{k=0}^{m} \left[ \left(-\frac{1}{2}\right)^k \frac{A_k \sigma^{k+1}}{(3k+2)!} \eta^{3k+2} \right] \Phi_{m,k}(h), \tag{4.88}$$

where $h \in (-2, 0)$ is a parameter and $\Phi_{m,k}(h)$ are well-defined power series of $h$. It can be shown that (4.88) converges in the whole $\eta \in [0, \infty)$ when $h \to 0$.

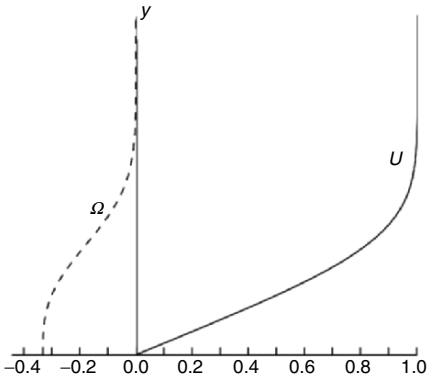


**Fig. 4.15.** Velocity and vorticity in Blasius boundary layer

As a result, Liao used computer-extended series to obtain the approximate analytical solutions up to the 35th order, with averaged error of $1.6 \times 10^{-4}$ compared to the numerical solution. The value of $f''(0) = 0.33206$ was also analytically obtained.

Having reviewed the basis of the boundary-layer theory near a solid wall, we now turn to the vorticity dynamics in such a boundary layer, which is nothing but an *attached vortex layer* (recall the remark of Lighthill (1963) quoted in Sect. 1.2). We start from the vorticity definition $\boldsymbol{\omega} = \nabla \times \boldsymbol{u}$, which now reads

$$\omega = \frac{\partial v}{\partial x} - \frac{\partial u}{\partial y} = \delta \frac{\partial V}{\partial X} - \frac{1}{\delta} \frac{\partial U}{\partial Y} = O(Re^{1/2}). \tag{4.89}$$

To obtain the rescaled vorticity of $O(1)$, we set

$$\Omega = \delta\omega = -\frac{\partial U}{\partial Y} + O(\epsilon), \tag{4.90}$$

so $U$ is simply the $y$-integral of $\Omega$. By (4.85c) and (4.90) as well as the adherence condition, there is

$$U(X,Y) = -\int_0^Y \Omega(X,Y')\,\mathrm{d}Y', \tag{4.91a}$$

$$V(X,Y) = \frac{\partial}{\partial X} \int_0^Y \mathrm{d}Y' \int_0^{Y'} \Omega(X,Y'')\,\mathrm{d}Y'', \tag{4.91b}$$

which is a simplification of the Biot–Savart formula (3.29). Note that according to the asymptotic matching principle

$$\lim_{y\to 0} u_\mathrm{e}(x,y) = \lim_{Y\to\infty} U(X,Y), \quad \epsilon \to 0,$$

there must be

$$u_\mathrm{e}(x) = -\int_0^\infty \Omega\,(X,Y')\,\mathrm{d}Y'. \tag{4.92}$$

By (4.90), the boundary-layer vorticity equation simply follows from the $Y$-derivative of (4.85a) along with using (4.85b,c):

$$U\frac{\partial \Omega}{\partial X} + V\frac{\partial \Omega}{\partial Y} = \frac{\partial^2 \Omega}{\partial Y^2} + O(\epsilon). \tag{4.93}$$

The kinematic boundary condition for solving $\Omega$ is (4.92), which is of integral type as expected. But, applying (4.85a) to the wall yields a local dynamic condition

$$-\frac{\partial \Omega}{\partial Y} = \frac{\partial p_\mathrm{e}}{\partial X} = -u_\mathrm{e}(X)\frac{\partial u_\mathrm{e}(X)}{\partial X} \quad \text{at} \quad Y = 0, \tag{4.94}$$

which is precisely the boundary vorticity flux $\sigma$. Note that the boundary-layer equations are effective only if $x \gg \delta$. This excludes the leading edge of the

wall where there is a singularity. In particular, for the Blasius solution, the boundary vorticity flux is zero for all $x \gg \delta$, implying no new vorticity is produced therefrom. Actually, as the flat plate starts moving at zero tangent pressure gradient, the vorticity in the transient boundary layer is created solely by $\boldsymbol{\sigma}_{\mathrm{a}}$ defined in (4.24a) and illustrated by (4.34). But once the starting process is over and a steady boundary layer is established, *the entire new vorticity in a Blasius boundary layer is exclusively created from the region near the leading edge*, which is continuously advected downstream. Equation (4.94) ensures the acceleration adherence on the wall and can replace (4.92), provided that the no-slip condition is imposed at an upstream point, see Sect. 2.2.4.

Moreover, the boundary enstrophy flux defined by (4.20) and its dissipation rate defined by (4.21) are very strong:

$$\eta = Re^{1/2}\frac{\partial}{\partial Y}\left(\frac{1}{2}\Omega^2\right), \quad \Phi_\omega = Re\left(\frac{\partial \Omega}{\partial Y}\right)^2. \tag{4.95a,b}$$

In contrast, the kinetic-energy dissipation rate is $\Phi \sim \nu\omega^2 = O(1)$.

Owing to the simplified local relation (4.90), solving the boundary-layer flow from (4.93) is operationally redundant. However, the physical purpose of solving the vorticity equation is to separate the shearing process from the momentum balance and focus on it; and this can also be achieved by projecting the momentum equation onto the solenoidal and curl-free spaces without raising the order of equations, see Sect. 2.3.1. Thus, we now consider this projection in the boundary-layer approximation. The special feature is that the decomposition can be made *locally* and *analytically*.[7]

The key quantity to be decomposed is the Lamb vector $\boldsymbol{l} \equiv \boldsymbol{\omega} \times \boldsymbol{u}$. We start from its *kinematic* Helmholtz–Hodge decomposition $\boldsymbol{l} = \boldsymbol{l}_\parallel + \boldsymbol{l}_\perp$, such that

$$\boldsymbol{l}_\parallel = \nabla\phi, \quad \boldsymbol{l}_\perp = \nabla \times \boldsymbol{\psi}, \quad l_{\perp y} = 0 \quad \text{at} \quad y = 0.$$

Since $\boldsymbol{\psi} = \boldsymbol{e}_z\psi$ (here $\psi$ is not the stream function), there is

$$\boldsymbol{l} = \boldsymbol{e}_x\left(\frac{\partial\phi}{\partial x} + \frac{\partial\psi}{\partial y}\right) + \boldsymbol{e}_y\left(\frac{\partial\phi}{\partial y} - \frac{\partial\psi}{\partial x}\right) = -\boldsymbol{e}_x\omega v + \boldsymbol{e}_y\omega u,$$

which in boundary-layer scales gives, by (4.90),

$$l_x = \frac{\partial\phi}{\partial X} + \frac{1}{\delta}\frac{\partial\psi}{\partial Y} = V\frac{\partial U}{\partial Y} + O(\delta^2),$$
$$l_y = \frac{1}{\delta}\frac{\partial\phi}{\partial Y} - \frac{\partial\psi}{\partial X} = -\frac{1}{\delta}U\frac{\partial U}{\partial Y} + O(\delta).$$

[7] This was first observed by S. Malhotra (1997, private communication). Any flows with scale separation along different directions, not necessarily boundary layers, can be similarly decomposed locally. Examples include free vortex layers and thin vortex filaments at large Reynolds numbers.

Thus, the term balance requires rescaling $\psi = \delta\Psi$ and $(l_x, l_y) = (L_X, \delta^{-1}L_Y)$, such that

$$L_X = \frac{\partial\phi}{\partial X} + \frac{\partial\Psi}{\partial Y} = V\frac{\partial U}{\partial Y} + O(\delta^2), \tag{4.96a}$$

$$L_Y = \frac{\partial\phi}{\partial Y} = -U\frac{\partial U}{\partial Y} + O(\delta^2). \tag{4.96b}$$

From (4.96b) we obtain

$$\phi = -\frac{1}{2}U^2 + C(X) + O(\delta^2);$$

hence

$$L_{\|X} = \frac{\partial\phi}{\partial X} = -U\frac{\partial U}{\partial X} + C'(X) + O(\delta^2), \tag{4.97}$$

and $L_{\|Y} = O(\delta^2)$. Since $\boldsymbol{L} = \boldsymbol{0}$ at the outer edge of the boundary layer, in (4.97) there must be $C'(X) = u_\mathrm{e}(X)u'_\mathrm{e}(X)$. Then, subtracting (4.97) from (4.96a) yields

$$L_{\perp X} = U\frac{\partial U}{\partial X} + V\frac{\partial U}{\partial Y} + \frac{\partial p_\mathrm{e}}{\partial X} + O(\delta^2) \tag{4.98}$$

and $L_{\perp Y} = O(\delta^2)$, indicating that $\boldsymbol{L}_\perp$ is indeed parallel to the wall.

We now introduce *dynamics*. Splitting the steady version of (4.81) into transverse and longitudinal parts gives

$$\boldsymbol{l}_\perp = \epsilon\nabla^2\boldsymbol{u}, \quad \boldsymbol{l}_\| = -\nabla\left(p_\infty + \frac{1}{2}q_\infty^2\right), \tag{4.99}$$

which is already a Helmholtz–Hodge decomposition for the Blasius boundary layer with $\sigma = 0$. After rescaling, (4.99) reads

$$L_{\perp X} = \frac{\partial^2 U}{\partial Y^2} + O(\delta^2), \tag{4.100a}$$

$$L_{\|X} = -\frac{\partial}{\partial X}\left(\frac{1}{2}U^2 + p_\mathrm{e}\right) + O(\delta^2). \tag{4.100b}$$

Therefore, equating (4.98) and (4.100a) recovers (4.85a), while equating (4.97) and (4.100b) recovers the Bernoulli integral (4.83) outside the layer. Note that although generically $\boldsymbol{L} = \boldsymbol{0}$ at $Y = 0$, this is not so for $\boldsymbol{L}_\perp$ and $\boldsymbol{L}_\|$ unless $\sigma = 0$. Indeed, (4.100a) indicates that

$$L_{\perp X} = -\frac{\partial\Omega}{\partial Y} \quad \text{or} \quad \boldsymbol{e}_y \times \boldsymbol{l}_\perp = -\boldsymbol{e}_z\epsilon\frac{\partial\omega}{\partial y} \quad \text{at} \quad Y = 0, \tag{4.101}$$

which is the boundary vorticity flux.

The preceding analysis shows that *the boundary layer equation is already only the transverse part of the momentum balance, and the longitudinal part degenerates to the Bernoulli integral outside the layer.* In other words, opposite to the close viscous boundary coupling between the shearing and compressing processes at small $Re$, the two processes are approximately *decoupled* for attached flow at large $Re$.

### 4.3.2 Vorticity Dynamics in Free-Surface Boundary Layer

If on an air–water interface the effect of the air motion on the water is negligible but only imposes a constant pressure on the surface, one obtains a *free surface*.[8] The free-surface motion has long been studied within the potential flow theory, in which one imposes the kinematic boundary condition (2.66) and normal dynamic condition (2.68a). The prediction of potential theory agrees well with experiment for long waves (e.g., Stoker (1958); Wehausen and Laitone (1960)). However, a free surface also has a boundary layer in which the flow is rotational and the shearing process is active; the difference from solid-wall boundary layer is that the former is strong only for short waves. In this case the water viscosity has to be retained and the Reynolds number is again very large. Our interest is the special physical features of the vorticity in a free-surface boundary layer and where they come from.

Let $S$ be a free surface. We use a reference velocity $U^*$ (say, a mean velocity of $S$) and a characteristic wave length $L$ to nondimensionalize the equations, in which three parameters are involved: the Reynolds number $Re$, the *Weber number* $We$, and the *Froude number* $Fr$:

$$We = \frac{T}{\rho U^{*2} L}, \quad Fr^{-1} \equiv g^* = \frac{gL}{U^{*2}}, \tag{4.102}$$

which measure the relative importance of surface tensor $T$ (assumed a constant) and gravitational force compared to the inertial force, respectively. We first show that on a curved $S$ there must be a distributed vorticity. This is a direct result of the stress continuity condition (2.68) and the triple decomposition (2.147) on $S$. In dimensionless form, this gives

$$p + We\kappa + \boldsymbol{n} \cdot \boldsymbol{t}_{\mathrm{s}} = 0, \quad \boldsymbol{n} \times (\epsilon \boldsymbol{\omega} \times \boldsymbol{n} + \boldsymbol{t}_{\mathrm{s}}) = \boldsymbol{0}, \tag{4.103a,b}$$

where $\kappa = -\nabla_\pi \cdot \boldsymbol{n}$ is twice of the mean curvature of $S$, and $\boldsymbol{t}_{\mathrm{s}}$ the surface-deformation stress. The suffix $\pi$ denotes tangent components, and the constant air pressure has been set zero. Let $\boldsymbol{U} = \boldsymbol{U}_\pi + \boldsymbol{n} U_{\mathrm{n}}$ be the velocity of $S$ and use (2.150), (2.151), and (2.137), from (4.103a,b) it follows that (Wu 1995; Longuet-Higgins 1998)

$$p = -We\kappa - 2\epsilon \nabla_\pi \cdot \boldsymbol{U}, \tag{4.104a}$$

$$\boldsymbol{\omega}_\pi = -2\boldsymbol{n} \times (\nabla_\pi U_{\mathrm{n}} + \boldsymbol{U} \cdot \mathbf{K}). \tag{4.104b}$$

These are the primary dynamic boundary conditions for a viscous free-surface problem, which is a typical situation where *all three processes in (2.147) enter into the play and are coupled*. Along the normal direction the water pressure

[8] This does not mean that the air motion itself is weak. From the tangent-stress continuity (Sect. 4.5) on a flat air–water interface with uniform velocity, one may find that the vorticity in the air is 56 times stronger than that in the water. But this does not conflict the neglect of its influence on water motion.

$p$ is balanced by the surface mean curvature through the surface tension, plus a very weak correction due to the viscous resistance to the change of surface area. In contrast, the change of surface shape (and hence the change of $\boldsymbol{n}$) is solely balanced by a tangent boundary vorticity, which is twice of the angular velocity of $\boldsymbol{n}$. It should be stressed that although (4.104b) does not contain viscosity, it holds for viscous flow only. The normal vorticity, if any, remains continuous due to no-slip, and is not involved in the stress continuity condition.

In two dimensions with $\boldsymbol{U} = (U_\mathrm{s}, U_\mathrm{n})$ (4.104b) is reduced to

$$\omega = 2\left(\frac{\partial U_\mathrm{n}}{\partial s} + U_\mathrm{s}\kappa\right). \tag{4.105}$$

If in addition $S$ is stationary, there must be $U_\mathrm{n} = 0$; so one simply has

$$\omega = 2U\kappa, \tag{4.106}$$

found by Longuet-Higgins (1953).

It is now clear that as long as $S$ is curved and in motion, adjacent to it there must be a boundary layer. If $\boldsymbol{U}$ and $\kappa$ are both of $O(1)$ then so is $\boldsymbol{\omega}_\pi$, weaker than the vorticity in wall boundary layer by a factor of $O(\epsilon^{1/2})$. Moreover, unlike the solid boundary $\partial B$ where the boundary vorticity can be known only after the boundary-layer equation is solved, now $\boldsymbol{\omega}_\pi$ is completely determined by the surface shape and motion, which to the leading order can be obtained by inviscid theory.[9] These differences from a solid-wall boundary layer are due to the arbitrary-deformation ability of free surface, which makes it possible to achieve a dynamic balance on $S$ mainly within inviscid and irrotational interactions. This key character can be further observed from the free-surface boundary layer equation, as derived in the follows.

In the incompressible version of the Navier–Stokes equation (2.134), the effect of gravity can be absorbed to a modified pressure or enthalpy $\tilde{h} = p + g^* z$, so

$$\boldsymbol{a} = -\nabla\tilde{h} - \epsilon\nabla\times\boldsymbol{\omega}, \quad \nabla\cdot\boldsymbol{u} = 0. \tag{4.107}$$

As we did for solid-wall boundary layer, the outer solution is inviscid, of which the quantities are denoted by suffix 0. We have seen that $\boldsymbol{\omega}_\pi$ is a viscous product but $\omega_n$ is not. Thus in general we allow the inviscid outer solution has a normal vorticity $\omega_{0\mathrm{n}}$, which happens, e.g., when a strong vertical vortex appears in the sea. Now, set

$$\begin{aligned} \boldsymbol{U} &= \boldsymbol{U}_0 + \boldsymbol{u}' = \boldsymbol{U}_0 + \nabla\times\boldsymbol{A}, \\ \nabla\cdot\boldsymbol{A} &= 0, \quad \boldsymbol{\omega}' = \nabla\times\boldsymbol{u}' = -\nabla^2\boldsymbol{A}, \\ \tilde{h} &= \tilde{h}_0 + h_\mathrm{e} \end{aligned} \tag{4.108}$$

where $h_\mathrm{e}$ is an excess enthalpy. Then the inviscid and irrotational solution $\boldsymbol{u}_0$ is *self-balanced* on $S$:

[9] The boundary vorticity flux on $S$ is still the measure of vorticity creation rate.

$$\frac{\mathrm{D}_0 \boldsymbol{U}_0}{\mathrm{D}t} = -\nabla \tilde{h}_0, \quad \tilde{h}_0 = -W\kappa + g^* z \quad \text{on} \quad S, \tag{4.109}$$

where $\mathrm{D}_0/\mathrm{D}t = \partial/\partial t + \boldsymbol{U}_0 \cdot \nabla$. It is in this self-balance of inviscid solution on $S$ where lies the very root of the difference between a free-surface boundary layer and its solid-wall counterpart. It explains why the former is weak, and indicates that the viscous perturbation is *regular*, being only a correction to the inviscid solution.

The governing equation for a three-dimensional free-surface boundary layer, in terms of the vector potential $\boldsymbol{A}$, was derived by Lundgren (1989). Denote $\delta = \epsilon^{1/2}$ as the boundary layer thickness. When $\kappa \ll \delta^{-1}$, an order-of-magnitude analysis shows that

$$\begin{aligned} \boldsymbol{u}'_\pi &= O(\delta), \quad u'_\mathrm{n} = O(\delta^2), \\ \boldsymbol{A}_\pi &= O(\delta^2), \quad A_\mathrm{n} = O(\delta^3), \\ \boldsymbol{\omega}'_\pi &= O(1), \quad \omega'_\mathrm{n} = O(\delta). \end{aligned}$$

Then it is easily shown that the boundary-layer equation can be linearized, yielding

$$\frac{\mathrm{D}_0 \boldsymbol{A}}{\mathrm{D}t} - \boldsymbol{A}_\pi \cdot \nabla_\pi \boldsymbol{U}_0 - 2\boldsymbol{A}_\pi \nabla_\pi \cdot \boldsymbol{U}_0 + \omega_{0\mathrm{n}} \boldsymbol{n} \times \boldsymbol{A} = \epsilon \frac{\partial^2 \boldsymbol{A}_\pi}{\partial n^2} + O(\delta^3). \tag{4.110}$$

This is a homogeneous equation and has nontrivial solution only if there exists a forcing mechanism provided by the free-surface condition following from (4.104b):

$$\frac{\partial^2 \boldsymbol{A}_\pi}{\partial n^2} = -\boldsymbol{\omega}'_\pi = 2\boldsymbol{n} \times (\nabla_\pi U_{0\mathrm{n}} + \boldsymbol{U}_{0\pi} \cdot \mathbf{K}_0) + O(\delta) \quad \text{on} \quad S, \tag{4.111}$$

where we recall that the right-hand side comes from $\boldsymbol{n} \times \boldsymbol{t}_\mathrm{s}$. Therefore, *the free-surface boundary layer is driven by the leading-order surface-deformation stress*.

Moreover, the excess enthalpy $h_\mathrm{e}$ is found to be

$$h_\mathrm{e} = -\boldsymbol{\omega}'_\pi \cdot \boldsymbol{A}_\pi + O(\delta^3) \quad \text{on} \quad S,$$

which is only an $O(\epsilon)$ correction to the surface shape. Finally, up to $O(\delta)$, the boundary vorticity flux is given by

$$\boldsymbol{\sigma}_\pi = \boldsymbol{n} \times \left( \frac{\mathrm{D}_0 \boldsymbol{u}'}{\mathrm{D}t} + \boldsymbol{u}'_\pi \cdot \nabla_\pi \boldsymbol{U}_0 \right) + O(\epsilon), \tag{4.112}$$

indicating that the leading-order source of vorticity on a free-surface is the *viscous correction of the surface acceleration*.

A simple example of free-surface boundary layer is viscous two-dimensional linear water wave sketched in Fig. 4.16. The problem was solved by Lamb (1932, Sect. 349) for a freely decaying wave, to which we impose an applied

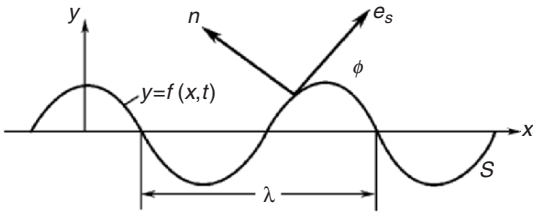


**Fig. 4.16.** A water wave

stress to maintain a constant amplitude. Lundgren (1989) has shown that this solution satisfies (4.111) and extended it to three-dimensional flow.

Assume the free-surface elevation is

$$y = f(x,t) = a\cos(kx - \gamma t), \quad \gamma^2 = gk + T'k^3, \quad ak = \frac{2\pi a}{\lambda} \ll 1,$$

where $T' = T/\rho$. The Cartesian components of the potential velocity are

$$u = a\gamma\, \mathrm{e}^{ky}\cos(kx - \gamma t), \quad v = a\gamma\, \mathrm{e}^{ky}\sin(kx - \gamma t), \quad y \le 0.$$

In this problem (4.111) is reduced to a linear equation for the scalar stream function, and the inviscid potential flow satisfies the Bernoulli equation. The resulting linearized vorticity solution is

$$\omega \simeq 2ak\gamma\, \mathrm{e}^{\beta y}\, \cos\{kx - (\gamma t + \beta y)\} = O(k), \tag{4.113}$$

where $\beta \equiv (\gamma/2\nu)^{1/2}$. The boundary vorticity flux and enstrophy flux are

$$\sigma \simeq \nu \frac{\partial \omega}{\partial y}\bigg|_{y=0} = 2ak\nu^{1/2}\gamma^{3/2}\, \sin\left(kx - \gamma t + \frac{\pi}{4}\right) = O(k\nu^{1/2}), \tag{4.114}$$

$$\eta \simeq a^2k^2\nu^{1/2}\gamma^{5/2}\left\{\sqrt{2} + 2\sin\left[2(kx - \gamma t) + \frac{\pi}{4}\right]\right\} = O(k^2\nu^{1/2}). \tag{4.115}$$

Like (4.50), $\eta$ has a nonzero positive average, showing that *the overall enstrophy in a forced water wave is increasing.*

If the wavelength is small or $k$ is large, the Froude number will be large, so by (4.113) there will be a nonnegligible vorticity in a thin boundary layer. The gravity-capillary wave belongs to this case, of which the vortical structures have been observed by many experimental and numerical studies (e.g., Lin and Rockwell 1995; Dommermuth and Mui 1995). Figure 4.17 shows a direct numerical simulation (DNS) of the surface vorticity $\omega$ on a two-dimensional unsteady near-breaking gravity capillary wave. The Reynolds number based on wavelength (5 cm) is of $O(10^4)$. The figure also shows the error of the DNS result compared with the prediction of (4.105). It is remarkable that, although in general on a free surface $\boldsymbol{\omega}_\pi = O(1)$, in gravity-capillary waves its peak value can be as large as $O(Re^{1/2})$, like the solid-wall case but confined to very

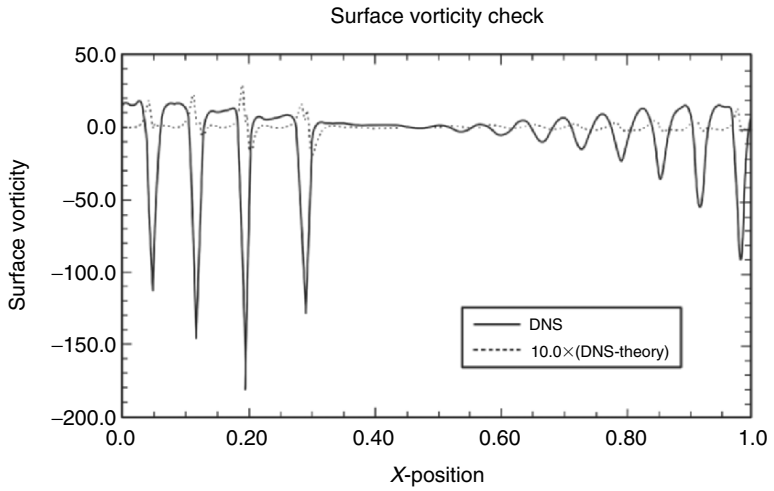


**Fig. 4.17.** Instantaneous surface vorticity for a two-dimensional unsteady near-breaking gravity-capillary wave, computed by DNS with a grid of $16,384 \times 4,097$ along the length and depth of the wave. The dotted line is 10 times the difference of the DNS result and (4.105). From Dommermuth and Mui (1995)

narrow regions of troughs. This is a sign that the traditional potential wave theory is insufficient for capturing the detailed structure of stiff short waves, since the created strong vorticity must reversely affect the surface motion.

Note that in the example of Fig. 4.17 the boundary-layer thickness is about 1 mm, but the required grid is extremely dense. Provided no boundary-layer separation occurs, such a thin layer can well be approximated by a vortex sheet, see Sect. 4.4. The distributed vorticity in the interior of the fluid and the free vortex sheet representing the free surface may coexist in the same theory. In this case a general result is worth noticing: the total vorticity is conserved if the vorticity contained in the sheet is included (Lundgren and Koumoutsakos 1999). Namely, there is

$$\int_V \boldsymbol{\omega}\,\mathrm{d}V + \int_S \boldsymbol{\gamma}\,\mathrm{d}S = \mathbf{0} \quad \text{for} \quad n = 3, \tag{4.116a}$$

$$\frac{\mathrm{d}}{\mathrm{d}t}\int_V \omega\,\mathrm{d}V + \frac{\mathrm{d}}{\mathrm{d}t}\int_S \gamma\,\mathrm{d}S = 0 \quad \text{for} \quad n = 2, \tag{4.116b}$$

which are the extension of (3.15) and (3.16), respectively. Therefore, if some vorticity moves out of $V$ and appears to be lost, then it is really gained by the vortex sheet.

## 4.4 Vortex Sheet Dynamics

We now proceed from the boundary-layer approximation at $Re \gg 1$ to the asymptotic state of a viscous fluid as $Re \to \infty$, which was called the Euler

limit of viscous flow in Sect. 2.2.5.[10] Due to (4.84), in this asymptotic state a wall boundary layer becomes an attached vortex sheet, while on an interface there is an interfacial vortex sheet. When the attached vortex sheet leaves the body which generates it, the wake is also sheet-like. The vorticity is confined in the sheets as a Dirac delta function. This state exists even if after taking $Re \to \infty$ the limit $t \to \infty$ is then taken. Being the asymptotic theory of shearing process, the *vortex sheet dynamics* has an important place in vorticity and vortex dynamics.

If the order of the earlier double-limit procedure is reversed, however, the situation can be different. At a large but finite $Re$, a closed flow bounded by thin vortex layers will be fulfilled by the vorticity via diffusion as $t \to \infty$, and then taking $Re \to \infty$ only makes the distributed vorticity obey a simpler law, see Sect. 7.2. Similarly, a thin vortex layer may roll many turns to form a tight spiral (Sect. 4.4.3), in which the diffusion will eventually smear out the layer structure so that the spiral becomes a concentrated vortex with disturbuted vorticity in its core (Chap. 6–8).

### 4.4.1 Basic Properties

We start from the basic jump conditions (2.81a) and (2.81b) and allow $[\![\rho]\!] \neq 0$ as in density-stratified or interface flow for generality. As said in the context of (2.81), to distinguish a vortex sheet $S$ from a shock we require the mass flux across $S$ be zero. Thus

$$\boldsymbol{n} \cdot [\![\boldsymbol{u}]\!] = 0, \quad [\![\boldsymbol{u}]\!] = \boldsymbol{u}_1 - \boldsymbol{u}_2, \tag{4.117}$$

i.e., $[\![\boldsymbol{u}]\!]$ must be along a tangent direction. We use the convention that the unit normal vector $\boldsymbol{n}$ is pointing from side 2 to side 1 of $S$. Then the sheet strength $\boldsymbol{\gamma}$ and velocity jump $[\![\boldsymbol{u}]\!]$ are related by (Fig. 4.18)

$$\boldsymbol{\gamma} = \boldsymbol{n} \times [\![\boldsymbol{u}]\!], \quad [\![\boldsymbol{u}]\!] = \boldsymbol{\gamma} \times \boldsymbol{n}. \tag{4.118a,b}$$

Let $\boldsymbol{u}_\gamma(\boldsymbol{x}, t)$ be the velocity of the vortex sheet itself. Since $[\![\boldsymbol{u}_\gamma]\!] = \boldsymbol{0}$, (4.117) can be rewritten

$$[\![u_\mathrm{n} - u_{\gamma\mathrm{n}}]\!] = 0. \tag{4.119}$$

We now impose the mass conservation condition (2.81a) and momentum balance (2.81b). By identity (2.82a) and using (4.119), it follows that

$$[\![\rho]\!](\overline{u}_\mathrm{n} - u_{\gamma\mathrm{n}}) = 0, \tag{4.120}$$

$$[\![\rho\boldsymbol{u}]\!](\overline{u}_\mathrm{n} - u_{\gamma\mathrm{n}}) = -[\![p]\!]\boldsymbol{n}, \tag{4.121}$$

[10] As stressed there, this asymptotic state should not be identified as an ideal fluid flow governed by the Euler equation and permitting slip velocity at boundaries. But, except within very thin sheets the flow is irrotational and indeed satisfies the Euler equation.

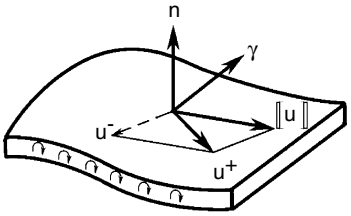


**Fig. 4.18.** A vortex sheet

where the overline denotes averaged value. Therefore, if $[\![\rho]\!] = 0$ so that $[\![\rho \boldsymbol{u}]\!] = \rho[\![\boldsymbol{u}]\!]$, the left-hand side of (4.121) will have vanishing normal component and hence so must the right-hand side, implying

$$[\![p]\!] = 0, \tag{4.122}$$

i.e., *unless there is a surface tension, a free vortex sheet cannot stand any pressure jump*. Then (4.121) yields

$$\boldsymbol{u}_\gamma \cdot \boldsymbol{n} = \frac{1}{2}(\boldsymbol{u}_1 + \boldsymbol{u}_2) \cdot \boldsymbol{n} = \bar{\boldsymbol{u}} \cdot \boldsymbol{n}. \tag{4.123}$$

Alternatively, if $[\![\rho]\!] \neq 0$ but the surface tension is zero (this happens if the flow is density-stratified but the stratification is concentrated in a thin layer that can be approximated by a singular surface), from (4.120) we still obtain (4.123), which by (4.121) implies (4.122). Hence, the two basic features of a vortex sheet, (4.122) and (4.123), are quite general.

There remains the determination of the tangent velocity of the sheet, which is meaningful only when the sheet is a material surface as we identified in Sect. 2.2.5. Denote $\boldsymbol{v} = \boldsymbol{u}_\gamma - \overline{\boldsymbol{u}}$ such that by (4.123) $\boldsymbol{v}$ is a tangent vector. Wu (1995) has proved that if and only if $\omega_\mathrm{n} \equiv 0$ all over the sheet then $\boldsymbol{v} = \boldsymbol{0}$, so we simply have

$$\boldsymbol{u}_\gamma = \bar{\boldsymbol{u}} \quad \text{if} \quad \omega_\mathrm{n} = 0. \tag{4.124}$$

This result applies to any two-dimensional vortex sheet. But more generally $\boldsymbol{v}$ satisfies a tangential vector equation:

$$\boldsymbol{n} \times \nabla(\boldsymbol{v} \cdot [\![\boldsymbol{u}]\!]) = \omega_\mathrm{n}[\![\boldsymbol{u}]\!], \tag{4.125}$$

which can be solved for the two components of $\boldsymbol{v}$ along the directions of $\boldsymbol{\gamma}$ and $[\![\boldsymbol{u}]\!]$. This may happen in some three-dimensional flows.

Suppose now $S$ is an interface of two different fluids with surface tension $T$ or a very thin solid surface (e.g., a thin wing with negligible thickness known as *lifting surface*) with velocity $\boldsymbol{u}_\mathrm{s}$, and on each side of $S$ there is an attached vortex sheet of strengths $\boldsymbol{\gamma}_1$ and $\boldsymbol{\gamma}_2$, forming a sandwich structure. Then

$$\boldsymbol{\gamma}_1 = \boldsymbol{n} \times (\boldsymbol{u}_1 - \boldsymbol{u}_\mathrm{s}), \quad \boldsymbol{\gamma}_2 = \boldsymbol{n} \times (\boldsymbol{u}_\mathrm{s} - \boldsymbol{u}_2). \tag{4.126}$$

This sandwich structure is often modeled by a single *net* vortex sheet *inside* $S$ with strength $\boldsymbol{\gamma} = \boldsymbol{\gamma}_1 + \boldsymbol{\gamma}_2$. If $S$ is a lifting surface, the net vortex sheet is conventionally called a *bound vortex sheet*. We use the same name for the net vortex sheet in an interface. In both cases a bound vortex sheet is no longer free, because across it there can be a pressure jump $[\![p]\!]$, which is either balanced by $T$ on an interface or provides a normal force to a lifting surface. Note that a bound vortex sheet by no means simply sticks to $S$; rather, as the net effect of $\boldsymbol{\gamma}_1$ and $\boldsymbol{\gamma}_2$ it is continuously produced from $S$ to update itself and advected downstream, becoming a free vortex sheet. Therefore, a bound vortex sheet also has a velocity $\boldsymbol{u}_\gamma$. But since now (4.122) is invalid, so is (4.123); thus, this $\boldsymbol{u}_\gamma$ has to be *defined*. When $\omega_\mathrm{n} = 0$, a consistent choice is to still set $\boldsymbol{u}_\gamma = \bar{\boldsymbol{u}}$. Note that by (4.118a) there is

$$\boldsymbol{u}_\mathrm{s} - \bar{\boldsymbol{u}} = \frac{1}{2}\boldsymbol{n} \times (\boldsymbol{\gamma}_1 - \boldsymbol{\gamma}_2), \tag{4.127}$$

indicating that generically a bound sheet does not move with $S$.

In the rest of this subsection we assume the flow is incompressible and away from vortex sheets the flow is irrotational with velocity potential $\phi(\boldsymbol{x}, t)$. Let $P$ be a point on $S$, and take a curve $C$ to connect $P^+$ and $P^-$. If the sheet has an edge, the curve can be made go across $S$ only once, see Fig. 4.19. Then the circulation along $C$ is

$$\oint_C \nabla\phi \cdot \mathrm{d}\boldsymbol{x} = \oint_C \mathrm{d}\phi = [\![\phi_P]\!] \equiv \mathit{\Gamma}. \tag{4.128}$$

Unlike the circulation along a generic loop, now this $\mathit{\Gamma}$ is a *point function* independent of the shape of $C$ so that we can consider $\mathrm{D}\mathit{\Gamma}/\mathrm{D}t$. This $[\![\phi]\!]$ or $\mathit{\Gamma}$ is nothing but the strength of *doublet* or *dipole* distributed on $S$. Then by (4.118b) there is

$$\boldsymbol{\gamma} = \boldsymbol{n} \times \nabla_\pi [\![\phi]\!] = \boldsymbol{n} \times \nabla_\pi \mathit{\Gamma}, \quad \nabla_\pi \mathit{\Gamma} = \boldsymbol{\gamma} \times \boldsymbol{n}. \tag{4.129a,b}$$

Moreover, we define the *vortex-sheet Lamb vector*

$$\boldsymbol{l}_\gamma \equiv \boldsymbol{\gamma} \times \bar{\boldsymbol{u}}. \tag{4.130}$$

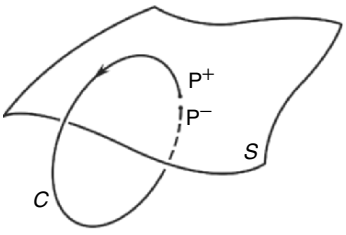


**Fig. 4.19.** A loop across the vortex sheet once

Set $\bar{\boldsymbol{u}} = \bar{\boldsymbol{u}}_\pi + \overline{u}_\mathrm{n}\boldsymbol{n}$, by (4.129) and noticing that $\nabla\Gamma = \nabla_\pi\Gamma$ since $\partial\Gamma/\partial n = [\![u_\mathrm{n}]\!] = 0$, it follows that

$$\boldsymbol{n}(\boldsymbol{l}_\gamma \cdot \boldsymbol{n}) = \boldsymbol{\gamma} \times \bar{\boldsymbol{u}}_\pi = -\boldsymbol{n}(\bar{\boldsymbol{u}}_\pi \cdot \nabla\Gamma), \tag{4.131a}$$

$$\boldsymbol{n} \times (\boldsymbol{l}_\gamma \times \boldsymbol{n}) = \boldsymbol{\gamma} \times \overline{u}_\mathrm{n}\boldsymbol{n} = \overline{u}_\mathrm{n}\nabla_\pi\Gamma. \tag{4.131b}$$

Thus, the normal and tangent components of $\boldsymbol{l}_\gamma$ are from the tangent and normal components of $\bar{\boldsymbol{u}}$, respectively.

Now, we further assume that the potential flows at both sides of a vortex sheet come from the same upstream flow.[11]. Then, applying the Bernoulli equation (2.177) to both sides of a bound or free vortex sheet and taking the jump, one has

$$\rho\left(\frac{\partial\Gamma}{\partial t} + \frac{1}{2}[\![q^2]\!]\right) = \begin{cases} -[\![p]\!] & \text{for bound sheet,} \\ 0 & \text{for free sheet,} \end{cases} \tag{4.132a}$$

where

$$\begin{aligned} \frac{1}{2}[\![q^2]\!] &= \frac{1}{2}(\boldsymbol{u}^+ + \boldsymbol{u}^-) \cdot (\boldsymbol{u}^+ - \boldsymbol{u}^-) = \bar{\boldsymbol{u}} \cdot [\![\boldsymbol{u}]\!] \\ &= \bar{\boldsymbol{u}} \cdot \nabla_\pi\Gamma = -\boldsymbol{n} \cdot (\boldsymbol{\gamma} \times \bar{\boldsymbol{u}}_\pi) \end{aligned} \tag{4.132b}$$

due to (4.131a). Therefore, one finds

$$\rho\left[\frac{\partial\Gamma}{\partial t} - \boldsymbol{n} \cdot (\boldsymbol{\gamma} \times \bar{\boldsymbol{u}}_\pi)\right] = \rho\frac{\mathrm{D}\Gamma}{\mathrm{D}t} = \begin{cases} -[\![p]\!] & \text{for bound sheet,} \\ 0 & \text{for free sheet.} \end{cases} \tag{4.133}$$

This equation contains rich information. First, for free vortex sheet it confirms that $\Gamma = [\![\phi]\!]$ is Lagrangian invariant as asserted by Kelvin's circulation theorem. Second, if the flow is steady, then there must be $\overline{u}_\mathrm{n} = 0$ and hence $\boldsymbol{l}_\gamma$ can only has normal component; but (4.133) implies that if the sheet is free this component must vanish. Therefore, *the Lamb vector of a steady free vortex sheet must vanish, or* $\boldsymbol{\gamma}$ *and* $\bar{\boldsymbol{u}}$ *must be aligned* (cf. Lighthill 1986b, p. 204). In contrast, when the flow is unsteady, by (4.131a) and (4.133) one has

$$\boldsymbol{\gamma} \times \bar{\boldsymbol{u}}_\pi = \boldsymbol{n}\frac{\partial\Gamma}{\partial t}. \tag{4.134}$$

Thirdly, since dynamics enters (4.133) via the Bernoulli equation, a close relation between the pressure jump across a thin wing and the behavior of bound and free vortex sheet is established. This is the very basis of the lifting-surface theory in classic aerodynamics, see Chap. 11.

Before closing this subsection, let us consider some vorticity integrals over the entire sheet $S$. In this case using (4.129) to express $\boldsymbol{\gamma}$ by $\boldsymbol{n} \times \nabla\Gamma$ is convenient as it permits useful transformations by the Stokes theorem. The simplest example is

[11] Thus, the vortex sheets considered here cannot be a free surface or the boundary of a closed separated bubble. For the latter case see Sect. 7.2

$$\int_S \boldsymbol{\gamma}\,\mathrm{d}S = \int_S \boldsymbol{n}\times\nabla\Gamma\,\mathrm{d}S = \oint_{\partial S}\Gamma\,\mathrm{d}\boldsymbol{x} = \boldsymbol{0} \tag{4.135}$$

because $\Gamma$ must vanish at the sheet boundary. In three dimensions (4.135) is a simplified version of the Föppl vorticity conservation theorem, indicating that the vector field $\boldsymbol{\gamma}$ must form closed loops on $S$.

Next, the integrals of the vector moments of $\boldsymbol{\gamma}$ are the vortical impulse and angular impulse of a vortex sheet, which by (3.78) and (3.79) read

$$\boldsymbol{I} = \frac{1}{n-1}\int_S \boldsymbol{x}\times(\boldsymbol{n}\times\nabla\Gamma)\mathrm{d}S, \quad \boldsymbol{L} = -\frac{1}{2}\int_S x^2\boldsymbol{n}\times\nabla\Gamma\,\mathrm{d}S.$$

An integration by parts, see formulas in Sect. A.2, casts each of these integrals to a boundary integral plus a surface integral. The former vanishes since $\Gamma = 0$ along $\partial S$; so we have a pair of neat formulas

$$\boldsymbol{I} = -\int_S \Gamma\boldsymbol{n}\,\mathrm{d}S = -\int_S [\![\phi]\!]\boldsymbol{n}\,\mathrm{d}S, \tag{4.136}$$

$$\boldsymbol{L} = -\int_S \Gamma\boldsymbol{x}\times\boldsymbol{n}\,\mathrm{d}S = -\int_S [\![\phi]\!]\boldsymbol{x}\times\boldsymbol{n}\,\mathrm{d}S, \tag{4.137}$$

which by (2.177) and (2.178) are precisely the jumps of potential impulse and angular impulse, respectively (the sign depends on the definition of the direction of $\boldsymbol{n}$).

The rate of change of $\boldsymbol{I}$ is

$$\frac{\mathrm{d}\boldsymbol{I}}{\mathrm{d}t} = -\int_S \frac{\mathrm{D}\Gamma}{\mathrm{D}t}\boldsymbol{n}\,\mathrm{d}S - \int_S \Gamma\frac{\mathrm{D}}{\mathrm{D}t}(\boldsymbol{n}\,\mathrm{d}S).$$

Here, by (4.133), $\mathrm{D}\Gamma/\mathrm{D}t \neq 0$ only if $S$ contains a bound vortex sheet of area $S_\mathrm{b}$, say; and the rate of change of $\boldsymbol{n}\,\mathrm{d}S$ is given by (2.29) with $\boldsymbol{u} = \bar{\boldsymbol{u}}$ now. But

$$-\Gamma(\boldsymbol{n}\times\nabla)\times\bar{\boldsymbol{u}} = -(\boldsymbol{n}\times\nabla)\times(\Gamma\bar{\boldsymbol{u}}) + (\boldsymbol{n}\times\nabla\Gamma)\times\bar{\boldsymbol{u}},$$

of which the integral is (again a line integral vanishes)

$$-\int_S \Gamma(\boldsymbol{n}\times\nabla)\times\bar{\boldsymbol{u}}\,\mathrm{d}S = \int_S \boldsymbol{\gamma}\times\bar{\boldsymbol{u}}\,\mathrm{d}S = \int_S \boldsymbol{l}_\gamma\,\mathrm{d}S.$$

If all vorticity is in $S$, by (3.72) the Lamb-vector integral vanishes. A similar transformation can be made for (4.137), leading to an integral of $\boldsymbol{x}\times\boldsymbol{n}\mathrm{D}\Gamma/\mathrm{D}t$ over $S_\mathrm{b}$ and an integral of $\boldsymbol{x}\times\boldsymbol{l}_\gamma$ that also vanishes. But, these Lamb-vector integrals will be nonzero if $\bar{\boldsymbol{u}}$ contains a possible potential velocity $\boldsymbol{u}_\mathrm{e}$ induced by other vortex systems. Thus, the final result is

$$\frac{\mathrm{d}\boldsymbol{I}}{\mathrm{d}t} = \int_S \boldsymbol{u}_\mathrm{e}\times\boldsymbol{\gamma}\,\mathrm{d}S + \frac{1}{\rho}\int_{S_\mathrm{b}} [\![p_\gamma]\!]\boldsymbol{n}\,\mathrm{d}S, \tag{4.138}$$

$$\frac{\mathrm{d}\boldsymbol{L}}{\mathrm{d}t} = \int_S \boldsymbol{x}\times(\boldsymbol{u}_\mathrm{e}\times\boldsymbol{\gamma})\mathrm{d}S + \frac{1}{\rho}\int_{S_\mathrm{b}} [\![p_\gamma]\!]\boldsymbol{x}\times\boldsymbol{n}\,\mathrm{d}S, \tag{4.139}$$

where the suffix $\gamma$ stresses that this pressure jump is caused by circulatory vortex sheets. These formulas are the Euler-limit form of (3.118) and (3.119), applied to an isolated vortex-sheet system.

### 4.4.2 Kutta Condition

In a viscous flow the velocity field is automatically free from singularity. But in the Euler limit the regularity has to be imposed, known as the **Kutta condition**: *The flow cannot turn around any corner with a nonzero velocity.* The condition is necessary for determining not only the strength of a bound vortex sheet but also the initial strength and orientation of a free vortex sheet as it just leaves the body. In other words, it determines how an attached vortex sheet becomes a free vortex sheet due to separation.

Assume a free vortex sheet $\boldsymbol{\gamma}$ leaves the body surface along a *separation line* $L$ thereon, which can be a sharp edge or on a smooth surface due to early separation. Let $\boldsymbol{e}_1$ be the unit tangent vector along $L$, and $\boldsymbol{e}_2$ be the unit vector tangent to the body surface and orthogonal to $\boldsymbol{e}_1$, such that $\boldsymbol{u}^{\pm} = u_1^{\pm}\boldsymbol{e}_1 + u_2^{\pm}\boldsymbol{e}_2$, see Fig. 4.20a. We examine how the Kutta condition determines the initial behavior of the free vortex sheet.

First, if the sheet leaves the wall not in a tangential direction, then the Kutta condition implies that there must be $u_2^{\pm} = 0$ and hence the flow can only be along the $\pm\boldsymbol{e}_1$-directions. If the flow is steady, by (4.132) there must be $[\![q^2]\!] = 0$ or $\boldsymbol{u}^+ = \pm\boldsymbol{u}^-$. If $\boldsymbol{u}^+ = \boldsymbol{u}^-$, we have $[\![\boldsymbol{u}]\!] = \boldsymbol{0}$, implying no vortex sheet at all; while if $\boldsymbol{u}^+ = -\boldsymbol{u}^-$, we have $\bar{\boldsymbol{u}} = \boldsymbol{0}$ and hence even a vortex sheet exists it cannot shed off from the body. Thus, a steady vortex sheet can leave the body surface only along the tangential direction (e.g., Smith (1984)). Then, for unsteady flow with $\boldsymbol{u}^+ \neq \boldsymbol{u}^-$, we will have $\bar{\boldsymbol{u}} = \overline{u}_1\boldsymbol{e}_1$, which however is along $L$ and still cannot send any vortex sheet into the flow. Therefore, in any case, *a free vortex sheet must leave a solid body tangentially.*

To put this conclusion in mathematic form, let $\boldsymbol{u}^-$ be on the inner side, so that $\boldsymbol{u}^- = u_1^-\boldsymbol{e}_1$ but $\boldsymbol{u}^+ = u_1^+\boldsymbol{e}_1 + u_2^+\boldsymbol{e}_2$. Thus,

$$\begin{aligned} [\![\boldsymbol{u}]\!] &= (u_1^+ - u_1^-)\boldsymbol{e}_1 + u_2^+\boldsymbol{e}_2, \\ \bar{\boldsymbol{u}} &= \frac{1}{2}[(u_1^+ + u_1^-)\boldsymbol{e}_1 + u_2^+\boldsymbol{e}_2]. \end{aligned} \tag{4.140}$$

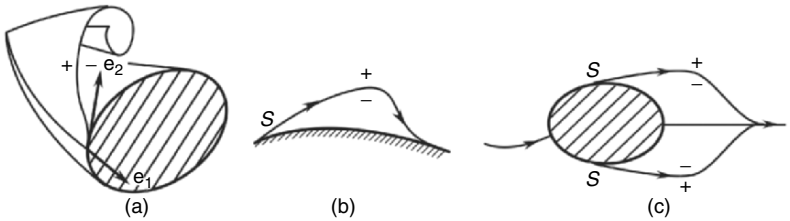


**Fig. 4.20.** Vortex sheet separating from a smooth surface. (**a**) Three dimensional flow; (**b**, **c**) two-dimensional flow

Then, let $\boldsymbol{n} = \boldsymbol{e}_2 \times \boldsymbol{e}_1$ point from the $-$ side to the $+$ side, we also have

$$\boldsymbol{\gamma} = u_2^+ \boldsymbol{e}_1 + (u_1^- - u_1^+)\boldsymbol{e}_2, \tag{4.141a}$$

$$q^{+2} = u_1^{+2} + u_2^{+2} = u_2^{-2} - 2\frac{\partial \Gamma}{\partial t}. \tag{4.141b}$$

Therefore, given $L$, $\boldsymbol{u}_1$, and $\partial\Gamma/\partial t$, the initial free vortex is completely determined.

In two dimensions (Fig. 4.20b,c) there is no velocity component along the $\boldsymbol{e}_1$ direction. Hence, for steady flow $\boldsymbol{u}^+ = \pm\boldsymbol{u}^- = \pm u_2 \boldsymbol{e}_2$, and by the same reasoning, *if all streamlines are from the same upstream flow, then no steady vortex sheet can shed off from a two-dimensional body.* This result permits an attached vortex bubble as a portion of the body, which is also enclosed by a vortex sheet. The reattachment point can be on the wall (Fig. 4.20b) or in the wake (Fig. 4.20c). But inside the bubble the flow is not from infinity and has lower total pressure or a smaller Bernoulli constant. Moreover, with minor modification of the argument, it can be shown that the bubble sheet must still leave the wall along a tangential direction, with the inside flow sitting in the cusp region (for more discussion see Sect. 7.2).

The classic application of the Kutta condition is to determine the circulation $\Gamma$ around a two-dimensional airfoil in a steady potential flow and hence the lift (Chap. 11). However, within the strictly inviscid potential flow theory, a flow can have $\Gamma \neq 0$ only if the body is multiply-connected, for which there exist irreducible loops surrounding the body. Since no surface lying within the fluid can span such a special loop, the circulation along it can be nonzero without violating the potential-flow condition. This is the case of two-dimensional airfoil flow. In and only in two dimensions, not only a potential flow can have $\Gamma \neq 0$ but also a *supplementary condition* is necessary to fix it along an irreducible loop, and hence the force. In contrast, for three-dimensional flow over a single-connected body, there is no room for an indeterminate $\Gamma$. However, the Kutta condition does exist in three dimensions as just given.

Finally, it should be stressed that on a smooth surface the location of separation line $L$ cannot be determined in the Euler limit, so (4.140) and (4.141) are still insufficient. An asymptotic viscous theory on the boundary-layer separation will be given in Sect. 5.2.

### 4.4.3 Self-Induced Motion

The velocity induced by a vortex sheet has been given by (3.31) or (3.35). When the flow is entirely induced by the sheet, these Biot–Savart formulas completely determine the flow including the motion of the vortex sheet itself, and the problem is purely kinematic. To compute this *self-induced motion* we let the point $\boldsymbol{x}$ remain on the sheet. In two-dimensional flow $\boldsymbol{x} = \boldsymbol{x}(s)$, where $s$ is the arclength of the sheet (a plane curve). Then (3.35) yields

$$\frac{\partial}{\partial t} Z^*(s,t) = \frac{1}{2\pi \mathrm{i}} \mathrm{pv} \int \frac{\gamma(s')\mathrm{d}s'}{Z(s,t) - Z'(s',t)}, \tag{4.142}$$

where pv means taking Cauchy principal value. Then, since $\gamma(s')\mathrm{d}s' = \mathrm{d}\Gamma'$ is the infinitesimal circulation increment, we may reversely view $s, s'$ as functions of $\Gamma$ and $\Gamma'$. Therefore, (4.142) becomes

$$\frac{\partial}{\partial t} Z^*(\Gamma, t) = \frac{1}{2\pi \mathrm{i}} \mathrm{pv} \int_{\Gamma_0}^{\Gamma_\mathrm{e}} \frac{\mathrm{d}\Gamma'}{Z(\Gamma, t) - Z'(\Gamma', t)}, \tag{4.143}$$

with $\Gamma_0$ and $\Gamma_\mathrm{e}$ being the circulations at two end points of the sheet. This integral-differential equation is called the *Birkhoff–Rott equation* and should be solved under initial condition

$$Z = Z(\Gamma, 0) \quad \text{at} \quad t = 0. \tag{4.144}$$

To ensure the uniqueness of the solution, $\Gamma$ should vary monotonically along the sheet. For example, one may impose a constraint

$$\frac{\mathrm{d}\Gamma}{\mathrm{d}s} \geq 0, \quad \Gamma_0 \leq \Gamma \leq \Gamma_\mathrm{e}. \tag{4.145}$$

A classic problem of the self-induced motion of a vortex sheet is the rolling up of the vortex sheet shed from the trailing edge of a large-span wing. Approximately, the bound vortex-sheet strength $\boldsymbol{\gamma}_\mathrm{b}$ equals the spanwise gradient of the circulation distribution on the wing (e.g., Prandtl and Tietjens 1934; Glauert 1947; see also Fig. 11.3). Assume that the streamwise velocity behind the wing is about the same as the uniform velocity $U$ at far upstream, such that an observer moving downstream with speed $U$ to different $x$-stations will see the same picture as the time evolution of the trace of the sheet in a fixed wake plane, with $t = x/U$. This reduces the problem to two-dimensional so that (4.143) applies. Moreover, assume the wing is flat, so on a wake plane right after the trailing edge the trace of the sheet is a straight line segment (see Fig. 4.21 later). The large span permits neglecting the mutual influence of the motion at the wing tips, thus the sheet can be simplified to a semiinfinite one and we only need to consider the rolling up process at one end. This theoretical model is called the *Kaden problem*, as Kaden (1931) first derived a similarity law of the geometry of a tightly rolled semiinfinite vortex sheet for the elliptical load distribution on the wing. Moore and Saffman (1973) found that the Kaden law can be neatly obtained by a dimensional analysis as follows.

Let the circulation distribution near a wingtip be given by

$$\Gamma(y) = 2Ay^{1-n}, \quad 0 < n < 1, \tag{4.146}$$

where $y$ is the spanwise coordinate with origin at the wing tip and $A$ is a constant. The sheet strength is

$$\gamma = \frac{\mathrm{d}\Gamma}{\mathrm{d}y} = 2(1-n)\Gamma_0 y^{-n}, \tag{4.147}$$

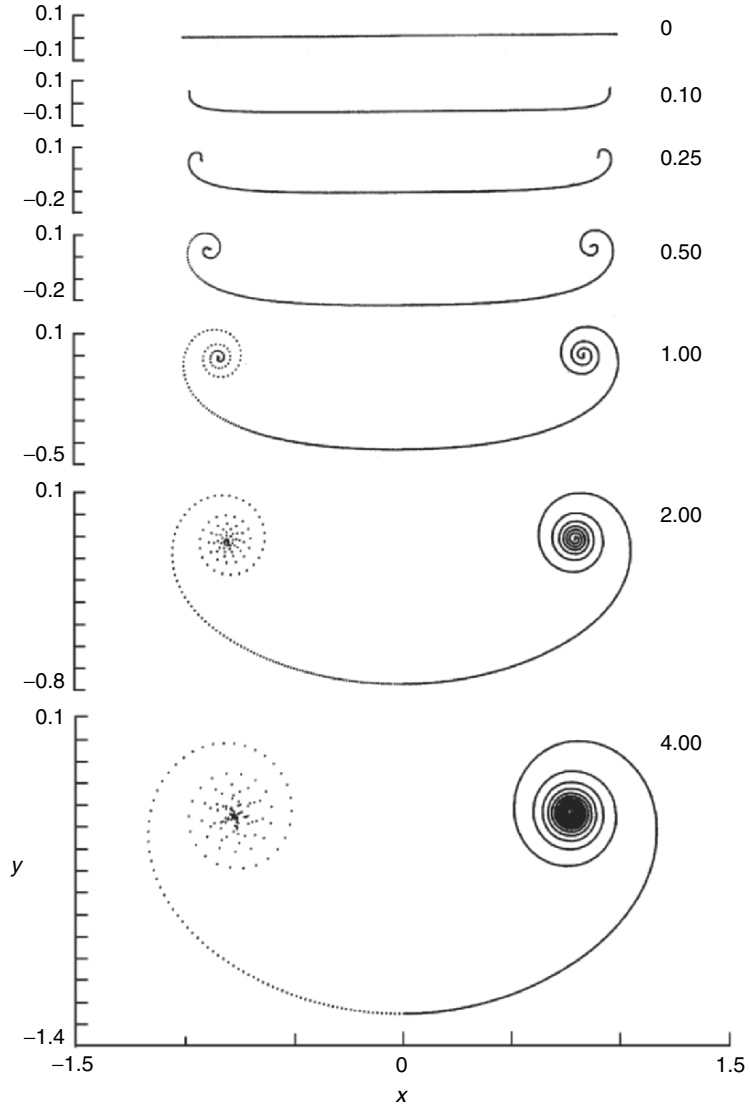


**Fig. 4.21.** Early stage of the roll-up. The vortex-blob positions are plotted on the left and an interpolation curve is on the right. From Krasny (1987)

which approaches infinity at $y = 0$ and must induce a very fast self-motion to make it quickly roll into tight spirals with many turns that can be approximated by concentric circles. In the Euler limit, the Kelvin circulation theorem implies that inside each circle the total vorticity remains unchanged as time goes on. Thus, in terms of polar coordinates $(r, \theta)$ we may write $\Gamma = \Gamma(r)$. Now $\Gamma$ and $A$ have dimensions $L^2/T$ and $L^{1+n}/T$, respectively; hence we may

immediately write

$$\Gamma = A\left(\frac{r}{k}\right)^{1-n} \quad \text{or} \quad r = k\left(\frac{\Gamma}{A}\right)^{1/(n-1)} \tag{4.148a,b}$$

with $k$ being a dimensionless constant.

Then, since the equi-$\Gamma$ lines are concentric circles, there must be

$$u_\theta = \frac{\Gamma}{2\pi r} = \frac{\beta}{r^n}, \quad \beta = \frac{A}{2\pi k^{1-n}}. \tag{4.149}$$

For a point $r_\mathrm{p}$ on the vortex sheet, since it moves with the sheet, there is $r_\mathrm{p}\mathrm{d}\theta/\mathrm{d}t = u_\theta$. Hence, by (4.148b) and (4.149),

$$\theta_P = \frac{\beta t}{r^{n+1}} + \theta_0, \quad \theta_0 = \theta_{t=0},$$

from which follows the spiral equation representing the *similarity law of tightly rolled sheet*:

$$r = \left(\frac{\beta t}{\theta - \theta_0}\right)^{1/(n+1)} \quad \text{as} \quad \theta \to \infty. \tag{4.150}$$

For the elliptical wing load (which has minimum induced drag in linearized wing theory; e.g., Prandtl and Tietjens (1934) and Glauert (1947)) there is $n = 1/2$ and (4.150) gives the *Kaden similarity law*

$$r = (4\pi^2 k)^{-1/3}\left(\frac{At}{\theta - \theta_0}\right)^{2/3}. \tag{4.151}$$

In principle, the prediction of Kaden's law can be tested by solving (4.143) if its solution exists for all $t > 0$. However, it has been proven that a singularity of the sheet curvature will spontaneously develop within a finite time $T$, which makes the solution for $t > T$ unobtainable (e.g., Saffman 1992). This problem was bypassed numerically by Krasny (1987) who replaced the singular kernel in (4.143) by a smoothed regular one. Fig. 4.21 shows his result for elliptical circulation distribution, of which the tightly rolled part fully confirms the Keden similarity law.

A vortex sheet in a three-dimensional space is defined by a pair of parameters $(\eta^1, \eta^2)$. Naturally, we use the surface-moving frame introduced in Appendix A3.2. Let $\boldsymbol{x} = \boldsymbol{x}(\eta^\alpha, t)$ with $\alpha = 1, 2$ be the sheet point where the velocity is to be estimated, and $\boldsymbol{x}' = \boldsymbol{x}'(\lambda^\alpha, t)$ be the integration point along the sheet. The covariant tangent vectors and normal vector of the sheet are

$$\boldsymbol{r}_\alpha = \frac{\partial \boldsymbol{x}}{\partial \eta^\alpha}, \quad \boldsymbol{n} = \frac{\boldsymbol{r}_1 \times \boldsymbol{r}_2}{\sqrt{g}}, \quad g = \det\{g_{\alpha\beta}\},$$

where $g_{\alpha\beta} = \boldsymbol{r}_\alpha \cdot \boldsymbol{r}_\beta$ are the covariant metric tensor. Then by (4.129a)

$$\boldsymbol{\gamma} = \frac{\boldsymbol{r}_1 \times \boldsymbol{r}_2}{\sqrt{g}} \times \nabla\Gamma = \frac{1}{\sqrt{g}}(\Gamma_{,1}\boldsymbol{r}_2 - \Gamma_{,2}\boldsymbol{r}_1),$$

where we used the notation $\Gamma_{,\alpha} = \boldsymbol{r}_\alpha \cdot \nabla \Gamma$. Moreover, we have $\mathrm{d}S = \sqrt{g}\mathrm{d}\lambda^1\mathrm{d}\lambda^2$. Hence, (3.31) yields the self-induction equation in three dimensions (Caflisch 1989; Kaneda 1990a)

$$\frac{\partial}{\partial t}\boldsymbol{x}(\eta^\alpha, t) = \frac{1}{4\pi}\mathrm{pv}\int_S \frac{\boldsymbol{\Gamma}\times\boldsymbol{R}}{R^3}\mathrm{d}\lambda^1\mathrm{d}\lambda^2, \tag{4.152a}$$

$$\boldsymbol{R}(\eta^\alpha, \lambda^\alpha, t) = \boldsymbol{x}(\eta^\alpha, t) - \boldsymbol{x}'(\lambda^\alpha, t),$$

$$\boldsymbol{\Gamma} = \sqrt{g}\boldsymbol{\gamma} = \Gamma_{,1}\boldsymbol{r}_2 - \Gamma_{,2}\boldsymbol{r}_1. \tag{4.152b}$$

It is convenient to take the variables $\eta^\alpha$ as two components of the Lagrangian label $\boldsymbol{X}$, since then $\Gamma(X^\alpha, t) = \Gamma(X^\alpha, 0)$. Choose the basis vector $\boldsymbol{r}_2$ parallel to $\boldsymbol{\gamma}$ at $t = 0$, so that the Lagrangian invariance of $\Gamma$ implies that $\Gamma_{,2} = 0$ at any time, and lines on the sheet with $X^1 = $ const. are vorticity lines. Consequently, $\Gamma$ is a function of $X^1$ only, say $\Gamma_{,1} = \gamma(X^1)$. Thus

$$\boldsymbol{\Gamma}(X^1, X^2, t) = \gamma(X^1)\boldsymbol{r}_2(X^1, X^2, t). \tag{4.153}$$

As a check, in two dimensions $\boldsymbol{r}_2$ is along the direction of $\boldsymbol{e}_3$ and (4.153) is reduced to $\boldsymbol{\Gamma} = \gamma(X^1)\boldsymbol{e}_3$. Rewrite $X^1 = s$ and $Y^1 = s'$, integrating (4.152a) over $\lambda^2$ gives

$$\frac{\partial}{\partial t}\boldsymbol{x}(s,t) = \frac{1}{2\pi}\mathrm{pv}\int_S \frac{(x_1 - x_1')\boldsymbol{e}_2 - (x_2 - x_2')\boldsymbol{e}_1}{(x_1 - x_1')^2 + (x_2 - x_2')^2}\gamma(s')\mathrm{d}s',$$

of which the complex-variable form with $Z(s,t) = x_1(x,t) + \mathrm{i}x_2(s,t)$ is precisely (4.142). Observe that the simplification in two dimensions is due to the $\lambda^2$-independence of the sheet or symmetry with respect to a translation along $\boldsymbol{e}_3$. There can also be a simplification in three dimensions if a symmetry exists, of which some examples are given by Kaneda (1990b).

In more general cases, (4.152a) has to be solved numerically. A striking example is the axisymmetric vortex sheet out of a nozzle computed by Nitsche and Krasny (1994), which evolves to vortex rings due to Kelvin–Helmholtz instability (Chap. 9) and self-induction. The computed vortex-sheet patterns at different evolution times are in excellent agreement with experimental flow visualization, one of which is shown in Fig. 4.22. Numerical computations of vortex-sheet evolution has recently been advanced to fully three-dimensional configurations (e.g., Pozrikidis 2000; Sakajo 2001).

### 4.4.4 Vortex Sheet Transport Equation

We now derive the transport equation of $\boldsymbol{\gamma}$ by looking at the evolution of vorticity in a material volume element $\delta v = \delta n \delta S$ with $\mathrm{D}(\delta v)/\mathrm{D}t = \vartheta \delta v$ and $\boldsymbol{\omega}\delta v = \boldsymbol{\gamma}\delta S$. By (3.98c) there is

$$\frac{\mathrm{D}}{\mathrm{D}t}(\boldsymbol{\gamma}\,\delta S) = \frac{\mathrm{D}\boldsymbol{\gamma}}{\mathrm{D}t}\delta S + \boldsymbol{\gamma}\frac{\mathrm{D}}{\mathrm{D}t}\delta S = (\boldsymbol{\omega}\cdot\nabla\boldsymbol{u} + \nabla\times\boldsymbol{a})\delta v.$$

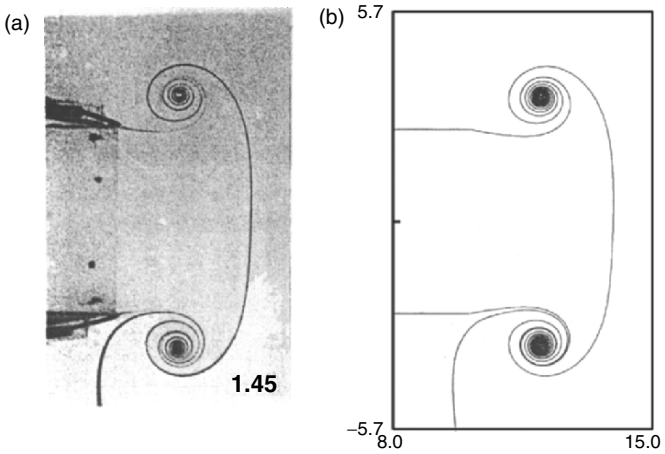


**Fig. 4.22.** Axisymmetric vortex sheet out of a nozzle. (**a**) Experimental visualization, (**b**) numerical solution. From Nitsche and Krasny (1994)

Here, three terms need to be transformed. First, by (2.139) and (2.140a) there is

$$\frac{\mathrm{D}}{\mathrm{D}t}\delta S = \nabla_\pi \cdot \boldsymbol{u}_\gamma \, \mathrm{d}S,$$

where we have replaced $\boldsymbol{u}$ by $\boldsymbol{u}_\gamma$ because $\nabla_\pi$ involves only tangent derivatives. Next, $\boldsymbol{\omega}\cdot\nabla\boldsymbol{u}\,\delta v = \boldsymbol{\gamma}\cdot\nabla\boldsymbol{u}\,\delta S$ is the stretching and tilting of $\boldsymbol{\gamma}\,\delta S$ by $\nabla\boldsymbol{u}$, where $\boldsymbol{u}$ can again be identified as $\boldsymbol{u}_\gamma$ since $\boldsymbol{\gamma}\cdot\nabla$ is a tangent gradient. Thirdly, to treat $\nabla\times\boldsymbol{a}\,\delta v$, in the limit $\delta v \to 0$ we write

$$\nabla\times\boldsymbol{a}\,\delta v = \int_{\delta v} \nabla\times\boldsymbol{a}\,\mathrm{d}v = \int_{\partial\,\delta v} \boldsymbol{n}'\times\boldsymbol{a}\,\mathrm{d}S,$$

where $\boldsymbol{n}'$ is the normal of $\partial\,\delta v$ out of $\delta v$, which equals $-\boldsymbol{n}$ on side 2 and $\boldsymbol{n}$ on side 1. Hence, the vorticity diffusion vector degenerates to the *tangent acceleration jump*:

$$\nabla\times\boldsymbol{a}\,\delta v = \boldsymbol{n}\times[\![\boldsymbol{a}]\!]\delta S.$$

Collecting these results, we obtain the *general vortex sheet transport equation*

$$\frac{\mathrm{D}\boldsymbol{\gamma}}{\mathrm{D}t} - \boldsymbol{\gamma}\cdot\nabla\boldsymbol{u}_\gamma + \boldsymbol{\gamma}\nabla_\pi\cdot\boldsymbol{u}_\gamma = \boldsymbol{n}\times[\![\boldsymbol{a}]\!], \quad \frac{\mathrm{D}}{\mathrm{D}t} = \frac{\partial}{\partial t} + \boldsymbol{u}_\gamma\cdot\nabla \tag{4.154a}$$

first derived by Wu (1995) using the vorticity transport equation (3.107) in reference space, who showed that it can also follow from the Kelvin circulation formula (2.32).[12] Alternatively, using (A.66), (4.154a) becomes

$$\frac{\partial\boldsymbol{\gamma}}{\partial t} + \nabla\times(\boldsymbol{\gamma}\times\boldsymbol{u}_\gamma) + \boldsymbol{\gamma}\nabla_\pi\cdot\boldsymbol{u}_\gamma + \boldsymbol{u}_\gamma[\![\omega_\mathrm{n}]\!] = \boldsymbol{n}\times[\![\boldsymbol{a}]\!]. \tag{4.154b}$$

[12] The unit normal vector used in Wu (1995) is opposite to that defined here.

The term-to-temathrmcorrespondence of (4.154a) and (4.154b) with the vorticity equation (3.98c) and (3.98a), respectively, is evident.

In what follows we assume the flow is incompressible. The left-hand side of (4.154a) and (4.154b) represents kinematics and the right-hand side is a dynamic effect. If $\boldsymbol{n} \times [\![\boldsymbol{a}]\!] = \boldsymbol{0}$, the equations become purely kinematic and carry no more information than (4.152), hence one does not need to solve them. This happens for a vortex sheet inside a homogeneous fluid, since then $[\![\boldsymbol{a}]\!] = -[\![\nabla p]\!]/\rho = 0$. This also happens for a vortex sheet attached to a stationary solid wall, since then the sheet location is known and its strength is determined by the external velocity $\boldsymbol{u}_{\mathrm{e}}$ obtained from the relevant Euler solution.

The dynamic source $\boldsymbol{n} \times [\![\boldsymbol{a}]\!]$ becomes important and nontrivial only when the sheet represents an interface, a free surface, or a freely moving singular layer of density stratification. The location of such a sheet is not known in advance, and (4.154a) or (4.154b) is necessary for solving its evolution. In this case, on each side of an interface, say, we have boundary vorticity fluxes $\boldsymbol{\sigma}_1$ and $\boldsymbol{\sigma}_2$, thus the total creation rate of the sandwich-like sheet is $\boldsymbol{\sigma}_1 + \boldsymbol{\sigma}_2 = \boldsymbol{n} \times [\![\boldsymbol{a}]\!]$. More specifically, taking the jump of the Euler equation with gravity, one has

$$\boldsymbol{n} \times ([\![\rho \boldsymbol{a}]\!] + \nabla [\![p]\!] + [\![\rho]\!] g \boldsymbol{k}) = \boldsymbol{0},$$

where $\boldsymbol{k}$ is the unit vertical vector. Then, define the *Atwood ratio*

$$A = \frac{[\![\rho]\!]}{\rho_1 + \rho_2} \tag{4.155}$$

such that by (2.82a) there is $[\![\rho \boldsymbol{a}]\!] = \overline{\rho}([\![\boldsymbol{a}]\!] + 2A\overline{\boldsymbol{a}})$ (on a free surface $A = 1$). After scaled by $U^*$, $L$, and $\overline{\rho}$, the dimensionless fomathrmof (4.154a) on an interface or singular density-stratified surface reads (Wu 1995; Pozrikidis 2000)

$$\frac{\mathrm{D}\boldsymbol{\gamma}}{\mathrm{D}t} - \boldsymbol{\gamma} \cdot \nabla \boldsymbol{u}_\gamma + \boldsymbol{\gamma} \nabla_\pi \cdot \boldsymbol{u}_\gamma = \boldsymbol{n} \times (2A\overline{\boldsymbol{a}} + We \nabla \kappa + 2Ag^* \boldsymbol{k}), \tag{4.156}$$

where $We$ is the Weber number defined in (4.102). In solving the motion of such a vortex sheet, this dynamic equation should be used along with the Biot–Savart formula (3.31) as well as the equation for $\overline{\boldsymbol{a}}$. Figure. 4.23 displays a numerical solution for two-dimensional interface instability (the *Rayleigh–Taylor instability*) obtained by Tryggvason (1988). Both mushroom-like interface pattern and vortex-sheet strength are shown at $A = 0$ and 0.6. The density difference tends to stabilize the interface, and the sheet strength $\gamma$ develops sharp peaks as it rolls into spirals.

## 4.5 Vorticity-Based Formulation of Viscous Flow Problem

We now move on to the general vorticity-based formulation of viscous incompressible flow, which is an important part of vorticity dynamics. The formulation not only provides a theoretical basis for developing numerical schemes

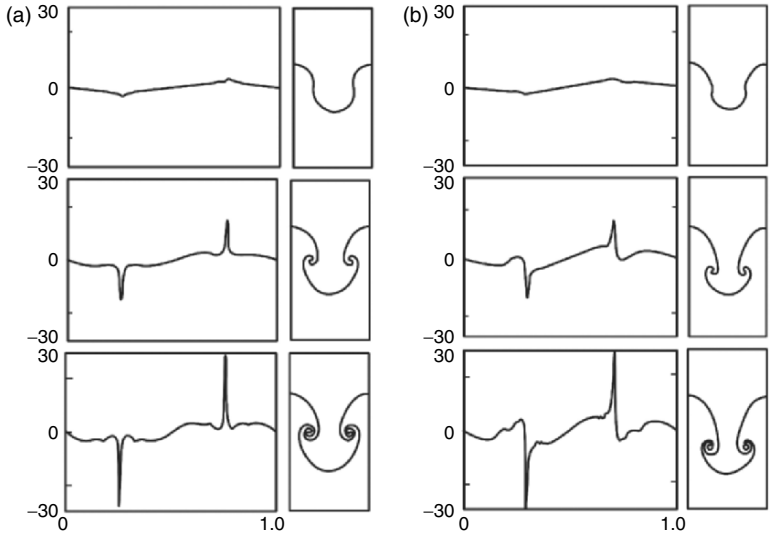


**Fig. 4.23.** Rayleigh–Taylor instability of an interfacial vortex sheet. (**a**) $A = 0$. (**b**) $A = 0.6$. *Right*: the sheet evolution as time. *Left*: vortex-sheet strength vs. normalized arc length. From Tryggvason (1988)

using vorticity as variable to solve the Navier–Stokes equations, but also leads to deeper understanding of the relevant physics.

Conventionally, one solves the velocity $\boldsymbol{u}$ and pressure $p$ from the Navier–Stokes and continuity equations. The velocity adherence condition (2.67) on $\partial B$ naturally matches this formulation. A subtle issue is the pressure, which for incompressible flow is no more than ensuring $\nabla \cdot \boldsymbol{u} = 0$ and has no natural boundary condition. Another disadvantage is that the skin-friction on a solid boundary, given by the negative of (2.151b), has to be estimated by a one-side interpolation of $\boldsymbol{u}$ that often results in a significant loss of accuracy, due to the $O(Re)$-large normal gradient of $\boldsymbol{\omega}$ near the wall. In contrast, in a vorticity-based formulation one focuses on the shearing process and solves the vorticity $\boldsymbol{\omega}$ and velocity $\boldsymbol{u}$ (or $\omega$ and stream function $\psi$ in two dimensions). The disadvantages of the $(\boldsymbol{u}, p)$ formulation are precisely the advantages of the $(\boldsymbol{\omega}, \boldsymbol{u})$ formulation. The need for solving $p$ is removed by keeping $\boldsymbol{u}$ divergence-free, and the skin-friction follows from the resolved $\boldsymbol{\omega}$ field. Since $\boldsymbol{\omega}$ is one order higher than $\boldsymbol{u}$, an accurate computation of the former usually implies an even more accurate estimate of the latter. Moreover, since at large $Re$ the vorticity is highly localized in the narrow wake region and exponentially decays elsewhere, the computational domain can be greatly reduced.

The advantages of the $(\boldsymbol{u}, p)$ formulation, however, are also precisely the disadvantages of the $(\boldsymbol{\omega}, \boldsymbol{u})$ formulation. First, one needs to solve $\boldsymbol{u}$ from computed $\boldsymbol{\omega}$ simultaneously. Second, the vorticity transport equation is one-order higher than the Navier–Stokes equation and may have spurious solutions that

are not solution of the latter, which has to be removed by a *compatibility condition*. But the most difficult issue is how to formulate the boundary condition for solving the vorticity transport equation.

A variety of vorticity-based numerical methods have been developed, all making great effort to cast one's physical understanding of vorticity creation at boundaries (Sect. 4.1.3; see also Lighthill 1963, Batchelor 1967) to a proper vorticity boundary condition. The methods fall into two categories. One category is grid-free *vortex method*, which can be traced back to Rosenhead (1931) and in which the viscous effect was first treated by Chorin (1973); for systematic presentation see, e.g., Gustafson and Sethian (1991) and Cottet and Koumoutsakos (2000). Another category uses conventional numerical methods with grid, in terms of differential or integral-differential formulation. Among the second category, Wu and coworkers (Wu and Thomson 1973; Wu 1976, 1984) pioneered a thorough study of the integral-differential formulation. For the *kinematic part* of the problem, he uses the generalized Biot–Savart formula (3.27) with known $\boldsymbol{\omega}$-field in the interior and *full velocity adherence* at the boundary to compute the $\boldsymbol{u}$-field. As noted in Sect. 3.2.2, this inevitably leads to a tangent-velocity discontinuity at the boundary, i.e., an attached vortex sheet $\boldsymbol{\gamma}$. The sheet strength is governed by an inhomogeneous Fredholm integral equation also derived from (3.27). Solving the integral equation for $\boldsymbol{\gamma}$ allows for an approximate estimate of the tangent boundary vorticity $\boldsymbol{\omega}_{\pi B}$, which just provides a *Dirichlet condition* for the *kinetic part*, i.e., solving the vorticity transport equation. This integral-differential approach has been applied to compute some aerodynamic flows (e.g., Sugavanam 1979; Wu and Gulcat 1981; Wang and Wu 1986; Kim et al. 1996).

Below we mainly present a formulation also of the second category, based on the work of Wu et al. (1994b) and Wu et al. (1995). As an interesting contrast to J. C. Wu's formulation, we will focus on a differential approach, using a locally derived dynamic *Neumann condition* for solving the vorticity transport equation.

### 4.5.1 Kinematical Well-Posedness

We first address the boundary-value problem for solving the kinematic aspect and the compatibility problem. As illustration, consider a laminar flow past a solid body surface $\partial B$ in an externally unbounded domain $V$ at a large Reynolds number. The kinematic problem can well be relaxed to include compressible flows; so we return to (3.24) and (3.25) for *given* $(\boldsymbol{\omega}, \vartheta)$ distribution:

$$\nabla \times \boldsymbol{u} = \boldsymbol{\omega}, \quad \nabla \cdot \boldsymbol{u} = \vartheta \quad \text{in } V, \tag{4.157a,b}$$

$$\int_V \vartheta \mathrm{d}V = \int_{\partial V} \boldsymbol{n} \cdot \boldsymbol{b} \, \mathrm{d}S, \quad \nabla \cdot \boldsymbol{\omega} = 0, \tag{4.158a,b}$$

where $\boldsymbol{b}$ is the velocity of $\partial B$. As shown in Sect. 3.2.2, the solution of this problem is unique if only the no-through condition is imposed:

$$\boldsymbol{n} \cdot \boldsymbol{u} = \boldsymbol{n} \cdot \boldsymbol{b} \quad \text{on } \partial B. \tag{4.159}$$

In two dimensions (4.158b) is trivial, but in three dimensions it may be violated by numerical errors. A common practice of enforcing (4.158b) is projecting the computed vorticity (with $\nabla \cdot \boldsymbol{\omega} \neq 0$) into the solenoidal space:

$$\boldsymbol{\omega} \Longrightarrow \widehat{\boldsymbol{\omega}} = \boldsymbol{\omega} - \nabla\psi, \quad \nabla \cdot \widehat{\boldsymbol{\omega}} = 0. \tag{4.160}$$

This projection requires solving a Poisson equation, a time-consuming step:

$$\nabla^2\psi = \nabla \cdot \boldsymbol{\omega} \quad \text{in } V, \quad \boldsymbol{n} \times \nabla\psi = \boldsymbol{0} \quad \text{on} \quad \partial B. \tag{4.161a,b}$$

We have seen that the integral approach of problem (4.157) to (4.159) leads to the generalized Biot–Savart formula (3.26) and (3.27), which can be directly used in numerical computation by some fast integration algorithms, e.g., Wang and Wu (1986) and Koumoutsakos et al. (1994). Here we focus on the differential approach.

To avoid the inconvenient cross interaction of different components of $\boldsymbol{\omega}$ and $\boldsymbol{u}$ in (4.157a), we replace (4.157a,b) by the curl of (4.157a), which is (2.86) but now serves as a Poisson equation for $\boldsymbol{u}$:

$$\nabla^2\boldsymbol{u} = \nabla\vartheta - \nabla \times \boldsymbol{\omega}. \tag{4.162}$$

This equation is one order higher than (4.157) and may have spurious solutions. They can be eliminated by proper boundary conditions, for which we set

$$\boldsymbol{n} \cdot \boldsymbol{u} = \boldsymbol{n} \cdot \boldsymbol{b}, \quad \boldsymbol{n} \times (\nabla \times \boldsymbol{u} - \boldsymbol{\omega}) = \boldsymbol{0} \quad \text{on } \partial B. \tag{4.163a,b}$$

While (4.163a) is the no-through condition (4.159), (4.163b) is an application of the tangent components of the original equation (4.157a) to the boundary. We then have the following theorem (Wu et al. 1995):

**Theorem (kinematic well-posedness).** *Suppose (4.158a) holds and the given $\vartheta$ and $\boldsymbol{\omega}$ are sufficiently smooth. Then problem (4.162) and (4.163) has a unique solution which satisfies almost everywhere the following equations in $V$:*

$$\nabla \cdot \boldsymbol{u} = \vartheta, \quad \nabla \times \boldsymbol{u} = \widehat{\boldsymbol{\omega}}, \tag{4.164}$$

*where $\widehat{\boldsymbol{\omega}}$ is defined by (4.160) with $\psi$ given by (4.161).*

The theorem implies that $\boldsymbol{u}$ can be solved from (4.162) and (4.163) with any given $\boldsymbol{\omega}$, which may not be solenoidal. The solution has correct $\vartheta$ and its curl is nothing but the projected $\widehat{\boldsymbol{\omega}}$. Consequently, the need for solving (4.161) is replaced by taking the curl at little cost. This remark also indicates that one can solve $n-1$ components of $\boldsymbol{u}$ in $n$-dimensional space and then compute the remaining one by integrating (4.157b).

To prove the theorem, we first notice that the existence of the solution is a direct consequence of problem (4.157) and (4.158) being well posed, as

seen clearly from the derivation of (4.162) if $\nabla \cdot \boldsymbol{\omega} = 0$. When $\nabla \cdot \boldsymbol{\omega} \neq 0$, we simply replace $\boldsymbol{\omega}$ by $\widehat{\boldsymbol{\omega}}$ in (4.157) and (4.158), which still fomathrma well-posed problem. The solution $\boldsymbol{u}$ satisfies (4.162) because $\nabla \times \boldsymbol{\omega} = \nabla \times \widehat{\boldsymbol{\omega}}$. It also satisfies the boundary condition (4.163b) due to (4.161b).

Next, let $\boldsymbol{v}$ be the difference of two solutions of (4.162) and (4.163), such that

$$\nabla^2 \boldsymbol{v} = \boldsymbol{0}, \quad \nabla \cdot \boldsymbol{v} = 0, \quad \boldsymbol{n} \times (\nabla \times \boldsymbol{v}) = \boldsymbol{0}.$$

Then, we have identity

$$\int_V [(\nabla \cdot \boldsymbol{v})^2 + (\nabla \times \boldsymbol{v})^2] \mathrm{d}V = -\int_V \boldsymbol{v} \cdot \nabla^2 \boldsymbol{v} \, \mathrm{d}V + \int_{\partial B} [(\boldsymbol{n} \cdot \boldsymbol{v}) \nabla \cdot \boldsymbol{v} + (\nabla \times \boldsymbol{v}) \cdot (\boldsymbol{n} \times \boldsymbol{v})] \mathrm{d}S, \qquad (4.165)$$

where

$$(\nabla \times \boldsymbol{v}) \cdot (\boldsymbol{n} \times \boldsymbol{v}) = -[\boldsymbol{n} \times (\nabla \times \boldsymbol{v})] \cdot \boldsymbol{v} = 0 \quad \text{on} \quad \partial B.$$

Thus, the right-hand side of (4.165) vanishes, and we have both $\nabla \cdot \boldsymbol{v} = 0$ and $\nabla \times \boldsymbol{v} = \boldsymbol{0}$ (almost everywhere), indicating $\boldsymbol{v} = \nabla \phi$ for some harmonic $\phi$. But by (4.159) there must be $\partial \phi / \partial n = 0$ on $\partial B$, so $\phi =$ const. and hence $\boldsymbol{v} = \boldsymbol{0}$ in $V$. Therefore, (4.162) and (4.163) has at most one solution.

Finally, from (4.162) we have

$$\nabla(\nabla \cdot \boldsymbol{u} - \vartheta) - \nabla \times (\nabla \times \boldsymbol{u} - \boldsymbol{\omega}) = \boldsymbol{0},$$

where the two terms must be orthogonal in the inner-product space (Sect. 2.3.1) owing to (4.163b):

$$\int_V \nabla \, (\nabla \cdot \boldsymbol{u} - \vartheta) \cdot [\nabla \times (\nabla \times \boldsymbol{u} - \boldsymbol{\omega})] \mathrm{d}V = \int_{\partial B} [\boldsymbol{n} \times (\nabla \times \boldsymbol{u} - \boldsymbol{\omega})] \cdot \nabla(\nabla \cdot \boldsymbol{u} - \vartheta) \mathrm{d}S = 0.$$

Thus, it follows that

$$\nabla(\nabla \cdot \boldsymbol{u} - \vartheta) = \boldsymbol{0}, \quad \nabla \times (\nabla \times \boldsymbol{u} - \boldsymbol{\omega}) = \boldsymbol{0}.$$

This implies $\nabla \times \boldsymbol{u} - \boldsymbol{\omega} = \nabla \xi$ for some $\xi$, of which the divergence is (4.161a); then (4.163b) implies (4.161b). Similarly, we have $\nabla \cdot \boldsymbol{u} - \vartheta =$ const. in $V$, but the constant must be zero due to (4.158a). Thus, the unique solution of (4.162) and (4.153) is also that of (4.157) and (4.158), which completes the proof.

From the theorem and its proof, the following corollary (Wu et al. 1995) is evident.

**Corollary.** *If (4.158a) and (4.158b) hold, then given sufficiently smooth $\vartheta$ and $\boldsymbol{\omega}$, problem (4.162) and (4.163) has the same solution as problem (4.157) to (4.159).*

The boundary condition (4.163b) is the key choice of the entire theorem and corollary.

### 4.5.2 Boundary Vorticity–Pressure Coupling

We now turn to the dynamic aspect of the vorticity-based formulation, confined to incompressible flow with $\rho = 1$. Define an operator on $\boldsymbol{u}$:

$$\mathcal{L}(\boldsymbol{u}) = \frac{\partial \boldsymbol{u}}{\partial t} + \boldsymbol{u} \cdot \nabla \boldsymbol{u} - \nu \nabla^2 \boldsymbol{u}. \tag{4.166}$$

Then symbolically the $(\boldsymbol{u}, p)$ formulation reads

$$\mathcal{L}(\boldsymbol{u}) = -\nabla p, \quad \nabla \cdot \boldsymbol{u} = 0. \tag{4.167a,b}$$

Similar to casting problem (4.157) and (4.159) to problem (4.162) and (4.163), we take the divergence of (4.167a) and use (4.167a) itself to construct a Neumann boundary condition for $p$ to ensure the compatibility:

$$\nabla^2 p = -\nabla \cdot \mathcal{L}(\boldsymbol{u}) \quad \text{in } V, \quad \left(\frac{\partial p}{\partial n}\right)_B = -\boldsymbol{n} \cdot \mathcal{L}(\boldsymbol{u})_B \quad \text{on } \partial B, \tag{4.168a,b}$$

where suffix $B$ means values on $\partial B$. Then, the dynamic $(\boldsymbol{\omega}, \boldsymbol{u})$ formulation is based on the curl of (4.166), for which we impose a *dynamic* boundary condition also constructed from (4.167a):

$$\nabla \times \mathcal{L}(\boldsymbol{u}) = \boldsymbol{0} \quad \text{in } V, \quad \boldsymbol{n} \times \mathcal{L}(\boldsymbol{u})_B = -\boldsymbol{n} \times \nabla p_B \quad \text{on } \partial B. \tag{4.169a,b}$$

Of course the dynamic process must be solved along with the kinematic problem, say (4.162) and (4.163) with $\vartheta = 0$. In (4.168b) and (4.169b) the acceleration no-through and no-slip conditions, (2.70a) and (2.70b), are imposed respectively. As quantities one-order higher than velocity, *the dynamic boundary conditions for the vorticity and pressure gradient match naturally the acceleration adherence*, which makes the boundary conditions and compatibility condition merge into one. This does reflect the correct physics, since as shown in Sects. 4.1.3 and 4.1.4 the acceleration adherence determines the vorticity creation (and "pressure creation") from the boundary.

Wu et al. (1994b) have proved that, after raising the equation's order, due to the viscous boundary $(\boldsymbol{\omega}, p)$ coupling, solving the pressure differential equation (4.168a) needs the satisfaction of the vorticity differential equation (4.169a) as a prerequisite, and vice versa. It is this boundary $(\boldsymbol{\omega}, p)$ coupling that causes the basic difficulty of the vorticity formulation, for which we now make a further observation.

Recall that the velocity adherence imposes a *kinematic integral constraint* to the possible $\boldsymbol{\omega}$-distribution, obtained by applying the generalized Biot–Savart formula (3.27) to the boundary. To match this fact, dynamically one should also cast the vorticity transport equation (2.168) to an integral representation. For neatness assume that the solid boundary $\partial B$ is stationary. Then by (3.23) and using the notation there, we have

$$\boldsymbol{\omega}(\boldsymbol{x},t)=\int_V G_0^*\boldsymbol{\omega}_0\,\mathrm{d}V'+\int_0^t \mathrm{d}t'\oint_{\partial B}\left(G^*\boldsymbol{\sigma}-\nu\boldsymbol{\omega}_{\mathrm{B}}\frac{\partial G^*}{\partial n}\right)\mathrm{d}S'$$
$$+\int_0^t \mathrm{d}t'\int_V \nabla G^*\times(\boldsymbol{\omega}\times\boldsymbol{u})\mathrm{d}V', \tag{4.170}$$

where $\boldsymbol{\omega}_{\mathrm{B}}$ and $\boldsymbol{\sigma}$ are the boundary vorticity and its flux. Now the boundary $(\boldsymbol{\omega},p)$ coupling appears via $\boldsymbol{\sigma}$, see (4.24b). Evidently, as long as a boundary-dependent Green's function $\widehat{G}^*$ with $\widehat{G}^*=0$ on $\partial B$ can be found, the coupling will be removed and an *integral-type Dirichlet boundary-value problem* for the vorticity follows:

$$\boldsymbol{\omega}(\boldsymbol{x},t)=\int_V \widehat{G}_0^*\boldsymbol{\omega}_0\,\mathrm{d}V'-\int_0^t \mathrm{d}t'\oint_{\partial B}\nu\boldsymbol{\omega}_{\mathrm{B}}\frac{\partial\widehat{G}^*}{\partial n}\mathrm{d}S'$$
$$+\int_0^t \mathrm{d}t'\int_V \nabla\widehat{G}^*\times(\boldsymbol{\omega}\times\boldsymbol{u})\mathrm{d}V'. \tag{4.171}$$

This equation, along with the Biot–Savart formula, shows that *in its strict nature the vorticity boundary condition for a viscous flow can only be of global type.*

Because conducting integrations with known Green's function does not need grid, (4.171) has served as a basis of some advanced *grid-free vortex methods* (e.g., Cottet and Koumoutsakos 2000), where the nonlinear advection represented by the last integral of (4.171) is also made grid-free by using fractional-step approach (see Sect. 4.5.3) and Lagrangian algorithm. However, finding a boundary-dependent Green's function $\widehat{G}^*$ for complicated boundaries, especially in three dimensions, is a difficult task. An alternative approach is to stay with differential formulation, but seek an approximate *local* vorticity boundary condition without coupling with $p$. We present such an approach later.

### 4.5.3 A Locally Decoupled Differential Formulation

The key issue of locally decoupled differential formulation is to estimate the strength of the coupling, dominated by the Reynolds number. For Stokes flows it is very strong, see the remark following (4.55a,b). But, in boundary layer theory at large $Re$ it vanishes approximately; the pressure is completely determined by the external Euler flow with an error of $O(Re^{-1})$, see (4.85b). This observation not only strongly suggests that the decoupling of $\boldsymbol{\omega}$ and $p$ is possible for arbitrary (not only attached) viscous flows at large $Re$, but also provides a clue to developing a general and rational approach that can lead to the desired decoupled approximation: splitting the Navier–Stokes equation into an Euler equation under the no-through condition, and an unsteady Stokes equation under the no-slip condition. Denoting the corresponding quantities by suffices $e$ and $s$, respectively, we then have

$$\frac{\partial \boldsymbol{u}_\mathrm{e}}{\partial t} + \boldsymbol{u}_\mathrm{e}\cdot\nabla\boldsymbol{u}_\mathrm{e} + \nabla p_\mathrm{e} = \boldsymbol{0}, \qquad \boldsymbol{n}\cdot\boldsymbol{u}_\mathrm{e} = 0 \quad \text{on} \quad \partial B, \tag{4.172a}$$

$$\frac{\partial \boldsymbol{u}_\mathrm{s}}{\partial t} + \nabla p_\mathrm{s} = \nu\nabla^2\boldsymbol{u}_\mathrm{s}, \quad \boldsymbol{n}\times\boldsymbol{u}_\mathrm{s} = \boldsymbol{0} \quad \text{on} \quad \partial B. \tag{4.172b}$$

Numerically, this splitting implies solving (4.172a) and (4.172b) successively within each time step $\Delta t$ rather than simultaneously. Physically, one conceives that during the Euler substep a slip velocity $\boldsymbol{u}_\mathrm{slip}$ of $O(\Delta t)$ is developed, which, once entering the Stokes substep with the no-slip condition turned on, becomes a newly created vortex sheet with strength $\boldsymbol{\gamma} = \boldsymbol{u}_\mathrm{slip}\times\boldsymbol{n}$, which is then diffused into the flow (Lighthill 1963). It has been rigorously proved that such a *fractional-step* approach converges to the true physics (the Navier–Stokes solution) as $\Delta t \to 0$, and for finite $\Delta t$ the error is of $O(\nu\Delta t)$ (Ying 1992; Beale and Greengard 1992). Corresponding to (4.172), the Helmholtz equation (2.168) is split to

$$\frac{\partial \boldsymbol{\omega}_\mathrm{e}}{\partial t} + \nabla\times(\boldsymbol{\omega}_\mathrm{e}\times\boldsymbol{u}_\mathrm{e}) = \boldsymbol{0}, \tag{4.173a}$$

$$\frac{\partial \boldsymbol{\omega}_\mathrm{s}}{\partial t} - \nu\nabla^2\boldsymbol{\omega}_\mathrm{s} = \boldsymbol{0}. \tag{4.173b}$$

Since the vorticity boundary condition is not needed at all in the Euler substep (Sect. 3.2.2), $\boldsymbol{\omega}_\mathrm{e}$ *is completely decoupled from* $p_\mathrm{e}$.[13]

Note that because the inviscid equations for $\boldsymbol{u}$ and $\boldsymbol{\omega}$ are nonlinear, in the above splitting $\boldsymbol{u} \neq \boldsymbol{u}_\mathrm{e}+\boldsymbol{u}_\mathrm{s}$ and $\boldsymbol{\omega} \neq \boldsymbol{\omega}_\mathrm{e}+\boldsymbol{\omega}_\mathrm{s}$. In contrast, the pressure equation (4.168a) is linear and one simply has $p = p_\mathrm{e} + p_\mathrm{s}$. Since $p_\mathrm{e}$ is completely decoupled from $\boldsymbol{\omega}_\mathrm{e}$, it takes care of the inhomogeneity of the equation. Then $p_\mathrm{s}$ takes care of the inhomogeneity of the boundary condition. Thus, the correct boundary-value problems for $p_\mathrm{e}$ and $p_\mathrm{s}$ are

$$\nabla^2 p_\mathrm{e} = -\nabla\cdot(\boldsymbol{u}\cdot\nabla\boldsymbol{u}) \quad \text{in } V, \quad \frac{\partial p_\mathrm{e}}{\partial n} = 0 \quad \text{on } \partial B, \tag{4.174a}$$

$$\nabla^2 p_\mathrm{s} = 0 \quad \text{in } V, \quad \frac{\partial p_\mathrm{s}}{\partial n} = -\nu(\boldsymbol{n}\times\nabla)\cdot\boldsymbol{\omega} \quad \text{on } \partial B. \tag{4.174b}$$

One may immediately recognize that problem (4.174b) is nothing but (2.100). The larger the Reynolds number is, the more dominant will $p_\mathrm{e}$ be and the weaker the boundary $(\boldsymbol{\omega}, p)$ coupling.

Now since the boundary coupling remains only between $\boldsymbol{\omega}_\mathrm{sB}$ and $p_\mathrm{sB}$, it will be weak if $p_\mathrm{sB}$ is small. To estimate $p_\mathrm{sB}$ we cast (4.174b) to the integral formulation in terms of free-space Green's function $G$:

$$\alpha p_\mathrm{s}(\boldsymbol{x}_\mathrm{B}) = -\mathrm{pv}\int_{\partial B}\nabla G_\mathrm{B}\cdot(\boldsymbol{n}p_\mathrm{sB} + \boldsymbol{n}\times\nu\boldsymbol{\omega}_\mathrm{B})\mathrm{d}S', \quad \boldsymbol{x}_\mathrm{B}\in\partial B. \tag{4.175}$$

[13] It is here that the grid-free Lagrangian vortex methods exhibit most of their strength. See, e.g., Gustafson and Sethian (1991) and Cottet and Koumoutsakos (2000).

Here, taking the Cauchy principal value leads to the factor $\alpha$ depending on the solid angle at each boundary point; for smooth $\partial B$ one has $\alpha = 1/2$. Now, we know $\boldsymbol{\omega}_{\mathrm{B}} = O(Re^{1/2})$ for $Re \gg 1$, and hence the linearity of (4.175) ensures that globally there must be $p_{\mathrm{sB}} = O(Re^{-1/2})$, which in turn implies that neglecting the $(\boldsymbol{\omega}_{\mathrm{s}}, p_{\mathrm{s}})$ coupling will bring an error of that order. This estimate may have a local change in the neighborhood of a separation line or sharp edge, but since in (4.175) $p_{\mathrm{sB}}$ affects $\boldsymbol{\omega}_{\mathrm{B}}$ through a surface integral, the $Re^{-1/2}$-dependence is a correct overall estimate.

We are now ready to find a local decoupled Neumann condition for the vorticity. To this end we estimate the boundary vorticity flux $\boldsymbol{\sigma}$ during one time step $\Delta t \ll 1$. First, the Euler substep (4.173a) generates an attached vortex sheet $\boldsymbol{\gamma} = \boldsymbol{u}_{\mathrm{slip}} \times \boldsymbol{n}$ as a result of the *driving force* $\nabla p_{\mathrm{e}} = O(1)$. It serves as the initial condition for (4.173b). As a specification of the symbolic condition (4.169b), we then apply (4.172b) to $\partial B$ and obtain

$$\boldsymbol{\sigma} = \boldsymbol{n} \times \frac{\partial \boldsymbol{u}_{\mathrm{s}}}{\partial t} + \boldsymbol{\sigma}_{\mathrm{sp}} + \boldsymbol{\sigma}_{\mathrm{svis}}, \tag{4.176}$$

where $\boldsymbol{\sigma}_{\mathrm{sp}}$ and $\boldsymbol{\sigma}_{\mathrm{svis}}$ are the boundary vorticity fluxes due to $p_{\mathrm{sB}}$ and $\boldsymbol{\omega}_{\mathrm{sB}}$, respectively, see (4.24b). Since $p_{\mathrm{s}}$ has a viscous origin, both $\boldsymbol{\sigma}_{\mathrm{sp}}$ and $\boldsymbol{\sigma}_{\mathrm{svis}}$ belong to the viscous part of $\boldsymbol{\sigma}$. Integrating (4.176) over $\Delta t$ and requiring that the resulted $\boldsymbol{\sigma}$ must ensure no-slip at $t = \Delta t$, there is

$$\overline{\boldsymbol{\sigma}} = \frac{\boldsymbol{\gamma}}{\Delta t} + \overline{\boldsymbol{\sigma}}_{\mathrm{sp}} + \overline{\boldsymbol{\sigma}}_{\mathrm{svis}}, \tag{4.177}$$

where overline means time-average. The first term on the right is the singular part of $\boldsymbol{\sigma}$ caused by advection, and the rest is the regular part caused by pure diffusion that contains the boundary $(\boldsymbol{\omega}_{\mathrm{s}}, p_{\mathrm{s}})$ coupling.

Then, since at the end of the Stokes substep the no-slip condition should be satisfied, there is $|\boldsymbol{\gamma}|/\Delta t = O(1)$. On the other hand, we have determined $p_{\mathrm{sp}} = O(Re^{-1/2})$; and, because $\boldsymbol{n} \times \nabla$ is a tangent differential operator of $O(1)$, $\boldsymbol{\sigma}_{\mathrm{svis}}$ should be of the same order as $\nu\boldsymbol{\omega}_{\mathrm{sB}}$. Therefore, $|\overline{\boldsymbol{\sigma}}_{\mathrm{sp}}|$, $|\overline{\boldsymbol{\sigma}}_{\mathrm{svis}}|$, and $\nu|\boldsymbol{\omega}_{\mathrm{B}}|$ are all of $O(Re^{-1/2})$, so (4.177) leads to a *decoupled approximation* (Wu et al. 1994b)

$$\boldsymbol{\sigma} = \frac{\boldsymbol{\gamma}}{\Delta t} + O(Re^{-1/2}). \tag{4.178}$$

Numerical tests have shown that (4.178) has higher accuracy than the corresponding local decoupled approximations of the Dirichlet condition, of which a commonly used fomathrmis

$$\Delta\boldsymbol{\omega}_{\mathrm{B}} \simeq \frac{\boldsymbol{\gamma}}{h}, \tag{4.179}$$

where $h$ is a chosen small normal diffusive distance, say $\sqrt{\pi\nu\Delta t}$.

Note that due to dropping the $O(Re^{-1/2})$-order regular part of (4.177), at the end of Stokes substep there may appear a residual slip velocity. If necessary, this can be effectively eliminated by a simple iteration procedure.

However, compared to those schemes which impose global vorticity boundary conditions (e.g., Wang and Wu 1986), an inevitable expense of the localized condition (4.178) is that the time step must be small.

Finally, once the $(\boldsymbol{\omega}, \boldsymbol{u})$ problem is solved, the pressure can be computed by solving (4.168a,b) or using integral-type formulation again, which for known Green's function can also be grid-free. But, in practice one's main concern is the pressure force on $\partial B$ only; in this case $p_{\mathrm{B}}$ can be simply obtained by integrating $\boldsymbol{\sigma}_{\mathrm{p}}$ over $\partial$B from a reference point with known $p_{\mathrm{B}}$.

Based on the above theoretical analysis, Wu (1994) developed a fractional finite-difference scheme with the approximate local Neumann condition (4.178) for both two- and three-dimensional flows, using $(\omega, \psi)$ and $(\boldsymbol{\omega}, \boldsymbol{u})$ as variables, respectively. As illustration, we show some two-dimensional numerical results that confimathrmthe efficiency and accuracy of the decoupling approximation, in particular the ability of accurately capturing the boundary vorticity (and hence skin friction) and its flux in complicated separated flows.

The first example is the flow over an impulsively started circular cylinder, for which the very careful experimental results at the Reynolds number based on cylinder radius up to 9,500 (Bouard and Coutaneau 1980) can be used for comparison. The scheme is of second order in space and first-order splitting in time. In the computation a grid of $7.7 \times 10^4$ (stretched in the radial direction) and time step 0.0025 for $Re = 9,500$ were used, and the computation was conducted on a workstation.

Figure 4.24 shows the computed flow pattern compared with experiment, which is however not critical; many schemes can produce almost the same flow patterns but only a few can predict the boundary vorticity or skin friction accurately. Figure 4.25 and 4.26 are the computed $\omega_{\mathrm{B}}$ and $\sigma$. The violent oscillations in the plots are due to separated vortices. The result is in good agreement with that of Anderson and Reider (1996) and Koumoutsakos and Leonard (1995). The former used a finite-difference scheme of fourth-order in both space and time, performed on a supercomputer with a uniform grid of $5 \times 10^5$ and time step $\Delta t = 3.3 \times 10^{-4}$. The latter used a grid-free deterministic vortex method to reach about the same accuracy as Anderson and Reider's, also performed on a supercomputer. In this scheme the dynamic Neumann condition for vorticity was employed, the time step for $Re = 9,500$ was 0.01, and the particle number increases as time, up to more than $10^6$ at $t = 6$. Both schemes by Anderson and Reider and by Koumoutsakos and Leonard retained the global nature of vorticity boundary condition. It is remarkable that the low-order differencing and a simple use of (4.178) on a coarse grid can already catch $\omega_{\mathrm{B}}$ and $\sigma$ satisfactorily.

Wu et al. (1994b) also tested the error estimate in (4.178), finding that for this cylinder-flow example it approaches almost exactly $Re^{-1/2}$ as $Re$ increases. In fact, Wu (1994) has constructed a nonfractional-step scheme where this error can well be removed; see also Wu et al. (1995). But this would be unable obtaining the boundary vorticity flux as a direct output.

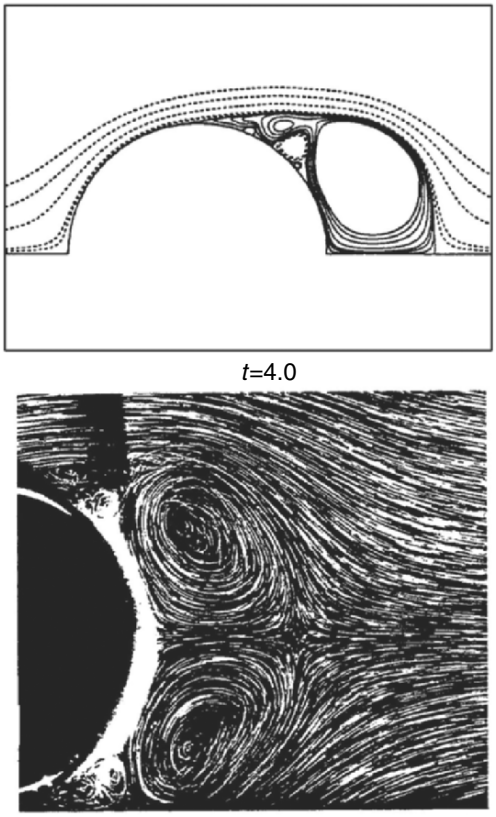


**Fig. 4.24.** Comparison of the computation of Wu et al. (1994b) and flow visualization of Bouard and Coutaneau (1980) on the flow patterns of an impulsively started flow over a circular cylinder at $Re = 9,500$ and $t = 4.0$

In two dimensions the local Neumann condition (4.178) contains *no* mechanism to ensure the conservation of total circulation (3.16), which is crucial when one computes an airfoil flow, say, with nonzero and variable circulation. A local approximation of the constraint imposed to $\sigma$ by this total-circulation conservation has been built into a generalized version (called CSOLVER) of the above frational-step scheme by Zhu (2000).

Figures 4.27 and 4.28 demonstrate the airfoil flows computed by CSOLVER (a one-equation turbulence model due to Spalart and Allmaras (1992) was used), compared with both experiment and the prediction of detached-eddy simulation (DES, see Shur et al. 1998), which combines the large-eddy simulation (LES) and Reynolds-averaged Navier–Stokes (RANS) computation and has to include the three-dimensional effect of the turbulence. The agreement with experiments and DES computation is good up to the stall angle, beyond which the accuracy of the turbulence model can hardly be judged.

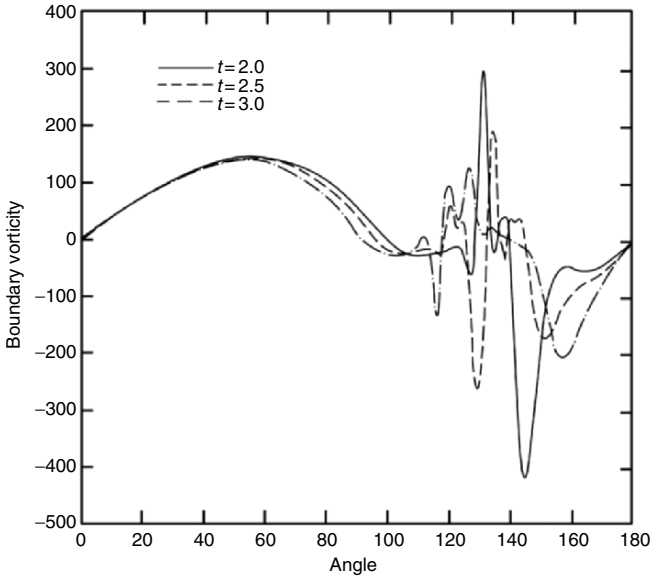


**Fig. 4.25.** Boundary vorticity of the same flow as in Fig. 4.23. Based on X.H. Wu (1994)

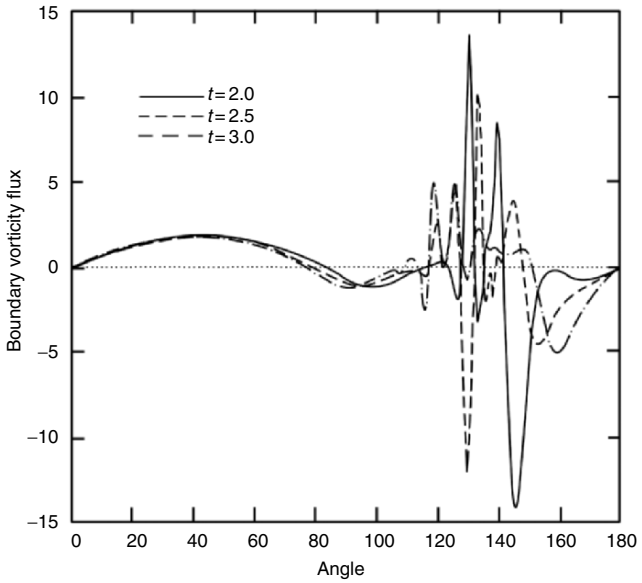


**Fig. 4.26.** Boundary vorticity flux of the same flow as in Fig. 4.23. Based on X.H. Wu (1994)

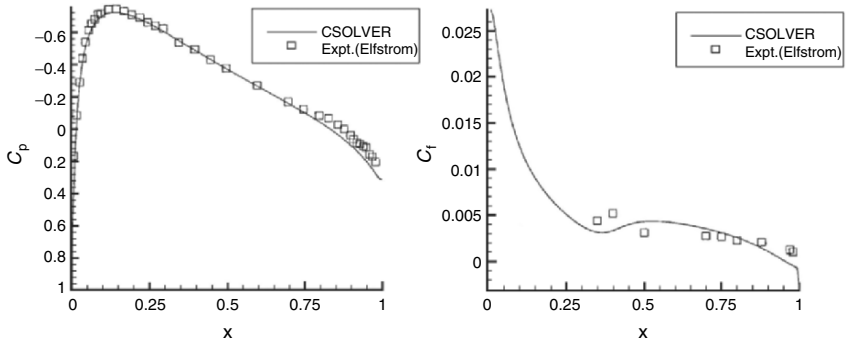


**Fig. 4.27.** Distribution of pressure and skin-friction coefficients over a NACA 0020 airfoil at $Re = 5 \times 10^6$ and $\alpha = 0°$. Comparison of numerical result and experiment. From Zhu (2000)

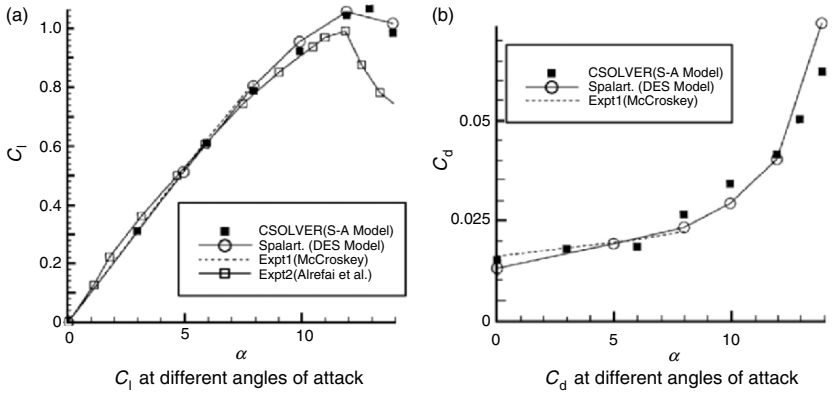


**Fig. 4.28.** Lift and drag coefficients of a NACA 0012 airfoil versus angle of attack at $Re = 10^5$. Comparison of numerical result with experiments and DES simulation. From Zhu (2000)

### 4.5.4 An Exact Fully Decoupled Formulation

The preceding analysis reveals that the vorticity–pressure coupling at boundary via the Navier–Stokes equation is the root of the trouble in formulating the vorticity boundary condition. A natural way to completely bypass this boundary coupling is to further raise the order of the governing equations by taking the curl of the vorticity transport equation

$$\left(\frac{\partial}{\partial t} - \nu\nabla^2\right)\boldsymbol{\omega} = \nabla \times \boldsymbol{l}_\perp, \quad \boldsymbol{l}_\perp = (\boldsymbol{\omega} \times \boldsymbol{u})_\perp, \tag{4.180}$$

where as before $(\cdot)_\perp$ denotes the transverse part with $(\cdot)_\perp \cdot \boldsymbol{n} = 0$ at boundary (assume stationary later). The curl of (4.180) yields a fourth-order equation

for $\boldsymbol{u}$:

$$\left(\frac{\partial}{\partial t} - \nu\nabla^2\right)\nabla^2\boldsymbol{u} = -\nabla^2\boldsymbol{l}_\perp. \tag{4.181}$$

Because of taking curl, a component equation of (4.180) and that of (4.181) *along the same direction* must be independent. For example, in a Cartesian coordinate system the $y$-component of (4.180) takes care of the flow in the $(x, z)$-plane, while that of (4.181) represents the flow along the $y$-direction. Consequently, the $y$-components of (4.180) and (4.181), along with the incompressibility condition and vorticity definition, fomathrma complete description of the flow field:

$$\left(\frac{\partial}{\partial t} - \nu\nabla^2\right)\omega_y = -(\nabla \times \boldsymbol{l}_\perp)_y \tag{4.182a}$$

$$\left(\frac{\partial}{\partial t} - \nu\nabla^2\right)\nabla^2 v = -\nabla^2 l_{\perp y}, \tag{4.182b}$$

$$\frac{\partial u}{\partial x} + \frac{\partial w}{\partial z} = -\frac{\partial v}{\partial y}, \tag{4.182c}$$

$$\frac{\partial u}{\partial z} - \frac{\partial w}{\partial x} = \omega_y. \tag{4.182d}$$

It is convenient to choose the $y$-axis normal to the boundary, say at $y = 0$, so that the velocity adherence can be explicitly imposed, which due to (4.182c,d) is fully reflected by

$$v = \frac{\partial v}{\partial y} = \omega_y = 0 \quad \text{at} \quad y = 0. \tag{4.183}$$

The boundary at the other side may be another solid wall as in a channel flow, or extends to infinity as in a boundary layer. The boundary conditions there is easily expressed as well, and then the problem is well-posed.

Essentially, (4.182) and (4.183) is the lowest-order formulation where the pressure is completely removed from both differential equations and boundary conditions. It demonstrates that *for incompressible flow the shearing (transverse) process alone can be solved without any involvement of the compressing (longitudinal) process*. This advantage has made the formulation convenient for studying incompressible flow bounded by flat walls. In particular, the formulation has been the basis of the classic shear-flow stability theory and the direct numerical simulation (DNS) of turbulent channel flow (Chap. 9). In the linear stability problem of parallel shear flow, one assumes the velocity and vorticity

$$\boldsymbol{u} = (U(y), 0, 0) + (u, v, w), \quad \boldsymbol{\omega} = (0, 0, -U'(y)) + (\xi, \eta, \zeta),$$

with lower-case components denoting disturbance. Then the linearized-disturbance version of (4.182a) and (4.182b) is well known (Thomson 1883;

Squire 1933) and will be discussed in Sect. 9.2.1:

$$\nabla^2 \frac{\partial v}{\partial t} + U\nabla^2 \frac{\partial v}{\partial x} - U'' \frac{\partial v}{\partial x} - \frac{1}{Re}\nabla^4 v = 0, \tag{4.184a}$$

$$\frac{\partial \eta}{\partial t} + U\frac{\partial \eta}{\partial x} + U' \frac{\partial v}{\partial z} - \frac{1}{Re}\nabla^2 \eta = 0. \tag{4.184b}$$

On the other hand, for DNS of turbulent channel flow, (4.182) is convenient especially when the boundary condition at $x$ and $z$ directions can be assumed periodic so that the *spectral method* can be applied. Then (4.182c) and (4.182d) are simplified to algebraic equations in spectral space that ensure the solenoidal condition for $\boldsymbol{u}$ and $\boldsymbol{\omega}$. Hence, only two scalar equations (4.182a) and (4.182b) are to be solved. This formulation has been used to obtain the first DNS result of turbulent channel flow by Kim et al. (1987), see also Sect. 9.2.4.

## Summary

1. Kinetics enters vorticity evolution through the vorticity diffusion vector $\nabla \times \boldsymbol{a}$, which comes from the effects of nonconservative body force, such as in rotating fluids and magnetohydrodynamics; baroclinicity, such as in density-stratified flow and non-isentropic flow; and viscosity. A nonzero $\nabla \times \boldsymbol{a}$ makes the flow no longer circulation-preserving and become history-dependent, where the vorticity can be created or eliminated.
2. Due to its universal existence in various fluids, the viscosity plays a crucial role in the evolution of vorticity field, including vorticity diffusion, dissipation, and creation at boundaries. For incompressible flow of uniform density without nonconservative body force, the no-slip condition at boundaries is the only source of vorticity in the whole flow field. The created new vorticity is diffused into the fluid, of which the rate is measured by the boundary vorticity flux. This flux joins the tangential momentum balance at the boundary, and hence can be caused by the tangent components of boundary acceleration, external body force, and pressure gradient, plus a three-dimensional viscous interaction. The boundary vorticity flux has important applications in the diagnosis of flow separation (Sect. 5.3.4) and aerodynamic configuration design (Sect. 11.4), in developing vorticity-based numerical methods (Sect. 4.5.3), and in flow control.
3. The key dimensionless parameter governing the dynamic evolution of a viscous vorticity field is the Reynolds number $Re$. The coupling between shearing and compressing processes is progressively weakened as $Re$ increases. At small $Re$ the vorticity diffusion prevails over its advection, as in a Stokes flow, with the strongest shearing-compressing coupling. For this flow a match of near-field Stokes approximation and far-field Oseen approximation yields a uniformly effective approximation. A two-term Oseen

approximation permits an analytical examination of the flow-separation mechanism based on vorticity dynamics.

4. At the opposite extremum when advection dominates the flow, vorticity is confined to narrow regions of which the simplest case is attached boundary layers adjacent to solid wall, interface, or free surface. These attached thin vortex layers are approximately described by boundary-layer theory, within which the shearing and compressing are decoupled and only the former needs to be solved. A unique feature of interfacial or free-surface boundary layer is that the surface-deformation process plays a crucial role and is coupled with both compressing process (as a viscous correction) and shearing process (to completely determine the surface vorticity).
5. As $Re \to \infty$ in a viscous fluid, the attached and free vortex layers can be further approximately described by vortex-sheet dynamics. Except for certain special cases such as closed flow, away from the sheets the flow is irrotational and governed by the Euler equation.

   Of course, to the earlier aspects one should immediately add that at large $Re$ the hydrodynamic instability, transition, and turbulence are all inevitable. These topics will be addressed in Chaps. 9 and 10.
6. The vorticity-based formulation of viscous flow aims at solving the shearing (transverse) process alone, without any involvement of the compressing (longitudinal) process. So far the success has been confined to incompressible flow. The advantages and disadvantages of this formulation are just complementary to those of the common velocity–pressure formulation. A key issue in vorticity-based formulation is to bypass the boundary coupling between the vorticity and pressure, which can be done by integral formulation, local fractional-step approach, or going into higher-order equations by taking double curls of the momentum equation.

# 5

# Vorticity Dynamics in Flow Separation

In the whole life of a vortical flow, if the first milestone is the generation of vorticity from a solid wall by the no-slip condition (Sect. 4.1.3) and the formation of attached shear flow (which appears as boundary layer at large Reynolds numbers), then the second milestone is *flow separation* which very often (not always) results in *separated flow*. These notions are closely related, but the former is a *local* process of the transition from attached flow to detached flow, while the latter concerns a *global* flow development after separation occurs. We defer the discussion of separated flow to Chap 7.

## 5.1 Flow Separation and Boundary-Layer Separation

In Sect. 4.2.3 we met an example of flow separation at small Reynolds numbers, while in Sect. 4.4.3 we revisited the subject at the opposite extreme of infinite Reynolds number. This chapter considers the general situation at finite and typically large Reynolds numbers. Before going into details, it is necessary to distinguish the general concept of flow separation and its subclass *boundary-layer separation*, since they will be treated by different theories.

Flow separation has been a quite vague concept.[1] In this book we define it as the process that fluid elements adjacent to the wall no longer move along the wall but turn into the interior of the fluid. The definition does not care how deep the "interior" could be. To study flow separation, therefore, one examines the flow behavior in an *infinitesimal neighborhood* of a *separation point* (in two dimensions) or a *separation line* (in three dimensions). This is precisely the approach that has led to the well-known *separation criteria* for two- and three-dimensional steady flows, due to Prandtl (1904) and Lighthill (1963) and others, respectively. Referring to the velocity and vorticity profiles before and after separation shown in Fig. 4.12, in two dimensions the separation

[1] Due to this vagueness, in literature it is often confused with boundary-layer separation, a situation partially responsible for some controversies.

point $x_s$ on a flat wall can be characterized by the special behavior of the skin friction $\tau_w$ or boundary vorticity:

$$\tau_w(s) = \mu u_{,y}(s) = -\mu\omega(s) = 0, \tag{5.1a}$$

$$\tau_{w,x}(s) = \mu u_{,xy}(s) = -\mu\omega_{,x}(s) < 0, \tag{5.1b}$$

where the inequality ensures $\tau_w$ changes sign across $x_s$. The flows from both sides of $x_s$ are divided by a unique *separation stream line* initiating from $x_s$, which serves as the skeleton of the separated shear later. Thus, $x_s$ appears as a *semiseddle point* (see Sect. 7.1 later). Equations (5.1a) and (5.1b) are Prandtl's local criteria expressed by *on-wall signatures* at $x_s$ and sufficient to describe a steady separation.

Three-dimensional flow separation is more complicated. Figure 5.1 shows a numerical visualization of fluid particle traces in a laminar flow over an 1:2 prolate spheroid at incidence $\alpha = 30°$ and $Re = 3.5 \times 10^4$ (based on the length of the short axis). One sees two separated free vortex layers rolling into concentrated vortices of opposite rotating directions. The upper vortex is from the primary separation, which induces a secondary separation that leads to the lower vortex.

Focusing on the process of flow separation, from Fig. 5.1 we may first identify two *separation zones* on the wall. Unlike (5.1a), in the major portion of both zones there is $\boldsymbol{\tau}_w \neq \mathbf{0}$. As the extension of two-dimensional separation, inside each zone there exists a *separation line* as the skeleton of the zone, from which initiates a unique *separation stream surface* as the skeleton of the separated free vortex layer. Since the separation line is the intersection of the separation stream surface and the wall, it must be a special skin-friction line ($\boldsymbol{\tau}$-line for short). To understand how separation happens, let $l$ be the

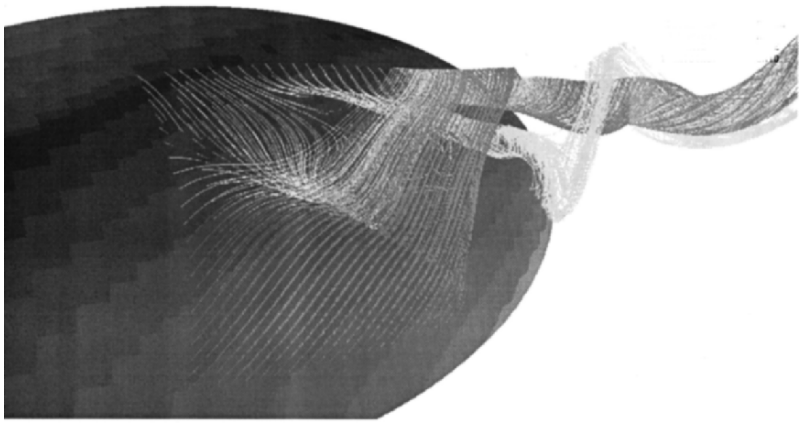

**Fig. 5.1.** A three-dimensional flow separation and separated flow from a prolate spheroid at incidence. From Wu et al. (2000)

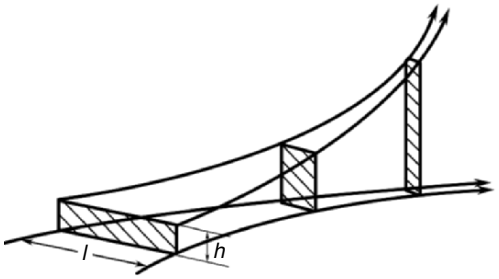


**Fig. 5.2.** Three-dimensional flow separation may follow from $\boldsymbol{\tau}$-line converging

distance of two $\boldsymbol{\tau}$-lines, above which we consider a flow tube of rectangular cross-section $l \times h$ with mean velocity $\overline{u}$ and mass flux $\rho hl\overline{u}$, see Fig. 5.2. Let $x_3$ be the normal coordinate from the wall. For sufficiently small $h$ the velocity profile is linear, yielding $\partial u/\partial x_3 = 2\overline{u}/h$ and $\tau = 2\mu\overline{u}/h$ or $\overline{u} = \tau h/(2\mu)$. Thus, since the mass flux $\rho hl\overline{u} = h^2 l\tau/2\nu$ must be constant, one obtains (Lighthill 1963)

$$h = C\left(\frac{\nu}{l\tau}\right)^{1/2}. \tag{5.2}$$

Therefore, $h$ will grow unboundedly not only as $\tau \to 0$ as is in two-dimensional case, but also as $l \to 0$. Namely, *$\boldsymbol{\tau}$-lines converging* toward each other causes an *upwelling* of the fluid as seen in Fig. 5.1. This and other similar criteria serve as either *separation warning* to pinpoint its location and special behavior, or *separation watch* to tell it is about to happen. These criteria are very useful in flow diagnosis and control. Mathematically, to study a flow separation in an infinitesimal neighborhood of a separation point or line, a Taylor expansion of the Navier–Stokes equations around that point or line is sufficient.

The flow-separation process may have different strengths and consequences. We say a *strong separation* if it causes *separated vortical flow* to be addressed in Chap. 7. We have already seen this situation in Sect. 4.2.3, where the flow separates at small Reynolds numbers to form stationary vortex bubbles with distributed vorticity. But a far more important strong separation is the *boundary-layer separation* at large Reynolds numbers, a concept introduced by Prandtl (1904) in the same seminal conference lecture in which the boundary layer theory was established. When a boundary-layer separation happens, the whole layer no longer moves along the wall but turns into the main stream and thereby alters the global flow field. This is one's main concern in engineering applications. Other weaker consequences of flow separation may exist, for example a very thin recirculation zone may develop underneath the main portion of the boundary layer but the entire layer remains attached. Or, the boundary layer instability may cause small-scale separation which leads to the formation of small vortices as observed in transition to turbulence, and

these vortices evolve to the coherent structures in turbulent boundary layer (Chap. 10).[2] In these cases the global feature of the outer flow is unchanged.

The local criteria of flow separation, such as (5.1) and its three-dimensional counterpart to be addressed later, are necessary but insufficient for fully describing strong or boundary-layer separation, since they cannot tell whether or not the whole layer will blow up. The characteristic length scale of the transition process from attached to detached vortex layer is the boundary-layer thickness $\delta = O(Re^{-1/2})$ along the normal, and another small scale $\delta^k$ along the wall ($k > 0$, to be determined later). To study boundary-layer separation in two dimensions, therefore, one has to consider the behavior of the vortex layer in a small but *finite* local region of $O(\delta \times \delta^k)$. This behavior can be obtained from either the full Navier–Stokes solution or proper approximate theory locally effective in the region. This is much more complicated than a Taylor expansion, especially when the flow is unsteady. Nevertheless, as will be seen, the flow separation theory provides a basis for the study of boundary-layer separation; and, in the Euler limit with $\delta \to 0$, the boundary-layer separation degenerates to the formation of free vortex sheet studied in Sect. 4.4.2. Note that the local theories alone, either in an infinitesimal neighborhood for flow separation or in a small but finite region for boundary-layer separation, cannot fully determine the global flow behavior. The goal of these local theories is to gain a clear physical understanding of what happens, and why, in the regions.

The theories of generic steady three-dimensional flow separation and steady boundary-layer separation in two and three dimensions are introduced in Sects. 5.2 and 5.3, respectively. In Sect. 5.4 we consider two-dimensional unsteady separation, including both theories of boundary-layer separation and generic flow separation. Throughout this chapter the flow is assumed incompressible and the solid wall is stationary. The emphasis will be the relevance of vorticity and vortex dynamics. Flow separation may also occur at free surface, for which the reader is referred to Lugt (1996) and references therein.

## 5.2 Three-Dimensional Steady Flow Separation

Like (5.1), Lighthill's hureristic argument on three-dimensional flow separation should be cast to a local quantitative theory in terms of the "roots" and "footprints" of vorticity dynamics on an arbitrary curved wall. Here we follow basically the formulation of Wu et al. (2000) but with renewed interpretation motivated by the very recent exact theory of Surana et al. (2005a) for three-dimensional steady separation of incompressible and compressible flow. This theory is based on *nonlinear invariant manifold theory*, of which a systematic presentation lies beyond the scope of this book. Thus, only some of its selected results will be briefly mentioned.

[2] Although the appearance of these coherent structures is random, each individual small-scale local separation process is still deterministic.

### 5.2.1 Near-Wall Flow in Terms of On-Wall Signatures

In this subsection we set up a general framework for developing the local flow separation theory solely in terms of on-wall flow signatures. On an arbitrarily curved stationary wall $\partial B$, let $\widehat{\boldsymbol{n}}$ be the unit normal of the wall pointing out of the solid and, as before, the suffix $\pi$ denote tangent components of any vector. For neatness set $\rho = 1$. Then, two pairs of orthogonal on-wall vector fields are of fundamental importance. The first pair is the $\boldsymbol{\tau}_w$-field and the boundary vorticity field $\boldsymbol{\omega}_{\mathrm{B}}$ related by (2.151b),

$$\boldsymbol{\tau}_w = \mu \boldsymbol{\omega}_{\mathrm{B}} \times \widehat{\boldsymbol{n}}, \quad \mu \boldsymbol{\omega}_{\mathrm{B}} = \widehat{\boldsymbol{n}} \times \boldsymbol{\tau}_w. \tag{5.3}$$

The second pair is $\nabla_\pi p$ and $\boldsymbol{\sigma}_p$ related by (4.24b):

$$\nabla_\pi p = \widehat{\boldsymbol{n}} \times \boldsymbol{\sigma}_p, \quad \boldsymbol{\sigma}_p = -\widehat{\boldsymbol{n}} \times \nabla p. \tag{5.4}$$

At large $Re$, $\boldsymbol{\sigma}_p$ dominates the entire boundary vorticity flux. Owing to (5.3) and (5.4), the analysis of the $(\boldsymbol{\tau}, \nabla_\pi p)$-field can be easily cast to that in terms of vorticity dynamics. The vector fields $(-\nabla_\pi p, \boldsymbol{\tau})$ or equivalently $(\boldsymbol{\sigma}, \boldsymbol{\omega})$ on $\partial B$ forms the basic on-wall signatures of the flow. For the flow over prolate spheroid given in Fig. 5.1, the two pairs of on-wall orthogonal vector lines are shown in Figs. 5.3 and 5.4.

Given an initial flow field, the on-wall flow signatures $(\boldsymbol{\sigma}, \boldsymbol{\omega})$ are sufficient for inferring the entire flow field, as can be convinced by inspecting (4.170). But in the present near-wall local analysis it suffices to use Taylor expansion. Assume the Navier–Stokes solution is analytic so that spatial derivatives of $\boldsymbol{u}$ and $\boldsymbol{\omega}$ of all orders exist. The pathlines are governed by a set of ordinary differential equations:

$$\frac{\mathrm{d}\boldsymbol{x}}{\mathrm{d}t} = \boldsymbol{u}(\boldsymbol{x}, t). \tag{5.5}$$

Due to analyticity, if at $t = 0$ a fluid element is at $\boldsymbol{x} = \boldsymbol{c}$ (so $\boldsymbol{c}$ is a label of the element), then the element at later time must follow a unique pathline

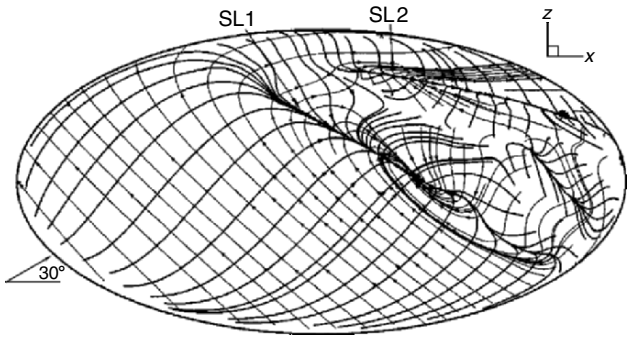


**Fig. 5.3.** Orthogonal $\boldsymbol{\tau}$-lines (*thick*) and $\boldsymbol{\omega}$-lines (*thin*). From Wu et al. (2000)

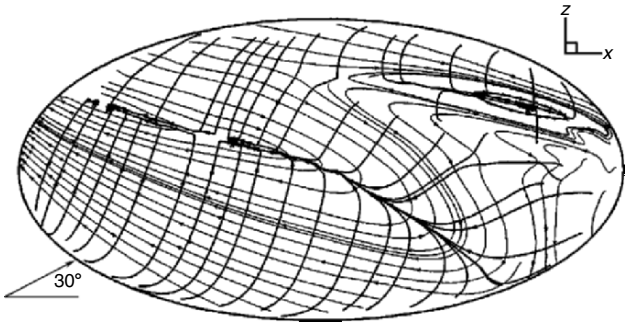


**Fig. 5.4.** Orthogonal $-\nabla_\pi p$-lines (*thick*) and $\boldsymbol{\sigma}$-lines (*thin*). From Wu et al. (2000)

$\boldsymbol{x}(t, \boldsymbol{c})$ of (5.5), which depends on $\boldsymbol{c}$ continuously (Sect. 2.1.1). If at a point $\bar{\boldsymbol{x}}$ there is $\boldsymbol{u} = \boldsymbol{0}$, then (5.5) has a solution $\boldsymbol{x}(t) = \bar{\boldsymbol{x}}$, i.e., the fluid element is fixed, and point $\bar{\boldsymbol{x}}$ is called a *fixed point* or *critical point*. Otherwise $\bar{\boldsymbol{x}}$ is an *ordinary point*. The same can be said for the on-wall $(\boldsymbol{\tau}_w, \boldsymbol{\omega}_\mathrm{B})$-field, but on the entire wall any $\boldsymbol{x}_\mathrm{B}$ is a fixed point of the $\boldsymbol{u}$-field. However, if the flow is steady, a unified local description of both near-wall $\boldsymbol{u}$-field and on-wall $\boldsymbol{\tau}$-field is possible. To see this, let $x_3$ be the normal distance of a point $P(\boldsymbol{x})$ above the wall $\partial B$, and introduce a new independent variable

$$s = \int_{t_0}^{t} x_3(r)\mathrm{d}r, \tag{5.6a}$$

which has dimension of length×time. Then $\mathrm{d}s = x_3\,\mathrm{d}t$ and (5.5) becomes

$$\frac{\mathrm{d}\boldsymbol{x}}{\mathrm{d}s} = \frac{1}{x_3}\boldsymbol{u}(\boldsymbol{x}), \tag{5.6b}$$

which is an *autonomous dynamic system* without singularity on the wall. Obviously, as $x_3 \to 0$ (5.6b) yields

$$\mu\frac{\mathrm{d}\boldsymbol{x}}{\mathrm{d}s} = \boldsymbol{\tau}_w(\boldsymbol{x}) \quad \text{on} \quad \partial B, \tag{5.7}$$

which generically has only isolated fixed points with $\boldsymbol{\tau}_w = \boldsymbol{0}$. Actually, (5.6a) represents a normally nonuniform rescaling of time[3]; as $x_3 \to 0$, any finite variation of $s$ requires an infinitely large variation of $t$, which reflects the physical fact that fluid elements move more and more slowly as approaching the wall. If we drop the constant $\mu$, then (5.7) represents the dynamic system for *limiting streamlines* as named by some authors.

We now consider the dynamic behavior of the Taylor expansion of (5.6b) around the origin $O$ on $\partial B$ for a point $P(\boldsymbol{x})$ in the flow field near $O$. The

[3] For unsteady flow the right-hand side of (5.6) and (5.7) become undefined.

approach is based on the operator splitting on a curved wall $\partial B$:

$$\nabla = \nabla_\pi + \widehat{\boldsymbol{n}}\partial_3, \quad \nabla^2 = \nabla_\pi^2 - \kappa_{\rm B}\partial_3 + \partial_3^2, \quad \partial_3 \equiv \frac{\partial}{\partial x_3}, \tag{5.8}$$

where $\kappa_{\rm B} = \mathrm{tr}\ \mathbf{K} = -\nabla_\pi \cdot \widehat{\boldsymbol{n}}$ is twice of the wall's *mean curvature*. Thus, we have $\boldsymbol{x} \cdot \nabla = \boldsymbol{x}_\pi \cdot \nabla + x_3\partial_3$, so that the Taylor expansion operator at $O$ can be formally written as

$$\mathcal{T} = \sum_{n=0}^{\infty} \frac{1}{n!}(\boldsymbol{x} \cdot \nabla)^n = \mathrm{e}^{\boldsymbol{x}\cdot\nabla} = \mathrm{e}^{\boldsymbol{x}_\pi\cdot\nabla}\,\mathrm{e}^{x_3\partial_3} = \mathcal{T}_\pi\mathcal{T}_3. \tag{5.9}$$

Here, we always compute normal derivatives first, and

$$\mathcal{T}_\pi = \sum_{n=0}^{\infty} \frac{1}{n!}(\boldsymbol{x}_\pi \cdot \nabla)^n, \quad \mathcal{T}_3 = \sum_{n=1}^{\infty} \frac{1}{n!}(x_3\partial_3)^n,$$

where we used the adherence condition

$$(\boldsymbol{x}_\pi \cdot \nabla)^n \boldsymbol{u} = 0, \quad n = 0, 1, 2, ..., \quad \text{on} \ \ \partial B.$$

Then, denoting $\mathrm{d}\boldsymbol{x}/\mathrm{d}s$ by $\boldsymbol{x}'$ and substituting (5.9) into (5.6), one obtains

$$\boldsymbol{x}'_P = \mathcal{T}(\partial_3\boldsymbol{u}) = \left[\sum_{n=0}^{\infty} \frac{1}{n!}(\boldsymbol{x}_\pi \cdot \nabla)^n\right]\left[\sum_{m=0}^{\infty} \frac{1}{(m+1)!}(x_3\partial_3)^m\right](\partial_3\boldsymbol{u}). \tag{5.10}$$

Here and below all terms on the right take their values at $O$. If $P$ is on $\partial B$, we have $\mathcal{T}_3 = 1$ and (5.10) reduces to the Taylor expansion of (5.7).

Just like in (5.3) and (5.4) $\partial_3\boldsymbol{u}_\pi$ and $\partial_3\boldsymbol{\omega}$ are expressed by on-wall quantities, by taking the $n$th-order normal derivatives of the Navier–Stokes equation along with solenoidal conditions $\nabla \cdot \boldsymbol{u} = 0$ and $\nabla \cdot \boldsymbol{\omega} = 0$, as well as using the adherence condition, one can obtain a set of recursive formulas by which all $\partial_3^n\boldsymbol{u}$, $\partial_3^n\boldsymbol{\omega}$, and $\partial_3^n p$ for $n = 1, 2, ...$, are expressible by on-wall quantities and their tangent derivatives (Wu et al. (1988a)). Namely, *any near-wall viscous flow can be inferred from its on-wall signatures*. For example, to the first two orders there is

$$\boldsymbol{x}'_P = \partial_3\boldsymbol{u} + \boldsymbol{x}_\pi \cdot \nabla_\pi(\partial_3\boldsymbol{u}) + \frac{1}{2}x_3(\partial_3^2\boldsymbol{u}_\pi + \widehat{\boldsymbol{n}}\partial_3^2 u_3) + O(|\boldsymbol{x}|^2), \tag{5.11}$$

where, by the Navier–Stokes equation, the normal derivatives on $\partial B$ can be expressed by tangent ones (recall $\rho = 1$ and hence $\mu = \nu$):

$$\partial_3 u_3 = 0, \tag{5.12a}$$

$$\nu\partial_3^2\boldsymbol{u}_\pi = \kappa_{\rm B}\boldsymbol{\tau}_w + \nabla_\pi p, \tag{5.12b}$$

$$\nu\partial_3^2 u_3 = \partial_3 p = -\nabla_\pi \cdot \boldsymbol{\tau}_w. \tag{5.12c}$$

Figure 5.1 and (5.2) indicate that a major part of three-dimensional flow separation takes place at ordinary points of the $(\boldsymbol{\tau}_w, \boldsymbol{\omega}_{\rm B})$-field, where as shown in Sect. 2.4.1 it is convenient to introduce a $\boldsymbol{\tau}$*-frame*, which is an intrinsic surface-moving orthogonal triad $(\boldsymbol{e}_1, \boldsymbol{e}_2, \boldsymbol{e}_3)$ with $\boldsymbol{e}_1$ and $\boldsymbol{e}_2$ being the unit vectors along the positive directions of $\boldsymbol{\tau}_w$ and $\boldsymbol{\omega}_{\rm B}$, respectively, and $\boldsymbol{e}_3 = \widehat{\boldsymbol{n}}$. The corresponding coordinates are denoted by $x_i$, $i = 1, 2, 3$. For a background knowledge of curvilinear orthonormal coordinates on surface see Sect. A.3.2. Following the notation there, we denote

$$\partial_i \equiv \frac{1}{h_i}\frac{\partial}{\partial x_i}, \quad i = 1, 2, 3, \tag{5.13}$$

with $h_i$ being the scale coefficients ($h_3 = 1$). In that appendix two sets of curvature components are introduced. One set is wall-curvature components $b_{\alpha\beta} = b_{\beta\alpha}$, $\alpha, \beta = 1, 2$, defined by

$$b_{\alpha\beta} = \boldsymbol{e}_\alpha \cdot \mathbf{K} \cdot \boldsymbol{e}_\beta, \quad \text{or} \quad \mathbf{K} = b_{\alpha\beta}\boldsymbol{e}_\alpha\boldsymbol{e}_\beta, \tag{5.14}$$

with $b_{11} + b_{22} = \kappa_{\rm B}$. The other set is

$$\begin{aligned} \kappa_1 &= (\partial_1 \boldsymbol{e}_1)\cdot \boldsymbol{e}_2 = -(\partial_1 \boldsymbol{e}_2)\cdot \boldsymbol{e}_1, \\ \kappa_2 &= (\partial_2 \boldsymbol{e}_2)\cdot \boldsymbol{e}_1 = -(\partial_2 \boldsymbol{e}_1)\cdot \boldsymbol{e}_2, \end{aligned} \tag{5.15a}$$

which now represent the *on-wall curvatures* of the $\boldsymbol{\tau}$-lines and $\boldsymbol{\omega}$-lines, respectively, dependent on the flow. Note that (A.81) indicates $\partial_\alpha$ and $\partial_\beta$ for $\alpha \neq \beta$ are not commutative:

$$\partial_1\partial_2 - \partial_2\partial_1 = \kappa_2\partial_2 - \kappa_1\partial_1. \tag{5.15b}$$

Moreover, owing to the orthogonality of the $x_1$-lines and $x_2$-lines, $\kappa_1$ and $\kappa_2$ are related by (A.82), for proof see A.3.2:

$$\partial_2\kappa_1 + \partial_1\kappa_2 = \kappa_1^2 + \kappa_2^2 + K, \tag{5.15c}$$

where $K = \det\{b_{\alpha\beta}\}$ is the *total curvature* of the wall.

It will be seen that the on-wall curvature $\kappa_2$ of the $\boldsymbol{\omega}$-lines is a key indicator of flow separation at large $Re$. Evidently, since $\boldsymbol{\tau}_w \cdot \boldsymbol{e}_2 \equiv 0$ and $\boldsymbol{\omega} \cdot \boldsymbol{e}_1 \equiv 0$, there is

$$\partial_1^n\omega_1 = \partial_2^n\omega_1 = \partial_1^n\tau_2 = \partial_2^n\tau_2 = 0, \quad n = 0, 1, 2, ...$$

at any ordinary points. Note that although $\omega_1 \equiv 0$ on $\partial B$, by (5.4) the *newly produced* vorticity from $\partial B$, which appears right above $\partial B$, is dominated by

$$\sigma_{p1} = \partial_2 p, \quad \sigma_{p2} = -\partial_1 p, \tag{5.16}$$

in which $\sigma_{p1}$ is along $\boldsymbol{e}_1$. Like the velocity profile, in a three-dimensional flow the vorticity profile may be twisted as one moves away from the wall. Moreover, (5.12c) is cast to

$$\nu\partial_3^2 u_3 = \partial_3 p = \tau\kappa_2 - \partial_1\tau = \nu(\omega\kappa_2 - \partial_1\omega) \quad \text{on } \partial B. \tag{5.17}$$

Then, by (A.83) and (5.15), in a $\boldsymbol{\tau}$-frame (5.11) has component form

$$\nu x'_{iP} = \tau_i + A_{ij}x_j, \quad |\boldsymbol{x}| \to 0, \tag{5.18a}$$

where $\boldsymbol{\tau}_w = (\tau, 0, 0)$ and

$$[A_{ij}] = \begin{bmatrix} \partial_1\tau & \partial_2\tau & \frac{1}{2}(\partial_1 p + \kappa_{\mathrm{B}}\tau) \\ \kappa_1\tau & -\kappa_2\tau & \frac{1}{2}\partial_2 p \\ b_{11}\tau & b_{12}\tau & \frac{1}{2}(\kappa_2\tau - \partial_1\tau) \end{bmatrix}. \tag{5.18b}$$

We also need to express the normal derivatives of $\boldsymbol{\omega}$ by on-wall signatures. The first-order derivatives simply follow from the component form of $\boldsymbol{\sigma}_p$ and $\boldsymbol{\sigma}_{\mathrm{vis}}$, see (4.24b) and (4.28):

$$\partial_3\omega_1 = -\frac{\sigma_{p1}}{\nu} + b_{12}\omega, \tag{5.19a}$$

$$\partial_3\omega_2 = -\frac{\sigma_{p2}}{\nu} + b_{22}\omega, \tag{5.19b}$$

$$\partial_3\omega_3 = -\partial_2\omega + \kappa_1\omega. \tag{5.19c}$$

Note that (5.19c) is a special form of (4.26b) due to $\nabla\cdot\boldsymbol{\omega} = 0$, which in $\boldsymbol{\tau}$-frame reads

$$\partial_1\omega_1 + \partial_2\omega_2 + \partial_3\omega_3 - \kappa_2\omega_1 - \kappa_1\omega_2 - \kappa_{\mathrm{B}}\omega_3 = 0. \tag{5.20}$$

Moreover, slightly away from the wall one can take the normal derivative of (5.20) and then apply the result on the wall, expressing the right-hand side by on-wall signature. By using the formulas given in A.3.2, this leads to

$$\nu(\partial_3^3\omega_3)_{\mathrm{B}} = (\kappa_2 b_{12} + \kappa_1 b_{22})\tau - \partial_1(b_{12}\tau) - \partial_2(b_{22}\tau) - \kappa_{\mathrm{B}}\sigma_3.$$

While on a flat wall the equation simply implies $\partial_3^2\omega_3 = 0$, on a curved wall one can remove $(\partial_3^2\omega_3)_{\mathrm{B}}$ by using the vorticity transport equation applied to the wall:

$$\nu\partial_3^2\boldsymbol{\omega} = \frac{\partial\boldsymbol{\omega}_{\mathrm{B}}}{\partial t} - \kappa_{\mathrm{B}}\boldsymbol{\sigma} - \nu\nabla_\pi^2\boldsymbol{\omega}_{\mathrm{B}}. \tag{5.21}$$

Wu et al. (2000) show that for steady flow this leads to a first-order *on-wall vorticity equation* (the suffix $B$ is dropped):

$$(b_{12}\partial_1 + b_{22}\partial_2)\omega = (b_{11}\kappa_1 + b_{12}\kappa_2)\omega, \tag{5.22}$$

which is nontrivial only when the wall is curved and the flow is three-dimensional.

### 5.2.2 Local Separation Criteria

We now consider the behavior and cause of a generic three-dimensional flow separation, in terms of the signatures of vorticity dynamics on an arbitrary curved stationary wall described in a $\boldsymbol{\tau}$-frame. First, from Fig. 5.3 one observes that *$\boldsymbol{\tau}$-lines will converge (or diverge) if and only if $\boldsymbol{\omega}$-lines have positive (or negative) on-wall curvature* $\kappa_2$. Therefore, Lighthill's $\boldsymbol{\tau}$-line converging criterion is cast to a simple inequality in terms of $\boldsymbol{\omega}$-line behavior:

$$\kappa_2 > 0. \tag{5.23}$$

On the other hand, the fluid upwelling is simply expressed by $u_{3P} \sim \partial_3^2 u_3 > 0$ at a point $P$ above the wall. By (5.12c) and (5.3), this condition can be cast to

$$\nabla_\pi \cdot \boldsymbol{\tau}_w < 0 \quad \text{or} \quad \boldsymbol{n} \cdot (\nabla \times \boldsymbol{\omega}) < 0. \tag{5.24a,b}$$

By (A.83), in the $\boldsymbol{\tau}$-frame both inequalities become $\omega\kappa_2 - \partial_1\omega > 0$ or

$$\kappa_2 - \partial_1(\ln \omega) > 0, \tag{5.25}$$

again in terms of vorticity. Inequality (5.24a) degenerates to (5.1b) in two dimensions, while in three dimensions it indicates that the on-wall signature of an upwelling is the *sink of the $\boldsymbol{\tau}$-field.*

The upwelling condition (5.25) and $\boldsymbol{\tau}$-line converging condition (5.23) differ by $\partial_1(\ln \omega)$, which describes the relative change of $\tau = \nu\omega$ along $\boldsymbol{\tau}$-lines, an effect neglected in Lighthill's (1963) argument. This extra term does not have a definite sign. In general (5.23) and (5.25) have different physical implications, and neither alone is sufficient to characterize a separation zone. Thus, Wu et al. (2000) proposed to take the simultaneous existence of (5.23) and (5.25) as a criterion for the *separation zone.* These inequalities have been obtained by Zhang (1985a) in terms of a local Cartesian frame (to be introduced in Sect. 5.2.3 later).

A more important and subtle issue is to identify a single *separation line*, say $L$, among all $\boldsymbol{\tau}$-lines in a zone where (5.23) and (5.25) hold. This requires introducing an *equality* to capture the unique feature of $L$. While in two-dimensional flow on the $(x_1, x_3)$-plane the separation point is simply fixed by equality (5.1a), in three dimensions the defining equality of $L$ is less obvious because $\tau \neq 0$ on $L$ except isolated points. In fact, the exact identification of the separation line cannot be answered by a simple three-dimensional extension of a local equality like (5.1a), but involves the global behavior of the $\boldsymbol{\tau}$-field. This issue is deferred to Sect. 7.1.2 as we discuss the topological property of the $\boldsymbol{\tau}$-field. Instead, here we return to Figs. 5.1 and 5.3 and make some further observations.

These figures indicate that the primary and secondary separation zones satisfying local inequalities (5.23) and (5.25) start to occur much more upstream than the separations start to become strong and produce separated shear layers that roll up into concentrated vortices. In other words, at large

$Re$, the initial (as well as terminal) location of a strong separation can be in the middle of the corresponding separation zones. Therefore, it is of interest to see if there are some criteria more localized than (5.23) and (5.25) which can pick up the large-$Re$ strong separation from a generic separation zone.

This issue was considered by Wu et al. (2000) in an attempt of identifying a separation line by a local equality. They conjectured that, compared to other $\boldsymbol{\tau}$-lines in the separation zone, along a separation line the neighboring $\boldsymbol{\tau}$-line converging and upwelling would be the strongest, so by (5.23) and (5.25) $\varphi = \kappa_2[\kappa_2 - \partial_1(\ln\omega)]$ takes maximum at that line. But in general this "ridge" condition cannot exist exactly on a $\boldsymbol{\tau}$-line (Surana et al. 2005a). Indeed, assume for *any* scalar $\varphi$ there is $\partial_2\varphi = 0$ at one station $x_1 = a$, say, then $\varphi$ will be extremum along the $\boldsymbol{\tau}$-line only if $\partial_1(\partial_2\varphi) = 0$. But by identity (5.15b), at point $a$ there is

$$\partial_1\partial_2\varphi = \kappa_2\partial_2\varphi + (\partial_2 - \kappa_1)\partial_1\varphi = (\partial_2 - \kappa_1)\partial_1\varphi.$$

Hence, for $\varphi$ to remain extremum there must be $\partial_1\varphi = 0$, i.e., $\varphi$ is independent of $x_1$, which cannot hold exactly.

At large $Re$, however, it can be shown that this extremal behavior does appear along certain separation lines as the leading-order approximation. Recall that in the Euler limit with $Re \to \infty$ the separation zone shrinks to a separation line, at a large but finite $Re$ the width $l$ of the separation zone must be small. This implies $\partial_2 = O(l^{-1}) \gg 1$ and so must be $\kappa_2$, but $\partial_1$ remains of $O(1)$. Consequently, $\partial_1(\ln\omega) = O(1)$ can be dropped from (5.25), making it identical to (5.23) as a single criterion of the separation zone:

$$\kappa_2 \gg 1 \quad \text{in separation zone.} \tag{5.26}$$

It will be seen in Sect. 5.3.4 that in a boundary-layer separation zone $\kappa_2$ is scaled to $Re^{3/8}$. Therefore, one may state

$$\partial_2\kappa_2 \simeq 0, \quad \partial_2^2\kappa_2 < 0, \quad \partial_1\kappa_2 \simeq 0 \tag{5.27a,b,c}$$

along an approximate strong separation line. Figure 5.5 confirms this feature in the secondary separation zone of Fig. 5.1, indicating that condition (5.27c) is indeed true.

A comparison of Figs. 5.1 and 5.3 indicates that before the formation of free vortex layer, in the separation zone the $\boldsymbol{\tau}$-line converging is associated with only modest positive $\kappa_2$. A data analysis of the spheroid flow indicates that, before strong separation happens nowhere in the $\boldsymbol{\tau}$-line converging region is (5.27) satisfied. This is shown in Fig. 5.6, where $\kappa_2$ has a peak only at stations 1, 2, and 3 but not 4.[4]

[4] The fluctuations in Fig. 5.6b indicate that the numerical resolution across the primary separation line is insufficient for estimating the on-wall curvature of vorticity lines, which requires computing second-order derivatives.

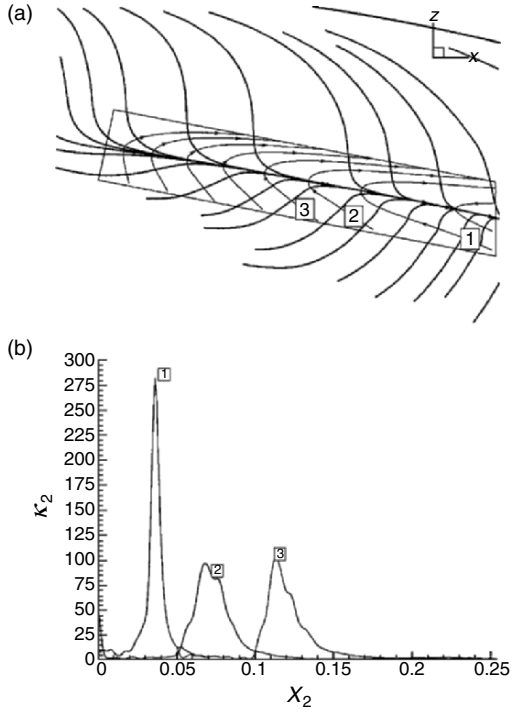


**Fig. 5.5.** (**a**) Local $(\boldsymbol{\tau}_w, \boldsymbol{\omega}_{\rm B})$-lines in the secondary separation zone of Fig. 5.1. The domain for sample data analysis is within the quadrilateral. (**b**) The on-wall curvature $\kappa_2$ of three $\boldsymbol{\omega}$-lines across the separation line, where the origin of abscissa for line 3 is shifted by 0.05. From Wu et al. (2000)

This being the case, we may state the following high-$Re$ approximate local criterion for "*strong separation warning*":

**Local criterion for strong separation.** *For a strong three-dimensional flow separation at large Reynolds numbers, to the leading order the separation zone is determined by local inequality (5.26), and the separation line therein can be identified by the occurrence of local maximum condition (5.27).*

This criterion is a local phenomenological description of strong flow separation after it takes place. Interestingly, its prediction is also in qualitative agreement with the exact theory of Surana et al. (2005a). The basic driving mechanism of separation is the same as explained in Sect. 4.2.3, see also Fig. 4.12: a tangent pressure gradient that creates new vorticity with direction different from the existing one. Note that by (5.12c), inequalities in (5.24) can be replaced by $\partial_3 p > 0$, implying that the upwelling must occur against an adverse normal pressure gradient. In either two or three dimensions this can happen only when the tangent pressure gradient is sufficiently strong to squeeze the fluid up. Therefore, the criterion for "*strong separation watch*" should be found from the behavior of $\nabla_\pi p$ or $\boldsymbol{\sigma}_p$, which will be visited later in Sect. 5.3.4.

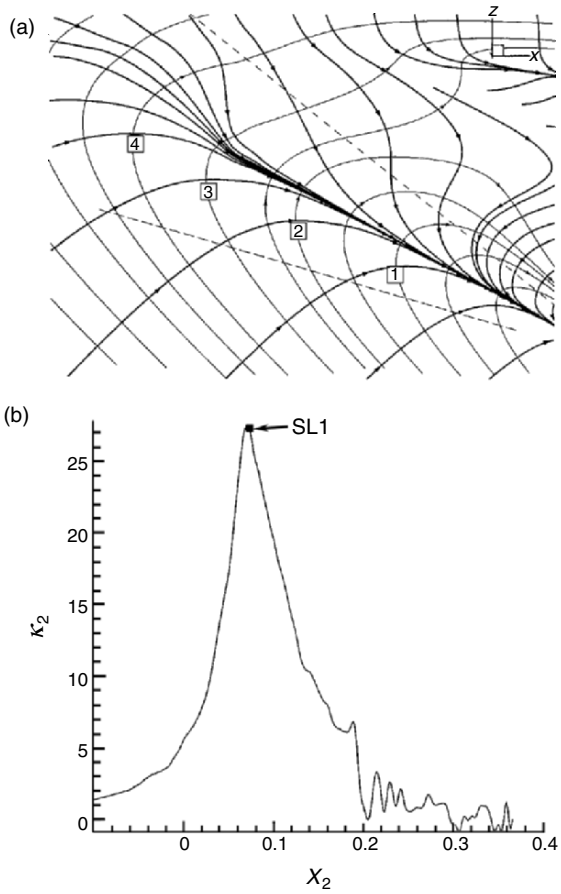


**Fig. 5.6.** (**a**)Local $(\boldsymbol{\tau}_w, \boldsymbol{\omega}_{\rm B})$-lines in the primary separation zone. (**b**) The on-wall curvature $\kappa_2$ of the $\boldsymbol{\omega}$-line 3 across the separation line. From Wu et al. (2000)

### 5.2.3 Slope of Separation Stream Surface

As the skeleton of the separated free shear layer, the *separation stream surface* plays a special role in determining the initial behavior of a separated flow. It intersects the wall at the separation line, so the determination of both separation stream surface and separation line should be considered simultaneously. Without going into detailed exact theory, here we follow the approximate approach of the preceding subsection on large-$Re$ strong separation, to seek a local expression of the slope of separation stream surface at an arbitrary $x_1$-station.

This problem cannot be conveniently analyzed in the $\boldsymbol{\tau}$-frame; so we turn to a local Cartesian coordinate system $(x, y, z)$, with the $(y, z)$-plane normal to the $\boldsymbol{\tau}$-line. Thus $(x, z) = (x_1, x_3)$, but the $y$-axis is *tangent* to the $\boldsymbol{\omega}$-line at

the origin. The two frames are different only in the $(y, z)$-plane, in which the corresponding part of (5.18a) and (5.18b) reads

$$\nu \begin{bmatrix} y'_P \\ z'_P \end{bmatrix} = \begin{bmatrix} \partial_y \tau_y & \frac{1}{2}\partial_y p \\ 0 & -\frac{1}{2}(\partial_y \tau_y + \partial_1 \tau) \end{bmatrix} \begin{bmatrix} y \\ z \end{bmatrix}. \tag{5.28}$$

Here, $\tau_y = -\omega_x = 0$ at origin only and we have $\partial_y \tau_y = -\kappa_2 \tau$, but the entry $b_{12}\tau$ in (5.18b) is absent (Wu et al. 2000).

Now, one is tempted to estimate the slope of the intersection line of the separation stream surface and the normal $(y, z)$-plane at each $x_1$ station. But, generically the influence of the flow at other $x_1$ stations cannot be neglected. In accordance with our approximate local criterion for strong separation, however, we may again be satisfied with assuming $\partial_2 \gg \partial_1$ so that the upstream and downstream influence can all be neglected. Indeed, it will be proved quantitatively in Sect. 5.3.4 that in boundary-layer separation $x_1$ serves merely as a parameter, and the entire separation pattern can be determined solely on each cross-sectional normal plane. Therefore, let $\phi$ be the angle between that line and the $y$-axis, such that

$$\tan\phi = \left(\frac{\mathrm{d}z}{\mathrm{d}y}\right)_{z=0} = \left(\frac{w_P}{v_P}\right)_{z\to 0},$$

then by (5.28) there is

$$\tan\phi = -\frac{(\partial_y \tau_y + \partial_1 \tau)\tan\phi}{2\partial_y \tau_y + \partial_y p \tan\phi},$$

of which one solution $\tan\phi = 0$ is the wall itself, and the other gives a local slope formula (Zhang 1985a; Wu et al. 2000)

$$\tan\phi = -\frac{1}{\partial_y p}(3\partial_y \tau_y + \partial_1 \tau) = \frac{\nu}{\partial_2 p}(3\kappa_2 \omega - \partial_1 \omega). \tag{5.29}$$

For two-dimensional flow in the $(y, z)$-plane, (5.29) reduces to (Legendre 1955; Oswatitsch 1957)

$$\tan\phi = -3\frac{\partial_y \tau}{\partial_y p}. \tag{5.30}$$

In fact, in our approximation $\partial_1 \omega$ can also be dropped from (5.29), so that the two-dimensional slope is a sufficiently good estimate. Note that unlike (5.30), (5.29) holds for all stream surfaces growing from any $\boldsymbol{\tau}$-lines in the separation zone, because no unique condition for the separation line is used. To pick up the slope of the approximate separation stream surface, one may simply require $\kappa_2$ to be maximum.

As a comparison, here we also cite an exact formula found by Surana et al. (2005a) for the slope of separation stream surface growing from a generic

closed separation line, applicable to arbitrary separation strength and $Re$. These authors start from the dynamic system (5.6b) with $s$ defined by (5.6a) as independent variable, and rewrite the equations as

$$\boldsymbol{x}'_\pi = \boldsymbol{A}(\boldsymbol{x}_\pi, z), \quad z' = zC(\boldsymbol{x}_\pi, z), \tag{5.31}$$

where

$$\begin{aligned} \boldsymbol{A}(\boldsymbol{x}_\pi, z) &= \int_0^1 \partial_z \boldsymbol{u}(\boldsymbol{x}_\pi, qz)\mathrm{d}q, \\ C(\boldsymbol{x}_\pi, z) &= \int_0^1 \int_0^1 \partial_z^2 w(\boldsymbol{x}_\pi, qrz)\mathrm{d}r\,\mathrm{d}q, \end{aligned} \tag{5.32}$$

which by the incompressibility is related by

$$\nabla_\pi \cdot \boldsymbol{A} + 2C + z\partial_z C = 0. \tag{5.33}$$

Then the linearized version of (5.31), similar to (5.18), is solved analytically. The separation line is defined by $\boldsymbol{x} = \boldsymbol{x}(\boldsymbol{x}_0, s)$, where $\boldsymbol{x}_0$ is a point at the line and $s$ now varies along the line like a rescaled "arclength" (with dimension of $LT$). For separation from a flat wall, after a lengthy derivation which is omitted here, Surana et al. (2005a) found, in terms of quantities in the $\boldsymbol{\tau}$-frame,

$$\cot\phi(\boldsymbol{x}_0) = \frac{1}{2\nu}\int_{-\infty}^0 \exp\left[\frac{1}{2}\int_0^s (3\kappa_2\omega - \partial_1\omega)\mathrm{d}r\right]\partial_2 p\,\mathrm{d}s, \tag{5.34}$$

where $s \to -\infty$ as one approaches the upstream fixed point of the separation line, which is a *saddle* (Sect. 7.1). Thus the upstream influence is naturally included. This formula reduces to (5.29) at fixed point or when the $\boldsymbol{\tau}$-field is linear and $\partial_2 p$ is $x_1$-independent, which is precisely the case in leading-order approximation of strong separation at large $Re$.

Note that as $Re \to \infty$, since $\tau = O(Re^{-1/2}) \to 0$, (5.29), (5.30), and (5.34) are all in consistency with the asymptotic behavior of a separating vortex sheet: it must leave the wall tangentially (Sect. 4.4.2).

### 5.2.4 A Special Result on Curved Surface

It has been observed that along certain separation or reattachment lines $\tau = \nu\omega$ is minimum or maximum compared to that at neighboring $\boldsymbol{\tau}$-lines. Whether this is a general phenomenon and, if not, when this happens, are of interest. The problem can be examined by applying the first-order equation (5.22) to a separation zone. Assume $\|\mathbf{K}\| = O(1)$. When (5.26) and (5.27) hold at $Re \gg 1$, we may simplify (5.22) to

$$\partial_2\omega = \frac{b_{12}}{b_{22}}\kappa_2\omega. \tag{5.35}$$

Thus, if $\tau = \nu\omega$ takes extremum on a separation line there must be $b_{12} = 0$. But by (A.78b) this happens only if the separation line is aligned to one of the principal directions $(\boldsymbol{p}_1, \boldsymbol{p}_2)$ of the curved wall. Assume this is so, then, by (5.27a) and (5.35) there is

$$\partial_2^2 \omega = -\kappa_2 \omega \frac{\mathrm{d}}{\mathrm{d}\beta}\left(\frac{b_{12}}{b_{22}}\right)\partial_2 \beta, \tag{5.36}$$

where $\beta \in [0, \pi/2]$ is the angle between the separation line and the principal directions of the wall, measured from $\boldsymbol{p}_1$ to $\boldsymbol{e}_1$ in counterclockwise sense, see A.3.2. An inspection of the $(\boldsymbol{\tau}, \boldsymbol{\omega})$-line patterns indicates that across *both* separation line *and* attachment line there must be $\partial_2 \beta > 0$. Then, from (A.78) it follows that (Wu et al. 2000)

$$\partial_2^2 \omega = \frac{\mathrm{d}}{\mathrm{d}\beta}\left(\frac{b_{12}}{b_{22}}\right) = \begin{cases} 1 - K_1/K_2, & \text{if} \quad \beta = 0, \\ 1 - K_2/K_1, & \text{if} \quad \beta = \pi/2, \end{cases} \tag{5.37}$$

where $K_1$ and $K_2$ are principal curvatures of the wall, for which one can define a set of sign convention for concave, convex, and concave–convex walls. Therefore, the sign of $\partial_2^2 \omega$ solely depends on the sign of two principal curvatures and can be easily identified.

This result shows that the extremal feature of $\omega$ or $\tau$ at a separation line is not unconditional. On a curved wall with $K_1 \neq K_2$, it happens only if there exists certain local symmetry due to the alignment of the separation line to a principal direction. For example, the outboard part of the trailing edge of a wing is a three-dimensional separation line, and we can judge that the skin-friction thereon reaches a minimum. Similarly, at a juncture locally like a saddle surface, if the separation line is aligned to any principal direction then $\tau = \nu\omega$ is always minimum. In contrast, for flow along a concave wall like the case in Görtler instability (Chap. 9), the skin-friction will reach maximum at alternative separation and reattachment lines.

Figure 5.1 indicates that the secondary separation line from the spheroid is basically aligned to the principal direction along which the principal curvature is $K_1$. Thus by the earlier analysis it is expected that $\omega$ is minimum and $\kappa_2\omega$ is maximum. This is confirmed by Fig. 5.7. In contrast, the primary separation line is not aligned to principal direction of the spheroid, and no such extremal behavior is found.

## 5.3 Steady Boundary Layer Separation

The preceding results of local analysis on strong separation are useful in the diagnosis of separating flows based on, say, numerical Navier–Stokes solutions. But they do not give a quantitative estimate of relevant flow quantities in the separation zone, nor reveal detailed physical interactions underlying a steady boundary-layer separation. In fact, once a boundary layer breaks away,

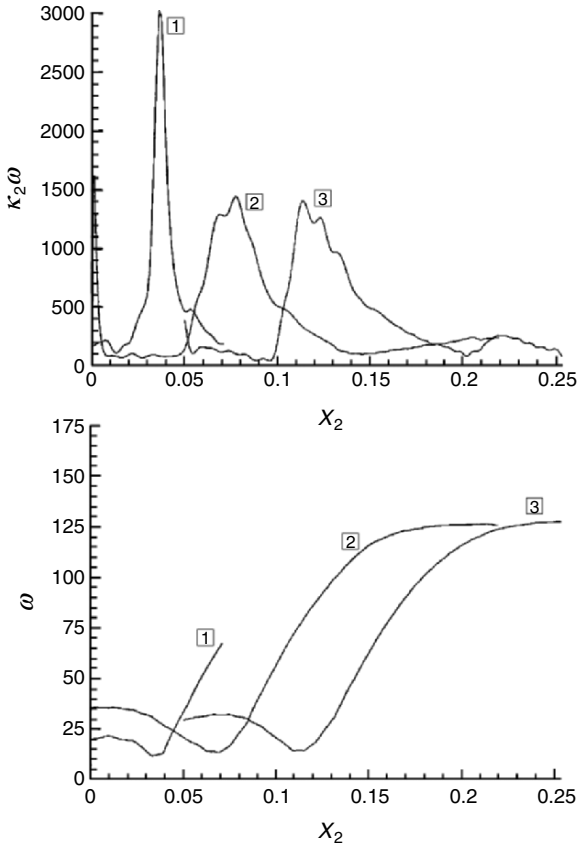


**Fig. 5.7.** $\omega$ and $\kappa_2\omega$ along three vorticity lines across the secondary separation line as shown in Fig. 5.5a. The origin of abscissa for line 3 is shifted by 0.05. From Wu et al. (2000)

the problem will involve the flow behavior in the whole layer. Physically, as Prandtl (1904) explained, since the fluid elements inside the boundary layer has smaller momentum and kinetic energy, under an adverse pressure gradient they are more vulnerable to be decelerated. In terms of vorticity dynamics, the adverse pressure gradient produces new vorticity at the wall with the sign opposite to the existing one, so to cause a *bifurcation* of upstream attached vortex layer into a detached free vortex layer and an attached vortex layer in the reversed flow (see Fig. 4.12). When this happens, Prandtl's theory for attached boundary layer no longer holds.

While this strong separation can be studied based on the full Navier–Stokes equations as we did earlier, a physically more appealing theoretical approach is still based on the matched asymptotic method, which has led to the elegant *triple-deck theory* as the second generation of boundary layer

theory. Although solving the full Navier–Stokes equation numerically is now more convenient than using the triple-deck theory, the latter is indispensable to a thorough physical understanding of boundary-layer separation, which is our main concern.[5]

### 5.3.1 Goldstein's Singularity and Triple-Deck Structure

Consider a two-dimensional *steady* boundary layer. Prandtl's equations (4.85) is based on rescaling coordinates, velocity, and vorticity by

$$(X, Y, U, V, \Omega) = (x, Re^{1/2}y, u, Re^{1/2}v, Re^{-1/2}\omega) = O(1), \tag{5.38}$$

derived for attached flow. The boundary layer separation must violate (5.38) around the separation point $x_\mathrm{s}$ where (5.1a) and (5.1b) hold as necessary but insufficient conditions. In particular, instead of the simple upwelling $v > 0$ for the general flow separation, there must be a strong upwelling

$$v(x, y) \gg Re^{-1/2} \quad \text{as} \quad x \to x_\mathrm{s}. \tag{5.39}$$

Once this happens, the boundary layer equations (4.85) has neither normal diffusion nor normal pressure gradient to balance the upwelling, so it grows unboundedly and thereby causes a singularity. The behavior of this singularity can be understood by the heuristic reasoning of Landau and Lifshitz (1944).

Since $V(x, 0) = 0$, by (4.85c) and (5.39) there must be $\partial V/\partial Y = -\partial u/\partial x = \infty$ or

$$\frac{\partial}{\partial u} x(u, Y)\Big|_{x=x_\mathrm{s}} = 0.$$

Thus, denoting $u_\mathrm{s}(Y) = u(x_\mathrm{s}, Y)$, when both $x_\mathrm{s} - x$ and $u - u_\mathrm{s}$ are small one has expansion

$$x_\mathrm{s} - x \simeq (u - u_\mathrm{s})^2 \frac{1}{2} \left[\frac{\partial^2}{\partial u^2}(x_\mathrm{s} - x)\right]_{x=x_\mathrm{s}} \equiv f(Y)(u - u_\mathrm{s})^2,$$

so that

$$u = u_\mathrm{s}(Y) + \alpha(Y)(x_\mathrm{s} - x)^{1/2}, \quad \alpha(Y) \equiv f^{-1/2}(Y), \tag{5.40a}$$

$$V = \beta(Y)(x_\mathrm{s} - x)^{-1/2}, \qquad \beta(Y) \equiv \frac{1}{2}\int_0^Y \alpha(Y)\mathrm{d}Y. \tag{5.40b}$$

Now the finite pressure gradient at the outer edge of the boundary layer is given, and so is $\partial^2 u/\partial Y^2$ by (5.40a). Therefore, the unbounded terms in (4.85a) must be self-balanced:

$$uu_{,x} + Vu_{,Y} = -uV_{,Y} + V\frac{\partial u}{\partial Y} = -u^2\frac{\partial}{\partial Y}\left(\frac{V}{u}\right) = 0 \quad \text{for} \quad x_\mathrm{s} - x \ll 1.$$

[5] The theory also provides a rational estimate for the grid density necessary in separation computation.

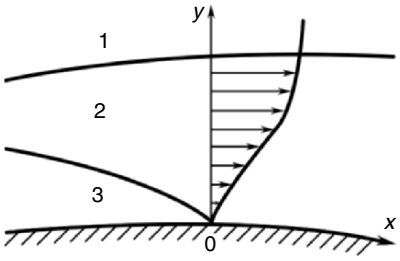


**Fig. 5.8.** Two-layer structure of a boundary layer before separation. After Sychev et al. (1998)

Since $u^2(x_\mathrm{s}, Y) \neq 0$, $V/u$ must be independent of $Y$. But by (5.40a,b) one has

$$\frac{V}{u} = \frac{\beta(Y)}{u_\mathrm{s}(Y)}(x_\mathrm{s} - x)^{-1/2} - \frac{\alpha(Y)\beta(Y)}{u_\mathrm{s}^2(Y)} + O((x_\mathrm{s} - x)^{1/2}),$$

so to the leading order there must be $\beta(Y) = Au_\mathrm{s}(Y)/2$ with $A$ being a constant. Then by (5.40b) $\alpha(Y) = 2\beta'(Y) = Au_\mathrm{s}'(Y)$, where a prime denotes derivative with respect to the argument. Thus one obtains

$$\begin{aligned} u(x, Y) &= u_\mathrm{s}(Y) + Au_\mathrm{s}'(Y)(x_\mathrm{s} - x)^{1/2}, \\ V(x, Y) &= \frac{1}{2}Au_\mathrm{s}(Y)(x_\mathrm{s} - x)^{-1/2}. \end{aligned} \tag{5.41}$$

Therefore, since generically $A \neq 0$, as $x \to x_\mathrm{s}$ there is an $O(x_\mathrm{s} - x)^{-1/2}$ singularity in $V$. The same singularity appears in the skin-friction gradient $\mathrm{d}\tau/\mathrm{d}x$.

This singularity was analyzed in most detail by Goldstein (1948) and is known as the *Goldstein singularity*. Assuming the existence of the singularity, Goldstein showed that, according to (4.85) with *given* adverse $p_e(x)$, as $x \to x_\mathrm{s}^-$ the boundary layer has a two-layer structure shown in Fig. 5.8. The sublayer adjacent to the wall has a thickness which decays as $Y \sim (x_\mathrm{s} - x)^{1/4}$, and the outer (main) layer has $Y = O(1)$. The asymptotic solutions in both layers were obtained, by which Goldstein proved that in general *it is impossible to continue the solution of the sublayer through the separation point.* Therefore, a generic boundary-layer calculation with given $p_e'(x) > 0$ will blow up once $x_\mathrm{s}$ is reached.[6]

Of course the Goldstein singularity never appears in real flows but is merely a reflection of the incompatibility of (5.38) and (5.39). Recall that scaling (5.38) reduces the elliptic Navier–Stokes equations (4.82) to the parabolic equations (4.85), of which the solution is fully determined by the upstream and

[6] The Goldstein singularity is not an inevitable existence. It has been found that some boundary-layer solutions can still be regular at separation (e.g., Liu and Lee 1982; Liu and Wan 1985).

side boundary conditions but is "blind" to any sudden change of downstream condition. Thus, to remove the Goldstein singularity, in a neighborhood of $x_s$ one should give up (5.38) to recover the elliptic feature of the model flow, to make it adaptive to the separation process. This adaptation needs a *local interaction* with the external flow which also changes the latter. Consequently, the external pressure gradient cannot be prescribed in advance but has to be solved from the interaction.

Specifically, recall that the basis of matched asymptotic method lies in the concept that, in an approximate theory, whenever there appears a singularity in one coordinate direction, one should perturb the singular equation by introducing a thin layer normal to that direction with different scaling. In Sect. 4.3.1 we have perturbed the Euler equation to replace the singular attached vortex sheet by an attached boundary layer; so now we should introduce a layer normal to the wall, of *streamwise* thickness $l \ll 1$ centered at $x_s$, in which the elliptic nature of the equations should be realized by rescaling such that the local interaction can be solved. The intersection of this new thin layer and the attached boundary layer forms a deck-like structure, of which the scales are the basis of the triple-deck theory and can be derived from the following simple reasoning.

First, the interaction of strong upwelling (5.39) in the separating flow with external pressure gradient causes a viscous response in a sublayer adjacent to the wall. Let this occur in a *lower deck* of normal thickness $y \sim Re^{-1/2}\delta$ in global scale, or $Y \sim \delta$ in boundary-layer scale, with $\delta \ll 1$ to be determined. Since adjacent to the wall the streamwise velocity profile can be represented by a uniform shear flow, we have $u(Y) \sim \Delta u(Y) \sim \delta$. Then by the momentum equation (4.85a), in the boundary-layer scale the balance between the inertial force and interactive pressure increment $\Delta p$ as well as the viscous force requires that

$$\frac{\delta^2}{l} \sim \frac{\Delta p}{l} \sim \frac{\delta}{\delta^2},$$

which gives $\Delta p = O(\delta^2)$ and $l = O(\delta^3)$. Finally, to determine $\delta$, we note that the appearance of the lower deck raises the rest of the boundary layer (the *main deck*) up by an additional displacement thickness $\delta$. The slope of this displacement is of $O(Re^{-1/2}\delta/l)$ in global scale. On the other hand, across the main deck the pressure remains unchanged, so that a $\Delta p = O(\delta^2)$ propagates all the way to the outer edge of the boundary layer and alters the external potential flow in a zone called the *upper deck*. The flow therein is inviscid and irrotational without preferred direction, so the upper-deck thickness should be of the same order as its streamwise length $l$. In the upper deck the displacement slope must be balanced by the interactive pressure. This yields $Re^{-1/2}\delta/l \sim \delta^2$, and hence $\delta = O(Re^{-1/8})$ and $l = O(Re^{-3/8})$. Therefore, a triple-deck structure as shown in Fig. 5.9 is established, which should replace the two-layer structure of Fig. 5.8.

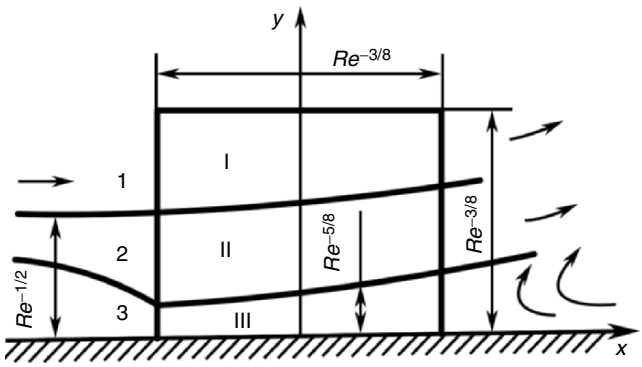


**Fig. 5.9.** Triple-deck structure and its scales. After Sychev et al. (1998)

Of the three decks the lower deck causing the displacement is most active, where the orders of magnitude of various quantities are

$$\begin{aligned} &\Delta x = O(Re^{-3/8}), \quad y = Re^{-1/2}\delta_{\text{lower}} = O(Re^{-5/8}), \\ &u = O(Re^{-1/8}), \quad v = O(Re^{-3/8}), \quad \Delta p = O(Re^{-1/4}). \end{aligned} \tag{5.42}$$

To the leading order, the role of the main deck is only passive. It is displaced by the lower deck so that the slope of the streamlines is transported from the lower deck to the upper deck. In the upper deck the interactive pressure due to this slope is to be solved, which eventually makes the triple-deck problem elliptic. This clear physical picture cannot be obtained by pure numerical computations. Notice that the thickness ratios of the three decks are

$$\frac{\delta_{\text{lower}}}{\delta_{\text{main}}} \sim \frac{\delta_{\text{main}}}{\delta_{\text{upper}}} \sim Re^{-1/8} \to 0 \quad \text{as} \quad Re \to \infty, \tag{5.43}$$

thus at large $Re$ the thickness of a thinner deck is asymptotically negligible in the scale of a thicker deck.

An inspection of the earlier derivation of the scales indicates that the same triple-deck structure exists in any laminar boundary layer which encounters a sudden change of whatever downstream flow conditions that vary for different flow problems. Therefore, the triple-deck structure has certain universal nature and appears in a variety of problems, see, e.g., the reviews of Smith (1982), Wu (1985), and Sychev et al. (1998).

### 5.3.2 Triple-Deck Equations and Interactive Vorticity Generation

We can now rescale the continuity and Navier–Stokes equations in each deck and match their solutions at each overlapping region of two decks. Here we consider two-dimensional flow, following basically the formulation of Smith

(1982) in terms of primitive variables $(u, v, p)$. To see the vorticity dynamics involved, we will also use the vorticity equation and boundary coupling relation (the boundary vorticity flux $\sigma$):

$$u\omega_{,x} + v\omega_{,y} = Re^{-1}(\omega_{,xx} + \omega_{,yy}), \tag{5.44}$$

$$\sigma \equiv -Re^{-1}\omega_{,y} = p_{,x} \quad \text{at} \quad y = 0. \tag{5.45}$$

As before, lower-case letters are used for variables in global scale and capital letters for variables in respective local scales. The rescaled variables of $O(1)$ in the main, upper, and lower decks will be distinguished by tilde, overbar, and asterisk, respectively. The basic small parameter is $\delta = Re^{-1/8}$.

1. *Main deck*
   According to Fig. 5.9, in the main deck we set

$$x - x_{\rm s} = \delta^3 \widetilde{X}, \quad y = \delta^4 \widetilde{Y}.$$

The solution should match the upstream boundary layer (see Sect. 4.3.1) at $x_{\rm s}^-$, which is function of $\widetilde{Y}$ only and denoted by suffix $B$:

$$u \to U_{\rm B}(\widetilde{Y}), \quad v \to \delta^4 V_{\rm B}(\widetilde{Y}), \quad \omega \to \delta^{-4}\Omega_{\rm B}(\widetilde{Y}) = -\delta^4 U_{\rm B}'(\widetilde{Y}).$$

Hence, the perturbation expansion is

$$(u, v, \omega) = (U_{\rm B}, \delta^4 V_{\rm B}, \delta^{-4}\Omega_{\rm B}) + (u^{(1)}, v^{(1)}, \omega^{(1)}) + \cdots ,$$

where the disturbance quantities should be rescaled to match the lower-deck solution. Since in lower deck $u = O(\delta)$, we set $u^{(1)} = \delta\widetilde{U}$, which by the continuity equation

$$\delta^{-2}\widetilde{U}_{,\widetilde{X}} + \delta^{-4} v^{(1)}_{,\widetilde{Y}} = 0$$

yields $v^{(1)} = \delta^2 \widetilde{V}$. Then there is $\omega^{(1)} = -\delta^{-3}\partial\widetilde{U}/\partial\widetilde{Y} = \delta^{-3}\widetilde{\Omega}$. Hence, the correct expansion is

$$(u, v, \omega) = (U_{\rm B}, \delta^4 V_{\rm B}, \delta^{-4}\Omega_{\rm B}) + (\delta\widetilde{U}, \delta^2\widetilde{V}, \delta^{-3}\widetilde{\Omega}) + \cdots .$$

We substitute this into (5.44) and subtract the attached boundary-layer vorticity equation (4.93). After letting $x \to \widetilde{X} = \delta^{-3}(x - x_{\rm s})$ and noticing $\partial\widetilde{\Omega}_{\rm B}/\partial\widetilde{X} = 0$, we obtain a linear equation

$$U_{\rm B}\widetilde{\Omega}_{,\widetilde{X}} + \widetilde{V}\Omega_{\rm B}'(\widetilde{Y}) = O(\delta) \quad \text{or} \quad U_{\rm B}\widetilde{V}_{,\widetilde{Y}\widetilde{Y}} = \widetilde{V}U_{\rm B}''$$

due to the continuity equation, of which the solution is

$$\begin{aligned} \widetilde{U} &= \widetilde{A}(\widetilde{X})U_{\rm B}'(\widetilde{Y}) = -\widetilde{A}(\widetilde{X})\Omega_{\rm B}(\widetilde{Y}), \\ \widetilde{V} &= -\widetilde{A}'(\widetilde{X})U_{\rm B}(\widetilde{Y}), \\ \widetilde{\Omega} &= -\widetilde{A}(\widetilde{X})U_{\rm B}''(\widetilde{Y}) = \widetilde{A}(\widetilde{X})\Omega_{\rm B}'(\widetilde{Y}), \end{aligned} \tag{5.46}$$

where $\widetilde{A}(\widetilde{X})$ is an unknown function of $\widetilde{X}$. Note that in the main deck $p = \delta^2 \widetilde{P}$, so by (4.85b) $\partial \widetilde{P}/\partial \widetilde{Y} = \delta^{-2} \partial p/\partial \widetilde{Y} = O(\delta^6)$, which is negligible.

The upper boundary condition of the main deck as $\widetilde{Y} \to \infty$ is (normalized) $U_{\rm B} \to 1$ and $U'_{\rm B} \to 0$. Thus,

$$u^{(1)} \to 0, \quad v^{(1)} \to -\delta^2 \widetilde{A}'(\widetilde{X}), \quad \omega^{(1)} \to 0. \tag{5.47}$$

We see that $-\widetilde{A}$ is the *additional displacement thickness* caused by viscous motion in the lower deck. As mentioned earlier, its slope

$$\widetilde{S}(\widetilde{X}) \equiv -\widetilde{A}'(\widetilde{X}) = \lim_{\widetilde{Y} \to \infty} \frac{\widetilde{V}(\widetilde{X})}{\widetilde{U}(\widetilde{X})} \tag{5.48}$$

will be related to the interactive pressure in the upper deck. On the other hand, at the lower boundary of the main deck with $\widetilde{Y} \to 0^+$ and at the upper boundary of the lower deck (not the wall, see (5.43)), $U_{\rm B}(\widetilde{Y})$ can be simplified to a simple shear flow. Denote

$$\lambda \equiv U'_{\rm B}(0) = -\Omega_{\rm B}(0) \tag{5.49}$$

as the skin friction at $x_{\rm s}^-$, by (5.46) there is

$$u = \lambda[\widetilde{Y} + \delta \widetilde{A}(\widetilde{X})], \quad \omega^{(1)} \to \delta^3 \widetilde{A}(\widetilde{X}) \Omega'_{\rm B}(0) \quad \text{at} \quad \widetilde{Y} = 0^+, \tag{5.50}$$

which is to be matched with lower-deck solution.

*2. Upper deck*

In the upper deck the flow is irrotational and isotropic, where

$$\overline{X} = \widetilde{X} = \delta^{-3}(x - x_{\rm s}), \quad \overline{Y} = \delta^{-3} y.$$

The zeroth-order basic flow is uniform with $(u^{(0)}, v^{(0)}, p^{(0)}) = (1, 0, 0)$, since within the length scale $l = \delta^3$ any inviscid streamwise variation above an attached boundary layer is negligible. The viscous motion in lower deck causes a disturbance $(u^{(2)}, v^{(2)}, p^{(2)})$, say, and the matching with the main-deck solution at $\overline{Y} = 0^+$ implies $v^{(2)} = O(\delta^2)$. The isotropy then implies so too must be $u^{(2)}$ and $p^{(2)}$. Thus the disturbance expansion reads

$$(u, v, p) = (1, 0, 0) + \delta^2 (\overline{U}, \overline{V}, \overline{P}) + \cdots .$$

Substituting this into the Euler equation yields a pair of linear potential-flow equations

$$\overline{U}_{,\widetilde{X}} = -\overline{P}_{,\widetilde{X}}, \quad \overline{V}_{,\widetilde{X}} = -\overline{P}_{,\overline{Y}}, \tag{5.51a,b}$$

which by the continuity yields a Laplace equation for $\overline{P}$:

$$\overline{P}_{,\overline{X}\,\overline{X}} + \overline{P}_{,\overline{Y}\,\overline{Y}} = 0. \tag{5.52a}$$

At the upper and upstream boundaries of the deck, both $\overline{P}$ and its normal derivative vanish. At the downstream boundary $\overline{P}$ is a constant that can be subtracted. The nontrivial boundary condition occurs only at the lower boundary $\overline{Y} = 0^+$ due to the matching with the main deck with $\widetilde{Y} \to \infty$. By (5.46) and (5.51b) this condition reads

$$\overline{P}(\widetilde{X}, 0) = \widetilde{P}(\widetilde{X}), \quad \overline{P}_{,\overline{Y}} = \widetilde{A}''(\widetilde{X}) \quad \text{at} \quad \overline{Y} = 0^+. \tag{5.52b}$$

Problem (5.52a,b) can be solved using complex-variable method or Green's function. In the latter approach, since we are only concerned with the solution at $\overline{Y} = 0^+$, the Cauchy principal value is to be taken, yielding

$$\frac{1}{2}\widetilde{P}(\widetilde{X}) = \text{p.v.} \int_{-\infty}^{\infty} (\overline{P} G_{,\overline{\eta}} - G\overline{P}_{,\overline{\eta}}) \mathrm{d}\widetilde{\xi},$$

where $G$ is the free-space Green's function (2.102) and the integration is along $\overline{Y} = 0^+$. Since $\partial G/\partial\overline{\eta} = 0$ at $\overline{Y} = \overline{\eta} = 0$, after an integration by parts one obtains a *pressure-displacement relation*

$$\widetilde{P}(\widetilde{X}) = \frac{1}{\pi} \text{p.v.} \int_{-\infty}^{\infty} \frac{\widetilde{S}(\widetilde{\xi}) \mathrm{d}\widetilde{\xi}}{\widetilde{\xi} - \widetilde{X}}, \tag{5.53}$$

where $\widetilde{S}$ is the displacement slope defined by (5.48).

*3. Lower deck*

In lower deck we have

$$X^* = \widetilde{X} = \delta^{-3}(x - x_\mathrm{s}), \quad Y^* = \delta^{-5} y = \delta^{-1}\widetilde{Y}.$$

The perturbation has magnitude comparable with that of the undisturbed basic flow. Then by (5.42) the expansion reads

$$(u, v, w) = (\delta U^*, \delta^3 V^*, \delta^4 \Omega^*) + \cdots,$$

of which the substitution into (5.44) yields the same boundary-layer vorticity equation as (4.93), of which an integration yields the same standard boundary-layer equation as (4.85). The upper boundary condition follows from (5.50):

$$U^* \sim \lambda[Y^* + \widetilde{A}(\widetilde{X})] \quad \text{as} \quad Y^* \to \infty. \tag{5.54}$$

The adherence requires $U^* = V^* = 0$ at $Y^* = 0$. It can be shown that $\partial\overline{P}/\partial Y^* = O(\delta^7)$, hence (5.54) holds throughout the entire lower deck as well.

We have now obtained a basic physical–mathematic picture of the triple-deck theory. The violation of scaling (5.38) due to a sudden change of boundary condition at $x_\mathrm{s}$ creates a lower deck where the flow is inherently viscous and rotational, as well as nonlinear. The lower deck represents an additional

displacement that is transported into the main deck, adding an inviscid, rotational, and linear disturbance to the upstream attached boundary layer solution which itself is viscous and rotational. Then the displacement is continued to be transported to the upper deck, adding an inviscid and irrotational disturbance to the external flow, which induces a pressure gradient to drive the lower-deck flow. In terms of our two fundamental processes, the main and lower decks are dominated by the shearing process, and the upper deck by the (degenerated) compressing process. Here we see a stronger coupling of both processes than in attached boundary layer theory.

The main and upper decks only serve as a scaffold in the development of the theory. Since the linearized solutions in these two decks have been used in the matching process, what remains is only the boundary-layer equation and the pressure-displacement relation, both in the lower-deck. These equations make the whole problem elliptic and can be cast to a canonic form by an $O(1)$ rescaling

$$(\widetilde{X}, Y^*, U^*, V^*, \widetilde{P}, \widetilde{A}) = (\lambda^{-5/4}X, \lambda^{-3/4}Y, \lambda^{1/4}U, \lambda^{3/4}V, \lambda^{1/2}P, \lambda^{-3/4}A), \tag{5.55}$$

where $\lambda$ is defined by (5.49). Consequently, one has a set of *canonical triple-deck equations* applicable to various problems with different streamwise boundary conditions at $x = x_{\mathrm{s}}^{\mp}$:

$$UU_{,X} + VU_{,Y} = -P_{,X} + U_{,YY}, \tag{5.56a}$$

$$U_{,X} + V_{,Y} = 0, \tag{5.56b}$$

$$P = \frac{1}{\pi}\text{p.v.}\int_{-\infty}^{\infty} \frac{A'(\xi)\mathrm{d}\xi}{X-\xi}, \tag{5.56c}$$

$$U \sim Y + A(X) \quad \text{as} \quad Y \to \infty, \tag{5.56d}$$

$$U = V = 0 \quad \text{at} \quad Y = 0. \tag{5.56e}$$

We mention that in supersonic flow (5.56c) is replaced by a much simpler one (Neiland 1969; Stewartson and Williams 1969):

$$P = -A'(X). \tag{5.56c$'$}$$

Consider now the vorticity-based formulation of the problem. Since (5.56c) holds at $Y = 0$, its streamwise derivative is actually the boundary vorticity flux due to the interaction, see (5.45) and (5.48):

$$-(\Omega_{,Y})_{Y=0} = P'(X) = \frac{1}{\pi}\text{p.v.}\int_{-\infty}^{\infty} \frac{S'(\xi)\mathrm{d}\xi}{\xi - X}.$$

The boundary vorticity flux may serve as the Neumann condition for the vorticity field (Sect. 4.5), but in attached boundary-layer theory the vorticity formulation is redundant due to the decoupling of the shearing and compressing processes (Sect. 4.3.2). But the two processes are now coupled so a vorticity

formulation of the triple-deck theory is no longer trivial:

$$U\Omega_{,X} + V\Omega_{,Y} = \Omega_{,YY}, \tag{5.57a}$$

$$U = -\int_0^Y \Omega(\eta)\mathrm{d}\eta, \tag{5.57b}$$

$$V = \int_0^Y \mathrm{d}\eta \int_0^\eta \Omega_{,X}(X,\eta')\mathrm{d}\eta', \tag{5.57c}$$

$$\Omega \sim -1 + S(X) \quad \text{as} \quad Y \to \infty, \tag{5.57d}$$

$$\Omega_{,Y} = \frac{1}{\pi}\text{p.v.}\int_{-\infty}^{\infty} \frac{S'(\xi)\mathrm{d}\xi}{X-\xi} \quad \text{at} \quad Y = 0. \tag{5.57e}$$

Here, like (4.91), (5.57b,c) is the simplified Biot–Savart formula. The pressure is removed as a part of scaffold. Evidently, (5.57) can be equally expressed as the stream-function equation with a *single* unknown $\Psi$, which reads

$$\Psi_Y\Psi_{,XYY} - \Psi_{,X}\Psi_{,YYY} = \Psi_{,YYYY}, \tag{5.58a}$$

$$\Psi = \Psi_Y = 0, \Psi_{,YYY} = -\frac{1}{\pi}\text{p.v.}\int_{-\infty}^{\infty} \frac{S'(\xi)\mathrm{d}\xi}{X-\xi}, Y = 0, \tag{5.58b}$$

$$\Psi_{,YY} \sim 1 - S(X), S(X) = -\lim_{Y\to\infty}(\Psi_X/\Psi_Y), Y \to \infty. \tag{5.58c}$$

A formulation in terms of both $\Psi$ and $P$ (so $\Psi$ is governed by a third-order equation equivalent to (5.56a,b)) has been extensively used by Sychev et al. (1998).

It is now clear that the key vorticity-dynamic event is the *self-induced creation of new vorticity*, say $\omega_{\text{in}}$, in the lower deck.[7] This boundary vorticity flux is proportional to the *curvature* of the displacement and very strong as can be seen by writing (5.57e) in global scale:

$$\Delta\sigma(x) = \Delta p'(x) = Re^{1/8}\frac{1}{\pi}\text{p.v.}\int_{-\infty}^{\infty} \frac{S'(\xi)\mathrm{d}\xi}{\xi - X}. \tag{5.59}$$

But since $\omega_{\text{in}}$ occurs only in the lower deck, its total convective flux at the downstream end of the deck is only $O(u\omega_{\text{in}}\delta^5) = O(Re^{-1/4})$ per unit time. It is diffused into the main deck where by (5.57d) $\omega_{\text{in}}$ is proportional to the displacement slope $S(X)$. This $\omega_{\text{in}}$ joins the vorticity advected from upstream boundary layer, $\omega_{\text{up}} = O(Re^{1/2}) < 0$ with total flux $O(u\omega_{\text{up}}\delta^4) = O(1)$, and that from downstream reverse-flow, $\omega_{\text{down}} > 0$, which is weaker than $\omega_{\text{up}}$. Therefore, the separated shear layer is still dominated by $\omega_{\text{up}}$, having a strength $\gamma < 0$ of $O(1)$.

[7] The self-induced adverse pressure gradient and boundary vorticity flux should not be confused with their counterparts caused by global flow condition as meant by Prandtl (1904). The former must and only appear in the narrow separation zone but with very strong peak.

### 5.3.3 Boundary-Layer Separation in Two Dimensions

We now apply the triple-deck theory to boundary-layer separation from a smooth surface. For this problem, the downstream condition of the triple deck should be a separated flow. As shown in Sect. 4.4.3, in the Euler limit a two-dimensional steady separated flow forms a closed bubble. The separated vortex sheet leaves the wall tangentially, so that between the sheet and the wall there is a cusp region right downstream of $x_s$. But this information is still insufficient for fully understanding the separation in the Euler limit. Later in Sect. 7.2.2 it will be shown that the local flow in the cusp region is a *Kirchhoff free-streamline flow* or *Helmholtz's motion* (e.g., Birkhoff and Zarantonello 1957; Milne-Thomson 1968). In this flow model the separated vortex sheet appears as a free streamline along which $q = |\boldsymbol{u}|$ and $p$ are constant, and the fluid in the cusp region is at rest. It can then be shown that near the separation point $x_s$ the local equation $y = f(x)$ and curvature $\kappa$ of the free vortex sheet are given by

$$\begin{aligned} &y \simeq -\tfrac{2}{3}k(x - x_s)^{3/2}, \\ &\kappa = -\tfrac{1}{2}k(x - x_s)^{-1/2} + \kappa_0, \quad x \to x_s^+, \end{aligned} \tag{5.60}$$

where $\kappa_0$ is the body curvature and $k$ an arbitrary constant; and, the local pressure along the body surface is

$$p \begin{cases} \simeq k(x_s - x)^{3/2} & \text{for} \quad x \to x_s^-, \\ = 0 & \text{for} \quad x > x_s. \end{cases} \tag{5.61}$$

These behaviors should be the external-flow condition of the triple-deck theory for boundary-layer separation from smooth surface. But the separation point $x_s$ cannot be determined by inviscid theory. Nevertheless, it has been found that there exists a point $x_0$ on the body surface such that

$$k \begin{cases} < 0 \text{ if } x_s > x_0, \\ = 0 \text{ if } x_s = x_0, \\ > 0 \text{ if } x_s < x_0. \end{cases} \tag{5.62}$$

Now, by (5.60) and (5.61), $k > 0$ has to be excluded since otherwise there would be $\kappa = -\infty$ at $x_s$ so that the vortex sheet would cut into the body (Fig. 5.10). $k < 0$ should also be rejected since it implies an infinitely large adverse pressure gradient at $x_s$ so that separation should have taken place earlier than $x_s$. Hence, the only choice in the Euler limit is $x_s = x_0$ with $k = 0$, known as *smooth separation*. But then at $x_s$ there is no adverse pressure at all, and the flow has no reason to separate.

The earlier dilemma was addressed by Sychev (1972), who proposed that $k$ is a Reynolds-number dependent negative number and $k(Re) \to 0$ as $Re \to \infty$. Thus, in the Euler limit the smooth separation is recovered, but at finite large Reynolds numbers there will be a very large positive adverse pressure

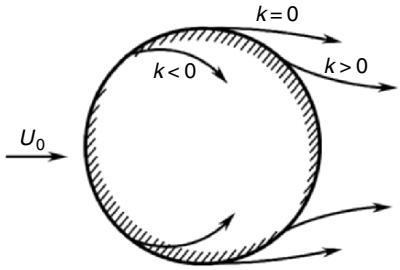


**Fig. 5.10.** The effect of the sign of $k$ on the separated streamline pattern. After Sychev et al. (1998)

gradient in a very narrow zone $\Delta x$ around $x_s$. Then, repeating the reasoning in Sect. 5.3.1, Sychev rearrived at exactly the same triple-deck structure as Fig. 5.9. Substituting (5.42) into (5.61) yields $k = O(Re^{-1/16}) = O(\delta^{1/2})$, so one may set

$$k = \widehat{\alpha}\, Re^{-1/16}, \quad \widehat{\alpha} > 0. \tag{5.63}$$

By (5.62), this implies that the separation point at finite $Re$ will be shifted downstream by a distance of $O(\delta^{1/2})$ from the smooth-separation point.

In order to complete the embedding of the triple-deck structure into the inviscid smooth-separation picture, some further analysis is necessary regarding the asymptotic flow behavior as $X \to \pm\infty$, of which for details see Smith (1982) and Sychev et al. (1998). The proper downstream condition is complicated since it must model separated flow. But to the leading order the fluid in the reverse flow region (in between the separated free vortex layer and the attached vortex layer) can be assumed at rest. A key observation is that the well-posed problem contains a single undetermined constant $\alpha$. If the solution exists and is unique, therefore, then there must exist one and only one value of $\alpha$ as a *universal constant* for various boundary-layer separation problems.

Assuming $u = 0$ in the recirculation region, Smith (1977) carried out the first numerical study of Sychev's proposal, which established the existence and uniqueness of problem (5.56) and (5.63) with $\alpha \simeq 0.44$ found by the calculation. The computed variation of $A$, $P$, and skin friction $\tau$ are shown in Fig. 5.11. Smith also made the first comparison of the asymptotic ($Re \to \infty$) pressure and skin-friction with available numerical and experimental results at low Reynolds numbers. The agreement is fairly good.

Smith's computation has been improved by others using fully consistent downstream condition (see the review of Sychev et al. (1998)). Figure 5.12 shows the asymptotic skin-friction computed by Korolev (1980), compared with the full-Navier–Stokes computation at $Re = 100$ and 300 by Fornberg (1980) and experimental measurement at $Re = 1.2 \times 10^4$ by Varty and Currie (1984). Considering that in the asymptotic theory $Re^{-1/16}$ is assumed much smaller than one (which for $Re = 1.2 \times 10^4$ and 200 is 0.556 and 0.718, respectively), the agreement is satisfactory.

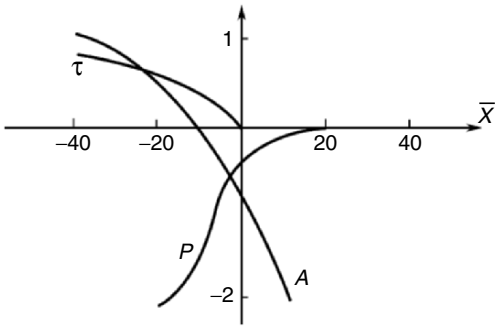


**Fig. 5.11.** Triple-deck solution of Smith (1977) for displacement $A$, pressure $P$, and skin-friction $\tau$ for two-dimensional boundary-layer separation. Reproduced from Smith (1977)

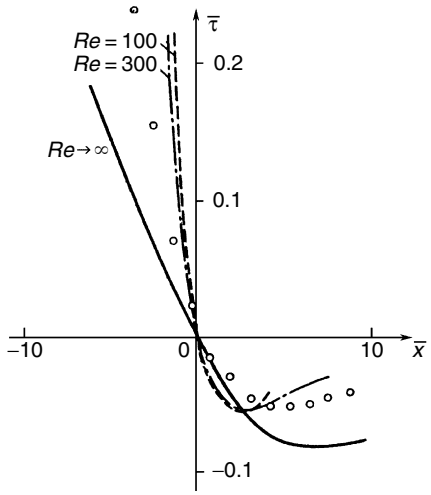


**Fig. 5.12.** Triple-deck solution of Korolev (1980) for skin-friction (*solid line*), compared with Navier–Stokes computation (*dashed and dashed-dot lines*) and experimental measurement (*circles*). From Sychev et al. (1998)

### 5.3.4 Boundary-Layer Separation in Three Dimensions

The formal extension of steady boundary-layer separation theory to three dimensions is straightforward, if the following conditions are satisfied (here we use the $\boldsymbol{\tau}$-frame developed in Sect. 5.2.1 and notations therein):

$$\| \mathbf{K} \| \ll Re^{1/8}, \tag{5.64}$$

$$\partial_1 = \frac{1}{h_1}\frac{\partial}{\partial x_1} = O(1). \tag{5.65}$$

Condition (5.64) implies that the wall curvature effect is negligible in the analysis. Consequently, a $\boldsymbol{\tau}$-frame with origin at separation line can be considered orthonormal in the entire separation zone and the scale factors $(h_1, h_2, h_3)$ are independent of the normal distance $x_3$. Condition (5.65) confines our analysis to ordinary points of a generic separation line not too close to the fixed points of the $\boldsymbol{\tau}$-field. Then, in the conventional boundary-layer scale with $\widetilde{X}_3 = Re^{1/2}x_3 = O(1)$ and $\widetilde{U}_3 = Re^{1/2}u_3$, denoting $\widetilde{D}_3 = \partial/\partial\widetilde{X}_3$, the continuity equation and momentum equation can be simplified to

$$\partial_2 u_2 + \widetilde{D}_3\widetilde{U}_3 - \kappa_2 u_1 = 0, \tag{5.66a}$$

$$u_2\partial_2 u_1 + \widetilde{U}_3\widetilde{D}_3 u_1 + \kappa_2 u_2^2 = \widetilde{D}_3^2 u_1, \tag{5.66b}$$

$$u_2\partial_2 u_2 + \widetilde{U}_3\widetilde{D}_3 u_2 - \kappa_2 u_1 u_2 = -\partial_2 p + \widetilde{D}_3^2 u_2, \tag{5.66c}$$

$$\widetilde{D}_3 p = 0, \tag{5.66d}$$

where $\kappa_2$ is the on-wall curvature of the $\boldsymbol{\omega}$-lines defined in Sect. 5.2. A scale analysis based on (5.64) to (5.66) can be made, which leads to exactly the same triple-deck scales as in two dimensions, but now the triple-deck width is along the $\boldsymbol{\omega}$-line direction and perpendicular to the separation line (Wu et al. 2000). Namely, in the region satisfying (5.64) and (5.65), the separation zone is a thin strip of width $O(Re^{-3/8})$ neighboring the separation line, see the sketch of Fig. 5.13.

In particular, we immediately obtain

$$\kappa_2 \sim \partial_2 \sim l^{-1} = O(Re^{3/8}), \tag{5.67}$$

which specifies (5.26). Then, from (5.16) and (5.19c) it follows that

$$\sigma_1 = \partial_2 p = O(Re^{1/8}), \tag{5.68a}$$

$$\sigma_2 = -\partial_1 p = O(1), \tag{5.68b}$$

$$\sigma_3 = Re^{-1}\partial_2\omega = O(Re^{-1/8}). \tag{5.68c}$$

This scaling characterizes the on-wall vorticity-dynamics signature in a boundary-layer separation zone. Moreover, in the most active lower deck the two-dimensional scaling (5.42) is extended to

$$\begin{array}{lll} u_1 = O(Re^{-1/8}), & u_2 = O(Re^{-1/8}), & u_3 = O(Re^{-3/8}), \\ \omega_1 = O(Re^{1/2}), & \omega_2 = O(Re^{1/2}), & \omega_3 = O(Re^{1/4}), \\ x_3 \sim Re^{-5/8}. & & \end{array} \tag{5.69}$$

Then, if a separation line and its neighboring $\boldsymbol{\tau}$-lines in the separation zone are given with known $\kappa_1$, one can infer the corresponding $\kappa_2$ from the general relation (5.15c) and thereby establish the curved $(x_1, x_2)$ grid in the separation strip.

With the earlier scaling, a set of triple-deck equations can be derived in terms of the $\boldsymbol{\tau}$-frame. Since all $x_1$-derivatives disappear from (5.66), at each

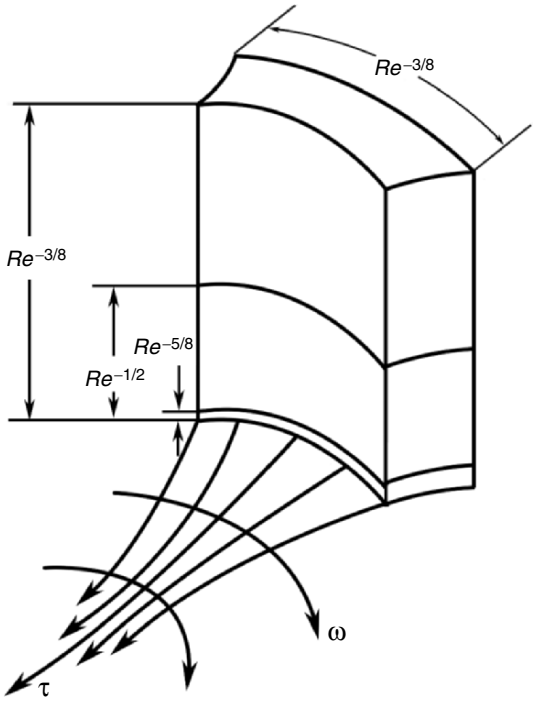


**Fig. 5.13.** Three-dimensional triple-deck structure

$x_1$-station *the triple-deck structure is completely determined by the flow variation in the* $(x_2, x_3)$*-surface*. In other words, under condition (5.64) and (5.65), $x_1$ serves as merely a parameter that gives the asymptotic flow conditions outside the triple-deck zone.

In fact, for the sake of solving the triple-deck equations, the $\boldsymbol{\tau}$-frame can even be replaced by the simpler normal-plane frame $(x, y, z)$ mentioned in Sect. 5.2.2. The reason is that one can well approximate the scale factors $h_\alpha(x_1, x_2)$, $\alpha = 1, 2$, by those right at $x_2 = 0$, i.e., $h_{\alpha 0} \equiv h_\alpha(x, 0)$, with error of $O(Re^{-3/8})$ (Smith 1978). Then all $x$-lines at different $y$-locations in the separation zone are parallel. This reduces (5.66) to a form very close to the two-dimensional form (5.56). The remaining three-dimensional effect is confined to the fact that in the boundary layers outside the separation zone there are two velocity-component profiles $\boldsymbol{U} = (U, V)$ along the streamwise and transverse directions, respectively. It is then found that in the matching conditions between the lower and main decks, and that between the lower deck and the near-wall approaching boundary layers as $X \to \pm\infty$, only the *streamwise component* $U_{\mathrm{B}}(Z)$ matters; but in the pressure-displacement relation or boundary vorticity flux-displacement curvature relation, only the *transverse component* $V(Z)$ matters (Wu et al. 2000).

Although so far no numerical solution of fully three-dimensional triple-deck equations is available, we may combine the preceding triple-deck scaling and the local vorticity-dynamics theory of general flow separation given in Sect. 5.2 to examine the boundary-layer separation behavior as a guidance to practical flow diagnosis. The flow data may well be obtained by numerical Navier–Stokes solutions.

*1. Separation watch criterion*

Since by (5.68) there is

$$\frac{|\sigma_1|}{|\sigma_2|} = O(Re^{1/8}) \quad \text{in separation zone,} \tag{5.70}$$

the tangent boundary vorticity flux vector $\boldsymbol{\sigma}_\pi$ (or tangent pressure gradient $\nabla_\pi p$) is almost aligned to the separation-line (or vorticity line) direction. The alignment is not exact because of the existence of $\sigma_2 = O(1)$; but it is in sharp contrast to attached three-dimensional boundary layer. In the latter, although the direction of external potential-flow driven by $\nabla_\pi p$ is generically different from the $\boldsymbol{\tau}$-line direction (the velocity profile inside the boundary layer has a twist), the difference can hardly be as large as $\pi/2$. Condition (5.71) holds only in the separation zone. Therefore, we may state

**Boundary-layer separation watch criterion.** *A boundary layer is about to separate as $\boldsymbol{\sigma}_\pi$ tends to be aligned to the $\boldsymbol{\tau}$-lines.*

Figure 5.14a plots both $\boldsymbol{\tau}$-lines and $\boldsymbol{\sigma}_\pi$-lines of the flow over inclined prolate spheroid studied before, which confirms the criterion. Figure 5.14b plots the $\sigma_1$-variation across the primary separation line at a few stations, indicating that when the boundary-layer separates (at stations 1, 2, and 3, see Fig. 5.6) $\sigma_1$ reaches a negative peak. In practical diagnosis the boundary-layer separation watch criterion can be checked more easily than examining the $\boldsymbol{\omega}$-line curvature $\kappa_2$.[8]

*2. Formation of streamwise separated vortex layer*

A major difference between three- and two-dimensional boundary-layer separation is that, although by (5.3) the $\boldsymbol{\omega}_\mathrm{B}$-lines are always perpendicular to $\boldsymbol{\tau}$-lines, as demonstrated in Fig. 5.1 the vorticity in a separated shear layer is basically aligned to the separation line so that the layer rolls up into a *streamwise* vortex. Behind this feature are the two basic vorticity-dynamics mechanisms discussed following (5.59): the strong self-induced vorticity creation and the vorticity advection. But what is new in three dimensions is that both mechanisms lead to an abrupt change of vorticity direction right above the wall. For definiteness, in the following discussion assume $\sigma_1 = \partial_2 p > 0$.

First, by (5.68a), the newly created $\boldsymbol{\omega}_\mathrm{in} = \boldsymbol{e}_1\omega_{\mathrm{in}\ 1} + \boldsymbol{e}_2\omega_{\mathrm{in}\ 2}$ with $\omega_{\mathrm{in}\ 1} = O(Re^{1/8}) > 0$ is almost aligned to the separation line. This is a very strong

[8] In numerical computation with adaptive grid, this criterion could be used to warn that the grid should be made locally denser for resolving the flow in the triple-deck strip.

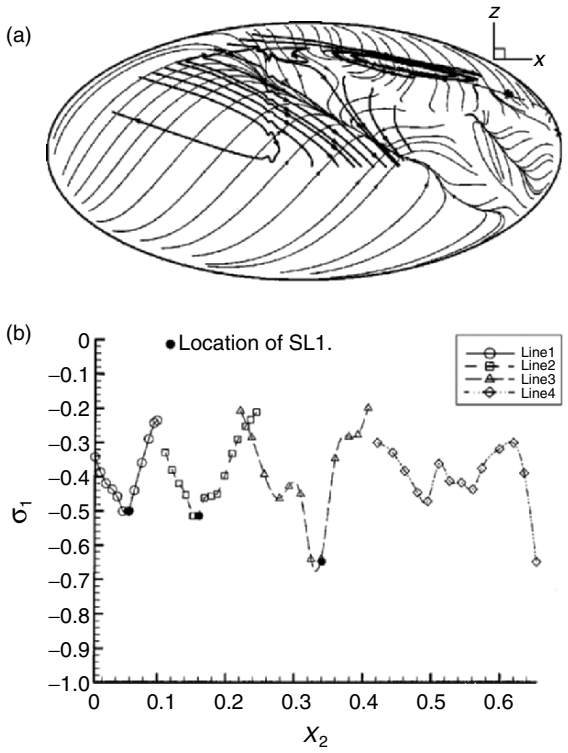


**Fig. 5.14.** The strong peak of interactive $\boldsymbol{\sigma}_1$ in the separation zone. (**a**) The $\boldsymbol{\tau}$-lines (*thin*) and $\boldsymbol{\sigma}_p$-lines (*thick*) on the prolate spheroid. (**b**) $\boldsymbol{\sigma}_1$ vs. $x_2$ at four $x_1$ station shown in Fig. 5.6. From Wu et al. (2000)

rotation (about 90°) from $\boldsymbol{\omega}_{\rm B} = \boldsymbol{e}_2\omega_{\rm B}$ on the wall during a very short normal distance within the lower deck. The rotation must be associated with a strong normal vorticity above the wall, and this is indeed so as shown by (5.68c) and (5.69): $\sigma_3$ and $\omega_3$ are both $O(Re^{3/8})$ times of their counterpart in attached boundary layer.

Second, the vorticity from the oncoming boundary layers also experiences an abrupt direction change as it is advected into the separation zone. To see this consider the transport equation for $\omega_1$ in the lower deck. By (5.69) we have $\omega_1 \simeq -\partial_3 u_2$, so taking the normal derivative of (5.66c) and using (5.66a,d), in global scale there is

$$(u_2\partial_2 + u_3\partial_3 - \nu\partial_3^2)\omega_1 = -\kappa_2 u_2\omega_2, \quad x_3 = O(Re^{-5/8}), \tag{5.71}$$

where each term is of $O(Re^{3/4})$. Evidently, the right-hand side serves as the source of $\omega_1$ due to the strong $\boldsymbol{\omega}$-line turning. The vorticity of the approaching boundary layer with $u_2 > 0$ above the wall no longer follows the $\boldsymbol{e}_2$ direction but quickly turns to an $\omega_1 = O(Re^{1/2}) < 0$, which is also raised up quickly.

The combined effect of these two mechanisms makes $\omega_1$ as strong as $\omega_2$ as entering the main deck. The overall vorticity flux budget is the same as in two dimensions, i.e., the vorticity in the separated vortex layer is dominated by that from the upstream boundary layer (with $\omega_1 < 0$ in this example). The layer then rolls into a vortex with total circulation $\Gamma_1 < 0$.

*3. Asymptote vs. envelope*

In a real flow governed by the Navier–Stokes equation, through a regular point on the wall there must be one and only one $\boldsymbol{\tau}$-line, including the separation line. But as $Re \to \infty$ some singular behavior may develop. The separation zone shrinks to an arbitrarily thin strip, and by (5.67) $\kappa_2 \to \infty$ in the strip. The strong separation-line criterion (5.27) assures that $\kappa_2$ *on* the separation line becomes singular earlier than any other neighboring $\boldsymbol{\tau}$-lines. This in turn results in a singular behavior of the separation line. In fact, denoting the curvature of separation line by $\kappa_{10}$, for the neighboring $\boldsymbol{\tau}$-lines there is

$$\kappa_1 = \kappa_{10} + (\partial_2 \kappa_1)_0 x_2 + O(x_2^2),$$

but by the general relation (5.15c), since $\partial_1 \kappa_2 = O(\kappa_2)$, we have

$$\partial_2 \kappa_1 = O(\kappa_2^2) = O(Re^{3/4}) \to +\infty.$$

Therefore, referring to Fig. 5.5a or Fig. 5.6a, as $x_2 \to \pm Re^{-3/4}$ and $Re \to \infty$, at each point of the separation line one sees three $\boldsymbol{\tau}$-lines tangent to each other but with different curvatures: in addition to the separation line itself, on the left ($x_2 < 0$) $\kappa_1$ jumps to a *finite* value smaller that $\kappa_{10}$, while on the right it jumps larger. In other words, *as $Re \to \infty$ the separation line degenerates from an asymptote of neighboring $\boldsymbol{\tau}$-lines to their envelope.* An envelope is a singular line since passing a regular point there are three vector lines.

While the earlier observation is made for real flow, the same degeneration of separation line occurs at a finite but large $Re$ if one uses three-dimensional attached boundary-layer equation to compute separating flow, since this implies that the triple-deck strip already shrinks to a line with $\kappa_2 = \infty$. The separation line then becomes a singular envelope where the computation must blow up. This is the *three-dimensional Goldstein singularity.* In early literature a separation line was identified as an envelope of neighboring $\boldsymbol{\tau}$-lines based on experimental and numerical visualization, but Lighthill (1963) identifies it as an asymptote. This controversy cannot be clarified solely by experiments due to the limited resolution of visualization. Zhang (1986b) was the first to conclude that, at a finite $Re$, one observes an asymptote in a full Navier–Stokes solution, but an envelope in boundary-layer approximation. The above simple argument supports Zhang's conclusion.

## 5.4 Unsteady Separation

For unsteady flow separation, one needs to predict not only where the separation happens but also when. Once again this can be done in two

categories: generic unsteady flow separation and unsteady boundary-layer separation at large Reynolds numbers. Despite the possibility of Navier–Stokes numerical solutions for some special cases at moderate Reynolds numbers, like the steady case locally effective theories are desired to reveal the key underlying physics and predict the separation character in both space and time. This section addresses theories in both categories according to the historic order. We first make an overall examination of the physical phenomena of unsteady boundary-layer separation, introduce an empirical separation criterion, and then present a rational theory based on unsteady boundary-layer equation in terms of *Lagrangian description*. We end the chapter by a new general theory of unsteady flow separation. For simplicity, this section is confined to two-dimensional incompressible flow; generalization of some of the theories to three-dimensional and/or compressible flow will be mentioned whenever available.

### 5.4.1 Physical Phenomena of Unsteady Boundary-Layer Separation

The most commonly encountered unsteady flows fall into two categories: periodic oscillating flow and transient flow between two steady states including starting flow. These are also the prototypes of studies on unsteady boundary-layer separation. We start from a few examples.

A familiar starting flow is the one over a circular cylinder impulsively brought into motion, for which rich experimental and numerical results are available. It is possible to perform a theoretical analysis of the flow shortly after the start. Scaled by the cylinder's radius and free-stream velocity, at $t = 0^+$ the flow is fully attached with potential velocity $U(x) = 2\sin x$ along the cylinder surface ($x$ is the arclength). For $t \ll 1$, the boundary layer is very thin (of thickness of $O(t^{1/2})$) and advection is weak, so $u_t$ is balanced by $\nu u_{yy}$ as in the case of the Rayleigh flow (Sect. 4.1.4).[9] Then $|\mathrm{d}U/\mathrm{d}x|$ reaches the maximum at the rear stagnation point ($\theta = 2\pi$) for the first time at $t \simeq 0.35$. This maximum point moves upstream, causing a thin embedded recirculation sublayer that signifies a weak separation (Sect. 5.1), but the boundary-layer equation remains valid. Then the boundary layer starts to thicken at $\theta \simeq 115^\circ$ at $t = 1.3$–$1.4$, followed by break-away separation and formation of separated vortex. This evolution can be seen from the numerical result of Ta Phuoc Loc and Bouard (1985) shown in Fig. 5.15 for the initial stage ($t \leq 1.6$) of the flow history at Reynolds number $Re = 9,500$ (a later-time state was shown in Fig. 4.24). The computed flow picture is in excellent agreement with an accurate experimental visualization of Bouard and Coutaneau (1980). Note that the separation point defined by (5.1) for steady flow, referred to as the zero-$\boldsymbol{\tau}$ point henceforth, differs significantly from the boundary-layer separation point.

[9] Here and below, whenever no confusion can be caused we neglect the suffix comma for partial derivatives.

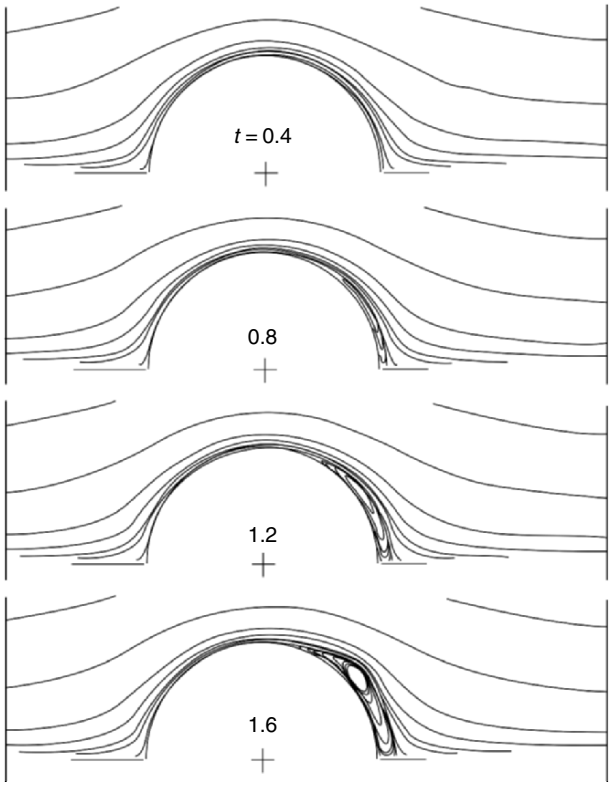


**Fig. 5.15.** Early stage of flow separation from an impulsively started circular cylinder at $Re = 9,500$. From Ta Phuoc Loc and Bouard (1985)

An unsteady boundary-layer separation with high-frequency oscillating components was carefully studied by Despard and Miller (1971), who also observed the difference of the zero-$\boldsymbol{\tau}$ point and separation point $S$. The zero-$\boldsymbol{\tau}$ point oscillates along the wall, generating a thin recirculation sublayer that shoots upstream ahead of $S$, then moving downstream to meet $S$ again, and then turning back. This is sketched in Fig. 5.16, where at each station two envelopes of the velocity profiles during a cycle are shown, and point $A$ is the farthest upstream end of the zero-$\boldsymbol{\tau}$ point during the cycle. The authors found that $S$ is basically fixed, until which the outer flow remains attached.

The preceding examples clearly indicate that Prandtl's criterion (5.1) cannot characterize unsteady boundary-layer separation at all, and generic flow separation is very different from boundary-layer separation. This is easily understood by considering the separation from down- and upstream moving walls (Fig. 5.17a,b), where there must be an attached sublayer below the separation point and hence no zero-$\boldsymbol{\tau}$ point on the wall exists. Consequently, instead of the zero-$\boldsymbol{\tau}$ point as a semisaddle on the wall, the boundary layer separation is

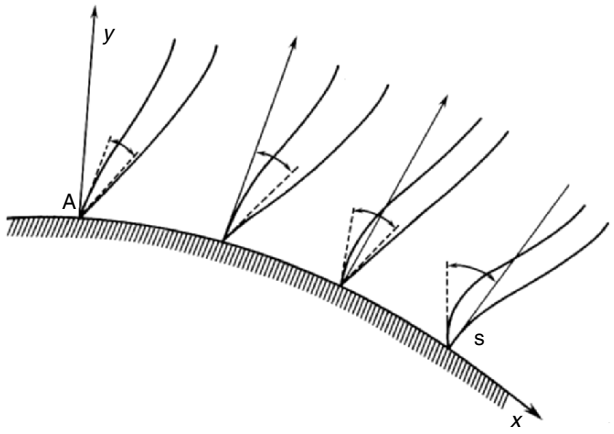


**Fig. 5.16.** Envelopes of velocity profiles for periodic oscillations. The dashed lines and arrows indicate the extreme positions of the tangents to the profile at the wall. From Telionis (1981)

now characterized by an *interior saddle point* where the vortex layer *bifurcates*. The two separation patterns in Fig. 5.17a,b can be realized at opposite sides of a single flow past a rotating circular cylinder, as has been confirmed by an experimental visualization of Koromilas and Telionis (1980). Note that while the moving-wall separations of Fig. 5.17a,b may still be steady, a Galilean transformation can cast them to unsteady flows with separation point moving up- and downstream as sketched in Fig. 5.17c,d, which correspond to the separation at adverse and favorable pressure gradients, respectively.

A truly unsteady flow with downstream-moving separation point has been experimentally realized by Didden and Ho (1985), who used a nozzle to produce a series of vortex rings impinging on a flat plate. Each primary vortex ring induces a local high-speed and low-pressure flow region near the wall, downstream which (with increased radial distance $r$) the pressure recovers to form an unsteady adverse pressure gradient that thickens the boundary layer and causes secondary separated vortex rings.[10] But the unsteady separation point is still in the region with $\mathrm{d}p/\mathrm{d}r < 0$, where a phase-averaged velocity profile similar to Fig. 5.17d was observed.

Like the study of steady boundary-layer separation, in unsteady case one also needs a set of criteria to identify where and when the separation happens. This was proposed by Moore (1958), Rott (1956), and Sears (1956) based on the inspection of flow patterns like Fig. 5.17. These authors assert that the separation point should be a zero-vorticity point inside the layer and move with local streamwise flow speed. Namely, using $s$ to denote both the

[10] The interaction of a vortex ring and a wall can be very complicated. Its two-dimensional counterpart, the interaction of a vortex couple and a wall, will be discussed in Sect. 8.4.1.

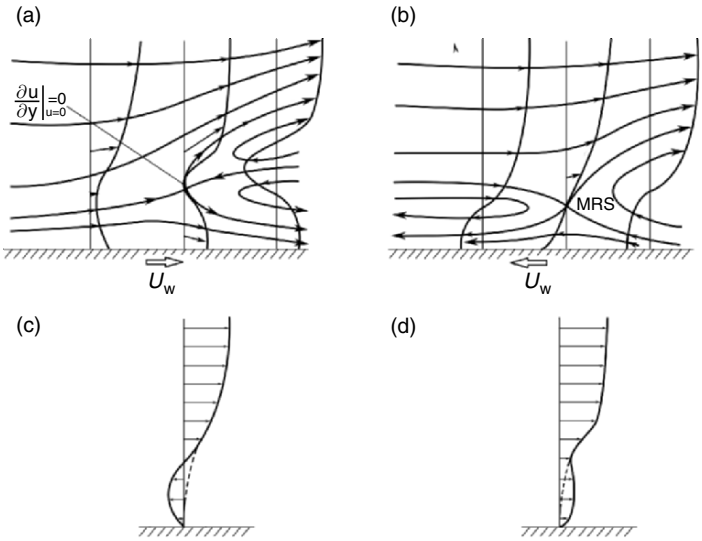


**Fig. 5.17.** Streamline patterns and velocity profiles near separation points viewed at different frame of references. The upper figures are steady separation over (**a**) downstream moving wall and (**b**) upstream moving wall. The lower figures are unsteady separation with (**c**) upstream moving separation point and (**d**) downstream moving separation point, compared with the profile (*dash lines*) at steady separation point. Based on Telionis (1981) and Didden and Ho (1985)

separation point and its coordinates,

$$\omega_{\rm s} = -u_y(s) = 0, \quad u_{\rm s} = x_t(s). \tag{5.72a,b}$$

This criterion is known as the *MRS criterion*.[11] Physically, during the separation the upper part of the boundary layer peels off from the wall with an attached vortex layer, and in between an irrotational region develops. The onset of this process is signified by the appearance of the interior saddle point. For steady flow this criterion evidently degenerates to (5.1) where the boundary vorticity $\omega_{\rm B} = 0$ at $s$.

Because near $s$ the boundary-layer thickness is much larger than $Re^{-1/2}$, like the Goldstein singularity in steady boundary-layer separation, $s$ is also a singular point of the unsteady boundary-layer equation (here and later we denote all variables in *boundary-layer scale* by lower-case letters)

$$u_t + uu_x + vu_y = u_{et} + u_e u_{ex} + u_{yy}. \tag{5.73}$$

Then Sears and Telionis (1975; see also Telionis 1981) show that the unsteady version of the heuristic reasoning of Sect. 5.3.1 leads to a generalization of

[11] One of the original statements of the MRS criterion says that $s$ is stationary in the frame of reference fixed to it, thus containing a logic cycle. Condition (5.72b) was derived by Sears and Telionis (1975), see later.

(5.41), from which (5.72) can be derived. In fact, let $s$ have streamwise coordinate $x_\mathrm{s}(t)$. The Landau–Lifshitz argument for the singularity with $v_y \to \infty$ (Sect. 5.3.1) now implies a coordinate expansion

$$x_\mathrm{s} - x = f(y,t)(u_\mathrm{s} - u)^2 + \cdots , \tag{5.74}$$

where $u_\mathrm{s} = u(x_\mathrm{s}, y, t) = u_\mathrm{s}(y,t)$. Then let the normal coordinate of $s$ be $y_\mathrm{s}(t)$, $u$ can be expanded to

$$u(x,y,t) = u_\mathrm{s}(y - y_\mathrm{s}, t) + f_{0,y}(x_\mathrm{s} - x)^{1/2} + f_{1,y}(x_\mathrm{s} - x)^{3/4} + \cdots , \tag{5.75a}$$

where $u_\mathrm{s}$ and $f_0$, $f_1$, ... are functions of $(y - y_\mathrm{s}, t)$. From (5.75a) and the continuity equation $u_x + v_y = 0$ it follows that

$$v(x,y,t) = \frac{1}{2} f_0 (x_\mathrm{s} - x)^{-1/2} + \frac{3}{4} f_1 (x_\mathrm{s} - x)^{1/4} + \cdots . \tag{5.75b}$$

Substituting (5.75a,b) into (5.73) yields an equation for the coefficients of the leading term $(x_\mathrm{s} - x)^{-1/4}$:

$$f_0 (u_\mathrm{s} - U_\mathrm{s})_{,y} - f_{0,y}(u_\mathrm{s} - U_\mathrm{s}) = 0,$$

where $U_\mathrm{s}(t) \equiv \mathrm{d}x_\mathrm{s}/\mathrm{d}t$ is the velocity of $s$. Thus $f_0 = A(t)[u_\mathrm{s}(y - y_\mathrm{s}, t) - U_\mathrm{s}(t)]$ with $A$ indeterminate. Putting this back to (5.75a,b) yields

$$u(x,y,t) = u_0 + A u_{\mathrm{s},y} (x_\mathrm{s} - x)^{1/2} + O((x_\mathrm{s} - x)^{3/4}), \tag{5.76a}$$

$$v(x,y,t) = \frac{1}{2} A (u_\mathrm{s} - U_s)(x_\mathrm{s} - x)^{-1/2} + O((x_\mathrm{s} - x)^{-1/4}), \tag{5.76b}$$

where $u_0$ and $u_\mathrm{s}$ are functions of $(y - y_\mathrm{s}, t)$, and $U_\mathrm{s}$ and $A$ depend on $t$. For steady flow over stationary wall all functions are independent of $t$, so $U_\mathrm{s} = 0$, $V_\mathrm{s} \equiv \mathrm{d}y_\mathrm{s}/\mathrm{d}t = 0$, and $y_\mathrm{s}$ is constant that can be set zero. Then since $u = 0$ on the wall, (5.76a) indicates that there is also $u_y(s) = -\omega_\mathrm{s} = 0$ at $y = 0$. This reduces to Prandtl's criterion (5.1a), and meanwhile (5.76) is reduced to (5.41).

For unsteady flow, the wall condition is no longer applicable. Because only the upper layer of the separating boundary layer becomes a free vortex layer, it can be argued that (5.76a) holds only for $y \geq y_\mathrm{s}(t)$. Moreover, assume that $v$ is regular at $s$ and hence the coefficient of $(x_\mathrm{s} - x)^{-1/2}$ in (5.76b) must vanish. Then we obtain

$$u(s,t) = U(s,t), \tag{5.77a}$$

indicating that the separation point is a bifurcation point *moving with local streamwise velocity*. Then, taking the derivative of (5.76a) with respect to $x_\mathrm{s} - x$ and requiring that $\partial u/\partial(x_\mathrm{s} - x)$ remains bounded at $y_\mathrm{s}$, we also have

$$\omega_\mathrm{s} = -\frac{\partial u_\mathrm{s}}{\partial y}\bigg|_{y = y_\mathrm{s}(t) > 0} = 0. \tag{5.77b}$$

Evidently, (5.77a,b) is precisely (5.72).

### 5.4.2 Lagrangian Theory of Unsteady Boundary Layer Separation

The earlier Sears–Telionis coordinate expansion provides a strong support to the MRS criterion but still in a heuristic way. One needs to develop a rational theory, which not only explains the physics behind the MRS criterion but also yields the time scale when the singularity happens, and furthermore to remove the singularity in a small space-time zone as was done by the triple-deck theory of Sect. 5.3 for steady boundary-layer separation. Unfortunately, adding the time dimension within the Eulerian description makes the required matched asymptotic expansion extremely complicated. Even in two dimensions such a task is still incomplete (e.g., Sychev et al. 1998). However, the difference between steady and unsteady flows disappears in the Lagrangian description, suggesting that *flow separation is essentially a material evolution process*. This observation motivated Van Dommenlen and Shen (1982) to formulate a Lagrangian theory of unsteady boundary-layer separation in late 1970s, which is free from many difficulties encountered in the Eulerian description. The theory has now been developed to cover three-dimensional compressible flow. Its two-dimensional incompressible version is presented later, mainly following Shen (1978), Van Dommenlen and Shen (1982), Van Dommenlen and Cowley (1990), and Cowley et al. (1990).

It has been remarked following (5.39) that in the boundary layer equation for attached flow there is neither normal diffusion nor normal pressure gradient to balance a strong upwelling $v \gg Re^{-1/2}$, and hence it may grow unboundedly to cause a singularity. This observation equally applies to unsteady flow, and implies that a material fluid element can be squashed to zero thickness in the $x$-direction but with an infinite length in the normal direction, as sketched in Fig. 5.18. Consequently, an infinite normal velocity is generated and the fluid elements above the squarshed one are ejected from the boundary layer. This is the basic mechanism that causes boundary-layer separation in both steady and unsteady flow, but for unsteady flow the Lagrangian description of such fluid element deformation is much simpler than the Eulerian description.[12]

The fluid element path is described by

$$x = x(\boldsymbol{\xi}, \tau), \quad y = y(\boldsymbol{\xi}, \tau), \tag{5.78}$$

where $\boldsymbol{\xi} = (\xi, \eta)$ are the initial coordinates of the element (its "labels") and $\tau = t$ the Lagrangian time. Then the velocity components are

$$u = x_\tau, \quad v = y_\tau. \tag{5.79}$$

[12] Like the Goldstein singularity in steady boundary-layer separation, the singularity in unsteady boundary-layer separation might not be inevitable either. On the other hand, it will be seen later (Fig. 5.22) that a sharp spike may develop near the separation point, but the flow remains regular.

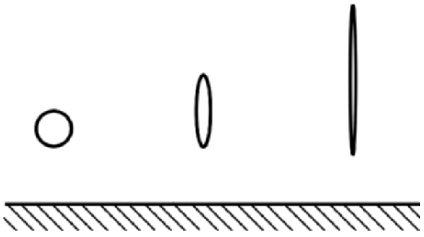

**Fig. 5.18.** Fluid element deformation leading to separation. From Cowley et al. (1990)

The derivatives in the two sets of coordinates $(x, y, t)$ and $(\xi, \eta, \tau)$ are related by

$$\begin{bmatrix} \xi_x & \xi_y & \xi_t \\ \eta_x & \eta_y & \eta_t \\ \tau_x & \tau_y & \tau_t \end{bmatrix} = \begin{bmatrix} x_\xi & x_\eta & x_\tau \\ y_\xi & y_\eta & y_\tau \\ t_\xi & t_\eta & t_\tau \end{bmatrix}^{-1} = J^{-1} \begin{bmatrix} y_\eta & -x_\eta & vx_\eta - uy_\eta \\ -y_\xi & x_\xi & uy_\xi - vx_\xi \\ 0 & 0 & J \end{bmatrix}, \tag{5.80}$$

where

$$J = x_\xi y_\eta - y_\xi x_\eta = 1 \tag{5.81a}$$

is the Jacobian for incompressible flow, see (2.40), which may then be written in characteristic form for numerical integration:

$$\mathrm{d}\xi : \mathrm{d}\eta : \mathrm{d}\tau : \mathrm{d}y = -x_\eta : x_\xi : 0 : 1. \tag{5.81b}$$

Moreover, by using (5.80) there is

$$\frac{\partial}{\partial x} = y_\eta \frac{\partial}{\partial \xi} - y_\xi \frac{\partial}{\partial \eta}, \quad \frac{\partial}{\partial y} = x_\xi \frac{\partial}{\partial \eta} - x_\eta \frac{\partial}{\partial \xi}. \tag{5.82}$$

Then, by (5.82), in (5.73) we have

$$\partial_y u = -\omega = x_\xi u_\eta - x_\eta u_\xi, \tag{5.83a}$$

which is also an expression in boundary-layer approximation of the Lagrangian vorticity $\Omega(\boldsymbol{\xi}, \tau)$ defined in the reference space spanned by $\boldsymbol{\xi}$, see (3.133a) and Sect. A.4, where it is shown that $\Omega = \omega$ for two-dimensional incompressible flow. In vector form, let $\nabla_\xi$ denote the gradient operator in the reference space, (5.83a) can be written

$$\boldsymbol{\omega} = \boldsymbol{\Omega} = \nabla_\xi u \times \nabla_\xi x. \tag{5.83b}$$

Then (5.73) is cast to the *Lagrangian boundary-layer equation*

$$u_\tau = u_{e,t} + u_e u_{e,x} - (x_\xi \Omega_\eta - x_\eta \Omega_\xi), \tag{5.84}$$

which is a dynamic system to be solved jointly with (5.79) and (5.83b) under given initial condition

$$x = \xi, \quad y = \eta, \quad u = u_0(\xi, \eta), \quad v = v_0(\xi, \eta) \quad \text{at} \quad \tau = 0. \tag{5.85}$$

The boundary conditions are essentially the same as in the Eulerian description:

$$(x, u) = (\xi, 0), \quad (y, v) = (0, 0) \quad \text{on} \quad \eta = 0, \tag{5.86a}$$

$$x_\tau = u \to U(x, t) \quad \text{as} \quad \eta \to \infty. \tag{5.86b}$$

Once the integration of (5.83) to (5.86) gives $x = x(\xi, \eta, \tau)$ at a subsequent time, one obtains $y(\xi, \eta, \tau)$ from (5.81b), and then velocities from (5.79).

An inspection of this Lagrangian formulation reveals a key simplification: owing to the approximate nature of (5.73), the streamwise position $x$ and velocity $u$ can be solved *independently* from solving the normal position $y$ and velocity $v$. Moreover, although a rigorous proof is not available, there has been strong evidence that the dynamic system (5.83–5.86) remains *regular* even after the singularity is formed (but the solution for $t > t_\mathrm{s}$ may not be physically realistic). Accepting this as a hypothesis, then, *the singularity develops solely from the continuity equation*. In this sense, the theory is entirely within kinematics. In particular, (5.81a) indicates that the mechanism for the singularity to occur is similar to the formation of shock in gas dynamics due to the coalescence of characteristics. In fact, the fluid-element normal location $y$ can be found by integrating (5.81b) along the curves $x = \text{const.}$ in the $(\xi, \eta)$ plane. Let $l$ be the arclength along such a curve with $l = 0$ at the wall $\eta = 0$, then

$$y = \int_0^l \frac{\mathrm{d}l}{|\nabla_\xi x|} = \int_0^s \frac{\mathrm{d}l}{(x_\xi^2 + x_\eta^2)^{1/2}}. \tag{5.87}$$

Now, at the separation point $u_x$ should be unbounded; so if $u_\xi$ and $u_\eta$ is bounded then (5.82) implies that $y_\xi$ and/or $y_\eta$ must be unbounded. Thus, the mapping between $(x, y)$ and $(\xi, \eta)$ is singular, which in (5.87) manifests as

$$\nabla_\xi x = 0 \quad \text{at} \quad (\boldsymbol{\xi}, t) = (\boldsymbol{\xi}_\mathrm{s}, t_\mathrm{s}). \tag{5.88}$$

This singularity condition has two effects. First, all infinitesimal deformations $\boldsymbol{\delta\xi}$ of fluid element do not cause any change of the streamwise position of the element in physical space:

$$\delta x = \boldsymbol{\delta\xi} \cdot \nabla_\xi x = 0 \quad \text{at} \quad (\boldsymbol{\xi}, t) = (\boldsymbol{\xi}_\mathrm{s}, t_\mathrm{s}). \tag{5.89}$$

Namely, as fluid elements move along their pathlines, they are blocked and squashed at a vertical barrier at some $x$, and hence must extend unboundedly along the normal as schematically shown in Fig. 5.18, resulting in the separation.

Second, by (5.83b) we see at once that (5.88) implies the first part of the MRS criterion, (5.72a) or (5.77b). Therefore, when the fluid-element squashing process reaches the singular state, it reaches zero-vorticity state too. Because the Lagrangian description does not distinguish steady and unsteady flow,

Shen (1978) points out that the same mechanism as sketched in Fig. 5.18 is also responsible for the Goldstein singularity in steady separation within boundary-layer approximation, and the MRS version of the Prandtl condition (5.1) is derivable from (5.87) that is *"no more than a formalized expression of the Prandtl concept — that the boundary layer must break away when a packet of fluid particles are stopped in their forward advance along the wall."*

The second part of the MRS criterion can also be derived from (5.88). In fact, denote the Lagrangian coordinates of the singularity point by $\boldsymbol{\xi}_{\mathrm{MRS}}$, of which the propagation speed is (a dot denotes $\mathrm{d}/\mathrm{d}t$), owing to (5.88),

$$\frac{\mathrm{d}}{\mathrm{d}t}x(\boldsymbol{\xi}_{\mathrm{MRS}},t)=\dot{x}+\dot{\boldsymbol{\xi}}_{\mathrm{MRS}}\cdot\nabla_{\xi}x=\dot{x}, \tag{5.90}$$

which is indeed the local streamwise velocity of the element, in agreement with (5.77a). Therefore, the MRS criterion is rationalized.

Van Dommenlen and Shen (1982) conducted a numerical calculation based on the earlier theory for flow over impulsively started circular cylinder. As sketched in Fig. 5.19, the singular point was found to appear at $\theta = 111^\circ$ and $t = 3.0045$, which moves upstream with $u = -0.52U$. The separation location differs from the full Navier–Stokes solution (Fig. 5.15) since the former is for $Re \to \infty$ asymptotically rather than at a finite Reynolds number. The separation location is also different from that of the Goldstein singularity for steady flow, $\theta = 104.5^\circ$. After the singularity is formed, the upper part of the boundary layer turns to a free separated vortex layer. On top of Fig. 5.19 are the profiles of velocity and vorticity (normalized by wall vorticity) close to separation, from which it is evident that as the bifurcation tears the boundary layer apart the irrotational region in between is enlarged.

We now introduce local scales in the neighborhood of $(\boldsymbol{\xi}_{\mathrm{s}}, t_{\mathrm{s}})$ so that the singularity can be removed. Assume $t_{\mathrm{s}}$ is the first time for a singular boundary-layer separation point to form. Since $x(\boldsymbol{\xi}, t)$ is a regular function of $\boldsymbol{\xi}$ and $t$ around $(\boldsymbol{\xi}_{\mathrm{s}}, t_{\mathrm{s}})$ one can perform a Taylor expansion of $x$ and form the deck structure thereby. Meanwhile, (5.88) should also be expanded to a Taylor series since it may not be satisfied anywhere for $\delta t = t - t_{\mathrm{s}} < 0$. To simplify the expansion, let $\delta\boldsymbol{\xi} = \boldsymbol{\xi} - \boldsymbol{\xi}_{\mathrm{s}}$, and make a proper shift and rotation of the previous arbitrarily chosen Lagrangian coordinate system to a new system $(l_1, l_2, t)$ . The Jacobian $J$ is invariant under the coordinate transformation, and has characteristics

$$\frac{\mathrm{d}l_1}{\mathrm{d}y}=-x_{,22}l_2+\cdots, \quad \frac{\mathrm{d}l_2}{\mathrm{d}y}=\frac{1}{2}x_{,111}l_1^2+\dot{x}_{,1}\delta t+\cdots, \tag{5.91a,b}$$

which results in a singularity when both right-hand side expressions vanish. Although at $t = t_{\mathrm{s}}$ the boundary-layer approximation blows up, at times shortly before $t_{\mathrm{s}}$ a rescaled asymptotic expansion can be conducted to describe the flow field. After some algebra, it can be found that the proper scales are

$$l_1=|\delta t|^{1/2}L_1, \quad l_2=|\delta t|^{3/4}L_2, \tag{5.92a,b}$$

$$\bar{x}\equiv x-x(\boldsymbol{\xi}_{\mathrm{s}},t)=|\delta t|^{3/2}X, \quad y=|\delta t|^{-1/4}Y, \tag{5.93a,b}$$

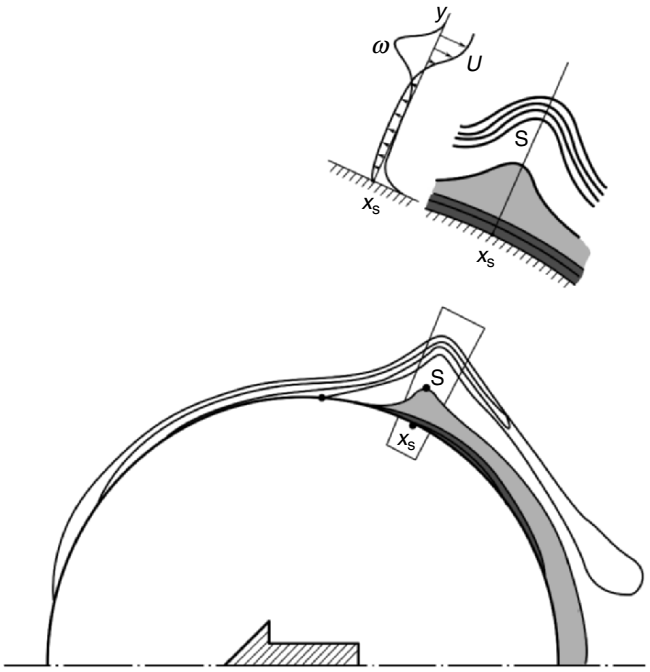


**Fig. 5.19.** Vorticity contours obtained from the Lagrangian boundary-layer equation for impulsively started circular cylinder. $t = 3.0045$. On top are the profiles of velocity and vorticity (normalized by wall vorticity) close to separation. Reproduced from Van Dommenlen and Shen (1982)

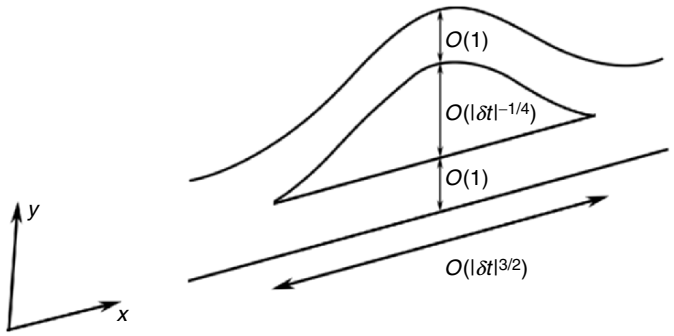


**Fig. 5.20.** Scales of unsteady boundary-layer bifurcation at $\delta t$ before singularity is formed. Reproduced from Cowley et al. (1990)

where $L_1, L_2, X, Y = O(1)$. These scales at a $\delta t < 0$ are shown schematically in Fig. 5.20.

Then, integrating (5.91) yields an analytical solution for $Y$, and a further $O(1)$ transformation $(L_1, X, Y) \rightarrow (L_1^*, X^*, Y^*)$ similar to (5.55) can scale out all coefficients. In terms of the variables with asterisk, the analytical solution takes canonical form

$$Y^* \sim \int_{-\infty}^{L_0^*} \frac{\mathrm{d}L^*}{(2X^* - 3L^* - L^{*3})^{1/2}} \pm \int_{L_1^*}^{L_0^*} \frac{\mathrm{d}L^*}{(2X^* - 3L^* - L^{*3})^{1/2}}, \qquad (5.94)$$

where $L_0^*$ is the real root of the cubic polynomial in the square root of the denominator. The solution (5.94) can be cast to elliptic integrals of the first kind. The signs of the square roots and the limits of integration are determined by the topology of the lines of constant $X^*$ that consists of three segments shown in Fig. 5.20. Leaving the mathematic details aside, the scaled vorticity contours of the nearly separated boundary layer is shown in Fig. 5.21, which also shows the sudden thickening of the boundary layer.

Finally, similar to the steady case where the scaling is closed by finding the relation of the lower-deck thickness $\delta$ and $Re$, we now need to close the theory by finding the relation of $\delta t$ and $Re$. Once again, since the MRS criterion implies the shearing is vanishingly small near $S$, the only possible mechanism to balance the normal extension of fluid elements is the normal pressure gradient $\Delta p_y \sim \Delta p_x$ in an irrotational *upper deck*. In the separation zone shown in Fig. 5.20, as a fluid element moves past a streamwise extent $O(|\delta t|^{3/2})$ but climbs up a thickness (in global scale) $O(Re^{-1/2}|\delta t|^{-1/4})$, it experiences a upwelling velocity $v$ of $O(Re^{-1/2}|\delta t|^{-7/4})$. The balance in the normal momentum, $\partial v/\partial x = -\partial p/\partial y$, together with the fact that $x \sim y$ in the upper deck, indicates that the locally induced pressure reads

$$\Delta p \sim v \sim Re^{-1/2}|\delta t|^{-7/4}.$$

So the pressure gradient is

$$\Delta p_x \sim Re^{-1/2}|\delta t|^{-7/4} \cdot |\delta t|^{-3/2} = Re^{-1/2}|\delta t|^{-13/4}.$$

Then an *unsteady triple-deck* interaction (strictly, it is a quadruple structure) appears if $\Delta p_x$ is of the same order as the acceleration $\overline{x}_{tt} = O(|\delta t|^{-1/2})$ in the expanding central region. This balance occurs when

$$Re^{-1/2}|\delta t|^{-13/4} = |\delta t|^{-1/2}, \quad \text{i.e.} \quad |\delta t| = O(Re^{-2/11}). \qquad (5.95)$$

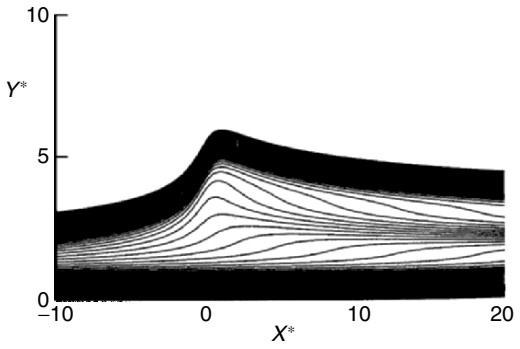


**Fig. 5.21.** Canonical vorticity contours near separation. From Cowley et al. (1990)

By (5.93b), at this time the scaled boundary-layer displacement thickness has grown to $O(Re^{1/22})$.

The earlier scalings are in agreement with the analysis in terms of Eulerian description (e.g., Elliott et al. 1983) as well as some numerical tests. However, the very small power of $Re$ may lead to large difference between theory and experiment at moderate $Re$. A more fundamental problem of unsteady boundary-layer separation theory, in either Lagrangian or Eulerian description, is that the unsteady triple-deck structure itself turns out to terminate at yet another finite-time singularity. While it is possible to rescale the variables at times close to this new singularity in an even shorter time-scale, the rescaling process may have to go on as a cascade. It remains an open issue on whether this situation reflects the physical cascade process in tranasition to turbulence associated with successive instabilities at a series of decreasing scales, or simply due to the limitation of the matched asymptotic theory itself.

### 5.4.3 Unsteady Flow Separation

We now turn to generic unsteady separation. Although some of the results of Sect. 5.2 are equally applicable to unsteady flow, a complete, general, and local unsteady separation theory had not been available until a very recent work of Haller (2004), who obtained an exact two-dimensional theory for both incompressible and compressible unsteady flow with general time dependence, applicable to arbitrary stationary or moving wall. The theory is essentially of kinematic nature, in which the separation point (to be defined later) can be either fixed on the wall or moving along the wall. The consistency of the theory with both Prandtl's theory for two-dimensional steady separation and the Lagrangian theory unsteady boundary-layer separation has been confirmed. The theory has been further improved by Haller and coworkers, and extended to three dimensions (Kilic et al. 2005; Surana et al. 2005b,c). Therefore, we devote this subsection to an introduction to Haller's unsteady separation theory based on Haller (2004) and Kilic et al. (2005), focusing on the simplest case. Namely, we assume the flow is incompressible with $\rho = 1$, and the separation point is *fixed* to a no-slip wall $\partial B$ at $y = 0$, referred to as *fixed separation*. Its results turn out to apply to any unsteady flow with a mean component, including turbulent boundary layers and flows dominated by vortex shedding.

The assertion made in Sect. 5.4.2, that flow separation is essentially a material evolution process, can be clearly demonstrated by the time evolution of a fixed separation and reattachment for an analytical periodic flow model shown in Fig. 5.22 (see (5.111) later). Similar to Fig. 5.19, a set of material lines initially aligned to the wall evolves to form an upwelling, then a singular-looking tip, and then a sharp spike. More crucially, there appears a distinguished material line, which attracts fluid particles released from its both sides and ejects them into the main stream. This special material line signifies the *separation profile*, of which a rational identification is the key

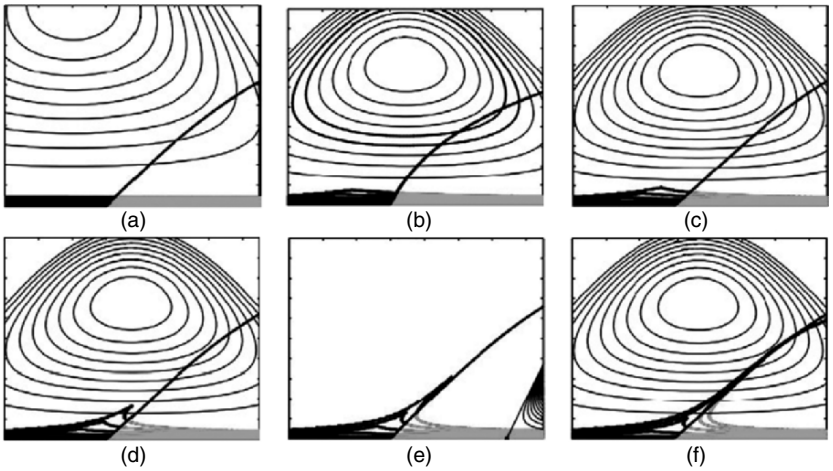


**Fig. 5.22.** Time evolution of material lines and streamlines for a periodic separation bubble model (5.109) with circular frequency $2\pi$. (**a**) $t = 0$, (**b**) $t = 8.2$, (**c**) $t = 9.95$, (**d**) $t = 15.0$, (**e**) $t = 18.65$, (**f**) $t = 25$. The time-dependent curve initially cutting the material lines but then serving as their approximate asymptotic line is the separation profile (up to quadratic order) to be identified later. From Haller (2004)

of a general separation theory. Note that Fig. 5.22 shows that instantaneous streamlines are irrelevant when the separation is unsteady.

This being the case, we start from the dynamic system (5.5):

$$\dot{x} = u(x, y, t), \quad \dot{y} = v(x, y, t), \tag{5.96}$$

which due to the no-slip condition and continuity can be cast to, similar to (5.31),

$$\dot{x} = yA(x, y, t), \quad \dot{y} = y^2 C(x, y, t), \tag{5.97}$$

where

$$\begin{aligned} A(x, y, t) &= \int_0^1 u_y(x, sy, t)\mathrm{d}s, \\ C(x, y, t) &= \int_0^1 \int_0^1 v_{yy}(x, sqy, t) q \, \mathrm{d}q \, \mathrm{d}s. \end{aligned} \tag{5.98}$$

The incompressibility further requires

$$A_x + 2C + yC_y = 0. \tag{5.99}$$

Now, denote the material line signifying the *separation profile* by $\mathcal{M}(t)$, which as seen in Fig. 5.22 is "anchored" to the fixed *separation point* $(x, y) = (\gamma, 0)$ for all $t$ by the no-slip condition. In dynamic system terms, $\mathcal{M}(t)$ is an *unstable manifold* for a fixed point on the wall, locally described by a time-dependent path

$$x = \gamma + yF(y, t). \tag{5.100}$$

While generic material lines emanating from the wall converge to the wall as $t \to -\infty$, $\mathcal{M}(t)$ is an exception, with the following properties:

1. it is *unique*, i.e., no other separation profile emerges from the same boundary point;
2. it is *transverse*, i.e., does not become asymptotically tangent to the wall in backward time;[13] and
3. it is *regular* up to $n$th order ($n \geq 1$), i.e., $\mathcal{M}(t)$ admits $n$ derivatives that are uniformly bounded at the wall for all $t$.

Then, substituting (5.100) into (5.97), one finds that $\mathcal{M}(t)$ satisfies a partial differential equation (the *separation equation*)

$$F_t = A(\gamma + yF, y, t) - yC(\gamma + yF, y, t)(F + yF_y), \tag{5.101}$$

from which unsteady separation criteria can be deduced. By (5.100), approximate separation profile can be expressed by series expansion

$$x = \gamma + f_0(t)y + f_1(t)y^2 + \frac{1}{2}f_2(t)y^3 + \frac{1}{6}f_3(t)y^4 + \cdots, \tag{5.102}$$

where $f_0(t)$ and $f_1(t)$ are the slope relative to the $y$-axis and curvature of $\mathcal{M}(t)$ at $(x, y) = (\gamma, 0)$, respectively.

Consider separation criteria first. Setting $y = 0$ in (5.101) yields a linear equation $\dot{f}_0(t) = a(t)$, thus ($t_0$ is an arbitrary reference time)

$$f_0(t) = f_0(t_0) + \int_{t_0}^{t} A(\gamma, 0, \tau)\mathrm{d}\tau. \tag{5.103}$$

Since by the earlier property (2) $\mathcal{M}(t)$ cannot become asymptotically tangent to the wall, $f_0(t)$ must be uniformly bounded. By (5.98) and $u_y = -\omega$ on the wall, therefore, a necessary separation criterion is

$$\lim_{t\to-\infty} \sup \left| \int_{t_0}^{t} u_y(s, \tau)\mathrm{d}\tau \right| = \lim_{t\to-\infty} \sup \left| \int_{t_0}^{t} \omega(s, \tau)\mathrm{d}\tau \right| < \infty, \tag{5.104}$$

where and below $s$ denotes the separation point $(\gamma, 0)$. For steady separation the integral becomes $\omega_\mathrm{s}(t-t_0)$, so (5.104) is reduced to Prandtl's first criterion (5.1a).

Then, as the generalization of (5.1b), by using $v_{yy} = -u_{yx} = \omega_x$ on the wall and after some algebra, it can be proved that the second necessary separation criterion is

$$\int_{t_0}^{-\infty} u_{xy}(s, \tau)\mathrm{d}\tau = -\int_{t_0}^{-\infty} \omega_x(s, \tau)\mathrm{d}\tau = \infty, \tag{5.105}$$

[13] All other material lines that start to be transverse remain so for any finite time, but become tangent to the wall as $t \to -\infty$ (G. Haller, 2005, private communication).

which for steady flow becomes $(t_0 + \infty)\omega_x = \infty$ and hence $\omega_x > 0$, equivalent to (5.1b). In particular, for periodic flow with period $T$, the integration interval in (5.104) can be replaced by $(0, T)$; while in (5.105) one splits the integrand into a mean and an oscillating part, with the former having to be negative. Thus, the two necessary separation criteria are simply reduced to

$$\int_0^T \omega(s,t)\mathrm{d}t = 0, \quad \int_0^T \omega_x(s,t)\mathrm{d}t > 0. \tag{5.106a,b}$$

In general, criterion (5.104) can be expressed in a form more suitable for computations. Recall that any material lines emanating from any wall points near $s$ will align with the wall as $t \to -\infty$, which by (5.103) is possible only if, for sufficiently small $|x - \gamma|$,

$$\int_{t_0}^{-\infty} u_y(x,0,\tau)\mathrm{d}\tau = \begin{cases} +\infty & \text{if} \quad x > \gamma, \\ -\infty & \text{if} \quad x < \gamma. \end{cases}$$

Thus, the backward integral of $u_y = -\omega$ at $s$ admits a sign change arbitrarily close to $s$ for sufficiently large $|t - t_0|$. Then, since the integral

$$i_t(x) \equiv \int_{t_0}^{t} u_y(x,0,\tau)\mathrm{d}\tau \tag{5.107}$$

is a continuous function of $x$ at any $t$, it must have at least one zero that approaches $s$ as $t \to -\infty$. Therefore, we may define an *effective separation point* $\gamma_{\mathrm{eff}}(t, t_0)$ by

$$\int_{t_0}^{t} u_y(\gamma_{\mathrm{eff}},0,\tau)\mathrm{d}\tau = 0 \quad \text{such that} \quad \gamma = \lim_{t\to-\infty} \gamma_{\mathrm{eff}}(t,t_0), \tag{5.108}$$

see Fig. 5.23. The reattachment point can be similarly defined.

Moreover, while criteria (5.104) and (5.105) permit *weak separation* by which particles near $s$ may turn back towards the wall for a finite period of time, a slight revision of (5.105) can give a sufficient condition for stronger *monotonic separation* by which particles near $s$ move away monotonically from the wall without turning back. Haller (2004) proves that this is simply ensured by

$$-u_{xy}(s,t) = \omega_x(s,t) > c_0 > 0, \tag{5.109}$$

of which the physical implication is obvious (cf. Fig. 4.12).

Haller (2004) has used the earlier theory to derive explicit general formulas for the time-dependent coefficients $f_0(t), f_1(t), \ldots$ of (5.106) up to quadratic order. In particular, for steady flow the slope of $\mathcal{M}$ reduces to

$$f_0 = -\frac{u_{yy}(s)}{3u_{xy}(s)} = -\frac{p_x(s)}{3\tau_x(s)},$$

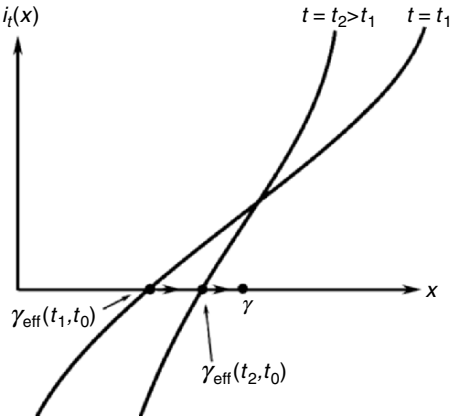


**Fig. 5.23.** The convergence of $\gamma_{\text{eff}}$ to $\gamma$

in agreement with (5.30) where $\phi$ is the angle of the separation line relative to the $x$-axis. The second equality uses the Navier–Stokes equation as we did in Sect. 5.2, except which all the earlier results are evidently kinematic; use was made of only the continuity equation.

The fixed separation conditions (5.104) and (5.105) have been improved by Kilic et al. (2005), assuming that the unsteady velocity fields under consideration admit a *finite time asymptotic average in time*. After some lengthy algebra, the authors show that (5.104) and (5.105) can be replaced by

$$\lim_{T\to\infty} \frac{1}{T} \int_{t_0-T}^{t_0} \omega(s,t)\mathrm{d}t = 0, \tag{5.110a}$$

$$\lim_{T\to\infty} \frac{1}{T} \int_{t_0-T}^{t_0} \omega_x(s,t)\mathrm{d}t > 0, \tag{5.110b}$$

which are a direct generalization of (5.106) to aperiodic flow.

As an analytic example, consider a periodic separation bubble model derived by Ghosh et al. (1998),

$$\begin{aligned} u(x,y,t) &= -y + 3y^2 + x^2 y - \tfrac{2}{3}y^3 + \beta xy \sin nt, \\ v(x,y,t) &= -xy^2 - \tfrac{1}{2}\beta y^2 \sin nt. \end{aligned} \tag{5.111}$$

Substituting this model into (5.108) yields $(\gamma^2 - 1)T = 0$ and $2\gamma T > 0$, $T = 2\pi/n$. Thus, the fixed separation point is at $\gamma = -1$ and the reattachment point at $\gamma = +1$, as shown in Fig. 5.22 for $n = 2\pi$ and $\beta = 3$, which is in agreement with the numerical observation of Ghosh et al. (1998). The expansion coefficients $f_0(t), ..., f_3(t)$ can also be derived, which gives the approximate separation profile also shown in Fig. 5.22.

The preceding unsteady separation theory indicates that the final results on the separation definition and criteria are fully *Eulerian* that do not require

the advection of fluid particles. This is a unique advantage of the theory. Like the general three-dimensional steady separation theory of Sect. 5.2, this unsteady theory meets three highly desired requirements proposed, respectively, by Sears and Telionis (1975), Cowley et al. (1990), and Wu et al. (2000), and summarized by Haller: *independent of our ability to solve the boundary-layer equations accurately; independent of the coordinate system selected; and expressible solely by quantities measured or computed along the wall.*

## Summary

1. Phenomenologically, flow separation is a local process in which fluid elements adjacent to a wall no longer move along the wall but turn to the interior of the fluid. In its strong form and at large Reynolds numbers, the process may evolve to boundary-layer separation where the whole layer breaks away and thereby significantly alters the global flow field. Physically, flow separation is due to the boundary coupling of the two fundamental dynamic processes. A near-wall adverse pressure gradient yields a boundary vorticity flux $\boldsymbol{\sigma}_p$, which creates new vorticity with direction different from that of existing one, so the accumulation of the former in space and time causes a transition of the near-wall vorticity from being carried along by the wall to shedding off. Thus, a vorticity-dynamics description of separation is especially illuminating, which can be obtained from the conventional momentum considerations owing to the on-wall equivalence between the $\boldsymbol{\tau}_w$-field and its orthogonal $\boldsymbol{\omega}_{\mathrm{B}}$-field, and that between the $\nabla_\pi p$-field and its orthogonal $\boldsymbol{\sigma}_p$-field.
2. A general flow-separation process without any specification to its strength can be studies in an infinitesimal neighborhood of a separation point or separation line, by using a Taylor expansion of the continuity and Navier–Stokes equations. The criteria for separation zone and separation line at large Reynolds numbers can be formulated in terms of the earlier two pairs of orthogonal on-wall vector fields. For steady separation and in two dimensions, the criteria amount to those well-known ones due to Prandtl. In three dimensions, the separation zone is characterized by the strong converging of $\boldsymbol{\tau}$-lines or large positive on-wall curvature of $\boldsymbol{\omega}$-lines. If the separation starts at a fixed point of the $\boldsymbol{\tau}$-field ("closed separation"), a generic separation line can be uniquely determined. But at large $Re$ a significant separated free shear layer may start to form and/or cease to shed off at ordinary points of a $\boldsymbol{\tau}$-line; for which the separation line may be approximately identified as the line with maximum $\boldsymbol{\omega}$-line curvature in the separation zone.
3. Boundary-layer separation at large $Re$ involves the flow behavior in the whole layer and its interaction with external flow in a small but finite zone. Although this process is governed by the Navier–Stokes equation, the matched asymptotic expansion has contributed an elegant triple-deck

theory that clarifies the underlying physics and represents the second generation of the boundary-layer theory. The triple-deck theory has been fully developed for steady separation, but becomes difficult for unsteady separation due to the involvement of different time scales at different stages of separation process. So far the only successful theory for this situation is based on the Lagrangian description, which confirms the MRS criterion and extends it to three dimensions.

4. Both generic flow separation and boundary-layer separation are essentially material evolution processes, and hence favors the use of Lagrangian description when the flow is unsteady. This explains the success of the Lagrangian approach and difficulty of the Eulerian approach to unsteady boundary-layer separation. For generic unsteady flow separation, a complete local theory can be developed also by starting from the Lagrangian description, of which however the final results on the separation criteria and separation profile can still be expressed by on-wall Eulerian variables. The on-wall signatures of separation can be used as a convenient tool in complex flow diagnosis and separation control.

# Part II

# Vortex Dynamics

# 6

# Typical Vortex Solutions

In Chap. 4 we have studied attached and free vortex layers, and seen that the rolling up of a free vortex layer forms a vortex which has the highest possible vorticity concentration as mentioned in the beginning of Sect. 1.3 (the formation process of vortices will be further discussed in Sect. 8.1). In this chapter we start the dynamics of *vortices* by presenting a number of typical exact viscous and inviscid vortex solutions, and asymptotically approximate vortex solutions, followed by a basic open issue on how to rationally define a vortex.

Exact solutions can provide a thorough physical understanding, serve as the testing bed of the accuracy of approximate approaches and as the basic flow in their stability analyses (Chap. 9). However, exact Navier–Stokes vortex solutions, mostly confined to incompressible flow (see reviews of Wang 1989, 1991), are obtainable only under highly idealized conditions. In certain aspects they behave quite unrealistic, and some solutions may correspond to real flows only in a local region and/or a finite period of time.

In reality there is no single isolated straight vortex with nonzero total circulation. Vortices always appear as loops (in three dimensions) or in pairs (in two dimensions), and hence each vortex is in the strain field caused by other vortices and boundary conditions. For a thin-core strained vortex one may find asymptotic solutions analytically, which complement the shortage of exact solutions and may also play similar roles as the exact solutions.

Unless stated otherwise, throughout this chapter we assume the flow is incompressible flow with $\rho = 1$.

## 6.1 Governing Equations

The geometric characters of columnar vortices and vortex rings makes it often convenient to use a cylindrical coordinate system $(r, \theta, z)$ with $\boldsymbol{u} = (u, v, w)$ and $\boldsymbol{\omega} = (\omega_r, \omega_\theta, \omega_z)$. By the general formula for any vector $\boldsymbol{A}$

$$\nabla \times \boldsymbol{A} = \frac{1}{r}\begin{vmatrix} \boldsymbol{e}_r & r\boldsymbol{e}_\theta & \boldsymbol{e}_z \\ \partial_r & \partial_\theta & \partial_z \\ A_r & rA_\theta & A_z \end{vmatrix}, \tag{6.1}$$

the vorticity components are given by

$$\omega_r = \frac{1}{r}\frac{\partial w}{\partial \theta} - \frac{\partial v}{\partial z}, \quad \omega_\theta = \frac{\partial u}{\partial z} - \frac{\partial w}{\partial r}, \quad \omega_z = \frac{1}{r}\frac{\partial (rv)}{\partial r} - \frac{1}{r}\frac{\partial u}{\partial \theta}. \tag{6.2}$$

The continuity equation reads:

$$\frac{1}{r}\frac{\partial (ru)}{\partial r} + \frac{1}{r}\frac{\partial v}{\partial \theta} + \frac{\partial w}{\partial z} = 0, \tag{6.3}$$

and the Crocco–Vazsonyi equation (2.163) along with (2.164) gives

$$\frac{\partial u}{\partial t} + (w\omega_\theta - v\omega_z) = -\frac{\partial H}{\partial r} - \nu\left(\frac{1}{r}\frac{\partial \omega_z}{\partial \theta} - \frac{\partial \omega_\theta}{\partial z}\right), \tag{6.4a}$$

$$\frac{\partial v}{\partial t} + (u\omega_z - w\omega_r) = -\frac{1}{r}\frac{\partial H}{\partial \theta} - \nu\left(\frac{\partial \omega_r}{\partial z} - \frac{\partial \omega_z}{\partial r}\right), \tag{6.4b}$$

$$\frac{\partial w}{\partial t} + (v\omega_r - u\omega_\theta) = -\frac{\partial H}{\partial z} - \frac{\nu}{r}\left(\frac{\partial (r\omega_\theta)}{\partial r} - \frac{\partial \omega_r}{\partial \theta}\right), \tag{6.4c}$$

where $H = q^2/2 + p$ is the total enthalpy. Whenever needed, substituting (6.2) to (6.4) yields the common component momentum equations in terms of velocity and pressure. One of the component forms of the vorticity transport equations is

$$\frac{\mathrm{D}\omega_r}{\mathrm{D}t} = \boldsymbol{\omega}\cdot\nabla u + \nu\left(\nabla^2\omega_r - \frac{\omega_r}{r^2} - \frac{2}{r^2}\frac{\partial \omega_\theta}{\partial \theta}\right), \tag{6.5a}$$

$$\frac{\mathrm{D}\omega_\theta}{\mathrm{D}t} + \frac{v\omega_r}{r} = \boldsymbol{\omega}\cdot\nabla v + \frac{\omega_\theta u}{r} + \nu\left(\nabla^2\omega_\theta + \frac{2}{r^2}\frac{\partial \omega_r}{\partial \theta} - \frac{\omega_\theta}{r^2}\right), \tag{6.5b}$$

$$\frac{\mathrm{D}\omega_z}{\mathrm{D}t} = \boldsymbol{\omega}\cdot\nabla w + \nu\nabla^2\omega_z, \tag{6.5c}$$

where

$$\frac{\mathrm{D}}{\mathrm{D}t} = \frac{\partial}{\partial t} + u\frac{\partial}{\partial r} + \frac{v}{r}\frac{\partial}{\partial \theta} + w\frac{\partial}{\partial z}, \tag{6.6}$$

$$\nabla^2 = \frac{1}{r}\frac{\partial}{\partial r}\left(r\frac{\partial}{\partial r}\right) + \frac{1}{r^2}\frac{\partial^2}{\partial \theta^2} + \frac{\partial^2}{\partial z^2}. \tag{6.7}$$

We now focus on axisymmetric flow, for which $H$ does not enter the azimuthal momentum balance. An inspection of (6.1.5) with $\partial/\partial\theta = 0$ indicates that if $\boldsymbol{u} = (0, v(r,t), 0)$, then $\boldsymbol{\omega} = (0, 0, \omega_z(r,t))$ has only one nonzero

component. This kind of vortices are called *pure vortices*, with all vorticity lines being along the axis and all streamlines are closed circles centered at the $z$-axis. Then, if $w$ is nonzero and $r$-dependent, $\omega_\theta$ will appear too such that the velocity and vorticity lines become helical. This kind of vortices are called *swirling vortices*, having nonzero helicity density $\boldsymbol{\omega} \cdot \boldsymbol{u}$.

We have seen in Sect. 3.3.1 that a *Stokes stream function* $\psi$ can be introduced to ensure the continuity, which expresses $u$ and $w$ by (3.57) but not $v$:

$$u = -\frac{1}{r}\frac{\partial \psi}{\partial z}, \quad w = \frac{1}{r}\frac{\partial \psi}{\partial r}. \tag{6.8}$$

Thus, the velocity and vorticity, and hence their governing equations, can be expressed in terms of two scalar functions, $\psi$ and $\Gamma = rv$ (differing from the circulation around a circle centered at $r = 0$ by a factor $1/2\pi$). Consequently, (6.2) and (6.8) yield

$$\omega_r = -\frac{1}{r}\frac{\partial \Gamma}{\partial z}, \tag{6.9a}$$

$$\omega_z = \frac{1}{r}\frac{\partial \Gamma}{\partial r}, \tag{6.9b}$$

$$\omega_\theta = -\left[\frac{\partial}{\partial r}\left(\frac{1}{r}\frac{\partial \psi}{\partial r}\right) + \frac{1}{r}\frac{\partial^2 \psi}{\partial z^2}\right]. \tag{6.9c}$$

The role of $\Gamma$ for $\omega_r$ and $\omega_z$ is exactly the same as that of $\psi$ for $u$ and $w$. Contours of $\Gamma$ and $\psi$ on an $(r, z)$-plane are the intersections of vorticity surfaces and stream surfaces with the plane, respectively. Then (6.4b) and (6.5b) can be cast to

$$\frac{\mathrm{D}\Gamma}{\mathrm{D}t} = \nu\left[r\frac{\partial}{\partial r}\left(\frac{1}{r}\frac{\partial \Gamma}{\partial r}\right) + \frac{\partial^2 \Gamma}{\partial z^2}\right], \tag{6.10a}$$

$$\frac{\mathrm{D}}{\mathrm{D}t}\left(\frac{\omega_\theta}{r}\right) = \nu\left(\nabla^2 + \frac{2}{r}\frac{\partial}{\partial r}\right)\left(\frac{\omega_\theta}{r}\right) + \frac{1}{r^4}\frac{\partial \Gamma^2}{\partial z}, \tag{6.10b}$$

which govern the azimuthal and meridional motions, respectively. $\Gamma$ and $\omega_\theta$ may serve as the basic variables to be solved, all other quantities can be inferred therefrom. They are coupled solely through the $z$-dependence of $v$, which happens, e.g., if the vortex hits a boundary at $z = 0$ as sketched in Fig. 3.5a.

Most of existing exact vortex solutions, either viscous or effectively inviscid, were found when (6.5) can be linearized. That is, when the flow is *generalized Beltramian* satisfying (3.63). It is therefore appropriate here to examine when this happens in general (not confined to two-dimensional or rotationally symmetric flows where $\omega$ or $\omega/r$ is a function $f(\psi, t)$). We consider *inviscid steady flow* and *viscous unsteady flow* separately.

Any incompressible, effectively inviscid, and *steady* flow must be generalized Beltramian, since then (2.163) is reduced to

$$\boldsymbol{\omega} \times \boldsymbol{u} = -\nabla H. \tag{6.11}$$

In this case (6.10a) and (6.10b) are reduced to

$$\boldsymbol{u} \cdot \nabla \Gamma = 0, \tag{6.12a}$$

$$\boldsymbol{u} \cdot \nabla \left(\frac{\omega_\theta}{r}\right) = \frac{1}{r^4} \frac{\partial \Gamma^2}{\partial z}. \tag{6.12b}$$

Thus, the circulation along any circle around the vortex axis is conserved. Since the flow is steady, a fluid particle moves along a streamline, and all fluid motion occurs on the revolution surfaces generated by the family of curves $\psi =$ constant around the $z$-axis. Therefore, by (6.12a) there is $\Gamma = C(\psi)$, from (6.9a,b) and (6.12b) it follows that:

$$\omega_r = -\frac{1}{r} \frac{\mathrm{d}C}{\mathrm{d}\psi} \frac{\partial \psi}{\partial z} = u \frac{\mathrm{d}C}{\mathrm{d}\psi}, \tag{6.13a}$$

$$\omega_z = \frac{1}{r} \frac{\mathrm{d}C}{\mathrm{d}\psi} \frac{\partial \psi}{\partial r} = w \frac{\mathrm{d}C}{\mathrm{d}\psi}, \tag{6.13b}$$

$$\frac{\omega_\theta}{r} = \frac{C}{r^2} \frac{\mathrm{d}C}{\mathrm{d}\psi} - \frac{\mathrm{d}H}{\mathrm{d}\psi}. \tag{6.13c}$$

The expression of $\omega_\theta / r$ can be more directly obtained by considering the $z$-component of (6.11):

$$u\omega_\theta - v\omega_r = \frac{\partial H}{\partial z};$$

then since by (6.11) $\boldsymbol{u} \cdot \nabla H = 0$, we also have $H = H(\psi)$, and hence (6.13c) comes from (6.8). Therefore, there remains only a single differential equation to be solved for steady inviscid axisymmetric flows:

$$r \frac{\partial}{\partial r} \left(\frac{1}{r} \frac{\partial \psi}{\partial r}\right) + \frac{\partial^2 \psi}{\partial z^2} = r^2 \frac{\mathrm{d}H}{\mathrm{d}\psi} - C \frac{\mathrm{d}C}{\mathrm{d}\psi}. \tag{6.14}$$

This equation is called the *Bragg–Hawthorne equation* (Bragg and Hawthorne 1950) or *Squire equation* since Squire (1956) re-derived it independently.

In passing, we note that (6.14) can be extended to nonaxisymmetric case by using the transformation (2.112), a special form of the Helmholtz decomposition:

$$\boldsymbol{u} = \nabla \phi + \nabla \psi \times \nabla \chi.$$

Since the two stream functions $\psi$ and $\chi$ define two families of stream surfaces, their intersections are streamlines along which $H$ is constant. Thus, we have

$H = H(\psi, \chi)$, and (6.11) becomes

$$\boldsymbol{\omega} \times (\nabla\psi \times \nabla\chi + \nabla\phi) + \frac{\partial H}{\partial \psi}\nabla\psi + \frac{\partial H}{\partial \chi}\nabla\chi = \mathbf{0}$$

of which the projection to the directions of $\nabla\psi$ and $\nabla\chi$ yields a pair of symmetric equations (Keller 1996)

$$\boldsymbol{\omega} \cdot \nabla\chi + \frac{\partial H}{\partial \psi} = 0, \quad \boldsymbol{\omega} \cdot \nabla\psi - \frac{\partial H}{\partial \chi} = 0, \tag{6.15a,b}$$

along with $\nabla^2\phi = 0$. This set of equations are applicable to any three-dimensional steady inviscid flows (still generalized Beltramian) and has been used by Keller (1996) to study axisymmetric vortices with helical waves and other relevant flows. When the flow is nonaxisymmetric, $\Gamma = rv$ is no longer an integral of the motion and the flow cannot be expressed by $\psi$ alone.

On the other hand, by directly looking at the Lamb-vector components in (6.4), we find that *a viscous axisymmetric vortex with* $\omega_z \neq 0$ *will be generalized Beltramian if and only if*

$$u = 0\ , \quad v = v(r,t), \quad w = w(r,t). \tag{6.16a}$$

$$\omega_r \ = \ 0, \quad \omega_\theta(r,t) = -\frac{\partial w}{\partial r}, \quad \omega_z(r,t) = \frac{1}{r}\frac{\partial (rv)}{\partial r}. \tag{6.16b}$$

In fact, (6.16) implies the three components of the Lamb vector are

$$l_r = -\frac{1}{2}\frac{\partial}{\partial r}(v^2 + w^2) - \frac{v^2}{r}, \quad l_\theta = 0, \quad l_z = 0.$$

But now (6.4a) can be reduced to $\partial p/\partial r = v^2/r$ with $H = p + (v^2 + w^2)/2$ even for viscous flow. Conversely, after rewriting (6.5) to make $\nabla \times (\boldsymbol{\omega} \times \boldsymbol{u})$ appear explicitly, an inspection of its component form indicates that with $\omega_z \neq 0$, for the flow to be generalized Beltramian it is necessary that $u, v, w$ are independent of $z$. Then (6.3) implies that $u = C(t)/r$, which would lead to a singularity at the vortex axis if $C \neq 0$. Hence (6.16) follows.

Once (6.16) holds, in (6.5) for $\boldsymbol{\omega} = (0, \omega_\theta, \omega_z)$, the viscous terms are solely balanced by the unsteady terms

$$\frac{\partial \omega_z}{\partial t} = \frac{\nu}{r}\frac{\partial}{\partial r}\left(r\frac{\partial \omega_z}{\partial r}\right), \tag{6.17a}$$

$$\frac{\partial \omega_\theta}{\partial t} = \nu\left[\frac{1}{r}\frac{\partial}{\partial r}\left(r\frac{\partial \omega_\theta}{\partial r}\right) - \frac{\omega_\theta}{r^2}\right]. \tag{6.17b}$$

Note that although for a generalized Beltrami vortex (6.5) is linearized and one has more chance to find analytical solutions, the most important physical feature of a vortex, the stretching, is missing. The significance of these generalized Beltrami vortices should not be overestimated.

## 6.2 Axisymmetric Columnar Vortices

### 6.2.1 Stretch-Free Columnar Vortices

We start from the simplest *stretch-free* vortex solutions of the form (6.16). In this case (6.4) is reduced to

$$\frac{\partial p}{\partial r} = \frac{v^2}{r}, \tag{6.18a}$$

$$\frac{\partial \Gamma}{\partial t} = \nu r \frac{\partial}{\partial r}\left(\frac{1}{r}\frac{\partial \Gamma}{\partial r}\right), \tag{6.18b}$$

$$\frac{\partial w}{\partial t} = -\frac{\partial p}{\partial z} + \frac{\nu}{r}\frac{\partial}{\partial r}\left(r\frac{\partial w}{\partial r}\right). \tag{6.18c}$$

Unlike (6.12b), $v$ and $w$ are now decoupled. If the flow is effectively inviscid, the only equation we can use is (6.18a) in which the pressure can automatically adjust itself to balance whatever centrifugal acceleration. Thus, *a stretch-free inviscid vortex can have arbitrary radial dependence*, providing a big freedom for constructing various inviscid vortex models. The most familiar example is the *q-vortex*, which fits many experimental data pretty well

$$u(r) = 0, \quad v(r) = \frac{q}{r}\left(1 - \mathrm{e}^{-r^2}\right), \quad w(r) = W_0 \pm \mathrm{e}^{-r^2}, \tag{6.19a}$$

$$\omega_z(r) = 2q\mathrm{e}^{-r^2}, \quad \omega_\theta(r) = \pm 2r\mathrm{e}^{-r^2}. \tag{6.19b}$$

In Chap. 8 it will be seen that (6.19) is actually the canonical form of an approximate viscous solution suitable to describe a wake vortex far downstream of an aircraft, found by Batchelor (1964). So the $q$-vortex is also called the *Batchelor vortex.* Evidently (6.19) satisfies (6.11). On the other hand, the vorticity has a Gaussian distribution, and hence the $q$-vortex is one of the family called *Gaussian vortices.*

In contrast, for viscous flow, if $\omega_\theta = 0$ as in the case of pure vortices, we have (6.18a) plus (6.17a). If the flow is steady, (6.17a) implies that $\omega_z$ must be a constant (can be zero), which by (6.2) leads to

$$v(r) = Ar + \frac{B}{r}, \tag{6.20}$$

where $A$ and $B$ are arbitrary constants. For a flow between two rotating coaxial circular cylinders with inner and outer radii $R_1$ and $R_2$ and angular velocity $\Omega_1$ and $\Omega_2$, respectively, the constants can be determined as

$$A = -\Omega_1 \frac{1 - \mu\eta^2}{1 - \eta^2}, \quad B = \Omega_1 \frac{R_1^2(1 - \mu)}{1 - \eta^2}, \tag{6.21}$$

where $\mu = \Omega_1/\Omega_2$ and $\eta = R_1/R_2$. This flow is known as the *Couette–Taylor flow.* But if the flow domain is unbounded as our present concern, (6.20)

implies either the well-known *line vortex* with $A = 0$ and constant $\Gamma = 2\pi rv$ or a *solid rotation* with $B = 0$. There is no smooth and steady stretch-free viscous solution in an unbounded domain, because to maintain a steady viscous flow a constant driving force is necessary. The best one can do is to artificially combine a solid core of radius $a$ and a potential outer flow, to form a *Rankine vortex*

$$v(r) = \begin{cases} \dfrac{\omega r}{2}, & \text{if} \quad r \le a, \\ \dfrac{\omega a^2}{2r}, & \text{if} \quad r > a, \end{cases} \tag{6.22}$$

where $\omega$ and $a$ are the constant core vorticity and core radius, respectively. Obviously, this is also an inviscid solution.

As we allow the flow to decay freely, (6.17a) permits uniformly effective viscous solutions. A complete set of similarity solutions has been given by Neufville (1957), who sets

$$\tau = \nu t, \quad \eta = \frac{r^2}{4\tau}, \tag{6.23}$$

which cast (6.17a) to

$$\eta \frac{\partial^2 \omega}{\partial \eta^2} + (\eta + 1)\frac{\partial \omega}{\partial \eta} - \tau \frac{\partial \omega}{\partial \tau} = 0.$$

A further transformation $\omega = \tau^{-(n+1)} \mathrm{e}^{-\eta} L(\eta)$ then yields the *Laguerre equation*

$$\eta L'' + (1 - \eta)L' + nL = 0,$$

of which the solutions are the *Laguerre polynomials* (e.g., Abramowitz and Stegun, 1972):

$$L_n(\eta) = \mathrm{e}^{\eta} \frac{\mathrm{d}^n}{\mathrm{d}\eta^n} \left( \frac{\eta^n}{\mathrm{e}^{\eta}} \right).$$

Therefore, the general solution of (6.17a) is

$$\omega(\eta, \tau) = \sum_{n=0}^{\infty} C_n \tau^{-(n+1)} \mathrm{e}^{-\eta} L_n(\eta). \tag{6.24}$$

The exponential decay of $\omega$ as $\eta$ indicates that the vorticity is concentrated in a region with $\eta \ll 1$. Note that $L_n(\eta)$ has $n$ zeros and can be inferred from recursive formulas:

$$L_0(\eta) = 1, \quad L_1(\eta) = 1 - \eta,$$

$$L_{n+1}(\eta) = (2n + 1 - \eta)L_n(\eta) - n^2 L_{n-1}(\eta).$$

Two special modes of (6.24) are well known. The mode $n = 0$ is the *Oseen–Lamb vortex* (Oseen 1912; Lamb 1932):

$$v(r,t) = \frac{\Gamma_0}{2\pi r}\left[1 - \exp\left(-\frac{r^2}{4\nu t}\right)\right], \tag{6.25a}$$

$$\omega_z(r,t) = \frac{\Gamma_0}{4\pi\nu t}\exp\left(-\frac{r^2}{4\nu t}\right). \tag{6.25b}$$

It represents the viscous decay process of a singular line vortex from $t = 0$, having a finite circulation $\Gamma = 2\pi r v$ that satisfies the following initial-boundary conditions:

$$\Gamma(0,0) = \Gamma_0, \quad \Gamma(0,t) = 0, \quad \Gamma(\infty,t) = \Gamma_0.$$

The behavior of (6.25) for $r \gg 4\nu t$ approaches that of line vortex. For small $r$, there is $v \simeq \Gamma_0 r/(8\pi\nu t)$, similar to a solid rotation. These two regions merge around $r_0 \sim \sqrt{4\nu t}$, which represents an expanding core radius, see Figs. 6.1a and b. Note that the $v(r)$ distribution of the $q$-vortex, (6.19), is essentially the same as an Oseen vortex if the latter is "frozen" at a time $t_0$ with radius rescaled by $\sqrt{4\nu t_0}$.

The Oseen–Lamb vortex may also be viewed as the axisymmetric counterpart of the Stokes first problem analyzed in Sect. 4.1.4. But, it is easily verified that in unbounded domain an isolated Oseen–Lamb vortex has infinite total kinetic energy and angular momentum.

Second, the mode $n = 1$ in (6.24) leads to the *Taylor vortex* (Taylor 1918):

$$v(r,t) = \frac{Mr}{8\pi\nu t^2}\exp\left(-\frac{r^2}{4\nu t}\right), \tag{6.26a}$$

$$\omega_z(r,t) = \frac{M}{2\pi\nu t^2}\left(1 - \frac{r^2}{4\nu t}\right)\exp\left(-\frac{r^2}{4\nu t}\right), \tag{6.26b}$$

where $M$ represents the total angular momentum about the axis

$$M = \int_0^\infty 2\pi r^2 v \mathrm{d}r. \tag{6.27}$$

This solution has *zero total circulation* (because $\omega$ changes sign once) and finite $M$. Note that (6.26) is nothing but the time derivative of (6.25). The velocity profiles of Oseen–Lamb vortex and Taylor vortex are compared in Fig. 6.1c. All higher modes with $n > 1$ in (6.24) have zero total circulation and zero total angular momentum (Neufville 1957).

Any pure vortices are two-dimensional generalized Beltrami flow, for which by (3.64) $\omega_z(r,t) = f(\psi,t)$. While for the Rankine vortex we simply have $f =$ constant, for Neufville's vortex family $f(\psi,t)$ is nonlinear.

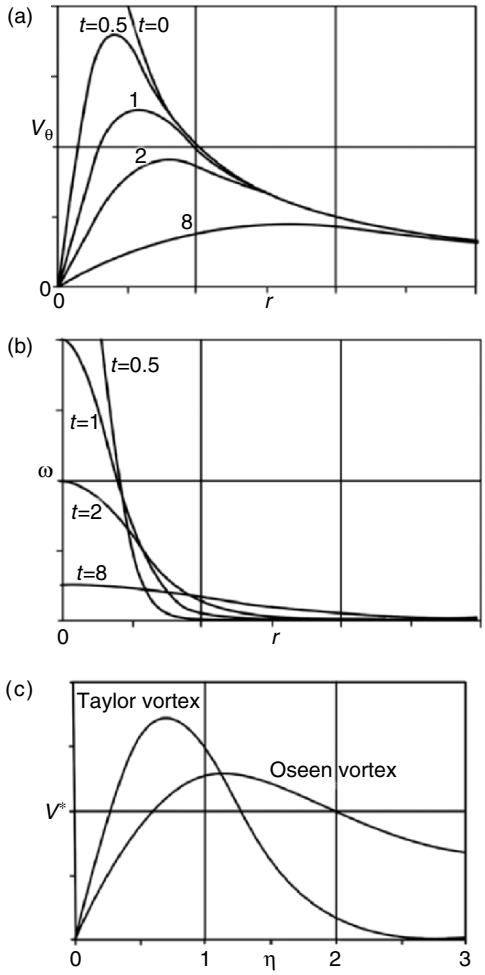


**Fig. 6.1.** The decay of the circumferential velocity (**a**) and vorticity (**b**) of the Oseen–Lamb vortex, and its comparison with the Taylor vortex in similarity variables (**c**). In (c) $V^* \propto v/t^{-1/2}$ and $v/t^{-3/2}$ for the Oseen–Lamb vortex and Taylor vortex, respectively. Reproduced from Panton (1984)

### 6.2.2 Viscous Vortices with Axial Stretching

Vortex stretching occurs if the axial velocity $w(r, z, t)$ is $z$ dependent. The simplest $z$-dependence of $w$ is linear and uniform

$$w(r,t) = \gamma(t)z, \quad u(r,t) = -\frac{1}{2}\gamma(t)r, \quad \gamma > 0, \tag{6.28}$$

where $u(r, t)$ is derived from (6.3). The vorticity has only a $z$-component. The flow can take this form only locally ($r < \infty, \quad |z| < \infty$). From (6.5c) and

(6.28), the vorticity equation reads:

$$\frac{\partial \omega}{\partial t} = \frac{\nu}{r}\frac{\partial}{\partial r}\left(r\frac{\partial \omega}{\partial r}\right) + \frac{1}{2}\gamma r\frac{\partial \omega}{\partial r} + \gamma\omega. \tag{6.29}$$

On the right-hand side, the second term is a radial advection, while the third term is a uniform stretching. If at $t = 0$ a vortex element has unit length, then at time $t$ its length will be

$$S(t) = \exp\left(\int_0^t \gamma(t')\mathrm{d}t'\right) \tag{6.30}$$

or $\mathrm{e}^{\gamma t}$ if $\gamma$ is a constant. Once again, we seek similarity solutions of (6.29). Following Lundgren (1982; see also Kambe 1984), we introduce new stretched variables:

$$\rho \equiv S^{1/2}(t)r, \quad \tau \equiv \int_0^t S(t')\mathrm{d}t', \tag{6.31}$$

such that (6.29) is cast to

$$S\frac{\partial \omega}{\partial \tau} = \gamma\omega + \nu\frac{S}{\rho}\frac{\partial}{\partial \rho}\left(\rho\frac{\partial \omega}{\partial \rho}\right).$$

But since

$$\frac{\partial S}{\partial \tau} = \frac{\partial S}{\partial t}\frac{\mathrm{d}t}{\mathrm{d}\tau} = \gamma,$$

we finally obtain the same equation as (6.17a) but in terms of $(\rho, \tau)$ variables:

$$\frac{\partial \omega^*}{\partial \tau} = \frac{\nu}{\rho}\frac{\partial}{\partial \rho}\left(\rho\frac{\partial \omega^*}{\partial \rho}\right), \quad \omega^* \equiv S^{-1}\omega,$$

Therefore, from any pure vortex one can generate a uniformly stretched vortex by the *Lundgren transformation*

$$\omega(r,t) = S(t)\omega^*\left(S^{1/2}(t)r, \int_0^t S(t')\mathrm{d}t'\right). \tag{6.32}$$

The two flows before and after transformation have similar behavior. Because $S(t) > 1$ implies $r < \rho$, $t < \tau$, and $\omega > \omega^*$, the velocity and vorticity of stretched vortex flow are enhanced, with shorter distances and faster rotation time, in agreement with the kinematics discussed in Sect. 3.5.3. For example, from the Oseen–Lamb vortex and a constant $\gamma$, we find a new solution

$$\omega(r,t) = \frac{\gamma\Gamma_0}{4\pi(1-\mathrm{e}^{-\gamma t})}\exp\left(-\frac{\beta r^2}{1-\mathrm{e}^{-\gamma t}}\right). \quad \beta \equiv \frac{\gamma}{4\nu}. \tag{6.33a}$$

Integrating this with respect to $r$ yields the circumferential velocity profile

$$v(r,t) = \frac{\Gamma_0}{2\pi r}\left[1 - \exp\left(-\frac{\beta r^2}{1+\alpha\mathrm{e}^{-2\nu t}}\right)\right], \tag{6.33b}$$

where $\alpha$ is an integration constant. This solution was studied by Rott (1958) and Bellamy-Knights (1970).

Then, let $t \to \infty$ in (6.33), we obtain an asymptotic steady solution of stretched vortex of radius $\delta \sim (\nu/\gamma)^{1/2}$, which exists only if $\gamma > 0$:

$$\omega(r) = \frac{\gamma \Gamma_0}{4\pi\nu} \mathrm{e}^{-\beta r^2}, \tag{6.34a}$$

$$u(r) = -\frac{\gamma}{2} r, \quad v(r) = \frac{\Gamma_0}{2\pi r}\left(1 - \mathrm{e}^{-\beta r^2}\right), \quad w(z) = \gamma z. \tag{6.34b}$$

This is the famous *Burgers vortex* (Burgers 1948). It can be directly obtained from the steady version of (6.29). If $\gamma < 0$, the vorticity will run away from the axis. If the time in (6.25) is frozen at $t = 1/\gamma$, the velocity distribution will be the same as that of the Oseen–Lamb vortex. This is because the radial flow $-\gamma r/2$ brings the far-field vorticity to the vortex core, which exactly compensates the viscous diffusion. But we have $\partial u/\partial r|_{r=0} = -\gamma/2$ and hence $u$ is not smooth at $r = 0$.

The Burgers vortex is the first stretched vortex solution to model turbulent eddies. As a remarkable feature, its total dissipation per unit length in the $z$-direction is finite but *independent of* $\nu$

$$\rho\nu \int_0^\infty 2\pi r \omega^2(r) \mathrm{d}r = \frac{\rho\gamma\Gamma_0^2}{4\pi}. \tag{6.35}$$

Thus, the dissipation remains finite as $\nu \to 0$, which is a fundamental assumption of turbulence theory (e.g., Frisch 1995). This vortex has served as a building block of various vortex models for fine-scale turbulent structures and starting point of searching for more complex vortex solutions (Sect. 6.5).

The Lamb vector of the Burgers vortex is

$$\boldsymbol{l}(r) = -\omega(r)\left[v(r)\boldsymbol{e}_r + \frac{1}{2}\gamma r \boldsymbol{e}_\theta\right] \tag{6.36}$$

from which it follows that

$$\nabla \cdot \boldsymbol{l}_\parallel = -\frac{1}{r}\frac{\partial}{\partial r}(rv\omega), \quad \nabla \times \boldsymbol{l}_\perp = -\boldsymbol{e}_z \frac{1}{2r}\frac{\partial}{\partial r}(\gamma r^2 \omega).$$

Equating $\nabla \cdot \boldsymbol{l}_\parallel$ to $\nabla^2 \phi_l$, by using (6.7) we find

$$\phi_l = \int_r^\infty v\omega \, \mathrm{d}r + C \log r,$$

where there must be $C = 0$. Thus, from the $r$-momentum equation

$$u\frac{\partial u}{\partial r} - \frac{v^2}{r} = -\frac{\partial p}{\partial r}$$

and using (6.4c), we can obtain $\boldsymbol{l}_{\parallel}$ and then $\boldsymbol{l}_{\perp}$ from (6.36)

$$\boldsymbol{l}_{\parallel} = -v(r)\omega(r)\boldsymbol{e}_r = -\nabla\left(H - \frac{1}{2}w^2\right), \tag{6.37a}$$

$$\boldsymbol{l}_{\perp} = -\frac{1}{2}\gamma r\omega(r)\boldsymbol{e}_{\theta} = -\frac{1}{2}\gamma\frac{\partial \Gamma}{\partial r}\boldsymbol{e}_{\theta}, \quad \Gamma = rv(r). \tag{6.37b}$$

While $\boldsymbol{l}_{\parallel}$ is independent of $\gamma$ and has the same form as nonstretched vortices, $\boldsymbol{l}_{\perp}$ is completely caused by the stretching as it should. Remarkably, $\boldsymbol{l}_{\parallel}$, $\boldsymbol{l}_{\perp}$, and $\boldsymbol{\omega}$ are *geometrically orthogonal*.

Moreover, the strain-rate tensor of the Burgers vortex is

$$\mathbf{D} = \frac{1}{2}\begin{pmatrix} -\gamma & R & 0 \\ R & -\gamma & 0 \\ 0 & 0 & 2 \end{pmatrix}, \quad R = r\frac{\partial}{\partial r}\left(\frac{v}{r}\right). \tag{6.38}$$

The deformation principal axes are the $z$-axis (stretching) and any pair of orthogonal axes on the $(r, \theta)$ plane, where shrinking occurs. As the vortex stretches at a rate $\gamma$, $\boldsymbol{l}_{\perp}$ shrinks at rate $\gamma/2$. Based on the transport equation for $\boldsymbol{l}$, Wu et al. (1999b) have shown that *vortex stretching is generically associated with the Lamb-vector shrinking*.

In this simplest model of stretched vortices, the nonlinearity caused by $\boldsymbol{l}_{\perp} \neq \mathbf{0}$ can be made disappear by the Lundgren transformation (6.32). When the axial velocity is nonuniform, one may consider more general families of semi-similarity solutions, in which if the nonlinear coupling between different components can be *artificially* removed then the solutions may have closed form. To this end, we seek steady solutions of the form

$$\begin{aligned} &\psi = g(r)z + f(r), \quad rv = \Gamma(r), \\ &\frac{\partial \psi}{\partial z} = g(r) = ru, \quad \frac{\partial \psi}{\partial r} = g'(r)z + f' = -rw. \end{aligned} \tag{6.39}$$

Substitute these into the dynamic equations (6.4b) for $v$ and (6.5b) for $\omega_{\theta}$, as well as the kinematic relation (6.9c), we obtain a set of ordinary differential equations. Recall that $v$ and $\psi$ determine the motion along the azimuthal direction and on the axial plane, respectively. The equations are decoupled, of which the ones for $g$ and $f$ can be integrated once, and the one for $\Gamma$ can be integrated twice

$$g\frac{\mathrm{d}}{\mathrm{d}r}\left(\frac{g'}{r}\right) - \frac{g'^2}{r} = \nu\frac{\mathrm{d}}{\mathrm{d}r}\left[r\frac{\mathrm{d}}{\mathrm{d}r}\left(\frac{g'}{r}\right)\right] + C_1 r, \tag{6.40a}$$

$$g\frac{\mathrm{d}}{\mathrm{d}r}\left(\frac{f'}{r}\right) - g'\frac{f'}{r} = \nu\frac{\mathrm{d}}{\mathrm{d}r}\left[r\frac{\mathrm{d}}{\mathrm{d}r}\left(\frac{f'}{r}\right)\right] + C_2 r, \tag{6.40b}$$

$$v(r) = \frac{\Gamma_0}{2\pi r}\left[\int_0^r s\exp\left(\int_0^s \frac{u(\tau)}{\nu}\,\mathrm{d}\tau\right)\mathrm{d}s + C_3\right], \tag{6.40c}$$

where $C_1, C_2, C_3$, and $\Gamma_0$ are integration constants. Then, if $f \equiv 0$, (6.40a) permits a simple solution $g'/r =$ constant, which includes the Burgers vortex. If $f(r) \neq 0$, a combination of the simple solution $g'/r =$ const. of (6.40a) and (6.40b) makes the latter have solution $(f'/r)' = C_4 r$, and hence

$$u(r) = A_1 r + A_2 r^{-1}, \quad f(r) = B_1 r^4 + B_2 r^2. \tag{6.41}$$

By different choices of the constants, one finds a linear superposition of some elementary vortices and axial flows, including (Xiong and Wei 1999): a superposition of a circular-pipe Poiseuille flow and a forced vortex and/or a line vortex; that of a circular-pipe Poiseuille flow and a Burgers vortex; and a swirling flow with singular sink (a simple model for *bathtub vortex*) or source.

Now, assume instead an $r$-dependent axial velocity with an exponential decay, similar to that in (6.19)

$$w = \gamma z \left(1 - b\,\mathrm{e}^{-\beta r^2}\right).$$

Substituting this profile into (6.39) and (6.40a), and equating terms, we find that a special solution exists if and only if

$$C_1 = -\gamma^2, \quad \beta = \frac{\gamma}{4\nu}, \quad b = 3.$$

The velocity profiles are found to be

$$u(r) = -\frac{1}{2}\gamma r + \frac{6\nu}{r}\left(1 - \mathrm{e}^{-\beta r^2}\right), \tag{6.42a}$$

$$v(r) = \frac{\Gamma_0 H\left(\beta r^2\right)}{2\pi r H(\infty)}, \tag{6.42b}$$

$$w(r,z) = \gamma z \left(1 - 3\mathrm{e}^{-\beta r^2}\right), \tag{6.42c}$$

where

$$H(x) \equiv \int_0^x \exp\left(-\eta + 3\int_0^\eta \frac{1 - \mathrm{e}^{-\zeta}}{\zeta} d\zeta\right) \mathrm{d}\eta, \quad H(\infty) = 37.905. \tag{6.43}$$

Sullivan (1959) wrote down this solution without giving derivation. The vorticity components of this *Sullivan vortex* are

$$\omega_r = 0, \tag{6.44a}$$

$$\omega_\theta = -\frac{3\gamma^2}{2\nu} r z \mathrm{e}^{-\beta r^2}, \tag{6.44b}$$

$$\omega_z = \frac{\gamma \Gamma_0}{2\nu H(\infty)} \exp\left(-\beta r^2 + 3\int_0^{\beta r^2} \frac{1 - \mathrm{e}^{-\zeta}}{\zeta} \mathrm{d}\zeta\right). \tag{6.44c}$$

Like the Burgers vortex, $u$ is not smooth at $r = 0$ either with $\partial u/\partial r|_{r=0} = \gamma$. But the most striking property of the Sullivan vortex is that it permits a *two-cell structure*. From (6.42a), there will be $u(r_0) = 0$ at an $r_0 = 3.36\sqrt{\nu/\gamma}$ that satisfies $\beta r_0^2 = 3(1 - \mathrm{e}^{-\beta r_0^2})$, and $u$ changes sign across $r_0$. Thus, $r = r_0$ is a *limit circle* (see Sect. 7.1.1): fluid outside $r_0$ will move inward to $r_0$, while that inside $r_0$ will move outward to $r_0$. Therefore, near $r_0$ there must be a strong axial flow, which in turn requires an axial flow of opposite direction near $r = 0$. So $w(r, z)$ has to change sign somewhere between $r_0$ and the axis as well. The one-cell Burgers vortex and two-cell Sullivan vortices are compared in Fig. 6.2. The two-cell structure has been observed in some hurricanes, so the Sullivan vortex is of special interest in meteorology.

### 6.2.3 Conical Similarity Swirling Vortices

In both Burgers vortex and Sullivan vortex the coupling of three velocity components are arbitrarily constructed rather than derived from reasonable boundary conditions. Thus, some behaviors of these vortices are lack of physical background. In seeking for fully nonlinear solutions of stretched swirling vortices one should avoid this arbitrariness.

The first step toward this goal is the *Long vortex*. Instead of assuming an axial flow of the form of $w = zf(r)$, Long (1958, 1961) assumes $rv$ approaches a constant for $r \gg 1$. Then, the similarity consideration gives a combined variable $x = Kr/(\sqrt{2}\nu z)$, and the dimensional analysis plus continuity equation leads to the following form of velocity components and pressure:

$$\begin{aligned} u &= K\left(-\frac{\epsilon}{r}f(x) + \frac{1}{\sqrt{2}z}f'(x)\right), \\ v &= \frac{K}{r}\Gamma(x), \quad w = \frac{K}{\sqrt{2}r}f'(x), \\ \frac{p}{\rho} + gz &= -\frac{K^2}{\epsilon^2 z^2}s(x), \end{aligned} \tag{6.45}$$

where $g$ is the gravitational acceleration and $\epsilon \equiv \nu/K = Re^{-1} \ll 1$. This implies $u/w = \sqrt{2}\epsilon(x - f/f') \ll 1$, and thus the flow is asymptotically cylindrical. Substituting (6.45) into (6.4) and neglecting $\mathrm{O}(\epsilon^2)$ terms, Long obtains coupled equations for $f(x)$, $\Gamma(x)$, and $s(x)$:

$$\begin{aligned} \Gamma^2 + 2x^3 s' &= 0, \\ xf'' + (f-1)f' - 4x^3 s &= 0, \\ x\Gamma'' + (f-1)\Gamma' &= 0. \end{aligned} \tag{6.46}$$

This approximation is called the *quasi-cylindric approximation*, which is the counterpart of boundary-layer approximation in studying concentrated

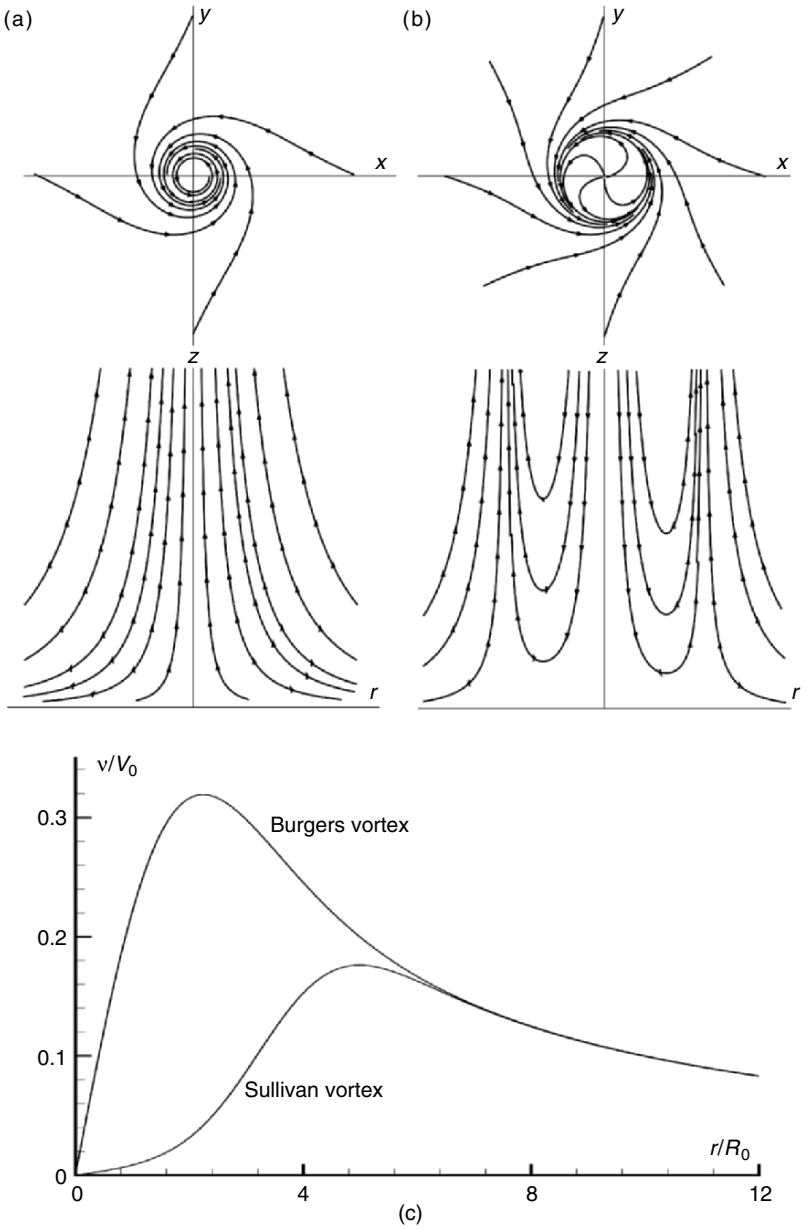


**Fig. 6.2.** The velocity profiles of one- and two-cell vortices. (**a**) One cell (Burgers vortex); (**b**) two cells (Sullivian vortex); (**c**) the circumferential velocity, where $V_0 = \Gamma/2\pi r_0$, $R_0 = (\nu/\gamma)^{1/2}$

vortices and will be further explored in Sect. 8.1. By requiring a finite velocity at $x = 0$, Long solved these equations numerically. This vortex is also widely used in meteorology.

Inspecting Long's similarity variable $x$, it is clear that before making the quasi-cylindrical approximation the flow has *conical similarity*, i.e., any function of $x$, such as $f(x)$, $\Gamma(x)$, and $s(x)$, will be invariant along a ray from the origin with constant $r/z$. According to Wang (1991), Slezkin (1934) was the first to note that when velocities are inversely proportional to $R = \sqrt{r^2 + z^2}$ the Navier–Stokes equation permits conical similarity solutions. Yih et al. (1982) have proved that among all axisymmetric solutions of the Navier–Stokes equation, only conical similarity solutions have finite (actually, zero) velocity at infinity. This avoids the divergence of the flow field as $z \to \infty$ as in the Burgers and Sullivan vortices.

Conical similarity solutions are best analyzed in spherical coordinates $(R, \theta, \phi)$, where $\phi$ is the azimuthal angle about the vortex axis $\theta = 0$. Let $x = \cos\theta$, so that $x = 0$ and 1 correspond to the equator plane and the vortex axis, respectively. Assume

$$u_R = \frac{F'(x)}{R}, \quad u_\theta = \frac{F(x)}{R\sin\theta}, \quad u_\phi = \frac{\Omega(x)}{R\sin\theta}, \tag{6.47}$$

where the form of $u_R$ is from the continuity equation. Substituting (6.47) into the axisymmetric momentum equation and eliminating pressure, one obtains a pair of coupled second-order equation for $\Omega$ and fourth-order equation for $F$. Integrating the latter three times and denoting $F = 2\nu(1 - x^2)f$, a pair of elegant coupled nonlinear integral-differential equations for $f(x)$ and $\Omega(x)$ follows:

$$f'^2 + f^2 = \frac{G(x)}{(1 - x^2)^2}, \tag{6.48a}$$

$$\Omega'' + 2f\Omega' = 0, \tag{6.48b}$$

where

$$G(x) \equiv -\int_0^x \mathrm{d}x \int_0^x \mathrm{d}x \int_0^x \frac{4\Omega\Omega'}{1 - x^2}\mathrm{d}x + Px^2 + Qx + R, \tag{6.48c}$$

with $P, Q, R$ being integration constants to be determined by boundary conditions. The Reynolds number has been normalized to unity. When $\Omega = 0$ (6.48a) describes a conical similarity momentum jet, and $\Omega \neq 0$ is a swirling vortex with all components coupled in a way determined by the equations and boundary conditions. Both cases have been studied by many authors as briefly reviewed by Wang (1991), see also Sozou et al. (1994).

If we require that at vortex axis there is no source or sink and all velocity components are finite, and if there is a solid wall at $x = 0$ ($\theta = \pi$) where the adherence condition holds, then the boundary conditions for (6.48) would be

$$\Omega = F = 0, \quad \text{and} \quad F' \quad \text{finite}, \quad \text{at} \quad x = 1, \tag{6.49a}$$

$$\Omega = F = F' = 0 \quad \text{at} \quad x = 0. \tag{6.49b}$$

However, by (6.48b), $\Omega'(x)$ cannot change sign for $x \in [0, 1]$, implying that for a swirling vortex with nonzero $\Omega(x)$ one of (6.49a) and (6.49b) has to be relaxed. If we relax the former, there can be a viscous boundary layer induced by the vertical vortex near the solid wall $x = 0$, but the vortex core is singular like a line vortex. If we relax the latter, the vortex core can be regular but on the plane $x = 0$ there must be a slip. These alternative choices have been studied by Goldshtik (1960) and Serrin (1972), and by Yih et al. (1982), respectively. The solutions for each choice can exhibit both one-cell and two-cell vortices, see Fig. 6.3 as an example.

Wu (1986b) attempted a fully regular solution by allowing the viscosity to be function of $x$, but unfortunately his modified $\Omega$-equation is incorrect as pointed out by Goldshtik and Shtern (1988). These authors conclude that, with any variable $\nu(x)$, conditions (6.49a) and (6.49b) still cannot be simultaneously satisfied. Therefore, the conical similarity vortex solutions cannot mimic the interaction of a tornado-like vortex and the ground, which is actually more complicated than any similarity solution can simulate, as will be seen in Sect. 8.4.

While concluding this section, we stress again that none of the exact solutions presented herein is completely realistic. The vorticity in the Rankine vortex has a discontinuity which is impossible when $\nu$ is finite. The Burgers and Sullivan vortices have infinite $u, w$ as $|z| \to \infty$, nonsmooth $u$ at $r = 0$, and a nonphysical decoupling between the motions in the azimuthal direction and on the meridional plane. After all, as long as the total circulation is finite there must be $v \sim r^{-1}$ as $r \to \infty$, which immediately implies that the total kinetic energy and axial angular momentum is infinity, see (6.27). The only exception is the Taylor vortex, which has two counter-rotating fluid bodies

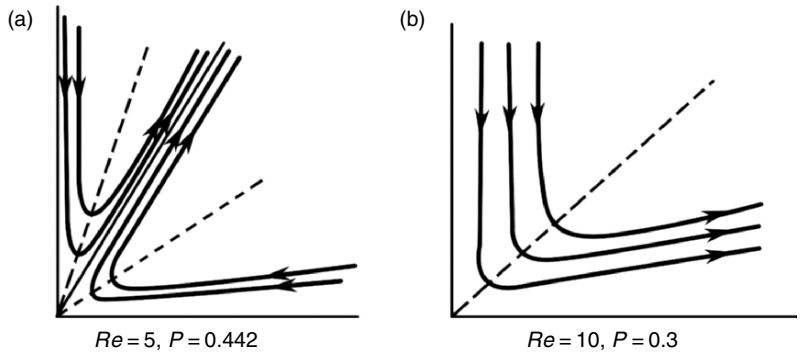


**Fig. 6.3.** Conical similarity vortices interacting a no-slip flat plate with singular core. Reproduced from Serrin (1972)

with one surrounding the other. Except some geophysical vortices (Chap. 12), however, such a vortex is seldom encountered due to instability (Chap. 9). Therefore, all these solutions can at most represent some local behavior of real vortices.

The lacking of "realistic" analytical solution for isolated axisymmetric vortices is also a reflection of the very basic physics. If the flow domain is bounded, there must be a boundary layer with distributed vorticity, and a columnar vortex solutions can be effective at most in a limited subdomain (e.g., in a circular vortex tube). Alternatively, if the fluid is unbounded at rest at infinity and the vorticity is created from a nonrotating moving body, say a flying wing, then vortices never appear as a single isolated one but form *closed loops* or *in pair* to ensure the total-vorticity conservation (3.15) or total-circulation conservation (3.16) in two dimensions. Therefore, none of the above isolated vortex solutions can be globally effective. It is therefore necessary to examine wider classes of vortex solutions that are more realistic. We pursue this task in Sects. 6.3–6.5.

## 6.3 Circular Vortex Rings

Due to the first Helmholtz theorem, in unbounded space a vortex must form a loop with compact support. The simplest vortex loop is a circular vortex ring, which in a sense is a more fundamental vortex structure than columnar vortices and can be easily produced experimentally (e.g., by an impulsive motion of a piston), see Fig. 4.22. Because of their frequent appearance in nature and technology, vortex rings have been a subject of active studies (see, e.g., the reviews of Shariff and Leonard 1992 and Lim and Nickels 1995). In this section we discuss incompressible axisymmetric circular vortex-ring solutions sketched in Fig. 6.4. If along the ring's circular axis $r = r_0$ the velocity is nonzero, the ring has a swirl.

### 6.3.1 General Formulation and Induced Velocity

Unlike a columnar vortex, a circular vortex ring in a fluid at rest at infinity will move along its axis due to its *self-induction* at $r = 0$, to which all ring elements of unit arclength have the same contribution, in contrast to nonuniform self-induction of noncircular loops, e.g., Fig. 3.15. It is then convenient to observe the ring in a comoving frame of reference, so that at infinity there is an opposite translational velocity. Consider a swirl-free vortex ring first. In cylindrical coordinates $(r, \theta, z)$ the total velocity is $U\boldsymbol{e}_z + \boldsymbol{u}$ with $\boldsymbol{u} = \boldsymbol{0}$ at infinity. $\boldsymbol{u}$ and $\boldsymbol{\omega}$ have components

$$\boldsymbol{u} = (u, 0, w), \quad \boldsymbol{\omega} = (0, \omega_\theta, 0), \tag{6.50}$$

indicating that the flow is rotationally symmetric and complex lamellar as observed in Sect. 3.3.1. Thus, kinematically, the flow field is fully described by

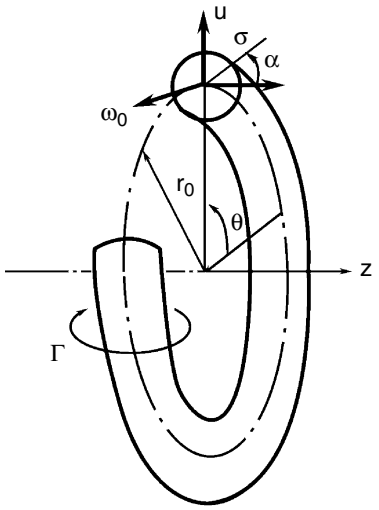


**Fig. 6.4.** Vortex-ring geometry and cylindrical coordinates

a Stokes stream function

$$\Psi = -\frac{1}{2}Ur^2 + \psi \tag{6.51}$$

with $\boldsymbol{u}$ and $\omega_\theta$ being solely determined by $\psi$ through (6.8) and (6.9c). Dynamically, (6.5b) is reduced to

$$\frac{\mathrm{D}\omega_\theta}{\mathrm{D}t} = \frac{\omega_\theta u}{r} + \nu\left(\nabla^2\omega_\theta - \frac{\omega_\theta}{r^2}\right) \tag{6.52}$$

of which a neater form is (6.10b):

$$\frac{\mathrm{D}f}{\mathrm{D}t} = \nu\left(\nabla^2 f + \frac{2}{r}\frac{\partial f}{\partial r}\right), \quad f \equiv \frac{\omega_\theta}{r}. \tag{6.53}$$

If in addition the flow is *generalized Beltramian*, then (3.63) and (3.67) hold. While (3.67) and (6.4) imply a Bernoulli equation

$$p + \frac{1}{2}q^2 + \int f(\psi)\,\mathrm{d}\psi = \text{const.}, \tag{6.54}$$

condition $\nabla \times (\boldsymbol{\omega} \times \boldsymbol{u}) = \boldsymbol{0}$ along with (6.3) simply leads to $\boldsymbol{u} \cdot \nabla f = 0$, indicating that *the advection of $\omega_\theta$ is always balanced by the vortex-tube tilting* which occurs everywhere in a circular vortex ring. Then (6.52) or (6.53) are linearized, yielding

$$\frac{\partial\omega_\theta}{\partial t} = \nu\left(\frac{\partial^2\omega_\theta}{\partial r^2} + \frac{1}{r}\frac{\partial\omega_\theta}{\partial r} - \frac{\omega_\theta}{r^2} + \frac{\partial^2\omega_\theta}{\partial z^2}\right), \tag{6.55a}$$

$$\frac{\partial f}{\partial t} = \nu\left(\frac{\partial^2 f}{\partial r^2} + \frac{3}{r}\frac{\partial f}{\partial r} + \frac{\partial^2 f}{\partial z^2}\right). \tag{6.55b}$$

Unlike two-dimensional flows, now the second-order differential operators in the kinematic relation (3.66) of $f(\psi, t)$ and its viscous dynamic constraint (6.55b) are different. This makes it much harder to find a viscous solution of generalized Beltrami vortex ring, except the simplest case $f = \text{const.}$, for which (6.53) or (6.55b) is trivially satisfied. This special case yields a family of solutions with $\omega_\theta = Cr$ and different vortex-core radii, known as the *Fraenkel–Norbury family* (Fraenkel 1970; Norbury 1973). Remarkably, the results agree very well with experimental measurement and viscous numerical solutions, see the comment of Fukumoto (2002). This solution family will be addressed in Sect. 6.3.2. Then in the next two sections we discuss the asymptotic thing-ring theory, where the viscous effect will also be introduced. Note that any *inviscid* and *steady* axisymmetric vortex ring is also generalized Beltramian due to (6.11), even if it has a swirl $rv \neq 0$. In this case, the flow is governed by the Bragg–Hawthorne equation (6.14) along with the three component expressions for $\boldsymbol{\omega}$ given by (6.13).

As a preparation of the these discussions, in the rest of this subsection we consider the vortex-ring induced Stokes stream function $\psi$ and especially its self-induced translation. The $\psi$ for given $\omega_\theta$ is obtained from the inversion of (6.9c), which is a special form of (2.104b) in unbounded domain with $\boldsymbol{\psi} = (0, r\psi, 0)$:

$$\psi(r, z) = \frac{1}{4\pi} \int \frac{r\omega'_\theta \boldsymbol{e}'_\theta \cdot \boldsymbol{e}_\theta}{R} \mathrm{d}V', \quad R = |\boldsymbol{x} - \boldsymbol{x}'|. \tag{6.56}$$

Using the notations defined in Fig. 6.4, (6.56) takes the form

$$\psi(r, z) = \int \omega_\theta G(r, r', z - z') \, \mathrm{d}r' \, \mathrm{d}z', \tag{6.57a}$$

$$G(r, r', z - z') = \frac{rr'}{4\pi} \int_0^{2\pi} \frac{\cos\beta}{R} \, \mathrm{d}\beta, \quad \beta = \theta - \theta', \tag{6.57b}$$

$$R = \sqrt{(z - z')^2 + r^2 + r'^2 - 2rr' \cos\beta}. \tag{6.57c}$$

Let the moving point $\boldsymbol{x}'$ be along a circle with varying $\theta'$ and fixed $(r', z')$. By (6.57c) and Fig. 6.4, in this circle

$$r_1 = \sqrt{(z - z')^2 + (r - r')^2}, \quad r_2 = \sqrt{(z - z')^2 + (r + r')^2} \tag{6.58}$$

are $R_{\min}$ and $R_{\max}$, respectively. We set

$$\phi = \frac{\beta}{2} - \frac{\pi}{2}, \quad k^2 = 1 - \frac{r_1^2}{r_2^2} = \frac{4rr'}{r_2^2}, \tag{6.59}$$

then in (6.57c)

$$R^2 = r_2^2(1 - k^2 \sin^2\phi),$$

$$2rr' \cos\beta = \frac{1}{2} r_2^2 (2 - k^2) - r_2^2 (1 - k^2 \sin^2\phi).$$

Hence, (6.57b) can be integrated to yield

$$G(r,r',z-z')=\frac{\sqrt{rr'}}{2\pi}\left[\left(\frac{2}{k}-k\right)K(k)-\frac{2}{E(k)}\right], \tag{6.60}$$

where

$$K(k)=\int_0^{\pi/2}\frac{\mathrm{d}\phi}{\sqrt{1-k^2\sin^2\phi}},\quad E(k)=\int_0^{\pi/2}\sqrt{1-k^2\sin^2\phi}\,\mathrm{d}\phi \tag{6.61}$$

are the first and second kinds of complete elliptic integrals, respectively.

As a simple but fundamental application of the Biot–Savart integral (6.57), consider a *circular line vortex* of circulation $\Gamma$ and radius $r_0$ at the $z=0$ plane, with singular vorticity distribution

$$\omega_\theta=\Gamma\delta(r-r_0)\delta(z). \tag{6.62}$$

Then, by (6.60), (6.56) becomes

$$\psi(r,z)=\Gamma\sqrt{\frac{rr_0}{2\pi}}\left[\left(\frac{2}{k}-k\right)K(k)-\frac{2}{k}E(k)\right],$$

so by (6.8) the motion on the axial plane is given by

$$u(r,z)=-\frac{\Gamma k}{4\pi r_0}\frac{z}{r_0}\left(\frac{r_0}{r}\right)^{3/2}\left[-K(k)+\frac{2-k^2}{2(1-k^2)}E(k)\right], \tag{6.63a}$$

$$w(r,z)=-\frac{\Gamma k}{4\pi r_0}\left(\frac{r_0}{r}\right)^{1/2}\left[K(k)+\frac{r_0}{2r}\frac{k^2}{1-k^2}-\frac{2-k^2}{2(1-k^2)}E(k)\right], \tag{6.63b}$$

$$k=2\sqrt{\frac{r_0 r}{z^2+(r+r_0)^2}}. \tag{6.63c}$$

In particular, at the ring center $(r,z)=(0,0)$ there is

$$\boldsymbol{u}_0=-\frac{\Gamma}{2r_0}\boldsymbol{e}_z, \tag{6.64}$$

indicating that the circular line vortex moves with constant velocity along the $-z$ direction without changing its shape. After imposing $U=\Gamma/2r_0$ to make the flow steady, the streamlines are shown in Fig. 6.5.

Equation (6.64) is the simplest example of the self-induced motion of a single vortex ring. A general method of determining the translation velocity for a circular viscous and unsteady ring has been given by Saffman (1970, see also Saffman 1992), who makes use of both the vortical impulse $\boldsymbol{I}$ given by (3.78) and Lamb's second formula (3.93) for kinetic energy $K$. The circular vortex ring is allowed to have arbitrary cross-sectional shape and vorticity distribution as well as swirl, so that all components of velocity and vorticity can

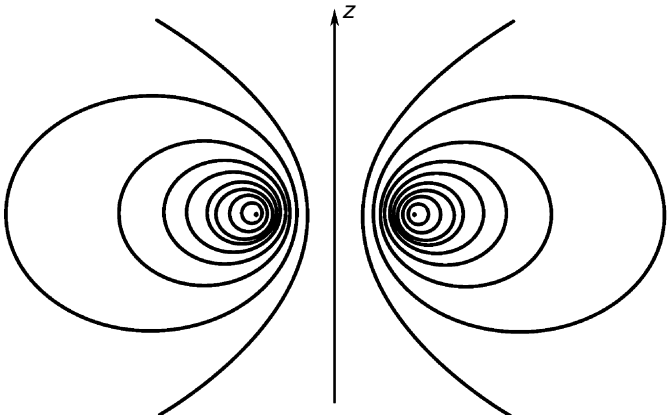


**Fig. 6.5.** Streamlines of a circular line vortex

be nonzero. Recall that the total velocity of the flow viewed in the comoving frame is $U\boldsymbol{e}_z + \boldsymbol{u}$, by (3.93) and (3.78) there is

$$K = 2UI_z + 2\pi \int [\omega_\theta(rw - zu) + v(z\omega_r - r\omega_z)]r \,\mathrm{d}r \,\mathrm{d}z,$$

where the second term is the vorticity-induced kinetic energy $K_v$, which by definition also reads:

$$\begin{aligned} K_v &= \pi \int (u^2 + v^2 + w^2) r \,\mathrm{d}r \,\mathrm{d}z \\ &= \pi \int \left( w\frac{\partial \psi}{\partial r} - u\frac{\partial \psi}{\partial z} \right) \mathrm{d}r \,\mathrm{d}z + \pi \int r v^2 \,\mathrm{d}r \,\mathrm{d}z \\ &= \pi \int \omega_\theta \psi r \,\mathrm{d}r \,\mathrm{d}z + \pi \int r v^2 \,\mathrm{d}r \,\mathrm{d}z \end{aligned}$$

by using integration by parts. The first integral is also derivable from Lamb's first formula (3.92). On the other hand, by using (6.2) there is

$$2\pi \int v(z\omega_r - r\omega_z) r \,\mathrm{d}r \,\mathrm{d}z = \pi \int r v^2 \,\mathrm{d}r \,\mathrm{d}z$$

plus line integrals that vanish due to $\boldsymbol{u} = \boldsymbol{0}$ at infinity. Thus, this integral is cancelled from $K$, yielding an exact relation

$$\pi \int \omega_\theta \psi r \,\mathrm{d}r \,\mathrm{d}z = 2UI_z + 2\pi \int \omega_\theta (rw - zu) r \,\mathrm{d}r \,\mathrm{d}z, \tag{6.65}$$

$$I_z = \frac{1}{2} \int \omega_\theta r^2 \,\mathrm{d}r \,\mathrm{d}z \,\mathrm{d}\theta. \tag{6.66}$$

Therefore, $U$ will be known if so are the rest parts of (6.65). To simplify the second term on the right-hand side of (6.65), Saffman (1970) appeals to the *Lamb transformation* (Lamb 1932, Sect. 162). Suppose the ring motion is already steady with a well-defined $U$. Then for inviscid axisymmetric flow we use (6.3) to transform (6.5b) to

$$\frac{\partial(u\omega_\theta)}{\partial r} + \frac{\partial(w\omega_\theta)}{\partial z} = \frac{1}{r}\frac{\partial v^2}{\partial z}.$$

Multiplying both sides by $zr^2$, we obtains

$$(r^2 w - rzu)\omega_\theta = rv^2 - 3rzu\omega_\theta + \frac{\partial}{\partial r}(zr^2 u\omega_\theta) + \frac{\partial}{\partial z}(zr^2 w\omega_\theta - zrv^2)$$

of which the integration over the entire flow field gives the desired relation

$$2\pi \int \omega_\theta (rw - zu) r \,\mathrm{d}r\,\mathrm{d}z = 2\pi \int (rv^2 - 3rzu\omega_\theta)\,\mathrm{d}r\,\mathrm{d}z. \tag{6.67}$$

Saffman (1970) further found that the Lamb transformation also holds for unsteady flow, provided $U$ is replaced by the axial velocity $\mathrm{d}Z/\mathrm{d}t$ of the vortex-ring centroid, which is defined by

$$\boldsymbol{X} = (X, Y, Z) = \frac{1}{2}\int \frac{\boldsymbol{I}\cdot(\boldsymbol{x}\times\boldsymbol{\omega})}{|\boldsymbol{I}|^2}\boldsymbol{x}\,\mathrm{d}V. \tag{6.68}$$

In this way, the viscous decay of thin vortex ring can be included even if the core has no sharp boundary or definite radius $a$.

### 6.3.2 Fraenkel–Norbury Family and Hill Spherical Vortex

As remarked in the context of (6.3.6), generalized Beltrami vortex rings with $\omega_\theta = \Omega r$ in the core form the Fraenkel–Norbury family of steady Euler solutions, which also satisfy the Navier–Stokes equation inside the core region $A$ with its shape to be solved. The problem can be stated as (Norbury 1973): given the free-stream axial velocity $(0, 0, U)$, the vorticity constant $\Omega$, and a constant $k > 0$, find the Stokes stream function $\Psi$ and boundary $\partial A$ of the core cross-section $A$ such that

$$\left(\frac{\partial^2}{\partial r^2} - \frac{1}{r}\frac{\partial}{\partial r} + \frac{\partial^2}{\partial z^2}\right)\Psi(r,z) = \begin{cases} -\Omega r^2 & \text{in } A, \\ 0 & \text{outside } A, \end{cases} \tag{6.69a}$$

and

$$\begin{gathered} \Psi \text{ and } \nabla\Psi \text{ are continuous across } \partial A, \\ \Psi = k \quad \text{on} \quad \partial A, \\ \Psi + \frac{1}{2}Ur^2 \to 0 \quad \text{as} \quad r^2 + z^2 \to \infty. \end{gathered} \tag{6.69b}$$

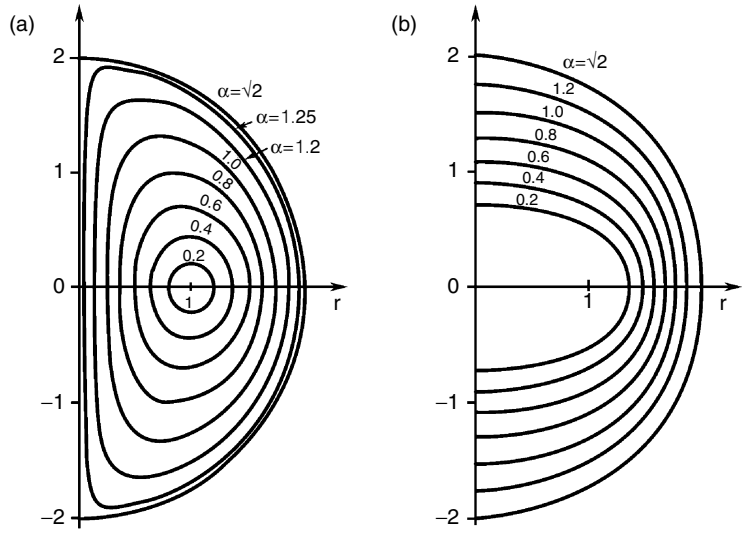


**Fig. 6.6.** Fraenkel–Norbury vortex rings. (**a**) Core shapes. (**b**) Dividing streamlines. After Norbury (1973)

Using the radial distance $L$ of the midpoint of the core at $z = 0$ as length scale, and introducing a single parameter $\alpha > 0$ by defining the area of $A = \pi L^2 \alpha^2$, one can choose a velocity scale $U^* = \Omega L^2 \alpha^2$. Then the dimensionless form of the problem (6.69b), scaled by $L$ and $U^*$, amounts to solving the boundary integral equation along $\partial A$ with a single parameter $\alpha$:

$$k(\alpha) = -\frac{1}{2} U(\alpha) r^2 + \frac{1}{2\pi\alpha^2} \int_{\partial A(\alpha)} G(r, r', z - z') \, \mathrm{d}r' \, \mathrm{d}z' \quad \text{for} \quad (r, z) \in \partial A(\alpha), \tag{6.70}$$

where $G$ is given by (6.60).[1] Fraenkel and Burgers (1974) have proved that for each $\alpha \in (0, \sqrt{2}]$ only one solution set $\{k, U, \partial A\}$ of (6.70) exists, in agreement with Norbury's (1973) numerical calculation. Figure 6.6 shows the computed core boundary $\partial A$ and dividing streamline $\Psi = 0$ of the family for different $\alpha$. The dividing streamline encloses a fluid body carried along by the vortex ring.

Of the Fraenkel–Norbury ring family, the case $\alpha = \sqrt{2}$ is the well-known *Hill spherical vortex* (Hill 1894) and has closed-form solution. In this case one sets $\omega_\theta = \Omega r$ inside a spherical region:

$$\frac{\omega_\theta}{r} = f(\psi) = \begin{cases} -\Omega & \text{if} \quad r^2 + z^2 < a^2, \\ 0 & \text{if} \quad r^2 + z^2 > a^2. \end{cases} \tag{6.71}$$

Thus, as mentioned following (6.55), the vorticity has no diffusion, and its adnvection is balanced by tilting. The problem is reduced to pure kinematics,

[1] This problem is a special case of contour dynamics of Sect. 8.3.2.

and (6.69b) has a solution in the sphere

$$\begin{aligned} \psi &= \frac{1}{10}\Omega r^2(r^2+z^2-a^2), \\ u &= -\frac{1}{5}\Omega r z, \quad w = \frac{1}{5}\Omega(2r^2+z^2-a^2). \end{aligned} \tag{6.72}$$

On the sphere surface $\psi = 0$, the tangent velocity is

$$q = \sqrt{u^2+w^2} = \frac{1}{5}\Omega a r, \quad r^2+z^2 = a^2. \tag{6.73}$$

The Hill spherical vortex is the "fattest" circular vortex ring. Its streamlines and vorticity lines are sketched in Fig. 6.7. On the plane $z = 0$ we have $u = 0$ while $w$ has the same magnitude but opposite signs at $r = 0$ and $r = a$. In the upper and lower hemispheres divided by the plane $z = 0$, the radial velocity $u$ has opposite signs. At the intersectional circle of the plane $z = h$ and the sphere, there is $w = \Omega(2r^2+h^2-a^2)/5$, which has opposite signs inside and outside the circle $r = \sqrt{(a^2-h^2)/2}$. Moreover, from (6.54), (6.71), and (6.73), the pressure is determined up to a constant $p_0 = p(0,0)$:

$$p = \frac{1}{50}\rho\Omega^2[r^2(r^2-a^2)+2z^2a^2-z^4]+2\rho\Omega\nu z+p_0. \tag{6.74}$$

In the above analysis our coordinate system is fixed to the spherical vortex. Outside the sphere the flow is irrotational. By (6.72), at the vortex center

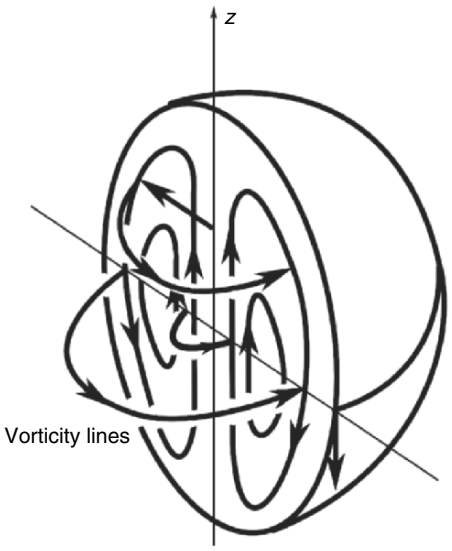


**Fig. 6.7.** The Hill spherical vortex. Based on Panton (1984)

$(r, z) = (0, 0)$ there is a self-induced velocity $\boldsymbol{u}_0 = -\Omega a^2 \boldsymbol{e}_z/5$, which is balanced by a potential flow with free-stream velocity $U\boldsymbol{e}_z$ while keeping its shape unchanged. Then the continuity of velocity and pressure at the sphere can determine the constants $\Omega$ and $p_0$. For potential flow over sphere, the velocity and pressure at the surface $r^2 + z^2 = a^2$ are given by (e.g., Milne-Thomson 1968)

$$q = \frac{3}{2a} U r, \quad p = \frac{1}{8}\rho U^2 \left( \frac{9z^2}{a^2} - 5 \right) + p_\infty. \tag{6.75a,b}$$

Comparing (6.3.26a) and (6.73) gives $\Omega = 15U/(2a^2)$, which also ensures the continuity of normal vorticity $\boldsymbol{\omega} \cdot \boldsymbol{n}$. Then (6.74) yields

$$p = \frac{9}{8a^2}\rho U^2 z^2 + 2\rho\Omega\nu z + p_0 \quad \text{on the sphere,}$$

of which the comparison with (6.3.26b) gives, in the Euler limit $\nu \to 0$,

$$p_0 = p_\infty - \frac{5}{8}\rho U^2. \tag{6.76}$$

Thus, $p_0$ is smaller than $p_\infty$ by an amount proportional to $\rho U^2$.

Since like the Rankine vortex the vorticity inside the sphere jumps from $-\Omega a$ to zero across the boundary, the shear-stress continuity cannot be satisfied at the boundary. Hence, although inside a spherical boundary the Hill vortex is both exact generalized Beltrami Navier–Stokes solution and Euler solution, after combining with the external potential flow the global flow is no longer a smooth viscous solution.

Then, as an *Euler solution*, the Hill spherical vortex can be extended to allow for a swirl with nonzero circumferential velocity $v$ that causes a circulation $C = rv$ around the $z$-axis. In this case the inviscid steady flow is still generalized Beltramian but no longer solely depends on $\psi$. Moffatt (1969; see also Saffman (1992)) has found a closed-form solution of the Bragg–Hawthorne equation (6.1.14) with $C = \pm\alpha r$ as well as $H = -A\psi$, which in spherical coordinates $(R, \Theta, \phi)$ reads

$$\Psi = R^2 \sin^2\Theta \left[ -\frac{A}{\alpha^2} + c \left( \frac{a}{R} \right)^{3/2} J_{\frac{3}{2}}(\alpha R) \right], \tag{6.77}$$

where $c$ is a constant. By setting $C = 0$ outside the sphere, the solution can match the external potential flow

$$\Psi = -\frac{1}{2} U \left( R^2 - \frac{a^3}{R} \right) \sin\Theta \tag{6.78}$$

with $\boldsymbol{U} = (0, 0, -U)$ at infinity. To ensure the velocity continuity across the sphere, the gradients of (6.77) and (6.78) must be equal at $R = a$, which determines

$$U = \frac{2Aa}{3\alpha}\frac{J_{\frac{5}{2}}(\alpha a)}{J_{\frac{3}{2}}(\alpha a)}, \qquad c = \frac{A}{\alpha^2}J_{\frac{3}{2}}(\alpha a). \tag{6.79}$$

Thus, with the swirl a global Euler solution is still possible. If $\alpha a$ is larger than the first zero of $J_{\frac{5}{2}}$ (about 5.6), then $U$ changes direction.

### 6.3.3 Thin-Cored Pure Vortex Ring: Direct Method

Asymptotic approximations to the Fraenkel–Norbury vortex-ring family have been studied for those rings with $\alpha \to \sqrt{2}$ (close to the Hill spherical vortex) by Norbury (1973), and for $\alpha \to 0$ (thing rings) by Fraenkel (1970, 1972) and Fukumoto (2002). We now consider the thin-ring asymptotics with $\alpha = \epsilon \sim a/L \ll 1$ in (6.70). Our main concern is the steady inviscid thin ring in a fluid with uniform velocity $-U\boldsymbol{e}_z$ at infinity.

Fraenkel (1970) has developed a systematic expansion scheme in $\epsilon$. To illustrate how the line vortex solution of Sect. 6.3.1 is modified to have a finite core, we consider the simplest case: the core has circular cross-section and $\omega_\theta = \omega_0$ is constant, so the core circulation is $\Gamma = \pi a^2\omega_0$ with $a$ being the core radius. We use the coordinates $(\sigma, \alpha)$ shown in Fig. 6.4 to find geometric relations. The approach is to integrate the stream function under the thin-core approximation, which is called the *direct method*.

We follow the algebra of Tong et al. (1994). From Fig. 6.4 there is

$$z = \sigma\cos\alpha, \quad r = r_0 + \sigma\sin\alpha,$$

and similarly for $z'$ and $r'$. Then (6.58) is cast to

$$r_1 = \sqrt{\sigma^2 + \sigma'^2 - 2\sigma\sigma'\cos(\alpha - \alpha')},$$
$$r_2 = \sqrt{4r_0^2(1+2\delta) + \sigma^2 + \sigma'^2 - 2\sigma\sigma'\cos(\alpha + \alpha')},$$

where

$$\delta = \frac{1}{2r_0}(\sigma\sin\alpha + \sigma'\sin\alpha') \ll 1.$$

When the field point $P$ is inside the core, $r_1$ and $r_2$ satisfy $k'^2 \equiv r_1^2/r^2 = 1 - k^2 \ll 1$. The asymptotic form of (6.60) is

$$G = \frac{r_0}{2\pi}(1+\delta)\left(\ln\frac{8r_0}{r_1} - 2\right) - \delta + \mathrm{O}\left(\frac{r^2}{r_0^2}\ln\frac{r_0}{r}\right). \tag{6.80}$$

On the other hand, for a circular core with uniform vorticity $\omega_0$, there is

$$\omega'_\theta = \omega_0\frac{r'}{r_0} = \omega_0\left(1 + \frac{\sigma'\sin\alpha'}{r_0}\right), \quad \mathrm{d}r'\,\mathrm{d}z' = \sigma'\,\mathrm{d}\sigma'\,\mathrm{d}\alpha'.$$

These results simplify (6.57a), of which the leading-order approximation can be integrated by using the identity

$$\int_0^{2\pi} \ln r_1 \, \mathrm{d}\alpha' = \begin{cases} 2\pi \ln r' & \text{if} \quad r' > r, \\ 2\pi \ln r & \text{if} \quad r' < r, \end{cases} \tag{6.81}$$

yielding

$$\psi(\sigma,\alpha) = \frac{\Gamma r_0}{2\pi} \left\{ \ln \frac{8r_0}{a} - \frac{3}{2} - \frac{\sigma^2}{2a^2} + \frac{\sigma}{2r_0} \sin\alpha \left( \ln \frac{8r_0}{a} + 1 - \frac{5\sigma^2}{4a^2} \right) \right.$$
$$\left. + \mathrm{O}\left( \frac{a^2}{r_0^2} \ln \frac{r_0}{a} \right) \right\}.$$

Now, the total streamfunction is

$$\Psi(\sigma,\alpha) = -\frac{1}{2} U r_0^2 \left( 1 + \frac{2\sigma}{r_0} \sin\alpha \right) + \psi(\sigma,\alpha),$$

and at the core boundary $\Psi(a,\alpha) =$ constant for any $\alpha$, where

$$\frac{r^2}{r_0^2} = 1 + \frac{2\sigma}{r_0} \sin\alpha + \mathrm{O}\left( \frac{\sigma^2}{r_0^2} \right)$$

but $r_0$ and $a$ are constant. Hence, to determine $U$ we only need the coefficients of $\sin\alpha$ in $\Psi$ to vanish. This gives

$$U = \frac{\Gamma}{4\pi r_0} \left( \ln \frac{8r_0}{a} - \frac{1}{4} \right) + \mathrm{O}\left( \frac{\Gamma a^2}{r_0^3} \ln \frac{R}{a} \right). \tag{6.82}$$

This well-known formula relating the thin-ring translation velocity to its circulation and size was first obtained by Kelvin (1867). It is evident that if two coaxial vortex rings 1 and 2 have the same $\Gamma$ but $r_{01} < r_{02}$, then $U_1 > U_2$. Hence, if initially ring 1 is behind ring 2, then ring 1 will catch up and run through ring 2. Then their mutual induction will increase $r_{01}$ but reduce $r_{02}$, so ring 2 will run through ring 1 and the process may be repeated a few times. This phenomenon known as *leap frog* has been well observed in experiments.

Finally, substituting (6.63) for $\sigma \le a$ into the expression of $\Psi$ and set $\Psi =$ const., we find the streamline shapes

$$\frac{\sigma^2}{a^2} - \frac{5\sigma}{4r_0} \sin\alpha \left( 1 - \frac{\sigma^2}{a^2} \right) = \text{const.} = \frac{\sigma_0^2}{a^2},$$

of which the leading-order approxiamtion is

$$\sigma = \sigma_0 + \frac{5}{8} \frac{a^2 - \sigma_0^2}{r_0} \sin\alpha, \quad 0 \le \sigma \le a. \tag{6.83}$$

This is a family of nonconcentric circles whose centers are a distance $r_0 + 5(a^2 - \sigma_0^2)/(8r_0)$ away from the $z$-axis. When $\sigma_0 = 0$, the streamlines shrink to a stagnation point at $r_0 + 5a^2/(8r_0)$. Note that in obtaining this result we have assumed $r_1^2 \ll r_2^2$ which is true only in the near field.

Higher-order expansions have been carried out by Fraenkel (1972), in which the cross-section of the thin ring is no longer a circle. A further higher-order asymptotic theory of the Fraenkel–Norbury family with $\omega_\theta = \Omega r$ has been obtained by Fukumoto (2002).

### 6.3.4 Thin-Cored Swirling Vortex Rings: Energy Method

In the preceding analysis the translation velocity $U$ of the ring was obtained by integrating the stream function. We now use (6.65)–(6.67) to calculate $U$. Since to the leading order the ring cross-section is a circle of radius $a$, we may set $\omega_\theta = \omega(\sigma)$. In the derivation some relations and notations will be useful:

$$\begin{gathered} \Gamma_\sigma(\sigma) = 2\pi \int_0^\sigma \omega_\theta(\sigma')\sigma' \,\mathrm{d}\sigma', \quad \omega_\theta(\sigma)\sigma \,\mathrm{d}\sigma = \frac{1}{2\pi}\,\mathrm{d}\Gamma_\sigma, \quad \Gamma_\sigma(a) \equiv \Gamma, \\ u = \frac{\Gamma_\sigma}{2\pi\sigma}\cos\alpha, \quad v = v(\sigma) \equiv \frac{C_\sigma(\sigma)}{2\pi\sigma}. \end{gathered} \tag{6.84}$$

First, by (6.66), in the thing-ring approximation we have

$$I_z = \pi \int (r_0 + \sigma\sin\alpha)^2 \omega_\theta(\sigma)\sigma \,\mathrm{d}\sigma \,\mathrm{d}\alpha \simeq \pi\Gamma r_0^2.$$

Second, on the left-hand side of (6.65) $\psi$ is given by (6.57a), in which to the leading order $G$ is given by (6.80) with $\delta = 0$. Hence, there is

$$\psi \simeq \psi(\sigma) = r_0 \int \omega_\theta(\sigma')(\ln 8r_0 - 2 - \ln\sigma^*)\sigma' \,\mathrm{d}\sigma',$$

where $\sigma^* = \sigma$ if $\sigma > \sigma'$ and $\sigma^* = \sigma'$ otherwise. Thus, an integration by parts yields

$$\psi(\sigma) = \frac{r_0\Gamma}{2\pi}\left(\ln\frac{8r_0}{a} - 2\right) + \frac{r_0}{2\pi}\int_\sigma^a \frac{\Gamma_s}{s}\,\mathrm{d}s,$$

and hence

$$\pi \int \omega_\theta\psi\sigma \,\mathrm{d}\sigma \,\mathrm{d}\alpha \simeq \frac{1}{2}r_0\Gamma^2\left(\ln\frac{8r_0}{a} - 2\right) + \frac{r_0}{2}\int_0^a \frac{\Gamma_\sigma^2}{\sigma}\,\mathrm{d}\sigma.$$

Thirdly, to the leading order, on the right-hand side of (6.67) there is

$$2\pi \int rv^2 \,\mathrm{d}r \,\mathrm{d}z = r_0 \int_0^a \frac{C_\sigma^2}{\sigma}\,\mathrm{d}\sigma, \quad 6\pi \int rzu\omega_\theta \,\mathrm{d}r \,\mathrm{d}z = \frac{3}{4}r_0\Gamma^2.$$

Therefore, substituting these results into (6.65), we finally obtain

$$U = \frac{\Gamma}{4\pi r_0}\left(\ln\frac{8r_0}{a} - \frac{1}{2} + \frac{1}{\Gamma^2}\int_0^a \frac{\Gamma_\sigma^2 - 2C_\sigma^2}{\sigma}\,\mathrm{d}\sigma\right), \tag{6.85}$$

and, for the kinetic energy associated with the vortex ring,

$$K = \frac{1}{2}r_0\Gamma^2\left(\ln\frac{8r_0}{a} - 2 + \frac{1}{\Gamma^2}\int_0^a \frac{\Gamma_\sigma^2 + C_\sigma^2}{\sigma}\,\mathrm{d}\sigma\right). \tag{6.86}$$

It is seen that $U$ and $K$ depend on the core structure. *The swirl enhances the kinetic energy but slows down the translation velocity* $U$. For swirl-free thin vortex ring with $\Gamma_\sigma/\Gamma = \sigma^2/a^2$, the above result is reduced to

$$U = \frac{\Gamma}{4\pi r_0}\left(\ln\frac{8r_0}{a} - \frac{1}{4}\right), \quad K = \frac{1}{2}r_0\Gamma^2\left(\ln\frac{8r_0}{a} - \frac{1}{4}\right), \tag{6.87}$$

with $I_z = \pi\Gamma r_0^2$, which returns to Kelvin's result (6.82).

Finally, for a viscous and unsteady vortex ring, Saffman (1970) found that if the $\omega_\theta$-distribution is assumed as the Oseen–Lamb vortex (6.25b) then the speed of the ring is

$$U = \frac{\Gamma}{r_0}\left[\ln\frac{8r_0}{\sqrt{4\nu t}} - 0.558 + \mathrm{O}\left(\frac{\nu t}{a^2}\right)^{1/2}\right], \tag{6.88}$$

which corrects a numerical error of an earlier result by Tung and Ting (1966; see also Ting and Klein 1991) by matched asymptotic expansion method to be introduced in Sect. 6.5.

In reality a viscous vortex ring has quite complicated structure, see, e.g., Maxworthy (1972). When two viscous rings of about the same radius move toward the same direction, in most cases one will entrain another to become a single vortex ring rather than making leap frog.

## 6.4 Exact Strained Vortex Solutions

Since no single straight vortex can be isolated in an unbounded space and each vortex is in the strain field induced by others, the cross-section of a generic vortex is not circular. For example, a row of vortices can be formed in a mixing layer or boundary layer due to the instability, where each vortex is in a background flow field which may contain both symmetric strain and antisymmetric shear. Figure 6.8 is a flow visualization photo that shows a row, where the vortices are approximately elliptic. Having discussed vortex rings, therefore, we now return to solutions of columnar vortices with *noncircular cross-section*. This section is confined to closed-form exact solutions, including elliptic vortex patches, vortex dipole, Stuart "cat-eyes" and viscous Taylor–Green vortex lattice. Except the last example they are Euler solutions. More realistic solutions with small viscosity can only be obtained asymptotically, which is the subject of Sect. 6.5.

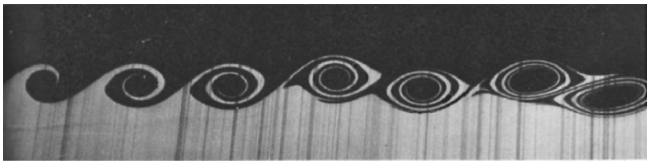

**Fig. 6.8.** A row of strained elliptic vortices. From Van Dyke (1982)

### 6.4.1 Strained Elliptic Vortex Patches

As the simplest extension of axisymmetric vortices, we first consider an inviscid vortex in an irrotational strain field, with elliptic cross-section and uniform vorticity $\omega$ in the ellipse. This kind of models are called *vortex patches*, of which a general treatment with arbitrary and variable boundary shape of the patch will be presented in Sect. 8.3.2. We start from the classic *Kirchhoff elliptic vortex* (e.g., Lamb 1932, Art. 159) without background strain, see Fig. 6.9.

Once an isolated circular vortex patch (a Rankine vortex) is deformed to an elliptic one with semi-major and minor axes $a$ and $b$, it will rotate under self-induction. Let $(x, y)$ be the coordinates along the major and minor axes which rotate with the ellipse, such that the patch contour is defined by

$$\frac{x^2}{a^2} + \frac{y^2}{b^2} = 1. \tag{6.89}$$

Then by $\nabla^2\psi = -\omega$ there is

$$\psi = -\frac{1}{2}\omega(Ax^2 + By^2), \quad A + B = 1. \tag{6.90}$$

This solution should be matched with an external potential flow, which can be conveniently done in terms of elliptic coordinates $(\xi, \eta)$ with

$$x = c\cosh\xi\cos\eta, \quad y = c\sinh\xi\sin\eta, \tag{6.91}$$

where $c = \sqrt{a^2 - b^2}$ is the focal distance from the origin, and $\xi = \text{const.}$ defines elliptic lines. The patch contour (6.89) is then given by $\xi = \xi_0 = a/c$ with $\sinh\xi_0 = b/c$. The solution of $\nabla^2\psi = 0$ for the irrotational motion of the fluid, otherwise at rest, produced by an elliptic cylinder rotating with angular velocity $\Omega$ is (Lamb 1932, Art. 72)

$$\psi = -\frac{1}{4}\Omega(a+b)^2\,\mathrm{e}^{-2\xi}\cos 2\eta - \frac{\kappa}{2\pi}\xi, \quad \xi > \xi_0, \tag{6.92}$$

where $\kappa$ is an arbitrary circulation since the domain is doubly-connected, which is now fixed by the circulation $\pi ab\omega$ of the Kirchhoff vortex. Thus the

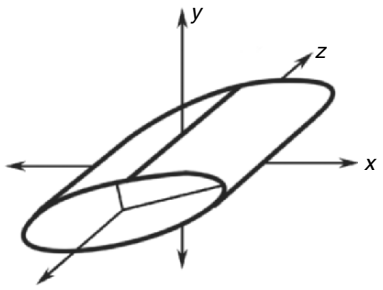


**Fig. 6.9.** An elliptic vortex

second term of (6.92) is $-\omega ab\xi/2$. Comparing (6.90) and (6.92), then, the continuity of $\psi$ and tangent velocity $\partial\psi/\partial\xi$ leads to $Aa = Bb = ab/(a+b)$ and (a dot denotes derivative with respect to time)

$$\dot{\theta} = \Omega = \frac{ab\omega}{(a+b)^2}. \tag{6.93}$$

For a different method to obtain the solution see Saffman (1992).

To the motion of this isolated Kirchhoff vortex we now add a three-dimensional uniform strain, which causes a velocity field

$$\boldsymbol{u}_s = \gamma_1 x\boldsymbol{e}_x - \gamma_2 y\boldsymbol{e}_y + \gamma_3 z\boldsymbol{e}_z, \tag{6.94}$$

$$\gamma_1 - \gamma_2 + \gamma_3 = 0. \tag{6.95}$$

Then the vortex will be deformed by $(\gamma_1, \gamma_2)$ and stretched by $\gamma_3$ as it rotates, so that $a$, $b$, as well as its area $\pi ab$ and vorticity $\omega$ are all time-dependent. The exact solution of this three-dimensionally strained elliptic vortex-patch problem has been studied by Neu (1984a), which includes earlier solutions as special cases. Thus, here we follow Neu's analysis.

A material point on the contour (6.89) has a path $\boldsymbol{x}(t) = x(t)\boldsymbol{e}_x + y(t)\boldsymbol{e}_y$. Like the three-dimensional quadratic form that defines the deformation ellipsoids (Sect. 2.1.2), we define the ellipse by the matrix equation (where $\boldsymbol{x}$ is a column matrix and the superscript T denotes transpose)

$$\boldsymbol{x}^{\mathrm{T}} E(a,b,\theta)\boldsymbol{x} = 1, \tag{6.96}$$

where $\theta(t)$ is the angle of the major axis with respect to a fixed $x'$-axis and

$$E = R(\theta)\begin{bmatrix} 1/a^2 & 0 \\ 0 & 1/b^2 \end{bmatrix} R(-\theta) \tag{6.97}$$

with

$$R(\theta) = \begin{bmatrix} \cos\theta & -\sin\theta \\ \sin\theta & \cos\theta \end{bmatrix} \tag{6.98}$$

being the rotation matrix. Since $\boldsymbol{x}(t)$ satisfies (6.89) at any $t$, we may differentiate it to obtain

$$\dot{\boldsymbol{x}}^{\mathrm{T}} E\boldsymbol{x} + \boldsymbol{x}^{\mathrm{T}}\dot{E}\boldsymbol{x} + \boldsymbol{x}^{\mathrm{T}} E\dot{\boldsymbol{x}} = 0, \tag{6.99}$$

where the particle velocity $\boldsymbol{u} = \dot{\boldsymbol{x}}$ is a linear function of $\boldsymbol{x}$ (cf. (2.24))

$$\dot{\boldsymbol{x}} = U(a,b,\theta)\boldsymbol{x}, \tag{6.100}$$

with matrix $U(a,b,\theta)$ determined by the self-induced velocity plus (6.95)

$$U(a,b,\theta) = -\frac{\omega}{a+b}R(\theta)\begin{bmatrix} 0 & a \\ -b & 0 \end{bmatrix} R(-\theta) + \begin{bmatrix} \gamma_1 & 0 \\ 0 & -\gamma_2 \end{bmatrix}. \tag{6.101}$$

Substituting (6.100) into (6.99) yields the equation

$$\boldsymbol{x}^{\mathrm{T}}(U^{\mathrm{T}}E + \dot{E} + EU)\boldsymbol{x} = 0,$$

which we satisfy by requiring

$$\dot{E} + U^{\mathrm{T}}E + EU = 0. \tag{6.102}$$

Then, substituting (6.97) and (6.101) into (6.102), we obtain a dynamic system

$$\begin{aligned}
&\dot{a} + (\gamma_2 \sin^2\theta - \gamma_1 \cos^2\theta)a = 0,\\
&\dot{b} + (\gamma_2 \cos^2\theta - \gamma_1 \sin^2\theta)b = 0,\\
&\dot{\theta} - \frac{\omega ab}{(a+b)^2} + \frac{1}{2}(\gamma_1 + \gamma_2)\frac{a^2+b^2}{a^2-b^2}\sin 2\theta = 0.
\end{aligned} \tag{6.103}$$

The system is *autonomous* if $\omega$ is constant. This happens when the vortex has no axial stretching, i.e., $\gamma_1 = \gamma_2 \equiv \gamma$ and $\gamma_3 = 0$, so that the total vorticity $\pi ab\omega$ is preserved. Elliptic vortex patches in such a general two-dimensional strain field were studied first by Kida (1981a), and then by Neu (1984a) and Bertozzi (1988) using neater approaches. Let us now consider in detail the evolution modes of this *Kida elliptic vortex* based on Bertozzi's approach.

Using $r \equiv \log\eta = \log(a/b)$ and $\phi \equiv 2\theta$ as new variables, and $\tau = \omega t$ as the dimensionless time, (6.103) can be cast to

$$\frac{\mathrm{d}r}{\mathrm{d}\tau} = 2\frac{\gamma}{\omega}\cos\phi, \tag{6.104a}$$

$$\frac{\mathrm{d}\phi}{\mathrm{d}\tau} = \frac{2\mathrm{e}^r}{(\mathrm{e}^r+1)^2} - 2\frac{\gamma}{\omega}\frac{\mathrm{e}^{2r}+1}{\mathrm{e}^{2r}-1}\sin\phi. \tag{6.104b}$$

The evolution modes of the vortex can be clearly visualized from the phase portraits on the plane with $(r, \phi)$ as polar coordinates, of which the results for a few typical values of parameter $\gamma/\omega$ are shown in Fig. 6.10. Note that $\phi$ varies from 0 to $\pi$ implies that the trajectory goes a cycle, which is possible only in the shaded region.

To read these plots, we first notice that if $\gamma/\omega = 0$ (no strain), then there is $r = \text{const.}$, i.e., all trajectories form concentric circles and the vortex just rotates with constant angular velocity given by the first term of (6.104b) or (6.93). Namely, we return to the Kirchhoff elliptic vortex, of which a special case is $r \equiv 0$, i.e., all trajectories shrink to the origin, corresponding to a stationary Rankine vortex.

Then, for $\gamma/\omega \neq 0$, we see two fixed points, a saddle and a center, where the solution is unstable and neutually stable, respectively.[2] Right at these fixed

[2] For the general definition, classification, and stability of fixed points see Sect. 7.1.1.

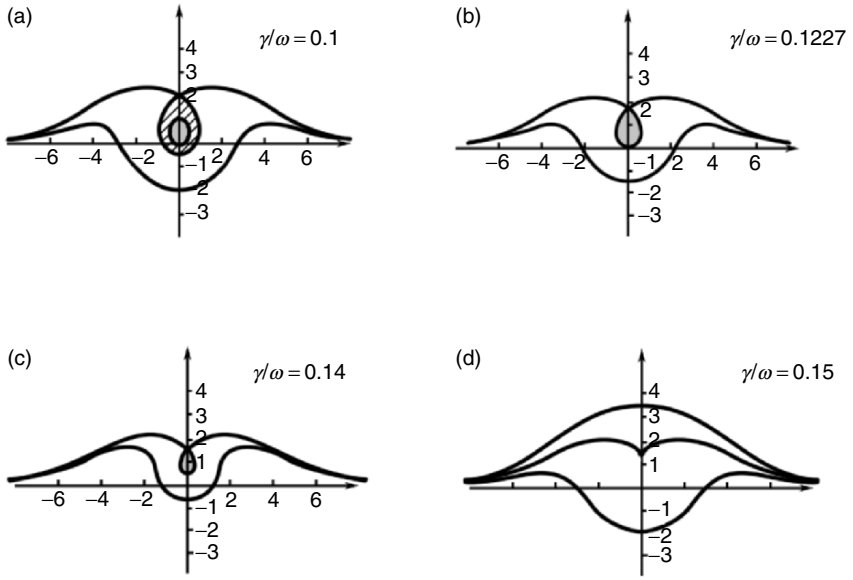


**Fig. 6.10.** Phase portraits for the evolution of the Kida vortices on the $(r, \phi)$-plane

points the vortex does not move and the solution is steady, as was first discovered by Chaplykin in 1899 (see Meleshko and van Heijst (1994), which also describes Chaplykin's contributions to other two-dimensional vortex solutions). This special case is of great interest in modern vortex dynamics as mentioned in the context of Fig. 6.8. Motivated by the need for understanding the stability of these vortices, the steady solution of the Chaplykin vortex was re-investigated independently by Moore and Saffman (1971).

Away from the saddle and center, for $0 < \gamma/\omega < 0.1227$ there are three evolution modes (Fig. 6.10a): rotation (in the hatched region), oscillation (inside the shaded region, where $\theta = \phi/2$ varies periodically but in an interval less than $2\pi$), and elongation (the remaining regions). As $t \to \infty$, the elongation mode reaches an asymptotic state with $a/b \to \infty$, $\theta \to 0$ or $\pi$, and $\omega \to \infty$; but $2\omega b$ remains finite, corresponding to a vortex sheet of length $2a$ along the $x$-axis. The sheet strength has an elliptic distribution and vanishes at $\pm a$.[3]

As $\gamma/\omega$ inceases from zero, the phase portrait bifurcates first at $\gamma/\omega = 0.1227$ (Fig. 6.10b) where the rotating mode ceases to exist. Away from the fixed points only oscillating and elongating modes are possible until the second bifurcation at $\gamma/\omega = 0.15$ (Fig. 6.10d), where the two fixed points merge to a

[3] The roll-up of a vortex sheet as in the Kaden problem of Sect. 4.4.2 is because the sheet strength at the wing tip is nonzero, implying a force normal to the sheet. The present vortex sheet does not roll up since no such force exists at its end points (cf. Saffman 1992).

higher-order one, beyond which no steady solution exists and any vortex will be continuously elongated.

Finally, in a three-dimensional strain field with $\gamma_3 \neq 0$ and $\gamma_1 \neq \gamma_2$, (6.103) gives

$$\frac{\mathrm{d}}{\mathrm{d}t}(ab) = (\gamma_1 - \gamma_2)ab,$$

so there is

$$\pi ab = \pi a_0 b_0 \mathrm{e}^{(\gamma_1-\gamma_2)t}, \quad \omega = \omega_0 \mathrm{e}^{(\gamma_2-\gamma_1)t}, \tag{6.105}$$

which shows explicitly the axial-stretching effect. The time-dependent $\omega(t)$ makes the system (6.103) nonautonomous. Further complexity of the evolution modes have been discussed by Neu (1984a).

### 6.4.2 Vortex Dipoles

Straight vortex pairs with the strength of the same magnitude but opposite sign are also called *vortex dipoles*. Lamb in 1895 and 1906 (the second and third editions of Lamb 1932) and Chaplykin in 1903 (see Meleshko and van Heijst 1994) independently found an effectively inviscid *circular* vortex dipole with distributed vorticity. Following both authors, we assume that outside the dipole the flow is irrotational and the dipole moves with a constant velocity $-U\boldsymbol{e}_x$. Then imposing a uniform flow $U\boldsymbol{e}_x$ to make the dipole stationary, the potential solution over a circular cylinder reads, in the polar coordinate system $(r, \theta)$ with

$$u = \frac{1}{r}\frac{\partial \psi}{\partial \theta}, \quad v = -\frac{\partial \psi}{\partial r}, \tag{6.106}$$

$$\psi_{\mathrm{ir}} = U\left(r - \frac{a^2}{r}\right)\sin\theta, \quad r > a. \tag{6.107}$$

Inside the circle $\psi$ must satisfy (6.11) since the flow is inviscid and steady, again a generalized Beltrami flow. Thus we may linearize (3.65) by setting $\omega = k^2\psi$ and obtain

$$\frac{\partial^2 \psi}{\partial r^2} + \frac{1}{r}\frac{\partial \psi}{\partial r} + \frac{1}{r^2}\frac{\partial^2 \psi}{\partial \theta^2} = -k^2\psi. \tag{6.108}$$

To match (6.107), there should be $\psi \propto \sin\theta$; so the solution of (6.108) is $\psi = CJ_1(kr)\sin\theta$. The first zero of $J_1(ka)$, $ka = 3.8317$, gives a closed circular streamline $\psi = 0$ at $r = a$ that matches $\psi_{\mathrm{ir}}$ in the circle. Then the velocity continuity requires $v = v_{\mathrm{ir}} = -2U\sin\theta$ at $r = a$, implying that

$$C = \frac{2U}{kJ_1'(ka)} = \frac{2U}{kJ_0(ka)}.$$

Hence, it follows that:

$$\psi = \frac{2UJ_1(kr)}{kJ_0(ka)}\sin\theta, \quad r \leq a. \tag{6.109}$$

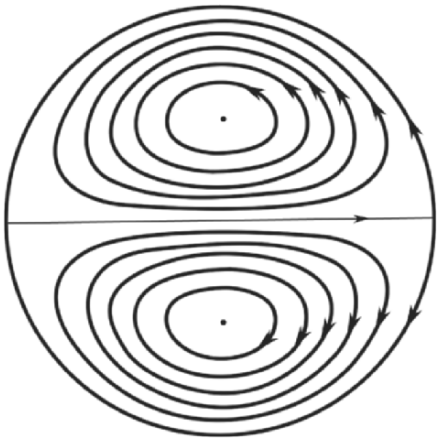

**Fig. 6.11.** The streamlines of the Chaplykin–Lamb dipole

Figure 6.11 shows the streamline pattern of this *Chaplykin–Lamb dipole* as a two-dimensional counterpart of the Hill spherical vortex ring. Moreover, the vorticity is

$$\omega = \begin{cases} 2Uk\dfrac{J_1(kr)}{J_0(ka)}\sin\theta & \text{for} \quad r < a, \\ 0 & \text{for} \quad r \geq a. \end{cases} \tag{6.110}$$

The circular-dipole streamlines (6.109) and its vorticity distribution (6.110) have been found in good agreement with two-dimensional experiment using soap film and numerical solution of the Navier–Stokes equation made by Couder and Basdevant (1986).

Chaplykin has further determined that inside the dipole the vorticity reaches maximum and minimum at

$$r_0 = \frac{c}{b}a = 0.48a, \quad \theta = \pm\frac{\pi}{2},$$

where $c = 1.8412$ is the smallest positive zero of $J_1'(c)$. At these points $\psi$ also takes maximum value. Then, since by (3.67) we now have

$$\boldsymbol{\omega} \times \boldsymbol{u} = \omega\nabla\psi = \frac{1}{2}\nabla(k^2\psi^2)$$

from (3.145) we find a Bernoulli integral for this generalized Beltrami flow

$$p = p_\infty + \frac{1}{2}[U^2 - (u^2 + v^2)] - \begin{cases} \dfrac{1}{2}k^2\psi^2 & \text{for} \quad r \leq a, \\ 0 & \text{for} \quad r > a. \end{cases} \tag{6.111}$$

Hence, at the extrema of vorticity, Chaplykin found that

$$p_{\min} = p_\infty + \frac{1}{2}U^2\left[1 - 4\frac{J_1^2(c)}{J_0^2(ka)}\right] = p_\infty - 3.69U^2, \tag{6.112}$$

so the condition $p_{\min} > 0$ imposes an upper bound for the dipole speed $U$.

Because the Chaplykin–Lamb dipole moves with a constant velocity in a fluid otherwise at rest, they must be *force-free*. This means that the rate of change of the total fluid momentum is zero, which by (3.80) implies a constant vortical impulse $\boldsymbol{I}$ (for systematic analysis see Sect. 11.3.1). Indeed, one finds

$$\boldsymbol{I} = \boldsymbol{e}_x \int\int y\omega r \,\mathrm{d}r \,\mathrm{d}\theta = Ck^2\pi \boldsymbol{e}_x \int_0^\infty r^2 J_1(kr)\,\mathrm{d}r = -2\pi a^2 U \boldsymbol{e}_x. \qquad (6.113)$$

More complicated dipoles, either circular or noncircular, which do not move with constant velocity, can be found in, e.g., Saffman (1992) and Meleshko and van Heijst (1994). Dipoles are of particular importance in large-scale geophysical vortical structures influenced by the variation of Coriolis force as latitude (Sect. 12.3).

### 6.4.3 Vortex Arrays

We now consider an array of infinitely many vortices of equal strength and distance, periodic in at least one direction. The simplest models are the single and double rows of point vortices well documented in relevant textbooks which, although not our main concern here, are briefly reviewed for later reference.

On a plane $z = x + \mathrm{i}y$, for a single row of vortices at $z = nl$ $(n = 0, 1, ...)$, each having strength $\Gamma$, the complex velocity potential reads:

$$W(z) = \frac{\Gamma}{2\pi\mathrm{i}} \sum_{n=-\infty}^{\infty} \ln(z - nl) = \frac{\Gamma}{2\pi\mathrm{i}} \sum_{n=0}^{\infty} \ln(z^2 - n^2 l^2)$$

$$= \frac{\Gamma}{2\pi\mathrm{i}} \ln \sin \frac{\pi z}{l} \qquad (6.114)$$

from which one easily confirms that the whole row is stationary. As $y \to \pm\infty$, there is uniform velocities $u = \mp\Gamma/2a$, representing parallel flows of opposite directions, see Fig. 6.12. Near each vortex the streamlines are closed, known as "*cat-eyes*". Therefore, for remote fluid the vortex row behaves as a straight vortex sheet, while at moderate distance one sees a set of discrete "*fluid roller bearing*".

If we add the second row with vortices of strength $-\Gamma$ located at $z = nl + h$, $h = a + \mathrm{i}b$, then

$$W(z) = \frac{\Gamma}{2\pi\mathrm{i}} \ln \frac{\sin(\pi z/l)}{\sin[\pi(z-h)/l]},$$

and the velocity of one row induced by the other (it suffices to compute the velocity of the vortex at $z = 0$) is

$$(u - \mathrm{i}v)_{z=0} = \left(\frac{\mathrm{d}W}{\mathrm{d}z}\right)_{z=0} = -\frac{\Gamma}{2l} \frac{\sinh(2\pi b/l) + \mathrm{i}\sin(2\pi a/l)}{\cosh(2\pi b/l) - \cos(2\pi a/l)}. \qquad (6.115)$$

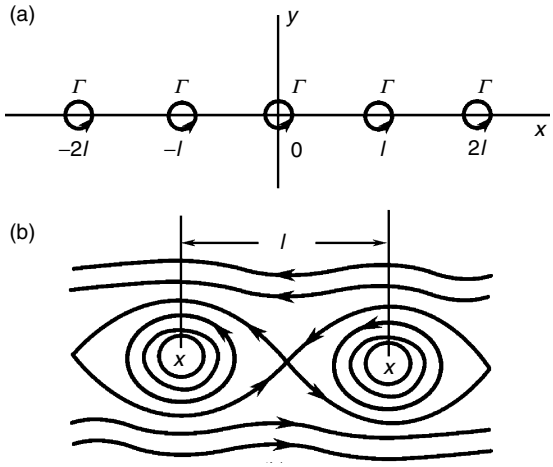


**Fig. 6.12.** Single vortex row (**a**) and associated streamlines (**b**)

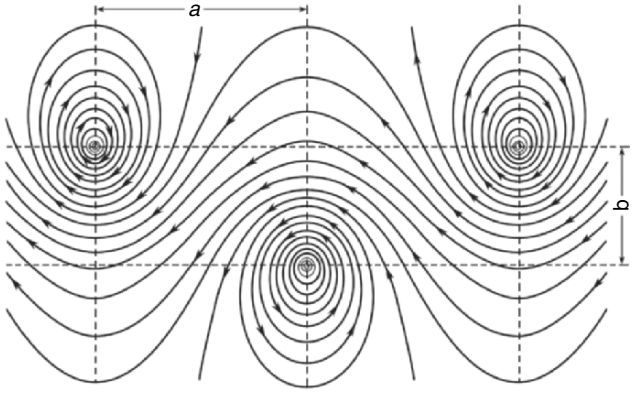


**Fig. 6.13.** Streamlines of Kármán vortex street, viewed in the frame of reference moving with vortices. From Oswatitsch (1959)

Each row will move parallel to itself only if $\sin(2\pi a/l) = 0$. In this case the rows will be symmetric or staggered if $a = 0$ or $l/2$, respectively. Kármán (1911,1912) found that only for the staggered configuration with

$$\cosh\left(\frac{\pi b}{l}\right) = \sqrt{2}, \quad \text{i.e.,} \quad \frac{b}{l} = 0.28055, \tag{6.116}$$

the rows are linearly stable (the stability boundary is shown in Fig. 8.20a), of which the streamline pattern viewed in the frame of reference moving with the vortices is shown in Fig. 6.13.

The staggered double-row point vortices are the simplest model of the observed *vortex street* shed from a buff body (Sect. 7.4). But Kochin et al.

(1964) have proved that the staggered rows of point vortices satisfying (6.116) are still unstable to nonlinear disturbance. The point-vortex arrays of either single or double row can be better modeled by vortex-patch arrays, which will be discussed in Sect. 8.3.2.

Our main concern is the exact solutions of vortex arrays with finite core. The only known exact inviscid and globally smooth solution of this kind is the steady single vortex row found by Stuart (1967). In this case (6.11) holds and the flow is generalized Beltramian with

$$\nabla^2\psi = -\omega = f(\psi), \tag{6.117}$$

where Stuart takes $f(\psi) = \mathrm{e}^{-2\psi}$. To seek the solution of this nonlinear equation for $\psi$, let $\psi = \ln[f(x) + g(y)]$ so that (6.117) is cast to (prime denotes the derivative with respect to the argument)

$$ff'' + gg'' + fg'' + gf'' - f'^2 - g'^2 = 1,$$

which holds if $f(x) = C\cosh x$ and $g(y) = A\cos y$ with $C^2 - A^2 = 1$. Therefore, we obtain an $x$-periodic solution, of which the stream function, velocity, and vorticity are given by

$$\psi = \log(C\cosh y + A\cos x), \quad C > 0, \quad A = \sqrt{C^2 - 1} > 0, \tag{6.118a}$$

$$u = \frac{C\sinh y}{C\cosh y + A\cos x}, \quad v = \frac{A\sin x}{C\cosh y + A\cos x}, \tag{6.118b}$$

$$\omega = -\mathrm{e}^{-2\psi} = -(C\cosh y + A\cos x)^{-2}. \tag{6.118c}$$

For any value of $C$ between 1 and $\infty$, the streamlines have the cat's eye pattern qualitatively similar to Fig. 6.12, typical for periodic disturbances of a shear layer. Stuart (1967) has shown that the total vorticity of each vortex is $\Gamma = -4\pi$, independent of $C$; so a change of $C$ only results in a re-distribution of vorticity.

In the extremal case of $C = 1, A = 0$, the cat's eye pattern degenerates to a *shear layer* $u = \tanh y$, a profile often used in shear-layer instability analysis. Then, if $A/C = \epsilon \ll 1$, we have a small perturbation to the shear layer. The linear approximation of (6.118a) is

$$\psi = \log\cosh y + \epsilon\sinh y\cos x + \mathrm{O}(\epsilon^2), \tag{6.119}$$

which satisfies the *Rayleigh equation* that is the basis of the inviscid linear stability theory for parallel shear flow (Sect. 9.2.1):

$$(U - c)(\phi'' - \alpha^2\phi) - U''\phi = 0. \tag{6.120}$$

In fact, with $U = \tanh y$, $c = 0$, $\alpha = 1$, and under the boundary condition $\phi \to 0$ at $y = \pm\infty$, the solution of this equation is exactly $\phi = \sinh y$. The

relation between (6.118) and linear-instability theory is therefore established. On the other hand, if $C \to \infty$, (6.118a) takes on the form

$$\psi - \log C = \log(\cosh y + \cos x). \tag{6.121}$$

Meanwhile, from (6.118c) we see that $\omega \to 0$ unless $x$ and $y$ are so chosen that

$$C \cosh y + A \cos x \to 0.$$

This happens if and only if

$$y = 0, \quad x = (2n+1)\pi, \quad n = 0, \pm 1, \ldots,$$

because $C \cosh y$ and $A \cos x$ cannot cancel each other due to the fact that

$$C > A > 0, \quad \cosh y \geq 1, \quad |\cos x| \leq 1.$$

Therefore, (6.121) returns to the single row of point vortices.

Finally, let us make a more general examination of the possibility of finding exact Navier–Stokes solution of strained vortices in two dimensions, within the range of generalized Beltrami flow. In addition to the kinematic condition (6.117), now $f(\psi, t)$ has to satisfy simultaneously the dynamic equation

$$\frac{\partial f}{\partial t} = \nu \nabla^2 f, \tag{6.122}$$

which can be cast to

$$q^2 \frac{\partial^2 f}{\partial \psi^2} + (\nabla^2 \psi - \nu^{-1} \psi_t) \frac{\partial f}{\partial \psi} = 0,$$

where $q^2 = u^2 + v^2 = \psi_x^2 + \psi_y^2$. Hence, denote

$$\beta(\psi, t) \equiv \frac{1}{q^2} (\nabla^2 \psi - \nu^{-1} \psi_t), \tag{6.123a}$$

we have

$$f(\psi, t) = C \int^{\psi} \mathrm{e}^{-\int^{\xi} \beta(\eta, t)\, \mathrm{d}\eta}\, \mathrm{d}\xi + D(t), \tag{6.123b}$$

which represents the general dynamic functional constraint on possible $f(\psi, t)$ for viscous flow and should be compatible with (6.117). The simplest solution of (6.123) is $C = 0$, which is the case of the Rankine vortex or other possible steady vortex patches that however oversimplifies the viscous effect. Next to $C = 0$, since (6.122) implies $\nabla^2(\psi_t - \nu \nabla^2 \psi) = 0$ which is consistent with $\beta = 0$, we get

$$f(\psi, t) = C\psi + D(t). \tag{6.124}$$

Substituting this into (6.117), a separation of variables yields a general solution (Wang 1989, 1990)

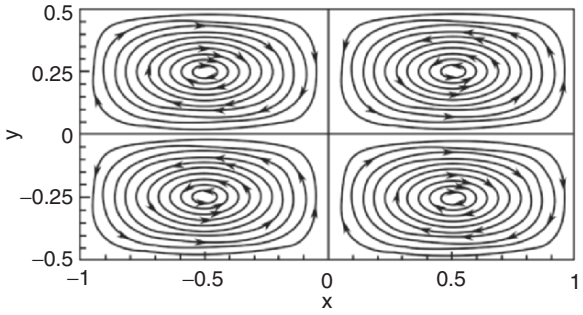


**Fig. 6.14.** Streamlines of a Taylor–Green vortex. Adapted from Sipp and Jacquin (1998)

$$\omega(x,y,t) = \mathrm{e}^{a\nu t} \sum_{\alpha} C_\alpha \mathrm{e}^{\pm\alpha x} \mathrm{e}^{\pm\sqrt{a^2-\alpha^2}\,y}, \tag{6.125}$$

where $\alpha$ and $C_\alpha$ can be complex. So far no viscous solution has been known for $\beta \neq 0$.

A special case of (6.125) is the *Taylor–Green vortex lattice*

$$\psi = \omega_0(t) \frac{\sin ax \sin by}{a^2+b^2}, \quad \omega_0(t) = \mathrm{e}^{-(a^2+b^2)\nu t}. \tag{6.126}$$

This vortex array is freely decaying, with the vorticity

$$\omega = \omega_0(t) \sin ax \sin by \tag{6.127}$$

satisfying (6.122). In each cell, the vorticity reaches the maximum value $\omega_0(t)$ at the center and reduces to zero at the boundary; the flow in such a cell may be viewed as a vortex confined by a rectangular free-slip boundary. The flow pattern is periodic with respect to both $x$ and $y$, with periods $A = 2\pi/a$ and $B = 2\pi/b$. The streamlines in four cells of total length $A$ and height $B$ are shown in Fig. 6.14. Note that a Taylor–Green vortex is also in a background strain field, and its stability character is of interest (e.g., Sipp and Jacquin 1998).

## 6.5 Asymptotic Strained Vortex Solutions

A common approach to approximate vortex solutions is the matched asymptotic method (and other singular perturbation methods if necessary). In this section we first outline its general formulation applied to a viscous vortex in a nonuniform flow, pioneered by Ting and Tung (1965). We then discuss a few typical asymptotic solutions for single columnar vortex in a two- or three-dimensional irrotational strain field. Some material on the solutions of strained vortices and vortex layers, complementary to this section, can be found in Rossi (2000).

### 6.5.1 Matched Asymptotic Expansion and Canonical Equations

Consider a vortex of finite circulation $\Gamma > 0$ in a nonuniform irrotational background flow $\boldsymbol{U}(\boldsymbol{x}, t)$ with a Reynolds number defined as $R_\Gamma = \Gamma/2\pi\nu$. Once $R_\Gamma^{-1} \ll 1$, the matched asymptotic expansion can be used as in the boundary layer theory (Sect. 4.3.1). Recall that the outer solution there is inviscid with a singular vortex sheet on the wall, which in the matched asymptotic expansion is replaced by a thin viscous vortex layer of thickness $\delta = \mathrm{O}(Re^{-1/2})$ as the inner solution. In contrast, the outer solution here is an inviscid global strain field $\boldsymbol{U}$ plus a singular *line vortex* (point vortex in two dimensions), and the matched asymptotic expansion will replace it by a thin viscous vortex with core radius $\delta = \mathrm{O}(R_\Gamma^{-1/2})$ as the inner solution. Just like in determining the boundary-layer solution at an $x$-station, we match it to the outer solution at the same $x$ and $y = 0$, now in determining the inner solution we match the viscous vortex to the strain field of outer flow at the point where the line vortex goes through. Consequently, for the inner solution the outer flow simply appears as a *constant strain field*.

Note, however, that, unlike a vortex sheet associated with only a finite jump of finite tangent velocities, a line vortex is more singular with infinite velocity at its axis. This makes the perturbation theory more complicated. One has to expand the series to higher orders to obtain the strained viscous vortex solution.

**Two-Dimensional Flow**

A two-dimensional strained vortex can be described by vorticity $\omega$ and stream function $\psi$. By (3.55), (3.56), and the two-dimensional version of (6.5c), the governing equations are

$$\frac{\partial \omega}{\partial t} + [\omega, \psi] = \nu \nabla^2 \omega, \tag{6.128a}$$

$$\nabla^2 \psi = -\omega, \tag{6.128b}$$

where

$$[\omega, \psi] \equiv \frac{\partial(\omega, \psi)}{\partial(x, y)} = \frac{\partial \omega}{\partial x}\frac{\partial \psi}{\partial y} - \frac{\partial \omega}{\partial y}\frac{\partial \psi}{\partial x} \tag{6.129a}$$

$$= \frac{1}{r}\frac{\partial(\omega, \psi)}{\partial(r, \theta)} = \frac{1}{r}\left(\frac{\partial \omega}{\partial r}\frac{\partial \psi}{\partial \theta} - \frac{\partial \omega}{\partial \theta}\frac{\partial \psi}{\partial r}\right) \tag{6.129b}$$

denotes the Jacobian of $\omega$ and $\psi$ in Cartesian and polar coordinates. We follow the approach of Ting and Tung (1965) to lay down a common basis of later analysis.[4]

[4] Ting and Tung (1965) include the fast unsteady motion of the line vortex around the origin, which involves multiple time scales and is beyond our concern.

Let the line vortex of circulation $\Gamma$ be at a saddle point of the external strained field $\boldsymbol{U} = \nabla\Psi \times \boldsymbol{e}_z$. For the global outer solution (the external strained field $\boldsymbol{U}$ plus a line vortex) we use $\Gamma$ and a global length scale $L$ to nondimensionalize the stream function. Then

$$\psi = \Psi(x, y) - \frac{1}{2\pi} \ln r, \quad \boldsymbol{u} = \nabla\Psi \times \boldsymbol{e}_z + \frac{1}{2\pi r}\boldsymbol{e}_\theta, \tag{6.130}$$

where $|\nabla\Psi| = \mathrm{O}(1)$. To seek the inner solution in terms of a stretched radial coordinate due to the smallness of the core radius $\delta$, we set

$$x = \delta\bar{r}\cos\theta, \quad y = \delta\bar{r}\sin\theta, \quad \bar{r} = \frac{r}{\delta}. \tag{6.131}$$

With the stretched $\bar{r}$, flow variables will still be denoted by $\psi$, $\omega$, and $\boldsymbol{u}$ for neatness. Equation (6.128a,b) is cast to

$$[\omega, \psi] = -\delta^2 \mathcal{L}\omega, \quad \mathcal{L} \equiv \frac{\partial}{\partial t} - \overline{\nabla}^2, \tag{6.132a}$$

$$\overline{\nabla}^2 \psi = -\delta^2 \omega. \tag{6.132b}$$

Here, the derivatives in the gradient operator and Jacobian $[\omega, \psi]$ are with respect to $(\bar{r}, \theta)$, so the order of magnitude is raised by $\mathrm{O}(\delta^{-2})$. At the vortex center we require

$$\psi = 0, \quad \frac{\partial\psi}{\partial\bar{r}} = 0 \quad \text{at} \quad \bar{r} = 0, \tag{6.133}$$

while for $\bar{r} \gg 1$ the solution must match (6.130) with $r \ll 1$, where we can make a Taylor expansion about the origin. Hence, the matching condition is

$$\begin{aligned} \delta^{-1}\overline{\nabla}\psi \times \boldsymbol{e}_z|_{\bar{r}\to\infty} &= \nabla\psi \times \boldsymbol{e}_z|_{r\ll 1} \\ &= \delta^{-1}\frac{1}{2\pi\bar{r}}\boldsymbol{e}_\theta + [(\nabla\Psi)_0 \\ &\quad + \delta\bar{\boldsymbol{r}} \cdot (\nabla\nabla\Psi)_0 + \cdots] \times \boldsymbol{e}_z. \end{aligned} \tag{6.134}$$

We now make regular inner power expansion for $\psi$. It turns out that the odd powers of $\delta$ are involved only in fast-time unsteady flow (Ting and Tung 1965), so by (6.132b) we set

$$\psi = \psi_0 + \delta^2\psi_2 + \cdots, \quad \omega = \delta^{-2}\omega_0 + \omega_2 + \cdots. \tag{6.135}$$

Then we find the leading-order inner solution must be *axisymmetric* and *generalized Beltramian*:

$$[\omega_0, \psi_0] = 0, \quad \omega_0 = \omega_0(\psi_0), \tag{6.136}$$

satisfying

$$\frac{\partial\psi_0}{\partial\bar{r}} \to \frac{1}{2\pi\bar{r}} \quad \text{as} \quad \bar{r} \to \infty. \tag{6.137}$$

Next, we substitute (6.135) into (6.132a,b) and the boundary conditions (6.133) and (6.134). Equating coefficients of like power of $\delta$ leads to the desired equations. First, from (6.132b) and (6.134) there is

$$\overline{\nabla}^2\psi_n = -\omega_n \quad \text{with} \quad \psi_n = 0 \text{ and } \frac{\partial\psi_n}{\partial\overline{r}} = 0 \text{ at } \overline{r} = 0. \tag{6.138}$$

Then, (6.132a) yields

$$\mathrm{O}(\delta^{-1}):\ \mathcal{D}\{\omega_1, \psi_1\} = 0, \tag{6.139a}$$

$$\mathrm{O}(\delta^{0}):\ \mathcal{D}\{\omega_2, \psi_2\} = -[\omega_1, \psi_1] - \mathcal{L}\omega_0, \tag{6.139b}$$

etc., each being a linear equation. Here, we have used (6.138) to simplify the sum of Jacobians and introduced the notation

$$\mathcal{D}\{\omega_n, \psi_n\} \equiv [\omega_0, \psi_n] + [\omega_n, \psi_0] = \frac{1}{\overline{r}}\frac{\partial}{\partial\theta}\left(\frac{\partial\omega_0}{\partial\overline{r}}\psi_n - \frac{\partial\psi_0}{\partial\overline{r}}\omega_n\right), \tag{6.140}$$

of which the $\theta$-average vanishes. It can then be proved that (Ting and Tung 1965, Ting and Klein 1991, p. 63) the $\theta$-average of $[\omega_1, \psi_1]$ also vanishes. Therefore, the $\theta$-average of (6.139b) implies that, as a *solvability condition* there must be

$$\mathcal{L}\omega_0 = 0, \quad \text{i.e.,} \quad \frac{\partial\omega_0}{\partial t} = \frac{1}{\overline{r}}\frac{\partial}{\partial\overline{r}}\left(\overline{r}\frac{\partial\omega_0}{\partial\overline{r}}\right), \tag{6.141}$$

precisely the dimensionless form of (6.17a). The matching condition (6.134) implies that the only permitted solution in the Neufville family (6.24) is the *Oseen–Lamb vortex* evolving from a point vortex at $t = 0$ ($\omega_0$ must freely decay since no mechanism can balance its diffusion):

$$\omega_0 = \frac{1}{4\pi t}\mathrm{e}^{-\overline{r}^2/4t}. \tag{6.142}$$

Therefore, unlike the boundary layer, now the leading-order inner solution is determined by an expansion to the second order rather than a leading-order analysis alone; the latter only gives (6.136) and (6.137). The $n$th-order solution for $n = 1, 2, ...$ is no longer axisymmetric, of which the specific form depends on the outer flow $\Psi(x, y)$.

Moreover, by (6.141), from (6.139b) and (6.140) there is

$$(\overline{\nabla}^2 + G)\psi_2 = 0, \tag{6.143a}$$

where

$$G(\overline{r}, t) \equiv \frac{\partial\omega_0/\partial\overline{r}}{\partial\psi_0/\partial\overline{r}} = -\frac{\partial\omega_0/\partial\overline{r}}{v_0(\overline{r}, t)}. \tag{6.143b}$$

Here, $\psi_2$ is $\theta$-dependent due to the matching with the outer solution. Thus, it is natural to set

$$\psi_2 = \sum_{k=0}^{\infty} [f_k^{(1)}(\overline{r}) \cos k\theta + f_k^{(2)}(\overline{r}) \sin k\theta], \tag{6.144a}$$

which casts (6.143) to

$$\left[\frac{\partial^2}{\partial \overline{r}^2} + \frac{1}{\overline{r}}\frac{\partial}{\partial \overline{r}} + \left(G - \frac{k^2}{r^2}\right)\right] f_k^{(\beta)} = 0, \quad \beta = 1, 2, \tag{6.144b}$$

The inner boundary condition is

$$f_k^{(\beta)} = 0, \quad \frac{\partial f_k^{(\beta)}}{\partial \overline{r}} = 0 \quad \text{at} \quad \bar{r} = 0. \tag{6.145}$$

Note that by requiring that near the center the core is solid-like and smooth to the leading order, the function $G$ must be finite as $\overline{r} \to 0$. On the other hand, by (6.134) the matching condition of $\psi_2$ with the outer flow reads

$$\nabla \psi_2 \to \overline{\boldsymbol{r}} \cdot (\nabla \nabla \Psi)_0, \quad \overline{r} \to \infty, \tag{6.146}$$

implying that, due to the irrotational condition $\nabla^2 \Psi = 0$,

$$\psi_2 \to \frac{1}{2}\overline{r}^2 \left[\left(\frac{\partial^2 \Psi}{\partial x^2}\right)_0 \cos 2\theta + \left(\frac{\partial^2 \Psi}{\partial x \partial y}\right)_0 \sin 2\theta\right], \quad \overline{r} \to \infty. \tag{6.147}$$

Except $k = 2$, the boundary conditions for all other $f_k^{(\beta)}$'s have to be homogeneous, permitting zero solution only. Therefore, we finally arrive at the *canonical equation* for a two-dimensional viscous strained vortex (Ting and Tung 1965)

$$\frac{\mathrm{d}^2 f}{\mathrm{d}\overline{r}^2} + \frac{1}{\overline{r}}\frac{\mathrm{d}f}{\mathrm{d}\overline{r}} + \left(G - \frac{4}{\overline{r}^2}\right) f = 0, \tag{6.148a}$$

$$f(\overline{r}) = 0, \quad \frac{\mathrm{d}f}{\mathrm{d}\overline{r}} = 0 \quad \text{at} \quad \overline{r} = 0, \tag{6.148b}$$

$$f(\overline{r}) \to \frac{1}{2}\overline{r}^2 \quad \text{as} \quad \overline{r} \to \infty. \tag{6.148c}$$

Once $f(\overline{r})$ is solved for a known $\omega_0$, the inner solution for the stream function follows:

$$\psi = \psi_0 + \delta^2 f(\overline{r})(A \cos 2\theta + B \sin 2\theta), \tag{6.149a}$$

$$A = \left(-\frac{\partial U}{\partial y}\right)_0, \quad B = \left(\frac{\partial U}{\partial x}\right)_0. \tag{6.149b}$$

Owing to its central role in studying strained vortices and their stability, after Ting and Tung (1965) the canonical equation (6.148) has been re-obtained independently (e.g., Moore and Saffman 1975, see also Saffman 1992). Its application will be exemplified in Sect. 6.5.2.

**Three-Dimensional Flow**

The matched asymptotic method of Ting and Tung (1965) can be directly extended to three dimensions (Moffatt et al. 1994; Jiménez et al. 1996). Assume the vortex axis (the $z$-axis) is aligned to a stretching principal axis of $\mathbf{D}$. The inner solution experiences a constant strain rate $\mathbf{D}$ with $\|\mathbf{D}\| = \mathrm{O}(1)$ and principal values $(\alpha, \beta, \gamma)$

$$\boldsymbol{U} = (\alpha x, \beta y, \gamma z), \quad \alpha + \beta + \gamma = 0, \quad \alpha < 0 \leq \gamma, \quad \beta \geq \alpha. \tag{6.150}$$

This background flow is called *triaxial strain*. The vorticity is $\boldsymbol{\omega} = (0, 0, \omega)$, which induces a velocity field $\boldsymbol{u}_v = (u, v, 0)$. Thus, the vorticity transport equation reads

$$\frac{\partial \omega}{\partial t} + (\alpha x + u)\frac{\partial \omega}{\partial x} + (\beta y + v)\frac{\partial \omega}{\partial y} = \gamma\omega + \nu\nabla^2\omega. \tag{6.151}$$

A two-dimensional stream function $\psi$ can be introduced on cross-plane, such that

$$\nabla^2\psi = -\omega, \quad u = \frac{\partial \psi}{\partial y}, \quad v = -\frac{\partial \psi}{\partial x}. \tag{6.152}$$

Different value ranges of the principal strain rates can be characterized by a single parameter, the *strain ratio*

$$\lambda = \frac{\alpha - \beta}{\alpha + \beta} = \frac{\beta - \alpha}{\gamma} \geq 0, \tag{6.153a}$$

so that

$$\alpha = -\frac{1}{2}\gamma(1+\lambda), \quad \beta = -\frac{1}{2}\gamma(1-\lambda), \quad \|\mathbf{D}\| = \alpha\beta\gamma = \frac{1}{4}\gamma^3(1-\lambda^2). \tag{6.153b}$$

Then several types of strain can be identified:

(i) $\lambda = 0$: $\alpha = \beta = -\gamma/2$, axisymmetric axial strain;
(ii) $0 < \lambda < 1$: $\alpha < \beta < 0$, nonaxisymmetric axial strain;
(iii) $\lambda = 1$: $\alpha = -\gamma$, $\beta = 0$, plane strain;
(iv) $1 < \lambda < 3$: $0 < \beta < \gamma$, biaxial strain;
(v) $\lambda = 3$: $\alpha = -2\gamma, \beta = \gamma$, axisymmetric biaxial strain;
(vi) $\lambda > 3$: $\beta > \gamma$, extreme biaxial strain;
(vii) $\lambda \to \infty$: $-\alpha \simeq \beta \gg 1$, $\gamma \to 0$, two-dimensional strain limit.

We have just examined the two-dimensional case (vii). For case (i), (6.151) has closed-form solution (6.33), of which the asymptotic steady state is the

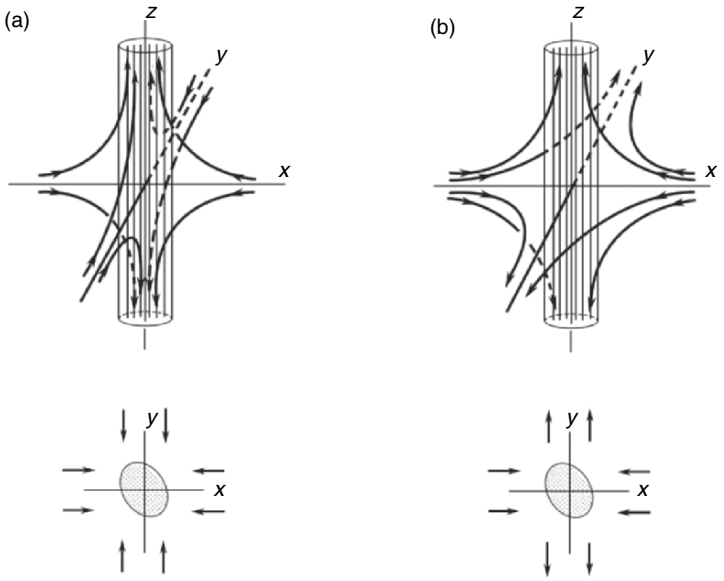


**Fig. 6.15.** Axial strain (**a**) and biaxial strain (**b**). From Moffatt et al. (1994)

Burgers vortex (6.34). In contrast, for case (iii) there is a layer-like steady solution known as the *Burgers vortex layer*:

$$\omega = \omega_0 \exp\left(-\frac{\gamma x^2}{4\nu}\right) \tag{6.154}$$

with $\omega_0$ being the maximum vorticity. On the other hand, if $\alpha \leq \beta < 0$ and if $R_\Gamma \to 0$ so that the vortex-induced velocity is negligible compared to $\boldsymbol{U}$, (6.151) has a nonaxisymmetric steady solution

$$\omega = \frac{(\alpha\beta)^{1/2}\Gamma}{2\pi\nu} \exp\left(\frac{\alpha x^2 + \beta y^2}{2\nu}\right). \tag{6.155}$$

For all other cases only asymptotic solutions can be obtained. The strain field for cases (ii) and (iv), i.e., the axial strain and biaxial strain, respectively, are sketched in Fig. 6.15.

While for types (i) and (ii) there is a tendency to form a concentrated vortex aligned with the $z$-axis, for types (iv), (v), and (vi) there is a tendency to form vortex sheets in the $(y, z)$ plane. The statistics of homogeneous isotropic turbulence has revealed that the ensemble average of $\alpha\beta\gamma$ is negative, indicating that there would be a bias towards biaxial strain. But the presence of the strained vortex modifies the local strain field, and as shown in Fig. 6.8 vortex sheets may tend to roll into concentrated vortices.

We focus on the asymptotic *steady* solution of (6.151), which is possible if the diffusion can be balanced by the strain. As in two dimensions, we make the

inner radial coordinate and stream function dimensionless by $\delta = R_\Gamma^{-1/2}$ and $\Gamma$. Besides, we use $\gamma$ to rescale $\alpha$ and $\beta$ such that $\lambda = \beta - \alpha$, $\alpha = -(1+\lambda)/2$, and $\beta = -(1-\lambda)/2$. Then, in polar coordinates $(\overline{r}, \theta)$, the dimensionless form of (6.152) can be cast to

$$\frac{1}{\overline{r}} \frac{\partial(\omega, \psi)}{\partial(\overline{r}, \theta)} = \delta^2(\mathcal{L}_0\omega + \lambda\mathcal{L}_1\omega), \tag{6.156a}$$

$$\mathcal{L}_0 = 1 + \frac{\overline{r}}{2}\frac{\partial}{\partial\overline{r}} + \nabla^2, \tag{6.156b}$$

$$\mathcal{L}_1 = \frac{1}{2}\left(\cos 2\theta\overline{r}\frac{\partial}{\partial\overline{r}} - \sin 2\theta\frac{\partial}{\partial\theta}\right). \tag{6.156c}$$

We now seek a solution of (6.156a) in the form

$$\psi = \psi_0 + \delta^2\psi_2 + \delta^4\psi_4 + \cdots, \tag{6.157}$$

and corresponding expansion for $(u, v)$ and $\omega$. Substituting these into (6.156a) and equating terms of like power of $\delta$, for $\mathrm{O}(\delta^0)$ one recovers the two-dimensional result (6.136), which now describes only the cross-plane behavior. Then for $\mathrm{O}(\delta^2)$ it follows the three-dimensional counterpart of (6.139b)

$$\frac{1}{\overline{r}}\frac{\partial}{\partial\theta}\left(\frac{\partial\omega_0}{\partial\overline{r}}\psi_2 + v_0\omega_2\right) = \mathcal{L}_0\omega_0 + \lambda_1\mathcal{L}_1\omega_0. \tag{6.158}$$

Due to the explicit form (6.156b) of $\mathcal{L}_1$, the $\theta$-average of (6.158) evidently yields the solvability condition $\mathcal{L}_0\omega_0 = 0$, implying that the *Burgers vortex* (6.34) is the leading-order inner solution at large $R_\Gamma$. Its dimensionless form is

$$\omega_0(\overline{r}) = \frac{1}{4\pi}\mathrm{e}^{-\overline{r}^2/4}, \tag{6.159a}$$

$$v_0(\overline{r}) = \frac{1}{2\pi\overline{r}}(1 - \mathrm{e}^{-\overline{r}^2/4}). \tag{6.159b}$$

This being the case, by using (6.156b), the $\theta$-integral of (6.158) yields

$$(\overline{\nabla}^2 + G)\psi_2 = -\frac{1}{4}\lambda\overline{r}^2 G(\overline{r})\sin 2\theta + g(\overline{r}), \tag{6.160}$$

where $G(\overline{r})$ is still defined by (6.143b) and it can be shown that $g(\overline{r}) = 0$ by higher-order solvability condition (Moffatt et al. 1994). This equation differs from (6.143a) by the inhomogeneous term on the right-hand side, which appears because the Burgers vortex is no longer generalized Beltramian. Now set

$$\psi_2 = \lambda f(r)\sin 2\theta, \tag{6.161}$$

from which and (6.160) follows the *canonical equation* for triaxially strained vortices (Moffatt et al. 1994):

$$\frac{\mathrm{d}^2 f}{\mathrm{d}\overline{r}^2} + \frac{1}{\overline{r}}\frac{\mathrm{d}f}{\mathrm{d}\overline{r}} + \left(G - \frac{4}{\overline{r}^2}\right) f = \frac{1}{4}\overline{r}^2 G(\overline{r}), \tag{6.162a}$$

$$f(\overline{r}) = 0, \quad \frac{\mathrm{d}f}{\mathrm{d}\overline{r}} = 0 \quad \text{at} \quad \overline{r} = 0, \tag{6.162b}$$

$$f(\overline{r}) \sim \overline{r}^2 \quad \text{as} \quad \overline{r} \to \infty. \tag{6.162c}$$

Before closing this section, we make a further comparison of (6.143) and (6.160). Let $\omega_0(\psi_0)$ be perturbed to $\omega = \omega_0 + \epsilon\omega^*$ with any $\epsilon \ll 1$. Then since $[\omega_0, \psi_0] = 0$, there is

$$[\omega, \psi] = \epsilon([\omega_0, \psi^*] + [\omega^*, \psi_0]) = \epsilon\mathcal{D}\{\omega^*, \psi^*\}.$$

Thus, whenever $\mathcal{D}\{\omega^*, \psi^*\} = 0$, the perturbed flow $(\omega, \psi)$ will be generalized Beltramian as well, with $\omega = F(\psi)$ for some $F$ which has Taylor expansion

$$F(\psi) = \omega_0 - \epsilon\nabla^2\psi^* = F(\psi_0 + \epsilon\psi^*) = F(\psi_0) + \epsilon\psi^* F'(\psi_0) + \mathrm{O}(\epsilon^2).$$

Hence, *if* there is also $\omega_0 = F(\psi_0)$, i.e., $\omega_0$ and $\psi_0$ are related by the *same* functional $F$ as $\omega$ and $\psi$:

$$\omega_0 = F(\psi_0) \Longleftrightarrow \omega = F(\psi), \tag{6.163}$$

then there will be

$$\nabla^2\psi^* + \psi^* F'(\psi_0) = 0, \quad \text{where} \quad F'(\psi_0) = \left(\frac{\mathrm{d}F}{\mathrm{d}\overline{r}}\frac{\mathrm{d}\overline{r}}{\mathrm{d}\psi}\right)_0 = -\frac{\omega_0'(\psi_0)}{v_0}.$$

Therefore, (6.143a) is recovered in a more general setting. This neat argument is due to Moore and Saffman (1975; see also Saffman 1992).

### 6.5.2 Strained Solution in Distant Vortex Dipole

As an application of the two-dimensional Ting–Tung theory, we return to the dipole problem. Opposite to the Chaplykin–Lamb dipole where the two vortices are very close to each other, now consider a pair of vortices of large distance $2L$, with circulation $\pm\Gamma$ and $R_\Gamma = \Gamma/\nu \gg 1$. The distant vortex dipole is the prototype of aircraft wake vortices, of which the instability is of great interest (Sect. 9.4.3).

At one vortex of core radius $\delta \ll L$ , the strain field of the other can be considered as caused by a point vortex. For the point-vortex pair located at $(x_0, y_0) = (\pm L, 0)$, the velocity of each vortex is $-\boldsymbol{e}_y\Gamma/4\pi L$. The dipole will be stationary if there is an upward uniform velocity $V = \Gamma/4\pi L$ at infinity to

cancel the downward motion of the dipole. Then the two-dimensional stream function $\psi(x, y)$ of the dipole is

$$\psi(x,y) = -\frac{\Gamma}{4\pi}\left[\frac{x}{L} + \ln\frac{(x-L)^2+y^2}{(x+L)^2+y^2}\right]. \tag{6.164}$$

Like the circular Chaplykin–Lamb vortex dipole, there is a closed streamline which separates the fluid extending to infinity and that carried along by the dipole; the latter is known as the *Kelvin oval*. By (6.164), the oval boundary $\psi = 0$ is given by the equation

$$\frac{(x-L)^2+y^2}{(x+L)^2+y^2} = \mathrm{e}^{-x/L} \tag{6.165}$$

from which one finds that, if $L = 1$ then the semi-major and minor axes of the oval are $(L_1, L_2) = (2.087, \sqrt{3})$, and the oval area is $A \simeq 11.4$.

Consider now the right-side vortex, which is allowed to have a $z$-independent axial velocity profile. The global scales are $L$ and $\Gamma > 0$. Introduce polar coordinates $(r, \theta)$ to the vortex center $(1, 0)$ and denote $r = \delta\overline{r}$ as before. In terms of $(\overline{r}, \theta)$, near the vortex center the outer solution (6.164) has dimensionless expansion

$$\begin{aligned}\psi &= -\frac{1}{4\pi}\left[1 + \delta\overline{r}\cos\theta + \ln\left(\frac{\delta^2\overline{r}^2/4}{1 + 4\delta\overline{r}\cos\theta + \delta^2\overline{r}^2/4}\right)\right] \\ &= -\frac{1}{2\pi}\left(\ln\overline{r} + \frac{1}{8}\delta^2\overline{r}^2\cos 2\theta + C\right) + \mathrm{O}(\delta^3),\end{aligned} \tag{6.166}$$

where the constant $C = 1/2 + \ln(\delta/2)$ can be removed by re-defining the zero streamline. The first term is caused by the right-side vortex alone, and the second term represents the $\mathrm{O}(\delta^2)$ effect of the left-side vortex. The effect of uniform stream has been cancelled, which removes terms linear to $\delta\overline{r}\cos\theta$.

The presence of the left-side vortex makes the right-side one no longer axisymmetric in the second-order inner solution $(\omega_2, \psi_2)$ via (6.166). To mimic the continuous vorticity feeding from wing tip instead of the decaying viscous vortex we seek an inviscid steady inner solution in cylindrical coordinates $(\overline{r}, \theta, z)$ with velocity

$$u = \delta u_2, \quad v = \delta^{-1}V + \delta v_2, \quad w = W + \delta w_2, \tag{6.167a}$$

$$\omega_r = \omega_{r2}, \quad \omega_\theta = \omega_{\theta 2}, \quad \omega_z = \delta^{-2}\frac{\Gamma'}{\overline{r}} + \omega_{z2}, \tag{6.167b}$$

where $\Gamma \equiv \overline{r}V(\overline{r})$. We have used $(V, W) = \mathrm{O}(1)$ to denote $(\delta v_0, w_0)$ which as shown in Sect. 6.2.1 can be arbitrarily prescribed, provided that $V \sim \overline{r}^{-1}$ and $W$ decays exponentially. The solution depends on both $\overline{r}$ and $\theta$ but not $z$. This is again a generalized Beltrami flow satisfying (6.11), and is quasi two-dimensional having a stream function $\psi$ to determine $(u, v)$. As to $w$, since $H$ is independent of $z$, by the inviscid and steady version of (6.4c) there must be

$$v\omega_r - u\omega_\theta = \frac{1}{r}\frac{\partial(w,\psi)}{\partial(r,\theta)} = 0,$$

implying that $w = w(\psi)$. Thus, we can use the same assumption as (6.163), with merely replacing $\omega$ by $w$. Then by the same Taylor expansion and noticing now

$$\left(\frac{\mathrm{d}F}{\mathrm{d}\psi}\right)_0 = \frac{\mathrm{d}W/\mathrm{d}\overline{r}}{\mathrm{d}\overline{r}/\mathrm{d}\psi_0} = -\frac{W'}{V}$$

it follows that (Saffman 1992)

$$w_2 = -\frac{W'}{V} f(\overline{r})\psi_2. \tag{6.168}$$

This result can be verified by substituting (6.167) into the inviscid and steady version of (6.5a) and integrating twice.

Now that everything is determined by a single $\psi$, which was already solved in the preceding subsection. To match with (6.166), the stream function must be

$$\psi = \psi_0 + \delta^2\psi_2 = \psi_0 + \frac{\delta^2}{4} f(\overline{r})\cos 2\theta, \tag{6.169}$$

where $f(\overline{r})$ satisfies canonical equation (6.148a). The function $G$ therein defined by (6.143b) can be written

$$G(\overline{r}) = -\frac{\overline{r}}{\Gamma}\left(\frac{\Gamma'}{\overline{r}}\right)'. \tag{6.170}$$

Then the solution directly follows (Zhu et al. 1999):

$$\begin{aligned} u &= -\frac{\delta}{2\overline{r}} f(\overline{r})\sin 2\theta, \\ v &= \delta^{-1}V(\overline{r}) - \frac{\delta}{4} f'(\overline{r})\cos 2\theta, \\ w &= W(\overline{r}) - \frac{\delta W'}{4V} f(\overline{r})\cos 2\theta; \end{aligned} \tag{6.171}$$

$$\begin{aligned} \omega_{\overline{r}} &= \frac{W'}{2\Gamma} f \sin 2\theta, \\ \omega_\theta &= -\delta^{-1}W' + \frac{1}{4}\left(\frac{W'}{V} f\right)' \cos 2\theta, \\ \omega_z &= \delta^{-2}\frac{\Gamma'}{\overline{r}} + \frac{1}{4} G f \cos 2\theta. \end{aligned} \tag{6.172}$$

Finally, by (6.171) and the $r$-component of the steady Euler equation, one finds

$$p = \delta^{-2}\left(p_\infty - \int_{\overline{r}}^{\infty} \frac{V^2}{\overline{r}}\,\mathrm{d}\overline{r}\right) - \frac{1}{2}\cos 2\theta \int_{\overline{r}}^{\infty} \frac{1}{\overline{r}^3} V(\overline{r}^2 f)'\,\mathrm{d}\overline{r} + \mathrm{O}(\delta^2), \quad (6.173)$$

where $p_\infty$ is the pressure of the background potential flow at vortex center.

For example, let $(V, W)$ be a $q$-vortex given by (6.19) with $q = W_0 = 1$, and taking the positive sign for $W$. Then (6.170) gives (the overbar for radial coordinate is dropped)

$$G(r) = \frac{4r^2}{\mathrm{e}^{r^2} - 1} > 0. \quad (6.174)$$

The core size $r = a$ is defined as where $V(r)$ reaches the maximum, which is the solution of $a^2 = 2\ln a$. By (6.19) and (6.174), near the axis (6.148a) is reduced to a Bessel equation:

$$f'' + \frac{1}{r}f' + 4\left(1 - \frac{1}{r^2}\right) f = \mathrm{O}(r^2)$$

with solution

$$f(r) = CJ_2(2r) + \mathrm{O}(r^4) = \frac{C}{2}r^2 + \mathrm{O}(r^4),$$

where constant $C$ has to be determined numerically by the entire solution satisfying (6.148c). Hence, we write

$$f(r,\theta) = \frac{r^2}{2}\left(1 + \beta\cos 2\theta\right) + \mathrm{O}(r^4), \quad \beta \equiv C\delta^2, \quad r \ll 1,$$

or, in terms of Cartesian coordinates with origin at the vortex center,

$$f(x,y) = \frac{1}{2}[(1+\beta)x^2 + (1-\beta)y^2] + \mathrm{O}(r^4).$$

Thus, for $r \ll 1$ the sectional streamlines are ellipses, but no longer so for $r = \mathrm{O}(1)$. Since $\Gamma' > 0$, $G > 0$, and $\psi \le 0$, (6.172) indicates that the strain field tends to reduce the axial vorticity for $|\theta| < \pi/4$ and $|\pi - \theta| < \pi/4$, but enhance it elsewhere. The streamlines and vorticity contours are no longer overlapped in this kind of strained vortices.

### 6.5.3 Vortex in Triaxial Strain Field

Motivated by the observed vortex patterns in turbulence, the asymptotic vortex solution and surrounding flow patterns in a triaxial strain field has been analyzed by Moffatt et al. (1994), Jiménez et al. (1996), and Prochazka and Pullin (1998), of which the main findings are outlined.

We start from the canonical equation (6.162). By using (6.159), the function $G$ defined by (6.143b) now reads

$$G(\overline{r}) = \frac{\overline{r}^2}{4(\mathrm{e}^{\overline{r}^2/4} - 1)} \tag{6.175}$$

from which the asymptotic behavior of $f(\overline{r})$ satisfying (6.162b,c) is further determined by Moffatt et al. (1994)

$$\begin{aligned} f(\overline{r}) &= a\overline{r}^2 + \frac{1}{12}\left(\frac{1}{4} - a\right)\left(\overline{r}^4 - \frac{5}{64}\overline{r}^6 + \cdots\right) \quad \text{as} \quad \overline{r} \to 0, \\ \overline{r}^2 f(\overline{r}) &\sim C+ \sim \frac{1}{4}\overline{r}^2 \mathrm{e}^{-\overline{r}^2/4} \quad \text{as} \quad \overline{r} \to \infty, \end{aligned} \tag{6.176}$$

where $a = -0.381475\ldots$ and $C = -17.4723\ldots$. Thus, by (6.161) one obtains

$$\begin{aligned} u(r,\theta) &= -\frac{1}{2}r + \left(\frac{\lambda}{2}r + \frac{2\epsilon_1}{r}f(r)\right)\cos 2\theta, \\ v(r,\theta) &= v_0(r) - \left(\frac{\lambda}{2}r + \epsilon_1 f'(r)\right)\sin 2\theta, \\ \omega(r,\theta) &= \omega_0(r) + \epsilon_1 \Omega(r)\sin 2\theta, \end{aligned} \tag{6.177}$$

where $\epsilon_1 = \lambda/R_\Gamma$ is the characteristic small parameter for strained vortices and

$$\Omega(r) = \left(f - \frac{r^2}{4}\right)\frac{r^2}{4(\mathrm{e}^{r^2/4} - 1)}. \tag{6.178}$$

The contours of vorticity and dissipation of strained vortices at different $\lambda$ has been extensively studied by Moffatt et al. (1994), who found that the peaks of enstrophy $\omega^2$ and dissipation rate $\Phi$ are dislocated. This occurs in two dimensions as well. Fig. 6.16 displays one of their asymptotic solutions for the contours of dissipation $\Phi$ with $\epsilon_1 = 0.00656$, which has a pair of maximal peaks and a pair of minimal peaks aligned to the major and minor axes, respectively. This pattern has been found in other direct numerical simulations, e.g., Fig. 3b of Su et al. (2002).

In contrast, the $\omega^2$ distribution (not shown) is nearly elliptic, with a pair of peaks located aligned to the minor axis. As mentioned following (2.155), the characteristic distribution of $\omega^2$ and $\Phi$ are good indicators of vortex structures in a complex flow, and their peak-value dislocation can be easily understood. In fact, even for an axisymmetric vortex these peaks are already dislocated: while the peak of $\omega^2$ is at the vortex center forming a "spaghetti structure", that of $\Phi$ is at the edge of the vortex core forming a "macaroni structure" (Wu et al. 1999a).

We remark that once $f(\overline{r})$ is solved, the Lamb vector of the vortex in triaxial strain can be readily obtained. Then the longitudinal and transverse

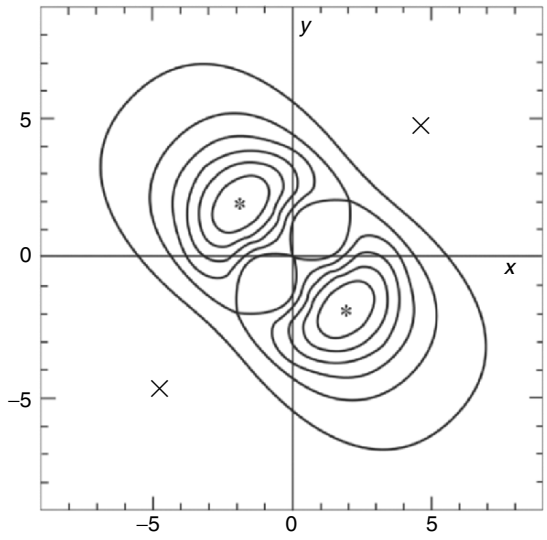


**Fig. 6.16.** Dissipation contours of an asymptotic strain vortex solution. The maxima and minima are marked with $*$ and $\times$, respectively. Reproduced from Moffatt et al. (1994)

parts of $\boldsymbol{l}$, $\boldsymbol{l}_{\parallel}$ and $\boldsymbol{l}_{\perp}$, can be expressed analytically in terms of $f(\overline{r})$. The patterns of the magnitude contours and vector lines of $\boldsymbol{\omega}$, $\boldsymbol{l}$, $\boldsymbol{l}_{\parallel}$, and $\boldsymbol{l}_{\perp}$ on the $(r, \theta)$ plane at $\lambda = 5$ are shown in Fig. 6.17. The topology of the vector fields of $\boldsymbol{l}$, $\boldsymbol{l}_{\parallel}$, and $\boldsymbol{l}_{\perp}$ in the entire plane is quite complex (not completely shown). While the center of a Burgers vortex is a stable spiral point of $\boldsymbol{l}$-field, it is now a saddle.

A special problem occurs for biaxially strained vortex when $\lambda \gg 1$. As sketched in Fig. 6.18, in this case the flow is divided to a few characteristic regions. In the *vortex-core region I* the vorticity diffusion is balanced by its enhancement due to stretching, which was just discussed. Outside the core region there is a *"cat-eye" region II* bounded by streamlines from two saddle points where $\overline{r} \gg 1$, but the asymptotic theory developed in Sect. 6.5.1 is effective only for $\overline{r} = \mathrm{O}(1)$. To fill this gap, Jiménez et al. (1996) apply the Lundgren transformation (6.32) and a singular perturbation technique called *coordinate stretching* (Van Dyke 1975) to delay the disordering to $\overline{r} = \epsilon_1^{-1/2}$. Then, Prochazka and Pullin (1998) construct a simple solution for region II, along whose bounding streamline the weak vorticity takes a constant value, and there is a weak *vorticity leakage* across that streamline to region III. Having determined these, the description of region II is complete.

All the theoretical predictions in this subsection have been confirmed by the numerical computation of Prochazka and Pullin (1998) with good accuracy.

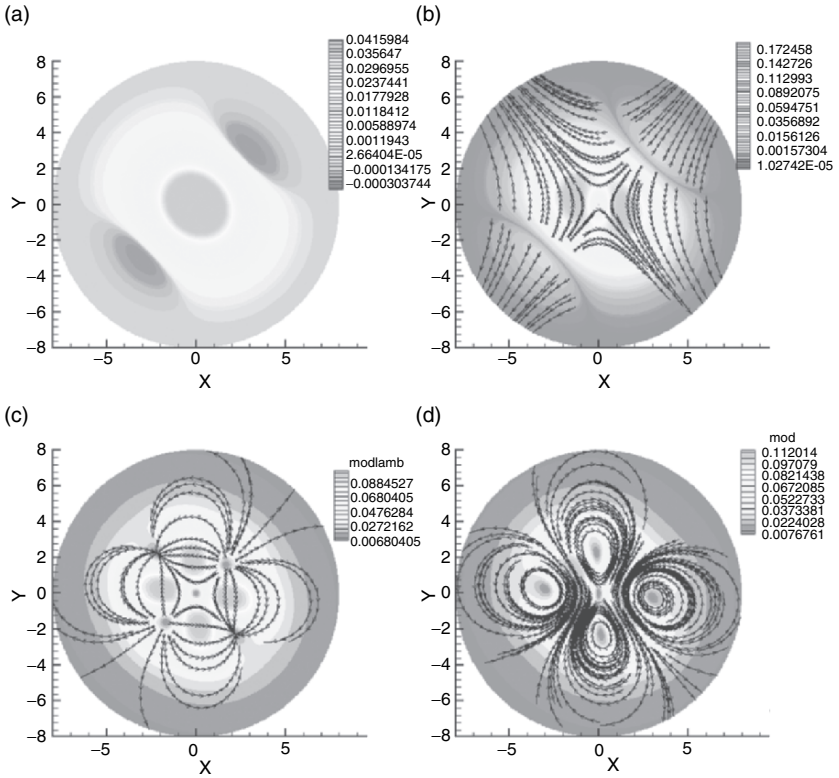


**Fig. 6.17.** The contours of vorticity (**a**), contours of magnitude and vector lines of Lamb vector (**b**), and its longitudinal (**c**) and transverse parts (**d**) for biaxially strained vortex at $\lambda = 5$. Courtesy of W.-D. Su, Q.-D. Cai, and H. Zhao

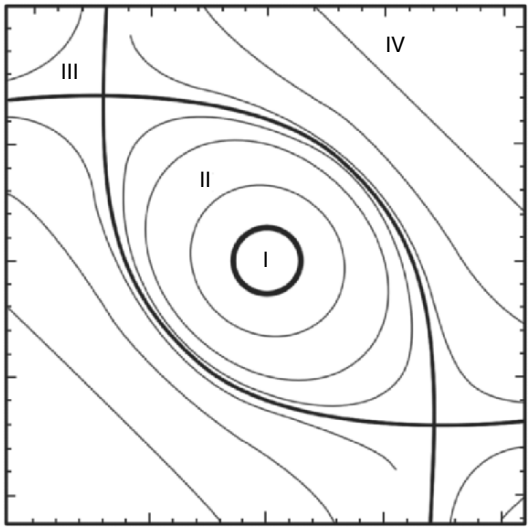


**Fig. 6.18.** Four regions for biaxial strained vortex with $\lambda \gg 1$

## 6.6 On the Definition of Vortex

Having studied various typical vortex solutions, we now visit a controversial but fundamental problem in vortex dynamics: the definition of a vortex in viscous flow. This issue turns out to be surprisingly difficult, although intuitively a vortex can be easily recognized (e.g., Lugt 1979). So far in this book we have only qualitatively identified a vortex as a connected fluid region with relatively high concentration of vorticity. But the need for a rational and quantitative definition has become increasingly pressing since the discovery of coherent vortical structures and their key role in turbulent flows (see Chap. 10). The lack of a consensus on vortex definition has caused considerable confusion in visualizing and understanding the coherent vortical structures, their evolution, and interaction. Currently the issue is still open.

In this section we follow a recent work of Wu et al. (2005b) to analyze the physical root of the controversy. We compare different invariant criteria for defining an incompressible vortex proposed in the past by an analytical diagnosis, exemplified by the Burgers vortex and Sullivan vortex. This analysis disqualifies some commonly used criteria and leads to a requirement that any generally applicable definition should satisfy.

### 6.6.1 Existing Criteria

One recognizes the existence of vortices first by their intuitive streamline patterns, which are however not Galilean invariant (Sect. 2.1) and cannot be used to define a vortex. A natural invariant approach could be based on the vorticity, from which one can extract vorticity lines and vorticity magnitude. A bundle of vorticity lines can ensure the correct topological property of the vortices, but does not tell the strength of the vortex. A better concept is vorticity tube, which has been used by Lamb (1932, p. 202) to define a vortex.

More precisely, we could define a vortex as a vorticity tube surrounded by irrotational flow, similar to the definition given by Saffman and Baker (1979). But the vortex boundary becomes fussy in viscous flow, and even some inviscid vortex models (say the $q$-vortex) may have exponentially decaying "tail" without sharp boundary. In that case one usually talks about the *vortex core* as we did for axisymmetric vortices in this chapter, of which the outer boundary is the radius $r_0$ where the circumferential velocity is maximum. However, this criterion cannot be generalized to more complex and nonaxisymmetric vortices.

A simple alternative to the vorticity-tube definition would be choosing a threshold magnitude, say $|\boldsymbol{\omega}_0|$, and identifying the fluid region with $|\boldsymbol{\omega}| \geq |\boldsymbol{\omega}_0|$ as a vortex. But the choice of $|\boldsymbol{\omega}_0|$ is subjective, and the side boundary of a vorticity tube may significantly differ from an isovorticity surface. This $|\boldsymbol{\omega}|$-criterion is also inadequate.

A natural basis for developing possible rational criteria is the symmetric–antisymmetric decomposition $\nabla \boldsymbol{u} = \mathbf{D} + \boldsymbol{\Omega}$, which suggests that a vortex may

be defined as a flow region where the vorticity prevails over the strain rate. This requires the calculation of the invariants of $\nabla \boldsymbol{u}$ through its representative matrix, say $\mathbf{A}$; which in cylindrical coordinates reads

$$\mathbf{A} = \begin{bmatrix} u_{,r} & v_{,r} & w_{,r} \\ (u_{,\theta} - v)/r & (v_{,\theta} + u)/r & w_{,\theta}/r \\ u_{,z} & v_{,z} & w_{,z} \end{bmatrix}. \tag{6.179}$$

The first criterion along this line was proposed by Weiss (1981) for two-dimensional flow $(u, v)$ based on the eigenvalues $\sigma$ of $\nabla \boldsymbol{u}$, of which the characteristic equation is

$$\sigma^2 + Q_{2\mathrm{D}} = 0, \tag{6.180a}$$

where

$$Q_{2\mathrm{D}} = \begin{vmatrix} u_{,x} & v_{,x} \\ u_{,y} & v_{,y} \end{vmatrix} = \frac{1}{2}(\|\boldsymbol{\Omega}\|^2 - \|\mathbf{D}\|^2) = \frac{1}{4}\omega^2 - \frac{1}{2}\|\mathbf{D}\|^2. \tag{6.180b}$$

is the second invariant of $\nabla \boldsymbol{u}$ (and also the negative of the discriminant $\Delta_{2\mathrm{D}}$; the first invariant is $\mathrm{tr}(\nabla \boldsymbol{u}) = 0$). Here we have used the notation $\|\mathbf{S}\| \equiv [\mathrm{tr}(\mathbf{S} \cdot \mathbf{S}^{\mathrm{T}})]^{1/2}$ for any tensor $\mathbf{S}$. When $Q_{2\mathrm{D}} > 0$ at a point, we have purely imaginary eigenvalues $\pm \mathrm{i}\sigma_i = \pm \mathrm{i}\sqrt{Q_{2\mathrm{D}}}$ and the flow there is called *elliptic* (otherwise is *hyperbolic*), which can measure how much the vorticity prevails over the strain rate. Thus, a vortex is defined as a connected fluid region with

$$Q_{2\mathrm{D}} = -\Delta_{2\mathrm{D}} = \sigma_i^2 > 0, \tag{6.181}$$

known as the *Weiss criterion*. In particular, for a two-dimensional axisymmetric vortex, by (6.179) there is

$$Q_{2\mathrm{D}} = \frac{1}{4}\left\{ \left[ \frac{1}{r}\frac{\partial}{\partial r}(rv) \right]^2 - \left[ r\frac{\partial}{\partial r}\left(\frac{v}{r}\right) \right]^2 \right\} = \frac{v}{r}\frac{\partial v}{\partial r} \tag{6.182}$$

and (6.181) precisely defines the vortex as the fluid within $r = r_0$ where $v = \max$, in consistency with our common concept of vortex core. The Weiss criterion has successfully passed the DNS tests for various two-dimensional turbulence (e.g., Brechet et al. 1988; Basdevant and Philipovich 1994).

Controversy on defining a vortex appears once we enter three-dimensional flow. The characteristic equation for the eigenvalues of $\nabla \boldsymbol{u}$ is

$$\sigma^3 + Q\sigma - R = 0, \tag{6.183}$$

where

$$Q \equiv -\frac{1}{2}u_{i,j}u_{j,i} = \frac{1}{2}(\|\mathbf{\Omega}\|^2 - \|\mathbf{D}\|^2)$$
$$= \frac{1}{2}\left(\frac{1}{2}\omega^2 - \|\mathbf{D}\|^2\right) = \sigma_1\sigma_2 + \sigma_1\sigma_3 + \sigma_2\sigma_3, \tag{6.184a}$$

$$R \equiv \det(u_{i,j}) = \frac{1}{3}u_{i,j}u_{j,k}u_{k,i}$$
$$= \frac{1}{3}\left(D_{ij}D_{jk}D_{ki} + 3D_{ij}\Omega_{jk}\Omega_{ki}\right) = \sigma_1\sigma_2\sigma_3 \tag{6.184b}$$

are the second and third invariants of $\nabla \boldsymbol{u}$, respectively. The discriminant of (6.183) is

$$\Delta = \left(\frac{Q}{3}\right)^3 + \left(\frac{R}{2}\right)^2. \tag{6.185}$$

Consequently, in three dimensions the question on how much the vorticity should prevail over the strain rate may have two possible answers, both being within kinematics: either

$$\Delta > 0 \tag{6.186}$$

or

$$Q > 0. \tag{6.187}$$

These are known as the *$\Delta$-criterion* (Dallmann 1983; Chong et al. 1990) and *$Q$-criterion* (Hunt et al. (1988)), respectively. The $Q$-criterion can be equally expressed in terms of the *kinematic vorticity number* $m$ introduced by Truesdell (1953) in both two and three dimensions:

$$m \equiv \frac{\|\mathbf{\Omega}\|}{\|\mathbf{D}\|} = \frac{\omega}{\sqrt{2}\|\mathbf{D}\|} > 1. \tag{6.188}$$

Moreover, in an axisymmetric stretch-free vortex, (6.18a) indicates that the centrifugal acceleration can only be balanced by the radial pressure gradient, so in each $(r, \theta)$-plane the pressure is minimum at the vortex center. This *sectional pressure-minimum* has been observed in some (not all) complicated vortices. One remarkable example is strong vortex filaments in turbulence with sectional diameter of the smallest possible turbulence scale, the *Kolmogorov dissipation scale* (Chap. 10). Thanks to the low-$p$ property, such vortex filaments can be experimentally visualized (Douady et al. 1991). This property has also been considered as a *dynamic* criterion for defining at least a class of *low-pressure vortices*.

To assure the low-pressure feature in an axial vortex, Hunt et al. (1988) proposed to add the low-pressure condition to (6.187). Jeong and Hussain (1995) proposed a replacement of these two conditions by a single one, that the *vorticity-induced* pressure is sectionally minimum in a vortex. They start from the gradient of the incompressible Navier–Stokes equation

$$a_{j,i} = -\frac{1}{\rho} p_{,ij} + \nu u_{j,ikk}, \tag{6.189}$$

where $a_{j,i}$ can be decomposed into symmetric and antisymmetric parts

$$a_{j,i} = \left( \frac{\mathrm{D}}{\mathrm{D}t} D_{ij} + \Omega_{ik}\Omega_{kj} + D_{ik}D_{kj} \right) + \left( \frac{\mathrm{D}}{\mathrm{D}t} \Omega_{ij} + \Omega_{ik}D_{kj} + D_{ik}\Omega_{kj} \right). \tag{6.190}$$

While the antisymmetric part just leads to the vorticity transport equation, the symmetric part yields

$$-\frac{1}{\rho} p_{,ij} = \frac{\mathrm{D}}{\mathrm{D}t} D_{ij} - \nu D_{ij,kk} + \Omega_{ik}\Omega_{kj} + D_{ik}D_{kj}. \tag{6.191}$$

In a plane the local pressure reaches a minimum at a point if the tangent gradient of $p$ vanishes there, and the second-order derivatives along two orthogonal tangent directions are both positive. Since $p_{,ij}$ is a symmetric tensor, the objective choice of the plane can be made in a principal-axis coordinate systems, where the plane is spanned by the two eigenvectors of $p_{,ij}$ and for $p$ to be minimum the associated two eigenvalues must be both positive (the third eigenvalue is the smallest). The eigenvalues of $p_{,ij}$ can be found from the right-hand side of (6.191), but for picking up the vorticity-induced $p_{\min}$ the effect of the material derivative of $D_{ij}$ (invariant following a fluid element) and its viscous diffusion should be excluded. Thus, the problem amounts to the real eigenvalues $\lambda_1 \geq \lambda_2 \geq \lambda_3$ of the symmetric tensor

$$\mathbf{G} \equiv \mathbf{D} \cdot \mathbf{D}^{\mathrm{T}} - \boldsymbol{\Omega} \cdot \boldsymbol{\Omega}^{\mathrm{T}}, \tag{6.192}$$

and the sectional pressure-minimum induced by a vortex is ensured by requiring the second eigenvalue of $\mathbf{G}$ be negative:

$$\lambda_2 < 0. \tag{6.193}$$

This is known as the $\lambda_2$-*criterion.* In two dimensions, one simply has $G_{\alpha\beta} = -Q_{2\mathrm{D}}\delta_{\alpha\beta}$, so (6.192) returns to (6.180b) and the $\Delta$-, $Q$-, and $\lambda_2$-criteria are all identical.

In their study of educing low-$p$ vortices, Kida and coworkers (e.g., Kida and Miura 1998) reconsidered the sectional $p_{\min}$ problem directly based on tensor $p_{,ij}$. The sectional plane was chosen to perpendicular to the third eigenvector associated with the smallest eigenvalue of $p_{,ij}$, say $\boldsymbol{e}_p$. These authors then apply the sectional minimum-pressure criterion to obtain the candidate of a *vortex axis.* To pick up $p_{\min}$ caused by vortices only, on the sectional plane the elliptic condition (6.181) is applied simultaneously. Then, the vortex core is defined as a radially concave region ($\partial^2 p/\partial r^2 > 0$) around each axis so that the core boundary is given by the inflection surface (Makihara et al. 2002).

Extensive numerical tests of the above three-dimensional invariant criteria have been conducted by many authors (e.g., Jeong and Hussain 1995; Kida

and Miura 1998; Cucitore et al. 1999; Dubief and Delcayre 2000) for various vortices, including exact isolated vortex solutions (some have been given in this chapter) and complex turbulent coherent vortices. These authors reported that, roughly speaking, the $\Delta$-criterion sometimes covers too much vortical flow region; the $Q$- and $\lambda_2$-criteria educe quite similar vortex plots in most tested cases, but the former may miss a part of vortex; the $\lambda_2$-isosurfaces cannot always capture the pressure minimum and also sometimes covers too much space to visualize the coherent vortex structure neatly, while in some other cases it may cut a connected vortex into segments as well. No commonly agreed conclusion has been reached.

### 6.6.2 An Analytical Comparison of the Criteria

In searching for a rational definition of a vortex, numerical tests are insufficient, because without knowing what is a vortex a priori the judgment of which criterion educes the best vortex patterns in complex flows cannot be completely objective. What is needed is a clear insight on the physical root of the difference between various proposed criteria, which can be gained only by theoretical diagnosis. We do this later, based on the *canonical matrix* of the tensor $\nabla \boldsymbol{u}$ introduced by Chong et al. (1990).

Since among various proposed criteria (6.186) is a condition that the others all satisfy, we proceed under the assumption that (6.183) has a pair of complex conjugate roots $\sigma_{1,2} = \sigma_r \pm \mathrm{i}\sigma_i$ and a real root $\sigma_3 = -2\sigma_r$. Then there exists a transforming matrix $\mathbf{P}$ such that after transformation ($\boldsymbol{x}$ and $\boldsymbol{y}$ are column matrices)

$$\mathbf{A} \to \mathbf{B} = \mathbf{P}^{-1}\mathbf{A}\mathbf{P}, \quad \boldsymbol{x} \to \boldsymbol{y} = \mathbf{P}^{-1}\boldsymbol{x}, \tag{6.194a,b}$$

the matrix representation $\mathbf{A}$ of $\nabla \boldsymbol{u}$ in an orthonormal coordinate system $(\boldsymbol{e}_1, \boldsymbol{e}_2, \boldsymbol{e}_3)$ is transformed to the canonical form

$$\mathbf{B} = \begin{bmatrix} \sigma_r & -\sigma_i & 0 \\ \sigma_i & \sigma_r & 0 \\ 0 & 0 & -2\sigma_r \end{bmatrix}. \tag{6.195}$$

Then the linear dynamic system

$$\frac{\mathrm{d}y_i}{\mathrm{d}t} = B_{ij}y_j, \quad i,j = 1,2,3$$

can be invariantly decomposed into the direct sum of a two-dimensional system and a one-dimensional system

$$\frac{\mathrm{d}x'_\alpha}{\mathrm{d}t} = A'_{\alpha\beta}x'_\beta, \quad \alpha,\beta = 1,2,$$

$$\frac{\mathrm{d}x'_3}{\mathrm{d}t} = \sigma_3 x'_3 \quad \text{i.e.,} \quad x'_3 = C\mathrm{e}^{\sigma_3 t}.$$

It then suffices to study the system in the invariant plane spanned by the complex eigenvectors $\boldsymbol{w} = \boldsymbol{p} \pm \mathrm{i}\boldsymbol{q}$ associated with $\sigma_r \pm \mathrm{i}\sigma_i$, where $\boldsymbol{p}$ and $\boldsymbol{q}$ are real vectors. We denote the normal of the $\boldsymbol{w}$-plane by $\boldsymbol{e}_3'$. The transforming matrix $\mathbf{P}$ is constructed by taking $(\boldsymbol{q}, \boldsymbol{p})$ as its columns (e.g, Hirsch and Smale 1974). In general, the transformation (6.194b) is *skewed* with $\boldsymbol{e}_3' \neq \boldsymbol{e}_3$, and hence $\mathbf{B}$ does not represent any real velocity-gradient tensor in physical space. However, $\mathbf{B}$ retains the same $\sigma$, $Q$, and $\Delta$, which is all what we need. An elliptical fixed point on the $\boldsymbol{w}$-plane has polar-coordinate expression (Chong et al. 1990)

$$r = C\mathrm{e}^{k\theta}, \quad k \equiv \frac{\sigma_r}{\sigma_i}, \tag{6.196}$$

where $C > 0$ depends on initial conditions.

Now, in terms of $\sigma_i$ and $k$ we have

$$\Delta = \frac{\sigma_i^6}{27}(1 + 9k^2)^2, \quad Q = \sigma_i^2(1 - 3k^2).$$

Hence, the $\Delta$- and $Q$-criteria amount to

$$\Delta\text{-criterion}: \quad \sigma_i^2 > 0; \tag{6.197}$$

$$Q\text{-criteron}: \quad \sigma_i^2 > 0, \quad -\frac{1}{\sqrt{3}} < k < \frac{1}{\sqrt{3}}. \tag{6.198}$$

Namely, the $\Delta$-criterion is not affected by the axial-strain ratio $k$ and always equivalent to (6.180b) with effective ingredient $Q_{2\mathrm{D}} = \sigma_i^2$, but now the subscript 2D stands for the invariant two-dimensional subspace. In contrast, the $Q$-criterion sets an upper bound for $k$, beyond which a swirling flow is not supposed to be a vortex.

Unlike the $\Delta$- and $Q$-criteria, the $\lambda_2$-criterion is based on a different invariant set of $\mathbf{G}$ defined by (6.192). To compare it with the preceding two, therefore, we re-express the eigenvalues of $\mathbf{G}$ by those of $\mathbf{A}$. For simplicity, assume the vortex axis is normal to the $\boldsymbol{w}$-plane, so that we only need to consider a $2 \times 2$ matrix of (6.179), symbolically denoted by

$$\mathbf{A} = \begin{bmatrix} a & b \\ -c & d \end{bmatrix} \tag{6.199}$$

with complex eigenvalues

$$\sigma_{1,2} = \frac{1}{2}(a + d) \pm \frac{\mathrm{i}}{2}\sqrt{4bc - (a - d)^2}, \quad (a - d)^2 < 4bc. \tag{6.200}$$

In this case

$$\mathbf{G} = \begin{bmatrix} a^2 - bc & (b - c)\sigma_r \\ (b - c)\sigma_r & d^2 - bc \end{bmatrix}. \tag{6.201}$$

But by (6.200) there is

$$bc = \sigma_i^2 + \frac{1}{4}(a-d)^2, \quad \sigma_r^2 = \frac{1}{4}(a+d)^2,$$

which enables writing the characteristic equation of (6.201) as

$$\lambda^2 - 2(\sigma_r^2 - \sigma_i^2)\lambda + (\sigma_r^2 - \sigma_i^2)^2 - \sigma_r^2[(a-d)^2 + (b-c)^2] = 0. \tag{6.202}$$

Consequently, under the assumed condition (6.193) yields an inequality equation

$$-\sigma_r^2 - \sigma_r\sqrt{(a-d)^2 + (b-c)^2} + \sigma_i^2 > 0,$$

of which the solution is

$$\sigma_i^2 > 0, \quad -(\sqrt{1+\beta^2} + \beta) < k < \sqrt{1+\beta^2} - \beta, \tag{6.203a}$$

where

$$\beta \equiv \frac{1}{2|\sigma_i|}\sqrt{(a-d)^2 + (b-c)^2}. \tag{6.203b}$$

We can now explore the physical root of the difference between the $Q$-, $\Delta$-, and $\lambda_2$-criteria. As seen from (6.196), for fixed $\sigma_i$ the larger $|k|$ is, the faster the streamlines merge into or diverge out of the fixed point, owing to the stronger strain rate $-2\sigma_r = -2k\sigma_i$ along the the principal direction $\boldsymbol{e}_3$ of $\nabla\boldsymbol{u}$. If the vortex axis has unit vector $\boldsymbol{e}_v$ and $\boldsymbol{e}_v = \boldsymbol{e}_3$, $k$ reflects the *axial strain ratio*. But, *there is no physical reason to set any upper bound to the axial strain*; in particular, an axial stretching with $k < 0$ will enhance the vortex, even if it makes $\|\mathbf{D}\|$ exceed $\|\boldsymbol{\Omega}\|$. Alternatively, if $\boldsymbol{e}_v \neq \boldsymbol{e}_3$, since they are not orthogonal in a generic vortex, permitting an arbitrary axial strain must requires permitting an arbitrary $\sigma_r$ or $k$. This key observation explains why some educed vortices based on the $Q$-criterion (6.187) may exhibit hollow or broken regions (Jeong and Hussain 1995). Then, the $\lambda_2$-criterion imposes unequal bounds for $k$, more stringent for shrink ($k > 0$) and looser for stretch ($k < 0$). Thus, the criterion is somewhat superior to the $Q$-criterion, and indeed it has helped study near-wall coherent structures (Jeong et al. (1997); Schoppa and Hussain (2002)). But, by (6.203), the $\lambda_2$-criterion may also break a vortex at locations with strong axial stretching (e.g., Kida and Miura 1998 and Figs. 6.19, 6.21). In contrast, the $\Delta$-criterion solely in terms of the projected flow pattern on the $\boldsymbol{w}$-plane is free from this trouble.

The Kida $p_{\min}$-criterion is not convenient to diagnose based on the invariant $\boldsymbol{w}$-plane but its performance will be exemplified later.

### 6.6.3 Test Examples and Discussion

We now illustrate the preceding diagnosis by considering two familiar vortices, both belonging to *necessary tests* that any general criterion should pass

through. Consider the Burgers vortex first. From (6.34) and (6.179) one easily finds

$$\sigma_r = -\frac{\gamma}{2} < 0, \quad \sigma_i^2 = Q_{2\mathrm{D}} = \frac{v}{r}\frac{\partial v}{\partial r}. \tag{6.204a,b}$$

Since $\boldsymbol{e}_3 = \boldsymbol{e}_v = \boldsymbol{e}_z$, (6.203) can be applied. The $\Delta$-, $Q$-, and $\lambda_2$-criteria are then specified to

$$\Delta = \frac{Q_{2\mathrm{D}}}{27}\left(Q_{2\mathrm{D}} + \frac{9}{4}\gamma^2\right)^2 > 0, \tag{6.205a}$$

$$Q = Q_{2\mathrm{D}} - \frac{3}{4}\gamma^2 > 0, \tag{6.205b}$$

$$-\lambda_2 = Q_{2\mathrm{D}} - \frac{1}{4}\gamma^2 - \frac{\gamma}{2}\left| r\frac{\mathrm{d}}{\mathrm{d}r}\left(\frac{v}{r}\right)\right| > 0, \tag{6.205c}$$

respectively, which can also be directly derived from (6.34). Now, by (6.204a,b), only the $\Delta$-criterion predicts the correct core radius $r_0 = 2.24\sqrt{\nu/\gamma}$ with $v(r_0) = v_{\max}$ for any $\gamma$. The core radius variation as $\gamma$ predicted by the three criteria are compared in Fig. 6.19 for $\beta = 10$, indicating that the $Q$- and $\lambda_2$-criteria may underestimate or even nullify the core radius.

On the other hand, the pressure distribution is

$$\frac{p}{\rho} = -\frac{1}{8}\gamma^2(r^2 + 4z^2) - \int_r^\infty \frac{v^2}{r}\mathrm{d}r,$$

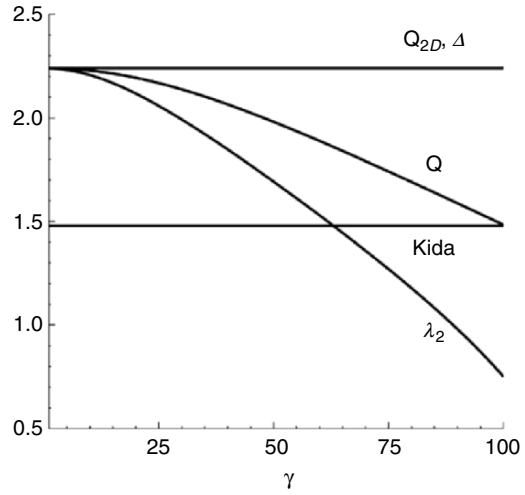


**Fig. 6.19.** Vortex-criteria test by a Burgers vortex with $\beta = 10$. Four predicted core radii $r_0\sqrt{\gamma/\nu}$ vs. $\gamma$. From Wu et al. (2005b)

so the cross-plane Laplacian of $p$ is

$$\frac{1}{r}\frac{\partial}{\partial r}\left(r\frac{\partial p}{\partial r}\right) = 2\left(Q_{2D} - \frac{\gamma^2}{4}\right).$$

Since $Q_{2D} = (\Gamma_0\gamma/8\pi\nu)^2$ at $r = 0$, Kida's $p_{\min}$-criterion requires

$$R_\Gamma = \frac{\Gamma_0}{\nu} > 4\pi, \tag{6.206}$$

otherwise the pressure takes maximum. This imposes a constraint not to $\gamma$ but to the Reynolds number, because at small $Re$ the centrifugal acceleration is mainly balanced by diffusion rather than pressure gradient. Unfortunately, as Kida and Miura (1998) have noticed and is plotted in Fig. 6.19 as well, the proposed concave condition $\partial^2 p/\partial r^2 > 0$ yields a core radius $1.48\sqrt{\nu/\gamma}$, smaller than the correct value by 34%.

The Burgers vortex is quite special since it has $\boldsymbol{e}_v = \boldsymbol{e}_3 = \boldsymbol{e}_3'$ and given axis location. In general, as a preferred direction permitting arbitrary strain, the vortex axis and its location must be clearly identified. This issue is nontrivial for those vortices with complicated shapes (Robinson 1991b). To further test the criteria, we need a vortex solution with both axial stretching and multiple vorticity components. Thus, let us turn to the two-cell Sullivan vortex (6.42) to (6.44). Its invariant $\boldsymbol{w}$-plane is found to coincide with the $(r, \theta)$-plane, i.e., $\boldsymbol{e}_v = \boldsymbol{e}_3'$; but the $\boldsymbol{\omega}$-lines and $\boldsymbol{e}_3$ form different spirals. Owing to (6.205a), it suffices to use the $Q_{2D}$-criterion to represent the effective part of (6.186). $\Delta$ or $Q_{2D}$ and $Q$ are functions of $r$ only, and numerical calcuation indicates that $\lambda_2$ is almost independent of $z$ except a small neighborhood of $(r, z) = (0, 0)$.

We set $\beta = 10$ again in calculation. In Figs. 6.20 and 6.21 we plot the $r$-dependence of $Q_{2D}$, $Q$, and $-\lambda_2$ at $z = 1$, resepctively, with $\gamma$ being a parameter. The sign of $Q_{2D}$ depends on the local competition of fluid rotation and radial strain, and takes a local minimum common to all $\gamma$ at $r = 0$. For small $\gamma$, while the $Q_{2D}$- and $\lambda_2$-criteria educe a single vortex with outer boundary larger than the limit cycle $r_0 = 3.36\sqrt{\nu/\gamma^2}$, the $Q$-criterion educes a hollow vortex. As $\gamma$ increases, the $Q_{2D}$-criterion educes a hollow vortex surrounding a thin vortex centered at the $z$-axis, but the region with $Q > 0$ disappears first, and then that with $-\lambda_2 > 0$. Therefore, as predicted by (6.198) and (6.203), the $Q$- and $\lambda_2$-criteria suffer from the same qualitative limitation. On the other hand, the $Q_{2D}$-criterion divides the Sullivan vortex into three subclasses as $\gamma$ varies but never denies the existence of the vortex.

Note that $Q_{2D}$ is not affected by the azimuthal vorticity $\omega_\theta$ on the $\boldsymbol{w}$-plane, which alone does not forms any axial structure. In other words, *a swirling flow is recognized as a vortex due solely to its axial vorticity.*[5] Thus one sees a general fact that, as a result of allowing for the arbitrariness of axial strain, the azimuthal and radial vorticity components should also have certain arbitrariness (subjected to some kinematic and dynamic constraints) and not

[5] This is also true for a swirling vortex ring, see Sect. 6.3.4.

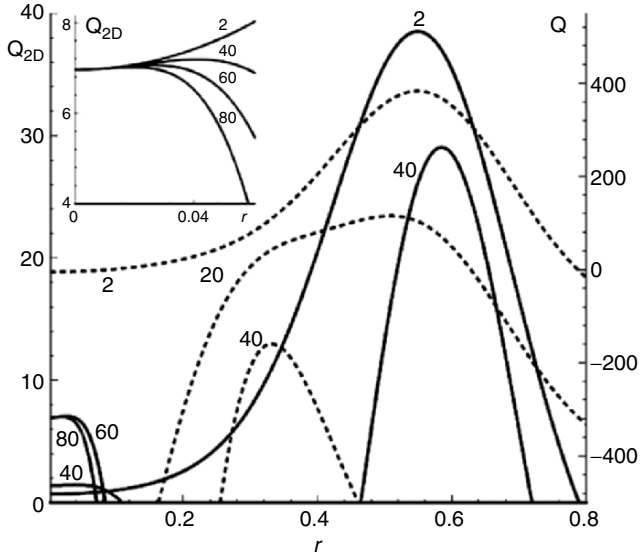


**Fig. 6.20.** The $r$-dependence of $Q_{2D}$ (*solid line*) and $Q$ (*dashed line*) for $\beta = 10$ and different $\gamma$ (values marked in the plot). To make the plot compact, the $Q_{2D}$ curves for $\gamma = 2$ and 40 are scaled down by 10 and 5 times, respectively. The upper-left zoom-in plot shows the behavior of $Q_{2D}$ at small $r$ in original scale. For $\gamma < 2$ and $\gamma > 60$ the qualitative feature of the curves in this and the next figures remain unchanged. From Wu et al. (2005b)

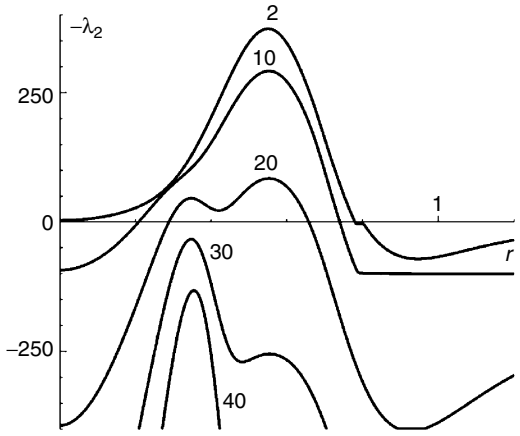


**Fig. 6.21.** The $r$-dependence of $-\lambda_2$ at $z = 1$ for $\beta = 10$ and different $\gamma$ (values marked in the plot). The straight segments are due to the interchange of $\lambda_2 < 0$ and $\lambda_3 < 0$ as the intermediate eigenvalue. From Wu et al. (2005b)

enter the vortex definition.[6] When the vortex axis $\boldsymbol{e}_v$ is aligned to neither the local vorticity nor $\boldsymbol{e}_3$, it seems that a natural kinematic choice would be to define the axis as normal to the invariant $\boldsymbol{w}$-plane or take $\boldsymbol{e}_v = \boldsymbol{e}_3'$.

Finally, it should be stressed that any inequalities like (6.186), (6.187), and (6.193) cannot identify a single line as the vortex axis but only a region as a vortex, in which $\boldsymbol{e}_v$ forms a bundle of axial directions. An equality is necessary for identifying a single axis as Kida's criterion does for low-pressure vortices by an extremal condition. Again, a natural kinematic choice would be $Q_{2D}$ = maximum in the vortex region. If this is accepted, then the axis of the Burgers vortex (and Batchelor vortex) would be retained, but the Sullivan vortex would be identified to have an *annular core* with its radius dependent on $\gamma$.

The preceding analysis and discussions can be summarized as a general requirement for any vortex definition:

*A generally applicable vortex definition should be able to identify the vortex axis and allow for arbitrary axial strain. What matters in the definition should be only the axial vorticity component or rotational motion of the fluid on a cross-plane, compared to the strain rate on that plane.*

## Summary

1. Axial vortices are the existence form of the highest concentration of vorticity. The study of these vortices is considerably benefited by examining a small number of typical vortex solutions of the Navier–Stokes and Euler equations, including single cylindrical vortices without and with axial strain, circular vortex rings, inviscid and viscous strained vortices, and vortex pairs or arrays. These theoretical models are widely used for understanding the basic physics and stability of vortices in reality.
2. A major part of exact vortex solutions were found when the nonlinearity in vorticity transport equation is absent, which is the case if the flow is generalized Beltramian. In particular, for inviscid generalized Beltrami flow there is a big freedom to construct exact vortex solutions. However, this simple class excludes some key effects such as nonuniform axial stretching (a vortex with uniform axial stretching can be cast to a vortex without axial stretching by the Lundgren transformation). Only a few truly nonlinear analytical vortex solutions are available, but in most of them different components are still artificially decoupled. The known nonlinear solutions with naturally coupled components as required by boundary conditions are even rarer.

[6] The Batchelor vortex (or $q$-vortex) (6.19) also has both axial and azimuthal vorticity components with helical vorticity lines. But due to the absence of axial strain, all the four considered criteria yield the correct core radius, because their effective ingredients are all simply (6.182).

3. The exactness of viscous or inviscid vortex solutions does not ensure that they are physically realistic, because they can hardly satisfy all physical conditions, such as the finiteness of the total kinetic energy and angular momentum. No isolated straight columnar vortex with nonzero total circulation is realistic. In reality, a vortex (or a segment of a curved vortex) is constantly in a strained field induced by other vortices (or other segments of the same curved vortex). In most cases the solutions for strained vortices can be found only approximately, for example by matched asymptotic expansion or other singular perturbation methods.
4. How to define an axial vortex in three dimensions is a subtle issue. While in many studies of vortex dynamics a qualitative definition is sufficient, quantitative criteria becomes necessary in understanding vortex structures, their evolution and interactions in very complicated flows especially in turbulence. A rational criterion must be invariant under Galilean and coordinate transformations, free from artificially defined threshold values, and should also be able to identify the vortex axis and allow for arbitrary axial strain. So far the definition problem still remains an open issue.

# 7

# Separated Vortex Flows

This chapter discusses global *separated flow*. We first introduce a general theory in Sect. 7.1 on the topological behavior of separated flow as well as the structural stability and bifurcation of the separated flow, where a discussion on the classification of flow separation will also be made. We then address two basic types of steady separated flow, the *separated bubble flow* and *free vortex-layer separated flow*, in Sects. 7.2 and 7.3, respectively. In a separated bubble flow, the separation stream surface (defined in Sect. 5.1) and a part of the solid wall from which the separation occurs form a closed boundary of the separated vortex bubble. Hence, the flow inside the bubble is isolated from external free stream and has only weak distributed vorticity. In contrast, in a free vortex-layer separated flow the fluids at both sides of the separation stream surface come from the same free stream. Thus, the separated vortices formed thereby are much stronger than that in closed bubbles. This difference makes the latter more important in engineering applications.

Unsteady separated flow is far more complicated than either type of steady separated flows, which we discuss in Sect. 7.4 with focus on its rich phenomena and relevant vorticity-vortex dynamics mechanisms.

## 7.1 Topological Theory of Separated Flows

In Sect. 5.2.1 we have mentioned the concept of fixed points or critical points of a the vector field. Like the knottness and tangledness of a vector field discussed in Sect. 3.3.2, the number and types of fixed points and closed pathlines as well as their connection by trajectories are the topological property of the flow, which for a given solid body may change as the flow condition varies, from simple to complex. Thus the flow topology is a powerful tool to rationally interpret separated-flow patterns over various configurations, obtained experimentally or numerically. This approach, based on Poincaré's (1882) qualitative theory of ordinary differential equations, was introduced to the studies

of three-dimensional separated flows by Legendre (1956) and Lighthill (1963); for reviews see Tobak and Peake (1982) and Délery (2001).

Like the flow separation theory of Sect. 5.2, the topological theory of separated flow is also based on the full Navier–Stokes equation with assumed analytic property, so that the Taylor expansion (5.10) exists. Although it can be applied to instantaneous unsteady flow (e.g., Srygley and Thomas 2002), the main development of the topological theory is for steady and incompressible flow which we assume in this section.

### 7.1.1 Fixed Points and Closed Orbits of a Dynamic System

Consider a general dynamic system (say, in three-dimensional space)[1]

$$\dot{\boldsymbol{x}} = \boldsymbol{f}(\boldsymbol{x}), \tag{7.1}$$

where the dot denotes $d/dt$ (in (5.6) $t$ is replaced by rescaled variable $s$) and $\boldsymbol{f}$ does not contain $t$ explicitly, as in the case of steady flows. Such a system is said to be *autonomous*. A *fixed point* or *critical point* $\bar{\boldsymbol{x}}$ is a stationary solution of (7.1), i.e., $\boldsymbol{f}(\bar{\boldsymbol{x}}) = \boldsymbol{0}$ or $\boldsymbol{x} = \bar{\boldsymbol{x}}$ for all $t$. If $\bar{\boldsymbol{x}}$ is the unique fixed point in its neighborhood, it is said to be *isolated*. In addition, if (7.1) has a solution $\boldsymbol{x}(t+T) = \boldsymbol{x}(t)$, then the pathline (trajectory, orbit) forms a *closed orbit*.

We have seen that a general flow separation can be studied by the low-order Taylor expansion of the governing equations, especially the linearization of (5.6), in a small neighborhood of an on-wall point. Now the linearization of (7.1) around a fixed point $\bar{\boldsymbol{x}}$ is also the basis of studying the topological property of the nonlinear system (7.1). In a convenient coordinate frame $(x_1, x_2, x_3)$, this linearized system reads

$$\dot{\boldsymbol{x}} = D\boldsymbol{f}(\bar{\boldsymbol{x}})\boldsymbol{x}, \tag{7.2a}$$

where

$$D\boldsymbol{f}(\boldsymbol{x}) \equiv \frac{\partial(f_1, f_2, f_3)}{\partial(x_1, x_2, x_3)} \tag{7.2b}$$

is the Jacobian matrix of $\boldsymbol{f}$ at $\boldsymbol{x}$. The solution behavior of (7.2) is completely determined by the eigenvalues $\lambda_k$ of the Jacobian matrix $D\boldsymbol{f}(\bar{\boldsymbol{x}})$, and can be constructed from eigenvectors $\mathrm{e}^{\lambda_k t}\boldsymbol{x}_k$. Then, if (7.2) has no eigenvalue with real part zero, it is called a *hyperbolic linear system*, and its fixed points are called hyperbolic (or nondegenerate) fixed points. *Hyperbolic fixed points* are robust, and we have the following theorem (e.g., Hirsch and Smale 1974; Guckenheimer and Holmes 1983):

[1] For clear definitions and a detailed index of relevant terminology of this section see, e.g., the textbook of Hale and Koçak (1991).

**Hartman–Grobman Theorem.** *If $\bar{\boldsymbol{x}}$ is an isolated hyperbolic fixed point of (7.1), then there is a neighborhood of $\bar{\boldsymbol{x}}$ in which $\boldsymbol{f}$ is topologically equivalent to the linear vector field (7.2).*

Depending on whether neighboring trajectories will approach, leave, or stay around a fixed point or closed orbit as $t \to \infty$, we may classify the fixed points or closed orbits as *asymptotically stable*, *unstable*, or *stable*, respectively. A hyperbolic fixed point can only be unstable or asymptotically stable, which repels or attracts neighboring trajectories. A closed orbit attracting or repelling neighboring trajectories is called a *limit cycle*. If a limit cycle is not surrounded by another one, it is said to be *single*. A single limit cycle is seen in Fig. 6.2.

A three-dimensional system (7.1) can be decomposed into three two-dimensional systems on three orthogonal planes, of which the behavior is easier to examined. In a two-dimensional $(x, y)$-plane, we write (7.1) as

$$\begin{aligned} \dot{x} &= ax + by + P_2(x, y), \\ \dot{y} &= cx + dy + Q_2(x, y), \end{aligned} \tag{7.3}$$

where $P_2, Q_2 = O(r^2)$ with $r = \sqrt{x^2 + y^2}$ are analytic near the origin. The locally linearized system of (7.3) is familiar:

$$\dot{x} = ax + by, \quad \dot{y} = cx + dy, \tag{7.4}$$

of which the eigenvalues $\lambda_1, \lambda_2$ are determined by characteristic equation $\lambda^2 - p\lambda + q = 0$, where $p = \lambda_1 + \lambda_2 = a + d$ and $q = \lambda_1\lambda_2 = ad - bc$. According to the sign of the discriminant $\Delta = p^2 - 4q$, the feature of $\lambda_1$ and $\lambda_2$, and hence the behavior of various fixed points of (7.4), can be inferred. The result is summerized in Fig. 7.1, the *p–q diagram*.

From the figure one sees the following types of fixed points:[2]

1. *Hyperbolic fixed points.* $p \neq 0$ and $q \neq 0$, so both eigenvalues $\lambda_1$ and $\lambda_2$ have nonzero real part:
   - $q < 0$: $\lambda_1, \lambda_2$ are real roots of opposite signs, and the fixed points are unstable *saddles*.
   - $0 < q < (p/2)^2$: $\lambda_1, \lambda_2$ are different real roots of the same sign, and the fixed points are *nodes*, which is stable if $p < 0$ and unstable if $p > 0$.
   - $q > (p/2)^2$: $\lambda_1, \lambda_2$ are conjugate complex roots with nonzero real part, and the fixed points are *spirals*. They are stable if $p < 0$ and unstable if $p > 0$.

[2] The terminology for the classification of fixed points of a two-dimensional vector field is not completely unified in literature. Due to the intuitive analogy with quadratic plane curves, saddles and centers are sometimes called hyperbolic and elliptic fixed points, respectively, while the fixed "points" with $q = 0$ are called parabolic fixed points (e.g., Tabor 1989).

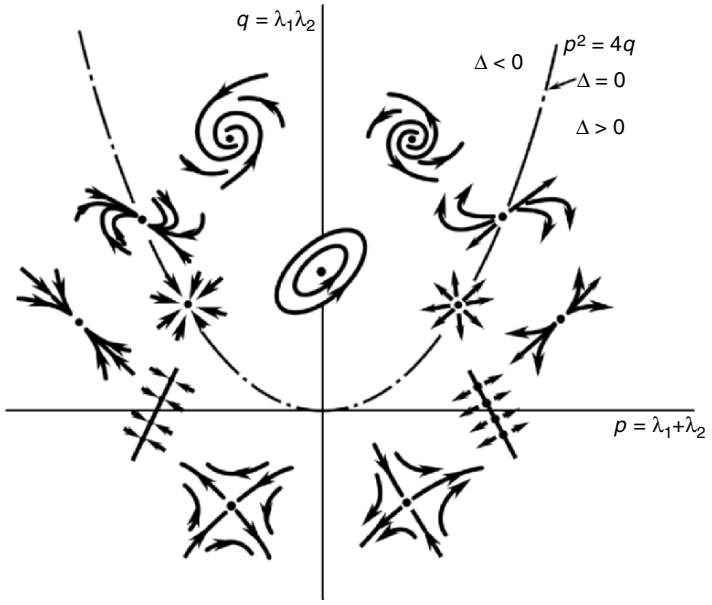


**Fig. 7.1.** The fixed points of two-dimensional linear systems

- $q = (p/2)^2$ and $p \neq 0$: $\lambda_1, \lambda_2$ are the same nonzero real root. In this case, we have *stars* (*critical nodes*) or *inflected nodes* depending on the form of the coefficient matrix being

$$\text{either} \quad \begin{bmatrix} \lambda & 0 \\ 0 & \lambda \end{bmatrix} \quad \text{or} \quad \begin{bmatrix} \lambda & 1 \\ 0 & \lambda \end{bmatrix},$$

  respectively. In the latter case, the trajectories approach the fixed point along a single direction, and tend to be parallel to the same direction again at infinity.

  It is easily seen that node, spiral, and star or inflected node are topologically the same. We refer all of them to as *topological nodes*. An unstable node is called a *source*, while an asymptotically stable node is a *sink*.

2. *Nonhyperbolic fixed points*:
   - $q > 0$ and $p = 0$: $\lambda_1, \lambda_2$ are pure imaginary roots, and the fixed points are *centers* which are merely neutrally stable.
   - $q = 0$ and $p \neq 0$: One of $\lambda_1$ and $\lambda_2$ is zero and the fixed points form a straight line rather than being isolated. The trajectories are a set of parallel straight lines.

By the Hartman–Grobman theorem, nonhyperbolic fixed points cannot retain their topological classes in (7.3). On the other hand, the nonlinear system (7.1) may have more kinds of nonhyperbolic fixed points, called higher-order or multiple fixed points. One such example is the *saddle–node*, consisting half saddle on one side and half node on the other side.

### 7.1.2 Closed and Open Separations

The above classification of fixed points enables a further classification on the local flow separation as a supplement to our discussion in Sect. 5.2. For a fully attached flow over a three-dimensional body surface, there can only be a front stagnation point where the oncoming flow hits the body first, and a rear stagnation point where the flow leaves the body. They are source and sink of the $\boldsymbol{\tau}_w$-field, respectively. But, if the $\boldsymbol{\tau}_w$-field has a saddle $O$, the two special $\boldsymbol{\tau}$-lines leaving $O$ will attract neighboring $\boldsymbol{\tau}$-lines and satisfy the converging condition (5.23), but repel neighboring streamlines above the wall and satisfy the upwelling condition (5.25). These special $\boldsymbol{\tau}$-lines are identified as separation lines by Lighthill's (1963). Then, as sketched in Fig. 7.2, from each separation line grows a separation stream surface, on which all streamlines must emanate from $O$ (Wu et al. 1988a), so $O$ is a *seminode* on this stream surface. On the normal plane perpendicular to the separation stream surface the projected velocity field will see $O$ as a *semisaddle*. This type of separation pattern initiating at a saddle of the $\boldsymbol{\tau}_w$-field is called the *closed separation*.

If in Fig. 7.2 the direction of all $\boldsymbol{\tau}_w$-lines and streamlines is reversed, and meanwhile the qualifiers "attracting" and "repelling" are exchanged, then one obtains possible patterns of *closed reattachment*.

In Sect. 5.2 we left the exact identification of a separation line, say $L$, an open issue. Now since for closed separation $L$ must uniquely initiate from a saddle of the $\boldsymbol{\tau}$-field, it can be unambiguously identified. What remains is to find the end point of $L$. Still in terms of the fixed points of the $\boldsymbol{\tau}$-field, Zhang (1985a) has shown that a closed separation line starting from a saddle must terminate at an attracting *node* or *spiral*. To this list Surana et al. (2005a) added that a closed separation line may also terminate at an attracting *limit*

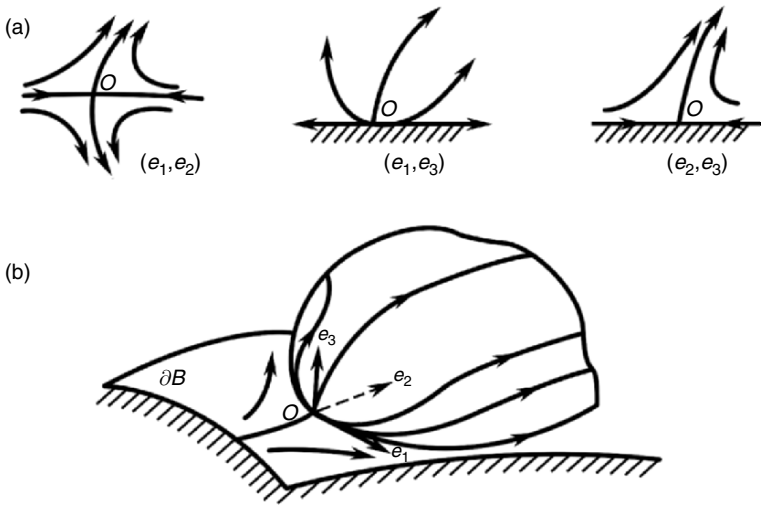


**Fig. 7.2.** Closed separation initiated from a saddle of the $\boldsymbol{\tau}_w$-field

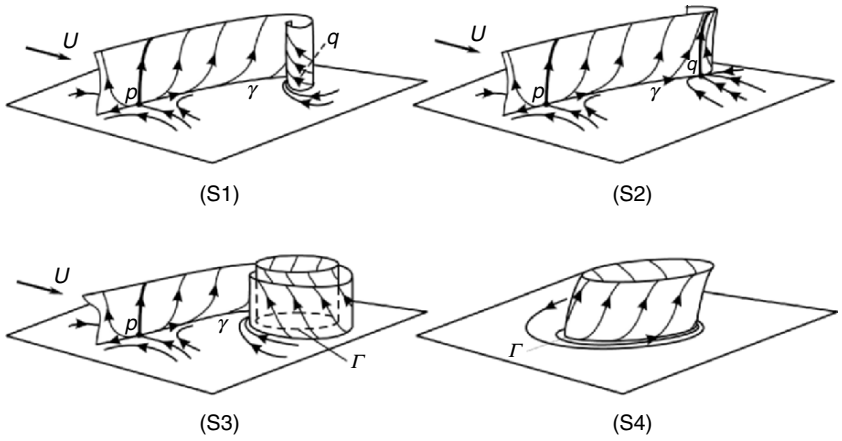


**Fig. 7.3.** The four robust closed separation patterns S1–S4. The separation line is denoted by $\gamma$. In terms of the fixed points of the $\boldsymbol{\tau}$-field on the wall, for S1 and S2 $\gamma$ initiates at a saddle $p$ and terminates at a spiral ($q$ in S1), a node ($q$ in S2), or a limit cycle $\Gamma$ in S3. In S4 $\gamma$ is simply a stable limit cycle $\Gamma$. From Surana et al. (2005a)

*cycle* or just be such a limit cycle. Based on the *invariant manifold theory*, these authors proved that any robust closed separation patterns, which deform smoothly but survive under small disturbance to the flow field, can only be these four kinds, see the sketches in Fig. 7.3. The corresponding separation stream surfaces can then be determined, with the exact formula (5.34) and its extension to curved wall describing their slope. Therefore, within the range of closed separation, the theory of generic steady flow separation is complete.

In addition to the closed separation, however, one cannot exclude the situation where the $\boldsymbol{\tau}$-lines emanating from the front node gradually turn from diverging to converging, causing a separation zone on halfway along the trajectories. Namely, inequalities (5.23) and (5.25) may start to hold at *ordinary points* of a bundle of $\boldsymbol{\tau}$-lines. This separation pattern has indeed been observed first by Wang (1970), who named it the *open separation*. The vortex formed due to a strong primary open separation may also induce a secondary open separation, with an *open reattachment* in between. This is actually the case shown in Fig. 5.1 and analyzed in Sect. 5.2 without concerning any fixed point of the $\boldsymbol{\tau}_w$-field. The flow-visualization experiment of Wang et al. (1990) demonstrates that for the flow over such a prolate spheroid, when the incidence gradually increases from zero, the separation pattern changes from closed type to open type and back to closed type again. Two situations are shown in Fig. 7.4.

The existence of open separation has been confirmed by several experiments as reviewed in Wang (1997). However, in contrast to closed separation,

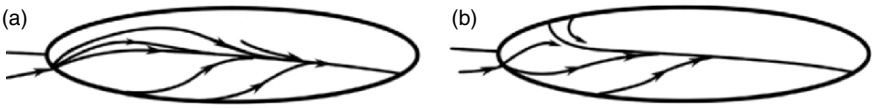


**Fig. 7.4.** (**a**) Open and (**b**) closed separation from prolate spheroid. From Wang (1982)

open separation is a stranger to the dynamic system theory and the topological theory. Surana et al. (2005a) argued that, within the invariant manifold theory, an open separation line segment is no more distinguished than any other segments in the separation zone. This makes it impossible to uniquely identify an open separation line and associated separation stream surface with well-defined slope. Moreover, the appearance of an open separation at ordinary points of some $\boldsymbol{\tau}$-lines emanating from the front node does not alter the topology of the separated flow to be discussed later (e.g., Tobak and Peake 1982), which makes it less certain to identify the qualitative behavior of a specific separated flow by its global topological structure.

So far the only available criteria applicable to open separation zone and separation line is the approximate relations (5.26) and (5.27). The slope of open separation stream surface may be approximately expressed by (5.30). Fortunately, the observed evidence of open separation has been exclusively for large-$Re$ boundary-layer separation, characterized by the boundary layer breaking away and formation of separated free shear layer. This is likely the only circumstance for open separation to occur. As a physical reality, a further theoretical study of open separation is highly desired.

The approximate relations (5.26), (5.27), and (5.30) may be equally applicable to closed separation if it becomes strong away from the upstream saddle.

The concepts of closed and open separation only involve the initial behavior of a separation line, which are less global than the concept of separated flow in the entire flow field. In particular, closed and open separations should not be confused with bubble-type and free vortex-layer types of separated flows, respectively, defined in the beginning of this chapter. While any sufficiently strong open separation must lead to free vortex-layer separated flow and hence is always associated with strong separated vortices, a closed separation may lead to a separated flow of either bubble type or free vortex-layer type. The latter may equally result in strong separated vortices; of which examples include the prolate-spheroid separated flow in Fig. 7.4b, the leading-edge vortices to be shown in Fig. 7.7, the necklace vortices to be shown in Fig. 7.29, and the hemisphere–cylinder separated flow to be shown in Fig. 10.45.

On the other hand, free vortex-layer type of separated flow can be either steady (in three dimensions only) and unsteady (e.g., the Kármán vortex street

behind circular cylinder to be addressed in Sect. 7.4); but most of bubble-type separated flows only exist under special conditions and are steady.

It should also be stressed that the concepts of closed and open separation as well as both types of separated flow apply well to turbulent flow, at least in certain averaged sense (e.g., Reynolds or ensemble average). Thus, when we discuss complex turbulent shear flow in Sect. 10.6, these concepts will be revisited and further clarified.

### 7.1.3 Fixed-Point Index and Topology of Separated Flows

Rewrite system (7.2) as

$$\dot{x} = P(x, y), \quad \dot{y} = Q(x, y), \tag{7.5}$$

which defines a two-dimensional vector $(P, Q)$. Let $C$ be a sufficiently small single closed curve that does not meet any fixed point of (7.5). Let a point move along $C$ a cycle counterclockwise, see Fig. 7.5, such that the vector $(P, Q)$ turns $j$ rounds over an angle $2\pi j$. The integer $j$ can be expressed by

$$j = \frac{1}{2\pi} \oint_C \mathrm{d}\left(\tan^{-1}\frac{Q}{P}\right) = \frac{1}{2\pi} \oint_C \frac{P\mathrm{d}Q - Q\mathrm{d}P}{P^2 + Q^2}. \tag{7.6a}$$

From Fig. 7.5 it is evident that, if $C$ is a closed path of (7.5) enclosing $(P, Q) = (0, 0)$ then $j = \pm 1$, while if $C$ does not enclose any fixed point then $j = 0$. This assertion is independent of the shape of $C$ since it can be continuously changed to another closed curve. We call $j$ the *index* of the fixed point, which is a topological feature.

To compute $j$ for various isolated fixed points, let the origin be at a hyperbolic fixed point so that it suffices to consider the linearized system (7.4). Take a small circle of radius $\delta$ surrounding the origin, such that $x = \delta\cos\theta$

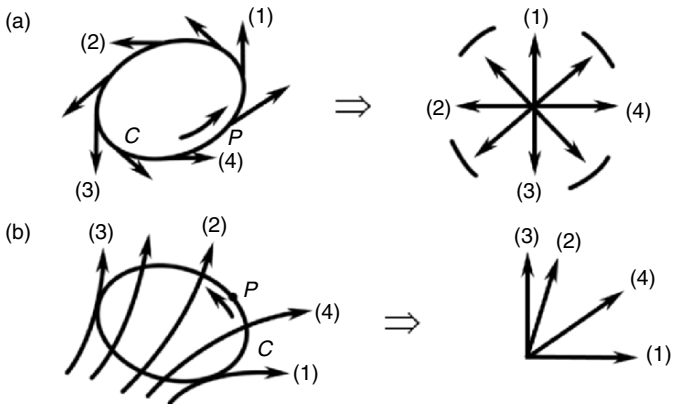


**Fig. 7.5.** Schematic interpretation of the index of a fixed point

and $y = \delta \sin\theta$, and substitute into the linearized version of (7.6a). We then obtain

$$j = \frac{ad - bc}{|ad - bc|}, \tag{7.6b}$$

where $a, b, c$, and $d$ are the coefficients in (7.4). Thus, Fig. 7.1 shows that the index of any nodes (source, sink, or spiral) is $+1$, while that of saddles is $-1$.

On a two-dimensional surface in the three-dimensional space, the sum of the indices of fixed points of a vector field must obey certain rules. For example, on a sphere $\sum j = 2$, and on a torus it is 1, etc. Any closed surface topologically equivalent to these typical shapes have the same $\sum j$. For separated flows, this allows us to identify the possible number and nature of fixed points of the $\boldsymbol{\tau}_w$-field on the body surface and the $\boldsymbol{u}$-field in the space.

The topological rule of $\sum j$ implies a simple relation between the total number of nodes and saddles, denoted by $\sum_{\mathrm{N}}$ and $\sum_{\mathrm{S}}$, respectively, (Hunt et al. 1978; Tobak and Peake 1982; Xia and Deng 1991). First, consider the $\boldsymbol{\tau}$-field and $\boldsymbol{\omega}_{\mathrm{B}}$-field on body surface. For the simplest attached flow over a single-connected closed surface which is topologically equivalent to a sphere, there is $\sum_{\mathrm{N}} = 2$ and $\sum_{\mathrm{S}} = 0$. But if a closed separation from a saddle point happens and hence the flow topology is altered, the general topological rule is

$$\sum_{\mathrm{N}} - \sum_{\mathrm{S}} = 2. \tag{7.7a}$$

Since open separation is not associated with saddles, the flow topology can be the same as that of fully attached flow.[3]

Next, if a three-dimensional body $B$ is connected to a plane P extending to up- and downstream infinity (e.g., a half-wing model mounted on a flat plate in a wind tunnel), then on the surface similar consideration implies

$$\left(\sum_{\mathrm{N}} - \sum_{\mathrm{S}}\right)_{B+\mathrm{P}} = 0. \tag{7.7b}$$

Moreover, let $\mathrm{N}'$ and $\mathrm{S}'$ be the seminode and semisaddle as those appeared on the boundary in a cross section of the flow field (Fig. 7.6). Then, assume a plane cuts one or more solid bodies in the flow field so that the sectional flow on the plane has $m$ isolated and finite holes and the connectivity of the sectional flow is $n = m+1$. Their $j$ must be $\pm 1/2$. Again starting the reasoning from the simplest attached flow, we find on the plane there is

$$\left(\sum_{\mathrm{N}} + \frac{1}{2}\sum_{\mathrm{N}'}\right) - \left(\sum_{\mathrm{S}} + \frac{1}{2}\sum_{\mathrm{S}'}\right) = 1 - n, \tag{7.7c}$$

[3] For this reason Tobak and Peake (1982) call open separation as "local separation", in contrast to the "global separation" with saddles.

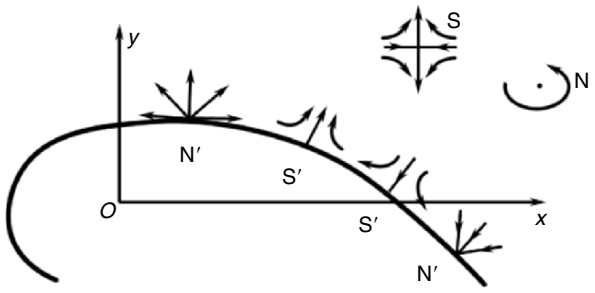


**Fig. 7.6.** Fixed points on a sectional plane of a three-dimensional flow

which for a single hole is $-1$. On the other hand, if a sectional plane cuts a surface that extends to infinity in all directions, there is

$$\left(\sum_{\mathrm{N}} + \frac{1}{2}\sum_{\mathrm{N}'}\right) - \left(\sum_{\mathrm{S}} + \frac{1}{2}\sum_{\mathrm{S}'}\right) = 0. \tag{7.7d}$$

The index of higher-order fixed points can be estimated as if they are combinations of low-order ones.

In experimental visualization of complex separated flows, one paints the model surface with a thin layer of thick oil, puts it into a wind tunnel, and observes the residual oil trace after the test as the footprint of the flow. The trace approximately reflects $\boldsymbol{\tau}$-lines. But since near fixed points $\boldsymbol{\tau}_w$ approaches zero, the trace there is very fussy. With the help of (7.7), a rational determination can be made on the types of fixed points. In so doing any sharp edges and apex should be made rounded to avoid singularity. The oil-flow method can be combined with other visualization techniques inside the flow field to gain a three-dimensional picture.

For example, Fig. 7.7 shows schematically a typical flow pattern over a slender delta wing at a large angle of attack, of which the visualized pattern is clarified by the topological interpretation based on (7.7a) and (7.7c). At the smoothed apex the separation line still initiates from a saddle, indicating a closed separation. Figure 7.8 compares the visualized cross-flow pattern with topological interpretation for asymmetric vortices over an elongated body at high incidence, and Fig. 7.9 is a similar comparison of *unsteady* vortex shedding behind a plate. Note that in two-dimensional flows to ensure the mass conservation the spirals like those in Fig. 7.9 must vary periodically between sources and sinks, otherwise there must be flow component along the third dimension.

### 7.1.4 Structural Stability and Bifurcation of Separated Flows

A further topic of the topological theory is how the topological structure varies as flow parameters. This question leads to the concept of *structural stability*

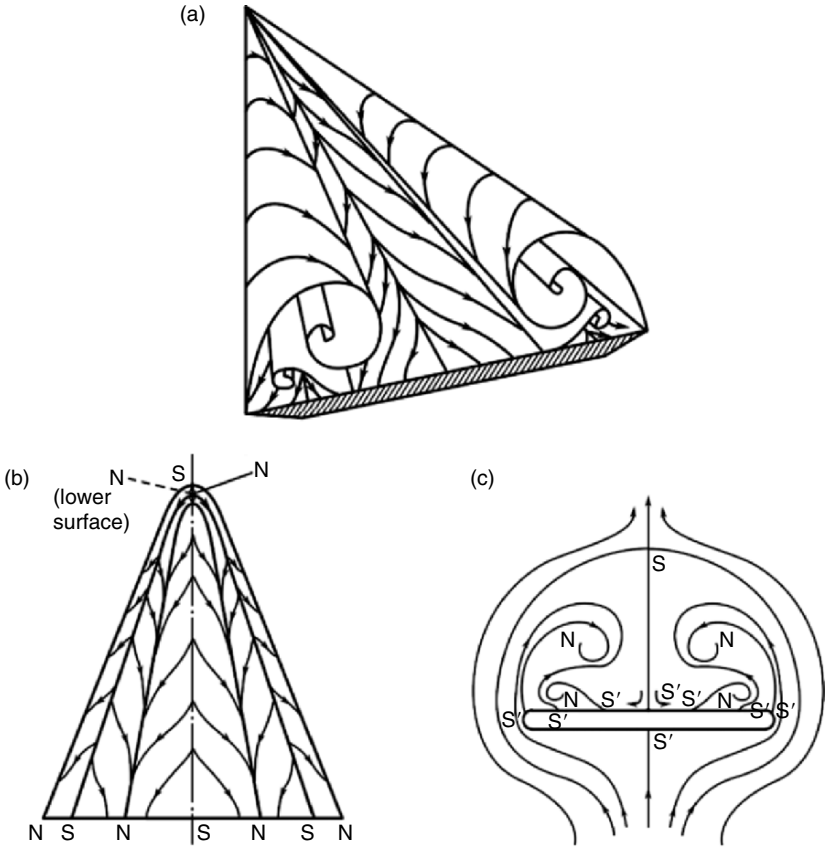


**Fig. 7.7.** Separated flow on a slender delta wing, (**a**) schematic stream surfaces, from Délery (2001), (**b**) skin-friction line topology, where the wing apex is rounded off to show the saddle point there (cf. Lighthill 1963), (**c**) cross-flow topology

and *bifurcation*. Let $\lambda = (\lambda_1, \lambda_2, ..., \lambda_n)$ be a set of flow conditions (e.g., Mach number, Reynolds number, geometric parameters, angle of attack, etc.). If for a fixed $\lambda_0$, an infinitesimal change $\delta\lambda$ does not change the topological structure of the *phase portrait*, then we say this portrait is *structurally stable*, otherwise it is structurally unstable. Note that the structural stability is different from the flow stability to be addressed in Chap. 9. A flow may be unstable under disturbance and evolve to another flow of the same topology, during which there is no structural instability. On the other hand, as a flow parameter goes across a critical value, the flow topology can change but during this process the flow remains hydrodynamically stable (e.g., Yin and Sun 2003). Once again, the concepts discussed here can be applied to both laminar and turbulent flows, at least the time average of the latter.

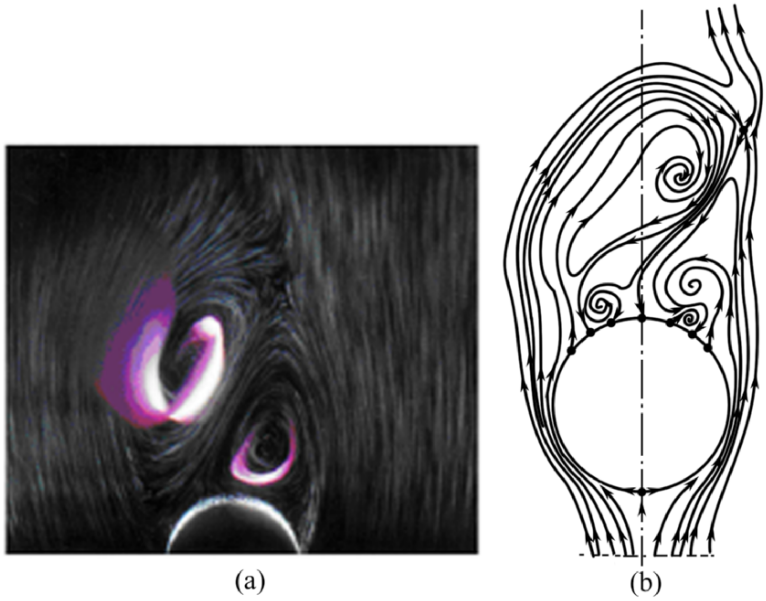


**Fig. 7.8.** Cross flow pattern of asymmetric vortices over an elongated body at high incidence. (**a**) Air-bubble visualization, (**b**) topological interpretation. From Délery (2001)

For two-dimensional vector fields, the structural stability is answered by the following theorem (e.g., Hirsch and Smale 1974), showing again the importance and robustness of hyperbolic fixed points:

**The Peixoto Theorem .** *A two-dimensional vector field has stable topological structure if and only if (1) the vector field has only finite number of hyperbolic fixed points and single limit cycles, and (2) there is no saddle-to-saddle trajectory.*

Here, the saddle–saddle connection includes closed loop emanating from and returning to the same saddle. The theorem is a powerful tool for identifying possible real vortical flows which are constantly exposed to some disturbances.

For example, in literature one often sees simple plots of two-dimensional or rotationally symmetric separated flow with saddle–saddle connection as sketched in Fig. 7.10a. So is in this book, such as small-$Re$ separated flow over sphere (Figs. 4.10 and 4.11) and large-$Re$ steady separated flows (Figs. 7.15 and 7.17 later). Some carefully controlled visualization photos of steady separated flows (e.g., Fig. 10.42b later; for more see Batchelor (1967) and Van Dyke (1982)) also tempt one to draw the corresponding topological portraits with saddle–saddle connection. Even the simplest two-dimensional, steady, and attached flow (e.g., Fig. 10.42a or Fig. 11.2 later) has inevitably a saddle–saddle connection, where no separation occurs at all. Now the Peixoto theorem asserts that these patterns are all structurally unstable. A small disturbance

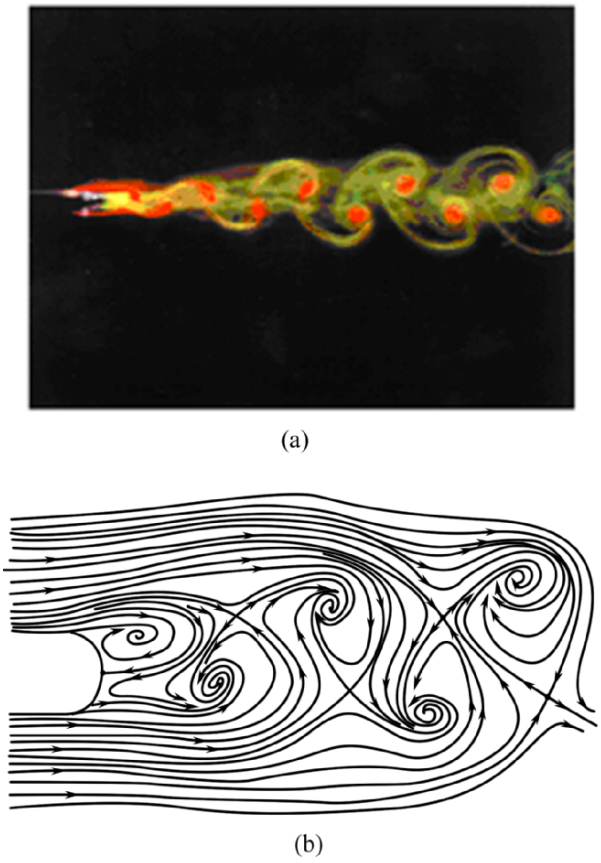


**Fig. 7.9.** Vortex shedding behind a plate, (**a**) dye filaments visualization, (**b**) topological interpretation. From Délery (2001)

may break the saddle–saddle connection of Fig. 7.10a to a robust saddle–node connection, as sketched in Fig. 7.10b or c. For more examples of breaking saddle connection see Bakker (1991).

In experiments, as long as disturbances cannot be completely eliminated, any observable nominally two-dimensional and steady flow patterns must be structurally stable. By the Peixoto theorem, if there appear any saddles or semisaddles, the flows should have Fig. 7.10b or c as building block but not a, although the latter could be a theoretical solution. Then, as argued before, if the flow is incompressible, Fig. 7.10b or c in turn implies that it must be unsteady with alternative periodic spiral sink and source, associated with a fluctuating velocity component along the third dimension.

The Peixoto structural stability theorem is equally applicable to the two-dimensional $\boldsymbol{\tau}$-field of a three-dimensional steady flow. In this regards it is of interest to note that, for a nominally two-dimensional steady flow over a cylinder, either fully attached or with separated bubble, the zero-$\boldsymbol{\tau}$ points

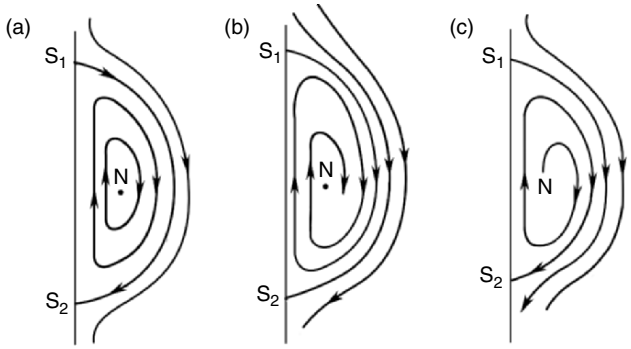


**Fig. 7.10.** Sketches of nominally two-dimensional and steady separated flow, (**a**) structurally unstable with saddle–saddle connection and a center; (**b**) structurally stable with a spiral sink; (**c**) structurally stable with a spiral source

on the cylinder surface seen in a flow plane are actually the degenerate fixed "points" of the $\boldsymbol{\tau}$-field, i.e., the $p$-axis of Fig. 7.1 along the span direction. They are structurally unstable. Therefore, what has been observed in experiments of nominally two-dimensional flows (including turbulence) is a $\boldsymbol{\tau}$-field having some spanwise periodic structures with alternative saddle and node distribution. To see this, consider a disturbance which alternatively stretches and compresses the fluid along the span. Then if a nominally two-dimensional separation point is in the stretching phase, it will be a saddle of the $\boldsymbol{\tau}$-field; while if it is in the compression phase, it will become a node. The situation is opposite for an attachment point. Therefore, the analysis of the two-dimensional $\boldsymbol{\tau}$-field and that of the two-dimensional flow field complement each other. They a lso explain why in a three-dimensional space any nominally two-dimensional or rotationally symmetric flows and vortices always have a tendency to become fully three-dimensional.

Unfortunately, it has been shown that there can be no analogue of the Peixoto theorem for dimensions greater than two. It is known that a saddle–saddle connection is still structurally unstable in three dimensions (e.g., Guckenheimer and Holmes 1983, p. 50), but all other flow patterns need to be studied on a case-by-case basis. Observing a three-dimensional flow by its projected patterns in three orthogonal planes, as we did in Fig. 7.2, cannot be used in the study of structural stability. The invariant direct-sum decomposition of matrices, as we used in Sect. 6.6.2, can well be applied to linear systems but not nonlinear ones. The latter may admit invariant subspaces, which however typically do not span the whole space, and hence the full dynamics of a three-dimensional system cannot be inferred from them. Actually, the fact that even a steady three-dimensional flow can have chaotic streamlines (the ABC flow, Sect. 3.3.1) has sufficed to exclude the possibility of constructing a general three-dimensional flow solely from the observations of lower-dimensional subspaces (Haller 2005, private communication).

Nevertheless, the spatial dimensions of the flow is reducible in some special cases, if the flow has a symmetry or a conserved quantity. For a recent a general coordinate-free theory for such an incompressible and inviscid flow, see Mezić and Haller 1998, which gives a unified geometric treatment of the *integrability* of three-dimensional steady Euler flows, two-dimensional unsteady Euler flows, as well as quasigeostrophic flows (Sect. 12.2.2) and magnetohydrodynamic flows (Sect. 4.1.1).

Once a flow field is structurally unstable, a small disturbance may cause a *topological bifurcation*. If the bifurcation is induced by a change of parameter $\lambda$, we say a *parametric bifurcation*. A bifurcation can be *local* if its consequence is confined to a local region. This happens when $\lambda$ (say the Reynolds number) is near a critical value corresponding to a nonhyperbolic fixed point, for example the splitting of a saddle-nodal point into a saddle and a node. Or, it can be *global* if its consequence is not local, for example opening a bubble to a free vortex layer. Flow analyses based on Taylor expansions as exemplified later can only handle local bifurcation.

To demonstrate some basic concepts of bifurcation, consider a one-dimensional "vector field" (Guckenheimer and Holmes 1983; Bakker 1991)

$$\frac{\mathrm{d}x}{\mathrm{d}t} = f(x) = -x^3, \tag{7.8}$$

which has only a third-order nonhyperbolic fixed point $x_0 = 0$ and is structurally unstable. Such a high-order fixed point behaves as if several hyperbolic fixed points fold together. To study the bifurcation of a nonhyperbolic system, one can introduce a minimum number of parameters (i.e., adding some perturbations) to "unfold" the high-order fixed point. The resulting perturbed system is called an *unfolding* of the nonhyperbolic system. For (7.8), a parametric perturbation $f(x) \to f_\lambda(x)$ may create one, two, or (at most) three fixed points in a neighborhood; thus a full unfolding is obtainable by adding two lower-order perturbations to (7.8), say

$$\frac{\mathrm{d}x}{\mathrm{d}t} = f_\lambda(x) = \lambda_1 + \lambda_2 x - x^3. \tag{7.9}$$

If $x_0$ is a fixed point, one may first study the local linearized system

$$\frac{\mathrm{d}x}{\mathrm{d}t} = f'_\lambda(x_0)(x - x_0) + O(|x - x_0|^2),$$

where $f'_\lambda(x_0)$ plays a role like the characteristic polynomial $\lambda^2 - p\lambda + q$ of (7.3): if the characteristic value of $f'_\lambda(x_0)$ has a zero real part, then the fixed point is nonhyperbolic, and otherwise is hyperbolic. From $f_\lambda(x_0) = 0$ (which determines $x_0$) and $f'_\lambda(x_0) = 0$ (which determines the characteristic values) one can eliminate $x_0$ to obtain a set of bifurcation parameters and the corresponding *phase portrait* and *bifurcation diagram*. Now, for

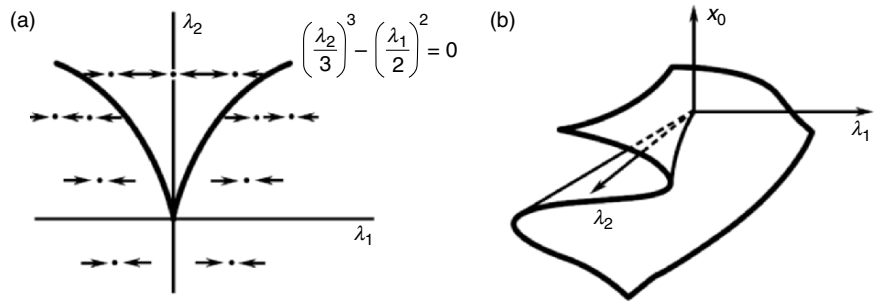


**Fig. 7.11.** The bifurcation diagram and phase portrait of perturbed system (7.9). Reproduced from Bakker (1991)

(7.9) there is $f'_\lambda(x) = \lambda_2 - 3x^2$, thus from $f_\lambda(x_0) = 0$ and $\lambda_2 - 3x_0^2 = 0$ it follows that

$$\left(\frac{\lambda_2}{3}\right)^3 - \left(\frac{\lambda_1}{2}\right)^2 = 0,$$

of which the bifurcation diagram and phase portrait are shown in Fig. 7.11. From Fig. 7.11a we see that on the curve $(\lambda_2/3)^3 = (\lambda_1/2)^2$, above it, and below it, respectively, there are two, three, and one fixed points. The relation of the $x_0$-location and $\lambda_1, \lambda_2$ is shown in Fig. 7.11b.

Returning to separated vortical flows, assume that in the steady version of (5.6b) there are some parameters, such that

$$\frac{\mathrm{d}\boldsymbol{x}}{\mathrm{d}s} = \frac{1}{x_3}\boldsymbol{u}_\lambda(\boldsymbol{x}), \quad \lambda = (\lambda_1, \lambda_2, ..., \lambda_n). \tag{7.10}$$

We assume that the solution of (7.10) for a given $\lambda$ is asymptotically stable in fluid-dynamics sense, i.e., an initial disturbance to the solution will eventually vanish (Chap. 9; note that a separated flow may be structurally stable but asymptotically unstable). Then, let $\lambda$ increases to a fixed value $\lambda_0$, making the solution asymptotically unstable and evolves to a new steady solution. Let $\psi$ be a quantity characterizing the solution. Then the solution evolution as $\lambda$ changes can be expressed as Fig. 7.12a. For $\lambda < \lambda_0$, we have original solution denoted by $\psi = 0$; when $\lambda$ exceeds $\lambda_0$, the new solution only slightly differs from the original one. Thus, the structural stability may still be retained; the appearance of this new solution does not imply a topological bifurcation. Such a bifurcation is called *supercritical bifurcation*. Only as $\lambda$ further increases to a higher level, could a new topological structure occur.

For example, for a flow over a round-nose revolutionary body with zero angle of attack $\alpha$, on the body surface there are only an attached node and a separation node, and the flow is highly symmetric. At a small $\alpha$ the flow is no longer symmetric but can still be attached without changing topological structure. Then, further increasing $\alpha$ may create a pair of saddles and a pair

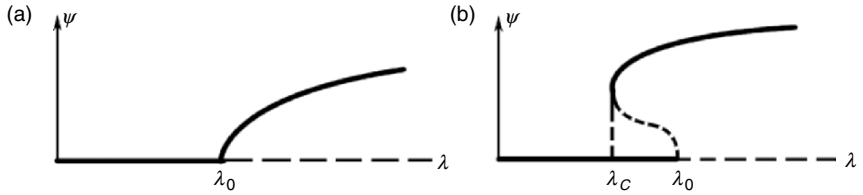


**Fig. 7.12.** Supercritical bifurcation (**a**) and subcritical bifurcation (**b**)

of nodes. During the transition process, it often happens that at first an even-order fixed point (e.g., a saddle–nodal) occurs, or an original hyperbolic fixed point becomes a third-order fixed point; then these high-order points split into new hyperbolic ones. As indicated by this example, in general the stronger is the symmetry, the smaller the energy content. The less symmetric steady solution, therefore, should exactly absorb the extra energy brought in by the change of parameter.

Figure. 7.12b shows a *subcritical bifurcation*. As $\lambda$ passes $\lambda_0$, the asymptotically stable new solution suddenly jumps to a state with a finite difference from the original one. This bifurcation may simultaneously break the structural stability of the original solution and lead to a new flow topology. A subcritical bifurcation has a hysteresis: if the bifurcation already occurs, to recover the original solution one has to reduce $\lambda$ to a value not only smaller than $\lambda_0$, but further smaller than $\lambda_c < \lambda_0$.

In theoretical study of the topological structure and bifurcation of three-dimensional, steady, and separated vortical flows, a basic tool is the high-order Taylor expansion in a neighborhood of the fixed point under consideration, based on (5.10), e.g., Dallmann (1983, 1984, 1988) and Perry and Chong (1986). A systematic background knowledge along with comprehensive case studies is given by Bakker (1991). In contrast to local analysis of Sect. 5.2.2, high-order expansion is necessary to include sufficiently many fixed points in the determination of topological structure.

## 7.2 Steady Separated Bubble Flows in Euler Limit

Separated flows with closed vortex bubbles can exist if the flow is strictly *two-dimensional* or *axisymmetric*, as well as *steady*. This kind of flows have simple topology and, in the limit of infinite Reynolds number, can be described by an asymptotic theory. Although we have just seen that these flows are structurally unstable, a more realistic flow may appear as a perturbation of these highly symmetric flows.

The study of steady separated flow in the Euler limit has long history, started from the *free-streamline theory* of Helmholtz (1868) and Kirchhoff (1869), of which some result was used in Sect. 5.3.3, where we saw that the

theory has to be combined with the viscous boundary-layer separation theory to determine the separation point and flow behavior nearby. For the global behavior of steady separated bubble flow, our concern is the Euler-limit behavior of the vorticity inside the bubble and the vortex layer enclosing the bubble. For the former the central result is the *Prandtl–Batchelor theorem* initiated by Prandtl (1905) and thoroughly examined by Batchelor (1956a); while for the latter the issue is solving a *cyclic* or *recirculating* vortex layer.

### 7.2.1 Prandtl–Batchelor Theorem

We are concerned with the Euler limit and steady state. The smaller the viscosity $\nu$ is, the longer time is needed to reach a steady state after the motion starts. Batchelor (1956a) points out that the correct Euler limit of a steady flow, that corresponds to practical experimental procedure, is established by *first taking* $t \to \infty$ such that the unsteadiness vanishes; and *then setting* $\nu \to 0$. Thus, in the final steady state the flow is governed by (assume $\rho = 1$)

$$-\nu\nabla \times \boldsymbol{\omega} = \boldsymbol{u} \cdot \nabla \boldsymbol{u} + \nabla p, \tag{7.11a}$$

$$= \boldsymbol{\omega} \times \boldsymbol{u} + \nabla H, \quad H = p + \frac{1}{2} q^2. \tag{7.11b}$$

In fact, except the highly viscous regions near the closed vortex layers, the flow is *circulation-preserving* and *generalized Beltramian* (Sect. 3.3.1):

$$\boldsymbol{u} \times \boldsymbol{\omega} = \nabla H, \tag{7.12}$$

which is to be solved in the region away from viscous layers. If the sheet is open to oncoming flow, the boundary condition necessary for solving (7.12) is obtainable from the vorticity or stagnation enthalpy on each streamline that extends to infinity. However, for a bubble flow surrounded by a closed vortex sheet, one has to find different conditions for the solution. The unique nature of these conditions is: they come from the viscous (7.11) and exist only when $\nu$ is not identically zero, but $\nu$ does not appear explicitly. Consequently, the conditions are *invariant* in the sense that they are valid for arbitrary $\nu$, so that in the Euler limit they still hold and provide additional information to the solution of (7.12) in the inner region of the bubble not very close to the surrounding vortex layers (*core region* for short). The solution of (7.12) obtained thereby is certainly the limit at $\nu \to 0$ of the Navier–Stokes solution rather than any other purely inviscid Euler solutions. This solution is called the *relevant Euler solution*.

The desired conditions have been found by Batchelor (1956a), who then obtained the relevant vorticity solution of (7.12) in the core region up to a constant factor to be determined by matching with the above-mentioned cyclic vortex layer solution. This result is stated as

**Prandtl–Batchelor Theorem.** *Under the steady Euler limit, for two-dimensional flow enclosed by vortex sheets, away from the sheets the vorticity is constant. For axisymmetric flow enclosed by vortex sheets, if the closed projected streamlines can shrink to a point at the center of the bubble, i.e., the bubble is not internally bounded by a torus, the vorticity must be along the azimuthal direction and proportional to the distance to the symmetry axis.* Namely,

$$\omega = \omega_0 \quad \text{for two-dimensional flow,} \tag{7.13}$$

$$\frac{\boldsymbol{\omega}}{r} = \alpha \boldsymbol{e}_\theta \quad \text{for axisymmetric flow,} \tag{7.14}$$

where $\omega_0$ and $\alpha$ are constant.

Note that (7.13) and (7.14) are a direct extension of the Rankine vortex and the Fraenkel–Norbury vortex-ring family (Sect. 6.3.2) to arbitrary core shape, respectively. If the closed boundary is entirely stationary, the asymptotic steady state in the bubble must be $\boldsymbol{u} = \boldsymbol{0}$ and $\boldsymbol{\omega} = \boldsymbol{0}$. In a nontrivial Prandtl–Batchelor flow, therefore, at least a part of boundary vortex sheet must be in tangent motion, which can have a variable velocity.

We now prove the theorem. For steady two-dimensional flow and rotationally symmetric flow (axisymmetric flow without swirl) in a bubble, there exists the stream function and Stokes stream function $\psi$, respectively, so that in the Euler limit (7.12) implies $H = H(\psi)$, and (3.64–3.67) hold where the scalar function $f(\psi)$ is nothing but $-\mathrm{d}H/\mathrm{d}\psi$. Namely,

$$\omega(\psi) = \begin{cases} -H'(\psi) & \text{for two-dimensional flow,} \\ -rH'(\psi) & \text{for rotationally symmetric flow.} \end{cases} \tag{7.15}$$

Hence, a single additional scalar condition is needed to solve (7.12). Because the streamlines are closed, provided $\nu \neq 0$, integrating (7.11b) along any streamline $C_\mathrm{s}$ yields

$$\oint_{C_\mathrm{s}} (\nabla \times \boldsymbol{\omega}) \cdot \mathrm{d}\boldsymbol{x} = 0. \tag{7.16}$$

Having obtained this *invariant condition*, we can combine it with the Euler-limit behavior (7.15). For two-dimensional flow, we use intrinsic frame $(\boldsymbol{t}, \boldsymbol{n})$ along $C_\mathrm{s}$, with unit vectors $(\boldsymbol{t}, \boldsymbol{n})$ being tangent and normal to the line, see Fig. 7.13. Then since $\mathrm{d}\psi = q\mathrm{d}n$, a straightforward algebra gives

$$\nabla \times \boldsymbol{\omega} = \boldsymbol{u}\frac{\mathrm{d}\omega}{\mathrm{d}\psi} = -\boldsymbol{u}\frac{\mathrm{d}^2 H}{\mathrm{d}\psi^2}.$$

Substituting this into (7.16), since $\psi$ is constant along $C_\mathrm{s}$, we simply obtain

$$\frac{\mathrm{d}\omega}{\mathrm{d}\psi} \oint_{C_\mathrm{s}} \boldsymbol{u} \cdot \mathrm{d}\boldsymbol{x} = \frac{\mathrm{d}\omega}{\mathrm{d}\psi} \Gamma_\mathrm{s} = 0.$$

If $\Gamma_\mathrm{s} = 0$, there must be $q = 0$ at all points of $C_\mathrm{s}$; such a streamline, if exists, must be in the near-boundary viscous region. Therefore, inside the bubble and away from boundary there must be $\mathrm{d}\omega/\mathrm{d}\psi = 0$, which proves (7.13).

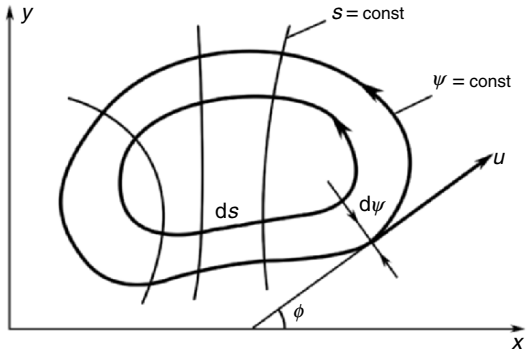


**Fig. 7.13.** The orthogonal curvilinear coordinates $(s, \psi)$

For rotationally symmetric flow, we consider an axial plane and introduce intrinsic orthonormal frame $(\boldsymbol{t}, \boldsymbol{n}, \boldsymbol{e}_\theta)$ thereon, with $s$ being the arc length along the streamlines $\psi =$ constant. The flow pattern is about the same as that in Fig. 7.13 with $(x, y)$ being replaced by $(z, r)$. In this frame $\boldsymbol{u} = (q, 0, 0)$, $\boldsymbol{\omega} = (0, 0, \omega_\theta)$, $\mathrm{d}\psi = rq\mathrm{d}n$, and $\mathrm{d}\boldsymbol{x} \cdot (\nabla \times \boldsymbol{\omega}) = (\boldsymbol{t} \times \nabla) \cdot \boldsymbol{\omega}\mathrm{d}s$. Then,

$$(\boldsymbol{t} \times \nabla) \cdot \boldsymbol{\omega} = \left(\boldsymbol{e}_\theta \partial_n - \boldsymbol{n}\frac{1}{r}\partial_\theta\right) \cdot (\boldsymbol{e}_\theta \omega_\theta) = \frac{\partial \omega_\theta}{\partial n} + \frac{\omega_\theta}{r}\cos\phi, \tag{7.17}$$

where, by (7.15) and referring to Fig. 7.13,

$$\frac{\partial \omega_\theta}{\partial n} = -\frac{\mathrm{d}H}{\mathrm{d}\psi}\cos\phi - r^2 q\frac{\mathrm{d}^2 H}{\mathrm{d}\psi^2},$$
$$\cos\phi = \boldsymbol{e}_z \cdot \boldsymbol{t} = \boldsymbol{e}_r \cdot \boldsymbol{n} = \frac{\partial r}{\partial n}.$$

Hence, (7.17) is cast to

$$(\boldsymbol{t} \times \nabla) \cdot \boldsymbol{\omega} = -2\frac{\mathrm{d}H}{\mathrm{d}\psi}\boldsymbol{e}_z \cdot \boldsymbol{t} - r^2 q\frac{\mathrm{d}^2 H}{\mathrm{d}\psi^2}.$$

But since $\oint \boldsymbol{t}\mathrm{d}s \equiv \boldsymbol{0}$, see (A.18), (7.16) simply yields

$$\frac{\mathrm{d}^2 H}{\mathrm{d}\psi^2}\oint_{C_\mathrm{s}} r^2 q\mathrm{d}s = 0. \tag{7.18}$$

Therefore, $\mathrm{dH}/\mathrm{d}\psi$ must be constant. This proves (7.14).

There remains extending (7.14) to steady axisymmetric bubble with swirl. In this case both streamlines and vorticity lines are spiral in the bubble, and $C_\mathrm{s}$ in (7.16) is the closed projection of a streamline on an axial plane ("projected streamline" for short). Besides, (6.13) indicates that, in the Euler

limit, in addition to $H(\psi)$ we need also $C(\psi) = \Gamma$, the circulation along a circle of radius $r$ from the axis. Hence one more condition is necessary to solve (7.12), which Batchelor (1956a) chose as the integral of (7.11b) along the closed projection $C_\omega$ of a spiral vorticity line on the axial plane:

$$\oint_{C_\omega} (\nabla \times \boldsymbol{\omega}) \cdot \mathrm{d}\boldsymbol{x} = 0.$$

But the proof is lengthy and needs some heuristic argument. We now follow a simpler proof with sufficient rigor due to Chernyshenko (2003, private communication).

We use intrinsic frame $(\boldsymbol{t}, \boldsymbol{n}, \boldsymbol{e}_\theta)$ along a closed projected stream line $C_\mathrm{s}$ as before. The velocity and vorticity are now $\boldsymbol{u} = (u_s, 0, v)$ and $\boldsymbol{\omega} = (\omega_s, \omega_n, \omega_\theta)$, where $v$ is the azimuthal velocity. The $(r, z)$-components of the vorticity in cylindrical coordinates, given by (6.9a,b), now yield

$$\omega_s = \frac{1}{r}\frac{\partial \Gamma}{\partial n}, \quad \omega_n = -\frac{1}{r}\frac{\partial \Gamma}{\partial s}. \tag{7.19a,b}$$

Assume $u_s \neq 0$ except at the center of the core region where $C_\mathrm{s}$ shrinks to a point. The two desired invariant conditions can be constructed from two tangent components of (7.11). Due to the axial symmetry, the $\boldsymbol{e}_\theta$-component of (7.11a) along with an inspection of (6.4b) and (6.10a), and the inner product of $\boldsymbol{u}$ and (7.11b), yield, respectively,

$$\boldsymbol{u} \cdot \nabla \Gamma = -\nu r \boldsymbol{e}_\theta \cdot (\nabla \times \boldsymbol{\omega}), \quad \boldsymbol{u} \cdot \nabla H = -\nu \boldsymbol{u} \cdot (\nabla \times \boldsymbol{\omega}),$$

where $\boldsymbol{u}$ on the left-hand side of both equations can be replaced by $u_s \boldsymbol{t}$ due to axial symmetry. Hence it follows that

$$\frac{\partial \Gamma}{\partial s} = -\nu \frac{r}{u_s} \boldsymbol{e}_\theta \cdot (\nabla \times \boldsymbol{\omega}), \quad \frac{\partial H}{\partial s} = -\nu \frac{\boldsymbol{u}}{u_s} \cdot (\nabla \times \boldsymbol{\omega}), \tag{7.20a,b}$$

of which the integral along $C_\mathrm{s}$ immediately yields the invariant conditions

$$\oint_{C_\mathrm{s}} \frac{r}{u_s} (\boldsymbol{e}_\theta \times \nabla) \cdot \boldsymbol{\omega} \, \mathrm{d}s = 0, \tag{7.21a}$$

$$\oint_{C_\mathrm{s}} \left[ \left( \boldsymbol{t} + \frac{v}{u_s} \boldsymbol{e}_\theta \right) \times \nabla \right] \cdot \boldsymbol{\omega} \, \mathrm{d}s = 0. \tag{7.21b}$$

Now, as $\nu \to 0$, (7.19a,bb) and (7.19a,ba) indicate $\omega_n = 0$, i.e., the stream surfaces are also vorticity surfaces (Lamb surfaces). In this case we have (6.13), so in terms of the intrinsic frame with $\mathrm{d}\psi/\mathrm{d}n = r u_s$ there is

$$\omega_s = u_s \frac{\mathrm{d}\Gamma}{\mathrm{d}\psi}, \quad \omega_n = 0, \quad \frac{\omega_\theta}{r} = \frac{\Gamma}{r}\frac{\mathrm{d}\Gamma}{\mathrm{d}\psi} - \frac{\mathrm{d}H}{\mathrm{d}\psi}. \tag{7.22a,b,c}$$

Thus, in (7.21), for the term with $\boldsymbol{t}$ we still have (7.17a,b), while for the terms with $\boldsymbol{e}_\theta$ we have, noticing $\partial_s \boldsymbol{t} = \kappa \boldsymbol{n}$ with $\kappa$ being the curvature of $C_\mathrm{s}$,

$$(\boldsymbol{e}_\theta \times \nabla) \cdot \boldsymbol{\omega} = (\boldsymbol{n}\partial_s - \boldsymbol{t}\partial_n) \cdot (\boldsymbol{t}\omega_s + \boldsymbol{e}_\theta \omega_\theta) = \kappa\omega_s - \partial_n \omega_s$$
$$= u_s(\kappa - \partial_n \log u_s)\frac{\mathrm{d}\Gamma}{\mathrm{d}\psi} - r u_s^2 \frac{\mathrm{d}^2\Gamma}{\mathrm{d}\psi^2}.$$

Therefore, (7.21a) yields

$$\frac{\mathrm{d}^2\Gamma}{\mathrm{d}\psi^2}\oint_{C_\mathrm{s}} r^2 u_s \,\mathrm{d}s - \frac{\mathrm{d}\Gamma}{\mathrm{d}\psi}\oint_{C_\mathrm{s}} r(\kappa - \partial_n \log u_s)\,\mathrm{d}s = 0,$$

where the integrals are functions of $\psi$ only. It thus follows that

$$\frac{\mathrm{d}\Gamma}{\mathrm{d}\psi} = C\mathrm{e}^{\int^\psi g(\eta)\,\mathrm{d}\eta}, \quad g(\psi) = \frac{\oint r(\kappa - \partial_n \log u_s)\,\mathrm{d}s}{\oint r^2 u_s \,\mathrm{d}s}. \tag{7.23}$$

But, as $C_\mathrm{s}$ shrinks to the core center as assumed, since $\boldsymbol{n}$ points toward the center there must be $u_s \to 0^+$ with $\partial_n u_s < 0$ and $\kappa \to +\infty$. Hence, $\Gamma$ would be singular if $C \neq 0$. The permissible solution is thus simply $\Gamma =$ constant, implying that $\omega_s = 0$ and $v = C/r$ ($C = 0$ if the bubble flow extends to the $z$-axis). On the other hand, this removes the $\boldsymbol{e}_\theta$-component in (7.21b), making it the same as (7.18) and recovering (7.14). The proof of the theorem is therefore completed.

We make two remarks on the theorem and closed bubble flow. First, the formation mechanism of these bubble flows is very different from that of concentrated vortices by the rolling up of free vortex layers. For the former the viscous effect has to take sufficient time to fully act on the motion, sending the vorticity from the sheet to the interior, which finally reaches an equilibrium steady state. The sheet vorticity is supplemented by the outer flow. But for the latter there is no sufficient time for diffusion to reach equilibrium state. Goldstein and Hultgren (1988) have pointed out that in this case the vorticity can have variable distribution in closed streamlines.

Second, the physical explanation of the theorem is simple. For steady two-dimensional flow, the viscous vorticity equation

$$\boldsymbol{u} \cdot \nabla\omega = \nu\nabla^2\omega$$

is a diffusion equation. If $\omega$ changes across streamlines, there must be an inward or outward vorticity diffusive flux. But at the center of closed streamlines there is no vorticity source or sink (Sect. 4.1); so in steady state this diffusion cannot exist. The only possibility is, therefore, a constant vorticity, which implies no vorticity diffusion. In contrast, for rotationally symmetric flow, in cylindrical coordinates $(x, r, \theta)$ by (7.15) one finds a uniform axial viscous force

$$\nu(\nabla \times \boldsymbol{\omega}) = -2\alpha\nu\boldsymbol{e}_x, \tag{7.24}$$

which is balanced by a uniform pressure gradient. Thus, the inviscid velocity distribution is not altered. Both this physical interpretation and the proof

procedure of the theorem stress the key role of vorticity diffusive flux $\boldsymbol{\sigma} = \nu\partial_n\boldsymbol{\omega}$ defined by (4.17) in the formation of the bubble's core region. In fact, that flux was precisely introduced from examining the line integral of $\nu\nabla\times\boldsymbol{\omega}$, and can well replace $\nu\nabla\times\boldsymbol{\omega}$ in the invariant conditions. To see this, we use the notation of (4.23) so that on a surface $S$

$$-\nu\boldsymbol{n}\times(\nabla\times\boldsymbol{\omega}) = \boldsymbol{\sigma} - \boldsymbol{\sigma}_{\rm vis}.$$

Then by (7.11) one easily obtains

$$(\boldsymbol{\sigma} - \boldsymbol{\sigma}_{\rm vis})\times\boldsymbol{n} = (\boldsymbol{u}\cdot\nabla\boldsymbol{u})_\pi + \nabla_\pi p = (\boldsymbol{\omega}\times\boldsymbol{u})_\pi + \nabla_\pi H, \tag{7.25}$$

where again suffix $\pi$ denotes tangent components. Now let $S$ be a stream surface with $u_n = 0$. Then for two-dimensional flow with both $\boldsymbol{\sigma}_{\rm vis}$ and $(\boldsymbol{\omega}\times\boldsymbol{u})_\pi$ vanishing, along an open segment of a streamline $C_{\rm s}$ we simply have

$$H_B - H_A = \int_A^B \sigma\,{\rm d}s \tag{7.26}$$

at any Reynolds number, indicating that the difference of stagnation enthalpy at ends points is solely due to vorticity diffusion across the streamline (Chernyshenko 1998). This is why in the Euler limit $H$ becomes constant along the streamline. The corresponding invariant condition for closed streamlines is, evidently,

$$\oint_{C_{\rm s}} \frac{\partial\omega}{\partial n}\,{\rm d}s = 0, \tag{7.27}$$

which is an alternative form of the two-dimensional version of (7.16).

For axisymmetric flow, from (7.20) it follows that

$$r(\boldsymbol{n}\times\boldsymbol{e}_\theta)\cdot(\boldsymbol{\sigma} - \boldsymbol{\sigma}_{\rm vis}) = u_s\frac{\partial\mathit{\Gamma}}{\partial s},$$
$$(\boldsymbol{n}\times\boldsymbol{u})\cdot(\boldsymbol{\sigma} - \boldsymbol{\sigma}_{\rm vis}) = u_s\frac{\partial H}{\partial s},$$

which are the alternative form of (7.21a,b) and yield, along a segment of a projected streamline,

$$\mathit{\Gamma}_B - \mathit{\Gamma}_A = \int_A^B \frac{r}{u_s}\boldsymbol{t}\cdot(\boldsymbol{\sigma} - \boldsymbol{\sigma}_{\rm vis})\,{\rm d}s, \tag{7.28a}$$

$$H_B - H_A = -\int_A^B \boldsymbol{e}_\theta\cdot(\boldsymbol{\sigma} - \boldsymbol{\sigma}_{\rm vis})\,{\rm d}s + \int_A^B \frac{v}{u_s}\boldsymbol{t}\cdot(\boldsymbol{\sigma} - \boldsymbol{\sigma}_{\rm vis})\,{\rm d}s, \tag{7.28b}$$

which explains the physical source of the variation of $\mathit{\Gamma}$ and $H$ along $C_{\rm s}$ at any Reynolds numbers. The invariant conditions alternative to (7.22a,b) are obvious. We just note that in the Euler limit with $\omega_n = 0$ (4.25) gives

$$\frac{1}{\nu}\boldsymbol{\sigma}_{{\rm vis}\pi} = \boldsymbol{\omega}\cdot\mathbf{K} = -\boldsymbol{\omega}\cdot\left(\boldsymbol{t}\frac{\partial}{\partial s} + \boldsymbol{e}_\theta\frac{1}{r}\frac{\partial}{\partial\theta}\right)\boldsymbol{n}$$
$$= -\boldsymbol{\omega}\cdot\left(\boldsymbol{t}\boldsymbol{t}\kappa - \frac{1}{r}\boldsymbol{e}_\theta\boldsymbol{e}_\theta\cos\phi\right) = \boldsymbol{t}\kappa\omega_s - \boldsymbol{e}_\theta\frac{\omega_\theta}{r}\cos\phi.$$

Thus the preceding component results can be recovered.

### 7.2.2 Plane Prandtl–Batchelor Flows

This subsection discusses the Euler limit of two-dimensional flow over a stationary body with steady separated vortex bubble of area $S$ bounded by $C$.[4] By (7.13), outside and inside the bubble the vorticity is zero and constant, respectively. We have Bernoulli integral not only outside the bubble but also in the core region of the bubble, since in (7.12) there is $\boldsymbol{\omega} \times \boldsymbol{u} = \nabla(\omega_0 \psi)$, yielding

$$\frac{1}{2}(\nabla\psi)^2 + \frac{p}{\rho} + \omega_0\psi = \frac{p_c}{\rho} + \omega_0\psi_c \quad \text{in the core region,} \tag{7.29}$$

where the suffix c denotes the bubble center where $q^2 = |\nabla\psi|^2 = 0$. Therefore, let $\psi = 0$ along $C$ with $\psi > 0$ and $n > 0$ in the bubble as in Fig. 7.13, the Euler limit of the flow is a solution of the following problem:

$$\nabla^2\psi = 0 \qquad \text{for} \quad \psi < 0, \tag{7.30a}$$

$$\nabla^2\psi = -\omega_0 \qquad \text{for} \quad \psi > 0, \tag{7.30b}$$

$$[\![|\nabla\psi|^2]\!] = 2[\![H]\!] = \text{const. along } \psi = 0, \tag{7.30c}$$

$$\nabla \times (\psi \boldsymbol{e}_z)|_{|\mathbf{x}|\to\infty} = \boldsymbol{U}_\infty, \tag{7.30d}$$

where $[\![\cdot]\!] = (\cdot)|_{\psi=0^-} - (\cdot)|_{\psi=0^+}$ denotes the jump across $C$. While in this inviscid formulation $\omega_0$ and $[\![H]\!]$ (or the separation point) are arbitrary parameters, only the *relevant Euler solution* is our concern, which is the limit of the true viscous solution as $\epsilon \equiv Re^{-1} \to 0$ and in which $\omega_0$ and $[\![H]\!]$ are specially determined. Here the Reynolds number is defined based on the body size $R$ and $U_\infty$. As said in the beginning of this section, this is achieved by returning to viscous analysis, where the boundary vortex sheet is replaced by a cyclic vortex layer of finite thickness. This issue will be addressed later after discussing some general properties of the solution of (7.30).

Let $U_e = \psi_{,n}|_{\psi=0_-}$ be the potential velocity at $C$, by (4.118a) the vortex sheet strength $\gamma = u - U_e$ is given by

$$\gamma = -\frac{[\![H]\!]}{U_m}, \quad U_m = \frac{1}{2}(U_e + u). \tag{7.31}$$

The stream function can be written as $\psi = U_\infty y + \psi_1 + \psi_2$, where the first term is the stream function of uniform oncoming flow, and by the Biot–Savart law

$$\begin{aligned} \psi_1(\boldsymbol{x}) &= \frac{\omega_0}{2\pi}\int_S \log r \, \mathrm{d}S(\boldsymbol{x}'), \\ \psi_2(\boldsymbol{x}) &= \frac{1}{2\pi}\int_C \gamma(s)\log r \, \mathrm{d}s(\boldsymbol{x}'), \quad r = |\boldsymbol{x} - \boldsymbol{x}'|, \end{aligned} \tag{7.32}$$

[4] Analyses of axisymmetric Prandtl–Batchelor flow are relatively rare. One example is the Hill spherical vortex with swirl (Sect. 6.3.2).

are the contributions of $\omega_0$ and $\gamma$, respectively. Moreover, since $\omega_0$ depends on $U_\infty$, we need a compatibility condition

$$U_\infty = \sqrt{2[\![H]\!]} - \frac{\partial}{\partial y}(\psi_1 + \psi_2) \quad \text{at the upstream end.} \tag{7.33}$$

Then the inviscid problem amounts to finding the shape and strength of the sheet for given $\omega_0$ and $[\![H]\!]$, including the separation and re-attachment points.

A closed vortex bubble carried by a body will produce a lift. Let $S$ and $\omega_0$ be the dimensionless area and vorticity of the bubble, respectively, scaled by $R$ and $U_\infty$. Then by the well-known (dimensional) *Kutta–Joukowski lift formula* $L = \rho U_\infty \Gamma$ (for more discussion see Chap. 11), with $\Gamma = \omega_0 S$ being the total vorticity or circulation of the bubble , the additional lift coefficient due to the bubble (not including the lift caused by vortex sheet $\gamma$) simply reads

$$\Delta C_l = \frac{\Delta L}{\frac{1}{2}\rho U_\infty^2 R} = 2\omega_0 S. \tag{7.34}$$

The small region near the separation point $A$ needs special consideration. As argued in Sect. 4.4.2, in order to have a shedding vortex sheet, at $A$ there must be $[\![H]\!] \neq 0$ and the external potential flow must be tangent to the surface, see Fig. 7.14 later. Thus, in a small neighborhood of $A$, in terms of local Cartesian coordinates $(x, y)$ the sheet equation $y = f(x)$ must satisfy $f(0) = f'(0) = 0$, i.e., $y = o(x)$. The flow inside the cusp varies mainly along the $y$-direction, so that (7.30b) is reduced to $\partial^2\psi/\partial y^2 \simeq -\omega_0$, of which the solution satisfying $\psi = 0$ along $y = f(x)$ is

$$\psi \simeq -\frac{1}{2}\omega_0 y[y - f(x)], \quad x \ll 1.$$

Thus, as $x \to 0$ we have $q = o(x)$ and by (7.30c) $U_e = \sqrt{2[\![H]\!]} + o(x^2)$. Therefore, near the separation point the fluid in the cusp is indeed stationary as we inferred from the Kutta condition in Sect. 4.4.3. This being the case, the local flow is nothing but a *Kirchhoff free-streamline flow*, which gives

$$f(x) = ax^{3/2} + bx^{5/2} + \cdots, \quad x \ll 1. \tag{7.35}$$

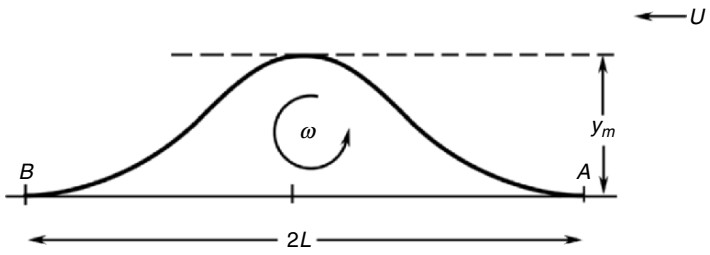


**Fig. 7.14.** Sadovskii flow

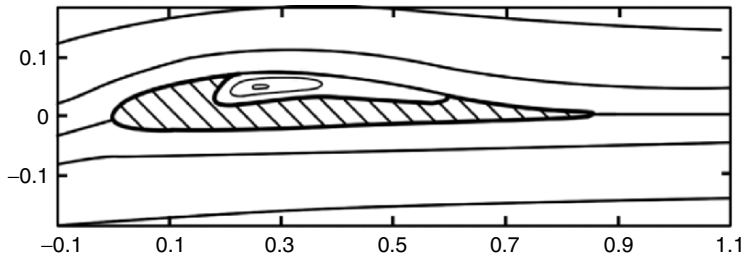


**Fig. 7.15.** Streamlines for airfoil with a trapped vortex. $\omega_0 = -20$, $[\![H]\!] = 0.53$. Adapted from Bunyakin et al. (1998)

Several Prandtl–Batchelor bubble flows with the above common features have been studied. Sadovskii (1971) was the first to solve the problem for the flow of Fig. 7.14, where a pair of Prandtl–Batchelor vortices of length $L$ are symmetrically in touch, known as the *Sadovskii flow*. He derived a pair of integral equations for the sheet shape $f(x)$ and strength $\gamma(x)$ with a given constant $[\![H]\!]$. The equations were solved numerically. The computation was improved by Moore et al. (1988) who gave a complete set of the solutions for Sadovskii flow.

Other investigated Prandtl–Batchelor flows include corner flows (e.g., Chernyshenko 1984; Moore et al. 1988) and flow over a flat plat with a forward-facing flap (Saffman and Tanveer 1984). The latter was motivated by the concept that if at a large angle of attack a stationary vortex can be captured, then the lift will be greatly enhanced. The most interesting configuration along this line is to capture a vortex by an airfoil with a cavity on its upper surface, studied by Bunyakin et al. (1996). Owing to (7.34), such an airfoil may have additional lift but avoid early separation under strong adverse pressure gradient on the upper surface, where the original solid wall is replaced by a free shear layer like a flexible moving belt.[5] The authors found that due to the structural instability 3 of closed bubble flow, the bubble shape is very sensitive to the given $\omega_0$ and $[\![H]\!]$, and only in a certain range of these parameters can a meaningful solution be obtained. Figure 7.15 plots the configuration and flow pattern.

We now turn to the cyclic viscous vortex-layer. Squire (1956) was the first to exemplify that a matched asymptotic expansion can be applied to fix the flow within the layer as well as $\omega_0$ and $[\![H]\!]$. We use the same intrinsic frame $(\boldsymbol{t}, \boldsymbol{n})$ as in Fig. 7.13, and let quantities be made dimensionless by body size $R$, density $\rho$, and $U_\infty$. Assume now Fig. 7.14 represents a bubble on a flat wall. Let $s$ move from $A$ ($s = 0$) to $B$ ($s = s_B$) along the separated vortex sheet

[5] As remarked in Sect. 7.1.2, the vortex in the cavity is much weaker than that formed by the rolling-up of a free vortex layer. The latter was proposed by Wu and Wu (1992). Such a strong vortex must have axial flow and is expected to be more stable as well.

(in free shear layer) and returns $A$ ($s = s_A > s_B$) along the wall (in attached boundary layer). Let $u(s, \psi)$ be the streamwise velocity in the vortex layer such that $\mathrm{d}\psi = u\mathrm{d}n$. Both free vortex layer and attached boundary layer are governed by a boundary-layer type of equation:

$$u\frac{\partial u}{\partial s} = U_e\frac{\partial U_e}{\partial s} + \epsilon\frac{\partial^2 u}{\partial n^2}, \quad \epsilon = Re^{-1}.$$

Introduce the well-known Mises transformation (e.g., Rosenhead 1963)

$$\frac{\partial^2 u}{\partial n^2} = \frac{\mathrm{d}\psi}{\mathrm{d}n}\frac{\partial}{\partial \psi}\left(\frac{\mathrm{d}\psi}{\mathrm{d}n}\frac{\partial u}{\partial \psi}\right) = \frac{1}{2}u\frac{\partial^2 u^2}{\partial \psi^2}$$

and a rescaled stream function $\Psi = Re^{1/2}\psi$, and denote the total enthalpy inside the viscous vortex layer by

$$g(s, \Psi) \equiv p_s + \frac{1}{2}u^2(s, \Psi).$$

Then the above boundary-layer equation reads

$$\frac{\partial g}{\partial s} = u\frac{\partial^2 g}{\partial \Psi^2}. \tag{7.36}$$

Assume the inviscid flow in the core region has been solved, so that at $s = 0_-$ there is a known potential flow with $g = g_0(\psi)$, and on the wall there is a known $p(s)$. Then the upstream condition, periodic condition, and wall condition for (7.36) are, respectively,

$$s = 0, \Psi < 0: \quad g = g_0(\psi); \tag{7.37a}$$

$$\Psi > 0: \quad g(0, \Psi) = g(s_A, \Psi); \tag{7.37b}$$

$$\Psi = 0, \quad s_B < s < s_A: \quad g = p(s). \tag{7.37c}$$

Besides, since $\psi = 0_+$ corresponds to $\Psi \to \infty$ in the Euler limit, (7.30c) gives the matching condition

$$\Psi \to \infty: \quad g \to H(\psi)|_{\psi=0_+} = H|_{\psi=0_-} - [\![H]\!] < \infty, \tag{7.37d}$$

which ensures the uniqueness of the solution.

Generically, the boundary-layer approximation cannot be applied to regions near $A$ and $B$, referred to as *turn regions*. But when a turn region has a cusp, only the normal variation is important, and the inviscid cusp flow away from the viscous free vortex layer and boundary layer is stationary. In fact, the characteristic flow rate $Q$ in the turn region must be of the same order as that in a boundary layer: $Q_{\text{turn}} \sim Re^{-1/2}$, so that locally there is

$$Re_{\text{turn}} \sim U_{\text{turn}}L_{\text{turn}}Re \sim Q_{\text{turn}}Re \sim Re^{\frac{1}{2}} \to \infty.$$

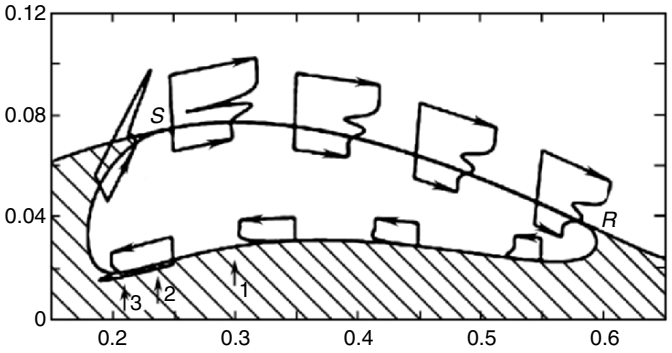


**Fig. 7.16.** Velocity profile as a function of $\psi$ in the cyclic layer of Fig. 7.15 for the relevant Euler solution of flow over an airfoil with trapped vortex. Adapted from Bunyakin et al. (1998)

Thus, to the leading order the flow is inviscid and Bernoulli integral holds. In this case it can be shown that when using (7.36) as the governing equation the turn region can be ignored (see Bunyakin et al. (1998) for references). Thus the formulation for the cyclic vortex layer is completed.

For example, by solving (7.36) under condition (7.37), as well as the conventional boundary-layer equation for flow over a wall, Bunyakin et al. (1998) extend their inviscid solution shown in Fig. 7.15 to include the viscous attached and free vortex layers. Then the whole flow field is determined. Figure 7.16 shows the velocity profiles in the cyclic vortex layer. The airfoil was carefully selected to avoid any smooth-surface separation other than the fixed front and rear points of the cavity. To make the airfoil look more realistic, tangent blowing was introduced at three points of the cavity wall (arrows in Fig. 7.16). This requires an extension of boundary conditions (7.37) and is omitted here.

### 7.2.3 Steady Global Wake in Euler Limit

The preceding discussion on plane Prandtl–Batchelor flows is for the situation where the bubble size is of the same order of the body size. A different and more challenging problem relevant to the Prandtl–Batchelor flow is the asymptotic form of the entire vortical wake behind a bluff body. It will be seen in Sect. 7.4 that as the Reynolds number $Re = UD/\nu$ (based on diameter $D$) increases to about 50 the wake behind a circular cylinder starts to be spontaneously unsteady and vortex shedding occurs. However, the *mathematical existence* of a steady but unstable wake cannot be excluded. Numerically, careful Navier–Stokes calculations (Fornberg 1985) which specifically eliminate the possibility of unsteadiness and asymmetry have shown that steady wake is a Navier–Stokes solution. Theoretically, such a mathematical solution has been obtained in the Euler limit. Roshko (1993) remarks that, while this

solution is mainly of academic interest, "it is an intriguing and important one for theoretical fluid mechanics and it provides perspective on the 'real problem'."

The classic Kirchhoff free-streamline wake, which is open at downstream end and the fluid therein is stationary, was criticized by Batchelor (1956b). The dilemma is: if the wake is open, how can the downstream boundary condition that the flow resumes uniform be satisfied? And, if the wake is closed, then the Prandtl–Batchelor theorem requires that the wake has a uniform vorticity rather than being stationary. Thus, Batchelor (1956b) proposed that the steady wake in the Euler limit is a closed bubble with $\omega_0$ and $[\![H]\!]$ as parameters. It has been found that the wake length increases linearly as $Re$; and its width increases initially as $O(Re^{1/2})$, but after $Re > 150$ turns to be $O(Re)$ as well, see Fig. 7.17. Moreover, in such a big pair of separated bubbles the vorticity is basically constant as predicted by the Prandtl–Batchelor theorem; and at the outer boundary of the bubbles there is a thin vortex layer, which tends to vanish as the characteristic velocity increases toward downstream.

After many researchers' effort, a complete asymptotic theory of steady separated flow has been established and supported by numerical tests. For comprehensive reviews see Sychev et al. (1998, Chap. 6) and Chernyshenko (1998); a few major points are briefly outlined here.

First, in the global bubble scale the flow is a uniquely determined inviscid Sadovski flow (where the cylinder shrinks to a point as $Re \to \infty$), of which the width-to-length ratio is $h/L = 0.300$ and the area is $S = \alpha L^2$ with $\alpha \simeq 0.44$. The vorticity $\omega_0$ is fixed such that, by the Bobyleff–Forsythe formula (2.159) and from (2.76), the total dimensionless dissipation rate and the total drag coefficient $C_\mathrm{d}$ (nondimensionalized by $\rho U_\infty^2 R$) are, respectively,

$$C = \omega_0^2 S \simeq 0.73, \tag{7.38}$$

$$C_\mathrm{d} = \frac{C}{Re}. \tag{7.39}$$

Secondly, in addition to the global bubble-scale flow, special care is needed for the flow in turn regions, cusp, and at the body scale, as well as their matching. In the body scale, the velocity in the bubble is found to be much less than outside, so that one returns to the inviscid Kirchhoff free-streamline flow with drag coefficient

$$C_\mathrm{d} = 2k_\mathrm{d}[\![H]\!], \tag{7.40}$$

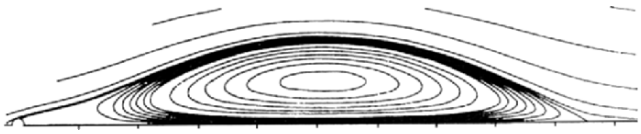

**Fig. 7.17.** Schematic flow pattern of steady global wake behind a circular cylinder (the small semicircle at the left end of the plot). From Chernyshenko (1998)

where $k_\mathrm{d}$ is drag coefficient in the Kirchhoff flow with the velocity magnitude on the free streamline equal to unity, depending on the body shape and separation point. Comparing (7.39) and (7.40) yields

$$[\![H]\!] = \frac{C}{2k_\mathrm{d}Re}. \tag{7.41}$$

Thirdly, to ensure the existence of the viscous solution in the cyclic vortex layer, there must be an equality among parameters (Chernyshenko 1988):

$$[\![H]\!] = \frac{1}{2D_0}\sqrt{\frac{C\omega_0}{2Re}}, \tag{7.42}$$

where $D_0$ is a constant; for flow past an isolated body $D_0 \simeq 0.235$. The key physics behind (7.42) is the vorticity balance. The vorticity diffuses toward the symmetry line where it vanishes, and also diffuses across the bubble boundary. This loss of vorticity must be compensated by that produced from the body surface and advected into the flow. In this problem one only needs the net effect of vorticity discharged from the body rather than the detailed diffusion and advection process; so it suffices to know the sum of vorticity diffusive flux $\sigma$ and advective flux $u_n\omega$ across any line segment, which is nothing but the end-point difference of the total enthalpy. Indeed, as an easy extension of (7.26), by applying (7.25) to any line segment there is (Chernyshenko 1998)

$$H_B - H_A = \int_A^B (u_n\omega - \sigma)\,\mathrm{d}s. \tag{7.43}$$

This is why $[\![H]\!]$ enters (7.41), which also shows that the jump must vanish in the Euler limit. The four equations (7.38–7.40) and (7.42) then determine the four unknowns $\omega_0$, $S$, $C_\mathrm{d}$, and $[\![H]\!]$, with only $k_\mathrm{d}$ depending on the body shape. Namely, in addition to (7.39) for the drag and (7.41) for $[\![H]\!]$, there is

$$\omega_0 = \frac{2CD_0}{k_\mathrm{d}^2 Re}, \quad S = \frac{k_\mathrm{d}^4 Re^2}{4CD_0^4}, \quad L = \frac{k_\mathrm{d}^2 Re}{2D_0\sqrt{\alpha C}}, \quad \alpha \simeq 0.44. \tag{7.44}$$

## 7.3 Steady Free Vortex-Layer Separated Flow

Closed-bubble separated flows discussed in Sect. 7.2 are relatively rare in reality. The common situation is *free vortex-layer separated flow*, in which a separated vortex layer rolls into a vortex and the flows at both sides of the layer come from the same main stream. As said in Sect. 7.1.2, the free vortex-layer may come from both *closed separation* initiating at a saddle point of the $\boldsymbol{\tau}_w$-field, for example at the apex of a slender delta wing as shown in Fig. 7.7b, and *open separation* initiating at an ordinary point of the $\boldsymbol{\tau}_w$-field, as seen

in Fig. 6.1. A prototype of free vortex-layer separated flow is a pair of vortex sheets shed from a slender wing, which roll into vortices above the wing and greatly enhance the lift. Being steady and stable in a range of parameters, this kind of *detached-vortex flow* has become the second generation of aeronautical flow type in practical use (after the attached flow type over streamlined body; e.g. Küchemann (1978)).

No general theory is available for free vortex-layer separated flow even in the Euler limit, because as seen in Sect. 4.4.4 the self-induced rolling-up process of a vortex sheet is inherently nonlinear. One has to appeal to approximate theories or numerical simulation. The simplest theory in the Euler limit is fully linearized, in which the vortex-sheet rolling up is completely ignored so that the sheet location is known. This is the case in Prandtl's classic lifting-line theory for a thin wing of large aspect ratio (e.g., Prandtl and Tietjens 1934; Glauert 1947; see also Chap. 11). But here we need to address the nonlinearity of the self-induction, with the expense that in some other aspects significant simplification has to be made. This is the case of the *slender-body theory* to be used throughout this section.[6] We consider the slender approximation of vortex-sheet conditions first, then review methods for computing the self-induced evolution of leading-edge vortex-sheet and free wake vortex sheet. Finally, we analyze the stability of a class of slender free vortex-layer separated flow.

### 7.3.1 Slender Approximation of Free Vortex Sheet

Consider a steady flow over a point-nose slender body shown in Fig. 7.18. In a body coordinate-system $Oxyz$ with the body axis along the $x$-direction and $z$-axis vertical up, let the local angle of attack at $x$ be $\alpha(x) = O(\epsilon) \ll 1$, so that the constant oncoming velocity $\boldsymbol{U}$ has $(x, z)$ components

$$\boldsymbol{U} = (U\cos\alpha, U\sin\alpha) = (U, U\alpha) + O(\epsilon^2), \tag{7.45}$$

and the disturbance velocity components are $(u', v, w) = O(\epsilon U)$. Due to the slenderness, the $x$-wise disturbance of the body to the fluid is much smaller than those in cross directions. Consequently, a three-dimensional flow problem is reduced to a cross-flow $U\alpha$ over two-dimensional sections of the body at different $x$, and away from the vortex sheet we only need to consider a two-dimensional disturbance velocity potential $\varphi(y, z; x)$. The three-dimensionality of the flow lies in the $x$-dependent boundary condition, with

[6] This section could be shifted to Chap. 11 on aerodynamics. We put it here for understanding the basic physics of free vortex-layer separated flow as the counterpart of closed-bubble separated flow. Although in engineering applications the slender-body theory has now been replaced by more numerically oriented methods, it provides an opportunity to demonstrate how the general theory of three-dimensional vortex sheet dynamics is specified to concrete problems of significant practical value.

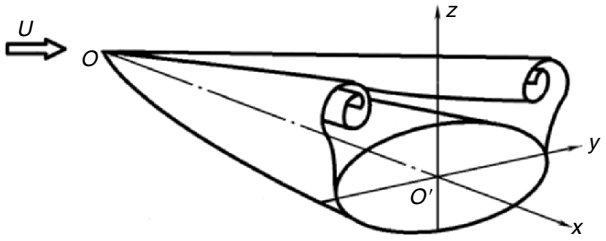


**Fig. 7.18.** Free vortex-layer separated flow from a slender body

$x$ being a parameter. Since $U\alpha \ll U$, the cross flow can always be assumed incompressible, so that

$$\frac{\partial^2 \varphi}{\partial y^2} + \frac{\partial^2 \varphi}{\partial z^2} = 0 \quad \text{at each } x \text{ station}, \tag{7.46}$$

implying that the general method of conformal mapping can be applied. Although (7.46) holds for both subsonic and supersonic oncoming flows, the accuracy is poorer for the former because the upstream influence of the after body cannot be taken into account. The usefulness of slender-body theory lies in its generality: for attached flow over a complicated configuration it is the only analytical method, and for separated flow it is the simplest semianalytical method.

The cross-flow potential $\varphi$ is to be superposed to potentials due to the uniform oncoming flow, angle of attack, and the body volume. Let the cross area of the body be $A(x)$ which for a remote observer appears as a source distribution $b_0(x)$ along the $x$-axis. The relation between $A(x)$ and $b_0(x)$ varies from subsonic to supersonic oncoming flows. The total potential and far-field boundary condition read

$$\Phi = U[x + b_0(x) + \alpha(x)]z + \varphi(y, z; x), \tag{7.47a}$$

$$\frac{\varphi}{U} \sim \alpha(x)z + \frac{A'(x)}{2\pi} \ln r, \quad r^2 = y^2 + z^2 \to \infty. \tag{7.47b}$$

Slender-body theory was developed first for airship aerodynamics, and then applied to attached flow over slender wing and body, wing-body combination, etc., based on (7.47); e.g., Nielsen (1960) and Ashley and Landahl (1965). In extending the theory to separated flow with slender free vortex sheets, the key issue is to ensure the vortex-sheet conditions. For steady flow, two of the conditions can be stated as

$$\boldsymbol{u}^+ \cdot \boldsymbol{n} = \boldsymbol{u}^- \cdot \boldsymbol{n} = \bar{\boldsymbol{u}} \cdot \boldsymbol{n} = 0, \quad \bar{\boldsymbol{u}} \cdot [\![\boldsymbol{u}]\!] = 0, \tag{7.48a,b}$$

Equation (7.48a) tells not only the continuity of normal velocity across any vortex sheet, but also the fact that the sheet must be a stream surface in steady flow. Equation (7.48b) is from the Kelvin circulation theorem $\mathrm{D}[\![\varphi]\!]/\mathrm{D}t = 0$,

which by (4.132) and (4.133) is equivalent to the pressure continuity. What we need now is to find the slender-approximation of (7.48a,b), the steady version of the Kutta condition (4.141), and the Biot–Savart formula (3.31) in convenient component form. The following algebra is based on the work of Clark (1976) and J.H.B. Smith (1978).

As shown in Fig. 7.19a, let a slender vortex sheet $\Sigma$ intersect a cross-plane $\pi$ with unit normal $\boldsymbol{e}_x$ at a curve $C$, which has unit tangent vector $\boldsymbol{t}$. Then $\boldsymbol{e}_x \times \boldsymbol{t} = \boldsymbol{n}_c$ is the unit vector normal to $C$, and $(\boldsymbol{e}_x, \boldsymbol{t}, \boldsymbol{n}_c)$ form a local orthonormal "$C$-frame", where by (7.45) we write

$$\boldsymbol{u} = (U + u_x)\boldsymbol{e}_x + u_s\boldsymbol{t} + u_n\boldsymbol{n}_c + O(\epsilon^2). \tag{7.49}$$

Alternatively, one can use a polar coordinate system $(r, \theta)$, see Fig. 7.19b, which leads to an orthonormal "$P$-frame" $(\boldsymbol{e}_x, \boldsymbol{e}_r, \boldsymbol{e}_\theta)$, by which we can define

$$\text{On vortex sheet } \Sigma: \ r = r(x, \theta) \tag{7.50a}$$

$$\text{Along separation line}: \ \theta = g(x), \quad r = f(x, g(x)). \tag{7.50b}$$

The two frames are related by a rotation about the $x$-axis by an angle $\phi$:

$$\begin{bmatrix} \boldsymbol{t} \\ \boldsymbol{n}_c \end{bmatrix} = \begin{bmatrix} \cos\phi & \sin\phi \\ -\sin\phi & \cos\phi \end{bmatrix} \begin{bmatrix} \boldsymbol{e}_r \\ \boldsymbol{e}_\theta \end{bmatrix}.$$

Now, since (7.48) is expressed in the vortex-sheet intrinsic frame, we need to use both $C$- and $P$-frames to construct that frame under slender approximation. By (7.50a) we have

$$\mathrm{d}r = \frac{\partial r}{\partial x}\mathrm{d}x + \frac{\partial r}{\partial \theta}\mathrm{d}\theta = \frac{\partial r}{\partial x}\mathrm{d}x + r\cos\phi\mathrm{d}\theta;$$

thus the vector increment $\mathrm{d}\boldsymbol{x}$ *tangent to* $\Sigma$ can be expressed as

$$\mathrm{d}\boldsymbol{x} = \boldsymbol{e}_x\mathrm{d}x + \boldsymbol{e}_r\mathrm{d}r + \boldsymbol{e}_\theta r\mathrm{d}\theta = \boldsymbol{e}\mathrm{d}x + \boldsymbol{t}r\csc\phi\mathrm{d}\theta + O(\epsilon^2),$$

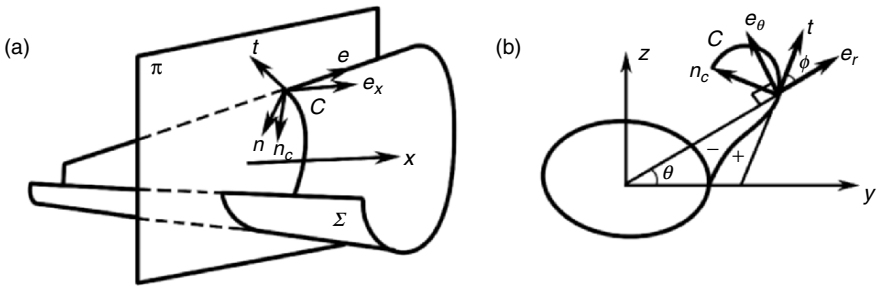


**Fig. 7.19.** Local coordinate systems for slender-approximation analysis, (**a**) the "$C$-frame"($\boldsymbol{e}_x$, $\boldsymbol{t}$, $\boldsymbol{n}_c$), (**b**) the "$P$-frame" ($\boldsymbol{e}_r$, $\boldsymbol{e}_\theta$) on a cross plane. The unit normal vector $\boldsymbol{n}$ of $\Sigma$ is generally not aligned to $\boldsymbol{n}_c$

where

$$\boldsymbol{e} = \boldsymbol{e}_x + \frac{\partial r}{\partial x}\boldsymbol{e}_r = \boldsymbol{e}_x + \boldsymbol{t}\frac{\partial r}{\partial x}\cos\phi - \boldsymbol{n}_c\frac{\partial r}{\partial x}\sin\phi \tag{7.51}$$

is also a unit vector tangent to $\Sigma$, generally not perpendicular to $\boldsymbol{t}$. Then by (7.49) and (7.51), the normal of $\Sigma$ is given by

$$\boldsymbol{n} = \frac{\boldsymbol{e}\times\boldsymbol{t}}{|\boldsymbol{e}\times\boldsymbol{t}|} = \boldsymbol{e}_x\frac{\partial r}{\partial x}\cos\phi + \boldsymbol{n}_c. \tag{7.52}$$

The triad $(\boldsymbol{e}, \boldsymbol{t}, \boldsymbol{n})$ is the desired intrinsic frame on slender $\Sigma$, which casts the exact vortex-sheet condition $[\![\boldsymbol{u}]\!]\cdot\boldsymbol{n} = 0$ to

$$[\![u_n]\!] = -[\![u_x]\!]\frac{\partial r}{\partial x}\sin\phi = O(\epsilon^2).$$

Thus, $u_n$ is approximately continuous across $\Sigma$, and hence

$$[\![\boldsymbol{u}]\!] = [\![u_x]\!]\boldsymbol{e}_x + [\![u_s]\!]\boldsymbol{t} + O(\epsilon^2). \tag{7.53}$$

Therefore, by (7.52) the *slender stream-surface condition* (7.48a) reads

$$\frac{1}{U}\frac{\partial\varphi}{\partial n} = -\frac{\partial r}{\partial x}\sin\phi. \tag{7.54}$$

On the other hand, because $\overline{u}_x = U$, (7.48b) and (7.53) yield

$$[\![u_x]\!] = [\![\boldsymbol{u}]\!]\cdot\boldsymbol{e}_x = -\frac{\overline{u}_s}{U}[\![u_s]\!] = O(\epsilon^2);$$

thus, actually $[\![u_n]\!] = O(\epsilon^3)$. But $[\![u_s]\!]$ has to be retained here since there is no $O(\epsilon)$ term. Note that $[\![\boldsymbol{u}]\!]\cdot\boldsymbol{e}_x$ cannot be simply identified as $\boldsymbol{e}_x\cdot\nabla[\![\varphi]\!] = [\![\varphi]\!]_{,x}$, because $\boldsymbol{e}_x$ is not a tangent vector and the resulting gradient will no longer be tangent to $\Sigma$. Rather, one has to express $\boldsymbol{e}_x$ by $\boldsymbol{e}$ via (7.52), which yields

$$[\![\boldsymbol{u}]\!]\cdot\boldsymbol{e}_x = \frac{\partial[\![\varphi]\!]}{\partial x} - [\![u_s]\!]\frac{\partial r}{\partial x}\cos\phi, \quad [\![\varphi]\!] = \Gamma.$$

Hence, the *slender pressure-continuity condition* reads

$$\frac{\partial\Gamma}{\partial x} = [\![u_s]\!]\left(\frac{\partial r}{\partial x}\cos\phi - \frac{\overline{u}_s}{U}\right). \tag{7.55}$$

Then, the Kutta condition (4.143) requires that in the "downstream side" of the vortex sheet $\Sigma$ (the cusp side is denoted by superscript bar, see Fig. 7.19b) the flow must be along the separation line. Since by (7.50b) the directional ratios of the separation line are

$$1 : \frac{\partial r}{\partial x} : r\frac{\partial\theta}{\partial x} = 1 : \left(\frac{\partial f}{\partial x} + \frac{\partial f}{\partial g}\frac{\mathrm{d}g}{\mathrm{d}x}\right) : f\frac{\mathrm{d}g}{\mathrm{d}x},$$

the same should be $U + u_x^- : u_r^- : u_\theta^-$. This yields, ignoring $O(\epsilon^2)$ terms,

$$u_r^- = U\left(\frac{\partial f}{\partial x} + \frac{\partial f}{\partial g}\frac{\mathrm{d}g}{\mathrm{d}x}\right), \quad u_\theta^- = Uf\frac{\mathrm{d}g}{\mathrm{d}x}. \tag{7.56}$$

Then, since $u_s = u_r\cos\phi + u_\theta\sin\phi$, and since by $\partial r/\partial\theta = r\cot\phi$ and (7.50b) there is $\partial f/\partial g = f\cot\phi$, from (7.56) it follows that

$$u_s^- = U\left(\frac{\partial f}{\partial x}\cos\phi + f\frac{\partial g}{\partial x}\csc\phi\right).$$

On the other hand, from the definition of $[\![u_s]\!]$ and $\overline{u}_s$ there is $[\![u_s]\!] = 2(\overline{u}_s - u_s^-)$; so applying (7.55) to the separation line yields

$$\frac{1}{U}\frac{\mathrm{d}\Gamma}{\mathrm{d}x} = 2\left(\frac{\overline{u}_s}{U} - \frac{\partial f}{\partial x}\cos\phi - f\frac{\partial g}{\partial x}\csc\phi\right)\left(\frac{\overline{u}_s}{U} - \frac{\partial f}{\partial x}\cos\phi\right),$$

from which one solves, dropping $O(\epsilon^2)$ terms,

$$\overline{u}_s = U\frac{\partial f}{\partial x}\cos\phi + \sqrt{\frac{U}{2}\frac{\mathrm{d}\Gamma}{\mathrm{d}x}} \quad \text{at} \quad \theta = g(x), \tag{7.57}$$

where the positive square root is taken to ensure $\overline{u}_s$ is toward downstream. This is the *slender Kutta condition*, which determines the total circulation of free vortex sheets shed from the separation line. The two terms represent the speeds needed for turning the free stream to the separation-line direction and feeding the circulation into the vortex sheet, respectively.

Finally, by (7.52) and (7.53), and recall that $[\![u_x]\!] = O(\epsilon^2)$, the slender vortex-sheet strength reads

$$\boldsymbol{\gamma} = \boldsymbol{n}\times[\![\boldsymbol{u}]\!] = -\boldsymbol{e}_x[\![u_s]\!] + O(\epsilon^2),$$

which causes an induced velocity $\boldsymbol{u}_\pi$ on the cross plane only, in consistency with the slender approximation (7.46). Therefore, it suffices to use the two-dimensional complex-variable form of the Biot–Savart formula:

$$\begin{aligned}\frac{\mathrm{d}W}{\mathrm{d}Z} &= v - iw = -\frac{1}{2\pi i}\int\frac{[\![u_s]\!]\mathrm{d}Z'}{Z - Z'} \\ &= \frac{1}{2\pi i}\int_{\Gamma_0}^{\Gamma_e}\frac{\mathrm{d}\Gamma'}{Z - Z'}, \quad Z = y + iz,\end{aligned} \tag{7.58}$$

where $\Gamma_0$ and $\Gamma_e$ are the values of the circulation at initial and terminal points of the vortex sheet. When $Z \to Z'$, the Cauchy principal value is implied in the integral and we return to the Birkhoff–Rott equation (4.143).

The above slender-body formulation can be simplified when the flow has conical similarity, which will be so when the body model is conical and extends infinitely long. In the body-axis frame (Fig. 7.18), a steady conical flow

(cf. Sect. 6.2.3) depends on only $(y/x, z/x)$ and keeps the same along each ray from the point nose. The body shape and separated vortices are all along rays. The lateral size of a slender conical body is characterized by its semiapex angle $\epsilon$ or semispan $s = kx$ with $k \equiv \tan\epsilon \simeq \epsilon \ll 1$. The flow can be conveniently described by *conical coordinates* $(y', z') = (y/s, z/s)$ in the cross-flow plane and it suffices to examine the flow in a single $(y', z')$ plane. Then in the preceding vortex-sheet conditions we simply have $\partial r/\partial x = k$, $\mathrm{d}g/\mathrm{d}x = 0$. At a spatial point $\boldsymbol{x}$, the ray has length $R = |\boldsymbol{x}|$ and unit vector $\boldsymbol{e}_R = \boldsymbol{x}/R$ given by

$$R = x\sqrt{1 + k^2(y'^2 + z'^2)} = x + O(\epsilon^2), \tag{7.59a}$$

$$\boldsymbol{e}_R = \frac{\boldsymbol{e}_x + k(y'\boldsymbol{e}_y + z'\boldsymbol{e}_z)}{\sqrt{1 + k^2(y'^2 + z'^2)}} = \boldsymbol{e}_x + k(y'\boldsymbol{e}_y + z'\boldsymbol{e}_z) + O(\epsilon^2). \tag{7.59b}$$

Therefore, up to $O(\epsilon)$, a spherical surface $R = \text{const.}$ can be replaced by a $(y', z')$ plane; but the difference between $\boldsymbol{e}_x$ and $\boldsymbol{e}_R$ has a non-negligible effect. *A slender conical vortex can be approximated by a quasi two-dimensional point vortex only on a spherical surface with normal* $\boldsymbol{e}_R$.

As indicated by (7.45–7.47), on a cross plane with normal $\boldsymbol{e}_x$, a slender conical-flow problem is the superposition of an *angle-of-attack problem* $\boldsymbol{u}_\alpha$ caused by a cross-flow $U_n \simeq U\alpha$, and a *thickness problem* $\boldsymbol{u}_a = \boldsymbol{u}_\mathrm{s}(y', z') + U\boldsymbol{e}_x$ caused by an axial flow $U_x \simeq U$ at $\alpha = 0$, where $\boldsymbol{u}_\mathrm{s}$ represents a two-dimensional source distribution due to the body thickness. Here, an important consequence of $\boldsymbol{e}_R \neq \boldsymbol{e}_x$ is: the axial flow $U\boldsymbol{e}_x$ should be further decomposed to $U\boldsymbol{e}_x = U\boldsymbol{e}_R + \boldsymbol{u}_c$, where by (7.59b)

$$\boldsymbol{u}_c(y', z') = -kU(y'\boldsymbol{e}_y + z'\boldsymbol{e}_z) = -\frac{U_n}{K}(y'\boldsymbol{e}_y + z'\boldsymbol{e}_z), \tag{7.60}$$

with

$$K \equiv \frac{\alpha}{\epsilon} \tag{7.61}$$

being a *conical similarity parameter* that measures the relative magnitude of $\alpha$. Obviously, the linear velocity field $\boldsymbol{u}_c$ exists in any slender conical flow, and represents a *uniform sink* everywhere in the $(y', z')$ plane. The boundary condition for the thickness problem has to be jointly satisfied by $\boldsymbol{u}_\mathrm{s}$ and $\boldsymbol{u}_c$:

$$\boldsymbol{n} \cdot \boldsymbol{u}_\mathrm{s} = -\boldsymbol{n} \cdot \boldsymbol{u}_c = \frac{U_n}{K}(y'n_y + z'n_z) \quad \text{on } C, \tag{7.62}$$

where $\boldsymbol{n}$ now denotes the unit normal vector of the cross-flow contour $C$. Consequently, what matters is the total cross-flow with free-stream velocity $U_n$ (Cai et al. 2003):

$$\boldsymbol{e}_y v(y', z') + \boldsymbol{e}_z w(y', z') = \boldsymbol{u}_\alpha(y', z') + \boldsymbol{u}_\mathrm{s}(y', z') + \boldsymbol{u}_c(y', z'). \tag{7.63}$$

### 7.3.2 Vortex Sheets Shed from Slender Wing

The quasi two-dimensional feature of the slender approximation naturally suggests extending the conformal-mapping method from body contour to the contour $C$ of a separated vortex sheet in a cross-flow plane $Z = y + iz$, where $C$ is treated as a cut. This approach was mainly developed at Royal Aeronautical Establishment (RAE) of the United Kingdom in 1960s and 1970s so we call it the *RAE method*. In this method (7.54), (7.55), (7.57), and (7.58) are all necessary input. A major difficulty is that once the vortex sheet rolls into a vortex with distributed vorticity and spiral arms (Chap. 8), inside the vortex core the conformal mapping can no longer be used. In the RAE method (Smith 1968) the tightly rolled-up part of the sheet is replaced by a single line vortex of circulation $\Gamma_v(x)$ at $Z_v$ on each cross plane, which is connected to the unrolled sheet by a cut that can satisfy (7.53) but not (7.54). The best one can do is to impose (7.54) in averaged sense, i.e., the total force acting on the point vortex plus the cut is zero. This condition determines $Z_v$.

Smith (1968) applied the RAE method to a slender flat-plate delta wing at incidence. The wing has infinite downstream extension so the flow is conical. On a cross plane the wing semispan is $s = kx$. Figure. 7.20 is the calculated location of vortex sheet and line vortex (appearing as a point) on the $Z$-plane at different $\alpha$. The agreement of computed spanwise pressure distribution with experimental data is reasonably good. The main discrepancy is due to the incapability of computing the secondary separation from the upper surface of the wing, induced by the primary leading-edge vortex (Fig. 7.7a). The secondary vortex has opposite circulation and weakens the suction peak caused by the primary vortex.

By using the RAE method, Fiddes (1980) calculated the symmetrically separated vortex sheets from a cone of elliptic cross section at incidence, which happens at the nose of aircrafts and missiles. In the Euler limit the location $\theta_s$ of separation line is indeterminate, which in Fiddes' calculation was taken from experimentally observed values. Fiddes (1980) also imbedded the triple-deck structure (Sect. 5.2) into the calculation to iteratively determine the separation line from an initially assumed $\theta_s$. The results are in reasonable agreement with experiments.

Most of the role of the RAE method has now been replaced by more efficient numerical methods.[7] Numerical computations can also be greatly simplified within the slender approximation (7.45) and (7.46). Write the local axial velocity as $U = x/t$, a steady three-dimensional flow problem at different $x$-stations is reduced to an unsteady two-dimensional cross-flow problem at different $t$.

[7] In numerical approaches the vortex-sheet conditions (7.48a) and (7.48b) are automatically satisfied, but the Kutta condition and Biot-Savart formula or its equivalence remain necessary.

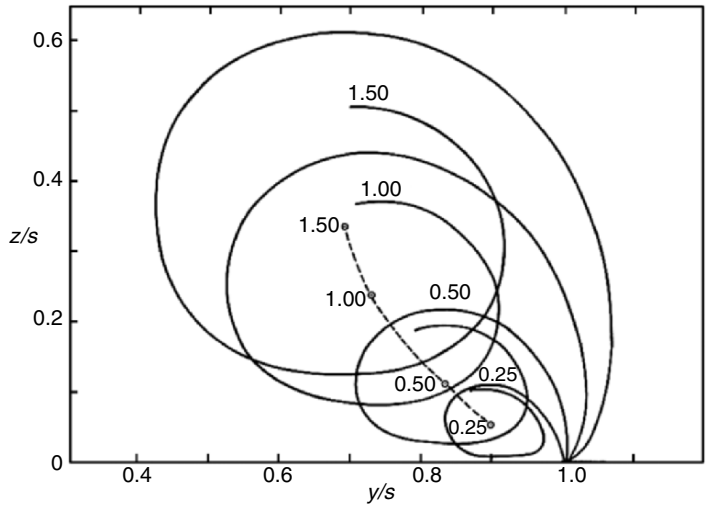


**Fig. 7.20.** Location of vortex sheet (*solid curve*) and line vortex (*circle*) over a slender delta wing for different $K = \alpha/k$ (*marked by numbers*), calculated by the RAE method. From Smith (1968)

Figure. 7.21a shows the pattern of a leading-edge vortex sheet from a slender delta wing of finite chord length (so the flow does not have conical similarity) at a typical cross-plane, computed by Ma and Jin (1991) using the viscous *vortex-in-cell method*. According to the Kutta condition, the vortex sheet is set to leave the leading edge tangentially. By carefully adjusting the grid, Ma and Jin were able to capture not only the global pattern but also the tendency of the sheet to break into discrete vortices due to the Kelvin–Helmholtz instability (Chap. 9).

Then, as the leading-edge vortex layer travels downstream to the wake, it must meet the trailing-edge vortex layer and merge to a single and complicated structure. The rolling-up of wake vortex-sheet alone has been beautifully computed by Krasny (1987) also within the same $U = x/t$ approximation, as already exemplified by Fig. 4.21; but the evolution of the merged leading- and trailing-edge vortex sheets is of particular interest. This has also been computed by Ma and Jin (1991), see Fig. 7.21b at a typical wake plane. Figure. 7.21c is the sketch of the vortex-sheet pattern by Küchemann (1978) for comparison.

It should be stressed that although numerically one can compute the tightly rolled-up part of a vortex sheet, this part cannot be accurately simulated on a cross plane. In the preceding analysis we have neglected the contribution of $[\![u_x]\!] = \boldsymbol{e}_x \cdot \nabla\Gamma$ to the vortex sheet strength $\boldsymbol{\gamma}$, which for an isolated vortex sheet is of $O(\epsilon^2)$. However, when many layers of the sheet squeeze together, $[\![u_x]\!]$ may have an $O(1)$ integrated effect and cause a strong

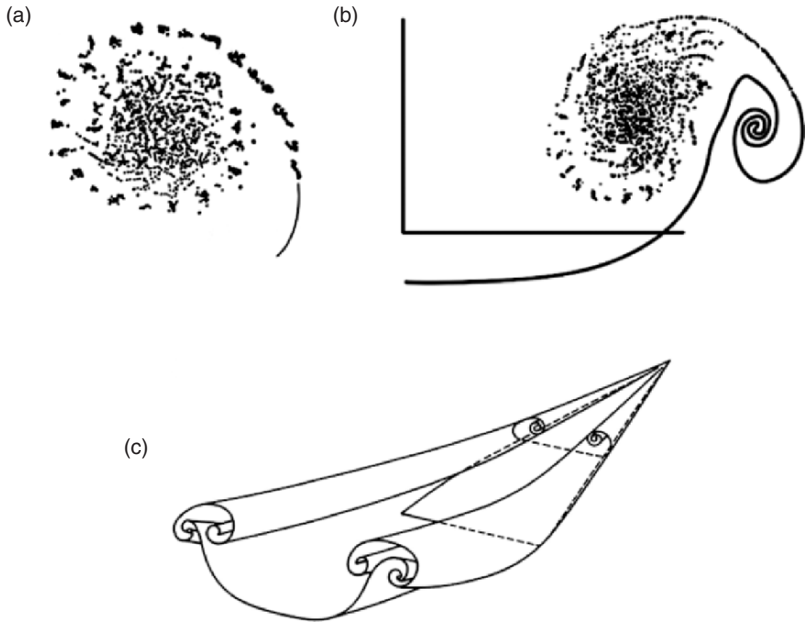


**Fig. 7.21.** The evolution of vortex sheets shed from a slender delta wing at $\alpha = 20.5^\circ$ and $Re = 10^6$ based on root-chord length, computed by Ma and Jin (1990), (**a**) a leading-edge vortex sheet upstream the trailing edge, (**b**) a merged leading- and trailing-edge vortex sheet in the wake, (**c**) is reproduced from Küchemann (1978)

axial velocity inside the vortex core (for an example see Sect. 11.5.4). This will make the flow inevitably three-dimensional, beyond the ability of any slender approximation.

### 7.3.3 Stability of Vortex Pairs Over Slender Conical Body

We now shift our focus from the rolling up process of vortex sheets shed from a slender body to the slender vortex pair formed thereby, which is the strongest structure in a free vortex-layer separated flow. As the angle of attack $\alpha$ increases to a critical value, an originally steady, stable, and symmetric vortex pair above a slender wing or body may become unstable, leading to asymmetric or unsteady structures, or both. The asymmetric vortices will cause a large rolling moment in the case of slender wing, or a large side force in the case of slender smooth body, even at zero roll and yawing angles, respectively. The underlying physical mechanism has been a controversial issue for long time. But, within the slender conical-flow approximation, simple inviscid analyses may explain the phenomenon quite well at least qualitatively, without the need for systematic knowledge of hydrodynamic stability.

The occurrence of the asymmetric vortex-flow solution besides the symmetric one over a circular cone at high enough angles of attack has been

found by Dyer et al. (1982) using the simplest cross-flow point-vortex model. They observed that at a critical similarity parameter $K$ defined by (7.61) the vortex flow has a bifurcation to a symmetric solution and an asymmetric solution even when the separation lines are postulated as symmetric. A systematic analysis of the instability of the symmetric and asymmetric vortex pair under small conical disturbances has been carried out by Cai et al. (2003, 2004) for various slender conical flows. In their analysis the feeding sheet is ignored which, although important in estimating the total force (e.g., Fiddes and Smith 1982), has negligible effect on vortex stability due to much weaker vorticity concentration.

In what follows we present the main analysis of Cai et al. (2003) for the stability of symmetric vortex pairs. Our concern is not the incompressible and potential flow field but the motion of point vortices in the $(y', z') = (y/x, z/x)$ plane, which is a *discrete* dynamic system constrained by the flow boundary conditions (for a general discussion of point-vortex system see Sect. 8.3.1). For example, with vortices 1 and 2 behind a slender cone of radius $a = kx$, the system has 4 degrees of freedom. By (7.62) and (7.63), the velocity of one such vortex is determined by the sum of the vortex-induced velocity $\boldsymbol{u}_\alpha$ (excluding the self-induction), the source-caused velocity $\boldsymbol{u}_\mathrm{s}$, and the velocity $\boldsymbol{u}_c$ caused by the sink. In terms of complex variable $Z = y' + iz'$, therefore, for vortex 1 we may write

$$\begin{aligned}\frac{\mathrm{d}Z_1}{\mathrm{d}t} &= \frac{\mathrm{d}Z_\alpha}{\mathrm{d}t} + \frac{\mathrm{d}Z_s}{\mathrm{d}t} + \frac{\mathrm{d}Z_c}{\mathrm{d}t} = F(Z_1, \overline{Z}_1, Z_2, \overline{Z}_2) \\ &= U_n\left(1 - \frac{a^2}{Z_1^2}\right) + \frac{i\Gamma}{2\pi}\left(\frac{1}{Z_1 - a^2/\overline{Z}_2} - \frac{1}{Z_1 - Z_2} - \frac{1}{Z_1 - a^2/\overline{Z}_1}\right) \\ &\quad + \frac{U_n a}{K Z_1} - \frac{U_n \overline{Z}_1}{aK}. \end{aligned} \tag{7.64}$$

The point-vortex velocity defined in this way represents the velocity at which the vortex would move, and will be called *vortex velocity* to be distinguished from the flow-field velocity. Note that the uniform sink flow is not an analytic function of $Z$. In general $\mathrm{d}Z/\mathrm{d}t = F(Z, \overline{Z})$ may not be two-dimensionally divergence-free although the flow is incompressible. This is not only due to the existence of variable axial velocity in three-dimensional slender-body theory, but also because we are dealing with a discrete system even for truly two-dimensional point vortices.

Now return to real variables, assume at $t = 0$ the vortex at $\boldsymbol{x}_0$ is stationary with $\boldsymbol{u}_0 = \boldsymbol{0}$ (a fixed point), and a disturbance shifts it to $\boldsymbol{x}_0 + \delta\boldsymbol{x}$ at $t = 0^+$ ($\delta\boldsymbol{x}$ is constrained by boundary conditions), such that similar to (2.13) or (7.3) but now for discrete vortices, the linearized system and solution read

$$\frac{\mathrm{d}}{\mathrm{d}t}\delta x_i = \delta x_j u_{0i,j} \quad \text{so that} \quad \delta x_i(t) = \delta x_i(0)\mathrm{e}^{\lambda_{1,2}t},$$

where $\lambda_1$ and $\lambda_2$ are the eigenvalues of vortex velocity gradient tensor $\nabla\boldsymbol{u}_0$. Thus, within the linearized theory, the vortex system will be stable (necessary

for nonlinearly stable), neutrally stable, and unstable (sufficient for nonlinearly unstable) if both $\lambda_1$ and $\lambda_2$ have negative real parts, are imaginary, and at least one of $\lambda_1$ and $\lambda_2$ has positive real part, respectively. It is easily verified that

$$\lambda_{1,2} = \frac{1}{2}\left(D_0 \pm \sqrt{D_0^2 - 4J_0}\right), \tag{7.65a}$$

in which

$$J_0 \equiv \left.\frac{\partial(v,w)}{\partial(y,z)}\right|_{\boldsymbol{x}_0}, \quad D_0 \equiv \nabla\cdot\boldsymbol{u}|_{\boldsymbol{x}_0} \tag{7.65b}$$

are the Jacobian of the gradient and divergence of the vortex velocity at $\boldsymbol{x}_0$, respectively. While the stability character can be readily identified if one of $D_0$ and $J_0$ vanishes, it is also easy to see that if both are nonzero then

$$\text{Unstable if } \begin{cases} D_0 > 0 & \text{for any} \quad J_0, \\ J_0 < 0 & \text{for any} \quad D_0; \end{cases} \tag{7.66a}$$

$$\text{Stable if } \; D_0 < 0 \quad \text{and} \quad J_0 > 0. \tag{7.66b}$$

In complex variable the disturbance displacement reads $(\delta Z_1, \delta Z_2)$ for vortices 1 and 2. Since for any disturbance there is

$$(\delta Z_1, \delta Z_2) = (\delta Z_s, \delta\overline{Z_s}) + (\delta Z_a, -\delta\overline{Z_a}) \quad \text{with}$$
$$\delta Z_s = \frac{1}{2}(\delta Z_1 + \delta\overline{Z_2}), \quad \delta Z_a = \frac{1}{2}(\delta Z_1 - \delta\overline{Z_2}),$$

it suffices to consider the stability under symmetric and antisymmetric disturbances separately.

We now apply the above simple theory to examine the stability of some symmetric slender vortex pair. As comparison, consider first the truly two-dimensional flow over a circular cylinder with a pair of symmetric separated vortices, for which the source and sink terms in (7.64) are absent, and there is $U_n = U$ and $Z_2 = \overline{Z}_1$, see Fig. 7.22. The stationary condition for undisturbed vortices is obtained by letting the right-hand side of (7.64) vanish, which leads to the famous *Föppl vortices* (Föppl 1913)[8]: stationary vortex pair must be located on a pair of special curves (*Föppl line*, see Fig. 7.22) with special circulations

$$z_0 = \pm\frac{1}{2}\left(r_0 - \frac{a^2}{r_0}\right), \quad \Gamma = \mp 4\pi U z_0\left(1 - \frac{a^4}{r_0^4}\right), \quad r_0 = \sqrt{y_0^2 + z_0^2}. \tag{7.67}$$

Then, Cai et al. (2003) have given a general proof that, for any two-dimensional flow fields obtainable from the circular-cylinder flow through a

[8] The Föppl vortices are the first theoretical model of closed-bubble separated flow, which we now see is very different from the corresponding Euler-limit.

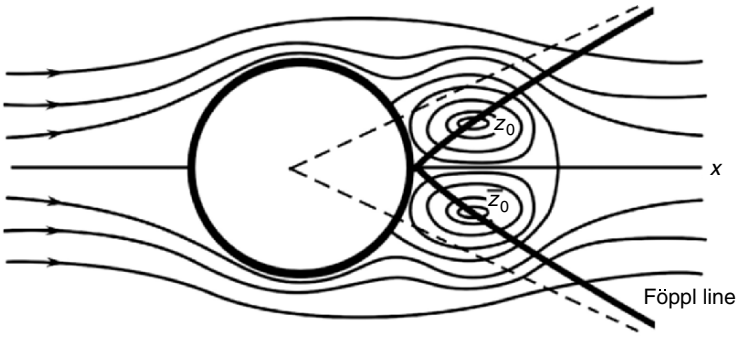


**Fig. 7.22.** Stationary vortex pair behind a circular cylinder and the Föppl line

series of conformal mappings, if the vortex system is initially placed symmetrically then there must be $D_0 = 0$, and hence (7.65a) is reduced to

$$\lambda_{1,2} = \pm\sqrt{-J_0}.$$

It is then easily seen that for antisymmetric disturbance there is $J_0 < 0$, and hence the flow is unstable (first proved by Föppl (1913)); while for symmetric disturbance there is $J_0 > 0$, and hence the flow is linear neutrally stable (first proved by Smith (1973)). Therefore, for an arbitrary small disturbance, *a* symmetric point-vortex pair in any two-dimensional incompressible flow cannot be stable.

In contrast to truly two-dimensional flow, the uniform sink (7.60) plays a crucial role in the slender-conical vortex stability, since solely by this term there is

$$D_0 = -\frac{2U_n}{aK} < 0, \tag{7.68}$$

no matter where the vortices locate. By (7.66b), the appearance of this sink is necessary for a pair of vortices to be stable. It reflects a basic stabilizing mechanism (in a highly simplified manner, of course): *t*he vorticity continuously generated from the body surface and entering slender free vortices can be balanced by its continuous axial advection, so the over-saturation and shedding of vorticity, typical in truly two-dimensional flow, can be avoided or delayed. Topologically, a vortex in a background sink-flow appears as a stable spiral on the $(y', z')$ plane rather than a center (Sect. 7.1.1). Note that since by (7.68) $D_0$ is inversely proportional to $K$, for fixed $\epsilon$ an increase of $\alpha$ always tends to make the flow less stable or more unstable. So does the thickness effect, which pushes the vortices away from the body. The thickness effect overrides the sink effect when $J_0 < 0$, for which the vortex will appear as a saddle point in the $(y', z')$ plane and is unstable.

Cai et al. (2003) have analyzed the stability property of several typical conical configurations as function of $K$ and the separation point (the semisaddle on the contour $C$). For slender circular cones the stationary symmetric vortex

flow is stable under small symmetric disturbances, but unstable under small antisymmetric disturbances as demonstrated by Fig. 7.23. Hence, an initially symmetric vortex flow tends to become asymmetric. The instability is mainly from the thickness effect.

In contrast, for slender flat-plate delta wing with $\boldsymbol{u}_{\rm s} = \mathbf{0}$ in (7.63), the angle-of-attack problem is obtainable from (7.64) by conformal mapping. It is found that $J_0 > 0$ for both symmetric and antisymmetric disturbances with $0 < K \leq 10$, see Fig. 7.24, and hence the symmetric vortex pair is stable. This confirms and extends an earlier result of Huang and Chow (1996). In between

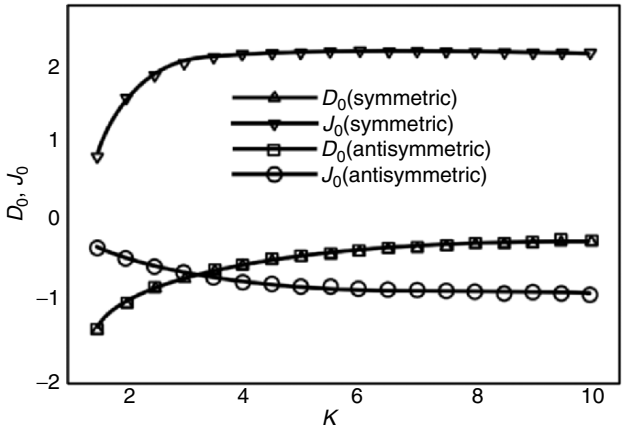


**Fig. 7.23.** $D_0$ and $J_0$ for symmetric vortices above slender circular cones of different $K$, under symmetric and antisymmetric disturbances. The separation angle is $\theta = 34^\circ$ (counted from the real total point). Reproduced from Cai et al. (2003)

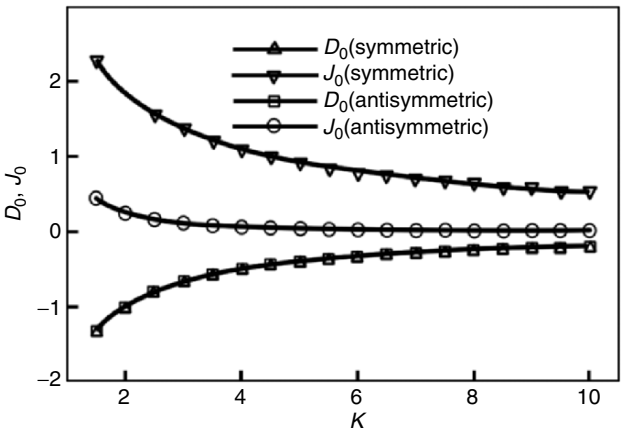


**Fig. 7.24.** $D_0$ and $J_0$ for symmetric vortices above slender delta wing of different $K$, under symmetric and antisymmetric disturbances. Reproduced from Cai et al. (2003)

the circular cones and flat-plate delta wing, slender elliptic cones with different thickness ratio $\tau$ and separation points have also been examined. For example, for antisymmetric disturbance, as $\tau$ increases from zero, the flow changes from stable to unstable. The stable spiral and saddle patterns in the $(y', z')$ plane for a stable and unstable vortex, respectively, are also illustrated.

Cai et al. (2003) have also studied the stabilizing effect of fins on cone and delta wing. Their predictions based on this simple model have been compared with available experimental results with reasonable agreement. Using the same approach, Cai et al. (2004) have further studied the stability of asymmetric vortex pair.

Needless to say, the conical-flow assumption employed in the preceding analysis cannot follow the development of disturbances along a vortex axis as in the case of *convective instability* (Chap. 9), which has been considered by some authors a preferred mechanism for certain vortex asymmetry problems (see the review of Cai et al. (2003)). Another possible mechanism for the appearance of asymmetric vortices having been argued is the asymmetry of flow separation/reattachment on both sides of the body (Ericsson 1992).

## 7.4 Unsteady Bluff-Body Separated Flow

Unlike steady separated bubble flow behind a bluff body discussed in Sect. 7.2, unsteady separated flow from bluff bodies is a very common existence and of great significance in engineering applications. It causes fluctuating drag and lateral force to the body and is a major source of flow-induced structural vibration and noise. Of various transient or periodic separated flows, the incompressible flow past a stationary and nominally two-dimensional bluff cylinder of cross-flow length $D$ is most important. It already possesses almost the entire complexity of shearing process, such as flow separation, free shear layer and its rolling up, vortex interactions, various shear instabilities, transition to three-dimensional flow and to turbulence, and unsteady turbulent separated flow. After over a century of effort since Strouhal (1878) observed that the frequency $f$ of vortex shedding is proportional to $U/D$ with the proportionality constant now being known as the *Strouhal number* $St = fD/U$, and Kármán (1912) constructed the vortex street model (Sect. 6.4.3) and estimated the drag, "the problem of bluff body flow remains almost entirely in the empirical, descriptive realm of knowledge." (Roshko 1993). The great complexity and importance in applications of bluff-body flows are well demonstrated by the comprehensive two-volume manograph of Zdravkovich (1997, 2002).

Nevertheless, the formation mechanism of vortex shedding has been clarified, and some of the mechanisms that cause sudden changes of the flow patterns, Strouhal number $St$, and drag coefficient $C_{\mathrm{D}}$ at different Reynolds numbers $Re = UD/\nu$ have been identified. For the latest comprehensive review see Williamson (1996). In this section we review the basic phenomena, discuss the formation process of the vortex shedding, and introduce a

model to predict the basic $Re$-dependence of $St$ and $C_{\mathrm{D}}$ in which the integrated vorticity and energy balances are incorporated.

### 7.4.1 Basic Flow Phenomena

Bluff bodies with smooth-surface separation and fixed separation are typified by circular cylinder and flat plate normal to the oncoming flow, respectively. In both cases the flow is characterized by high $C_{\mathrm{D}}$ and periodic vortex shedding, of which the quantitative behavior depends on the Reynolds number. The key issue of bluff-body flow is the $Re$-dependence of $St$ and $C_{\mathrm{D}}$, and the underlying mechanisms. In Fig. 7.25 we plot the curves of $St$, the time-averaged $C_{\mathrm{D}}$, and the time-averaged *base suction coefficient* $-C_{\mathrm{p_b}}$ versus $Re$ for circular cylinder, based on experimentally measured data.[9] The $-C_{\mathrm{p_b}}$ is defined as negative of the pressure coefficient at the downstream end $b$ of the body:

$$-C_{\mathrm{pb}} = -\frac{p_{\mathrm{b}} - p_{\infty}}{\frac{1}{2}\rho U^2}, \tag{7.69}$$

which reflects the sensitivity of the flow pattern to $Re$ more adequately than that of $C_{\mathrm{D}}$. The $-C_{\mathrm{p_b}}$ for Navier–Stokes solutions of the *steady* attached and separated flow (Dennis and Chang 1970; Fornberg 1985) at $Re < 700$ are also shown for comparison, of which the trend is opposite to the realistic unsteady flow.

Figure 7.25 reveals that there are different regimes divided by some critical $Re$ marked by A, B,...., J. Each regime has its special flow pattern, as summarized schematically in Fig. 7.26 for side view and top view. A few typical visualization photos are shown in Fig. 10.42 of Chap. 10; for more see Van Dyke (1982). In each regime, both $St$ and $-C_{\mathrm{pb}}$ have corresponding special features. The physical events behind Figs. 7.25 and 7.26 are briefly outlined below (Roshko 1993; Williamson 1996; Noack 1999).

1.*Steady flow* (regime before A, $Re < 49$).
Similar to the separated bubble flow over a sphere seen in Sect. 4.2.2, at $Re = 4$ a pair of standing vortices appears behind the circular cylinder due to a local topological bifurcation at the rear stagnation point, characterized by the appearance of new fixed points (Bakker 1991). But, no hydrodynamic instability occurs (Yin and Sun 2003); so we say a *kinematic bifurcation*. Then, in the steady separated-bubble regime ($4 < Re < 49$) the flow is globally stable with respect to all three-dimensional disturbances.

2.*Laminar parallel and oblique shedding* (regime A–B, $49 < Re < 140$–$194$). At the first critical Reynolds number $Re_{\mathrm{cr1}} \simeq 49$ the flow becomes linearly

[9] The real measured data have certain diversity due to the difference of experimental conditions such as cylinder roughness, amplitude and spectra of free-stream turbulence, aspect ratio of the cylinder, end conditions, and blockage ratio, etc.

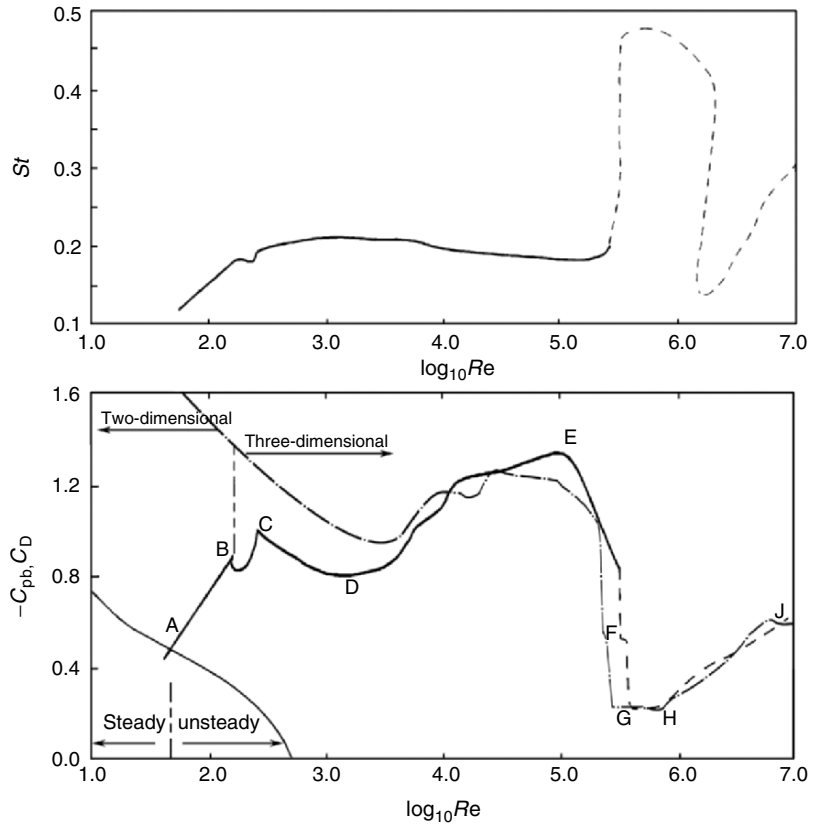


**Fig. 7.25.** The variation of (**a**) $St$, and (**b**) $-C_{\mathrm{pb}}$ (*solid and dashed lines*) and $C_{\mathrm{D}}$ (*dashed-dotted line*) as $Re$. Based on Schewe (1983), Roshko (1993), Norberg (1994), and Williamson (1996)

unstable with respect to two-dimensional disturbances and experiences a (dynamic) supercritical *Hopf bifurcation*, leading to laminar and parallel vortex shedding, which forms a Kármán vortex street that is linearly stable to three-dimensional disturbances.

The experimental conditions at the spanwise ends of the cylinder always cause some three-dimensional disturbances, which when $Re > 64$ will propagate to the midspan region of the cylinder and lead to *oblique shedding* (vorticity lines make an angle $\theta \neq 0$ to the cylinder axis) with lower frequency $St_\theta = St_0 \cos\theta$. In different spanwise regions the oblique shedding may have different $St_\theta$, as sketched in Fig. 7.26, so as $Re$ increases at the measurement point the measured signal may jump from one mode to another to manifest as a discontinuity in the $St$-curve. This was observed at $Re \simeq 75$ (not shown in Fig. 7.25). The end-conditions can be carefully controlled to resume parallel

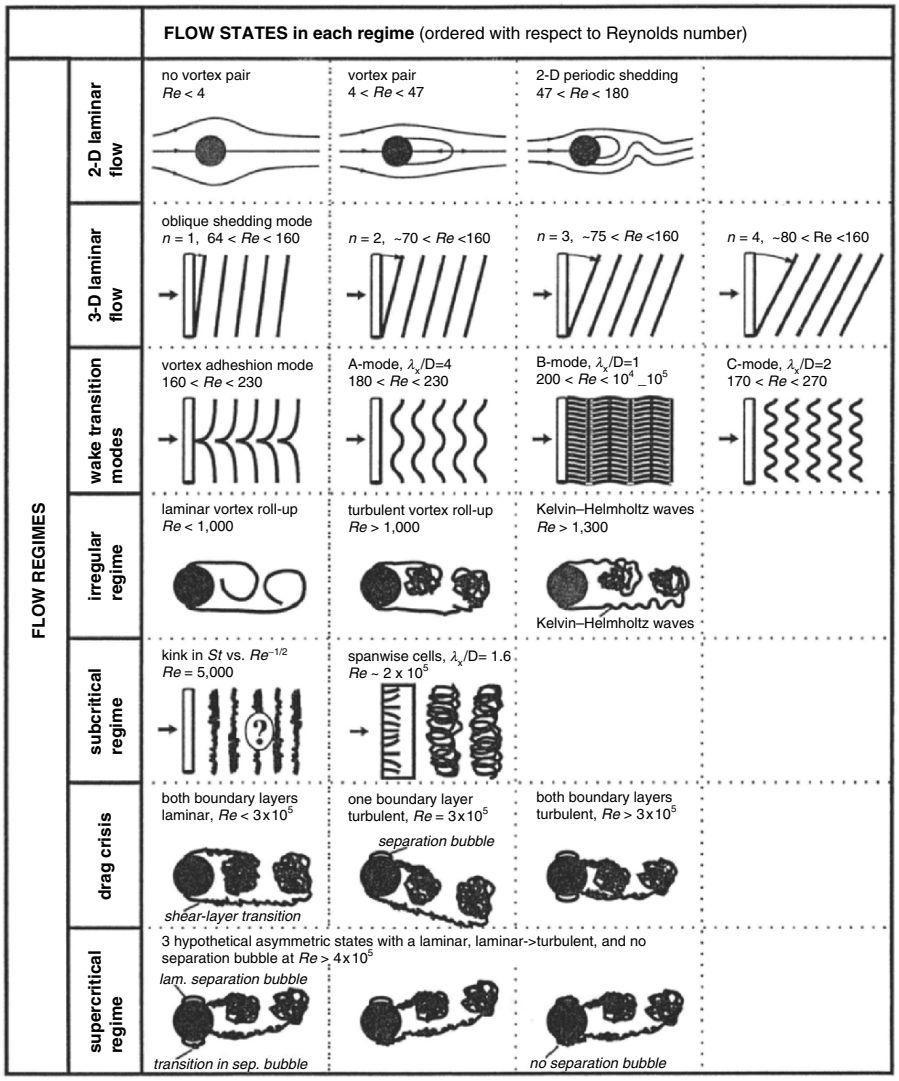


**Fig. 7.26.** Schematic patterns of unsteady bluff-body flow in different regimes. Based on Noack (1999)

shedding, and a "universal" smooth $St$-curve can be obtained if for oblique shedding one plots $St_\theta / \cos\theta$.

3. *Three-dimensional wake* (regime B–C, $190 < Re < 260$).
The wake becomes intrinsically three dimensional (not associated with end-effect) due to two bifurcations at $Re_{\mathrm{cr}2} = 190$ and $Re_{\mathrm{cr}3} = 260$ (Henderson and Barkley 1996; Barkley and Henderson 1996). At $Re_{\mathrm{cr}2}$ the flow is linearly

unstable with respect to a spanwise wavelength of $\lambda_s/D = 4$, called "mode A" instability, leading to a slightly subcritical onset of three dimensionality. Flow visualization shows the inception of vortex loops and formation of streamwise vortex pairs (Fig. 7.27a). This instability causes the discontinuity of both $St$ and $-C_{pb}$ curves at $Re_{cr2}$. Then for $Re$ in 230–260 there is a graduate energy transfer from the mode A shedding to a "mode B" shedding in which finer-scale streamwise vortices of $\lambda_s/D \sim 1$ appear (Fig. 7.27b) due to a supercritical bifurcation at $Re_{cr3}$. In this regime of transition to three-dimensional wake, the local shedding-phase difference along the span also causes some large-scale dislocations of the shed vortices.

The formation mechanism of wake vortices changes in this regime. We have seen that at small $Re$ the wake vortices are formed due to a kinematic topological bifurcation. Only when $Re^{-1/2} \ll 1$, i.e., $Re = O(10^2)$ and above, can a boundary layer and its separated shear layer be sufficiently thin, and wake vortices be formed by shear-layer rolling-up.

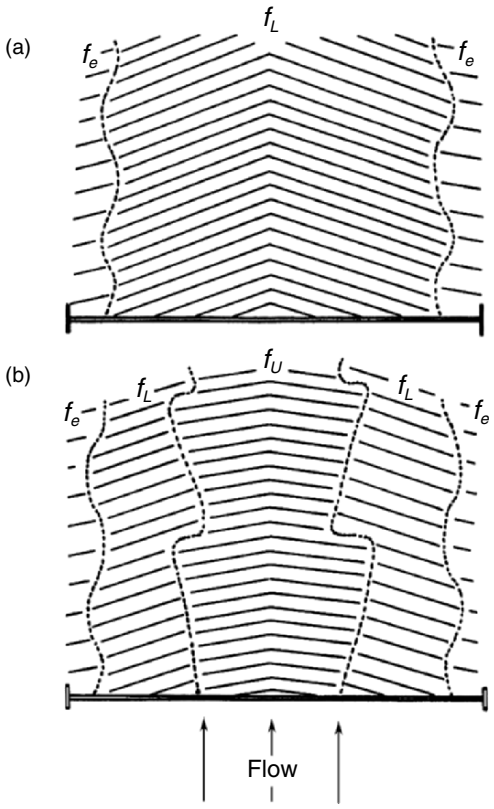


**Fig. 7.27.** Sketch of oblique shedding, (**a**) periodic mode with a chevron-shaped oblique vortex pattern ($64 < Re < 178$), (**b**) quasi-periodic mode ($Re < 64$). From Williamson (1989)

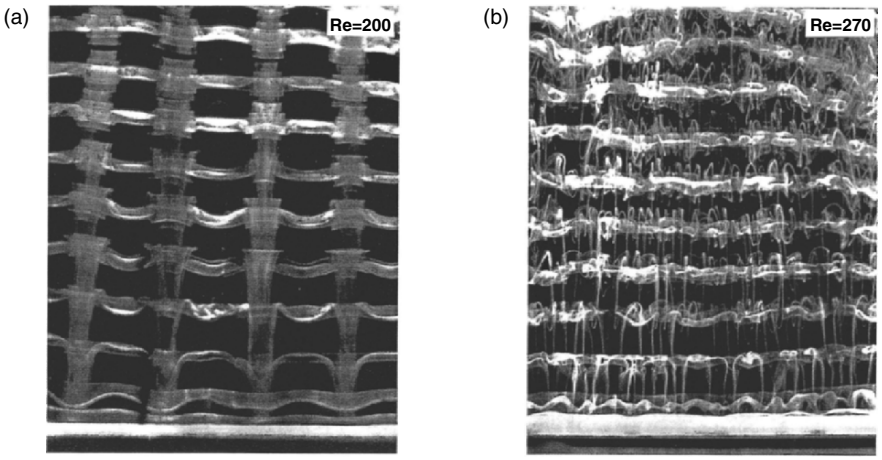


**Fig. 7.28.** Flow visualization of (**a**) mode A instability at $Re = 200$ and (**b**) mode B instability at $Re = 270$. From Williamson (1996)

4. *Transitional and turbulent flow* (regimes C–D to H–J, $Re > 260$).
To gain a complete idea of the complicated $Re$-dependence of unsteady separated flows in the full $Re$ range, we continue our discussion on the physics behind Fig. 7.25 to transitional and turbulent flow that may also be a part of Chap. 10. As $Re$ increases from 260, the flow starts the transition process to turbulence. The transition first occurs in the wake, where fine-scale three-dimensional structures are more and more disordered. This causes a reduction of the base suction, associated with an increase of $St$ and the length of vortex-street formation region. Then, in regime D–E the free shear layer transition starts at about $Re \sim 1,300$ due to the *Kelvin–Helmholtz instability* (Sect. 9.2.2), where $St$ and $-C_{\rm pb}$ reach a minimum and maximum, respectively. As the shear layer becomes turbulent, $-C_{\rm pb}$ and $C_D$ increase, while $St$ and the length of formation region are gradually reduced.

Then, for $Re < 3 \times 10^5$, the boundary layers at both sides are still laminar although the wake and free shear layers have become turbulent. Around point $E$ ($Re \simeq 3 \times 10^5$) the boundary-layer at one side starts transition and hence can remain attached at stronger adverse pressure gradient. This shifts the separation much further downstream. The transition does not occur simultaneously at the other side, implying an asymmetric state with nonzero mean lift. At higher $Re$ the boundary layers at both sides are turbulent, causing a drastic drop of the $C_D$ and $-C_{\rm pb}$ down to 0.2 ("*drag crisis*") and rise of $St$ (up to 0.5), and a reduction of the vortex-street formation region. But the flow is not completely random. Roshko (1961) has discovered the reappearance of periodic turbulent vortex shedding in the H–J regime, indicating that the alternative fully turbulent shear-layer rolling-up mechanism reappears at very large $Re$.

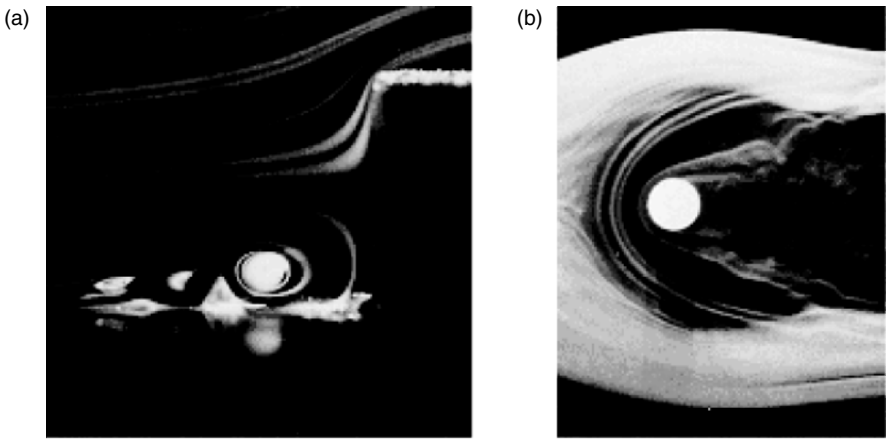


**Fig. 7.29.** Necklace vortices, (**a**) side view, (**b**) top view. From Van Dyke (1982)

Note that all the flow patterns over the circular cylinder so far discussed at different $Re$ cannot be applied to the portion near the ends of the cylinder, which always exist in reality, e.g., a free end or bounded by a flat plate. Once the end effect is considered, inherently three-dimensional new vortex structures must occur that are very different from those observed in the normally two-dimensional mid-portion of the cylinder. A familiar example is the *necklace vortices* at the juncture of the cylinder and a perpendicular flat plate (the prototype of wing-fuselage juncture), see Fig. 7.29. The oncoming attached boundary layer along the wall encounters a strong adverse pressure gradient as approaching the cylinder and separates ahead of it, forming a separated vortex of which the two legs are advected downstream at both sides. As $Re$ increases the primary necklace vortex may induce a secondary one, which could causes a tertiary one, etc., so that the vortex system at the juncture is increasingly complicated and finally become turbulent.

### 7.4.2 Formation of Vortex Shedding

At the critical value $Re_{\rm cr} \simeq 49$, one observes disturbance waves traveling downstream on the sides of the steady closed separated bubbles. The velocity fluctuation causes a Reynolds stress, which makes the base suction start to be higher than that it would take in steady flow at the same $Re$, see Fig. 7.25b. A further increase of $Re$ then causes a sudden inception of the wake instability and growth of fluctuations, making the bubble break into vortex-shedding mode. This happens in a near-wake *vortex formation region*, which is crucial for the entire wake since it is the region where vortex shedding is initiated at *all* Reynolds numbers.

At $Re \gg 1$, the interaction of the upper and lower separated shear layers plays an important role in this vortex-formation region (Gerrard 1966).

Consider the upper shear layer which rolls into a vortex with $\omega < 0$ of increasing strength due to the continuous feeding of vorticity from the upstream boundary layer. Suppose the vortex is stronger than that from the lower shear layer due to an asymmetric disturbance. It then entrains the lower-side fluid with positive and zero vorticity across the wake to enter the upper side. This causes a vorticity cancellation, which eventually cuts off the feeding sheet so that the vortex with $\omega < 0$ has to shed downstream. The lower shear layer will then roll into a stronger vortex and the process is repeated to form a cycle.

Gerrard (1966) further proposed that the entrained fluid from opposite side may enter different regions of the other side in a delicate balanced manner, see the sketch of Fig. 7.30. Fluid $a$ enters the vortex and weakens it; fluid $b$ enters the feeding shear layer and plays the key role to cut it; and fluid $c$ moves back toward the cylinder where it is cancelled in the next half of the cycle. Therefore, the vorticity in the formation region and shed vortices (denoted by $V$ in the figure) is considerably weaker than that in the shear layers. This overall picture has been confirmed and refined by Green and Gerrard (1993) for $Re > 500$.

According to Green and Gerrard (1993), the end-point location of the vortex formation region coincides with the overall location in the wake where the vortex strength is a maximum. As $Re$ increases, the vortex formation region shrinks, while the base suction coefficient grows (a larger drag) as seen from Fig. 7.25, which is progressively dominated by the Reynolds stress in the shear layers.

The above qualitative understanding of the vortex street formation process via shear-layer interaction can be enriched by topological analysis of the type of Sect. 7.1. In two-dimensional steady separated flow there can only be saddles and centers, and the saddle–saddle connection is structurally unstable. As the energy level increases and saturated, the closed bubble opens and instantaneous "alleyways" of fluid can penetrate the separated flow region. A series of instantaneous streamline patterns in different phases of a period, from an impulsively started cylinder motion and viewed in the frame fixed to the cylinder, is analyzed by Perry et al. (1982) based on the flow visualization movie made under the direction of Prandtl, and Fig. 7.31 reproduces their sketch. The strength of vortex $A$ with $\omega < 0$ is growing in (a)–(d); but in

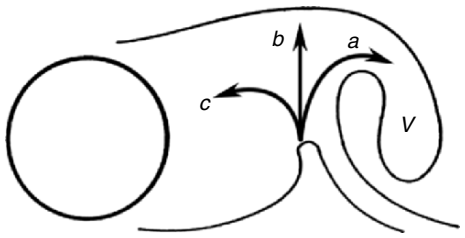


**Fig. 7.30.** Sketch of vortex formation region behind bluff body. Arrows show reverse flow ($c$) and entrainment ($a$) and ($b$). Reproduced from Gerrard (1966)

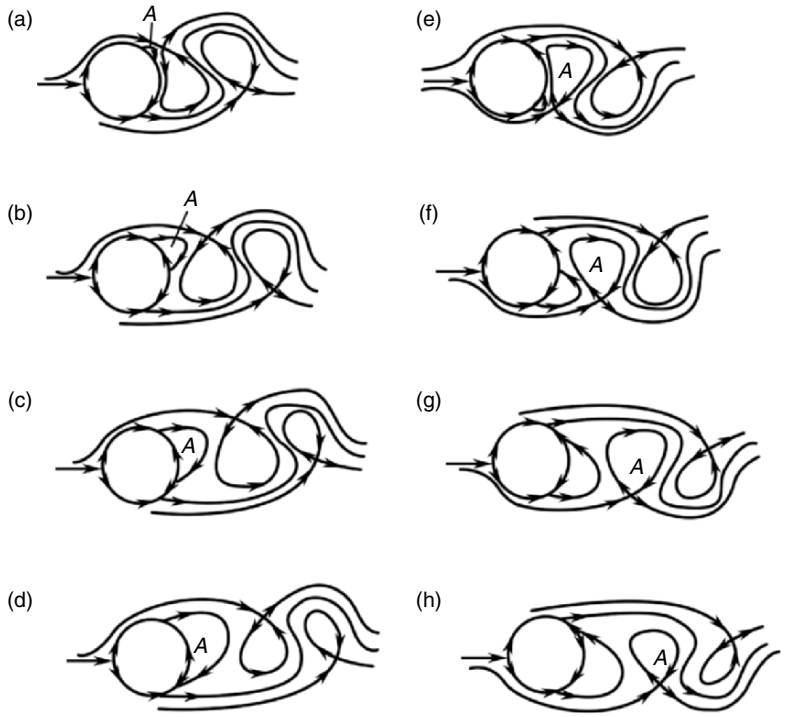


**Fig. 7.31.** Sketch of vortex shedding by the topology of instantaneous streamlines. Plotted are only those streamlines which leave or terminate at saddle points. From Williamson (1996). Note the generation and evolution of vortex $A$

(e) a new saddle forms at the lower side, which cuts off the vorticity feeding to vortex $A$, making it shed away, and meanwhile forms a new vortex with $\omega > 0$. Actually steps (e)–(h) are just half-cycle difference from (a) to (d), respectively.

The preceding qualitative picture needs to be quantitized by careful instability analysis, which will be briefly mentioned at the end of Sect. 9.1.1. While the stability analysis has now been able to predict very precisely the most unstable frequencies at which small disturbances have the highest growth rate, these frequencies are not identical to the vortex shedding frequency or $St$ that is still beyond the capability of stability theories. Moreover, the stability analysis neither identifies the basic mechanisms that limit the amplitude of large transverse displacement of fluid elements in the vortex street, nor reveals the forces that drive the system back toward equilibrium. As a complement to the preceding detailed local analysis, a global vorticity balance in the formation region can be easily obtained, by which one may gain further insight to the overall physical picture.

Consider a two-dimensional incompressible flow on the $(x, y)$-plane past a cylinder, with wake vortices shedding alternatively from upper and lower

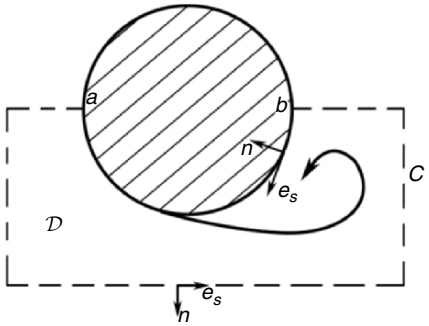


**Fig. 7.32.** The flow region where the vorticity generated at the lower surface is forming a counterclockwise wake vortex

sides of the cylinder surface contour $\partial B$. As shown in Fig. 7.32, we focus on the process in which the vorticity is generated from the lower part of $\partial B$ and forms a new wake vortex during half period $T/2$ (cf. Figs. 7.31e–h). Let $\mathcal{D}$ be a flow domain bounded by $C$ that includes the vorticity-generation region as well as the whole newly formed vortex but not any earlier ones. A segment of $C$ coincides with $\partial B$ from the front stagnation point $a$ to the downstream end $b$ of the cylinder. The normal and tangent unit vectors along $C$ are denoted by $(\boldsymbol{n}, \boldsymbol{e}_s)$, with $\boldsymbol{n}$ pointing out of $\mathcal{D}$ and $\boldsymbol{e}_s$ along the counterclockwise direction so that $\boldsymbol{n} \times \boldsymbol{e}_s = \boldsymbol{e}_z$. Then by the vorticity equation

$$\frac{\mathrm{D}\omega}{\mathrm{D}t} = \nu \nabla^2 \omega,$$

the rate of change of the total vorticity in $\mathcal{D}$ is

$$\frac{\mathrm{d}}{\mathrm{d}t} \int_{\mathcal{D}} \omega \mathrm{d}S = \oint_C \sigma \mathrm{d}s,$$

where $\sigma$ is the vorticity diffusive flux defined by (4.17), which on the stationary $\partial B$ becomes boundary vorticity flux given by $\sigma = \rho^{-1} \partial p / \partial s$, see (4.29). Therefore, by using (7.69) and the fact $p_a = p_\infty + \rho U^2/2$, we obtain (Ahlborn et al. 1998)

$$\frac{\mathrm{d}}{\mathrm{d}t} \int_{\mathcal{D}} \omega \mathrm{d}S = \frac{U^2}{2}(1 - C_{\mathrm{pb}}) + \nu \int_a^b \frac{\partial \omega}{\partial n} \mathrm{d}s. \tag{7.70}$$

Here, the term with base pressure $C_{\mathrm{pb}}$ is the result of vorticity generation by on-wall tangent pressure gradient, which as said in Sect. 4.1.3 is independent of the Reynolds number $Re = UD/\nu$; and the integral of the diffusive flux $\sigma$ is taken along the contour $ab$ in the fluid. $\sigma$ will be strong at a segment of $ab$ where the vorticity is cancelled by the diffusive mixing with opposite vorticity entrained from the upper side. Thus (7.70) provides a clear global interpretation of the Hopf bifurcation at $Re > Re_{\mathrm{cr1}}$. The vorticity generated at the cylinder surface by a strong adverse pressure gradient (characterized

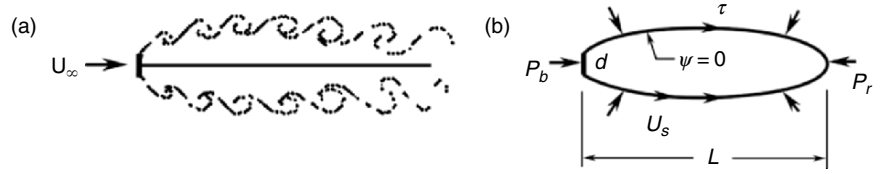


**Fig. 7.33.** Flow past a bluff body with splitter plate, (**a**) instantaneous flow, (**b**) wake defined by zero streamline of the mean flow. From Roshko (1993)

by base suction $-C_{\rm pb}$) is too much to be balanced by diffusion and steady advection, so the flow has to become unsteady which in turn significantly alters the vorticity generation process to achieve a new periodic balance.

The key role of shear-layer interaction in the formation region implies that, as the pioneer work of Roshko (1955) first discovered, vortex shedding can be suppressed if one places a sufficiently long splitter plate along the oncoming flow at the lee side of the cylinder to block this interaction. In that case the upper and lower shear layers will evolve separately due to Kelvin–Helmholtz instability (Sect. 9.2.2), see Fig. 7.33a; and the mean flow will be a pair of long symmetric closed bubbles sketched in Fig. 7.33b (the mean flow with vortex shedding is a much shorter pair of bubbles). This control effect can also be interpreted by (7.70), in which $\mathcal{D}$ should now be extended to the downstream end of the splitter plate, where $p$ recovers nearly to $p_\infty$ and hence $C_p \simeq 0$. The base suction is thereby removed, and the integrated vorticity generation from the bluff-body surface is significantly weakened ( the new $\sigma$ along the splitter plate should be even much weaker). Therefore, in lower half of Fig. 7.33b, since $\omega > 0$ and hence $\sigma < 0$ at the outer edge of the vortex bubble where $u_n = 0$, by (7.70) and (7.26) a mean steady integral balance (Fig. 7.33b) is possible:

$$\frac{U^2}{2} \simeq -\int_a^b \sigma \mathrm{d}s = H(b) - H(a),$$

where $H$ is the total enthalpy.

### 7.4.3 A Dynamic Model of the $(St, C_D, Re)$ Relationship

Once the vortex shedding mode is established, downstream of the formation region (near wake) the fully developed vortices in the far wake vortex street are no longer sensitive to the cross-sectional shape of the body that generates the wake, but evolve as a self-excited periodic system with a *single dominant frequency*. In fact, numerical experiments have shown that a Kármán vortex street can be produced without really computing the cylinder flow, as long as the upstream flow condition is set as the most unstable mean velocity profile of a circular-cylinder wake (Triantafyllou and Karniadakis 1990), or even simply an absolutely unstable Gaussian wake profile (Maekawa et al. 1992). Therefore, some quite universal laws on the $Re$-dependence of $St$ and

$C_D$ or $-C_{\mathrm{pb}}$ (or the $St$–$C_D$ or $St - C_{\mathrm{pb}}$ relationship) should exist in a large range of $Re$ for buff cylinders of various cross sections. The Kármán vortex-street model is the first and most famous example.

Since Strouhal's (1878) pioneer work, it has long been known that the Strouhal number $St$ due to vortex shedding is almost a constant around 0.2 at large Reynolds numbers (till $Re\ 2 \times 10^5$ according to Fig. 7.25), and several empirical models for the $St$–$Re$ relation have been proposed based on fitting with experimental data. At the low $Re$ end, Roshko (1954a,b) was the first to discover the vortex-street similarity behind cylinders of different sectional shapes and to extract an empirical relation from a large data base for the universal $St$–$Re$ relationship for different bluff cylindrical bodies:

$$St = 0.212 \left(1 - \frac{b}{Re}\right), \tag{7.71}$$

where $b = 21.2$ for $45 \leq Re \leq 200$ and 12.7 for $300 \leq Re \leq 800$. His work has been modified and extended to a larger range of $Re$ by many authors. Fey et al. (1998) found a good fitting up to $Re < 2 \times 10^5$ (before drag crisis) if one assumes

$$St = St^* + \frac{m}{\sqrt{Re}}, \tag{7.72}$$

with different constants $St^*$ and $m$ in different regimes.

Compared to the $St$–$Re$ relation, less work (even purely empirical) has been done on the relation between $C_D$ or $C_{\mathrm{pb}}$ and $Re$. In fact, *two* equations are needed to relate $St$, $C_D$, and $Re$, which may well be coupled; hence, further refinement of (7.71) and (7.72) should be anticipated. Now, the appearance of $C_{\mathrm{pb}}$ in (7.70), which was derived by the global momentum and vorticity balance, suggests that the physics in the formation region is at least as important as the vortex-street region, and should be included in searching for the universal laws. As stressed in the context of (7.70), the flow at $Re > Re_{\mathrm{cr1}}$ is characterized by a spontaneously periodic balance between the vorticity creation, advection, and diffusion in the near field, which bears direct relevance to the force acting to the body.[10] The entire cycle is synchronized by a *clockwork*, of which the key mechanism should be in the formation region.

The first step from purely empirical relationships toward semianalytical ones among $(St, C_D, Re)$ was made by Ahlborn et al. (1998, 2002) based on (7.70) and kinetic-energy balance in the vortex-street region. These authors obtained a *dynamic* model for the desired relationships (the effects of three dimensionality and turbulence outlined in Sect. 7.4.1 cannot be treated in the model), of which the core content is presented below with improved rationality. Since relevant flow variables can only be estimated by scale analysis, there will inevitably be a few coefficients to be fixed by experimental data.

[10] It will be shown in Sect. 11.5 that this force can well be obtained by the flow data in this formation region only, and the effect of the Kármán vortex street on the force is nearly indirect only via its upstream influence.

We first consider the vorticity balance in the formation region based on the space-time averaged version of (7.70). Let $n = 2\pi f$ be the circular shedding frequency. From the derivation of (7.70) it is evident that the domain $\mathcal{D}$ has to contain both the lower-surface boundary layer and the newly separated vortex, including possible secondary and tertiary vortices. To avoid dealing with the average of the advective vorticity flux $\omega u_n$ across $\partial\mathcal{D}$, we assume $\mathcal{D}$ is a material fluid body.[11] Thus, $\mathcal{D}$ is strongly $t$-dependent; as suggested by Fig. 7.31, it deforms and changes shape and area as the boundary-layer separates, small vortex-bubble forms, grows, detaches, and finally sheds off. Nevertheless, we may introduce a nominal radius $R(t)$ so that $\mathcal{D}(t) = \pi R^2(t)$.

Now, denote the time average over $T/2 = \pi/n$ and spatial average over $\mathcal{D}$ for any function $F(\boldsymbol{x}, t)$ by

$$\overline{F} = \frac{n}{\pi}\int_0^{\pi/n} F\mathrm{d}t, \quad \langle F\rangle = \frac{1}{\pi R^2}\int_{\mathcal{D}} F\mathrm{d}S.$$

Averaging (7.70) over $T/2$ yields

$$nR^2\langle\omega\rangle - \nu\overline{\left(\int_a^b \frac{\partial\omega}{\partial n}\mathrm{d}s\right)} = \frac{U^2}{2}(1-\overline{C}_{\mathrm{pb}}).$$

Dividing this equation by $U^2/2$ and noticing $n = 2\pi USt/D$, we obtain

$$\frac{\pi R^2 St}{UD}\langle\omega\rangle - \frac{1}{2Re}\frac{D}{U}\overline{\left(\int_a^b \frac{\partial\omega}{\partial n}\mathrm{d}s\right)} = \frac{1}{4}(1-\overline{C}_{\mathrm{pb}}), \tag{7.73}$$

where all three parameters $St$, $C_{\mathrm{pb}}$, and $Re$ appear. Then, as a material loop, the curve $ab$ deforms and changes shape during $T/2$ as significantly as $\mathcal{D}$. But since $\partial\omega/\partial n < 0$ along the curve $ab$, by the mean-value theorem there must exist an $N(t) > 0$ such that

$$\int_a^b \frac{\partial\omega}{\partial n}\mathrm{d}s = -2\pi N(t)R(t)\frac{\langle\omega\rangle(t)}{R(t)} = -2\pi N(t)\langle\omega\rangle(t)$$

at any $t \in [0, T/2]$. Physically, $N(t)$ measures how much the real $\partial\omega/\partial n$ along $ab$ differs from $\langle\omega\rangle/R$ and how much the arclength of the curve $ab$ differs from $2\pi R$. Therefore, (7.73) becomes

$$\left(\frac{\beta^2}{4}St + \frac{\overline{N}}{Re}\right)\frac{D}{U}\overline{\langle\omega\rangle} = \frac{1}{4\pi}(1-\overline{C}_{\mathrm{pb}}), \tag{7.74}$$

where $\overline{\langle\omega\rangle}$ is the constant space-time averaged vorticity in the deformable $\mathcal{D}$, $\beta = 2\pi R/D$ is the dimensionless nominal diameter of $\mathcal{D}$, and $\overline{N} > 0$ is a mean

[11] This fluid body has to extend sufficiently far upstream so that in the entire $s$ T/2 it can cover the lower-surface boundary layer as required in deriving (7.70).

value of $N$ in $T/2$ that can hardly be estimated in practice nor is independent of the cross-section shapes.

We now observe that $\overline{\langle\omega\rangle}$ is twice of the mean angular velocity of $\mathcal{D}$, so $2\pi/\overline{\langle\omega\rangle}$ is half of the mean turn-over time of the vortex in $\mathcal{D}$, which should scale with $T/2$. Therefore, we are led to setting $\overline{\langle\omega\rangle} = 2An$ with $A = O(1)$. By (ideally) adjusting the domain $\mathcal{D}$, we can set $A = 1$ without loss of generality,[12] obtaining

$$\overline{\langle\omega\rangle} = 2n \quad \text{or} \quad \frac{D}{U}\overline{\langle\omega\rangle} = 4\pi St. \tag{7.75}$$

From this equation and (7.74), and dropping the overline for neatness, we arrive at the first dynamic relation (Ahlborn et al. 1998):

$$St^2 + \frac{4N}{\beta^2 Re} St = \frac{1 - C_{\mathrm{pb}}}{4\pi^2\beta^2}. \tag{7.76}$$

Next, consider the balance of work rate and kinetic energy. In the frame of reference fixed to the undisturbed fluid, the body has speed $U$ and experiences a drag $F_x$, so the work rate needed for maintaining the body motion is governed by (2.76):

$$F_x U = \frac{\mathrm{d}}{\mathrm{d}t}\int_{\mathcal{D}} \frac{1}{2}\rho q^2 \mathrm{d}S + \int_{\mathcal{D}} \Phi \mathrm{d}S, \tag{7.77}$$

where $\Phi$ is the dissipation rate. This formula holds only when $\mathcal{D}$ surrounds the body, and hence we are still working in the vortex-formation region, but the role of viscosity in (7.77) is different from that in (7.70). It now controls the dissipation, which however occurs at small scales with large wave numbers that appear in the wake when $Re > 190$. Here, the mechanism responsible for vortex shedding with $St < 0.5$ in both laminar and turbulent regimes must be associated with large structures with negligible dissipation. Therefore, in the present context the dissipation terms in (7.77) should be dropped, so its spatial average over $\mathcal{D}$ and time average over $T$ simply yield

$$\overline{C}_D = \frac{1}{2}\pi\beta^2 St \frac{\overline{\langle q^2\rangle}}{U^2},$$

where $\langle q^2\rangle$ scales with $U^2$. Thus, we obtain the second dynamic relation (Ahlborn et al. 2002)

$$C_D = \beta^2 K St, \quad K \equiv \frac{\pi}{2}\frac{\overline{\langle q^2\rangle}}{U^2} = O(1). \tag{7.78}$$

Having obtained dynamic relations (7.76) and (7.78), Ahlborn et al. (1998) note that $C_{\mathrm{pb}}$ and $C_D$ are related by

$$1 - C_{\mathrm{pb}} = (1 - \gamma)(1 + C_D), \quad \gamma = \frac{C_D + C_{\mathrm{pb}}}{1 + C_D}, \tag{7.79}$$

[12] Ahlborn et al. (1998, 2002) set $A = \sqrt{2}$.

and experimental data of vertical flat plate with round edge of varying aspect ratio indicate $|\gamma| = O(10^{-2}) \ll 1$ (for circular cylinder, $\gamma$ can be inferred from Fig. 7.25). Hence, as a rough approximation, they replaced $1 - C_{\rm pb}$ in (7.76) by $1 + C_D$. This enables eliminating $\beta^2$ from (7.76) and (7.78), obtaining an $St$–$C_D$ relation

$$St = \frac{K}{2\pi^2}\frac{C_D + 1}{C_D + Re^*/Re} = \frac{St_\infty}{1 + Re^*/(ReC_D)}, \tag{7.80}$$

where

$$St_\infty = \frac{K}{2\pi^2}\left(1 + \frac{1}{C_D}\right), \tag{7.81a}$$

$$Re^* = 4NK \tag{7.81b}$$

are the asymptotic Strouhal number as $Re \to \infty$ and a finite-$Re$ correction coefficient, respectively.

We have obtained two dynamic relations (7.78) and (7.80) for the three parameters $(St, C_D, Re)$, along with three empirical coefficients $K$, $\beta^2$, and $Re^*$ that need to be fixed by fitting with experimental data. A simple way to obtain $K$ and $\beta$ is to drop $Re^*/Re$ in (7.80), which and (7.78) then yield

$$K = 2\pi^2\frac{C_D St}{1 + C_D}, \tag{7.82a}$$

$$\beta St = \frac{1}{\pi}\sqrt{\frac{1 + C_D}{2}}. \tag{7.82b}$$

Thus, $K$ and $\beta^2$ are as universal as $St$ and $C_D$. Note that

$$\beta St \equiv St^* = \frac{2fR}{U} \tag{7.83}$$

is the universal Strouhal number in terms of the *wake width*, first introduced by Roshko (1954b). By using the experimentally measured $St$ and $C_D$ for a circular cylinder in a very large range of $Re$ from $2 \times 10^4$ to $10^7$ (Fig. 7.25), and for cylinders of various cross sections, Ahlborn et al. (2002) have found that (7.82a) gives $K \simeq 1.53$ as almost a universal constant (even in the "drag crisis" regime in Fig. 7.25b where $C_D$ drops significantly), and (7.82b) indeed leads to a universal weak dependence of $\beta St$ on $C_D$.

Some previously known results can be recovered and interpreted by the present dynamic model. For example, if $C_D$ roughly takes constant in the considered $Re$ regimes and $b = Re^*/C_D$, (7.80) recovers (7.71). Thus, using Roshko's values for $45 \le Re \le 200$ and with $C_D = 1.1$ at $Re \sim 100$, it follows roughly that $Re^* \approx 23$, and $N \approx 3.8$ by (7.81b). The former is close to the upper bound of diffusion-dominated regime $Re < 25$, and the latter implies that the diffusion layer is $Re$-independent (recall that $N$ measures the dimensionless vorticity gradient at the outer edge of a newly formed vortex).

Since it is more plausible that this diffusion layer scales with the boundary-layer thickness $\delta$, a better estimate is $N \sim D/\delta \propto \sqrt{Re}$ in laminar regime. Consequently, to the leading order of $1/\sqrt{Re}$, (7.80) modifies (7.71) to

$$St = St_\infty \left(1 - \frac{\eta}{C_D\sqrt{Re}}\right),$$

which will recover (7.72) if $St_\infty = St^*$ and coefficient $\eta$ is properly chosen. This conveys a little physics to (7.72), but still cannot explain its effectiveness in turbulent regimes.

## Summary

1. The topological theory provides a general tool to rationally analyze the overall qualitative structure of a separated vortex flow, in terms of critical points and their connections on body surface and inside the fluid. It has mainly been applied to steady flow but in principle can also be used to study unsteady flow. The theory helps distinguish closed separation (separation line initiates from a fixed point) and open separation (separation line initiates from an ordinary point). It also leads to the concept of structural stability and topological bifurcation of the flow.
2. Under certain special conditions, a separated vortex flow takes the simplest form, confined in a steady laminar bubble enclosed by a shear layer. In the Euler limit of two-dimensional and axisymmetric flows, the Prandtl–Batchelor theorem gives constant and linear vorticity distribution, respectively, in the core region of the bubble. For some simple cases, the cyclic vortex layer surrounding the bubble can be solved asymptotically, so a complete solution is obtained. This Prandtl–Batchelor flow has been applied not only to the study of closed vortex bubbles of body scale, but also to the construction of an asymptotic model for steady global wake as $Re \to \infty$. This global-wake model is of academic interest since it leads to a well-posed problem with unique solution; but it is too far from any realistic separated vortex flow at large $Re$, which are inherently unsteady with various instabilities and transition to turbulence (item 4 later).
3. In the steady-flow regime, the counterpart of bubble-type separated flow is free vortex-layer separated flow, typically associated with moving vehicle at large Reynolds numbers. To such a flow only the highly simplified slender-body theory can provide a general treatment, including useful yet simple models for the rolling-up process of separated free shear layers. The shear layer rolling-up results in strong vortices near a vehicle and has considerable influence on the vehicle's performance. When the flow has conical similarity as well as being slender, the stability problem of these vortices can be analyzed by a simple inviscid and two-dimensional theory.
4. The unsteady separated flow with periodic or quasiperiodic vortex shedding occurs widely in various external and internal viscous flows with solid

boundaries, either laminar or turbulent. The physics involved in such a flow covers almost every aspect of vorticity and vortex dynamics, and so far one's understanding of the flow has largely been based on experimental observations even for the simplest body geometries. On the other hand, in wake-flow properties some universality has been observed in the empirical relationships among $St, C_D$, and $Re$, regardless the cross shape of bluff bodies. A preliminary step is made toward basing these relations on a more rational dynamic background.

# 8

# Core Structure, Vortex Filament, and Vortex System

## 8.1 Vortex Formation and Core Structure

The analysis in Sects. 4.4.2 and 7.3 has indicated that, in a fluid of small viscosity, the most fundamental mechanism for the formation of a vortex is the rolling-up of vortex layer. Indeed, if one wishes to produce a vortex by a solid-body motion relative to the fluid, the first naive idea could be rotating a thin rod in the fluid about its axis (or letting the fluid container rotate). The essence of this mechanism is to transfer the angular momentum of the solid to a fluid layer adjacent to the solid via the no-slip condition, and then let the vorticity diffuse into the interior of the fluid. However, as $\mu \to 0$, the required time for such diffusion would be infinity, and hence it would take very long time to form a vortex. But in reality once the solid is in motion the vortex appears very quickly. Producing vortices by an oar during boat rowing is a common experience. This fast formation mechanism of vortex can only be the rolling-up of the separated vortex layer at its free end (Betz 1950). Owing to the singularity of a flat vortex sheet, the smaller the fluid viscosity is, the thinner will be the vortex layer, and the faster will the vortex be formed.

Based on this understanding, the present section discusses the core structure of vortices formed from the rolling-up of vortex layers. We assume the vortex axis is straight. It is then convenient to use cylindrical coordinates $(r, \theta, z)$, so we have (6.2) for vorticity components $(\omega_r, \omega_\theta, \omega_z)$ in terms of velocity components $(u, v, w)$. The corresponding continuity and Navier–Stokes equations for incompressible fluid are (6.3) and (6.4), respectively.

Now, in the rolling process, the distance between two neighboring turns of the vortex layer must eventually be reduced to the same order of the layer thickness. Then the viscous diffusion will smear out the spiral structure in the tightly rolled-up region to form a *vortex core* with smooth vorticity distribution, to which the Euler theory no longer applies. On the other hand, inside the vortex core the axial velocity in general has a strong radial variation, so any two-dimensional model will not be appropriate either. While it will be too complicated to study the entire vortex core by three-dimensional and

nonaxisymmetric viscous flow, we may divide problem into two phases: the vortex-core formation phase and its matured phase, to which we can employ different approximations as presented later.

### 8.1.1 Vortex Formation by Vortex-Layer Rolling Up

The phase of vortex-core formation by vortex-layer rolling up may be further subdivided into two stages: the early stage characterized by vortex-layer rolling up, and the late stage characterized by the formation of viscous vortex core. In order to cover both stages by a single theoretical model, we abandon the axial-flow effect and assume the flow is two-dimensional, but retain the unsteadiness, nonaxisymmetry, and viscosity. In this case $\omega = \omega \boldsymbol{e}_z$, so (6.4b) is reduced to

$$\frac{\partial v}{\partial t} + \frac{1}{r}\frac{\partial}{\partial \theta}\left(\frac{1}{2}q^2\right) + u\omega + \frac{1}{\rho r}\frac{\partial p}{\partial \theta} = \nu \frac{\partial \omega}{\partial r}. \tag{8.1}$$

To eliminate one more variable, we may take average of (8.1) for $\theta$ varying from 0 to $2\pi$. A physical model for the vortex formation within this approximation has been introduced by Kurosaka (see Dang 1986) and is presented here (see the sketch of Fig. 8.1).

In the early stage, we consider inviscid flow first and simplify the first few turns of the vortex layer outside the core to a single vortex sheet. Away from the sheet the flow is assumed irrotational and governed by

$$\frac{\partial v}{\partial t} + \frac{1}{r}\frac{\partial}{\partial \theta}\left(\frac{1}{2}q^2\right) = -\frac{1}{\rho r}\frac{\partial p}{\partial \theta}. \tag{8.2}$$

Taking the $\theta$-average at fixed $r$, since $p$ is continuous across the sheet but tangent velocity $u_s$ has discontinuity, there is

$$\frac{\partial \overline{v}}{\partial t} = -\frac{1}{4\pi r}[\![u_s^2]\!]. \tag{8.3}$$

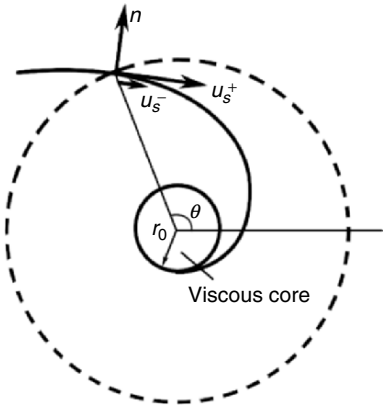


**Fig. 8.1.** Vortex-core structure

Let $\boldsymbol{e}_s$ and $\boldsymbol{e}_n$ be the unit tangent and normal vectors of the sheet, respectively. Let us thicken the sheet to a vortex layer of thickness $\delta$. The Lamb vector of the layer is

$$\boldsymbol{\omega} \times \boldsymbol{u} = \omega \boldsymbol{e}_z \times (u_s \boldsymbol{e}_s + u_n \boldsymbol{e}_n) = \omega u_s \boldsymbol{e}_n - \omega u_n \boldsymbol{e}_s,$$

so that $\boldsymbol{e}_n \cdot (\boldsymbol{\omega} \times \boldsymbol{u}) = \omega u_s$. Thus, let $Q$ be the vorticity flux advected by $u_s$ into the vortex, there is

$$Q = \int_0^\delta u_s \omega \, \mathrm{d}n = \int_0^\delta (\boldsymbol{\omega} \times \boldsymbol{u}) \cdot \boldsymbol{e}_n \, \mathrm{d}n, \tag{8.4}$$

which by (6.11) with $H = p + q^2/2$ is cast to

$$Q = \int_0^\delta (\boldsymbol{\omega} \times \boldsymbol{u}) \cdot \boldsymbol{n} \, \mathrm{d}n = -\left( p + \frac{1}{2} q^2 \right) \Big|_0^\delta = -\frac{1}{2} [\![ u_s^2 ]\!], \tag{8.5}$$

so that

$$\frac{\partial \overline{v}}{\partial t} = \frac{1}{2\pi r} Q(t).$$

We now add the viscous term, which can only smear out but never produce new discontinuities. Thus, after averaging over $\theta$, the viscous equation reads

$$\frac{\partial \overline{v}}{\partial t} = \frac{1}{2\pi r} Q(t) + \nu \frac{\partial \overline{\omega}}{\partial r}. \tag{8.6}$$

Assume the vortex layer is disconnected from its generating body at $t = \tau$ such that $Q$ vanishes by then. Denote the viscous core radius by $r = f(t)$, then (8.6) is modified to

$$\frac{\partial \overline{v}}{\partial t} = \frac{1}{2\pi r} Q(t) H(\tau - t) H(r - f(t)) + \nu \frac{\partial \overline{\omega}}{\partial r}, \tag{8.7}$$

where $H$ is the step function. The $\theta$-averaged vorticity equation reads

$$\frac{\partial \overline{\omega}}{\partial t} - \frac{\nu}{r} \frac{\partial}{\partial r} \left( r \frac{\partial \overline{\omega}}{\partial r} \right) = \frac{1}{2\pi r} Q(t) \delta(r - f(t)) H(\tau - t), \tag{8.8}$$

which is an inhomogeneous and axisymmetric heat equation, with a source term from the input vorticity flux. Under the initial-boundary conditions

$$\overline{\omega}(r, 0) = 0, \quad \overline{\omega}(\infty, t) = 0,$$

we find the solution

$$\overline{\omega}(r, t) = \frac{1}{4\pi\nu} \int_0^T \frac{Q(\eta)}{t - \eta} \exp\left( -\frac{r^2 + f^2(\eta)}{4\nu(t - \eta)} \right) I_0 \left( \frac{r f(\eta)}{2\nu(t - \eta)} \right) \mathrm{d}\eta, \tag{8.9}$$

in which $T = t$ if $t < \tau$, otherwise $T = \tau$, and $I_0$ is the zeroth-order modified Bessel function of the first kind. By using the integral formula

$$\int_0^\infty r \exp(-p^2 r^2) I_0(ar)\,\mathrm{d}r = \frac{1}{2p^2} \exp\left(\frac{a^2}{4p^2}\right), \tag{8.10}$$

we can also find the total vorticity of this vortex (the circulation along a circle with $r = \infty$) from (8.9):

$$\Gamma_\infty = \int_0^\infty 2\pi r \overline{\omega}\,\mathrm{d}r = \int_0^T Q(\eta)\,\mathrm{d}\eta. \tag{8.11}$$

This is a result that can physically be anticipated: at the early stage $T = t < \tau$, the circulation comes from the input vorticity flux through the feeding sheet from $t = 0$ to $t$; while at the later stage $T = \tau$, the circulation comes from the entire vorticity flux of the early stage. The unique feature of the Kurosaka model is the combined consideration of vorticity transport, vortex-layer rolling up, and viscous diffusion. At the early stage of the rolling up, both the vorticity flux $Q(t)$ and core radius $f(t)$ increase as $t$, so we can set $f(t) = \alpha t^m$ and $Q(t) = 2\pi\beta t^n$, with $m, n$ being constants. Then, Kurosaka has proved that, in the limit of $\nu \to 0$, (8.9) is reduced to

$$\bar{\omega} = \begin{cases} \dfrac{\beta}{m\alpha^2}\left(\dfrac{r}{\alpha}\right)^{(n+1)/m-2}, & r < \alpha t^m \\ 0, & r > \alpha t^m \end{cases} \tag{8.12}$$

$$\bar{v} = \begin{cases} \dfrac{\beta}{(n+1)\alpha^{(n+1)/m}} r^{(n+1)/m-1}, & r < \alpha t^m \\ \dfrac{\beta}{n+1}\dfrac{t^{n+1}}{\alpha}, & r > \alpha t^m. \end{cases} \tag{8.13}$$

Therefore, inside the viscous core the flow is rotational, with vorticity and circumferential velocity depending only on $r$ but not $t$; while outside the core the flow is irrotational, with averaged circumferential velocity being enhanced as $t$. This result is similar to the Kaden similarity law (Sect. 4.4.4), but no assumption is made here on the initial distribution of the vortex-sheet strength.

At the late stage when the feeding vortex layer has been disconnected from its generating body, the flow can be assumed axisymmetric with relatively small radial velocity $u$. Then (8.1) is reduced to

$$\frac{\partial v}{\partial t} = \nu \frac{\partial \omega}{\partial r}. \tag{8.14}$$

By using (8.9) with $T = \tau$ and $t \to \infty$, one obtains

$$\omega(r, t) \sim \frac{\Gamma_\infty}{4\pi\nu t} \exp\left(-\frac{r^2}{4\nu t}\right), \tag{8.15}$$

which is the familiar Oseen vortex. Both asymptotic results (8.12) and (8.15) are satisfactory. Although the Kurosaka model is confined to two-dimensional flow, it does capture the main physics of the dynamic evolution process from vortex-layer rolling up to the formation of viscous core of a vortex.

### 8.1.2 Quasicylindrical Vortex Core

We now move on from the formation phase of a vortex to its matured phase, where any vortex layer disconnected from its generating body has entirely rolled into the vortex core, and the unsteadiness due to viscous diffusion is basically canceled by the energy supplement from outside flow. Then we can make simplified assumptions opposite to those of Sect. 8.1.1: The flow is steady and axisymmetric, but the three dimensionality is retained to allow for variable axial flow in the vortex core. Moreover, for an infinitely extended straight vortex, the axial variation of the flow is much smaller than its radial variation. Therefore, like the boundary-layer approximation, the continuity equation (6.3) implies that the radial velocity is much smaller than axial velocity, namely

$$\frac{\partial}{\partial z} \ll \frac{\partial}{\partial r}, \quad u \ll w.$$

This leads to the *quasicylindrical approximation* used in studying the Long vortex (Sect. 6.2.3). Now the governing equations are reduced to

$$\frac{v^2}{r} = \frac{1}{\rho}\frac{\partial p}{\partial r}, \tag{8.16a}$$

$$u\frac{\partial v}{\partial r} + w\frac{\partial v}{\partial z} + \frac{uv}{r} = \nu\left(\nabla^2 v - \frac{v}{r^2}\right), \tag{8.16b}$$

$$u\frac{\partial w}{\partial r} + w\frac{\partial w}{\partial z} = -\frac{1}{\rho}\frac{\partial p}{\partial z} + \nu\nabla^2 w, \tag{8.16c}$$

and

$$\nabla^2 = \frac{\partial^2}{\partial r^2} + \frac{1}{r}\frac{\partial}{\partial r}. \tag{8.17}$$

A vortex core under this approximation is called a *quasicylindrical vortex core*, which has two significant simplifications: similar to (6.18a), (8.16a) is independent of viscosity, so the centrifugal force is entirely balanced by the radial pressure gradient; and, the Laplace operator $\nabla^2$ is degenerated to a parabolic operator, requiring only three boundary conditions at vortex axis, outer edge of the core, and upstream flow. At the vortex axis, the viscous-flow condition requires

$$u = 0, \quad v = 0, \quad \frac{\partial w}{\partial r} = 0, \tag{8.18}$$

where $\partial w/\partial r = 0$ is due to the smoothness. Correspondingly, the vorticity at the axis should satisfy

$$\omega_r = 0, \quad \omega_\theta = 0, \quad \frac{\partial \omega_z}{\partial r} = 0. \tag{8.19}$$

The other two boundary conditions vary as specific vortices. For a *trailing vortex* (the vortex formed from the rolling up of the vortex layer separated at the trailing edge of a wing), after the vortex layer is fully rolled into the core, the external flow can be assumed irrotational; but for a leading-edge vortex with feeding vortex-layer that is not tightly rolled (Sect. 7.3.1), the flow at the outer edge of the core is rotational and inviscid. There is a bigger variety for the upstream condition.

To this axisymmetric flow we introduce the Stokes stream function. Recall that the Euler limit of a steady axisymmetric flow has circulation $rv = C(\psi)$ and stagnation enthalpy $H = p/\rho + q^2/2 = H(\psi)$, governed by the elliptic Bragg–Hawthorne equation (6.14). The quasicylindrical approximation casts this equation to

$$\frac{\partial^2 \psi}{\partial r^2} - \frac{1}{r}\frac{\partial \psi}{\partial r} = r^2 \frac{\mathrm{d}H}{\mathrm{d}\psi} - C\frac{\mathrm{d}C}{\mathrm{d}\psi}. \tag{8.20}$$

We now follow the analysis of Hall (1966) to examine a few basic characters of a quasicylindrical vortex core. First, as $r \to \infty$ there is $p = p_\infty$, so by (8.16a) we have

$$\frac{p_\infty - p}{\rho} = \int_0^\infty \frac{v^2}{r}\,\mathrm{d}r = \int_0^\infty \frac{C^2}{r^3}\,\mathrm{d}r. \tag{8.21}$$

If all fluid comes from the far-upstream uniform flow $(0, 0, W)$, as in the case of free vortex-layer separated flow of Sect. 7.3, then by the Bernoulli equation, after neglecting the small amount $u^2/2$ at a point in the core there is

$$\frac{p}{\rho} + \frac{1}{2}(v^2 + w^2) = \frac{p_\infty}{\rho} + \frac{1}{2}W^2 - \Delta H, \tag{8.22}$$

where $\Delta H$ is the loss of the stagnation enthalpy due to viscosity. Thus, by (8.21) there is

$$w^2 = W^2 - \frac{C^2}{r^2} + 2\int_0^\infty \frac{C^2}{r^3}\,\mathrm{d}r - 2\Delta H,$$

i.e.,

$$w^2 = W^2 + \int_0^\infty \frac{1}{r^2}\frac{\partial C^2}{\partial r}\,\mathrm{d}r - 2\Delta H. \tag{8.23}$$

Let us examine the physical implication of this equation. Rayleigh (1916) and Synge (1933) have proved that the inequality

$$\frac{1}{r^3}\frac{\mathrm{d}C^2}{\mathrm{d}r} > 0,$$

i.e., the magnitude of the circulation is a nondecreasing function of $r$, is the sufficient and necessary condition for a two-dimensional, axisymmetric, steady, and inviscid flow to be stable with respect to axisymmetric disturbances (see Sect. 9.3.1). At large Reynolds numbers the same conclusion should hold. Hence, for a stable vortex flow the second term on the right-hand side of (8.23) should be positive. We then see that inside the vortex core the viscous effect always causes an axial-flow deficit, while the radial variation of circumferential velocity always results in an axial-flow increment (Batchelor 1964). Equations (8.16a) and (8.22) indicate that this axial-flow increment comes from the radial pressure gradient necessary for balancing the centrifugal force. The centrifugal force leads to a low pressure at the axis and hence larger axial velocity.

For example, for the Rankine vortex (6.22) with rigid (and inviscid) core of radius $a$, we have $\Delta H = 0$ for $r \le a$. Let the core angular velocity be $\Omega$, (8.23) then implies

$$\begin{aligned} &v = \Omega a^2/r, \quad w = W, && r \ge a \\ &v = \Omega r, \quad w = [W^2 + 2\Omega^2(a^2 - r^2)]^{1/2}, && r \le a \end{aligned} \tag{8.24}$$

where the second expression shows clearly the coupling between $w$ and $v$.

The second basic character of a quasicylindrical vortex core is the sensitivity of the axial velocity at vortex center to that at the outer edge of the core (Hall 1966). Denote by subscripts 0 and $a$ the flow quantities at $r = 0$ and $r = a$. In the inviscid approximation, the Bernoulli equation yields

$$\frac{p_\infty - p_0}{\rho} = \frac{1}{2}(w_0^2 - w_a^2) - \frac{1}{2}\frac{C_a^2}{a^2}.$$

Differentiating this equation with respect to $z$ and neglecting the small amount $\mathrm{d}C/\mathrm{d}z$, we obtain

$$\frac{\mathrm{d}}{\mathrm{d}z}\left(\frac{p_\infty - p_0}{\rho}\right) = \frac{1}{2}\left(\frac{\mathrm{d}w^2}{\mathrm{d}z} - \frac{\mathrm{d}w_a^2}{\mathrm{d}z}\right) + \frac{C_a^2}{a^3}\frac{\mathrm{d}a}{\mathrm{d}z}. \tag{8.25}$$

On the other hand, setting $r = 0$ and replacing $\infty$ by $a$ in (8.21), we also have

$$\frac{\mathrm{d}}{\mathrm{d}z}\left(\frac{p_\infty - p_0}{\rho}\right) = \int_0^a \frac{1}{r^3}\frac{\partial C^2}{\partial z}\,\mathrm{d}r + \frac{C_a^2}{a^3}\frac{\mathrm{d}a}{\mathrm{d}z}.$$

A comparison of these two equations yields

$$\frac{\mathrm{d}w_0^2}{\mathrm{d}z} - \frac{\mathrm{d}w_a^2}{\mathrm{d}z} = 2\int_0^a \frac{1}{r^3}\frac{\partial C^2}{\partial z}\,\mathrm{d}r. \tag{8.26}$$

But, from the inviscid version of (8.16b)

$$\frac{\partial v}{\partial z} = -\frac{u}{w}\left(\frac{\partial v}{\partial r} + \frac{v}{r}\right)$$

one easily obtains

$$\frac{\partial C^2}{\partial z} = -\frac{u}{w}\frac{\partial C^2}{\partial r},$$

so (8.26) becomes

$$\frac{\mathrm{d}w_0^2}{\mathrm{d}z} - \frac{\mathrm{d}w_a^2}{\mathrm{d}z} = -2\int_0^a \frac{1}{r^3}\frac{u}{w}\frac{\partial C^2}{\partial r}\,\mathrm{d}r. \tag{8.27}$$

Now, if the vortex core is expanding in the $z$-direction such that $u > 0$, the axial flow at $r = a$ will usually be decelerated, i.e., $\mathrm{d}w_a^2/\mathrm{d}z < 0$. Thus, because $\partial C^2/\partial r > 0$ and $w > 0$, (8.27) implies that the rotation effect reduces the axial acceleration $\mathrm{d}w^2/\mathrm{d}z$ at the axis to below $\mathrm{d}w_a^2/\mathrm{d}z$. On the contrary, if the vortex core is shrinking, $\mathrm{d}w^2/\mathrm{d}z$ will be increased to above $\mathrm{d}w_a^2/\mathrm{d}z$. Therefore, the variation of axial velocity at the outer edge of the core always causes a magnification effect at the vortex axis.

### 8.1.3 Core Structure of Typical Vortices

Having discussed the general formation process and some thin-core characters of vortices, we now focus on the core structures of two typical types of vortices formed by vortex-layer rolling up: the trailing vortices and leading-edge conical vortices.

The core structure of a trailing vortex at far downstream has been examined by Batchelor (1964), who obtained the first asymptotic solution of the viscous core. After a long-time diffusion, at far downstream the axial flow cannot have large radial gradient. So if the axial velocity $w$ takes a constant value $W$ outside the core, we may set $\mid w - W \mid \ll W$ and meanwhile $u \simeq 0$ by continuity. Hence, the steady quasicylindrical equations (8.16b) and (8.16c) are further linearized:

$$W\frac{\partial C}{\partial z} = \nu\left(\frac{\partial^2 C}{\partial r^2} - \frac{1}{r}\frac{\partial C}{\partial r}\right), \tag{8.28a}$$

$$W\frac{\partial w}{\partial z} = -\frac{1}{\rho}\frac{\partial p}{\partial z} + \nu\nabla^2 w, \tag{8.28b}$$

with boundary condition

$$C(z,0) = 0, \quad C(z,\infty) = \Gamma, \quad w(z,\infty) = W. \tag{8.29}$$

Equation (8.28a) is an axisymmetric heat equation which has an asymptotic similarity solution independent of the initial condition:

$$C = rv = \Gamma(1 - \mathrm{e}^{-\eta}), \quad \eta = \frac{Wr^2}{4\nu z}. \tag{8.30}$$

After a rescaling of $r$, this solution is the $q$-vortex or Batchelor vortex of Sect. 6.2.1. Substituting it into (8.16a) gives

$$\frac{p_\infty - p}{\rho} = \frac{\Gamma^2 W}{8\nu z} P(\eta), \tag{8.31a}$$

$$P(\eta) = \int_\eta^\infty \frac{(1 - \mathrm{e}^{-\xi})^2}{\xi^2}\,\mathrm{d}\xi \tag{8.31b}$$

$$= \frac{(1 - \mathrm{e}^{-\eta})^2}{\eta} + 2\mathrm{ei}(\eta) - 2\mathrm{ei}(2\eta), \tag{8.31c}$$

where $\mathrm{ei}(\eta) = \int_\eta^\infty (\mathrm{e}^{-\xi}/\xi)\,\mathrm{d}\xi$ is the exponential integral.

Then, substituting (8.31a) into (8.28b), it follows that

$$W\frac{\partial w}{\partial z} - \nu\left(\frac{\partial^2}{\partial r^2} + \frac{1}{r}\frac{\partial}{\partial r}\right) w = -\frac{\Gamma^2 W}{8\nu z^2}\left(P + \eta\frac{\mathrm{d}P}{\mathrm{d}\eta}\right).$$

After some algebra, Batchelor (1964) obtained

$$w = W - \left(\frac{\Gamma^2}{8\nu z}\ln\frac{Wz}{\nu}\right)\mathrm{e}^{-\eta} + \frac{\Gamma^2}{8\nu z} f(\eta) - \frac{BW^2}{8\nu z}\mathrm{e}^{-\eta}, \tag{8.32}$$

where $B$ is a constant determined by upstream condition, while

$$f(\eta) = \mathrm{e}^{-\eta}[\ln\eta + \mathrm{ei}(\eta) - 0.807] + 2\mathrm{ei}(\eta) - 2\mathrm{ei}(2\eta).$$

For sufficiently large $z$, the leading terms of (8.32) is

$$W - w \sim \frac{\Gamma^2}{8\nu z}\ln\left(\frac{Wz}{\nu}\right)\mathrm{e}^{-\eta}. \tag{8.33}$$

The solutions (8.30), (8.31a), and (8.32) have been independent of the upstream condition. This result indicates that even if there is an axial-flow excess ($w > W$) at upstream, it must eventually become a deficit due to viscous dissipation.

The above analysis applies to the case with $\eta = O(1)$, which by (8.30) implies the core radius

$$a \sim O\left(\sqrt{\frac{\nu z}{W}}\right), \tag{8.34}$$

comparable to the boundary-layer thickness.

Now, assume that the trailing vortex is caused by a wing with span $b$ and one may estimate $a \sim 0.1b$. Then since the Reynolds number based on the chord length $c$ is $Re_c = Wc/\nu$, (8.34) implies that Batchelor's linearized vortex-core theory is applicable at

$$z \sim 0.01c\,Re_c\,A^2,$$

where $A = b^2/S_\mathrm{w}$ is the aspect ratio of the wing, with $S_\mathrm{w}$ being the wing area. The water-tank experiment of Olsen (1971) indicated that the axial-velocity deficit at the trailing-vortex core starts to appear at $10c \sim 60c$ downstream the trailing edge, but the above estimate requires several thousands of $c$ under that experimental condition. Thus, Batchelor's model is oversimplified.

An improved core model for trailing vortices has been introduced by Moore and Saffman (1973). They proved that, at near-wake region, in most part of the trailing-vortex core the viscosity can still be neglected, and hence there is an axial-flow excess. But there exists a *viscous subcore* where the axial flow tends to become deficit. Outside the subcore the flow is not yet a uniform stream as set in (8.29), but an inviscid vortex solution suggested by the Kadan similarity law. The asymptotic solution (8.15), i.e., the Oseen vortex, indicates that the size of viscous subcore is of the order of $(\nu t)^{1/2}$; while by (4.150) the radius of the surrounding inviscid core should be

$$a(t) \propto (\gamma t)^{1/(n+1)}, \quad 0 \le n \le 1$$

where $\gamma$ is a constant. Thus, to ensure the viscous subcore is much thinner than $a(t)$, there must be

$$(\nu t)^{1/2} \ll (\gamma t)^{1/(n+1)},$$

i.e.,

$$t \gg \left(\frac{\nu^{1+n}}{\gamma^2}\right)^{1/(1-n)}. \tag{8.35}$$

For a wing with elliptic load distribution we have $n = 1/2$ and $\gamma = \Gamma_0 b^{-1/2}$, so if we set $z = Wt$, (8.35) will imply

$$z \gg \frac{Wb^2\nu^3}{\Gamma_0^4} = \frac{16cA^2}{C_l^4 Re_c^3},$$

where $C_l = 2\Gamma_0/(Wc)$ is the sectional lift coefficient at wing root. For a typical wing, the right-hand side of this relation is much smaller than the chord length $c$, so (8.35) holds right at the trailing edge, indicating that a model with inviscid outer core fits better the realistic flow.

The viscous subcore is still governed by the linear equation (8.28a) and (8.28b), but cast to unsteady form by $z = Wt$:

$$\frac{\partial C}{\partial t} = \nu\left(\frac{\partial^2 C}{\partial r^2} - \frac{1}{r}\frac{\partial C}{\partial r}\right), \tag{8.36a}$$

$$\frac{\partial w}{\partial t} = -\frac{1}{\rho W}\frac{\partial p}{\partial t} + \nu\nabla^2 w. \tag{8.36b}$$

The inner boundary condition is the same as before:

$$r = 0: \quad v = 0, \quad w \text{ finite}, \tag{8.37}$$

but the boundary condition at the outer edge of the viscous core (i.e., the "boundary-layer variable" $r/(\nu t)^{1/2} \to \infty$) should be matched with the inviscid trailing-vortex solution in the limit $r \to 0$. Once again this is a problem of matched asymptotic expansion. Substituting (4.149) into (8.16a) yields

$$\frac{p}{\rho} \sim -\frac{1}{2n}\frac{\beta^2}{r^{2n}}, \quad \text{as } r \to 0 \tag{8.38}$$

where $\beta$ is a constant. This is then substituted into the approximate Bernoulli equation between two neighboring turns of the vortex sheet,

$$\frac{p_\infty - p}{\rho} = Ww + \frac{1}{2}v^2$$

(where it is assumed that $u \ll w$ and $\mid W - w \mid \ll W$), yielding

$$w \sim \frac{\beta^2}{2W}\left(\frac{1}{n} - 1\right) r^{-2n} > 0, \quad \text{as } r \to 0. \tag{8.39}$$

Along with the limiting form of (4.149) itself,

$$v \sim \frac{\beta}{r^n}, \quad r \to 0, \tag{8.40}$$

the three equations give the asymptotic matching condition of the inner solution determined by (8.36a), (8.36b), and (8.37) at $r/(\nu t)^{1/2} \to \infty$. Note that (8.39) has singularity at $r = 0$, indicating at the outer edge of viscous subcore there is a strong axial flow.

Equations (8.38) and (8.40) represent an already smoothed inviscid vortex core. One should check if the matching between the viscous subcore and smoothed inviscid core is reasonable. By (4.150), the distance between two neighboring turns of the vortex sheet is $2\pi r^{n+2}/[(n+1)\gamma t]$. Thus, as long as $r \ll (\gamma \nu^{1/2} t^{3/2})^{1/(n+2)} \equiv a$, this distance will be much smaller than the vortex-layer thickness $(\nu t)^{1/2}$, or the radius of the smoothed inviscid core is much larger than that of viscous subcore. Hence the above matching condition is correct. In this way, we obtain a trailing-vortex core structure consisting of three regions as shown in Fig. 8.2. Moore and Saffman (1973) show that the viscous subcore in a trailing vortex will have axial-velocity deficit if $n > 0.44$.

Consider now the core structure of a leading-edge conical vortex, which was first studied by Hall (1961) using matched asymptotic expansion method. Then Stewartson and Hall (1962) improved the solution of the viscous subcore. Similar to the trailing-vortex solution of Moore and Saffman (1973), the leading-edge vortex core can also be divided into an inviscid outer region and a viscous inner region. Due to the conical similarity, $(u, v, w, p)$ are functions of only a single variable $r/z$, and the outer edge of the core is $r = az$. Thus, we can introduce a similarity variable $\eta = r/(az)$ to cast the quasi-cylindrical equation (8.16a) and (8.16b), along with the continuity equation (6.3) to a

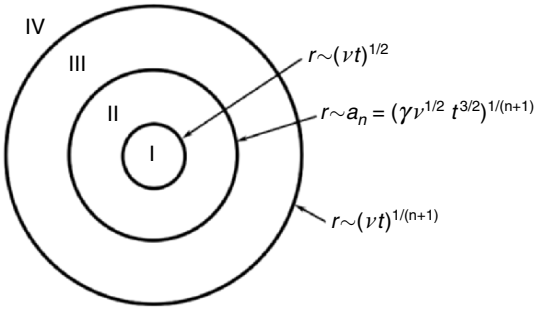


**Fig. 8.2.** The core structure of a trailing vortex

set of ordinary differential equations. For the inviscid outer core $(u_i, v_i, w_i, p_i)$ with boundary condition

$$\eta = 0: \quad u_i = 0; \quad \eta = 1: \quad (v_i, w_i, p_i) = (V, W, P),$$

where $V, W, P$ are given constants, Hall (1961) obtained

$$u_i = -\frac{1}{2} W \alpha \eta, \tag{8.41a}$$

$$v_i = (V^2 - W^2 \alpha^2 \ln \eta)^{1/2}, \tag{8.41b}$$

$$w_i = W(1 - \alpha \ln \eta), \tag{8.41c}$$

$$\frac{p_i - p}{\rho} = V^2 \ln \eta - \frac{1}{2} W^2 \alpha^2 \ln \eta, \tag{8.41d}$$

where

$$\alpha = \left(1 + \frac{2V^2}{W^2}\right)^{1/2} - 1 > 0. \tag{8.42}$$

Ludwieg (1962) also obtained this solution. Guiraud and Zeytounian (1977) have applied the multiscale expansion to the rolling-up solution of a leading-edge conical vortex sheet, and found that (8.41) corresponds to the lowest-order smooth approximation of their solution.

As $\eta \to 0$, singularity appears in (8.41), implying a need for introducing viscous subcore. By the substitution of (8.41) into (8.16), it can be found that the viscous effect becomes important once

$$r \sim z \left(\frac{W \alpha z}{\nu}\right)^{1/2} \quad \text{or} \quad \nu \sim \frac{W \alpha r^2}{z}. \tag{8.43}$$

By the principle of matched asymptotic expansion, the boundary condition

for the viscous inner solution is

$$r = 0: \quad u = v = \frac{\partial w}{\partial r} = 0;$$

$$\frac{r}{z}\left(\frac{W\alpha z}{\nu}\right)^{1/2} \to \infty: \quad (u, w, p) \to (u_i, w_i, p_i). \tag{8.44}$$

However, a further analysis indicates that the order of magnitude of terms in (8.16) depends on two factors $W\alpha/z$ and $\ln(r/z)$ rather than a single one as so far we have met. It is necessary to introduce new variables based on these factors and using them to expand the outer solution, and then establish the corresponding inner expansion. The desired equations then follow from substituting the outer and inner expansions into (8.16) and collect terms of the same orders. Stewartson and Hall (1962) found that the proper inner variables are

$$\zeta = \frac{r}{z}\left(\frac{W\alpha\chi z}{\nu}\right)^{1/2}, \quad \chi = \ln\left[\alpha\left(\frac{W\alpha z}{\nu}\right)^{1/2}\right]. \tag{8.45}$$

In terms of these variables, the edge of viscous subcore becomes $\zeta/\chi^{1/2} \to \infty$, while the edge of the entire core is at $\zeta = \chi^{1/2}\mathrm{e}^{\chi}$. By (8.45), the viscous subcore radius is $\zeta = O(\chi^{1/2})$ instead of $O(1)$ in an ordinary boundary layer.

### 8.1.4 Vortex Core Dynamics

In Sects. 8.1.1–8.1.3 we discussed the models for different phases in the formation of vortices and typical core structures. We now discuss the dynamic evolution of a vortex core itself, which can be named *vortex-core dynamics*. Recall that the helical-wave decomposition introduced in Sect. 2.3.4 is a further sharpening of the Helmholtz decomposition, which splits a vector potential into the left- and right-handed components, and thereby introduces an additional intrinsic degree of freedom. Consequently, in the helical-wave spectral space a flow evolution problem appears as a dynamic system. This decomposition is a natural tool in the study of vortex-core dynamics, as demonstrated by Melander and Hussain (1993a). But their analysis is in the physical space.

Consider an axisymmetric columnar vortex in the cylindrical coordinates $(r, \theta, z)$. A helical-wave decomposition splits $\boldsymbol{\omega}$ into a right-handed polarized component $\boldsymbol{\omega}_{\mathrm{R}}$ and a left-handed polarized vorticity component $\boldsymbol{\omega}_{\mathrm{L}}$, along with corresponding polarized velocity distribution; for the orthogonal helical-wave basis vectors in terms of cylindrical coordinates see (2.127). The vector lines of $(\boldsymbol{\omega}_{\mathrm{R}}, \boldsymbol{u}_{\mathrm{R}})$ and $(\boldsymbol{\omega}_{\mathrm{L}}, \boldsymbol{u}_{\mathrm{L}})$ are right-handed and left-handed spirals, respectively. The two sets of spirals move along the vortex axis toward opposite directions: the right-handed spirals move right and vice versa. The core vorticity field is therefore the superposition of the two polarized vorticity fields, see Fig. 8.3. To study the core dynamics, we introduce a sinusoidal disturbance

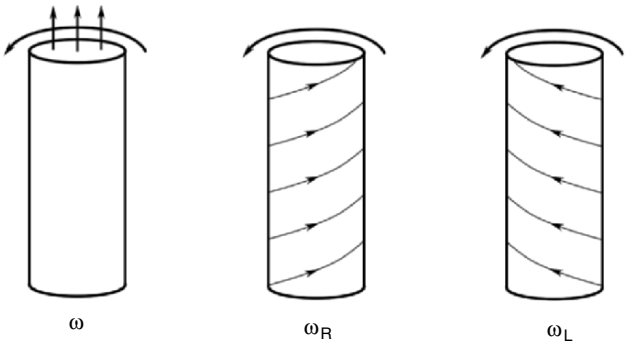


**Fig. 8.3.** Left and right polarized vorticity components of a vortex column. Adapted from Melander and Hussain (1993a)

to the columnar vortex and examine its evolution. Assume an initial vorticity distribution

$$\omega_r(r,\theta,z) = \Omega\left(\frac{r}{s(z)}\right)\frac{r}{s(z)^3}\frac{\mathrm{d}s}{\mathrm{d}z}, \tag{8.46a}$$

$$\omega_\theta(r,\theta,z) = 0, \tag{8.46b}$$

$$\omega_z(r,\theta,z) = \Omega\left(\frac{r}{s(z)}\right)\frac{1}{s(z)^2}, \tag{8.46c}$$

where $\Omega$ is the axial vorticity and $s(z)$ defines the boundary shape of the axisymmetric vortex. Melander and Hussain (1993a) adopt a distribution function

$$\Omega(\zeta) = \begin{cases} \omega_0 \exp(-\dfrac{4\zeta^2}{1-\zeta^2})\exp(4\zeta^4+4\zeta^6+4\zeta^8), & 0 \le \zeta < 1 \\ 0, & 1 \le \zeta \end{cases} \tag{8.47}$$

$$s(z) = r_0(1-\mu\cos(2\pi z/\lambda)), \tag{8.48}$$

where $\omega_0$ is the peak value of vorticity, $r_0$ is the radius of the undisturbed vortex core, and $\lambda$ and $\mu$ are, respectively, the disturbance wavelength and amplitude of the disturbance wave along the core. Obviously, when $\zeta = r/s(z) \ll 1$ the vorticity distribution is nearly Gaussian.

Melander and Hussain (1993a) used a three-dimensional spectral method to conduct a numerical computation under periodic boundary condition, of which the main results are as follows.

Consider first the time-variation of the vorticity magnitude. The computed vorticity contours at a sequence of times during the core evolution are shown in Fig. 8.4a, where the variation of the core boundary is marked by thick lines. Here, the core boundary is defined by the kinematic vorticity number

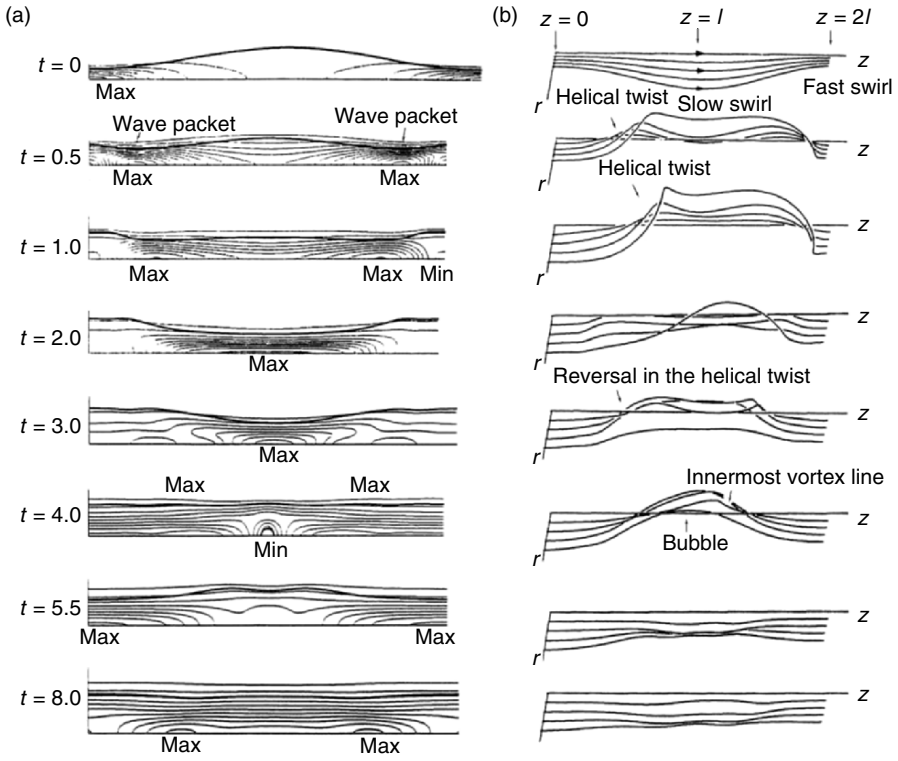


**Fig. 8.4.** (**a**) The instantaneous isovorticity contours of the vortex column. Along the axis some local minima and maxima of $\omega$ are indicated. (**b**) The evolution of four typical vortex lines. From Melander and Hussain (1993a)

$m = \sqrt{(\omega^2/2S_{ij}S_{ij})} = 1$, see (6.188). In order to see the three-dimensional evolution of the core, Fig. 8.4b shows the twisting deformation of four typical vorticity lines.

From these figures we see that the main character of the vortex-core evolution is the propagation of wave packets and the formation of low enstrophy bubble. The wave pockets propagating toward opposite axial directions carry opposite polarized vorticities. The core evolution can be interpreted by the propagation of polarized wave packets and their interaction. It is known that the opposite polarized vorticities distribute separately. Some regions are dominated by $\boldsymbol{\omega}_{\mathrm{R}}$, while some others by $\boldsymbol{\omega}_{\mathrm{L}}$. The twisting of the vorticity lines in Fig. 8.4b is determined by the dominance of certain polarized vorticity. In a region dominated by $\boldsymbol{\omega}_{\mathrm{R}}$, the vorticity lines twist to the right-hand direction, and vice versa. Meanwhile, the right-polarized vorticity moves right and vice versa as well. The trend of moving toward opposite directions of the helical-wave decomposed polarized vorticity-wave packets is a result of the

nonlinearity of the vorticity equation. More precisely, as will be seen below, it is a result of the helical-wave decomposed transverse Lamb vector.

Associated with their motion, there is also a deformation of wave packets, including elongation, broadening, and low enstrophy bubble formed behind the wave packets. While the wave-packet broadening is a viscous diffusion effect, the other two kinds of deformation are due to the interaction of left- and right-polarized vorticity. To see this, we just observe the evolution of a single isolated polarized wave packet and then their interaction. The former is exemplified by $\boldsymbol{\omega}_{\mathrm{R}}$ shown in Fig. 8.5. There, the wave-packet simply translates slowly toward right, with a much smaller speed than the case with both polarized vorticities. Therefore, the nonlinear character of vortex-core evolution must be from the interaction of left- and right-polarized vorticities. For convenience, introduce a pair of projection operators $P^+$ and $P^-$, which define the right- and left-handed components of a vector, respectively. Then the vorticity transport equation can be decomposed into a pair of coupled evolution equations for two polarized vorticities (Melander and Hussain 1993a):

$$\frac{\partial \boldsymbol{\omega}_{\mathrm{R}}}{\partial t} = -\nabla \times (\boldsymbol{\omega}_{\mathrm{R}} \times \boldsymbol{u}_{\mathrm{R}}) + \nabla \times P^-(\boldsymbol{\omega}_{\mathrm{R}} \times \boldsymbol{u}_{\mathrm{R}}) - P^+[(\boldsymbol{u}_{\mathrm{L}} \cdot \nabla)\boldsymbol{\omega}_{\mathrm{R}}] + P^+[(\boldsymbol{\omega}_{\mathrm{R}} \cdot \nabla)\boldsymbol{u}_{\mathrm{L}}] - \nabla \times P^+(\boldsymbol{\omega}_{\mathrm{L}} \times \boldsymbol{u}) + \frac{1}{Re}\nabla^2 \boldsymbol{\omega}_{\mathrm{R}}, \tag{8.49a}$$

$$\frac{\partial \boldsymbol{\omega}_{\mathrm{L}}}{\partial t} = -\nabla \times (\boldsymbol{\omega}_{\mathrm{L}} \times \boldsymbol{u}_{\mathrm{L}}) + \nabla \times P^+(\boldsymbol{\omega}_{\mathrm{L}} \times \boldsymbol{u}_{\mathrm{L}}) - P^-[(\boldsymbol{u}_{\mathrm{R}} \cdot \nabla)\boldsymbol{\omega}_{\mathrm{L}}] + P^-[(\boldsymbol{\omega}_{\mathrm{L}} \cdot \nabla)\boldsymbol{u}_{\mathrm{R}}] - \nabla \times P^-(\boldsymbol{\omega}_{\mathrm{R}} \times \boldsymbol{u}) + \frac{1}{Re}\nabla^2 \boldsymbol{\omega}_{\mathrm{L}}. \tag{8.49b}$$

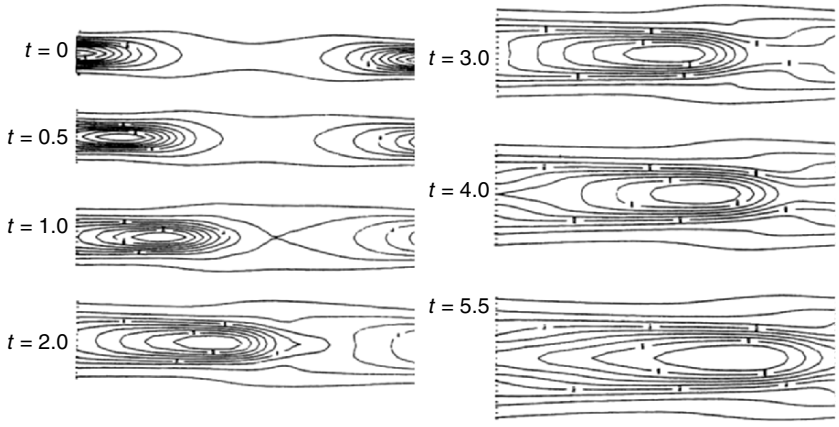


**Fig. 8.5.** Evolution of $\omega_{\mathrm{R}}$ in the absence of the initial left-handed component $\omega_{\mathrm{L}}$. The letters on the left-hand side of figure show the different time of evolution. From Melander and Hussain (1993a)

In (8.49a), the six terms on the right-hand side are, respectively, the inviscid self-evolution of $\boldsymbol{\omega}_{\mathrm{R}}$, the production of left-polarized vorticity due to the right-polarized vorticity, the advection of $\boldsymbol{\omega}_{\mathrm{R}}$ by the velocity $\boldsymbol{u}_{\mathrm{L}}$ of the left-handed vorticity, the stretching of $\boldsymbol{\omega}_{\mathrm{R}}$ due to the gradient of $\boldsymbol{u}_{\mathrm{L}}$, the production of $\boldsymbol{\omega}_{\mathrm{R}}$ due to the evolution of $\boldsymbol{\omega}_{\mathrm{L}}$, and the viscous diffusion of the right-polarized vorticity.

The numerical result of Melander and Hussain (1993a) indicates that the second term is quite weak, but the third term, i.e., a polarized vorticity advected by the opposite polarized velocity, plays a dominant role. Next to this is the self-evolution of the polarized vorticity. Therefore, to a big extent the evolution of $\boldsymbol{\omega}_{\mathrm{R}}$ may amount to these two mechanisms. The self-evolution effect tends to move the $\boldsymbol{\omega}_{\mathrm{R}}$-wave packet to the right, adding enstrophy in front of the wave packet but subtracting enstrophy behind it. On the other hand, the $\boldsymbol{u}_{\mathrm{L}}$ associated with the $\boldsymbol{\omega}_{\mathrm{L}}$ tends to advect $\boldsymbol{\omega}_{\mathrm{R}}$ to the left. Because the rightward self-induced motion of the $\boldsymbol{\omega}_{\mathrm{R}}$-packet is slower than the leftward advection by $\boldsymbol{u}_{\mathrm{L}}$, the net effect is a left drift of the packet although the $\boldsymbol{\omega}_{\mathrm{R}}$-packet has a self-induced motion to the right. Thus, there is a backward drift of the polarized wave packets caused by the advection of opposite polarized velocities, leading to the wave-packet elongation.

The formation of low enstrophy bubble is also due to the wave-packet advection by opposite polarized vorticities. This advection reaches a maximum at the axis, so the wave-packet is dragged at maximum velocity near the axis. The mutual dragging of the wave packets of opposite polarized vorticity results in an overlap near the axis, leading to the formation of low enstrophy bubble.

## 8.2 Dynamics of Three-Dimensional Vortex Filament

The quasicylindrical vortex-core theory provides a detailed understanding of the core structure and dynamics at large Reynolds numbers, but is confined to an isolated and straight vortex core. It cannot deal with a curved vortex and its interaction with surrounding flow field. One of the essential properties inherent in vortex motion is its three dimensionality. Once we consider a curved vortex in three-dimensional space, then, the first remarkable feature is that each segment of the vortex experiences an "induction" of the rest, known as the *self-induction* of three-dimensional vortices.[1] The self-induction causes the vortex not only to move but also, except a small number of special cases such as circular vortex rings, to deform continuously, including nonuniform stretching and tilting. Similar effect exists when a curved vortex is in a nonuniform background flow field as in contrast to the straight-vortex case (Sect. 6.5) which remains straight. The motion and deformation of a curved vortex due to self-induction and background-field effect are very important mechanisms and

[1] The self-induction of a vortex sheet or layer exists in both two and three dimensions, see Sect. 4.4.4.

play a key role in many complex flows as exemplified by vortical structures in turbulence (Chap. 10). During the self-induced motion of a three-dimensional vortex, the vortex core is a waveguide tube that can support the propagation of disturbances and even solitary waves along the core. These interesting issues are the subject of the present section.

As the vortex shape becomes more complicated, the corresponding theoretical models have to be cruder approximations. In this section we consider the *vortex-filament* model, which is an isolated thin vortex with so small cross-section that the core structure is simplified to have uniform vorticity distribution. The significant role of vortex filaments has been widely confirmed by numerical computations and experiments; in particular, they are often observed in turbulence as the strongest coherent structures (e.g., She et al. 1990), see Fig 8.6.

The central idea of our analysis in this section is applying asymptotic expansion to the Biot–Savart formula (3.32) to obtain the self-induced velocity. The expansion should be compatible with the Navier–Stokes equation at large $Re$. Assume the vorticity is concentrated in a vortex tube of local radius $a$ with $Re = \Gamma/\nu \to \infty$, and meanwhile the curvature of the filament $\kappa < \infty$. Then the balance of $a$ and $Re$ requires $a = O(Re^{-1/2})$.

We first introduce a local-induction approximation, within which we have the elegant self-induced solitary-wave theory of Hasimoto (1972) for very thin

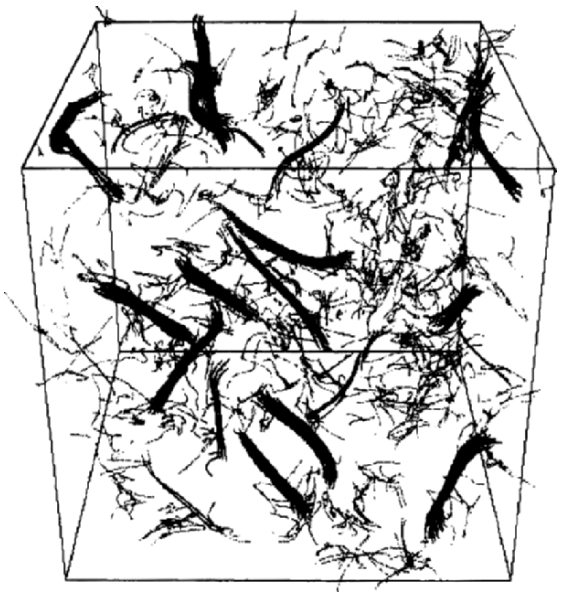

**Fig. 8.6.** Intermittent vortex filaments in a three-dimensional turbulent fluid simulated on a computer. From She et al. (1990)

core. We then generalize Hasimoto's theory to include the effects of finite core and stretching.

### 8.2.1 Local Induction Approximation

Consider an isolated and closed vortex filament of strength $\Gamma$, of which a point $P(\boldsymbol{X})$ experiences a self-induced velocity determined by the Biot–Savart formula (3.32), which now reads

$$\boldsymbol{u}(\boldsymbol{X}) = -\frac{\Gamma}{4\pi}\int \frac{\boldsymbol{r}\times \mathrm{d}\boldsymbol{l}}{r^3}, \tag{8.50}$$

where $\boldsymbol{r} = \boldsymbol{X} - \boldsymbol{\xi}$ , with $\boldsymbol{X}$ and $\boldsymbol{\xi}$ being the position vectors of $P$ and a moving point along the filament, respectively, and $\mathrm{d}\boldsymbol{l} = \boldsymbol{t}\,\mathrm{d}s$ is the vector line element of the filament at $\xi$. As shown by (3.33), the self-induced circumferential velocity has a $1/r$-singularity at the filament. In three dimensions, the self-induction will also cause a curvature-related $\ln r$-singularity in the binormal velocity as will be seen later. To bypass the singularities, we first estimate the induced velocity at a point $Q$ near the filament, and then let $Q$ approach the filament asymptotically. We take the intrinsic coordinates along the filament as shown in Fig. 8.7, with the origin at $P$ and $\boldsymbol{t}, \boldsymbol{n}, \boldsymbol{b}$ being the unit vectors along tangent, normal, and binormal directions, respectively (see Sect. A.3.1). Then a point $Q$ on the normal plane of the filament can be expressed as

$$\boldsymbol{x} = x_2\boldsymbol{n} + x_3\boldsymbol{b}. \tag{8.51}$$

What we need is the asymptotic induced velocity of $Q$ as $\rho = \sqrt{x_2^2 + x_3^2} \to 0$. In a neighborhood of $P$ $(L \geq s \geq -L)$, we may write approximately

$$\boldsymbol{\xi} \sim \kappa\boldsymbol{t} + \frac{1}{2}\kappa s^2\boldsymbol{n}, \quad \delta\boldsymbol{l} \sim (\boldsymbol{t} + \kappa s\boldsymbol{n})\delta s,$$

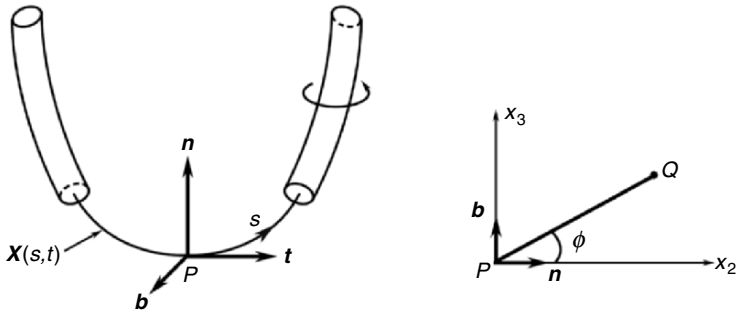


**Fig. 8.7.** Three-dimensional vortex filament and coordinates

where $s$ is the arclength. Substituting these relations into (8.50), when $\rho \to 0$ the entire integral over the closed filament approaches asymptotically (for details see Callegari and Ting 1978; Ting and Klein 1991)

$$\boldsymbol{u} = \frac{\partial \boldsymbol{X}}{\partial t} = \frac{\Gamma}{2\pi\rho}\boldsymbol{e}_\theta + \frac{\Gamma\kappa}{4\pi}\ln\left(\frac{L}{a}\right)\boldsymbol{b} + \boldsymbol{Q}_{\mathrm{f}}, \tag{8.52}$$

where $\boldsymbol{Q}_{\mathrm{f}}$ denotes the finite single-valued part of the velocity as $r \to 0$. It is now evident that to the leading order the velocity at $P$ is dominated by the induction of its nearby segment $L \geq s \geq -L$ bounded by a cut-off arclength $L$. The finite part $\boldsymbol{Q}_{\mathrm{f}}$ is negligible as compared to the very large local induction that approaches infinity asymptotically as $a, \rho \to 0$. This implies the validity of the *localized induction approximation*, by which only the induced motion of $P$ by the local segment of length $2L$ needs to be taken into account. Note that the local-induction approximation cannot be applied to short-wave disturbances, say near a knot of the filament.

Clearly, on the right-hand side of (8.52), the first term is the familiar self-induced circumferential velocity, which has a $1/r$-singularity but does not change the shape of the filament. The second term is a self-induced motion along the binormal, of which the magnitude depends not only on $\Gamma$ but also on the curvature $\kappa$ of the filaments, having a weak logarithmic singularity. Thus, due to the self-induction, an infinitely thin vortex filament will move at an infinitely large velocity; and in general it will also deform at an infinitely large rate. It is only the second term of (8.52), therefore, that dominates the self-induced motion of a vortex filament. An infinitely long straight line vortex filament has no self-induced motion; but once it is disturbed to deviate from the straight line, it will deform immediately and this deformation will continue as time goes on.

We now see that, to the leading order, the self-induced motion of a vortex filament is given by

$$\boldsymbol{u} = \frac{\Gamma\kappa}{4\pi}\ln\Big(\frac{L}{a}\Big)\boldsymbol{b} + O(1). \tag{8.53}$$

If the core radius $a$ is sufficiently small so that the variation of $L/a$ along the filament can be ignored, (8.53) becomes approximately $\boldsymbol{u} = c\kappa\boldsymbol{b}$, where $c$ is a constant. Then a rescaling of time and length casts the self-induction equation to a very compact form:

$$\boldsymbol{X}_t = \kappa\boldsymbol{b}, \tag{8.54}$$

where and below the subscripts $t$ and $s$ denote partial derivatives with respect to these variables, respectively. Since $\boldsymbol{b} = \boldsymbol{t} \times \boldsymbol{n}$ and $\boldsymbol{t} = \boldsymbol{x}_s$, by the Frenet–Serret formulas (A.39),

$$\boldsymbol{t}_s = \kappa\boldsymbol{n}, \quad \boldsymbol{n}_s = -\kappa\boldsymbol{t} + \tau\boldsymbol{b}, \quad \boldsymbol{b}_s = -\tau\boldsymbol{n}, \tag{8.55}$$

with $\tau$ being the torsion of the curve, we can rewrite (8.54) as

$$\boldsymbol{X}_t = \boldsymbol{X}_s \times \boldsymbol{X}_{ss}. \tag{8.56}$$

Therefore, the self-induced motion of a vortex filament is completely reduced to the *geometric motion of a spatial curve* governed by (8.56).

The most significant results under the local-induction approximation are due to Betchov (1965) and Hasimoto (1972). Betchov was the first to find that (8.56) can be cast to a pair of partial-differential equations for the curvature $\kappa$ and torsion $\tau$ of the filament, with $(s,t)$ as arguments. These equations are known as the Betchov intrinsic equations. He has used these equations to study the self-induced motion of helical and planar filaments, and examined the feature of the equations at two extreme cases, proving that they have nonlinear wave solutions. Then, on the basis of Betchov's work, Hasimoto elegantly transformed (8.56) to the nonlinear Schrödinger equation.

Following Hasimoto (1972), we first combine the second and third formulas of (8.55) to a complex-variable formula

$$(\boldsymbol{n}+\mathrm{i}\boldsymbol{b})_s = -\mathrm{i}\tau(\boldsymbol{n}+\mathrm{i}\boldsymbol{b}) - \kappa\boldsymbol{t}. \tag{8.57}$$

The form of this formula naturally suggests introducing a complex scalar

$$\psi = \kappa\,\mathrm{e}^{\mathrm{i}\Phi} \quad \text{with} \quad \Phi(s,t) = \mathrm{i}\int_0^s \tau(s',t)\,\mathrm{d}s' \tag{8.58}$$

and a new complex vector

$$\boldsymbol{N} = (\boldsymbol{n}+\mathrm{i}\boldsymbol{b})\,\mathrm{e}^{\mathrm{i}\Phi}, \tag{8.59}$$

such that (8.57) is cast to $\boldsymbol{N}_s = -\psi\boldsymbol{t}$. This change of variables is known as the *Hasimoto transformation*. Scalar $\psi$ represents a wave function with amplitude $\kappa$ and phase $\tau$, called the *filament function*. The task then is to find the wave equation satisfied by $\psi$. To this end, we use $\psi, \boldsymbol{t}$ and their spatial derivatives to express $\boldsymbol{N}_s$ and $\boldsymbol{N}_t$, obtaining two expressions for $\boldsymbol{N}_{st}$ and let them equal each other. In the derivation the following orthogonal relations are employed:

$$\boldsymbol{t}\cdot\boldsymbol{t} = 1, \quad \boldsymbol{N}\cdot\boldsymbol{N}^* = 2,$$
$$\boldsymbol{N}\cdot\boldsymbol{N} = \boldsymbol{N}^*\cdot\boldsymbol{N}^* = 0,$$

where the asterisk denotes complex conjugate. After some algebra, we find that (8.54) yields

$$-\psi_t = -\mathrm{i}(\psi_{ss} + R\psi), \quad \frac{1}{2}\psi\psi_s^* = R_s - \frac{1}{2}\psi_s\psi^*. \tag{8.60}$$

Here, the unknown function $R$ is determined by integrating (8.60):

$$R = \frac{1}{2}(\psi\psi^* + A) = \frac{1}{2}(|\psi|^2 + A),$$

where $A$ is an arbitrary real function of $t$ and can be removed without loss of generality (corresponding to a shift of the origin in the integration). Thus,

we finally arrive at the famous *nonlinear Schrödinger equation* for curvature $\kappa$ and torsion $\tau$:

$$\frac{1}{\mathrm{i}}\frac{\partial\psi}{\partial t} = \frac{\partial^2\psi}{\partial s^2} + \frac{1}{2}|\psi|^2\psi. \tag{8.61}$$

Owing to the Hasimoto transformation, this equation combines two aspects of the self-induced motion of a vortex filament into a whole: the geometric aspect governed by the Serret–Frenet formula and the dynamic aspect governed by the local-induction approximation. The nonlinear Schrödinger equation has extensive applications in theoretical physics, and has been studied in depth by many researchers. As a significant implication of Hasimoto's work, it represents a completely integrable Hamilton system of infinite dimensions, permitting *solitary-wave solutions*.

The simplest example is a solitary wave moving along the filament with constant speed $c$. Let $\kappa = 0$ at infinity and view the problem in a frame of reference fixed to the wave. Then $\kappa$ and $\tau$ become functions of $\xi = s - ct$, so

$$\psi = \kappa(\xi)\exp\left(\mathrm{i}\int_0^s \tau(\xi)\,\mathrm{d}\xi\right).$$

Substituting this into (8.61), one finds that the real and imaginary parts yields, respectively,

$$-c\kappa[\tau(\xi) - \tau(-ct)] = \kappa_{ss} - \kappa\tau^2 + \frac{1}{2}\kappa^3, \tag{8.62a}$$

$$c\kappa_s = 2\tau\kappa_s + \kappa\tau_s, \tag{8.62b}$$

where (8.62b) can be directly integrated to yield

$$(c - 2\tau)\kappa^2 = 0.$$

Thus, as long as $\kappa$ is not identically zero (rectilinear filament), there must be

$$\tau = \tau_0 = \frac{1}{2}c = \text{const.} \tag{8.63}$$

Hence, the torsion $\tau$ is invariant along the filament and the solitary wave propagates with a speed of $2\tau$. On the other hand, by using the boundary condition at infinity, the integration of (8.62a) gives

$$\kappa = \pm 2\tau_0\,\mathrm{sech}(\pm\tau_0(s - ct)). \tag{8.64}$$

This is a solitary-wave solution propagating along the filament, of which the shape can be determined by using (8.56). Several different shapes are possible depending on the value of the torsion; a typical Hasimoto solitary-wave solution is plotted in Fig. 8.8.

As pointed out earlier, generically a curved vortex filament will move and deform by self-induction, but in a few special cases the shape can be preserved.

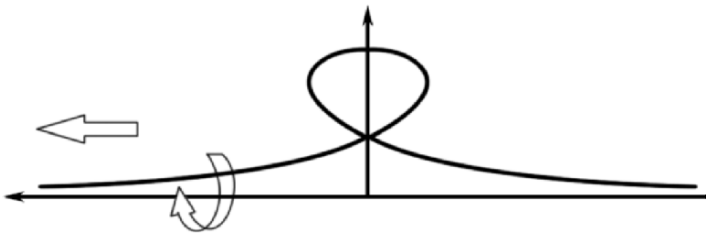

**Fig. 8.8.** Hasimoto solitary-wave solution

The above self-induced solitary wave is such an example: it slides along the filament with constant speed as well as rotates as the filament, but the wave shape keeps unchanged. In fact, all shape-preserved waves can be expressed by

$$\boldsymbol{X}_t = -c\boldsymbol{X}_s + \boldsymbol{\Omega} \times \boldsymbol{X} + \boldsymbol{V}, \tag{8.65}$$

where $c, \boldsymbol{\Omega}$, and $\boldsymbol{V}$ are constants. $\boldsymbol{V}$ and $\boldsymbol{\Omega}$ represent a translation and a rigid rotation, respectively; while $c$ is the sliding speed along the filament of a disturbance of fixed shape. More specifically, from (8.56) and (8.65) follows:

$$\boldsymbol{X}_s \times \boldsymbol{X}_{ss} = -c\boldsymbol{X}_s + \boldsymbol{\Omega} \times \boldsymbol{X} + \boldsymbol{V}, \tag{8.66}$$

which permits the following types of solutions:

1. $c = 0$, $\boldsymbol{\Omega} = 0$, $\boldsymbol{V} = 0$: rectilinear vortex.
2. $c = 0$, $\boldsymbol{\Omega} = 0$: circular vortex-filament ring, along which all points have the same curvature $\kappa$ and hence by (8.54) also the same velocity. Thus, it only translates but never changes shape (Sect. 6.3).
3. $\boldsymbol{\Omega} = 0$: helical vortex filament.
4. $c = 0$, $\boldsymbol{V} = 0$, Euler elastic loop.
5. Solitary waves.

For more discussions of shape-preserved vortex filaments the reader is referred to Kida (1981b).

More important than the integrability of the self-induced motion equation, Hasimoto's work confirms that a vortex core is a waveguide tube of solitary waves. It is this wave-propagation feature that explains many nonlinear phenomena and considerably enriches the vortex-filament dynamics. This conclusion of Hasimoto has been verified by experiments. Hopfinger et al. (1982) found that in a rotating circular-cylindrical container a thin vortex may have twisting deformation, very similar to the shape of Hasimoto's solitary-wave solution. Maxworthy et al. (1983, 1985) further found that this twisting deformation is stable during a collision process, with only a phase shift. Such a shape-preserved property during collision is exactly a character of solitary waves. Interestingly, observations have indicated that even a tornado can produce a solitary wave by twisting (Aref and Flinchem 1984).

Inspired by Hasimoto's work, Leibovich and Ma (1983) have extended the solitary-wave propagation along a vortex filament to a more general case, taking into consideration of vortex-core structure and axial velocity. By using singular perturbation method, these authors also derived the nonlinear Schrödinger equation

$$\mathrm{i}\frac{\partial A}{\partial \tau} + \alpha\frac{\partial^2 A}{\partial z^2} + \beta A|A|^2 = 0, \tag{8.67}$$

where $\tau = \varepsilon^2 t$, $z = \varepsilon(s - C_{\mathrm{g}}t)$, and $\varepsilon$ are the small parameters in perturbation expansion with $C_{\mathrm{g}}$ being the group velocity of the wave packet. Coefficients $\alpha$ and $\beta$ depend on the core structure and axial-velocity distribution. This work further confirms the existence of solitary waves along a vortex core and, by a comparison with the experimental results of Hopfinger et al. (1982), strongly supports a basic fact having been observed in Sect. 8.1.4: *being able to transport waves is a common and intrinsic property of various vortices*. For further references on the solitary-wave propagation along vortex filaments, see also Lamb (1980) and Newell (1985). The propagation and interaction of several solitary waves along a vortex filament have been discussed by Aref and Flinchem (1984) and Fukumoto and Miyazaki (1986, 1991).

It is of interest to look at the motion invariants under the local-induction approximation. The total length of a vortex filament is invariant (cf. Sect. 8.2.3) and the total vorticity is preserved. Fukumoto (1987) has shown that both the angular momentum $I(t)$ and helicity $J(t)$ of a closed vortex-filament loop are preserved. But, since the far-field influence has been neglected, the global information about the degree of knottedness of a filament should be lost, and hence $J(0)$ should be zero (see the context of (3.76)). Besides, although the total enstrophy is not preserved by the three-dimensional Euler equation, it is preserved under this approximation (Ricca 1992); and so is the total kinetic energy. Therefore, all known invariant quantities of the Euler equation remain effectively invariant under the local-induction approximation. Besides, it can be proved that the total torsion, i.e., Hasomoto's phase function $\Phi$ defined in (8.58) is preserved as well:

$$\Phi = \int_s \tau \,\mathrm{d}s = \text{const.}$$

Having seen the elegance of the Hasimoto theory, its limitation should also be recognized. First, owing to the neglect of vortex-core structure, the self-induced motion of very slender vortex filaments contains singular velocity and deformation, and the $L/a$ in (8.53) is also indeterminate. Second, in the Hasimoto theory the self-stretching of the filament, a very crucial mechanism in vortex-filament evolution and instability, is completely absent.

To see the second limitation clearly, we write the general motion of a very slender vortex filament as

$$\boldsymbol{u} = \boldsymbol{X}_t = \beta(s,t)\boldsymbol{n} + \gamma(s,t)\boldsymbol{b}, \tag{8.68}$$

where the tangent velocity along the filament itself has been dropped without loss of generality, because this motion can be removed by a reparameterization. On the other hand, following (2.17), the time-rate of the length $\delta s$ of a vortex-filament element $\delta \boldsymbol{x} = \boldsymbol{t}\,\delta s$ is

$$\frac{1}{\delta s}\frac{\mathrm{D}\delta s}{\mathrm{D}t} = \frac{1}{\delta s}\boldsymbol{t}\cdot\delta\boldsymbol{u} = \boldsymbol{t}\cdot\boldsymbol{u}_s,$$

where by (8.68) and (8.55), see also (3.127), the only $\boldsymbol{t}$-component of $\boldsymbol{u}_s$ is $-\kappa\beta = -\kappa\boldsymbol{n}\cdot\boldsymbol{X}_t$. Thus, there is

$$\frac{1}{\delta s}\frac{\mathrm{D}\delta s}{\mathrm{D}t} = -\kappa\boldsymbol{n}\cdot\boldsymbol{X}_t, \tag{8.69}$$

which by (8.54) is identically zero in the Hasimoto theory. It is these limitations that have motivated a few extensions of the Hasimoto theory, as presented later.

### 8.2.2 Vortex Filament with Finite Core and Stretching

To remove the singularity in (8.53) as $a \to 0$, it is necessary to consider the internal structure of the vortex core. Local-induction models with *inviscid* finite core and axial flow have been studied by Widnall and Bliss (1971) to the first order, and by Moore and Saffman (1972) to the second order by using an elegant force-balance procedure. The Moore–Saffman equation for the motion of a finite-core filament was rederived by Fukumoto and Miyazaki (1991) more systematically using matched asymptotic expansions. These authors then proceed to apply the Hasomoto transform (8.58) and (8.59) to a filament with finite core, and thereby extend Hasimoto's equation (8.61) to an integrable *Hirota equation* (Hirota 1973)

$$\mathrm{i}\psi_t + \psi_{ss} + \frac{1}{2}|\psi|^2\psi - \mathrm{i}W\left(\psi_{sss} + \frac{3}{2}|\psi|^2\psi_s\right) = 0, \tag{8.70}$$

where function $W(s,t)$ depends on the core structure. The Hirota equation reduces to the nonlinear Schrödinger equation when $W \to 0$ and to the *modified* $K$-d$V$ *equation* when $W \to \infty$. Therefore, within the local-induction approximation, at least for inviscid fluid the vortex-filament equation is always integrable even with finite core.

As exemplified in Chap. 6, however, the circumferential and axial velocity profiles of an inviscid vortex solution may have certain arbitrariness. In general, the axial velocity in an inviscid core does not match with the outer flow and discontinuities may appear. A vortex filament with finite *viscous* core was first studied by Ting (1971) and then developed by Callegari and Ting (1978) to a complete second-order theory with decaying vortex core and axial velocity. Their filament-evolution equation reduces to that of Moore and Saffman (1972) as $\nu \to 0$, except for the difference in axial-velocity distribution.

This work has inspired a series of subsequent developments (e.g., Klein and Majda 1991a,b, 1993; Klein et al. 1992, 1996; Klein and Ting 1992, 1995; Klein and Knio 1995), including neater derivation of the Callegari–Ting equation, extending it to contain the nonlocal effect on filament self-stretching, improving the theoretical basis of thin-tube numerical method for the computation of filament motion, and various numerical tests of the theoretical predictions (e.g., Zhou 1997).

In particular, Klein and Majda (1991a,b) have shown that, under short-wavelength disturbances of great practical interest, the local self-induction and nonlocal self-stretching of a slender vortex filament will directly compete. On the other hand, a theory with nonlocal stretching needs finite-core theory as a necessary constituent. Therefore, in this case the two limitations mentioned at the end of Sect. 8.2.1 have to be removed simultaneously.

In this section we focus on the Callegari–Ting theory, following the neater approach of Klein and Knio (1995) but omit detailed algebra. Before entering the mechanics, we need to construct a proper coordinate system with origin $O$ moving along the vortex axis with arclength $s$, curvature $\kappa$, and torsion $\tau$. Similar to the case of circular vortex ring (Fig. 6.4), we introduce not only an orthonomal curvilinear triad $(\boldsymbol{t}, \boldsymbol{n}, \boldsymbol{b})$ at any point $O$ at the axis, but also polar coordinates $(r, \phi)$ on the crossplane spanned by $(\boldsymbol{n}, \boldsymbol{b})$, with $\phi$ being the angle between $\boldsymbol{e}_r$ and $\boldsymbol{n}$, see Fig. 8.9a. However, unlike the circular vortex ring, the corresponding three-dimensional curvilinear coordinates $(r, \phi, s)$ are not orthogonal in general due to the existence of torsion $\tau$, which makes the orientation of $\boldsymbol{n}$ and $\boldsymbol{b}$ rotate around the axis. To compensate this effect, we replace $\phi$ by

$$\theta \equiv \phi + \Phi(s, t)$$

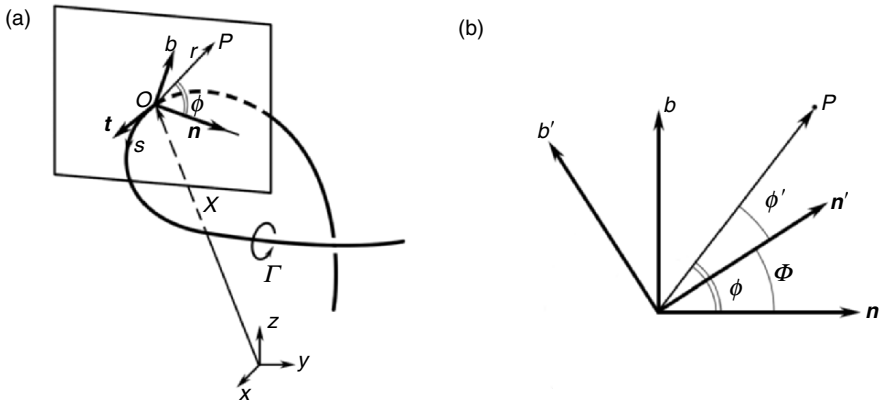


**Fig. 8.9.** Three-dimensional curvilinear coordinates systems. (**a**) The $(\boldsymbol{t}, \boldsymbol{n}, \boldsymbol{b})$ and $(r, \phi, s)$ frames. (**b**) The orthogonal $(r, \theta, s)$ frame, where primed quantities are evaluated at $s + ds$ and $\theta = \phi + \Phi$

as the polar angle (see Fig. 8.9b), where $\Phi$ is Hasimoto's phase function defined in (8.58) such that $\Phi_s = \tau$. Then the orthogonality of the $(r, \theta, s)$ coordinates is ensured. Indeed, consider a point $P$ away from the vortex axis, we can describe its position vector $\boldsymbol{x}$ in terms of the above coordinates with origin $O$ be the on-axis point $\boldsymbol{X}(s,t)$ nearest to $P$:

$$\boldsymbol{x}(P) = \boldsymbol{X}(s,t) + r\boldsymbol{e}_r. \tag{8.71}$$

Then there is an orthogonal decomposition (Callegari and Ting 1978)

$$\mathrm{d}\boldsymbol{x} = \boldsymbol{e}_r\,\mathrm{d}x + r\boldsymbol{e}_\theta\,\mathrm{d}\theta + h\boldsymbol{t}\,\mathrm{d}s, \tag{8.72}$$

where $h = 1 - \kappa\cos\phi$.

Now, in view of the finiteness of the vortex core, we start from the general vorticity–velocity formulation (Sect. 4.5) with the full Biot–Savart formula (3.29) and vorticity transport equation as the kinematic and kinetic aspects of the problem, respectively:

$$\boldsymbol{u}(\boldsymbol{x}_0,t) = \frac{1}{4\pi}\int \frac{\boldsymbol{\omega}\times\boldsymbol{r}}{r^3}dV, \quad \boldsymbol{r} = \boldsymbol{x}_0 - \boldsymbol{x}, \tag{8.73}$$

$$\boldsymbol{\omega}_t = \nabla\times(\boldsymbol{u}\times\boldsymbol{\omega}) + \nu\nabla^2\boldsymbol{\omega}, \tag{8.74}$$

where and in the following no super- or subscript is attached to quantities at the moving point $\boldsymbol{x}$ for neatness.

We take the filament curvature radius $R = O(1)$ as global length scale, and core radius $a$ as local scale, so $a/R \equiv \delta = Re^{-1/2} \ll 1$. Consider the kinematic aspect (8.73) first. At any point $O : s \to \boldsymbol{X}(s,t)$ at the filament axis under consideration, introduce a ball $B$ of radius $\delta_{\mathrm{B}}$, with

$$1 \gg \delta_{\mathrm{B}} \gg \delta^{1/2},$$

centered at $O$ to divide the space $R^3$ into a local and a nonlocal part. Let $R^3 - B$ be the nonlocal part, so (8.73) can be split into

$$\boldsymbol{u}(\boldsymbol{x}_0,t) = \frac{1}{4\pi}\left(\int_{R^3-B} + \int_B\right)\frac{\boldsymbol{\omega}\times\boldsymbol{r}}{r^3}\,\mathrm{d}V.$$

Then we seek the inner solution in $B$ and outer solution in $R^3 - B$.

Inside $B$ we use stretched radial and axial coordinates

$$\overline{r} = \delta^{-1}r, \quad z = \delta^{-1}(s_0 - s).$$

Since all geometric variations of the filament axis are weak, $\boldsymbol{r}$ can be expanded to a Taylor series of $z$ around $\boldsymbol{x}_0$. In the $(r,\theta,s)$-coordinates we have

$$\boldsymbol{r} = \boldsymbol{x}_0 - \boldsymbol{X} = \delta(z\boldsymbol{t} + \overline{r}\boldsymbol{e}_r) + \delta^2\left(\frac{1}{2}z^2\kappa\boldsymbol{b} - \overline{r}z\cos\phi\kappa\boldsymbol{t}\right) + O(\delta^3), \tag{8.75}$$

where we have used identity $\partial \boldsymbol{e}_r/\partial s = -\cos\phi\kappa\boldsymbol{t}$ due to (8.55). Then, as in Sect. 6.5.1, the vorticity $\boldsymbol{\omega} = (\xi, \eta, \zeta)$ permits a perturbation expansion

$$\begin{aligned}\boldsymbol{\omega} &= \delta^{-2}(\eta^{(0)}\boldsymbol{e}_\theta + \zeta^{(0)}\boldsymbol{t}) + \delta^{-1}(\xi^{(1)}\boldsymbol{e}_r + \eta^{(1)}\boldsymbol{e}_\theta + \zeta^{(1)}\boldsymbol{t}) + O(1)\\ &= \delta^{-2}(\eta^{(0)}\boldsymbol{e}_\theta + \zeta^{(0)}\boldsymbol{t}) + \delta^{-1}[\xi^{(1)}\boldsymbol{e}_r + \eta^{(1)}\boldsymbol{e}_\theta + z(\eta^{(0)}\boldsymbol{e}_\theta + \zeta^{(0)}\boldsymbol{t})_s]\\ &\quad + O(1). \end{aligned} \tag{8.76}$$

We substitute these expansions into (8.73), where the volume element $\mathrm{d}V$ comes from (8.72). In fact, we only need the transverse velocity $\boldsymbol{u}^\perp$ in the $(r, \theta)$-plane, since it solely causes the filament displacement. Assuming the leading-order vorticity and velocity are *axisymmetric*, the resulting asymptotic inner induced velocity is

$$\begin{aligned}\boldsymbol{u}^\perp_{\mathrm{inn}} = \frac{\kappa\boldsymbol{b}}{2}\left\{\frac{\varGamma}{2\pi}\left[\ln\left(\frac{\delta_{\mathrm{B}}}{\delta}\right) - 1\right] - \int_0^\infty \left(\frac{1}{\kappa}\zeta^{(1)}_{11} + \overline{r}\ln\overline{r}\zeta^{(0)}\right)\mathrm{d}\overline{r}\right\}\\ + O(1), \quad \text{as} \quad \delta_{\mathrm{B}}/\delta \to \infty,\end{aligned} \tag{8.77}$$

where $\zeta^{(1)}_{11}$ is the real part of the Fourier component of $\zeta^{(1)}$:

$$\zeta^{(1)}_{11} + \mathrm{i}\zeta^{(1)}_{12} = \frac{1}{\pi}\int_0^{2\pi} \zeta^{(1)}(\overline{r}, \theta, s, t)\mathrm{e}^{\mathrm{i}\theta}\,\mathrm{d}\theta.$$

The above development is confined within kinematics, and so is the entire outer solution, which amounts to the Biot–Savart integral over $R^3 - B$ with $\boldsymbol{r} = \boldsymbol{X}_0 - \boldsymbol{X} + \delta\overline{r}\boldsymbol{e}_r$. This yields

$$\boldsymbol{u}_{\mathrm{out}}(\boldsymbol{X}_0) = \frac{\varGamma}{4\pi}\int_{L-I_{\mathrm{B}}} \frac{\boldsymbol{r}\times\boldsymbol{t}}{r^3}\mathrm{d}s\cdot(1 + O(\delta)),$$

where $I_{\mathrm{B}}$ is the interval $s_0 - \delta_{\mathrm{B}} < s < s_0 + \delta_{\mathrm{B}}$. Thus, to the leading order (8.73) indeed reduces to the line-integral version (8.50). The result is already known to be (8.53) but now reads

$$\boldsymbol{u}^\perp_{\mathrm{out}} = \frac{\varGamma\kappa}{4\pi}\ln\left(\frac{L}{\delta_{\mathrm{B}}}\right)\boldsymbol{b} + \boldsymbol{Q}^\perp, \tag{8.78}$$

where $L$ is a cut-off length comparable with $R$ (Callegari and Ting (1978) take $L/\delta_{\mathrm{B}} = R/\delta = (\delta\kappa)^{-1}$), $\boldsymbol{Q}$ is the finite nonlocal part of the Biot–Savart integral and, if exists, the contribution of a regular background flow field. Then an asymptotic matching of inner and outer solutions at $\delta_{\mathrm{B}}$, as $\delta_{\mathrm{B}} \to \infty$, yields the unified evolution equation for the filament axis:

$$\boldsymbol{X}^\perp_t(s,t) = \frac{\varGamma\kappa}{4\pi}\left[\ln\left(\frac{L}{\delta_{\mathrm{B}}}\right) + C\right]\boldsymbol{b} + \boldsymbol{Q}^\perp, \tag{8.79a}$$

$$C(t) = -\frac{1}{2}\left[1 + \frac{4\pi}{\varGamma}\int_0^\infty \left(\frac{1}{\kappa}\zeta^{(1)}_{11} + \overline{r}\ln\overline{r}\zeta^{(0)}\right)\mathrm{d}\overline{r}\right], \tag{8.79b}$$

where $C(t)$ is called the *core-structure function*, depending on the axial-vorticity distribution. Note that (8.69) and (8.79) imply

$$\frac{1}{\delta s}\frac{\mathrm{D}\delta s}{\mathrm{D}t} = -\kappa \boldsymbol{n}\cdot\boldsymbol{Q}, \tag{8.80}$$

clearly indicating that *any filament stretching must be a nonlocal effect*. Its special form will be given in Sect. 8.2.3.

There remains solving $\zeta(\overline{r},\theta,s,t)$ from the viscous dynamic equation (8.74) in the inner region. In this region the temporal variation scales to the very short "turnover time" of $O(\delta^2/\Gamma)$, during which the core-flow can be assumed quasisteady. Corresponding to (8.71), the velocity is split to

$$\boldsymbol{u}(P,t) = \boldsymbol{X}_t + \boldsymbol{v}, \quad \boldsymbol{v} = u\boldsymbol{e}_r + v\boldsymbol{e}_\theta + w\boldsymbol{t}, \tag{8.81}$$

with $u = v = 0$ at $r = 0$. This condition ensures that the vortex axis is a material line. We then expand $\boldsymbol{v}$ as

$$\boldsymbol{v} = \delta^{-1}(v^{(0)}\boldsymbol{e}_\theta + w^{(0)}\boldsymbol{t}) + (u^{(1)}\boldsymbol{e}_r + v^{(1)}\boldsymbol{e}_\theta + w^{(1)}\boldsymbol{t}) + O(\delta), \tag{8.82}$$

where by assumption $v^{(0)}$ and $w^{(0)}$ are independent of $\theta$. Substitute (8.76) and (8.82) into (8.74), it is found that, due to the quasisteadiness,

$$\nabla\times(\boldsymbol{v}\times\boldsymbol{\omega})\cdot(1+O(\delta^2)) = \boldsymbol{0},$$

implying a self-balance of the vorticity advection and stretching/tilting. Thus, to the first two orders the core flow is generalized Beltramian and (8.74) can be linearized (cf. Sect. 6.5.1). It then turns out that the leading-order equations can be trivially satisfied by any axisymmetric core structure at a time instance; but they cannot evolve freely because the core structure should properly response the filament stretching and viscous diffusion. Before seeking this core evolution, we first reexpress (8.79b) by the leading-order axial and circumferential velocities. By (8.74) and using (6.2), the integrand in (8.79b) can be expressed in terms of leading-order circumferential and axial velocity. This casts (8.79b) to

$$C(t) = C_v(t) + C_w(t),$$

$$C_v(t) = \lim_{\overline{r}\to\infty}\left(\frac{4\pi^2}{\Gamma^2}\int_0^{\overline{r}} r' {v^{(0)}}^2\,\mathrm{d}r' - \ln\overline{r}\right) - \frac{1}{2}, \tag{8.83a}$$

$$C_w(t) = -\frac{8\pi^2}{\Gamma^2}\int_0^{\infty} r' {w^{(0)}}^2\,\mathrm{d}r'. \tag{8.83b}$$

This result was also first obtained by Callegari and Ting (1978).

Now, regarding to the evolution of the core-structure function $C(t)$, Klein and Ting (1995) have shown that its time rate can be expressed in terms of leading-order axial vorticity $\zeta$ and velocity $w$ (recall the remark following

(4.181); superscript (0) is omitted). Let $S(t)$ be the total length of the filament normalized by its initial value at $t = 0$, and introduce a dimensionless viscosity

$$\tilde{\nu} = \left(\frac{\nu}{\Gamma\delta^2}\right)^2 = \frac{1}{\delta^4 R_\Gamma^2} = O(1), \tag{8.84}$$

from (8.83) there is (dot denotes $\mathrm{d}/\mathrm{d}t$)

$$\dot{C}_v(t) = -\frac{8\pi^2\tilde{\nu}}{\Gamma^2}\int_0^\infty r'\zeta^2\,\mathrm{d}r' + \frac{\dot{S}}{2S}, \tag{8.85a}$$

$$\dot{C}_w(t) = \frac{16\pi^2}{\Gamma^2}\left(\tilde{\nu}\int_0^\infty r'w^2\,\mathrm{d}r' + \frac{3\dot{S}}{2S}\int_0^\infty r'w^2\,\mathrm{d}r'\right). \tag{8.85b}$$

Here, from the linearized version of (8.74) it follows that

$$w_t = \frac{\tilde{\nu}}{\overline{r}}(\overline{r}w_{\overline{r}})_{\overline{r}} + \frac{\overline{r}^3}{2}\frac{\dot{S}}{S}\left(\frac{w}{\overline{r}^2}\right)_{\overline{r}}, \tag{8.86a}$$

$$\zeta_t = \frac{\tilde{\nu}}{\overline{r}}(\overline{r}\zeta_{\overline{r}})_{\overline{r}} + \frac{\dot{S}}{S}\frac{\overline{r}^2\zeta_{\overline{r}}}{2\overline{r}}. \tag{8.86b}$$

Moreover, we apply the Lundgren transformation (6.32) to (8.85) but with different meaning for $S$, i.e., introduce stretched time (not to be confused with torsion) and radial variables

$$\tau \equiv \int_0^t S(t')\,\mathrm{d}t', \quad \rho \equiv S^{\frac{1}{2}}(t)\overline{r}. \tag{8.87}$$

Then, let $f_1 = S(t)w$, $f_2 = S(t)\zeta$, the two equations in (8.86) are both transformed to the two-dimensional axisymmetric heat equation, again the same form as (6.17a):

$$\frac{\partial f_\beta}{\partial\tau} - \frac{\tilde{\nu}}{\rho}\frac{\partial}{\partial\rho}\left(\rho\frac{\partial f_\beta}{\partial\rho}\right) = 0, \quad \beta = 1, 2,$$

which as we know from Sect. 6.2.1 has a family of time-decaying solutions in terms of the Laguerre polynomials, see (6.24). The series coefficients are determined by initial condition. It is not surprising that the simplest solution of this family is nothing but an extension of the Burgers vortex, which by the Ludgren transformation reduces to the Oseen vortex (Sect. 6.2.2). Note that in the Euler limit with $\tilde{\nu} \to 0$, (8.85) reduces to

$$C_v(t) = \frac{1}{2}\ln S(t) + C_v(0), \quad C_w(t) = S^{-3}(t)C_w(0). \tag{8.88}$$

### 8.2.3 Nonlocal Effects of Self-Stretch and Background Flow

It is well known that the vortex self-stretching as well as the stretching by background flow field is an extremely active mechanism in vortex dynamics at large Reynolds numbers (Sects. 3.5.3 and 6.5.3), in particular in the energy cascade process of turbulence. Without vortex-filament stretching, neither can one reveal the physics of kinks and folds during its evolution, nor the formation of hairpin vortices. In particular, numerical tests (e.g., Chorin 1982, 1994; Siggia 1985, see Fig. 3.15) have shown that a disturbance to a vortex filament, of wavelength $\lambda$ much shorter than the vortex-filament curvature radius but much larger than core radius $a$, often causes the appearance of folds and kinks, and hairpins. This observation suggested Klein and Majda (1991a,b) to introduce a disturbance of wavelength $\lambda = \epsilon R$ to a straight vortex filament, such that

$$1 \gg \epsilon \gg \delta \geq O(Re^{-1/2}). \tag{8.89}$$

This disturbance implies a rescaled length $\sigma = s/\epsilon$ and time $\tau = t/\epsilon^4$. Now, specifically, imposing such a disturbance to a straight vortex filament with fixed tangent vector $\boldsymbol{t}_0$ will lead to a disturbed position vector

$$\boldsymbol{X}(s,t,\epsilon) = \epsilon\sigma\boldsymbol{t}_0 + \epsilon^2\boldsymbol{X}^{(2)}(\sigma,\tau) + o(\epsilon^2) \tag{8.90}$$

for the filament axis, which has disturbed tangent vector and velocity

$$\boldsymbol{X}_s = \boldsymbol{t}_0 + \epsilon\boldsymbol{X}^{(2)}_\sigma + o(\epsilon), \quad \boldsymbol{X}_t = \epsilon^{-2}\boldsymbol{X}^{(2)}_\tau + o(\epsilon^{-2}).$$

Thus, the leading term of $\boldsymbol{X}_t$ due to the local induction is of $O(\epsilon^{-2})$, which by (8.79a) with $L/\delta_{\mathrm{B}}$ being set as $\epsilon/\delta$ implies the distinguished limit

$$\epsilon^2 = \frac{1}{\ln(\epsilon/\delta) + C}. \tag{8.91}$$

Here, as remarked before, the structure function $C$ can be considered constant over a stretched time period of $O(\tau)$. Therefore, normalize the velocity by $\Gamma/4\pi$, from (8.78) there is

$$\boldsymbol{X}_t = \epsilon^{-2}\kappa\boldsymbol{b} + \boldsymbol{Q}. \tag{8.92}$$

To compute the finite nonlocal effect $\boldsymbol{Q}$, denote the integrand of the line Biot–Savart formula (8.50) as

$$\boldsymbol{F}(s) = \frac{\boldsymbol{X}_0 - \boldsymbol{X}}{|\boldsymbol{X}_0 - \boldsymbol{X}|^3} \times \boldsymbol{t} = \boldsymbol{F}_1(s) + O(1) \quad \text{as} \quad s_0 - s \to 0,$$

where $\boldsymbol{X}$ is given by (8.90) and by (8.75)

$$\boldsymbol{F}_1(s) = \frac{\kappa \boldsymbol{b}}{2|s_0 - s|}$$

is the local-induction effect. Thus, the finite $\boldsymbol{Q}$ can be written as

$$\boldsymbol{Q} = \int [\boldsymbol{F}(s) - H(1 - \epsilon^{-1}|s_0 - s|)\boldsymbol{F}_1(s)]\,\mathrm{d}s,$$

where $H$ is the Heaviside step function. Substituting this into (8.92), Klein and Majda (1991a) obtain

$$\boldsymbol{X}_t = \kappa \boldsymbol{b} + \epsilon^2 I[\boldsymbol{X}^{(2)}] \times \boldsymbol{t}, \tag{8.93}$$

where $I[w]$ defines a linear *nonlocal operator* for any function $w(\sigma)$:

$$I[w](\sigma) \equiv \int_{-\infty}^{\infty} \frac{1}{|h|^3} \Big[ w(\sigma + h) - w(\sigma) - h w_\sigma(\sigma + h) + \frac{1}{2} h^2 H(1 - |h|) w_{\sigma\sigma}(\sigma) \Big]\,\mathrm{d}h. \tag{8.94}$$

This linear operator incorporates the leading-order nonlocal effect of the Biot–Savart integral (8.50) under the scale assumption (8.91).

Then, by extending the Hasimoto transformation (8.58) and (8.59) to include a nonlocal disturbance, the spatial curve $\boldsymbol{X}(s,t)$ can again be expressed by the filament function $\psi(s,t)$, of which the asymptotic equation reads

$$\frac{1}{\mathrm{i}} \psi_\tau = \psi_{\sigma\sigma} + \epsilon^2 \Big( \frac{1}{2} |\psi|^2 \psi - I[\psi] \Big). \tag{8.95}$$

This is a perturbed nonlinear Schrödinger equation. It is remarkable that the nonlocal but linear stretching $I[\psi]$ directly competes the local but nonlinear self-induction at the same order of magnitude. This apparent paradox is explained by a careful calculation using (8.80), which shows that the rate of self-stretching of a vortex-filament element is given by

$$\frac{1}{\delta s} \frac{\partial \delta s}{\partial t} = \frac{\epsilon^2}{4}\,\mathrm{i} \int_{-\infty}^{\infty} \frac{1}{|h|} \left[ \psi^*(\sigma + h)\psi(\sigma) - \psi(\sigma + h)\psi^*(\sigma) \right] \mathrm{d}h, \tag{8.96}$$

namely, the stretching rate is a quadratically nonlinear process. Thus, the nonlocal term $I[\psi]$ in (8.94) is essentially a nonlinear effect.

Klein and Knio (1995) and Klein et al. (1996) have used their theoretical results to propose some improvements of a numerical scheme for computing slender vortex filaments called *thin-tube method* (Knio and Ghoniem 1990). As a critical verification of both the asymptotic theory and the scheme, they compared the prediction of above asymptotic theory and the improved thin-tube method for some typical filament configurations and obtained convincing agreement for $\sigma$ as large as $1/2$. A further comparison of the predictions of the Hasimoto local-induction equation (8.61), the Callegari–Ting equation

(8.79) with $C(t)$ given by (8.83), and the Klein–Majda equation (8.93) for the sideband instability of Kelvin waves on a vortex filament has been conducted by Zhou (1997), which however indicates that all these approximations still cannot capture the behavior of turbulent vortices.

Klein and Majda (1993) further proceed to consider the effect of a nonuniform background flow field on the asymptotic evolution of a vortex filament. Introduce a small-amplitude disturbance wave to deform a straight vortex filament under the above-assumed conditions for asymptotic expansion, but now the evolution goes on under a background flow field

$$\delta \boldsymbol{v}_b = \frac{1}{\epsilon^2} \mathbf{A} \cdot \boldsymbol{x}, \tag{8.97}$$

where

$$\{A_{ij}\} = \begin{pmatrix} s_{11} & -\frac{1}{2}\omega + s_{12} & 0 \\ \frac{1}{2}\omega + s_{12} & s_{22} & 0 \\ 0 & 0 & s_{33} \end{pmatrix}$$

which satisfies the incompressibility condition

$$\operatorname{tr} A = s_{11} + s_{22} + s_{33} = 0. \tag{8.98}$$

Since $x_3$ is along the undisturbed vortex axis,

$$S_2 = \begin{pmatrix} s_{11} & s_{12} \\ s_{12} & s_{22} \end{pmatrix}$$

obviously represents the deformation matrix perpendicular to the undisturbed axis. By using the asymptotic expansion method, Klein and Majda (1993) generalize (8.95) to

$$\begin{aligned} \frac{1}{\mathrm{i}}\psi_\tau = \psi_{\sigma\sigma} &+ \epsilon^2 \left( \frac{1}{2}|\psi|^2\psi - I[\psi] \right) \\ &+ \epsilon^2 \left[ \omega\psi + \mathrm{i}s_{33} \left( \frac{2}{5}\psi + \sigma\psi_\sigma \right) + \left( s_{12} - \mathrm{i}\frac{s_{11} - s_{22}}{2} \right) \psi^* \right], \end{aligned} \tag{8.99}$$

in which the last part in the square bracket is the effect of background flow. The specific physical roles of its three terms are as follows:

- *The first term.* $\psi_\tau = \mathrm{i}\epsilon^2\omega\psi$, which is the rotation of the background flow around the vortex axis, corresponding to the rotation of $\psi$ on the complex plane with angular velocity $\epsilon^2\omega$.
- *The second term.* $\psi_\tau = -\epsilon^2 s_{33}(2\psi/5 + \sigma\psi_\sigma)$, which indicates that the growth or decay of the disturbance amplitude of the filament depends on the flow convergence or divergence in the normal plane and on the advection along the $x_3$ axis.

– *The third term.* $\psi_\tau = \mathrm{i}\epsilon^2 \left[s_{12} - \mathrm{i}(s_{11} - s_{22})/2\right] \psi^*$, which represents the effect of the planar strain $S_2$ normal to the filament axis. This term has both damping and growing solutions corresponding to the strain axis of the background flow field.

Having obtained the filament-evolution equation that contains self-stretching and hence is able to reveal the formation mechanism of kink, folds, and hairpins, we can now examine these phenomena frequently seen in experiments and numerical simulations. They are the result of nonlinear instability of vortex filaments, and actually the interaction between the nonlocal linear operator on the filament function and the local nonlinear term of the function in (8.95) and (8.99).

For example, consider a helical vortex filament which is a solution of (8.65). Introducing a small disturbance to this filament with $\epsilon^2 = 0.25$, and then conducting the numerical resolution of (8.95) under periodic spatial boundary condition for convenience, one obtains the time evolution of the filament curvature shown in Fig. 8.10. It is seen that as time goes on there appears a big curvature peak at a location of the filament, indicating the formation of a kink. The corresponding spatial curves are shown in Fig. 8.11. Therefore, *the formation of the kink is precisely the interaction between the linear operator reflecting the nonlocal stretching and the local nonlinear term reflecting the self-induction.*

Similarly, the formation of hairpin structure is due to the interaction between the background flow field and self-induction as well as self-stretching. Consider a simple case with a constant strain field $\gamma$ perpendicular to the vortex axis. Then (8.99) is reduced to

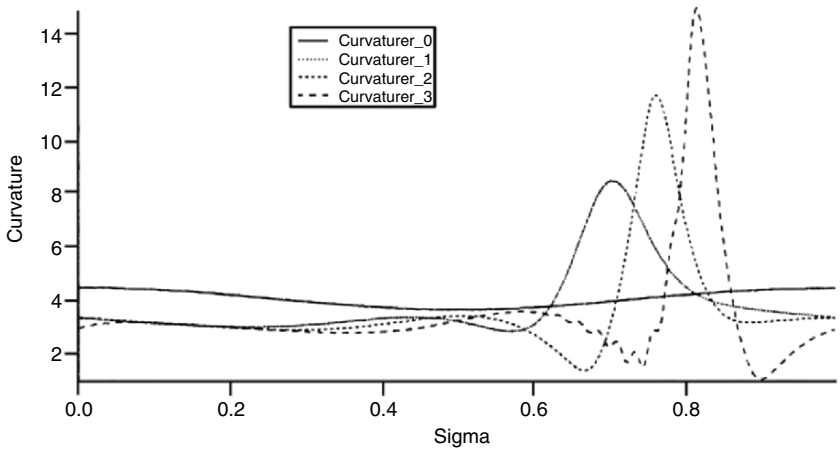


**Fig. 8.10.** Time series of curvature distribution for perturbation of a helical vortex filament. From Klein and Majda (1991a)

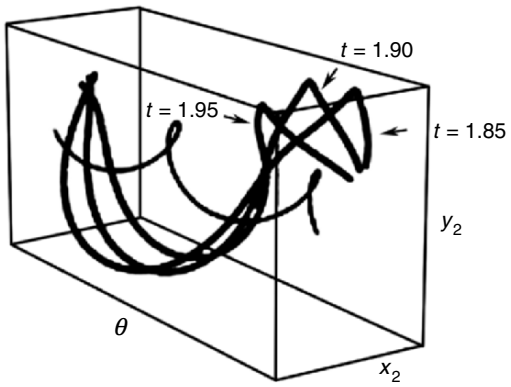


**Fig. 8.11.** Time evolution of the vortex filament. From Klein and Majda (1991a)

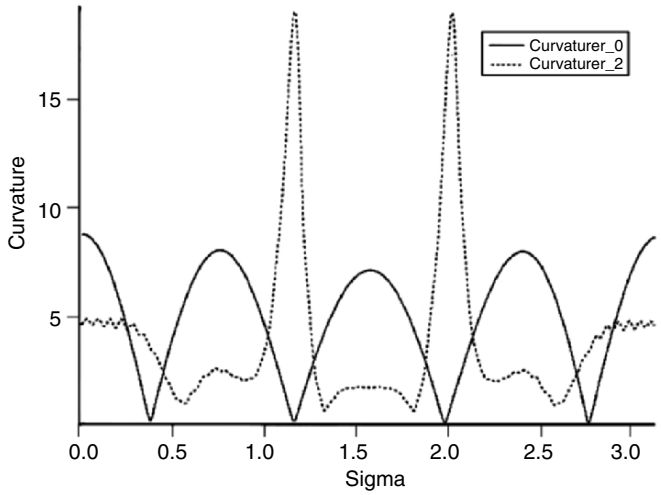


**Fig. 8.12.** The curvature distribution at different times for a vortex filament under the effect of the background flow field. From Klein et al. (1992)

$$\frac{1}{\mathrm{i}}\psi_\tau = \psi_{\sigma\sigma} + \epsilon^2\Big(\frac{1}{2}|\psi|^2\psi - I[\psi] - \mathrm{i}\gamma\psi^*\Big). \tag{8.100}$$

Assuming spatial periodicity and taking $\gamma = 2$, $\epsilon^2 = 0.25$, the numerical solution of (8.100) yields the time-evolution of the filament curvature shown in Fig. 8.12, in which two local peaks appear at the late stage of the evolution. Since each curvature peak represents a kink, two peaks are necessary for producing a hairpin-like vortex filament. Indeed, the hairpin can be clearly seen in the time-evolution of the spatial curve shown in Fig. 8.13.

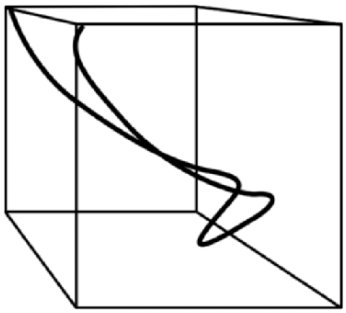

**Fig. 8.13.** The hairpin creation. From Klein et al. (1992)

## 8.3 Motion and Interaction of Multiple Vortices

The motion and interaction of a multiple-vortex system are far more complicated than the motion and self-interaction of an isolated vortex. To such a system the role of theoretical analyses is quite limited. So far a complete theory exists only for two-dimensional point-vortex system, which is to be introduced in Sect. 8.3.1. The problem becomes more difficult once a finite core is introduced to each vortex, and simplified approach is available for two-dimensional vortex-patch system only, with uniform vorticity distribution in the cores; yet the final resolution of a specific problem still has to rely on numerical computation, see Sect. 8.3.2. The viscous interactions of three-dimensional vortices, in general, have to be understood by experiments and numerical computations, of which a typical example will be discussed in Sect. 8.3.3.

### 8.3.1 Two-Dimensional Point-Vortex System

We consider a system of infinitely long and parallel straight line vortices in an irrotational flow. In this model the vortex tilting and stretching are all omitted, so that it can be treated as a point-vortex system on a two-dimensional cross plane. While the theoretical foundation and classic applications of such a system are already well known, they have attracted renewed interest. This is because, on the one hand, the discrete vortex method for solving two-dimensional Euler equation in computational fluid dynamics is precisely based on the dynamics of point-vortex systems, and on the other hand some remarkable new phenomena stemming from computations have motivated deeper explorations of the dynamic behavior of the systems, in particular the chaotic property of a set of point vortices as a Hamiltonian system. People have also attempted to find new clues to the understanding of turbulence from the study

of point-vortex systems. In fact, the extensive study of point-vortex systems provides an ideal entry into the field of the nonlinear dynamics (see Newton 2001).

A point-vortex system consists of $N$ point vortices of circulations $\gamma_k$ located at $z_k = x_k + \mathrm{i}y_k, (k = 1, 2, \ldots, N)$, with singular vorticity field

$$\omega = \sum_{k=1}^{N} \gamma_k \delta(z - z_k), \tag{8.101}$$

and associated complex velocity potential

$$\chi(z) = \frac{1}{2\pi \mathrm{i}} \sum_{k=1}^{N} \gamma_k \ln(z - z_k). \tag{8.102}$$

For a free point-vortex system, which experiences no external force and in which each vortex moves under the induction of others, the governing equations follow from (3.34):

$$\frac{\mathrm{d}}{\mathrm{d}t} z_m(t) = -\mathrm{i} \sum_{n=1}^{N}{}' \frac{\gamma_n}{z_m - z_n}, \tag{8.103}$$

where the notation $\sum'$ implies excluding $m = n$ during summation. Equation (8.103) can also be derived by using asymptotic expansion as the high-Reynolds-number limit of the two-dimensional Navier–Stokes solution (see Ting and Klein 1991). If there is an irrotational background flow, its complex velocity potential can be added to (8.102).

The Hamiltonian of the point-vortex system is defined as

$$H = \sum_{m \neq n}^{N} \gamma_m \gamma_n \ln r_{mn}, \tag{8.104}$$

where

$$\sum_{m \neq n}^{N} = \sum_{m=1}^{N} \sum_{n=1}^{N}{}', \quad r_{mn} = |z_m - z_n| = \sqrt{(x_m - x_n)^2 + (y_m - y_n)^2}.$$

By (8.104) there is

$$\frac{\partial H}{\partial z_m} = \frac{\gamma_m}{2} \sum_{n=1}^{N}{}' \frac{\gamma_m}{(z_m - z_n)}.$$

Hence, the motion equation (8.103) of the system can be cast to

$$\gamma_m \frac{\mathrm{d}z_m}{\mathrm{d}t} = -2\mathrm{i} \frac{\partial H}{\partial z_m}, \tag{8.105}$$

of which the splitting of real and imaginary parts leads to Hamilton's canonical equations

$$\gamma_m \frac{\mathrm{d}x_m}{\mathrm{d}t} = -\frac{\partial H}{\partial y_m}, \tag{8.106a}$$

$$\gamma_m \frac{\mathrm{d}y_m}{\mathrm{d}t} = \frac{\partial H}{\partial x_m}. \tag{8.106b}$$

Here, $\gamma_m x_m, \gamma_m y_m$ correspond to the generalized momentum and coordinates, respectively, in Hamilton's equations for particle dynamics (e.g., Lanczos 1970). This Hamiltonian structure of point-vortex systems is revealed by Kirchhoff and Poincare more than a century ago, indicating that a series of methods and results of classic particle dynamics can well be applied to the dynamics of point-vortex system.

The Hamiltonian $H$ is the interaction energy of the vortex system. By the Noether theorem (e.g., Arnold 1989), several invariants of the system can be deduced from the symmetry of a Hamiltonian system. Because the Hamiltonian depends only on the relative locations of the vortices, $H$ must be invariant during the translation and rotation of the entire system. The translational invariance implies

$$I = Q + \mathrm{i}P = \sum_{m=1}^{N} \gamma_m z_m = \text{const.}, \tag{8.107}$$

where $Q$ and $P$ are the impulses along the $x$- and $y$-direction. On the other hand, the rotational invariance implies

$$L = \sum_{m=1}^{N} \gamma_m (x_m^2 + y_m^2) = \text{const.}, \tag{8.108}$$

where the conserved quantity $L$ is the angular impulse. $I$ and $L$ are, respectively, the counterparts of the impulse (3.78) and angular impulse (3.79) defined for a continuously distributed vorticity field, the latter are also invariant for circulation-preserving flow (see the remark at the end of Sect. 3.6.1).

Now, assume that the distances among the vortices are uniformly changed by a factor $\lambda$, i.e., $r'_{mn} = \lambda r_{mn}$, $\lambda = 1 + \delta\lambda$, where $\delta\lambda$ is small, so that

$$\delta x_m = x_m \delta\lambda, \quad \delta y_m = y_m \delta\lambda,$$

then

$$\delta H = \sum_{m\neq n}^{N} \gamma_m \gamma_n (\ln \lambda r_{mn} - \ln r_{mn}) = \sum_{m\neq n}^{N} \gamma_m \gamma_n \ln(1+\delta\lambda) = \delta\lambda \sum_{m\neq n}^{N} \gamma_m \gamma_n.$$

On the other hand, we have

$$\delta H = \sum_{m=1}^{N} \frac{\partial H}{\partial x_m}\delta x_m + \frac{\partial H}{\partial y_m}\delta y_m = \delta\lambda \sum_{m=1}^{N} \left( \gamma_m x_m \frac{\mathrm{d}y_m}{\mathrm{d}t} - \gamma_m y_m \frac{\mathrm{d}x_m}{\mathrm{d}t} \right).$$

Thus,

$$\sum_{m\neq n}^{N}\gamma_m\gamma_n=\sum\left(\gamma_m x_m\frac{\mathrm{d}y_m}{\mathrm{d}t}-\gamma_m y_m\frac{\mathrm{d}x_m}{\mathrm{d}t}\right)=\text{const.} \tag{8.109}$$

indicating the conservation of the angular momentum of the system respect to the origin.

Finally, for the time rate of the Hamiltonian there is

$$\begin{aligned}\frac{\mathrm{d}H}{\mathrm{d}t}&=\sum_{m=1}^{N}\left(\frac{\partial H}{\partial x_m}\frac{\mathrm{d}x_m}{\mathrm{d}t}+\frac{\partial H}{\partial y_m}\frac{\mathrm{d}y_m}{\mathrm{d}t}\right)\\&=\sum_{m=1}^{N}\left(\gamma_m\frac{\mathrm{d}y_m}{\mathrm{d}t}\frac{\mathrm{d}x_m}{\mathrm{d}t}-\gamma_m\frac{\mathrm{d}x_m}{\mathrm{d}t}\frac{\mathrm{d}y_m}{\mathrm{d}t}\right)=0.\end{aligned} \tag{8.110}$$

Namely, the Hamiltonian itself is also an invariant.

If we introduce the *canonical Poisson bracket* (Lanczos 1970)

$$\{f,g\}\equiv\sum_{m=1}^{N}\frac{1}{\gamma_m}\left(\frac{\partial f}{\partial x_m}\frac{\partial g}{\partial y_m}-\frac{\partial f}{\partial y_m}\frac{\partial g}{\partial x_m}\right), \tag{8.111}$$

then it easily follows three involutive conservation relations:

$$\{H,L\}=0, \tag{8.112}$$

$$\left\{H,P^2+Q^2\right\}=0, \tag{8.113}$$

$$\left\{P^2+Q^2,L\right\}=0. \tag{8.114}$$

Meanwhile, we have the following useful relations:

$$\{Q,P\}=\Gamma, \tag{8.115}$$

$$\{Q,L\}=2P, \tag{8.116}$$

$$\{P,L\}=-2Q, \tag{8.117}$$

where $\Gamma=\sum_{m=1}^{N}\gamma_m$.

Now, an important observation is that, by the theory of Hamiltonian systems of finite degrees of freedom, it can be shown that there exists a critical number $N_\mathrm{c}$ of the point vortices, such that the motion of the system is integrable when $N\leq N_\mathrm{c}$, but not integrable when $N>N_\mathrm{c}$ (for the definition of integrability see Sect. 3.3.1). It is surprising that the value of $N_\mathrm{c}$ for point-vortex systems is very small, depending on the existence of solid boundary and background potential-flow field. For unbounded fluid there is $N_\mathrm{c}=3$. A four-vortex system will also be integrable if its total circulation is zero. $N_\mathrm{c}$ decreases once there appears solid boundary or background flow. It is now known that in a half-plane domain or inside a circular boundary we have

$N_c = 2$, while for a general boundary we simply have $N_c = 1$. For example, Hasimoto (1985) has computed the motion of two point vortices of equal strength $\gamma_1 = -\gamma_2 = 1$ in a semicircular domain. The initial locations of the vortices were

$$z_1 = \mathrm{i}(\sqrt{17} - 4)^{1/4}\, \mathrm{e}^{\mathrm{i}\pi/4}, \quad z_2 = r_2\, \mathrm{e}^{3\mathrm{i}\pi/4},$$

where $r_2$ was given different values. The result is shown in Fig. 8.14. We see that a small change of the vortex locations and their distances from the boundary makes the system's motion vary from double periodic to chaotic, and then back to double periodic. A slight difference of the initial locations implies a significant difference in the system's evolution. This fact confirms that the two-vortex system in a semicircular domain is not integrable, i.e., $N_c = 1$.

Another example is four point vortices in an unbounded fluid. When the initial locations have central symmetry ($z_1 = -z_2, z_3 = -z_4$), the motion is periodic as seen from Fig. 8.15a, but if the initial locations differ slightly from the above symmetric configuration chaos appears at once, see Fig. 8.15b. This confirms $N_c = 3$ for unbounded fluid.

The preceding observation has a deep impact on one's understanding of the formation mechanism of turbulence. Actually, a point-vortex system with $N > N_c$ may be viewed as a highly simplified model for turbulence, of which the description inevitably requires the introduction of statistic approach; for details see the review of Aref (1983).

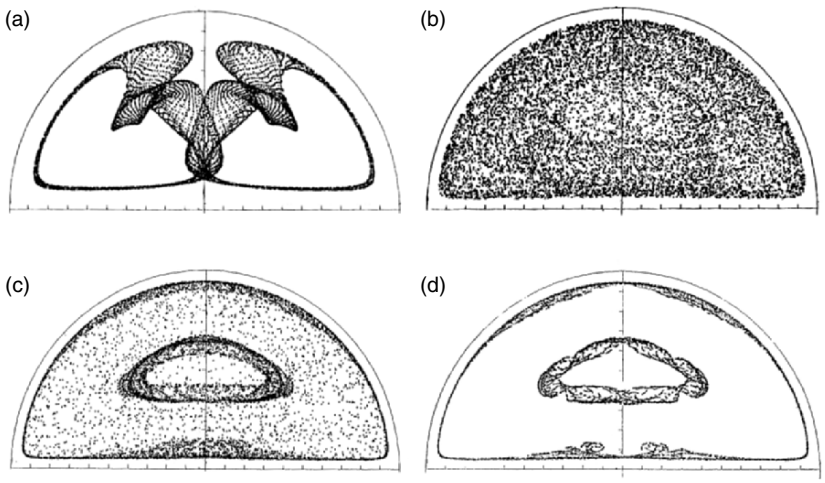


**Fig. 8.14.** The motion of two point vortices in a semicircular domain. The initial locations $z_1$ and $z_2$ have only one parameter $r_2$, which in (**a**–**d**) takes 0.18, 0.10, 0.0817, 0.0815, respectively. From Hasimoto (1985)

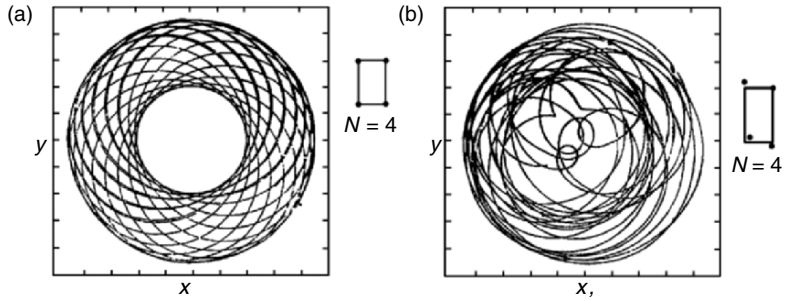


**Fig. 8.15.** The motion of four point vortices in unbounded fluid. From Aref and Pomphrey (1982)

In addition to the integrability and chaos, the evolution of the relative locations $r_{ij} = |z_i - z_j|$ of point vortices is also of interest (Novikov 1975). From (8.104), (8.106a), and (8.106b) one may derive the evolution equation of $r_{ij}$:

$$\frac{\mathrm{d}}{\mathrm{d}t} r_{ij}^2 = \frac{2}{\pi} \sum_{k \neq i,j}^{N} \gamma_k \epsilon_{ijk} A_{ijk} \left( \frac{1}{r_{jk}^2} - \frac{1}{r_{ki}^2} \right), \tag{8.118}$$

where $A_{ijk}$ is the area of the triangle formed by three vortices at $z_i, z_j, z_k$, and $\epsilon_{ijk}$ is the Kronecker symbol: if $z_i, z_j, z_k$ is ordered clockwise then $\epsilon_{ijk} = 1$, otherwise it is $-1$. Unless the three vortices are on a straight line, (8.118) provides a closed set of equations for the evolution of $r_{ij}$, which has only two motion integrals given by $r_{ij}$, i.e., $H$ itself, and

$$\frac{1}{2} \sum_{i,j} \gamma_i \gamma_j r_{ij}^2 = \left( \sum \gamma_i \right) I - (P^2 + Q^2). \tag{8.119}$$

By (8.118), it is evident that the three-vortex system is of fundamental significance: The sum of the distance variation of each three-vortex system constitutes the distance variation of the entire vortex system. Therefore, the interaction of the whole point-vortex system can be decomposed into a set of interactions of three-vortex systems. If the distances between point vortices are taken as the motion scales in the fluid, then the three-vortex interaction is the lowest-order dynamic process in which new length and time scales are produced. Then, since three-vortex systems are integrable, a general nonintegrable vortex system ($N > 3$) can be considered the dynamic interaction of integrable triads. This view means that the three-vortex problem is the basis of understanding two-dimensional point-vortex systems. For further analysis see Newton (2001).

For a three-vortex system, (8.118) becomes

$$\frac{\mathrm{d}}{\mathrm{d}t} r_{ij}^2 = \frac{2}{\pi} \gamma_k A \left( \frac{1}{r_{jk}^2} - \frac{1}{r_{ki}^2} \right), \tag{8.120}$$

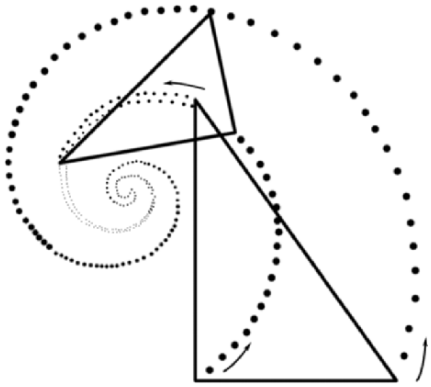

**Fig. 8.16.** The point-vortex collapse. From Marchioro and Pulivirenti (1984)

while (8.119) reduces to

$$\gamma_1\gamma_2 r_{12}^2 + \gamma_2\gamma_3 r_{23}^2 + \gamma_1\gamma_3 r_{13}^2 = \text{const.} \tag{8.121}$$

In particular, when $\gamma_1\gamma_2+\gamma_2\gamma_3+\gamma_1\gamma_3 = 0$, the triangle formed by the vortices may remain as a similarity triangle, which shrinks or enlarge monotonically. In the former case, the three vortices merge to a point in a finite time, called the *point-vortex collapse*. For example, let $\gamma_1 = \gamma_2 = 2$ and $\gamma_3 = -1$, and at $t = 0$ there is $z_1 = (-1, 0), z_2 = (1, 0), z_3 = (1, \sqrt{2})$, then (8.120) becomes

$$\frac{\mathrm{d}}{\mathrm{d}t} r_{ij}^2(t) = -\frac{2}{3\sqrt{2}\pi} r_{ij}^2(0),$$

so that

$$r_{ij}(t) = r_{ij}(0)\sqrt{1 - \frac{t}{3\sqrt{2}\pi}}. \tag{8.122}$$

Hence, $r_{ij} = 0$ at $t = 3\sqrt{2}\pi$. The triangles at $t = 1$ and 20 are plotted in Fig. 8.16.

### 8.3.2 Vortex Patches

A natural extension of two-dimensional point-vortex system is to consider a system of two-dimensional vortices, each now having a finite area with uniformly distributed vorticity called a *vortex patch*. The simplest vortex patch is the Rankine vortex, next to which is the Kirchhoff elliptical vortex (Sect. 6.4.1). The vortex-patch model provides a convenient mathematic means for the studies of the motion and interaction of finite-core vortices, since as shown by the *contour dynamics* proposed by Zabusky et al. (1979), the time evolution of the interaction of vorticity field can be reduced to that

of the boundaries of the patches, so that the original two-dimensional problem is reduced to the motion of one-dimensional curves. The velocity of a system of $N$ vortex patches is the superposition of the velocities induced by all vortex patches; but the evolution and interaction of the system are more complicated than point-vortex system. Although the area of a vortex patch is conserved, its boundary may deform dramatically. The contour-dynamics method has been applied extensively to the studies of two-dimensional vortex motions at large Reynolds numbers, especially the evolution and interaction of vortex cores, such as the dynamic mechanisms in the initial formation of coherent vortical structures in mixing layers, jets, and wakes, as well as the geophysical fluid dynamics relevant to the motion of atmosphere and ocean. For reviews see Dritschel (1989) and Pullin (1992).

Consider a two-dimensional system of $N$ vortex patches, where a typical patch has vorticity $\omega_i$, area $A_i$, and contour $C_i$. By (2.104b), for $N$ vortex patches we have

$$\psi(\boldsymbol{x}) = -\sum_{i=1}^{N} \omega_i \int_{A_i} G(\boldsymbol{x}, \boldsymbol{x}') \, \mathrm{d}S', \quad G = \frac{1}{2\pi} \ln r, \quad r = |\boldsymbol{x} - \boldsymbol{x}'|, \tag{8.123}$$

Thus, in terms of complex variable,

$$u + \mathrm{i}v = -\mathrm{i}(\psi_{,x} + \mathrm{i}\psi_{,y}) = \mathrm{i} \sum_{i=1}^{N} \omega_i \int_{A_i} (G_{,x} + \mathrm{i}G_{,y}) \, \mathrm{d}S,$$

by using the complex-variable form (A.32) of the Stokes theorem, there is

$$u + \mathrm{i}v = -\sum_{i=1}^{N} \omega_i \oint_{C_i} G \, \mathrm{d}z.$$

Multiplying both sides by $\boldsymbol{e}_x$, noticing $\mathrm{i}\boldsymbol{e}_x = \boldsymbol{e}_y$, $\boldsymbol{e}_x \, \mathrm{d}z = \mathrm{d}\boldsymbol{x}$ (see Sect. A.2.4), and $\mathrm{d}\boldsymbol{x} = \boldsymbol{t} \, \mathrm{d}s$, where $\boldsymbol{t}$ is the unit tangent vector of $C_i$ and $\mathrm{d}s$ the arclength, it follows at once that

$$\boldsymbol{u} = \frac{1}{2\pi} \sum_{i=1}^{N} \omega_i \oint_{C_i} \ln |\boldsymbol{x} - \boldsymbol{x}'| \boldsymbol{t} \, \mathrm{d}s. \tag{8.124}$$

We follow the Lagrangian evolution of the patches. In terms of complex variable $z = x + \mathrm{i}y$, if at $t = 0$ the contours of the patches have material arc element $\mathrm{d}s$, then (8.124) reads

$$\frac{\mathrm{d}z}{\mathrm{d}t}(\alpha, t) = \frac{1}{2\pi} \sum_{i=1}^{N} \omega_i \oint \ln |z(\alpha, t) - z(\alpha', t)| \frac{\partial z}{\partial s}(\alpha', t) \, \mathrm{d}s, \tag{8.125a}$$

$$z(\alpha, 0) = z_0(\alpha), \tag{8.125b}$$

$$C_i(t) = z(\alpha), \quad \alpha \in C_{i0}. \tag{8.125c}$$

This set of equations describes the time evolution of the contour $C_i$, which is similar to the Birkhoff–Rott equation (4.143) for the self-induced motion of a vortex sheet. Both are self-deforming curve equations for the position $z$ of the curve by use of a Lagrangian parameterization. However, they have a fundamental difference: while the Birkhoff–Rott equation is ill-posed, the contour-dynamics equation is not.

One of the basic applications of contour dynamics is the evolution of an isolated vortex core. For a circular Rankine vortex, it is found that, under a disturbance $\exp(\mathrm{i}(n\theta - \sigma t))$ with $n$ being the circumferential wave number, the patch can still rotate at constant angular velocity. But when $\sigma = 0$ the circular patch may bifurcate to $n$-fold symmetric noncircular equilibria (e.g., Batchelor 1967). The case with $n = 2$ is the Kirchhoff elliptic vortex, which has highly robust structure. We have seen that even in a constant strain field the patch can remain to be elliptic. Numerical computations have indicated that this evolution trend happens under quite wide initial conditions. This is why the elliptic vortex-patch model may simulate more accurately the evolution of a two-dimensional inviscid vorticity field than circular vortices. But the computation of Deem and Zabusky (1978) has shown that in addition to elliptic patches, there also exist vortex patches of three, four, and five edges rotating with constant angular velocity, known as the V-states equilibria of the patches (Fig. 8.17).

By using the contour dynamics and numerical computation, Saffman and Szeto (1981) and Pierrehumbert and Widnall (1981) have studied the motion of a single row of identical elliptic vortex patches of circulation $\Gamma$, area $A$, and separation $L$. The motion depends on parameter $\alpha = A/L^2$. Smaller $\alpha$ implies smaller and nearly circular patches, and at larger $\alpha$ we have more elliptic ones. Under the assumption that the patches have elliptical symmetry, it has been found that solutions exist for $\alpha < 0.2377$ only, see Fig. 8.18. This value of $\alpha$ is a fold or limit point but not the critical value at which patches

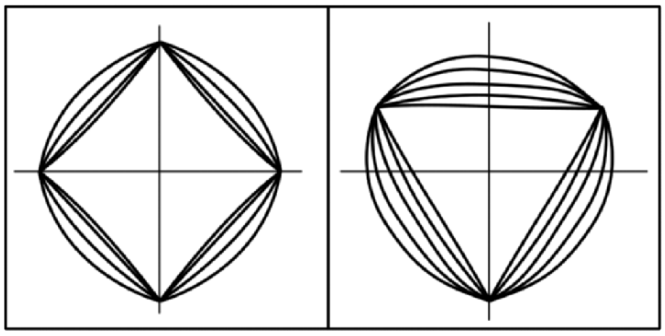

**Fig. 8.17.** Vortex patches rotating with constant angular velocity. From Deem and Zabusky (1978)

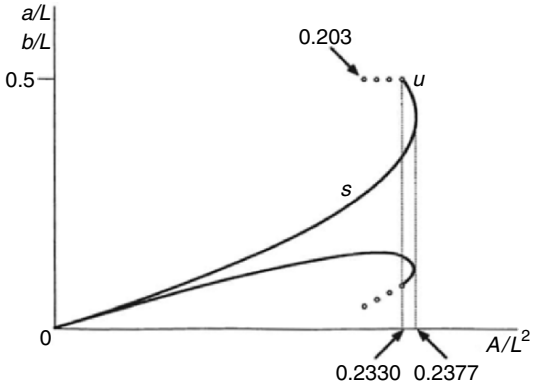


**Fig. 8.18.** The motion property of a single vortex-patch row. *Dotted line* is the family of connected vortices. From Saffman (1992)

touch. The appearance of the fold point implies the existence of neighboring solutions of the same area, due to the transition from stability to instability (Saffman 1992). On the other hand, when the system reaches the critical value $\alpha = 0.2330$, the patches evolve continuously to a family of connected vortices or finite-amplitude waves on a vortex layer of finite thickness.

Although the stability of vortical flows is the subject of Chap. 9, we briefly mention here the stability of single and double vortex-patch rows with respect to two-dimensional disturbance. This has been discussed by Meiron et al. (1984; see Saffman (1992)) using normal-mode analysis (see Sect. 9.1) and *Floquet theory*. Let the $x$-periodic streamfunction $\psi_0$ of the basic patch-row flow be disturbed to

$$\psi(x, y, t) = \psi_0(x, y) + \epsilon \mathrm{e}^{\sigma t}\psi(x, y)\mathrm{e}^{\mathrm{i}px(2\pi/L)}, \quad \epsilon \ll 1. \tag{8.126}$$

Here, $\psi(x, y)$ is the eigenfunction and $\sigma = \sigma_r + \mathrm{i}\sigma_i$ the eigenvalue, with $\sigma_r$ being the disturbance growth rate. The wave number $p$ is an arbitrary real number. When $p = 0$ or is any integer, the disturbance wave has the same wavelength as the undisturbed vortex-patch row, and is said to be superharmonic. If $0 < p < 1$, the disturbance is called subharmonic. In particular, for vortices with small area, the most unstable disturbance happens when $p = 1/2$. In this case every second vortex deforms in the same way, so the disturbance wavelength is $2L$, which is called *pairing instability*. The instability property of single-row of vortex patches under subharmonic disturbances is shown in Fig. 8.19 for four values of $\alpha$. When $p = 1/2$, the disturbance propagation speed is zero, so the pairing instability is stationary. Note that when $\alpha = 0.235$, superharmonic disturbance ($p = 0$, $p = 1$) is also unstable.

The same method has been applied to the stability of the Kármán vortex street of finite-area vortex patches (Meiron et al. 1984), focusing on the

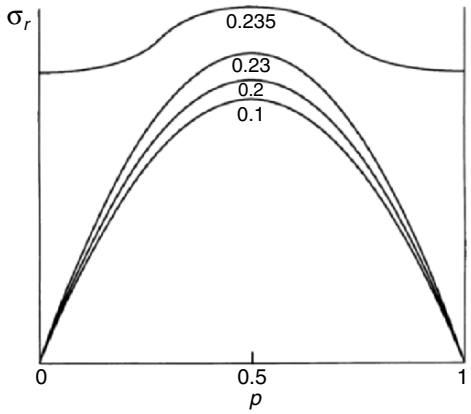


**Fig. 8.19.** The growth rate of subharmonic disturbances for single rows of vortex patches. From Saffman (1992)

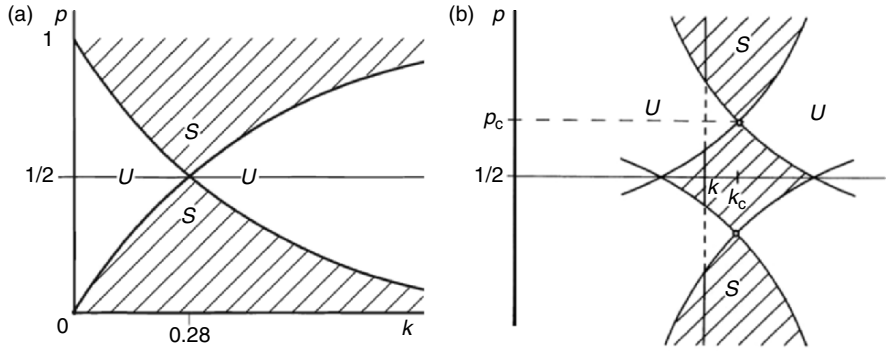


**Fig. 8.20.** Stability boundaries for Kármán vortex street consisting of point vortices (**a**), and finite-core vortex patches (**b**). Regions marked by $S$ and $U$ are stable (*hatched*) and unstable, respectively. Unless going through crosses at specific $k_c$, *vertical lines* for any $k$ will always meet unstable region(s). Based on Saffman (1992)

influence of finite patch area on the stability character of the street. Let $k = H/L$ be the aspect ratio of the street and $p$ the wavenumber as above, the numerically obtained stability boundaries on the $(k, p)$-plane are shown in Fig. 8.20b. As comparison, also shown in the Fig. 8.20a is the corresponding stability boundaries of the classic point-vortex street (Sect. 6.3.3). For the latter, except the single cross at $(k_c, p) = (0.28055, 0.5)$, for any aspect ratio $k$ there exists certain range of $p$ with growing disturbances, and hence the street is linearly unstable as mentioned in Sect. 6.4.3. For the former, the conclusion remains qualitatively the same. There appear a pair of crosses $(k_c, p_c)$ with their location depending on the patch area $A$, such that except these crosses

one can always find some range of $p$ with unstable modes. Jiménez (1988) has shown analytically that for finite-core patches the new crosses appear at

$$k_c = 0.28055 + 0.55536A^2 + O(A^4),$$
$$p_c = 0.5 \pm 4.63089A^2 + O(A^4).$$

While not all wavenumbers are unstable, only one unstable wavenumber suffices for the flow to be unstable. Therefore, except $k_c$, in both point-vortex and finite-patch models there are always unstable wavenumbers, and hence the flow is unstable. In other words, *finite core neither stabilizes nor destabilizes the vortex street* (MacKay and Meiss 1987; Jiménez 1988).

In the study of vortex-core evolution by using contour dynamics, it is natural to ask whether there exists an asymptotic equilibrium state for an isolated inviscid vortex core with continuous or piecewise continuous initial vorticity distribution. Melander et al. (1987) proposed that the axisymmetrinization should be a general equilibration principle. But a counterexample has been given by Dritschel (1989), see Fig. 8.21, where an elliptic vortex patch with continuous vorticity distribution finally evolves to an elliptic vortex core with surrounding complicated filament debris.

Our main concern here is the evolution of multiple vortex patches. The simplest multiple-patch system is a vortex pair, of which the nonlinear evolution is shown in Fig. 8.22 computed by contour dynamics for four initial separations at $t = 0$. Clearly, between two corotating vortices there exists a critical separation, below which the vortices will "merge." So the result can be viewed as a numerical experiment on vortex merging. Relevant theory has pointed out that, depending on the initial separation, the vortex–pair

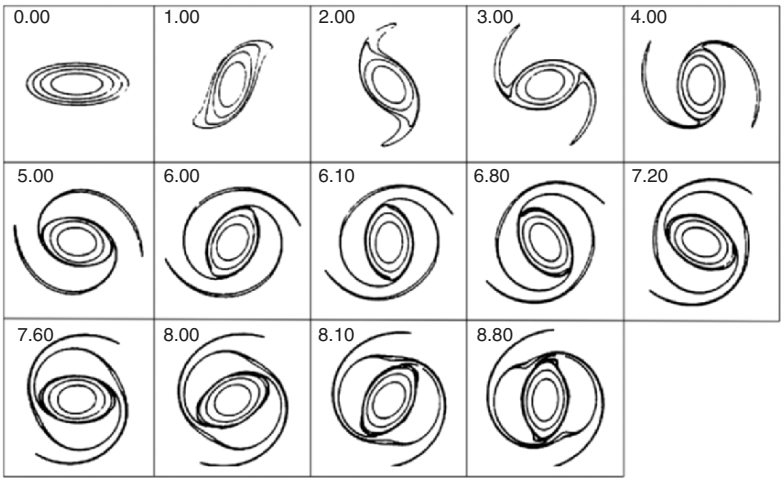


**Fig. 8.21.** The evolution of an elliptical distribution of vorticity computed with contour dynamics. From Dritschel (1989)

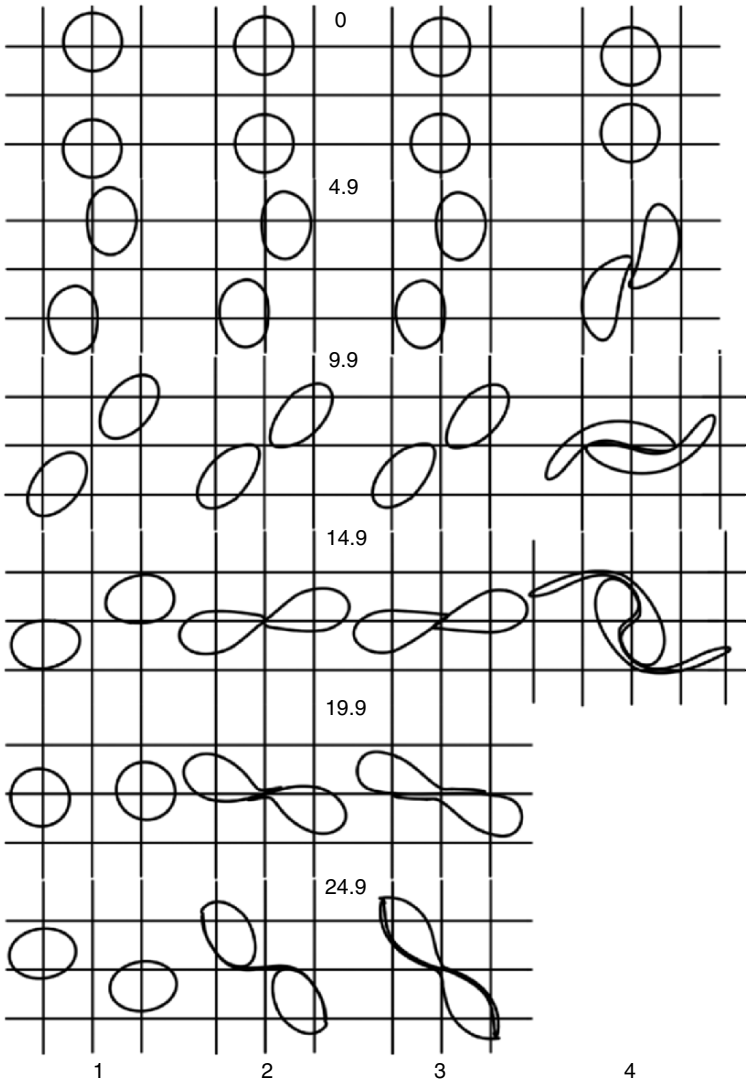


**Fig. 8.22.** Interaction of a vortex pair. From Zabusky et al. (1979)

interaction may evolve to "merging" (also known as centroid collapse), corotation without merging, nutation, etc. It should be stressed that, however, the word "merge" here means only the deformation of the pair. The contour dynamics applies only to two-dimensional inviscid flow, so during such an evolution the topological feature of vortex patches cannot change. The interaction can only deform the patches but not really make them merge or reconnect.

### 8.3.3 Vortex Reconnection

We conclude our discussion on vortex interactions by introducing the viscosity. Perhaps the most important viscous vortex interaction is the *cut-and-reconnect* process (reconnection for short), which alters the topological structure of the vorticity field. Vortex reconnection involves many phenomena of fundamental significance in vortex dynamics, such as vortex stability, dynamics of helicity, selective dissipation in fluid of small viscosity, and the possible generation of singularity in the vorticity field. The study of vortex reconnection is of particular importance in understanding the evolution of vortical structures in turbulence.

One's attention to vortex reconnection started from the late-stage evolution of the Crow instability (Crow 1970b) of wingtip vortices, since then there have appeared many systematic experimental, theoretical, and numerical studies. The focus of experiments has been on the simplest case, i.e., the collision of two circular vortex rings (Fohl and Turner 1975; Oshima and Asaka 1977; Schatzle 1987; Oshima and Izutsu 1988). Hussain and Husain (1989) have also studied the self-collision and reconnection of an elliptic vortex ring which is deformed by its own induction. Progress has also been made by numerical simulation, e.g., the interactions of two vorticity tubes (Zabusky et al. 1991; Boratav et al. 1992; Shell et al. 1993), two circular vortex rings (Kida and Takaoka 1991a; Aref and Zawadzki 1990), and two elliptic vortex rings (Aref and Zawadzki 1991). Based on their experimental observations, Lee and Fu (2001) have proposed that the cut-and-reconnect of near-wall vortex structures is a universal process in transitional and turbulent boundary layers. The very high resolution in numerical visualization has considerably enhanced our understanding of the cut-and-reconnect process. For review of this subject see Kida and Takaoka (1994).

As discussed in Sect. 6.6, so far a general and rigorous definition of a vortex is still unavailable, which direct results in the lack of a commonly agreed clear definition of vortex reconnection, as well as the lack of the consensus on relevant physical mechanisms. In experiments, one usually identifies a vortex reconnection by the topological change of dye or smoke structures, which however constitute a scalar field (the density of the medium) that may have very different behavior from the vorticity field. On the other hand, in numerical simulation one usually identifies a vortex reconnection by the topological change of isosurface of vorticity magnitude, which as noted in Sect. 6.6 may differ significantly from the vorticity surfaces that consist of vorticity lines and form vorticity tubes but on which the vorticity magnitude varies in general. Therefore, one has to make distinction among *scalar reconnection*, *isovorticity reconnection*, and *vorticity-tube reconnection*, which are referred to the topological-structure variations of the isoscalar surfaces, isosurface of vorticity magnitude, and vorticity tube, respectively. It is well known that Helmholtz's vorticity theorems imply that in an inviscid and incompressible

fluid it is impossible to have vorticity-tube reconnection, but it is possible for scalar and isovorticity reconnections.

We now look at the process and main mechanisms during vorticity-tube reconnection. Consider two parallel vorticity tubes with opposite-signed vorticity, which approach each other under mutual induction. As they get closer, they will deform to a "head–tail" shape (Fig. 8.23a). Then, the viscosity enters into the play to cancel opposite-signed vorticity (Fig. 8.23b), which changes the topology of the tubes (Fig. 8.23c). However, the detailed reconnection process is much richer than viscous cancellation alone. The key mechanism is called *bridging*, which involves complicated interactions such as the stretching, self-induction, and viscous diffusion of the vorticity lines. Referred to Fig. 8.24a, after the viscous dissipation cancels the closest vorticity lines of opposite signs in the interaction zone, the remaining vorticity lines are connected with their counterparts in the other tube which, due to the diffusion and self-induction, will retreat (Fig. 8.24b). Thus, the flow on the crossplane behaves like a doublet. The doublet induces an advection normal to the plane of Fig. 8.24, causing a vorticity-line stretching and rotation around the doublet. This process results in a crosslinking of the interacting vorticity lines. As the process continues, the vorticity is accumulated and a "bridge" is formed. During the bridging new vorticity normal to the original interaction plane is

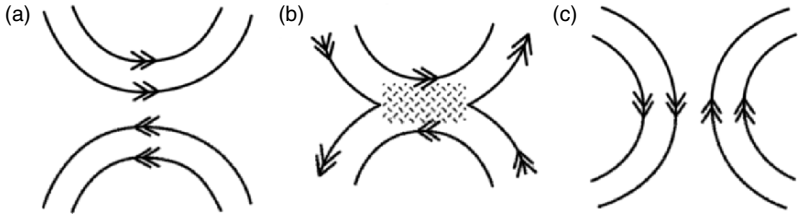


**Fig. 8.23.** Sketch of vortex reconnection: viscous cancellation. Based on Kida and Takaoka (1994)

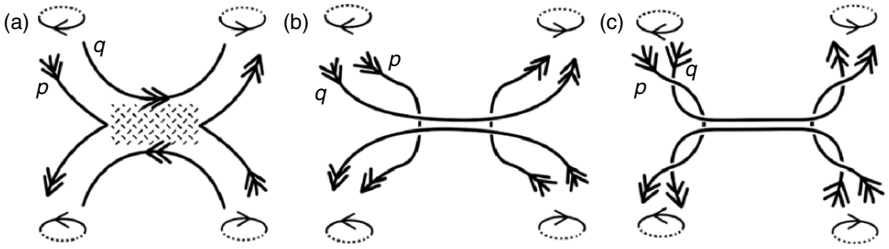


**Fig. 8.24.** Sketch of vortex reconnection: bridging process. Based on Kida and Takaoka (1994)

also formed, which has even stronger intensity than the original one owing to the stretching. The global topological structure of the vorticity tubes is thereby altered.

The detailed structural evolution during the bridging process can be revealed by direct numerical simulation. Figure 8.25 exhibits such a structure during the reconnection of a trifold vorticity tube (Kida and Takaoka 1991b), where the drawn isosurface of vorticity magnitude is taken as 10% of the maximum value. The formation of the bridge is clearly seen, near which the vorticity lines are pulled out of the main tube at the bridge as a hairpin vortex.

Owing to the key role of the viscosity, the above vortex reconnection process is not circulation preserving. Thus, the change of topology and that of helicity, see (3.75) and (3.115), no longer have a one-to-one correspondence. On the left-hand side of (3.75) there is not only the winding number $\alpha_{ij}$ but also circulations $\kappa_i$ and $\kappa_j$ which are now time dependent due to diffusion. Hence, the change of one of the three: topology, circulation, and helicity, may or may not cause the change of the other two. Moreover, the reconnection is a local process that cannot be fully reflected by integral relations of the type of (3.75). Therefore, for viscous flow the helicity is not a good indicator of reconnection.

Nevertheless, it is of interest to look at the variation of helicity due to viscosity. In an unbounded domain, the rate of change of helicity is given by the general formula (3.115). Now by (4.15) and Green's identity

$$\int \boldsymbol{u} \cdot \nabla^2 \boldsymbol{\omega} \, \mathrm{d}V = \int \boldsymbol{\omega} \cdot \nabla^2 \boldsymbol{u} \, \mathrm{d}v = - \int (\nabla \times \boldsymbol{\omega}) \cdot \boldsymbol{\omega} \, \mathrm{d}V,$$

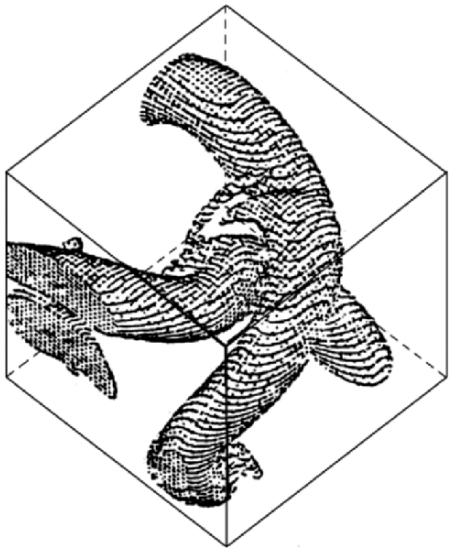

**Fig. 8.25.** Numerical simulation of the bridging process of a trifold vorticity tube. Adapted from Kida and Takaoka (1994)

(3.115) yields

$$\frac{\mathrm{d}}{\mathrm{d}t}\int(\nabla\times\boldsymbol{u})\cdot\boldsymbol{u}\,\mathrm{d}V=-2\nu\int(\nabla\times\boldsymbol{\omega})\cdot\boldsymbol{\omega}\,\mathrm{d}V. \tag{8.127}$$

Therefore, the integrand on the right is of exactly the same form as that on the left, with $\boldsymbol{u}$ being replaced by $\boldsymbol{\omega}$. One may call $(\nabla\times\boldsymbol{\omega})\cdot\boldsymbol{\omega}$ the *vorticity helicity density* and its integral the *vorticity helicity*. For the helicity density we may use the intrinsic coordinates along a streamline, see (3.2) and (3.3), such that $\boldsymbol{\omega}\cdot\boldsymbol{u}=\xi q^2$; while for the vorticity helicity density we use the intrinsic coordinates along a *vorticity line* and denoting $\boldsymbol{\omega}=\boldsymbol{t}_\omega\omega$ such that

$$(\nabla\times\boldsymbol{\omega})\cdot\boldsymbol{\omega}=\zeta\omega^2, \tag{8.128}$$

with $\zeta\equiv\boldsymbol{t}_\omega\cdot(\nabla\times\boldsymbol{t}_\omega)$ being the *torsion of neighboring vorticity lines*. Then (8.127) is cast to a neat form

$$\frac{\mathrm{d}}{\mathrm{d}t}\int\xi q^2\,\mathrm{d}V=-2\nu\int\zeta\omega^2\,\mathrm{d}V. \tag{8.129}$$

Moreover, corresponding to (3.52) there is

$$|\nabla\times\boldsymbol{\omega}|^2=\zeta^2\omega^2+|(\nabla\times\boldsymbol{\omega})\times\boldsymbol{t}_\omega|,$$

and the vorticity field will be Beltramian if the "vorticity Lamb vector" $(\nabla\times\boldsymbol{\omega})\times\boldsymbol{\omega}$ vanishes. Therefore, (8.127) indicates that the strongest change of helicity density happens at places where the viscous vorticity field is locally Beltramian. Note however not all Beltrami vorticity field has this function. An exception is *Trkalian flows*, which is a Beltrami flow with constant $\xi$, so that $\zeta=\xi$. Then (8.129) degenerates to the balance of the rate of change of total kinetic energy and dissipation, losing any relevance to the helicity. But for a linear combination of Trkalian flows with each constituent having its own $\xi$, such as the ABC flow met in Sect. 3.3.1, (8.129) is not trivial. Kida and Takaoka (1991b) have shown that the helicity of the viscous ABC flow decreases in time due to the diffusion, while no reconnection occurs.

## 8.4 Vortex–Boundary Interactions

The interaction of vortices and boundaries is a very wide subject. The boundary can be a rigid or flexible wall, and an interface of two fluids or a free surface. A clear understanding of the interaction mechanisms and, whenever possible, imposing proper control of the interactions, are extremely important at both fundamental and applied levels.

Depending on the specific vortex and boundary, the relative scale of the vortex and body, the interaction orientation, etc., as well as other flow parameters and boundary geometry, there can be a huge variety of interaction

patterns, impossible to be examined in a section. However, a vortex–boundary interaction problem can always be decomposed into several more primary physical processes, of which most have been or to be addressed in this book: the vorticity generation from boundaries (Sect. 4.1), interaction-caused boundary motion and deformation (Sects. 4.3.2 and 4.4.4), as well as unsteady boundary-layer separation (Sect. 5.4), the rolling-up and evolution of separated vortex layer (Sects. 4.4, 7.3, 7.4, and 8.1), vertical-flow instability and vortex breakdown (Chap. 9), and the interaction-caused aerodynamic force and moment on the body surface (Chap. 11). In a broad sense, vortex-boundary interactions also include the formation of near-wall vortical structures in wall-bounded turbulence (Chap. 10) and their reaction to the wall. Besides, vortex-induced structure vibration should be within one's concern as well, but is beyond the scope of this book. A good knowledge of these primary physical processes certainly makes it easier to understand various complicated composite interactions encountered in practice. Therefore, in this section we only discuss a few typical examples. For further materials the reader is referred to the reviews of Doligalski et al. (1994) and Rockwell (1998).

### 8.4.1 Interaction of Vortex with a Body

The examples of vortex–solid wall interactions to be discussed here are: the interactions between an isolated vortex and a solid wall parallel or perpendicular to the vortex axis, and the rebound of vortices from a solid boundary.

First, consider the interaction of an isolated straight vortex and a parallel wall. When the vortex scale is much smaller than the body scale, at the simplest approximation level the problem can be modeled by a two-dimensional point vortex of circulation $\Gamma$ above an infinitely extended flat wall at hight $a$, with a uniform oncoming flow $U_0$. The Reynolds number is defined as $Re = \Gamma/2\pi\nu$. To satisfy the no-through condition, we introduce an image vortex below the wall, which induces a velocity $V = \Gamma/4\pi a$ at the real vortex. Thus, the net advection speed is

$$V_\mathrm{c} = U_0 - \frac{\Gamma}{4\pi a}, \tag{8.130}$$

which suggests introducing an advection rate

$$\alpha = \frac{V_\mathrm{c}}{U_0} = 1 - \frac{\Gamma}{4\pi a U_0} \tag{8.131}$$

depending on the strength and height of the vortex. A smaller $\alpha$ implies a stronger vortex–wall interaction.

At low Reynolds numbers, the influence of the vortex–wall interaction on the surrounding flow is quite weak. In contrast, when $Re$ is large, the interaction can trigger a series of complex responses in the nearby boundary layer. The vortex induces a reversed flow and an adverse pressure gradient

in a local region inside the boundary layer. The fluid elements in this region are compressed along the streamwise direction, associated with a local vorticity concentration. Consequently, a thin fluid layer is quickly squeezed up from the interior of the boundary layer, moving through the strong vorticity-gradient layer near the wall and suddenly erupting into the external flow. This is precisely an unsteady boundary-layer separation process addressed in Sect. 6.4.2 in terms of the Lagrangian description. The separated shear layer carries strong vorticity, often rolls into vortices, and produces a strong interference to the external flow.

The above interaction process has been confirmed by theoretical analysis and numerical simulation. The process is hard to be studied experimentally, because the unsteady boundary-layer separation develops rapidly at very small spatial scales. But various experiments have verified the late-stage evolution of the boundary-layer separation, namely the suddenly erupted thin fluid layer has very strong vorticity and quickly rolls into new vortices, known as *secondary separated vortices*. An instantaneous streamline pattern of vortex–wall interaction obtained by the numerical simulation of Peridier et al. (1991) is shown in Fig. 8.26. The primary vortex is centered right above $x = 0$ (beyond the figure) and rotates in counterclockwise direction, while the secondary vortex rotates in clockwise direction. On the left of the secondary vortex we see the converging of streamlines that leads to a spike of the boundary-layer displacement thickness.

Not only the boundary-layer behavior is altered by the vortex–wall interaction, but also the motion of the primary vortex can be significantly changed by the formation of secondary vortex in a complicated manner. A typical example is the rebound of a vortex pair or vortex ring from the wall. We consider the vortex pair rebound phenomenon from a surface. A pair of inviscid vortices of

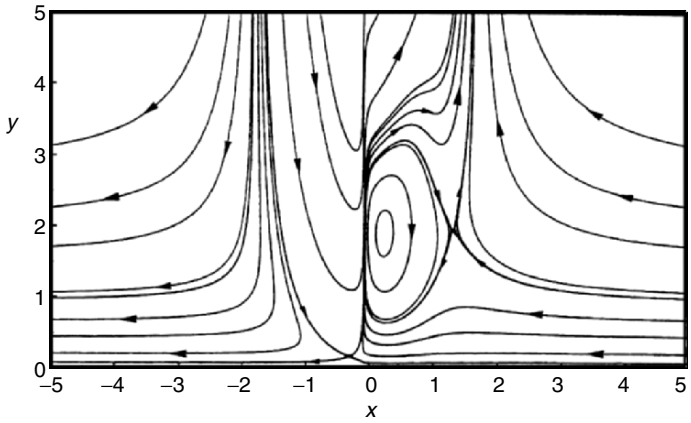


**Fig. 8.26.** Instantaneous streamlines in the boundary layer at $t = 0.75$ showing a secondary vortex. From Peridier et al. (1991)

equal and opposite circulation at the same height above a flat boundary, either a solid wall or a free surface, may approach the boundary under their mutual induction. In this process the vortices will separate from each other and never rebound from the boundary (Lamb 1932; Saffman 1979, 1991). The observed vortex pair rebounding from a ground has been attributed to the viscous separation induced by the vortex pair and the formation of secondary vortices (Harvey and Perry 1971; Peace and Riley 1983; Orlandi 1990). Figure 8.27, from the direct numerical simulation of Orlandi (1990), clearly explains the entire interaction process.

We focus on the left part of the vortex pair, which has $\omega < 0$ and induces a strong vortex layer on the wall with $\omega > 0$. The action of the primary vortex makes the layer sheds out of the wall and then rolls into a secondary vortex, which has a strong core and is connected to the near-wall shear layer by a

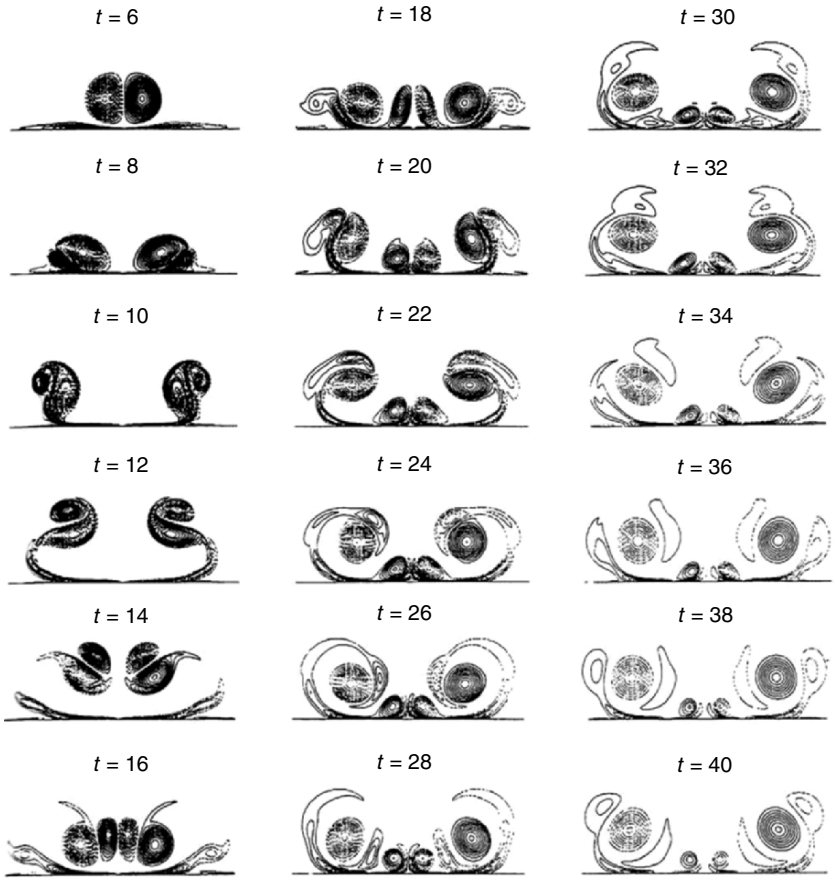


**Fig. 8.27.** Vortex dipole rebound from a wall. The contour plots of vorticity at $Re = 800$. From Orlandi (1990)

feeding sheet. Note that the secondary vortex also induces a weak tertiary vortex. The upward motion of the secondary vortex just blocks the trend of the primary vortex to move outward parallel to the wall (see the plot at $t = 10$). Consequently, the primary and secondary vortices form a vortex couple, whose interaction results in an upward motion away from the wall ($t = 12$). This is the rebounding. In this newly formed vortex couple the circulation of the primary vortex is larger, and hence the couple follows a circular trajectory bending toward the primary vortex ($t = 14$). Consequently, the couple turns toward the wall again, causing another rebounding. Theoretically, this rebounding process may repeat many times, but due to the viscous dissipation the vortex couple eventually becomes a circular vortex rotating around its center.

Similar phenomena can be observed in the interaction of a vortex ring and a solid wall parallel to the ring plane. The vortex ring induces unsteady boundary-layer separation followed by the eruption of the secondary vortex ring, and then the appearance of even a series of rings. It is worth noticing that the circulation of the secondary ring can be comparable with that of the primary one; thus, their interaction may alter the latter to a significant extent.

A more complicated vortex–wall interaction happens when the vortex axis is normal rather than parallel to the wall. The primary importance of this vertical interaction lies in the fact that it is the simplest fluid dynamics model for understanding the mechanisms involved in meteorological tornados. However, even such an apparently simple model has already contained complicated fluid dynamic mechanisms, of which a complete knowledge is not yet available. We have briefly encountered this problem in Sect. 6.2.3 on conical similarity vortex solutions, where we saw the nonexistence of steady and regular conical similarity solution satisfying both no-slip condition on the wall and the regularity condition at the vortex axis. The interaction of a tornado-like vortex with the ground is far more complicated than any similarity solutions can simulate. The vertical interaction of a vortex and a no-slip wall has been studied by many investigators, both experimentally and numerically (Maxiworthy 1982; Lewellen 1993; Arrese and Fernandez-Feria 1996; Lewellen and Lewellen 1997; Nolan and Farrell 1999b; Hirsa et al. 2000).

Hirsa et al. (2000) have conducted experimental and numerical simulations of the early stage of the vertical interaction of a columnar vortex and a no-slip wall at low Reynolds numbers. The experiment was carried out in a water tank which produced a Burgers vortex, and in the numerical simulation the unsteady Navier–Stokes equation was solved in order to capture the rich mechanisms during the interaction evolves as time. In the computation the experimentally produced Burgers vortex was used. Both experiment and computation did show strong unsteadiness of the flow in the early stage of this vertical interaction. The key character of the flow field is a spatially oscillating boundary-layer structure of the Bödewadt type near the vortex core.[2] Typical numerical results of this oscillating structure are shown in Fig. 8.28.

[2] On Bödewadt-type boundary layer see Bödewadt (1940) and Lugt (1996).

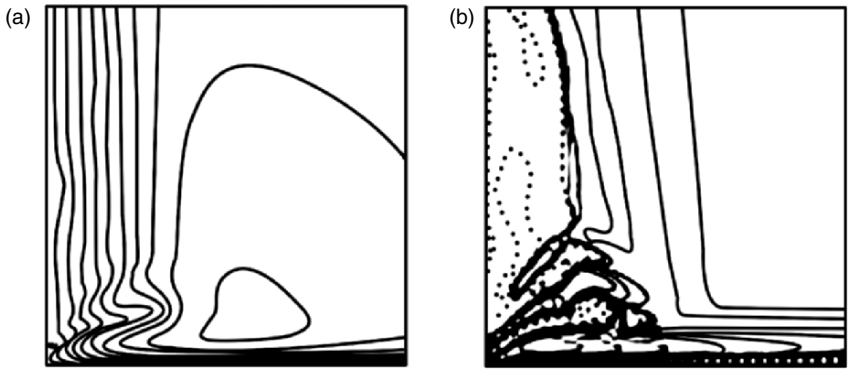


**Fig. 8.28.** Interactions of a laminar vortex with the ground. (**a**) Contour of $\Gamma$ for $Re = 125$ at time $t = 20$. (**b**) Contour of the azimuthal vorticity $\eta$. From Hirsa et al. (2000)

In Fig. 8.28a are the isocirculation lines (which are actually vorticity lines in a meridian plane), of which the spatial oscillation is obvious. Figure 8.28b plots the contours of azimuthal vorticity $\eta$ on the meridian plane. The basic physical mechanism behind the figures is as follows.

Due to the induction of the secondary flow in the interaction zone, adjacent to the wall there appears a strong inflow from the boundary layer at large radius, which forms a very thin shear layer (a vortex layer) with azimuthal vorticity right above the wall. Initially, this thin layer cannot be easily identified, but the inward radial flow has to turn up near $r = 0$ and then becomes an outward radial flow. The advective velocity makes the near-wall vorticity lines tilt away from the wall and form a new shear layer, in which the azimuthal vorticity is of opposite sign to that in the primary wall layer. The new layer moves outward and leads to the formation of the third shear layer with different signed azimuthal vorticity and inward radial velocity. It is this mechanism of the formation of shear layers with alternative signed azimuthal vorticity and radial velocity that forms the spatially oscillating boundary-layer structure. But, as the distance from the wall increases, the amplitude and strength of azimuthal vorticity are decaying due to viscosity. Besides, the shear layers may roll up at their edges to form the toroidal vortex structure. This is the most significant property in the effusive corner region of the vertical vortex–wall interaction. Note that the large toroidal vortex structure does not develop from the columnar vortex itself as in the case of vortex breakdown (Sect. 9.4). Rather, it comes from the spatially oscillating boundary layer.

The preceding examples have demonstrated the great complexity of the vortex–wall interactions, yet they are confined to two-dimensional and axisymmetric flows. In a fully three-dimensional interaction the situation is further complicated, including the change of the flow topology. As an illustration of three-dimensional vortex–body interactions, Fig. 8.29 sketches a complex vortex system observed in a jet in crossflow (Shi et al. 1991). The jet is issued

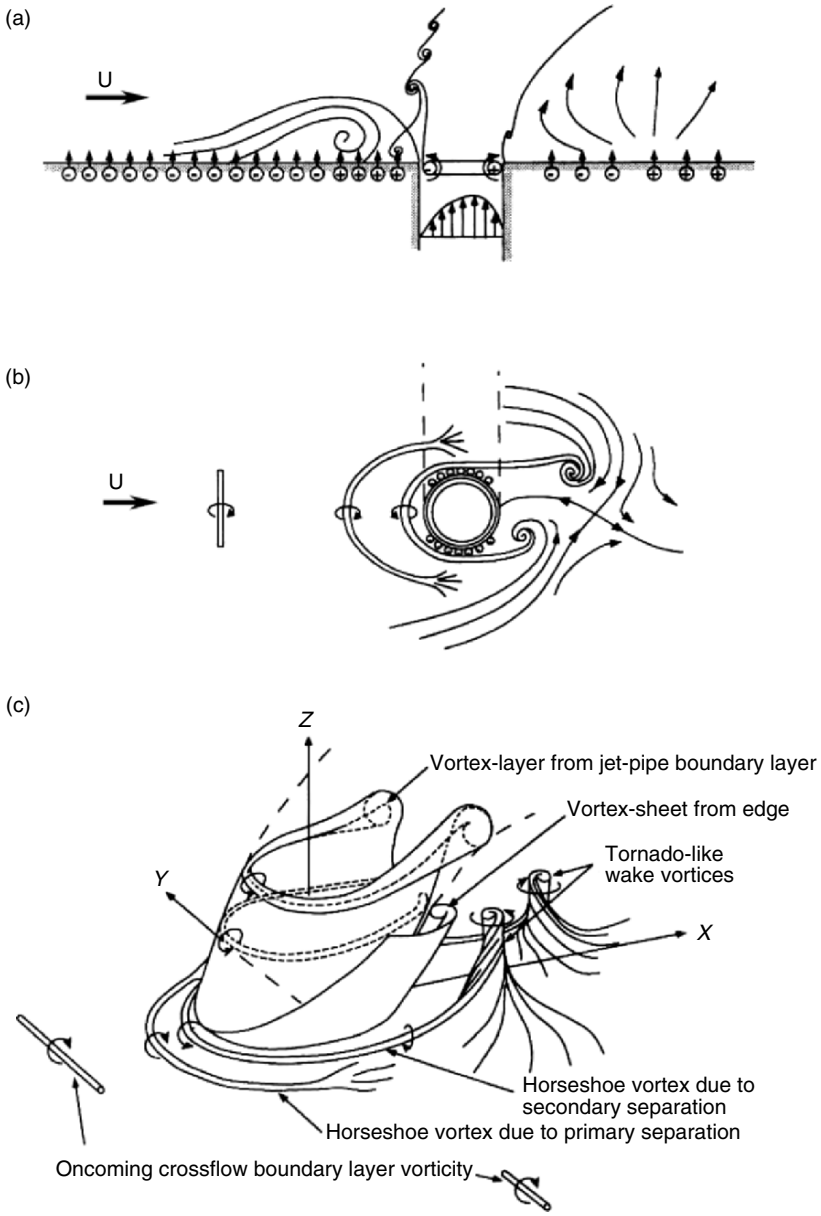


**Fig. 8.29.** The near-field vortex system in jet in crossflow. Sketched based on an experiment: (**a**) the side view (central plane), (**b**) the top view, (**c**) a perspective view. From Shi et al. (1991)

normally out of an orifice of a flat plate and interacts with the oncoming boundary-layer flow. The flow is incompressible, so the vorticity of this vortex system is created entirely from the solid surface, including the flat plate, the inner wall of orifice, and their juncture. From the figure we first see the vorticity in the attached boundary layer (on the left). Approaching the jet, an adverse pressure gradient causes the boundary layer to separate and form a horseshoe vortex. The separated flow reattaches in front of the jet and there is a secondary separation and another horseshoe vortex.

Similarly, inside the jet pipe the vorticity in the pipe shear flow eventually leaves the orifice and becomes a free vortex layer. Then, because along the side edge of the orifice $\boldsymbol{\tau}_w = \mu \boldsymbol{n} \times \boldsymbol{\omega}$ has a nonzero component and the wall curvature is very large, a pair of weak vortex layers is formed near the edge by the mechanism of $\boldsymbol{\sigma}_{\text{vis}}$ defined by (4.25), which is experimentally distinguishable from the orifice vortex layer. Finally, as the horseshoe vortices are advected downstream of the jet, some horn vortices appeared. These microtornados are somewhat similar to the Kármán vortices. However, the fundamental difference is that, unlike a solid cylinder, no new vorticity can be created from the jet plume boundary, as stressed by Shi et al. (1991).

### 8.4.2 Interaction of Vortex with Fluid Interface

As another type of vortex–boundary interaction, the interaction of vortices and a free surface is again a very complicated nonlinear and unsteady process involving vortex–vortex and vortex–wave interactions. Understanding this type of interactions has profound theoretical value and important applications.

In Sect. 8.4.1 we discussed the rebounding of a vortex pair from a solid wall. Whether or not a viscous vortex pair rebounds from a free surface is a more delicate problem. The experiment of Baker and Crow (1977) and low-Reynolds-number computation of Peace and Riley (1983) intended to support the rebounding phenomenon, but Orlandi (1990) and Tryggvason et al. (1992) showed numerically that, on a flat, "free-slip" (in fact, shear-free) surface the rebound does not occur at high Reynolds numbers. Tryggvason et al. have attributed the previously observed rebounding to the effect of surface contamination. However, it seems that most of these discussions can be settled by the simple analysis of Saffman (1991), who provides a mathematic proof that on a flat free surface the vorticity centroid does not approach the surface monotonically. We now present Saffman's analysis.

Assume the vortex pair initially moves down toward a flat free surface $y = 0$, with the vorticity antisymmetric about $x = 0$. By (4.105), there is $\omega = 0$ at $y = 0$. Let

$$\Gamma = \int_0^\infty \int_0^\infty \omega \, \mathrm{d}x \, \mathrm{d}y > 0, \quad \bar{y} = \frac{1}{\Gamma} \int_0^\infty \int_0^\infty \omega y \, \mathrm{d}x \, \mathrm{d}y > 0$$

be the total strength and the height of the centroid of the vorticity in the first quadrant, respectively. The boundary conditions are

$$u = 0, \quad \omega = 0, \quad \text{on } x = 0, \tag{8.132a}$$

$$v = 0, \quad \omega = 0, \quad \text{on } y = 0. \tag{8.132b}$$

Note that no free-slip condition is imposed. The vanishing vorticity on the free surface is a direct consequence of (4.104b) on a flat and stationary free surface.

Introduce the horizontal component of the impulse in the first quadrant

$$I_x = \Gamma \bar{y} = \int_0^\infty \int_0^\infty \omega y \, \mathrm{d}x \, \mathrm{d}y. \tag{8.133}$$

Differentiate this and using the vorticity transport equation

$$\frac{\partial \omega}{\partial t} = -u \frac{\partial \omega}{\partial x} - v \frac{\partial \omega}{\partial y} + \nu \nabla^2 \omega,$$

it follows that

$$\begin{aligned} \Gamma \frac{\mathrm{d}\bar{y}}{\mathrm{d}t} + \bar{y} \frac{\mathrm{d}\Gamma}{\mathrm{d}t} &= \iint \left[ -y \left( u \frac{\partial \omega}{\partial x} + v \frac{\partial \omega}{\partial y} \right) + \nu y \nabla^2 \omega \right] \mathrm{d}x \, \mathrm{d}y \\ &= \iint \left( v\omega + \nu y \frac{\partial^2 \omega}{\partial x^2} + \nu y \frac{\partial^2 \omega}{\partial y^2} \right) \mathrm{d}x \, \mathrm{d}y. \end{aligned} \tag{8.134}$$

Let us calculate each terms on the right-hand side of (8.134) by using the boundary condition (8.132). The first term yields

$$\iint v\omega \, \mathrm{d}x \, \mathrm{d}y = -\frac{1}{2} \int_0^\infty v_0^2 \, \mathrm{d}x \, \mathrm{d}y,$$

where $v_0 = v(0, y)$, while the second term is

$$\iint \nu y \frac{\partial^2 \omega}{\partial x^2} \, \mathrm{d}x \, \mathrm{d}y = -\nu \int_0^\infty y \frac{\partial \omega}{\partial x} \Big|_{x=0} \mathrm{d}y < 0,$$

where use has been made of the fact that, due to the vorticity diffusion, at $x = 0$ and $y > 0$ there must be $\partial \omega / \partial x > 0$. Then the third term yields

$$\iint \nu y \frac{\partial^2 \omega}{\partial y^2} \, \mathrm{d}x \, \mathrm{d}y = -\nu \iint \left[ \frac{\partial}{\partial y} \left( y \frac{\partial \omega}{\partial y} \right) - \frac{\partial \omega}{\partial y} \right] \mathrm{d}x \, \mathrm{d}y = 0.$$

Thus, we obtain

$$\frac{\mathrm{d}}{\mathrm{d}t} (\Gamma \bar{y}) = -\frac{1}{2} \int_0^\infty \left( v^2 + 2\nu y \frac{\partial \omega}{\partial x} \right) \Big|_{x=0} \mathrm{d}y < 0. \tag{8.135}$$

But, since

$$\frac{\mathrm{d}\Gamma}{\mathrm{d}t} = -\nu \int_0^\infty \left.\frac{\partial \omega}{\partial x}\right|_{x=0} \mathrm{d}y - \nu \int_0^\infty \left.\frac{\partial \omega}{\partial y}\right|_{y=0} \mathrm{d}x < 0, \tag{8.136}$$

there is no reason to infer from (8.135) the conclusion that $\mathrm{d}\bar{y}/\mathrm{d}t < 0$, i.e., to assume the vorticity centroid $\bar{y}$ should decrease monotonically.

Apply an analysis similar to the derivation of (8.135), we also obtain

$$\frac{\mathrm{d}}{\mathrm{d}t}(\Gamma \bar{x}) = \frac{1}{2} \int_0^\infty \left( u^2 + 2\nu x \frac{\partial \omega}{\partial y} \right) \Big|_{y=0} \mathrm{d}x > 0. \tag{8.137}$$

Then, as Saffman argued, as $t \to \infty$, (8.137) indicates that the vorticity moves asymptotically away from $x = 0$ and hence the right-hand side of (8.135) will tend to zero. Therefore, there is

$$\Gamma \bar{y} \sim \text{const. as } t \to \infty.$$

Thus, along with (8.136), we see that a continuous vorticity reduction due to dissipation leads to an increase of $\bar{y}$, implying a rebound in a way which will depend upon the value of viscosity and the initial distribution of vorticity.

While the above discussion is limited to highly idealized simple circumstances, we now turn to some more complex interaction of vortices with a free surface, focusing on the vorticity generation from the free surface and corresponding vortex deformation.

A typical complicated vortex–free surface interaction occurs when a pair of submerged vortices or a vortex ring moves to a free surface $S$ as revealed by the experiments of Sarpkaya and coworkers (e.g., Sarpkaya 1992, 1996; Sarpkaya and Suthon 1991). First, consider a pair of vortices. The experiments have shown that as a vortex pair approaches the free surface $S$ by mutual induction, the surface will be humped up to form a *Kelvin oval*, and at mean time a series of lateral vortices appears, riding on the quasicylindrical oval ("*striations*"), bounded by two rows of "*scars*" and whirls digging into the water at the roots of the oval (Fig. 8.30). This interesting finding has excited many numerical simulations, such as those based on two-dimensional vortex sheet model for the free surface (e.g., Tryggvason 1989; Yu and Tryggvason 1990) and Navier–Stokes solver (Ohring and Lugt 1991; Lugt and Ohring 1992), as well as fully three-dimensional Navier–Stokes simulation (Dommermuth 1993).

Based on the results of these computations, Wu and Wu (1996) outlined the physics relevant to the vorticity creation in this interacting process. Initially, the interaction of the rising vortex pair with $S$ is apparently a two-dimensional inviscid process and can be mimicked by taking the pair as point vortices and $S$ as a weak boundary vortex sheet. As the Kelvin oval is formed, the surface tangent vorticity $\boldsymbol{\omega}_\pi$ increases to $O(1)$ as indicated by (4.105), or equivalently, the sheet strength $\boldsymbol{\gamma}$ is of $O(\delta)$, $\delta = Re^{-1/2}$. Note that the variation of $\boldsymbol{\gamma}$ already contains the vorticity creation process as seen from (4.154a) or (4.154b). Between the vortex pair and $S$, the flow can still be irrotational.

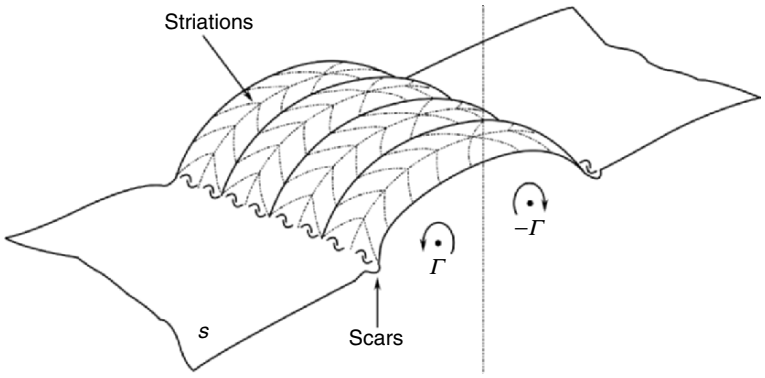


**Fig. 8.30.** Striations and scars. Based on Sarpkaya and Suthon (1991)

Then, at a finite $Re$, new vorticity produced at $S$ is diffused into the fluid; and at a certain stage of the early interaction, the vortex sheet needs to be refined as a free-surface boundary layer. By (4.112), then, the boundary vorticity flux on $S$ is dominated by the boundary layer correction of surface acceleration; that is, $\boldsymbol{\sigma} = O(\delta)$. In two-dimensions (4.112) is reduced to

$$\sigma = -\frac{\mathrm{D}_0 u_s'}{\mathrm{D}t} + u_s' \left\{ -\frac{\partial}{\partial s} U_{0s} + \kappa U_{0s} \right\} + O(\delta^2), \tag{8.138}$$

where $u_s'$ can be solved in boundary-layer approximation (Sect. 4.3.2), provided that the elevation of $S$ and its velocity induced by the primary vortices have been known from inviscid calculation. Qualitatively, $\boldsymbol{\sigma}$ concentrates in the local region of high curvature, where separation may happen at a sufficiently large Froude number (about 0.5 and larger), so that a pair of secondary vortices of opposite sign is formed below $S$. Then, toward the end of this stage the boundary layer approximation is no longer applicable. This newly produced secondary vortex pair is responsible for the observed scars and possible rebounding of the primary vortices.

The preceding two-dimensional picture cannot explain the observed striation, which are related to the vortex instability along the axis. In a three-dimensional Navier–Stokes simulation, Dommermuth (1993) has introduced an initial disturbance of the location and vorticity distribution of the primary vortices to observe the effect of instability. He finds that, as a vortex tube interacts itself and its neighbors, sheets of helical vorticity are spiraled off. Due to shortwave inviscid instability, these sheets manifest themselves as a briads of crossaxis vorticity, a structure independent of the presence of $S$. But, as they rotate around and translate with the primary vortices, some braids will approach $S$ and their open ends become normal to $S$ to form the observed whirls as the outer boundary of the scars.

The interaction of a vortex ring and a free surface can be similarly analyzed. In an experimental study of the normal collision process of a horizontal

vortex ring and an initially flat free surface, Song et al. (1992) have found that different vortex-ring strengths will produce different wave patterns on the free surface. In the initial stage of the interaction there appears a single circular sunken on the free surface; and as the ring strength increases on the free surface there may also appear rapidly developed axisymmetric traveling waves. In the later stage of the interaction, there will be fully three-dimensional surface waves with their pattern depending on the core structure. Similar phenomena can be observed on a density interface, for which Maxworthy (1977), Sarpkaya (1983) and Dahm et al. (1989) have carried out experimental studies. They found that a strong vortex ring can move across the interface, a weaker one can only go through partially, and a very weak one cannot at all. This observation has been confirmed by numerical simulation.

Finally, because an interface or free surface may propagate traveling waves, the vortex–interface interaction can modulate these waves. This is another unique feature of vortex–interface interactions. We exemplify this modulation by a numerical study of Fish (1989). At small Froude numbers, Fish applied the perturbation technique to linearize the governing equations and boundary conditions, and thereby obtained the deformation of the surface traveling waves due to the interaction with a vortex pair. It is found that, because of the interaction of the vortex-induced flow and the group velocity of the traveling wave, on the free surface a part of waves is compressed to have shorter wavelength, and another part is stretched to have longer wavelength, see Fig. 8.31.

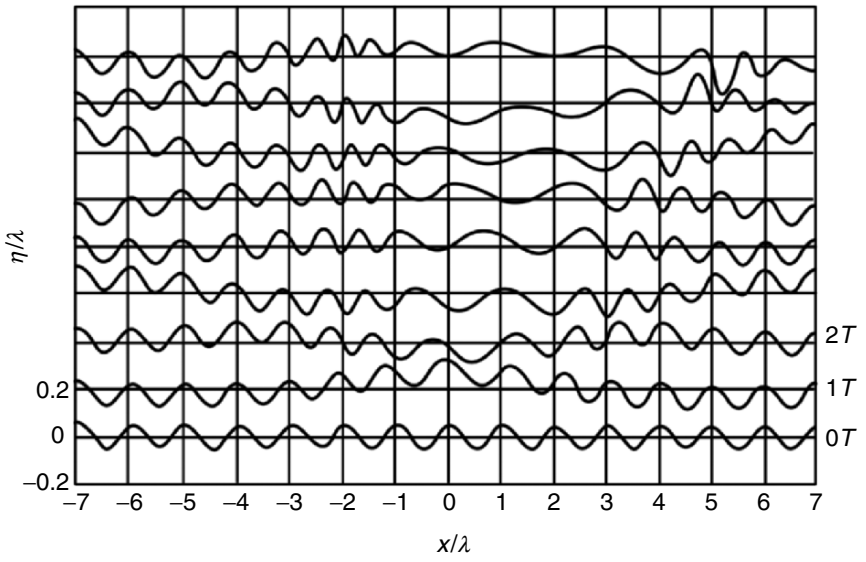


**Fig. 8.31.** The modulation of free-surface traveling wave with amplitude $\eta$ by a vortex pair. Based on Fish (1989)

## Summary

1. A vortex is typically, though not always, formed due to the motion of a solid body moving through a fluid of small viscosity. This involves a sequence of processes, from flow separation and formation of free vortex layer to the latter's rolling up into spiral structure, and to the smearing out of the multilayer structure by viscous diffusion. This sequence of processes makes the vorticity further concentrate in a thin smooth vortex core.
2. The wide variety of vortex core structures can be seen from those specific vortex solutions studied in Chap. 6. But generally a vortex core is more complicated than those analytic solutions under idealized conditions. A vortex may have a feeding shear layer to continuously send the vorticity created at solid surface into the core that is then advected by axial velocity (e.g., leading-edge vortex), or until it is saturated and sheds off from the body (e.g., newly produced wake vortex behind a cylinder). For a quasicylindrical vortex core, the radial variation of circumferential velocity always enhances the core axial-flow velocity, so that the variation of axial velocity at the outer edge of the core has a magnification effect at the vortex axis. On the contrary, the viscosity plays a key role in the inner core and always results in a deficit of the axial velocity. Moreover, the vortex core itself has special dynamics and evolution processes, as revealed by using the helical-wave decomposition.
3. Once a generic curved vortex is to be considered, its self-induction (a purely kinematic effect) becomes a dominant mechanism in its motion. Bold approximations have to be made for theoretical analysis, and significant insight has been gained thereby. The simplest model is a thin vortex filament of negligible core structure under local-induction approximation (the Hasimoto theory), by which a vortex core was found to be a waveguide for the first time and can support nonlinear solitary waves in its curvature and torsion. The Hasomoto theory has been extended to include the effects of finite core, nonlocal induction, self-stretching, and background flow, which can explain more phenomena observed in vortex motion. In fact, the aforementioned helical wave propagating along a finite core indicates that the core may also serve as waveguide of different kinds of vortical waves.
4. As one proceed to consider the motion and interaction of a system of multiple vortices, further simplifications have to be introduced. The simplest vortex-system model consists of two-dimensional point vortices, which is a Hamiltonian system and has well studied properties such as invariants, integrability, and chaos. Next to the point-vortex system is the inviscid vortex-patch system consisting of two-dimensional finite patches of arbitrary shape, with a constant vorticity in each patch. The two-dimensional motion and interaction of the patches can be reduced to the Lagrangian evolution of the one-dimensional boundary curves of each patch. While both point-vortex system and vortex-patch system cannot address the

viscous effect in vortex interaction, this effect is of particular importance in changing the topology of the system, because it can cause two approaching vortices (or two segments of a single vortex) to be cut and reconnected (reconnection for short) as observed in the evolution of aircraft trailing vortices and turbulence. The reconnection process involves many aspects of viscous vorticity and vortex dynamics, well beyond the reach of any circulation-preserving theory.

5. The vortex–boundary interactions form another rich category of vortex dynamics of significant practical importance. The interaction of a vortex and a solid wall may have various patterns depending on their shapes and relative orientation, and may cause strong generation of new vorticity from the wall that forms secondary vortices. The interaction of a vertical vortex and a flat wall, apparently a quite simple configuration, turns out to be unexpectedly complicated and likely to be spontaneously unsteady. This explains in part the full complexity in understanding meteorological tornados from fluid-dynamics side. In contrast, the interaction of a vortex and a free surface or interface can be more subtle since the shape of the surface keeps changing during the interaction process. It is this shape evolution that forms a detectable trace of the vortex motion and is of practical interest.

# Part III

# Vortical Flow Instability, Transition and Turbulence

# 9

# Vortical-Flow Stability and Vortex Breakdown

Flow stability theory is an important area of fluid mechanics that explores how a flow loses its stability and becomes turbulence eventually. Similarly, vortex stability theory is an important portion of vortex dynamics. Many complicated phenomena appearing in vortex motion can only be explained in terms of vortex instability. Miscellaneous vortices of various scales may occur in the complicated process as a flow loses its stability and gradually becomes turbulent. Typical examples include the Taylor vortices between two concentric circular cylinders, streamwise and hairpin vortices in boundary layers, the Görtler vortices in concave-wall boundary layers, etc.

The very rich contents and wide variety of vortical-flow instabilities cannot be fully covered by a single chapter. The choice of materials here is based on the following considerations. First, the basic concepts of hydrodynamic instability, mainly that of shear layers, should be introduced as a foundation of later discussions on the vortical structures in transitional and turbulent flows (Chap. 10). Second, the priority is given to the new progresses on the vortex instability theory in recent years, such as the absolute/convective instability, the nonmodal instability, strained vortex instability, and the improved theoretical explanation of the mechanisms in vortex breakdown. Throughout this chapter we assume the flow is incompressible.

Abundant literatures are available related to hydrodynamic stabilities, for example the books of Drazin and Reid (1981), Schmid and Henningson (2001), Drazin (2002), and Zhou and Zhao (2004). Detailed materials of vortical-flow stability can be found in the book of Yin and Sun (2003) and the review article of Ash and Khorrami (1995); see also the reviews of Huerre and Rossi (1998) and Rossi (2000).

## 9.1 Fundamentals of Hydrodynamic Stability

A flow that one is interested in its stability is called a basic flow, which is a solution of the Navier–Stokes or Euler equation. The velocity and pressure of

the basic flow are denoted by $(\boldsymbol{U}(\boldsymbol{x},t), P(\boldsymbol{x},t))$, which is subjected to disturbances $(\boldsymbol{u}(\boldsymbol{x},t), p(\boldsymbol{x},t))$ under natural or laboratory conditions. The disturbed flow is

$$(\boldsymbol{u}^*(\boldsymbol{x},t), p^*(\boldsymbol{x},t)) = (\boldsymbol{U}(\boldsymbol{x},t), P(\boldsymbol{x},t)) + (\boldsymbol{u}(\boldsymbol{x},t), p(\boldsymbol{x},t))\,. \tag{9.1}$$

If the disturbances decay as they evolve in space and time so that the flow recovers its original basic-flow state, the flow is said to be stable. If the disturbances continuously grow so that the basic flow develops to another state or becomes turbulent, the flow is said unstable.

Mathematically, a basic flow is *stable* (in the sense of Liapounov) if for all $\epsilon > 0$ there exists $\delta(\epsilon)$ such that when

$$\|\boldsymbol{u}(\boldsymbol{x},0)\|, \quad \|p(\boldsymbol{x},0)\| < \delta,$$

then

$$\|\boldsymbol{u}(\boldsymbol{x},t)\|, \quad \|p(\boldsymbol{x},t)\| < \epsilon \quad \text{for all } t > 0.$$

Here the norm $\|\cdot\|$ can be chosen in different ways. A flow is said to be *asymptotically stable* if it is stable and, moreover,

$$\|\boldsymbol{u}(\boldsymbol{x},t)\|, \quad \|p(\boldsymbol{x},t)\| \to 0, \quad \text{as } t \to \infty.$$

In particular, when the norm is the total disturbance kinetic energy

$$K_v(t) = \int_{\mathcal{D}} \frac{1}{2}|\boldsymbol{u}|^2 \mathrm{d}V \tag{9.2}$$

with initial value $K_v(0)$, then if

$$\lim_{t\to\infty} \frac{K_v(t)}{K_v(0)} \to 0 \tag{9.3}$$

the basic flow is asymptotically stable. If there exists a threshold energy $\delta > 0$, and the flow is stable for $K_v(0) < \delta$, it is said *conditionally stable*. If $\delta \to \infty$, the flow is *unconditionally stable*. If

$$\frac{\mathrm{d}K_v}{\mathrm{d}t} < 0 \quad \text{for all} \quad t > 0, \tag{9.4}$$

then the flow is said *monotonically stable*. These concepts in terms of energy norm are the basis of *energy method* in stability analysis (e.g., Serrin 1959, Joseph 1976, Schmid and Henningson 2001).

The stability behavior of a flow usually depends on the critical values of some characteristic parameters of the flow. Hence, these critical values determine the stability criteria. Since the shearing process is dominated by the Reynolds number, several *critical Reynolds numbers* can be defined for different types of flow stability. In Fig. 9.1, the abscissa is the Reynolds number

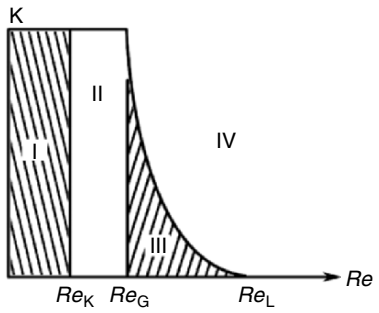


**Fig. 9.1.** Sketch illustrating critical Reynolds numbers. *Region I*: monotonically stable; *region II*: globally stable but not necessarily monotonically stable; *region III*: conditionally stable; *region IV*: possibly unstable. Reproduced from Schmid and Henningson (2001)

and the ordinate, the initial disturbance energy $K_v(0)$. The curve that divides regions III and IV is the stability characteristic curve. Its intersection with the $Re$-axis is the critical Reynolds number $Re_{\mathrm{L}}$ for linear instability with $K_v(0) \to 0$. For $Re > Re_{\mathrm{L}}$, the flow is unstable to certain infinitesimal disturbances. For $Re = Re_{\mathrm{L}}$, the flow is at least unstable to infinitesimal disturbance of one frequency. $Re_{\mathrm{G}}$ dividing regions II and III is the critical Reynolds number of global stability. For $Re_{\mathrm{G}} < Re < Re_{\mathrm{L}}$, the flow is conditionally unstable, since the disturbances will decay if $K_v(0)$ is smaller than a threshold and otherwise the flow is unstable. For $Re < Re_{\mathrm{G}}$, the flow is globally stable. One may imagine that $Re_{\mathrm{G}}$ corresponds to the lowest Reynolds number for which turbulence can be sustained. The region of $Re < Re_{\mathrm{G}}$ can be further divided into subregions I and II, with their border being $Re_{\mathrm{K}}$. For $Re < Re_{\mathrm{K}}$ the flow is monotonically stable. Note that in a flow that is stable but not monotonically stable, growing disturbances may exist in some finite time period, called *transient growth*.

### 9.1.1 Normal-Mode Linear Stability

The most mature and popular method in the study of flow stability is linear analysis for sufficiently small disturbances. A linear theory can give sufficient condition for instability, since if the flow is unstable to small disturbances it must be so to large ones. But a linearly stable flow may not be nonlinearly stable.

In the linear theory, the disturbance equations become homogeneous linear partial differential equations. For flows with vanishing disturbance at boundary, which is our present concern, the boundary conditions are homogeneous as well. It is well known that such a boundary-value problem implies an *eigenvalue problem*.

Consider a columnar vortex with axis along the $z$-direction as example. By the Laplace and Fourier transforms, the following expression can be obtained in the cylindrical coordinates $(r, \theta, z)$:

$$\boldsymbol{u}(\boldsymbol{x}, t) = \mathrm{Re} \int_{-\infty}^{\infty} \mathrm{d}k \sum_{n=-\infty}^{\infty} \int \mathrm{d}\omega \hat{\boldsymbol{u}}(r, k, n, \omega) \mathrm{e}^{\mathrm{i}(kz+n\theta-\omega t)}, \tag{9.5}$$

where Re represents the real part, $k$ and $n$ ($n$ is a discrete integer) are the wave numbers along $z$ and $\theta$ directions, respectively. Substituting (9.5) into the linearized disturbance equations, one obtains a *dispersion relation* for the eigenvalues of $k, n$, and $\omega$

$$\mathcal{F}(k, n, \omega; Re, ...) = 0. \tag{9.6}$$

This approach is usually referred to as the *normal-mode analysis*, in which one used to consider either *temporal mode* or *spatial mode*. In temporal-mode analysis, the variation of disturbances as time is the concern, where $k$ and $n$ are given real values. The eigenvalue $\omega$ is complex, $\omega = \omega_r + \mathrm{i}\omega_i$. Thus, for a given mode, the velocity disturbance can be expressed as

$$\boldsymbol{u}(\mathbf{x}, t) = \widehat{\boldsymbol{u}}(r, k, n) \mathrm{e}^{\omega_i t} \cdot \mathrm{e}^{i(kz+n\theta-\omega_r t)}, \tag{9.7}$$

where $\widehat{\boldsymbol{u}}$ is the amplitude and $\omega_r$ is the frequency. As time goes on, $\widehat{\boldsymbol{u}}$ will vary while the disturbance is propagating as a travelling wave. $\omega_i$ is the growth rate of the disturbance. The flow is stable or asymptotically stable if $\omega_i < 0$, and *neutrally stable* if $\omega_i = 0$. When $\omega_i > 0$, the disturbance grows exponentially with time and the flow is unstable.

In the spatial-mode analysis, frequency $\omega$ and wave number $n$ are chosen real but eigenvalue $k = k_r + \mathrm{i}k_i$ is complex. Then (9.7) is replaced by

$$\boldsymbol{u}(\boldsymbol{x}, t) = \widehat{\boldsymbol{u}}(r, n, \omega) \mathrm{e}^{-k_i x} \cdot \mathrm{e}^{\mathrm{i}(k_r x+n\theta-\omega t)}. \tag{9.8}$$

The flow is linearly stable or neutrally stable in its spatial development if $k_i \geq 0$. When $k_i < 0$, the disturbance grows exponentially in space and the flow is unstable. In a laboratory experiment, a vibrating ribbon is often used to introduce a small disturbance of given frequency and amplitude so that the development of the disturbance along the downstream direction can be measured. This corresponds to the spatial mode. But, the spatial-mode analysis is mathematically more difficult than the temporal-mode one, so most of the theoretical works are based on temporal-mode analysis.

Although the temporal-mode analysis can explain certain flow instability behaviors, one may be more interested in the flow response to an initial and localized disturbance, i.e., the spatio-temporal development of the response to an impulsive disturbance (*impulsive response*), which is more inherently related to the physical stability concept. This has led to the development

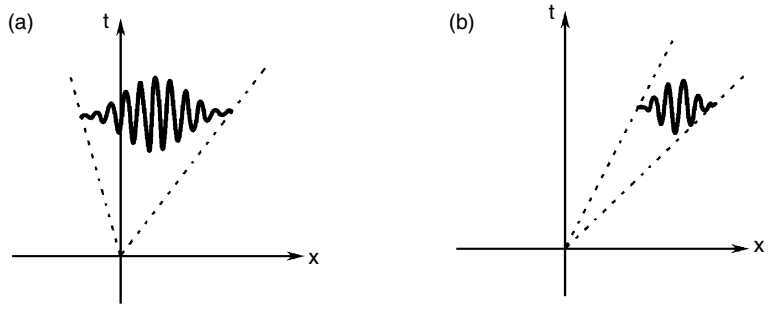


**Fig. 9.2.** Sketches of the impulse response. (**a**) Absolutely unstable; (**b**) Convectively unstable

of the theory of absolute and convective stability, which has revealed more comprehensive and profound flow instability behavior both qualitatively and quantitatively.

*Absolute instability* (AI) is referred to the situation where local disturbances can propagate both upstream and downstream (Fig. 9.2a) so that an unstable flow is gradually contaminated everywhere by a point-source input. In contrast, *convective instability* (CI) is referred to the situation where local disturbances propagate and develop only in downstream direction (Fig. 9.2b) so that the flow can eventually recover its original undisturbed state at the location where the disturbance is initially introduced.

Strictly, the aforementioned spatial-mode analysis is applicable only to a flow that is convectively unstable. For an absolutely unstable flow, the region influenced by an impulsive disturbance will be large enough after certain time, leading to an onset of synchronized self-sustained oscillation, or self-excited resonance, which can bury the initial disturbances. In this case, observing spatial propagation of an initial disturbance is obviously meaningless. Thus, the AI/CI theory is a powerful tool to clearly distinguish the temporal and spatial development of disturbances.

One of the purposes of stability analysis is for flow control, where the AI/CI analysis is of crucial importance. Depending on different applications, in a vortex-control problem it is desired to either enhance a favorable vortex or disrupt an unfavorable one. Many experimental and numerical studies have shown that an unsteady forcing with a very small power input may cause essential changes of the flow state, hence is an efficient method for flow control (e.g., Wu et al. 1998; Seifert and Pack 1999). Here, to answer the question such as how to impose the forcing, where to impose the forcing, and what kind of disturbance modes to pose for the maximum absolute growth rate, requires a clear understanding of the specific AI/CI character of the flow.

A full presentation of the AI/CI theory involves quite delicate mathematics and complicated calculations, for which the reader is referred to Huerre and Monkwwitz (1990), Huerre and Rossi (1998), and Yin and Sun (2003). Here, we only briefly outline its basic concepts and research methodology. Our task

is to study the spatial-temporal development of an impulsive response within the framework of the linear normal-mode analysis. The disturbance velocity can be decomposed to

$$\boldsymbol{u}(\boldsymbol{x},t) = \widehat{\boldsymbol{u}}(r,n)\mathrm{e}^{\mathrm{i}(kz+n\theta-\omega t)}. \tag{9.9}$$

Unlike the temporal or spatial mode alone, both the axial wavenumber $k$ and frequency $\omega$ are now complex. Thus, corresponding to (9.9), for the example of a swirling vortex, (9.6) may take the form

$$D(k,\omega;n,a,s,Re) = 0, \tag{9.10}$$

where dimensionless parameters $a$ and $s$ characterize the axial velocity profile and rotation level in a swirling flow (see (9.76)).

To determine the complex $k$ and $\omega$ in the spatio-temporal evolution of an impulsive response, the *Briggs–Bers criterion* (Briggs 1964; Bers 1975, 1983) should be applied. Mathematically, based on the steepest-descent integral it can be shown that to find the asymptotic temporal growth rate (at large time after the impulse) is equivalent to finding those points with vanishing group velocity; that is

$$\frac{\partial\omega}{\partial k}(k^0;n,a,s,Re) = 0, \tag{9.11a}$$

$$\omega^0 = \omega(k^0;n,a,s,Re), \tag{9.11b}$$

where $k^0$ is the *saddle point* of the dispersion relation in the complex $k$-plane, or equivalently, the *branch points* $\omega^0$ in the complex $\omega$-plane, see Fig. 9.3. $k^0$ and $\omega^0$ at a saddle point are called the *absolute complex wave number* and *absolute complex frequency*, respectively. The imaginary part of absolute complex frequency, $\omega_i^0$, is the absolute growth rate. An unstable flow will be absolutely unstable if at least one of the branch-point singularities of the dispersion relation lies on the upper half of the $\omega$-plane (i.e. some $\omega_i^0 > 0$); and the saddle point obtained thereby is the coalescence of a downstream travelling wave $k^+(\omega)$ and an upstream travelling wave $k^-(\omega)$, which can be judged from the saddle point diagram by checking whether $k^+(\omega)$ and $k^-(\omega)$ are from the upper and lower halves of the complex $k$-plane. This is

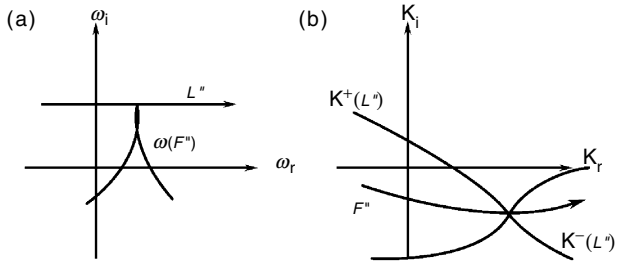


**Fig. 9.3.** Sketches for Briggs method. (**a**) Complex $\omega$-plane; (**b**) Complex $k$-plane

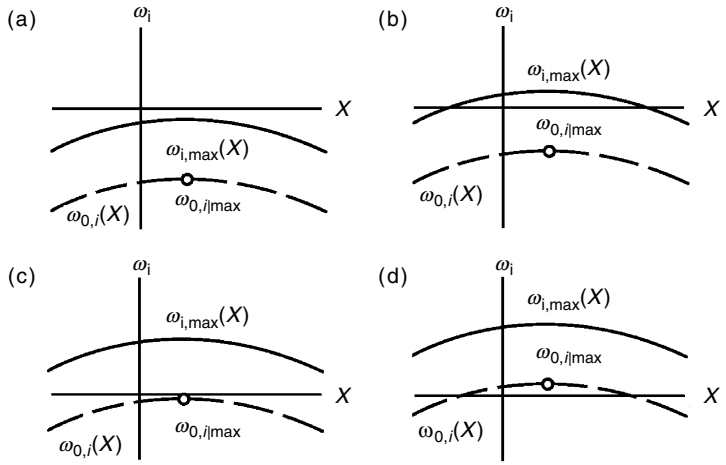


**Fig. 9.4.** The local stability categories of the spatially developing flow. (**a**) Uniformly stable, (**b**) convectively unstable, (**c**) almost absolutely unstable, (**d**) pocket of absolute instability

the so-called pinching requirement for the path integral of wave package on the $k$-plane. If these conditions do not hold, the unstable flow is convectively unstable.

The above AI/CI theory is valid for strictly parallel flows. For weakly non-parallel flows, the simplest approach is to apply local parallel assumption at several streamwise locations and then perform AI/CI analysis at each location. For this purpose, the local maximal temporal growth rate and local absolute growth rate can be defined, respectively, as

$$\omega_{i,\max}(z;Re) = \omega_i(k_{\max};z;Re), \tag{9.12a}$$

$$\omega_i^0(z;Re) = \omega_i^0(k^0;z;Re). \tag{9.12b}$$

Here, $k_{\max}$ corresponds to $\partial\omega/\partial k(k_{\max};z;Re) = 0$, $k$ is real; $k^0$ corresponds to $\partial\omega/\partial k(k^0;z;Re) = 0$, $k$ is complex. The maximum of the local absolute growth rate is denoted by $\omega_{i,\max}^0$. According to the distribution of $\omega_{i,\max}$ and $\omega_{i,\max}^0$, a flow can be divided into four categories as shown in Fig. 9.4, by which one can make following identifications:

(a) If $\omega_{i,\max} < 0$ and $\omega_{i,\max}^0 < 0$ for all locations, the flow is locally and homogeneously stable everywhere. Consequently, it is also globally stable.
(b) If $\omega_{i,\max} > 0$ for a part of the flow field but $\omega_{i,\max}^0 < 0$, the flow is convectively unstable in certain local region. The disturbances will grow in a finite region but the flow is still globally stable.
(c) If at certain locations $\omega_{i,\max}^0 \approx 0$, a region of absolute instability is about to or already occur, though small. The flow is still globally stable. There

exits a stable global mode of certain frequency decaying or growing very slowly. An external excitation close to this frequency can easily lead to an abrupt growth of the global mode and cause global resonance.

(d) When the region of absolute instability is greater than certain critical size, the flow becomes *globally unstable*, and a global self-sustained oscillation may occur. On the global instabilities for a spatially developing flow, see Chomaz (2005).

A typical example to which the AI/CI analysis has been successfully applied is the wake instability behind a blunt body (Triantafyllou and Triantafyllou 1986, Karniadakis and Triantafyllou 1989, Monkewitz and Nguyen 1987, Monkewitz 1988a). The authors performed AI/CI analysis at various downstream locations of a circular cylinder based on the parallel flow assumption (although the wake flow is already quite far from being parallel). The results show that even at a Reynolds number lower than the critical one, an absolutely unstable flow region already occurs locally in the wake. However, the flow field is only convectively unstable and globally stable. For the flow with Reynolds number greater than the critical one, the flow becomes absolutely unstable in a region between the cylinder and certain location in the reverse flow. Downstream of it, the flow is convectively unstable. The Kármán vortex street is just a phenomenon of self-sustained oscillation in a globally unstable system. The energy to maintain the oscillation comes from the absolute instability region in the wake. Thus, the AI/CI analysis clarifies the formation mechanism of the Kármán vortex street, which was discussed qualitatively in Sect. 7.4.

### 9.1.2 Linear Instability with Non-normal Operator

In all preceding normal-mode analyses a single representative mode is considered sufficient for finding linear instability. Despite the simplicity and wide applications of this approach, however, difficulties have been encountered. While the critical Reynolds number predicted by normal-mode analysis agrees very well with experiments in some special flows such as the Benard flow and narrow-gap Taylor–Couette flow, it fails in most vortical flows. Examples include the plane Couette flow, plane Poiseuille flow, boundary layers, free shear layers, and concentrated vortices. The critical Reynolds number predicted by normal-mode theory in these flows may be much larger (or even infinity) than the Reynolds number at which experiments found the flow becoming unstable. To explain the discrepancies, a natural consideration is that real disturbances are never infinitesimal but a finite-amplitude disturbance is beyond the ability of linear analysis. Therefore, weakly nonlinear stability theory has been developed and proved successful (e.g., Stuart 1984, Craik 1985, Zhou and Zhao 2004).

Recent studies have revealed that, however, the linear effect on instability is indispensable although nonlinearity is inevitable and necessary in the

transition from laminar to turbulent flow. In fact, the property of the linear operator in the disturbance equation, i.e., whether it is symmetric, normal, or self-adjoint, plays a critical role, is of close relevance to the aforementioned discrepancies.

Consider a linear operator $L$ defined on a *Hilbert space* (complete inner-product space) and its complex-conjugate transverse $L^\dagger$, the later being defined by the inner-product integral relation

$$\langle v, Lu\rangle = \langle u, L^\dagger v\rangle$$

over the same domain $\mathcal{D}$ as $L$ for any vectors $u$ and $v$. A linear operator is called *normal* if $LL^\dagger = L^\dagger L$, which includes *symmetric* and *self-adjoint* operators.[1] If $L$ is normal and compact, its eigenfunctions form a complete orthogonal set, so that the solution of the linear disturbance equation can be expanded in terms of the eigenfunctions of $L$. To know whether a disturbance will grow, therefore, it suffices to observe the subspace of growing modes: a single (exponentially) growing mode will imply the linear instability, while without such modes the flow is linearly stable. This is why the normal-mode analysis can well predict linear instability. The linear operators in the stability analysis of the Bernard flow and narrow-gap Taylor–Couette flow are of this kind.

In contrast, if $L$ is non-normal, although its eigenfunctions may still form a complete set, they can be nonorthogonal. In this case, even if all individual disturbance modes decay, a linear combination of some of them may lead to *transient algebraic growth*. Thus, one cannot judge the stability simply through a single-mode analysis.

To see how this happens, we express the disturbance evolution as a linear dynamic system (e.g., Nolan and Farrell 1999a)

$$\dot{v} = Tv, \tag{9.13a}$$

where $v$ is a (column matrix) function describing the state of the disturbance and $T$ the time evolution operator. Define a positive-definite Hermitian operator $M$ such that the energy of the system can be expressed by

$$E = v^* M v, \tag{9.13b}$$

where $v^*$ is the transpose complex conjugate of $v$. We transfer $v$ to generalized velocity coordinates

$$u = M^{1/2} v, \quad A = M^{1/2} T M^{-1/2}, \tag{9.14a,b}$$

such that

$$\dot{u} = Au, \quad \dot{u}^* = u^* A^\dagger, \quad E = u^* u. \tag{9.15a,b}$$

[1] Boundary conditions should be understood implicitly built in the operator $L$.

Since (9.14b) is a similarity transformation, the eigenvalues of $A$ are the same as those of $T$. Assume $A$ is an autonomous operator for simplicity, the explicit solution of (9.15a) is

$$u(t) = u(0)\mathrm{e}^{At}, \tag{9.16}$$

where the exponential of operator $\mathrm{e}^{At}$ is called the *propagator* (for its properties and calculations see, e.g., Hirsch and Smale 1974, Hale and Koçak 1991). Then by (9.15) there is

$$\frac{\partial E}{\partial t} = \dot{u}^* u + u^* \dot{u} = u^* A^\dagger u + u^* A u = u^*(A^\dagger + A)u,$$

which and (9.16) yield

$$E(t) = u^*(0)\mathrm{e}^{(A^\dagger + A)t}u(0). \tag{9.17}$$

Now, since the energy operator $(A^\dagger + A)$ is always normal no matter whether or not $A$ is, instead of examining the asymptotic behavior of the eigenvalues $\lambda_i$ of $A^\dagger + A$ as $t \to \infty$ as we did in normal-mode analysis, we can now examine the *finite-time* variation of $\lambda_i(t')$ during $(0, t)$. Then the eigenvector associated with the largest eigenvalue $\lambda_{\max}$ will have the fastest growth (or least decay) in energy during this interval, called *finite-time optimal*:

$$\left(\frac{1}{E}\frac{\partial E}{\partial t}\right)_{\max} = \lambda_{\max} \quad \text{or} \quad \left(\frac{E(t')}{E(0)}\right)_{\max} = \mathrm{e}^{\lambda_{\max} t'}, \quad t' \in (0, t). \tag{9.18}$$

If $A$ is normal, evidently its eigenvalues are the same of $A^\dagger + \mathbf{A}$; otherwise they will be different, associated with nonorthogonal eigenvectors. Consequently, even all eigenmodes of $A$ are decaying, the disturbance energy may have a finite-time transient growth.

For example, let $\boldsymbol{u}_1$ and $\boldsymbol{u}_2$ be two normal modes such that $\langle \boldsymbol{u}_1, \boldsymbol{u}_2 \rangle$ vanishes due to orthogonality, then their contributions to the kinetic energy can be superposed

$$\langle \boldsymbol{u}_1 + \boldsymbol{u}_2, \boldsymbol{u}_1 + \boldsymbol{u}_2 \rangle = \langle q_1^2 + q_2^2 \rangle, \quad q_\alpha = |\boldsymbol{u}_\alpha|, \quad \alpha = 1, 2.$$

Thus, if the kinetic energy of all normal modes decays, so must be that of any disturbance. But if these modes are nonorthogonal, then

$$q^2 = |\boldsymbol{u}_1 + \boldsymbol{u}_2|^2 = q_1^2 + q_2^2 + 2q_1 q_2 \cos\theta,$$

where $\theta \neq \boldsymbol{\pi}/2$ is the angle between $\boldsymbol{u}_1$ and $\boldsymbol{u}_2$ in functional space. Thus, assuming $\theta$ is time-independent, there is

$$\dot{q^2} = \dot{q_1^2} + \dot{q_2^2} + 2(\dot{q_1} q_2 + q_1 \dot{q_2}) \cos\theta.$$

Thus, if $\theta > \boldsymbol{\pi}/2$ , $q^2$ may have algebraic growth even if both $\dot{q_1^2}$ and $\dot{q_2^2}$ are negative. But this growth can happen only in a finite time, because it

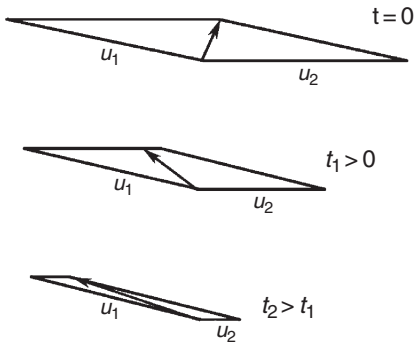


**Fig. 9.5.** Sketch illustrating transient growth due to nonorthogonal superposition of two eigenvectors that decay at different rates as time evolves

will eventually tend to zero as $q_1^2$ and $q_2^2$ continue to decay as $t \to \infty$. This situation is sketched in Fig. 9.5.

In recent years, many researchers have reexamined the linearized Navier–Stokes equation or Euler equation, of which the operator is intrinsically non-normal especially for vortical basic flows as to be shown in Sect. 9.1.4. It has been demonstrated that the early algebraic linear growth of some finite but small disturbances, known as *nonmodal instability*, can reach surprisingly large amplitude on a time scale shorter than that for asymptotically growing mode encountered in normal-mode analysis, and thereby trigger their nonlinear growth mechanisms very rapidly. For example, in a Poiseuille flow at Reynolds number 5,000, Butler and Farrel (1992) found disturbances that could grow in energy by a factor 4,897, despite the fact that the flow is asymptotically stable at this Reynolds number. For plane Couette flow, at $Re = 4{,}000$ the disturbance-energy growth can be as large as by a factor of 18,000. This kind of transient growth is responsible for triggering the transition at a Reynolds number lower than the critical value predicted by the normal-mode theory. It is the very reason for *subcritical transition* to occur in a plan Poiseuille or Couette flow. This type of transition is also known as *bypass transition*, i.e. a transition emanating from nonmodal growth mechanisms. In addition, there is special concern on the transient growth of disturbances in some fields of physics, for example, geophysics and meteorology.

For transient growth, since the mode analysis becomes insufficient, the linear stability theory need to be generalized to include both normal and non-normal operators. This has been benefited from some theories developed in matrix analysis, among which the *pseudo-spectrum method* (e.g., Trefethen 1991, 1997; Reddy et al. 1993; Trefethen et al. 1993) and the *singular-value method* (e.g., Noble and Daniel 1988; Golub and van Loan 1996; Farrell and Ioannou 1996) are of special importance. Chomaz (2005) has discussed the relations between the non-normality and nonlinearity for the global instabilities in a spatially developing flow.

The singular-value method deserves a brief outline here, by which both asymptotic modal instability and nonmodal transient instability can be studied simultaneously. In fact, the method has been generalized to nonlinear operator by Mu (2000) to study finite-time nonlinear evolution of disturbances. Return to (9.16), where the propagator $\mathrm{e}^{At}$ of operator $A$ transforms the unitary initial states (the column vectors $v_i$ of unitary matrix $V$, say) of the disturbance to its final states (column vectors $u_i$ of unitary matrix $U$, say). During the transformation each initial state $\mathbf{V}_i$ realizes a growth $\sigma_i$ under the action of the propagator. Then, finding the complete set of unitary initial and final states as well as the growths amounts to constructing a *singular-value decomposition* of the propagator:

$$\mathrm{e}^{At} = U\Sigma V^{\dagger}, \tag{9.19}$$

where $\Sigma = \mathrm{diag}(\sigma_1, ..., \sigma_n)$ is a diagonal matrix. As explained by Farrell and Ioannou (1996), this decomposition can be visualized as the simultaneous formation of a particular orthogonal basis in the domain and the range space of a matrix, such that each basis vector $v_i$ (the $i$th domain vector or *right singular vector*) in the domain space is mapped to a corresponding basis vector $u_i$ (the $i$th range vector or *left singular vector*). Moreover, because

$$\mathrm{e}^{A^{\dagger}t}\mathrm{e}^{At} = V\Sigma U^{\dagger}U\Sigma V^{\dagger} = V\Sigma^2 V^{\dagger}, \tag{9.20}$$

we see that, given domain vectors, the growth $\sigma_i$ of range vector $u_i$ is simply the corresponding element of the diagonal matrix $\Sigma$, which is the *singular value* of the propagator. $\sigma_i$ will be the same as eigenvalues $\mathrm{e}^{\lambda_i t}$ if $A$ is normal; but more generally it is the $\sigma_{\max}$ rather than $\lambda_{\max}$ that determines the maximum growth at a given time. In fact, there is (Farrell and Ioannou 1996)

$$\sigma_{\min}^2 \leq \mathrm{e}^{(\lambda_i + \lambda_i^*)t} \leq \sigma_{\max}^2, \tag{9.21}$$

where $\lambda_i$ ranges over all eigenvalues of $A$. The initial disturbance that gives the maximum growth at a given $t$ is referred to as the *optimal disturbance* at that $t$, and the maximum growth that occurs when all time intervals are surveyed is called the *global optimal*.

### 9.1.3 Energy Method and Inviscid Arnold Theory

In addition to small-disturbance analysis, the energy method is also often applied based on (9.2) to (9.4). While small-disturbance analysis usually gives the sufficient condition for a flow to be unstable, the energy method gives the sufficient condition for a flow to be stable.

Using the same notation as in (9.1), from the full disturbed Navier–Stokes equation with $\rho = 1$

$$\frac{\partial \boldsymbol{u}^*}{\partial t} + \boldsymbol{\omega}^* \times \boldsymbol{u}^* = -\nabla\left(p^* + \frac{1}{2}|\boldsymbol{u}^*|^2\right) - \nu\nabla \times \boldsymbol{\omega}^*. \tag{9.22}$$

We subtract the basic-flow equation to obtain the nonlinear equation for disturbance dynamics

$$\frac{\partial \boldsymbol{u}}{\partial t} + \boldsymbol{L} = -\nabla H - \nu \nabla \times \boldsymbol{\omega} \tag{9.23}$$

with boundary condition

$$\boldsymbol{u} = \boldsymbol{0} \quad \text{at} \quad \partial\mathcal{D}. \tag{9.24}$$

Here, we use notations

$$H \equiv p + \boldsymbol{U} \cdot \boldsymbol{u} + \frac{1}{2}|\boldsymbol{u}|^2, \tag{9.25}$$

$$\boldsymbol{L} \equiv \boldsymbol{\Omega} \times \boldsymbol{u} + \boldsymbol{\omega} \times \boldsymbol{U} + \boldsymbol{\omega} \times \boldsymbol{u}. \tag{9.26}$$

$\boldsymbol{L}$ is referred to as the *disturbance Lamb vector*. Note that $\boldsymbol{\omega} \times \boldsymbol{u}$ is the only source of all nonlinear instabilities in vorticity evolution. Another nonlinear term $\nabla|\boldsymbol{u}|^2/2$ has been absorbed into the unknown stagnation enthalpy $H$ in (9.23).

Making inner product of (9.23) and $\boldsymbol{u}$, and integrating over the domain $\mathcal{D}$, using (9.24) and identities

$$\boldsymbol{u} \cdot [(\boldsymbol{\Omega} + \boldsymbol{\omega}) \times \boldsymbol{u}] = 0, \quad \boldsymbol{u} \cdot (\boldsymbol{\omega} \times \boldsymbol{U}) = -(\boldsymbol{\omega} \times \boldsymbol{u}) \cdot \boldsymbol{U}, \quad \boldsymbol{u} \cdot \nabla\phi = \nabla \cdot (\boldsymbol{u}\phi),$$
$$\boldsymbol{u} \cdot (\nabla \times \boldsymbol{\omega}) = \nabla \cdot (\boldsymbol{\omega} \times \boldsymbol{u}) + \omega^2,$$

it follows that:

$$\frac{\mathrm{d}K_v}{\mathrm{d}t} = \int_{\mathcal{D}} (\boldsymbol{\omega} \times \boldsymbol{u}) \cdot \boldsymbol{U} \mathrm{d}V - \nu \int_{\mathcal{D}} \omega^2 \mathrm{d}V. \tag{9.27}$$

This equation is the vortical form of the classical *Reynolds–Orr equation*

$$\frac{\mathrm{d}K_v}{\mathrm{d}t} = \int_{\mathcal{D}} \boldsymbol{u} \cdot \mathbf{D} \cdot \boldsymbol{u} \mathrm{d}V - \nu \int_{\mathcal{D}} \nabla \boldsymbol{u} : \nabla \boldsymbol{u} \mathrm{d}V, \tag{9.28}$$

where $\mathbf{D}$ is the symmetric strain rate of the basic flow.

Equation (9.28) is the basis of the energy method in stability analysis (e.g., Serrin 1959; Joseph 1976). On the right-hand side, the second term is the viscous dissipation of the disturbance kinetic energy and always negative; while the first term represents the transfer between the basic flow and disturbances. If there is certain mechanism that leads to energy transfer from the basic flow to disturbances and causes a growth of the latter, there may be $\mathrm{d}K_v/\mathrm{d}t > 0$ that implies the basic flow is unstable. Obviously, (9.27) provides a physically more revealing information than (9.28): *The net energy-transfer direction between the basic flow and disturbances depends solely on the mean geometric relation of the disturbance Lamb vector* $\boldsymbol{\omega} \times \boldsymbol{u}$ *and the local basic-flow velocity* $\boldsymbol{U}$.

Now, (9.28) ensures the existence of a critical Reynolds number $Re_{\mathrm{K}}$, below which any distrubance decays and the flow is monotonically stable. In fact, make all quantities in (9.28) dimensionless, we may set $Re_{\mathrm{K}} = v_{\mathrm{K}}^{-1}$, where

$$v_{\mathrm{K}} = \sup_{t>0} \max_{\boldsymbol{u}} \frac{-\int_{\mathcal{D}} \boldsymbol{u}\cdot\mathbf{D}\cdot\boldsymbol{u}\mathrm{d}V}{\int_{\mathcal{D}} \nabla\boldsymbol{u} : \nabla\boldsymbol{u}\,\mathrm{d}V} \tag{9.29}$$

is a positive and finite stability limit (Joseph 1976). Here, the incompressibility implies that the numerator in (9.29), with a minus sign, has a positive upper bound. For the estimate of $\nu_{\mathrm{K}}$, Serrin (1959) applied the calculus of variation to show that the minimum-value problem (9.29) is equivalent to a linear eigenvalue problem

$$\boldsymbol{u}\cdot\mathbf{D} - \nu_{\mathrm{K}}\nabla^2\boldsymbol{u} = -\nabla\pi, \qquad \nabla\cdot\boldsymbol{u} = 0, \qquad \boldsymbol{u}|_{\partial\mathcal{D}} = \mathbf{0}. \tag{9.30}$$

Here, $\pi_K(\boldsymbol{x}, t)$ and $\nu_{\mathrm{K}}$ are Lagrangian multipliers to ensure divergence-free condition and normalize the total dissipation, respectively, such that the minimum eigenvalue of $\nu_{\mathrm{K}}$ gives a stability boundary $Re_{\mathrm{K}}$ to any disturbance.

We make an observation on (9.27) and (9.28). Since the disturbance energy is related to quadratic terms of $\boldsymbol{u}$ and/or $\boldsymbol{\omega}$, nonlinear effect, if any, should appear as cubic terms of the disturbance, which is however absent due to $(\boldsymbol{\omega}\times\boldsymbol{u})\cdot\boldsymbol{u} \equiv 0$. To look at this fact in a general operator form, let $L$ and $N$ be linear and nonlinear operators, respectively, and consider a dynamic system ($u$, $L$, and $N$ stand for column vector and matrices, respectively)

$$\frac{\partial u}{\partial t} = Lu + Nu, \quad u|_{t=0} = u_0, \quad u = 0 \ \text{ at } \partial\mathcal{D}, \tag{9.31}$$

of which (9.23) is a specific case. The energy of (9.31) is given by

$$\frac{1}{2}\frac{\mathrm{d}}{\mathrm{d}t}\langle u, u\rangle = \langle (L+N)u, u\rangle. \tag{9.32}$$

But, (9.27) indicates that the choice of energy norm excludes the effect of any nonlinear disturbance, leading to

$$\langle Nu, u\rangle = 0 \tag{9.33}$$

for viscous incompressible fluid, although formally the energy method permits any disturbance of arbitrary amplitude. *The energy method has exactly the same information as that can be obtained from a linear stability analysis.*

The above observation, along with the observation made in Sect. 9.1.2, that *the classic energy method only includes the role of the normal part of* $L$, has been proven rigorously and independently by Galdi and Padula (1990) and Henningson and Reddy (1994) by different approaches. Together these observations imply an interesting equivalence of the "nonlinear" energy method and linear normal-mode method: if the operator is normal, their prediction of asymptotic stability boundary should be the same, i.e., $Re_{\mathrm{K}} = Re_{\mathrm{L}}$. This has indeed been proven by Padula (1988) and Galdi and Padula (1990), who extended the classic energy stability method to *energy instability method*. Therefore, a fundamental conclusion can be made that *linear mechanism is necessary for transition to turbulence*. One more conclusion is that *non-normality is necessary for sub-critical transition at a Reynolds number smaller than* $Re_{\mathrm{L}}$.

The above energy method studies the growth rate of *disturbance energy*. From (9.1) and (9.2), one may also study the *total* kinetic energy directly based on the Liapounov formal stability theory. A system is called *formally stable* if for the system one can construct a conserved scalar such that its first variation is zero, while its second variation is positively or negatively definite. Formal stability implies linear stability because the second variation of this conserved scalar is invariant in the linearized dynamics. But the formal stability is stronger than the linear one. In a finite-dimensional system formal stability implies nonlinear stability; whereas in infinite dimensions it is a necessary prerequisite for nonlinear stability. The condition for formal stability may not be the same as that for linear stability. The result can be obtained without considering whether the operator is normal. In this area, one of the important achievements is due to Arnold (1965b,c; 1969). As seen in Sect. 3.6.4, Arnold proves that the first variation of total kinetic energy $K$ for a steady inviscid circulation-preserving flow is zero, i.e. $K$ reaches its stationary value. Then, the second energy variation is (3.187):

$$\delta^2 K = \frac{1}{2}\int_{\mathcal{D}} \left\{(\delta \boldsymbol{u})^2 + \delta\boldsymbol{\omega}\cdot(\boldsymbol{U}\times\boldsymbol{\xi})\right\} \mathrm{d}V, \tag{9.34}$$

where $\delta\boldsymbol{\omega} = \nabla\times(\boldsymbol{\xi}\times\boldsymbol{\Omega})$ and $\boldsymbol{\xi}$ is an arbitrary divergence-free vector field with $\boldsymbol{\xi}\cdot\boldsymbol{n} = 0$ on boundary, and we have denoted the basic flow by capital letters. Thus, for a steady and inviscid circulation-preserving flow, if $\delta^2 K$ is definitely positive or definitely negative, then $K$ is a Liapounov function and the flow is formally stable.

In two-dimensional flow with $\boldsymbol{\xi} = (\xi_1, \xi_2)$ and stream function $\Psi$ for basic flow, since the steady basic flow is generalized Beltramian with $\Omega = \Omega(\Psi)$, we have

$$\delta\boldsymbol{\omega} = \nabla\times(\boldsymbol{\xi}\times\boldsymbol{\omega}) = -(\boldsymbol{\xi}\cdot\nabla)\Omega\boldsymbol{e}_3,$$
$$\delta\boldsymbol{\omega}\cdot(\boldsymbol{U}\times\boldsymbol{\xi}) = \frac{\mathrm{d}(\Delta\Psi)}{\mathrm{d}\Psi}(\boldsymbol{\xi}\cdot\nabla\psi)^2,$$

where $\Delta = \nabla^2$. Thus, (9.34) is reduced to

$$\delta^2 K = \frac{1}{2}\int_{\mathcal{D}} \left\{(\delta\boldsymbol{u})^2 + \frac{\mathrm{d}(\Delta\Psi)}{\mathrm{d}\Psi}(\boldsymbol{\xi}\cdot\nabla\Psi)^2\right\} \mathrm{d}V, \tag{9.35}$$

and there must be $\delta^2 K > 0$ if

$$\frac{\mathrm{d}(\Delta\Psi)}{\mathrm{d}\Psi} \geq 0, \tag{9.36}$$

which is a sufficient condition for a two-dimensional inviscid and steady flow to be formally stable. Arnold (1965b,c) has also found a class of stable two-dimensional steady flow with $\delta^2 K < 0$ , which is omitted here. We shall demonstrate the application of the Arnorld theory in the stability analysis of parallel shear flows in Sect. 9.2.1 and columnar vortices in Sect. 9.3.1.

Inspired by the Arnold theory, Carnevale and Vallis (1990) introduced a virtual additional term to the Euler equation to force a monotonic temporal evolution of $K$ to seek possible formally stable steady vortical flows from various initial states. The virtual term was designed to eventually vanish when the flow approaches steady-state. Thus, only the final state is physically meaningful but the evolution process is not. Examples of their numerical experiments with periodical boundary conditions are shown in Fig. 9.6.

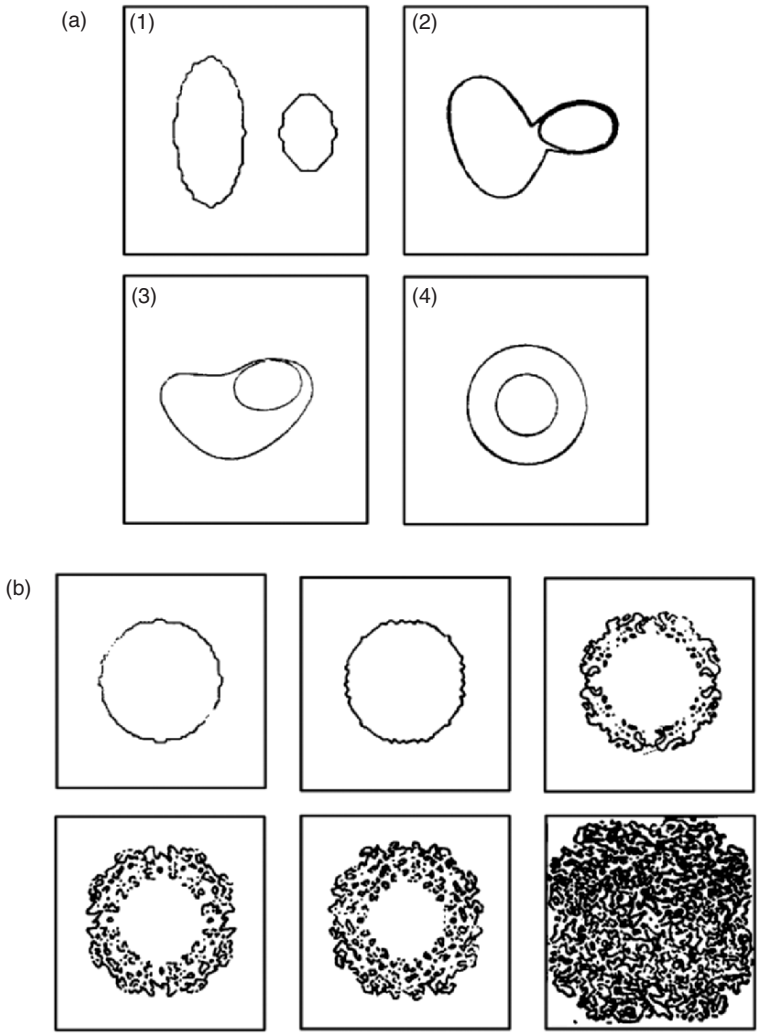


**Fig. 9.6.** Evolution of the two-dimensional vorticity field. (**a**) Addition of energy into the vorticity field; (**b**) subtraction of energy from the vorticity field. From Carnevale and Vallis (1990)

The evolution of a vortex system by energy addition is shown in Fig. 9.6a. The initial vorticity distribution of the system is two elliptical vortex patches of the same sign. They eventually evolve to a circular vortex with concentric vorticity distribution: the stronger vorticity patch is surrounded by the weaker one. Opposite to this trend, the evolution of a vortex system by energy subtraction is shown in Fig. 9.6b. The initial circular vortex patch evolves to a constant vorticity distribution ("Kelvin sponge"). Note that this nonlinear stabilizing approach to circulation-preserving flows offers a theoretical guidance for vortex control.

The Arnold theory has now been extended to two-dimensional inviscid, isentropic, and compressible flow. However, extension of the theory to three dimensions has never been successful. Recent studies (Rouchon 1991; Sadun and Vishik 1993) have indicated that in three dimensions the sign of $\delta^2 K$ is usually uncertain, of which the physical root is vortex stretching.

### 9.1.4 Linearized Disturbance Lamb Vector and the Physics of Instability

Since our concern is the instability of free and attached vortex layers and vortices, it is informative to make a general identification of the vorticity-dynamic mechanisms responsible for the linear instability, both normal and non-normal.

The curl of (9.23) yields the disturbance vorticity equation

$$\frac{\partial \boldsymbol{\omega}}{\partial t} + \nabla \times \boldsymbol{L} = \nu \nabla^2 \boldsymbol{\omega}, \tag{9.37}$$

where by (9.26) the only nonlinear term is $\nabla \times (\boldsymbol{\omega} \times \boldsymbol{u}) = \boldsymbol{u} \cdot \nabla \boldsymbol{\omega} - \boldsymbol{\omega} \cdot \nabla \boldsymbol{u}$ that represents the convection and stretching/tilting of disturbance vorticity by disturbance velocity. Within the linear approximation, therefore, in addition to a viscous diffusion the key to the stability of a vortical flow is $\nabla \times (\boldsymbol{\Omega} \times \boldsymbol{u} + \boldsymbol{\omega} \times \boldsymbol{U})$. To see the respective roles of these two terms, similar to the fractional-step approach to the vorticity-based formulation of viscous flow problems (Sect. 4.5.3), we follow Orszag and Patera (1983; see also Huerre and Rossi 1998) to split the inviscid and linearized version of (9.37) into two sub-processes, each being driven by one term

$$A: \quad \frac{\partial \boldsymbol{\omega}}{\partial t} = -\nabla \times (\boldsymbol{\Omega} \times \boldsymbol{u}) = \boldsymbol{\Omega} \cdot \nabla \boldsymbol{u} - \boldsymbol{u} \cdot \nabla \boldsymbol{\Omega}, \tag{9.38a}$$

$$B: \quad \frac{\partial \boldsymbol{\omega}}{\partial t} = -\nabla \times (\boldsymbol{\omega} \times \boldsymbol{U}) = \boldsymbol{\omega} \cdot \nabla \boldsymbol{U} - \boldsymbol{U} \cdot \nabla \boldsymbol{\omega}. \tag{9.38b}$$

From (9.26) and (9.27), it is immediately evident that for process $A$ there is $\mathrm{d}K_v/\mathrm{d}t = 0$. Thus, by (9.38a) this process can only redistribute the disturbance kinetic energy over the flow via the convection, stretching, and tilting of $\boldsymbol{\Omega}$ by $\boldsymbol{u}$. In contrast, any increase of $K_v$ must be solely from process $B$, which by (9.38b) is the convection, stretching, and tilting of $\boldsymbol{\omega}$ by $\boldsymbol{U}$, during

which the disturbance may absorb energy from the basic flow to enhance itself and lead to instability.

To demonstrate these roles, assume the basic flow is in the $(x, y)$-plane and along the $x$-direction

$$\boldsymbol{U}(x, y) = \mathbf{e}_x U(x, y), \quad \boldsymbol{\Omega} = \Omega \mathbf{e}_z,$$

and denote the disturbance velocity and vorticity components by $\boldsymbol{u} = (u, v, w)$ and $\boldsymbol{\omega} = (\xi, \eta, \zeta)$. As always, we denote a vector on the $(x, y)$-plane by suffix $\boldsymbol{\pi}$. In process $A$, in addition to the stretching of $\boldsymbol{\Omega}$ by $\partial w/\partial z$, the tilting

$$\boldsymbol{\Omega} \cdot \nabla \boldsymbol{u}_\pi = \Omega \frac{\partial \boldsymbol{u}_\pi}{\partial z}$$

produces *new* disturbance vorticity $\boldsymbol{\omega}_\pi = (\xi, \eta)$ as a consequence of three-dimensional disturbance. This process stops once $\boldsymbol{u}_\pi$ becomes $z$-independent. Then, in the context of the secondary instability of a shear flow, Orszag and Patera (1983) use an elegant argument to prove that process $B$ will cause a transient increase of the newly produced $\boldsymbol{\omega}_\pi$ and turn it to the basic-flow direction, which stops once the alignment is complete. Thus, neither $A$ nor $B$ alone can lead to instability but only a combination of both can, in which process $A$ continuously produces $\boldsymbol{\omega}_\pi$ from $\Omega \mathbf{e}_z$ so that process $B$ is able to continuously amplify $\boldsymbol{\omega}_\pi$ and tilt it to streamwise direction.

The role of process $B$ can be demonstrated analytically for a unidirectional shear flow $U(y)$ with $\Omega = -\mathrm{d}U/\mathrm{d}y$. Then (9.38b) yields

$$\frac{\partial \xi}{\partial t} + U \frac{\partial \xi}{\partial x} = -\eta \Omega, \tag{9.39a}$$

$$\frac{\partial \eta}{\partial t} + U \frac{\partial \eta}{\partial x} = 0, \tag{9.39b}$$

$$\frac{\partial \zeta}{\partial t} + U \frac{\partial \zeta}{\partial x} = 0. \tag{9.39c}$$

Let $\xi + \mathrm{i}\eta = \omega_\pi \mathrm{e}^{\mathrm{i}\theta}$ and $\tau = x + Ut$ such that (9.39a) and (9.39b) become

$$\frac{\mathrm{d}}{\mathrm{d}\tau}(\ln \omega_\pi) \cos\theta - \frac{\mathrm{d}\theta}{\mathrm{d}\tau} \sin\theta = -\frac{\Omega}{2U} \sin\theta,$$

$$\frac{\mathrm{d}}{\mathrm{d}\tau}(\ln \omega_\pi) \sin\theta + \frac{\mathrm{d}\theta}{\mathrm{d}\tau} \cos\theta = 0,$$

which can be cast to

$$\frac{\mathrm{d}\theta}{\mathrm{d}\tau} = -\alpha \sin^2\theta, \quad \frac{\mathrm{d}}{\mathrm{d}\tau}(\ln \omega_\pi) = \frac{1}{2}\alpha \sin 2\theta, \tag{9.40}$$

where $\alpha \equiv -\Omega/2U$. Hence, as long as $\omega_\pi \neq 0$, one obtains

$$\theta = \cot^{-1}[\alpha(\tau - \tau_0)], \quad \omega_\pi = \omega_{\pi 0} \sqrt{1 + \alpha^2(\tau - \tau_0)^2}, \tag{9.41}$$

where $\tau_0$ and $\omega_{\pi 0}$ are integration constants corresponding to $\theta_0 = \pi/2$. Therefore, as $t$ and/or $x$ increases unboundedly, $\theta$ tends to zero or $\boldsymbol{\omega}_\pi$ is aligned to the $\boldsymbol{U}$ direction, and $|\boldsymbol{\omega}_\pi|$ increases algebraically. Here, (9.39a) indicates that the strong shear $U'(y) = -\Omega$ is the major mechanism to form the streamwise vorticity $\xi$ by process B; but in so doing there must be $\eta \neq 0$, which is prepared by the $y$-component of (9.38a) in process A

$$\frac{\partial \eta}{\partial t} = \Omega \frac{\partial v}{\partial z}, \tag{9.42}$$

that tilts the vorticity in basic flow to the $y$-direction, as long as $\partial v/\partial z \neq 0$.

It should be stressed that the linear operators contained in processes A and B are both non-normal. Indeed, in operator form, we have

$$-(\boldsymbol{\Omega} \times \boldsymbol{u})_i = L^{(1)}_{ik} u_k, \quad L^{(1)}_{ik} = -\epsilon_{ijk}\Omega_j, \tag{9.43}$$

$$-(\boldsymbol{\omega} \times \boldsymbol{U})_i = L^{(2)}_{ik} u_k, \quad L^{(2)}_{ik} = U_k \partial_i - \delta_{ik} U_j \partial_j, \tag{9.44}$$

where $L^{(1)}$ is antisymmetric and $L^{(2)}$ is neither symmetric nor antisymmetric. Therefore, we conclude that the disturbance Lamb vector is the physical source of various hydrodynamic instability and implies a non-normality of the stability operator. A complete analysis of linear stability or instability can be made only if the disturbance Lamb vector is fully considered (along with the viscous diffusion operator), otherwise certain instability mechanisms may be missing. The disturbance-energy consideration alone is insufficient, since it only involves a scalar process but the real physics involves vector processes.

## 9.2 Shear-Flow Instability

Having reviewed the basic concepts and theories of general flow stability, we now consider the stability of shear flows and swirling flows by applying some of those theories, including both normal-mode (temporal and AI/CI) and nonmodal analyses.

### 9.2.1 Instability of Parallel Shear Flow

Parallel shear flow is a prototype of various vortex layers with vorticity concentration in one spatial dimension, which includes the plan Couette flow, the plan Poiseuille flow, and the Poiseuille flow in a circular pipe. Nearly parallel flows include boundary layers, jets, wakes, and free shear layers. In stability analysis the latter can also be regarded as parallel as first approximation.

Let the basic parallel shear flow be given by

$$\boldsymbol{U} = U(y)\boldsymbol{e}_x, \tag{9.45}$$

so that the disturbed flow is

$$\boldsymbol{u}^* = (U(y), 0, 0) + (u, v, w). \tag{9.46}$$

The linearized disturbance equations for normal velocity $v$ and normal vorticity $\eta$ are (4.184a) and (4.184b)

$$\left(\frac{\partial}{\partial t} + U\frac{\partial}{\partial x} - \nu\nabla^2\right)\nabla^2 v = \frac{\mathrm{d}^2 U}{\mathrm{d}y^2}\frac{\partial v}{\partial x}, \tag{9.47}$$

$$\left(\frac{\partial}{\partial t} + U\frac{\partial}{\partial x} - \nu\nabla^2\right)\eta = -\frac{\mathrm{d}U}{\mathrm{d}y}\frac{\partial v}{\partial z}. \tag{9.48}$$

The boundary conditions are, taking the channel flow between parallel plates as example,

$$v = \frac{\partial v}{\partial y} = 0, \quad \eta = 0, \quad \text{at} \quad y = \pm 1. \tag{9.49}$$

Introducing normal modes

$$v(\boldsymbol{x}, t) = \hat{v}(y, t)\mathrm{e}^{\mathrm{i}\alpha x + \mathrm{i}\beta z}, \quad \eta(\boldsymbol{x}, t) = \hat{\eta}(y, t)\mathrm{e}^{\mathrm{i}\alpha x + \mathrm{i}\beta z} \tag{9.50}$$

to (9.47) and (9.48), and denoting $D = \partial/\partial y$ and $k^2 = \alpha^2 + \beta^2$, in matrix operator form we obtain

$$\frac{\partial}{\partial t}\begin{bmatrix}\hat{v}\\ \hat{\eta}\end{bmatrix} = -\mathrm{i}\begin{bmatrix}L_{\mathrm{os}} & 0\\ L_{\mathrm{c}} & L_{\mathrm{sq}}\end{bmatrix}\begin{bmatrix}\hat{v}\\ \hat{\eta}\end{bmatrix}, \tag{9.51}$$

where, with $U' = \mathrm{d}U/\mathrm{d}y$,

$$L_{\mathrm{os}} = -\frac{1}{(D^2 - k^2)}\left[\frac{(D^2 - k^2)^2}{\mathrm{i}Re} - \alpha U(D^2 - k^2) + \alpha U''\right], \tag{9.52a}$$

$$L_{\mathrm{c}} = \beta D U, \tag{9.52b}$$

$$L_{\mathrm{sq}} = \alpha U - \frac{D^2 - k^2}{\mathrm{i}Re} \tag{9.52c}$$

are called the *Orr–Sommerfeld operator*, the *coupling operator*, and the *Squire operator*, respectively, since the differential equations for $\widehat{v}$ and $\widehat{\eta}$ are known as the *Orr–Sommerfeld equation* and *Squire equation*, respectively, which are coupled by $L_c$ for three-dimensional disturbances.

Squire (1933) obtained a transformation that can convert any three-dimensional normal-mode disturbance to an equivalent two-dimensional one. He then proved that the parallel shear flows first become unstable to two-dimensional disturbance wave at a value of the Reynolds number smaller than any value for which three-dimensional disturbances can grow. Thus, to find sufficient condition of flow instability, one only needs to consider two-dimensional disturbance.[2] In this case $L_{\mathrm{c}} = 0$ and $\eta = 0$, and hence one only

[2] It has to be stressed that since the Squire theorem is proved within the normal-mode analysis, it is no longer effective whenever the operator non-normality is involved. But even the Orr–Sommerfeld operator alone is non-normal as well, as seen from (9.41) and (9.42). This non-normality effect will be discussed in Sect. 9.2.4.

needs to work on the Orr–Sommerfeld equation. Then, let the stream function $\psi(x, y, t)$ take the form

$$\psi(x, y, t) = \varphi(y) \exp(\mathrm{i}\alpha(x - ct)) \tag{9.53}$$

and substitute into (9.51), we obtain the conventional form of the Orr–Sommerfeld equation

$$(\mathrm{i}\alpha Re)^{-1}(D^2 - \alpha^2)^2\varphi = (U - c)(D^2 - \alpha^2)\varphi - U''\varphi. \tag{9.54}$$

The boundary condition (9.49) now reads

$$\varphi = D\varphi = 0 \quad \text{at} \quad y = \pm 1. \tag{9.55}$$

For inviscid flow, set $Re \to \infty$, (9.54) degenerates to

$$(U - c)(\varphi'' - \alpha^2\varphi) - U''\varphi = 0, \tag{9.56}$$

called the *Rayleigh equation*. In an inviscid flow where $U(y)$ can be arbitrary assumed, by (9.56) Rayleigh (1880) stated that an inviscid parallel flow $U(y)$ is unstable only if there is an interior point $y_s$ where $U''(y_s) = 0$, i.e., the velocity profile has an inflectional point or the vorticity $\Omega = -U'$ has an extremum (known as the *Rayleigh theorem*). This condition was later sharpened by Fjørtoft (1950) by adding a requirement that $U''(U - U_s) \leq 0$ in certain interval of $y$, where $U_s = U(y_s)$ (known as the *Fjørtoft theorem*). For the proof of these theorems see Drazin and Reid (1981). Now, it can be shown that the latter is equivalent to a physically more appealing condition (Yin and Sun 2003), which we state as:

**The Fjørtoft theorem.** *The necessary condition for an inviscid parallel shear flow to be unstable is that inside the flow the vorticity has a maximum where $\Omega > 0$ or a minimum where $\Omega < 0$.*

To demonstrate these theorems, six types of velocity and vorticity distributions are shown in Fig. 9.7. In Figs. 9.7a and 9.7b the flows have no vorticity extremum, so they are inviscidly stable. Fig. 9.7c and 9.7d have vorticity extremum, and hence by Rayleigh's condition they should be unstable. However, according to Fjørtoft, only the flow in Fig. 9.7d is unstable where $\Omega < 0$, and it has a minimum. The case (e), (f) are similar to (c), and (d). For case (f) there is $\Omega > 0$, and it has a maximum, so this case is unstable.

Tollmien (1935) has shown that the instability conditions of the Fjørtoft theorem become sufficient for symmetric profiles in a channel or monotone profiles in a boundary layer.

More generally, the Fjørtoft theorem can be recovered and extended by the Arnold stability theorem (Sect. 9.1.3). In (9.33) we now have

$$U = \frac{\mathrm{d}\psi}{\mathrm{d}y}, \quad \omega = -\Delta\psi = -U', \quad \frac{\mathrm{d}(\Delta\psi)}{\mathrm{d}y} = U''.$$

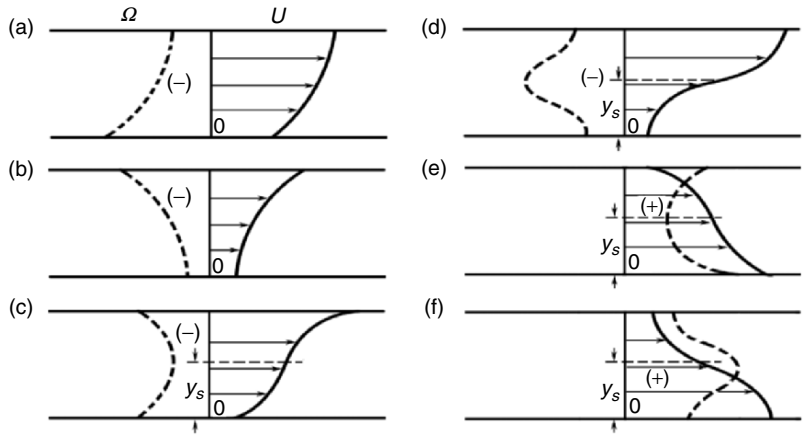


**Fig. 9.7.** Velocity and vorticity profiles for the parallel shear flows: (**a**) stable; (**b**) stable; (**c**) stable according to Fjørtoft; (**d**) unstable according to Fjørtoft; (**e**) stable according to Fjørtoft; (**f**) unstable according to Fjørtoft

Thus in the flows of Figs. 9.7a and 9.7b, the sign of $\mathrm{d}(\Delta\psi)/\mathrm{d}\psi$ does not change. Then one can always make the sign of $\mathrm{d}\psi$ the same as that of $\mathrm{d}(\Delta\psi)$ through a Galilean transformation (which does not alter the stability behavior[3]), such that (9.34) holds. Hence both flows are stable. Then, in the case of Fig. 9.7c, one can nullify the velocity at the inflection through a Galilean transformation so that $U - U_s = 0$ and the sign of $\mathrm{d}\psi$ is the same as that of $\mathrm{d}(\Delta\psi)$, and hence the flow is stable according to the Arnold theorem. Thus, the theorem not only extends the Rayleigh–Fjørtoft theorem to nonlinear regime but also yields the *sufficient condition for a parallel shear flow to be stable*. In contrast, for the case shown in Fig. 9.7d, the sign of $\mathrm{d}\psi$ is opposite to that of $\mathrm{d}(\Delta\psi)$ and the flow is inviscidly unstable, as asserted by the Fjørtoft theorem.

### 9.2.2 Instability of free shear flow

Stability analyses on free shear flows originated from the pioneering works of Helmholtz (1868) and Kelvin (1871), and thus named as *Kelvin–Helmholtz instability*. In recent decades, experimental, theoretical and numerical studies on the stability of the free shear layers have been extremely active. Organized spanwise vortex structures have been found in experiments after free shear flow becomes unstable, followed by vortex pairing and tearing due to their interactions. These processes are associated with three-dimensional vortical structures including streamwise vortices. The spanwise vortical structures due to the Kelvin–Helmholtz instability can survive up to an Reynolds number as high as $10^7$; and other organized structures can also be observed in mixing

[3] But the AI/CI behavior depends on the frame of reference, see Sect. 9.3.1.

layers. Hence, the investigation on the formation and evolution of the ordered vortical structures in free shear flows will offer important analogy and hint to the analysis of coherent structures in turbulence.

Moreover, the interaction between spanwise vortices and streamwise vortices may modify the structure of a shear layer, thickening it, enhancing the mixing between the fluids with different ingredients or concentrations, or enhancing chemical reactions. The study of the stability of free shear flows can therefore provide important physical insight for flow control and guidance in fluid machinery design.

To illustrate the instability mechanism of free shear flows, consider the simplest basic flow, an inviscid incompressible flow consisting of two layers with different velocities:[4]

$$(\boldsymbol{U}, \rho) = \begin{cases} U_2 \boldsymbol{e}_x & \text{for} \quad y \geq 0, \\ U_1 \boldsymbol{e}_x & \text{for} \quad y < 0, \end{cases} \tag{9.57}$$

which has a flat vortex sheet at $y = 0$. Assuming that the flows in both upper and lower regions are irrotational (reasonable for instability analysis), with potentials

$$\phi(z) = \begin{cases} \phi_2 & : \quad y \geq \zeta, \\ \phi_1 & : \quad y < \zeta, \end{cases} \tag{9.58}$$

where $y = \zeta(x, t)$ is the elevation of the disturbed vortex sheet. Substituting the normal mode decomposition

$$(\zeta, \phi_1, \phi_2) = (\hat{\zeta}, \hat{\phi_1}, \hat{\phi_2}) \exp(\mathrm{i}(\alpha x + \beta z) + st) \tag{9.59}$$

into the inviscid version of (9.47) and the corresponding boundary conditions, for the eigenvalue of $s$ one obtains

$$s = \mathrm{i}k\overline{U} \pm \frac{1}{2} k[\![U]\!], \tag{9.60}$$

where $\overline{U} = (U_1 + U_2)/2$ is the mean basic-flow velocity. Hence,

$$(\zeta, \phi_1, \phi_2) = (\hat{\zeta}, \hat{\phi_1}, \hat{\phi_2}) \mathrm{e}^{(1/2)k[\![U]\!]t} \mathrm{e}^{\mathrm{i}(\alpha x + \beta z + k\overline{U}t)}, \tag{9.61}$$

indicating that *a free flat vortex sheet is always inviscidly unstable*. Disturbance waves with any wavelength must be amplified and will propagate downstream with speed of $c = \overline{U}$.

The Kelvin–Helmholtz instability of a vortex sheet can well be explained in terms of vorticity (Batchelor 1967). Introduce transformation

$$kx' = \alpha x + \beta z, \quad kz' = -\beta x + \alpha z,$$

[4] Here we omit the case with density difference and gravitational effect, which can be easily added; e.g., Drazin and Reid (1981) and Drazin (2002).

such that the disturbed flow becomes two-dimensional on the $(x', y)$-plane. Then by using (4.129a) and $(\boldsymbol{e}'_x, \boldsymbol{e}'_z) = (\nabla x', \nabla z')$, for the vortex-sheet strength $\boldsymbol{\gamma}$ we obtain

$$\boldsymbol{\gamma} = \gamma \boldsymbol{e}'_z, \quad \gamma = -\mathrm{i}k[\![\hat{\phi}]\!]\mathrm{e}^{(1/2)k[\![U]\!]t}\mathrm{e}^{\mathrm{i}(kx'+k\overline{U}t)}. \tag{9.62}$$

Notice that (9.61) and (9.62) imply a phase lag of $\pi/2$ between $\zeta$ fluctuation and $\gamma$. In Fig. 9.8, the thick solid curve shows the periodical deformation of the vortex sheet, and its varying thickness denotes the accumulation (e.g., around point $A$) or rarefication (e.g., around point $C$) of the disturbance vorticity. Thus, according to the Biot–Savart law, the segment of vortex sheet around $A$ with $\zeta > 0$ must move downward and will induce a negative velocity component in the $x$ direction. This action is the most obvious at point $B$ to make it move towards $A$ and hence strengthen the sinusoidal deformation of the sheet. The more the vortex sheet deforms, the more accumulation of vorticity disturbance around $A$ will occur. This mechanism develops a positive feedback and leads to exponential growth of disturbances.

Consider now a vortex layer with finite thickness, a commonly used basic-flow profile is

$$U(y) = \overline{U}\left(1 + Ra\tanh\left(\frac{y}{2\theta}\right)\right). \tag{9.63}$$

Here, the velocity ratio $Ra = (U_1 - U_2)/2\overline{U}$ represents the shear level of the basic flow. The flows with $Ra = 0$ and 1 correspond to a wake and a jet, respectively. $\theta$ is the momentum thickness that is the only length scale that one can get in the two-dimensional free shear layer. Monkewitz and Huerre (1982) have calculated the spatial growth rates of disturbances with tanh and Blasius velocity profiles, and found that the growth rate $(-\alpha_i\theta/Ra)$ and phase velocity $c_r/\overline{U} = \omega/(\alpha_r\overline{U})$ are both related to the Strouhal number $St = f\theta/\overline{U}$ ($f$ is the frequency of disturbance). The most amplified wave corresponds to $St = 0.032$, with the corresponding natural frequency $f_n$ of the mixing layer. For all the cases from $Ra = 0$ to $Ra = 1$, the variation of $St_n$ is within 5% only (see Fig. 9.9).

The linear stability theory of free shear flows describes the initial stage of the Kelvin–Helmholtz instability. Its prediction of the growth rate and the

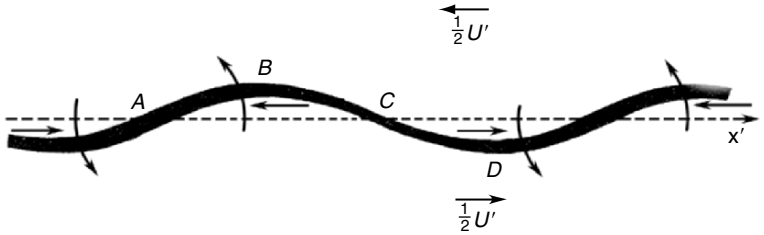


**Fig. 9.8.** The instability of a vortex sheet on the $(x', y)$-plane. From Batchelor (1967)

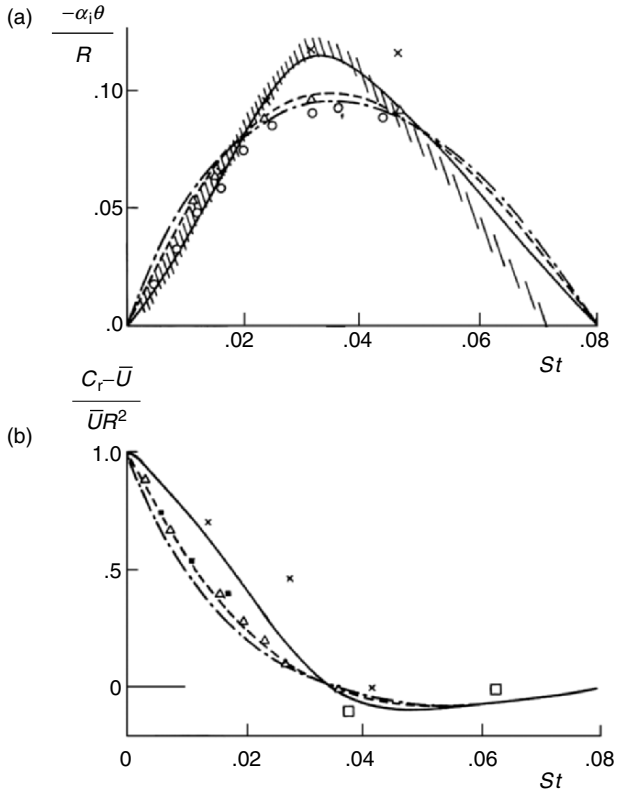


**Fig. 9.9.** Variation of (**a**) normalized amplification rate and (**b**) normalized phase velocity with Strouhal number $St = f\theta/\overline{U}$. From Ho and Huerre (1984)

phase velocity of the instability waves agrees well with experiments. After that stage, the shear layer will quickly roll up to form a row of spanwise vortices as the consequence of Kelvin–Helmholtz instability. The later development of vortical structures will be addressed in Sect. 10.2.

In reality an unstable free vortex layer is often under a strain field. Neu (1984b) has studied this interesting and complicated problem.

### 9.2.3 Instability of Boundary Layer

It is well known that, as the Reynolds number increases, a laminar boundary layer will become turbulent through transition. Reynolds was the first to realize that transition is caused by boundary-layer instability. He then developed this concept into a theory, see (9.23). However, the boundary-layer instability alone does not immediately lead to turbulence; it involves a series of complicated transitional processes.

Consider a flat-plate boundary layer in a uniform incompressible free stream. The flow near the leading edge is laminar, and the local Reynolds number $Re_x$ increases as $x$. Once $Re_x$ passes a critical value, the flow will lose its stability and there will appear two-dimensional travelling waves, known as the *Tollmien–Schlichting waves*, which propagate downstream with certain frequencies, wavelengths and growing amplitudes. The neutral curve for the Blasius boundary layer is shown in Fig. 9.10.

Tani (1969) has correctly called the Tollmien–Schlichting wave as *vorticity wave*. Indeed, a boundary layer is an attached vortex layer with continuous vorticity distribution (Sect. 4.3). The vorticity in a shear layer always tends to organize itself into vortical structures. This tendency is suppressed by the vorticity diffusion. However, toward downstream the boundary layer is thickened, the vorticity diffusion becomes weaker due to progressively smaller vorticity gradient. Sufficiently far downstream from the leading edge, the tendency of forming organized structure will overcome the diffusion effect.

Because only infinitesimal disturbances are considered, the prediction of linear stability on the growth rate of selective Tollmien–Schlichting waves is effective only in the region close to the neutral curve. Nonlinear theory is necessary after the disturbances have grown to certain level, see Stuart (1963), Craik (1971), Itoh (1974, 1980), Herbert (1975), Zhou (1982) and Zhou and Zhao (2004).

During the downstream propagation of the Tollmien–Schlichting waves, two-dimensional disturbances will gradually evolve to three-dimensional ones, which lead to streamwise vortices in the boundary layer, characterized by their axes parallel to the free-stream direction and each neighboring pair of vortices being counter-rotating. The streamwise vortices or rolls have been identified

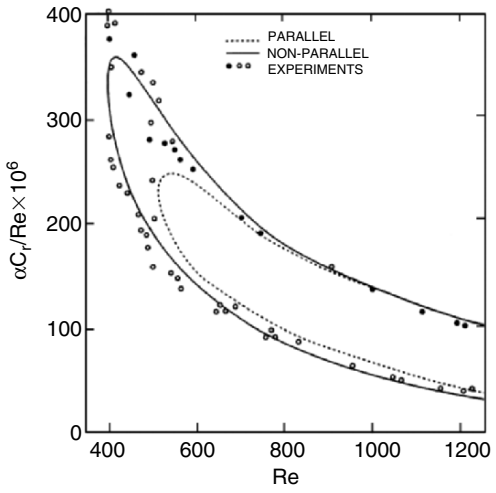


**Fig. 9.10.** The curve of the neutral stability of the Blasius boundary-layer profile. From Saric and Nayfeh (1975)

as the dominant vortical structure in the boundary layer. The appearance of streamwise vortices modifies the mean velocity distribution in the boundary layer and induces the so-called *secondary instability*. A detailed description of the boundary-layer transition process including secondary instability, and the corresponding vortical structures, will be given in Sect. 10.3.

### 9.2.4 Non-Normal Effects in Shear-Flow Instability

On the basis of the general discussion of the nonmodal instability, we can now analyze in more detail the relation between the operator non-normality and flow instability in parallel shear flow, for which the relevant operators are given by (9.52). It is known that for the plane Couette flow with $U = y$, the normal-mode analysis fails to find any linear instability, contradicting experimental results. Within linear theory, to this paradox there have appeared two interpretations, both in terms of the operator non-normality.

The first interpretation is the transient growth in the $v$-equation (9.47), first studied by Orr in 1907. This *Orr mechanism* has been thoroughly studied by Case (1960) for inviscid Couette flow by solving an initial-value problem. He found that the plane Couette flow has only a continuous spectrum that is ignored in the normal-mode approach. The disturbance has transient growth and then decays as $t^{-1}$ or faster. Case also proves that the solution of the initial-value problem has just the form of a conventional normal mode expansion, indicating that the latter is complete as later generally proved by DiPrima and Habetler (1969).

A more powerful transient-growth mechanism than the Orr mechanism is in the $\eta$-equation (9.48) or (9.51), where the coupling operator $L_{\mathrm{c}}$ connects the variable $v$ in (9.47) to (9.48) as an inhomogeneous term. It exists for three-dimensional disturbances only and is the main source of the eigen-mode non-orthogonality in the linearized Navier–Stokes equations. As a simplified mathematic model of (9.51) to illustrate this mechanism, Waleffe (1995a) considers a pair of linear equations

$$\frac{\mathrm{d}}{\mathrm{d}t}\begin{bmatrix} v \\ \eta \end{bmatrix} = \begin{bmatrix} -\lambda & 0 \\ 1 & -\mu \end{bmatrix}\begin{bmatrix} v \\ \eta \end{bmatrix}, \tag{9.64}$$

where $\lambda$, $\mu > 0$ of $\mathrm{O}(Re^{-1})$ are decay rates. The solution of (9.64) is

$$v(t) = v(0)\mathrm{e}^{-\lambda t} \tag{9.65a}$$

$$\eta(t) = -v(0)\frac{\mathrm{e}^{-\lambda t} - \mathrm{e}^{-\mu t}}{\lambda - \mu} + \eta(0)\mathrm{e}^{-\mu t}. \tag{9.65b}$$

The first term on the right-hand side of (9.65b) grows algebraically like $t$ at small times and decays exponentially at large times. The maximum amplification is at $t^* = (\ln\lambda - \ln\mu)/(\lambda - \mu)$, with

$$\eta_{\max} = v(0)\frac{\mathrm{e}^{-\mu t^*}}{\lambda} = \mathrm{O}(\epsilon Re). \tag{9.66}$$

The transient algebraic growth caused by the non-normality of linear systems has been studied by, e.g., Trefethen et al. (1993), Waleffe (1995a,b), and Baggett and Trefethen (1997). The last paper summarizes various low-dimension dynamic system models proposed by five research groups for parallel shear flows at various high Reynolds numbers. These models confirm that when $Re \to \infty$, the threshold value for a disturbance to cause subcritical transition is $\epsilon = \mathrm{O}(Re^{-\alpha})$ with $\alpha > 1$. Actually, the subcritical transition in a real flow can be triggered by a very small disturbance, and this kind of dynamic characteristics does result from the joint effects of linear non-normality and nonlinearity.

The respective effects on physical turbulence of the linear non-normal and nonlinear operators in the full Navier–Stokes equation (adding nonlinear operators $N_v$ and $N_\eta$ to (9.51)),

$$\frac{\partial}{\partial t}\begin{bmatrix}\hat{v}\\ \hat{\eta}\end{bmatrix} = -\mathrm{i}\begin{bmatrix}L_{\mathrm{os}} & 0\\ L_{\mathrm{c}} & L_{\mathrm{sq}}\end{bmatrix}\begin{bmatrix}\hat{v}\\ \hat{\eta}\end{bmatrix} + \begin{bmatrix}N_v(\widehat{v},\widehat{\eta})\\ N_\eta(\widehat{v},\widehat{\eta})\end{bmatrix}, \tag{9.67}$$

have been examined by Kim and Lim (2000) by a direct numerical simulation of a fully developed turbulent channel flow at turbulence Reynolds number $Re_\tau = u_\tau h/\nu = 100$, where $h$ is the width of the channel. Kim and Lim divided the channel into upper and lower portions in their simulation. The governing equation for the upper portion was a modified Navier–Stokes equation, where the coupling operator $L_{\mathrm{c}}$ was turned off, so that the strong non-normality mechanism of the operator is absent. The governing equation for the lower portion remained the full Navier–Stokes equation. The initial condition was a regular channel turbulence. The variation of mean shear stress with time on both channel walls is shown in Fig. 9.11. Obviously, without $L_{\mathrm{c}}$ the turbulent shear stress cannot be maintained.

For further illustration, the left column of Fig. 9.12 shows the contours of streamwise vorticity on the $(y, z)$-plane at different times. We see that at large time the streamwise vorticity in the upper portion disappears. The reduction of wall shear stress and streamwise vorticity implies a reduction of turbulence intensity. This example well demonstrates that the operator non-normality is necessary for maintaining turbulence intensity even in a fully developed turbulent flow.

Kim and Lim (2000) carried out an even more interesting numerical experiment for the same fully developed turbulent channel flow, but the initial condition was changed to random disturbances instead of organized turbulence structures. Three cases were simulated as shown at the right column of Fig. 9.12, of which the streamwise vorticity contours are at $t = 80$. The full Navier–Stokes equation was applied for case (a); $L_{\mathrm{c}}$ was turned off for case (b); and the nonlinear operators $N_v$ and $N_\eta$ were turned off in case (c). For case (b), the streamwise vorticity disappears very quickly in particular near the wall. For case (c) the random vorticity distribution is replaced by some larger spanwise-scale structures. These simulations clearly emphasize

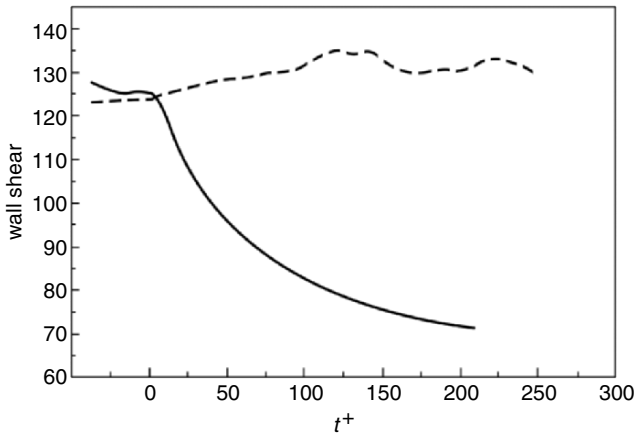


**Fig. 9.11.** Time evolution of mean shear at wall: *solid line* is for the upper wall, and the *dashed line* is for lower wall. From Kim and Lim (2000)

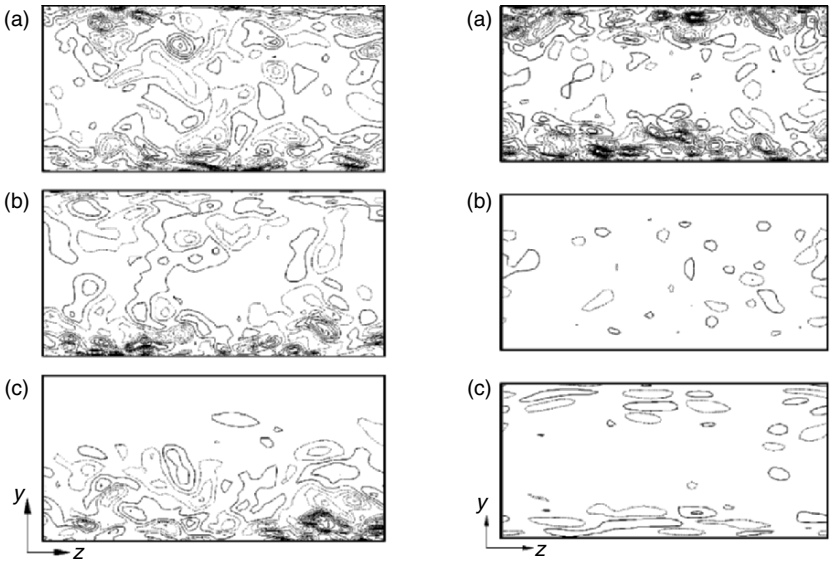


**Fig. 9.12.** Contour of streamwise vorticity on a $y$-$z$ plane from two numerical experiments of channel turbulence. *Left*: Evolution as time, where in the upper portion $L_c$ is dropped. (**a**) $t = 0$; (**b**) $t = 20$; (**c**) $t = 200$. *Right*: Effect of different operators at $t = 80$. (**a**) Full Navier–Stokes; (**b**) linear coupling operator $L_c$ is turned off; (**c**) nonlinear operator $N_v$ and $N_\eta$ are turned off. From Kim and Lim (2000)

the important role of both non-normality and nonlinearity in sustained wall turbulence. In short, turbulence cannot be formed without nonlinearity and wall-layer structures cannot be formed without non-normality. Lacking either mechanism, turbulence would cease to exist.

## 9.3 Instability of Axisymmetric Columnar Vortices

Beginning from this section, we discuss the stability character of columnar vortices. Some of these vortices contain axial flow and are also called *swirling flow* or *swirling vortex*. A vortex without axial flow is called a *pure vortex* (Chap. 6). In this section, we consider the instability of an isolated and axisymmetric vortex without axial stretching, mainly its linear normal-mode instability including temporal, spatial, and temporal–spatial modes. A formally nonlinear stability theory for a pure vortex and the nonmodal instability of a vortex will also be briefly discussed.

Since the basic flow is axisymmetric without axial stretching, its velocity profiles take the form $\boldsymbol{U} = (0, V(r), W(r))$ in cylindrical coordinates $(r, \theta, z)$. Then from (6.2) to (6.4) the linearized disturbence equations read

$$\frac{\partial u}{\partial r} + \frac{u}{r} + \frac{1}{r}\frac{\partial v}{\partial \theta} + \frac{\partial w}{\partial z} = 0, \tag{9.68a}$$

$$\frac{\partial u}{\partial t} + \frac{V}{r}\frac{\partial u}{\partial \theta} + W\frac{\partial u}{\partial z} - 2\frac{Vv}{r} = -\frac{\partial p}{\partial r} + \nu\left(\Delta u - \frac{u}{r^2} - \frac{2}{r^2}\frac{\partial v}{\partial \theta}\right), \tag{9.68b}$$

$$\frac{\partial v}{\partial t} + u\frac{\mathrm{d}V}{\mathrm{d}r} + \frac{V}{r}\frac{\partial v}{\partial \theta} + W\frac{\partial v}{\partial z} + \frac{uV}{r} = -\frac{1}{r}\frac{\partial p}{\partial \theta} + \nu\left(\Delta v - \frac{v}{r^2} + \frac{2}{r^2}\frac{\partial u}{\partial \theta}\right), \tag{9.68c}$$

$$\frac{\partial w}{\partial t} + u\frac{\mathrm{d}W}{\mathrm{d}r} + \frac{V}{r}\frac{\partial w}{\partial \theta} + W\frac{\partial w}{\partial z} = -\frac{\partial p}{\partial z} + \nu\Delta w, \tag{9.68d}$$

where $\Delta = \partial^2/\partial r^2 + 1/r\partial/\partial r + 1/r^2\partial^2/\partial\theta^2 + \partial^2/\partial z^2$.

### 9.3.1 Stability of Pure Vortices

For normal-mode analysis, we write

$$(u, v, w, p) = (\mathrm{i}F(r), G(r), H(r), P(r))\,\mathrm{e}^{\mathrm{i}(kz+n\theta-\omega t)}, \tag{9.69}$$

where $F(r), G(r), H(r), P(r)$ are amplitude functions with the factor $i$ of $F(r)$ expressing the phase difference between the velocity components; $k$ and $n$ are axial and circumferential wave numbers, respectively. An axisymmetric disturbance corresponds to $n = 0$ and a spiral mode has $n \neq 0$.

Consider the inviscid instability of a pure vortex $\boldsymbol{U} = (0, V(r), 0)$. Based on the angular-momentum conservation, Rayleigh (1916) found that the criterion

$$\frac{\mathrm{d}\Gamma^2}{\mathrm{d}r} = \frac{\mathrm{d}}{\mathrm{d}r}(rV)^2 > 0, \quad \Gamma = rV, \tag{9.70}$$

is a sufficient condition for the vortex to be stable to an axisymmetric disturbance. By a more rigorous mathematical analysis, Synge (1933) has proved that (9.70) is actually a sufficient and necessary condition.

Similar to the Rayleigh–Fjørtoft theorem for parallel shear flows (Sect. 9.2.1), we can also find that the necessary condition for a pure vortex to be unstable to nonaxisymmetric disturbances is the existence of mean vorticity extremum, i.e. the mean vorticity gradient becomes zero at certain location inside the flow field.

Consider the simplest model of an isolated circular pure vortex, consisting of a core of constant vorticity $\Omega_0$ surrounded by a ring of oppositely signed vorticity $-\Omega_0$. Flierl (1988) solved the normal-mode stability equation and found that when $\Omega_0 < 1/3$ the vortex is linearly stable. Observations (Kloosterziel and Heijst 1991) and several numerical and analytical studies indicate that a critical steepness of the vorticity distribution is needed for a vortex to become unstable. Kloosterziel and Carnevale (2004) applied Arnold's stability theory (Sect. 9.1.3) to investigate the formal stability of such a vortex in unbounded inviscid fluid. They derived the first and second variations of the angular momentum $M$ and kinetic energy $K$ for the basic flow, and proved that under the condition of vortex-area preserving, the first variations of both $M$ and $K$ are zero. They defined a linear combination of the second variation of $M$ and $K$: $\delta^2(K+1/2\mu M)$, and proved that if $\Omega_0 < 1/3$, there is always a $\mu$ such that $\delta^2(K + 1/2\mu M)$ is negatively definite. Then according to Arnold's theorem, this flow is formally stable. It is concluded that for this vortex the linear-stability regime coincides with the formal-stability regime. It should be noticed that this method can be applied to more complicated circular pure vortices.

### 9.3.2 Temporal Instability of Swirling Flow

Swirling flows are very often encountered in various applications. Swirling jets and wakes can be found in internal flows of many industrial facilities and in the flows around the flying vehicles. In the design of high-efficiency combustion chambers or control of airplane wakes, it is very important to understand the dynamic characteristics of swirling flows, in particular their stability behavior. Besides, swirling flows exist in many atmospheric phenomena, such as tornadoes and dust devils. While the instability mechanism of a pure vortex is due to the centrifugal force, the instability of a swirling vortex appears to be a very complicated coupling of the centrifugal instability and the Kelvin–Helmholtz instability due to axial shear. For a comprehensive review of the linear instability of a swirling vortex based on temporal normal-mode analysis, the reader is referred to Ash and Khorrami (1995).

For a swirling vortex with variable axial flow $W(r)$, Howard and Gupta (1962) derived an equation for inviscid instability analysis

$$\gamma^2 D\left[SD_* u\right] - u\left\{\gamma^2 + \gamma r D\left[S\left(\frac{D\gamma}{r} + 2n\frac{V}{r^3}\right)\right] - 2kS\frac{V}{r^2}\left(krD_* V - nDW\right)\right\} = 0. \tag{9.71}$$

Here, $\gamma(r) = nV/r + kW - \omega$ is the Doppler frequency, $S = r^2/(n^2 + k^2 r^2)$, $D = \mathrm{d}/\mathrm{d}r$, $D_* = 1/r + D$. Then, as an extension of the Rayleigh criterion (9.70) for pure vortices, they showed that the sufficient but not necessary condition for a swirling flow to be stable to axisymmetrical disturbances is

$$\frac{1}{r^3}\frac{\mathrm{d}\Gamma^2}{\mathrm{d}r} \geq \frac{1}{4}\left(\frac{\mathrm{d}W}{\mathrm{d}r}\right)^2. \tag{9.72}$$

Unfortunately, no general solution of the *Howard–Gupta equation* (9.71) can be found for three-dimensional disturbances. Hence, so far the results obtained from this equation are either general criteria but under certain simplified asymptotic limit, or the detailed instability characters for specific swirling flows.

Based on (9.71) and using an energy consideration, Leibovich and Stewartson (1983) have carried out an asymptotic analysis for $|n| \gg 1$ and achieved a finite upper limit of the growth rate $\omega_i$ for inviscid disturbances as $-n \to -\infty$. Based on this result and within the normal-mode framework, Leibovich and Stewartson obtained a sufficient condition for a columnar vortex to be unstable to small disturbance

$$V\frac{\mathrm{d}\Omega}{\mathrm{d}r}\left[\frac{\mathrm{d}\Omega}{\mathrm{d}r}\frac{\mathrm{d}\Gamma}{\mathrm{d}r} + \left(\frac{\mathrm{d}W}{\mathrm{d}r}\right)^2\right] < 0, \tag{9.73}$$

where $\Omega = V/r$, and $\Gamma = rV$. Emanuel (1984) has proven that (9.73) is a direct extension of the Rayleigh criterion (9.70) to the vortex with nonzero axial velocity and with disturbances not necessarily axisymmetric.

Note that (9.73) is not a necessary condition for instability either; examples exist where the flow condition does not satisfy (9.73) but the vortex is still unstable. Similarly, for large $k$ and $|n|$, Staley and Gall (1984) have found a sufficient condition for temporal instability, which, in terms of the basic-flow velocities, can be cast to (Yin et al. 2000)

$$k\frac{\mathrm{d}\Gamma}{\mathrm{d}r} - n\frac{\mathrm{d}W}{\mathrm{d}r} < 0. \tag{9.74}$$

Thus, when $k\mathrm{d}\Gamma/\mathrm{d}r > 0$ as usual, the sign of $n$ for unstable helical mode depends on that of $\mathrm{d}W/\mathrm{d}r$. Namely, there is $n < 0$ if the swirl is jet-like ($\mathrm{d}W/\mathrm{d}r < 0$) and $n > 0$ if it is wake-like ($\mathrm{d}W/\mathrm{d}r > 0$). But this sign change (a change of the orientation of the disturbance wave relative to the basic rotating flow) does not matter in temporal-mode analysis, since a Galilean transformation can cast a jet-like flow to a wake-like one and vise versa.

Having discussed some general but approximate results deduced from the Howard–Gupta equation (9.71), we now illustrate its application to a widely used special vortex model, the Batchelor vortex or $q$-vortex (6.19). In (6.19a), the constant $W_0$ and the indefinite sign of the axial velocity permit modelling both jets and wakes. Similar to what has just been said, in temporal normal-mode these factors merely change the frequency $\omega_r$ but not affect whether the

flow is stable; only the shape of mean axial velocity profile matters. Thus $W_0$ can be removed by a Galilean transformation, yielding

$$U = 0, \quad V = \frac{q}{r}\left(1 - \mathrm{e}^{-r^2}\right), \quad W = \mathrm{e}^{-r^2}. \tag{9.75}$$

In consistent with the remark following (9.75), Khorrami (1991) has confirmed that the inversion of the axial velocity profile lead to a sign change of the unstable azimuthal wave number $n$.

Lessen et al. (1974), Duck and Faster (1980), Ma (1984), Yin and Xia (1991), and Mayer and Powell (1992), among others, have studied the linear stability character of the $q$-vortex, in terms of either temporal or spatial mode. The main results on the temporal mode are as follows.

First, so far it has never been found that to an axial disturbance ($n = 0$) the flow can become unstable. For $n > 0$, i.e., an increase of rotation by the disturbance, even a weak rotation will stabilize all the modes as long as $q > 0.08$. In other words, the rotation increase helps the flow to resist further disturbances.

In contrast, a swirling flow is unstable to negative azimuthal wave numbers $n < 0$, and the temporal growth rate $\omega_i$ will increase as $|n|$. For a given $n$, if $q$ is gradually increased, the flow will become stable again to all the disturbance modes after $q > 1.5$. A typical result is shown in Fig. 9.13.

The maximum unstable region in the parameter $(k, q)$-plane corresponds to the flow with $n = -1$, for which extremely complicated flow pattern may

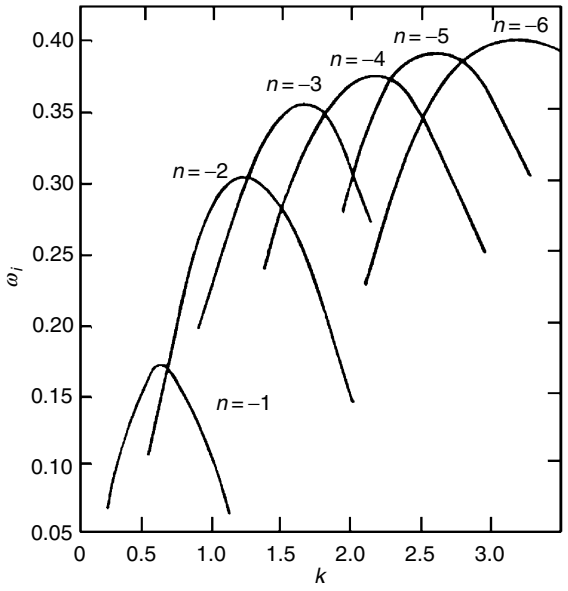


**Fig. 9.13.** Variation of the growth rate $\omega_i$ as the axial wave number $k$ with different azimuthal wave numbers $n$ for $q = 0.8$. From Lessen et al. (1974)

occur. Leibovich et al. (1986) found two bifurcated branches in the dispersion relation $\omega_r(k, n, q)$. One branch is called the fast mode, and the corresponding phase velocity of the disturbance wave tends to infinity when $k \to 0$. The other is called the slow mode with frequency

$$\omega_r = -\frac{n\Gamma_1}{4\pi} k^2 \left[ \ln\left(\frac{2}{|k|}\right) + c_1 - 0.5772 \right],$$

where $\Gamma_1$ and $c_1$ are determined by the velocity profile, and the associated phase and group velocities tend to zero when $k \to 0$,

$$c = \frac{\omega_r}{k} \to 0, \quad c_\mathrm{g} = \frac{\partial \omega_r}{\partial k} \to 0.$$

The zero group velocity suggests these disturbances tend to become absolutely unstable.

For most vortex flows of interest in engineering or geophysical fluid dynamics, centrifugal force is indeed the source to cause instability and it is essentially an inviscid mechanism. Therefore, it had long been confident that viscosity acts only on dissipation as an stabilizing effect. However, Khorrami's (1991) calculation revealed two purely viscous instability modes in the $q$-vortex, which are different from the viscous instability of plane shear layers due to the existence of centrifugal force.[5]

Consider first the viscous instability of an inviscidly unstable swirling flow. For $n = -1$ we have the lowest critical Reynolds number. As the Reynolds number increases, azimuthal instability modes $-n$ of higher and higher orders will be activated. Both critical axial wave number $k_\mathrm{c}$ and critical Reynolds number $Re_\mathrm{c}$ are not sensitive to swirling parameter $q$; but $Re_\mathrm{c}$ grows as $n^2$ when $-n$ grows. Thus, small-scale disturbances decay quickly due to viscosity and eventually the dominant disturbances should be those modes with small azimuthal wave numbers.

Then, consider the purely viscous instability modes when the basic flow is inviscidly stable. Khorrami (1991) worked out two cases, $n = 0$ and $n = +1$, which are known to be both stable according to the inviscid theory. Calculations for $q = 1.0$ and $Re = 10^4$ yields the results shown in Fig. 9.14, in which the variation of frequency $\omega_r$ and the growth rate of disturbance $\omega_i$ with wavenumber $k$ are given. Note however that Schmid et al. (1993) have noticed that the stability operator is highly non-normal for the specific unstable mode $n = +1$. Thus, the transient growth of disturbances plays an

[5] Strictly, the purely viscous instability is meaningful only if the basic flow is an exact Navier–Stokes solution. But the Batchelor vortex is not (see Sects. 6.2.1 and 8.1.3), although the Reynolds-number effect on its inviscid instability modes and its viscous instability modes have been widely investigated. In fact, in these studies the Batchelor vortex is used as a fitting model of experimentally observed vortices or an approximate viscous solution. This makes sense because the linear instability analysis is also approximate.

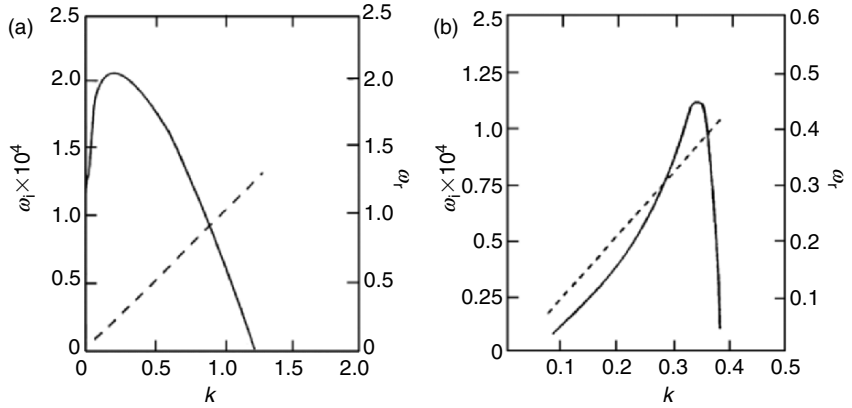


**Fig. 9.14.** Disturbance growth rate $\omega_i$ and frequency $\omega_r$ vs axial wavenumber $k$ for viscous disturbances with $q = 1.0$ and $Re = 10^4$. *Solid line* for $\omega_i$, and *broken line* for $\omega_r$. (**a**) Axisymmetric mode $n = 0$; (**b**) asymmetric mode $n = +1$. From Khorrami (1991).

important role and the normal-mode approach alone cannot give the whole scenario for the growth of disturbances.

### 9.3.3 Absolute and Convective Instability of Swirling Flow

We now proceed from temporal-mode analysis of swirling-vortex instability to some recent AI/CI analyses. The inviscid and viscous AI/CI characters of a Batchelor vortex have been studied by Olendraru et al. (1999) and Olendraru and Sellier (2002) using linear theory, and by Delbende et al. (1998) using direct numerical simulation. The two approaches may check and complement each other. On the other hand, Loiseleux et al. (1998) discussed the AI/CI of a Rankine vortex with a method similar to Olendraru and coworkers, while Yin et al. (2000) studied the AI/CI of slender vortices for both incompressible and compressible flows, including high Mach-number effect.

To consider the Batchelor vortex, we return to (6.19a) and write

$$U(r) = 0, \quad V(r) = \frac{q}{r}(1 - \mathrm{e}^{-r^2}), \quad W(r) = a + \mathrm{e}^{-r^2}, \tag{9.76}$$

which has two parameters

$$a = \frac{W_\infty}{\Delta W}, \quad q = \frac{\Omega_\mathrm{c} R}{\Delta W}, \tag{9.77}$$

where $R$ is the radius of the vortex core, $\Omega_\mathrm{c}$ is the angular velocity at the axis, and $\Delta W = W_\mathrm{c} - W_\infty$, with $W_\mathrm{c}$ and $W_\infty$ being the axial velocity at $r = 0$ and the free-stream velocity at $r = \infty$ respectively. Thus, $a$ and $q$ characterize the axial velocity distribution and the level of swirl for a Batchelor vortex,

respectively. Along with these profile parameters, the Reynolds number is defined by $Re = \Delta WR/\nu$. We stress that, while for temporal-mode analysis $a$ can be eliminated by a Galilean transformation, it does have important influence on the AI/CI behavior and the spatial propagation of disturbances. As discussed in Huerre and Monkwwitz (1990), it is precisely in the situation where Galilean invariance is broken that absolute-convective instability acquires physical significance. Associated with this is the fact that the sign of azimuthal wave number $n$ of the disturbance matters (see the remark following (9.74)).

The azimuthal and axial velocity distributions of a typical swirling flow are shown in Fig. 9.15, where

| | |
|---|---|
| $a < -1$, | coflow wake; |
| $a = -1$, | wake with $W(0) = 0$; |
| $-1 < a < 0$, | counter-flow wake or jet; |
| $a = 0$, | jet with $W_\infty = 0$; |
| $a > 0$, | coflow jet. |

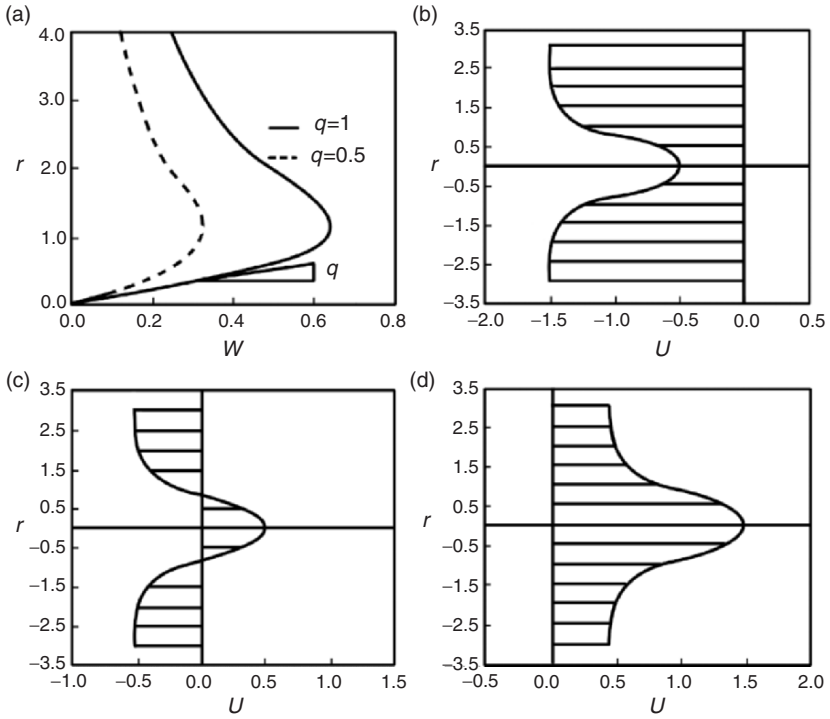


**Fig. 9.15.** Batchelor vortex velocity profiles. (**a**) Azimuthal velocity profile $V(r)$. Axial velocity profile $W(r)$ for (**b**) coflowing wakes( $a < -1$); (**c**) counter-flowing wakes or jets($-1 < a < 0$); (**d**) coflowing jets( $a > 0$ ). From Olendraru et al. (1999)

In the $(a, q)$-space, the half planes $a > -0.5$ and $a < -0.5$ represent the jet side and wake side, respectively. Figure 9.16 plots the AI/CI boundaries for $n = \pm 1, -2, ..., -7$ at $Re = 667$, which divide the $(a, q)$-plane into three distinct regions: a stable (S) region, an AI region, and two CI outer regions at both the jet side and wake side. Recall that if $\Omega_c > 0$, then there is $q > 0$ for jet flow with $\Delta W < 0$ and $q < 0$ for wake flow with $\Delta W < 0$. For the latter, we have mentioned in Sect. 9.3.2 that the temporal-mode unstable azimuthal wavenumber $n$ is positive. But it can be shown that the instability equation is invariant under transformation $(q, -n) \to (-q, n)$; so the AI/CI boundaries with $n = 1$ for a wake-type Batchelor vortex can still be read off from Fig. 9.16 by taking $q > 0$ and $n < 0$.

A close look of Fig. 9.16 shows that the transitional helical mode from CI to AI is very sensitive to the wake-like or jet-like nature of the flow, as well as to the level of swirl. For wakes-like flow, the critical transitional mode is always $n = -1$. But on the jet side $(a > -0.5)$, the critical transitional mode may have different azimuthal wave numbers $n = -1, -2, ...$ . Moreover, when $q = 0$, there is no swirl and the flow is a pure wake or jet, and there is a small AI region in a narrow range of $a$. An increase of $q$ will cause significant enlargement of the AI region.

Note that the inviscid stability analysis, limited by the numerical method applied, cannot determine the neutral boundary accurately. Once the viscous effect is involved the situation is changed. As shown in Fig. 9.17 for the helical

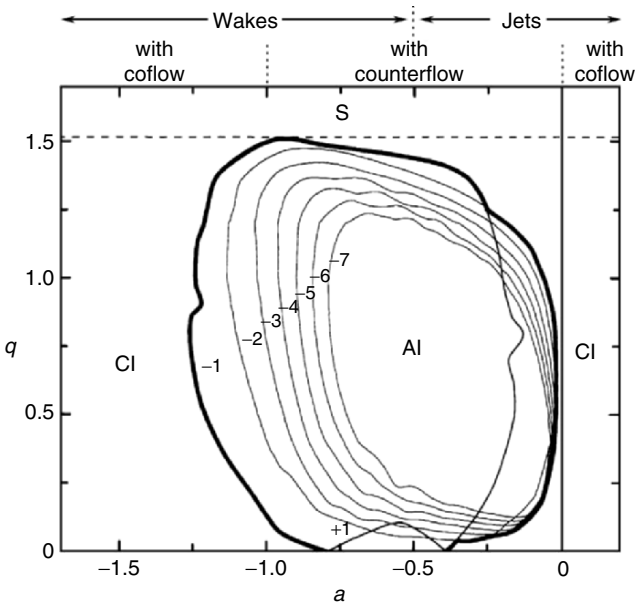


**Fig. 9.16.** AI/CI boundaries of the helical mode $n = \pm 1, -2, \ldots, -7$ in the $(a, q)$-plane for $Re = 667$. From Delbende et al. (1998)

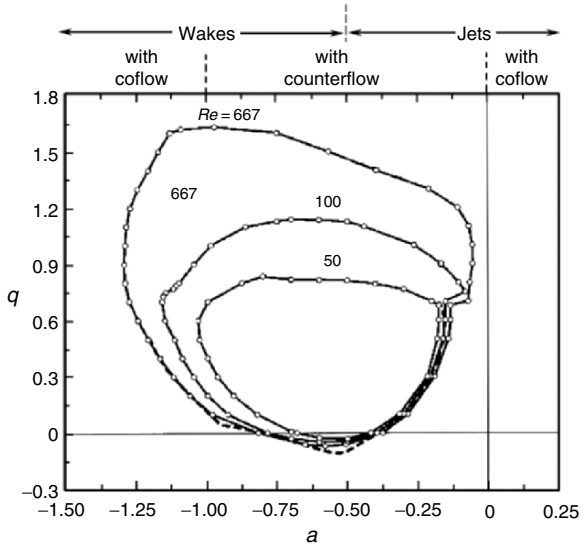


**Fig. 9.17.** AI/CI boundaries of the helical mode $n = -1$ in the $(a, q)$-plane at different Reynolds numbers. From Olendraru and Sellier (2002)

mode $n = -1$ and different $Re$, the increase of $Re$ also enlarges the AI region significantly. But, since both AI and CI regions are subregions of the temporal instability, and as remarked in Sect. 9.3.2 the Batchelor vortex will be linearly stable if $q > 1.5$, the AI regions for any $Re$ have a common upper bound at $q \simeq 1.5$.[6]

The absolute growth rate $\omega_i^0$ of the Batchelor vortex is illustrated in Fig. 9.18 for wake-like flow with different $(a, q)$ and $n = 1, 2$. Initially, an increase of $q$ leads to a corresponding increase of $\omega_i^0$, which then starts to decrease for larger $q$. Thus, for each pair of $(a, n)$, there is a maximum $\omega_i^0$, denoted by $\omega_{i,\max}^0$. It is evident that the axial flow has a strong effect on the absolute growth rate, which reaches the largest value when there is a counterflow ( $a = -0.8$), and this rate reduces as the axial velocity deficit $a$ does.

### 9.3.4 Non-Modal Instability of Vortices

Finally, having discussed the normal-mode instabilities of a swirling vortex, we turn to the non-normality effects on the vortex instability. Smith and Rosenbluth (1990) and Nolan and Montgomery (2000) have studied the transient algebraic growth of the disturbance energy in inviscid hollow hurricane-like vortices.

[6] The top boundary of AI/CI for $Re = 667$ in Fig. 9.17 is beyond $q = 1.5$, possibly due to numerical error.

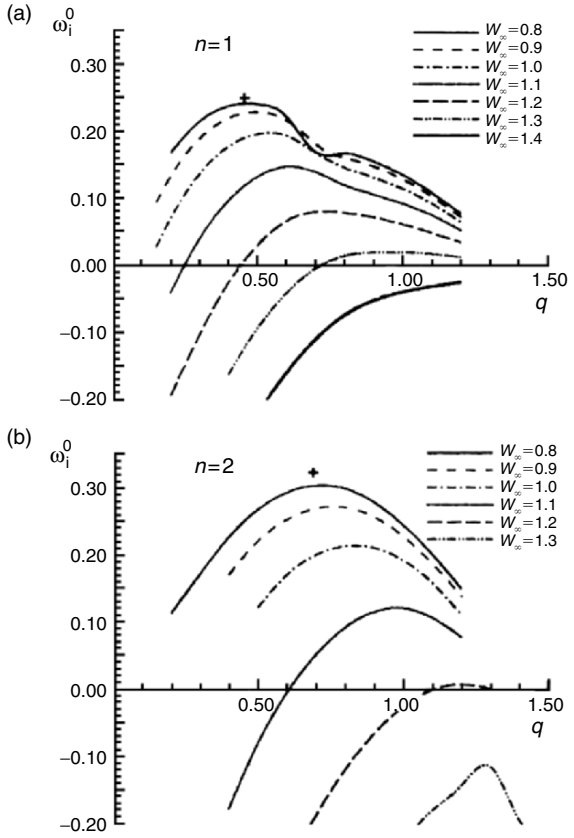


**Fig. 9.18.** The variation of absolute growth rate $\omega_i^0$ for wake-type $q$-vortex. (**a**) $n = 1$; (**b**) $n = 2$. The sign + marks the corresponding maximum temporal growth rate $\omega_{i,\max}$, which is the upper bound of all $\omega_i^0$. From Yin et al. (2000)

Nolan and Farrell (1999a) have studied the dynamics of both transient and exponentially growing disturbances in two-dimensional one- and two-cell vortices, which are maintained by the radial inflow of a fixed cylindrical deformation field. Taking the linear evolution of asymmetric disturbances as a dynamic system like (9.13), they found that the mean-flow shear results in a non-normal operator that indeed allows for the transient growth of disturbances even when all modes of the operator are decaying. While the unstable modal disturbances convert the mean-flow deformation to disturbance vorticity, the instantaneous optimal disturbances use the mean-flow deformation to *rearrange* their own vorticity into configurations with higher energy. A hybrid use of these two mechanisms was found to achieve substantial finite-time energy growth. The authors also found that the radial flow causes vorticity advection and stretching, which is extremely important in assessing the potential

for transient growth and instability of the vortices. This phenomenon can be interpreted based on our general discussion on the key role of the curl of the disturbance Lamb vector (Sect. 9.1.4).

Miyazaki and Hunt (2000) pointed out that bending waves can be excited by the interaction between the vortex and three-dimensional external turbulence through a dominantly linear process. Choosing the Oseen–Lamb pure vortex (6.25) as their basic flow, Antkowiak and Brancher (2004) have analyzed in detail the transient growth of vortex energy. This flow is always stable in temporal-mode analysis, no matter if the disturbance is two- or three-dimensional. By introducing normal-mode disturbances $\boldsymbol{v}(r,\theta,z,t) = \widehat{\boldsymbol{v}}(r,t)\exp(\mathrm{i}(kz+n\theta))$, the authors looked for the initial disturbance corresponding to maximum gain of disturbance energy (the optimal disturbance) $G(t) = K_v(t)/K_v(0)$ by optimum control theory. Their work revealed that the optimal disturbance may involve strong transient growth in the linear regime, which gradually triggers a nonlinear transition to the originally (linearly) stable vortex.

Figure 9.19 gives the gain of the optimal disturbance energy with various wave numbers $k$ for $n = 1$, where the maximal gain of the energy occurs at $k \approx 1.4$. The gain can be as high as $10^3$ for a high Reynolds number flow. However, the optimal wave number is found to be independent of the Reynolds number, indicating that there exists certain size of three-dimensional disturbed vortex cores that is the most effective for their energy to be transferred from the mean to disturbance motions. Figure 9.20 shows the structure of the optimal disturbance. Initially, it is a group of left-handed spiral vorticity sheets (Fig. 9.20a). After a while, they can evolve to strong bending waves in the vortex core (Fig. 9.20b).

Following Antkowiak and Brancher (2004), the transient growth of disturbance energy in the Oseen–Lamb vortex involves two mechanisms. One is similar to what has been discussed in Sect. 9.2.4; there is also a coupling operator similar to $L_c$ in (9.51) for small disturbances. Except for the trivial case $k = n = 0$ and the extremely special case like a rotating rigid body,

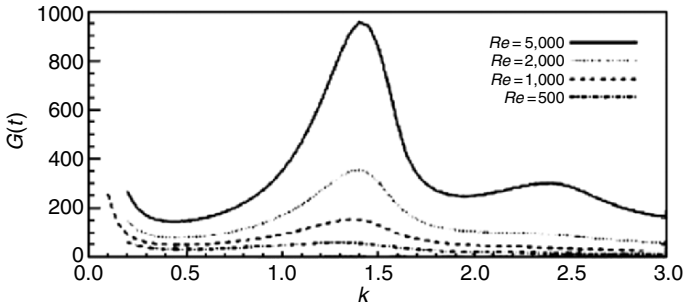


**Fig. 9.19.** Optimal energy growth versus axial wavenumber $k$ for $n = 1$. From Antkowiak and Brancher (2004)

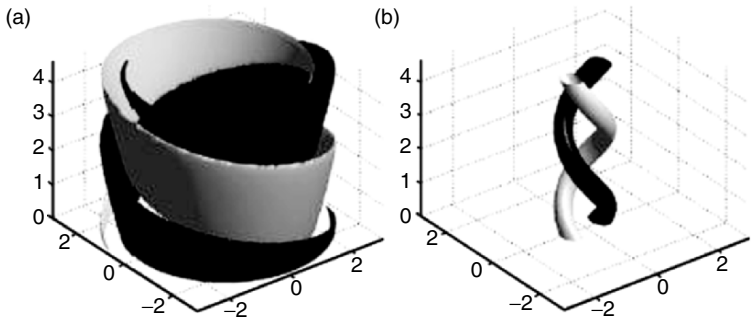


**Fig. 9.20.** Isosurfaces of axial vorticity for the optimal 3D case. The levels correspond to ±80% of maximum vorticity. (**a**) At initial time; (**b**) at the optimal time. From Antkowiak and Brancher (2004)

the operator is highly non-normal. With three-dimensional disturbances, one can extend the Orr mechanism and the lifting-up mechanism discussed in Sect. 9.2.4 to analyze the transient growth of the disturbance energy caused by the operator non-normality, but now more complicated dynamic processes such as vorticity stretching and tilting enter into the play.

The second physical mechanism is closely related to the vortex motion, i.e., the interaction between the vorticity convection and induction. Taking two-dimensional disturbances as example, the linearized equation for the disturbance vorticity reads:

$$\frac{\partial \omega}{\partial t} + \frac{V}{r}\frac{\partial \omega}{\partial \theta} + u\frac{\mathrm{d}\Omega}{\mathrm{d}r} = \frac{1}{Re}\nabla^2\omega, \tag{9.78}$$

where $\omega$ is the axial disturbance vorticity, $u$ is radial disturbance velocity, $V(r)$ and $\Omega(r) = 2\exp(-r^2)$ are the circumferential velocity and axial vorticity of the basic Oseen–Lamb vortex. The second terms on the left-hand side of (9.78) is the convection effect on $\omega$, while the third one expresses the axial vorticity transfer from the mean to the disturbance motion due to the interaction between the mean vorticity gradient and the radial disturbance velocity.

Now, as just seen in Fig. 9.20a, the initial structure of the optimal disturbance is a set of spiral vortex sheets located at the edge of the vortex, where the induction term is negligible. As time goes on, the spiral sheets are convected and unfolded by an analogy of the Orr mechanism, which leads to a local reorganization of the disturbance vorticity. The latter in turn enhances the induction of the vortex at its axis. Thus, the initially occurred Orr mechanism at the edge of the vortex core gradually influences the vortex core and causes bending waves there. The helical vortex-dipole structure in the core then grows quickly so that most of disturbance energy is concentrated in the bending waves. This is how the joint effect of the local Orr mechanism and the

global vortex induction leads to a transient growth of the disturbance energy in the Oseen–Lamb vortex.

It should be pointed out here that the above phenomenon and physical mechanisms take place in fact in all flows where shear and swirl coexistence.

An important question in any nonmodel instability analysis is whether theoretically predicted optimal disturbances (see Sect. 9.1.2) can exist in reality, e.g., a rotational weather system, and what would happen if the initial disturbance is not optimal. This question has been addressed by Nolan and Farrell (1999b), who imposed a stochastic asymmetric forcing to the same one- and two-cell vortex models with radial inflow studied by Nolan and Farrell (1999a). The authors found that those structures generated by vortex instability, that can most effectively induce the energy transfer from mean to disturbance field, are close to the *global optimals* defined in Sect. 9.1.2. Physically, as long as a stochastic forcing contains a constituent that belongs to the optimal disturbance, it will be rapidly amplified in finite time by the operator non-normality and become dominant.

## 9.4 Instabilities of Strained Vortices

It has been stressed in Chap. 5 that in reality a vortex often exists in a strain field, so that the cross shape of the vortex and surrounding streamlines become elliptical. The instability of such a vortex is called *elliptical instability*. This instability is invariably three-dimensional and has linear growth rates scaled with strain rate, so that the flow becomes very complicated and leads to small-scale disorder.

As is known, the linear stability analysis for parallel shear flows can describe only the initial development of the disturbances after the flow becomes unstable. The further transition of the flow into turbulence is related to the secondary instability of the unstable flow where the stream lines of the basic flow are no longer parallel but usually elliptical due to the strain field. The elliptical instability on a two-dimensional basic vortex just represents a simple model for the secondary instability. Moreover, elliptical instability gives a universal mechanism for two-dimensional large-scale coherent structures to directly evolve to complicated three-dimensional motions. This direct transfer mechanism plays a dominant role in transition of the flows like wakes, mixing layers and vortex pairs. On the other hand, since the existence of strong vortex filaments with various sizes in turbulence has been well established, and all these filaments are subject to the background strain field caused by surrounding vortices (Sect. 6.5), one expects that elliptical instability of these vortex filaments would have important influences on the evolution of coherent structures and the intermittency of turbulence.

For these reasons, elliptical instability has recently become a new active research subject in the field of hydrodynamic instability. For more information see the review of Kerswell (2002).

### 9.4.1 Elliptical Instability

The simplest example of elliptical instability is an unbounded strained vortex, i.e., the basic flow is a superposition of an unbounded fluid at uniform rotation as rigid body with angular velocity $\omega/2 = 1$ and stagnation potential flow with stretching in the $-45^\circ$ direction

$$\boldsymbol{U} = \begin{bmatrix} 0 & -1-\epsilon & 0 \\ 1-\epsilon & 0 & 0 \\ 0 & 0 & 0 \end{bmatrix} \boldsymbol{x} = \mathbf{A} \cdot \boldsymbol{x}, \tag{9.79}$$

where $\epsilon > 0$ is the strain rate. Craik and Criminale (1986) have proven that this flow is an exact solution of the Navier–Stokes equation with stream function

$$\psi = -\frac{1}{2}[(1-\epsilon)x^2 + (1+\epsilon)y^2] \tag{9.80}$$

for $\epsilon < 1$, so the streamlines are elliptical with eccentricity rate

$$E = \sqrt{(1+\epsilon)(1-\epsilon)}. \tag{9.81}$$

We now introduce a *Kelvin-mode* disturbance

$$(\boldsymbol{u}', p') = (\hat{\boldsymbol{u}}(t), \hat{p}(t)) \exp(\mathrm{i}\boldsymbol{k}(t) \cdot \mathbf{x}), \tag{9.82}$$

which differs from the convential normal modes in that $\hat{\boldsymbol{u}}(t), \hat{p}(t)$, and wave number $\boldsymbol{k}(t)$ are all functions of time. Then (9.68) becomes

$$\dot{u}_j + \mathrm{i}\dot{\hat{k}}_l x_l \hat{u}_j + \mathrm{i}k_m A_{ml} x_l \hat{u}_j + A_{jl}\hat{u}_l = -\mathrm{i}k_j \hat{p} - \nu k^2 \hat{u}_j, \tag{9.83a}$$

$$k_j \hat{u_j} = 0. \tag{9.83b}$$

The continuity equation (9.83b) implies that the disturbance is a transverse wave, by which the nonlinear terms in (9.83a) can be cancelled automatically. Thus, (9.83) are equally applicable to nonlinear disturbances of arbitrary amplitude. Moreover, by setting

$$\widehat{\boldsymbol{u}} = \exp\left(-\nu \int_0^t k^2 \mathrm{d}\tau\right) \widehat{\boldsymbol{v}}, \tag{9.84}$$

the viscous term in (9.83a) can also be eliminated in the equation for $\widehat{\boldsymbol{v}}$. Then, if the wave vector $\boldsymbol{k}$ is so selected that

$$\frac{\mathrm{d}\boldsymbol{k}}{\mathrm{d}t} = -\mathbf{A}^{\mathrm{T}} \cdot \boldsymbol{k}, \tag{9.85}$$

then terms depending on $\boldsymbol{x}$ in (9.83a) can be eliminated as well, yielding

$$\frac{\mathrm{d}\widehat{v}_j}{\mathrm{d}t} + A_{jl}\widehat{v}_l = -\mathrm{i}k_j \widehat{p}. \tag{9.86}$$

Multiplying both sides of this equation by $k_j$, and using the time derivative of (9.83b)

$$k_j \frac{\mathrm{d}\widehat{v}_j}{\mathrm{d}t} = -\widehat{v}_j \frac{\mathrm{d}k_j}{\mathrm{d}t} = k_j A_{jl} \widehat{v}_l,$$

one obtain

$$\widehat{p} = 2\mathrm{i} k^{-2} k_j A_{jl} \widehat{v}_l.$$

Combining this and (9.86) to eliminate $\widehat{p}$, we obtain an important equation

$$\frac{\mathrm{d}\widehat{v}_i}{\mathrm{d}t} = \left(2k^{-2} k_i k_j - \delta_{ij}\right) A_{jl} \widehat{v}_l, \tag{9.87}$$

or in invariant form

$$\frac{\mathrm{d}\widehat{\boldsymbol{v}}}{\mathrm{d}t} = \mathbf{Q}(t) \cdot \widehat{\boldsymbol{v}}, \qquad \mathbf{Q}(t) = \left( \frac{2\mathbf{k}\mathbf{k}^{\mathrm{T}}}{|\mathbf{k}|^2} - \mathbf{I} \right) \cdot \mathbf{A}, \tag{9.88}$$

where $\mathbf{I}$ is the unit matrix.

Bayly (1986) has reduced (9.87) to a Floquet problem for $\widehat{\boldsymbol{v}}$ and demonstrated instability by searching over all possible wave numbers. The so-called *Floquet problem* is to express a solution operator with respect to time by a product of two operators:

$$\mathcal{A}(t) = \mathcal{P}(t) \exp(\mathcal{B}t),$$

where $\mathcal{P}(t)$ is a time periodic operator and $\mathcal{B}$ a time-independent operator. The eigenvalues of $\mathcal{B}$ are referred to as *Floquet exponents* (Schmid and Henningson 2001).

By a different approach, Waleffe (1990) has casted (9.87) to an equation for a single component $\widehat{v}_z$. Our presentation below follows a slightly different version due to Yin and Sun (2003). From (9.85) and (9.87) one obtains:

$$\frac{\mathrm{d}(k^2 \widehat{v}_i)}{\mathrm{d}t} = -k^2 A_{il} \widehat{v}_l + 2k_j A_{jl} \left( \widehat{v}_l k_i - k_l \widehat{v}_i \right)$$

of which the time derivative yields

$$\begin{aligned} \frac{\mathrm{d}^2 k^2 \widehat{v}_i}{\mathrm{d}t^2} = {} & k^2 A_{il} A_{lj} \widehat{v}_j - 4(k_m A_{ml} A_{lj} \widehat{v}_j) k_i + 2(k_m A_{ml} A_{lj} k_j) \widehat{v}_i \\ & -2(k_m A_{ml} \widehat{v}_l)(k_j A_{ji}) + 2(k_m A_{ml})(k_j A_{jl}) \widehat{v}_i + 2(k_m A_{ml} \widehat{v}_l) A_{ij} \widehat{v}_j. \end{aligned}$$

After some algebra, we find a homogeneous second-order ordinary differential equation

$$\left[1 - a \cos 2\Omega(t - t_0)\right] \frac{\mathrm{d}^2 k^2 \widehat{v}_z}{\mathrm{d}t^2} + \Omega^2 \left[c - 4a \cos 2\Omega(t - t_0)\right] (k^2 \widehat{v}_z) = 0, \tag{9.89}$$

where $\Omega = \sqrt{1-\epsilon^2}$ and

$$a = \frac{\epsilon \sin^2\theta}{1-\epsilon\cos^2\theta}, \quad c = \frac{4(1-\epsilon)\cos^2\theta}{1-\epsilon\cos^2\theta}.$$

The coefficients of (9.89) have period $\pi/\Omega$. From this equation we may obtain the elliptical instability boundary as shown in Fig. 9.21 on the $(a, \sqrt{c})$-plane. Note that $\Omega\sqrt{c}$ and $2\Omega$ are the natural and forcing frequencies of (9.89), respectively, implying that subharmonic instability will occur when $\sqrt{c} = 1$. Thus, in Fig. 9.21 the instability boundary starts from the point $(a, \sqrt{c}) = (0, 1)$.

For small $\epsilon$, it can be found that the maximum growth rate $\sigma$ depends linearly on the strain rate $\epsilon$:

$$\sigma = \frac{9}{16}\epsilon. \tag{9.90}$$

In the above discussion of elliptic instability the basic flow is two-dimensional unbounded strained vortex. The theory has been extended to three-dimensional basic flow, where the triaxial instability of a triaxial ellipsoid is analyzed; for review see Kerswell (2002). Figure 9.22 shows the dependence of $\sigma$ on $\epsilon$ in the full range of $\epsilon$ for both two- and three-dimensional basic flows. The left end of the curve corresponds to rigid rotation, while the right end represents a Couette flow.

Finally, we remark that the mechanism of linear elliptical instability discussed here is a *parametric resonance* where a normal mode, or a pair of normal modes, of the undistorted rotating flow resonates with the underlying strain field. Thus, it is also called the *co-operative instability* (Kerswell 2002). In particular, since the above simple model assumes an unbounded uniform rotation and strain as the basic flow that is not altered by the disturbance, for a vortex with finite core radius $a$ the model is only an asymptotic approximation for $ka \gg 1$ or the disturbance wave-length is much smaller than $a$. Thus, this model represents an *unltra short-wave instability* (Saffman 1992).

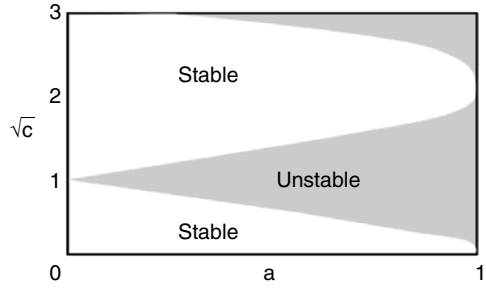


**Fig. 9.21.** The stability boundary for the elliptical flow on $(a, \sqrt{c})$-plane. From Huerre and Rossi (1998)

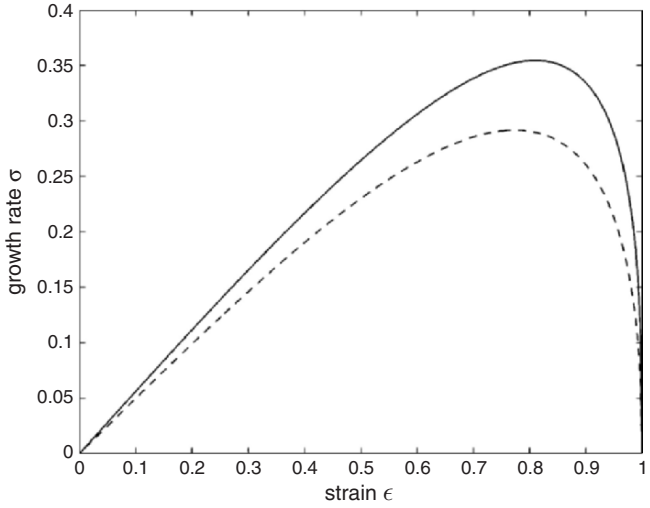


**Fig. 9.22.** The relation between the maximum growth rate $\sigma$ and strain rate $\epsilon$ for the inviscid Kelvin wave. The *solid line* is for an unbounded strained vortex, and the *dashed line* is for the triaxial instability of a triaxial ellipsoid. From Kerswell (2002)

### 9.4.2 A Columnar Vortex in a Strained Field

We proceed from the simple model of ultra short-wave instability to a more realistic case, i.e., the instability of a straight vortex filament in a strain field on the plane perpendicular to its axis. In this case elliptical streamlines occur only near the vortex core. Moore and Saffman (1975) considered the instability of a two-dimensional inviscid vortex in a weak strain field (see the strained vortex solution in Sect. 6.5.2) with respect to three-dimensional disturbances, while Tsai and Widnall (1976) considered the instability of a strained Rankine vortex. These authors found that in this case the most amplified disturbances have wavelength of $k \sim \mathrm{O}(1)$, namely the vortex is unstable to short-wave disturbance. Therefore, this "Tsai–Widnall–Moore–Saffman (TWMS) instability" is a *short-wave elliptical instability* near the vortex core. It has recently been extended by Eloy and Le Dizès (1999, 2001) to the Burgers and Oseen vortices, which we outline later.

The axial vorticity distributions of the Burgers and Oseen vortices have a common form

$$\omega_z = \frac{\Gamma}{\delta^2} G(\bar{r}), \quad \bar{r} = \frac{r}{\delta}, \tag{9.91}$$

where $\Gamma$ is the circulation, $\delta$ the radius of vortex core, and

$$G(\bar{r}) = \frac{1}{4\pi} \mathrm{e}^{-\bar{r}^2/4} \tag{9.92}$$

is the normalized Gaussian function. For the difference of these vortices see Sect. 6.2. We now add a background strain field

$$\boldsymbol{U}_\epsilon = (\epsilon x, -\epsilon y, 0) = (\epsilon r\cos 2\theta, -\epsilon r \sin 2\theta, 0)$$

perpendicular to the vortex axis, which makes the vortex-core shape become elliptical. Consequently, (9.80) is no longer a solution of the Navier–Stokes equation. However, it has been shown in Sect. 6.5 that in the limit of large Reynolds number $Re = \Gamma/\nu$, the main features of the vortex is retained near its core. Referring to (6.172), the axial vorticity reads:

$$\omega_z = \frac{\Gamma}{\delta^2} G\left(\bar{r}\right) + \epsilon\eta\left(\bar{r}\right) F\left(\bar{r}\right)\sin 2\theta + \mathrm{O}\left(\frac{\epsilon\gamma\delta^2}{\Gamma}, \frac{\epsilon^2\delta^2}{\Gamma}\right), \tag{9.93}$$

where $\gamma$ is the stretched rate of the Burgers vortex, and by (6.175) and (6.148a) there is

$$\eta(\bar{r}) = \frac{\bar{r}^2}{4(\mathrm{e}^{\bar{r}^2/4} - 1)}, \tag{9.94}$$

$$F'' + \frac{1}{\bar{r}}F' - \frac{4}{\bar{r}^2}F + \eta(\bar{r})F = 0. \tag{9.95}$$

The function $F$ measures the interaction of the vortex with the strain field. Then the velocity and pressure distributions of the vortex in the strain field are given by

$$V_r = \epsilon\delta^2\frac{4}{r}F\left(\bar{r}\right)\cos 2\theta - \frac{\gamma}{2}\Gamma + \mathrm{O}\left(\frac{\epsilon^2\delta^3}{\Gamma}, \frac{\epsilon\gamma\delta^3}{\Gamma}\right), \tag{9.96a}$$

$$V_\theta = \frac{\Gamma}{\delta}V\left(\bar{r}\right) - 2\epsilon\delta F'\left(\bar{r}\right)\sin 2\theta + \mathrm{O}\left(\frac{\epsilon^2\delta^3}{\Gamma}, \frac{\epsilon\gamma\delta^3}{\Gamma}\right), \tag{9.96b}$$

$$V_z = \gamma z, \tag{9.96c}$$

$$P = -\frac{\Gamma^2}{2\delta^2}\left[V\left(\bar{r}\right)\right]^2 + \epsilon\frac{\Gamma}{\delta}F'\left(\bar{r}\right)V\left(\bar{r}\right)\sin 2\theta + \mathrm{O}\left(\epsilon^2\delta, \epsilon\gamma\delta\right), \tag{9.96d}$$

where $\gamma$ is the axial stretching rate for the Burgers vortex only and

$$V(\bar{r}) = \frac{1}{2\pi\bar{r}}(1 - \mathrm{e}^{-\bar{r}^2/4}) \tag{9.97}$$

is the azimuthal velocity profile of the Burgers and Oseen vortices. The above asymptotic results are valid if $\Gamma/\delta^2 \gg \epsilon, \gamma$. Thus, they can be applied to analyze the vortex instability in a weak strain field.

First, Eloy and Le Dizès (1999) neglect the effects of stretching and viscous diffusion, and using the same method as TWMS to conduct the stability analysis. Since in weak-strain approximation ($\epsilon \ll \Gamma/\delta^2$) (9.92) indicates

axisymmetry to the leading order, one can superimpose to the basic flow a Kelvin wave

$$\hat{\boldsymbol{u}} = \boldsymbol{\Phi}(r)\mathrm{e}^{\mathrm{i}(kz+n\theta-\omega t)} + \text{c.c.}, \tag{9.98}$$

where c.c. denotes complex conjugate, while $\omega$, $k$, and $n$ are related by the dispersion relation $D(\omega, k, n) = 0$. Because the interaction of the $n$-Kelvin wave and the strain field can produce two additional azimuthal wavenumbers $n \pm 2$, the $n$-wave and $n+2$-wave can resonate via the strain field under the resonance condition

$$D(\omega, k, n) = D(\omega, k, n+2) = 0.$$

For this flow the dispersion relation has symmetry $D(\omega, k, n) = D(-\omega, k, -n)$, so the resonance condition can be satisfied by the stationary helical waves $(\omega, n) = (0, \pm 1)$, and there is $D(0, \kappa/\delta, 1) = 0$ for arbitrary dimensionless axial wavenumber $\kappa$. Hence, this special combination of helical modes will always be amplified by the strain field to make the vortex unstable. This parametric resonant instability is characterized by a disturbance growth rate $\sigma = \mathrm{O}(\epsilon)$, a critical wave number $\kappa_\mathrm{c} = \mathrm{O}(1)$, and an instability disturbance wave-band range $\Delta\kappa = \mathrm{O}(\epsilon\delta^2/\Gamma)$ around $\kappa_\mathrm{c}$.

Next, interestingly, Eloy and Le Dizès (1999) observed that the effect of axial stretching and viscous diffusion on the elliptical instabilities of the Burgers vortex and Oseen vortex, respectively, is to make the dimensionless axial wavenumber $\kappa$ of the resonant helical waves *time-dependent*, such that their instabilities has a *transient* feature. The core radius of an Oseen vortex $\delta_\mathrm{L}$ grows with time as $(\nu t)^{1/2}$ due to viscosity, i.e., on a time scale $t_\mathrm{L} = \mathrm{O}(\delta^2/\nu) = \mathrm{O}(\delta^2 Re/\Gamma)$. Thus, if the initial configuration is unstable, at later times $k\delta$ will increase and go out the unstable band centered at the critical wave number $\kappa_\mathrm{c}$, so the helical waves are no longer unstable (see Fig. 9.23a). The amplitude gain of the instability wave may be estimated as

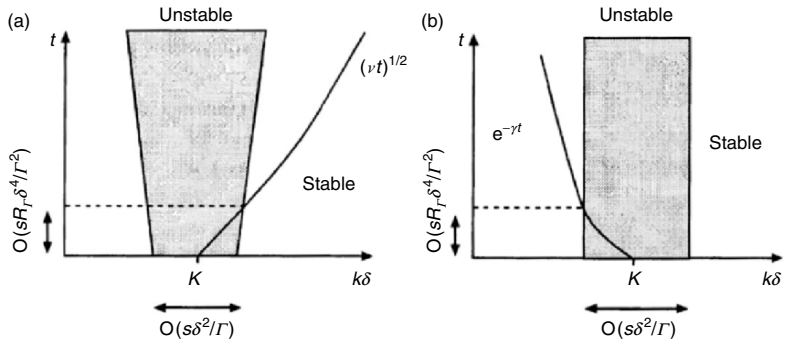


**Fig. 9.23.** Time evolution of $k\delta$ for the Oseen vortex (**a**) and the Burgers vortex (**b**). In both cases, $k\delta$ remains in the unstable band around $k$ only for a finite time. From Eloy and Le Dizès (1999)

$G \sim \exp(\tau\sigma)$, where $\tau$ is the time during which the wave passes the instability wave band and $\sigma = \mathrm{O}(\epsilon)$ is the mean disturbance growth rate. Thus, $\tau = \mathrm{O}((\Delta\kappa)t_\mathrm{L}) = \mathrm{O}(\epsilon Re\delta^4/\Gamma^2)$ and $G \sim \exp\left(\epsilon^2 Re\delta^4/\Gamma^2\right)$. Therefore, the vortex can be considered unstable if $\epsilon \gg \Gamma/\left(\delta^2 Re^{1/2}\right)$.

In contrast, to a Burgers vortex, the stretching decreases its axial wave number according to $k_b = k_0 \exp(-\gamma t)$. Hence if a helical wave is initially unstable, after a finite time $\tau = \Delta\kappa/\gamma = \mathrm{O}(\epsilon Re\delta^4/\Gamma^2)$, $k\delta$ will decrease and likewise go out of the unstable band $\Delta\kappa$ (see Fig. 9.23b). Thus, the growth is also transient, again under the condition $\epsilon \gg \Gamma/(\delta^2 Re^{1/2})$.

### 9.4.3 Instability of a Vortex Pair

A pair of parallel and counter-rotating vortices is one of the basic vortex structures (Sect. 6.5.2). Their stability behavior are important not only in academic studies but also for engineering applications.

Motivated by the need for studying the evolution of aircraft trailing vortices, Crow (1970b) was the first to study the *long-wave instability* (known as the *Crow instability*) of a vortex pair. He modelled the vortex pair by two infinitely long filaments subjected to a harmonic disturbance of wavelength $2\pi/k \gg a$, where $a$ is the core radius, and used the Biot–Savart formula with cutoff approximation (see Sect. 8.2.1; the cutoff parameter depends on the core structure) to calculate the vortex-induced velocities. Then three mechanisms are involved in the disturbance development (i) the self-induction of each individual vortex, (ii) the mutual induction between the two vortices, and (iii) the action of the strain field. Crow found that (i) is a stabilizing factor but (iii) is destabilizing. The resultant instability is due to the resonance of a long, bending Kelvin wave on the vortex filament with the external strain field imposed by the other vortex filament. The disturbances can be classified into symmetric and antisymmetric modes. Calculation indicates that the latter is decaying, while the stability boundary for the former is shown in Fig. 9.24, where $a$ is the vortex-core radius and $b$ the distance between the vortices. The flow is unstable only for long-wave disturbances, also called *long-wave cooperative instability* (Saffman 1992). In fact, there is a critical wavenumber $k = k_\mathrm{c}$, such that for $k > k_\mathrm{c}$ the flow is stable, because the filament rotation due to self-induction exceeds the rate of convection away from the hyperbolic stagnation point of the strain flow.

Moore and Saffman (1975), Tsai and Widnall (1976), and Leweke and Williamson (1998, 2000) have further studied the short-wave instability of the vortex pair and revealed again the same mechanism based on the parametric resonance. Figure 9.25 shows the flow visualization of the vortex pair at various evolution stages. In the beginning of vortex-pair formation, the vortices are straight and uniform along their axes. Later, two different instability behaviors occur. The large-scale symmetric deformation with axial wavenumber of about $6b$ corresponds to the Crow instability, while the growing disturbance

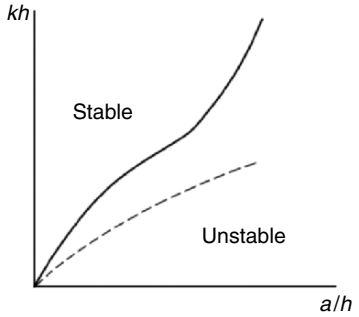


**Fig. 9.24.** Stability boundary for symmetric modes of trailing vortex pair. The *dashed line* is the maximum growth rate of disturbances. From Saffman (1992)

with $\lambda \ll b$ is due to the short-wave instability which, unlike the Crow instability, will change the vortex-core structure. The amplitude is larger in the regions where the Crow instability brings the two vortices closer with stronger mutually induced strain rate. A close look at Fig. 9.25c indicates that the initial reflectional symmetry of the flow with respect to the plane separating the vortices is lost, and the displacements of the two vortices are out of phase. Thus, the two instabilities are closely coupled in their evolution.

If only the Crow instability acts, the vortex pair will experience a vortex-reconnection process (Sect. 8.3.3) to form a periodic array of vortex rings, which persist for a long time. Hence, most of the initial circulation is retained in the long-life and large-scale structures. But, when long- and short-wave instabilities coexist, their mutual interaction significantly complicates the late-stage evolution pattern. The mutually induced shift velocity of the vortex pair due to long-wave instability is a constant; but with the existence of short-wave instability this velocity will shortly become much smaller but finally tend to a constant again, about only 1/3 of its initial value. This reduction of the shift velocity is an indication of the breakdown of the complicated and organized structures formed by both instabilities.

In fact, as just said, in a region where the vortices are brought closer by the Crow instability, the elliptical instability develops more rapidly, and hence at these periodic axial locations the primary organized vortical structures break down first, resulting directly in a mixing through a cross over of the fluid originally rotating around only one vortex. This process leads to the formation of an array of transverse counter-rotating secondary vortex pairs. The axial vorticity is thereby pulled out, and is subsequently tilted and stretched by the strain field. Therefore, the circulation of the primary vortices is considerably weakened, which is why the mutual-induction speed is reduced. Obviously, compared to the Crow instability alone, the interaction of long- and short-wave instabilities can destroy the large-scale vortex structures more efficiently.

Finally, an important issue in trailing-vortex instability is the AI/CI character of the counter-rotating vortex pair in the presence of a uniform

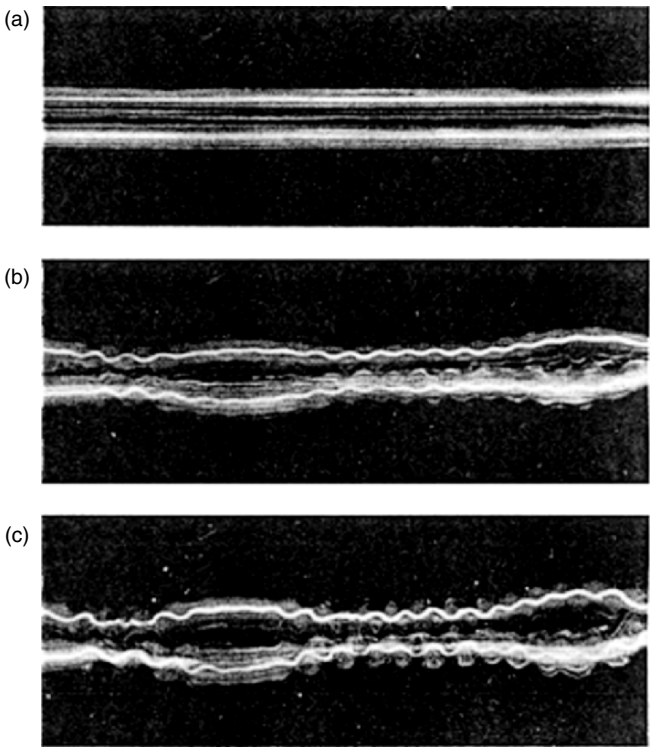


**Fig. 9.25.** Visualization of vortex pair evolution under the combined action of long-wavelength and short-wavelength instabilities at different dimensionless time $t^*$. (**a**) $t^* = 1.7$; (**b**) $t^* = 5.6$; (**c**) $t^* = 6.8$. From Leweke and Williamson (1998)

axial advection velocity. This spatial-temporal development of trailing vortices has been examined by Fabre et al. (2000a,b). The trailing vortices have a downstream advection velocity $U_0$ and a mutually induced downwash velocity $W_0 = \Gamma/2\pi b$. The dispersion relation for spatio-temporal mode analysis has the form

$$D\left(k, \omega; \frac{a}{b}, \frac{W_0}{U_0}\right) = 0$$

of which Fabre et al. studied two asymptotic cases.

At the long-wave asymptotic end with $(a/b)^2 \ll 1$, the AI/CI regions are shown in Fig. 9.26a in the parametric $(W_0/U_0, a/b)$-plane. As $W_0/U_0$ increases the flow changes from CI to AI, and in the limit of $a/b \to 0$ a finite ratio $W_0/U_0 > 0.14$ is needed to promote the absolute instability. On the other hand, in the CI region on the left part of the figure one may perform a spatial-mode analysis. Then the ratio of the spatial and temporal growth rates can

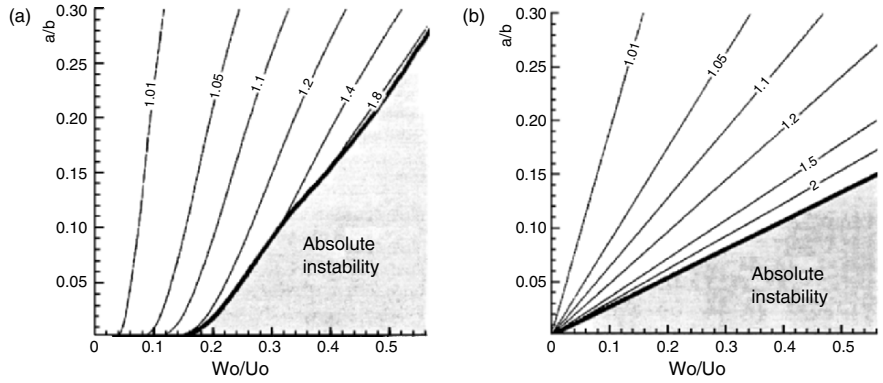


**Fig. 9.26.** The absolute and convective instability regions of a vortex pair. (**a**) Short-wave instability; (**b**) long-wave instability. The ratio of spatial to temporal growth rates is displayed in the convective region. From Fabre et al. (2000b)

be compared, also shown in the CI region of Fig. 9.26. The spatial growth is seen increasingly larger than the temporal growth as the AI region is closer.

At the opposite short-wave asymptotic end with $|ka| = \mathrm{O}(1)$, the AI/CI boundary is shown in Fig. 9.26b. Qualitatively similar to the long-wave case, the flow is convectively unstable when $W_0/U_0 \to 0$, and its spatial growth rate is larger than the temporal one as $W_0/U_0$ increases.

The AI/CI character of trailing vortices is of great value in aeronautical application. Let the aircraft flight speed be $U_0$, then the downwash velocity of the trailing vortices is given by (e.g., Prandtl and Tietjens 1934)

$$\frac{W_0}{U_0} = \frac{C_\mathrm{L}}{4\pi \mathrm{AR}} \left(\frac{b_0}{b}\right)^2 ,$$

where $C_\mathrm{L}$ is the lift coefficient of the wing, AR is its aspect ratio, and $b_0$ its wing span. Assume $\mathrm{AR} \gg 1$ and the wing load has elliptic distribution, then $b/b_0 = \pi/4$ and $W_0/U_0 \simeq 0.13 C_\mathrm{L}/\mathrm{AR}$. For a common transport aircraft in the lending state there is $C_\mathrm{L} \approx 2$, $\mathrm{AR} \approx 10$, and $W_0/U_0 \approx 0.026$. Thus, by Fig. 9.26 the trailing vortices are convectively unstable, and spatial-mode analysis can be applied to study their evolution. The obtained maximum spatial growth rate of the disturbance is close to the maximum temporal growth rate. But, for wings with small AR or high-lift devices, the trailing vortices may exhibit absolute instability.

## 9.5 Vortex Breakdown

*Vortex breakdown* is a sudden and abrupt structural change in the evolution of a concentrated vortex, as a typical appearance of the nonlinear instability

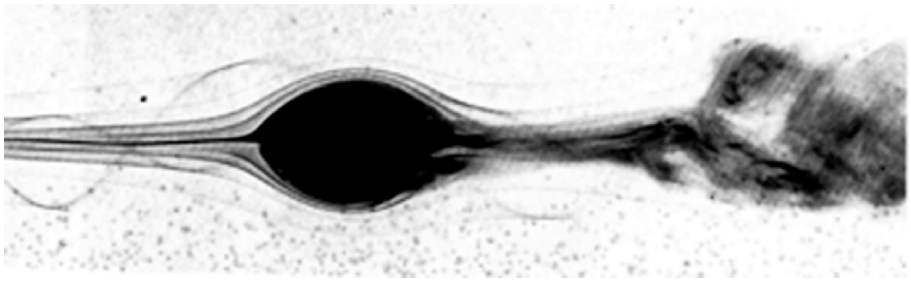

**Fig. 9.27.** A bubble-type vortex breakdown. Reproduced from Van Dyke (1982)

of vortex motion. Different patterns of vortex breakdown may occur, such as nearly-axisymmetric bubble type, spiral type, and double helix type. Fig. 9.27 is a typical photo of the bubble-type vortex breakdown.

At low Reynolds numbers, vortex-breakdown patterns have three most essential features: the appearance of a stagnation point at the vortex axis; a finite recirculation zone following the stagnation point; and the sudden expansion of the vortex core. But at very high $Re$ Sarpkaya (1995) observed a quite different breakdown pattern in swirling flow: a kink appears in the vortex core, followed by a spiral. The nascent spiral adjacent to the kink directly bursts into turbulence and quickly rotates. The reminder of the breakdown transforms into a nominally axisymmetric core of swirling turbulent flow. The breakdown bubble and recirculation zone are no longer observable.

Vortex breakdown plays an important favorable or unfavorable role in nature and technology. It has been observed in tornadoes, dust devils, and water spouts. In a combustion chamber the recirculation zone after the breakdown of the swirling flow may support and stabilize the flame, and enhance the mixing of the fuel and air. The trailing vortices behind large aircrafts may be destructed by breakdown, and thereby their threat to a following aircraft is reduced during take-off and landing. However, the breakdown of the leading-edge vortices of a slender-wing aircraft at large angles of attack may significantly decrease the nonlinear vortex lift, increase the drag, and deteriorate the controllability.

At the fundamental level, as a typical and extremely complicated nonlinear-dynamics phenomenon, a clear understanding of the vortex breakdown is of significant value in theoretical studies.

All these explain why the vortex breakdown has become a research area of vortex dynamics that has been attracting great attention of many researchers ever since it was first observed by Peckham and Atkison (1957) in the leading-edge vortex evolution of low-speed flow over a slender wing. Considerable progresses have been achieved by various experiments, numerical studies and theoretical analyses during the past five decades. For reviews of experimental findings, physical observations, and theoretical developments at different

stages see Sarpkaya (1971), Hall (1972), Leibovich (1978, 1983), Stuart (1987), Escudier (1988), Althaus et al. (1995), Lucca-Negro and Doherty (2001).

The current status in the researches of vortex breakdown may be roughly summarized as follows. In experimental studies, the description of its phenomena and basic characters has been gradually completed, and one's interest has turned to the breakdown control since 1990s (e.g., the review of Mitchell and Délery (2001)).

In computational studies, the current focus is the numerical solutions of the unsteady Navier–Stokes equation with high accuracy and resolution, which has not only enabled pretty good simulation of experimentally observed flow patterns but also revealed some new phenomena, and hence promoted relevant theoretical developments.

In theoretical studies, various models have been proposed toward a rational understanding of the physical mechanisms involving in vortex breakdown, of which the basic aspects have now been clarified.

Owing to its inherent complexity, however, so far a unified, satisfactory and commonly accepted theory on the physics and topological structure of vortex breakdown has not yet appeared. This situation is also responsible for the lacking of technical means in achieving effective and efficient control of vortex breakdown. Therefore, it is still necessary to continue relevant fundamental researches, of which the recent progresses are outlined in this section.

### 9.5.1 Vorticity-Dynamics Mechanisms of Vortex Breakdown

The physical mechanism of vortex breakdown can well be qualitatively understood in terms of vorticity dynamics (Brown and Lopez 1990).

Consider an axisymmetric and steady swirling motion of an incompressible fluid, and neglect the viscosity first. As shown in Sect. 6.1, in cylindrical coordinates $(r, \theta, z)$ with velocity components $(u, v, w)$ and vorticity components $(\omega_r, \omega_\theta, \omega_z)$, this flow is generalized Beltramian and can be described by the Stokes streamfunction $\psi$, circulation $\Gamma(\psi)$, and stagnation enthalpy $H(\psi)$. In the discussion of vortex-core dynamics of a swirling flow (see (8.25) and (8.26)), we have shown that the axial pressure gradient (and axial acceleration $w\,\mathrm{d}w/\mathrm{d}z$ at the vortex axis) has two constituents, imposed at the outer edge of the core by the exterior boundary condition and caused by the rotational effect of the swirl, respectively. Even under an externally imposed favorable pressure gradient there can still be an adverse pressure gradient (and axial deceleration) at the vortex axis. Actually, in practical circumstances where vortex breakdown takes place, either in a vortex generator with a straight circular pipe followed by an expanding section (most of experimental studies of vortex breakdown were conducted in this kind of apparatus) or on the lee side of a slender wing at large angles of attack. The axial deceleration must then cause an outward radial flow due to the continuity. Consequently, the balances of momentum and angular momentum will force a redistribution of $\omega_z$ and $\omega_\theta$, of which the detailed process is as follows.

First, from the observed velocity distribution upstream the breakdown point, it is known that in the early stage of the flow evolution the axial vorticity $\omega_z$ is dominant, while $\omega_\theta$ takes a weak and positive value. However, to have an internal stagnation point at the vortex axis that signifies the onset of vortex breakdown and is followed by a recirculating zone, the axial velocity $w$ must become negative at the vortex axis $r = 0$. Then, by the Biot–Savart formula for axisymmetric flow and applied to the axial velocity at $r = 0$,

$$w(0,z) = \frac{1}{2}\int_0^\infty \int_{-\infty}^\infty \frac{r^2\omega_\theta}{[r^2+(z-z')^2]^{3/2}}\mathrm{d}r\,\mathrm{d}z', \tag{9.99}$$

it is evident that $w(0,z) < 0$ must be associated by a change in sign of the azimuthal vorticity $\omega_\theta$. Therefore, as pointed out by Brown and Lopez (1990) based on their numerical simulation, the generation of negative vorticity (hence the swirling flow is of wake-type if $u = 0$) is a necessary condition for the appearance of the internal stagnation point and recirculating zone.

Next, to explain how $\omega_\theta$ becomes negative, notice that by (6.12b) there is

$$\frac{\mathrm{D}}{\mathrm{D}t}\left(\frac{\omega_\theta}{r}\right) = \frac{1}{r^4}\frac{\partial \Gamma^2}{\partial z} = -\frac{u}{r^3}\frac{\partial \Gamma^2}{\partial \psi}. \tag{9.100}$$

But, as sketched in Fig. 9.28, an expansion of the flow tube will cause an increase of the circulation $\Gamma$; and, in most practical cases with vortex breakdown, one observes $\mathrm{d}\Gamma^2/\mathrm{d}\psi \geq 0$. This is a tilting effect of the vorticity. Therefore, a positive radial velocity $u > 0$ as asserted above will cause a decrease of $\omega_\theta$. If this trend continues, $\omega_\theta$ will eventually become negative.

Then, the azimuthal vorticity in an axisymmetric flow can be viewed as a bundle of thin vortex rings, each having a length $l = 2\pi r$ that is enlarged by the outward flow $u > 0$. Therefore, once appears, the negative $\omega_\theta$ will be enhanced due to stretching, which will in turn induced a stronger negative axial velocity at the axis.

We thus see a *positive-feedback mechanism*: an adverse pressure gradient reduces the axial velocity and causes an outward radial velocity, associated with a reduction of the azimuthal vorticity due to the vorticity tilting; once the azimuthal vorticity becomes negative, it is enhanced by the stretching effect due to the outward radial flow and hence causes a further reduction

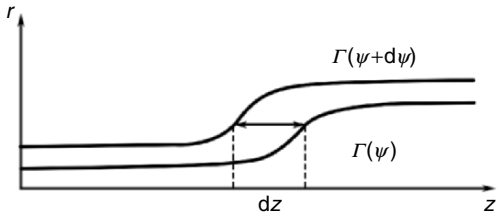


**Fig. 9.28.** The generation the axial gradient of the circulation

of the axial velocity and to make the latter become zero and even negative. This nonlinear positive-feedback mechanism finally leads to the formation of an internal stagnation point and vortex breakdown.

Only the above positive-feedback mechanism, however, cannot stabilize the breakdown bubble at an equilibrium position. This mechanism has to be counteracted by a *negative-feedback mechanism*. In fact, the latter does exist, again due to the vorticity stretching and tilting. Once is formed, the breakdown bubble will force the external fluid to move outward like passing a bluff body, making the vorticity tubes tilted outward too and stretched as well. These two effects enhance the outward radial velocity from the vortex axis, which supplements the fluid momentum far from the axis to suppress the external axial adverse pressure gradient. It is the coexistence and dynamic balance of the positive and negative feedback mechanisms that forms a complete vorticity-dynamics interpretation of the vortex breakdown.

Recent direct numerical simulations have confirmed the preceding analysis. Darmofal's (1993) computation demonstrated the variation of axial and azimuthal vorticities during the vortex breakdown. Ruith et al. (2003) have applied a high-accuracy scheme to compute the unsteady axisymmetric and three-dimensional swirling laminar jets and wakes, with flow domains unbounded in the downstream and radial directions. They simulated the spatial and temporal evolution of swirling Navier–Stokes flows. The numerical results agree well with the experiments of Garg and Leibovich (1979), and show that viscous diffusion of axial vorticity away from the axis starts the evolution of the flow. It effectively reduces the induced velocity on the vortex axis, thereby increasing the pressure locally. Adverse pressure gradient and viscous diffusion yield a divergent vortex core. Thus, the preceding inviscid feedback mechanisms are extended to viscous flow. Then the flow evolves toward an axisymmetric, quasi-steady bubble breakdown state, enclosing an ovoid region of circulating fluid. The axisymmetric breakdown configuration eventually becomes unstable to helical disturbances in the wake of the bubble, yielding a helical breakdown (see Sect. 9.5.3).

### 9.5.2 Onset of Vortex Breakdown: Fold Catastrophe Theory

Theoretically, one approach to the interpretation of vortex breakdown is using hydrodynamic stability theory, which was first attempted by Ludwieg (1960, 1965). He considered the formation of the breakdown internal stagnation point at the vortex axis as a result of loosing stability of the vortex core to helical disturbances. However, linearly stability analysis and experiments (Escudier 1988) indicated that the flow upstream breakdown point is at worst still critically stable; and, even if it is linearly unstable there exist no sufficient space and time to allow for any small disturbance to evolve to such a strong one that can cause the observed abrupt and violent change in the vortex structure. In fact, according to the linearly stability theory, under certain external-flow conditions one can find a flow region unstable to helical disturbances, but

observe no breakdown. Conversely, some axisymmetric breakdown can occur without loosing stability, as shown for a swirling flow in a sealed cylinder with a rotating endwall. Thus, the vortex breakdown is not a direct consequence of the hydrodynamic instability.

The suddenness of vortex breakdown makes some researchers more inclined to consider it as a jump from one swirling-flow state to another. This concept was initiated by Benjamin (1962) in his "*conjugate theory*", in which the breakdown is viewed as a critical state very similar to a shock wave in gas dynamics or a hydraulic jump in open channel flows. According to the theory, the flow upstream the breakdown is supercritical, where the disturbance can only propagate in downstream direction; while the flow downstream the breakdown is subcritical, where the disturbance can propagate in both upstream and downstream directions. Thus, the breakdown is a transition process from supercritical to subcritical. Under this critical state, Leibovich and Randall (1972), Randall and Leibovich (1973), Leibovich and Kribus (1990) have obtained solitary wave solutions of weakly nonlinear and fully nonlinear evolution equations to mimic axisymmetric bubble-type breakdown.

During this period, several researchers have also considered the vortex breakdown as a *fold catastrophe* that cause a sudden transition to a different flow state. Batchelor (1967) was the first to notice that the solution for inviscid swirling flow in a diverging pipe have a fold bifurcation as the swirl is increased. This concept has been extended by Saffman (1992) and Buntine and Saffman (1995). The fold catastrophe theory has been further developed by Wang and Rusak (1997a), Goldshtik and Hussain (1997, 1998), and Rusak et al. (1998). Meanwhile, numerical simulations of swirling flows in circular tube and the flow in a rotating, sealed cylinder with a differentially rotating endwall also confirmed the existence of the nonuniqueness of the solutions corresponding to the fold bifurcation.

The fold catastrophe theory for vortex breakdown has now become an active research direction, which provides a new interpretation of the breakdown and serves as a new departure point for its understanding. In what follows we first review the results of direct numerical simulations of swirling flow, and then outline the theoretical work of Wang and Rusak (1997a).

In most of early numerical computations on vortex breakdown in a circular tube, the obtained solutions are unique. But later more accurate computation indeed found the solution nonuniqueness (Leibovich and Kribus 1990). Beran and Culick (1992) have conducted a numerical simulation specifically for testing the uniqueness of the solution. They computed the steady and axisymmetric swirling flow of a viscous incompressible fluid through a circular pipe of constant radius and circular pipes with throats. The variation of the solution as a characteristic parameter $\lambda$ was numerically determined, where $\lambda$ is taken as the value $q$ of a $q$-vortex. The authors found that the axial velocity at the centerline

$$w_{\mathrm{c}}(z) = w(z, r)|_{r=0}$$

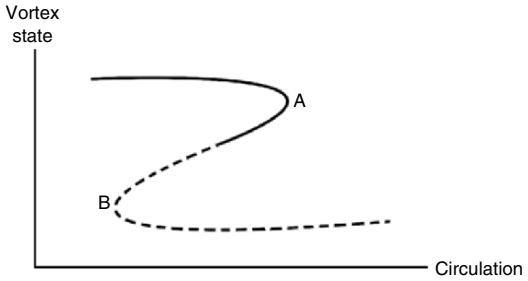


**Fig. 9.29.** A representative solution diagram that relates vortex state to vortex circulation. A, primary limit point; B, secondary limit point; *solid line* – nonreversed flow; *dashed line* – reversed flow.

is a good measure of the behavior of the vortex-core flow that gives a direct indication of where vortex breakdown occurs. Furthermore, the quantity

$$Q \equiv \min_{z}[w_{\mathrm{c}}(z)], \tag{9.101}$$

was used to represent the computed solution in the presentation of solution path. A typical numerical result is shown in Fig. 9.29. The figure indicates that the solution depends on the vortex circulation, and the nonuniqueness comes about through the formation of two limit points on the path, in between of which the vortex may have three possible solutions. Along the direction of circulation increase, for the uppermost branch of solution points there is no reversed flow. This branch ends at a limit point A. After A is passed, the path of solution folds, and a solution with reversed flow gradually develops as the circulation increases. This branch ends at the second limit point B. As the incoming swirl is further increased, the solutions after passing B have a large separation zone. Thus, the existence of the solution nonuiqueness and a fold bifurcation is confirmed.

The studies of Wang and Rusak (1997a,b) have unified the major previously theoretical and numerical approaches (see also Wang and Rusak 1996a,b; Rusak et al. 1998). They have obtained the global bifurcation diagram for the Euler solution of steady and axisymmetric swirling flow, and studied the linear stability of different branches of the bifurcated solution at the critical state. In this way, they are able to give a consistent explanation of the axisymmetric vortex breakdown.

Wang–Rusak's study includes three main steps. The first step is the global analysis of Euler equation of the axisymmetric swirling flow in a pipe. Consider the axisymmetric and incompressible swirling flow in a straight circular pipe of finite length $z_0$. Introduce the Stokes stream function $\psi(z, r)$, so that the flow is generalized Beltramian and governed by the Bragg–Hawthorne equation (6.14)(it is also known as Squire–Long equation). For mathematical convenience, set $y = 1/2r^2$, so that equation becomes

$$\psi_{yy} + \frac{\psi_{zz}}{2y} = H'(\psi) - \frac{I'(\psi)}{2y}, \tag{9.102}$$

where $H = p/\rho + 1/2(u^2+v^2+w^2)$ is the total head and $I = \Gamma^2/2$ the extended circulation function, both are nonlinear functions of $\psi$. This nonlinearity may lead (9.102) to have multiple solutions at a given *swirling level* $s$, defined as the ratio of the maximum circumferential velocity and the characteristic axial velocity.

In order to study the solution bifurcation, it is necessary to find a representative scalar of the flow status. WR pointed out that the solutions of (9.102) are well known to correspond to the stationary points of the following functional:

$$E(\psi) = \int_0^{x_0} \int_0^{1/2} \left( \frac{\psi_y^2}{2} + \frac{\psi_z^2}{4y} + H(\psi) - \frac{I(\psi)}{2y} \right) \mathrm{d}x\, \mathrm{d}y, \tag{9.103}$$

of which the variational principle had been introduced by Benjamin (1962) in his vortex-breakdown study.

The global variational analysis determines the topology of the functional $E$ for various fixed swirl level $s$. Numerical analysis shows that there exist two critical swirl levels of the incoming vortex flow, $s_0$ , $s_1$ and $s_1 > s_0$. Refer to Fig. 9.30a, when $s < s_0$, the inlet flow develops as a columnar flow state all along the pipe and is a global minimizer of $E(\psi)$ and unique solution of (9.102). When $s > s_0$ (Fig. 9.30b), three possible steady-state solutions of the problem are found. One is the trivial columnar state $\psi_0(y)$ that is now a local minimizer of $E(\psi)$. The two other states bifurcate at about $s_0$ from a certain state which is a large disturbance to the columnar solution. One solution is the global minimizer of $E(\psi)$ and describe an open, stagnant separation zone. The second solution is the min–max point of $E(\psi)$ which describe a localized (solitary) wave in the swirling flow. The critical swirling level $s_1$ (Fig. 9.30c) is corresponding to Benjamin's critical swirling level, but modified due to the effect of the finite length of pipe. As swirl is further increased above $s_1$, the columnar flow solution becomes a min–max point of $E(\psi)$. The third possible solution is the global minimizer solution, and the separation zone becomes much large in its size and its leading point moves toward the pipe inlet. It describes a vortex breakdown state.

The earlier mentioned bifurcation diagram can be plotted in a different way, see Fig. 9.31, to see more clearly the variation of the solution status as the swirl level. The characteristic parameter of the solutions is taken as the

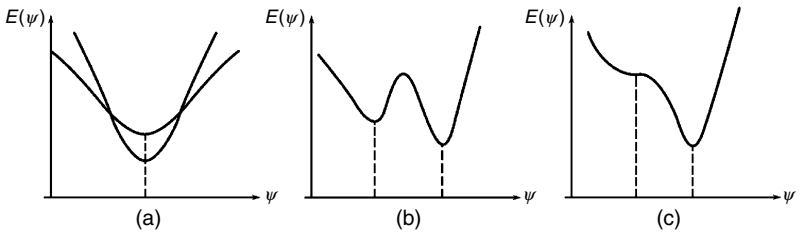


**Fig. 9.30.** The function $E(\psi)$ for (**a**) $s > 0$ but small; (**b**) $s_0 < s < s_1$; (**c**) $s = s_1$. Based on Wang and Rusak (1997a)

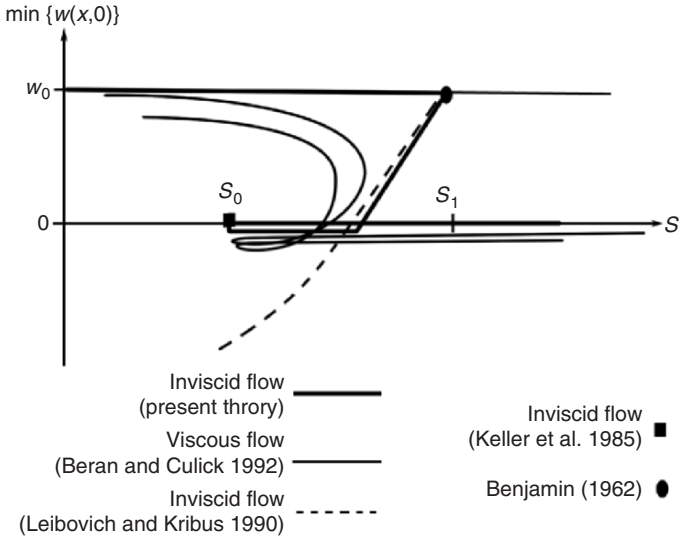


**Fig. 9.31.** The bifurcation diagram of solutions and the corresponding theoretical studies. From Wang and Rusak (1997a)

minimum axial velocity along the vortex axis. In this bifurcation diagram of (9.102) also plotted the predictions of the theories of Benjamin (1962), Keller et al. (1985), and Leibovich and Kribus (1990). It is evident that the Wang–Rusak theory coincides well with the reasonable parts of the previous theories, provides their natural interrelations, and meanwhile fills the gap between them. It can also be seen that the Wang-Rusak theory is well correlated to the numerical results of Beran and Culick (1992), indicating that the main effect of viscosity is to smooth the bifurcation diagram. This has been studied theoretically by Wang and Rusak (1997b) as well, in good agreement with the results of Beran and Culik. Therefore, it can be concluded that the bifurcation of steady and viscous solutions is dominated by that of steady and inviscid solutions.

While the earlier bifurcation analysis of (9.102) explains the mechanism of vortex breakdown in terms of nonlinear dynamic system, it is more desired that the mechanism can be clarified in terms of fluid dynamics. In the second step of Wang–Rusak's analysis, they have considered the linear stability of different branches of the bifurcation solution at critical state to axisymmetric disturbances. They found that when $s < s_0$ the branch of the columnar flow solutions is unconditionally stable to any axisymmetric disturbance. This means that any axisymmetric disturbance to a base columnar flow will decay in time and the flow return to a columnar state when the incoming swirl in the range of $s < s_0$. In a range of $s_0 < s < s_1$, two stable steady-state solutions coexist, one is a local minimizer solution that describe a columnar swirling flow and the other is a global minimizer that describe a swirling flow

with a large open stagnation zone. The two branches of solutions are connected by a branch of min–max solutions that are unstable. This means that in the range $s_0 < s < s_1$ there exist two basins of attraction. In the range of $s > s_1$ the equilibrium columnar flow state is unstable and it is expected to be absolutely unstable. If the swirl is relatively large, the global minimizer solution is a strong attractor, then the flow will develop with time in a nonlinear dynamics from a columnar state into the vortex breakdown.

In the third step of Wang–Rusak's analysis, they discuss the effects of slight viscosity, pipe divergence and the inlet vorticity perturbations. They have shown that when the flow Reynolds number is relatively high, the pipe is straight (a small adverse pressure gradient), and there are no vorticity perturbation at the pipe inlet, the mechanism of vortex breakdown is dominated by the loss of stability of the columnar state as the swirl level is increased above the critical value and the nonlinear transition to a relatively stable lower energy breakdown state which contains a large open near stagnant separation zone. On the other hand, if the Reynolds number is lower, the adverse pressure gradient and the negative inlet azimuthal vorticity perturbation are strong, the breakdown state develops as a result of those decelerating effects and breakdown appears as solitary wave disturbance.

Wang–Rusak's theory is limited to the axisymmetric swirling flow. For a complete understanding of the vortex breakdown phenomenon a study of the axisymmetric solutions to the nonaxisymmetric disturbances is necessary to be developed.

### 9.5.3 Vortex Breakdown Development: AI/CI Analysis

The AI/CI analysis of vortices introduced in Sect. 9.3.1 enables the hydrodynamic stability theory to proceed from local temporal-mode to global spatial-temporal mode. It is reasonable to believe that the theory may reveal the mechanism of the breakdown development after its sudden onset, especially the mode selection in the breakdown zone, i.e., under what conditions there appear axisymmetric bubble breakdown, and helical or double-helical breakdown.

In fact, some elements of the AI/CI concepts have been implied in certain early theoretical attempts of vortex-breakdown. For example, the CI corresponds to a supercritical flow of Benjamin's (1962) "conjugate-flow theory", while the AI corresponds to its subcritical flow. On the other hand, Bilanin and Widnall (1973) proposed that in a breakdown region waves are trapped with vanishing group velocity. This concept may also be considered as the simplest AI/CI analysis. Therefore, the AI/CI theory of vortex breakdown is a natural generalization of the in-depth development of the conjugate-flow theory and group-velocity criterion.

Monkewitz (1988b) has shown the existence of a finite pocket of local absolute instability in the wake of axisymmetric bluff bodies. Correspondingly, with a bubble-type breakdown, the upstream flow is decelerated, the stream

tube is expanded, and an internal stagnation point is formed. These processes are just like a flow over a bluff body, and hence suggest that the key to understanding breakdown and its different modes observed in experiments lies in the consideration of the flow field created by vortex breakdown itself. Thus, many studies have used the AI/CI analysis to elucidate the physical evolution in the breakdown zone, e.g., Olendraru et al. (1996, 1999), Delbende et al. (1998), Loiseleux et al. (1998), Yin et al. (2000), Ruith et al. (2003), and Gallaire and Chomaz (2003a,b, 2004).

Loiseleux et al. (1998) have examined the relation between vortex breakdown and the AI/CI characters of a prebreakdown vortex, for the latter they used the Rankine vortex as the basic flow, with axial velocity profile being a plug flow. The shape of AI domain is qualitatively similar to its counterpart for the Batchelor vortex (Figs. 9.16 and 9.17). The authors found that for $n = -2$, when the external axial velocity becomes zero and the swirl number $S = 1.61$ (or the Rossby number $Ro = S^{-1} = 0.62$), the flow becomes absolutely unstable. They compared this prediction with several experimental data measured in vortex generators and above slender wings, see Fig. 9.32 on the $(Re, Ro)$-plane, where $Ro = 0.62$ is marked by a dashed line. Despite its simplicity, the AI/CI criterion is seen to provide a reasonable estimate of vortex breakdown onset.

Yin et al. (2000) have used the experimental data of vortex breakdown obtained by Garg and Leibovich (1979) in a pipe to conduct an AI/CI numerical analysis, where the basic flow is assumed as a Batchelor vortex ($q$-vortex) that fits the experimental profiles quite well. The result is listed in Table 9.1,

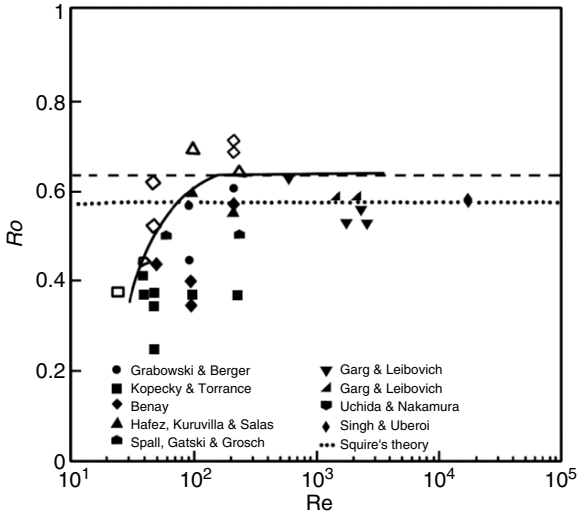


**Fig. 9.32.** Reynolds number–Rossby number plane for various numerical and experimental studies of swirling flows and trailing wing-tip vortices. The *dashed line* corresponds to the AI/CI transition for a Rankine vortex with plug flow and a zero external axial velocity. From Loiseleux et al. (1998)

**Table 9.1.** AI character in near wake of breakdown based on experimental profiles of Garg and Leibovich (1979). From Yin et al. (2000)

| Case | $Re$ | $W_\infty/W_d$ | $q$ | $k_r^o$ | $k_i^o$ | $\omega_r^o$ | $\omega_i^o$ |
|---|---|---|---|---|---|---|---|
| 1 | 9892 | 1.066 | 1.140 | 1.65922 | −0.563106 | 3.556942 | 0.242629 |
| 2 | 9577 | 1.094 | 1.037 | 1.433490 | −0.804143 | 2.919500 | 0.244768 |
| 3 | 7196 | 1.035 | 1.094 | 1.630081 | −0.547424 | 3.143451 | 0.270133 |
| 4 | 5575 | 1.151 | 1.182 | 1.374675 | −0.724399 | 3.766633 | 0.156573 |
| 5 | 4830 | 1.036 | 1.086 | 1.600400 | −0.568426 | 3.081507 | 0.264991 |
| 6 | 4684 | 1.064 | 0.965 | 1.144451 | −0.705080 | 2.293895 | 0.226299 |

showing that for all tested cases the flow in the near wake of breakdown bubble is indeed absolutely unstable. Yin et al. also computed the AI/CI character using the experimental data of Pagan and Solignac (1986) by fitting their velocity profiles by a modified version of the Batchelor vortex. Once again the flows were found absolutely unstable.

Yin et al. (2000) have further applied the AI/CI theory to predict an important property of the vortex breakdown: the dominant frequency in a breakdown bubble. Based on Bilanin's (1973) concept of vanishing group-velocity $C_\mathrm{g}$ in a breakdown region and noticing that from the AI/CI point of view $C_\mathrm{g}$ should be computed in the complex $k$-plane, for trapped waves there is

$$C_\mathrm{g} = \frac{\mathrm{d}\omega}{\mathrm{d}k} = \frac{x}{t} = 0 \quad \text{for complex} \quad \omega, k, \tag{9.104}$$

which may yield the corresponding absolute frequency $f^0$ for given $W_\infty$, $q$, and $n$. To simplify their analysis, Yin et al. introduced some approximations based on the experimental data of Garg and Leibovich (1979), and adopted a speculation of Koch (1985) that the dominant frequency could be determined from an $\omega^0$ at the boundary of AI and CI regions, for which $\omega_i^0 = 0$. Then, in the experimental low Reynolds-number range, they found that the Strouhal number (dominant frequency $f^0$ nondimensionalized by the core radius and characteristic axial velocity of the basic flow) predicted by AI/CI analysis takes about the same value around 0.17, in reasonable agreement with the experimentally observed value around 0.15, see Fig. 9.33. All these tests strongly suggest that the absolute instability should be a common character in vortex breakdown.

Once it is established that in the breakdown zone the flow is absolutely unstable, the key issue is whether the AI/CI analysis can reveal the physical mechanism of the mode selection, including the transition from an axisymmetric bubble-type breakdown to a spiral-type breakdown. This has been addressed by Ruith et al. (2003) based on their direct numerical simulation using a two-parameter axisymmetric columnar vortex model as basic flow. Their computation shows that the basic breakdown form is an axisymmetric bubble as predicted by the fold catastrophe theory, and in the wake of the bubble there exists a sufficiently large AI pocket that causes a transition to helical breakdown modes, giving rise to a self-excited global mode.

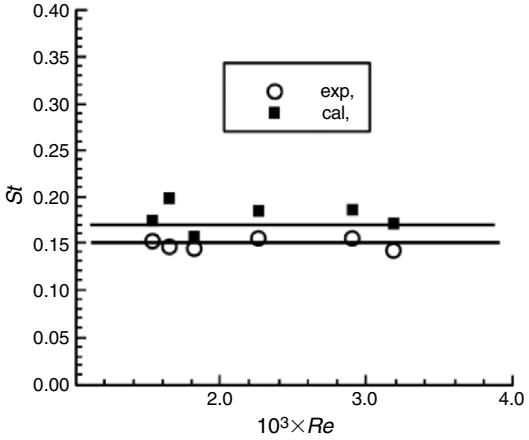


**Fig. 9.33.** Dominant Strouhal number in a breakdown bubble. $St = 0.171$: theoretical predication. $St = 0.15$: average of measured values. From Yin et al. (2000)

To clarify the mode selection mechanism, Ruith et al. (2003) approximated the numerically computed swirling vortex by a Batchelor vortex with varying swirling level $s$ and parameter $a$ (see Sect. 6.2.1) at different $z$-stations, so that the AI/CI characters of the flow at each section can be analyzed using the AI/CI boundary plots of Fig. 9.16. The results are shown in Fig. 9.34 for four different swirling level $s$ that quantifies the relative importance of the swirl velocity with respect to the axial velocity.

For each selected $s$, the dash-dotted line connects the $(a, s)$ values computed at different $z$-stations, with the arrow pointing to the direction of $z$ increase. This figure should be read along with Fig. 9.35, the corresponding numerically simulated flow pattern at the same $S$, from which one can find what physical event happens at the characteristic $z$-stations marked by the value of $z$ in Fig. 9.34.

Consider first Figs. 9.34a and 9.35a at a relatively small swirl level $s = 0.8944$ first. In this case, the velocity profiles at $z = 3.0$ has entered the AI region but not deeply, and then retreats to the CI region. Since the AI pocket in the physical space is not large enough, this low-swirl case is unable to support self-sustained disturbances, and hence we observe an axisymmetric bubble-type breakdown.

As $s$ is increased to 1.0, see Figs. 9.34b and 9.35b, one finds the $(a, s)$ trajectory enters the AI regions twice as $z$ increases and then returns to the CI region: $z = 1.8$, in the bubble; and $z = 5.3$ in the wake of the bubble. The AI pocket for the latter is considerably larger than that in the bubble itself, and also much larger than the pocket for $s = 0.8944$. This indicates that the critical size able to support a global self-excited mode might be reached first in the wake of the bubble. Owing to this global self-excited disturbance, the axisymmetric bubble is unstable to the helical disturbance wave with

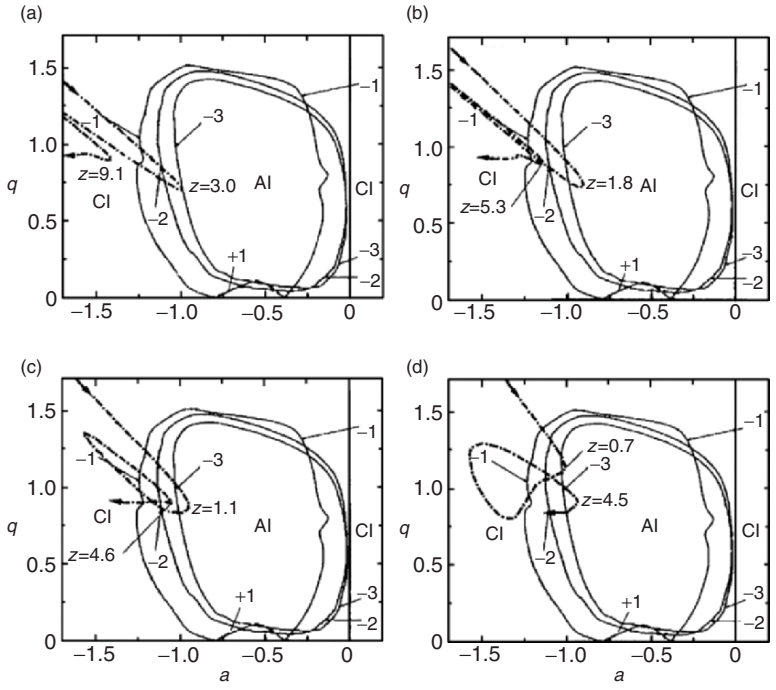


**Fig. 9.34.** AI/CI transition curves (*dash-dotted lines*) for a Batchelor vortex with azimuthal modes $n = \pm 1, -2, -3$ at $Re = 667$ as an observer moves along the vortex axis. *Solid lines*: the AI/CI boundaries taken from Fig. 9.16. (**a**) $s = 0.8944$, (**b**) $s = 1.0$, (**c**) $s = 1.095$, (**d**) $s = 1.3$. From Ruith et al. (2003)

$n = -1$ ($z$=5.3), and thereby starting the transition to spiral breakdown. As $s$ is continuously increased to 1.095 and 1.3, then, the AI pocket in the wake region is further enlarged, indicating more pronounced helical breakdown. And, as seen from Figs. 9.34c,d and 9.35c,d, the AI pockets corresponding to higher azimuthal wave numbers are even larger, leading to the possibility of breakdown modes with higher helical wave numbers: for $s = 1.3$ we have double-helical ($n = -2$) breakdown mode.

## Summary

1. The products of the shearing process, i.e., free or attached vortex layers (free shear layers or boundary layers) and vortices, are subjected to various hydrodynamic instabilities that form the most commonly encountered route to transition and turbulence. Many hydrodynamic stability theories outlined in Sect. 9.1 have been motivated and critically tested by, and found important applications to, these vortical structures. Within linear

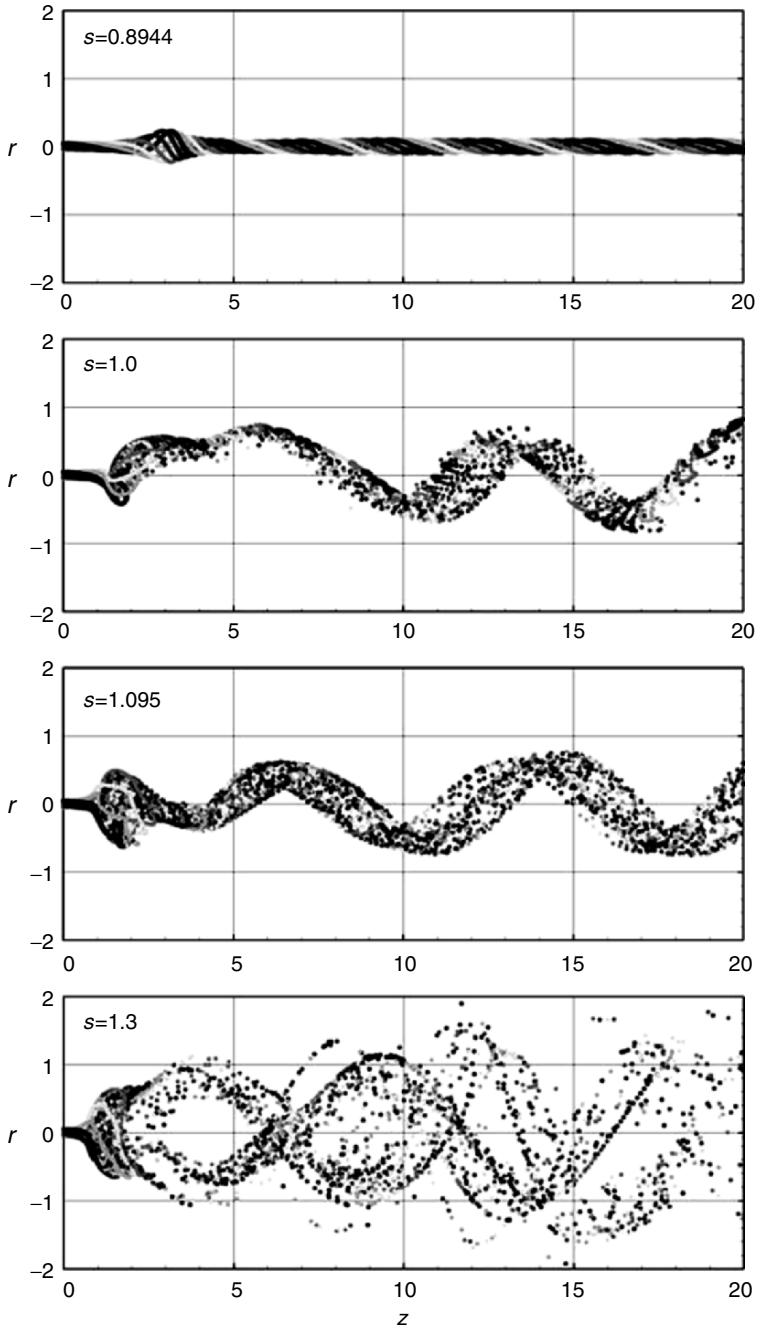


**Fig. 9.35.** The streaklines from the numerical computation of the incompressible time-dependent three-dimensional Navier–Stokes equation for a swirling flow. (**a**) $s = 0.8944$, a steady bubble breakdown; (**b**) $s = 1.0$, the quasi-steady axisymmetric bubble breakdown is helical unstable; (**c**) $s = 1.095$, a helical breakdown; (**d**) $s = 1.3$, the double-helical breakdown mode. From Ruith et al. (2003)

approximation, the classic local analysis based on normal-mode approach has now been enriched by the important distinction between the absolute and convective instabilities (AI/CI), and supplemented by the analysis of the effect of transient algebraic growth of disturbances due to the non-normality of the relevant operator, even if the flow is stable with respect to any nomal-mode disturbances.

As the only active nonlinear term in the momentum and energy balance, the disturbance Lamb vector plays a key role in the instability mechanisms of vortical flows, either locally or globally. Inspecting the interaction of this vector with the basic flow may lead to a clear understanding of the physical processes that make the flow unstable. This knowledge enriches the usually computed stability boundaries and disturbance growth rates.

2. Free and attached vortex layers belong to weakly nonparallel flow. The theories for their instability are developed from the classic results on parallel shear-flow instability, notably the Rayleigh–Fjørtoft theorem for inviscid flow and Orr–Summerfeld equation for viscous flow.

   A free shear layer is subjected to the Kelvin–Helmholtz instability at any Reynolds numbers, by which the layer rolls into a row of spanwise vortices. The dimensionless frequency (Strouhal number) associated with the most amplified disturbance is nearly independent of the detailed basic-flow velocity profile across the layer, which is a key parameter in free shear-layer control.

   A boundary layer becomes unstable as the Reynolds number passes a critical value, for which the normal-mode solution of the Orr–Summerfeld equation, the Tollmian–Schlishting wave, may grow. This wave is a vortical wave.

   In both unstable free shear layer and boundary layer, the spanwise vortical structures will become three-dimensional due to the secondary instability, from which streamwise vortical structures are formed as a further step of transition. In addition, a strong transient growth may trigger nonlinear instabilities, a mechanism that is necessary for subcritical transition of laminar shear flows and for wall-bounded turbulence to be self sustained.

3. The instability of a free straight vortex is caused by the interaction of centrifugal instability and shear instability. Except pure vortices to which Arnold's nonlinear stability theory may apply, this interaction is complicated owing to the wide variety of the velocity–vorticity distribution in a swirling vortex, so that within the linear approximation the governing Howard–Gupta equation has to be solved case by case. Moreover, in addition to the swirl ratio, the AI/CI character of the vortex is not Galilean invariant and depends critically on the axial velocity profile. Besides, the non-normality effect always exists in a vortex and may cause some different route to transition.

4. A strained vortex, including that under the strain field of another neighboring vortex, has abundant instability mechanisms depending on the ratio of disturbance wave length to the vortex core radius. The ultra short-wave instability or elliptical instability is found to be a universal

mechanism for direct transition to turbulence. When the disturbance wave length is of the same order as the core radius (short-wave), the vortex axis may be deformed by the bending and twisting modes of disturbance. When the wave length is long compared to the core radius, the Crow instability comes into play and is responsible for the aircraft trailing vortex pair to be cut and reconnected to discrete vortex rings. This process can be accelerated by the cooperative effect of the long- and short-wave instabilities.

5. As a sudden and abrupt structural change of the vortex core, vortex breakdown is a highly nonlinear process and remains one of the most complicated vortex-dynamics phenomenon not fully understood. Recent progresses, however, have been so significant that basic aspects of the breakdown are gradually clarified. Qualitatively, the breakdown involves the balance of a positive-feedback and a negative-feedback mechanism, both having root at vorticity stretching and tilting. Quantitatively, the onset of vortex breakdown is an axisymmetric and inviscid process of fold catastrophe due to the Euler solution becoming nonunique as the swirl increases, so that the thin-core solution is nonlinearly and globally unstable that has to jump to a stable one with expanded core region. Then, this onset is followed by a disturbance enhancement in an absolutely unstable breakdown region, which forms a bubble or spiral flow depending on the dominant azimuthal disturbance mode.

# 10

# Vortical Structures in Transitional and Turbulent Shear Flows

Problems related to turbulence phenomena have already been mentioned in several previous chapters showing that vorticity and vortex dynamics have made important contributions to turbulence research in many aspects. For example, the instability of shear flows and formation of concentrated vortices are closely related to laminar-turbulence transition. The vortex instability, interaction, and breakdown are closely related to the formation of turbulence. The fundamental laws in vorticity and vortex dynamics are powerful tools to describe and explain the very complicated vortical motions in turbulence. On the other hand, studies in turbulence have in turn enhanced and will continue to motivate the development of vorticity and vortex dynamics. It is therefore logically natural to include this chapter in the present book.

Turbulence is the most difficult problem in classical mechanics. As a complicated, nonlinear dynamic system, a turbulence field consists of many time-dependent vortical structures of various characteristics, interacting nonlinearly with each other. If one regards vortices as the sinews and muscles of fluid motions, there is no doubt that vortices should also be the sinews and muscles of turbulence. The generation, evolution, interaction, and dissipation of these vortical structures dominate the nature of turbulence fields. To understand, prescribe, and control turbulent flows, we have to discuss these vortical structures.

Classic turbulence descriptions focusing on the statistic characteristics of turbulence quantities have made significant contributions to turbulence studies (Bradshaw 1971; Townsend 1976). However, they cannot look into details of the specific structures though the statistics is indeed constrained by these structures. In contrast, we shall focus on the specific motions of the coherent structures in this chapter. The vortical structures in typical turbulent flows will be introduced as examples. For better understanding of their historical evolution, discussions on structures in transitional flows will also be involved in some cases.

Traditional flow visualization techniques may offer important information and have made significant contribution to the studies of vortical structures in

turbulence. However, the results are sometimes confusing and even misleading due to the fact that the image shows streak lines or time lines, etc. instead of streamlines (see Figs. 2.2, 2.3, and Sect. 2.1.1). In particular, the flow markers quite often deviate from the regions of vorticity concentration and accumulate in regions of lower vorticity, which smears out dynamically significant structures from visualization. Fortunately, recent developments in particle image velocimetry (PIV), direct numerical simulation (DNS), and large-eddy simulation (LES) have revealed much more information in turbulent flows and made more detailed structural studies possible.

Based on the knowledge of structure evolution, the importance of vorticity and vortex dynamics in turbulence studies will be addressed. *Our purpose is to attract the readers interested in turbulence into this book. On the other hand, we also try to attract the readers interested in vorticity and vortex dynamic into turbulence studies.* However, this chapter is not a review article, nor do we have intention to compress the abundant turbulence phenomena into one chapter. Only limited typical materials are selected as examples to serve what we try to address. Besides, due to imperfection of the analytical means of studying the vortical motions in turbulence, the major materials will be leaned upon intuitive physical descriptions with some brief analytical explanations wherever convenient.

## 10.1 Coherent Structures

### 10.1.1 Coherent Structures and Vortices

A homogeneous isotropic turbulence field and a typical turbulent shear flow are compared in Fig. 10.1, where (a) is a turbulence field generated by a grid and (b) is a turbulent mixing layer formed by two confluent flows with higher speed on the top and lower at the bottom. No organized structure can be observed at certain distance downstream of the grid in (a). However, there appears rolling up of the spanwise vortices in (b) due to the inflectional instability in the shear region. One can observe that the sizes of individual vortical structures are significantly different; the small vortical structures are random motions while the large spanwize structures are fairly well organized. These relatively organized vortical structures in turbulence are known as *coherent structures*. The coherent structures usually contain a major portion of the turbulence energy and dominate turbulence transport. Thus, they are crucial for understanding and modeling of turbulence, as well as for controlling turbulence phenomena relevant to mixing, heat transfer, combustion, turbulence drag, and aerodynamic noise. So far, quite different definitions were given to the flow structures as coherent. In this book, we suggest the following definition: *coherent structures are groups of evolving structures, mainly vortical structures in turbulence which are spatially well-organized and contain essential portion of turbulence energy. They can be identified from the turbulent*

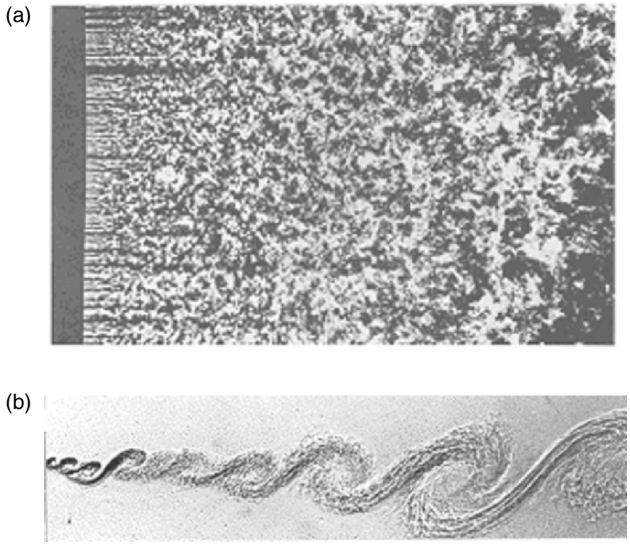


**Fig. 10.1.** Examples of turbulence structures. (**a**) Homogeneous isotropic turbulence behind a grid. (**b**) Large-scale turbulence structures in a turbulent mixing layer. From Van Dyke (1982)

*flow field as quasideterministic structures in the sense that they are more unpredictable in spatial or temporal phases than in size or in shape.*

Special attentions should be paid to some aspects related to coherent structures. First, the concept of coherent structure is varying with the knowledge of turbulence gained in the history. During the infancy of revealing coherent structures, a term "large" coherent structure was often used. However, it was found later that the size of structures is not necessarily a criterion to identify the coherent structures; rather, the level of organization is. We shall see later that the large overturning motion in a turbulent boundary layer is usually not regarded as a coherent structure or at least its coherence is weak, but the relatively small streamwise vortices in the wall region of the boundary layer are coherent. The concept of a coherent structure is based on the common understanding that this organized portion of characteristic structures can be identified from the whole turbulent flow field. Their characteristic shapes are somehow preserved although they are always evolving in space and time.

Associated with the above progress of our understanding, the criteria for identifying coherent structures or in what sense a structure is regarded as organized are also varying. Actually, different experimental techniques or different definitions of a vortex (Sect. 6.6) could lead to different identifications of coherent structures from the same physical flow structures. The phase-locked components of turbulent fluctuations were once regarded as the only criterion to identify coherent motions. After the *phase jitter* was noticed, it has been realized that the phase relation is not always of crucial to the

concept of coherence in many flows, and then pattern-matching techniques became well accepted. To date, there exist many vortex-identification or wave-decomposition techniques applied to identifying coherent structures. The results are often quite scattered. For example, vortex identification can be based on isosurfaces of various scalar fields, such as components of vorticity, enstrophy, or pressure (Sect. 6.6). For the last option, although remarkable concurrence between pressure minima and vortices was found (Robinson 1991a) the relation is not necessarily one-to-one (Kim 1989).

Second, exact occurrence of coherent structures is not predictable although they are quite well organized and quasideterministic. The coherent structures in turbulence are not like the concentrated vortices in a laminar flow; they always coexist with its random partners in a turbulence background, i.e., there is *an order underlying the disorder of fluid turbulence* (Lesieur 1990, pp. 6–7). The nonlinear interactions between the coherent and random structures are always there. Recent studies on the coupling between coherent structures and fine-scale turbulence show that a coherent structure is not a simple vortex. Due to the interaction between a coherent vortex and its turbulence surroundings, there are always secondary structures (threads) spun azimuthally around it (Melander and Hussain (1993a,b)). It forms a typical view of internal intermittency in turbulence where a group of highly dissipative (high vorticity) structures embedded into an irrotational flow region. One can also observe from Fig. 10.1 that those organized large vortical structures are not all the same in shape, in spacing and in the small structures they are carrying. Up to now, no one can predict these structures with exact shape or size, at exact location and exact instance. Instead, the prediction can be made for certain coherent structures to occur under given condition, and the probability of its occurrence is certainly greater than others. That is to say that coherent structures are a sort of organized structures appearing in turbulence with high probability.

### 10.1.2 Scaling Problem in Coherent Structure

Scaling of coherent structures is one of the major problems in scaling of turbulence. As is well known, one employs quite often the concept of *eddy viscosity* to simulate the effect of turbulence on the mean flow. Similar to the averaged free path and averaged velocity of the molecule motion, eddy viscosity in turbulence also contains two scales, one velocity scale and one length scale. But in reality none of the turbulence structures are with fixed size and fixed intensity. What can be observed in a turbulence field are instantaneous frames of fluid motions with at least two physical processes involved. One is the formation and growth of the coherent structures due to instability or self-organization, where the size and energy involved in the coherent structures are growing. The other is the process of cascade where the sizes of the individual vortical structures become smaller and smaller due to the interaction between coherent structures as well as between coherent and random motions.

By its very nature, turbulence is a *multiscale* physical phenomenon. The well-known *Kolmogorov scaling law* (Kolmogorov 1941) revealed the physics that turbulence consists of a continuum of scales from the largest ones determined by the flow geometry to the smallest ones at the Kolmogorov dissipation scale (see details explained later). The largest ones are usually coherent. The smaller ones include cascaded coherent structures and random motions. Thus, there is in fact no distinct scale separation in most turbulent flows as large coherent structures and small random eddies. The classical scale separation concept can only be regarded as a hypothetical possibility, by which the fine scales are supposed to be statistically isotropic in any turbulent shear flows and the coupling between the largely disparate scales is assumed to be weak.

The *universal scaling law* (She and Leveque 1994) also revealed the existence of multiscale structures in turbulence, where the coherent motions correspond to the most intermittent structures and there exists cascading similarity in structures with different length scales. Both of the above theories express very well the existence of multiscale structures in turbulence. The concepts like eddy viscosity or *mixing length* etc. only reflect statistically averaged effects of all the scales in oversimplified ways.

Of all length scales in turbulence, quite a few particular ones have been introduced into turbulence studies, such as Kolmogorov scale, Taylor microscale, integral length scale and viscous length scale, etc. (Tennekes and Lumley 1972; Frisch 1995). The *Kolmogorov scale* (or *dissipation scale*) $\eta = (\nu^3/\varepsilon)^{1/4}$ (for details see Sect. 10.5.2) represents statistically the smallest possible eddy structures before being dissipated by viscosity where $\varepsilon$ is dissipation rate (see (2.54)) and $\nu$, kinematic viscosity. *Taylor microscale* $\lambda$ represents a statistical length of the small eddies supposing the turbulence is isotropic, where $\overline{(\partial u_1/\partial x_1)^2} \equiv \overline{u_1^2}/\lambda^2$. *Integral length scale* $L$ represents statistically a characteristic size related to the largest coherent structures defined by integration of correlation. And the *viscous length scale* $\nu/u_\tau$ is a viscosity-dominated characteristic length usually used in the wall-bounded layers.

For the scaling of coherent structures, more detailed scales could be involved than those stated above. But, the basic concept of multiscales and statistical viewpoint remain the same. There are many different definitions of scales for different coherent structures or in different regions; and all of these definitions are related to certain structures in statistical sense. For example, the spatial scales of the spanwise coherent structures in free shear layers are of the same order of the layer thickness, while the scales of the streamwise structures in a wall-bounded shear layer depends on the viscous scales. However, these scales are only in a statistical sense and never mean that there is no structure of other size. More specifically, any scales obtained by correlation and spectrum, etc. reflect only the structures with an averaged probability of occurrence. Once again, the continuous spectrum is a good evidence that in turbulence fields there exist structures of all the possible sizes ranging from the maximum (integral) scale to the smallest (dissipation) scale.

As will be seen later, there are many types of scales for the coherent structures even for a simple shear layer. There are global scales related to the whole shear layer and local scales related to the local shear region around certain coherent structures. In complex shear flows, there will be even more characteristic scales (Sect. 10.6): the global scales for the whole layer, individual scales for individual mean shear zones and local scales for the local shear region inside each mean shear zone. In general, each scale is related to its own instability mechanism and the production of the corresponding coherent structure. Apparently, the scale of the largest coherent structures depends on the boundary condition of the total shear layer.

### 10.1.3 Coherent Structure and Wave

In turbulence studies, vorticity or vortices are closely related to waves. The relation between the two deserves a thorough clarification in order to understand many important phenomena. In particular:

(1) *Coexistence and interaction of vortices and waves.*
As mentioned in Sect. 2.3, there may be two types of waves in a flow field. One is the dilatation wave or longitudinal wave, by which the energy propagates via normal stress in a compressing process. The other is the transverse wave or vorticity wave, by which the energy propagates via the shear stress. Section 2.4 shows further that the Stokes–Helmholtz decomposition of the Navier–Stokes equation leads to separate equations for stagnation enthalpy and vorticity, i.e., (2.170) and (2.166). The former, characterizing all longitudinal interactions, is directly related to the acoustic wave and becomes dominant at high Mach number. The latter, characterizing all transverse interactions, is directly related to the vorticity wave. It becomes dominant in the high shear region and is the subject of vorticity dynamics. Under certain conditions, the energy of the two can transfer to each other. It is the subjects like *vortex sound* (briefly mentioned in Sect. 2.4.3, see, e.g., Howe (2003)) and *shear flow receptivity* (e.g., Goldstein and Hultgren (1989)), which are beyond the scope of this book.

Vorticity in a flow can be transported by vortex motions or by vorticity waves. A vortex motion is related to the mass transport while a vorticity wave is the motion transfer without mass transport such as the T–S waves (Chap. 9). The vorticity wave is one of the processes to propagate and accumulate vorticity. The distributed vorticity in a shear layer would be accumulated and concentrated through certain instability mechanism (Fig. 9.8 and Chap. 9) and eventually role up to become vortices. In general, while the instability wave is growing, so will be the vorticity concentration; but the distribution of vorticity concentration is still continuous. When a single vortex layer is rolled up, there is a catastrophe from continuous vorticity concentration to a discrete one.

In a turbulent flow, the growth of instability waves and rolling up of vortical structures, as well as their cascade and breakdown, occur everywhere and all the time. Thus, the vorticity waves are coexisting with the vortical structures in turbulence. In fact, the unstable vorticity waves prepare themselves for rolling up and produce new vortices. The formed vortices, in turn, generate new local shear region and prepares condition for other instability waves to grow.

Besides, the formed vortical structures themselves could also be the carrier of waves. For example, a vortex supports waves that travel along its axis. These waves may be axisymmetrically traveling along the core of a columnar vortex (Leibovich and Ma 1983; Melander and Hussain 1994), bending waves of the vortex axis (Sect. 9.3), or helical waves along the core.

(2) *Vortices in one inertial frame of reference can be observed as waves in another frame of reference.*
Here discussed is an important point that often causes confusion in turbulence studies. One example is shown in Fig. 10.2a where a row of spanwise vortices is transported by a two-dimensional uniform background flow. An observer moving with the uniform flow can easily see that the background flow and the true vortex pattern are steady. However, a measuring probe fixed in space can sense the periodical velocity signals induced by the vortex row. The frequency of the wave depends on the length scale of the vortices and the velocity of the background flow. A row of smaller vortices or a higher uniform velocity leads to a higher frequency.

Similar phenomena can happen to more complicated traveling structures. For example, in the intermittency region at the edge of a turbulence boundary layer, the passing alternative potential regions and turbulence regions would be observed by the fixed sensor as a wave. It is also true in the region with internal intermittency where the passing alternative high-shear structures and low-shear regions would be seen as a wave. In particular, the intermittently

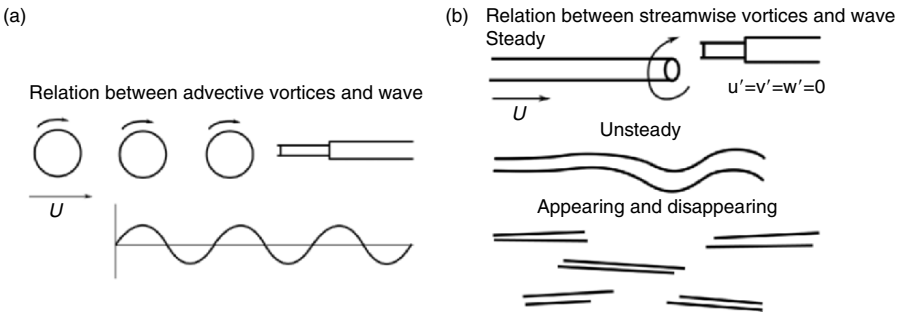


**Fig. 10.2.** Relation between vortices and waves. (**a**) Advective vortices. (**b**) Streamwise vortices

passing small-scale structures in a transitional boundary layer would be observed as high frequency "spike."

The above phenomenon exists, however, only if the traveling structures move with velocity components in the direction perpendicular to the vortex axis. For the vortices traveling in the direction parallel to their axis, the situation would be entirely different. An extreme case is shown in Fig. 10.2b with steady streamwise vortices in the flow. A fixed measuring sensor cannot detect any velocity fluctuations at all. If the vortices are drifting in space, what the probe measures is velocity variation due to spatial migration of the vortices rather than the characteristic quantities of the vortices. This observation is very important in our later discussion related to by-pass transition and to flows involving streamwise vortices.

In view of the above discussion, one should pay enough attention to the difference between temporal waves and spatial waves. For example, if streamwise vortices are steady in temporal domain, then no temporal waviness can be observed by a fixed sensor; but they are related to spatial (spanwise) waves. Obviously, waves measured by a fixed one-dimensional sensor are just one aspect of the structures.

## 10.2 Vortical Structures in Free Shear Flows

We first discuss a nominally two-dimensional mixing layer under zero pressure gradient as an example of the coherent structures in free shear layers, because it is the simplest and also one of the best understood free shear layers so far. In a turbulent mixing layer, there exist vortical structures of various scales, from the largest, with the length scale comparable to the local thickness to the smallest, with the length scale of the order of Kolmogorov length scale.

### 10.2.1 Instability of Free Shear Layers and Formation of Spanwise Vortices

The fundamental coherent structures in a two-dimensional mixing layer are sketched in Fig. 10.3. Assume that the incoming flows on both sides of the splitter plate are laminar with velocities $U_1 > U_2$, where the free stream is from left to right, $U_1$ and $U_2$ are the velocities on the top and bottom sides respectively. As discussed in Sect. 9.2, this flow is subject to Kelvin–Helmholtz instability. According to the linear stability theory and under parallel-flow

**Fig. 10.3.** The fundamental coherent structures in a mixing layer

assumption, two-dimensional disturbances will grow exponentially with downstream distance, and the dimensionless spatial growth rate $(-\alpha_i\theta/R)$ is shown in Fig. 9.9a (Ho and Huerre 1984). The main conclusion is that this growth rate is dependent on the Strouhal number $St = f\theta/\overline{U}$. The most amplified frequency at $St = 0.032$ corresponds to the natural frequency $f_n$ of the mixing layer. The associated phase velocity at maximum amplification equals to the average velocity $\overline{U}$ of the mixing layer.

Downstream of the region of exponential growth, the instability waves evolve into a nonlinear region and the amplitude of the fundamental mode approaches its saturation. Meanwhile, the fundamental instability wave leads to roll-up of a periodical row of spanwise vortices (Figs. 10.1 and 10.3) moving at the average velocity $\overline{U}$ with a wavelength $\lambda_n = \overline{U}/f_n$.

As mentioned in Sect. 10.1, the vorticity in the shear layer is gradually accumulated and concentrated through the instability mechanism. As the instability wave is growing, so is the fluctuation of vorticity concentration; but the concentrated vorticity is still continuously distributed (Fig. 9.8). When the shear layer with concentrated vorticity finally rolls up, there is a catastrophe from continuous vorticity to discrete spanwise vortices as sketched in Fig. 10.4. Experimental observations indicate that the roll-up process is completed where the fundamental mode reaches its maximum amplitude. The roll-up process has also been confirmed by numerical simulations (e.g., Aref 1980; Riley and Metcalfe 1980). As will be discussed later, the subharmonic component of disturbance waves will also start growing that is related to vortex pairing.

After roll-up, a topological sketch of the mixing layer structure is shown in Fig. 10.5, indicating a row of vortices with saddle points in between. It is well known that any structures defining the topology of the velocity field are not Galilean invariant. Thus, one has to keep in mind its dependence on the frame of reference in viewing the topology. Figure 10.5 is made in a reference frame moving at the same velocity as the average velocity of the mixing layer.

**Fig. 10.4.** Rolling process of a thin wavy vortex layer

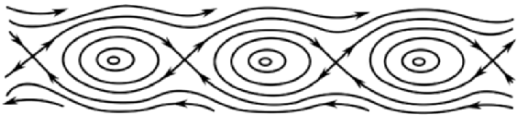

**Fig. 10.5.** Topology of the fundamental coherent structures in a mixing layer. Based on Dallmann (1984)

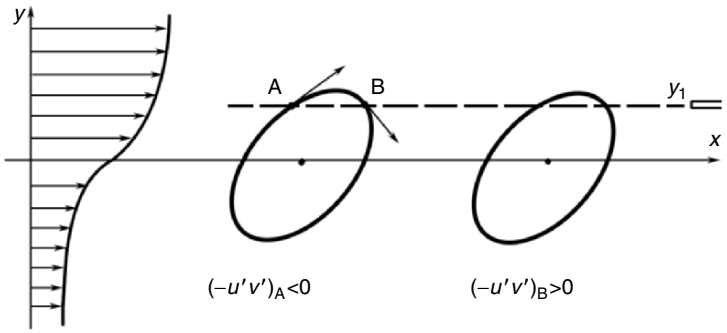


**Fig. 10.6.** Relation between Reynolds stress and tilting of the spanwise vortices

The fundamental vortices with wavelength $\lambda_n$ are not stable structures. All the vortices are living in a background of mean shear field and subject to mutual interactions, so they continue to evolve. They will be deformed, subjected to pairing or tearing, as well as develop to three-dimensional structures. These structure evolutions are the dominant mechanism for the growth of mixing layers. One of the physics showing how the vortex evolution controls the turbulent momentum transfer is the relation between Reynolds stress and deformation of the spanwise vortices (Browand and Ho 1983). The qualitative result indicates that the Reynolds shear stress is positive where the spanwise vortices are tilted backwards at the top, and negative when they tilted forward.

One can easily understand this mechanism from Fig. 10.6. The tilted spanwise vortex array is advected by the flow from left to right. A sensor fixed at $y = y_1$ will continuously sense the velocity fluctuations caused by the induced velocity of the passing vortices. When point B passes the sensor, it causes $u' > 0$, $v' < 0$ and so $(-u'v')_B > 0$. For the same reason, $(-u'v')_A < 0$ when point A passes the sensor. According to conservation of angular momentum, the point closer to the vortex center should have larger induced velocity and so $|(-u'v')_A| > |(-u'v')_B|$. Thus, the Reynolds stress, i.e., the long time average of $(-u'v')$ measured by this sensor, is negative. This relation was further examined by Zhou and Wygnanski (2001). The tilting angles of the elliptical spanwise vortices calculated from the measured coherent Reynolds stress in a forced mixing layer match very well with the experimental observations of the vorticity contours (Fig. 10.7).

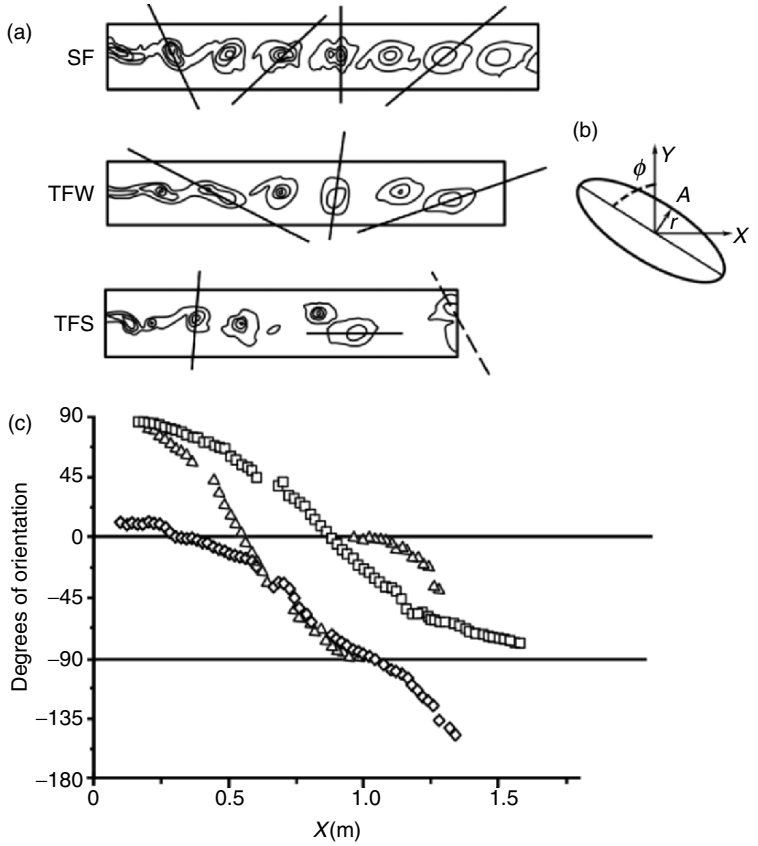


**Fig. 10.7.** Calculated orientation of tilted spanwise coherent vortices. (Δ) forced by single frequency (SF), (□) forced by two frequencies – fundamental and subharmonic, weaker (TFW), (◇) forced by two frequencies, stronger (TFS). From Zhou and Wygnanski (2001)

During the rolling up of the fundamental vortices, subharmonic component of disturbance waves also starts growing. The growth of disturbance with half of the fundamental instability frequency $1/2f_n$, or with double wavelength $2\lambda_n$, corresponds to a pairing process (Fig. 10.8). It is one of the major physical processes in the continuing evolution of the mixing layer. Although more than two vortices involved in one merging have been observed in unforced mixing layers (Ho 1982), the amalgamation was most often a pairing between neighboring spanwise vortices (Winant and Browand 1974).

The location where the pairing occurs can be expressed by a dimensionless streamwise distance $x^* = Rx/\lambda_0$ from the splitter plate, where $\lambda_0 = \overline{U}/f_0$ is the initial instability wavelength. Experiments in a forced mixing layer indicate that the first pairing happens at $x^* = 4$, the second at $x^* = 8$, and the third, $x^* = 16$ (Ho and Huang 1982). However, for a naturally developing

**Fig. 10.8.** Pairing process of the spanwise vortices

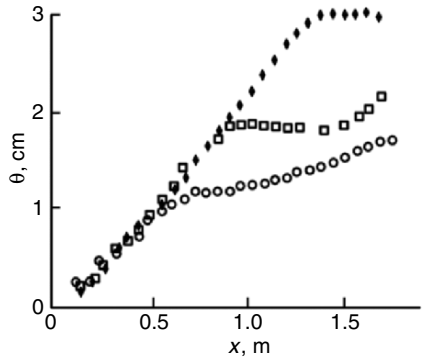


**Fig. 10.9.** Growth rate of a mixing layer forced in various ways. (○) forced by single frequency, (□) forced by two frequencies (weaker), (◇) forced by two frequencies (stronger). From Wygnanski and Petersen (1987)

mixing layer, the spatial location where the pairing occurs is fairly random. This is why the mean velocity profiles in a naturally developing mixing layer will not show any abrupt thickening. Rather, a linear spatial growth will be observed.

Pairing, though important, is not the only mechanism that causes the growth of a mixing layer. The photo in Fig. 10.1 by Brown and Roshko (1974) on a naturally developing mixing layer reveals that the mixing layer is growing in the downstream direction due to vorticity diffusion but no obvious pairing is involved. In contrast, for a forced mixing layer, a rather weak periodical disturbance can dramatically influence the pairing process and result in significant modification of mixing properties. This is one of the physical backgrounds of the active flow control. An example is shown in Fig. 10.9, where the same mixing layer was forced in different ways and the growth rate exhibits entirely different behaviors (Wygnanski and Petersen 1987).

### 10.2.2 The Secondary Instability and Formation of Streamwise Vortices

The roll-up of spanwise vortices and their pairing are not a purely two-dimensional process. They always coexist with nonuniformity in the spanwise direction due to three-dimensional disturbances, which eventually leads to streamwise streaks (Konrad 1976) or counter-rotating streamwise vortex pairs (Lin and Corcos 1984; Lasheras et al. 1986). Experiments indicate that

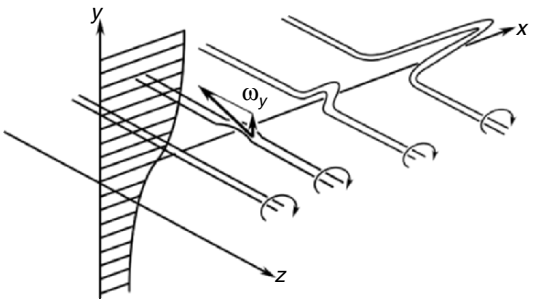


**Fig. 10.10.** Initiation of streamwise vortices in a strain field

these secondary vortices develop together with the spanwise structures from the very beginning of the mixing layer (Huang and Ho 1990).

The physical mechanism for initiation of the streamwise vortices in a shear layer can be explained in Fig. 10.10 intuitively. Consider a large spanwise vortex consisting of many spanwise vortex filaments. If any of these filaments is deformed by three-dimensional disturbances and results in a small waviness in $y$ direction, the humped-up portion of the vortex would be advected faster than the rest due to the shear field, thus initiating a streamwise vortex pair. A discussion in Sect. 9.4 on the elliptical instability further gives a universal mechanism for the two-dimensional large-scale deformed spanwise vortices to be directly transferred to complicated three-dimensional motions. This direct transfer mechanism plays a dominant role not only in mixing layer but also in flows like wakes and vortex pairs. More discussion on the formation of streamwise vortices will be made in Sect. 10.3.1.

The strain field mentioned above is not only related to the mean shear field of the mixing layer. Refer to Fig. 10.5, where the strongest stretching and compression exist along the streamline passing through saddle points. Thus, there is more chance for this mechanism to work near the saddle point. In this region, the so formed initial streamwise vortex filaments will be further stretched so that they will be strengthened and wrapped onto the existing large spanwise vortices. These streamwise vortices are referred to as "braids" and are sketched in Fig. 10.11 (Bernal and Roshko 1986). The average spanwise spacing of these secondary structures increases in size with downstream distance and remain to be of the same order of magnitude as the local thickness of the mixing layer. The thickness of the braid region connecting the spanwise vortex core is suggested to be of the order of Taylor microscale (Browand 1986).

The occurrence of streamwise vortices is important in the evolution of mixing layers because it enhances the mixing efficiency. Furthermore, the interaction of the spanwise and streamwise vortices has considerable influence on the transition to small scales and the further development of the whole mixing layer.

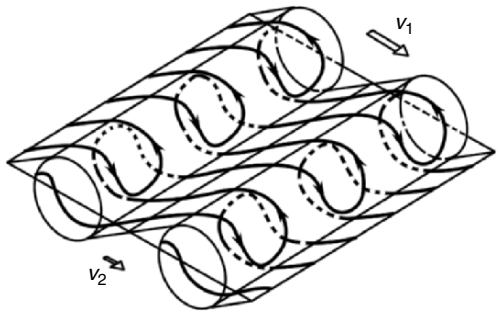


**Fig. 10.11.** A conceptual sketch of streamwise vortices in a mixing layer. Reproduced based on Bernal and Roshko (1986)

### 10.2.3 Vortex Interaction and Small-Scale Transition

In general, the entire process from occurrence of instability wave in a laminar flow to a fully developed turbulence is regarded as the *laminar-turbulent transition*. However, in more detailed structural studies, one can also apply this concept to local properties in the flow field. For example, the aforementioned spanwise and streamwise vortices may still be "laminar." With further development, including interaction of various structures, these vortices are stretched, twisted or broken down to be random, small-scale vortices or *eddies*, and eventually become "real" turbulence. This final stage of transition is thus referred to as *small-scale transition*. It belongs to the category of *cascade*.

From Fig. 10.5, we can imagine that stretching and compression between two neighboring spanwise vortices would be enhanced during pairing so that the streamwise vortices will be subjected to stronger strain, which may lead to the small-scale transition. If one takes Kolmogorov's 5/3-power law in energy spectrum (Tennekes and Lumley 1972) as a criterion to identify a fully developed turbulence, this expectation has indeed been proven by experiments. As an example, the fine-scale turbulence was first found in the cores of the streamwise vortices at the point where the spanwise structures rolled around and were coalesced (Huang and Ho 1990). Then, the asymptotic value of the $-5/3$ power law in spectra is reached and the flow becomes turbulence around the second pairing, $x^* = 8$ (Fig. 10.12). The above experiment was carried out at Reynolds number of $(1.3 \sim 1.9) \times 10^4$ based on the local maximum vorticity thickness $\delta_\nu = (U_1 - U_2)/(\partial U/\partial Y)_{\max}$ . At much lower Reynolds number, this location could move to approximately the place where the third pairing occurs.

The small-scale transition involves continuous vortex interaction between coherent vortices, as well as between coherent and random vortices. The appearance of small-scale filaments during the onset of transition due to successive interactions between a large, coherent vortex, and its surrounding smaller scales has been simulated numerically (Melander and Hussain 1993b; Pradeep

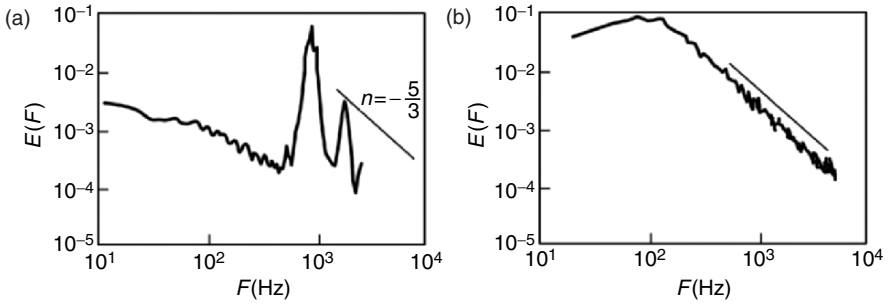


**Fig. 10.12.** Power spectra of longitudinal velocity fluctuation. (**a**) $x^* = 2$; (**b**) $x^* = 8$. From Huang and Ho (1990)

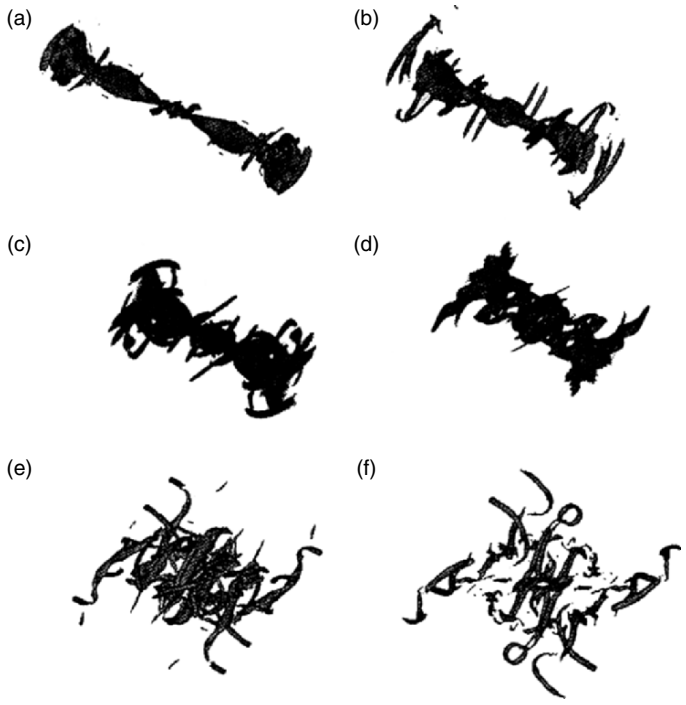


**Fig. 10.13.** Iso-vorticity contours illustrating appearance of small scale filaments during onset of transition. From Pradeep and Hussain (2000)

and Hussain 2000) and a sequence of views is shown in Fig. 10.13. It indicates vividly how the energy cascade from large to small scales takes place.

Actually, during the whole process of small-scale transition, the vortex cut-and-reconnection plays a key role in the final formation of small-scale structures. The physical mechanism and the theoretical background of vortex

reconnection have been discussed in Sect. 8.3.3. Sketches of the vortex reconnection can be seen in Figs. 8.23 and 8.24. A complete process obtained by numerical simulation is shown in Fig. 10.14, where there are successive steps, such as continuous formation of bridge and head–tail (c), separation of head from tail (d), formation of thread (e), successive reconnection of thread, etc. (Hussain 1992). In this way, smaller secondary structures take energy from the coherent vortices, and so on.

After the small-scale transition has happened, a global view of the vortical structures in a mixing layer is shown in Fig. 10.15. The previously formed large vortical structures still exist; but they are in a turbulent rather than laminar background. Melander and Hussain (1993b) point out that when a coherent vortex is embedded in a sea of fine-scale turbulence, the large-scale coherent structure organizes the nearby fine-scale turbulence into a family of highly polarized (see Sect. 10.4.3) vortex threads spun azimuthally around the coherent vortex. They suggest that small-scale polarized structures are unavoidable components of coherent structures and that an essential part of the internal intermittency is generated by large-scale coherent structures.

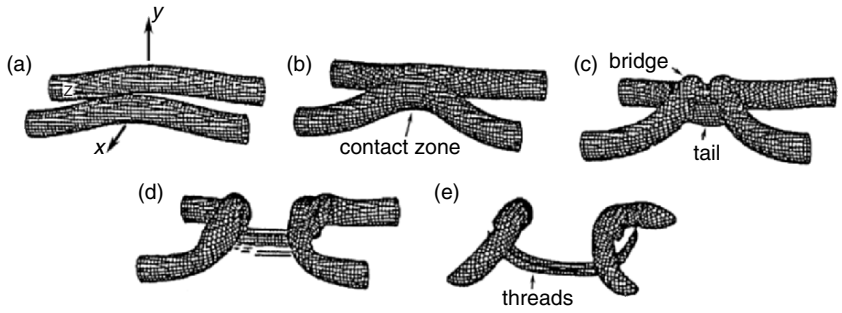


**Fig. 10.14.** Iso-vorticity surface to show the successive steps of small-scale formation during vortex reconnection. From Hussain (1992)

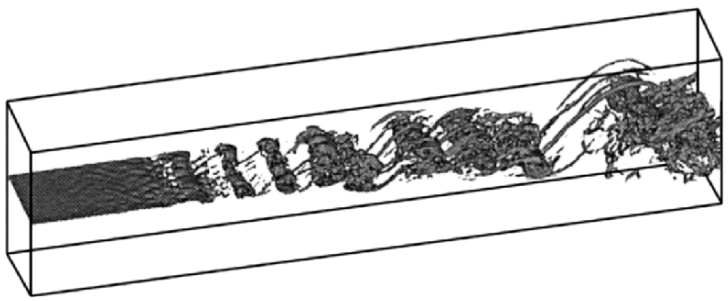

**Fig. 10.15.** A global view of the vortical structures in a mixing layer. From Lesieur et al. (2000)

The preceding discussion can now be summerized as follows. In a turbulent mixing layer, two physical processes are going on simultaneously. One is that the large-scale vortices are gradually organized from the concentration of initially distributed vorticity through the instability mechanism. The other is that the energy contained in large-scale vortices are successively transferred to smaller vortices and eventually to small random vortices, or eddies. Both processes continue in the whole turbulent flow field so that the coexistence of vortices and waves as well as that of multiscale structurtes can be observed. These coexisting waves and multiscale vorticies continue to grow or decay, as well as interact with each other. Thus, any flow structures that one can observe in experiments or numerical simulations are only snapshots in a continuously developing field.

## 10.3 Vortical Structures in Wall-Bounded Shear Layers

The essential difference between a wall-bounded shear layer and a free shear layer is obvious. In a free shear layer, there is no boundary and hence no vorticity source for the incompressible flow without nonconservative body force. In contrast, in a wall-bounded shear layer, the nonslip condition on the wall generates new vorticity via the boundary vorticity flux (Sect. 4.1). The wall-produced vorticity will enter the flow field continuously and make the boundary-layer structures significantly more complicated than a free shear layer.

Unlike mixing layers, many controversial issues exist in understanding of the structures in boundary layers. Most of them have been caused by the limitation to low-Reynolds number flow in laboratory experiments or numerical simulations. The vortical structures in a boundary layer, in particular at relatively low-Reynolds numbers, are closely related to the boundary layer transition process with varying details, depending on the specific boundary condition (e.g., surface roughness, free-stream turbulence) and initial condition (e.g., upstream forcing).

Fortunately, recent studies have found certain universality in wall-bounded shear layers. Some dominant transitional vortical structures are independent of specific type of wall-bounded basic flow (whether it is a boundary layer, a channel flow, or a pipe flow, etc.) and initial conditions (whether naturally developed or forced). For example, one may speculate that a *hairpin vortex*, either symmetric or asymmetric, is a common element in transition. Then, certain characteristics of wall turbulence are only weakly dependent on specific type of outer flow (Kachanov 2002). Furthermore, it is well known that similarity exists in the mean velocity profiles of the fully developed turbulent boundary layers at high Reynolds number (Fig. 10.16, where $y^+ = yu_\tau/\nu$ and $u^+ = u/u_\tau$ are the viscous length scale and velocity scales, respectively, $u_\tau = \sqrt{\tau_\mathrm{w}/\nu}$ is the friction velocity, $\tau_\mathrm{w}$ is the wall-shear stress and $\nu$ is the kinematic viscosity). By convention, $y^+ = yu_\tau/\nu \leq 100$ is considered the *wall*

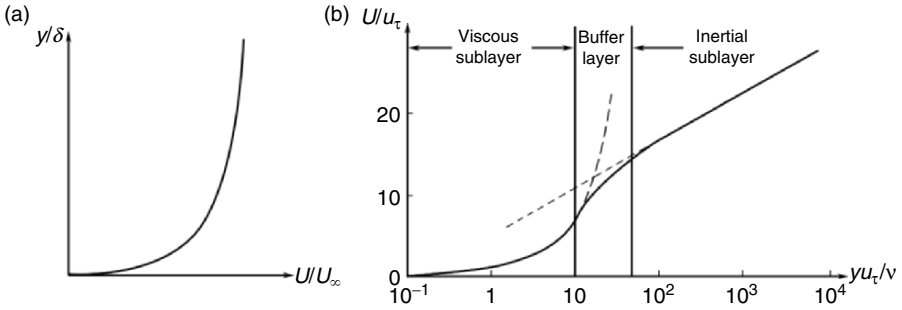


**Fig. 10.16.** Mean velocity profile of a turbulent boundary layer at high Reynolds number. (**a**) Linear coordinates. (**b**) Semi-logarithmic coordinates

*region*, including the *sub layer*, *buffer region* and at least part of the *logarithmic region*. The rest of the layer is commonly referred to as the outer region (Robinson 1991b). The similarity in mean velocity profiles means a similarity of mean vorticity profiles, thus also implies a possible similarity in the vortical structures. Consequently, though complicated, a brief discussion on the nature of vortical structures in a typical boundary layer is still possible.

In Sect. 10.2, we took a two-dimensional mixing layer as an example to discuss the coherent structures of free shear layers, because it is the simplest and also one of the best understood free shear layers. For the same reason, we now take a two-dimensional boundary layer on a smooth flat plate in the absence of streamwise pressure gradient to exemplify the coherent structures in wall-bounded shear layers. The main discussion below is based on the *Klebanoff-type transition* (K-type, where a peak-valley pattern of $\Lambda$ waves occurs in transition, Fig. 10.17a,) because it can often be observed in naturally developed boundary layers, although their original studies (Klebanoff et al. 1962) were performed in a forced boundary layer. Other types of transition (e.g., H-type and C-type, where staggered pattern of $\Lambda$ waves occurs in transition; see Fig. 10.17) mainly found in controlled boundary layers will not be discussed in this section. The special issues related to *by-pass transition* will be briefly addressed in a separate section (Sect. 10.3.5) associated with a discussion on streamwise vortices.

### 10.3.1 Tollmien–Schlichting Instability and Formation of Initial Streaks

In Sect. 9.2.3 we have seen that, when the Reynolds number reaches certain critical value, the laminar boundary layer will be subjected to Tollmien–Schlichting (T–S) instability. The neutral curve (Fig. 9.10) can be obtained by the linear stability theory. Any single disturbance at a frequency within the unstable region will grow exponentially. If there were any chance to keep a perfect two-dimensionality of the growing instability waves, the wave would

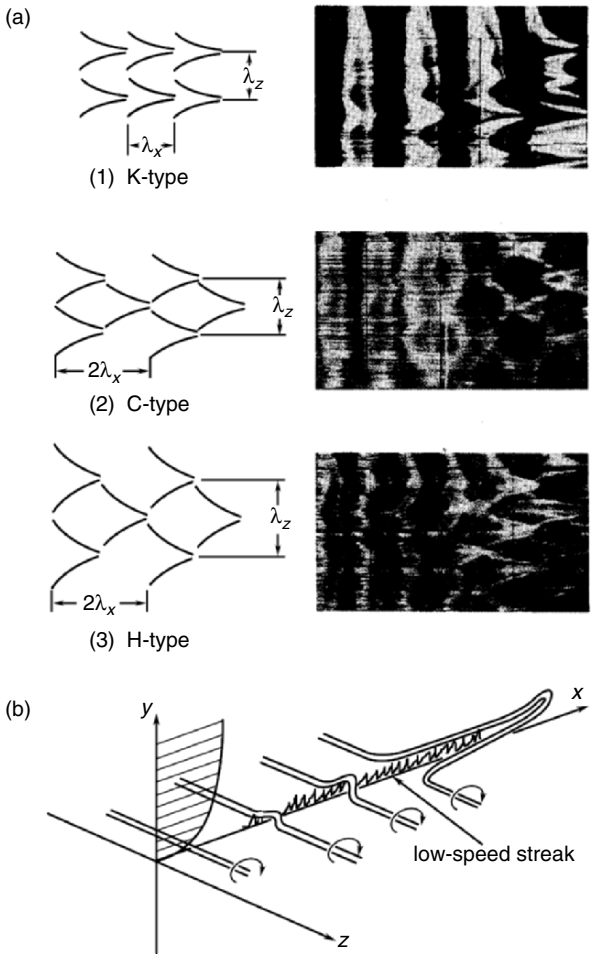


**Fig. 10.17.** Formation of streamwise vortices and streaks. (**a**) The $\Lambda$-waves, from Saric and Thomas (1983). (**b**) The $\Lambda$-vortices and streamwise vortices

reach a maximum strain rate and the vortex sheet would roll-up to become spanwise vortices as it happens in a mixing layer. However, there has never been such a chance in a boundary layer. Even in a laminar boundary layer on a smooth plate, the flat plate can never be perfectly smooth and the free stream is never perfectly disturbance-free. This is why streamwise *streaks* (with the spanwise fluctuations of the mean velocity) can be observed even in a laminar flow before the occurrence of T–S waves, no matter how weak they could be.

After the occurrence of T–S waves, even if the T–S waves may shortly keep its two-dimensionality during the stage of linear growth, they will never be two-dimensional in nonlinear stage, no matter which type of transition

they are subjected to (Fig. 10.17a). Considering the most common K-type transition in a naturally developing boundary layer, the $\Lambda$-shaped waves will appear and are aligned to each other in the streamwise direction. As can be seen later, the observed growing of the oblique waves is actually related to the rolling up of vortex sheet to become streamwise vortices and the latter will produce further streamwise streaks.

Fig. 10.17b indicates that while the two-dimensional instability wave is growing and the vorticity sheet is rolling up, the three-dimensional disturbance will cause certain slight bending. Due to the very strong shear at the wall, the vortex segment at a little farther away from the wall will be transported much faster than the segments closer to the wall, and the segments connecting them will be stretched and strengthened to become $\Lambda$-shaped vortices (e.g., Fig. 4.5), and then further stretched to be the streamwise vortices. This mechanism is similar to the formation of streamwise vortices in a mixing layer (Fig. 10.10); but the mean shear in the vicinity of the wall as well as three-dimensional disturbances in a boundary layer is so strong that there is never a chance for the vortex sheet to roll up to become observable two-dimensional spanwise vortices in a boundary layer.

Comparing Fig. 10.17 with Fig. 10.10, one can also see a major difference, i.e., the occurrence of the low-speed streaks beneath the $\Lambda$-vortices/streamwise vortices. The formation of the low-speed streaks is, first, due to momentum transfer in the mean shear field. In the regions where the vortex legs pump the near wall low-speed fluid away from the wall, the flow will slow down and form low-speed streaks (on the contrary, in regions where the vortex pairs pump the outer high-speed fluid towards the wall, high-speed streaks will form). Second, even if there is no mean shear normal to the wall, in the region where the vortex legs cause an induced velocity away from the wall, the flow near the wall will slow down due to the continuity, and hence form the low-speed streaks. This is why, more often than not, the streamwise streaks are observed coexisting with streamwise vortices.

Besides, the two legs of a $\Lambda$-vortex, once formed, will be subject to two opposite actions. On the one hand, they will be tilted further towards downstream direction due to the mean shear and become streamwise vortices (Jiménez and Pinelli 1997). On the other hand, the mutual induction between the two legs intends to lift both vortex legs upward. Thus, their orientation depends on the relative intensity of the two. Obviously, the strong shear dominates in the near wall region so that the upstream roots of the legs develop to streamwise vortices. The downstream portions of the legs farther away from the wall will be lifted up to become elongated *hairpin vortices* that asymptotically tend to the direction of maximum production of $\overline{\omega_x^2}$, i.e., $\overline{\omega_x\omega_y}(\partial U/\partial y)$ (Brooke and Hanratty 1992) or to the direction of maximum stretching (45° from the wall). After the heads of the initial $\lambda$ vortices have swept over, some portions of their legs or the streamwise vortices could be gradually dissipated by viscosity; but streaks would still leave behind.

### 10.3.2 Secondary Instability and Self-Sustaining Cycle of Structure Regeneration

After the appearance of the streaks caused by streamwise vortex pairs, there occurs the secondary instability and the consequent *self-sustaining cycle* of structure regeneration.

Swearingen and Blackwelder (1987) are among the earliest who argue that the low-speed streaks instability is responsible for the turbulence sustaining cycle. Recent numerical experiments have shown that the dominant physics in the turbulent sustaining mechanism consists of three steps: streak formation related to streamwise vortices, streamwise vortex regeneration/re-energizing, and breakdown of streaks due to streak instability (Hamilton et al. 1995; Waleffe 1997). There is little argument on the mechanism how the streaks are produced by the streamwise vortices as was stated in Sect. 10.3.1. However, no consensus has been reached in how the streamwise vortices are regenerated. This problem is at least partly due to the fact that three-dimensional vortices are extremely difficult to characterize in the laboratory. Many possible mechanisms were suggested, for example, the "wall cycle" (Jiménez and Pinelli 1997, 1999), the "streak transient growth" (Schoppa and Hussain 2002), etc. The following picture is one of the possible mechanisms.

Figure 10.18a is a simplified sketch of the secondary instability and the related vortex generation. Once low-speed streak is formed, the normal and spanwise distributions of the streamwise velocity cause an inflectional instability in both directions. Similar to what happens in a mixing layer, the instability waves will grow around the low-speed streak and the $\Lambda$-shaped vortex will roll up.

As can be seen conceptually in Fig. 10.18b (top and side views) and c (oblique view), the above mechanism of $\Lambda$-vortex formation does not work individually. Instead, it occurs successively, aligned to each other, and produce $x$-dependent waviness of the vorticity layer around the low-speed streak. Combined with the disturbance from the fundamental T–S wave, these periodical $\Lambda$-vortices may occur with a period of (or lock-on to) the fundamental T–S wave. As a consequence, the upstream roots of the group of $\Lambda$-vortices, i.e., the group of streamwise vortices, will not only re-energize the original streamwise vortices on both sides of the original low-speed streak, but also in turn strengthen the upward pumping of the low-momentum fluids and strengthen the low-speed streak.

From Figs. 10.18b and c, one can also see that the streamwise length of a streak is much longer than the legs of the streamwise vortices. The latter stays in the near-wall region with a length of around $x^+ \approx 200$ and each spacing around $x^+ \approx 400$, while the former occupies a region of $x^+ \approx 1{,}000$ (Blackwelder and Eckelmann 1978). Experiments and numerical studies have also shown that the spanwise scale of the hairpin vortices and spanwise wavelength of the streaks are both $\lambda_z u_\tau/\nu \approx 100$ (Kline et al. 1967). Jiménez and Moin (1991) regard this dimensionless spanwise scale as a Reynolds number

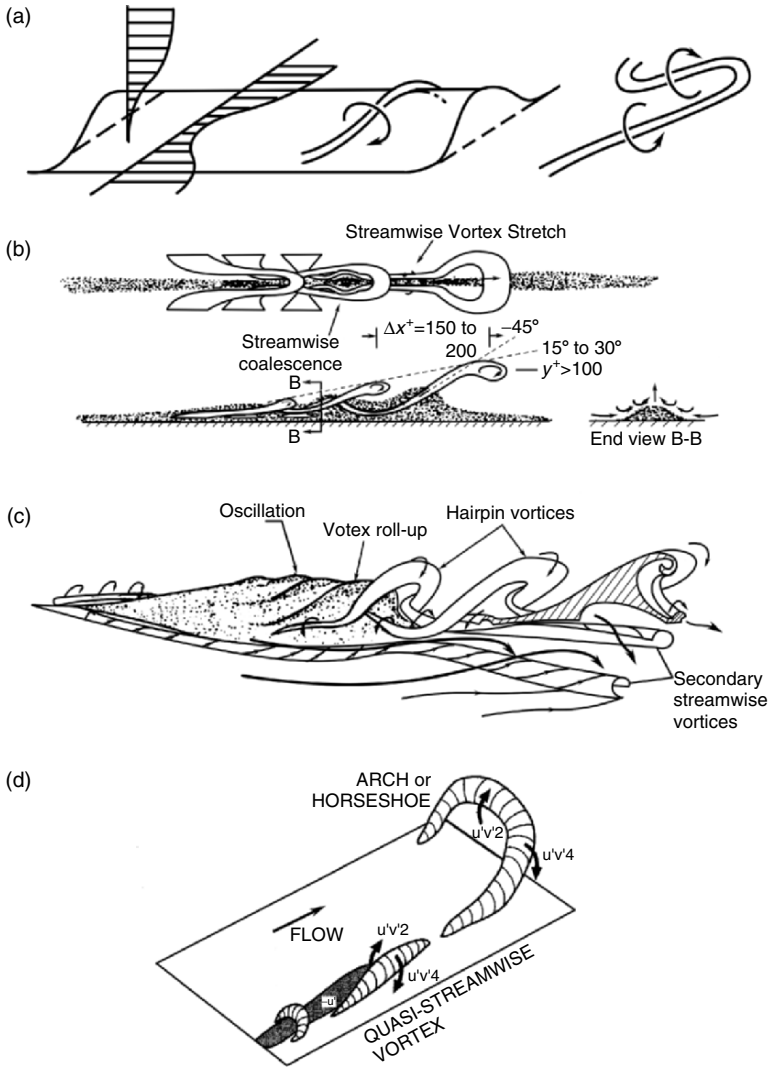


**Fig. 10.18.** Structure regeneration. (**b**) is reproduced from Smith (1984), (**c**) is from Acarlar and Smith (1987b), and (**d**) is based on Robinson (1991b). In (**d**), $u'v'2$ denotes $u' < 0$ and $v' > 0$, while $u'v'4$ denotes $u' > 0$ and $v' < 0$

and have shown that turbulence cannot be self-sustained at Reynolds numbers lower than this value. Thus, it is proposed that this may be a universal critical Reynolds number for self-sustaining of turbulence.

In a real flow, the vortex structures are much more complicated than what have been said. For example, secondary streamwise vortices with opposite sign may also be formed due to inrush fluid (Fig. 10.18c). Furthermore, the $\Lambda$- or horseshoe-like vortices are not necessarily symmetrical with respect to their

central normal plane (Fig. 10.18d) unless the disturbances develop symmetrically. Symmetrical hairpins were observed in some flows (e.g., Head and Bandyopahyay 1981; Adrian et al. 2000; Kachanov 2002), but found rare in other studies (e.g., Kline and Robinson 1989; Kim et al. 1987; Spalart 1986). An analogy between the wake instability and the flow instability caused by the spanwise velocity distribution around a low-speed streak might be helpful. The former indicates that various modes of inflectional instability can be expected, including fundamental varicose mode, fundamental sinusoidal mode, as well as the subharmonic modes. The fundamental sinusoidal mode will likely lead to the typical staggered row of vortices, while the fundamental varicose mode would lead to symmetrical horseshoe structures (Acarlar and Smith 1987a,b; Swearingen and Blackwelder 1987; Waleffe 1997). Since the fundamental varicose mode is expected to be the least unstable, it is reasonable that the numerical simulations rarely found vortices in the shape of complete horseshoes, i.e., asymmetric structures occur more often.

To summarize, both normal and spanwise inflectional instabilities contribute to rolling up of vortices and breakdown of T–S waves into three-dimensional turbulence (Blackwelder 1979). The presence of highly inflectional profiles (high-shear regions) is the key to the secondary instabilities that lead to the structure regeneration cycle. As one of the evidences, the high-shear layer shown in numerical simulation (Rist and Fasel 1995) matches the experiments (Kachanov 1994) very well, where a hairpin vortex riding above the low-speed streak is the main conclusion of their simulation. Moreover, it is worthy mentioning that when the Reynolds number is low, the regeneration cycle could be limited in certain local regions and develop *turbulent spots*. In a high Reynolds-number field, this regeneration cycle, combining with further wave interaction and small-scale transition (to be shown later), will become the major physical background of the self-sustaining turbulence in the whole turbulence field.

### 10.3.3 Small-Scale Transition in Boundary Layers

We have mentioned in Sect. 10.2 that the whole process from occurrence of instability wave in a laminar flow to a fully developed turbulent flow is regarded as laminar-turbulent transition, and the local breakdown of the "laminar" coherent structures is referred to as small-scale transition. In general, the occurrence of spikes in the velocity signals is the symbolic starting of the small-scale transition in a boundary layer. However, it is very difficult to set up a criterion on when or where the small-scale transition starts. For example, while the breakdown of early streaks already produces spikes and small random eddies, the newborn hairpin vortices could still be "laminar" in the local sense.

After hairpin vortices are formed, complicated vortex interactions can be observed up to a fully developed turbulent boundary layer. Various interpretations have been proposed for the formation of spikes and related structure

interactions. The continuous production of turbulence (or small-scale transition) in turbulent boundary layers was first considered as *bursts* by Kline et al. (1967). They discovered that the low-speed streaks are subjected to periodical motion of sweep (or inrush), lift (or ejection), oscillate, and burst with an averaged period of $300\nu/u_\tau^2$. The corresponding streamwise extent of the low-speed streak is approximately $x^+ = xu_\tau/\nu = 300-2000$ (Blackwelder and Haritonidis 1983).

Later studies considered that this quasicyclic process may be logically related to the self-sustaining cycle of structure regeneration at high Reynolds number (Kline et al. 1967; Hinze 1975; Landahl 1975). During this sequence, there are two major events, *ejection* and *sweep*. Ejections are associated with events $u' < 0$ and $v' > 0$ (marked as $u'v'2$ in Fig. 10.18d). Sweeps are associated with $u' > 0$ and $v' < 0$ ( $u'v'4$ in Fig. 10.18d). The head portion of the $\Lambda$-vortex will produce an inrush motion on its downstream side and introduces adverse pressure gradient to its upstream field. The latter, combined with the shear-layer instability caused by the low-speed streak, initiates the burst (breakdown) of the low-speed streak and breakdown of the parent vortices into small-scale structures (Fig. 10.19), see Sect. 9.5 for more detail on vortex breakdown.

It has been found that almost 80% of the turbulence production in the entire boundary layer occurs in the buffer region during intermittent, violent outward ejections of low-speed fluid and inrushes of high-speed fluid toward the wall (Lu and Willmarth 1973). This near-wall turbulence-production process, in particular the sweep events, is important for the generation of turbulent wall-shear stress (Choi 1989; Kravchenko et al. 1993; Orlandi and Jiménez 1994).

More detailed structural studies have shown that many specific vortex interactions play significant roles in small-scale transition. The formation of $\Omega$-vortices and the ring-like vortices close to the tip of the $\Lambda$-vortex is one

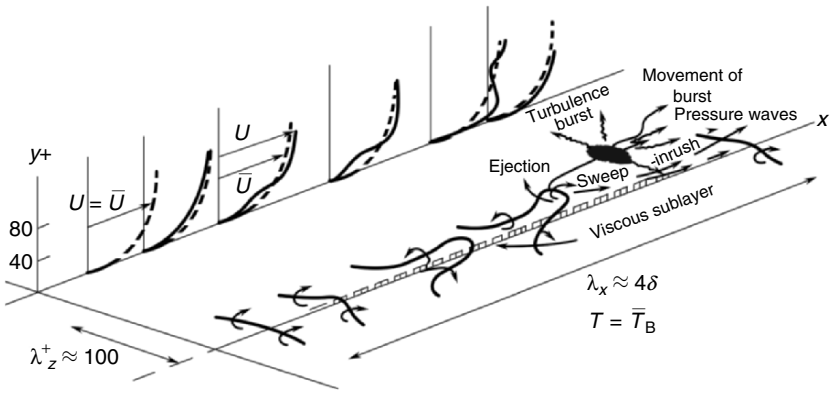


**Fig. 10.19.** Relation between burst and vortex regeneration. From Hinze (1975)

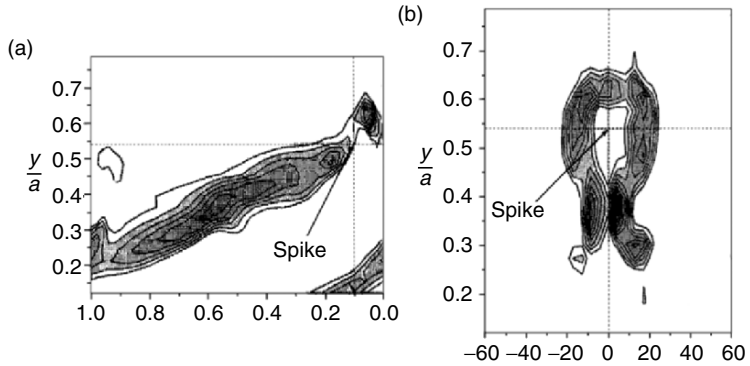


**Fig. 10.20.** The ring-like vortex at the tip of hairpin in a pipe flow. *Left* – side view, *right* – front view. From Han et al. (2000)

of the typical phenomena. It is caused by inviscid self-induction followed by the viscous cut-and-reconnection. The self-induction of the head of a hairpin vortex will cause its bending and expansion, and narrow its neck (Fig. 10.20). The neck of two sides will eventually touch each other and a vortex ring will be separated from the mother hairpin vortex due to cut-and-reconnect mechanism. This sequence is very much similar to what happens to the Crow instability of a vortex pair and its eventual breakdown into small vortices (see Sect. 9.4.3 for more detail on Crow instability). The vortex loop near the head of the $\Lambda$-vortex has been found both numerically and experimentally (Fig. 10.21) in boundary layers (Kachanov 1994; Rist and Fasel 1995; Rist and Kachanov 1995), as well as in pipe flows (Han et al. 2000; Reuter and Rempfer 1999).

Recently, another explanation is proposed on the small-scale transition based on different observations. Lee (2000, also Lee and Lee 2001) found a kind of rhombus-shaped coherent structure in the near wall region, called the soliton-like coherent structure (SCS) that is related to wave resonance during the development of three-dimensional disturbances. Figure 10.22 is a plan-view of several soliton-like coherent structures (marked by SCS1 and SCS2) forming a long streak. These SCSs appear periodically from early transitional flow and are transported downstream to the later stages of transition. The rhombus-shaped SCS could be another view of the sub layer phenomenon in the K-type transition (Fig. 10.17a). However, Lee's observation gives more details in the later stage of vortex interaction and small-scale generation (or spike generation). The SCS causes strong periodical humping up of the low-speed streak and periodical ejections (Fig. 10.22). The ejection is strong enough to cause a secondary vortex ring around it, similar to the vortex ring produced by a pulsed jet. When the secondary vortex ring is advected downstream, it will interact with the existing hairpin vortices or other vortical structures and form a series of small-scale vortex loops (Lee and Fu 2001).

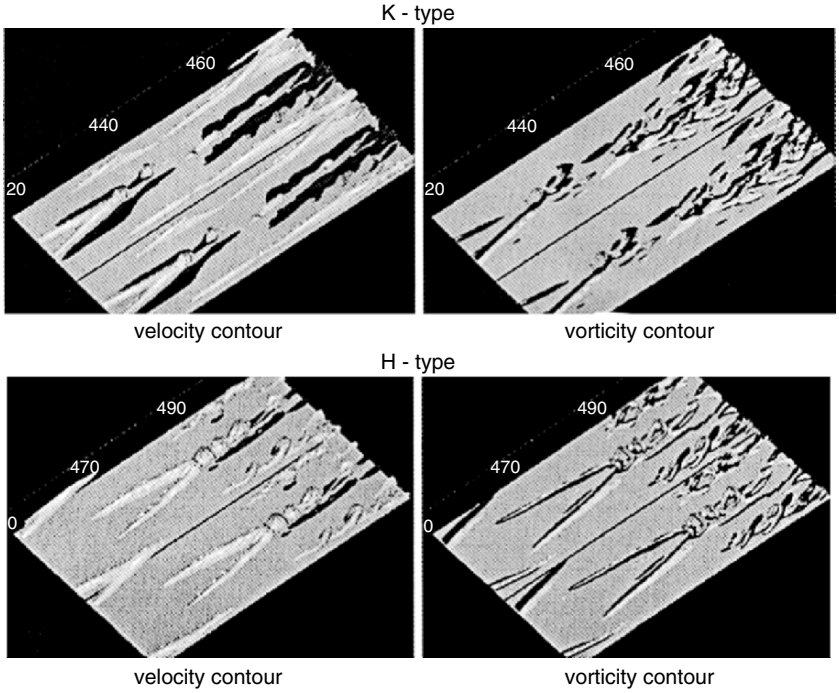


**Fig. 10.21.** The ring-like vortex at the tip of hairpin in a boundary layer. From Kachanov (1994)

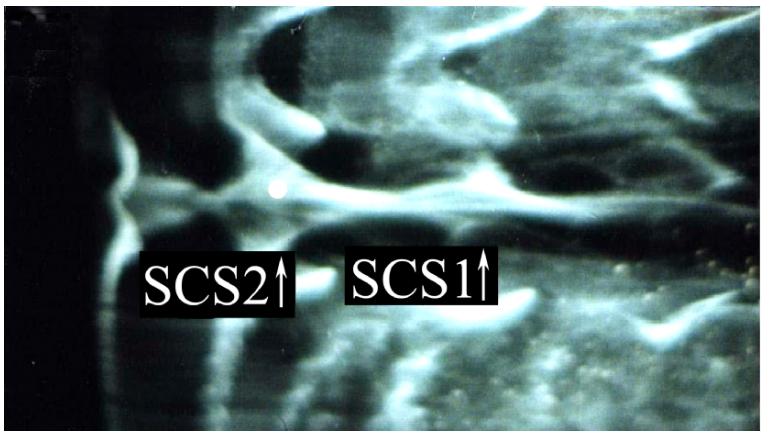


**Fig. 10.22.** Hydrogen bubble visualization of the soliton-like coherent structures. From Lee and Chen (2006)

### 10.3.4 A General Description of Turbulent Boundary Layer Structures

In Sects. 10.3.1–10.3.3 we did not describe the vortical structures in the transitional and turbulent flows separately because they are, in many aspects, of the same nature. The main difference lies in Reynolds numbers and consequently different background flow field, but appearance and dynamics of the main vortical structures are similar. For example, the $\Lambda$-vortices, streamwise vortices, and low-speed streaks; the secondary instability caused by the inflectional profiles; the growing of oscillations and breakdown into fine turbulence, etc.

By a scaling argument, Blackwelder (1983) pointed out that there exists indeed a similarity between transitional boundary layers and turbulent boundary layers. For example, the length scales of the vortical structures near the wall in transitional boundary layers on either curved or flat plates are similar to those associated with the bursting process in turbulent boundary layers if normalized with the viscous scale. Their inflectional profiles and oscillations both have a spanwise extent of typically $z^+ \approx 50\nu/u_\tau$. Besides, in both cases the maximum instantaneous shear appears in the range of $20 < y^+ < 70$ and has a maximum comparable to the shear at the wall.

Kachanov (2002) suggested that in both transitional and turbulent wall-bounded shear flows a common mechanism of turbulent production seems to exist in the following processes: the warping of the wave front and formation of the initial vortex loop related to the resonant wave interaction; formation of the $\Lambda$-vortices, high-shear layer, and the first spike; and multiple reconnection of the $\Lambda$-vortex legs leading to formation of a train of very intensive ring-like vortices attributed to spikes. Here, the high-frequency "spike" is just another view of the passage of small-scale structure (Sect. 10.1.3).

Figure 10.23 sketches the vortical structures from transitional to turbulent boundary layer. Fig. 10.23a shows the sequence of transition: region (1) is a low Reynolds-number, stable laminar flow; region (2) is a linear instability region with growth of two-dimensional T–S waves; In region (3) nonlinear growth of two-dimensional T–S waves occurs, along with the growth of three-dimensional disturbances, as well as the rolling up of initial streamwise vortices and streamwise streaks; region (4), successive production of hairpin structures due to secondary instability; and region (5), vortex-ring formation and breakdown of vortical structures due to vortex interaction. Up to here, these vortical structures occupy only limited local spaces and form turbulent spots or localized turbulence. It is usually characterized by a group of observable mushroom-like structures in the cross-section of the vortex pairs (see Figs. 109 to 111 of Van Dyke 1982). Finally, region (6) is the spatial spreading of turbulent spots that eventually form fully developed turbulent boundary layer, in which the main structures are shown in Fig. 10.23b.

In the wall region of a fully developed turbulent boundary layer, there are spanwisely distributed streamwise vortices (Lesieur et al. 2003) and

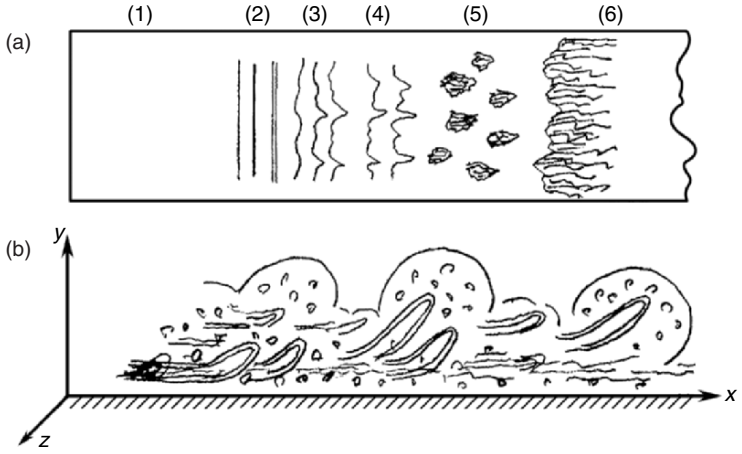


**Fig. 10.23.** A global view of the vortical structures from transitional to a turbulent boundary layer. (**a**) Sequence of transition. (**b**) Fully developed turbulence

corresponding high-speed and low-speed streaks. The averaged spanwise wavelength of the streaks in the sub layer is typically 100 viscous lengths (up to at least $Re_\theta \approx 6000$ based on momentum thickness $\theta$). The streamwise structures are broken from time to time under influence of vortex interaction with surrounding. They will also be reformed and strengthened around the high-shear region through the instability mechanism as stated before. Unlike the early stage of transition, all the aforementioned structures are now coexisting with the background of small random eddies produced by vortex breakdown or burst.

From the wall region to the outer edge of the boundary layer, there appear hairpin structures inclined to the wall at an angle of approximately 45°(Fig. 10.23b). At lower Reynolds number, the vortices are less elongated and more like horseshoe shaped. Low-Reynolds number simulations indicate that they most often occur asymmetrically or even singly (sometimes named *hooks*), with only occasional instances of counter-rotating pairs. At moderate or relative higher Reynolds numbers, the vortices are elongated and more hairpin-shaped.

There is a controversy on whether the hairpin vortices could remain up to the fully developed turbulent region downstream and how large an area they can occupy in the outer region. Head and Bandyopahyay (1981) reported that a turbulent boundary layer is filled with hairpin vortices in their smoke tunnel experiment; but it is not so from many other results. Thus, it might be helpful to discuss the Reynolds-number effect on the hairpin structures.

The viscous dissipation of a vortex pair of separation $\lambda_z$ depends on the viscous cancelation of the vorticity with opposite sign, which happens due to the vorticity diffusion from both legs at a rate proportional to $\nu\omega/\lambda_z$.

The lifetime of the hairpin votices, $t_{\text{life}}$, should be proportional to $\omega$, $\lambda_z$ and inversely proportional to the diffusion rate, and thus $t_{\text{life}}$ can be scaled to $\lambda_z^2/\nu$. On the other hand, the lift-up velocity of the hairpin vortices depends on the induced velocity caused by the mutual induction of the vortex pair and is proportional to $\Gamma/\lambda_z$, where the circulation $\Gamma \sim \omega\lambda_z^2$. Furthermore, $\omega$ depends on the wall shear, $\omega \sim \partial U/\partial y|_{\text{w}} \sim u_\tau/\delta$ and so the time $t_{\text{p}}$ required for the hairpin vortices to lift up and penetrate the whole boundary layer of thickness $\delta$ can be scaled to $\delta^2/u_\tau\lambda_z$. This gives $t_{\text{p}}/t_{\text{life}} \sim \delta^2\nu/u_\tau\lambda_z^3$. Then, since $\lambda_z$ is known to be scaled to the viscous length $\nu/u_\tau$, the ratio $t_{\text{p}}/t_{\text{life}}$ is actually the square of the Reynolds number, $(\delta u_\tau/\nu)^2$. This argument can at least qualitatively explain why one observes larger number of horseshoe-shaped structures and hairpins in transitional or relatively low-Reynolds number flows than that of hairpin-shaped structures at high Reynolds numbers. For the latter the time required for the hairpin vortices to lift up and penetrate to the outer edge of the boundary layer will be much longer than their life time and most of them would be dissipated before penetrating through the whole layer.

The outer edge of the turbulent boundary layer consists of three dimensional bulges, the turbulent/nonturbulent interface with the same scale of the boundary-layer thickness $\delta$. Deep irrotational valleys occur at the edges of the bulges, through which free-stream fluid is entrained into the turbulent region (Robinson 1991b). Inside the bulges are slow over-turning motions with a length scale of $\delta$. They have relatively long life times compared with the quasistreamwise vortices that form, evolve, and dissipate rapidly in the near-wall region. These large-scale structures at the outer edge are also related to the induced velocities of groups of hairpin heads.

The inner–outer region interaction is one of the major controversial issues in turbulent boundary layer theories. It is now almost a common understanding that the outer-region structures have a definite effect on the near-wall production process (Praturi and Brodkey 1978; Nakagawa and Nezu 1981) but not play a governing role (Falco 1983). The large over-turning motions are weak, though they have influence on bursting and thus on small-scale transition. Although the outer layer also contains energetic structures, recent numerical experiments (Jiménez and Pinelli 1999) have confirmed that the essential inner-layer dynamics ($y^+ < 60$) can operate *autonomously*.

One of the interesting issues relevant to the inner–outer region interaction is whether the large over-turning motion has important influence on the formation of streamwise vortices. It was suggested (Brown and Thomas 1977; Cantwell et al. 1978) that the successive passing of the large over-turning motions would cause waviness of near-wall streamlines. The *Görtler instability* on a concave boundary layer might have influence on the formation or growing of the streamwise vortices. This suggestion is similar to the "*Görtler-Witting mechanism*," which conjectured that large amplitude T–S waves will locally induce concave curvature in the streamlines and hence a Görtler instability (Lesson and Koh 1985). But, by a computation on a wavy wall,

Saric and Benmalek (1991) showed that the wall section with convex curvature had an extraordinary stabilizing effect on the Görtler vortex so that the net result of the whole wavy wall (or the large amplitude T–S waves) was stabilizing. However, the flow waviness caused by the large over-turning motion is not sinusoidal (or the convex and concave portions of the curvature are not symmetrical), so the net effect of the overturning motion is still to be clarified in the future.

### 10.3.5 Streamwise Vortices and By-Pass Transition

Streamwise vortices are seen in all high Reynolds number shear flows, including free shear layers (mixing layer, wake, and jet, etc.) and wall-bounded shear layers (boundary layer, wall jet, wall wake, etc.). In the former, the inflectional instability leads to spanwise vortices first. A streamwise vortex is a product of secondary instability of the existing spanwise structures. In the latter, the streamwise vortex starts immediately after the nonlinear process starts in the wall region, so one never sees an observable spanwise vortex. However, the background mechanism of streamwise vortices formation is in common, both due to sufficiently strong shear field and three-dimensional disturbances.

The processes described so far are not the only mechanism to form streamwise vortices. Corotating streamwise vortices can be formed in the boundary layer on a sweepback wing due to the crossflow instability. Counter-rotating streamwise vortices can also be formed due to centrifugal instability, such as the *Dean vortices* in curved channels (Dean 1928), the *Görtler vortices* near a concave surface (Görtler 1940; Drazin and Reid 1981), the *Taylor vortices* between concentric cylinders with the inner one rotating, or the streamwise vortices in the outer region of the wall jet on a convex wall, etc. Thus, streamwise vortices are a popular flow phenomenon in turbulent shear layers.

It has been shown in Sect. 10.3.2 that the streamwise vortices play a dominant role in the self-sustaining mechanism of boundary-layer turbulence. Actually, the momentum transported by the streamwise vortices not only generates the streaks but also account for the increase of skin friction in the turbulent boundary layer (Orlandi and Jiménez 1994). The dominant roles of streamwise vortices near the wall in turbulence production and drag generation is now widely accepted (e.g., Kim et al. 1987). In engineering applications, the influences of streamwise vortices in mass transfer (e.g., mixing), momentum transfer (e.g., Reynolds shear stress and skin friction), and energy transfer (e.g., heat transfer) are also significant. Besides, as will be discussed below, streamwise vortices is a key mechanism in the *by-pass transition* to turbulence. All of these explain why we have to pay enough attention to the specific nature related to streamwise vortices.

Figure 10.2 has shown that traveling vortices may be detected as and expressed by waves. This is however not the case for a steady streamwise vortex. Correspondingly, the mechanism of disturbance growth related to streamwise vortices cannot be expressed by the growth of normal modes either. The current understanding of the streak development is the *nonmodal growth*

(*transient growth*) introduced in Sect. 9.1.2 and discussed in Sect. 9.2.4 in the context of shear-layer instability, which has been shown to have potential importance for studies of by-pass transition (e.g., Gustavsson 1991; Butler and Farrel 1992).

A pair of counter rotating streamwise vortices in a boundary layer will cause wall-normal velocity disturbance that accumulates (or grows) algebraically along the streamwise direction $x$ (Fig. 10.24). Even if the streamwise vortices decay along $x$, the normal velocity disturbance could still grow as an integrated effect. The closely related phenomenon is the occurrence of low-speed streaks and the surrounding high shear layers. Actually we have already come across similar phenomenon in the discussion of self-sustaining mechanism in boundary layers (Fig. 10.18). The later breakdown of low speed streaks occurs through a secondary instability, which is developed on the local shear layer between high- and low-speed streaks when a critical Reynolds number based on their size is sufficiently large (Sect. 9.1.2 and Sect. 9.2.4). If this mechanism overwhelms the normal-mode transition, there occurs by-pass transition.

Let us discuss in a little more detail. The T–S waves in a boundary layer on a smooth plate will start when the Reynolds number reaches certain critical value. The disturbances with frequencies within the unstable region will grow exponentially in the linear regime. If, by any mechanism, there occurs a pair of relatively weak streamwise vortices, then their induced velocity disturbances cannot compete with those induced by the T–S waves (the normal mode) because the former grows algebraically. However, if the flow is stable to normal-mode disturbances or there are sufficiently strong initial streamwise vortices for the transient growth to be overwhelming, transition to turbulent flow will take place without passing through the stage of exponential grow of T–S waves. This is called *by-pass transition*.

The transition of the Couette flow and circular-pipe flow are good examples where the velocity profiles are linearly stable to normal modes. Subcritical transition in an ordinary boundary layer is another example where the T–S

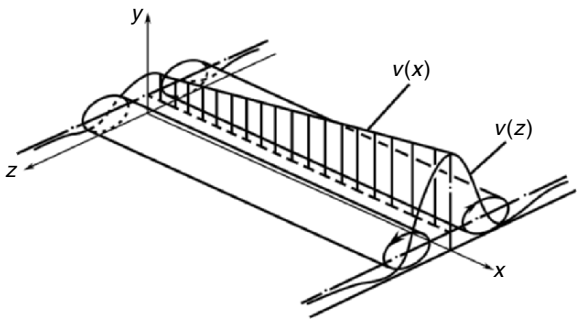


**Fig. 10.24.** Transient growth and counter rotating vortices

wave is linearly stable due to the low Reynolds number. For all these cases, the transition scenario can occur only if there is a mechanism other than passing through the exponential growth of T–S waves.

Besides, if the initial disturbance amplitude exceeds a threshold level, by-pass transition will take place (Darbyshire and Mullin 1995; Draad et al. 1998), such as in a boundary layer on a rough surface or a boundary layer under a surrounding of high turbulence intensity (e.g., a turbine blade). This result is independent of whether the shear flow is unstable to exponential growth of wave-like disturbances. As discussed above, a boundary layer subjected to a free-stream turbulence of moderate levels would develop unsteady streamwise oriented streaky structures with high and low streamwise velocity. This phenomenon was observed even as early as Klebanoff et al. (1962) who observed a by-pass of linear stage whenever the initial amplitude of the perturbation was large, and also discovered the existence of streamwise vortices in the flow field near the surface by measuring two velocity components. Subcritical transitions have recently been investigated in more detail for a variety of flows, for examples, in circular pipes (e.g., Morkovin and Reshotko 1990; Morkovin 1993; Reshotko 1994), in plane Poiseuille flows and in boundary layer flows (e.g., Nishioka and Asai 1985; Kachanov 1994; Asai and Nishioka 1995, 1997; Asai et al. 1996; Bowles 2000).

## 10.4 Some Theoretical Aspects in Studying Coherent Structures

Having seen the significant role of coherent structures in the development of the two example flows, their physical understanding, prediction, and control have become a very active area in turbulence studies. However, a turbulent flow is full of vortical structures of various scales, which can all cause the stretching or tilting of local vorticity. It is not an easy job to calculate all these influences unless a direct numerical simulation is performed, which up to now is still limited to relatively low Reynolds number flows. Thus, the traditional way in turbulence studies is the statistical method.

The famous Kolmogorov (1941, 1962) theory and the recent development of the universal scaling law of cascading (She and Leveque 1994; She 1997, 1998) belong to the statistical method. They both revealed the multiscale structures in turbulence and contributed firmly to the physical background of cascading. Recently, the latter theory has made progresses in combining the knowledge of their universal scaling law with those of coherent structures in shear flows (Gong et al. 2004). However, there is still a long way to go before it can help turbulence modeling to solve the problem of turbulence development in a flow field. So, the most convenient statistical method to date is still based on the Reynolds decomposition.

As has been pointed out in the context of Fig. 10.2 and Sect. 10.3.5, turbulent disturbances related to steady components of streamwise vortices cannot

be expressed by the temporal fluctuations of the velocity field. This brings us to a further discussion on the limitation of the Reynolds decomposition. A combination of triple decomposition and vortex dynamics has shed light on building up *statistical vortex dynamics* and may be a more powerful way out in turbulence studies. But more detailed studies on the vortical structures in turbulence require DNS or deterministic theories.

Many achievements have been made on the relevance of vortex dynamics to turbulence. Theoderson (1952) was the first to predict theoretically the generation of hairpin-shaped structures in a boundary layer as early as 1952. Since then, abundant experimental and computational results have been obtained in the past half century, which have prepared a condition for applying vortex dynamics to predict the coherent structures or explain their evolution (e.g., Saffman and Baker 1979; Leonard 1985; Hunt 1987; Ashurst and Meiburg 1988; Virk and Hussain 1993; Hunt and Vassilicos 2000; Lesieur et al. 2000; Schoppa and Hussain 2002; Lesieur et al. 2003). As mentioned in Sect. 1.2, these efforts have naturally in turn enriched the content of vorticity and vortex dynamics (e.g., Melander and Hussain 1993a and 1994, Pradeep and Hussain 2000; Hussain 2002). We expect that the present section can offer readers some brief concepts related to the basic theories that are important in handling coherent structures.

### 10.4.1 On the Reynolds Decomposition

The Reynolds decomposition has been the most popularly applied statistical method and has contributed tremendously to turbulence studies. While extended to triple decomposition of the velocity field, it has shown its potential also in studies of coherent structures.

In the triple decomposition method, one expresses any instantaneous quantity $\varphi$ as

$$\varphi = \Phi + \varphi_{\mathrm{c}} + \varphi_{\mathrm{r}}, \tag{10.1}$$

where $\Phi$ is its time-mean, and $\varphi_{\mathrm{c}}$ and $\varphi_{\mathrm{r}}$ are its coherent and random components, respectively.

Neglecting the correlation between the coherent and random motions, the coherent energy equation can be written as (Hussain 1983)

$$\begin{aligned} U_j \frac{\partial}{\partial x_j}\left(\frac{1}{2}\overline{u_{\mathrm{c}i}u_{\mathrm{c}i}}\right) = &-\frac{\partial}{\partial x_j}\left(\overline{u_{\mathrm{c}j}p_{\mathrm{c}}} + \underbrace{\frac{1}{2}\overline{u_{\mathrm{c}i}u_{\mathrm{c}i}u_{\mathrm{c}j}}}_{1}\right) - \underbrace{\overline{u_{\mathrm{c}i}u_{\mathrm{c}j}}\frac{\partial U_i}{\partial x_j}}_{2} \\ &+ \underbrace{\overline{\langle u_{\mathrm{r}i}u_{\mathrm{r}j}\rangle\frac{\partial u_{\mathrm{c}i}}{\partial x_j}}}_{3} - \underbrace{\frac{\partial}{\partial x_j}\overline{u_{\mathrm{c}i}\langle u_{\mathrm{r}i}u_{\mathrm{r}j}\rangle}}_{4} - \underbrace{\overline{\epsilon_{\mathrm{c}}}}_{5}, \end{aligned} \tag{10.2}$$

where $u_i = U_i + u_{\mathrm{c}i} + u_{\mathrm{r}i}$.

The viscous diffusion term and the energy production due to normal stresses have been neglected in (10.2) due to their little contribution to the coherent energy balance.

The left-hand side of the equation is the advection of coherent energy by the mean. The terms on the right-hand side are: (1) the diffusion of the coherent energy by coherent velocity and pressure fluctuations; (2) the coherent production by the mean shear; (3) the intermodal energy transfer that expresses the rate of energy transfer from coherent motions to random ones; (4) the diffusion of the coherent energy by random velocity fluctuations; and (5) the viscous dissipation of coherent energy that is usually negligible.

Equation (10.2) shows very clearly the energy transfer between mean, coherent, and random motions and is helpful in understanding, prediction, and control of coherent structures (see Sect. 10.5.3). However, due to the problem revealed by Fig. 10.2 and discussed in Sect. 10.3.5, one should be able to imagine that the existence of streamwise vortices would also cause problem on both the traditional Reynolds decomposition and the triple decomposition of the velocity field as discussed later.

The most representative product from the Reynolds decomposition is the Reynolds shear stress $-\overline{u'v'}$ that is a particular correlation function in turbulence studies. For generality, we take the correlation function between velocity components measured at two separate points to discuss the influence of streamwise vortices. In a statistically steady turbulence, it is defined as

$$R_{ij}(x_k; r, \tau) = \overline{u_i'(x_k, t)u_j'(x_k + r, t + \tau)}, \tag{10.3}$$

where $u_i'(x_k, t)$ is the instantaneous value of the $i$th component of the temporal velocity fluctuation at position $x_k$ and time instant $t$; $r$ and $\tau$ are the spatial and temporal spacing between the measuring location of $u_i'$ and $u_j'$ respectively. The over-bar expresses time averaging. For example, $-R_{12}(x_k; 0, 0)$ just represents the Reynolds shear stress $-\overline{u'v'}$ at location $x_k$.

As is known, the correlation function can usually characterize coherent structures in turbulent flows. However, it has a fundamental defect if streamwise vortices are involved. Without loss of generality, consider the simultaneous two-point spatial correlation of spanwise velocity components $w$ with spanwise spacing $\Delta z$ in a statistically two-dimensional flow, i.e., $i = j = k = 3$ and $\tau = 0$, that is the most characteristic quantity related to streamwise vortices. Thus, we have:

$$R_{33}(z; \triangle z, 0) = \overline{w'(z, t)w'(z + \triangle z, t)}, \tag{10.4}$$

where the velocity fluctuation $w'$ is a *temporal* fluctuation.

Now, the problem comes because an ideally steady streamwise vortex will generate only a steady induced velocity, but no temporal velocity fluctuations. Even if in real flows the so-called streamwise vortices are not entirely streamwise and not ideally steady, at least their steady streamwise component will generate no temporal velocity fluctuations. Therefore, the above correlation

function cannot reflect the full contribution of turbulence structures, especially, the influence of the steady components of streamwise vortices. Thus, the traditional correlation function has to be reconsidered.

A possible way to express the fluctuations caused by streamwise vortices in a statistically steady two-dimensional flow is to replace the temporal fluctuations of the velocity components by spatial ones. Namely, instead of (10.4) we set

$$g_{33}(z;\Delta z,0)=[w(z,t)-\langle w(t)\rangle][w(z+\Delta z,t)-\langle w(t)\rangle], \tag{10.5}$$

where $g_{33}$ is an instantaneous value of the spatial correlation and $\langle\ \rangle$ denotes the spanwise spatial averaging. In order to obtain a satisfactory statistical quantity, the procedure used to obtain the instantaneous spatial correlation function should be repeated for enough times to form an ensemble average. In statistically steady flows, the ensemble-averaged quantity may be replaced by a time-averaged value and we obtain

$$G_{33}(z;\Delta z,0)=\overline{(w_1-w_{\rm av})(w_2-w_{\rm av})}, \tag{10.6}$$

where we use the following abbreviations for neatness, $w_1=w(z,t)$, $w_2=w(z+\Delta z,t)$ and $w_{\rm av}=\langle w(t)\rangle$.

By further decomposing $w_1$, $w_2$, $w_{\rm av}$ into time means and temporal fluctuations, the following expression can be obtained

$$\begin{aligned}G_{33}=&\overline{w_1'w_2'}+\overline{w_1}\cdot\overline{w_2}+\overline{w_{\rm av}}\cdot\overline{w_{\rm av}}-\overline{w_1}\cdot\overline{w_{\rm av}}-\overline{w_2}\cdot\overline{w_{\rm av}}\\&+\overline{w_{\rm av}'^2}-\overline{w_1'w_{\rm av}'}-\overline{w_2'w_{\rm av}'},\end{aligned} \tag{10.7}$$

where $w_1$ and $w_2$ are the instantaneous values of the spanwise velocity at location 1 and 2, respectively, $w_1'$ and $w_2'$ are the corresponding temporal fluctuations and $w_{\rm av}'$ is the time fluctuation of $w_{\rm av}$. This decomposition contains many additional terms since (10.6) is nonlinear.

In a statistically steady two-dimensional flow, $w_{\rm av}=0$ at any time so that we have

$$G_{33}=\overline{w_1'w_2'}+\overline{w_1}\cdot\overline{w_2}=\overline{w_1\cdot w_2}, \tag{10.8}$$

Here $w_1$ and $w_2$ are the instantaneous values instead of the temporal velocity fluctuations. We suggest that this $G_{33}$ is referred to as the *total correlation* to distinguish it from the traditional one. If and only if the turbulent flow is ideally two-dimensional with no steady component of $w$ caused by streamwise vortices, can it then recover to the traditional correlation function:

$$G_{33}=\overline{w_1'w_2'}. \tag{10.9}$$

A comparison of the two correlation functions obtained in two extreme cases is shown in Fig. 10.25 (Xu et al. 2000). The results in figure (a) were taken in a wall jet at a sufficient downstream distance of the jet exit, where

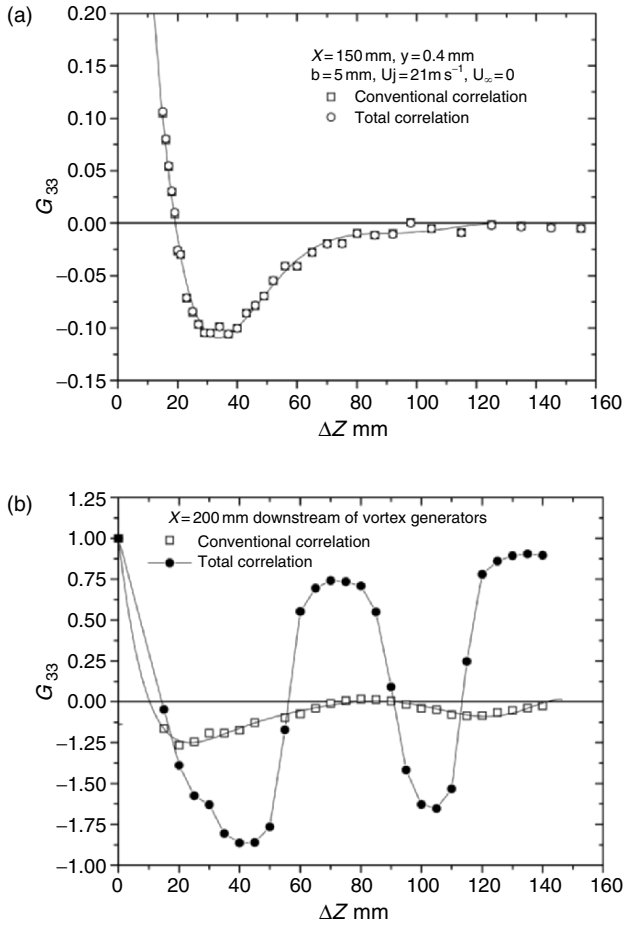


**Fig. 10.25.** The conventional and total correlation. (**a**) The correlation coefficient in a two-dimensional wall jet. (**b**) The correlation coefficient in a two-dimensional boundary layer with a spanwise row of symmetrical vortex generators (wavelength = 70 mm). From Xu et al. (2000)

the turbulence was almost statistically steady and two-dimensional. The two curves computed by conventional and total correlations are almost identical. It indicates that even if there were streamwise vortices in the flow, they migrated or appeared and disappeared in a random way so that the streamwise vortices did not cause significant steady component of $w$. Figure (b) shows the opposite extreme where the results were obtained in a boundary layer with a row of symmetrical vortex generators, which were so arranged that all odd-number generators were tilted to one side at a given angle relative to the $x$-axis and those in even numbers were in the opposite side and symmetrical to the former.

The total correlation reaches the level of O(1) while the conventional one is very low in spite of the existence of strong streamwise vortices along with their steady component.

In a real turbulent flow region, the steady component of streamwise vortices could vary between these two extreme experimental conditions. On the relatively more serious side, for example, Saric (1994) points out that the Görtler-vortex motion produces a situation in spatially developing flows where the disturbance is inseparable in three dimensions from the basic-state motion and that it seems as if all interesting phenomena associated with Görtler vortices share this three-dimensional inseparability. Actually, they are only inseparable from the time-mean value because the disturbances themselves involve steady components. On the less serious side, for example, in a turbulent boundary layer, the streamwise vortices have limited lifetime, within which there would be more obvious steady component, but less or even none in long time average (Bernard et al. 1993). This is believed to be the reason why this problem did not attract enough attention and people have been confined to the conventional correlation in turbulence studies for so long.

Since the Reynolds stresses $-\rho\overline{u'v'}$, $-\rho\overline{v'w'}$, $-\rho\overline{u'w'}$, and turbulence energy $-\rho\overline{u'u'}$, $-\rho\overline{v'v'}$, $-\rho\overline{w'w'}$, etc. are all correlation functions, a logical extension of the above argument is that inherent defect may exist in the traditional concept on turbulence quantities based solely on the Reynolds decomposition. Within that framework, all turbulence quantities are expressed only in terms of temporal fluctuations and are supposed to represent all the actions that the turbulence adds to the mean field. The major efforts of the traditional turbulence modeling have been trying to model these quantities. However, once the steady component of streamwise vortices appears, the traditional definition of turbulence energy and turbulent shear stresses will miss an invisible fraction. This is believed to be one of the basic reasons for the difficulties in modeling the wall region where the streamwise vortices are so critical.

One might argue that there is nothing wrong with the Reynolds equation. The lost fraction of turbulence contained in the steady components of streamwise vortices should enter the mean field. This is true. But in doing so the steady components of the streamwise turbulence structures are not expressed as turbulence. Many physical and technical problems would then follow. For example, the entire concept based on the turbulence energy equation has to be reconsidered. How can one count the turbulence production, advection, diffusion, and dissipation if the steady component of the streamwise vorticity has to be ruled out from turbulence? Besides, if one tried to absorb the steady component of the streamwise vortices into mean flow, the traditional Reynolds-averaged Navier–Stokes (RANS) solution for the mean field of a nominally two-dimensional turbulent flow would become three-dimensional and hence lose its simplicity.

As the above total correlation suggests, one of the ways out could be to apply both temporal decomposition and spatial decomposition in the spanwise

direction to the velocity. In this way, both temporal fluctuation and the time-mean effect of the streamwise vortices will be counted into turbulence quantities. Further studies are desired before a full solution of this problem can be reached.

### 10.4.2 On Vorticity Transport Equations

An alternative or even more powerful approach in studying coherent structures might be the *statistical vorticity dynamics*. Instead of applying the Reynolds decomposition and triple decomposition to the velocity field only, the statistical vorticity dynamics applies the triple decompositions to both velocity and vorticity field:

$$\begin{aligned} \boldsymbol{u}(x,t) &= \boldsymbol{U}(x,t) + \boldsymbol{u}_{\mathrm{c}}(x,t) + \boldsymbol{u}_{\mathrm{r}}(x,t), \\ \boldsymbol{\omega}(x,t) &= \boldsymbol{\Omega}(x) + \boldsymbol{\omega}_{\mathrm{c}}(x,t) + \boldsymbol{\omega}_{\mathrm{r}}(x,t), \end{aligned} \tag{10.10}$$

where $\boldsymbol{u}$, $\boldsymbol{\omega}$ are the instantaneous quantities, $\boldsymbol{U}$, $\boldsymbol{\Omega}$ are time mean quantities, and subscripts c and r denote coherent and random constituents, respectively.

The instantaneous vorticity equation (2.168) reads

$$\frac{\mathrm{D}\boldsymbol{\omega}}{\mathrm{D}t} = \frac{\partial \boldsymbol{\omega}}{\partial t} + (\boldsymbol{u}\cdot\nabla)\boldsymbol{\omega} = (\boldsymbol{\omega}\cdot\nabla)\boldsymbol{u} + \nu\nabla^2\boldsymbol{\omega} \tag{10.11}$$

indicating that the rate of change of the vorticity is due to stretching and tilting of the vorticity caused by the instantaneous velocity gradient (the first term) as well as to viscous diffusion (the second term). This equation can be applied to any instantaneous velocity and vorticity field in both laminar and turbulent flows (Sects. 3.5.1 and 3.5.3).

As the first step of applying (10.11) to coherent structures, dimensional analysis may give a simple but important concept. Take the spanwise vortices in a mixing layer as example. Assuming that the mean velocity difference is of $\mathrm{O}(U)$ and the thickness of the mixing layer is of $\mathrm{O}(\delta)$, then we have the estimates:

$$\begin{aligned} |\omega| = \mathrm{O}(U/\delta), \quad |\nabla u| = \mathrm{O}(U/\delta), \\ |(\boldsymbol{\omega}\cdot\nabla)\boldsymbol{u}| = \mathrm{O}(U^2/\delta^2), \quad |\nu\nabla^2\omega| = \mathrm{O}(\nu U/\delta^3). \end{aligned} \tag{10.12}$$

Hence, the ratio of the first term on the right-hand side of (10.11) to the second term is of $\mathrm{O}(U\delta/\nu)$, i.e., the Reynolds number based on the radial size of large spanwise vortices, which is usually a very large number. Thus, the development of large coherent structures in the mixing layer can be regarded as an invicid process.

For statistical analysis, substitute (10.10) into (10.11) and take time average, we obtain the mean vorticity equation.

$$\frac{\mathrm{D}\boldsymbol{\Omega}}{\mathrm{D}t} = (\boldsymbol{\Omega}\cdot\nabla)\boldsymbol{U} + \nu\nabla^2\boldsymbol{\Omega} + \nabla\times\overline{(\boldsymbol{u}_{\mathrm{c}}\times\boldsymbol{\omega}_{\mathrm{c}})} + \nabla\times\overline{(\boldsymbol{u}_{\mathrm{r}}\times\boldsymbol{\omega}_{\mathrm{r}})}. \tag{10.13}$$

Compared to (10.11), the first two terms on the right-hand side of (10.13) are of the same form, but the stretching and tilting here are caused by the mean velocity gradient only. Moreover, there occur two extra nonlinear interaction terms on the right-hand side, which are the curl of the coherent and random Lamb vectors and have very clear physical meaning. The third term represents the time-averaged effect of the interaction (i.e., stretching and advection) between the coherent vorticity and coherent velocity fluctuations. The fourth term is the time-mean effect of the interaction between the random vorticity and velocity fluctuations. These terms are very helpful in understanding the development of a turbulent shear flow.

As an illustration, consider a forced mixing layer (Zhou and Wygnanski 2001). The viscous effect in (10.13) is small as discussed earlier. By assuming that the time-mean spanwise coherent motion is basically two-dimensional and that the influence of the random motion is negligible in a mixing layer under two-dimensional forcing, the first and fourth terms can also be dropped from (10.13). The rates of change of $\Omega$ from direct measurement (expressed by symbols in Fig. 10.26) and calculated from the third term (by solid line) at the right side of (10.13) are plotted in Fig. 10.26. The balance of data indicates that the above assumptions are valid. Thus, $\mathrm{D}\Omega/\mathrm{D}t$ is indeed dominated by the curl of the time-mean coherent Lamb vector, including the change in the

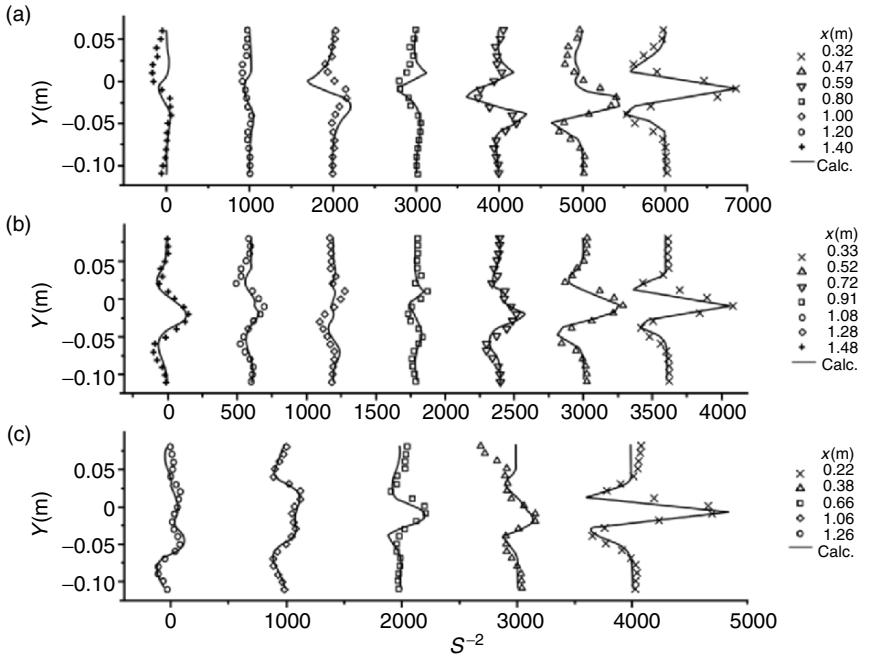


**Fig. 10.26.** Mean vorticity balance in a forced mixing layer (**a**) Forced by single frequency, (**b**) Forced by two frequencies (fundamental and subharmonic), (**c**) Forced by two frequencies but with stronger amplitude. From Zhou and Wygnanski (2001)

mean vorticity profile along the flow and the spreading of the entire mean shear field. It also explains why the spreading rate depends on the variation of the forcing condition.

This example clearly demonstrates the benefit of the mean vorticity equation as compared to the Reynolds equation combining with the turbulence energy equation or the Reynolds stress transport equations. The latter can express the interaction of mean flow field with the turbulence field or that between turbulent velocity fluctuations themselves. The function of coherent motions is buried in the turbulence fluctuations and cannot be revealed explicitly.

For analysis of coherent motions, we assume that the coherent quantities can be represented by the phase-locked ensemble averaged quantities and further assume that the coherent and random motions are uncorrelated. Substituting (10.10) into (10.11), taking the phase-locked ensemble average, and neglecting the higher order quantities, the coherent vorticity equation reads (based on Hussain 1983)

$$\begin{aligned}\frac{\mathrm{D}\boldsymbol{\omega}_c}{\mathrm{D}t} = {} & \overset{1}{(\boldsymbol{\omega}_c\cdot\nabla)\boldsymbol{U}} + \overset{2}{(\boldsymbol{\Omega}\cdot\nabla)\boldsymbol{u}_c} + \overset{3}{\nu\nabla^2\boldsymbol{\omega}_c} + \overset{4}{\nabla\cdot(\boldsymbol{\omega}_c\boldsymbol{u}_c - \overline{\boldsymbol{\omega}_c\boldsymbol{u}_c})} \\ & \overset{5}{-\nabla\cdot(\boldsymbol{u}_c\boldsymbol{\omega}_c - \overline{\boldsymbol{u}_c\boldsymbol{\omega}_c})} \overset{6}{-\nabla\cdot(\boldsymbol{u}_c\boldsymbol{\Omega})} + \overset{7}{\nabla\cdot(\langle\boldsymbol{\omega}_r\boldsymbol{u}_r\rangle - \overline{\boldsymbol{\omega}_r\boldsymbol{u}_r})} \\ & \overset{8}{-\nabla\cdot(\langle\boldsymbol{u}_r\boldsymbol{\omega}_r\rangle - \overline{\boldsymbol{u}_r\boldsymbol{\omega}_r})}. \end{aligned} \tag{10.14}$$

where the over-bar denotes the time mean quantities and the bracket $\langle\ \rangle$, the phase locked quantities. Compared to the mean vorticity equation, the first three terms of the right side are of the same form as the first two terms of (10.13). Instead of the stretching and tilting of the mean vorticity caused by the mean velocity gradient in the first term of (10.13), here the first and second terms on the right side represents the stretching/tilting of the coherent vorticity by the mean velocity gradients and that of the mean vorticity by the coherent velocity gradients. The third term is the viscous diffusion of the coherent vorticity. The fourth and fifth terms represent the *residual* coherent interaction (after subtracting the mean) between the coherent vorticity and the coherent velocity fluctuations, where the summation of the time mean components is the same as, but of the opposite sign to the third term in (10.13). It means that while coherent interaction causes an increase of mean vorticity, the mean coherent vorticity would be reduced by the same amount, i.e., an energy transfer from the coherent to the mean, or vice versa. The sixth term represents the advection of mean vorticity by the coherent velocity fluctuations. The seventh and eighth terms involve special physical mechanisms. They are the residual (after subtracting the mean) coherent interaction between the random vorticity and velocity fluctuations. The seventh is due to stretching and tilting, and the eighth due to advection. By these interactions,

the coherent vorticies may be sliced into random eddies or the latter may be reorganized into coherent ones (see Sect. 10.5.1).

As has been shown in Figs. 10.10 and 10.17b, the main mechanism of streamwise vortices formation in a shear layer is due to the three dimensional deformation of the spanwise vortices in a strong shear field. From the coherent vorticity equation (10.14), this mechanism can be easily examined. Considering $\mathrm{D}\omega_{xc}/\mathrm{D}t$, a small normal coherent vorticity component $\omega_{yc}$ in a region of strong mean shear $\partial U/\partial y$ will lead to a significant value of $\omega_{yc}(\partial U/\partial y)$, and so to a dominant first term to produce streamwise vorticity (see also Williamson 1996).

### 10.4.3 Vortex Core Dynamics and Polarized Vorticity Dynamics

The discussions in Sect. 10.4.2 are based on the statistic point of view. Neither (10.13) nor (10.14) can describe any deterministic structure of the individual coherent vortices. In order to apply vortex dynamics to study more detailed coherent structures in turbulence, there are yet two major difficulties: the influence of internal vorticity distribution in a vortex core on the dynamics of the vortex is not well understood; and, the structure and dynamics of a large-scale coherent structure in a turbulent environment are not clear. For these purposes vortex core dynamics and polarized vorticity dynamics would be helpful, of which the basic theories have been discussed in Sect. 8.1.2–8.1.4 (see also Melander and Hussain 1994, and Melander and Hussain 1993a). Here, we only list some results to show their contributions in understanding turbulence.

Figure 10.27 is a typical result from the core dynamics showing periodical deformation of a coherent vortex core. Assume that the initial shape of a vortex core is distorted as (A). The vorticity lines are being uncoiled because the two ends of the vortex segment in the figure are thinner and rotate faster

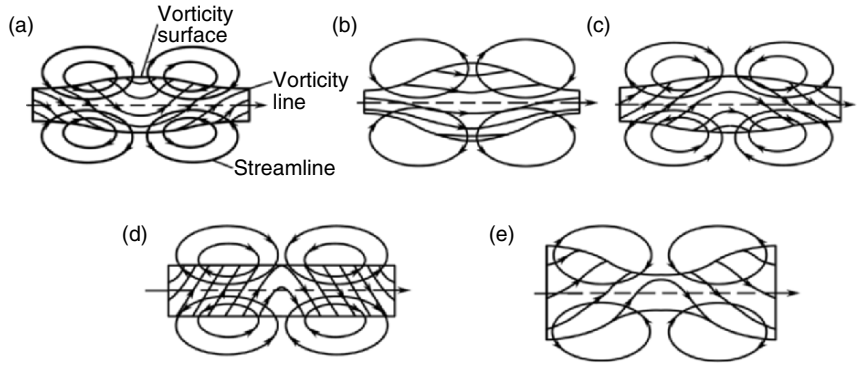


**Fig. 10.27.** Schematic of the coupling between swirling and meridional flows. From Melander and Hussain (1994)

than the midportion. Meanwhile, the meridional flow induced by the vorticity lines will continue to distort the shape of a vorticity surface sketched in the figure further away from that of a rectilinear vortex (B). When the vorticity lines are entirely uncoiled, the difference in rotating speed between the two ends and the midportion is even larger so that the differential rotation causes new coiling of the vorticity line to the opposite direction (C). Then the new coiling with opposite sign induces a meridional flow of opposite sign and brings the vorticity surface towards rectilinear (D). When the shape of vorticity surface becomes rectilinear the vorticity lines are highly coiled and its induced meridional flow causes distortion of the vortex away from rectilinear, but in a way opposite to the original one (E), i.e., thicker and rotates slower at the two ends than the midportion of the vortex. The dynamic procedure can be continued in the same way as above and an oscillation of vortex shape and coiling of vorticity lines can be easily seen. This kind of dynamic oscillation is expected to be one of the typical behaviors of the coherent vortices in turbulence and affects the collectively induced velocity field in turbulence. It will also have important influence on the interaction between coherent vortices and the surrounding random eddies.

The above oscillating mechanism is also an evidence on the coexistence of vortices and waves in turbulence, as well as an evidence on the vortical structures as a carrier of vorticity waves (Sect. 10.1.3). While a vortex is associated with the mass transport, a wave is the motion transfer without mass transport; in many cases they are not separable. We see that generically the core dynamics involves neither a pure wave motion nor a pure mass transport, but a combination of both. However, in the above example, the vorticity can be transported as waves in a vortex core without corresponding mass transport due to the coupling between swirl and meridional flow (Hussain 1992).

Figure 10.27 has also shown that the vortices are usually *polarized*, i.e.,, with a preferred swirling direction (either left-handed or right-handed, Fig. 10.28a). Thus, the polarized vorticity dynamics (Sect. 8.1.4) becomes an important tool in quantitative understanding of the evolution of coherent structures. It can handle the problems related to mutual interactions of the coherent structures, their coupling with fine-scale turbulence and their break down and reorganization. The polarized vorticity equations are shown in (8.49a) and (8.49b). Comparing with the usual vorticity equation, these equations involve additional terms expressing that the evolution of the one handed mode (say the left-handed) is coupled with the other (say the right-handed). In developing the polarized vorticity dynamics, the basic analytical tool is the complex *helical wave decomposition* (HWD) introduced in Sect. 2.3.4.

One of the major achievements from the polarized vorticity equation is the structure of a coherent vortex column in an environment of random eddies (Fig. 10.28). Due to the interaction between the coherent vortices and the turbulence surroundings, there are always secondary structures (threads) spun azimuthally around it. The vorticity in the threads is mostly azimuthal

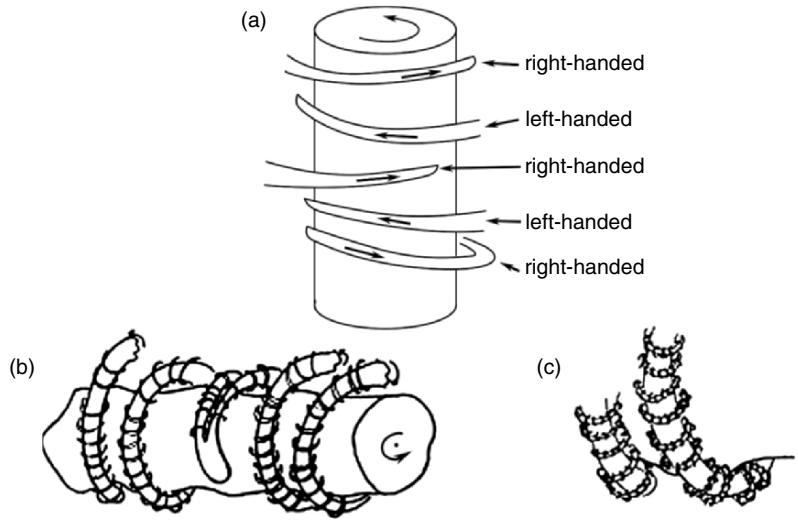


**Fig. 10.28.** Schematic illustration of coherent-random interaction. (**a**) polarized structures, (**b**) primary, (**c**) secondary. From Melander and Hussain (1993b)

and the threads are highly polarized (Melander and Hussain 1993a and b). It not only gives a clear view on the turbulence cascade, but also enriches the concept of a coherent vortex: in a turbulent flow a coherent vortex should not be only an isolated single vortex. Rather, it is always coupled with a group of surrounding small-scale, polarized vortices winding around it. This phenomenon also gives a good explanation of internal intermittency in turbulence – the highly dissipative structures embedded into an irrotational flow.

## 10.5 Two Basic Processes in Turbulence

In either a free shear layer or a wall-bounded shear layer, we have seen one thing in common. The observed vortical structures appear as the instantaneous frames of mainly two developing processes. The first process starts from a laminar/locally laminar, or a random turbulence background. Disturbances of selected modes (not necessary normal modes) are growing and lead to the formation of vortical structures with larger and larger scales. The second process is the structural evolution in the opposite direction, i.e., the *cascade*. Large coherent structures are getting smaller and smaller due to vortex interaction and gradually pass their energy to random eddies. As the cascade continues, the random energy will eventually dissipate to heat. From the equations in Sect. 10.4, we can easily find out those terms representing either process.

### 10.5.1 Coherence Production – the First Process

This process is the physical source to generate and maintain a turbulence, without which even an existing turbulence cannot survive. For example, the turbulence generated by a grid in a uniform flow will eventually disappear due to dissipation. This process is also the source to cause anisotropy and the variety of the coherent structures in a turbulence field, without which even existing coherent structures will eventually pass their energy to isotropic small eddies.

In terms of energy transfer, this process transfers energy from the mean to coherent energy (through instability and *coherence production* – second term of (10.2)) and from random to coherent (negative intermodal transfer – third term of (10.2)). The appearance of the organized structures as a result of an instability mechanism was also emphasized by Prigogine (1980) from the viewpoint of thermodynamics. As a consequence of self-organization, the number of degrees of freedom (Lesieur 1990, p. 141) is reduced and thus it is a procedure that leads to a negative entropy generation. In terms of synergetics (Haken 1984), it is the process that the orderly motion evolves from the disordered (molecular motions or random eddies) background, and hence represents *self-organization* (the organization of random eddies is related to the last two terms of (10.14)).

The self-organization of coherent vortices from random ones can be illustrated by two examples. One is an experiment in a rotation tank (Hopfinger et al. 1982) where the preferred orientation of the axes of the high-vorticity eddies are parallel to the rotation axis due to the Taylor–Proudman theorem (see Sect. 12.1). Imagine that the rotating tank is similar to the motion of a tornado and the surrounding eddies are the random atmospheric turbulence, then the tornado will give the surrounding eddies a preferred orientation and eventually strengthen the tornado. The other is a numerical study of a coherent structure embedded in the surrounding fine-scale turbulence (Melander and Hussain 1993b) as has been shown in Fig. 10.28. The small-scale random eddies in the absence of coherent vortex are isotropic and homogeneous. The appearance of coherent vortices destroys the isotropy by aligning the random vortices to the swirl direction of the vortex, thereby giving the random vortices a preferred direction, and hence increases the coherent vorticity.

We should stress here that the negative entropy generation in a turbulence field is not in conflict with the second law of thermodynamics. The latter asserts that the entropy is always increasing in an isolated system, but a given turbulence region is an open system which exchanges mass and energy with its neighboring. The given turbulence region may obtain a negative entropy flux from its neighbor so that its entropy would be locally reduced while the entropy in the neighboring region is increased. If the two regions add up to be one isolated system, the total system should still have positive entropy generation. As an interesting example from a mixing layer experiment, Huang and Ho (1990) found that the small-scale transition was first produced by the

strain field of the pairing vortices imposed on the streamwise vortices. The strained streamwise vortices were unstable and initiated the random fine-scale turbulence. That is to say, the vortex merging (with negative entropy generation) is accompanied by the small-scale transition (with positive entropy generation) and the total entropy generation should still be positive.

In Sects. 10.2 and 10.3, we have seen that the stability mechanism dominates the coherent production. In a mixing layer, there occur typically the Kelvin–Helmholtz instability and the formation of the spanwise vortices, the subharmonic instability and pairing etc. In a boundary layer, there occur typically the T–S instability, the local inflectional instability and the formation of hairpin structures, etc. They start from laminar or locally laminar background with distributed mean vorticity (shear) and develop to organized vortices. The background can even be turbulent; e.g., a flow field with mean shear and filled with small eddies, where large vortices can also be produced by certain instability mechanism. Thus, it will be interesting to discuss the similarity and difference in applying stability theory in a turbulent and in a laminar flow.

The linear stability theory in laminar flows like those presented in Chap. 9 has been well accepted for a long history and is even taken for granted although a so-called laminar flow is in fact full of random molecular motions. Only because the length scale of molecular motion are so small compared to the wavelength of the instability waves, the latter can be regarded as approximately independent of the details of time-dependent motions of fluid molecules. It is this independence that ensures the physical validity of the entire continuum mechanics including hydrodynamic stability theory. The molecular motions do have influence on the instability mechanism; they can usually be counted by a molecular viscosity – a statistical isotropic time-mean scalar (if without additives). Consider now a turbulence field. If the wavelength of the concerned instability waves is much greater than the average length scale of the background eddies, and if the latter is almost isotropic, then the situation is similar to the laminar case. The coherent instability waves may be considered approximately independent of the details of the surrounding time-dependent motion of the small turbulent eddies, so that the physical nature of flow instability should work. Of course, small eddies also have influence on the instability waves; but they could be likewise counted by certain statistical time-mean quantities such as *eddy viscosity*. In particular, the mean velocity field of a mixing layer is subject to an *inviscid* instability. Thus, the instability mechanism is independent of the molecular motion, or similarly, independent of the small-scale isotropic random eddies in turbulence. That is to say, neither molecular viscosity nor eddy viscosity affects the inviscid instability mechanism. Thus, it is not surprising that the stability analysis for laminar mixing layers can work very well also in turbulent mixing layers (see details explained later).

It should be emphasized here that enough disparity in length scale is essential for the instability mechanism to be independent of the background turbulence. This is true not only for the case where the length scale of background

turbulence is much smaller than the wavelength of the instability waves as stated above, but also for the opposite case where the length scale of the background turbulence is much larger than the wavelength of the instability waves. For the latter, one just needs to think about what happens in the atmosphere or an ocean. Miscellaneous flow instability phenomena take place in local regions (local instability) although the whole atmosphere or ocean is already turbulent.

The linear instability analysis was shown successful to predict the most amplified frequencies and the amplification rates of the large spanwise vortices in an externally excited turbulent mixing layer (Oster and Wygnanski 1982; Monkewitz and Huerre 1982). Gaster et al. (1985) further found that their measured disturbance matched perfectly with the linear stability calculations in both amplitude and phase distributions in a forced turbulent mixing layer. Morris et al. (1990, see also Roshko 2000) made a good progress in modeling a turbulent mixing layer based on the concept that the turbulence production is dominated by coherent production and is caused by the amplification of the instability modes. This idea was examined by Zhou and Wygnanski (2002) based on the data measured by Weisbrot and Wygnanski (1988). The result from the mixing layer excited at moderate amplitude level is shown in Fig. 10.29, where "forced by two frequencies" means forced by a fundamental frequency and its subharmonic. Figure (a) indicates that the growth rate of the mixing layer depends directly on the turbulence production, and figure (b) indicates that the turbulence production term is indeed dominated by the coherent production mainly related to the spanwise coherent vortices.

Though successful in the above examples, the applicability of the instability theory in turbulence is limited. If the scales of the coherent structures of interest are close to that of the background eddies and strong interactions happen between the two, the instability waves can no longer be independent of the turbulence background, and thus the similarity in the instability mechanisms between laminar and turbulent flows is no longer valid. It is also important to mention the role of the isotropic property for the viscosity. Even in a laminar flow, very small amount of the polymer additive may cause a dramatic change in the stability character because instability wave may cause a feedback effect on the viscosity tensor so that the growth of the instability wave is no longer independent of molecular motions. The same is true in a turbulence field. If the background turbulence eddies cause significant anisotropy, the conventional stability calculation would not be applicable.

All that stated above will add complexity to a turbulent boundary layer and make the application of stability theory in its downstream locations difficult. In a boundary layer, new vorticity is continuously sent into the flow field and new vortical structures are continuously formed at downstream locations, similar to what happens in a transitional boundary layer. Kachanov (2002) described this phenomenon as a *continuous transition*. The downstream flow is under the influence of background turbulent structures advected from upstream, including organized structures like hairpins, streamwise vortices and random vortex rings, etc. The latter may have the length scales close to

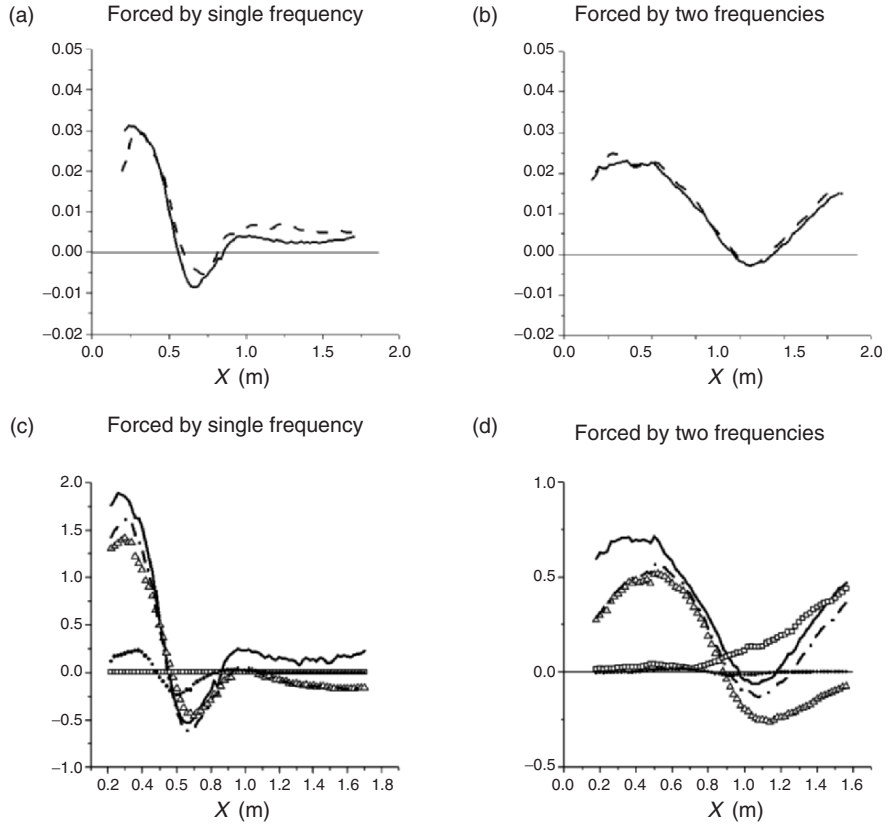


**Fig. 10.29.** The relation between growth of mixing layer and the coherent production. (**a**) and (**b**) Growth rate versus turbulence production. *Dashed line* – $\mathrm{d}\theta/\mathrm{d}x$; *solid line* – $(U_2+U_1)/(U_2-U_1)^2\int_{-\infty}^{\infty}(-\text{Production})/U^2\,\mathrm{d}y$; (**c**) and (**d**): Turbulence production versus coherent production, where *solid line* – total turbulence production, *dash-dotted line* – summation of the coherent production, *triangle* – fundamental, *square* – subharmonic, and *solid circle* – high harmonic. From Zhou and Wygnanski (2002)

the downstream instability waves. In addition, they are highly anisotropic. It is believed to be the reason why so far attempts to apply instability theory in a turbulent boundary layer has had little success except in separated boundary layers, where there is a region similar to a mixing layer so that an inviscid instability mechanism becomes dominant (see Sect. 10.6.1).

The little success in applying instability theory to analyze the whole turbulent boundary layer, however, does not mean that the stability mechanism does not exist physically in turbulent boundary layers. For example, the local inflectional instability mechanism around low speed streaks is still a key point in the self-sustaining mechanism of turbulence in fully developed turbulent boundary layers.

### 10.5.2 Cascading – the Second Process

This is an entropy generation process, including cascade, intermodal (coherent-random) energy transfer (the third term of (10.2)), and dissipation. A cascade process involves complicated iterative operation of vortex stretching, tilting and folding (Sect. 3.5.3). However, the tendency of cascading can be explained by a simplified sketch with only stretching involved (Fig. 10.30). Suppose that a turbulence field is filled with many vortical structures. If a vortex filament along the $x$-direction is stretched by the induction of other vortices, this vortex filament will become thinner and rotates faster, which enhances the local induced velocity in the $y$- and $z$-directions. This in turn increases the local velocity gradient and causes stretching of neighboring vortices in those directions. Consequently, the latter also becomes thinner and their rotation is speeded up. Such a procedure will continue and every step will cause further decrease of the length scale of the vortices. Accordingly, turbulence energy will gradually be transferred to smaller and smaller scales.

Note that the probabilities of the cascade process as described above are uniform in all directions, and thus the turbulent structures will approach homogeneous and isotropic after several steps of cascade if there is no anisotropic influence from the first process. In fact, this process exists in all types of shear flow; and the final products of the cascade, the random eddies, are almost the same. This is why the background random eddies in turbulent shear flows are almost not dependent of the boundary conditions but coherent structures are.

In a real viscous shear flow, the largest scales are usually related to the production of coherent structures. Below that, there often exists a range of eddy sizes called the inertial subrange. In the *inertial subrange* and in average sense, no energy is added by the mean flow and no energy is taken out by viscous dissipation, so that the energy flux across each wave number is constant and the energy cascade is conservative (Tennekes and Lumley 1972). If there is no influence from the first process, both Kolmogorov's spectrum and She's universal scaling law can express the cascading very well. However, where there is influence from an instability mechanism that causes production and anisotropy, a variation of the similarity parameter in the She–Leveque scaling law (She and Leveque 1994) can be seen (Gong et al. 2004).

Besides, this cascading process cannot continue unlimitedly. With the process of stretching, thinning, and faster rotating going on, the dissipation

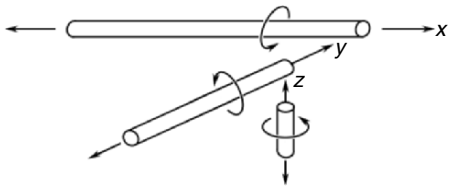


**Fig. 10.30.** A sketch of turbulence cascade. Based on Chen (1986)

rate due to the molecular viscosity is greatly enhanced. (recall 2.54, 2.155 and 4.21 for the energy and enstrophy dissipation rates, their dependence on the vorticity and its gradient, respectively). Eventually, eddies smaller than the *dissipation scale* or *Kolmogorov scale* will be entirely dissipated with their energy being transferred to random molecular motion, the heat, and cannot be maintained in any turbulence field.

The dissipation scale can be directly obtained from dimensional analysis. Experimental observations indicate that the dissipation scale $\eta$ depends on dissipation rate $\varepsilon$ and kinematic viscosity $\nu$. Thus we may write, dimensionally (denoted by $[\,]$), $[\eta] = [\nu]^m[\varepsilon]^n$, where $[\nu] = L^2T^{-1}$; $[\eta] = L$; $[\varepsilon] = L^2T^{-3}$. This yields $m = 3/4$, $n = -1/4$, and so

$$[\eta] = [\nu]^{3/4}[\varepsilon]^{-1/4}, \quad \eta = k(\nu^3/\varepsilon)^{1/4}. \tag{10.15}$$

Then the Kolmogorov scale $\eta = (\nu^3/\varepsilon)^{1/4}$ by setting $k = 1$.

Therefore, for a given $\varepsilon$ , a smaller $\nu$ leads to smaller dissipation scale, implying that smaller vortices can survive at higher Reynolds numbers. For example, in a high Reynolds number boundary layer, the order of $\eta$ can be as small as tens of microns, and the corresponding timescale is of the order of microseconds (Karniadakis and Choi 2003). This is why direct numerical simulations to date are still confined to low Reynolds numbers.

The above discussion only gives an overall mechanism of cascade. Its real physical details are miscellaneous and very complicated. Not only the vortex stretching but also more complicated vortex interactions will be involved, such as vortex pair instability, vortex cut-reconnection etc. as shown in Fig. 10.13 and 10.14. Furthermore, the cascading process happens often simultaneously with the production process. Let us make use of Fig. 10.28 again to summarize the last statements. On the one hand, it is a vivid view of fractal cascading by the successive interactions between a coherent vortex and its surrounding small scales. When the coherent motion defines a preferred orientation to small random eddies, the latter are stretched in the expanse of the coherent energy. The interaction generates further a local shear that can sustain turbulence also in consuming the energy contained in the coherent vortex. Thus, the energy is passed from large to secondary and continuously to even smaller scales. On the other hand, the small scales, aligned and stretched by the coherent vortex are self-organized into increasingly large scales through vortex merging; thus, the interaction also involves a negative cascade or self-organization process.

### 10.5.3 Flow Chart of Coherent Energy and General Strategy of Turbulence Control

Flow control in a shear layer is important in engineering applications, for examples, lift augmentation, drag reduction, noise suppression, heat transfer, mixing enhancement, improving combustion, or other chemical reaction, etc. All these performances are closely related to turbulence structures. In general,

the development of a turbulent flow depends on the generation, transfer, and dissipation of turbulence energy (Bradshaw et al. 1967). It can be seen below, the flow control in a shear layer is indeed a control of coherent structures, i.e., a control of the generation, transfer, and dissipation of coherent energy. Thus, flow control is also of interest for physical studies as a diagnostic tool in enhancing or destruction of coherent structures.

In the coherent energy equation (10.2) the viscous dissipation of coherent energy is usually negligible (Sect. 10.4.2). Of the rest terms, the streamwise diffusion is relatively small, and the integrations of the two diffusion terms (by coherent – term 1 of 10.2, and random fluctuations – term 4) across the flow are approximately zero. Thus, the advection of the coherent energy depends only on the two source terms, i.e., the coherent production (term 2 of 10.2) and the intermodal (coherent-random) energy transfer (term 3). The former is usually positive except in some limited narrow regions of certain asymmetrical turbulent shear layers where the production could be negative (Eskinazi and Erian 1969; Hinze 1970). The latter is usually negative except in some special regions where self-organization mechanism becomes dominant (such as a region where a typhoon is being formed). Thus, the main flow chart of the coherent energy is clear. While the mean energy is being transferred to coherent energy through instability mechanism, the coherent energy is transferred to random energy through cascade. The random energy is then transferred to the heat (the molecular energy) through dissipation. Thus, the level of coherent energy just depends on the balance of the two processes. Although the feedback from the random to the coherent energy always exist, such as the reorganization of surrounding random eddies by the coherent vortices (Fig. 10.28), it is usually of secondary importance in the energy balance.

Based on the above discussions, the basic energy chart can be expressed schematically by Fig. 10.31, where solid lines denote the major route and the dashed lines, the minor feedback. The water level mimics the coherent level or the negative entropy level. The coherent production or self-organization process that increases the negative entropy is expressed by pumps. The cascading, dissipation process, and negative production are illustrated by valves.

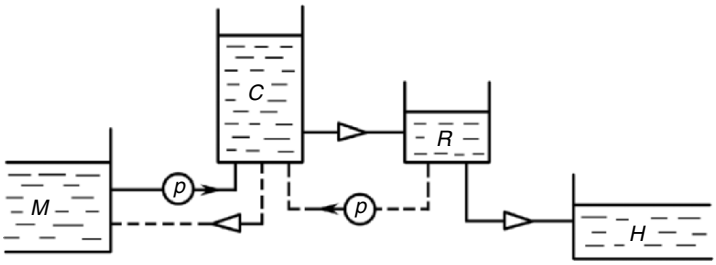


**Fig. 10.31.** A flow chart of energy transfer. $M$ – Mean energy, $C$ – Coherent energy, $R$ – Random energy, $H$ – Heat (molecular energy), $P$ – Pump, *Triangle* – Valve

Apparently the level of coherent energy in a flow just depends on how to adjust the pumps and valves. For examples, stimulating coherent production can lead to increase of coherent energy; suppressing it or enhancing dissipation can reduce the level of coherent motion.

Specific methods of flow control depend on nature of the flow, purposes of application, and techniques available. Detailed techniques are very much different, from controlling a convectively unstable flow to a globally unstable flow, from stimulation to suppression of coherent production, from passive to active, from open-loop to close-loop, etc. For example, a global instability may be stimulated very efficiently by a single sensor–actuator feedback control; while using the same technique to suppress the global instability (where all the global modes have to be attenuated) is difficult (Huerre and Monkwwitz 1990).

In recent two decades, amazingly large amount of studies have been conducted on flow control for various purposes and with various techniques (for reviews see, e.g., Bushnell and McGinley 1989; Fiedler and Fernholz 1990; Gad-el-Hak 1996, 2000; Karniadakis and Choi 2003). A detailed discussion is beyond the scope of this book. It is in order, however, to pick up a few examples to explain the basic control strategy stated above.

**Enhancement of Coherent Production**

In this category, a successful example is to introduce periodical blowing on the knee of a trailing flap to delay separation so that the lift on the wing can be augmented (Seifert et al. 1993). Since the outer portion of the mean velocity profile of the separated boundary layer on the flap is similar to a mixing layer (Fig. 10.36g and Sect. 10.6.1). The periodic forcing enhanced the coherent production of the spanwise vortices and increases the entrainment of the high-energy fluid into the separation region. Then, if one regards the separation region as a reservoir with the solid boundary as its one side, the streamline of the other side will bend towards the wall due to enhanced entrainment (Katz et al. 1989). Thus, the separation will be weakened or even eliminated.

Another example is also introducing periodical excitation at the outer edge of the separation region of an airfoil for lift augmentation. But the physical idea is different. The introduced disturbance is so controlled that the outer edge of the mean separation region is bent towards and reattaches at the trailing edge of the airfoil. The target is not to eliminate separation at large angle of attack but to enhance the coherent production to form a series of spanwise vortices traveling through the upper surface of the wing, so that a strong time-mean vortex is seemingly "*captured*" (Fig. 10.32a) and the vortex lift is obtained (Zhou et al. 1993).

The major criterion to distinguish the above two types of separation control is the skin friction. In the first example, the separation suppression is targeted so that an increase of skin friction is expected as a measure of success. But in the second example, the formation of a strong mean vortex is

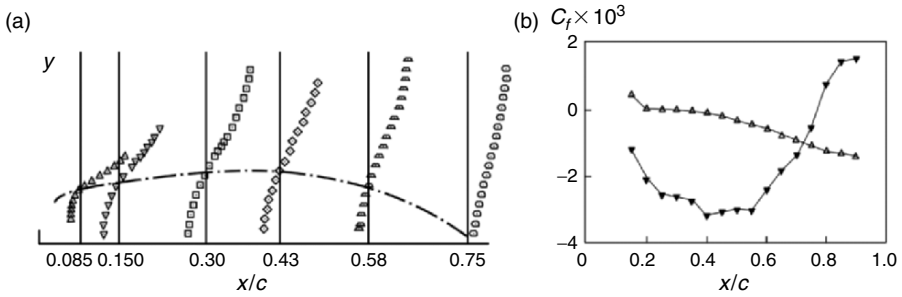


**Fig. 10.32.** The mean vortex enhancement on an airfoil at large angle of attack by periodical forcing. ($\alpha = 27°$, $Re = 6.71 \times 10^5$, forced with $fU_\infty/c = 2$). (**a**) Mean-velocity profile at various streamwise locations on the upper surface of the airfoil. (**b**) Distribution of skin friction. In (**b**) *open symbols* – unforced; *closed symbols* – forced. From Zhou et al. (1993)

expected so that a reduction of skin friction to a strong negative value is a measure of success (Fig. 10.32b). This idea can be extended to (Zhou 1992) and has been applied successfully in augmentation of lift in dynamic stall (Wygnanski 1997), where, judged by the results, the dynamic stall vortex was actually enhanced and captured in the ensemble averaged sense.

### Suppression of Coherent Production

Many studies for drag reduction belong to this category (e.g., Karniadakis and Choi 2003). Since in wall-bounded flows the sweeps and ejections in the turbulence regeneration cycle are the major activities related to turbulence production and generation of turbulent wall-shear stress (Sect. 10.3.2), interrupting the regeneration cycle artificially should lead to large drag reduction and even flow relaminarization, such as riblets (Walsh (1990)), opposition control (Jacobson and Reynolds 1998), spanwise wall oscillations (Jung et al. 1992), and spanwise traveling waves (Du et al. 2002; Zhao et al. 2004).

The *opposition control* is an example that offers a very clear physical mechanism to the coherent-structure suppression. As is shown in Fig. 10.33, the strength of near-wall streamwise vortex would be substantially reduced by blowing and suction with normal velocities equal and opposite to that induced by the streamwise vortex. Numerical computations have confirmed this mechanism (Kim 2003). In experiments, the drag can be reduced by approximately 25–30% (Choi et al. 1994).

Spanwise wall oscillation is another vivid example for the suppression of turbulence regeneration process. The key mechanism identified is the control of the near-wall streamwise vortices and corresponding suppression of the low-speed streak instability (Dhanak and Si 1999). Note that the spanwise locations of the low-speed streaks are at the symmetric lines of the streamwise

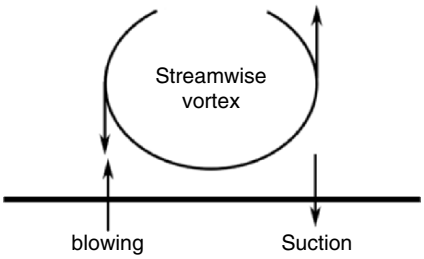


**Fig. 10.33.** A sketch of opposition control. Based on Kim (2003)

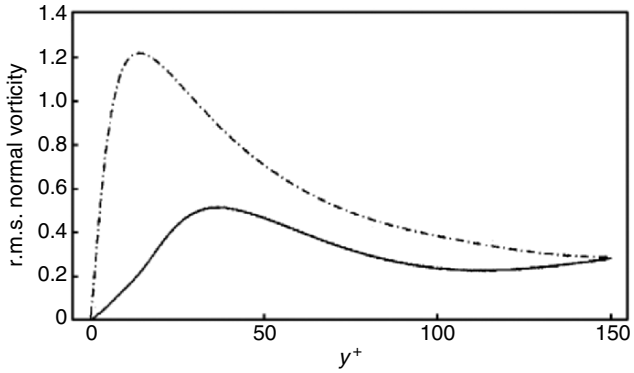


**Fig. 10.34.** Suppression of normal vorticity fluctuation by the spanwise wall oscillations. *Dash-dotted line* – no wall oscillation; *solid line* – spanwise wall oscillation at $T^+ = 100$. From Karniadakis and Choi (2003)

vortex pairs where the induced velocities of the latter are pumping the low momentum fluid away from the wall (Fig. 10.18b). Now imagine, when the wall surface suddenly moves in the spanwise direction, the originally existing low-speed streaks and streamwise vortices will also be moved in the same direction due to influence of the Stocks layer caused by the moving wall. Since the low-speed streaks and streamwise vortices locate at different distances from the wall, their spanwise displacements caused by the Stocks layer are different. Assume that the differential displacement between the low-speed streaks and streamwise vortices equals their half spanwise wavelength, the spanwise locations of the low-speed streaks are now between different streamwise vortex pairs where the latter would pump the high-speed fluid toward the wall and weaken the low-speed streaks, thereby the process of turbulent energy production would be disrupted (Baron and Quadrio 1996). Figure 10.34 indicates the effect of spanwise wall oscillation on the wall-normal vorticity fluctuations. As a result, the skin friction drag reduction in excess of 40% can be achieved.

### Enhancement of Dissipation

An example of using dissipation enhancement to reduce the coherent energy was presented by Wiltse and Glezer (1998). The flow was forced by cantilevered piezoelectric actuators at a frequency approximately an order of magnitude lower than the Kolmogorov wave number of the base flow. The velocity power spectra $S(f)$ measured downstream of the jet exit are shown in Fig. 10.35, where $f_{\mathrm{r}}$ is the resonance frequency of the actuator. Above a critical frequency of $f/f_r = 0.05$, the turbulence energy of the forced flow is *higher* than the unforced flow even though the excitation is applied at frequencies above $f/f_r = 1$. On the contrary, the energy at all frequencies below that value is *lower* than the unforced flow. Apparently, the forcing induces coupling or long-range interactions between small and large scales within the flow and thus leads to an accelerated energy cascade from the large scales (Yeung et al. 1995). This phenomenon can be explained by the energy flow chart in Fig. 10.31. Direct small-scale excitation works as a wider opening of the dissipation valve and faster draining of the random energy to heat. It increases the "water" level difference across the valve of intermodal energy transfer, and in turn increases the energy flux to drain the coherent energy out to the random. Thus, the coherent energy is reduced.

Following the above discussions, a logical question is whether the coherent production control and the dissipation control can be combined for particular purposes. The answer is yes. It has already been demonstrated that large and small vortical structures between widely disparate scales in turbulent flows are *directly* and *bi-directionally* coupled, which can be stimulated through coherent narrow-band forcing at either the large or small scales (Wiltse and

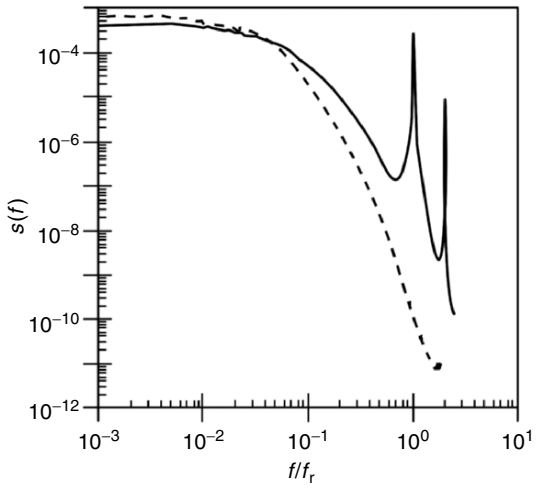


**Fig. 10.35.** Velocity power spectra of the forced (*solid line*) and unforced (*dashed line*) flow. From Wiltse and Glezer (1998)

Glezer 1993; Yeung et al. 1995). This phenomenon can also be mimicked by playing with the pumps and valves simultaneously (Fig. 10.31). Thus, a properly designed combination of multiple-control toll should be able to control the turbulence level at desired scale more effectively.

## 10.6 Vortical Structures in Other Shear Flows

In Sects. 10.2 and 10.3, we have exemplified free shear layers and wall-bounded shear layers by two-dimensional mixing layer and two-dimensional boundary layer respectively. In Sects. 10.4 and 10.5 we discussed more general knowledge in transitional and turbulent flows. Now we should be able to extend our knowledge obtained in Sects. 10.1–10.5 to discuss the vortical structures in more general turbulent flow fields. The discussions are mainly based on comparisons of the particular shear layer with the above simplest examples to find their similarity and difference. The vorticity budget will be applied to explain the flow phenomena wherever convenient. A central concept in Sects. 10.1–10.5 is that coherent structures start from an instability mechanism, which will still be followed.

### 10.6.1 Vortical Structures in Plane Complex Turbulent Shear Flows

Let us call all the plane shear layers other than the mixing layer and boundary layer *plane complex shear layers*. Although traditionally the plane wake and jet are also considered as simple shear layers, it will be made clear that they actually possess certain characters of complex shear flows.

We first introduce the concepts of *partial similarity* and *local similarity*. Partial similarity means that two flows are dynamically similar only in their dominant feature but not perfectly similar. A well-known example is high- and low-speed wind tunnel tests, each taking care of only either the Reynolds-number effect or the Mach-number effect on the real flow but seldom both. Thus the tested flow and real flow are only partially similar. In contrast, local similarity means that the similarity exists in some local regions rather than globally. For example, the mean velocity profile around the low-speed streak is locally similar to a mixing layer and is subject to an inflectional instability (Fig. 10.18a).

In terms of the concept of partial similarity and local similarity, one can extend the knowledge on vortical structures in Sects. 10.1–10.5 to complex shear layers. Since these structures are formed from instability mechanisms of the shear field, one can also expect the coherent structures produced in certain local regions of the complex turbulent shear flows to be similar to those in simple shear layers. Figure 10.36 shows the mean velocity profiles of various kinds of plane complex turbulent shear flows that can, at first glance, be regarded as the combination of a few simple mixing layers or boundary

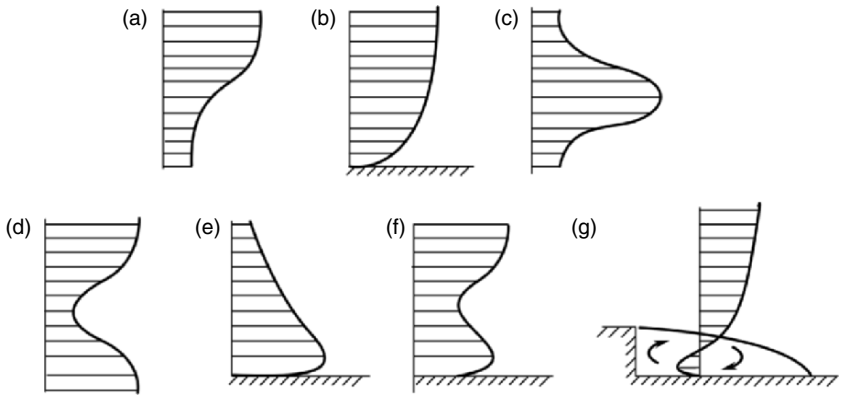


**Fig. 10.36.** Mean velocity profiles of the complex turbulent shear flows

layers. The plane jet (c) and plane wake (d) can be regarded as combination of two mixing layers (a) symmetrical with respect to the centerline. The wall jet (e) can be regarded as combination of a mixing layer (a) and a boundary layer (b). A weak wall jet or a wake-boundary-layer confluent flow (f) is a combination of three regions, two mixing layer regions, and one boundary layer region. Even a separated flow (g) can be regarded as a combination of mixing layer and a boundary layer but with opposite flow directions close to the wall.

It is reasonable, therefore, to conceive as the first approximation that each shear layer might behave independently, and the flow in each shear region would have a specific instability mechanism and produce corresponding coherent structures. The flow behavior in each region should satisfy its own boundary condition, and hence the development of the structures therein should have their own scale. Then, the interaction between different regions should be considered.

The coherent structures sketched in Fig. 10.37 can be taken as an example. The coherent vortices in the upper or lower portions of a wake behind a bluff-body are quite similar to those in a mixing layer. They are subject to the inviscid instability and develop large spanwise vortices on each side, wound around by streamwise vortex pairs as in a mixing layer. These coherent structures also subject to small-scale transition downstream, and afterward the spanwise vortices still survive but become a component of the structures in the fully developed turbulent wake.

The separated bubble behind a backward-facing step is a good example of separated flows, where the outer region is similar to a mixing layer and the wall region is similar to a boundary layer but with mean flow direction opposite to the free stream (Fig. 10.36g). Eaton and Johnson (1981) found that the mean velocity profiles upstream of reattachment are almost identical to a mixing layer in the outer three quarter of the separated shear layer. They further

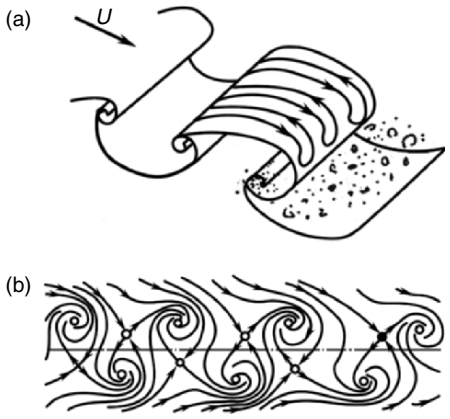


**Fig. 10.37.** A sketch of plan wake. (**a**) oblique view and (**b**) side view (see also Fig. 7.9b)

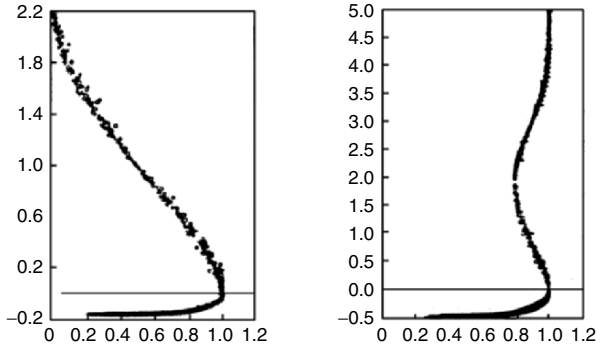


**Fig. 10.38.** Collapsing of wall jet and wall-wake profiles. For the coordinates see the main text below. From Zhou and Wygnanski (1993) and Weidemann (1996)

found that growth rates of these shear layers in many other experiments are also comparable to that of the plane-mixing layer, although the turbulence level is very high in the neighboring boundary layer region.

The scaling of wall jets and wall wakes is another good evidence of the local similarity. If a complex turbulent shear flow can be viewed as a combination of simple shear regions, its number of scales should depend on that of these simple shear regions. This assertion is confirmed by Fig. 10.38. In a strong wall jet (Fig. 10.36e), two velocity scales ($U_{\max}$ for inner region and $U_{\max} - U_\infty$ for outer) and two length scales ($y$ at $U_{\max}$ for inner and $y$ at $(U_{\max} + U_\infty)/2 - y$ at $U_{\max}$ for outer) are required to collapse the mean velocity profiles measured at various streamwise locations (Zhou and Wygnanski 1993). However, three velocity scales and length scales are necessary in a weak wall jet or wall-wake (Fig. 10.36f).

On the instability behavior, it was found that when certain periodical disturbances are introduced into a wall jet or a separated flow, the response of the flow in the mixing-layer region is also similar to that in a simple mixing layer. Therefore, it is a very useful approach to regard complex shear flows as combinations of simple shear layers as the first approximation.

It should be born in mind, however, that the discussed similarity is not only local but also partial. The shear regions in a complex shear flow are not really independent of each other. In the above discussions the border of different shear regions was taken at the surface with the maximum or minimum mean velocity, where the Reynolds shear stress is generally nonzero. This implies inevitable interactions between the two regions. Even if the Reynolds shear stress is zero in long-time average at the center of a symmetrical shear layer, say a plan wake or a plan jet, the instantaneous shear stress is still nonzero. Even if the shear stress is zero the mass transfer may still not be zero. Thus, the coherent structures in each region of a complex shear flows cannot be entirely the same as those in a simple shear layer of corresponding type.

In general, to what extent a local similarity holds depends on how well we can separate the two neighboring regions or how strong their interaction is, which is closely related to the characteristic scales of the neighboring regions. If the disparity of scale is significant, the interaction is relatively weak and different regions can almost be considered as independent. For example, in a wall-wake flow, if the boundary-layer thickness is very large and the wake is produced by a thin circular cylinder at the outer region of the boundary layer, the interaction between the mixing layer region and the boundary layer region is weak. The vortex street in the wake will keep its own behavior almost independent of the boundary-layer structures. In the opposite situation, the interaction will be strong and resonance may even occur. This is the case in a plane wake (or a plane jet), where the two opposite shear regions have exactly the same length and velocity scales, so actually there is resonance between the two. As a consequence of interaction, the two rows of the spanwise vortices of opposite vorticity have to be staggered. Figure 10.37b clearly shows that all vortex centers and saddle points are connected to the streamlines of both sides. Thus, the vortical structures on both sides are coupled and the two regions are not separable. Moreover, it is well known that in a two-dimensional far wake the coherent structures appear not only in the characteristic sinuous mode (antisymmetric), but also, for an appreciable percentage, in the varicose (symmetric) mode (Fiedler 1988). Thus, the mixing layer region of a wake is not really the same as a simple mixing layer.

Besides, the development of a complex shear layer is influenced not only by the individual stability mechanisms in local regions but also by the instability mechanism of its global scale. For example, in the separated flow shown in Fig. 10.36g, in addition to the thickness of the mixing-layer region and boundary-layer region, the total thickness of the separated boundary layer or the total length of the separation bubble is a new length scale, which affects the structures of the separated bubble as a whole. In particular, if the

flow structure governed by this length scale (say the oscillation of the bubble) resonates with those governed by the length scales of the individual region (say the rolling up or pairing of the spanwise vortices in the mixing-layer region), the effect of global length scale may even be dominant. One of the significant examples occurs in the separation control on an airfoil or flap. In order to increase the mixing between the separated region and the outer high-momentum free stream, a preferred dimensionless frequency to maximally amplify the disturbances in the mixing-layer region should be a reasonable choice. Since the bandwidth of the unstable range in a mixing layer is quite wide, eventually the frequency able to resonate with the global instability frequency becomes the preferred frequency. As is well known, the global instability of the separation bubble is governed by the length of the separation region (the chord of airfoil or flap). Thus, the chord of airfoil or flap becomes the length scale of the commonly used Strauhal number applied in the separation control (Zhou et al. 1993; Wygnanski 1997; Wu et al. 1998).

### 10.6.2 Vortical Structures in Nonplanar Shear Flows

Many turbulent shear flows in applications are far from being planar. It is of interest that even for these flows the above discussion can be helpful as long as the similarity and the difference between the planar and nonplanar flows can be carefully addressed. The scaling consideration is also a useful tool for the nonplaner shear layers.

Take an axisymmetric jet as example. In a meridian sectional plane, the shape of the mean velocity distribution looks similar to a plane jet (Fig. 10.36c). One might imagine an instability mechanism similar to a plane jet or the combination of two symmetrical mixing layer regions. The streamwise development of this instability would form vortices similar to the spanwise vortices in the mixing layer, which would be vortex rings (Maxworthy 1977). Indeed, this seems to be the case close to the jet exit (Fig. 10.39). However, the finite diameter of the axisymmetric jet offers an additional scale $R_{1/2}/\theta$

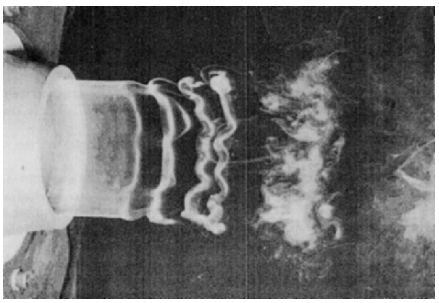

**Fig. 10.39.** Instability of the vortex rings in an axisymmetric jet. From Fiedler (1988)

(where $\theta$ is the momentum thickness of the mixing layer on one side of the jet, and $R_{1/2}$ is the radial distance from the center to the location where the mean velocity equals half of the maximum velocity) affecting the instability of the whole flow, which causes the azimuthal instability (Plaschko 1979).

From the linear stability analysis, many meaningful results can be obtained by solving the eigen problem (Cohen and Wygnanski 1987a,b). As in most axisymmetric flows, mainly the first three azimuthal modes ($n = 0$, $n = \pm 1$, and $n = \pm 2$, i.e., ring, single helix, and double helix, respectively) are of main interest in the mode analysis. At jet exit, almost all modes are unstable; but, at certain location in the region where $x/\mathrm{D} \geq 3$ ($R_{1/2}/\theta \leq 4.82$), the unstable helix mode becomes so dominant that the whole flow structures from there on depend on the growth of unstable helix waves. It is the reason why the vortex ring at certain distance downstream of the jet exit consists of many vortex sections at spiral angle relative to the jet cross-section, i.e., the dents-shaped vortex ring (Fig. 10.39). Then formation of streamwise vortices and small-scale transition will follow. The continuing development of the axisymmetric jet was also studied by the polarized vorticity dynamics (Melander et al. 1991). The result shows that during rolling up of the ring vortex and the development of azimuthal instability, different polarized vorticity components start to separate spatially. When the ring structures break down, the jet structure consists of mainly streamwise vortical structures having the form of lobes or asymmetric hairpins.

If the jet exit is elliptical, we have two additional length scales instead of one. The downstream development of the vortex ring is much more complicated due to different self-induction and the consequent mutual induction at different azimuthal locations (Fig. 10.40). For example, the high curvature near two ends of the major axis will make these portions of the vortex ring move faster and twist an originally planar vortex ring to nonplanar. The bent-forward vortex branch near the major axis will produce an outward induced

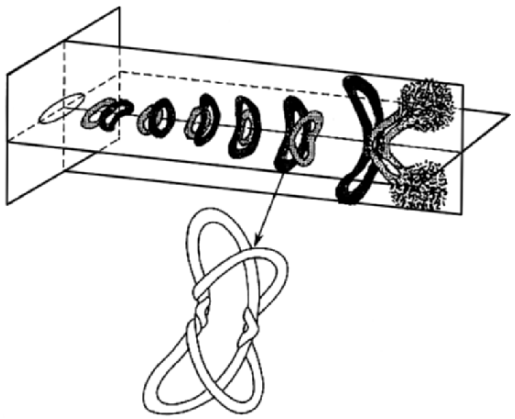

**Fig. 10.40.** Elliptic jet. From Husain and Hussain (1991)

velocity near the ends of the minor axis. Thus, in the streamwise view, the major and minor axes of the vortex ring will exchange their positions periodically (Koshigoe et al. 1989; Zaman 1996; Gutmark and Grinstein 1999); in the side view, the pairing partners will bend in opposite ways and be entangled to each other (Husain and Hussain 1991).

Similar to the large spanwise coherent vortices in mixing layers, the zigzag vortex rings in a jet start from the transition stage but still exist after small-scale transition occurs. The only difference is that the large coherent ones exist now in a turbulence background.

The preceding comparison of two- and three-dimensional jets is also useful for understanding the nature of structures in wakes due to the similarity between wakes and jets. An axisymmetric wake will also develop vortex ring, the dents-shaped deformation and streamwise vortices, but with vorticity of sign opposite to that of the jet. The reader may compare the sphere wake (Fig. 55 of Van Dyke 1982) and the round jet (Fig. 118 of Van Dyke 1982). One can also imagine that if the cross-section of the wake is elliptical, the vortex ring will also be subject to nonuniform self-induction, the consequent three-dimensional deformations, etc. But, due to the strong disturbances, these structural developments may not be observable as clearly as in jets.

We should now emphasize that many nonplanar shear layers have other behavior that cannot be solely accounted by the consideration of additional scales. Consider the flow around a delta wing at high angles of attack sketched in Fig. 10.41 (see also Figs. 7.7). According to the slender body approximation in Sect. 7.3.1 the flow can be decomposed into that parallel to and that normal to the axis of the slender body. Although the flow is truly three-dimensional, if one observes the flow on a sectional plane normal to the leading edge, the mean velocity profile is still similar to that on a two-dimensional separated airfoil, having a combination of an outer mixing-layer region and an inner boundary-layer region. Both experimental observations (Gad-el-Hak and Blackwelder 1985, 1986) and numerical calculations (Fig. 7.21a,b) have shown that a series of discrete vortices are formed in the outer region similar to the spanwise vortices in a mixing layer. This is why an active flow control, which can enhance a separated vortex on a two-dimensional wing, may also have chance

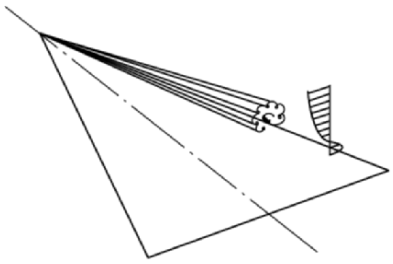

**Fig. 10.41.** The flow around a delta wing. Sketched based on Gad-el-Hak and Blackwelder (1985)

to enhance the lifting vortex and delay its breakdown on a delta wing (Gad-el-Hak and Blackwelder 1986; Teng et al. 1987). But there is an essential difference between this three-dimensional flow and its two-dimensional counterpart: the three-dimensional vorticity transportation. Due to the axial flow, a part of the vorticity can be advected downstream. If the sweepback angle is so large that the rate of the vorticity transportation in the axial direction can balance the boundary vorticity flux from the wall around the leading edge, the rolled-up main vortex can remain steady above the upper surface of the wing and produce a vortex lift, rather than shed off as in two dimensions. Besides, as is well known, the lifting vortex on the delta wing may breakdown in the downstream region due to the strong adverse pressure gradient.

### 10.6.3 Vortical Flow Shed from Bluff Bodies

The transitional and turbulent flow field downstream of a bluff body depends on the flow pattern around the bluff body. The simplest and most carefully studied example of the flows around a bluff body is the flow over circular cylinder (Roshko 1961; Zdravkovich 1997, 2002). A detailed description of the flow phenomena around a circular cylinder is given in Sect. 7.4.1. Here offers further a brief explanation of the transition of flow pattern and their influence on the downstream flow structures based on vorticity balance.

Figure 10.42 shows some typical views in the whole sequence of the flow patterns at various Reynolds numbers. When the Reynolds number is very low ($Re = 1.54$), the vorticity produced by the wall and diffused into the surrounding laminar flow is transported downstream except for those lost by the viscous dissipation. Due to this balancing of vorticity, no separation

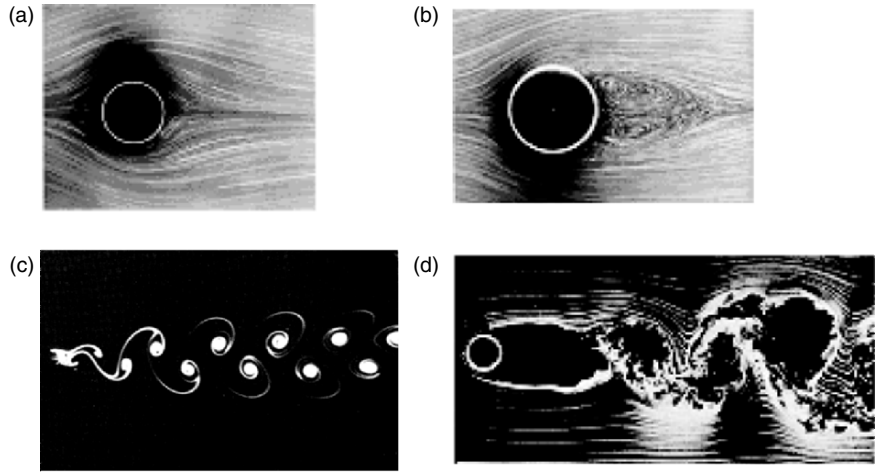


**Fig. 10.42.** The flow over a circular cylinder. (**a**) $Re = 1.54$, (**b**) $Re = 26$, (**c**) $Re = 105$, (**d**) $Re = 10,000$. From Van Dyke (1982)

is observed. At relatively higher Reynolds number ($Re = 26$), the vorticity produced at the wall is increased due to higher shear and cannot be balanced by the above mechanism so that the produced vorticity accumulates to become two symmetrical, steady separated bubbles. These two bubbles reduce the area where the vorticity of the favorable sign is produced; instead, in the separated region the wall produces the vorticity of opposite sign. On the mean while, the transportation of vorticity produced in the region upstream of the separated bubbles is enhanced due to the larger velocity at outer border of the bubbles so that the vorticity balance can be kept in a steady flow. If Reynolds number is increased further ($Re = 105$), even the second mechanism cannot be kept, i.e., the production of the vorticity is so large and the vorticity is accumulated so fast that the vorticity accumulated in the separated bubble has to shed away in a certain rate to keep the vorticity balance. Thus, a periodical vortex shedding starts. If the Reynolds number is high enough ($Re = 10{,}000$), the wake becomes turbulent and the vortices shed from the circular cylinder become a part of the coherent structures in the wake. At even higher Reynolds numbers, no matter the incoming flow is laminar or turbulent the major vortical flow patterns are similar, i.e., the major downstream vortex patterns are usually not Reynolds-number sensitive though the dimensionless vortex shedding frequency may (Fig. 7.25a).

Based on the same concept of vorticity balance, the flow pattern on an inclined cylindrical body can also be explained. Consider a slender cylindrical body with an inclination angle relative to the spanwise direction (Fig. 10.43). The incoming velocity can be decomposed into two components, normal and parallel to the cylinder axis. To the leading approximation with the viscous effect of the axial flow neglected, the normal component would play the similar role as that of the two-dimensional case. The axial velocity in this flow will transport away part of the vorticity by advection in the axial direction and weaken the vortex shedding. By increasing the inclination angle relative to the spanwise direction, the influence of the axial advection will also increase. At certain angle this influence may become so large that all the vorticity produced at the wall can be balanced by the axial advection and the vortex shedding

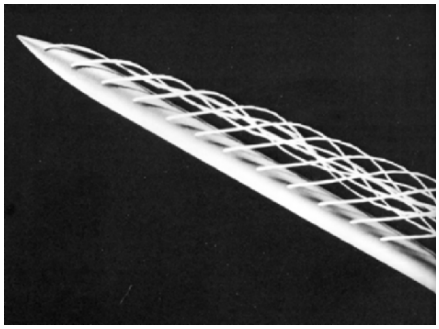

**Fig. 10.43.** A slender body at angle of attack. From Van Dyke (1982)

in the normal direction will stop. Once it stops, the vortex system around the slender body becomes steady so that the contents of coherent structures in the wake change dramatically. This is exactly what happens, for example, on the fuselage of an airplane at large enough angle of attack but not at deep stall.

Another interesting feature that is closely related to the downstream coherent structures in the wake is how the separation originates. For this purpose, one has to pay attention to open and closed separation (Sect. 7.1, also refer to Wang 1982). The closed separation originates from the critical points (termed as fixed points in Sect. 7.1) of the skin-friction lines and the separation line is closed in front of the separation region (Figs. 7.3 and 7.4b). On the contrary, in open separation, the separation line originates from an ordinary point of a skin-friction line and is not closed in the front leeside surface (Fig. 7.4a). Apparently the separation on a rectangular wing at high angle of attack is a closed separation and the flow around the prolate spheroid shown in Fig. 10.44 is an open separation.

The judgment of open and closed separations will help predicting the coherent structures in the downstream turbulent flow field. For example, closed separation usually (in particular, in two dimensions) leads to unsteady vortex shedding into the wake region; and open separation, to steady separated flow as seen from the sharp contrast of the flow patterns discussed in Sect. 7.3 and Sect. 7.4. However, the closed separation is not necessarily related to the unsteady vortex shedding. A three-dimensional free vortex-layer separated flow can start from close separation as well. For example, the necklace vortex shown in Fig. 7.29 starts from a closed separated vortex at its center. The strong axial flow on both side transports the vorticity away so that there is no continuous accumulation of vorticity in the central portion where a separation bubble would have been formed if it were a two-dimensional forward facing step. More complicated flows that start from closed separation and with no unsteady vortex shedding can be found on a hemisphere-cylinder at large angles of attack (Fig. 10.45). Judge from the surface pattern, both flow patterns belong to closed separation. In each pattern, there exists a separated vortex in the central symmetric plane that starts from a saddle point and ends (reattach) at a node. However, each separated vortex at the center is immediately combined with a pair of tornado-like vortices that transports away the vorticity accumulated in the center so that no unsteady vortex shedding can be observed.

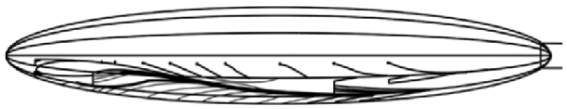

**Fig. 10.44.** The surface limiting flow pattern of a prolate spheroid at angle of attack $30^\circ$ and $U_\infty = 45\,\mathrm{m\,s^{-1}}$. From Kreplin et al. (1980)

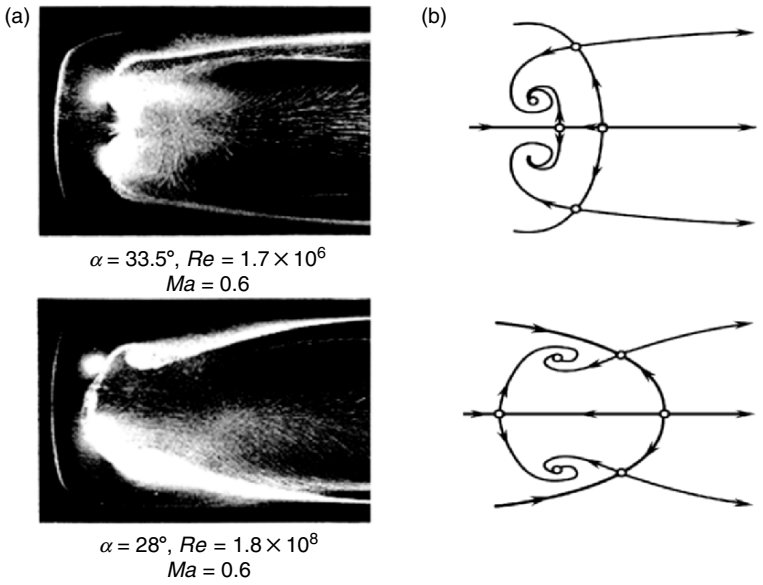


**Fig. 10.45.** The surface flow patterns (**a**) (Bippes and Turk 1983) and the corresponding topological structures (**b**) (Dallmann 1984) of a hemisphere-cylinder at large angles of attack

## Summary

In this chapter, we choose the mixing layer as an example of free shear layers and the simple boundary layer as an example of wall-bounded shear layers to describe the evolution of coherent vortices. After the related theoretical aspects and the general physics have been summarized, the knowledge introduced in the two examples is extended to more complicated turbulent shear flows.

The most important viewpoints are listed:

1. The usually observed turbulence phenomena are instantaneous frames of two physical processes, the coherent production or self-organization process and the cascading/dissipation process. All the vortical structure evolution depends on the balancing between the two. Based on the belief that coherent structures are caused by the instability mechanism, the coherent structures in many flows other than the two simplest examples can be understood within the local/partial similarity limit.
2. The conventional statistical theory, the statistical vorticity theory, and the deterministic vorticity theory are three major categories of methods in turbulence studies. The fact that a steady streamwise vortex cannot produce any temporal velocity fluctuation has challenged greatly to the traditional turbulence theory, including the normal mode transition and

the Reynolds decomposition. Thus, the spatial decomposition approach, or the statistical vorticity theory may be more powerful ways to study coherent structures. Considering the statistical theories smear out some important information on the coherent structures, the deterministic vorticity theory and DNS might be the final solution to study details of individual vortical structures if necessary.

3. Vorticity balance and coherent energy balance are powerful tools in explaining the turbulence phenomena. The flow pattern around a bluff body and the turbulent wake behind it depend on how the separation initiates and whether vortex shedding occurs, and both can be explained in term of vorticity balance. Many flow control techniques can be understood based on the coherent energy balance. The control strategy based on this point of view may help future development in flow control.

# Part IV

# Special Topics

# 11

# Vortical Aerodynamic Force and Moment

## 11.1 Introduction

As an applied branch of fluid dynamics, aerodynamics (and hydrodynamics) studies the force and moment experienced by solid bodies moving through the fluid. In order to fully understand relevant mechanisms, aerodynamics has a task in common to general fluid dynamics: investigating various flow phenomena generated by the body motion. In addition, the ultimate concern of aerodynamics, also its unique task, is *expressing the force and moment in a way that can precisely capture the key physical mechanisms contributing to these integrated performances.*

*Low-speed aerodynamics* is dominated by the shearing process, of which the necessary physical knowledge has been discussed in preceding chapters. Therefore, it is natural now to further identify those specific key shearing processes that contribute most significantly to the force and moment for any given body motion at low Mach numbers. This task requires developing some special theories. We focus on incompressible flow, but some theories also cover compressible flow. It can then be seen that, as the Mach number increases, the compressing process is progressively important for the force and moment and becomes dominant in supersonic flow.

The main concern of this chapter is a basic external-flow problem: a material body of volume $B$ moves arbitrarily in a viscous fluid. The body may have arbitrarily deformable boundary, as encountered in several areas such as fish swimming and insect flight in external biofluiddynamics, nonlinear fluid–solid coupling, and flow control by flexible walls, etc.[1] Thus, we assume the body surface $\partial B$ has specified velocity distribution $\boldsymbol{u} = \boldsymbol{b}(\boldsymbol{x}, t)$. The fluid volume $V_\mathrm{f}$ is bounded internally by the material surface $\partial B$ and externally by a control surface $\Sigma$. The latter may have arbitrary velocity $\boldsymbol{v}(\boldsymbol{x}, t)$ or extend to infinity where the fluid is at rest or in uniform translation. The flow domain is sketched in Fig. 11.1.

[1] Some of the theories can also be applied to gas–liquid two-phase flow by adding the surface tension effect.

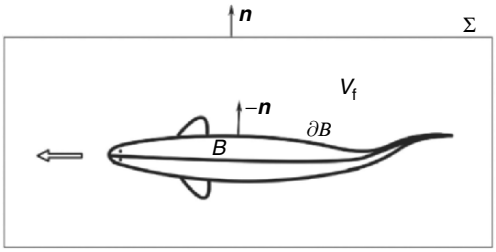


**Fig. 11.1.** Flow domain to be analyzed and notations

### 11.1.1 The Need for "Nonstandard" Theories

The general expressions of aerodynamic force and moment are *"standard"* formulas (2.71) and (2.72). For an incompressible external flow defined in Fig. 11.1, by the Reynolds transport theorem (2.37), these formulas take the following alternative forms, based on (a) direct integrals of surface stresses and their moments over $\partial B$, (b) integrals of local balance of momentum and angular momentum, and (c) the rate of change of total momentum and angular momentum in a generic control volume:

$$\boldsymbol{F} = -\int_{\partial B} (-p\boldsymbol{n} + \boldsymbol{\tau})\,\mathrm{d}S \tag{11.1a}$$

$$= -\rho \int_{V_f} \boldsymbol{a}\,\mathrm{d}V + \int_{\Sigma} (-p\boldsymbol{n} + \boldsymbol{\tau})\,\mathrm{d}S \tag{11.1b}$$

$$= -\rho \frac{\mathrm{d}}{\mathrm{d}t} \int_{V_f} \boldsymbol{u}\,\mathrm{d}V + \int_{\Sigma} [-p\boldsymbol{n} + \boldsymbol{\tau} - \rho\boldsymbol{u}(u_n - v_n)]\,\mathrm{d}S, \tag{11.1c}$$

$$\boldsymbol{M} = -\int_{\partial B} \boldsymbol{x} \times (-p\boldsymbol{n} + \boldsymbol{\tau})\,\mathrm{d}S + \boldsymbol{M}_{\mathrm{s}B} \tag{11.2a}$$

$$= -\rho \int_{V_\mathrm{f}} \boldsymbol{x} \times \boldsymbol{a}\,\mathrm{d}V + \int_{\Sigma} \boldsymbol{x} \times (-p\boldsymbol{n} + \boldsymbol{\tau})\,\mathrm{d}S + \boldsymbol{M}_{\mathrm{s}\Sigma} \tag{11.2b}$$

$$= -\rho \frac{\mathrm{d}}{\mathrm{d}t} \int_{V_\mathrm{f}} \boldsymbol{x} \times \boldsymbol{u}\,\mathrm{d}V + \int_{\Sigma} \boldsymbol{x} \times [-p\boldsymbol{n} + \boldsymbol{\tau} - \rho\boldsymbol{u}(u_n - v_n)]\,\mathrm{d}S + \boldsymbol{M}_{\mathrm{s}\Sigma}. \tag{11.2c}$$

Here, $\boldsymbol{a} = \mathrm{D}\boldsymbol{u}/\mathrm{D}t$ is the fluid acceleration and we have used the triple decomposition of the stress $\boldsymbol{t} = -p\boldsymbol{n} + \boldsymbol{\tau} + \boldsymbol{t}_\mathrm{s}$, with $\boldsymbol{\tau} = \mu\boldsymbol{\omega} \times \boldsymbol{n}$ and $\boldsymbol{t}_\mathrm{s}$ being the shear stress and the stress due to surface deformation, respectively, see (2.149) and (2.150). We have bypassed the need for calculating the local $\boldsymbol{t}_\mathrm{s}$ (which may

be complicated on a deformable surface) as much as possible. The effect of $\boldsymbol{t}_\mathrm{s}$ vanishes in (11.1), while that of $\boldsymbol{x} \times \boldsymbol{t}_\mathrm{s}$ in (11.2) has been integrated out, see (2.153):

$$\boldsymbol{M}_{\mathrm{s}B} = -2\mu \int_{\partial B} \widehat{\boldsymbol{n}} \times \boldsymbol{b} \, \mathrm{d}S = -2\mu \int_B \boldsymbol{\omega}_B \, \mathrm{d}V, \tag{11.3a}$$

$$\boldsymbol{M}_{\mathrm{s}\Sigma} = -2\mu \int_\Sigma \boldsymbol{n} \times \boldsymbol{u} \, \mathrm{d}S = -2\mu \int_V \boldsymbol{\omega} \, \mathrm{d}V, \tag{11.3b}$$

where $\widehat{\boldsymbol{n}} = -\boldsymbol{n}$ is the outward normal of $\partial B$ and $V = V_\mathrm{f} + B$. The total vorticity in $B$ or $V$ can evidently be expressed by the total circulation in two dimensions and by (3.14) in three dimensions. Of these alternative formulas, forms (b) and (c) will be identical if $V_\mathrm{f}$ is a material fluid volume. Form (a) is most primary but may also be viewed as the special case of (b) or (c): If $\Sigma$ shrinks to the body surface $\partial B$ so that $V_\mathrm{f} = 0$, then since the direction of $\boldsymbol{n}$ on $\Sigma$ is opposite to that on $\partial B$, (b) or (c) is reduced to (a).

These formulas, however, are not physically most revealing. What appear in their integrand are variables like velocity, pressure, and density themselves, but the mechanisms leading to their specific distribution in a flow field and at the body surface are hidden. These mechanisms come from *local dynamics* governed by

$$\rho \boldsymbol{a} = -\nabla p + \mu \nabla^2 \boldsymbol{u} = -\nabla p - \mu \nabla \times \boldsymbol{\omega}, \tag{11.4}$$

$$\nabla \times \boldsymbol{a} = \frac{\partial \boldsymbol{\omega}}{\partial t} + \nabla \times (\boldsymbol{\omega} \times \boldsymbol{u}) = \nu \nabla^2 \boldsymbol{\omega}, \quad \nu = \mu/\rho, \tag{11.5}$$

where one sees the *spatial and temporal derivatives* of the relevant variables. It is the interactions of these derivatives that form various flow structures which at large Reynolds numbers are highly localized but may dominate the integrated performance. Thus, there is a theoretical gap between standard formulas and local dynamics. This gap cannot be eliminated by simply substituting (11.4) into (11.1b) and (11.2b), because the pressure $p$ is a global effect of all interactions; it is actually the quantity that one wishes most to remove or replace by other local dynamic processes.

For example, at large Reynolds numbers, by (11.1a) we know that the lift on an airfoil is dominated by the pressure difference on its both surfaces, which is in turn explainable by the Bernoulli equation due to a larger fluid speed on the upper surface. But a deeper physical question is: Why the fluid runs faster on the upper surface?

A popular heuristic answer to this question is: The fluid particles that separate at the front stagnation point have to meet again at the trailing edge. This story is, however, wrong. The timelines (Sect. 2.1) in Fig. 11.2 indicate that the fluid on the upper surface runs even faster than needed for meeting the fluid from the lower surface at the trailing edge. No explanation can be directly found from (11.1).

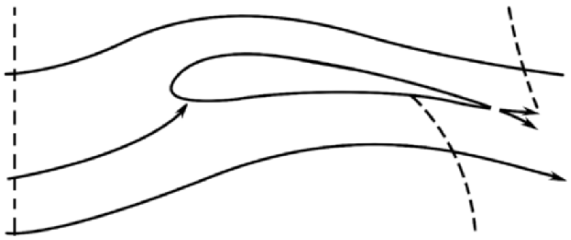

**Fig. 11.2.** Potential flow over a Joukowski airfoil. *Dashed lines* are time lines. Reproduced from Panton (1984)

More generally, the above theoretical gap exists between any integrated performances and their key local contributors. It makes the physical understanding, flow diagnosis, and configuration design lose the most valuable guidance. The awareness of this gap is becoming clearer as one's strong pursuit of carefully and optimally designed high-performance configurations. Suppose one is given a set of finite-domain data for a viscous flow over a body. One can then calculate the stress on the wall and apply (11.1a) to get the force. Then one may look at various fields in the domain: streamlines, velocity vectors, the contours of pressure and vorticity, etc. These together form a quite complete physical picture of the flow. However, if one wishes to identify the physical mechanisms that result in that force status, only some qualitative assessments can be drawn from these plots. They are still insufficient to pinpoint what flow structures have net contribution to the force, in what way, how, and why.

### 11.1.2 The Legacy of Pioneering Aerodynamicist

In fact, filling the aforementioned gap has been a long-term effort in the development of aerodynamics, where the "standard" formulas are only a starting point rather than the final form of the theory. Instead, a great milestone in the development of classic aerodynamics is the well-known *circulation theory*, where the aerodynamic force is expressed by elegant "*nonstandard*" formulas in terms of the circulation $\Gamma$ of a wing section. The historical significance of the circulation theory has been well described by Wu (2005):

*"The task of finding theoretical solutions to practical aerodynamic flow problems was (and still is) formidably difficult. Bypassing flow details as much as possible was indeed the only strategy open to the pioneering aerodynamicist. Together with simplifications of the inviscid-fluid assumption, this strategy served as the springboard for the dazzling developments of aerodynamics a century ago by leading scholars in Europe: Kutta, Joukouski, Lanchester, Prandtl, among others."*

To see how this strategy worked so successfully, let us briefly recall the circulation theory for steady flow. This includes the Kutta–Joukowski formula (see Joukowski 1931)

$$L = -\rho U \Gamma \tag{11.6}$$

for the lift of a two-dimensional airfoil, and Prandtl's *lifting-line theory* for the lift and *induced drag* of a three-dimensional wing (e.g., Prandtl and Tietjens 1934; Glauert 1947)[2]:

$$L \simeq \rho U \int_{-s}^{s} \Gamma(y)\,\mathrm{d}y, \tag{11.7a}$$

$$D_{\mathrm{in}} \simeq -\rho \int_{-s}^{s} w(y)\Gamma(y)\,\mathrm{d}y, \tag{11.7b}$$

where $s$ is the semi-span and

$$w(y) = -\frac{1}{4\pi}\int_{-s}^{s} \frac{\mathrm{d}\Gamma(y')}{\mathrm{d}y'}\frac{\mathrm{d}y'}{y-y'} < 0 \tag{11.8}$$

is the *downwash velocity* (usually estimated at the 1/4-chord point, i.e., the aerodynamic center). Both theories are valid for streamlined wings in the limit of $Re \to \infty$. Note that $\Gamma$ does not appear in (11.1) at all; but it is this quantity that immediately reveals that the physical root of the force and moment is the vorticity in wing boundary layers and vortical wake formed thereby. In particular, the key to arriving at (11.7) was the ingenious insight of Prandtl and Lanchester that, owing to Helmholtz's vorticity theorems and in linearized approximation, a finite-span wing produces a *horseshoe vortex system* consisting of a bound line vortex (the *lifting line*) along the 1/4-chord line of the wing and a flat wake vortex sheet with variable strength[3]

$$\boldsymbol{\gamma}(y) = \boldsymbol{e}_x \gamma(y) = -\boldsymbol{e}_x \frac{\mathrm{d}\Gamma}{\mathrm{d}y}, \tag{11.9}$$

Fig. 11.3.[4] Then, (11.8) is merely a simple application of the Biot–Savart formula (3.31) to the horseshoe vortex system.

Evidently, the circulation theory has indeed bypassed the flow details as much as possible, narrowing the unknowns down to a single circulation $\Gamma$ to be solved for calculating the forces. In two dimensions, it is obtainable by using complex variable and conformal mapping (e.g., Lighthill 1986b). On the flow plane $z = x + \mathrm{i}y = r\mathrm{e}^{\mathrm{i}\varphi}$ there exists analytical complex velocity potential $w(z) = \phi + \mathrm{i}\psi$, and one maps the airfoil onto $a$ unit circle $\zeta = \mathrm{e}^{\mathrm{i}\theta}$ on the

[2] For two-dimensional flows we work on the $(x, y)$-plane, so that a clockwise circulation is negative as in the case around an airfoil with positive lift. But for three-dimensional flows we follow the convention that, in a *wind-axis system*, $(x, y, z)$ are along the oncoming flow, wing-span, and vertical up directions, respectively, see Fig. 7.18. Thus on an $(x, z)$-plane a clockwise circulation is positive.

[3] In linear approximation the rolling-up of vortex sheet due to self-induction, see Sects. 4.4.4 and 7.3, is entirely ignored.

[4] Ideally, the horseshoe vortex system becomes closed loop by the starting vortex at downstream infinity that retreats continuously with velocity $U$.

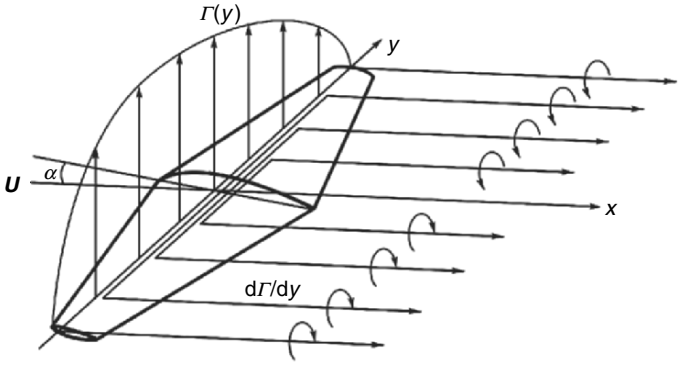


**Fig. 11.3.** The steady horseshoe vortex system of a thin wing

$\zeta$ plane. In that plane one considers the flow $U\mathrm{e}^{\mathrm{i}\alpha}$ over the circle at incidence $\alpha$ with *arbitrary* circulation $\Gamma$:

$$\frac{\mathrm{d}w}{\mathrm{d}\zeta} = u - \mathrm{i}v = U\left(\mathrm{e}^{-\mathrm{i}\alpha} - \frac{\mathrm{e}^{\mathrm{i}\alpha}}{\zeta^2}\right) + \frac{\Gamma}{2\pi\mathrm{i}\zeta},$$

which yields

$$\frac{\mathrm{d}w}{\mathrm{d}\zeta} = -\mathrm{i}\mathrm{e}^{-\mathrm{i}\theta}\left[2U\sin(\alpha-\theta) + \frac{\Gamma}{2\pi}\right] \quad \text{at} \quad \zeta = \mathrm{e}^{\mathrm{i}\theta}.$$

The trailing edge of the airfoil can always be managed to map to $\zeta = 1$, thus the Kutta condition (Sect. 4.4.2) requires $\mathrm{d}w/\mathrm{d}\zeta = 0$ at $\theta = 0$. This gives $\Gamma = -4\pi U \sin\alpha$, so by (11.6) the lift coefficient is

$$C_l = \frac{L}{\frac{1}{2}\rho U^2 c} = \frac{8\pi}{c}\sin\alpha, \tag{11.10}$$

where the chord length $c$ of the airfoil depends on the specific mapping function and equals 4 for a flat plate, which is almost true for any thin airfoil as well. This leads to the well-known simple formula

$$C_l = 2\pi\sin\alpha \simeq 2\pi\alpha \quad \text{for} \quad \alpha \ll 1. \tag{11.11}$$

Then, for a large-span wing, (11.6) holds approximately at every wing section, so $\Gamma(y)$ in (11.7) is known. However, the relative downwash $w/U$ implies a reduction of the effective angle of attack that reduces the circulation and causes the induced drag (11.7b). This observation leads to an integral equation

$$\Gamma(y) = \pi U c(y)\left[\alpha(y) - \frac{1}{4\pi U}\int_{-s}^{s}\frac{\mathrm{d}\Gamma(y')}{\mathrm{d}y'}\frac{\mathrm{d}y'}{y-y'}\right], \quad \alpha \ll 1, \tag{11.12}$$

of which the solution can be obtained analytically (e.g., Glauert 1947; Anderson 1991), with the famous conclusion that *a wing with elliptical load distri-*

*bution has minimum induced-drag.* Note that, remarkably, in the above entire two- and three-dimensional circulation theory one only needs to find the mapping function $\zeta = f(z)$; no flow field needs to be solved at all.

Now, modern aerodynamics is facing many new challenging problems, in which the flow complexity is far beyond the reach of any analytical solutions. Meanwhile, advanced experimental and numerical techniques have made it possible, at least in principle, to obtain detailed and complete data bases for such complex flows. Thus, the force $\boldsymbol{F}$ and moment $\boldsymbol{M}$ may follow at once by substituting the data into (11.1) and (11.2) or their compressible version. This being the case, then, is there still any need for "nonstandard" formulas as those pioneers did to explicitly reveal the key physical mechanisms responsible $\boldsymbol{F}$ and $\boldsymbol{M}$?

The answer is positive. Modern aerodynamics is not merely a simple combination of the flow data and standard formulas like (11.1) and (11.2). The more complicated the flow is, the more important role will the key physical factors play. "Bypassing flow details as much as possible" so as to reveal the key physical factors to $\boldsymbol{F}$ and $\boldsymbol{M}$ is actually the most valuable legacy of the pioneering aerodynamicists, which should be continued and further enriched. Modern versions of the "nonstandard" formulas are still highly desired, but their integrand can now be obtained experimentally or numerically rather than necessarily by approximate theories. Namely, the formulas should be exact and general. They can serve not only as a basis for deducing various approximate theories (including the circulation theory) but also as a powerful tool in flow analysis, diagnosis, and optimal configuration design.

### 11.1.3 Exact Integral Theories with Local Dynamics

In order to bridge the theoretical gap between integral performance and local dynamics, we need systematic approaches able to transform standard integral formulas to nonstandard forms, so that the local dynamic processes that have crucial *net* contribution to the force and moment can stand out explicitly. Currently, there are two types of theories that fit this need, to which this entire chapter is devoted.

One type is the *projection theory* to be presented in Sect. 11.2, which projects each term of the Navier–Stoke equation onto a vector space spanned by properly chosen harmonic vectors. The force and moment due to nonlocal pressure effect is replaced by other quantities describing local shearing and compressing processes. The theory has been formulated for externally unbounded flow problems.

Another type of theories with wider versatility is based on various *derivative moment transformations* (DMT for short), which execute multidimensional integration by parts to cast the original integrand to a moment of its derivatives (see Appendix A.2), and of which we have seen a few kinematic examples in Chap. 3. Of this type of DMT-based force and moment theories, there first appeared the *vorticity moment theory*, which expresses the

total force and moment by the rate of change of vortical impulse and angular impulse (the first- and second-order vorticity moments, respectively) introduced in Sect. 3.4.1. The theory is valid for incompressible flow and contains classic results like (11.6) and (11.7) as its direct corollaries. Then, after this theory there appeared the *boundary vorticity-flux theory*, which expresses the total force and moment in terms of the first and second moments of the stress-related boundary vorticity fluxes introduced in Sect. 4.1.3. The theory may cover viscous compressible flow over any deformable closed or open solid surface or fluid interface, and has been applied to innovative aerodynamic diagnosis and configuration design in both external and internal flow problems. Actually, the boundary vorticity-flux theory is a special case of a more general DMT-based theory for an arbitrary domain, whose consistency with the vorticity moment theory can also be easily verified.

DMT-based theories will be presented in Sects. 11.3–11.5. Typical applications of the projection theory and DMT-based theories in theoretical development and flow diagnosis will be exemplified, and their linkage to classic aerodynamics will be addressed. Whenever possible, we shall also point out how to extend the theory to compressible flow with constant or variable $\mu$ governed by (2.134) or (2.160), respectively. Here we just mention that the vortical form of (2.134) is[5]

$$\rho \boldsymbol{u}_{,t} + \rho \boldsymbol{\omega} \times \boldsymbol{u} - \frac{1}{2} q^2 \nabla \rho = -\nabla \Pi_0 - \nabla \times (\mu \boldsymbol{\omega}), \quad \Pi_0 = \Pi + \frac{1}{2} \rho q^2. \quad (11.13)$$

## 11.2 Projection Theory

Consider a set of basis vectors $\nabla \psi_i$ satisfying $\nabla^2 \psi_i = 0$, $i = 1, ..., n$, $n = 2, 3$. Take the inner product of (11.13) and $\nabla \psi_i$, and integrate the result over $V_\mathrm{f}$. By using identities

$$\nabla \psi_i \cdot \nabla \beta = \nabla \cdot (\beta \nabla \psi_i), \quad \nabla \psi_i \cdot (\nabla \times \boldsymbol{A}) = \nabla \cdot (\boldsymbol{A} \times \nabla \psi_i)$$

for any scalars $\beta$ and vector $\boldsymbol{A}$, we obtain $n$ scalar equations

$$\int_{V_\mathrm{f}} \left( \rho \frac{\partial \boldsymbol{u}}{\partial t} + \rho \boldsymbol{l} - \frac{1}{2} q^2 \nabla \rho \right) \cdot \nabla \psi_i \, \mathrm{d}V = \int_{\partial B} (-\Pi_0 \boldsymbol{n} + \boldsymbol{\tau}) \cdot \nabla \psi_i \, \mathrm{d}S - \int_{\Sigma} \Pi_0 \boldsymbol{n} \cdot \nabla \psi_i \, \mathrm{d}S, \quad (11.14)$$

where $\boldsymbol{l} \equiv \boldsymbol{\omega} \times \boldsymbol{u}$ is the Lamb vector. The control surface $\Sigma$ is assumed fixed and sufficiently large with $\boldsymbol{\omega} = \boldsymbol{0}$ thereon. In (11.14) each term is a weighted integral of a constituent of inertial or surface force. Depending on the specific choice of $\psi_i$, two versions of the theory have been developed. We focus on the total force; the total moment can be similarly treated by a different set of basis vectors as will be briefly mentioned.

[5] Unlike the analysis of vorticity evolution and interaction, in considering the force and moment the equations for momentum and angular momentum have to be expressed in terms of per unit volume.

### 11.2.1 General Formulation

The primary goal of the projection theory is to re-express the integrated pressure force over $\partial B$ by the integrations of vorticity and density gradient. The approach was first introduced by Quartapelle and Napolitano (1983) for viscous incompressible flow. For compressible flow considered by Chang and Lei (1996a), we replace the total pressure force by that due to normal stress $\varPi$, denoted by $\boldsymbol{F}_{\varPi}$. Its difference from $\boldsymbol{F}_{\mathrm{p}}$ is small at large Reynolds numbers.

An inspection of (11.14) indicates that to construct the $i$th component of $\boldsymbol{F}_{\varPi}$ we simply need $\boldsymbol{n}\cdot\nabla\psi_i = \boldsymbol{n}\cdot\boldsymbol{e}_i$ on $\partial B$, where $\boldsymbol{e}_i$ is the unit vector along the $i$th Cartesian coordinate, since then $-\varPi_0\boldsymbol{n}\cdot\nabla\psi_i = -\varPi_0 n_i$. To remove the integral over $\varSigma$ or make it able to be explicitly estimated, we need $\boldsymbol{n}\cdot\nabla\psi_i$ to vanish at infinity. This pair of boundary conditions for $\psi_i$ is nothing but (2.185) for the potential $\widehat{\phi}_i$ caused by the body motion with unit velocity $\boldsymbol{U} = -\boldsymbol{e}_i$. By (2.174), $\nabla\widehat{\phi}_i$ decays as $O(|\boldsymbol{x}|^{-n})$ as $|\boldsymbol{x}|\to\infty$. More precisely, when the body moves with constant velocity, let $\varSigma$ be a big sphere of radius $|\boldsymbol{x}| = x = R$, then the boundary integral is negligible if (Chang and Lei 1996a)

$$\frac{1}{R}\max_{x=R}(|\varPi|, \rho q^2, |\boldsymbol{t}_{\mathrm{vis}}|)\to 0 \quad \text{uniformly as} \quad R\to\infty. \tag{11.15}$$

Chang et al. (1998) demonstrate that this condition imposes no strict limitation to flows of practical interest. When the body has acceleration, somecontribution from $\varSigma$ will appear due to compressibility(Chang and Lei 1996a). Thus, for a nonaccelerating body, from (11.14) and (2.185) it follows that

$$F_{\varPi i} = -\int_{V_{\mathrm{f}}}\left(\rho\frac{\partial\boldsymbol{u}}{\partial t} + \rho\boldsymbol{l} - \frac{1}{2}q^2\nabla\rho\right)\cdot\nabla\widehat{\phi}_i\,\mathrm{d}V + \int_{\partial B}\boldsymbol{\tau}\cdot\nabla\widehat{\phi}_i\,\mathrm{d}S. \tag{11.16}$$

Now the integral of $\boldsymbol{u}_{,t}$ is well convergent. This effect can be further localized in incompressible flow (Howe 1995). For example, for a linearly accelerating body with velocity $\boldsymbol{U}(t)$, since

$$\int_{V_{\mathrm{f}}}\boldsymbol{u}_{,t}\cdot\nabla\widehat{\phi}_i\,\mathrm{d}V = \int_{\partial B}\boldsymbol{u}_{,t}\cdot\boldsymbol{n}\widehat{\phi}_i\,\mathrm{d}S = \dot{U}_j\int_{\partial B}n_j\widehat{\phi}_i\,\mathrm{d}S,$$

the first term of (11.16) can be written in terms of the *virtual mass tensor* defined by (2.186). Thus the total force due to pressure reads

$$F_{\mathrm{p}i} = -M_{ij}\dot{U}_j - \rho\int_{V_{\mathrm{f}}}(\boldsymbol{\omega}\times\boldsymbol{u})\cdot\nabla\widehat{\phi}_i\,\mathrm{d}V + \int_{\partial B}(\mu\boldsymbol{\omega}\times\boldsymbol{n})\cdot\nabla\widehat{\phi}_i\,\mathrm{d}S.$$

Moreover, set $\boldsymbol{u} = \boldsymbol{U} + \boldsymbol{v}$ such that $\boldsymbol{v}$ is the relative velocity (the velocity viewed in the frame fixed to the body), since

$$\begin{aligned}(\boldsymbol{\omega}\times\boldsymbol{U})\cdot\nabla\widehat{\phi}_i &= \widehat{\phi}_{i,k}(U_j u_{k,j} - u_{j,k}U_j) = u_{k,j}(U_j\widehat{\phi}_{i,k} - U_k\widehat{\phi}_{i,j})\\ &= [U_j u_k\widehat{\phi}_{i,k} - U_k u_j\widehat{\phi}_{i,k} - U_k u_k\widehat{\phi}_{i,j}]_{,j},\end{aligned}$$

the volume integral of $(\boldsymbol{\omega}\times\boldsymbol{U})\cdot\nabla\widehat{\phi}_i$ can be cast to surface integral over $\partial B$ with $\boldsymbol{u}=\boldsymbol{U}$ thereon. Thus, what left is an integral of $\boldsymbol{n}\cdot\nabla\widehat{\phi}_i\,\mathrm{d}S=n_i\,\mathrm{d}S$ by (2.185a), which, however, vanishes on closed surface. Therefore, we have

$$F_{\mathrm{p}i}=-M_{ij}\dot{U}_j-\rho\int_{V_{\mathrm{f}}}(\boldsymbol{\omega}\times\boldsymbol{v})\cdot\nabla\widehat{\phi}_i\,\mathrm{d}V+\int_{\partial B}(\mu\boldsymbol{\omega}\times\boldsymbol{n})\cdot\nabla\widehat{\phi}_i\,\mathrm{d}S, \quad (11.17)$$

indicating that the contribution from the Lamb vector comes from the flow region away from $\partial B$. Equation (11.17) decomposes $\boldsymbol{F}_{\mathrm{p}}$ into a virtual mass effect, an inviscid Lamb-vector integral, and a viscous surface-vorticity integral. Note that, however, in real viscous fluid the acyclic potential flow and its associated virtual-mass effect must cause a vortex sheet $\boldsymbol{\gamma}_{\mathrm{ac}}$, which holds exactly in the asymptotic limit of $\nu\to 0$ but is only an approximation at finite Reynolds numbers (for further discussion see Sect. 11.3.3).

The total moment due to the normal stress can be similarly expressed, of which the details is omitted here. We just observe that since the $i$-component of $\boldsymbol{M}_{\Pi}$ is

$$M_{\Pi i}=\int_{\partial B}\boldsymbol{e}_i\cdot(\boldsymbol{x}\times\boldsymbol{n})\Pi\,\mathrm{d}S,$$

one simply needs to replace the harmonic function $\widehat{\phi}_i$ by a potential $\widehat{\chi}_i$ that would be induced in an inviscid fluid by rotation of $\partial B$ at unit angular velocity about an axis through the origin in the $i$-direction. Namely, $\widehat{\chi}_i$ satisfies the boundary condition (Quartapelle and Napolitano 1983)

$$\boldsymbol{n}\cdot\nabla\widehat{\chi}_i=(\boldsymbol{x}\times\boldsymbol{n})\cdot\boldsymbol{e}_i=\boldsymbol{n}\cdot(\boldsymbol{e}_i\times\boldsymbol{x})\quad\text{at}\quad\partial B. \quad (11.18)$$

Note that for rotating and/or deforming body $\boldsymbol{M}$ contains an extra term $\boldsymbol{M}_{\mathrm{s}}$ due to the surface-deformation stress.

Alternative to the choice $\psi_i=\widehat{\phi}_i$, it is natural to consider taking $\psi_i$ in (11.14) as the acyclic potential for the idealized irrotational flow over a body with unit velocity $\boldsymbol{e}_i=\nabla x_i$ at infinity, viewed in a frame of reference fixed to the center of $B$ which has no angular momentum. The body surface $\partial B$ may have arbitrary velocity $\boldsymbol{b}(\boldsymbol{x},t)$. Denote the harmonic basis vectors so constructed by $X_i$ (not the Lagrangian coordinates in early chapters), then instead of (2.185) we now have

$$\boldsymbol{n}\cdot\nabla X_i=0\quad\text{at}\quad\partial B, \quad (11.19a)$$

$$\boldsymbol{n}\cdot\nabla X_i=n_i\quad\text{at infinity}. \quad (11.19b)$$

Evidently $X_i$ and $\widehat{\phi}_i$ are related by

$$X_i=x_i-\widehat{\phi}_i. \quad (11.20)$$

This set of basis vectors has been used by Howe (1989, 1991, 1995), who developed a projection theory for the *total force* $\boldsymbol{F}$ exerted to rigid body by incompressible flow with uniform density.

Set $\psi_i = X_i$, the incompressible version of (11.14) reads

$$\rho \int_{V_\mathrm{f}} \frac{\partial \boldsymbol{u}}{\partial t} \cdot \nabla X_i \,\mathrm{d}V + \int_\Sigma p n_i \,\mathrm{d}S = -\rho \int_{V_\mathrm{f}} \boldsymbol{l} \cdot \nabla X_i \,\mathrm{d}V + \int_{\partial B} \boldsymbol{\tau} \cdot \nabla X_i \,\mathrm{d}S. \quad (11.21)$$

While (11.16) directly follows from the integral of normal stress over the body surface, we now use (11.1c) instead, assuming that $\Sigma$ is large enough to enclose all vorticity with negligible $|\boldsymbol{u}|^2$:

$$F_i = -\rho \frac{\mathrm{d}}{\mathrm{d}t} \int_{V_\mathrm{f}} u_i \,\mathrm{d}V - \int_\Sigma p n_i \,\mathrm{d}S. \quad (11.22)$$

A combination of (11.21) and (11.22) eliminates the pressure integral and introduces $F_i$. To simplify the result, we transform the unsteady term in (11.21). After dropping all surface integrals over $\Sigma$, we find

$$\int_{V_\mathrm{f}} X_{i,j} u_{j,t} \,\mathrm{d}V = \frac{\mathrm{d}}{\mathrm{d}t} \int_{V_\mathrm{f}} u_i \,\mathrm{d}V - \frac{\mathrm{d}}{\mathrm{d}t} \int_{\partial B} \widehat{\phi}_i u_n \,\mathrm{d}S - \int_{\partial B} u_n \frac{\mathrm{D}X_i}{\mathrm{D}t} \mathrm{d}S,$$

where $\widehat{\phi}_i$ is the potential used before. Thus, we arrive at a general force formula found by Howe (1995):

$$F_i = -\rho \frac{\mathrm{d}}{\mathrm{d}t} \int_{\partial B} \widehat{\phi}_i u_n \,\mathrm{d}S - \rho \int_{\partial B} \frac{\mathrm{D}X_i}{\mathrm{D}t} u_n \,\mathrm{d}S + \rho \int_{V_\mathrm{f}} \boldsymbol{l} \cdot \nabla X_i \,\mathrm{d}V - \int_{\partial B} \boldsymbol{\tau} \cdot \nabla X_i \,\mathrm{d}S. \quad (11.23)$$

In particular, for a rigid body moving with uniform velocity $\boldsymbol{b} = \boldsymbol{U}(t)$ the second integral in (11.23) vanishes; thus we obtain a decomposition very similar to (11.17) but now for the entire total force:

$$F_i = -M_{ij} \dot{U}_j + \rho \int_{V_\mathrm{f}} (\boldsymbol{\omega} \times \boldsymbol{v}) \cdot \nabla X_i \,\mathrm{d}V - \int_{\partial B} (\mu \boldsymbol{\omega} \times \boldsymbol{n}) \cdot \nabla X_i \,\mathrm{d}S. \quad (11.24)$$

Subtracting (11.17) from (11.24) should give the force due to skin friction, i.e., the integral of $\boldsymbol{\tau}$ over $\partial B$. This can indeed be verified.

For the total moment, similar to (11.18) but corresponding to $X_i$, the basis vectors for projection is taken as (Howe 1995)

$$\nabla Y_i \equiv \boldsymbol{e}_i \times \boldsymbol{x} - \nabla \widehat{\chi}_i. \quad (11.25)$$

Howe (1995) has applied (11.23) to re-derive several classic results at high and low Reynolds numbers. These include airfoil lift, induced drag, rolling and yawing moment (within the lifting-line theory), drag due to Kármán vortex street and on small sphere and bubble.

### 11.2.2 Diagnosis of Pressure Force Constituents

Owing to the fast decay of $\nabla \widehat{\phi}_i$, the projection theory for externally unbounded flow can be used to practically diagnose flow data obtained in a

*finite but sufficiently large* domain. In addition to the replacement of pressure force by local dynamic processes, this is another advantage of the projection theory. Equation (11.16) has been applied by Chang et al. (1998) to analyze the numerical results of several typical separated flows in transonic–supersonic regime. In the frame fixed to the body moving with $\boldsymbol{U} = -U\boldsymbol{e}_x$, they found that the dominant source elements of $\boldsymbol{F}_{\Pi}$ are

$$R(\boldsymbol{x}) = -\frac{1}{2}q^2\nabla\rho\cdot\nabla\phi, \tag{11.26a}$$

$$V(\boldsymbol{x}) = \rho(\boldsymbol{\omega}\times\boldsymbol{u})\cdot\nabla\phi \tag{11.26b}$$

with $\phi = U_i\widehat{\phi}_i$, which contribute to 95% or more of the total drag and lift. The positive or negative contributions to the lift and drag of major flow structures (shear layers, vortices, and shock waves) via $V(\boldsymbol{x})$ and $R(\boldsymbol{x})$ can be clearly identified. We cite two examples here. The first is a steady supersonic turbulent flow over a sphere, computed by Reynolds-average Navier–Stokes equations. The key structures are shown in Fig. 11.4.

It was found that the computational domain needs a radius of 17–22 diameters of the sphere to make the contribution to $\boldsymbol{F}_{\Pi}$ of the flow outside the domain negligible. Denote the drag coefficients due to $R(\boldsymbol{x})$ and $V(\boldsymbol{x})$ by $C_{\mathrm{DR}}$ and $C_{\mathrm{DV}}$, respectively. Their variation as free-stream Mach number $M_\infty$ is shown in Fig. 11.5. As $M_\infty$ increases, $R(\boldsymbol{x})$ due to density gradient

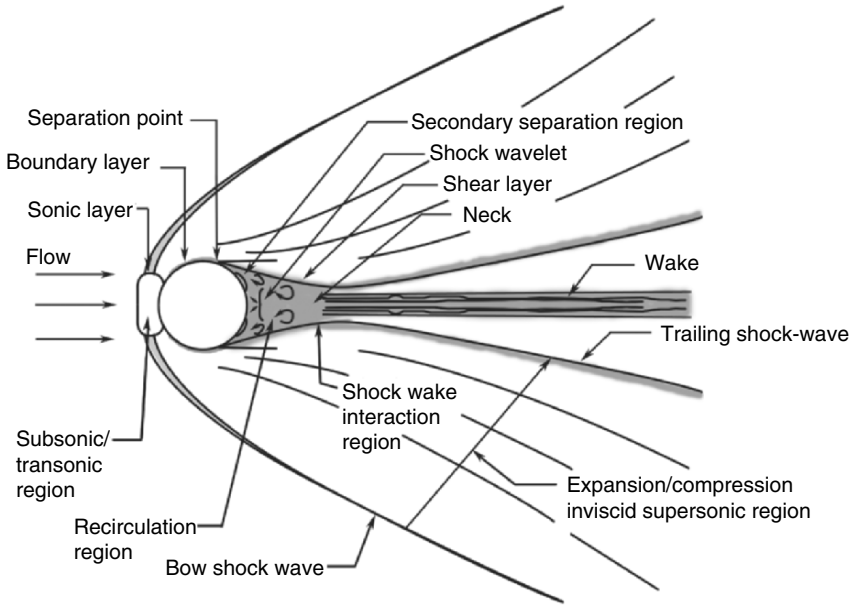


**Fig. 11.4.** Typical flow pattern of a supersonic flow around a sphere. Reproduced from Chang and Lei (1996a)

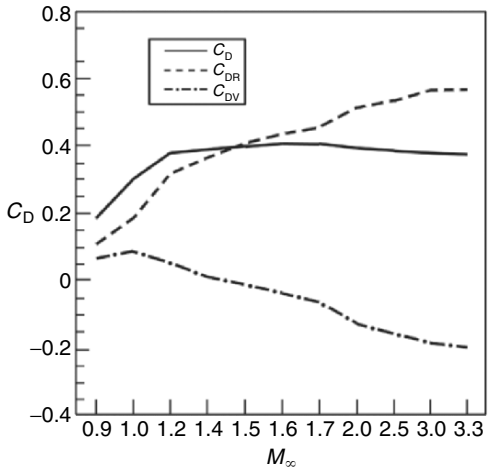


**Fig. 11.5.** Variation of $C_{\mathrm{D}}$, $C_{\mathrm{DR}}$ and $C_{\mathrm{DV}}$ with $M_\infty$ for supersonic flow over a sphere. Based on Chang and Lei (1996a)

is progressively important relative to $V(\boldsymbol{x})$ due to vorticity. It is well known that the drag reaches a maximum at a transonic Mach number; remarkably, Fig. 11.5 provides an interpretation of this phenomenon: the decrease of $C_{\mathrm{D}}$ as $M_\infty$ further increases is due to the fact that the contribution of the Lamb vector to the axial force changes from a drag to a thrust.

The second numerical example is steady flow over a slender delta wing with sweeping angle of 70° and an elliptic cross-section of the axis ratio 14:1. $M_\infty$ varies from 0.6 to 1.8, and the angle of attack $\alpha$ varies from 5° to 19°. The flow relative to the leading edge is still subsonic so in a transonic range vortices may still be the major source of lift and drag, see the sketch of Fig. 7.6. Figure 11.6 shows the situation by plotting the variation of $C_{\mathrm{LV}}$ and $C_{\mathrm{LR}}$ as $\alpha$ at two values of $M_\infty$. Also shown in the figure is the separate contribution to $C_{\mathrm{LV}}$ of the vorticity on windside ($C_{\mathrm{LV}(w)}$) and leeside ($C_{\mathrm{LV}(l)}$) of the wing surface, indicating that $V(\boldsymbol{x})$ on windside always contributes a negative vortical lift, which at a special Mach number $M_\infty = 1.2$ just cancels the positive contribution of $V(\boldsymbol{x})$ at wing side and leads to $C_{\mathrm{LV}} \simeq 0$. This behavior involves the relative orientation of $\boldsymbol{u}$, $\boldsymbol{\omega}$, and $\nabla\phi$ in different regions of the flow (for detailed analysis see Chang and Lei (1996b)).

## 11.3 Vorticity Moments and Classic Aerodynamics

The vorticity moment theory is the first version of the derivative-moment type of theories in aerodynamics, applied to a moving body $B$ in an incompressible fluid with uniform density. Assuming the external boundary $\Sigma$ retreats to

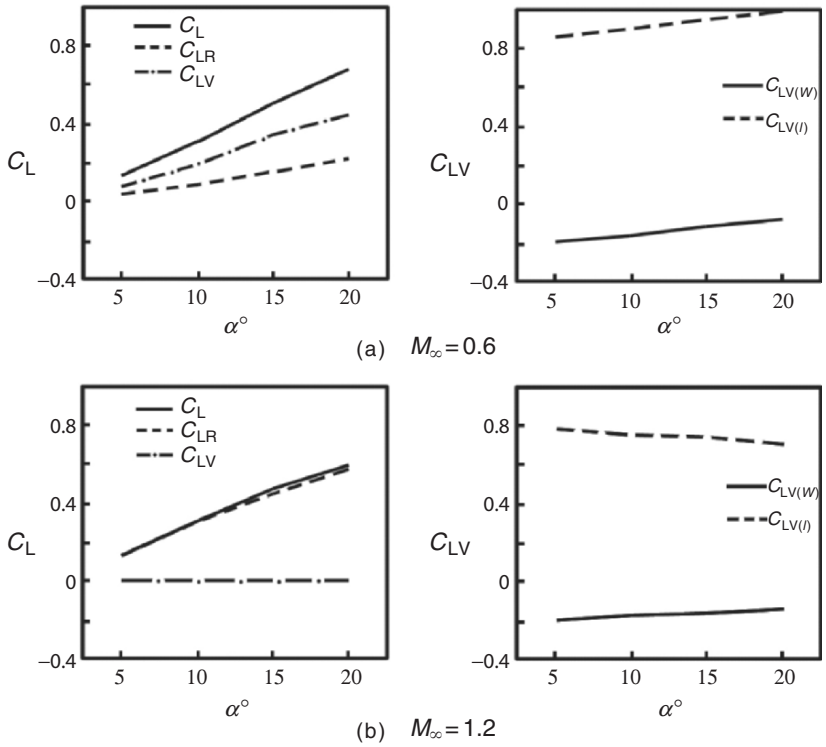


**Fig. 11.6.** Variation of $C_{\mathrm{L}}$, $C_{\mathrm{LV}}$, $C_{\mathrm{LR}}$, and $C_{\mathrm{LV}(w)}$ and $C_{\mathrm{LV}(l)}$ as $\alpha$ for transonic flow over a slender delta wing. (**a**) $M_\infty = 0.6$. (**b**) $M_\infty = 1.2$. Based on Figs. 8 and 11 of Chang and Lei (1996b)

infinity where the fluid is at rest, the theory casts $\boldsymbol{F}$ and $\boldsymbol{M}$ to the rate of change of the vortical impulse $\boldsymbol{I}$ and angular impulse $\boldsymbol{L}$ defined by (3.78) and (3.79), respectively. Thus, it represents a *global view*. Since $V_{\mathrm{f}}$ must include the starting vortex system (cf. Fig. 3.5c) and as the body keeps moving the wake region must grow, the flow in $V_{\mathrm{f}}$ is *inherently unsteady*. In this section we derive the theory, discuss its physical implication and exemplify its application, and then show how it reduces to the classic "inviscid" aerodynamics theory. Useful identities for derivative-moment transformation are listed in Sect. A.2.2.

### 11.3.1 General Formulation

For generality and better understanding, we first examine the force and moment under a weaker assumption than that stated above: The flow is irrotational at and near its external boundary $\Sigma$, so that $\boldsymbol{\omega}$, $\nabla \times \boldsymbol{\omega}$, and $\boldsymbol{l} = \boldsymbol{\omega} \times \boldsymbol{u}$ vanish on $\Sigma$. We then start from the standard force formula (11.1b), where the acceleration integral can be expressed by identity (3.117a) or (3.117b),

each representing a derivative-moment transformation. From both we have obtained the rate of change of the vortical impulse for any material volume $\mathcal{V}$ as given by (3.118). Now, set $\mathcal{D} = V_\mathrm{f}$ with $\partial V_\mathrm{f} = \partial B + \Sigma$ in (3.117b) and substitute the result into (11.1b). Since under the assumed condition on $\Sigma$ there is $\rho \boldsymbol{a} = -\nabla p$ there, by the derivative-moment transformation identity (A.25) the pressure term in (11.1b) is exactly canceled. Hence, it follows that

$$\boldsymbol{F} = -\frac{\rho}{k}\int_{V_\mathrm{f}} \boldsymbol{x} \times \boldsymbol{\omega}_{,t}\,\mathrm{d}V - \int_{V_\mathrm{f}} \boldsymbol{l}\,\mathrm{d}V + \frac{\rho}{k}\int_{\partial B} \boldsymbol{x} \times [\boldsymbol{n} \times (\boldsymbol{a}_B - \boldsymbol{l})]\,\mathrm{d}S, \quad (11.27)$$

where and below $k = n - 1$ and $n = 2, 3$ is the spatial dimensionality, $\boldsymbol{a}_B = \mathrm{D}\boldsymbol{b}/\mathrm{D}t$ is the acceleration of the body surface due to adherence, and

$$\boldsymbol{n} \times \boldsymbol{l} = \boldsymbol{\omega} u_n - \boldsymbol{u}\omega_n. \quad (11.28)$$

Thus, by the Reynolds transport theorem (2.35b), we obtain

$$\boldsymbol{F} = -\rho\frac{\mathrm{d}\boldsymbol{I}_f}{\mathrm{d}t} - \rho\int_{V_\mathrm{f}} \boldsymbol{l}\,\mathrm{d}V + \frac{\rho}{k}\int_{\partial B} \boldsymbol{x} \times (\boldsymbol{a}_B + \boldsymbol{b}\omega_n)\,\mathrm{d}S, \quad (11.29)$$

where $\boldsymbol{I}_\mathrm{f}$ is for volume $V_\mathrm{f}$. On the other hand, set $\mathcal{D} = B$ in (3.117b) and notice that the outward unit normal of $\partial B$ is $-\boldsymbol{n}$ (Fig. 11.1), since $B$ is a material body, by (2.35b) we have

$$\frac{\mathrm{d}}{\mathrm{d}t}\int_B \boldsymbol{b}\,\mathrm{d}V = \frac{\mathrm{d}\boldsymbol{I}_B}{\mathrm{d}t} + \frac{1}{k}\int_{\partial\mathcal{B}} \boldsymbol{x} \times (\boldsymbol{n} \times \boldsymbol{a}_B + \boldsymbol{b}\omega_n)\,\mathrm{d}S.$$

Comparing this with (11.29) yields

$$\boldsymbol{F} = -\rho\frac{\mathrm{d}\boldsymbol{I}_V}{\mathrm{d}t} - \rho\int_V \boldsymbol{l}\,\mathrm{d}V + \rho\frac{\mathrm{d}}{\mathrm{d}t}\int_B \boldsymbol{b}\,\mathrm{d}V, \quad (11.30)$$

where $V = V_\mathrm{f} + B$ has only an external boundary $\Sigma$. This "nonstandard" formula tells that if $\Sigma$ does not cut through any rotational-flow region then the total force has three sources: the rate of change of the impulse of domain $V_\mathrm{f} + B$, the *vortex force* given by the Lamb-vector integral (which has long been known; e.g., Saffman (1992)), and the inertial force of the virtual fluid displaced by the body.

We now shift $\Sigma$ to infinity so that $V = V_\infty$. In this case the vortex force vanishes due to the kinematic result (3.72).[6] Hence, (11.30) reduces to

$$\boldsymbol{F} = -\rho\frac{\mathrm{d}\boldsymbol{I}_\infty}{\mathrm{d}t} + \rho\frac{\mathrm{d}}{\mathrm{d}t}\int_B \boldsymbol{b}\,\mathrm{d}V. \quad (11.31)$$

[6] Recall that in deriving (3.72) and (3.73) use has been made of the asymptotic far-field behavior of the irrotational velocity.

A similar approach to the moment based on (11.2b), using derivative-moment transformation identities (A.24a) and (A.28a) as well as (3.73), yields

$$\boldsymbol{M} = -\rho \frac{\mathrm{d}\boldsymbol{L}_\infty}{\mathrm{d}t} + \rho \frac{\mathrm{d}}{\mathrm{d}t} \int_B \boldsymbol{x} \times \boldsymbol{b} \, \mathrm{d}V. \tag{11.32}$$

When $B$ is a flexible body, its interior velocity distribution may not be easily known. In that case, it is convenient to replace the body-volume integrals in (11.31) and (11.32) by the rate of change of identities (3.80) and (3.81a) applied to $B$. This yields

$$\boldsymbol{F} = -\rho \frac{\mathrm{d}\boldsymbol{I}_\mathrm{f}}{\mathrm{d}t} + \frac{\rho}{k} \frac{\mathrm{d}}{\mathrm{d}t} \int_{\partial B} \boldsymbol{x} \times (\boldsymbol{n} \times \boldsymbol{b}) \, \mathrm{d}S, \tag{11.33}$$

$$\boldsymbol{M} = \frac{\rho}{2} \frac{\mathrm{d}\boldsymbol{L}_\mathrm{f}}{\mathrm{d}t} - \frac{\rho}{2} \frac{\mathrm{d}}{\mathrm{d}t} \int_{\partial B} x^2 \boldsymbol{n} \times \boldsymbol{b} \, \mathrm{d}S, \tag{11.34}$$

where only the body-surface velocity needs to be known.

Equations (11.31–11.34) are the basic formulas of the vorticity-moment theory (Wu 1981, 2005). Recall that at the end of Sect. 3.5.2 we have shown that $\boldsymbol{I}_\infty$ and $\boldsymbol{L}_\infty$ of an unbounded fluid at rest at infinity is time invariant, even if the flow is not circulation-preserving. This invariance, however, was obtained under an implicit assumption that no vorticity-creation mechanism exists in $V_\infty$. Saffman (1992) has shown that a distributed nonconservative body force in $V_\infty$ will make $\boldsymbol{I}_\infty$ and $\boldsymbol{L}_\infty$ no longer time-invariant. Now, $V_\mathrm{f}$ is bounded internally by the solid body $B$, of which the motion and deformation is the only source of the vorticity in $V_\infty$; in this sense it has the same effect as a nonconservative body force. Then the variation of $\boldsymbol{I}_\infty$ and $\boldsymbol{L}_\infty$ caused by the body motion just implies a force and moment to $B$ as reaction. A clearer picture of this reaction to vorticity creation at body surface will be discussed in Sect. 11.4.

An interesting property of the vorticity moment theory is the *linear dependence* of $\boldsymbol{F}$ and $\boldsymbol{M}$ on $\boldsymbol{\omega}$ due to the disappearance of vortex force and moment. Hence, they can be equally applied to the total force and moment acting to a set of multiple moving bodies (Wu 1981), but not that on an individual body of the set. This property makes the theory very similar to the corresponding theory for potential flow, see (2.183) and (2.184), which by nature is always linear. The analogy between (11.31) and (2.183), and likewise for the moment, becomes perfect if $\boldsymbol{b}$ is constant so that in the former the integrals over $B$ are absent.

Except the unique property of linear dependence on vorticity, the vorticity moment theory exhibits some features common to all derivative-moment based theories. Firstly, owing to the integration by parts in derivative-moment transformation, the new integrands (in the present theory, the first and second moments of $\boldsymbol{\omega}$) do not represent the local density of momentum and angular

momentum. Rather, they are *net contributors* to $\boldsymbol{F}$ and $\boldsymbol{M}$. The entire potential flow, which occupies a much larger region in the space, is filtered out by the transformation and no longer needs to be one's concern (its effect on the vorticity advection, of course, is included implicitly).

Secondly, the new integrands have significant peak values only in considerably smaller local regions due to the exponential decay of vorticity at far field. This is a remarkable focusing, a property also shared by the projection theory.

Thirdly, since the derivative-moment transformation makes the new local integrands $\boldsymbol{x}$-dependent, if the same amount of vorticity, say, locates at larger $|\boldsymbol{x}|$, then its effect is amplified, and vice versa. This *amplification effect* by $\boldsymbol{x}$ further picks up fewer vortical structures that are crucial to $\boldsymbol{F}$ and $\boldsymbol{M}$.[7]

### 11.3.2 Force, Moment, and Vortex Loop Evolution

The core physics of vorticity moment theory and its special forms have been known to many researchers for long time (cf. Lighthill 1986a,b). Because under the assumed condition the total vorticity (total circulation if $n = 2$) is zero, the vorticity tubes created by the body motion and deformation must form closed loops (vortex couples for $n = 2$). Thus, if the circulation $\Gamma$ and motion of a vortex loop or couple are known, then so is their contribution to the force and moment. The problem is particularly simple in the Euler limit with $\mathrm{d}\Gamma/\mathrm{d}t = 0$.

von Kármán and Burgers (1935) have essentially used (11.31) to give a simple derivation of the Kutta–Joukwski formula (11.6). Consider the two-dimensional vortex couple introduced in Sect. 3.4.1, see (3.87) and Fig. 3.12. Let $\Gamma < 0$ be the circulation of the *bound vortex* of the airfoil in an oncoming flow $\boldsymbol{U} = U\boldsymbol{e}_x$, and assume the near-field flow is steady. As shown in Sect. 4.4.2, in this case no vortex wake sheds off. Thus, $-\Gamma > 0$ must be the circulation of the starting vortex alone, which retreats with speed $U$. The separation $r$ of the vortex couple then increases with the rate $\mathrm{d}r/\mathrm{d}t = U$, and hence (11.6) follows at once.

In three dimensions, as shown by (3.88), (3.89), and Fig. 3.13, the impulse and angular impulse caused by a thin vortex loop $C$ of circulation $\Gamma$ are precisely the vectorial area spanned by the loop and the moment of vectorial

[7] The origin of the position vector (which has been set zero here and below) can be arbitrarily chosen (a general proof is given in Sect. A.2.3). Hence whether a local vortical structure has favorable contribution to total force also depends on the subjective choice of the origin. But one can always make a convenient choice such that the flow diagnosis is most intuitive. See the footnote following (11.54a,b) below.

surface element, respectively. Hence a single evolving vortex loop will contribute a force and moment

$$\boldsymbol{F} = -\rho\Gamma\frac{\mathrm{d}}{\mathrm{d}t}\int_S \mathrm{d}\boldsymbol{S}, \tag{11.35}$$

$$\boldsymbol{M} = -\frac{2}{3}\rho\Gamma\frac{\mathrm{d}}{\mathrm{d}t}\int_S \boldsymbol{x}\times\mathrm{d}\boldsymbol{S}. \tag{11.36}$$

For a flow over a three-dimensional wing of span $b$ with constant velocity $\boldsymbol{U} = U\boldsymbol{e}_x$, a remote observer will see such a single vortex loop sketched in Fig. 3.5c. Then the rate of change of $\boldsymbol{S}$ equals $-bU\boldsymbol{e}_z$, solely due to the continuous generation of the vorticity from the body surface. Therefore, (11.35) gives

$$\boldsymbol{F} \simeq \rho\boldsymbol{U}\times\boldsymbol{\Gamma}b, \tag{11.37}$$

which is asymptotically accurate for a rectangular wing with constant chord $c$ and $b\to\infty$; each wing section of unit thickness will then have a lift given by (11.6).

Better than (11.37), we may replace the single pair of vorticity tubes with distance $b$ by distributed $\omega_x(y,z)$ in the wake vortices, which correspond to a bundle of vortex loops. This leads to

$$L \simeq \rho U\int_W y\omega_x\,\mathrm{d}S, \tag{11.38}$$

where $W$ is a $(y,z)$-plane cutting through the wake (cf. Fig. 11.20). Then, if $\omega_x$ is confined in a thin flat vortex sheet with strength $\gamma(y)$ as in the lifting-line theory (Fig. 11.3), by a one-dimensional derivative-moment transformation and (11.9) there is

$$y\gamma = \Gamma - \frac{\mathrm{d}(y\Gamma)}{\mathrm{d}y}.$$

Substituting this into (11.38) and noticing $\Gamma = 0$ at $y = \pm s$, we recover (11.7a) at once.

The multiple vortex-loop argument has been used by Wu et al. (2002) in analyzing various constituents of the force and moment on a helicopter rotor. An interesting application of (11.31) is given by Sun and Wu (2004) in a simulation of insect flight. Insects may fly at a Reynolds number as small as of 100, for which the lift predicted by classic steady wing theory is far lower than needed for supporting the insect weight. The crucial role of unsteady motion of lifting vortices was experimentally discovered only recently (e.g., Ellington et al. 1996). To further understand the physics, Sun and Wu conducted a Navier–Stokes computation of a thin wing which rotates azimuthally by 160° at constant angular velocity and angle of attack after an initial start, see Fig. 11.7. Numerical tests have confirmed that to a great extent this model can well mimic a down- or upstroke of the flapping motion of insect wings, yielding lift $L$ and drag $D$ in good agreement with experimental results.

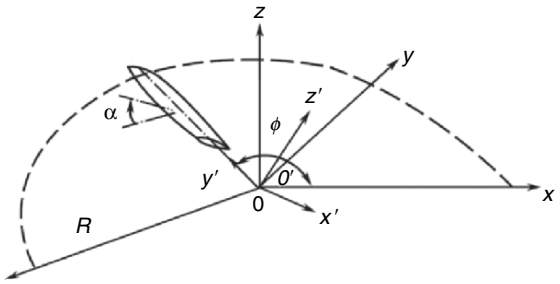


**Fig. 11.7.** Rotating wing; fixed $(x, y, z)$ frame and rotating $(x', y', z')$ frame. From Sun and Wu (2004)

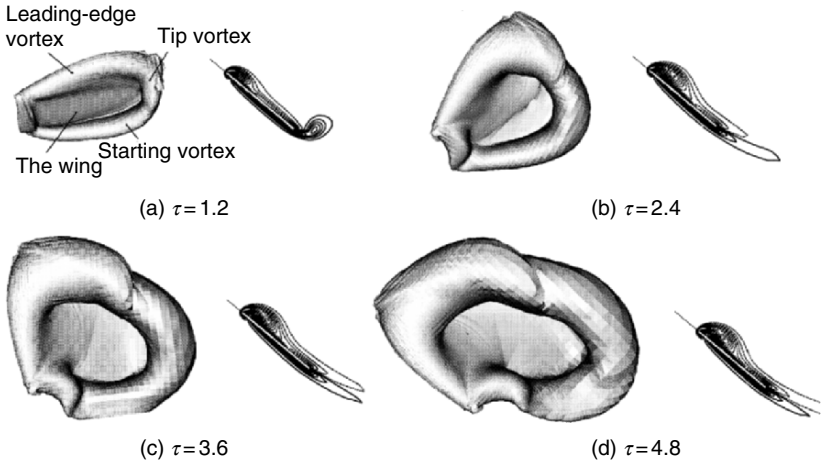


**Fig. 11.8.** Time evolution of isovorticity surface (*left*) around the wing and contours of $\omega_{y'}$ at wing section $0.6R$. From Sun and Wu (2004)

Sun and Wu (2004) found that $L$ and $D$ computed from (11.31) is in excellent agreement with that obtained by (11.1a). Figure 11.8 shows the isovorticity surface and the contours of $\omega_{y'}$ at wing section $0.6R$ ($R$ is the semi wingspan) and different dimensionless time $\tau$. A strong separated vortex *remains attached* to the leading edge in the whole period of a single stroke, which connects to a wingtip vortex, a wing root vortex, and a starting vortex to form a closed loop. As the wing rotates, the vector surface area spanned by the loop increases almost linearly and the loop is roughly on an inclined plane. Therefore, almost constant $L$ and $D$ are produced after start. The authors further found that the key mechanism for the leading-edge vortex to remain attached is a spanwise pressure gradient (at $Re = 800$ and 3,200), and its joint effect with centrifugal force (at $Re = 200$). Similar

to the leading-edge vortices on slender wing (Chap. 7), now these spanwise forces advect the vorticity in leading-edge vortex to the wingtip to avoid oversaturation and shedding.

### 11.3.3 Force and Moment on Unsteady Lifting Surface

Various classic external aerodynamic theories can be deduced from the vorticity moment theory in a unified manner at different approximation levels. This theoretical unification is a manifestation of the physical fact that all incompressible force and moment are from the same vortical root. We demonstrate this in the Euler limit.

The simplest situation is the force and moment due purely to body acceleration, for which (11.33) and (11.34) should reduce to (2.183) and (2.184) but with viscous interpretation. The body acceleration creates an unsteady boundary layer attached to $\partial B$ but inside $V_{\rm f}$, of which the effect is in $\boldsymbol{I}_{\rm f}$ and $\boldsymbol{L}_{\rm f}$. Namely, *an accelerating body must be dressed in an acyclic attached vortex layer*. Let $\widehat{\boldsymbol{n}} = -\boldsymbol{n}$ be the unit normal of $\partial B$ pointing into the fluid, in the Euler limit this layer becomes a vortex sheet of strength

$$\boldsymbol{\gamma}_{\rm ac} = \widehat{\boldsymbol{n}} \times [\![\boldsymbol{u}]\!] = \widehat{\boldsymbol{n}} \times (\nabla \phi_{\rm ac} - \boldsymbol{b}), \tag{11.39}$$

where suffix ac denotes acyclic and $\phi_{\rm ac}$ can be solved from (2.173) solely from the specified body-surface velocity $\boldsymbol{b}(\boldsymbol{x}, t)$. Then

$$\boldsymbol{I}_{\rm f} = \frac{1}{k} \int_{\partial B} \boldsymbol{x} \times \boldsymbol{\gamma}_{\rm ac} \, {\rm d}S = \frac{1}{k} \int_{\partial B} \boldsymbol{x} \times [\widehat{\boldsymbol{n}} \times (\nabla \phi_{\rm ac} - \boldsymbol{b})] \, {\rm d}S.$$

Here, after being substituted into (11.33), the integral of $\boldsymbol{b}$ is canceled, while like (3.84) the integral of $\phi_{\rm ac}$ is cast to

$$\frac{1}{k} \int_{\partial B} \boldsymbol{x} \times (\widehat{\boldsymbol{n}} \times \nabla \phi_{\rm ac}) \, {\rm d}S = - \int_{\partial B} \phi_{\rm ac} \widehat{\boldsymbol{n}} \, {\rm d}S = \boldsymbol{I}_{\phi}.$$

Thus, along with a similar approach to $\boldsymbol{L}_{\rm f}$, in (11.33) and (11.34) what remains is just (2.183) and (2.184):

$$\boldsymbol{F}_{\rm ac} = -\rho \frac{{\rm d}\boldsymbol{I}_{\phi}}{{\rm d}t}, \quad \boldsymbol{M}_{\rm ac} = -\rho \frac{{\rm d}\boldsymbol{L}_{\phi}}{{\rm d}t}.$$

Therefore, denote the impulse and angular impulse of $V_{\rm f}$ excluding the contribution of $\boldsymbol{\gamma}_{\rm ac}$ by $\boldsymbol{I}_{\rm f^-}$ and $\boldsymbol{L}_{\rm f^-}$, respectively, the force and moment can be simply expressed by

$$\boldsymbol{F} = -\rho \frac{\rm d}{{\rm d}t} (\boldsymbol{I}_{\rm f^-} + \boldsymbol{I}_{\phi}), \tag{11.40}$$

$$\boldsymbol{M} = -\rho \frac{\rm d}{{\rm d}t} (\boldsymbol{L}_{\rm f^-} + \boldsymbol{L}_{\phi}), \tag{11.41}$$

with the understanding that $\phi_{\rm ac}$ has influence on the vorticity advection.

We digress to note that the concept of vortex sheet can well be applied to flow at finite Reynolds numbers, as explained by Wu (2005). During a small time interval $\delta t$, the body-surface acceleration $\boldsymbol{a}_B$ causes a velocity increment $\delta \boldsymbol{b} = \boldsymbol{a}_B \delta t$, which by (11.39) yields a vortex layer of strength $\delta \boldsymbol{\gamma}_{\rm ac}$, so that the rate of change of $\boldsymbol{\gamma}_{\rm ac}$ is proportional to $\boldsymbol{a}_B$. This picture becomes exact as $\delta t \to 0$ no matter if $Re \to \infty$. Wu (2005) has demonstrated that, by substituting this $\delta \boldsymbol{\gamma}_{\rm ac}$ into (11.33), one obtains exactly the same $\boldsymbol{F}_{\rm ac}$ as calculated by the virtual mass approach based on inviscid potential-flow theory (Sect. 2.4.4).

Having clarifying the role of body-surface acceleration, we now focus on the rest part of force and moment caused by attached vortex sheet with nonzero circulation and free vortex sheet in the wake, denoted by suffix $\gamma$. We consider a thing wing represented by a bound vortex sheet or *lifting surface* as in Sect. 4.4.1. The interest in unsteady *flexible lifting surface theory* has recently revived due to the need for a theoretical basis of studying thin fish swimming and animal flight (Wu 2002).

In the Euler limit, the expressions of $\boldsymbol{I}$ and $\boldsymbol{L}$ and their rates of change have been given by (4.136–4.139), with vanishing Lamb-vector integrals. From these and (4.133) that tells how an unsteady bound vortex sheet induces a pressure jump $[\![p_\gamma]\!]$:

$$-[\![p_\gamma]\!]\boldsymbol{n} = \rho \boldsymbol{n} \frac{{\rm D}\Gamma}{{\rm D}t} = \rho \left( \bar{\boldsymbol{u}}_\pi \times \boldsymbol{\gamma}_{\rm b} + \frac{\partial \Gamma}{\partial t} \boldsymbol{n} \right),$$

we obtain the force and moment on a rigid or flexible lifting surface:

$$\boldsymbol{F}_\gamma = -\int_{S_{\rm b}} [\![p_\gamma]\!] \boldsymbol{n} \, {\rm d}S = \rho \int_{S_{\rm b}} \frac{{\rm D}\Gamma}{{\rm D}t} \boldsymbol{n} \, {\rm d}S \tag{11.42a}$$

$$= \rho \int_{S_{\rm b}} \bar{\boldsymbol{u}}_\pi \times \boldsymbol{\gamma}_{\rm b} \, {\rm d}S + \rho \int_{S_{\rm w}} \frac{\partial \Gamma}{\partial t} \boldsymbol{n} \, {\rm d}S, \tag{11.42b}$$

$$\boldsymbol{M}_\gamma = -\int_{S_{\rm w}} [\![p_\gamma]\!] \boldsymbol{x} \times \boldsymbol{n} \, {\rm d}S = \rho \int_{S_{\rm b}} \frac{{\rm D}\Gamma}{{\rm D}t} \boldsymbol{x} \times \boldsymbol{n} \, {\rm d}S \tag{11.43a}$$

$$= \rho \int_{S_{\rm b}} \boldsymbol{x} \times (\bar{\boldsymbol{u}}_\pi \times \boldsymbol{\gamma}_{\rm b}) \, {\rm d}S + \rho \int_{S_{\rm b}} \frac{\partial \Gamma}{\partial t} \boldsymbol{x} \times \boldsymbol{n} \, {\rm d}S, \tag{11.43b}$$

where $S_{\rm b}$ is the area of the bound vortex sheet, i.e., the wing area. These formulas are the basis of unsteady *lifting-surface theory*, which clearly reveal the vortical root of pressure jump on a wing.

Then, in linearized approximation, the vortex sheet has known location as we saw in the lifting-line theory. This greatly simplifies the above formulas and leads one back to almost entire classic wing aerodynamics. For example, it is easily verified that, the three-dimensional steady version of (11.42) returns to (11.7), while its two-dimensional unsteady version returns to the oscillating-airfoil theory. For details of these classic theories see, e.g., Prandtl and Tietjens (1934), Glauert (1947), Bisplinghoff et al. (1955), and Ashley and Landahl (1965).

## 11.4 Boundary Vorticity-Flux Theory

Opposite to the global view implied by the vorticity moment theory, we now trace the physical root to the body surface, where the entire vorticity field is produced. Then, the derivative-moment transformation leads to the *boundary vorticity-flux theory* as an *on-wall close view*.

### 11.4.1 General Formulation

Return to the incompressible flow problem stated in Sect. 11.1.1 (See Fig. 11.1), but now start from (11.1a) and (11.2a) where $\boldsymbol{F}$ and $\boldsymbol{M}$ are expressed by the body-surface integrals of the on-wall stress $\boldsymbol{t}$ and its moment, respectively. Naturally, the desired local dynamics on $\partial B$ that has net contribution to $\boldsymbol{F}$ and $\boldsymbol{M}$ should follow from proper transformation identities for surface integrals, which are given in Sect. A.2.3. To employ these identities we have to decompose the stress $\boldsymbol{t}$ into normal and tangent components first. Because the effect of $\boldsymbol{t}_{\rm s}$ has been integrated out, it suffices to deal with the orthogonal components of the reduced stress $\widehat{\boldsymbol{t}} = -p\boldsymbol{n} + \mu\boldsymbol{\omega} \times \boldsymbol{n}$, see (2.149). Therefore, using (A.25) and (A.26) to transform (11.1a), and using (A.28a) and (A.29) to transform (11.2a), in three dimensions we immediately obtain (Wu 1987)

$$\boldsymbol{F} = -\int_{\partial B} \rho \boldsymbol{x} \times \left( \frac{1}{2}\boldsymbol{\sigma}_{\rm p} + \boldsymbol{\sigma}_{\rm vis} \right) {\rm d}S, \tag{11.44}$$

$$\boldsymbol{M} = \int_{\partial B} \rho \left[ \frac{1}{2} x^2 (\boldsymbol{\sigma}_{\rm p} + \boldsymbol{\sigma}_{\rm vis}) - \boldsymbol{x}\boldsymbol{x} \cdot \boldsymbol{\sigma}_{\rm vis} \right] {\rm d}S + \boldsymbol{M}_{{\rm s}B}, \tag{11.45}$$

where $\boldsymbol{\sigma}_{\rm p}$ and $\boldsymbol{\sigma}_{\rm vis}$ are the stress-related boundary vorticity fluxes defined in (4.24b), and $\boldsymbol{M}_{{\rm s}B}$ is given by (11.3a). These formulas are the main result of the boundary vorticity flux theory. If one wishes, $\boldsymbol{M}_{{\rm s}B}$ can be absorbed into the first term of (11.45) by using the full normal and tangent stresses on deformable surface, see (2.151). Therefore, we conclude that

*For three-dimensional viscous flow over a solid body or a body of different fluid performing arbitrary motion, a body surface element has net contribution to the total force and moment only if the stress-related boundary vorticity fluxes are nonzero on the element.*

For example, for flow over sphere of radius $R$ at $Re \ll 1$, the Stokes drag law (4.59) can be quickly inferred from (11.44) by the vorticity distribution (4.57a) alone, which has led to (4.60a).[8] Thus, (4.59) follows at once, indicating that the pressure force and skin-friction force provide 1/3 and 2/3 of the total drag, respectively. On the other hand, by (11.45), for flow over any non-rotating sphere at *arbitrary* $Re$, we simply have

$$\boldsymbol{M} = \frac{1}{2}\rho R^2 \int_{\partial B} (\boldsymbol{\sigma}_{\rm p} + \boldsymbol{\sigma}_{\rm vis})\, {\rm d}S,$$

[8] This involves only the near-wall vorticity distribution, regardless the failure of the Stokes solution at far field.

where by (4.24b) both $\boldsymbol{\sigma}_{\rm p}$ and $\boldsymbol{\sigma}_{\rm vis}$ are under the operator $\boldsymbol{n}\times\nabla$ and hence integrate to zero by the generalized Stokes theorem. Thus the sphere is moment-free as it should. But if the sphere rotates the entire vorticity field will be redistributed, and there will be a nonzero moment

$$\boldsymbol{M} = \mu R^2 \int_{\partial B} \boldsymbol{e}_R \nabla_\pi \cdot \boldsymbol{\omega}\, {\rm d}S - \frac{8\pi R^3}{3}\mu\boldsymbol{\Omega}.$$

The theory can be easily generalized in a couple of ways (Wu et al. 1988b; Wu 1995; Wu and Wu 1993, 1996). Firstly, a simple replacement of pressure $p$ by $\mathit{\Pi} = p - (\lambda + 2\mu)\vartheta$ immediately extends the theory to viscous compressible flow with constant $\mu$. Here, expressing $\boldsymbol{F}$ and $\boldsymbol{L}$ by boundary vorticity fluxes does not conflict the dominance of the compressing process in supersonic regime. Rather, due to the viscous boundary coupling via the no-slip condition (Sect. 2.4.3), a shearing process must appear adjacent to the wall as a *byproduct* of compressing process. For example, when a shock wave hits the wall, the associated strong adverse pressure gradient will enter the boundary vorticity flux through $\boldsymbol{\sigma}_{\mathit{\Pi}}$ and hence causes a strong creation of vorticity opposite to that upstream the shock, somewhat similar to case that the interactive pressure gradient of $O(Re^{1/8})$ in the boundary-layer separation zone causes a strong peak of $\boldsymbol{\sigma}_{\rm p}$ (Sect. 5.3). In other words, *as an on-wall footprint of the flow field, the boundary vorticity flux can faithfully reflect the effect of compressing process on the wall.*

Secondly, owing to the transformation identities in Sect. A.2.3, we can consider the force and moment on an *open* surface, such as a piece of aircraft wing or body, a turbo blade, or the under-water part of a ship. This extension is done by simply adding proper line-integrals, including those due to $\boldsymbol{t}_{\rm s}$ given by (2.152a,b). Thus, for incompressible flow, we may write

$$\boldsymbol{F} = \boldsymbol{F}_{\rm surf} + \boldsymbol{F}_{\rm line}, \quad \boldsymbol{M} = \boldsymbol{M}_{\rm surf} + \boldsymbol{M}_{\rm line},$$

where $\boldsymbol{F}_{\rm surf}$ and $\boldsymbol{M}_{\rm surf}$ are given by (11.44) and (11.45), respectively, while

$$\boldsymbol{F}_{\rm line} = \frac{1}{2}\oint_{\partial S} \boldsymbol{x}\times(p\,{\rm d}\boldsymbol{x} + 2\mu\boldsymbol{\omega}\times{\rm d}\boldsymbol{x}) + 2\mu\oint_{\partial S}\boldsymbol{u}\times{\rm d}\boldsymbol{x}, \tag{11.46}$$

$$\boldsymbol{M}_{\rm line} = -\frac{1}{2}\oint_{\partial S}[x^2 p\,{\rm d}\boldsymbol{x} + (x^2\mathbf{I} - 2\boldsymbol{x}\boldsymbol{x})\cdot(\mu\boldsymbol{\omega}\times{\rm d}\boldsymbol{x})] + 2\mu\oint_{\partial S}\boldsymbol{x}\times(\boldsymbol{u}\times{\rm d}\boldsymbol{x}). \tag{11.47}$$

Note that with the help of these open-surface formulas, the $(p,\boldsymbol{\omega})$-distribution in (11.44) and (11.45) only needs to be *piecewise smooth*, because the boundary line-integral of each open piece must finally be cancelled. This is useful when the body surface has sharp edges, corners, or shock waves across which the tangent gradients of $\mathit{\Pi}$ and $\boldsymbol{\omega}$ are singular.

Thirdly, when $\mu$ is variable as in flows with extremely strong heat transfer, a simple way to generalize the preceding formulas is to take $\mu\boldsymbol{\omega}$ as a whole, including redefining the boundary vorticity flux as $\boldsymbol{\sigma}^d = \boldsymbol{n} \cdot \nabla(\mu\boldsymbol{\omega})$ so it has a dynamic dimension (denoted by superscript $d$), see Wu and Wu (1993). Moreover, since now $\nabla\cdot(2\mu\mathbf{B}) \neq \mathbf{0}$ and the local effect of $\boldsymbol{t}_\mathrm{s}$ has to be included, we should use (2.151) and define

$$\boldsymbol{\sigma}^d_{\tilde{\Pi}} \equiv \boldsymbol{n} \times \nabla\tilde{\Pi}, \quad \boldsymbol{\sigma}^d_\mathrm{vis} \equiv (\boldsymbol{n} \times \nabla) \times (\mu\boldsymbol{\omega}_r). \tag{11.48}$$

Correspondingly, (11.44) and (11.45) are extended to

$$\boldsymbol{F} = -\int_{\partial B} \boldsymbol{x} \times \left(\frac{1}{2}\boldsymbol{\sigma}^d_{\tilde{\Pi}} + \boldsymbol{\sigma}^d_\mathrm{vis}\right) \mathrm{d}S, \tag{11.49}$$

$$\boldsymbol{M} = \int_{\partial B} \left[\frac{1}{2}x^2(\boldsymbol{\sigma}^d_{\tilde{\Pi}} + \boldsymbol{\sigma}^d_\mathrm{vis}) - \boldsymbol{x}\boldsymbol{x} \cdot \boldsymbol{\sigma}^d_\mathrm{vis}\right] \mathrm{d}S, \tag{11.50}$$

where density $\rho$ as well as $\boldsymbol{M}_{\mathrm{s}B}$ in (11.45) has been absorbed into $\boldsymbol{\sigma}^d$s. This generalization makes the resulting force and moment formulas have exactly the same application range as that of the Navier–Stokes equation. Note that for variable $\mu$ the Navier–Stokes equation has an extra term, see (2.160a), which adds a viscous constituent $\boldsymbol{\sigma}^d_\mu \equiv 2\boldsymbol{n} \times (\nabla\mu \cdot \mathbf{B})$ to the boundary vorticity flux studied in Sect. 4.1.3. However, $\boldsymbol{\sigma}^d_\mu$ is not stress-related and does not explicitly enter the force and moment.

Finally, two-dimensional flow on the $(x, y)$-plane needs special treatment. We illustrate this by incompressible flow over an open deformable contour $C$ with end points $a$ and $b$. The positive direction of a boundary curve is defined by the convention that as one moves along it the fluid is kept at its left-hand side. Thus, on body surface we let $s$ increase along clockwise direction such that $(\boldsymbol{n}, \boldsymbol{e}_s, \boldsymbol{e}_z)$ form a right-hand triad. Then by (A.36) and (A.37), and noticing that the two-dimensional version of (2.152a,b) is

$$\int_a^b \boldsymbol{t}_\mathrm{s}\,\mathrm{d}s = 2\mu(v\boldsymbol{e}_x - u\boldsymbol{e}_y)|_a^b, \tag{11.51a}$$

$$\int_a^b \boldsymbol{x} \times \boldsymbol{t}_\mathrm{s}\,\mathrm{d}s = 2\mu\boldsymbol{e}_z \left[(\boldsymbol{x} \cdot \boldsymbol{u})|_a^b - \int_a^b u_\mathrm{s}\,\mathrm{d}s\right], \tag{11.51b}$$

we obtain

$$F_x = \rho\int_a^b \left(-y\sigma_\mathrm{p} + \nu x\frac{\partial\omega}{\partial s}\right) \mathrm{d}s + (yp - \mu x\omega + 2\mu v)|_a^b, \tag{11.52a}$$

$$F_y = \rho\int_a^b \left(x\sigma_\mathrm{p} + \nu y\frac{\partial\omega}{\partial s}\right) \mathrm{d}s - (xp + \mu y\omega + 2\mu u)|_a^b. \tag{11.52b}$$

Moreover, for $\boldsymbol{M} = M_z \boldsymbol{e}_z$, as observed at the end of Sect. A.2.4 it is impossible to express the boundary integral of $\boldsymbol{x} \times (\mu \boldsymbol{\omega} \times \boldsymbol{n}) = \boldsymbol{e}_z \mu \omega (\boldsymbol{x} \cdot \boldsymbol{n})$ by $\partial\omega/\partial s$. Thus by (A.38) and (11.51b), the result is

$$M_z = \rho \int_a^b \left( \frac{1}{2} x^2 \sigma_\mathrm{p} + \nu \boldsymbol{x} \cdot \boldsymbol{n} \omega \right) \mathrm{d}s - 2\mu (xu + yv)|_a^b + 2\mu \int_a^b u_\mathrm{s} \, \mathrm{d}s. \quad (11.53)$$

For a closed loop the last term is $-2\mu \Gamma_\mathrm{C}$ by our sign convention.

### 11.4.2 Airfoil Flow Diagnosis

While for Stokes flow the boundary vorticity flux distributes quite evenly, at large Reynolds numbers it typically has high peaks at very localized regions of $\partial B$, see the discussion following (4.94). It is this property in the high-$Re$ regime that makes the theory a valuable tool in flow diagnosis and control. So far it has been applied to the diagnosis of aerodynamic force on several configurations at different air speed regimes (Wu et al. 1999c), including airfoils and delta wing-body combination in incompressible flow, fairing in transonic flow, and wave rider in hypersonic flow. Zhu (2000) has demonstrated that the $\sigma_\mathrm{p}$-distribution can be posed in the objective function for optimal airfoil design.

To demonstrate the basic nature of this kind of diagnosis, we now consider the total force acting to a stationary two-dimensional airfoil by steady incompressible flow. At $Re \gg 1$ the contribution of skin friction can be neglected. In the wind-axis coordinate system $(x, y)$, (11.52) yields the lift and drag formulas

$$L = \rho \int_C x \sigma_\mathrm{p} \, \mathrm{d}s, \quad D = -\rho \oint_C y \sigma_\mathrm{p} \, \mathrm{d}s. \quad (11.54\text{a,b})$$

For convenience let the origin of $(x, y)$ be at the mid-chord point of the airfoil. Then by (11.54a) a negative $\sigma$-peak implies a positive lift for $x < 0$ and negative lift for $x > 0$. If for $x < 0$ there is a positive $\sigma$-peak on the upper surface, say, it not only produces a negative lift but also tends to cause early separation since it will be stronger as $\alpha$ increases. Moreover, the vorticity created by this unfavorable $\sigma$ adds extra enstrophy to the flow field, implying larger viscous drag. Therefore, ideally one wishes the sign of $\sigma$ over the upper surface to be like that sketched in Fig. 11.9a without front positive $\sigma$-peak and rear negative $\sigma$-peak on the upper surface.[9] In the figure the sign of $\sigma$

[9] Whether a boundary vorticity flux peak is favorable depends on the choice of the origin of the coordinates. For example, shifting the origin to the trailing edge would imply that negative boundary vorticity flux peaks on upper surface are all favorable, but by (11.54a) the contribution to the lift of a rear peak is less than that of a front one. However, this does not influence the net effect on the lift and drag, and setting the origin at the mid-chord is most convenient.

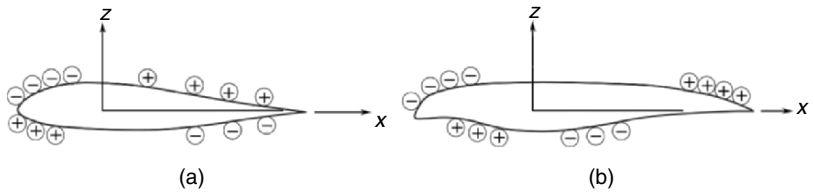


**Fig. 11.9.** Idealized boundary vorticity flux distribution over airfoil. (**a**) The boundary vorticity flux is completely favorable on upper surface. (**b**) An even more favorable boundary vorticity flux distribution

over the lower surface is qualitatively estimated by pressure gradient and the constraint

$$\oint_C \sigma_{\mathrm{p}}\,\mathrm{d}s = -\oint_C \frac{\partial p}{\partial s}\,\mathrm{d}s = 0. \tag{11.55}$$

Given the favorable sign distribution of $\sigma_{\mathrm{p}}$, however, (11.54a) indicates that there is still a room to further enhance $L$ by shifting the location of $\sigma$-peaks. On the upper surface, the front negative $\sigma$-peak and rear positive $\sigma$-peak will produce more lift if their $|x|$ is larger, while on the lower surface these peaks will produce less negative $L$ if their $|x|$ is smaller. This simple intuitive observation suggests a modification of the airfoil shape of Fig. 11.9a to that of Fig. 11.9b, which is precisely of the kind of *supercritical airfoils* originally designed for alleviating transonic wave drag. The present argument indicates that a supercritical airfoil must also have better aerodynamic performance at low Mach numbers.

Quantitatively, consider the relation between $\sigma$ and the airfoil geometry. For steady and attached airfoil flow at large $Re$, this relation can be obtained analytically in the Euler-limit by the potential-flow theory. Let $C$ be any streamline in the potential-flow region, of which the arc element $\mathrm{d}s$ has inclination angle $\chi$ with respect to the $x$-axis, see Fig. 11.10. Thus, in terms of complex variables $z = x + \mathrm{i}y$ and $w = \phi + \mathrm{i}\psi$ as used in deriving (11.10), we have

$$\begin{gathered} \mathrm{d}x = \cos\chi\,\mathrm{d}s,\ \mathrm{d}y = \sin\chi\,\mathrm{d}s,\ \ \mathrm{d}z = \mathrm{d}s\,\mathrm{e}^{\mathrm{i}\chi}, \\ u = q\cos\chi, \quad v = q\sin\chi, \quad \frac{\mathrm{d}w}{\mathrm{d}z} = q\,\mathrm{e}^{-\mathrm{i}\chi}. \end{gathered} \tag{11.56}$$

And, the tangent component of the Euler equation $C$ reads

$$a_{\mathrm{s}} = \frac{1}{2}\frac{\partial q^2}{\partial s} = -\frac{\partial p}{\partial s} \quad \text{on} \quad C. \tag{11.57}$$

Now, denote

$$\rho(z) = \log q - \mathrm{i}\chi = \log\left(\frac{\mathrm{d}w}{\mathrm{d}z}\right)$$

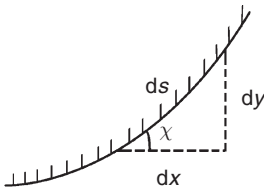


**Fig. 11.10.** Geometric relation of a contour $C$

such that

$$\frac{\mathrm{d}\rho}{\mathrm{d}z} = \frac{\mathrm{d}z}{\mathrm{d}w}\frac{\mathrm{d}^2 w}{\mathrm{d}z^2} = \frac{1}{2q^2}\frac{\mathrm{d}q^2}{\mathrm{d}z} - \mathrm{i}\frac{\mathrm{d}\chi}{\mathrm{d}z}.$$

Then by using $\mathrm{d}z = \mathrm{d}s\,\mathrm{e}^{i\chi}$ and (11.57) we find $\mathrm{e}^{i\chi}\mathrm{d}\rho/dz = q^{-2}\sigma_\mathrm{p} - \mathrm{i}\kappa$, where $\kappa \equiv \mathrm{d}\chi/\mathrm{d}s$ is the curvature of $C$. But by (11.56) $\mathrm{e}^{i\chi} = q\,\mathrm{d}z/\mathrm{d}w$, so

$$\frac{a_\mathrm{s}}{q^3} - \frac{\mathrm{i}\kappa}{q} = \left(\frac{\mathrm{d}z}{\mathrm{d}w}\right)^2 \frac{\mathrm{d}^2 w}{\mathrm{d}z^2} \quad \text{on} \quad C.$$

Therefore, $a_\mathrm{s}/q^3$ and $-\kappa/q$ are the real and imaginary parts of an analytical function (which is known once so is $\mathrm{d}w/\mathrm{d}z$).

Finally, let the streamline $C$ be the airfoil contour *underneath* the attached vortex sheet where the no-slip condition still works and $a_\mathrm{s}$ drops to zero. But the viscosity comes into play, producing a boundary vorticity flux $\sigma$ to replace $a_\mathrm{s}$ to balance the pressure gradient. Namely, we have

$$\frac{\sigma_\mathrm{p}}{q^3} - \frac{\mathrm{i}\kappa}{q} = \left(\frac{\mathrm{d}z}{\mathrm{d}w}\right)^2 \frac{\mathrm{d}^2 w}{\mathrm{d}z^2} \quad \text{on airfoil,} \tag{11.58}$$

indicating that if $q \sim 1$ then $\sigma_\mathrm{p}$, or pressure gradient, is directly linked to the local airfoil curvature.[10] But strictly the $\sigma_\mathrm{p}$–$\kappa$ relation is nonlinear and of global nature.

Equation (11.58) can be used to calculate $\sigma_\mathrm{p}$ over a realistic airfoil as long as the flow is attached. Figure 11.11a shows the $\sigma$-distribution computed thereby for a helicopter rotor airfoil VR-12 at $\alpha = 6°$, compared with the Navier–Stokes computation at $Re = 10^6$ using an one-equation turbulence model (Zhu 2000). The difference is very small except at the trailing edge, where the "inviscid" $\sigma$ approaches $\pm\infty$. But it can be shown that this singularity is symmetric and precisely canceled in (11.54).

The VR-12 airfoil has higher maximum lift before stall and larger stall angle of attack than a traditional airfoil, say NACA-0012. By (11.54a), the

[10] This result can be compared with that in the linearized supersonic aerodynamic theory, where the pressure is simply proportional to the local wall slope, as exemplified by (5.56c′).

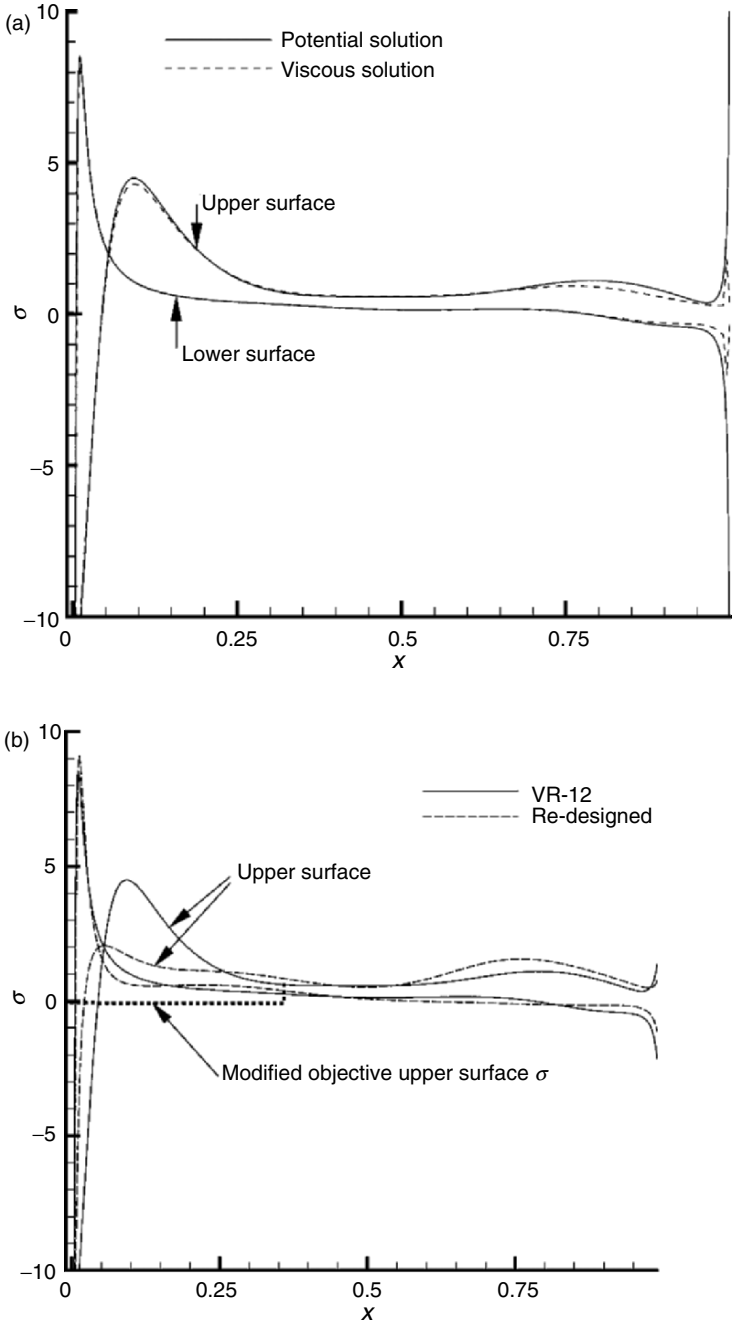


**Fig. 11.11.** Boundary vorticity flux distributions on VR-12 airfoil (**a**) and a re-designed airfoil (**b**). The design scheme sets a projective boundary vorticity flux only in the marked local region. From Zhu (2000)

major net contributor to the total lift is the primary negative $\sigma$-peak in a very narrow region on the upper surface, right downstream of the front stagnation point. But the effect of the following positive $\sigma$-peak associated with an adverse pressure gradient is unfavorable. Suppressing this front positive peak should lead to an even better performance. By (11.55), this suppression may also cause a favorable positive rear boundary vorticity-flux peak on the upper surface.

This conjecture has been confirmed by Zhu (2000) using a simple optimal design scheme, where the objective function includes minimizing the unfavorable $\sigma$ in a front-upper region. Some airfoils with better $\sigma$-distributions were produced thereby, of which one is shown in Fig. 11.11b associated with larger stall angle and maximum lift coefficient.

### 11.4.3 Wing-Body Combination Flow Diagnosis

Compared to airfoils, much less has been known on the optimal shapes of a three-dimensional wing. An interesting boundary vorticity-flux based diagnosis of a flow over a delta wing-body combination, see Fig. 11.12, has been made by Wu et al. (1999c). The flow parameters are $\alpha = 20°$, $M = 0.3$, and $Re = 1.744 \times 10^6\,\mathrm{ft}^{-1}$.

The model has an infinitely extended cylindrical afterbody, so the flow data on the body base were not available. Therefore, the body surface is open, of which the boundary is a circle $C$ of radius $a$ on the $(y, z)$-plane at the trailing edge. The line integrals in (11.46) have to be included; in the body-axis

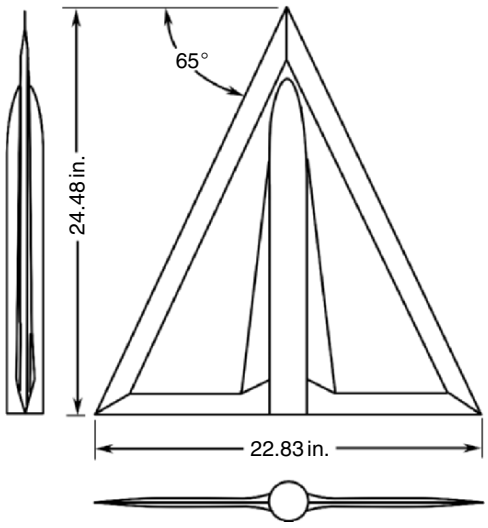


**Fig. 11.12.** A wing–body combination. From Wu et al. (1999c)

coordinate system with origin at the apex, the extended force formula gives (again ignore the skin-friction and denote $\boldsymbol{\sigma}_{\mathrm{p}}$ simply by $\boldsymbol{\sigma}$)

$$F_x = \frac{1}{2}\int_S \rho(z\sigma_y - y\sigma_z)\,\mathrm{d}S + \frac{a^2}{2}\int_0^{2\pi} p\,\mathrm{d}\theta, \tag{11.59a}$$

$$F_z = \frac{1}{2}\int_S \rho(y\sigma_x - x\sigma_y)\,\mathrm{d}S, \tag{11.59b}$$

where $S$ is the open surface of wing–body combination and $\tan\theta = z/y$. The surface integral of (11.59a) is found to provide a negative axial force (thrust), which is upset by the line integral, resulting in a net drag. The integrand $p\,\mathrm{d}\theta$ is zero except a pair of sharp positive peaks at the wing–body junctures. Thus a fairing of the junctures would reduce the drag.

On the other hand, (11.59b) traces the normal force $F_z$ to the root of the leading-edge vortices, i.e., the root of the net free vortex layers shed from the leading edges. These layers are dominated by the lower-surface boundary layer but partially cancelled by the upper-surface boundary layer. Thus, the $\boldsymbol{\sigma}$ on the upper and lower surfaces should provide a negative and positive lift, respectively. Indeed, a survey indicates that the lower-surface gives about 200% of $F_z$, but half of it is canceled by the unfavorable $\boldsymbol{\sigma}$ on the upper surface.

Moreover, it is surprising that $\boldsymbol{\sigma}$ is highly localized very near the leading edges, as demonstrated in Fig. 11.13 by the distribution of $\rho(y\sigma_x - x\sigma_y)/2$ on the contour of a cross-flow section at $x/c_0 = 0.24$, where $c_0$ is the root-chord length. The data analysis shows that an area around the leading edges, only of 1.7% of $S$, contributes to 104% of the total $F_z$. The remaining area of 98.3% $S$ merely gives $-4$% of $F_z$. This diagnosis underscores the very crucial

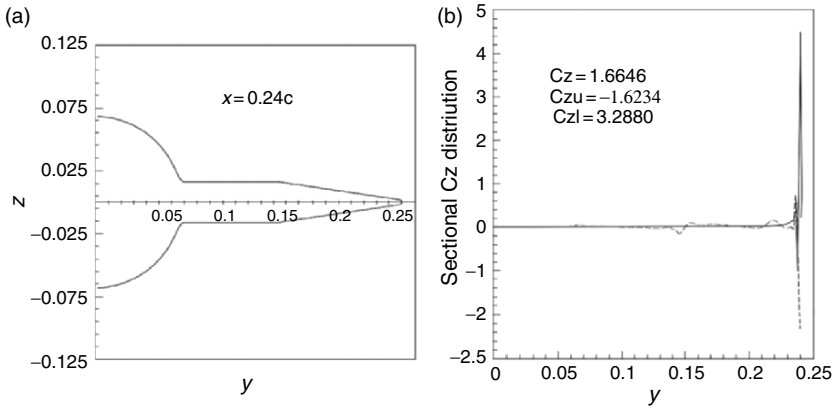


**Fig. 11.13.** (**a**) Sectional contour of the wing–body combination at $x/c_0 = 0.24$. (**b**)Boundary vorticity flux distribution. *Solid line*: lower surface, *dash line*: upper surface. From Wu et al. (1999c)

importance of near leading-edge flow management in the wing design. Should the spanwise flow on the upper surface be guided more to the $x$-direction, not only can it provide an axial momentum to reduce the drag but also the shed vortex layers from the lower surface could be less cancelled. Then stronger leading-edge vortices could be formed to give a higher normal force.

A different wing-flow diagnosis will be presented in Sect. 11.5.4.

## 11.5 A DMT-Based Arbitrary-Domain Theory

As a global view, the vorticity moment theory of Sect. 11.3 requires the data of the entire vorticity field in an externally unbounded incompressible fluid, but in flow analysis the available data are always confined in a finite and sometimes quite small domain. As an on-wall close view, boundary vorticity-flux theory of Sect. 11.4 requires only the flow information right on the body surface ("footprint" and "root" of the flow field), but is silent about how the generated vorticity forms various vortical structures that evolve, react to the body surface, and act to other downstream bodies. The shortages of these theories can be overcome by considering an *arbitrary domain* $V_f$, which has resulted in the finite-domain extensions of the above two theories, given by Noca et al. (1999) and Wu et al. (2005a), respectively.

The extension of vorticity-moment theory follows the same derivation of (11.29) from (11.27), but with all vortical terms retained at an arbitrary $\Sigma$. Like the original version, in this extension the rate of change $d/dt$ is calculated after integration is performed. The results are convenient for practical estimate of the force and moment acting to a body moving and deforming in an incompressible fluid, using measured or computed flow data. A more convenient formulation, obtained by a different DMT identity, will be given in Sect. 11.5.4. In particular, these progresses have excited significant interest in applying the new expressions to estimate the unsteady forces based on flow data measured by the particle-image velocimetry (PIV).

In contrast, the extension of the boundary vorticity-flux theory to include the flow structures in a finite $V_f$ is characterized by shifting the operator $d/dt$ into relevant integrals. This shift permits a direct generalization of the results to compressible flow, and makes it possible to quantitatively identify how each flow structure localized in both space and time affects the total force and moment, from a more fundamental point of view. The convenience of practical force estimate is not a mojor concern. This formulation is presented below. Once again we work on incompressible flow; as in Sects. 11.2 and 11.4, the compressibility effect can be easily added.

### 11.5.1 General Formulation

The formulation is based on proper derivative-moment transformation of the full expressions of $\boldsymbol{F}$ and $\boldsymbol{M}$ given by (11.1b) and (11.2b).

**Diffusion Form**

We start from identity (3.117a) for the fluid acceleration, and set $\mathcal{D} = V_\mathrm{f}$ with $\partial\mathcal{D} = \partial B + \Sigma$. Substitute this into (11.1b) and replace $\nabla \times \boldsymbol{a}$ by $\nu\nabla^2\boldsymbol{\omega}$ due to (11.5). On $\partial B$, we recognize that $\boldsymbol{n} \times \boldsymbol{a}$ is the boundary vorticity flux $\boldsymbol{\sigma}_\mathrm{a}$ due to acceleration of $\partial B$, defined in (4.24a). On $\Sigma$, we use (11.4) as well as identities (A.25) for $n = 3$ and (A.36) for $n = 2$ to transform $\boldsymbol{n} \times \boldsymbol{a}$, which makes the pressure integral in (11.1b) canceled. Therefore, we obtain (Wu and Wu 1993)

$$\boldsymbol{F} = -\frac{\mu}{k}\int_{V_\mathrm{f}} \boldsymbol{x} \times \nabla^2\boldsymbol{\omega}\,\mathrm{d}V + \boldsymbol{F}_B + \boldsymbol{F}_\Sigma, \tag{11.60}$$

where $\boldsymbol{F}_B$ and $\boldsymbol{F}_\Sigma$ are boundary integrals over $\partial B$ and $\Sigma$, respectively:

$$\boldsymbol{F}_B = \frac{1}{k}\int_{\partial B} \rho\boldsymbol{x} \times \boldsymbol{\sigma}_\mathrm{a}\,\mathrm{d}S, \tag{11.61a}$$

$$\boldsymbol{F}_\Sigma = -\frac{\mu}{k}\int_\Sigma \boldsymbol{x} \times [\boldsymbol{n} \times (\nabla \times \boldsymbol{\omega})]\,\mathrm{d}S + \mu\int_\Sigma \boldsymbol{\omega} \times \boldsymbol{n}\,\mathrm{d}S. \tag{11.61b}$$

Note that (11.61b) consists of only viscous vortical terms.

By using (A.24a), a similar approach to the moment yields

$$\boldsymbol{M} = \frac{\mu}{2}\int_{V_\mathrm{f}} x^2\nabla^2\boldsymbol{\omega}\,\mathrm{d}V + \boldsymbol{M}_B + \boldsymbol{M}_\Sigma, \tag{11.62}$$

where

$$\boldsymbol{M}_B = -\frac{1}{2}\int_{\partial B} \rho x^2\boldsymbol{\sigma}_\mathrm{a}\,\mathrm{d}S, \tag{11.63a}$$

$$\boldsymbol{M}_\Sigma = \frac{\mu}{2}\int_\Sigma x^2\boldsymbol{n} \times (\nabla \times \boldsymbol{\omega})\,\mathrm{d}S + \mu\int_\Sigma \boldsymbol{x} \times (\boldsymbol{\omega} \times \boldsymbol{n})\,\mathrm{d}S + \boldsymbol{M}_{\mathrm{s}\Sigma}, \tag{11.63b}$$

in which $\boldsymbol{M}_{\mathrm{s}\Sigma}$ is given by (11.3b).

Like $\boldsymbol{F}_B$ and $\boldsymbol{M}_B$, the integrals of $\boldsymbol{\tau}$ in $\boldsymbol{F}_\Sigma$ and $\boldsymbol{x} \times \boldsymbol{\tau}$ in $\boldsymbol{M}_\Sigma$ can be further cast to derivative-moment form as well, in terms of *vorticity diffusion flux* on a surface given by (4.23) and (4.24). Then (4.22) implies

$$-\boldsymbol{n} \times (\nabla \times \nu\boldsymbol{\omega}) = \begin{cases} \nu\boldsymbol{n} \cdot \nabla\boldsymbol{\omega} = \boldsymbol{\sigma} & \text{for } n = 2, \\ \nu\boldsymbol{n} \cdot \nabla\boldsymbol{\omega} - (\boldsymbol{n} \times \nabla) \times \nu\boldsymbol{\omega} = \boldsymbol{\sigma} - \boldsymbol{\sigma}_\mathrm{vis} & \text{for } n = 3. \end{cases} \tag{11.64}$$

Thus, for three-dimensional flow, by using (A.26) and (A.29) we obtain

$$\boldsymbol{F}_\Sigma = \frac{1}{2}\int_\Sigma \rho\boldsymbol{x} \times (\boldsymbol{\sigma} + \boldsymbol{\sigma}_\mathrm{vis})\,\mathrm{d}S, \tag{11.65}$$

$$\boldsymbol{M}_\Sigma = \frac{1}{2}\int_\Sigma \rho(2\boldsymbol{x}\boldsymbol{x} \cdot \boldsymbol{\sigma}_\mathrm{vis} - x^2\boldsymbol{\sigma})\,\mathrm{d}S + \boldsymbol{M}_{\mathrm{s}\Sigma}. \tag{11.66}$$

For flow with $Re \gg 1$, generically $|\boldsymbol{\sigma}_\mathrm{vis}| \ll |\boldsymbol{\sigma}|$.

Equations (11.60) to (11.66), characterized by the moments of $\mu\nabla^2\boldsymbol{\omega}$, can be called the *diffusion form* of the arbitrary-domain theory. It is easily seen that they hold true for compressible flow with constant $\mu$ as well. These formulas reveal explicitly the viscous root behind the classic circulation theory. The direct contribution of the body motion and deformation to the force and moment amounts to the moments of $\boldsymbol{\sigma}_a$, which is solely determined by the specified $\boldsymbol{b}(\boldsymbol{x}, t)$ and independent of the flow.

In contrast, for two-dimensional flow on the $(x, y)$-plane, apply the convention and notation defined in Sect. 11.4.1 to $\Sigma$, from (11.64) and a one-dimensional derivative-moment transformation we obtain the drag and lift components:

$$\begin{aligned} D_\Sigma &= \mu \oint_\Sigma \left( y\frac{\partial\omega}{\partial n} - x\frac{\partial\omega}{\partial s} \right) \mathrm{d}s, \\ L_\Sigma &= -\mu \oint_\Sigma \left( y\frac{\partial\omega}{\partial s} + x\frac{\partial\omega}{\partial n} \right) \mathrm{d}s, \end{aligned} \tag{11.67}$$

indicating that the local dynamics on $\Sigma$ is reflected by the *vorticity gradient vector* $\nabla\omega$. But, for $\boldsymbol{M}_\Sigma = M_\Sigma \boldsymbol{e}_z$, due to the same reason as that leading to (11.53), we stop at

$$M_\Sigma = \mu \oint_\Sigma \left( \frac{1}{2}x^2\frac{\partial\omega}{\partial n} + \boldsymbol{x}\cdot\boldsymbol{n}\omega \right) \mathrm{d}s - 2\mu\Gamma_\Sigma. \tag{11.68}$$

For flow with $Re \gg 1$, generically $|\partial\omega/\partial s| \ll |\partial\omega/\partial n|$ in (11.67) and (11.68).

### Advection Form

Owing to (11.5), $\nu\nabla^2\boldsymbol{\omega}$ in (11.60) and (11.62) can be replaced by $\nabla\times\boldsymbol{a} = \boldsymbol{\omega}_{,t} + \nabla\times\boldsymbol{l}$, where $(\cdot)_{,t} = \partial(\cdot)/\partial t$ and $\boldsymbol{l} \equiv \boldsymbol{\omega}\times\boldsymbol{u}$ is the Lamb vector. Therefore, the force and moment can be equally interpreted in terms of the local unsteadiness, advection, and stretching/tilting of the vorticity field in $V_\mathrm{f}$. But to retain the vortex force as in (11.30), we switch to identity (3.117b) that has led to the force formula (11.27). A corresponding formula for the moment can be derived from identity (A.24a). Consequently, (11.60) and (11.62) can be alternatively expressed as

$$\begin{aligned} \boldsymbol{F} = &-\rho\int_{V_\mathrm{f}} \left( \frac{1}{k}\boldsymbol{x}\times\boldsymbol{\omega}_{,t} + \boldsymbol{l} \right) \mathrm{d}V - \frac{\rho}{k}\int_{\partial V_\mathrm{f}} \boldsymbol{x}\times(\boldsymbol{n}\times\boldsymbol{l})\,\mathrm{d}S \\ &+\boldsymbol{F}_B + \boldsymbol{F}_\Sigma, \end{aligned} \tag{11.69}$$

$$\begin{aligned} \boldsymbol{M} = &\rho\int_{V_\mathrm{f}} \left( \frac{1}{2}x^2\boldsymbol{\omega}_{,t} + \boldsymbol{x}\times\boldsymbol{l} \right) \mathrm{d}V + \frac{\rho}{2}\int_{\partial V_\mathrm{f}} x^2\boldsymbol{n}\times\boldsymbol{l}\,\mathrm{d}S \\ &+\boldsymbol{M}_B + \boldsymbol{M}_\Sigma, \end{aligned} \tag{11.70}$$

where $\boldsymbol{n} \times \boldsymbol{l}$ is given by (11.28). We call this set of formulas the *advection form* of the general derivative-moment theory. The splitting of the moments of $\mu\nabla^2\boldsymbol{\omega}$ into three inviscid terms (two volume integrals and one boundary integral) further decomposes the physical mechanisms responsible for the total force and moment to their most elementary constituents. The role of the vortex force and the boundary integral of $\boldsymbol{x} \times (\boldsymbol{n} \times \boldsymbol{l})$ will be addressed in Sect. 11.5.4 for steady flow. To have a feeling on the role of $\boldsymbol{x} \times \boldsymbol{\omega}_{,t}$, consider a fish $B$ just starting to flap its caudal fin for forward motion so that $|\boldsymbol{\omega}|$ is increasing, as sketched in Fig. 11.14. Putting the other terms in (11.69) aside, based on the sign of $x$ and $y$ we can readily infer the qualitative effect of the tail swinging on the thrust and side force of the fish as indicated in the figure.

Due to the arbitrariness of the domain size, the theory can be applied to obtain the force and moment acting on any individual of a group of deformable bodies, which may perform arbitrary relative motions.

Now, as remarked earlier, as long as we use the full expression (11.69) to replace (11.27) and repeat the same steps there, a fully general version of (11.29) follows at once as the main result of the finite-domain vorticity moment theory (Noca et al. 1999). The original vorticity moment theory (J.C. Wu 1981) is then a special case of it as $\Sigma$ retreats to infinity where the fluid is at rest. On the other hand, as $\Sigma$ shrinks to the body surface $\partial B$, what remains in (11.60) and (11.62) is

$$\boldsymbol{F} = \boldsymbol{F}_B + \boldsymbol{F}_\Sigma, \quad \boldsymbol{M} = \boldsymbol{M}_B + \boldsymbol{M}_\Sigma,$$

where the normal vector $\boldsymbol{n}$ on $\Sigma$ now equals $\widehat{\boldsymbol{n}} = -\boldsymbol{n}$. Hence, substituting (11.61), (11.63), (11.65), and (11.66) into the above expressions, and using (4.23) and (4.24), we recover (11.44) and (11.45) of the boundary vorticity-flux theory for three-dimensional flow at once. The proof for two-dimensional flow is similar. A unification of various DMT-based theories is therefore achieved.

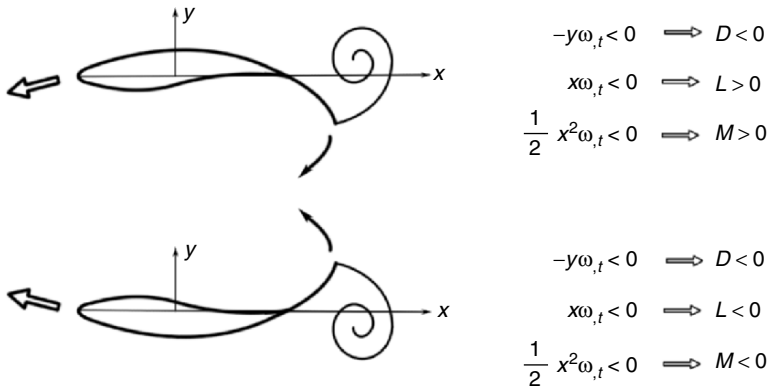


**Fig. 11.14.** A qualitative assessment of the effect of unsteady vorticity moments on the total force and moment

**The Effect of Compressibility**

By an inspection of the structure of (11.69) and (11.70) as well as a comparison of (11.4) and (11.13), we find that to generalize these formula to compressible flow it suffices to make simple replacements

$$\rho\boldsymbol{\omega}\times\boldsymbol{u}\Longrightarrow\rho\boldsymbol{\omega}\times\boldsymbol{u}-\frac{1}{2}q^2\nabla\rho,\quad \rho\boldsymbol{\omega}_{,t}\Longrightarrow\nabla\times(\rho\boldsymbol{u}_{,t}).$$

This leads to

$$\begin{aligned}\boldsymbol{F}=&-\frac{1}{k}\int_{V_\mathrm{f}}\boldsymbol{x}\times\nabla\times(\rho\boldsymbol{u}_{,t})\,\mathrm{d}V-\int_{V_\mathrm{f}}\left(\rho\boldsymbol{l}-\frac{1}{2}q^2\nabla\rho\right)\mathrm{d}V\\&-\frac{1}{k}\int_{\partial V_\mathrm{f}}\boldsymbol{x}\times\left[\boldsymbol{n}\times\left(\rho\boldsymbol{l}-\frac{1}{2}q^2\nabla\rho\right)\right]\mathrm{d}S+\boldsymbol{F}_B+\boldsymbol{F}_\Sigma,\end{aligned}\tag{11.71}$$

$$\begin{aligned}\boldsymbol{M}=&-\frac{1}{2}\int_{V_\mathrm{f}}x^2\nabla\times(\rho\boldsymbol{u}_{,t})\,\mathrm{d}V-\int_{V_\mathrm{f}}\boldsymbol{x}\times\left(\rho\boldsymbol{l}-\frac{1}{2}q^2\nabla\rho\right)\mathrm{d}V\\&+\frac{1}{2}\int_{\partial V_\mathrm{f}}x^2\boldsymbol{n}\times\left(\rho\boldsymbol{l}-\frac{1}{2}q^2\nabla\rho\right)\mathrm{d}S+\boldsymbol{M}_B+\boldsymbol{M}_\Sigma.\end{aligned}\tag{11.72}$$

The analogy between (11.71) and (11.16) is obvious. By using the numerical scheme developed by Chang and Lei (1996a) in their diagnosis of transonic viscous flow over circular cylinder based on the projection theory (Sect. 11.2.2), a similar diagnosis has been performed by Luo (2004) based on (11.71), for which $\Sigma$ can be quite small. The flow remains steady in the computed Mach-number range $M\in[0.6,1.6]$. Among Luo's results an interesting finding is that the compressing effect $-q^2\nabla\rho/2$ prevails over the vortex force $\rho\boldsymbol{\omega}\times\boldsymbol{u}$ at the same subsonic Mach number as Chang and Lei found, and that the vortex force changes from a drag to a thrust at the same supersonic Mach number as Chang and Lei found. These qualitative turning points, therefore, are independent of the specific local-dynamics theories.

### 11.5.2 Multiple Mechanisms Behind Aerodynamic Forces

In addition to the global view represented by the vorticity moment theory and the on-wall close view represented by the boundary vorticity flux theory, the present arbitrary-domain theory further enriches one's views of the physical mechanisms that have net contribution to the force and moment. How this is so has been exemplified by Wu et al. (2005a), using the unsteady two-dimensional and incompressible flow over a stationary circular cylinder of unit radius at $Re=500$ based on diameter. The flow field was solved numerically using a scheme developed by Lu (2002). An instantaneous plot of vorticity contours, in which the Kármán vortex street is clearly seen, is shown in Fig. 11.15. Since the computational domain does not cover the entire vorticity field, the figure represents a *mid-field view*.

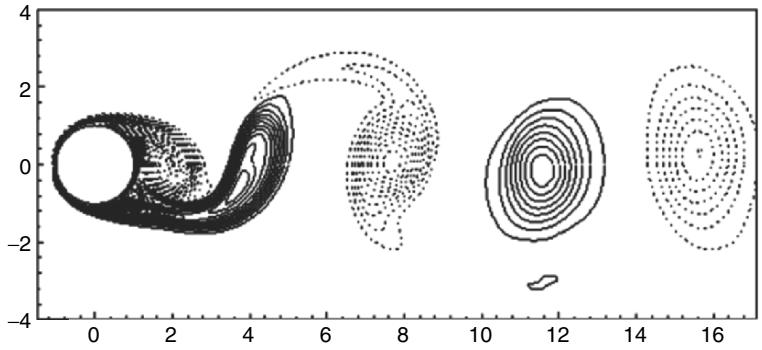


**Fig. 11.15.** An instantaneous vorticity contour (from −20 to 20 with increment 0.25) of flow over circular cylinder. In this and following figures solid and dashed lines represent positive and negative values, respectively. From Wu et al. (2005a)

It is well known that the unsteady force and moment acting to the cylinder are associated with the motion of the vortex street. However, as pointed out in Sect. 11.1, this common flow-visualization plot (along with the plots of velocity field and pressure contours, etc.,) does not tell precisely which part of each vortex in the street has a positive, negative, or zero instantaneous contribution to the total drag and lift. This information can only be found from the integrand distributions of the derivative-moment formulas (as well as those of the projection-theory of Sect. 11.2), obtained by a simple postprocessing of the flow data. Let us focus on the total drag and lift.

Take $\Sigma$ as concentric circles of varying radius $R$. In the following expressions the integrands of field integrals are expressed in Cartesian coordinates, while those in boundary integrals in polar coordinates $(r, \theta)$. Then (11.60) yields

$$\begin{aligned} D(t) &= -\mu \int_{V_\mathrm{f}} y\nabla^2\omega \,\mathrm{d}S + \mu R^2 \oint_\Sigma \left( \frac{\partial \omega}{\partial r}\sin\theta - \frac{1}{R}\frac{\partial \omega}{\partial \theta}\cos\theta \right) \mathrm{d}\theta \\ &= D_1 + D_2 + D_3, \end{aligned} \tag{11.73a}$$

$$\begin{aligned} L(t) &= \mu \int_{V_\mathrm{f}} x\nabla^2\omega \,\mathrm{d}V - \mu R^2 \oint_\Sigma \left( \frac{\partial \omega}{\partial r}\cos\theta + \frac{1}{R}\frac{\partial \omega}{\partial \theta}\sin\theta \right) \mathrm{d}\theta \\ &= L_1 + L_2 + L_3, \end{aligned} \tag{11.73b}$$

where and below $D_1, ..., L_3$ etc. denote corresponding integrals symbolically. In these formulas, by (11.69) there is

$$\begin{aligned} D_1 &= \int_{V_\mathrm{f}} \rho \left( -y\frac{\partial \omega}{\partial t} + v\omega \right) \mathrm{d}S + R \oint_\Sigma \rho\omega u_r \sin\theta \,\mathrm{d}\theta \\ &= D_4 + D_5 + D_6, \end{aligned} \tag{11.74a}$$

$$\begin{aligned} L_1 &= \int_{V_\mathrm{f}} \rho \left( x\frac{\partial \omega}{\partial t} - u\omega \right) \mathrm{d}S - R \oint_\Sigma \rho\omega u_r \cos\theta \,\mathrm{d}\theta \\ &= L_4 + L_5 + L_6. \end{aligned} \tag{11.74b}$$

In particular, when $\Sigma$ shrinks to the cylinder surface at $r = 1$, (11.73) reduces to the boundary vorticity-flux formulas

$$D = (D_2 + D_3)_{r=1}, \tag{11.75a}$$

$$L = (L_2 + L_3)_{r=1}. \tag{11.75b}$$

Equations (11.73–11.75) form a set of derivative-moment formulas for the force diagnosis, each yielding a special insight into the physics responsible for $D$ and $L$. Below we look at the distributions of their integrands.

### Mid-Field View

The inviscid decompositions of $D_1$ and $L_1$ given by (11.74) are shown in Figs. 11.16 and 11.17, respectively. As a mid-field view, these plots exhibit the same vortex structures as Fig. 11.15. But, due to the sign change of $\omega_{,t}, v$ and $y$, as a vortex passes a spatial point $\boldsymbol{x}$ the contribution of a single wake vortex may be split into two or even four pieces. It is this further identification of the net effect of every piece of a vortex constitutes the additional information carried by the local dynamics of the wake field. Note that the integrand of $L_4$, i.e., the unsteady term $\rho x \omega_{,t}$, does not reduce as $x$ increases (see Fig. 11.16a). But this does not matter since in a finite domain the integral-convergence problem does not exist, while when $\Sigma$ retreats to infinity the theory becomes the vorticity-moment theory with well-behaved convergence.

### Near-Field View

Although mathematically the diffusion form (11.60) is exactly equivalent to the advection form (11.69), for a flow at large Reynolds numbers that is our main interest the flow regions where the peak integrands of these alternative forms are very different. In the well-developed wake vortices $\mu|\nabla^2\boldsymbol{\omega}|$ has become quite weak, but it is very strong in boundary layers and free shear layers, across which $\mu|\nabla^2\boldsymbol{\omega}| \simeq \mu|\boldsymbol{\omega}_{,nn}|$ reaching $O(1)$. While in the advection form one already sees highly localized wake-vortex structures, in the diffusion form the key contributors to $\boldsymbol{F}$ and $\boldsymbol{M}$ are even more compact. Consequently, for flow with $Re \gg 1$, switching from the advection form to diffusion form implies tracking the more upstream vortical structure of those shown in Fig. 11.15. An observer watching the diffusion form naturally gains a *near-field view*, as demonstrated by Fig. 11.18 that shows the field of the integrand of $D_1$ and $L_1$.

It is remarkable that, as a sharp contrast to Figs. 11.16 and 11.17, according to (11.73) the near-field boundary layers and separated shear layers right before the formation of the Kármán vortex street have about 90% of the net contribution to $D$ and $L$. Each free vortex layer exhibits a sandwich structure because across such a layer $\omega_{,nn}$ changes sign twice. Once a concentrated wake vortex is formed and sheds downstream with its feeding sheet being cut off, it joins the rows of wake vortices which as a whole have only about 10% direct contribution to the forces.

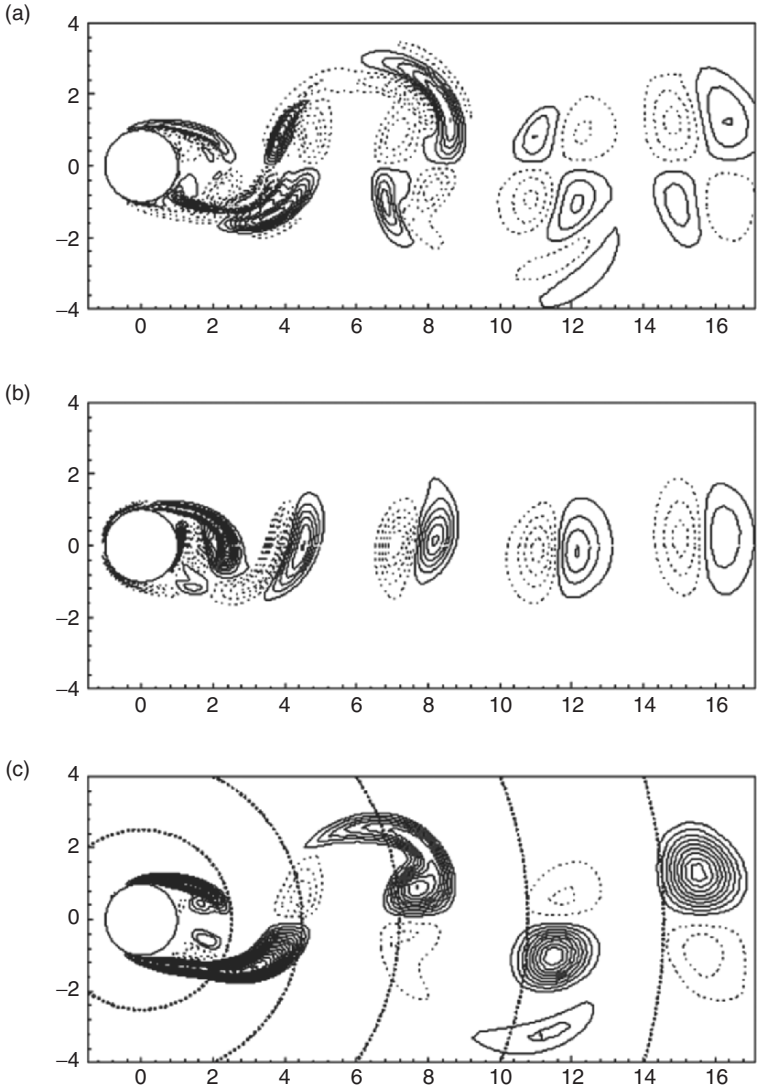


**Fig. 11.16.** Distribution of integrand of (**a**) $D_4$ from $-5$ to 5 with increment 0.5; (**b**) $D_5$ from $-5$ to 5 with increment 0.25; and (**c**) $D_6$ from $-2$ to 6 with increment 0.2. The $\theta$-variation of the integrand of $D_6$ depends on $R$, which can be qualitatively read off in (c) from the intersections of the field distribution and a few concentric circles. From Wu et al. (2005a)

The vortices in the vortex street are all product of the rolling-up of these separated shear layers, and Fig. 11.18 convincingly indicates that (11.60) can indeed trace the key local dynamic structures for the total force toward their

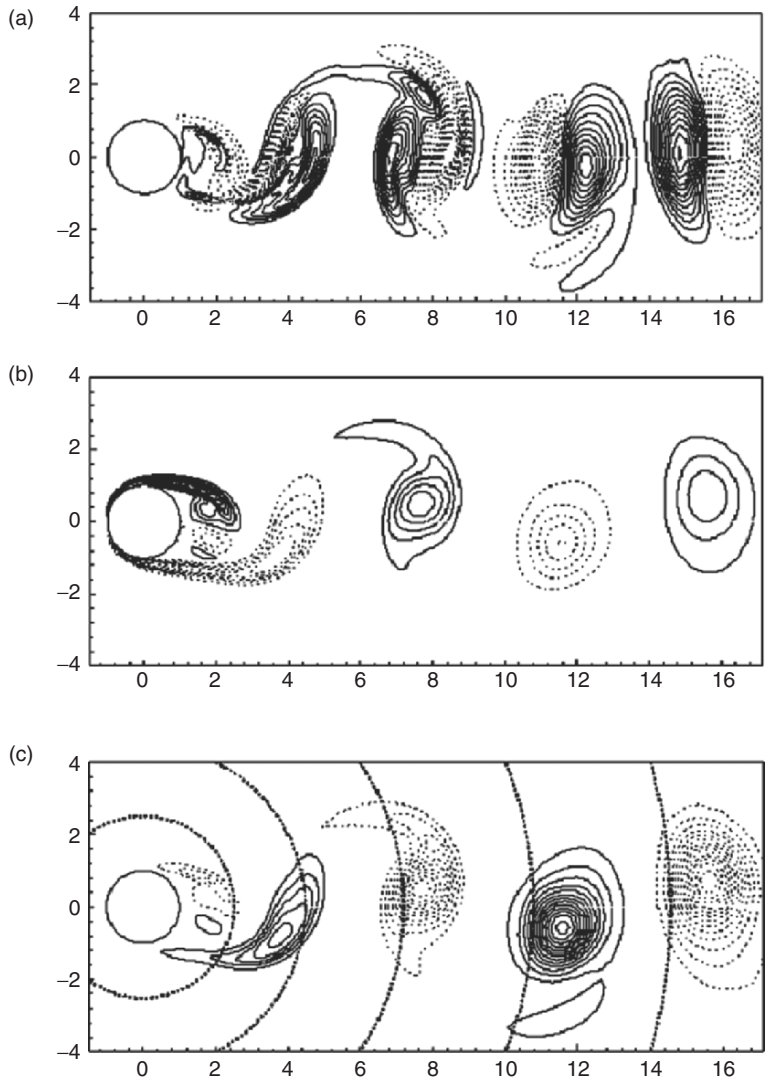


**Fig. 11.17.** Distribution of integrand of (**a**) $L_4$ from $-25$ to 25 with increment 0.5; (**b**) $L_5$ from $-10$ to 10 with increment 0.5; and (**c**) $L_6$ from $-40$ to 40 with increment 2. The $\theta$-variation of the integrand of $L_6$ can be qualitatively read off similar to Fig. 11.16c. From Wu et al. (2005a)

origin, a task that cannot be achieved by standard formulas. Of course, the Kármán street does strongly influence the total force; but its major effect is indirect through its induced unsteadiness of the flow, including the periodic swing of the peak $\nabla^2\omega$ in near-field vortex layers.

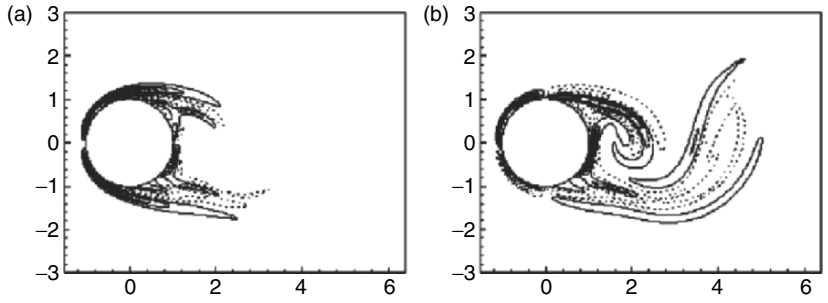


**Fig. 11.18.** Distribution of integrand of (**a**) $D_1$ and (**b**) $L_1$. Contours from $-10$ to 10 with increment 0.5. From Wu et al. (2005a)

### On-Wall Close View

If the radius of $\Sigma$ is $R_0 = 1 + \delta$ with $\delta \ll 1$ such that $V_\mathrm{f}$ is well within the sublayer of the boundary layer adjacent to the cylinder and the flow therein is dominated by diffusion, then $\boldsymbol{F}_\Sigma$ contributes to almost all $\boldsymbol{F}$ and the Stokes approximation (Sect. 4.2.1) can be applied in a way very similar to that discussed in Sect. 11.4.1. The result is actually independent of $R_0$ and equal to that obtained by (11.75) since the radius is canceled during integration. Therefore, to the above physical pictures we may add Fig. 11.19, which shows the $\theta$-variation of the two terms in (11.75a,b) as the on-wall close view. Recall that the normal and tangent components of $\nabla\omega$ are from respectively the pressure gradient ($\sigma = \sigma_\mathrm{p}$) and skin-friction, and the former is much stronger than the latter, it is still the moments of $\sigma$ that dominate the drag and lift. We have seen in the context of Fig. 4.12 that the sign change of $\sigma_\mathrm{p}$ signifies that the boundary layer is about to separate; now $x = \cos\theta$ and $y = \sin\theta$ in (11.75) add additional sign changes of the integrand in $D$ and $L$, resulting in their different $\theta$-dependence.

Notice the physical relation between Figs. 11.18 and 11.19. The boundary layers and their separation in the former are the *spatial and temporal accumulated effect* of the boundary vorticity fluxes in the latter (Sect. 4.2.3). This could be clearly seen by comparing a time sequence of both kinds of figures.

The above discussions have shown how different views capture different stages of the evolution of the same vorticity field, and how the physics of these stages are consistent and complementary to each other. Taking together, they form a complete multidimensional picture of the mechanisms responsible for the force and moment.

It should be stressed that a vortical structure favorable to the force and moment at one of its evolution stage may become unfavorable at another stage, although in terms of the flow data at any stage one can always infer the same force and moment. Therefore, as yet another *evolution view*, one may trace the motion of each individual structure (or a group of structures),

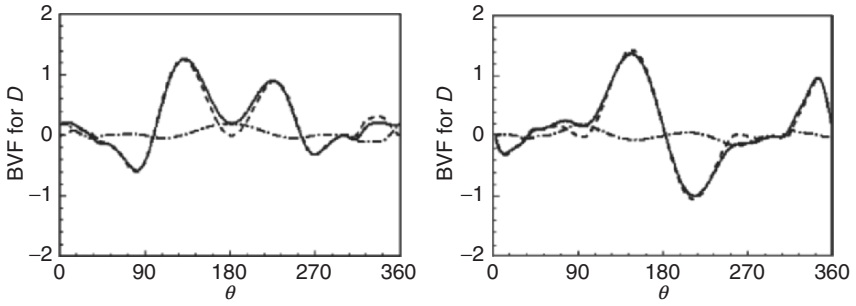


**Fig. 11.19.** Distributions of the integrands of (**a**) drag and (**b**) lift for the moments of vorticity-gradient components on the cylinder surface, see (11.75). *Solid lines*: total force, *dashed lines*: contribution of $\mu\partial\omega/\partial r$, *dashed–dot lines*: contribution of $\mu\partial\omega/\partial s$. From Wu et al. (2005a)

observing its "role switch," and assess its merit. Such a thorough quantitative assessment would be very beneficial in creating new configurations and flow-control strategy.

### 11.5.3 Vortex Force and Wake Integrals in Steady Flow

We now return to classic aerodynamics on steady flow over a stationary rigid body. Assume the Reynolds number is sufficiently large, all the attached boundary layers of the body are enclosed by $\Sigma$ which only cuts vortical flow in the wake. The preceding example of circular-cylinder flow has indicated that in the fully developed wake region the viscous vorticity gradient is much smaller than $O(1)$. This is generally true in high Reynolds-number steady aerodynamics, and right on $\Sigma$ one can neglect the effect of $\mu\nabla\boldsymbol{\omega}$ compared to the pressure force; namely, the entire $\boldsymbol{F}_\Sigma$ and $\boldsymbol{M}_\Sigma$ in (11.69) and (11.70) can be dropped.[11] Therefore, since $\boldsymbol{F}_B$ and $\boldsymbol{M}_B$ also vanish, we simply have

$$\boldsymbol{F} = -\rho\int_{V_\mathrm{f}} \boldsymbol{l}\,\mathrm{d}V - \frac{\rho}{k}\int_\Sigma \boldsymbol{x}\times(\boldsymbol{n}\times\boldsymbol{l})\,\mathrm{d}S \tag{11.76a}$$

$$= -\frac{\rho}{k}\int_{V_\mathrm{f}} \boldsymbol{x}\times(\nabla\times\boldsymbol{l})\,\mathrm{d}V = -\frac{\mu}{k}\int_{V_\mathrm{f}} \boldsymbol{x}\times\nabla^2\boldsymbol{\omega}\,\mathrm{d}V, \tag{11.76b}$$

$$\boldsymbol{M} = -\rho\int_{V_\mathrm{f}} \boldsymbol{x}\times\boldsymbol{l}\,\mathrm{d}V + \frac{\rho}{2}\int_\Sigma x^2\boldsymbol{n}\times\boldsymbol{l}\,\mathrm{d}S \tag{11.77a}$$

$$= \frac{\rho}{2}\int_{V_f} x^2\nabla\times\boldsymbol{l}\,\mathrm{d}V = \frac{\mu}{2}\int_{V_\mathrm{f}} x^2\nabla^2\boldsymbol{\omega}\,\mathrm{d}V. \tag{11.77b}$$

[11] This does not imply the neglect of viscosity inside $V_\mathrm{f}$. It is the accumulated effect of the viscous force in $V_\mathrm{f}$ that forms the dominant feature of the wake.

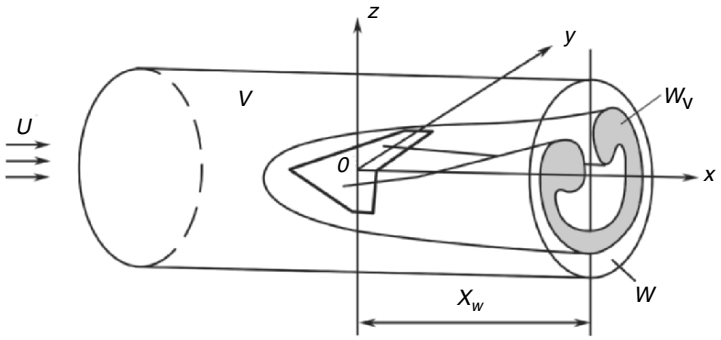


**Fig. 11.20.** Control volume $V$ in which the flow is steady, wake plane $W$, and its vortical part $W_\mathrm{v}$. From Wu and Wu (1996)

Therefore, *for steady flow at large Re, no transverse Lamb vector, no force and moment.*

Let us concentrate on the force given by (11.76) and consider a wing flow schematically drawn in Fig. 11.20. The oncoming flow has uniform velocity $\boldsymbol{U} = U\boldsymbol{e}_x$ in the wind-axis coordinate system $(x, y, z)$. The flow in a cylindrical control volume $V$ is assumed steady and symmetric with respect to the $(x, z)$-plane. $V$ has sufficiently remote side boundary $S$ and a downstream boundary $W$ on the $(y, z)$-plane (a *Wake plane*) at an arbitrary fixed $x$ location with $\boldsymbol{n} = \boldsymbol{e}_x$ there, such that the vorticity can be set zero over $\Sigma$ except a small vortical part of $W$, $W_\mathrm{v} \ll W$. Hence, in (11.76a) the $\Sigma$-integral reduces to a $W_\mathrm{v}$-integral.

One's concern in the flow property on a wake-plane is mainly from experimental aerodynamics. It has long been hoped that for steady flow a wake-plane survey may permit inferring the lift and drag on the body as an alternative to the balance measurement and the very difficult measurement of body-surface skin friction. For example, the approximate lift formula (11.38) has been used for decades. In what follows we use (11.76a) to address three problems of considerable practical interest. We denote

$$\boldsymbol{u} = (U + u', v, w), \quad p = p_\infty + p'. \tag{11.78}$$

### On the Distinction of Induced and Profile Drags

In steady flow, the drag consists of induced drag (see (11.7b)) and *profile drag.* The latter is associated with the shedding of low-energy viscous boundary-layer flow into the wake. Unlike the lift and induced drag which exist even in the Euler limit ($Re \to \infty$), the profile drag appears only at finite $Re$. How to rationally distinct the two drag constituents for a general nonlinear and viscous flow is important, since to alleviate them one has to use different methods based on their respective physical roots (cf. Kroo 2001).

Consider the Euler limit first, where the vortex-sheet Lamb vector (Sects. 4.4.1 and 11.3.3) in steady flow is nonzero only in the "bound vortex," i.e., the boundary layers attached to the wing. Thus, in (11.76a) the $W_\mathrm{v}$-integral disappears, and we see at once that the vortex force must be the only source of both lift and induced drag:

$$L = -\rho \int_V l_x \,\mathrm{d}V = \rho \int_V (u\omega_y - v\omega_x)\,\mathrm{d}V, \tag{11.79a}$$

$$D_\mathrm{in} = -\rho \int_V l_y \,\mathrm{d}V = \rho \int_V (v\omega_z - w\omega_y)\,\mathrm{d}V. \tag{11.79b}$$

In fact, from these formulas one may easily deduce (11.7a) and (11.7b) as linearized approximation.

We can also recover (11.38) from the vortex force, by using (A.22):

$$-\rho \int_{V_\mathrm{f}} \boldsymbol{l}\,\mathrm{d}V \simeq \rho \boldsymbol{U} \times \int_{V_\mathrm{f}} \boldsymbol{\omega}\,\mathrm{d}V = \rho U \boldsymbol{e}_z \int_{W_\mathrm{v}} y\omega_x \,\mathrm{d}S. \tag{11.80}$$

Note that, as a mid-field view, here the relevant vortex dynamics mechanism is more upstream than that in deriving (11.38) based on the global view. While in the latter we focused on the increase of the vortex-loop area, now we are focusing on the vorticity inside the wing boundary layers. This is evident in two-dimensional flow, for which (11.5) directly follows from (11.79b) without appealing to the starting vortex.

The induced drag can also be approximately expressed by a wake-plane integral. Similar to the derivation of (11.7a) from (11.38), by (11.9) and the same one-dimensional derivative-moment transformation for $\Gamma$ used there, since the integral of $wd(y\Gamma)/dy$ vanishes due to the symmetry, (11.7b) is cast to (Wu et al. 2002)

$$D_\mathrm{in} = -\rho \int_{-s}^{s} yw(y)\gamma(y)\,\mathrm{d}y, \tag{11.81a}$$

which is the vortex-sheet form of a more general wake integral for distributed vorticity, in pair with (11.38):

$$D_\mathrm{in} \simeq -\rho \int_{W_\mathrm{v}} yw\omega_x \,\mathrm{d}S. \tag{11.81b}$$

We now turn to the finite-$Re$ effect reflected by the boundary integral of (11.76), which is a wake integral of

$$\boldsymbol{x} \times (\boldsymbol{n} \times \boldsymbol{l}) = \boldsymbol{e}_x(\boldsymbol{x} \cdot \boldsymbol{l}) - x\boldsymbol{l} = \boldsymbol{e}_x(\boldsymbol{x}_\pi \cdot \boldsymbol{l}) - x\boldsymbol{l}_\pi,$$

where the suffix $\pi$ denotes the $(y, z)$ components tangent to $W$. On $W$ the Lamb vector can be replaced by the total-pressure gradient due to the steady Crocco equation

$$\rho\boldsymbol{\omega} \times \boldsymbol{u} = -\nabla P, \quad P \equiv p + \frac{1}{2}\rho q^2, \tag{11.82}$$

of which both sides approach zero simultaneously in the Euler limit. Since $x = x_w$ is fixed and $\nabla P = \nabla P'$ where $P' = P - P_\infty$ vanishes at $\partial W$, the integral of $\rho x \boldsymbol{l}_\pi = -x\nabla_\pi P'$ over $W$ vanishes. Thus, the wake integral yields a drag only, which is the profile drag:

$$D_{\text{prof}} = -\frac{\rho}{k}\boldsymbol{e}_x \int_{W_\text{v}} \boldsymbol{x}_\pi \cdot \boldsymbol{l}\, \mathrm{d}S \tag{11.83a}$$

$$= -\boldsymbol{e}_x \int_{W_\text{v}} P'\, \mathrm{d}S. \tag{11.83b}$$

Equation (11.83b) is the exact formula for deducing the profile drag from the measured total-pressure deficit over $W_\text{v}$. Its vorticity-dynamics origin is revealed by (11.83a): the nonBeltramian behavior of the viscous flow at finite $Re$. To see relevant mechanisms explicitly, denote the Euler-limit values of $\boldsymbol{l}$, $\boldsymbol{\omega}$, and $\boldsymbol{u}$ by suffix 0 and their residual values at finite $Re$ by a tilde, so that

$$\tilde{\boldsymbol{l}} = \boldsymbol{\omega}_0 \times \tilde{\boldsymbol{u}} + \tilde{\boldsymbol{\omega}} \times \boldsymbol{u}_0 + \tilde{\boldsymbol{\omega}} \times \tilde{\boldsymbol{u}}.$$

we may then replace $\boldsymbol{l}$ in (11.83a) by $\tilde{\boldsymbol{l}}$, and find a leading-order cause of the profile drag

$$D_{\text{prof}} \simeq \frac{\rho}{k} U \int_{W_\text{v}} (z\tilde{\omega}_y - y\tilde{\omega}_z)\, \mathrm{d}S. \tag{11.84}$$

As shown in Fig. 11.21, the wing boundary layers from upper and lower surfaces have positive and negative $\tilde{\omega}_y$, respectively, which merge at the trailing edge and form a wake of finite thickness, with $z\tilde{\omega}_y > 0$. This is the entire $D_{\text{prof}}$ in two dimensions. In three dimensions the side edges of the wing also have boundary layers, which yields $-y\tilde{\omega}_z > 0$ at both sides.

### On the Forces by Vortical-Wake Integrals

It has been highly desired to express, if possible, the forces by integrals only over the vortical part of the wake plane, $W_\text{v} \ll W$, because the entire $W$ is

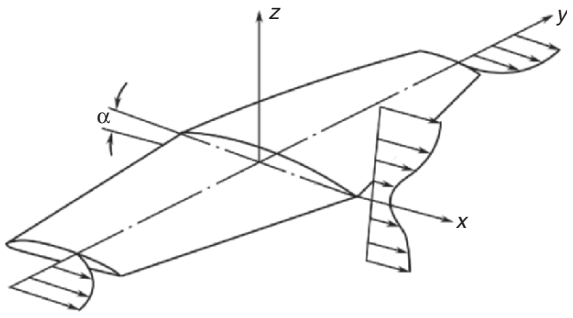


**Fig. 11.21.** Viscous sources of profile drag according to (11.84)

often too large to make a velocity survey. We have just seen that the profile-drag formula satisfies this need. To see to what extent the lift and induced drag can be likewise expressed, we first notice that the vortex force can be cast to an integral over a full $W$. By using the mass conservation one has the balance of momentum-flux through $W$ and side boundary $S$ (Batchelor 1967):

$$\int_S \boldsymbol{u} u_n \,\mathrm{d}S = -\boldsymbol{e}_x \int_W U u' \,\mathrm{d}S,$$

by which and identity (3.69) one transforms (11.79) to (Yates and Donaldson 1986)

$$L = -\int_W uw \,\mathrm{d}S, \quad D_{\mathrm{in}} = \frac{1}{2}\int_W (q_\pi^2 - u'^2)\,\mathrm{d}S, \tag{11.85}$$

where $q_\pi^2 = v^2 + w^2$. Note in passing that substituting these and (11.83) into (11.76), we recover the conventional wake integrals for lift and drag, which are a component form of (2.74) and have been the standard starting point of flow diagnosis by experimentally measured wake data:

$$L = -\rho \int_W uw \,\mathrm{d}S, \tag{11.86a}$$

$$D = \int_W [(p_\infty - p) + u(U-u)]\,\mathrm{d}S. \tag{11.86b}$$

However, (11.85) no longer has vortical form nor exhibits local dynamics. Unfortunately, there is no other way but the kinematic identity (3.69) to cast the Lamb-vector volume integral to boundary integral. Therefore, in exact form one has to be satisfied with either the compact vortical form (11.76) but allowing for volume integral, or wake integrals (11.85) over a large $W$. In other words, *it is impossible to exactly express the lift and induced drag by any wake integrals over the vortical region only.*

Nevertheless, some approximate formulas solely in terms of integrals over $W_{\mathrm{v}}$ are available. For the induced drag, so far the best result is the leading-order approximation (11.81b). For the lift, the best result follows from transforming (11.86b) by identity (A.26) (Wu and Wu 1989):

$$L = \rho \int_{W_{\mathrm{v}}} y[u\omega_x - (v\omega_y + w\omega_z)]\,\mathrm{d}S + \rho \int_W (wv_{,x} - vw_{,x})\,\mathrm{d}S, \tag{11.87}$$

of which the leading order is (11.80) or again (11.38). The second integral in (11.87) represents a small near-field correction to ensure the lift is independent of $x$, of which the integrand is not confined to $W_{\mathrm{v}}$.

Equation (11.87) has been applied to the diagnosis of a steady incompressible flow over a delta wing with leading-edge vortices, based on the measured data over a wake plane near the trailing edge (Wu et al. 1996).[12]

[12] In Wu and Wu (1989) and Wu et al. (1996) the drag formula is in error.

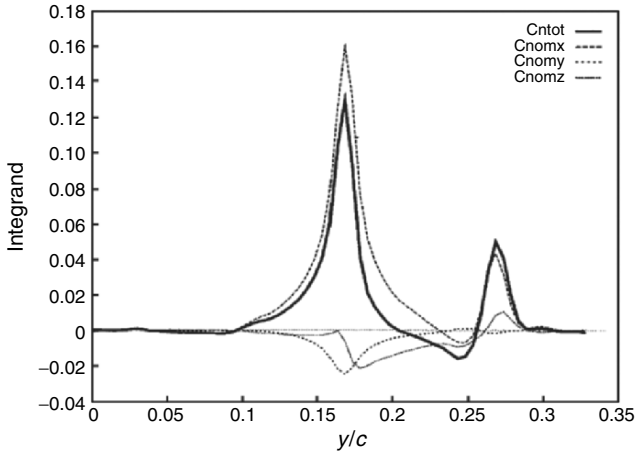


**Fig. 11.22.** Spanwise distribution of normal force and its vortical constituents over a half delta wing. From Wu et al. (1996)

The wing has sharp leading edge of 76° sweeping angle, and is at $\alpha = 20°$ and $Re = 1.14 \times 10^6\,\mathrm{ft}^{-1}$. With coordinates fixed to the wing, the wake plane $W$ is at $x/c = 0.075$ downstream of the trailing edge, on which a set of measured data of $(u, v, w, p, P)$ for half wing was utilized to infer the three vorticity components. The data show a strong leading-edge vortex, of which the core axial velocity is as high as $u = 1.8U$. This is the key structure of producing the normal force along with a negative axial force.

Figure 11.22 shows the spanwise normal load distribution from wing centerline to wing tip (integration along $z$ has been performed) computed from (11.87). Also shown are separate contributions from $\omega_x$, $\omega_y$, and $\omega_z$ in its $W_\mathrm{v}$-integral. The vortical wake integral of $yu\omega_x$ is dominant, leading to a local peak of lift/drag ratio of order 10 at the leading-edge vortex location. A weaker peak of normal load appears outside the wing tip, which is the place where boundary layers (dominated by that from the lower surface) leave the wing, with very low total pressure and hence a large axial force. The local $C_\mathrm{l}/C_\mathrm{d}$ there is only of order one. Therefore, a better aerodynamic performance would be gained if the wing tip is properly cut off, as in many successful wing designs.

### Forces in Terms of Flow Data Downstream of a Wake Plane

There are occasions where the flow-field survey can hardly be done around the body, and what one can measure is only a downstream wake. Hence, it is of interest to see whether an observer sitting in such the wake, without seeing the flow around body at all, can still infer exactly the same $\boldsymbol{F}$ as (11.86). We show that the answer is positive.

Use a wake plane $W$ to cut the whole space $V_\infty$ into a "front" and a "rear" control volumes, $V$ and $R$, respectively, see Fig. 11.23. Conceive that

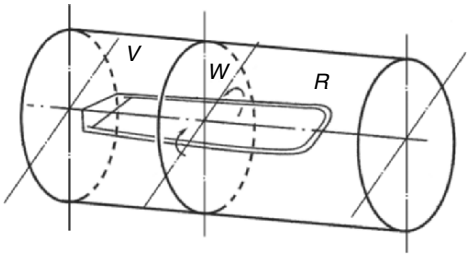


**Fig. 11.23.** The "front" and "rear" control volumes $V$ and $R$ divided by a wake plane $W$, with $V + R = V_\infty$

a front observer $A$ and a rear observer $B$ can only see the flows in $V$ and $R$, respectively. Kinematically, the two observers are linked by relations

$$\int_V \boldsymbol{\omega}\,\mathrm{d}V = \int_{W_\mathrm{v}} \omega_x \boldsymbol{x}\,\mathrm{d}S, \quad \int_{W_\mathrm{v}} \omega_x\,\mathrm{d}S = 0, \tag{11.88}$$

$$\int_R \boldsymbol{l}(\boldsymbol{x},t)\,\mathrm{d}V = -\int_V \boldsymbol{l}(\boldsymbol{x})\,\mathrm{d}V. \tag{11.89}$$

Dynamically, their bridge can be found from the vorticity-moment formula (11.48), by which it easily follows that

$$\boldsymbol{F} = -\rho\left(\frac{\mathrm{d}\boldsymbol{I}_V}{\mathrm{d}t} + \frac{\mathrm{d}\boldsymbol{I}_R}{\mathrm{d}t}\right) = -\rho\frac{\partial \boldsymbol{I}_R}{\partial t}. \tag{11.90}$$

Shifting $\partial/\partial t$ into the integral over $R$ and using (A.23) to manipulate the result, since viscous terms are dropped on $W$, (11.90) becomes

$$\boldsymbol{F} = \rho\int_R \boldsymbol{l}\,\mathrm{d}V + \frac{\rho}{2}\int_{W_\mathrm{v}} \boldsymbol{x}\times(\widehat{\boldsymbol{n}}\times\boldsymbol{l})\,\mathrm{d}S, \quad \widehat{\boldsymbol{n}} = -\boldsymbol{e}_x, \tag{11.91}$$

which is evidently nothing but (11.76) due to (11.89). Physically, the rear observer sees that at the upstream end of $R$ there comes a vortex pair satisfying (11.88), carrying a flux of vorticity moment into $R$ through $W_\mathrm{v}$ via the second term of (11.91). This vortex pair is connected to the starting-vortex system to form an unsteady horseshoe vortex, and the area spanned by the vortex (cut by $W_\mathrm{v}$) is increasing as shown by (11.90), which implies the vortex force in (11.91).

### 11.5.4 Further Applications

Before closing this section, we present two more applications of the derivative-moment transformation. We first extend our discussion on experiment-oriented force formulas to unsteady flow. We have seen that to obtain exact lift and drag in steady flow, the minimum requirement is to survey at least a large area of a wake plane where $\boldsymbol{u}' \neq \boldsymbol{0}$. The question now is what is the corresponding

minimum requirement if the flow around the body is *unsteady*. Experimental survey on a wake plane is certainly insufficient since the flow unsteadiness propagates to all directions. Thus we go to the next: How about on a control surface enclosing the body?

It has been believed that the answer is negative due to the extra volume integral of $\partial \boldsymbol{u}/\partial t$. Moreover, even if one can make the flow survey in a finite domain rather than merely on a wake plane, the gathered data may still be unable to fulfill the entire $V_{\mathrm{f}}$. For example, PIV can hardly detect the velocity distribution adjacent to the body surface.

Contrary to the conventional idea, however, we now show that the force formula by control-surface integral alone can be easily found once we enter the DMT-based formulation, as first shown by Noca et al. (1999). Here we follow Wu et al. (2005d), starting from (11.1c). When the flow is *incompressible*, an application of (A.22) to its first term immediately yields the desired result:

$$\boldsymbol{F} = -\rho \frac{\mathrm{d}}{\mathrm{d}t} \left( \int_{\partial B} \boldsymbol{x} b_n \, \mathrm{d}S + \int_{\Sigma} \boldsymbol{x} u_n \, \mathrm{d}S \right) - \int_{\Sigma} [p\boldsymbol{n} + \rho \boldsymbol{u}(u_n - v_n) - \boldsymbol{\tau}] \, \mathrm{d}S. \quad (11.92)$$

Alternatively, by (A.25) and (11.4) we have

$$-\int_{\Sigma} p\boldsymbol{n} \, \mathrm{d}S = -\frac{\rho}{k} \int_{\Sigma} \boldsymbol{x} \times (\boldsymbol{n} \times \boldsymbol{a}) \, \mathrm{d}S - \frac{\mu}{k} \int_{\Sigma} \boldsymbol{x} \times [\boldsymbol{n} \times (\nabla \times \boldsymbol{\omega})] \, \mathrm{d}S,$$

where the second term and the integral of $\boldsymbol{\tau}$ in (11.92) just combine to form $\boldsymbol{F}_{\Sigma}$ given by (11.65) or (11.67). Therefore, the involvement of pressure can be replaced by that of acceleration:

$$\boldsymbol{F} = -\rho \frac{\mathrm{d}}{\mathrm{d}t} \left( \int_{\partial B} \boldsymbol{x} b_n \, \mathrm{d}S + \int_{\Sigma} \boldsymbol{x} u_n \, \mathrm{d}S \right) - \frac{\rho}{k} \int_{\Sigma} \boldsymbol{x} \times (\boldsymbol{n} \times \boldsymbol{a}) \, \mathrm{d}S + \boldsymbol{F}_{\Sigma}. \quad (11.93)$$

For a specified body motion, since the PIV can yield the material acceleration $\boldsymbol{a}$ (e.g., La Porta et al. 2001; Christensen and Adrian 2002) on $\Sigma$, by which the pressure can be inferred (e.g., Liu and Katz 2004), the unsteady force can be deduced from (11.92) or (11.93).

Unfortunately, for the total moment a formula corresponding to (11.92) does not exist, since $\boldsymbol{x} \times \boldsymbol{u}$ is not divergence-free even for incompressible flow.

Equations (11.92) and (11.93) have been verified by numerical tests. One example is a two-dimensional uniform oncoming flow $\boldsymbol{U} = U\boldsymbol{e}_x$ past a *deformable* airfoil at $Re = 10^4$, of which the centerline oscillates as a traveling wave

$$y = a(x) \sin[2\pi(x - ct)], \quad (11.94)$$

where the amplitude $a(x)$ is a parabolic curve. The deformable airfoil is shown in Fig. 11.24, along with three different deformable control surfaces. Figure 11.25 is an instantaneous vorticity contour plot at phase speed $c/U = 0.5$,

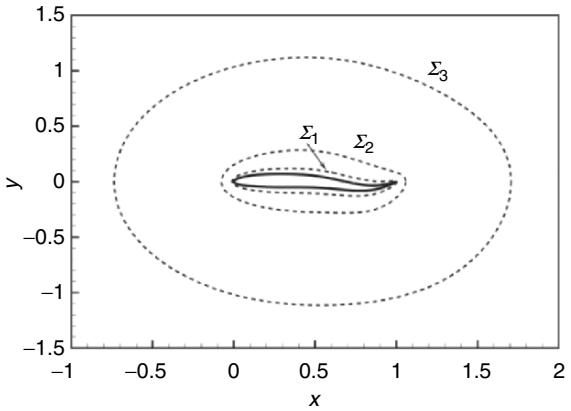


**Fig. 11.24.** A flexible airfoil with centerline defined by (11.94). Airfoil shape and three selected deformable control surfaces $\Sigma_i,\ i = 1,2,3$. From Wu et al. (2005d)

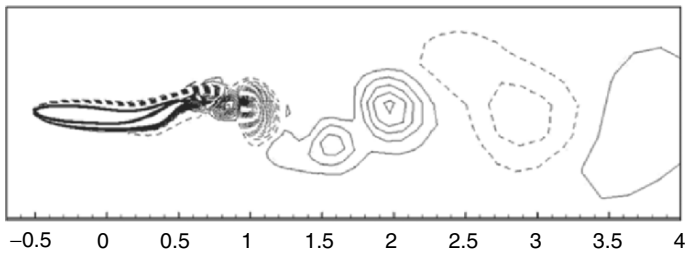


**Fig. 11.25.** An instantaneous vorticity contour plot for $c/U = 0.5$. Courtesy of Lu

and in Fig. 11.26 we plot the varying drag and lift computed by (11.92) and (11.93) over a period for the three $\Sigma$-locations at this phase speed. For comparison the result computed by (11.1a) is also shown. This example confirms the correctness of the derivative-moment formulas and the $\Sigma$-independent of of the results. The drag will become a thrust when $c/U > 1$ (not shown).

The second example is a local-dynamics diagnosis of the internal incompressible flow in a turbofan compressor, where the performance is no longer characterized by force and moment but the derivative-moment transformation can still be applied. After passing a row of rotor blades of angular velocity $\Omega$ about the $z$-axis, the fluid gains pressure and is slowed down at the exit. We analyze the flow in a domain $V$ consisting of a passage between two neighboring blades. Let the inlet plane at $z = z_0$ and exit wake plane at $z = z_1$ be perpendicular to the $z$-axis, and denoted by $S_0$ and $S_1$, respectively. Then a key stationary performance parameter is the *total-pressure ratio*, which should be as high as possible:

$$\beta \equiv \frac{1}{S_1 P_\infty} \int_{S_1} \overline{P}\, \mathrm{d}S, \quad P \equiv p + \frac{1}{2}\rho q^2, \tag{11.95}$$

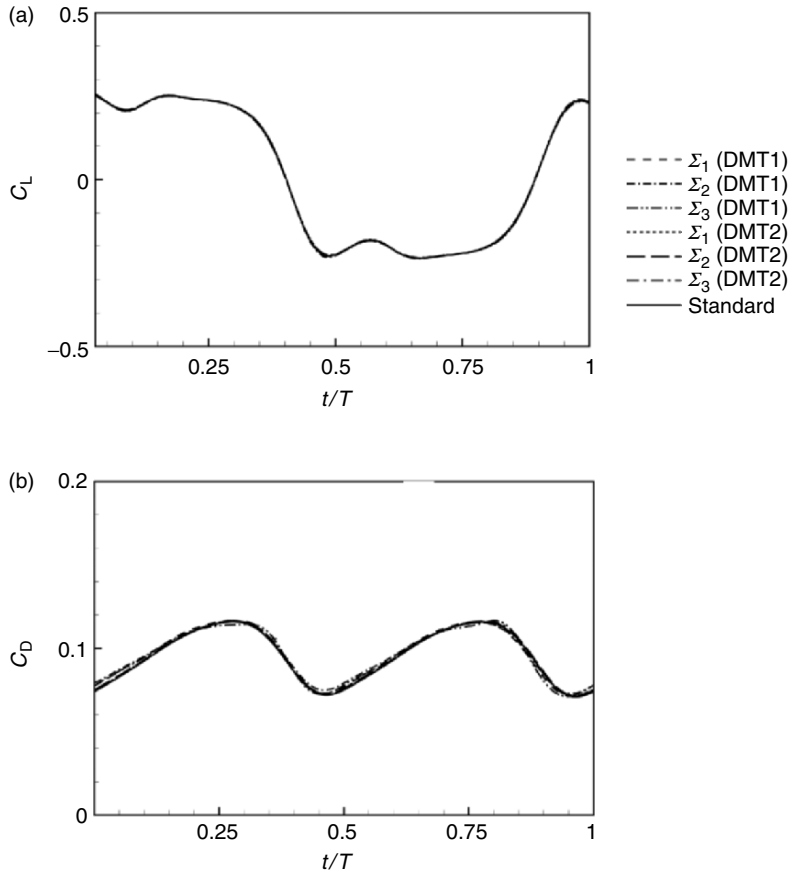


**Fig. 11.26.** The time history of drag and lift coefficients of the flexible airfoil for $c/U = 0.5$, computed by (11.1a), (11.92), and (11.93) for three deformable $\Sigma_i$, $i = 1, 2, 3$. The curves computed by these formulas are marked by standard, DMT1, and DMT2, respectively. From Wu et al. (2005d)

where $q = |\boldsymbol{u}|$ and the overline denotes the time average over a cycle. Another stationary performance parameter is the compressor *efficiency* $\eta$, which we define based on (2.76):

$$\eta \equiv \frac{1}{\Omega \overline{M}_z} \left( \int_{S_1} \overline{Pu}_z \, \mathrm{d}S - P_\infty U S_0 \right), \tag{11.96}$$

where $M_z$ is the moment acting to the flow by the rotating blade. Since on both the solid blade/hub surface and the exit plane $S_1$ the work rate done by pressure force is much larger than that done by viscous stress, the latter is neglected. $Pu_z$ represents the *total-pressure flux* entering into the combustor.

Now, to find the local flow structures that influence the total-pressure radio $\beta$, we use cylindrical coordinates $(r, \theta, z)$ and write $\mathrm{d}S = r\,\mathrm{d}r\,\mathrm{d}\theta$ in (11.95). Since for any function $f(r, \theta, z, t)$ there is

$$fr = \frac{1}{2}\frac{\partial}{\partial r}(fr^2) - \frac{r^2}{2}\frac{\partial f}{\partial r},$$

we can make an one-dimensional derivative-moment transformation:

$$\int_{S_1} Pr\,\mathrm{d}r\,\mathrm{d}\theta = \frac{1}{2}\left[\int_0^{2\pi}(P_\mathrm{s}R_\mathrm{s}^2 - P_\mathrm{h}R_\mathrm{h}^2)_{z_1}\,\mathrm{d}\theta - \int_{S_1} r^2\frac{\partial P}{\partial r}\,\mathrm{d}r\,\mathrm{d}\theta\right], \tag{11.97}$$

where $r = R_\mathrm{s}(z)$ and $r = R_\mathrm{h}(z)$ define the generators of the shroud and hub, respectively, and

$$P_\mathrm{s} \equiv P(R_\mathrm{s}, z_1, \theta) = p(R_\mathrm{s}, z_1, \theta), \tag{11.98a}$$

$$P_\mathrm{h} \equiv P(R_\mathrm{h}, z_1, \theta) = p(R_\mathrm{h}, z_1, \theta) + R_\mathrm{h}^2\Omega^2 \tag{11.98b}$$

due to the adherence condition. It is now evident that the local dynamics enters the last term on the right-hand side of (11.97), through the momentum equation (11.4). Hence, (11.95) is cast to

$$\beta = \frac{1}{2S_1P_\infty}\left[\int_0^{2\pi}(\overline{P}_\mathrm{s}R_\mathrm{s}^2 - \overline{P}_\mathrm{h}R_\mathrm{h}^2)_{z_1}\,\mathrm{d}\theta + \int_{S_1}\rho r(\overline{\omega_\theta u}_z - \overline{\omega_z u}_\theta)\,\mathrm{d}S\right], \tag{11.99}$$

which clearly reveals that, except the boundary line integrals, the key mechanism is the $r$-component of the Lamb vector. A similar derivative-moment transformation can be made for the integral of $Pu_z$ in determining the efficiency $\eta$, see (11.96):

$$\int_{S_1}\overline{Pu}_z\,\mathrm{d}S = \frac{1}{2}\int_{S_1} r\left[\overline{\omega_\theta(\rho u_z^2 + P)} - \rho\overline{u_z u_\theta \omega}_z - \overline{P\frac{\partial u_r}{\partial z}}\right]\mathrm{d}S. \tag{11.100}$$

On the other hand, applying (11.45) along with (11.47) to the open surface of the blade, after neglecting the viscous stresses we obtain

$$M_z = -\frac{1}{2}\int_{S_\mathrm{b}}\rho r^2\sigma_{pz}\,\mathrm{d}S + \frac{1}{2}\oint_{\partial S_\mathrm{b}} pr^2\,\mathrm{d}z, \tag{11.101}$$

where $S_\mathrm{b}$ is the area of the blade surface with $\partial S_\mathrm{b}$ being its boundary line at the juncture with the hub. Therefore, a simultaneous analysis of the integrand of $\beta$, $\eta$, and $\boldsymbol{M}$ forms a basis of local-dynamics diagnosis and can fill the gap between conventional analysis and blade design. the extension to compressible flow is straightforward.

Li and Guo (2005) have applied (11.99) and (11.100) to diagnose the blade design of a test model of low-speed compressor. Under the design condition, the rotational speed is 3000 rpm, total-pressure ratio was 150 mm (water),

total mass flux was $2.4\,\mathrm{m}^3\,\mathrm{s}^{-1}$, and efficiency was 85%. They found that the dominant local-dynamics mechanism in both (11.99) and (11.100) is a strong $\omega_\theta > 0$, of which the best favorable effect occurs at large $r$, i.e., near the shroud. By a Reynolds-averaged Navier–Stokes computation, Li and Guo observed a quite uniform distribution of the total-pressure flux $Pu_z$ across a sectional plane at the blade trailing edge, but this performance was deteriorated under small-flux condition and became the worst when stall occurred. The corresponding distributions of $\omega_\theta$ indicated that the efficiency drop is associated with the accumulation of large $\omega_\theta$ toward the region of smaller $r$. Based on this diagnosis and using (11.101), then, Li and Guo conducted a redesign of the blade shape, see Fig. 11.27, which improved significantly the uniformity of the $\omega_\theta$-distribution under the off-design conditions.

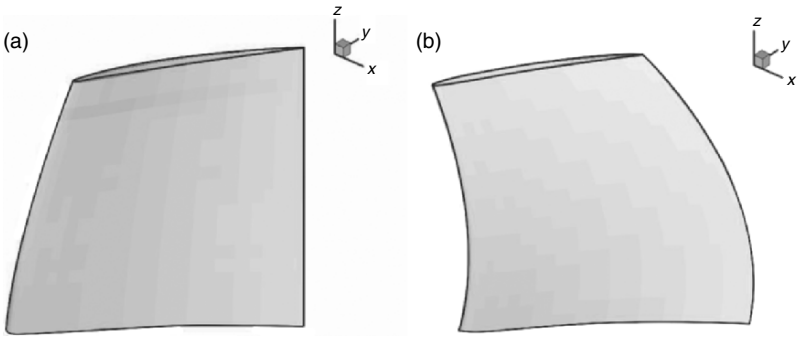


**Fig. 11.27.** (**a**) The original blade shape of a test model of low-speed compressor, and (**b**) the improved shape based on local-dynamics diagnosis. Courtesy of Li

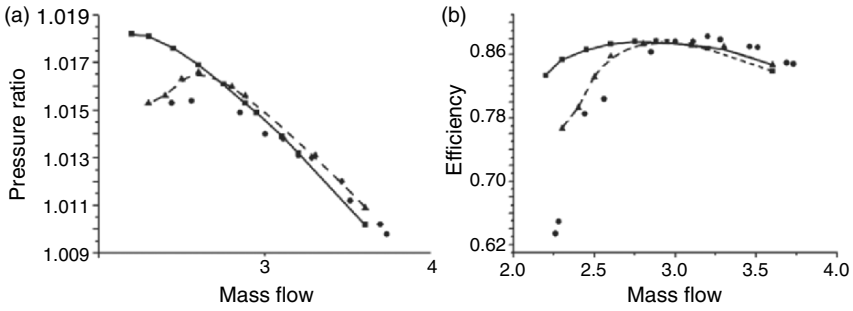


**Fig. 11.28.** The performance of the two blade shapes of Fig. 11.27. (**a**) total pressure ratio. (**b**) Efficiency. *Dashed line* and *solid line* represent the numerical results for the original blade and new blade, respectively. The *filled circles* are the experimental results of the original blade. Reproduced from Li and Guo (2005)

The total-pressure ratio and efficiency were accordingly enhanced at small-flux side, as evidenced by Fig. 11.28. The stall margin is considerably enlarged.

## Summary

1. The emphasis of the aerodynamics theories presented in this chapter is to reveal the local dynamic processes that have net contribution to the total force and moment. This information is very valuable for understanding the physics and in flow diagnosis, configuration design, and flow control. The local dynamic processes are measured by the spatial–temporal derivatives of relevant flow quantities, which at large Reynolds numbers are highly localized to a few discrete peaks associated with key flow structures. These structures have full appearance only in differential equations, but can be made reappear in integrated force and moment by projection or derivative-moment transformations (DMT). Both types of approaches arrive at the same overall physical picture: at low Mach numbers the dominant mechanism in the force and moment is the shearing process, while at supersonic Mach numbers it becomes the compressing process.
2. The projection theory projects the Navier–Stokes equation onto the vector space spanned by the unit acyclic potential velocities and then take integration. In particular, the integrated pressure force is replaced by those terms in the momentum balance that characterize the shearing and compressing processes, mainly the Lamb vector (vortex force) and density variation. The theory applies to externally unbounded fluid at rest at infinity or having uniform velocity. Due to the fast far-field convergence of the acyclic potential velocity, the force can be calculated from the flow data in a sufficiently large but finite domain.
3. The DMT-based theory transforms the integrands of standard force and moment formulas by the moments of their spatial–temporal derivatives that represent the local dynamics. In its general form, the theory is formulated for arbitrary domain, of which the outer boundary can extend to infinity, remain finite, or shrink to the body surface. This flexibility permits a global view, a mid-field view, a near-field view, and an on-wall close view, respectively. At two opposite extremal views, the theory recovers the infinite-domain vorticity-moment theory and boundary vorticity-flux theory, respectively. The former is the first systematic DMT-based theory for the force and moment, with very intuitive vortex-dynamics interpretation. The classic incompressible aerodynamic theories can be easily deduced from these DMT-based theories at certain approximate levels.
4. For the same flow field, each view of the DMT-based arbitrary-domain theory has its own key dynamic mechanism as the net contributor to the total force and moment. These include the rate of change of impulse and angular impulse, the Lamb-vector integrals along with unsteady vorticity moments, the vorticity diffusion moments, and the stress-related

boundary vorticity fluxes, etc. These multiple pictures reflect different evolution stages or aspects of the same flow; capturing any one of them can lead to the correct total force and moment. Therefore, a rich "multi-dimensional" means is available for a thorough flow analysis.

5. High-accuracy estimate of total force by experimentally measured data also calls for unconventional expressions with easily measurable integrand. Vorticity dynamics and DMT help achieve this goal and clarify some long-standing issues. For steady incompressible flow at large Reynolds numbers, the minimum requirement for the measurement is to survey a wake plane over the region where disturbance velocity is nonzero. To survey a small vortical region of the wake plane, one can obtain the profile drag but at most a good yet still approximate estimate of the lift, and a rough estimate of the induced drag. For unsteady incompressible flow, the use of a proper DMT identity permits an accurate estimate of total force by surveying the flow data on a control surface alone.
6. The application of derivative-moment transformations is not confined to external flow problems. The theory may well be applied to local-dynamics diagnosis of internal flows with different performance parameters.

# 12

# Vorticity and Vortices in Geophysical Flows

Geophysical fluid dynamics studies the motion of the atmosphere and oceans that cover the earth, which is the basis of meteorology and oceanography, where the vorticity and circulation are also among the most basic concepts as pioneered by the work of Bjerknes (1898, 1902). The self-rotation of the earth produces the Coriolis force, which brings in many unique and attractive topics to the vorticity dynamics and vortex motion in *rotating fluid dynamics*. In particular, the conservation of the *potential vorticity* is so fundamental that *to a large extent the geophysical fluid dynamics may be regarded as the dynamics of the potential-vorticity conservation*.

Moreover, the coherent vortical structures in a rotating fluid are relevant to large-scale geophysical flows, and hence to the understanding of atmospheric and oceanic circulations as well as turbulence therein. Thus, it is important to investigate isolated vortices, including their dynamics, instability properties, mutual interaction, and motion in rotating fluid. Owing to the Coriolis force and approximate two-dimensionality of geophysical flows, in several basic aspects these structures and interactions are quite different from those in a three-dimensional flow without system rotation as treated in preceding chapters.

This chapter is an introduction to geophysical vorticity and vortex dynamics. We start from the basic equations in rotating and density-stratified fluid, discussing relevant dimensional parameters, scalings, and a few frequently used simplified models derived thereby. The concept of potential vorticity is then introduced and some of its most significant applications are illustrated. The evolution process of vortical structures, as well as the structures of barotropic and baroclinic vortices, are discussed later within the two-dimensional approximation. We finally discuss the motion of strong large-scale atmospheric vortices. For more comprehensive and in-depth materials of some of these topics, the interested reader may consult, e.g. Gill (1982a), Bengtsson and Lighthill (1982), Hoskins et al. (1985), Pedlosky (1987), Hopfinger and van Heijst (1993), Voropayev and Afanasyev (1994), Salmon (1998), and McWilliams (2005).

## 12.1 Governing Equations and Approximations

### 12.1.1 Effects of Frame Rotation and Density Stratification

The fluids in both atmosphere and oceans are weakly density-stratified, with the density $\rho$ varying as the height when the fluid is at rest. For the atmosphere we use the perfect-gas equation $p = \rho RT$ where $R$ is the gas constant. For seawater the equation of state can be approximated by

$$\rho = \rho_0[1 - \alpha_1(T - T_0) + \alpha_2(S - S_0)],$$

where $S$ is the *salinity* (grams/kilograms), and $\alpha_1$ and $\alpha_2$ are empirically determined constants. For large-scale fluid motion under gravity, we may assume incompressibility, but general thermodynamic relations introduced in Sect. 2.3.3 are applicable whenever necessary. Then, in an inertial frame of reference ("absolute frame") $\Sigma$, the continuity equation and momentum equation read, respectively,

$$\frac{\mathrm{D}\rho}{\mathrm{D}t} = 0 \quad \text{or} \quad \frac{\partial\rho}{\partial t} + \boldsymbol{u}\cdot\nabla\rho = 0, \tag{12.1}$$

$$\frac{\mathrm{D}\boldsymbol{u}}{\mathrm{D}t} = -\frac{1}{\rho}\nabla p + \boldsymbol{g} + \nu\nabla^2\boldsymbol{u}, \tag{12.2}$$

where $\boldsymbol{g}$ is the gravitational acceleration at the earth surface. In geophysics, however, the flows are observed in a frame of reference $\Sigma'$ fixed to the earth, which has angular velocity $\boldsymbol{\Omega} = \Omega\boldsymbol{k}$, with $\boldsymbol{k}$ being the unit vector along the rotating axis. To establish the hydrodynamic equations in such a rotating frame, we first recall the relation between the relative acceleration viewed in $\Sigma'$ and the "absolute acceleration" in an inertial frame $\Sigma$.

Let a vector $\boldsymbol{e}$ of constant magnitude rotate with angular velocity $\boldsymbol{\Omega}$, such that

$$\frac{\mathrm{d}\boldsymbol{e}}{\mathrm{d}t} = \boldsymbol{\Omega}\times\boldsymbol{e}. \tag{12.3}$$

Thus, if $\Sigma'$ rotates about a point $O$ with angular velocity $\boldsymbol{\Omega}$ in which the orthonormal basis vectors are $\boldsymbol{e}'_i$ $(i = 1, 2, 3)$, then the rate of change of an arbitrary vector $\boldsymbol{b}$, appearing as $b'_i\boldsymbol{e}'_i$ in $\Sigma'$, reads

$$\frac{\mathrm{d}\boldsymbol{b}}{\mathrm{d}t} = \frac{\mathrm{d}b'_i}{\mathrm{d}t}\boldsymbol{e}'_i + b'_i\frac{\mathrm{d}\boldsymbol{e}'_i}{\mathrm{d}t} = \left(\frac{\mathrm{d}\boldsymbol{b}}{\mathrm{d}t}\right)_{\mathrm{r}} + \boldsymbol{\Omega}\times\boldsymbol{b}, \tag{12.4}$$

where $(\mathrm{d}\boldsymbol{b}/\mathrm{d}t)_{\mathrm{r}}$ is the relative rate of change of $\boldsymbol{b}$. Denoting $\mathrm{d}\boldsymbol{\Omega}/\mathrm{d}t$ by $\dot{\boldsymbol{\Omega}}$, and applying (12.4) to the position vector $\boldsymbol{r}$ of a fluid element from $O$ and the "absolute velocity" $\boldsymbol{u}$, we have

$$\frac{\mathrm{d}\boldsymbol{r}}{\mathrm{d}t} = \left(\frac{\mathrm{d}\boldsymbol{r}}{\mathrm{d}t}\right)_{\mathrm{r}} + \boldsymbol{\Omega}\times\boldsymbol{r} \quad \text{or} \quad \boldsymbol{u} = \boldsymbol{u}' + \boldsymbol{\Omega}\times\boldsymbol{r}, \tag{12.5}$$

$$\frac{\mathrm{D}\boldsymbol{u}}{\mathrm{D}t} = \left(\frac{\mathrm{D}\boldsymbol{u}}{\mathrm{D}t}\right)_{\mathrm{r}} + \boldsymbol{\Omega}\times\boldsymbol{u} + \dot{\boldsymbol{\Omega}}\times\boldsymbol{r}, \tag{12.6}$$

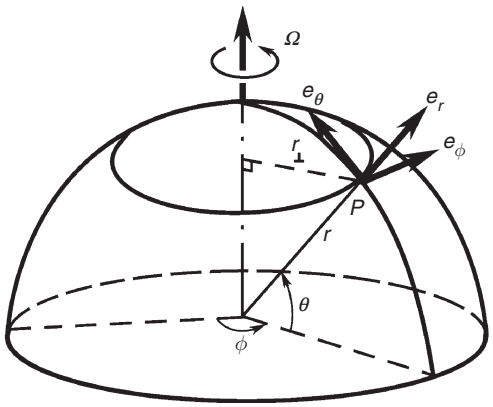


**Fig. 12.1.** Local orthonormal triad at latitude $\theta$

respectively, where $\boldsymbol{u}' = (\mathrm{d}\boldsymbol{r}/\mathrm{d}t)_\mathrm{r}$ is the relative velocity, which is related to the absolute vorticity by

$$\boldsymbol{\omega} = \boldsymbol{\omega}' + 2\boldsymbol{\Omega}, \tag{12.7}$$

Conventionally, one calls $2\boldsymbol{\Omega}$ the *planetary vorticity*. Thus, the "absolute acceleration" $\boldsymbol{a} = \mathrm{D}\boldsymbol{u}/\mathrm{D}t$ and the relative acceleration $\boldsymbol{a}' = (\mathrm{D}\boldsymbol{u}'/\mathrm{D}t)_\mathrm{r}$ are related by

$$\boldsymbol{a} = \boldsymbol{a}' + 2\boldsymbol{\Omega} \times \boldsymbol{u}' + \boldsymbol{\Omega} \times (\boldsymbol{\Omega} \times \boldsymbol{r}) + \dot{\boldsymbol{\Omega}} \times \boldsymbol{r}, \tag{12.8}$$

where the *centrifugal acceleration* is independent of the flow and conservative:

$$\boldsymbol{\Omega} \times (\boldsymbol{\Omega} \times \boldsymbol{r}) = \nabla\phi_\mathrm{c}, \quad \text{where} \quad \phi_\mathrm{c} = \frac{1}{2}[(\boldsymbol{\Omega} \cdot \boldsymbol{r})^2 - \Omega^2 r^2] \tag{12.9}$$

is the *centrifugal potential*. Its sum with the gravitational potential $\phi_\mathrm{g} = -GM/r$ ($M$ and $G$ are the earth's mass and universal gravitational constant, respectively), $\Phi = \phi_\mathrm{c} + \phi_\mathrm{g}$, is called the *geopotential*. The direction and magnitude of $\nabla\Phi$ are still called "vertical" and the "acceleration $g$ due to gravity", respectively.

The form of $\phi_\mathrm{c}$ suggests that, at a point $P$ of latitude $\theta$, it is natural to decompose $\boldsymbol{\Omega}$ into components normal and tangent to the spherical earth surface of radius $R$. As shown in Fig. 12.1, we introduce spherical coordinates $(\phi, \theta, r)$ with basis vectors $(\boldsymbol{e}_\phi, \boldsymbol{e}_\theta, \boldsymbol{e}_r)$ at a point $P$, pointing to east, north, and up, respectively,[1] so that

$$\boldsymbol{\Omega} = \boldsymbol{\Omega}_\perp + \boldsymbol{\Omega}_\pi, \quad \boldsymbol{\Omega}_\perp = \boldsymbol{e}_r \Omega \sin\theta, \quad \boldsymbol{\Omega}_\pi = \boldsymbol{e}_\theta \Omega \cos\theta. \tag{12.10}$$

[1] In conventional spherical coordinates the meridian angle is measured from the north pole, i.e., $90^\circ - \theta$. Note that the earth is not precisely a sphere, and for high-accuracy analysis more complicated coordinates are necessary (e.g., Gill 1982a).

Then (12.9) yields

$$\nabla\phi_{\rm c} = \Omega_\pi r(\boldsymbol{e}_\theta\Omega_\perp - \boldsymbol{e}_r\Omega_\pi), \quad \phi_{\rm c} = -\frac{1}{2}\Omega_\pi^2 r^2 = -\frac{1}{2}\Omega^2 r_\perp^2, \tag{12.11}$$

where $r_\perp = r\cos\theta$ is the perpendicular distance to the earth's rotating axis. Thus, the centrifugal force is solely due to $\boldsymbol{\Omega}_\pi$.

Substituting (12.7), (12.8), and (12.9) into (12.2), and neglecting $\dot{\boldsymbol{\Omega}}$, we obtain the Navier–Stokes equation for the relative motion of the atmosphere and ocean in the earth's rotating frame $\Sigma'$:

$$\frac{{\rm D}\boldsymbol{u}'}{{\rm D}t} = -2\boldsymbol{\Omega}\times\boldsymbol{u}' - \frac{1}{\rho}\nabla p - \nabla\Phi - \nu\nabla\times\boldsymbol{\omega}', \tag{12.12}$$

of which the curl yields the transport equation for the relative vorticity:

$$\frac{\partial\boldsymbol{\omega}'}{\partial t} + \boldsymbol{u}'\cdot\nabla\boldsymbol{\omega}' = (\boldsymbol{\omega}' + 2\boldsymbol{\Omega})\cdot\nabla\boldsymbol{u}' + \frac{1}{\rho^2}\nabla\rho\times\nabla p + \nu\nabla^2\boldsymbol{\omega}'. \tag{12.13}$$

Note that because $\boldsymbol{\omega}'_{,t} = \boldsymbol{\omega}_{,t} - 2\dot{\boldsymbol{\Omega}}$ and $\nabla\boldsymbol{\omega}' = \nabla\boldsymbol{\omega}$, (12.13) can well be expressed in terms of absolute vorticity $\boldsymbol{\omega} = \boldsymbol{\omega}' + 2\boldsymbol{\Omega}$:

$$\frac{\partial\boldsymbol{\omega}}{\partial t} + \boldsymbol{u}'\cdot\nabla\boldsymbol{\omega} = \boldsymbol{\omega}\cdot\nabla\boldsymbol{u}' + \frac{1}{\rho^2}\nabla\rho\times\nabla p + \nu\nabla^2\boldsymbol{\omega}, \tag{12.14}$$

which enables computing only the absolute vorticity and relative velocity.

Recall the discussions of Sect. 4.1, we see that (12.12) contains two interior sources of relative vorticity. One is the *Coriolis acceleration* $2\boldsymbol{\Omega}\times\boldsymbol{u}'$, of which the curl can be cast to

$$2\nabla\times(\boldsymbol{\Omega}\times\boldsymbol{u}') = 2\mathbf{B}'\cdot\boldsymbol{\Omega}, \tag{12.15}$$

where $\mathbf{B}' = \vartheta\mathbf{I} - (\nabla\boldsymbol{u}')^{\rm T}$ is the surface deformation tensor viewed in $\Sigma'$, which depends on the flow. To see how $\boldsymbol{\omega}'$ is created by the Coriolis force, consider the rate of change of circulation of a closed material loop $\mathcal{C}$. To isolate this effect, assume the flow is homoentropic and inviscid. Then in (3.157) we simply have $\nabla\times\boldsymbol{a}' = -2\mathbf{B}'\cdot\boldsymbol{\Omega}$, so the Kelvin circulation formula (2.32) yields

$$\frac{{\rm d}\Gamma'_{\mathcal{C}}}{{\rm d}t} = \int_{\mathcal{S}}(\nabla\times\boldsymbol{a}')\cdot{\rm d}\boldsymbol{S} = -2\boldsymbol{\Omega}\cdot\int_{\mathcal{S}}{\rm d}\boldsymbol{S}\cdot\mathbf{B}' = -2\boldsymbol{\Omega}\cdot\frac{{\rm d}\boldsymbol{\mathcal{S}}}{{\rm d}t} \tag{12.16}$$

due to (2.26), where $\boldsymbol{\mathcal{S}}$ is the vectorial surface spanned by $\mathcal{C}$. Therefore, as sketched in Fig. 12.2, if $\boldsymbol{\mathcal{S}}$ is reduced due to a velocity component $\boldsymbol{u}'_\perp$ normal to $\mathcal{C}$, and if this vectorial area change is not perpendicular to the direction of $\boldsymbol{\Omega}$, then there will be a net *relative-vorticity creation* inside the loop $\mathcal{C}$. In other words, a relative velocity gradient may create new $\boldsymbol{\omega}'$ even if the latter is initially zero, and then stretch and tilt the created vorticity tubes. This is a basic property of rotating fluid motion.

The second internal vorticity source is the *baroclinicity* due to density stratification, see (3.157) and Sect. 4.1.2, although the fluid is treated as

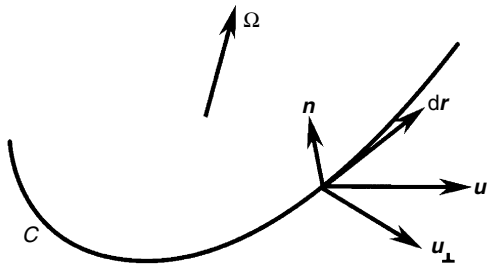


**Fig. 12.2.** A net relative vorticity creation inside a loop

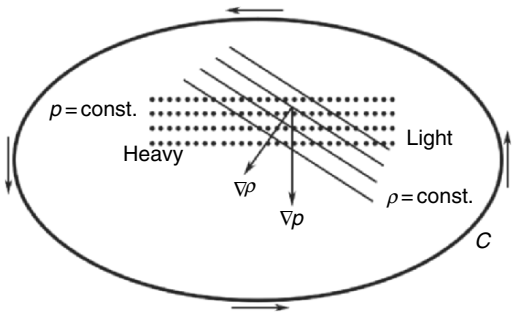


**Fig. 12.3.** Vorticity creation by baroclinicity

incompressible. The density variation in ocean is merely a few percentages, so the baroclinicity effect occurs mainly in the atmosphere. To isolate this effect, ignore the Coriolis force and viscosity, so that in the place of (12.16) we now have (4.10a):

$$\frac{\mathrm{d}\Gamma_C}{\mathrm{d}t} = -\oint_C \frac{1}{\rho}\mathrm{d}p = \int_S \frac{1}{\rho^2}\boldsymbol{n}\cdot(\nabla\rho\times\nabla p)\,\mathrm{d}S. \tag{12.17}$$

For example, if the air on the right is lighter than that on the left but both experience the same upward pressure force $-\nabla p$, see Fig. 12.3, then the right part ascends faster, resulting in a counterclockwise circulation. This circulation finally disappears as $\nabla\rho$ gradually turns to the direction of $\nabla p$. Note that the difference of the Coriolis force and baroclinicity is that while the former creates only relative vorticity but no absolute vorticity at all, the latter creates both in general.

The earlier exact equations are quite complicated in applications. Since geophysical fluid dynamics covers very wide range of length and time scales, a rich hierarchy of simplified models of the Navier–Stokes equation (12.12) and corresponding vorticity equation (12.13) has been developed and applied to different problems as surveyed by McWilliams and Gent (1980). A few major models will be introduced later.

### 12.1.2 Boussinesq Approximation

The first significant simplification is the well-known *Boussinesq approximation*, which assumes the density variation in the atmospheric region under study is small compared to a reference density $\rho_0(z)$ at each height $z$ from the earth, which is related to the reference pressure $p_0(z)$ by the hydrostatics equation

$$\frac{\mathrm{d}p_0}{\mathrm{d}z} = -\rho_0 g. \tag{12.18}$$

Namely, the effect of density stratification amounts to merely causing a *buoyancy*. Putting the system-rotation effect aside temporarily and letting the real pressure and density be $(p, \rho) = (p_0 + p', \rho_0 + \rho')$ with dynamic part $(p', \rho')$, (12.12) is cast to

$$\rho \frac{\mathrm{D}\boldsymbol{u}}{\mathrm{D}t} = -\nabla p' + \rho' \boldsymbol{g} + \mu \nabla^2 \boldsymbol{u}, \quad \boldsymbol{g} = -g\boldsymbol{e}_z.$$

Since by assumption $\rho'/\rho_0 \ll 1$, $\rho$ can be replaced by $\rho_0$ on the left-hand side:

$$\frac{\mathrm{D}\boldsymbol{u}}{\mathrm{D}t} = -\frac{1}{\rho_0}\nabla p' + \sigma \boldsymbol{g} + \nu \nabla^2 \boldsymbol{u}, \quad \sigma \equiv \frac{\rho'}{\rho_0} \ll 1, \quad \nu = \frac{\mu}{\rho_0}. \tag{12.19}$$

Thus, the dynamic pressure force per unit mass recovers curl-free, but $\nabla\sigma \times \boldsymbol{g}$ replaces the baroclinic term in (12.12) to become a source of vorticity.

In passing, we mention that under this approximation the continuity equation for stratified incompressible flow and the vertical component of the momentum equation for slow motion are

$$\frac{\partial \rho'}{\partial t} + w\frac{\mathrm{d}\rho}{\mathrm{d}z} = 0, \quad \rho_0 \frac{\partial w}{\partial t} = -\frac{\partial p'}{\partial z} - \rho' g,$$

respectively. Eliminating $\rho'$ then yields

$$\frac{\partial^2 w}{\partial t^2} + N^2 w = -\frac{1}{\rho_0}\frac{\partial^2 p'}{\partial z \partial t}, \tag{12.20}$$

where

$$\pm N \equiv \pm\sqrt{-\frac{g}{\rho_0}\frac{\mathrm{d}\rho}{\mathrm{d}z}} \tag{12.21}$$

has dimension $[T]^{-1}$ and is referred to as as the *buoyancy frequency* (commonly known as the *Brunt–Väisälä frequency*), because if $p' = 0$ in (12.20) then a vertical motion of a fluid parcel will be produced solely by the buoyancy as restoring force at frequency $N$. Under the Boussinesq approximation, a density-stratified flow will be hydrostatically stable if $\mathrm{d}\rho/\mathrm{d}z < 0$ and unstable if $\mathrm{d}\rho/\mathrm{d}z > 0$.

Evidently, the Boussinesq approximation of (12.13) is

$$\frac{\partial \boldsymbol{\omega}'}{\partial t} + \nabla \times (\boldsymbol{\omega}' \times \boldsymbol{u}') = 2\boldsymbol{\Omega} \times \boldsymbol{u}' + \nabla\sigma \times \boldsymbol{g} + \nu\nabla^2\boldsymbol{\omega}'. \tag{12.22}$$

Further approximations require scale analysis to identify the leading-order mechanisms. To this end we nondimensionalize (12.22). Let $L$ and $U$ be the characteristic length and velocity scales of the relative fluid motion under consideration so that the time scale is $L/U$, we obtain (dimensionless relative quantities are denoted by the asterisk)

$$Ro\left\{\frac{\partial \boldsymbol{\omega}^*}{\partial t^*} + \nabla^* \times (\boldsymbol{\omega}^* \times \boldsymbol{u}^*)\right\} = 2\boldsymbol{k} \cdot \nabla^* \boldsymbol{u}^* - \frac{1}{Fr}\nabla^*\sigma \times \boldsymbol{e}_z + Ek\nabla^{*2}\boldsymbol{\omega}^*, \tag{12.23a}$$

where, with the Reynolds number defined by $Re = UL/\nu$ as usual,

$$Ro = \frac{U}{\Omega L}, \quad Ek = \frac{\nu}{\Omega L^2} = \frac{Ro}{Re}, \quad Fr = \frac{\Omega U}{g} \tag{12.23b}$$

are the *Rossby number*, *Ekman number*, and *Froude number*, respectively. The Rossby number measures the relative importance of the relative and planetary vorticities. Then, since $Ek \sim Ro/Re$, except within the terrestrial boundary layer where the viscous effect is significant, large-scale flows with $Ro = O(1)$ or smaller all have $Ek \ll 1$ (for ocean there is $Ek = 10^{-14}$). Thus we ignore the viscosity in the rest of this chapter.

The orders of magnitude of the Rossby numbers for several typical flows on the earth, along with their characteristic length and velocity scales, are listed in Table 12.1. The most intense atmospheric vortices are *hurricanes* (*typhoons* in the North-Western Pacific) and tornados at small and large $Ro$, respectively, which are associated with extreme and hazardous weather events.

**Table 12.1.** The orders of magnitude of the Rossby numbers for typical geophysical fluid flows

| flow phenomena | length scales | velocity scales | orders of $Ro$ |
|---|---|---|---|
| bath-stub vortex | 1 cm | $0.1\,\mathrm{m\,s^{-1}}$ | $10^5$ |
| dust devil | 3 m | $10\,\mathrm{m\,s^{-1}}$ | $3 \times 10^4$ |
| tornado | 50 m | $150\,\mathrm{m\,s^{-1}}$ | $3 \times 10^4$ |
| hurricane | 500 km | $50\,\mathrm{m\,s^{-1}}$ | 1 |
| low-pressure system | 1,000 km | $1.5\,\mathrm{m\,s^{-1}}$ | $10^{-1}$ |
| oceanic circulation | 3,000 km | $1.5\,\mathrm{m\,s^{-1}}$ | $3 \times 10^{-3}$ |

From Lugt (1983)

### 12.1.3 The Taylor–Proudman Theorem

If the inviscid fluid motion is barotropic, the Rossby number will be the only dimensionless parameter. It is then evident from (12.23a) that a small-$Ro$ flow has yet another remarkable feature:

$$\lim_{Ro\to 0} 2\boldsymbol{k}\cdot\nabla\boldsymbol{u}^* = \boldsymbol{0}. \tag{12.24}$$

Namely, any slow steady motion in a rapidly rotating system tends to be independent of the axial position. This result was first pointed out by Hough (1897) according to Gill (1982a,b), then by Proudman (1916), and then experimentally confirmed by Taylor (1923). Taylor's flow visualization photos with a rotating dish are shown as Plate 23 of Batchelor (1967). A drop of colored fluid is quickly drawn out into a thin cylindrical sheet parallel to the rotating axis. More astonishingly, a short obstacle moving at the bottom of the dish can carry an otherwise stagnant column of the fluid with it (the *Taylor column*), see the sketch of Fig. 12.4. Although not in mathematical rigor, this result is now known as (cf. Batchelor 1967).

**The Taylor–Proudman Theorem.** *Steady motions at small Rossby number must be a superposition of a two-dimensional motion in the lateral plane and an axial motion which is independent of the axial position.*

The considerable significance of the Taylor–Proudman theorem in geophysical flows was later realized, and since then many experiments and numerical simulations have confirmed the tendency of the flow to be two-dimensionalized as $Ro \to 0$; e.g., Carnevale et al. (1997) and references therein. Recent studies have explored into the dynamic process toward two-dimensionalization and into rotating turbulence, e.g., Wang et al. (2004), Chen et al. (2005), and references therein.

We remark that the Taylor–Proudman theorem can be understood in a different way. If an inviscid and barotropic relative flow is steady with nonlinear

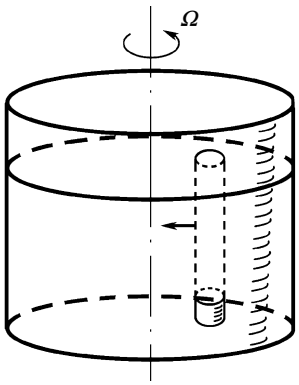


**Fig. 12.4.** The Taylor column in a rapidly rotating fluid

advection being identically zero, then the motion must be exactly described by the theorem even if $Ro$ is not small.[2]

### 12.1.4 Shallow-Water Approximation

We return to the general inviscid equations and from now on drop the prime for relative quantities. While for planetary-scale motion the spherical coordinates $(\phi, \theta, r)$ of Fig. 12.1 are appropriate (cf. Batchelor 1967), our main concern will be the motion with characteristic horizontal length $L \sim R\Delta\theta$ of order of 100 km or larger ($\Delta\theta$ is the latitude variation around a reference value $\theta_0$), but still much smaller compared to the earth radius $R$. Namely, if $D$ is the average depth of the atmosphere and oceans, we have

$$\frac{L}{R} \ll 1, \quad |\Delta\theta| \ll 1, \quad \frac{D}{L} = \epsilon \ll 1, \tag{12.25a,b,c}$$

by which some further simplifications can be made.

First, inequality (12.25a) implies that the effect of the earth curvature can be neglected, thus we may replace the spherical coordinates $(\phi, \theta, r)$ in Fig. 12.1 by local Cartesian coordinates $(x, y, z)$ on the earth surface, with velocity components $(u, v, w)$. This simplifies the inviscid version of (12.12) to

$$\frac{\mathrm{D}u}{\mathrm{D}t} + 2\Omega_\pi w - 2\Omega_\perp v = -\frac{1}{\rho}\frac{\partial \tilde{p}}{\partial x}, \tag{12.26a}$$

$$\frac{\mathrm{D}v}{\mathrm{D}t} + 2\Omega_\perp u = -\frac{1}{\rho}\frac{\partial \tilde{p}}{\partial y}, \tag{12.26b}$$

$$\frac{\mathrm{D}w}{\mathrm{D}t} - 2\Omega_\pi u = -\frac{1}{\rho}\frac{\partial \tilde{p}}{\partial z} - g, \tag{12.26c}$$

where$\Omega_\perp$ and $\Omega_\pi$ are given by (12.10), and $\tilde{p} = p + \rho\phi_\mathrm{c}$ is the modified pressure.

Secondly, let $U$ be the characteristic horizontal velocity. Then (12.25c) implies $w = O(\epsilon U)$ and $\omega_x, \omega_y = O(\epsilon\omega_z)$. Retaining the $O(1)$ terms only in (12.26) then leads to the *shallow-water approximation* for large-scale geophysical flows, where the fluid motion is basically horizontal (horizontal components are denoted by subscript $\pi$). The bottom boundary of the flow is allowed to have slowly-varying topography $z = h_\mathrm{B}(x, y)$, and the upper free boundary $z = \eta(x, y, t)$ may similarly have slow tidal motions at the scale of $L$, see Fig. 12.5.

We now combine the shallow-water model and Bousinnesq approximation. Let $\tilde{p} = p_0(z) + p'$ as before and denote $p' = \rho_0(z)\pi$, such that only the

[2] For example, Carnevale (2005, private communication) noticed that this would be the case if the relative motion is a steady axisymmetric and inviscid pure vortex, strictly governed by (6.18).

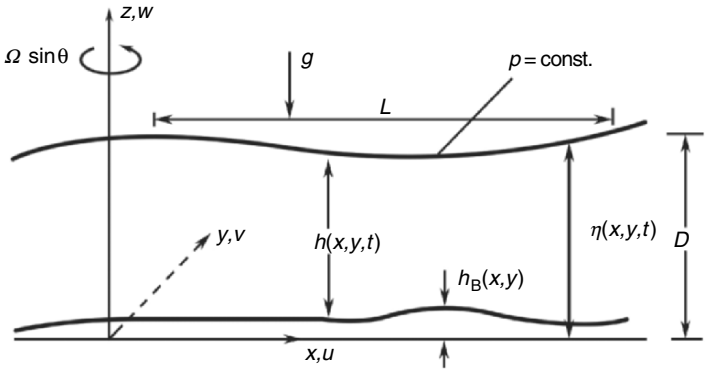


**Fig. 12.5.** Shallow-water approximation for large-scale geophysical fluid motion

vertical gradient of $p_0$ balances the gravitational force and that of $\pi$ balances the vertical acceleration $\mathrm{D}w/\mathrm{D}t$. Then integrating (12.18) from $z$ to $\eta$ yields

$$\tilde{p}(x, y, z, t) = \rho_0 g[\eta(x, y, t) - z] + \rho_0 \pi(x, y, z, t). \tag{12.27}$$

But, there is

$$\nabla_\pi \pi \sim \frac{D}{L}\frac{\partial \pi}{\partial z} \sim \frac{D}{L}\frac{\mathrm{D}_\pi w}{\mathrm{D}t} \sim \epsilon^2 \frac{U^2}{L},$$

which can be dropped. On the other hand, in (12.26a) we have $|\Omega_\pi w| \ll |\Omega_\perp v|$, so the $\Omega_\pi$-term can be dropped. Another $\Omega_\pi$-term in (12.26c) should then be dropped simultaneously, for otherwise the energy conservation would be violated (e.g., Salmon 1998). Consequently, the Coriolis force is solely controlled by

$$2\boldsymbol{\Omega}_\perp = 2\boldsymbol{e}_z \Omega \sin\theta \equiv \boldsymbol{f} = \boldsymbol{e}_z f, \tag{12.28}$$

where $f$ is called the *Coriolis parameter*. In contrast, $\boldsymbol{\Omega}_\pi$ only contributes to $\nabla\phi_\mathrm{c}$ as a modification of the "vertical" direction and the "acceleration $g$ due to gravity" (see the context following (12.9)). Therefore, by using (12.27) with $\nabla_\pi \pi$ dropped, and denoting $\boldsymbol{u} = \boldsymbol{v} + w\boldsymbol{e}_z$ with horizontal velocity $\boldsymbol{v} = (u, v)$ independent of $z$, the momentum equation is simplified to

$$\frac{\mathrm{D}_\pi \boldsymbol{v}}{\mathrm{D}t} + f\boldsymbol{e}_z \times \boldsymbol{v} = -g\nabla_\pi \eta = -\frac{1}{\rho_0}\nabla_\pi p, \tag{12.29}$$

where and below $\mathrm{D}_\pi/\mathrm{D}t \equiv \partial/\partial t + \boldsymbol{v} \cdot \nabla$. Thus, the horizontal fluid motion is somewhat like a Taylor column.[3]

[3] The quasi two-dimensional feature exists in shallow-water approximation even without system rotation. This feature is then enhanced by the rotation if the Rossby number is small.

Moreover, although $w$ is neglected in (12.28), as in the boundary layer theory the continuity equation $\nabla \cdot \boldsymbol{u} = 0$ has to be exactly satisfied:

$$\nabla_\pi \cdot \boldsymbol{v} \equiv \delta = -\frac{\partial w}{\partial z}. \tag{12.30a}$$

But since $\delta$ equals the rate of change of the cross area $A$ of a vertical fluid column, which is in turn related to that of the column height $h(x, y, t) = \eta(x, y, t) - h_{\mathrm{B}}(x, y)$, we have

$$\frac{\partial w}{\partial z} = -\frac{1}{A}\frac{\mathrm{D}_\pi A}{\mathrm{D}t} \quad \text{or} \quad \delta = -\frac{1}{h}\frac{\mathrm{D}_\pi h}{\mathrm{D}t}. \tag{12.30b}$$

Combining this and (12.30a) yields

$$\frac{\partial h}{\partial t} + \nabla_\pi \cdot (\boldsymbol{v}h) = 0. \tag{12.31}$$

Equations (12.29) and (12.31) are the *primitive equations* in shallow-water approximation. Note that $w$ depends on $z$ only linearly.

Then, (12.25b) implies that, in considering the variation of the Coriolis parameter at latitude, it suffices to retain the first two terms of the Taylor expansion:

$$\begin{aligned} f(\theta) &\simeq 2\Omega \sin\theta_0 + 2\Omega(\theta - \theta_0)\cos\theta_0 \\ &= 2\Omega \sin\theta_0 + 2\Omega \cos\theta_0 \frac{y}{R} \equiv f_0 + \beta_0 y, \end{aligned} \tag{12.32a}$$

where

$$\beta_0 \equiv \frac{2}{R}\Omega \cos\theta_0, \quad y = R(\theta - \theta_0). \tag{12.32b}$$

Then (12.29) is reduced to

$$\frac{\mathrm{D}_\pi \boldsymbol{v}}{\mathrm{D}t} + (f_0 + \beta_0 y)\boldsymbol{e}_z \times \boldsymbol{v} = -g\nabla_\pi \eta = -\frac{1}{\rho_0}\nabla_\pi p, \tag{12.33}$$

which is called *$\beta$-plane model* although $(x, y)$ vary along the sphere, and is accurate near $\boldsymbol{x} = \boldsymbol{0}$. The motion caused by the variation of $f$ with $\theta$ is called the *$\beta$-effect*. Simpler than this, if $L/R$ is negligible, we may simply take $f = f_0$ and obtain an approximation called the *$f$-plane model*.

It is of interest to look at the dimensionless form of (12.29) made by the horizontal characteristic length $L$ and velocity $U$, but $\eta$ is set to be $\eta = \mathrm{D}\eta^*$. Then

$$Ro\frac{\partial \boldsymbol{v}^*}{\partial t^*} + \boldsymbol{e}_z \times \boldsymbol{v}^* = -\frac{\epsilon}{Fr}\nabla_\pi^* \eta^*, \quad \epsilon = \frac{D}{L}, \tag{12.34}$$

where $Fr$ is the same as in (12.23b) and $Ro = U/fL$ is the *local Rossby number*. Sometimes the Froude number is alternatively defined as

$$F' \equiv \frac{U}{\sqrt{gD}} \quad \text{or} \quad F'' \equiv \frac{U}{ND}, \tag{12.35a}$$

where $N$ is the buoyancy frequency and, as will be seen in Sect. 12.3.3, $\sqrt{gD}$ is the phase velocity of the *gravity wave*, which for $D = 2\,\mathrm{km}$ is about $440\,\mathrm{m\,s^{-1}}$. Then (12.34) can be rewritten

$$Ro\frac{\partial \boldsymbol{v}^*}{\partial t^*} + \boldsymbol{e}_z \times \boldsymbol{v}^* = -\frac{Ro}{F'^2}\nabla_\pi^* \eta^*. \tag{12.35b}$$

Thus, for a steady flow with $Ro \ll F'^2$, the Taylor–Proudman theorem holds.

Finally, it is often convenient to replace (12.29) by the equivalent equations for vertical vorticity $\zeta$ and horizintal divergence $\delta$. Denote $\boldsymbol{\zeta}_\mathrm{a} = \boldsymbol{e}_z(\zeta + f)$ as the absolute vertical vorticity and recast (12.29) to

$$\frac{\partial \boldsymbol{v}}{\partial t} + \boldsymbol{\zeta}_\mathrm{a} \times \boldsymbol{v} = -g\nabla_\pi \left(\eta + \frac{1}{2g}|\boldsymbol{v}|^2\right),$$

so that its curl yields

$$\frac{\partial \boldsymbol{\zeta}_\mathrm{a}}{\partial t} + \boldsymbol{v} \cdot \nabla_\pi \boldsymbol{\zeta}_\mathrm{a} + \boldsymbol{\zeta}_\mathrm{a}\delta = 0. \tag{12.36}$$

Thus, along with the horizontal divergence of (12.29) and substituting $h(x, y, t) = \eta(x, y, t) - h_\mathrm{B}(x, y)$ into (12.31), see Fig. 12.5, we obtain the primitive shallow-water equations for three scalar variables $(\zeta, \delta, \eta)$:

$$\frac{\partial \zeta}{\partial t} + f\delta + \beta v = -\nabla_\pi \cdot (\boldsymbol{v}\zeta), \tag{12.37a}$$

$$\frac{\partial \delta}{\partial t} - f\zeta + \beta u + g\nabla_\pi^2 \eta = -\nabla_\pi \cdot (\boldsymbol{v} \cdot \nabla_\pi \boldsymbol{v}), \tag{12.37b}$$

$$\frac{\partial \eta}{\partial t} - \nabla_\pi \cdot (\boldsymbol{v} h_\mathrm{B}) = -\nabla_\pi \cdot (\boldsymbol{v}\eta), \tag{12.37c}$$

where the nonlinear advection terms are put on the right-hand side for clarity. Of course we may also introduce scalar potential $\chi(x, y, t)$ and stream function $\psi(x, y, t)$ by

$$\boldsymbol{v} = \nabla_\pi \chi + \boldsymbol{e}_z \times \nabla\psi, \tag{12.38}$$

such that $\delta = \nabla_\pi^2 \chi$ and $\zeta = \nabla_\pi^2 \psi$, and use $(\chi, \psi, \eta)$ as dependent variables.

## 12.2 Potential Vorticity

In geophysical flows the *potential vorticity* defined by (3.106) plays a key role. In a rotating system its general definition is

$$P \equiv \frac{1}{\rho}(\boldsymbol{\omega} + 2\boldsymbol{\Omega}) \cdot \nabla\phi \tag{12.39}$$

for any scalar $\phi$ satisfying $\mathrm{D}\phi/\mathrm{D}t = 0$. When the absolute flow is circulation-preserving or $\nabla\phi$ is perpendicular to the vorticity diffusion vector $\nabla \times \boldsymbol{a}$, the

*Ertel potential-vorticity theorem* stated in Sect. 3.6.1 holds true and has been proved extremely useful:

$$\frac{\mathrm{D}P}{\mathrm{D}t} = 0. \tag{12.40}$$

Rossby (1936, 1940) was the first to introduce the concept of potential vorticity to the fluid motion in oceans. Quite soon afterwards Ertel (1942) established independently the theorem now associated with his name, but with $\phi$ being a meteorological quantity. For a review of this early history and later developments see Hoskins et al. (1985).

In this section we first introduce the barotropic (Rossby) potential vorticity and illustrate its rich consequences in both atmospheric and oceanic motions. We then turn to baroclinic (Ertel) potential vorticity and go beyond the conservation condition, to see in what situation and how the combined distributions of entropy and Rossby–Ertel potential vorticity can characterize and uniquely determine the entire atmospheric motion.

### 12.2.1 Barotropic (Rossby) Potential Vorticity

Consider the shallow-water approximation and observe that (12.36) has the same form as (3.98c) for two-dimensional compressible and circulation-preserving flow. Moreover, a comparison of (12.30b) and the general continuity equation (2.40) clearly indicates that the role of variable density in the latter is now played by the variable fluid-layer depth. Therefore, by inspecting the two-dimensional and circulation-preserving version of the Beltrami equation (3.99), namely (3.137), we see at once that, as the *Beltramian form* of the vorticity equation for barotropic flow under the shallow-water approximation, there is (Rossby 1936, 1940)

$$\frac{\mathrm{D}_\pi}{\mathrm{D}t}\left(\frac{f+\zeta}{h}\right) = 0. \tag{12.41}$$

The quantity in the brackets is referred to as the *barotropic potential vorticity* or *Rossby potential vorticity* $P$, of which the corresponding Lagrangian invariant scalar $\phi$, see (12.39), can be found by inspecting (12.30b) where $A$ and $h$ are independent of $z$. Thus, $w$ depends on $z$ *linearly*:

$$w = (h_\mathrm{B} - z)\vartheta_\pi + w_\mathrm{B},$$

where $w_\mathrm{B}$ is the vertical velocity at the bottom $z = h_\mathrm{B}(x, y)$ determined by the no-through condition

$$w_\mathrm{B} = \frac{\mathrm{D}_\pi h_\mathrm{B}}{\mathrm{D}t} = \boldsymbol{v} \cdot \nabla h_\mathrm{B}.$$

Hence, by (12.30b), it follows that

$$w - \boldsymbol{v} \cdot \nabla h_\mathrm{B} = \frac{\mathrm{D}_\pi}{\mathrm{D}t}(z - h_\mathrm{B}) = \frac{z - h_\mathrm{B}}{h}\frac{\mathrm{D}_\pi h}{\mathrm{D}t},$$

from which we find

$$\phi = \frac{z - h_{\mathrm{B}}}{h}, \quad \frac{\mathrm{D}_\pi \phi}{\mathrm{D}t} = 0. \tag{12.42}$$

The simple conservative equation (12.41) has very clear physical meaning and significant consequence. First, for constant $h$, if a vertical fluid column (since the flow is treated as inviscid, the vorticity can terminate at upper and lower boundaries) on the northern hemisphere moves northward into a region of larger $f$, its relative vorticity will decrease, and vice versa if it moves southward.

Then, for constant $f > 0$ (say, a column in a rotating tank of fluid or carried by a west wind), the absolute vertical vorticity $\zeta_{\mathrm{a}}$ in the tube must be proportional to $h$. Larger $h$ must be associated with the stretching of the tube, and vice versa. Thus, assuming $|\zeta| < |f|$, if initially $\zeta = 0$, as the column moves to a deeper $h$ a $\zeta > 0$ must be produced, just as if it moves southward with constant $h$; while at shallower $h$ a $\zeta < 0$ will be created just as if it moves northward. These relative rotating flows are called *cyclone* and *anticyclone* in meteorology. In short, *a vorticity column stretching produces cyclonic vorticity, and its shrinking produces anticyclonic vorticity.* Therefore, a proper choice of the bottom topography in a rotating-tank experiment may lead to the same dyanamic effect as the Coriolis parameter varies (e.g., Carnevale et al. 1991a,b; Hopfinger and van Heijst 1993), which provides a convenient method to experimentally study the motion of barotropic vortices.

Moreover, assume for simplicity the flow is along a latitude line $\theta_0$ with $v = 0$. Then if at some $x$-location the air raises up due to a local high temperature and form a low pressure region at low altitude so that the surrounding air merges toward this location, then by (12.41) at the low-pressure center a cyclone can be formed. But when the up-raising air stream reaches high altitude to form a local high-pressure region, the air stream will move away to surrounding regions, so by (12.41) an anticyclone can be formed. Therefore, the cyclone in low-pressure region and anticyclone in high-pressure region appear in pair, see the sketch of Fig. 12.6.

### 12.2.2 Geostrophic and Quasigeostrophic Flows

In terms of the streamfunction introduced by (12.38), (12.41) can be cast to

$$\frac{\partial P}{\partial t} + [\psi, P] = 0, \tag{12.43}$$

where $[\psi, \cdot]$ is the horizontal Jacobian operator similar to that used in Sect. 6.5.1 for two-dimensional flow. However, this equation alone cannot be solved for $\zeta$ and $h$ which are still coupled with $\delta$ in (12.37). In studying large-scale geophysical flows approximations derived from but simpler than (12.37) are often used. The relative importance of the inertial force and Coriolis force depends on the local Rossby number $Ro = U/fL$. For the earth we have $\Omega = 7.29 \times 10^{-5}\mathrm{s}^{-1}$ and $f = 1.03 \times 10^{-4}\mathrm{s}^{-1}$ at $\theta = 45^\circ$. If

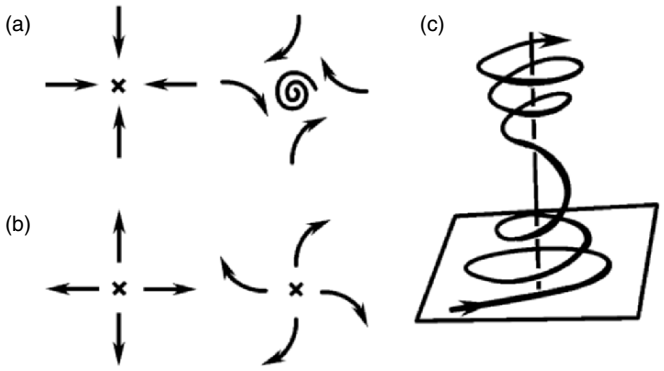


**Fig. 12.6.** The formation of a cyclone (**a**) and anticyclone (**b**) due to the potential-vorticity conservation, and their connection (**c**) by vertical airstream. From Lugt (1983)

$L \sim 1,000\,\mathrm{km}$, the inertial force could be comparable with the Coriolis force only if $U \sim 100\,\mathrm{m\,s^{-1}}$, which seldom occurs. Therefore, as a crude approximation at $Ro \ll 1$, we neglect the relative acceleration so that the pressure gradient or free-surface elevation is solely balanced by the Coriolis force. The flow under this balance is called the *geostrophic flow*, which must be *steady*:

$$f_0 \boldsymbol{e}_z \times \boldsymbol{v} = -g\nabla_\pi \eta \quad \text{or} \quad f_0 \boldsymbol{v} = g\boldsymbol{e}_z \times \nabla\eta. \tag{12.44}$$

By (12.38), we see $\chi = 0$ so the $\boldsymbol{v}$-field is incompressible. The streamlines must be perpendicular to the pressure gradient, or along a streamline the pressure is constant. Moreover, $\psi$ must be proportional to $\eta$ up to an additive constant; so we write

$$\psi = \lambda^2 \Delta\eta^*, \quad \lambda^2 \equiv \frac{gD}{f_0}, \quad \Delta\eta^* \equiv \frac{\eta - D}{D}. \tag{12.45}$$

The scalar $\lambda$ has the dimension of length and is known as the *Rossby deformation radius*, which characterizes the behavior of rotating flow subject to gravitational restoring force. The large-scale flows on the earth, such as the westerly belt at middle latitudes, the atmospheric low-pressure system, hurricane or typhoon, and oceanic circulation, all have small Rossby numbers and to the leading order can be modeled as geostrophic flow. Note that a geostrophic flow satisfies the condition of the Taylor–Proudman theorem.

Despite its simplicity, the steady solution (12.44) involves no evolution and is useless in weather and ocean prediction. To find the the next-order approximation called the *quasigeotrosphic flow*, denote $h_\mathrm{B}^* = h_\mathrm{B}/D$ such that

$$h = D(1 + \Delta\eta^* - h_\mathrm{B}^*), \tag{12.46}$$

and assume

$$Ro = \frac{U}{f_0 L} \ll 1, \quad \beta^* \equiv \frac{\beta L}{f_0} \ll 1, \quad |\Delta\eta^*|, |h_{\rm B}^*| \ll 1. \tag{12.47}$$

Then we can substitute the geostrophic $\psi$–$\eta$ relation (12.45) into the potential vorticity equation (12.41), retain the leading-order terms, to remove $\eta$ in an iterative way. Denote $y^* = y/L$ and replace $P$ by $\widehat{P} = DP$ in (12.43), we find (Salmon 1998)

$$\begin{aligned} \widehat{P} = \frac{D}{h}(f+\zeta) &\simeq f_0(1+\beta^* y^* + \nabla_\pi^2\psi/f_0)(1-\Delta\eta^* + h_{\rm B}^*) \\ &\simeq (\nabla_\pi^2 - \lambda^{-2})\psi + f + f_0 h_{\rm B}^* = f_0 + P', \end{aligned}$$

where $f_0(1+h_{\rm B}^*)$ is a background potential vorticity and

$$P' = (\nabla_\pi^2 - \lambda^{-2})\psi + f_0 h_{\rm B}^* + \beta y \tag{12.48}$$

is the potential vorticity due to the relative motion. Recall that $\lambda^{-2}\psi = \Delta\eta^*$ in geostrophic model represents the *stretching effect* of vertical vorticity due to the depth variation caused by the upper-boundary elevation. Then the governing equation for quasigeotrosphic flow with a single unknown $\psi$ follows from substituting (12.48) into (12.43):

$$(\nabla_\pi^2 - \lambda^{-2})\frac{\partial\psi}{\partial t} + [\psi, \nabla_\pi^2\psi + f_0 h_{\rm B}^*] + \beta\frac{\partial\psi}{\partial x} = 0, \tag{12.49}$$

which has been widely utilized in studies of large-scale barotropic geophysical vortices and will serve as the basic equation for most of our analyses in the rest of this chapter. We stress that solving (12.49) for specified initial and boundary conditions is a typical geophysical vorticity-vortex dynamics problem. An important example will be given in Sect. 12.3.4.

### 12.2.3 Rossby Wave

In the atmosphere and ocean there are many types of waves, such as internal-gravity wave, tropographic wave, Kelvin wave, etc. which are modified by the system rotation. Weak wave solutions are obtained from the linearized governing equations. For example, in the shallow-water approximation, by neglecting the nonlinear advections in (12.37), and using the $(\chi, \psi)$ expression of $\boldsymbol{v}$ given by (12.38), one can obtain coupled wave equations for $(\chi, \psi, \eta)$, which permitting free traveling waves. If we assume a constant $f = f_0$ and $\beta = 0$ so that it suffices to consider only the $x$-wise traveling wave of the form $\exp[{\rm i}(kx - \omega t)]$, then for $h_{\rm B} = 0$ one finds a dispersive relation (e.g., Pedlosky 1987; Gill 1982a,b; Salmon 1998)

$$\omega[\omega^2 - (f_0^2 + gDk^2)] = 0. \tag{12.50}$$

Here, $\omega = 0$ corresponds to steady geostrophic flow (no wave), and $\omega = \pm\sqrt{f_0^2 + gDk^2}$ correspond to *inertial-gravity waves* traveling in opposite directions. In the long-wave limit $\lambda^2 k^2 \ll 1$ we have *inertial wave* with $\omega \simeq \pm f_0$, corresponding to neglecting $-g\nabla_\pi \eta$ in (12.29); while in the short-wave limit $gDk^2 \gg 1$ we have *gravity wave* with $\omega \simeq \pm\sqrt{gD}k$, corresponding to neglecting the Coriolis force in (12.29). The gravity wave has phase speed $c = \omega/k = \sqrt{gD}$.

While by (12.50) all inertial-gravity waves have $\omega \geq |f|$, one type of wave is of extreme importance for large-scale meteorological process. This is the *Rossby wave*, a planetary vorticity wave as the direct consequence of the absolute-vorticity conservation motion caused solely by the $\beta$-effect. While the Rossby wave can be studied by the linearized version of (12.37) by retaining the $\beta$-effect, a simple way is to use the quasigeostrophic equation (12.49) of which the only wave solution is the Rossby wave.[4] Here we consider free plane Rossby wave as an elementary description of the phenomenon. Comprehensive reviews on various Rossby waves have been given by Platzman (1968) and Dickinson (1978).

For flat bottom topography, the linearized form of (12.49) is

$$(\nabla_\pi^2 - \lambda^{-2})\frac{\partial \psi}{\partial t} + \beta\frac{\partial \psi}{\partial x} = 0, \quad \psi = \lambda^2 \Delta\eta^*, \tag{12.51}$$

which permits plane traveling wave solution $\psi = \psi_0 \exp[\mathrm{i}(kx + ly - \omega t)]$. Let $l = 0$ for neatness, by (12.51) we find the dispersive relation

$$\omega = -\frac{\beta\lambda^2 k}{1 + \lambda^2 k^2}, \tag{12.52}$$

so the phase velocity $c = \omega/k$ and group velocity $c_\mathrm{g} = \partial\omega/\partial k$ are

$$c = -\frac{\beta\lambda^2}{1 + \lambda^2 k^2}, \quad c_g = -\beta\lambda^2 \frac{1 - \lambda^2 k^2}{(1 + \lambda^2 k^2)^2}. \tag{12.53}$$

Hence, if $f = f_0$ and $\beta = 0$, there is no wave again as in steady geostrophic flow. For $\beta \neq 0$ not assumed in deriving (12.50), when $k = \lambda^{-1} \equiv k_R$ we have maximum frequency $\omega_\mathrm{max} = -\beta\lambda/2$ and minimum period $T_\mathrm{min} = 4\pi/\beta\lambda$ (about 4.5 days at midlatitude, longer than the earth-rotation period). Note that on the northern hemisphere with $\beta > 0$ the zonal phase velocity is always westward, but the group velocity changes from westward to eastward as $k$ reduces through $-\lambda^{-1}$ and reaches $c_\mathrm{gmax} = \beta\lambda^2/8$ at $\lambda k = -\sqrt{3}$. The situation is plotted in Fig. 12.7. Only in the short-wave limit $\omega \simeq -\beta/k$ is independent of the deformation radius, corresponding to a simplified potential vorticity $P \simeq \zeta + f$ in (12.41), which is just the absolute vertical vorticity.

If there is a westerly belt along the altitude $\theta_0$ with constant basic state $u = U$ on which a free Rossby wave happens, then the phase speed will

[4] As one goes from more refined approximations to rougher ones, less types of waves can be studied.

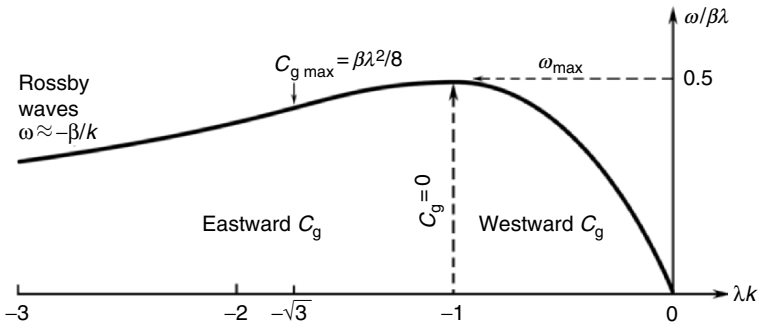


**Fig. 12.7.** The dispersion relation of the Rossby wave on the $(\lambda k, \omega/\beta\lambda)$-plane. Reproduced from Gill (1982a)

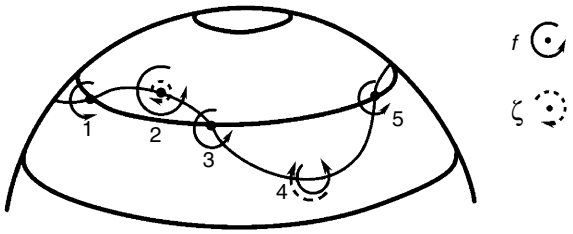


**Fig. 12.8.** The Rossby wave in the westerly belt. Solid and dashed marks represent the ambient potential vorticity $f$ and newly produced relative vorticity $\zeta$, respectively. The larger and smaller sizes of the solid marks indicate $f$ increase or decrease as altitude. Adapted from Lugt (1983)

be $U + c$. Assume the variation of $h$ is negligible, then the vorticity-dynamic mechanism for its formation is solely the conservation of $f + \zeta$ or the variation of $f$ as $y$. To gain an intuitive understanding, consider fluid columns 1, 2, and 3 as shown in Fig. 12.8, which are initially at the same latitude with the same $f_0$. Suppose a disturbance shifts column 2 northward as shown, so that its $f$ is increased. To reserve the potential vorticity, $\zeta_2$ must be accordingly reduced, or a new $\zeta_2 < 0$ or clockwise circulation is created. This negative $\zeta_2$ will induce column 1 to move northward where a new $\zeta_1 < 0$ must be created too; but meanwhile induce column 3 to move southward where a new $\zeta_3 > 0$ has to be created. Then, the newly created $\zeta_1$ and $\zeta_3$ will in turn induce column 2 to move back to the south, but due to the inertia it will go beyond the initial equilibrium position and gain some new $\zeta_2 > 0$. In this way, the oscillation is continued.

Mason (1971) reported that, to observe the Rossby wave in the westerly belt, a balloon was released from New Zealand and maintained at about the height of 12 km, which floated as the west wind. The balloon moved around the earth by 8.5 cycles during 102 days and its location was recorded by radio

signals which visualized the Rossby wave. The result is qualitatively similar to the sketch of Fig. 12.8.

### 12.2.4 Baroclinic (Ertel) Potential Vorticity

Rossby's concept of potential vorticity was given a full generality by the Ertel theorem, which holds for any Lagrangian invariant scalar $\phi$ in three-dimensional flow under the assumed condition. A few different special potential vorticities have then been proposed, of which the most important one that finds wide applications in meteorology is the *isentropic potential vorticity*.

Assume the motion of an air parcel is inviscid and without internal heat addition and conduction. Then by (2.61) the flow is *adiabatic* with $\mathrm{D}s/\mathrm{D}t = 0$. Substituting $p = \rho RT$ into (2.64) yields

$$\mathrm{d}s = C_\mathrm{p}\mathrm{d}\ln T - R\mathrm{d}\ln p,$$

of which the integration from state $(p, T)$ to a reference state $(p_\mathrm{r}, T_\mathrm{r})$ yields

$$T_\mathrm{r} = T\left(\frac{p_\mathrm{r}}{p}\right)^{R/C_\mathrm{p}} \exp\left[(s_\mathrm{r} - s)/C_\mathrm{p}\right]. \tag{12.54}$$

Thus, the temperature that a dry fluid parcel at $(p, T)$ would have, if it were compressed or expanded adiabatically to the reference pressure $p_\mathrm{r}$, is

$$\theta \equiv T\left(\frac{p_\mathrm{r}}{p}\right)^{R/C_\mathrm{p}}, \tag{12.55}$$

which is called the *potential temperature*.[5] In an adiabatic process $\theta$ and $s$ are both Lagrangian invariant; a fluid motion along an iso-$\theta$ surface must be isentropic. This observation permits defining an *isentropic potential vorticity* (IPV)

$$P = \frac{\boldsymbol{\omega} + 2\boldsymbol{\Omega}}{\rho} \cdot \nabla\theta, \tag{12.56}$$

of which the Lagrangian invariance is the specification of the Ertel theorem to the inviscid and adiabatic motion of the atmosphere.

Moreover, for the stably stratified atmosphere with $\partial p/\partial z = -\rho g$, $\theta$ must be a monotonically increasing function of height $z$, and hence can serve as an independent vertical coordinate. Since now a mass element can be expressed as

$$\delta m = \rho\delta A\delta z = -\frac{1}{g}\delta A\delta p = \frac{\delta A}{g}\left(-\frac{\partial p}{\partial\theta}\right)\delta\theta$$

we see that the "density" in the $(x, y, \theta)$ space is

$$\sigma \equiv -\frac{1}{g}\frac{\partial p}{\partial\theta}. \tag{12.57}$$

[5] Here the notation $\theta$ should not be confused with the latitude.

Then, similar to the horizontal gradient $\nabla_\pi$ in Sect. 12.2.1, we may now introduce the isetropic gradient $\nabla_\theta$, with the subscript $\theta$ denoting derivatives along an iso-$\theta$ or isentropic surface. For instance, the *isentropic vorticity* is defined as

$$\zeta_\theta = \boldsymbol{k} \cdot (\nabla_\theta \times \boldsymbol{u}) = \left(\frac{\partial v}{\partial x}\right)_\theta - \left(\frac{\partial u}{\partial y}\right)_\theta . \tag{12.58}$$

Therefore, the IPV defined by (12.54) can also be written as

$$P = \frac{f + \zeta_\theta}{\sigma}, \quad \frac{\mathrm{D}_\theta P}{\mathrm{D}t} = 0, \tag{12.59}$$

which is the commonly used form.

In meteorology, along with the potential temperature and specific humidity, the barotropic (Rossby) or isentropic potential vorticity is the third Lagrangian marker to identify an air parcel. This is true even diabatic heating and frictional or other forces are acting, due to the following theorem proved by Haynes and McIntyre (1987):

**Theorem .** *There can be no net transport of Rossby–Ertel potential vorticity (PV) across any isentropic surface. Within a layer bounded by two isentropic surfaces, PV can neither be created nor destroyed.*

Starr and Neiburger (1940) were the first to construct *IPV maps* for the 299–303K isnetropic layer over North America for 21 and 22, November 1939, and found that for three air parcels the conservation of IPV was approximately satisfied. However, their work as well as the later important studies by, e.g. Kleinschmidt (1950a,b, 1951, 1955, 1957), Reed and Sanders (1953), Obukhov (1964), and Danielsen (1967, 1968), among others, have made it clear that the significance of PV is far more than being an air-tracer.

Most importantly, PV maps are a natural diagnostic tool for making dynamic processes directly visible and comparisons between atmospheric models and reality meaningful. Just like from a given vorticity field one can reversely obtain its "induced" entire flow field under proper boundary conditions (Sect. 4.5.1), there is also an *invertibility principle* that allows one to deduce the "induced" stream function and hence the wind field by a given PV map. In fact, combined with potential temperature maps, the invertibility principle holds true even for the potential vorticity in baroclinic flow. The situation is very similar to that in classic aerodynamics as we saw in Chap. 11; to quote Hoskins et al. (1985):

*"Thus one can, if one wishes, think entirely in terms of the (barotropic) vorticity field, since this contains all the relevant information; and indeed the simplifying power and general usefulness of this particular mode of thinking about rotational fluid motion has long been recognized, and made routine use of, in another field, that of classic aerodynamics"* (e.g. Prandtl and Tietjens 1934; Goldstein 1938; Lighthill 1963; Batchelor 1967; Saffman 1981).

Hoskins et al. (1985) stress that, as in deducing the flow field from a given vorticity distribution, given an IPV map that by (12.56) is the *product* of absolute vorticity and static stability, additional information is necessary for determining both separately, and hence the wind, pressure, and temperature fields. This includes:

1. specify some kind of balance condition;
2. specify some reference state, expressing the mass distribution of $\theta$;
3. solve the inversion problem *globally* with proper boundary conditions (a purely local knowledge of $P$ cannot determine the local absolute vorticity and static stability separately).

Hoskins et al. (1985) have constructed daily Northern Hemisphere IPV maps for numerous isentropic surfaces for the 42 days from 20 September to 31 October 1982, and made a detailed analysis to demonstrate the invertibility principle. Here we illustrate how the principle works by a simple theoretical model problem (Thorpe 1985; Hoskins et al. 1985).

Let the reference state be a horizontally uniform atmosphere with constant $f$. The mass distribution of potential temperature $\theta$ is specified by prescribed static pressure $p$ as a monotonically decreasing function of $\theta$: $p = p_{\mathrm{ref}}(\theta)$, so the reference state is stable. On each isentropic surface the reference state has a constant IPV. Assume now that there is a circularly symmetric PV anomaly on some of the isentropic surfaces, centered at $r = 0$. Then since the adiabatic heating and friction are ignored, the flow must be steady, nondivergent and purely azimuthal with only a circumferential wind velocity $v(r, \theta)$, where $\theta$ is the potential temperature. Thus, in polar coordinated $(r, \theta)$ the relative vorticity is

$$\zeta_\theta = \frac{1}{r}\frac{\partial (rv)}{\partial r}. \tag{12.60}$$

Denote the absolute vorticity $f + \zeta_\theta$ by $\zeta_{\mathrm{a}\theta}$, differentiate (12.60) with respect to $r$, and using (12.59) and the constancy of $f$, it follows that

$$\frac{\partial}{\partial r}\left(\frac{1}{r}\frac{\partial (rv)}{\partial r}\right) - \frac{\zeta_{\mathrm{a}\theta}}{\sigma}\frac{\partial \sigma}{\partial r} = \sigma \frac{\partial P}{\partial r}. \tag{12.61}$$

Here, by using the isentropic form of the *thermal wind equation* (e.g. Hoskins et al. 1985)

$$f_{\mathrm{loc}}\frac{\partial v}{\partial \theta} = R(p)\frac{\partial p}{\partial r}, \quad f_{\mathrm{loc}} = f + 2\frac{v}{r}, \quad R(p) = \frac{1}{\rho\theta},$$

from the definition of $\sigma$ given in (12.57) there is

$$-g\frac{\partial \sigma}{\partial r} = \frac{\partial^2 p}{\partial r \partial \theta} = \frac{\partial}{\partial \theta}\left(\frac{f_{\mathrm{loc}}}{R}\frac{\partial v}{\partial \theta}\right). \tag{12.62}$$

Thus, from (12.59) and (12.62), (12.61) can finally be cast to a nonlinear equation for solving the wind field from given PV distribution:

$$\frac{\partial}{\partial r}\left(\frac{1}{r}\frac{\partial(rv)}{\partial r}\right)+\frac{P}{g}\frac{\partial}{\partial\theta}\left(\frac{f_{\rm loc}}{R}\frac{\partial v}{\partial\theta}\right)=\sigma\frac{\partial P}{\partial r}, \tag{12.63}$$

which is the mathematic form of the invertibility principle for this simple model problem. The isentropic gradient of $P$ appears on the right-hand side as the driving mechanism. The equation can be linearized by assuming $f_{\rm loc}\simeq f$, $R\simeq R_{\rm ref}(\theta)$, and $\sigma\simeq\sigma_{\rm ref}$:

$$\frac{\partial}{\partial r}\left(\frac{1}{r}\frac{\partial(rv)}{\partial r}\right)+\frac{f^2}{g\sigma_{\rm ref}}\frac{\partial}{\partial\theta}\left(\frac{1}{R_{\rm ref}}\frac{\partial v}{\partial\theta}\right)=\sigma_{\rm ref}\frac{\partial P}{\partial r}. \tag{12.64}$$

The left-hand side is a linear elliptical operator, which by proper rescaling can be reduced to the Laplace operator.

A pair of exact solutions of (12.64) "induced" by isolated upper air PV anomalies of either sign is plotted in Fig. 12.9a,b, under the boundary condition $v\to 0$ as $r\to\infty$ and $\theta=$ constant at 60 and 1,000 mb. The qualitative resemblance of these figures to the observed meteorological structures has been confirmed.

The earlier *potential vorticity inversion* method is essentially a time-stepping approach for weather prognosis. From a given initial map of velocity, pressure, etc. one computes the Rossby–Ertel PV map, advects it to the next timestep by (12.40), and then applies an inversion operator to obtain the velocity field. McIntyre and Norton (2000) have used the primitive shallow-water equations (12.37) and their hemisphere extension[6] to conduct the Rossby-PV inversion at a few different orders of accuracy and compared the results with direct numerical simulation of (12.37). The accuracy attained by the highest-order inversion is found to be surprisingly high in a prognosis period of 10 days.[7] The authors remark that the inversion operator they constructed has actually been close to the *ultimate limitation* of the inversion method.

In order to understand what the "ultimate limitation" is, we compare the situation with a two-dimensional circulation-preserving flow. In the conventional vorticity inversion (Sects. 3.2.2 and 4.5.1), a full velocity field can be exactly obtained from a given vorticity field only if the flow is incompressible; then we can make time-march of the vorticity due to $\mathrm{D}\omega/\mathrm{D}t=0$. Once the flow is compressible, the dilatation $\vartheta=\nabla\cdot\boldsymbol{u}$ has to join the inversion at each time step (e.g., (3.27) and (4.162)) and its evolution equation has to be used for the purpose of prognosis, which is however not Lagrangian invariant but depends on the history (Sect. 3.6.2). In particular, unsteady vorticity motion is a spontaneous source of sound that propagates with finite speed, see (2.170) and (2.171). Due to the sound emission, therefore, if an inversion was

[6] For weather prognosis one has to consider atmospheric motion of scales much smaller than quasigeostrophic scale, with Rossby number of order one.

[7] One result of this chapter has been reported as Fig. 2 of McIntyre and Norton (1990).

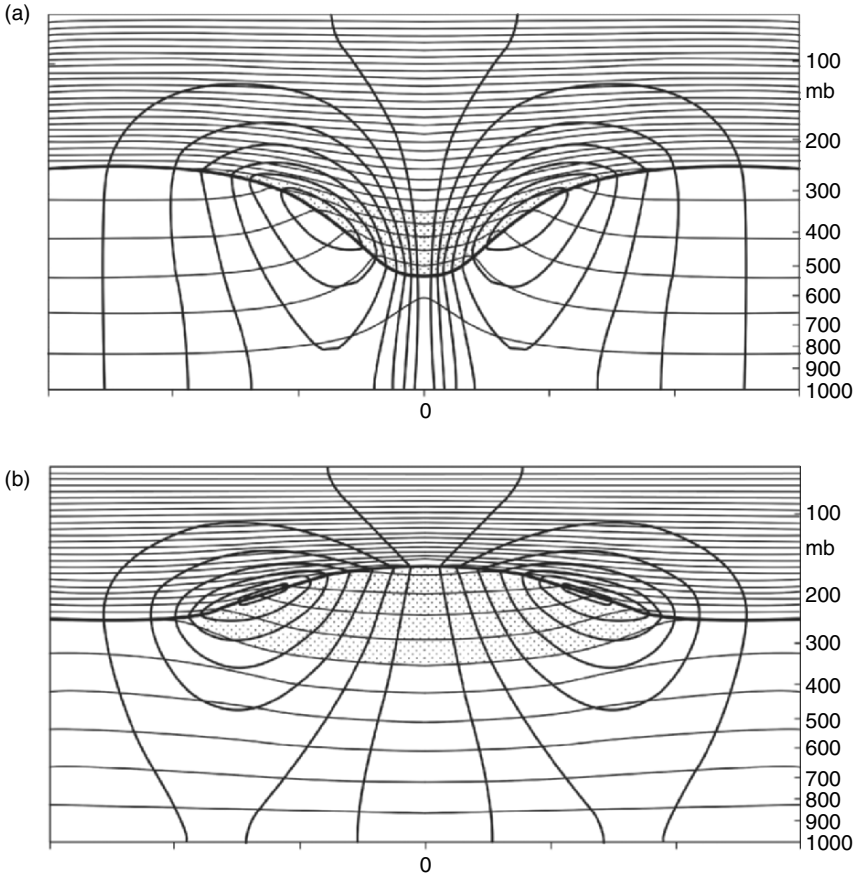


**Fig. 12.9.** Circularly symmetric flows "induced" by simple isolated IPV anomalies. In (**a**) the sense of the azimuthal wind is cyclonic, and in (**b**) it is anticyclonic. The thick line represents the tropopause and the two sets of thin lines are the isentropes every 5 K and transverse velocity every $3\,\mathrm{m\,s^{-1}}$. Reproduced from Hoskins et al. (1985)

to be made, backward time integration would be necessary, which is however impossible in practice.

The ultimate limitation of the potential-vorticity inversion has exactly the same physical root (another trouble is associated with coupled oscillators and chaos), but the role of acoustic wave is now played by gravity wave with phase speed $c = \sqrt{gD}$ (Sect. 12.2.3), of which the relative strength can be seen from (12.35):

$$F'^2 \left( Ro \frac{\partial \boldsymbol{v}^*}{\partial t^*} + \boldsymbol{e}_z \times \boldsymbol{v}^* \right) = -Ro \nabla^*_\pi \eta^*, \;\; F' = \frac{U}{c}, \;\; Ro = \frac{U}{fL} = O(1), \;\; (12.65)$$

where $F'$ corresponds to the Mach number in compressible fluid dynamics. No spontaneous gravity-wave emission from the evolving potential vorticity only if $F'$ is sufficiently small. Taking $F'$ as a small parameter, by improving a matched asymptotic expansion method devised in developing the theory of vortex sound, and considering (12.37) on an $f$-plane ($\beta = 0$), Ford et al. (2000) have proved that the potential vorticity inversion holds up to $O(F'^4 \ln F')$. In the worked out examples of potential-vorticity inversion by McIntyre and Norton (2000), $F'_{\max}$ has reached about 0.5–0.7.

## 12.3 Quasigeostrophic Evolution of Vorticity and Vortices

Sections 12.1 and 12.2 have set a basic framework for large-scale *geophysical vorticity dynamics*, of which the key is the concept and conservation of Rossby–Ertel potential vorticity. This section turns to some selected topics of large-scale geophysical vortices. The existence of such strong but usually localized large-scale vortical structures, some with extremely long life, is a remarkable character of geophysical flows. A primary example is the Great Red Spot on the Jupiter, which has remained rotating ever since it was first observed some 300 years ago, despite the strong shear flow and collision of many small vortices at its boundary. On the earth, a typical example in ocean is Gulf Stream rings, and that in the atmosphere is hurricanes and typhoons. These vortices are basically governed by the synoptic-scale dynamics and in geostrophic balance, with potential-vorticity gradient in their background flow field.

In Chaps. 4–10 we have discussed almost the whole life of some typical vortices, from their formation, motion and interaction, instability and breakdown, till becoming small-scale turbulent eddies and being dissipated. But, those discussions were mostly confined to incompressible flow with uniform density and without nonconservative body force, observed in an inertial frame of reference. They cannot be extended in similar detail to typical geophysical vortices. The detailed formation process of a hurricane, for example, cannot be included since it involves very complicated thermodynamic processes which produce absolute vorticity and are closely coupled with three-dimensional fluid motion, with some issues still to be clarified (interested readers may consult Bengtsson and Lighthill (1982) and references therein). Neither will a detailed discussion be included on the interactions of large-scale vortices, for which the reader is referred to Hopfinger and van Heijst (1993) and a three-dimensional analysis of Carnevale et al. (1997).

The selected topics in this section are all within quasigeostrophic approximation. It permits a discussion of the evolution of vertical vorticity and formation of vortical structures as a purely two-dimensional process (Sect. 12.3.1), followed by two-dimensional structures and evolution of barotropic vortices

(Sect. 12.3.2). The baroclinic effect on large-scale vortices will be demonstrated by a two-layer model of stratified fluid without the involvement of thermodynamics (Sect. 12.3.3). Finally, in Sect. 12.3.4 we discuss the prognosis of the motion of strong tropical cyclones, which is well known to be of crucial importance in weather forecast.

### 12.3.1 The Evolution of Two-Dimensional Vorticity Gradient

In quasigeostrophic approximation, we further assume that the variation of fluid-layer depth $h$ is negligible, and along the vertical direction the fluid is in hydrostatic balance. Then the flow is fully *two-dimensional* and incompressible. Thus, we may recover the convention in general fluid dynamics to denote the vertical vorticity by $\omega$ and drop the suffix $\pi$ for horizontal components. Now the Rossby potential vorticity is $P = f + \omega$, and for the relative vorticity (12.37a) is reduced to

$$\frac{\mathrm{D}\omega}{\mathrm{D}t} + \beta v = 0. \tag{12.66}$$

The two-dimensionality simplifies our analysis but also brings in some physical mechanisms different from those in three dimensions, from the formation of the structures to turbulence.

In a quasigeostrophic turbulent flow, most of the phenomena can be interpreted by the coexistence and mutual interaction of three mechanisms: isolated coherent vortices, two-dimensional turbulence, and Rossby waves (McWilliams 1984). Although the vorticity intensification by stretching does not exist, the *gradient of vorticity*, denoted by $\boldsymbol{s} \equiv \nabla\omega$, experiences a similar intensification and reduction as the vorticity does in three dimensions, causing the formation of isolated vortices. Taking the gradient of (12.66) yields

$$\frac{\mathrm{D}\boldsymbol{s}}{\mathrm{D}t} = -\nabla\boldsymbol{u}\cdot\boldsymbol{s} - \beta\nabla v = -\mathbf{D}\cdot\boldsymbol{s} + \frac{1}{2}\boldsymbol{\omega}\times\boldsymbol{s} - \beta\nabla v. \tag{12.67}$$

A reduction of $\boldsymbol{s}$ implies that the vorticity is spread more evenly, which happens in those long-life vortices. The merger of like-sign vortices (as well as the dissipation of small weak ones) makes the evolution toward a few large like-sign vortices (*coherent production* or *inverse cascade*, see Sect. 10.5.1). In fact, we have seen such an example in Fig. 9.6a in the context of Arnold's formal stability theory. Recall that a two-dimensional vortex can well be identified by the Weiss criterion (6.181) as an *elliptic region* with $Q_{2\mathrm{D}} = \det(\nabla\boldsymbol{v}) > 0$. Figure 12.10 shows an example of this process. As time goes on, the number of vortices becomes fewer, and each vortex becomes stronger and more isolated from the others and hence tends to be axisymmetric.

Opposite to the earlier process, an enhancement of $\boldsymbol{s}$ implies that the vorticity field is compressed in the direction of $\boldsymbol{s}$ and hence must be stretched in the direction normal to $\boldsymbol{s}$, evolving toward filament-like structures with smaller scales (*cascade*, see Sect. 10.5.2). The filaments (sheets extending along

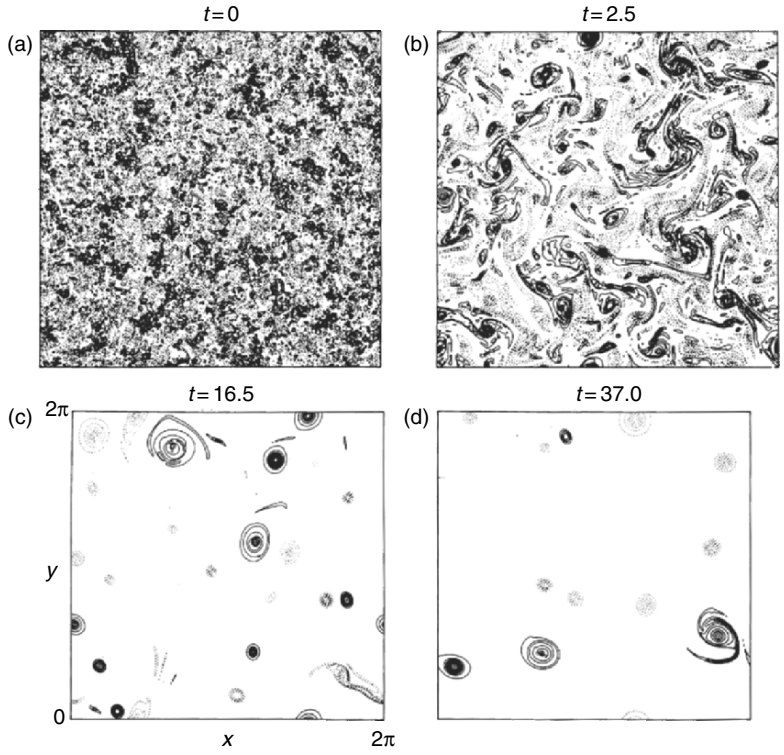


**Fig. 12.10.** Vorticity contours of a two-dimensional homogeneous and isotropic turbulence at different times. Direct numerical simulation based on (12.66) with $\beta = 0$ but a forcing at low wavenumbers and a hyperviscosity term $-\nu\nabla^4\omega$ are added on the right-hand side. The contour interval is 8 for (a) and 4 thereafter. From McWilliams (1984)

the third dimension) are in the *hyperbolic regions* according to the Weiss criterion, located in between isolated vortices as shown in Fig. 12.11.

We now make a closer look at (12.67) regarding the earlier opposite processes. To simplify our algebra, we convert plane vectors to complex variables on plane $z = x + \mathrm{i}y$. The conversion rules are given in A.2.4, see (A.31) to (A.33). We thus have ($\phi$ is any scalar)

$$\begin{aligned}
\nabla\phi &\Longrightarrow 2\boldsymbol{e}_x\partial_{\bar{z}}\phi,\\
\nabla\cdot\boldsymbol{v} = 0 &\Longrightarrow \partial_z w + \partial_{\bar{z}}\bar{w} = 0,\\
\boldsymbol{e}_z\omega &\Longrightarrow \mathrm{i}\boldsymbol{e}_z(\partial_{\bar{z}}\bar{w} - \partial_z w) = -2\mathrm{i}\boldsymbol{e}_z\partial_z w,\\
\boldsymbol{s} &\Longrightarrow 2\boldsymbol{e}_x\partial_{\bar{z}}\omega = -4\mathrm{i}\boldsymbol{e}_x\partial_z\partial_{\bar{z}}w,\\
\mathbf{D}\cdot\boldsymbol{s} &\Longrightarrow \boldsymbol{e}_x\eta\partial_z\omega,
\end{aligned} \tag{12.68}$$

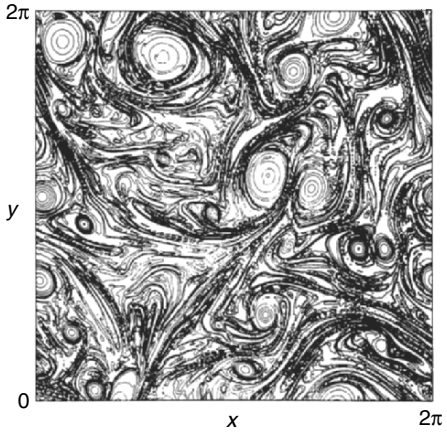


**Fig. 12.11.** $\mathrm{Log}_{10}|\omega|$ of the same vorticity field as Fig. 12.10c at $t = 16.5$ with contours step 0.25 between $-0.5$ and 1.5. From McWilliams (1984)

in which

$$\eta = u_{,x} - v_{,y} + \mathrm{i}(u_{,y} + v_{,x}) = 2\partial_{\bar{z}} w, \quad \text{with} \tag{12.69a}$$

$$\frac{1}{4}\eta\overline{\eta} = \frac{1}{2}D_{ij}D_{ij} = v_{,x}u_{,y} - u_{,x}v_{,y} + \frac{1}{4}\omega^2 = \lambda^2, \tag{12.69b}$$

where $\pm\lambda$ are the eigenvalues of $\mathbf{D}$ with $\lambda > 0$. Therefore, the complex-variable form of (12.67) easily follows:

$$\frac{\mathrm{D}}{\mathrm{D}t}\partial_{\bar{z}}\omega = \frac{1}{2}(\mathrm{i}\omega\partial_{\bar{z}}\omega - \eta\partial_z\omega) - 2\beta\partial_{\bar{z}}v, \tag{12.70}$$

which was first obtained by Weiss (1981) for $\beta = 0$. The first two terms on the right-hand side are the effects on $\mathrm{D}\boldsymbol{s}/\mathrm{D}t$ by the rotation by angular velocity $\omega/2$ and coupling with $\mathbf{D}$, respectively, and the third term is the $\beta$-effect.

We set $\boldsymbol{s} = \boldsymbol{e}_x s\,\mathrm{e}^{\mathrm{i}\alpha}$ in (12.70) and separate its real and imaginary parts. The result will be neat in the principal-axis frame of the strain-rate tensor $\mathbf{D}$ with eigenvalues $\pm\lambda$, where $\eta = \eta_{\mathrm{r}} + \mathrm{i}\eta_i = (2\lambda, 0)$. Let $\boldsymbol{p}_\pm$ be the eigenvectors associated with $\pm\lambda$, $\alpha_\lambda$ be the angle between $\boldsymbol{s}$ and $\boldsymbol{p}_+$, and $\phi_\lambda = \alpha + \alpha_\lambda$ be the angle between $\boldsymbol{p}_+$ and $\boldsymbol{e}_x$. We then find, since $v_{,y} = -u_{,x}$,

$$\frac{1}{s}\frac{\mathrm{D}s}{\mathrm{D}t} = -\lambda\cos 2\alpha_\lambda + \frac{\beta}{s}(u_{,x}\sin\phi_\lambda - v_{,x}\cos\phi_\lambda), \tag{12.71a}$$

$$\frac{\mathrm{D}\alpha_\lambda}{\mathrm{D}t} = \lambda\sin 2\alpha_\lambda + \frac{\omega}{2} + \frac{\beta}{s}(u_{,x}\cos\phi_\lambda + v_{,x}\sin\phi_\lambda), \tag{12.71b}$$

as obtained by Xiong (2002) for $\beta = 0$. We consider this case first. As Xiong (2002) emphasized, at a small neighborhood of any point, it is the intensification or weakening of the *magnitude* of the vorticity gradient $\boldsymbol{s}$ rather than

the change of its *direction* that dominates the direction of cascade (forward or inverse). More specifically, if $\alpha_\lambda = \pm\pi/2$ ($\boldsymbol{s}$ is aligned to $\boldsymbol{p}_-$), the strain rate causes the strongest intensification of $s$, along with rotation $\mathrm{D}\alpha_\lambda/\mathrm{D}t = \omega/2$. When this happens, since the isovorticity lines are orthogonal to $\boldsymbol{s}$, a circular vortex will be compressed along the $\boldsymbol{p}_-$ direction and stretched along the $\boldsymbol{p}_+$ direction. This is the mechanism responsible for the formation of sheet-like structures. If $\alpha_\lambda = 0$ or $\pi$ ($\boldsymbol{s}$ is aligned to $\boldsymbol{p}_+$), there is the strongest weakening of $s$ also along with rotation $\mathrm{D}\alpha_\lambda/\mathrm{D}t = \omega/2$. Finally, when $\alpha_\lambda = \pm\pi/4$, $\boldsymbol{s}$ experiences a pure rotation by $\mathbf{D}$ at a rate $\pm\lambda$ plus a rotation by $\omega/2$. The rotation may cause two or more like-sign vortices to turn around each other and merge to a larger vortex due to viscosity.

Figure 12.12 confirms the key role of $\mathrm{D}s/\mathrm{D}t$ in the formation of sheet-like and patch-like structures. Shown in the figure are the sign of $\mathrm{D}s/\mathrm{D}t$ and vorticity contours. In the positive regions the isovorticity lines are highly clustered, implying large vorticity gradient, while in the negative regions the isovorticity lines are quite loose. Note that in a similar plot for $\mathrm{D}\alpha/\mathrm{Dt}$ (not shown) one cannot find any correlations between the sign of $\mathrm{D}\alpha/\mathrm{D}t$ and isovorticity lines. Rather, the former is quite consistent with the sign of vorticity itself. However, since $\mathrm{D}\alpha/\mathrm{D}t$ and $\omega$ are not uniformly distributed, their spatial variation will inevitably alter the pattern of elliptic and hyperbolic regions of a flow, and thereby influence $\mathrm{D}s/\mathrm{D}t$ as well.

We stress that $\mathbf{D}$ and $\boldsymbol{s}$ in (12.67) or $\eta$ and $s\mathrm{e}^{\mathrm{i}\alpha}$ in (12.70) are closely coupled as found in numerical tests (e.g., Xiong 2002), implying that these

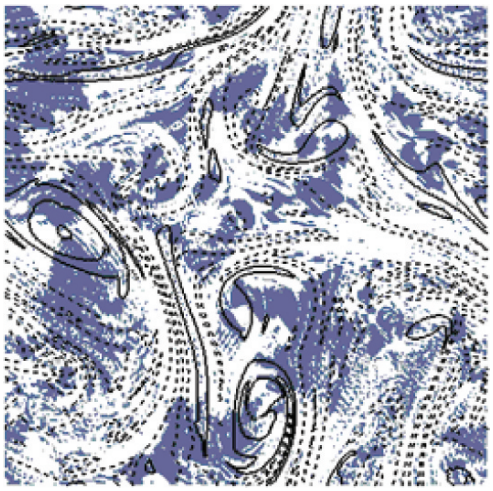

**Fig. 12.12.** An instantaneous plot of a two-dimensional vorticity evolution. Shown in the figure are the sign of $\mathrm{D}s/\mathrm{D}t$ (*white, positive; grey, negative*) and isovorticity lines (*solid, positive; dashed, negative*). From the direct numerical simulation of Xiong (2004, private communication)

equations are highly nonlinear. Thus, in analyzing the evolution of vorticity gradient, the strain rate cannot be assumed as a prescribed background field. This coupling can be understood in terms of complex-variable formulation. First, by (12.68) and (12.69a), the identity $2\nabla \cdot \mathbf{D} = -\nabla \times \boldsymbol{\omega} = \nabla^2 \boldsymbol{u}$ has complex-variable form

$$\partial_z \eta = \mathrm{i}\partial_{\bar{z}} \omega = \frac{1}{2}\nabla^2 w. \tag{12.72}$$

Therefore, the strain rate and vorticity have identical power spectrum in wave space, differing purely in phase (Weiss 1981). Next, by the *area theorem* (A.35), there is

$$2\mathrm{i} \int_S \partial_{\bar{z}} \omega \, \mathrm{d}S = \oint_{\partial S} \omega \, \mathrm{d}z = 2 \int_S \partial_z \eta \, \mathrm{d}S = \mathrm{i} \oint_{\partial S} \eta \, \mathrm{d}\bar{z} \tag{12.73a}$$

or

$$\oint_{\partial S} (\omega \, \mathrm{d}z - \mathrm{i}\eta \, \mathrm{d}\bar{z}) = 0. \tag{12.73b}$$

Namely, *the averaged vorticity gradient in an area $S$ is determined by the boundary integral of the strain rate, and vice versa.*

As the local mechanism responsible for the cascade and inverse cascade processes in two-dimensional vortical flows, the interaction between the vorticity gradient and the strain field discussed earlier must be constrained by some global conservative quantities. These constraints are especially important in the *inertial range* (the wavenumber range where the viscosity can be neglected) of two-dimensional turbulence, which is the leading-order approximation of geophysical turbulence. In inviscid, unbounded and incompressible flow, either two or three dimensions, the first conservative quantity is the total kinetic energy, see (2.52), which is *positively definite*. Besides, in three dimensions the helicity is the second conservative scalar, see (3.141), which can be either positive or negative. In contrast, in two dimensions the second conservative scalar is the total enstrophy, see (3.124) with both $\alpha$ and $\nabla \times \boldsymbol{a}$ vanishing, which is again positively definite.

It is the difference of whether the second scalar has positive definiteness that makes the cascade process in two-dimensional turbulence very different from that in three dimensions (Chap. 10). Fjørtoft (1953) was perhaps the first to prove that for two-dimensional flow on a sphere the kinetic energy is inversely cascaded up to large scales, who also argued the crucial importance of the vorticity conservation ($\beta = 0$ in 12.66)) in discussing the stability of steady flow. While the two-dimensional turbulence theory is beyond the scope of this book (see, e.g., Kraichnan 1967; Leith 1968; Batchelor 1969; Rhines 1979; Kraichnan and Montgomery 1980; Lesieur 1990; Salmon 1998), the basic conclusion is simple: unlike three-dimensional turbulence, *in the inertial range of two-dimensional turbulence the enstrophy is cascaded down to small scales but the kinetic energy is inversely cascaded up to large scales.* This result has been confirmed by direct numerical simulations (e.g. Ohkitani 1990; Rivera et al. 1998 and S.Y. Chen et al. 2003), and is in consistent with the preceding

analysis on the vorticity gradient. In particular, based on their direct numerical simulation, Chen et al. (2003a,b) calculated the alignment angle between the enstrophy flux among scales and the vorticity gradient. They found that the key mechanism for the enstrophy cascade is that the compressing effect of large-scale strain-rate field steepens the vorticity gradient.

Finally, the $\beta$-term in (12.71) has an asymmetric effect on vorticity gradient evolution. As a simple illustration, consider an initially axisymmetric vortex with azimuthal velocity $\boldsymbol{v} = g(r)\boldsymbol{e}_\alpha$ in the polar coordinates $(r, \alpha)$. Since $\boldsymbol{s} = s(r)\boldsymbol{e}_r$ for any $\alpha$, $\boldsymbol{e}_r$ is always aligned to $\boldsymbol{p}_+$ so that $\alpha_\lambda = 0$ and $\phi_\lambda = \alpha$. Then, in Cartesian coordinates with $(u, v) = g(-\sin\alpha, \cos\alpha)$, there is

$$\frac{\partial u}{\partial x} = \left(\frac{g}{r} - g'\right)\sin\alpha\cos\alpha, \quad \frac{\partial v}{\partial x} = g'\cos^2\alpha + \frac{g}{r}\sin^2\alpha.$$

Hence, in (12.71), the rate of change of the vorticity gradient due to the $\beta$-effect reads

$$\left(\frac{1}{s}\frac{\mathrm{D}s}{\mathrm{D}t}\right)_\beta = \frac{\beta}{s}(u_{,x}\sin\alpha - v_{,x}\cos\alpha) = -\frac{\beta}{s}g'(r)\cos\alpha, \tag{12.74a}$$

$$\left(\frac{\mathrm{D}\alpha}{\mathrm{D}t}\right)_\beta = \frac{\beta}{s}(u_{,x}\cos\alpha + v_{,x}\sin\alpha) = \frac{\beta}{s}\frac{g(r)}{r}\sin\alpha, \tag{12.74b}$$

which causes a nonuniform twisting and rotating of the velocity gradient, so that the vortex quickly becomes asymmetric.

### 12.3.2 The Structure and Evolution of Barotropic Vortices

We now turn to discuss already formed large-scale geophysical vortices. The vortices generated in a barotropic flow with negligible buoyancy effect are called *barotropic vortices*. In this case the fluid is assumed homogeneous. Under the same quasigeostrophic assumption as in the preceding subsection, one has freedom to construct various two-dimensional inviscid models for mesoscale atmospheric and oceanic vortices (see Sect. 6.2.1). Some early models have been reviewed by Flierl (1987).

In cylindrical coordinates $(r, \theta, z)$ the radial component of (12.8) for an axisymmetric flow reads, cf. (6.18a),

$$\frac{v^2}{r} + fv = \frac{1}{\rho}\frac{\partial p}{\partial r}, \tag{12.75}$$

indicating that the centrifugal acceleration due to both relative motion and rotating system is balanced by the radial pressure gradient. Thus, if the Coriolis parameter $f$ is constant, from (12.75) one obtains

$$v(r) = -\frac{1}{2}fr \pm \left[\left(\frac{1}{2}fr\right)^2 + \frac{r}{\rho}\frac{\partial p}{\partial r}\right]^{1/2}. \tag{12.76}$$

Solving this equation yields four types of vortices, of which the most important ones are the *cyclonic vortex* and *anticyclonic vortex* surrounding a

low-pressure and high-pressure center, with the senses of their rotation being the same of and opposite to the ambient vorticity $f$, respectively (Sect. 12.2.1).

If the pressure gradient is absent, there simply is

$$v(r) = -fr, \tag{12.77}$$

which is called the *inertia motion* as has been observed in the ocean.

Near the equator with small $f$, (12.75) is reduced to *cyclostropic motion*,

$$\frac{v^2}{r} = \frac{1}{\rho}\frac{\partial p}{\partial r}, \tag{12.78}$$

the same as (6.18a) in an inertial frame. The pressure gradient is always positive no matter what rotating direction is. In this case, some of those basic vortex solutions introduced in Chap. 5 may be applied to simulate the two-dimensional geophysical vortices, such as the Oseen vortex, Taylor vortex, and even the Burgers vortex (with stretching of shrinking due to the variation of the vortex-column height).

Recall that, in an inertial frame of reference, for the stability of a two-dimensional and inviscid axisymmetric vortex under axisymmetric disturbance we have the Rayleigh criterion (9.70), where $V$ is the azimuthal velocity of the basic flow. Now suppose the vortex is at the center of a rotating tank of angular velocity $\Omega = f/2$ such that $V = v + \Omega r$ with $v$ being the relative azimuthal velocity of the basic flow, then (9.70) takes the form

$$\frac{\mathrm{d}}{\mathrm{d}r}\left(rv + \frac{1}{2}fr^2\right)^2 \geq 0. \tag{12.79}$$

Kloosterziel and van Heijst (1991) have proved that this stability criterion holds generally true for two-dimensional inviscid vortices on an $f$-plane as well as for vortices that are off-center in a rotating fluid system. Thus, (12.79) represents a *generalized Rayleigh criterion*.

The simplest stable vortex structure is *monopolar vortex* consisting of circular streamlines about a common center, with positive or negative vorticity. Its simplest model is circular vortex patch. A more commonly seen but more complicated monopolar vortex consists of a vortex core of certain rotating sense surrounded by the vorticity of opposite sign (similar to the Taylor vortex). These large-scale monopolar vortices may come from the inverse energy cascade or self-organization process as addressed in Sect. 12.3.1 and shown in Fig. 12.10.

A class of relatively simple isolated vortical structures has often been used to study the instability of a monopolar vortex (Carton and McWilliams 1989; Carnevale and Kloosterziel 1994), which has smooth vorticity and velocity distributions. Its dimensionless form is

$$\omega = \omega_0\left(1 - \frac{1}{2}\alpha r^\alpha\right)\mathrm{e}^{-r^\alpha}, \tag{12.80}$$

where $\alpha$ is the steepness factor that controls the shape of vorticity distribution. The special case of $\alpha = 2$ is a *Gaussian vortex*:

$$\omega(r) = \left(1 - r^2\right) \mathrm{e}^{-r^2}, \quad v = \frac{1}{2} r \, \mathrm{e}^{-r^2}. \tag{12.81}$$

A class of structures more complicated than monopolar vortices is *dipolar vortices*, which is a self-propeled pair of counter-rotating closely packed patches with opposite vorticities. An exact inviscid dipolar-vortex solution, the circular Chaplykin–Lamb dipole, has been discussed in Sect. 6.4.2. A dipolar vortex has nonzero momentum but zero angular momentum. More complicated than this is *tripolar vortex* consisting of three patches in which the vorticity has alternative signs. For example, an elliptical vortex core with $\omega > 0$ along with two vortices with $\omega < 0$, each on one side, is a tripolar vortex. Furthermore, there can be *quadrupolar vortex*, etc. These typical structures are sketched in Fig. 12.13.

These abundant vortex patterns appear in geophysical flow because the instability of a monopolar vortex must lead to various compound vortices. Since the vorticity distribution determined by (12.80) has inflection point, according to the analysis of Sect. 9.3.1, the vortex will be unstable when $\alpha$ is sufficiently large. For example, it is unstable to the disturbance with azimuthal wave number $n = 2$ when $\alpha > 1.85$. Kloosterziel and Carnevale (1999) have examined a monopolar vortex with $\alpha = 3.0$ and initial state shown in Fig. 12.14a. They added a disturbance of the form

$$\omega' = \mu \cos(n\theta) \exp\left(-\frac{(\alpha r^\alpha - 2)^2}{2\sigma^2}\right), \tag{12.82}$$

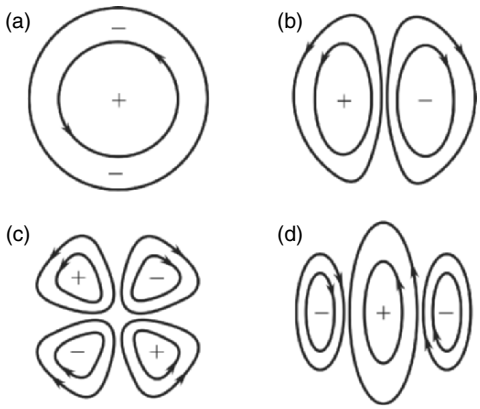


**Fig. 12.13.** Multipole structures. (**a**) vortex monopole; (**b**) vortex dipole; (**c**) symmetrical vortex quadrupole; (**d**) vortex tripole. Reproduced from Voropayev and Afanasyev (1994)

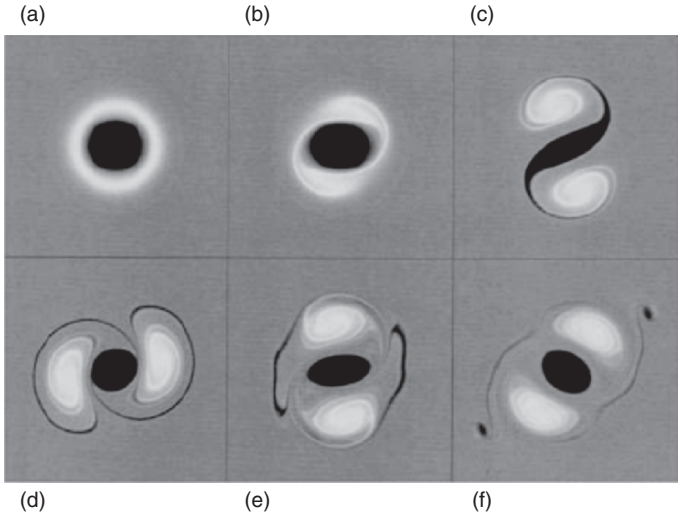


**Fig. 12.14.** Vorticity evolution of a monopolar vortex with a perturbation of type (12.46) with $n = 2$, $\mu = 0.1$, and $\sigma = 0.25$. Nondimensional time are (**a**) $t = 0$, (**b**) $t = 25$, (**c**) $t = 50$, (**d**) $t = 75$, (**e**) $t = 100$, and (**f**) $t = 200$. From Kloosterziel and Carnevale (1999)

where $n = 2$ is the azimuthal wave number, and $\mu$ and $\sigma$ are adjustable constants. A numerical calculation was conducted, see Fig. 12.14b–f. In Fig. 12.14b the vortex core has been elongated, indicating an increase of the disturbance amplitude. When $t = 50$, two hemicircular regions with opposite vorticities start to form, around which tendrils of core vorticity have been wrapped (Fig. 12.14c). Finally, the unstable monopolar vortex evolves to its mature stage, forming a tripole vortex (Fig. 12.14f) that can remain for long. Since it was found in laboratory and numerical simulation, the tripolar vortex has been an object of intense interest (van Heijst et al. 1991; Flor and van Heijst 1996). One has also observed tripolar vortex in ocean.

Further increasing the steepness parameter $\alpha$ may excite disturbances with higher azimuthal wave numbers. Figure 12.15 shows the evolution of a monopolar vortex with $\alpha = 7.0$ under an initial disturbance with $n = 3$ in (12.82). It eventually becomes a quadrupolar vortex, with a triangular vortex core surrounded by three satellite vortices of opposite vorticity. Then, in the numerical experiment of Kloosterziel and Carnevale (1999), a disturbance with $n = 4$ led the core of the same monopolar vortex with $\alpha = 7.0$ to become square in shape and four satellites are formed. The square vortex rotates but is unstable. Eventually, the core becomes elongated and breaks up into two pieces of dipoles. Beckers et al. (2003) have observed a transitory square vortex in their laboratory.

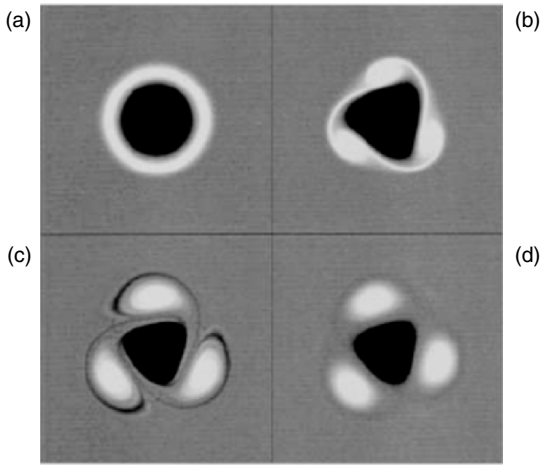


**Fig. 12.15.** Vorticity evolution of a monopolar vortex with a perturbation of type (12.81) with $n = 3$, $\mu = 0.1$, and $\sigma = 0.5$. Nondimensional time are (**a**) $t = 0$, (**b**) $t = 20$, (**c**) $t = 40$, and (**d**) $t = 200$. From Kloosterziel and Carnevale (1999)

Among various barotropic vortices discussed earlier, *dipole* solutions have the most general existence in both the atmosphere and ocean due to the following observation.

Consider an isolated cyclonic circulating flow at the northern hemisphere, of which the north side moves westward and experiences a southward Coriolis force, while the south side moves eastward and experiences a northward Coriolis force. Due to the $\beta$-effect, however, the latter is weaker than the former, forming a net north–south force on the flow not balanced by any other forces. Consequently, as a theorem proved by Flierl et al. (1983), *isolated structures with flat upper and lower boundaries cannot exist and remain isolated unless they have no net angular momentum.*

In other words, an isolated long-life vortical structure in the $\beta$-plane cannot be a simple monopolar vortex. If initially an isolated vortex in the $\beta$-plane has a nonzero net angular momentum, it will break apart rapidly, generating long barotropic Rossby wave that propagates quickly to the boundary (e.g., Flierl 1987). Therefore, the simplest form of isolated vortices in the $\beta$-plane are dipole solutions, also called *modons* or *$\beta$-gyres*.

The modons are exact, permanent-form, uniformly propagating solutions to the quasigeostropic potential vorticity equation (12.49) with flat bottom boundaries ($h_{\mathrm{B}}^{*} = 0$), characterized by closed streamlines that transport certain amount of the fluid with their traveling speed $c$ depending on their size (e.g. Stern 1975; Larichev and Reznik 1976; Berestov 1979; Flierl et al. 1980; Carnevale et al. 1988). They are actually the generalization of a classic Chaplykin–Lamb dipoles to geostrophic flow. The motion of modon depends on nonlinear effects. Rossby wave would tend to flatten out the modon, while

nonlinear effects would tend to steepen it, resulting in an equilibrium state. This nonlinear feature enables one to use the modon model to explain the dispersion and nonlinear phenomena in isolated geophysical flows.

We set $h_{\mathrm{B}}^{*} = 0$ in (12.48) which defines the potential vorticity $P'$ due to relative motion, and seek steady solution viewed in the frame of reference moving with the modon's traveling speed $c$ along the $x$-axis. Then $P'$ satisfies (12.43) with $\psi$ therein replaced by $\psi + cy$. The flow steadiness implies $[\psi + cy, P'] = 0$, and this will be so if $P'$ is any functional of $\psi + cy$. This reasoning is closely similar to that used in Sect. 6.4.2, where the flow being generalized Beltramian implied $\omega = F(\psi)$ for any $F$, which permits choosing $\omega = k^2\psi$ to linearize the equation for $\psi$ and obtaining the analytical solution of the Chaplykin–Lamb dipole. Now we can also linearize the equation for $\psi$ by setting

$$P' = (\nabla^2 - \lambda^{-2})\psi + \beta y = m(\psi + cy),$$

where $m$ is a constant. Assume $\psi$ vanishes fast enough at large $y$, we obtain $\beta = mc$ and thus the equation becomes

$$\nabla^2\psi = \rho^2\psi, \quad \rho^2 \equiv \frac{\beta}{c} + \lambda^{-2}.$$

Like the Chaplykin–Lamb dipole, this equation is also solved on the interior and exterior of a circle $r = a$ in polar coordinates, by separation of variables and requiring the continuity of $\psi$ and $\partial\psi/\partial r$ at $r = a$. The vorticity field of this modon solution on the $\beta$-plane, propagating due east, is given by

$$\omega(\theta, r) = -\beta' a \frac{J_1(kr)}{J_1(ka)} \sin\theta, \qquad (r \le a) \tag{12.83a}$$

$$= -\beta' a \frac{K_1(\rho r)}{K_1(\rho a)} \sin\theta, \qquad (r > a) \tag{12.83b}$$

where $\beta' = \beta + \lambda^{-2} = \rho^2 c$, $J_1$ and $K_1$ are the Bessel functions and modified Bessel functions, respectively, and $a$ is called the radius of the modon. Obviously, in the limit of $\lambda^{-2} = 0$ and $\beta \to 0$, the modon solution reduces to the Chaplykin–Lamb dipole (6.110).

The traveling speed $c$ and radius $a$ of modons may vary significantly. If $\lambda^{-2} = 0$, all values of $c \in [0, \infty)$ are possible. Once $a$ and $c$ are given, so will be $\rho$ and then the parameter $k$ is derived from a dispersion relation which assures the continuity of the tangential velocity at $r = a$:

$$-\frac{J_2(ka)}{kJ_1(ka)} = \frac{K_2(\rho a)}{\rho K_1(\rho a)}. \tag{12.84}$$

This equation has an infinity of branches, but the customary modon is the one corresponding to the branch with the lowest value of $k$, having the simplest structure. For example, at $\theta = 45^\circ$ there is $\beta \simeq 0.0014/(\mathrm{km\,day})$, for which Carnevale et al. (1988) considered a modon with radius $a \simeq 1000\,\mathrm{km}$ in ocean

and a special traveling speed $c = \beta a^2 \simeq 14\,\mathrm{km/day} \simeq 16\,\mathrm{cm\,s^{-1}}$. They found that the variation of the velocity from its center to $r \simeq a$ will be $U \simeq 5\beta a^2 \simeq 70\,\mathrm{km/day}$.

The stability of modon model has been a major concern owing to its importance in geophysical fluid dynamics. Unfortunately, while many numerical investigations have demonstrated that the modon is stable to rather strong perturbations, the problem of establishing its entire stability character, assuming it exists, remains to be unsolved.

Finally, we make a very brief discussion on the interactions between barotropic vortices, which is also a complicated issue. Two like-sign vortices with finite cores may merge into one when their distance $r$ is smaller than a critical value $r_c$. This merging process is the main mechanism for the turbulence decay in two-dimensional geophysical flow. Zabusky et al. (1979), Overman and Zabusky (1982), Melander et al. (1988), and others, have performed theoretical and numerical studies on this topic. For two vortex patches of the same size $R$ with uniform vorticity, the predicted critical distance is $d_c/R = 3.2$, in good agreement with experimentally observed critical value for the symmetric merging of anticyclonic vortices.

For cyclonic vortices, however, early experiments (Griffiths and Hopfinger 1986) by rotating tank with free surface found a significant variance from theoretical prediction; merging may occurs even when $d/R = 4.5$. This anomalous merger was explained by Carnevale et al. (1991b) as due to a topographic effect caused by the parabolic shape of the free surface in the rotating tank. Their prediction was confirmed by Fine et al. (1991) using an electron plasma experiments (which have no such topographic effect), who obtained the original merger rule $d_c/R = 3.2$ very accurately; and then by Nuijten and Velasco Fuentes (1994) using a rotating tank with rigid lid.

The isolated vortex structures presented here, such as monopolar vortices and modons, provide a simple way to explain many nonlinear phenomena in the atmospheric, oceanic, and planetary flows. As this explanation is combined with the interactions of coherent vortices, waves, and turbulence, a more complete physical interpretation of the nonlinear phenomena may be formed which, in turn, would help a deeper understanding of the role of these isolated vortices in geophysical fluid dynamics.

### 12.3.3 The Structure of Baroclinic Vortices

Baroclinic vortices exist in stratified fluid. Due to the coexistence of the effects of density and rotation, there is a direct and intimate relation between the structure of the density and velocity fields, characterized by the *Rossby radius of deformation* $\lambda$, see (12.45), which represents the distance over which the gravitational tendency to render the free surface flat is balanced by the tendency of Coriolis acceleration to deform the surface. Here, we consider the stratified fluid motion by a two-layer quasigeostrophic model rather than continuously stratified fluid. The thicknesses of the two layers are $H_\alpha$,

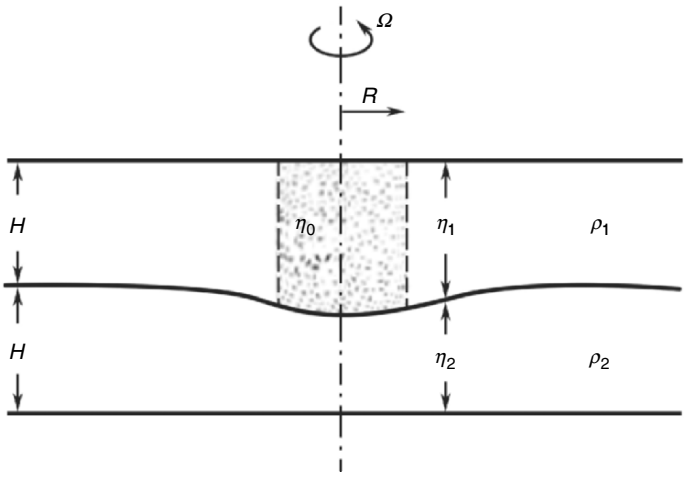


**Fig. 12.16.** Two-layer model of stratified fluid

with $\alpha = 1, 2$ for the upper and lower layers, respectively, see Fig. 12.16. Despite of its simplicity, this model does reflect the basic characters of stratified rotating fluid motion. By this simple two-layer model, analytical solutions of an isolated baroclinic vortex have been found by Pedlosky (1985), Griffiths and Hopfinger (1986), and Helfrich and Send (1988). In this model the Rossby radius of deformation is redefined by

$$\Lambda = \frac{\sqrt{g'H}}{f} \quad g' \equiv g\frac{\rho_2 - \rho_1}{\rho_2}. \tag{12.85}$$

If the flow scale $L \ll \Lambda$, then the effect of finite $\Lambda$ is negligible and the free surface has no difference from a rigid surface. If $L \gg \Lambda$, then the effect of finite $L$ becomes unimportant, and the horizontal flow velocity is uniform. Each layer satisfies the conservative equation (12.43) of the potential vorticity in quasigeostrophic flow:

$$\frac{\mathrm{D}P_\alpha}{\mathrm{D}t} = 0, \qquad \frac{\mathrm{D}}{\mathrm{D}t} = \frac{\partial}{\partial t} + [\psi_\alpha, \ \ ], \quad \alpha = 1, 2, \tag{12.86}$$

where $\psi_\alpha$ are the stream functions, the potential vorticities are

$$P_\alpha = \nabla^2\psi_\alpha + (-1)^\alpha \frac{f^2}{g' H_\alpha}(\psi_1 - \psi_2), \tag{12.87}$$

and the displacement of the contact surface is

$$\eta_\alpha - H = \pm\frac{f}{g'}(\psi_2 - \psi_1). \tag{12.88}$$

Consider now a *steady* vortex of core radius $R$ in the upper layer, which has uniform potential vorticity $P_0$. Outside the vortex core the relative vorticity

$\omega$ vanishes and the potential vorticity is $P = f/H$. In the lower layer, there is no vortex initially. Then

$$\nabla^2\psi_1 + \frac{1}{2}\lambda^{-2}(\psi_2 - \psi_1) = P_1, \qquad r < R \tag{12.89a}$$

$$\nabla^2\psi_1 + \frac{1}{2}\lambda^{-2}(\psi_2 - \psi_1) = 0, \qquad r > R \tag{12.89b}$$

$$\nabla^2\psi_2 + \frac{1}{2}\lambda^{-2}(\psi_1 - \psi_2) = 0, \tag{12.89c}$$

where $\lambda = \Lambda/\sqrt{2}$, $P_1 = \omega_0 = HP_0 - f$ is the relative vorticity. From these equations one can solve the azimuthal velocity induced by the baroclinic vortex:

$$\frac{v_\alpha}{R\omega_0} = \frac{r}{4R} \pm \frac{1}{2}K_1\left(\frac{R}{\lambda}\right) I_1\left(\frac{r}{\lambda}\right), \qquad r < R, \tag{12.90a}$$

$$\frac{v_\alpha}{R\omega_0} = \frac{R}{4r} \pm \frac{1}{2}I_1\left(\frac{R}{\lambda}\right) K_1\left(\frac{r}{\lambda}\right), \qquad r > R, \tag{12.90b}$$

in which $K_1$ and $I_1$ are modified Bessel functions, signs + and − correspond to layers 1 and 2, respectively. The velocity distribution is shown in Fig. 12.17, where solid and dashed lines are the velocities in the upper and lower vortices. For comparison, the velocity of a barotropic vortex is also shown by short dashed line.

It is seen from Fig. 12.17 that although initially the lower layer has no vortex, the baroclinic effect creates an obvious vortical motion as a baroclinic

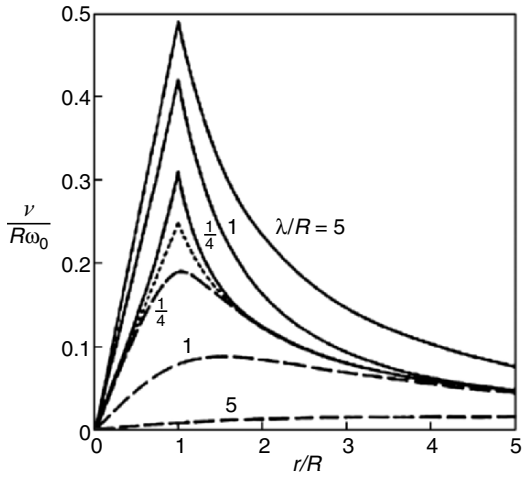


**Fig. 12.17.** The azimuthal-velocity distribution of a theoretical baroclinic vortex model. Top layer velocities (*solid lines*), bottom layer (*long dashed lines*), barotropic limit (*short dashed line*). Reproduced from Griffiths and Hopfinger (1987)

vortex. Its azimuthal velocity profile depends on the characteristic motion scale of the vortex, i.e., the ratio of the core radius $R$ and the Rossby radius of deformation $\Lambda$. First, let $R/\lambda \to 0$ so that $I_1(R/\lambda) \to 1/2R/\lambda$, then for $r > R$ there is

$$v_\alpha = \frac{1}{2}\frac{s}{r}\left[1 \pm \frac{r}{\lambda}K_1\left(\frac{r}{\lambda}\right)\right]. \tag{12.91}$$

where $s = (R^2\omega_0)/2$ is the vortex intensity. This is the solution obtained by Hogg and Stommel (1985). In the upper-layer, when $r > R$ the variation of azimuthal velocity significantly differs from the irrotational rule $v \sim 1/r$. In contrast, in the lower layer, the azimuthal velocity is obviously smaller that that in the upper layer for $r < R$, but approaches a constant for $r > R$.

Next, let $\lambda/R \to 0$, for which the effect of density gradient disappears and the flow tends to the Rankine vortex:

$$v_1 = v_2 = \begin{cases} \dfrac{sr}{2R^2} & r < R, \\ \dfrac{s}{2r} & r > R. \end{cases} \tag{12.92}$$

When $r > R$, the flow is actually independent of the depth, i.e., the fluid motion in both layers tends to be the same.

Finally, we briefly discuss the interaction of baroclinic vortices. By (12.92), owing to the interaction of $N$ vortices, the $k$th vortex has velocity in the $x$-direction

$$u_k = \sum_{n\neq k}^{n=N} \frac{s_n}{2}\left(\frac{y_k - y_n}{r_{kn}^2}\right)\left[1 + \Phi\frac{r_{kn}}{\lambda}K_1\left(\frac{r_{kn}}{\lambda}\right)\right], \tag{12.93}$$

where $r_{kn}^2 = (x_k - x_n)^2 + (y_k - y_n)^2$, and $\Phi = -1$ if the $n$th and $k$th vortices are in different fluid layers, or $\Phi = 1$ if otherwise. The velocity in the $y$-direction is similar. This interaction is determined by the modified Bessel function and hence is of short range. Thus, if the distance between two baroclinic vortices in the same fluid layer reduces, the velocity by which they propel each other will be larger than barotropic vortices; and inversely, if the two vortices are in different layers, then their interaction velocity will approaches zero as their distance. The integral invariance during the interaction of these vortices has been given by Hogg and Stommel (1985).

An interesting property of baroclinic–vortex interaction is that it can transport heat and other scalars. The vortex with negative sign in the upper layer will make the contact surface move down, and meanwhile so will the vortex with positive sign in the lower layer, resulting in a downward motion of hotter fluid. Thus, this couple of vortices, one on top of the other, is called a *hot heton*. The situation will be opposite if the sign of the vortices in upper and lower layers is reversed, for which the vortex couple becomes a *cold heton*. When these couples are not aligned, they will have displacement due to self-propulsion. This is the case when more than one vortex couples appear in the system, which can make the couple split due to the induction of other

couples. This interaction weakens the heat conduction and system's potential energy. Hogg and Stommel (1985) found that the heat transport by discrete vortex couples is inversely proportional to $r/\lambda$.

The baroclinic–vortex interaction may form interesting paths and partner exchange, in particular in the case with two hot hetons. If their distance $d$ is greater than the Rossby radius then hot hetons repel each other; while if $d$ is smaller than or equal to the Rossby radius, they will cohere together.

Like barotropic vortices, if the distance between two baroclinic vortices is smaller than a critical value, they will merge. For the latter, however, in addition to the effect of velocity field, the buoyancy due to density stratification also has a strong effect. For the two-layer model of the stratified fluid, if in the upper layer there are two vortices of the same sign and strength, then the merge will occur when their distance is smaller than a critical value. But for baroclinic vortices, the time needed from their initial rolling around each other to eventual merging will be much longer that the corresponding value of barotropic vortices. We call a vortex couple stable if the vortices do not merge, and unstable if they do.

The earlier discussion on vortex merging is for two vortices of the same strength and core radius. Two baroclinic vortices with similar potential vorticity but different strength and core radii will interact asymmetrically with larger critical distance, and the weaker vortex was always drawn out to surround the stronger one. Overman and Zabusky (1982) described the asymmetric interaction as "entrainment" of the region of greater vorticity density (the stronger vortex core) within the region of small vorticity density.

### 12.3.4 The Propagation of Tropical Cyclones

So far we have discussed the key role of potential vorticity, the evolution of two-dimensional vorticity field, and the structures of some barotropic and baroclinic vortices. Yet another key issue is the propagation of intense large-scale vortices, such as *Gulf Stream rings* in the ocean and *tropical cyclones* in the atmosphere. Due to the nonlinear advection under the $\beta$-effect, these structures can travel over thousands of kilometers while maintain their identities. They have very significant influence of the ocean and weather systems of the earth, and the prediction of their propagation paths is of crucial importance. We now conclude this chapter by considering the propagation of tropical cyclones, i.e., *hurricanes* in the North Atlantic Ocean and *typhoons* in the western North Pacific Ocean. The basic mechanisms can be clarified within quasigeostrophic approximation (12.49), and are about the same for the motion of of rings in ocean.

Figure 12.18 shows the track of a typhoon observed in 1990 as an example. Before entering the circled region, the typhoon had an initial tendency to propagate to the northwest, which is actually in common to all cyclones in the northern hemisphere. Therefore, we first focus on the theory and underlying physics of this "*northwest rule*".

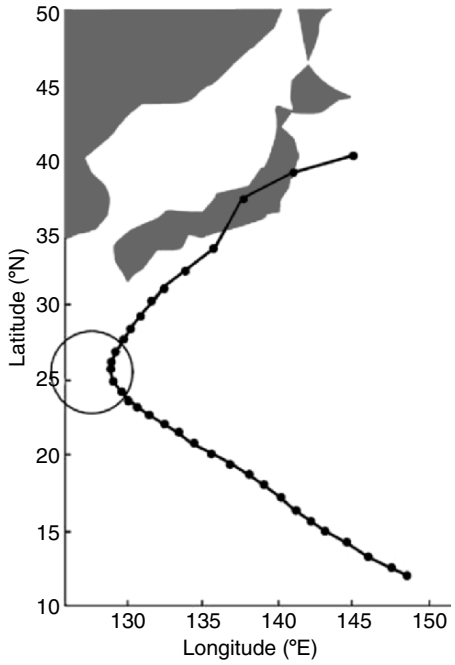


**Fig. 12.18.** Track of Typhoon Flo (1990). The time interval between two successive positions is 6 h, and the period of the segment within the circle is from 16 September 1990 at 1800 Universal Time Coordinate (UTC) to 17 September 1990 at 1800 UTC (the four-digit number is ddhh, dd and hh representing date and hour, respectively). From Chan (2005)

For a feature common to all cyclones, the bottom topography is beyond our concern. Thus the quasigeostrophic equation (12.49) is reduced to

$$(\nabla^2 - \lambda^{-2})\frac{\partial \psi}{\partial t} + [\psi, \nabla^2 \psi] + \beta \frac{\partial \psi}{\partial x} = 0, \tag{12.94}$$

where $\lambda$ is the deformation radius defined in (12.45) to approximate the vortex stretching due to horizontal divergence with low *Ro*. When $\lambda \to \infty$, (12.94) is valid for arbitrary *Ro*. An inspection of this equation reveals that it is invariant under the transformation $(\psi, y) \to (-\psi, -y)$, thus for any nonzero Rossby number, if in the northern hemisphere a cyclone moves to the northwest, an anticyclone will move to the southwest (and vice versa in the southern hemisphere).[8] Since the characteristic size of a tropical cyclone is much smaller than its distance to another cyclone, each cyclone is assumed *isolated*.

[8] "Cyclonic" implies counterclockwise/clockwise in the northern/southern hemisphere, so the terms cyclonic and anticyclonic can be used without reference to the specific hemisphere.

The studies of "northwest rule" were pioneered by Rossby (1948) and Adem (1956). Adem took $\lambda = \infty$ in (12.94), expanded the stream function $\psi$ in a Taylor series in time $t$, and showed that the combination of the lowest-order effects, i.e., terms with $\beta t, \beta t^2$ and $\beta t^3$, leads to the northwest rule. With the advance in satellite and computational technologies, since then the northwest rule has been repeatedly confirmed and the theoretical analysis based on (12.94) has been developed (Hopfinger and van Heijst 1993). Here we present a quite thorough analytical theory of Sutyrin and Flierl (1994), which is also taken as the unique example in this book to illustrate how to solve a specific nonlinear vorticity-vortex dynamics problem.

For later convenience, we rewrite the dimensional equation (12.94) in capital letters. Assume that the background flow is a zonal flow with uniform velocity $U\boldsymbol{e}_x$, so that the stream function $\Psi' = \Psi + UY$ and the associated potential vorticity $P'$ (not Lagrangian invariant) are governed by

$$\frac{\partial P'}{\partial T} + [\Psi' - UY, P'] = -\beta' \frac{\partial \Psi'}{\partial X}, \tag{12.95a}$$

$$(\nabla_\pi^2 - \lambda^{-2})\Psi' = P', \tag{12.95b}$$

where $\beta' \equiv \beta - U\lambda^{-2}$ is the effective $\beta$-term. Let the vortex center be at $(X_0, Y_0)$ with velocity $(U_0, V_0) = (\dot{X}_0, \dot{Y}_0)$ relative to the background zonal flow. We use the characteristic horizontal length scale $R$ and rate of rotation $\Omega_v$ of the vortex to nondimensionalize (12.95) and introduce dimensionless polar coordinates $(r, \theta)$ comoving with the vortex. Thus, we set $t = \Omega_v T$, $\omega = P'/\Omega_v$, $\psi = \Psi'/\Omega_v R^2$, $\gamma = R/\lambda$, and $\epsilon = \beta' R/\Omega_v$, such that (12.95) is recast to

$$\frac{\partial \omega}{\partial t} + [\psi^*, \omega] + \epsilon[\psi, r\sin\theta] = 0, \tag{12.96a}$$

$$(\nabla^2 - \gamma^2)\psi = \omega, \tag{12.96b}$$

where

$$\psi^* = \psi + \epsilon r(u\sin\theta - v\cos\theta) \tag{12.97}$$

describes the fluid motion relative to the vortex center, with $(u, v) = (\dot{X}_0, \dot{Y}_0)/\beta' R^2$ being the dimensionless propagation velocity of the center.

If there were no $\beta$ effect, the $r\sin\theta$ term in (12.96a) would vanish and an initially axisymmetric vortex would remain so. Thus, it is natural to decompose $\omega$ into a vortex part and a coupled $\beta$-caused residual anomaly, denoted by

$$\psi = \Phi + \epsilon\phi, \quad \omega = Q + \epsilon q.$$

Then, Sutyrin and Flierl (1994) simplify the formulation by replacing the smooth $\omega$-field by *nested vortex patches* of piecewise constant potential vorticity, so that the vortex patch theory and contour dynamics of Sect. 8.3.2 can

be applied. Specifically, let $\hat{r}_j = r_j + \epsilon\eta_j$ be the $j$th contour boundary with $\eta_j$ being the distortion from circular shape, we write

$$Q = (\nabla^2 - \gamma^2)\Phi = \sum \Delta_j H(\hat{r}_j - r), \tag{12.98}$$

in which $H$ is the Heaviside step function and $\Delta_j$ is the $j$th jump at $\hat{r}_j$. Since $\nabla Q$ gives $\delta$-functions, there is

$$\frac{\mathrm{D}Q}{\mathrm{D}t} = \sum \Delta_j \delta(\hat{r}_j - r)\left(\epsilon\frac{\mathrm{D}\eta_j}{\mathrm{D}t} - \frac{\mathrm{D}r}{\mathrm{D}t}\right).$$

Equating the coefficients for all the $\delta$-function terms to zero and dividing by $\epsilon$ yield

$$\frac{\partial\eta_j}{\partial t} + \Omega_j\frac{\partial\eta_j}{\partial\theta} + \frac{1}{\hat{r}_j\epsilon}\frac{\partial\Phi_j}{\partial\theta} = -\frac{1}{\hat{r}_j}\frac{\partial\phi^*}{\partial\theta}, \tag{12.99}$$

where

$$\Omega_j = \frac{1}{\hat{r}_j}\frac{\partial}{\partial\theta}(\Phi + \epsilon\phi_j^*), \quad \phi_j^* = \phi_j + r(u\sin\theta - v\cos\theta).$$

Subtracting the $(Q, \Phi)$ part from (12.96a) yields the the equation for residual potential vorticity anomaly, the $(q, \phi)$ part:

$$\frac{\partial q}{\partial t} + \epsilon[\phi^*, q] + \epsilon(\phi, r\sin\theta) = -[\Phi, q + r\sin\theta] \tag{12.100a}$$

$$(\nabla^2 - \gamma^2)\phi = q, \tag{12.100b}$$

which are actually equations for a *forced Rossby wave*. Physically, like a moving vorticity field will produce sound wave (Sect. 2.4.3), now a moving quasigeostrophic vortex will produce long Rossby wave. Similar to the limitation of potential-vorticity inversion (Sect. 12.2.4) due to the emission of gravity wave, the isolated vortex motion solved from the earlier equations is also effective only in a period in which the Rossby-wave radiation is negligible. Beyond this time scale the vortex will no longer be isolated but become an "inner solution" to be matched with the far-field Rossby wave radiation as the "outer solution".

Equations (12.98)–(12.100) are still nonlinear. Since $\beta'$ is weaker than the potential vorticity anomaly of an intense vortex, we assume $\epsilon \ll 1$ and expand the solution in $\epsilon$ to linearize the problem. Namely, we write $\Phi = \Phi_0(r) + \epsilon\Phi_1(r, \theta, t)$, where $\Phi_0$ is a symmetric part specified by the initial condition and $\Phi_1$ an asymmetric part from the relative shift of the vorticity contours. This regular perturbation is valid for $t \ll \epsilon^{-1}$. Then the axisymmetric part $\Phi_0$ is governed by a Helmholtz equation that can be easily solved using the Green's function

$$G_1(r, r') = \begin{cases} -r' I_1(\gamma r)K_1(\gamma r') & \text{for} \quad r < r', \\ -r' I_1(\gamma r')K_1(\gamma r) & \text{for} \quad r > r', \end{cases} \tag{12.101}$$

to yield

$$\Omega_0(r) \equiv \frac{1}{r}\frac{\mathrm{d}\Phi_0}{\mathrm{d}r} = -\frac{1}{r}\sum \Delta_j G_1(r, r_j). \tag{12.102}$$

Next, the asymmetric part with nonzero $\eta_j$ is governed by the linear set

$$(\nabla^2 - \gamma^2)\Phi_1 = \Delta_j \eta_j, \tag{12.103a}$$

$$\frac{\partial \eta_j}{\partial t} + \Omega_{0j}\frac{\partial \eta_j}{\partial \theta} + \frac{1}{r_j}\frac{\partial \Phi_{1j}}{\partial \theta} = -\frac{1}{r_j}\frac{\partial \phi_j}{\partial \theta} - u\cos\theta + v\sin\theta, \tag{12.103b}$$

$$\frac{\partial q}{\partial t} + \Omega_0 \frac{\partial q}{\partial \theta} = -\Omega_0 r\cos\theta, \tag{12.103c}$$

where $\phi_j = \phi(r_j, \theta, t)$ and repeated indices imply summation henceforth. Then, assuming $q = 0$ at $t = 0$, the solution of (12.103c) and hence that of (12.100b) can be easily obtained:

$$q = r\sin(\theta - \Omega_0 t) - r\sin\theta, \tag{12.104a}$$

$$\phi = \frac{r\sin\theta}{\gamma^2} + I_1(\gamma r)\int_r^\infty K_1(\gamma r')\sin(\Omega_0 t - \theta) r'^2\,\mathrm{d}r' + K_1(\gamma r)\int_0^r I_1(\gamma r')\sin(\Omega_0 t - \theta) r'^2\,\mathrm{d}r'. \tag{12.104b}$$

Remarkably, owing to the vortex-patch approximation, the $(q, \phi)$ part is independent of the vortex distortion $\eta_j$ but simply advected by the planetary vorticity $r\sin\theta$ and the axisymmetric vortex with rate of rotation $\Omega_0(r)$. Note that (12.104a) indicates explicitly that for long times the disturbances would be unrealistically large, a sign of the aforementioned limitation imposed by the radiation of Rossby wave.

The coupled equations (12.103a) and (12.103b) can be solved by expanding relevant variables in azimuthal modes as $F(r, \theta, t) = \hat{F}(r, t)\mathrm{e}^{\mathrm{i}m\theta}$ to remove their $\theta$-dependence. Recall the theorem of Sect. 12.3.2 that only dipoles with antisymmetric mode $m = -1$ can persist a long time, we should focus on this *modon* or *β-gyres* mode. Then (12.103a) has solution $\hat{\Phi}_1(r, t) = \Delta_j \eta_j G_1(r, r_j)$, and (12.103b) reduces to a set of ordinary differential equations:

$$\frac{\mathrm{d}\hat{\eta}_j}{\mathrm{d}t} - \mathrm{i}A_{jk}\hat{\eta}_j = \mathrm{i}r_j^{-1}\hat{\phi}_j - (u + \mathrm{i}v), \tag{12.105a}$$

$$A_{jk} = \Omega_0(r_j)\delta_{jk} + r_j^{-1}\Delta_k G(r_j, r_k), \tag{12.105b}$$

which can be solved by normal-mode expansion in terms of the eigenvectors of $A_{jk}$. We thus see that a $\beta$-gyre has two parts. One is expressed by (12.104) and generated directly by the advection of the planetary vorticity $r\sin\theta$,

and the other part is induced by distortions in the vortex shape (12.103b), due to the radial advection of contours relative to the vortex center by the first part.

Once $\hat{\phi}_j$ and $\hat{\eta}_j$ are known, from (12.105a) we can further obtain the velocity and trajectory of the vortex center analytically, which are our ultimate concern. The result depends on the definition of the center of an irregular vortex, of which a few alternative choices were considered by Sutyrin and Flierl (1994). They recommend that the most appropriate choice is to let $\eta = 0$ at the innermost contour (assumed at $r = 1$) of the vortex, implying a *solid-like core*. It then follows that

$$x + \mathrm{i}y = -\frac{t}{\gamma^2} + \mathrm{i}\frac{\mathrm{e}^{\mathrm{i}\Omega_0(r)t} - 1}{\Omega_0(r)} \int G_1(1,r)r \, \mathrm{d}r + i \sum_k A_{0k} \int_0^t \eta_k \, \mathrm{d}t. \quad (12.106)$$

In particular, if the vortex is represented by a single patch with $j = 0$ (a Rankine vortex at $t = 0$), for $\gamma \ll 1$ it is found that $x + \mathrm{i}y$ approaches asymptotically to a northwest accelerating motion

$$x + \mathrm{i}y \simeq \frac{t^2}{8}\left(\frac{\pi}{2} + \mathrm{i}\,\ln\frac{1}{\gamma^2 t}\right), \quad (12.107)$$

as previously found by Sutyrin (1988) and Reznik (1992) for a geostrophic point-vortex.

A two-contour vortex model having jumps $\Delta_0$ and $\Delta_1$ can mimic tropical cyclones quite well. Typically, the radius of the inner contour with large vorticity is on the order of 100 km, and the radius of the outer contour that encloses the cyclonic circulation is an order larger. We thus have $r_0 = 1$ with the peak rotation rate $\Omega_0(1) = 1$, and $r_1 \sim 10$ with $\delta \equiv -\Delta_1/2 \ll 1$. Assuming the nondivergent limit $\gamma \to 0$ such that (12.105) can be simplified, Sutyrin and Flierl derived an explicit universal formula for the highly nonlinear time-dependence of the propagation velocity of the vortex, in terms of both $t$ and a slow time $\tau = t\delta$:

$$\begin{aligned} u + \mathrm{i}v = {} & \frac{1 - \mathrm{i}\tau}{8}(1 - \mathrm{e}^{\mathrm{i}t}) \\ & + \frac{t + \tau}{4}\left(\mathrm{i} + \frac{\tau}{2}\right)\mathrm{e}^{-\mathrm{i}\tau}[\mathrm{Ei}(\mathrm{i}(t + \tau)) - \mathrm{Ei}(\mathrm{i}\tau)], \end{aligned} \quad (12.108)$$

where $\mathrm{Ei}(x)$ is the Eiry function, of which the asymptotic behavior naturally divides the vortex track into three stages. The *initial stage* for $t < 1$ and $\tau \ll 1$ has the track

$$x_0 \simeq -\frac{1}{2}\left[\frac{y_0}{\ln(r_1)}\right]^{3/2}, \quad (12.109)$$

so the vortex center accelerates predominately to the north with increasing westward displacement. Then, in the *advanced stage* for $1 < t < \delta^{-1}$ and

$\tau < 1$, the corresponding length scale is $R' = \beta' R^2/\Omega_v \delta^2$, so let $(X_0, Y_0) = R'(\hat{x}, \hat{y})(\tau)$ one has the universal vortex track, depending on the slow time $\tau$ only:

$$\hat{x} + \mathrm{i}\hat{y} = \delta \int (u + \mathrm{i}v)\mathrm{d}\tau = -\frac{1}{4} \int \tau \mathrm{e}^{-\mathrm{i}\tau} \left(\mathrm{i} + \frac{\tau}{2}\right) \mathrm{Ei}(\mathrm{i}\tau)\mathrm{d}\tau, \qquad (12.110)$$

of which a plot is shown in Fig. 12.19. Also shown in the figure is the track computed without considering the distortion in the vortex shape, for which the factor $\mathrm{i} + \tau/2$ in (12.110) would be absent. The significant difference of the two curves indicates the crucial influence of the shape distortion. This advanced stage is followed by a *mature stage* with $\tau > 1$, which we omit here (see Sutyrin and Flierl 1994).

The prediction of the earlier analytical theory has been compared with the motion of typical tropical cyclones by Sutyrin and Flierl (1994), who also discuss its application to oceanic rings. But for better comparison it seems necessary to go to at least two-layer modeling of stratification as exemplified in Sect. 12.3.3 for either atmospheric and oceanic phenomena (Carnevale et al. 1988), of which for some earlier studies see, e.g., McWilliams and Flierl (1979) and Mied and Lindemann (1979).

The universal northwest rule for the initial movement of cyclones is of course insufficient for predicting the specific track of each intense vortex, although returning to dimensional form with original variables (12.108) already implies a big variety of cyclone tracks. More physical factors have to be taken into consideration. First, the *bottom topography* has a strong influence on the track, of which a basic model is the quasigeostrophic flow governed

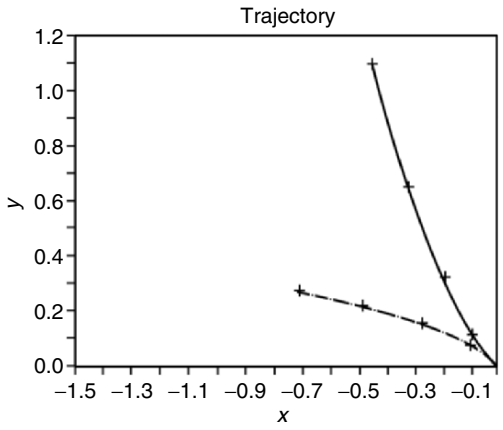


**Fig. 12.19.** Universal vortex track (*solid line*) for the advanced stage of two-contour vortex, computed by (12.110). The dash-dotted line is the result without considering the vortex-shape distortion. Crosses denote $\tau = 1, 2, 3, 4$. Adapted from Sutyrin and Flierl (1994)

by (12.49) with $\lambda^{-2} = 0$. At the fundamental level, Carnevale et al. (1988) have used a two-point-vortex model to approximate a modon and conducted comprehensive numerical experiments on the propagation of barotropic modons over a variety of topography, such as ridges, valleys, axially symmetric hills and holes, and randomly generated topographies. For example, cyclones would climb hills but anticyclones would move downhill.

Carnevale et al. (1991a) have further used rotating-tank experiment to investigate the effect of topography on the propagation of both isolated cyclones (with zero total circulation) and nonisolated cyclones (with nonzero circulation). Briefly, if the horizontal scale of a vortex is much smaller than that of the topography over which it lies, the latter can be modeled by a constant slope of which the direction defines local compass directions and hence a local "$\beta$-effect". Thus, a cyclone over such a broad topography will propagate toward the "local northwest" (upslope and toward left), which alters the direction of the vortex track. For example, a cyclone would climb up out of a valley in a cyclonic spiral around the center, and up the slope of a hill in an anticyclonic spiral around the peak. More complicated than this, sufficiently strong topographic disturbances can destroy a modon into two nearly independent oppositely signed vortices.

At the applied level, among others, Luo and Chen (1995) have used (12.49) with $\lambda^{-2} = 0$ to perform nine numerical experiments on the topographic effect of Taiwan island on typhoon tracks, and obtained right deviation of the tracks.

Secondly, baroclinicity implies the appearance of horizontal temperature gradient accompanied by vertical wind shear in the vortex, resulting in low-level cyclonic and high-level anticyclonic structure as sketched in Fig. 12.6. In this case one has to use the isentropic potential vorticity (IPV) defined in (12.59).

Once the vertical flow enters into the play, however, a thorough theoretical analysis becomes impossible. Instead, in developing practical forecast methods one substitutes the observed data into the governing equations more general than (12.49), to infer the local time derivative of $P$ ($\partial P/\partial t$ or simply $P_t$) called the *IPV tendency*, and use it to predict the vortex position shortly afterward. Here, the key issue is to identify the mechanisms or terms that dominant the IPV tendency qualitatively. This strategy is reviewed by Chan (2005) and outlined later.

Generically, the IPV tendency can be symbolically expressed by

$$P_t = \mathrm{HA} + \mathrm{VA} + \mathrm{DH} + \mathrm{FR}, \tag{12.111}$$

where HA, VA, DH, and FR represent horizontal advection, vertical advection, diabatic heating, and friction, respectively. The friction is important only in the planetary boundary layer, so baroclinicity adds two extra mechanisms, the *vertical advection* and *diabatic heating*.[9] Then, Wu and Wang (2000) found

[9] The diabatic heating in tropics is largely the difference between latent heat release and radiative cooling, and for the former to happen it is necessary to consider the *moisture field* (e.g., Gill 1982b), that makes the problem even more involved.

that the tropical cyclone tends to move toward the area of $\max\{P_{1t}\}$, where $P_1$ denotes the azimuthal mode of $P$ with wavenumber 1 (WN-1), which we recall in the quasigeostrophic model is modons or gyres. Using a projection operator $\Lambda_1$ to project both sides of (12.111) into the WN-1 mode, from observed data the authors diagnosed that the strongest vertical gradient of $P_{1t}$ is near the eyewall in the tropical cyclone and the tropopause in the tropical atmosphere, respectively. Therefore, away from these regions the dominant causes of vortex motion is horizontal advection and diabatic heating. Then the WN-1 mode of the former can be further decomposed to (Chan et al. 2002)[10]

$$\Lambda_1\{\mathrm{HA}\} = -(\boldsymbol{v}_1 \cdot \nabla P_s + \boldsymbol{v}_s \cdot \nabla P_1), \tag{12.112}$$

where the first term denotes the asymmetric advection of symmetric potential vorticity (AASPV) in the vortex and environment, including the contribution of the $\beta$-effect and other asymmetric convection; while the second term is the symmetric advection of asymmetric WN-1 potential vorticity (SAAPV) consisting of the $\beta$-gyres, vertical shear, and asymmetric convection. On the other hand, diabatic heating is found strong mainly when the convection is quite asymmetric and the vortex track is not smooth.

Chan et al. (2002) have applied (12.111) and (12.112) to diagnose the data of more than 300 typhoons, which led them to propose the following conceptual framework to interpret their motions (see also Chan 2005):

*The potential vorticity tendency of WN-1 determines the motion of a tropical cyclone, due mainly to the horizontal advection and diabatic heating.* While the former dominates when the motion is steady, a significant contribution of the latter, especially the rotation of its asymmetric part, can lead to a non-smooth vortex track. Within this azimuthal mode, changes in the distribution of one or more of AASPV, SAAPV, and adiabatic heating, lead to subsequent changes of the vortex motion direction.

Evidently, this conceptual framework has to be supplemented by the aforementioned bottom topography effect. Nevertheless, we can now follow the analysis of Chan (2005), applying (12.111) and (12.112) to interpret Fig. 12.18, especially the physics that caused the turn of the track of the Typhoon Flo from a northwestward to a northeast direction. The turn started at 0000 Universal Time Coordinate (UTC) on 17 September associated with a maximum AASPV to the northeast of the vortex and about perpendicular to its motion direction, see Fig. 12.20a. Thus by (12.112), the large-scale flow had changed, to advecting the vortex toward the *northeast*. But the vortex turning is an integrated effect of maximum relative vorticity tendency over time, and hence happened later. Meanwhile, the SAAPV caused a significant $\max P_{1t}$ opposite to the AASPV term at the left of the vortex direction, see Fig. 12.20b. The effect of diabatic heating DH is small (Fig. 12.20c). Thus, both terms in (12.112) jointly determined the instantaneous direction of the total $P_t$ maximum as shown in Fig. 12.20d.

[10] Advection of WN-1 mode by the WN-1 flow no longer yields a WN-1 mode.

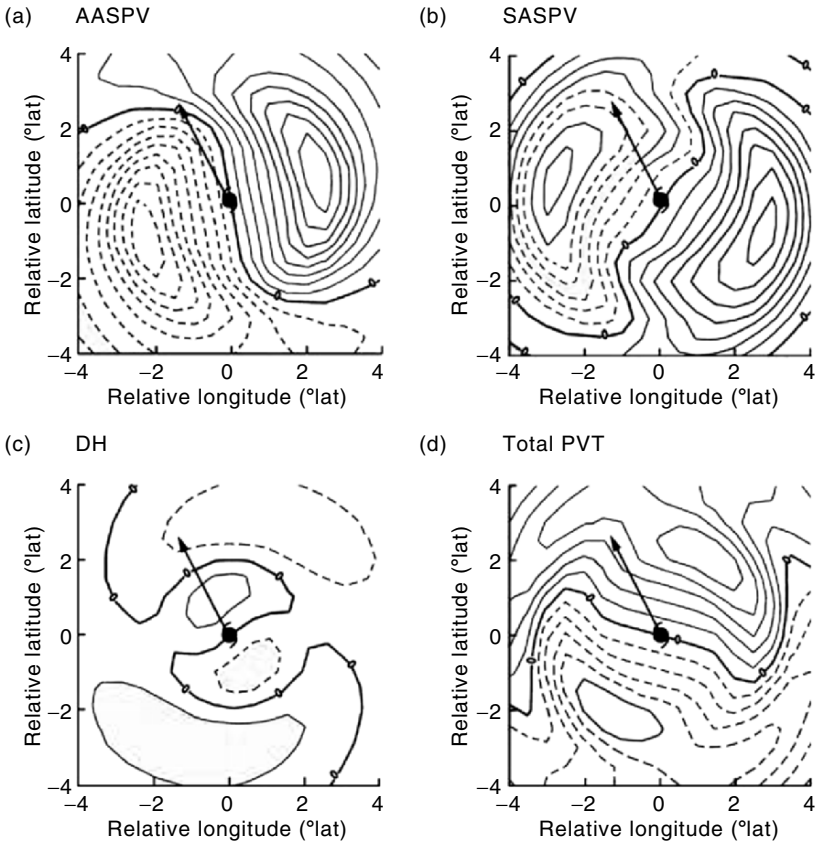


**Fig. 12.20.** Contributors to WN-1 potential vorticity tendency $P_{1t}$ in the midtroposphere for Typhoon Flo at 0000 UTC on 17 September 1990. (**a**) and (**b**) are the contributions of AASPV and SAAPV terms in horizontal advection, of $P_t$, and (**c**) is the contribution of DH term, and (**d**) total potential vorticity tendency (PVT). The contour intervals are $0.5 \times 10^{-9} \mathrm{m^2 s^{-2}\,K\,kg^{-1}}$. thin solid (*dashed*) lines are positive (negative) values. The arrow points to the direction of vortex motion, with the typhoon symbol at its center. Adapted from Chan (2005)

The vortex track turned toward the north-northeast 18 h later, so the patterns of Fig. 12.20 became those in Fig. 12.21. In WN-1 horizontal advection, the AASPV pattern (Fig. 12.21a) again rotated clockwise, with maximum on the southeast side and ahead of the vortex motion, while the SAAPV pattern (Fig. 12.21b) rotated similarly with different maximum direction and location. Both horizontal advections were significantly stronger than that in Fig. 12.20 due to the enhancement of potential vorticity in the vortex. On the other hand, the diabatic heating (Fig. 12.21c) was also enhanced, with maximum on the left of the vortex motion direction. Again the vortex motion

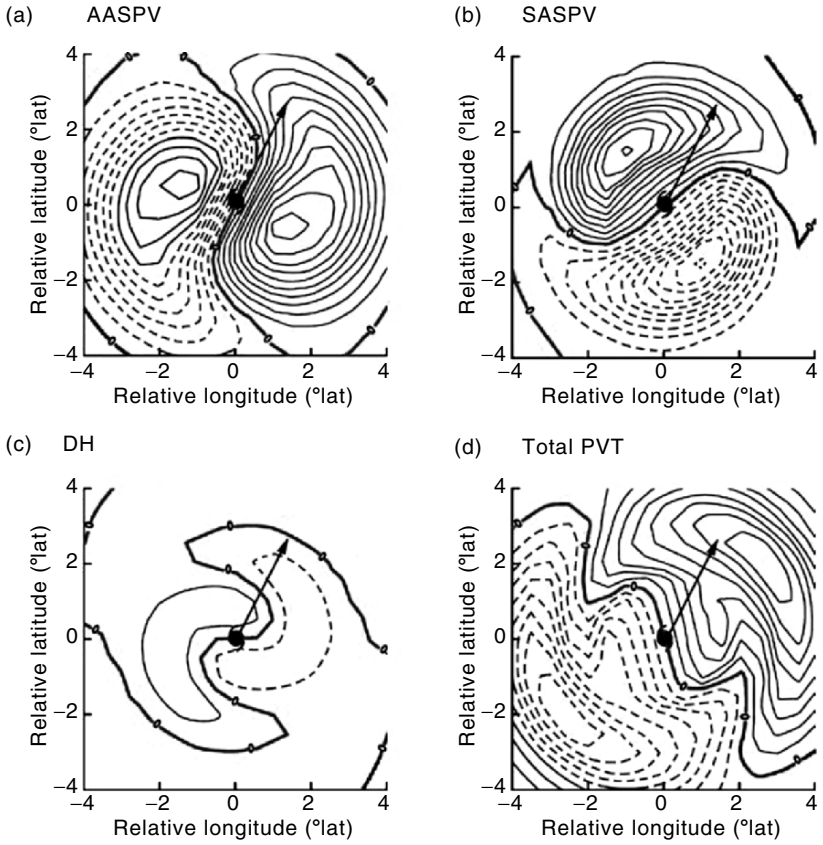


**Fig. 12.21.** As in Fig. 12.20 except after the track turned (1800 UTC on 17 September 1990). The contour intervals are $1 \times 10^{-9} \mathrm{m^2 s^{-2}\,K\,kg^{-1}}$. From Chan (2005)

direction was aligned better to the total $P_{1t}$ maximum than any individual term (Fig. 12.21d), indicating that all the three mechanisms should be considered especially when the motion changes direction.

## Summary

1. Vorticity and vortex dynamics is of considerable importance in atmospheric and oceanic fluid dynamics. Geophysical vortical structures have some unique properties. In general, the formation and structures of strong vortices of various scales, from turbulent coherent structures to tornados and to hurricanes, involve the coupling with density–temperature stratification as an internal baroclinic source of absolute vorticity.

   Specifically, large-scale vortical structures, which is the concern of this chapter, are influenced by the earth's rotation through the Coriolis force with latitude-dependent strength (the $\beta$ effect), which creates new relative vorticity.

On the other hand, large-scale vortices can be treated within the shallow-water model, and even by two-dimensional approximation due to both the shallow-water model and the Taylor–Proudman theorem for slow motion in rapidly rotating system.

2. The concept of potential vorticity and its conservation is the key to almost the entire geophysical fluid dynamics. In shallow-water approximation, the barotropic potential-vorticity conservation along with the $\beta$ effect directly implies the stretching (vorticity enhancement) and shrinking (vorticity weakening) of vertical vortex columns, and leads to the existence of dissipative Rossby waves. In meteorology, under certain balanced-flow condition the global weather map can be constructed from the isentropic potential-vorticity map and isentropic temperature map through an inversion principle, just like in incompressible flow the velocity field can be constructed from the vorticity field through the Biot–Savart formula.
3. Compared to three-dimensional flow, in two dimensions the vorticity has no stretching and tilting, but the vorticity gradient vector does have similar behavior. Its enhancement generates filament-like structures, and its weakening implies more evenly distributed vorticity. The vorticity gradient field and strain-rate field are closed coupled, which governs the entire evolution of kinetic energy and enstrophy of a two-dimensional turbulence: while the former is toward larger structures (inverse cascade), the latter is toward finer structures (cascade). In a rotating system the $\beta$-effect joints this coupling mechanism.
4. Studies of barotropic vortices focus on their two-dimensional instability under the $\beta$ effect. The existence of the $\beta$-effect implies that the only isolated vortical structure that can persist and remain isolated is dipoles (modons, or gyres). Thus, a monopolar vortex must evolve to multipolar structures as often observed in geophysical flows. In contrast, baroclinic vortices are more complicated due to the stratification, of which the theoretical studies are confined to the simplest models such as two-layer model.
5. In the study of intense tropical cyclones, an issue of great practical importance is the prediction of their propagation. As a universal rule, any cyclones have an initial tendency to propagate toward northwest due to the $\beta$-effect, as can be thoroughly analyzed by quasigeostrophic vortex model. But the initial tendency of each cyclone is subjected to change due to several complicated factors. The specific propagation track of a tropical cyclone is determined by the maximum temporal tendency of isentropic potential vorticity of azimuthal wave-number 1. For steady propagation, the dominant mechanism of this tendency is horizontal advection including the $\beta$ effect, which can be predicted by barotropic vortex models. But, the "local $\beta$-effect" caused by the bottom topography as well as the baroclinic effect, especially diabatic heating, can cause non-smooth cyclone track with sudden turn.

# A

# Vectors, Tensors, and Their Operations

## A.1 Vectors and Tensors

A spatial description of the fluid motion is a geometrical description, of which the essence is to ensure that relevant physical quantities are invariant under artificially introduced coordinate systems. This is realized by tensor analysis (cf. Aris 1962). Here we introduce the concept of tensors in an informal way, through some important examples in fluid mechanics.

### A.1.1 Scalars and Vectors

Scalars and vectors are geometric entities independent of the choice of coordinate systems. This independence is a necessary condition for an entity to represent some physical quantity. A scalar, say the fluid pressure $p$ or density $\rho$, obviously has such independence. For a vector, say the fluid velocity $\boldsymbol{u}$, although its three components $(u_1, u_2, u_3)$ depend on the chosen coordinates, say Cartesian coordinates with unit basis vectors $(\boldsymbol{e}_1, \boldsymbol{e}_2, \boldsymbol{e}_3)$, as a single geometric entity the one-form of $\boldsymbol{e}_i$,

$$\boldsymbol{u} = u_1\boldsymbol{e}_1 + u_2\boldsymbol{e}_2 + u_3\boldsymbol{e}_3 = u_i\boldsymbol{e}_i, \quad i = 1, 2, 3, \tag{A.1}$$

has to be independent of the basis vectors. Note that Einstein's convention has been used in the last expression of (A.1): unless stated otherwise, a repeated index always implies summation over the dimension of the space.

The inner (scalar) and cross (vector) products of two vectors are familiar. If $\theta$ is the angle between the directions of $\boldsymbol{a}$ and $\boldsymbol{b}$, these operations give

$$\boldsymbol{a} \cdot \boldsymbol{b} = |\boldsymbol{a}||\boldsymbol{b}| \cos\theta, \quad |\boldsymbol{a} \times \boldsymbol{b}| = |\boldsymbol{a}||\boldsymbol{b}| \sin\theta.$$

While the inner product is a projection operation, the cross-product produces a vector perpendicular to both $\boldsymbol{a}$ and $\boldsymbol{b}$ with magnitude equal to the area of the parallelogram spanned by $\boldsymbol{a}$ and $\boldsymbol{b}$. Thus $\boldsymbol{a} \times \boldsymbol{b}$ determines a vectorial area

with unit vector $\boldsymbol{n}$ normal to the $(\boldsymbol{a}, \boldsymbol{b})$ plane, whose direction follows from $\boldsymbol{a}$ to $\boldsymbol{b}$ by the right-hand rule. In particular, the inner and cross-products of Cartesian basis vectors satisfy

$$\left.\begin{array}{l} \boldsymbol{e}_i \cdot \boldsymbol{e}_j = \delta_{ij} \\ \boldsymbol{e}_i \times \boldsymbol{e}_j = \boldsymbol{e}_k, \quad i,j,k = 1,2,3 \text{ and cycles} \end{array}\right\}, \tag{A.2a,b}$$

where

$$\delta_{ij} = \begin{cases} 1 \text{ if } & i = j, \\ 0 \text{ if } & i \neq j \end{cases}$$

is the Kroneker symbol.

The gradient operator

$$\nabla = \boldsymbol{e}_i \frac{\partial}{\partial x_i} \tag{A.3}$$

is also a vector, which as a single entity is invariant under any coordinate transformations. Thus, the pressure gradient $\nabla p$ is a vector; the divergence and curl of velocity,

$$\nabla \cdot \boldsymbol{u} = \vartheta, \quad \nabla \times \boldsymbol{u} = \boldsymbol{\omega},$$

are the *dilatation* scalar and *vorticity* vector, respectively.

### A.1.2 Tensors

Scalar and vectors can be considered as special tensors of rank (or order) zero and one respectively. In general, as the immediate extension of vectors, in an $n$-dimensional Euclidean space *a tensor* $\mathbf{T}$ *of rank* $m$ *is a geometric entity independent of the choice of coordinate systems*, and has $n^m$ components with respect to a given coordinate system. When $n = 3$, like the one-form (A.1) for a vector, these $3^m$ components $T_{ij\ldots k}$ constitute the coefficients of an $m$-form of the given base vectors, i.e.,

$$\mathbf{T} = T_{ij\ldots k} \boldsymbol{e}_i \boldsymbol{e}_j \ldots \boldsymbol{e}_k, \quad i,j,\ldots,k = 1,2,3,$$

and obey certain transformation rule to keep the invariance of $\mathbf{T}$.[1] The necessity of introducing tensors of ranks higher than one can be illustrated by the following simple example.

Assume the fluid velocity at a spatial point $\boldsymbol{x}$ is $\boldsymbol{u}$, and consider the velocity change at any neighboring point $\boldsymbol{x} + \mathrm{d}\boldsymbol{x}$, see Fig. A.1. To the first-order of $\mathrm{d}\boldsymbol{x}$, there is

$$\mathrm{d}\boldsymbol{u} = (\mathrm{d}\boldsymbol{x} \cdot \nabla)\boldsymbol{u} = \mathrm{d}x_j \boldsymbol{u}_{,j}\,, \tag{A.4a}$$

where $\mathrm{d}x_j \quad (j = 1,2,3)$ are Cartesian coefficients of $\mathrm{d}\boldsymbol{x}$. Here and throughout the book we have used a simple notation $(\cdot)_{,j}$ to indicate the derivative with

[1] In many books a tensor is defined by requiring their components to obey this transformation rule, which is the inverse of that of the basis vector, to ensure the invariance of the tensor.

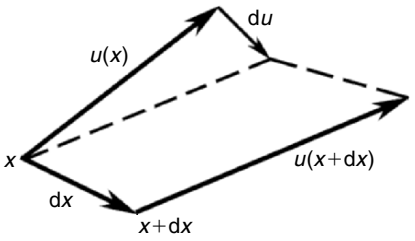


**Fig. A.1.** A schematic interpretation of (A.4a)

respect to $x_j$; sometimes we also denote $\partial/\partial x_i$ by $\partial_i$. So $\boldsymbol{u}$ has three directional derivatives

$$\boldsymbol{u}_{,j} \equiv \frac{\partial \boldsymbol{u}}{\partial x_j}, \quad j = 1, 2, 3,$$

each being a vector. Thus we may further expand them as

$$\boldsymbol{u}_{,j} = \boldsymbol{e}_k u_{k,j}, \qquad j, k = 1, 2, 3. \tag{A.4b}$$

Then, just as $p_{,j}$ is the $j$th component of pressure gradient vector $\nabla p$, the vector $\boldsymbol{u}_{,j}$ is the $j$th component of a geometric entity, velocity gradient, defined as

$$\nabla \boldsymbol{u} = \boldsymbol{e}_j \boldsymbol{u}_{,j} = \boldsymbol{e}_j \boldsymbol{e}_k u_{k,j}, \quad j, k = 1, 2, 3, \tag{A.5}$$

where summation is to be taken twice, once for $j$ and once for $k$. This is a two-form of $\boldsymbol{e}_i$ $(i = 1, 2, 3)$, an example of tensors of rank 2, can also be directly obtained from (A.1) and (A.3). Note that in (A.5) the index $j$ implies the components of $\nabla$ and goes first, while the index $k$ implies the components of $\boldsymbol{u}$ and goes after $j$. The order inverse in $u_{k,j}$ is only apparent, because this component of $\nabla \boldsymbol{u}$ is merely an abbreviation of $\partial u_k/\partial x_j$. Since $\nabla \boldsymbol{u}$ is independent of the magnitude and direction of $\mathrm{d}\boldsymbol{x}$, in comparison with (A.4a) it is a more general description of the velocity variation at the neighborhood of a point.

In physical and numerical experiments one always uses certain coordinate systems, and the direct output is always components of tensors. Using component operations is also convenient in deriving formulas, and sometimes only one typical component is sufficient. For example, for the velocity gradient we may just write down a representative component $u_{k,j}$. But writing the final equations in coordinate-independent tensorial form enables seeing the physical objectivity of these equations clearly.

Any tensor of rank 2 can be expressed by a square matrix, but not vise versa. Like any square matrix, the deformation tensor, or generally any tensor of rank 2, can always be decomposed into a symmetric part and an anti symmetric part, each being a tensor of rank 2

$$\nabla \boldsymbol{u} = \mathbf{D} + \boldsymbol{\Omega}, \tag{A.6a}$$

where

$$\mathrm{D}_{ij} \equiv \frac{1}{2}(u_{j,i} + u_{i,j}) = \mathrm{D}_{ji} \tag{A.6b}$$

is called the *strain-rate tensor*, having six independent components, and

$$\Omega_{ij} \equiv \frac{1}{2}(u_{j,i} - u_{i,j}) = -\Omega_{ij} \tag{A.6c}$$

is the *spin tensor* or *vorticity tensor*, having three independent components.

As illustrated by (A.6a), the addition (as well as differentiation and integration) of tensors is the same as that of vectors. The multiplication of tensors, in general, results in a tensor of higher rank. A new operation of tensors is *contraction* by summing a pair of components with the same index (*"dummy index"*). This reduces the rank by two. The simplest example is the inner product of vectors: $\boldsymbol{a} \cdot \boldsymbol{b} = a_i b_i$ or $\nabla \cdot \boldsymbol{u} = \vartheta$. Similarly, for two tensors of rank 2 there is

$$A_{ij} B_{jk} = C_{ik}.$$

### A.1.3 Unit Tensor and Permutation Tensor

The most fundamental symmetric tensor of rank 2 is the *unit tensor*

$$\mathbf{I} \equiv \boldsymbol{e}_i \boldsymbol{e}_j \delta_{ij} \tag{A.7}$$

of which the components in any Cartesian coordinates are invariably the Kronecker delta. The contraction of two unit tensors gives

$$\delta_{ij}\delta_{jk} = \delta_{ik} \quad \text{or} \quad \mathbf{I} \cdot \mathbf{I} = \mathbf{I}.$$

Making contraction again (denoted by double dots) yields

$$\mathbf{I} : \mathbf{I} = \delta_{ii} = n \quad \text{(dimension of the space)}.$$

Clearly, the contraction of two tensors of rank 2 is the same as the multiplication of two matrices.

With a few exceptions in Sect. 3.2, all tensors we need in this book but one will be of ranks no more than 2. Like (A.2b), the cross-product of vectors in three-dimensional space can be expressed by

$$(\boldsymbol{a} \times \boldsymbol{b})_i = \boldsymbol{e}_i \cdot (\boldsymbol{e}_j a_j \times \boldsymbol{e}_k b_k) = a_j b_k \boldsymbol{e}_i \cdot (\boldsymbol{e}_j \times \boldsymbol{e}_k) = \epsilon_{ijk} a_j b_k,$$

where $\epsilon_{ijk}$ are the Cartesian components of a tensor of rank 3

$$\mathbf{E} \equiv \boldsymbol{e}_i \boldsymbol{e}_j \boldsymbol{e}_k \epsilon_{ijk}. \tag{A.8a}$$

To find these components, we use the familiar rule of vector product

$$\epsilon_{ijk} \equiv \boldsymbol{e}_i \cdot (\boldsymbol{e}_j \times \boldsymbol{e}_k) = \begin{vmatrix} \boldsymbol{e}_i \cdot \boldsymbol{e}_1 & \boldsymbol{e}_i \cdot \boldsymbol{e}_2 & \boldsymbol{e}_i \cdot \boldsymbol{e}_3 \\ \boldsymbol{e}_j \cdot \boldsymbol{e}_1 & \boldsymbol{e}_j \cdot \boldsymbol{e}_2 & \boldsymbol{e}_j \cdot \boldsymbol{e}_3 \\ \boldsymbol{e}_k \cdot \boldsymbol{e}_1 & \boldsymbol{e}_k \cdot \boldsymbol{e}_2 & \boldsymbol{e}_k \cdot \boldsymbol{e}_3 \end{vmatrix} = \begin{vmatrix} \delta_{i1} & \delta_{i2} & \delta_{i3} \\ \delta_{j1} & \delta_{j2} & \delta_{j3} \\ \delta_{k1} & \delta_{k2} & \delta_{k3} \end{vmatrix}$$
$$= \begin{cases} 1 & \text{if} \quad (ijk) = (123), (231), (312), \\ -1 & \text{if} \quad (ijk) = (132), (213), (321), \\ 0. & \text{otherwise.} \end{cases} \tag{A.8b}$$

Therefore, these components in any Cartesian coordinates are invariably the *permutation symbol* $\epsilon_{ijk}$, completely anti symmetric under exchange of any pair of its three indices. For this reason, tensor $\mathbf{E}$ is called *permutation tensor*. It is used frequently whenever there is a cross-product. If more than one cross-products appear, one need the multiplication of two permutation tensors. In a three-dimensional space, from (A.8b) there is

$$\epsilon_{ijk}\epsilon_{lmn} = \begin{vmatrix} \delta_{il} & \delta_{im} & \delta_{in} \\ \delta_{jl} & \delta_{jm} & \delta_{jn} \\ \delta_{kl} & \delta_{km} & \delta_{kn} \end{vmatrix}. \tag{A.9a}$$

Contraction with respect to $k, n$ yields

$$\epsilon_{ijk}\epsilon_{lmk} = \delta_{il}\delta_{jm} - \delta_{im}\delta_{jl}. \tag{A.9b}$$

Continuing the contraction with respect to $j, m$ then gives

$$\epsilon_{ijk}\epsilon_{ljk} = (3-1)\delta_{il} = 2\delta_{il}, \tag{A.9c}$$

and continuing again

$$\epsilon_{ijk}\epsilon_{ijk} = 3(3-1) = 6. \tag{A.9d}$$

One often needs to handle two-dimensional flow. If $\boldsymbol{a}$ and $\boldsymbol{b}$ are vectors in the flow plane such that $\boldsymbol{a} \times \boldsymbol{b}$ is along the third direction $\boldsymbol{e}_3$ normal to the plane, then in $\epsilon_{ijk}a_j b_k$ one of the $i, j, k$ must be 3 due to (A.8b), with the other two varying between 1 and 2. In this case (A.9b) yields

$$\epsilon_{3jk}\epsilon_{3lm} = \begin{vmatrix} \delta_{jm} & \delta_{jn} \\ \delta_{km} & \delta_{kn} \end{vmatrix}, \quad j, k, m, n = 1, 2. \tag{A.10a}$$

Contracting with respect to $k, n$ yields

$$\epsilon_{3jk}\epsilon_{3mk} = (2-1)\delta_{jm} = \delta_{jm}, \tag{A.10b}$$

and continuing again,

$$\epsilon_{3jk}\epsilon_{3jk} = 2(2-1) = 2. \tag{A.10c}$$

The particular importance of the permutation tensor in vorticity and vortex dynamics lies in the fact that

$$\omega_i = \epsilon_{ijk} u_{k,j} = \epsilon_{ijk} \Omega_{jk}, \tag{A.11a}$$

due to (A.3) and (A.6). Inversely, by using (A.9b) it is easily seen that

$$\Omega_{jk} = \frac{1}{2} \epsilon_{ijk} \omega_i. \tag{A.11b}$$

This pair of intimate relations between vorticity vector and spin tensor show that they have the same nonzero components and hence can represent, or are dual to, each other. Note that (A.11b) also indicates that the inner product of a vector and an antisymmetric tensor can always be conveniently expressed as the cross-product of the former and the dual vector of the latter; for instance,

$$\boldsymbol{a} \cdot \boldsymbol{\Omega} = \frac{1}{2} \boldsymbol{\omega} \times \boldsymbol{a}, \quad \boldsymbol{\Omega} \cdot \boldsymbol{a} = \frac{1}{2} \boldsymbol{a} \times \boldsymbol{\omega}. \tag{A.12a,b}$$

Obviously, we also have

$$\nabla \cdot \boldsymbol{\Omega} = -\frac{1}{2} \nabla \times \boldsymbol{\omega}. \tag{A.13}$$

## A.2 Integral Theorems and Derivative Moment Transformation

The key result of tensor integrations is the extension of the fundamental theorem of calculus in one dimension

$$\int_a^b f'(x)\, \mathrm{d}x = \int_a^b \mathrm{d}f(x) = f(b) - f(a)$$

to multidimensional space. We state two classic theorems without giving proof (e.g., Milne-Thomson 1968), which are then used to derive useful integral transformations.

### A.2.1 Generalized Gauss Theorem and Stokes Theorem

First, let $V$ be a volume, having closed boundary surface $\partial V$ with outward unit normal vector $\boldsymbol{n}$ and $\circ$ denote any permissible differential operation of the gradient operator $\nabla$ on a tensor $\mathcal{F}$ of any rank. Then the *generalized Gauss theorem* states that $\nabla \circ \mathcal{F}\, \mathrm{d}V$ must be a total differentiation, and its integral can be cast to the surface integral of $\boldsymbol{n} \circ \mathcal{F}\, \mathrm{d}S$ over the boundary surface $\partial V$ of $V$, where $\boldsymbol{n}$ is the unit outward normal vector:

$$\int_V \nabla \circ \mathcal{F}\, \mathrm{d}V = \int_{\partial V} \boldsymbol{n} \circ \mathcal{F}\, \mathrm{d}S. \tag{A.14}$$

In particular, if $\mathcal{F}$ is constant, (A.14) yields a well-known result

$$\int_{\partial V} \boldsymbol{n}\,\mathrm{d}S = \int_{\partial V} \mathrm{d}\boldsymbol{S} = \boldsymbol{0}, \tag{A.15}$$

i.e., the integral of vectorial surface element $\mathrm{d}\boldsymbol{S} = \boldsymbol{n}\,\mathrm{d}S$ over a closed surface must vanish. Moreover, for the total dilatation and vorticity in $V$ we have

$$\int_V \vartheta\,\mathrm{d}V = \int_{\partial V} \boldsymbol{n}\cdot\boldsymbol{u}\,\mathrm{d}S, \tag{A.16a}$$

$$\int_V \boldsymbol{\omega}\mathrm{d}V = \int_{\partial V} \boldsymbol{n}\times\boldsymbol{u}\,\mathrm{d}S. \tag{A.16b}$$

One often needs to consider integrals in two-dimensional flow. In this case the volume $V$ can be considered as a deck on the flow plane of unit thickness. Then (A.14) and some of the volume-integral formulas below remain the same in both two and three dimensions, but care is necessary since in $n$-dimensions $\delta_{ii} = n$ is $n$-dependent. Some formulas for $n = 3$ need to be revised or do not exist at all; see Sect. A.2.4 for issues special in two dimensions.

Next, let $S$ be a surface with unit normal $\boldsymbol{n}$, then without leaving $S$ only tangential derivatives can be performed and have chance to be integrated out, expressed by line integrals over the boundary loop $\partial S$. The tangent differential operator is naturally $\boldsymbol{n}\times\nabla$, and the line element of $\partial S$ has an intrinsic direction along its tangent, $\mathrm{d}\boldsymbol{x} = \boldsymbol{t}\,\mathrm{d}s$, where $\boldsymbol{t}$ is the tangent unit vector and $ds$ the arc element. The directions of the normal $\boldsymbol{n}$ of $S$ and $\boldsymbol{t}$ obey the right-hand rule. Then, as the counterpart of (A.14), the *generalized Stokes theorem* states that on any open surface $S$ any $(\boldsymbol{n}\times\nabla)\circ\mathcal{F}\mathrm{d}S$ must be the total differentiation, and its surface integral can be cast to the line integral of $\mathrm{d}\boldsymbol{x}\circ\mathcal{F}$ along $\partial S$:

$$\int_S (\boldsymbol{n}\times\nabla)\circ\mathcal{F}\,\mathrm{d}S = \oint_{\partial S} \mathrm{d}\boldsymbol{x}\circ\mathcal{F}. \tag{A.17}$$

Thus, if $\mathcal{F}$ is constant, (A.17) shows that the integral of element $\mathrm{d}\boldsymbol{x}$ over a closed line must vanish

$$\oint \boldsymbol{t}\,\mathrm{d}s = \oint \mathrm{d}\boldsymbol{x} = \boldsymbol{0}; \tag{A.18}$$

and if $\mathcal{F} = \boldsymbol{x}$, since

$$[(\boldsymbol{n}\times\nabla)\times\boldsymbol{x}]_i = \epsilon_{ijk}\epsilon_{jml}n_l x_{k,m} = -2n_i,$$

we obtain the well-known formula for the integral of a vectorial surface

$$\int_S \boldsymbol{n}\,\mathrm{d}S = \frac{1}{2}\oint_{\partial S} \boldsymbol{x}\times\mathrm{d}\boldsymbol{x} \tag{A.19}$$

with (A.15) as its special case since a closed surface has no boundary. In general, (A.17) implies

$$\int_S (\boldsymbol{n} \times \nabla) \circ \mathcal{F} \, \mathrm{d}S = \boldsymbol{0} \quad \text{on closed } S. \tag{A.20}$$

The most familiar application of (A.17) to fluid mechanics is the relation between total vorticity flux through a surface and *circulation* along the boundary of the surface. Since $(\boldsymbol{n} \times \nabla) \cdot \boldsymbol{u} = \boldsymbol{n} \cdot (\nabla \times \boldsymbol{u})$, there is

$$\int_S \boldsymbol{\omega} \cdot \boldsymbol{n} \, \mathrm{d}S = \oint_{\partial S} \boldsymbol{u} \cdot \mathrm{d}\boldsymbol{x}. \tag{A.21}$$

### A.2.2 Derivative Moment Transformation on Volume

The Gauss and Stokes theorems permit the construction of useful identities for integration by parts. In particular, we need to generalize the one-dimensional formula

$$\int_a^b f(x)\mathrm{d}x = bf(b) - af(a) - \int_a^b xf'(x) \, \mathrm{d}x,$$

which expresses the integration of $f(x)$ by the $x$-moment of its derivative, to various integrals of a vector $\boldsymbol{f}$ over a volume or surface, so that they are cast to the integrals of proper moments of the derivatives of $\boldsymbol{f}$ plus boundary integrals. We call this type of transformations the *derivative moment transformation*.

We first use the generalized Gauss theorem (A.14) to cast the volume integral of $\boldsymbol{f}$ to the moments of its divergence and curl. Since

$$\begin{aligned} (f_i x_j)_{,i} &= f_j + f_{i,i} x_j, \\ \epsilon_{ijk}\epsilon_{jlm}(f_m x_k)_{,l} &= \epsilon_{ijk}(\epsilon_{jlm} f_{m,l}) x_k + \epsilon_{ijk}\epsilon_{jkm} f_m, \end{aligned}$$

where $\boldsymbol{x}$ is the position vector, by (A.14) we find a pair of vector identities

$$\int_V \boldsymbol{f} \, \mathrm{d}V = -\int_V \boldsymbol{x}(\nabla \cdot \boldsymbol{f})\mathrm{d}V + \int_{\partial V} \boldsymbol{x}(\boldsymbol{n} \cdot \boldsymbol{f}) \, \mathrm{d}S, \tag{A.22}$$

$$\int_V \boldsymbol{f} \, \mathrm{d}V = \frac{1}{n-1}\int_V \boldsymbol{x} \times (\nabla \times \boldsymbol{f})\mathrm{d}V - \frac{1}{n-1}\int_{\partial V} \boldsymbol{x} \times (\boldsymbol{n} \times \boldsymbol{f}) \, \mathrm{d}S, \tag{A.23}$$

where $n = 2, 3$ is the space dimension. The factor difference comes from the use of (A.9c) for $n = 3$ and (A.10b) for $n = 2$. Note that for two-dimensional flow, (A.22) still holds if $\boldsymbol{f}$ is on the plane (e.g., velocity), but becomes trivial if $\boldsymbol{f}$ is normal to the plane (e.g., vorticity).[2]

[2] This can be verified by considering a deck-like volume of unit thickness. When the vector is normal to the deck plane, one finds $0 = 0$ from (A.22).

Then, we need to cast the first vector moment $\boldsymbol{x}\times\boldsymbol{f}$ to the second moments of its curl, say $\boldsymbol{F}=\nabla\times\boldsymbol{f}$. When $n=3$, $\boldsymbol{F}$ has three second moments $x^2\boldsymbol{F}$, $\boldsymbol{x}\times(\boldsymbol{x}\times\boldsymbol{F})$, and $\boldsymbol{x}(\boldsymbol{x}\cdot\boldsymbol{F})$, related by

$$\boldsymbol{x}\times(\boldsymbol{x}\times\boldsymbol{F})=\boldsymbol{x}(\boldsymbol{x}\cdot\boldsymbol{F})-x^2\boldsymbol{F}.$$

Note that $\boldsymbol{x}(\boldsymbol{x}\cdot\boldsymbol{F})=\boldsymbol{0}$ for $n=2$. Then one finds

$$2\int_V \boldsymbol{x}\times\boldsymbol{f}\,\mathrm{d}V=-\int_V x^2\boldsymbol{F}\,\mathrm{d}V+\int_{\partial V} x^2\boldsymbol{n}\times\boldsymbol{f}\,\mathrm{d}S,\quad n=2,3, \tag{A.24a}$$

$$\int_V \boldsymbol{x}\times\boldsymbol{f}\,\mathrm{d}V=\int_V \boldsymbol{x}(\boldsymbol{x}\cdot\boldsymbol{F})\,\mathrm{d}V-\int_{\partial V}\boldsymbol{x}(\boldsymbol{n}\times\boldsymbol{f})\cdot\boldsymbol{x}\,\mathrm{d}S,\quad n=3, \tag{A.24b}$$

$$3\int_V \boldsymbol{x}\times\boldsymbol{f}\,\mathrm{d}V=\int_V \boldsymbol{x}\times(\boldsymbol{x}\times\boldsymbol{F})\,\mathrm{d}V-\int_{\partial V}\boldsymbol{x}\times\boldsymbol{x}\times(\boldsymbol{n}\times\boldsymbol{f})\,\mathrm{d}S,\quad n=3. \tag{A.24c}$$

Here, (A.24c) is the sum of (A.24a) and (A.24b). The trick of proving the first two is using (A.14) to cast the surface integrals therein to volume integrals first. In so doing $\boldsymbol{n}$ becomes operator $\nabla$ which then has to act on both $\boldsymbol{f}$ and $\boldsymbol{x}$.

If we make a Helmholtz–Hodge decomposition $\boldsymbol{f}=\boldsymbol{f}_\perp+\boldsymbol{f}_\parallel$, see (2.87) and associated boundary conditions (2.98a) or (2.98b), then we can replace $\boldsymbol{f}$ by $\boldsymbol{f}_\parallel$ on the right-hand side of (A.22). Namely, *the integral of a vector is expressible solely by the derivative-moment integrals of its longitudinal part*. However, (A.23) is not simply a counterpart of this result in terms of the transverse part of the vector. Rather, as long as $\boldsymbol{n}\times\boldsymbol{f}_\parallel\neq\boldsymbol{0}$ on $\partial V$, a boundary coupling with the longitudinal part must appear. For some relevant discussions see Wu and Wu (1993).

### A.2.3 Derivative Moment Transformation on Surface

By similar procedure, we may use the Stokes theorem (A.17) to cast surface integrals of a vector to that of its corresponding derivative moments plus boundary line integrals. To this end we first decompose the vector to a normal vector $\phi\boldsymbol{n}$ and a tangent vector $\boldsymbol{n}\times\boldsymbol{A}$, since they obey different transformation rules. Then for the normal vector we find a surface-integral identity effective for $n=2,3$

$$\int_S \phi\boldsymbol{n}\,\mathrm{d}S=-\frac{1}{n-1}\int_S \boldsymbol{x}\times(\boldsymbol{n}\times\nabla\phi)\,\mathrm{d}S+\frac{1}{n-1}\oint_{\partial S}\phi\boldsymbol{x}\times\mathrm{d}\boldsymbol{x}. \tag{A.25}$$

And, *for* $n=3$ *only*, the integral of tangent vector can be cast to

$$\int_S \boldsymbol{n}\times\boldsymbol{A}\,\mathrm{d}S=-\int_S \boldsymbol{x}\times[(\boldsymbol{n}\times\nabla)\times\boldsymbol{A}]\,\mathrm{d}S+\oint_{\partial S}\boldsymbol{x}\times(\mathrm{d}\boldsymbol{x}\times\boldsymbol{A}). \tag{A.26}$$

In deriving these identities the operator $\boldsymbol{n}\times\nabla$ should be taken as a whole for the application of (A.17). Setting $\phi=1$ in (A.25) returns to (A.19). In fact,

(A.25) is also a special case of (A.23) with $\boldsymbol{f} = \nabla\phi$. Note that the cross-product on the right-hand side of (A.26) can be replaced by inner product

$$\int_S \boldsymbol{n} \times \boldsymbol{A}\,\mathrm{d}S = \int_S \boldsymbol{x}(\boldsymbol{n} \times \nabla) \cdot \boldsymbol{A}\,\mathrm{d}S - \oint_{\partial S} \boldsymbol{x}(\boldsymbol{A} \cdot \mathrm{d}\boldsymbol{x}), \tag{A.27}$$

where $(\boldsymbol{n} \times \nabla) \cdot \boldsymbol{A} = \boldsymbol{n} \cdot (\nabla \times \boldsymbol{A})$.

Then, for both $n = 2$ and 3, the integral of the first moment $\boldsymbol{x} \times \boldsymbol{n}\phi$ can be transformed to the following alternative forms:

$$\int_S \boldsymbol{x} \times \boldsymbol{n}\phi\,\mathrm{d}S = \frac{1}{2}\int_S x^2 \boldsymbol{n} \times \nabla\phi\,\mathrm{d}S - \frac{1}{2}\oint_{\partial S} x^2\phi\,\mathrm{d}\boldsymbol{x} \tag{A.28a}$$

$$= -\int_S \boldsymbol{x}[\boldsymbol{x} \cdot (\boldsymbol{n} \times \nabla\phi)]\,\mathrm{d}S + \oint_{\partial S} \phi\boldsymbol{x}(\boldsymbol{x} \cdot \mathrm{d}\boldsymbol{x}) \tag{A.28b}$$

$$= -\frac{1}{3}\int_S \boldsymbol{x} \times [\boldsymbol{x} \times (\boldsymbol{n} \times \nabla\phi)]\,\mathrm{d}S + \frac{1}{3}\oint_{\partial S} \phi\boldsymbol{x} \times (\boldsymbol{x} \times \mathrm{d}\boldsymbol{x}). \tag{A.28c}$$

Finally, to cast the surface integral of

$$\boldsymbol{x} \times (\boldsymbol{n} \times \boldsymbol{A}) = \boldsymbol{n}(\boldsymbol{x} \cdot \boldsymbol{A}) - \boldsymbol{A}(\boldsymbol{x} \cdot \boldsymbol{n})$$

to the second-moment of the derivatives of $\boldsymbol{A}$, we start from two total derivatives

$$\begin{aligned}
\epsilon_{ijk}(\boldsymbol{n} \times \nabla)_j(x^2 A_k) &= x^2\epsilon_{ijk}(\boldsymbol{n} \times \nabla)_j A_k + A_k\epsilon_{ijk}(\boldsymbol{n} \times \nabla x^2)_j \\
&= x^2\epsilon_{ijk}(\boldsymbol{n} \times \nabla)_j A_k + 2(x_i n_k A_k - n_i x_k A_k), \\
\epsilon_{ljk}(\boldsymbol{n} \times \nabla)_j(x_i x_l A_k) &= x_i x_l \epsilon_{ljk}(\boldsymbol{n} \times \nabla)_j A_k + A_k\epsilon_{ljk}(\boldsymbol{n} \times \nabla)_j(x_i x_l) \\
&= x_i x_l \epsilon_{ljk}(\boldsymbol{n} \times \nabla)_j A_k + 3x_i n_k A_k - A_i x_k n_k.
\end{aligned}$$

Here, since what matters in $\boldsymbol{x} \times (\boldsymbol{n} \times \boldsymbol{A})$ is only the tangent components of $\boldsymbol{A}$, we may well drop its normal component $n_k A_k$. Hence, subtracting the second identity from 1/2 times the first yields an integral of $\boldsymbol{x} \times (\boldsymbol{n} \times \boldsymbol{A})$. Using (A.17) to cast the left-hand side to line integral then leads to the desired identity

$$\int_S \boldsymbol{x} \times (\boldsymbol{n} \times \boldsymbol{A})\,\mathrm{d}S = \int_S \mathbf{S} \cdot [(\boldsymbol{n} \times \nabla) \times \boldsymbol{A}]\,\mathrm{d}S - \oint_{\partial S} \mathbf{S} \cdot (\mathrm{d}\boldsymbol{x} \times \boldsymbol{A}), \tag{A.29a}$$

where

$$\mathbf{S} = \frac{1}{2}x^2\mathbf{I} - \boldsymbol{x}\boldsymbol{x} \quad \text{or} \quad S_{ij} = \frac{1}{2}x^2\delta_{ij} - x_i x_j. \tag{A.29b}$$

is a tensor depending on $\boldsymbol{x}$ only.

As a general comment of derivative moments, we note that, since in (A.22),(A.23), and (A.25)–(A.27) the left-hand side is independent of the choice of the origin of $\boldsymbol{x}$, so must be the right-hand side. In general, if $I$

represents any integral operator (over volume or surface or a sum of both), than the above independence requires

$$I\{(\boldsymbol{x}_0 + \boldsymbol{x}) \circ \mathcal{F}\} = I\{\boldsymbol{x} \circ \mathcal{F}\}$$

for any constant vector $\boldsymbol{x}_0$. Thus, we have

$$\boldsymbol{x}_0 \circ I\{\mathcal{F}\} + I\{\boldsymbol{x} \circ \mathcal{F}\} = I\{\boldsymbol{x} \circ \mathcal{F}\},$$

which implies that, due to the arbitrariness of $\boldsymbol{x}_0$, there must be

$$I\{\mathcal{F}\} = 0. \tag{A.30}$$

Namely, if we remove $\boldsymbol{x}$ from the right-hand side of (A.22), (A.23), and (A.25)–(A.27), the remaining integrals must vanish. It is easily seen that this condition is precisely the Gauss and Stokes theorem themselves.

### A.2.4 Special Issues in Two Dimensions

The preceding integral theorems and identities are mainly for three-dimensional domain, with some of them also applicable to two-dimensional domain. A few special issues in two dimensions are worth discussing separately.

In many two-dimensional problems it is convenient to convert a plane vector $a\boldsymbol{e}_x + b\boldsymbol{e}_y$ to a complex number $z = x + \mathrm{i}y$ by replacing $\boldsymbol{e}_z\times$ by $\mathrm{i} = \sqrt{-1}$ (Milne-Thomson 1968), so that

$$\boldsymbol{e}_y = \boldsymbol{e}_z \times \boldsymbol{e}_x \Longrightarrow \mathrm{i}\boldsymbol{e}_x \tag{A.31a}$$

and hence

$$a\boldsymbol{e}_x + b\boldsymbol{e}_y = (a + b\boldsymbol{e}_z\times)\boldsymbol{e}_x \Longrightarrow \boldsymbol{e}_x(a + \mathrm{i}b). \tag{A.31b}$$

Then the immaterial $\boldsymbol{e}_x$ can be dropped. Thus, denoting the complex conjugate of $z$ by $\bar{z} = x - \mathrm{i}y$, for derivatives there is

$$\partial_x = \partial_z + \partial_{\bar{z}}, \quad \partial_y = \mathrm{i}(\partial_z - \partial_{\bar{z}}), \tag{A.32a}$$

$$2\partial_z = \partial_x - \mathrm{i}\partial_y, \quad 2\partial_{\bar{z}} = \partial_x + \mathrm{i}\partial_y, \tag{A.32b}$$

so by (A.31)

$$\nabla \Longrightarrow 2\boldsymbol{e}_x\partial_{\bar{z}}, \quad \nabla^2 \Longrightarrow 4\partial_z\partial_{\bar{z}}. \tag{A.33}$$

The replacement rule (A.31) cannot be extended to tensors of higher ranks. If in a vector equation one encounters the inner product of a tensor $\mathbf{S}$ and a vector $\boldsymbol{a}$ that yields a vector $\boldsymbol{b}$, then (A.31) can be applied after $\boldsymbol{b}$ is obtained by common real operations. For example, consider the inner product of a trace-free symmetric tensor

$$\mathbf{S} = \boldsymbol{e}_x\boldsymbol{e}_x S_{11} + \frac{1}{2}(\boldsymbol{e}_x\boldsymbol{e}_y + \boldsymbol{e}_y\boldsymbol{e}_x)S_{12} + \boldsymbol{e}_y\boldsymbol{e}_y S_{22}, \quad S_{11} + S_{22} = 0,$$

and a vector $\boldsymbol{a} = \boldsymbol{e}_x a_1 + \boldsymbol{e}_y a_2 \Longrightarrow \boldsymbol{e}_x(a_1 + \mathrm{i}a_2)$. After obtaining $\boldsymbol{a} \cdot \mathbf{S} = \mathbf{S} \cdot \boldsymbol{a}$ by real algebra, we use (A.31) to obtain

$$2\boldsymbol{a} \cdot \mathbf{S} \Longrightarrow \boldsymbol{e}_x(a_1 - \mathrm{i}a_2)(2S_{11} + \mathrm{i}S_{12}), \quad S_{11} + S_{22} = 0. \tag{A.34}$$

In this case $\mathbf{S}$ appears as a complex number $S_{11} + \mathrm{i}S_{12}/2$ but $\boldsymbol{a}$ appears as its *complex conjugate* $a_1 - \mathrm{i}a_2$.

Now, if $\mathcal{F} = f(x, y)$ is a scalar function, (A.17) is reduced to

$$\boldsymbol{e}_z \times \int_S \left( \boldsymbol{e}_x \frac{\partial f}{\partial x} + \boldsymbol{e}_y \frac{\partial f}{\partial y} \right) \mathrm{d}S = \int_S \left( \boldsymbol{e}_y \frac{\partial f}{\partial x} - \boldsymbol{e}_x \frac{\partial f}{\partial y} \right) \mathrm{d}S = \oint_{\partial S} \mathrm{f}\, \mathrm{d}\boldsymbol{x}.$$

Hence, by (A.31) this formula becomes

$$\mathrm{i} \int_S \left( \frac{\partial f}{\partial x} + \mathrm{i} \frac{\partial f}{\partial y} \right) \mathrm{d}S = \oint_{\partial S} f \, \mathrm{d}z,$$

which by (A.32) is further converted to

$$\oint_{\partial S} f(z, \overline{z}) \, \mathrm{d}z = 2\mathrm{i} \int_S \frac{\partial f}{\partial \overline{z}} \, \mathrm{d}S, \tag{A.35a}$$

$$\oint_{\partial S} f(z, \overline{z}) \, \mathrm{d}\overline{z} = -2\mathrm{i} \int_S \frac{\partial f}{\partial z} \, \mathrm{d}S, \tag{A.35b}$$

the second formula being the complex conjugate of the first. Milne-Thomson (1968) calls this result the *area theorem*.

The two-dimensional version of the derivative-moment transformation on surface, i.e., the counterpart of (A.25) and (A.26), also needs special care. We proceed on the real $(x, y)$-plane. Let $C$ be an open plane curve with end points $a$ and $b$, and $\boldsymbol{e}_s$ and $\boldsymbol{n}$ be the unit tangent and normal vectors along $C$ so that $(\boldsymbol{n}, \boldsymbol{e}_s.\boldsymbol{e}_z)$ form a right-hand orthonormal triad. Then since

$$\frac{\partial \boldsymbol{x}}{\partial s} = \boldsymbol{e}_s, \quad \boldsymbol{n} \times \nabla \phi = \boldsymbol{n} \times \left( \boldsymbol{e}_s \frac{\partial}{\partial s} + \boldsymbol{n} \frac{\partial}{\partial n} \right) \phi = \boldsymbol{e}_z \frac{\partial \phi}{\partial s}$$

for any scalar $\phi$ and tangent vector $\boldsymbol{t}A$, there is

$$\int_C \boldsymbol{n}\phi \, \mathrm{d}s = -\boldsymbol{e}_z \times (\boldsymbol{x}\phi)\big|_a^b - \int_C \boldsymbol{x} \times (\boldsymbol{n} \times \nabla \phi) \, \mathrm{d}s, \tag{A.36}$$

$$\int_C \boldsymbol{t}A \, \mathrm{d}s = (\boldsymbol{x}A)\big|_a^b - \int_C \boldsymbol{x} \frac{\partial A}{\partial s} ds. \tag{A.37}$$

The transformation of the first-moment integral of a normal vector $\boldsymbol{n}\phi$ has been given by (A.28). But that of a tangent vector, say $\boldsymbol{x} \times \boldsymbol{e}_s A$, cannot be similarly transformed at all, because

$$\boldsymbol{x} \times \boldsymbol{e}_s A = \frac{\partial}{\partial s}(\boldsymbol{x} \times \boldsymbol{x}A) - \boldsymbol{e}_s \times \boldsymbol{x}A - \boldsymbol{x} \times \boldsymbol{x} \frac{\partial A}{\partial s}$$

simply leads to a trivial result. What we can find is only a scalar moment

$$\int_a^b \boldsymbol{x} \cdot A\boldsymbol{t}\,\mathrm{d}s = -\frac{1}{2}\int_a^b x^2 \frac{\partial A}{\partial s}\,\mathrm{d}s + \frac{1}{2}x^2 A\Big|_a^b. \tag{A.38}$$

## A.3 Curvilinear Frames on Lines and Surfaces

In the above development we only encountered Cartesian components of vectors and tensors. In some situations curvilinear coordinates are more convenient, especially when they are orthonormal. Basic knowledge of vector analysis in a three-dimensional orthonormal curvilinear coordinate system can be found in most relevant text books (e.g., Batchelor 1967), where the coordinate lines are the intersections of a set of triply orthogonal surfaces. But, the *Dupin theorem* (e.g., Weatherburn 1961) of differential geometry requires that in such a system *the curves of intersection of every two surfaces must be the lines of principal curvature on each.* While the concept of *principal curvatures* of a surface will be explained later, here we just notice that the theorem excludes the possibility of studying flow quantities on an *arbitrary* curved line or surface and in its neighborhood by a three-dimensional orthonormal curvilinear coordinate system. These lines and surfaces, however, are our main concern. Therefore, in what follows we construct local coordinate frames along a single line or surface only and as intrinsic as possible, with an arbitrarily moving origin thereon.

### A.3.1 Intrinsic Line Frame

If we are interested in the flow behavior along a smooth line $C$ with length element $\mathrm{d}s$, say a streamline or a vorticity line, the intrinsic coordinate frame with origin $\mathrm{O}(\boldsymbol{x})$ on $C$ has three orthonormal basis vectors: the tangent vector $\boldsymbol{t} = \partial\boldsymbol{x}/\partial s$, the *principal normal* $\boldsymbol{n}$ (toward the center of curvature), and the *binormal* $\boldsymbol{b} = \boldsymbol{t} \times \boldsymbol{n}$, see Fig. A.2. This $(\boldsymbol{t}, \boldsymbol{n}, \boldsymbol{b})$ frame can continuously move along $C$ and is known as *intrinsic line frame*. The key of using this frame is to know how the basis vectors change their directions as $s$ varies. This is given by the *Frenet–Serret formulas*, which form the entire basis of spatial curve theory in classical differential geometry (e.g., Aris 1962):

$$\frac{\partial \boldsymbol{t}}{\partial s} = \kappa\boldsymbol{n}, \quad \frac{\partial \boldsymbol{n}}{\partial s} = -\kappa\boldsymbol{t} + \tau\boldsymbol{b}, \quad \frac{\partial \boldsymbol{b}}{\partial s} = -\tau\boldsymbol{n}, \tag{A.39a,b,c}$$

where $\kappa$ and $\tau$ are the curvature and torsion of $C$, respectively. The curvature radius is $r = -1/\kappa$ with $\mathrm{d}r = -\mathrm{d}n$. The torsion of $C$ measures how much a curve deviates from a plane curve, i.e., it is the curvature of the projection of $C$ onto the $(\boldsymbol{n}, \boldsymbol{b})$ plane. For a plane curve $\tau = 0$ and we have a $(\boldsymbol{t}, \boldsymbol{n})$ frame as already used in deriving (A.36)–(A.38).

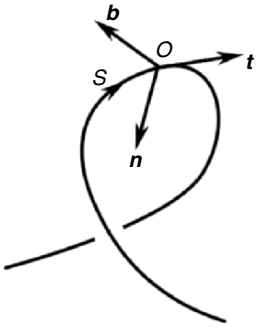


**Fig. A.2.** Intrinsic triad along a curve

Now, let the differential distances from O along the directions of $\boldsymbol{n}$ and $\boldsymbol{b}$ be d$n$ and d$b$, respectively. Then

$$\nabla = \boldsymbol{t}\frac{\partial}{\partial s} + \boldsymbol{n}\frac{\partial}{\partial n} + \boldsymbol{b}\frac{\partial}{\partial b}, \tag{A.40}$$

which involves curves along $\boldsymbol{n}$ and $\boldsymbol{b}$ directions that have their own curvature and torsion. Then one might apply the Frenet–Serret formulas to these curves as well to complete the gradient operation. But due to the Dupin theorem we prefer to leave the two curves orthogonal to $C$ undetermined.

For example, if $C$ is a streamline such that $\boldsymbol{u} = q\boldsymbol{t}$, then the continuity equation for incompressible flow reads

$$\nabla \cdot \boldsymbol{u} = \frac{\partial q}{\partial s} + q\nabla \cdot \boldsymbol{t} = 0, \tag{A.41}$$

where, by using (A.39),

$$\nabla \cdot \boldsymbol{t} = \boldsymbol{n} \cdot \frac{\partial \boldsymbol{t}}{\partial n} + \boldsymbol{b}\frac{\partial \boldsymbol{t}}{\partial b}. \tag{A.42}$$

Similarly, there is

$$\nabla \times \boldsymbol{t} = \kappa \boldsymbol{b} + \left(\boldsymbol{n} \times \frac{\partial \boldsymbol{t}}{\partial n} + \boldsymbol{b} \times \frac{\partial \boldsymbol{t}}{\partial b}\right).$$

Here, since $|\boldsymbol{t}| = 1$, it follows that:

$$\boldsymbol{n} \cdot \left(\boldsymbol{n} \times \frac{\partial \boldsymbol{t}}{\partial n} + \boldsymbol{b} \times \frac{\partial \boldsymbol{t}}{\partial b}\right) = \boldsymbol{t} \cdot \frac{\partial \boldsymbol{t}}{\partial b} = \frac{1}{2}\frac{\partial}{\partial b}|\boldsymbol{t}|^2 = 0,$$

$$\boldsymbol{b} \cdot \left(\boldsymbol{n} \times \frac{\partial \boldsymbol{t}}{\partial n} + \boldsymbol{b} \times \frac{\partial \boldsymbol{t}}{\partial b}\right) = -\boldsymbol{t} \cdot \frac{\partial \boldsymbol{t}}{\partial n} = -\frac{1}{2}\frac{\partial}{\partial n}|\boldsymbol{t}|^2 = 0.$$

Therefore, the second term of $\nabla \times \boldsymbol{t}$ must be along the $\boldsymbol{t}$ direction, with the magnitude

$$\xi \equiv \boldsymbol{t} \cdot (\nabla \times \boldsymbol{t}) = \boldsymbol{b} \cdot \frac{\partial \boldsymbol{t}}{\partial n} - \boldsymbol{n} \cdot \frac{\partial \boldsymbol{t}}{\partial b}. \tag{A.43}$$

The scalar $\xi$ is known as the *torsion of neighboring vector lines* (Truesdell 1954). Thus, using this notation we obtain

$$\nabla \times \boldsymbol{t} = \xi \boldsymbol{t} + \kappa \boldsymbol{b}. \tag{A.44}$$

This result enables us to derive the vorticity expression in the streamline intrinsic frame

$$\boldsymbol{\omega} = \nabla \times (q\boldsymbol{t}) = \nabla q \times \boldsymbol{t} + q \nabla \times \boldsymbol{t} = \nabla q \times \boldsymbol{t} + \xi q \boldsymbol{t} + \kappa q \boldsymbol{b}.$$

The first term of is

$$\nabla q \times \boldsymbol{t} = \frac{\partial q}{\partial b} \boldsymbol{n} - \frac{\partial q}{\partial n} \boldsymbol{b},$$

so we obtain (Serrin 1959)

$$\boldsymbol{\omega} = \xi q \boldsymbol{t} + \frac{\partial q}{\partial b} \boldsymbol{n} + \left( \kappa q - \frac{\partial q}{\partial n} \right) \boldsymbol{b}. \tag{A.45}$$

Thus, $\xi 0$ if $\boldsymbol{\omega} \cdot \boldsymbol{u} \neq 0$. Note that in a three-dimensional orthonormal frame there must be $\xi \equiv 0$, so by the Dupin theorem a curve with $\xi \neq 0$ cannot be the principal curvature line of any orthogonally intersecting surfaces.

### A.3.2 Intrinsic operation with surface frame

Derivatives of tensors along a curved surface $S$ can be made simple by an intrinsic use of an intrinsic surface frame, which is more complicated than the intrinsic line frame since now there are two independent tangential directions on $S$.

#### Covariant Frame

At a given time, a two-dimensional surface $S$ in a three-dimensional space is described by the position vector $\boldsymbol{x}$ of all points on $S$, which is a function of two independent variables, say $u^\alpha$ with $\alpha = 1, 2$. Then

$$\boldsymbol{r}_\alpha(u^1, u^2) \equiv \frac{\partial \boldsymbol{x}}{\partial u^\alpha}, \quad \alpha = 1, 2, \tag{A.46}$$

define two nonparallel tangent vectors (not necessarily orthonormal) at each point $\boldsymbol{x} \in S$, see Fig. A.3. Note that by convention when an upper index appears in the denominator it implies a lower index in the numerator, and

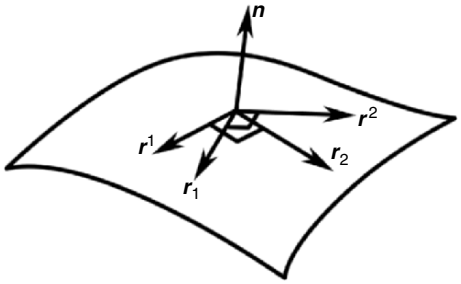


**Fig. A.3.** Covariant and contravariant frames on a surface

vise versa. $\boldsymbol{r}_\alpha$ are used as the *covariant* tangent basis vectors characterized by lower indices. Their inner products

$$g_{\alpha\beta} \equiv \boldsymbol{r}_\alpha \cdot \boldsymbol{r}_\beta, \quad \alpha, \beta = 1, 2, \tag{A.47}$$

form a $2 \times 2$ matrix which gives the covariant components of the so-called *metric tensor* and completely determine the feature of $\boldsymbol{r}_\alpha$. Note that the area of the parallelogram spanned by $\boldsymbol{r}_1$ and $\boldsymbol{r}_2$ is $|\boldsymbol{r}_1 \times \boldsymbol{r}_2| = \sqrt{g} = \det\{g_{\alpha\beta}\}$.

From $\boldsymbol{r}_\alpha$ one can obtain the unit normal vector

$$\boldsymbol{n}(u^1, u^2) = \frac{\boldsymbol{r}_1 \times \boldsymbol{r}_2}{|\boldsymbol{r}_1 \times \boldsymbol{r}_2|} = \frac{\boldsymbol{r}_1 \times \boldsymbol{r}_2}{\sqrt{g}}. \tag{A.48}$$

Then the set $(\boldsymbol{r}_1, \boldsymbol{r}_2, \boldsymbol{n})$ form a covariant right-handed *surface frame*. We stress that *only* $\boldsymbol{n}$ is the intrinsic feature of the surface, but $\boldsymbol{r}_\alpha$ created by $u^\alpha$ are artificially chosen. If we introduce a variable $u^3$ along the $\boldsymbol{n}$ direction, then since for the given surface $\boldsymbol{r}_\alpha$ and $\boldsymbol{n}$ depends only on $u^1, u^2$, there is $\partial \boldsymbol{r}_\alpha / \partial u^3 = 0$ and $\partial \boldsymbol{n} / \partial u^3 = 0$.

### Contravariant Frame

A vector $\boldsymbol{f}$ can be decomposed in terms of $(\boldsymbol{r}_\alpha, \boldsymbol{n})$

$$\boldsymbol{f} \cdot \boldsymbol{r}_\alpha = f_\alpha, \quad \boldsymbol{f} \cdot \boldsymbol{n} = f_3.$$

However, to recover the vector from its components, one *does not* have $\boldsymbol{f} = \boldsymbol{r}_\alpha f_\alpha + f_3 \boldsymbol{n}$, since then $\boldsymbol{f} \cdot \boldsymbol{r}_\beta = f_\beta$ would equal $\boldsymbol{r}_\alpha \cdot \boldsymbol{r}_\beta f_\alpha = g_{\alpha\beta} f_\alpha$, which is possible only if $g_{\alpha\beta} = \delta_{\alpha\beta}$, but in general this is not the case. Thus, *a covariant frame alone is insufficient*; one has to construct another frame conjugate to it. This is similar to the situation in complex domain, where a complex basis-vector set, say $\boldsymbol{a}_i$, needs be complemented by its complex conjugate $\boldsymbol{a}_i^*$ with $\boldsymbol{a}_i \cdot \boldsymbol{a}_j^* = \delta_{ij}$, such that if $\boldsymbol{f} \cdot \boldsymbol{a}_i = f_i$ then there should be $\boldsymbol{f} = f_i \boldsymbol{a}_i^*$.

We therefore introduce the second pair of tangent vectors $\boldsymbol{r}^\alpha$ with upper index, by requiring the hybrid components of the metric tensor be a unit matrix

$$\boldsymbol{r}^\alpha \cdot \boldsymbol{r}_\beta \equiv g^\alpha_\beta = \delta^\alpha_\beta. \tag{A.49}$$

To this end, we set (see Fig. A.3)

$$\boldsymbol{r}^1 = \frac{\boldsymbol{r}_2 \times \boldsymbol{n}}{\sqrt{g}}, \quad \boldsymbol{r}^2 = \frac{\boldsymbol{n} \times \boldsymbol{r}_1}{\sqrt{g}}. \tag{A.50}$$

Then obviously $\boldsymbol{r}^\alpha \cdot \boldsymbol{r}_\beta = 0$ for $\alpha \neq \beta$, and by (A.48) $\boldsymbol{r}^\alpha \cdot \boldsymbol{r}_\beta = 1$ for $\alpha = \beta$ as desired. Moreover, by using identity

$$(\boldsymbol{a} \times \boldsymbol{b}) \times (\boldsymbol{c} \times \boldsymbol{d}) = \boldsymbol{b}[\boldsymbol{a} \cdot (\boldsymbol{c} \times \boldsymbol{d})] - \boldsymbol{a}[\boldsymbol{b} \cdot (\boldsymbol{c} \times \boldsymbol{d})] \tag{A.51}$$

there is

$$\boldsymbol{r}^1 \times \boldsymbol{r}^2 = \frac{1}{g}(\boldsymbol{r}_2 \times \boldsymbol{n}) \times (\boldsymbol{n} \times \boldsymbol{r}_1) = \frac{1}{g}\boldsymbol{n}[\boldsymbol{n} \cdot (\boldsymbol{r}_1 \times \boldsymbol{r}_2)] = \frac{\boldsymbol{n}}{\sqrt{g}},$$

so we have

$$\boldsymbol{n} = \sqrt{g}\boldsymbol{r}^1 \times \boldsymbol{r}^2, \quad |\boldsymbol{r}^1 \times \boldsymbol{r}^2| = \frac{1}{\sqrt{g}}. \tag{A.52}$$

Thus, we have a *contravariant* right-handed frame $(\boldsymbol{r}^1, \boldsymbol{r}^2, \boldsymbol{n})$. Similar to (A.46), $\boldsymbol{r}^\alpha$ can be created by a pair of covariant variables $u_1, u_2$:

$$\boldsymbol{r}^\alpha(u_1, u_2) = \frac{\partial \boldsymbol{x}}{\partial u_\alpha}, \quad \alpha = 1, 2. \tag{A.53}$$

With

$$g^{\alpha\beta} = \boldsymbol{r}^\alpha \cdot \boldsymbol{r}^\beta, \quad \alpha, \beta = 1, 2, \tag{A.54}$$

being the contravariant components of the metric tensor. Substituting (A.50) into (A.54), and using (A.47) and identity

$$(\boldsymbol{a} \times \boldsymbol{b}) \cdot (\boldsymbol{c} \times \boldsymbol{d}) = (\boldsymbol{a} \cdot \boldsymbol{c})(\boldsymbol{b} \cdot \boldsymbol{d}) - (\boldsymbol{a} \cdot \boldsymbol{d})(\boldsymbol{b} \cdot \boldsymbol{c}), \tag{A.55}$$

we find

$$g^{11} = \frac{g_{11}}{g}, \quad g^{22} = \frac{g_{22}}{g}, \quad g^{12} = g^{21} = -\frac{g_{12}}{g}.$$

Namely, $g^{\alpha\beta}$ are the *cofactors* of $g_{\alpha\beta}$, or the two matrices are inverse of each other:

$$g^{\alpha\beta} g_{\beta\gamma} = \delta^\alpha_\gamma. \tag{A.56}$$

Since in both frames $\boldsymbol{n}$ is the same and normal to any tangent basis vectors, the covariant and contravariant component of a vector $\boldsymbol{f}$ along $\boldsymbol{n}$ coincide and will be denoted by $f_n$. We thus write

$$\boldsymbol{f} = \boldsymbol{r}_\alpha f^\alpha + f_n \boldsymbol{n} = \boldsymbol{r}^\beta f_\beta + f_n \boldsymbol{n}. \tag{A.57}$$

This time the result is correct

$$\boldsymbol{f}\cdot\boldsymbol{r}^{\gamma}=f^{\alpha}\delta_{\alpha}^{\gamma}=f^{\alpha},\quad \boldsymbol{f}\cdot\boldsymbol{r}_{\gamma}=f^{\beta}\delta_{\gamma}^{\beta}=f_{\gamma}.$$

Here we see a *hybrid use* of the two frames. Accordingly, the summation convention over the repeated index is implied only if one index is upper and the other is lower.

Moreover, by (A.57) we have

$$\begin{aligned} f^{\alpha}&=\boldsymbol{r}^{\alpha}\cdot\boldsymbol{f}=\boldsymbol{r}^{\alpha}\cdot\boldsymbol{r}^{\beta}f_{\beta}=g^{\alpha\beta}f_{\beta},\\ f_{\beta}&=\boldsymbol{r}_{\beta}\cdot\boldsymbol{f}=\boldsymbol{r}_{\beta}\cdot\boldsymbol{r}_{\alpha}f^{\alpha}=g_{\beta\alpha}f^{\alpha}. \end{aligned}\tag{A.58}$$

Thus, raising or lowering the index of a component can be achieved by using the metric tensor $g^{\alpha\beta}$ or $g_{\alpha\beta}$, respectively. Actually, in (A.56) we have done this for the metric tensor itself.

A tensor of higher rank can be similarly decomposed by its repeated inner products with basis vectors. Depending on the choice of basis vectors, the components of a tensor of rank 2 can be covariant, contravariant, or hybrid. For example, if a tensor $\mathbf{T}$ has only tangent component, we can write

$$\mathbf{T}=T_{\alpha\beta}\boldsymbol{r}^{\alpha}\boldsymbol{r}^{\beta}=T_{\alpha\cdot}^{\cdot\beta}\boldsymbol{r}^{\alpha}\boldsymbol{r}_{\beta}=T_{\cdot\beta}^{\alpha\cdot}\boldsymbol{r}_{\alpha}\boldsymbol{r}^{\beta}=T^{\alpha\beta}\boldsymbol{r}_{\alpha}\boldsymbol{r}_{\beta},$$

where the dots indicate the order of components which cannot be exchanged unless the tensor is symmetric with respect to relevant indices.

### Tangent Derivatives of a Vector

The most important differential operations on a surface $S$ is the tangent derivatives of vectors and tensors. We split the gradient vector into

$$\nabla=\nabla_{\pi}+\boldsymbol{n}\frac{\partial}{\partial n},\quad \nabla_{\pi}(\cdot)=\boldsymbol{r}^{\alpha}\frac{\partial(\cdot)}{\partial u^{\alpha}}=\boldsymbol{r}^{\alpha}(\cdot)_{,\alpha},\tag{A.59}$$

where a hybrid use has been made: $\boldsymbol{r}^{\alpha}$ is not created from $u^{\alpha}$ but from $u_{\alpha}$.

Now, for the tangent derivatives of a vector $\boldsymbol{f}$, there is

$$\begin{aligned} \nabla_{\pi}\boldsymbol{f}&=\boldsymbol{r}^{\alpha}(\boldsymbol{r}^{\beta}f_{\beta}+f_{n}\boldsymbol{n})_{,\alpha}\\ &=\boldsymbol{r}^{\alpha}(\boldsymbol{r}_{,\alpha}^{\beta}f_{\beta}+\boldsymbol{r}^{\beta}f_{\beta,\alpha}+\boldsymbol{n}_{,\alpha}f_{n}+\boldsymbol{n}f_{n,\alpha}). \end{aligned}$$

Here, the derivatives of $f_{\beta}$ and $f_{n}$ are merely that of numbers; the key is the derivatives of basis vectors $\boldsymbol{r}_{\alpha},\boldsymbol{r}^{\beta}$, and $\boldsymbol{n}$. These vectors are not coplaner, and hence their derivatives with respect to $u^{\alpha}$ can be expressed by their linear combinations. The result is given by the classic *Gauss formulas*

$$\boldsymbol{r}_{\beta,\alpha}=\Gamma_{\alpha\beta}^{\lambda}\boldsymbol{r}_{\lambda}+b_{\alpha\beta}\boldsymbol{n},\quad \boldsymbol{r}_{,\alpha}^{\beta}=-\Gamma_{\alpha\lambda}^{\beta}\boldsymbol{r}^{\lambda}+b_{\alpha}^{\beta}\boldsymbol{n},\quad \Gamma_{\alpha\beta}^{\lambda}=\Gamma_{\beta\alpha}^{\lambda},\tag{A.60a,b,c}$$

and *Weingarten formulas*

$$\boldsymbol{n}_{,\alpha} = -b_\alpha^\beta \boldsymbol{r}_\beta = -b_{\alpha\beta}\boldsymbol{r}^\beta, \quad b_{\alpha\beta} = b_{\beta\alpha} = b_\beta^\gamma g_{\alpha\gamma}. \tag{A.61a,b}$$

The six coefficients $\Gamma_{\alpha\beta}^\lambda = \Gamma_{\beta\alpha}^\lambda$ in (A.60) are called *Christoffel symbols of the second kind*. They do not form a tensor since $\boldsymbol{r}_\alpha$ are artificially chosen. In contrast, three coefficients $b_{\alpha\beta} = g_{\gamma\alpha}b_\beta^\alpha = b_{\beta\alpha}$ are covariant components of the symmetric *curvature tensor*, defined by the intrinsic operation

$$\mathbf{K} \equiv -\nabla_\pi \boldsymbol{n} = -\boldsymbol{r}^\alpha \boldsymbol{n}_{,\alpha} = \boldsymbol{r}^\alpha \boldsymbol{r}_\beta b_\alpha^\beta = \boldsymbol{r}^\alpha \boldsymbol{r}^\beta b_{\alpha\beta}. \tag{A.62}$$

### Intrinsic Operation on Surface

In view of the complicated involvement of nontensorial $\Gamma_{\alpha\beta}^\lambda$ in the derivatives of $\boldsymbol{r}^\alpha$ or $\boldsymbol{r}_\beta$, it is desired to bypass these operations. We call this kind of operation *intrinsic operation*. To start, we look at some more intrinsic properties of the normal vector $\boldsymbol{n}$. First, the *mean curvature* $\kappa$ is defined as half of the two-dimensional divergence

$$2\kappa \equiv -\nabla_\pi \cdot \boldsymbol{n} = b_\alpha^\beta \delta_\beta^\alpha = g^{\alpha\beta} b_{\alpha\beta} = b_\alpha^\alpha. \tag{A.63}$$

This result directly comes from the contraction of (A.62. Second, by (A.61a,b) there is

$$\nabla_\pi \times \boldsymbol{n} = \boldsymbol{r}^\alpha \times \boldsymbol{n}_{,\alpha} = -b_{\alpha\beta}\boldsymbol{r}^\alpha \times \boldsymbol{r}^\beta = \mathbf{0}. \tag{A.64}$$

Finally, (A.61a) implies

$$\boldsymbol{n} \cdot \boldsymbol{n}_{,\alpha} = 0. \tag{A.65}$$

From the derivation of (A.64 we can already see the main feature of the intrinsic operation: (1) *The operation is in vector form rather than component form*; and (2) *the tangent basis vectors are carried along in the operation but their derivatives do not appear*. The final result will be automatically free from these vectors. The following examples further show the strategy.

First, we compute the jump of normal vorticity across a vortex sheet

$$[\![\omega_n]\!] = \boldsymbol{n} \cdot [\![\nabla \times \boldsymbol{u}]\!] = (\boldsymbol{n} \times \nabla) \cdot (\boldsymbol{n} \times \boldsymbol{\gamma}),$$

where $\boldsymbol{\gamma}$ is the sheet strength. Using the surface frame, we have

$$[\![\omega_n]\!] = (\boldsymbol{n} \times \boldsymbol{r}^\alpha) \cdot (\boldsymbol{n} \times \boldsymbol{\gamma}_{,\alpha} + \boldsymbol{n}_{,\alpha} \times \boldsymbol{\gamma}),$$

which amounts to common vector algebra. Thus, by (A.55),

$$\begin{aligned}[\![\omega_n]\!] = {} & (\boldsymbol{n} \cdot \boldsymbol{n})(\boldsymbol{r}^\alpha \cdot \boldsymbol{\gamma}_{,\alpha}) - (\boldsymbol{n} \cdot \boldsymbol{\gamma}_{,\alpha})(\boldsymbol{r}^\alpha \cdot \boldsymbol{n}) \\ & + (\boldsymbol{n} \cdot \boldsymbol{n}_{,\alpha})(\boldsymbol{r}^\alpha \cdot \boldsymbol{\gamma}) - (\boldsymbol{n} \cdot \boldsymbol{\gamma})(\boldsymbol{r}^\alpha \cdot \boldsymbol{n}_{,\alpha}),\end{aligned}$$

where $\boldsymbol{n}\cdot\boldsymbol{\gamma}=0$, $\boldsymbol{r}^{\alpha}\cdot\boldsymbol{n}=0$, and we have (A.65). Thus, we simply obtain (Saffman 1992; where no proof is given)

$$[\![\omega_n]\!]=\boldsymbol{r}^{\alpha}\cdot\boldsymbol{\gamma}_{,\alpha}=\nabla_{\pi}\cdot\boldsymbol{\gamma}. \tag{A.66}$$

Second, we show that for any vectors $\boldsymbol{A}$ and $\boldsymbol{B}$ satisfying $\boldsymbol{n}\cdot\mathbf{A}=0$ and $\boldsymbol{B}=\boldsymbol{n}\times\mathbf{A}$, there is

$$\nabla_{\pi}\cdot\boldsymbol{A}=(\boldsymbol{n}\times\nabla)\cdot\boldsymbol{B}=\boldsymbol{n}\cdot(\nabla\times\boldsymbol{B}). \tag{A.67}$$

Indeed, since $\boldsymbol{n}\times\nabla=\boldsymbol{n}\times\nabla_{\pi}$, we have

$$\begin{aligned}(\boldsymbol{n}\times\nabla)\cdot\boldsymbol{B}&=\boldsymbol{n}\cdot(\nabla_{\pi}\times\boldsymbol{B})=\boldsymbol{n}\cdot[\boldsymbol{r}^{\alpha}\times(\boldsymbol{n}_{,\alpha}\times\boldsymbol{A}+\boldsymbol{n}\times\boldsymbol{A}_{,\alpha})]\\&=\boldsymbol{n}\cdot\boldsymbol{n}_{,\alpha}(\boldsymbol{r}^{\alpha}\cdot\boldsymbol{A})-\boldsymbol{n}\cdot\boldsymbol{A}(\boldsymbol{r}^{\alpha}\cdot\boldsymbol{n}_{,\alpha})+\boldsymbol{r}^{\alpha}\cdot\boldsymbol{A}_{,\alpha},\end{aligned}$$

in which the first two terms vanish due to (A.65) and assumed feature of $\boldsymbol{A}$. The last term gives (A.67).

Third, $(\boldsymbol{n}\times\nabla)\times\boldsymbol{A}$ is a tangent-derivative operation and we develop it to several fundamental constituents. There is

$$\begin{aligned}(\boldsymbol{n}\times\nabla)\times\boldsymbol{A}&=(\boldsymbol{n}\times\boldsymbol{r}^{\alpha})\times\boldsymbol{A}_{,\alpha}=\boldsymbol{r}^{\alpha}(\boldsymbol{A}_{,\alpha}\cdot\boldsymbol{n})-\boldsymbol{n}(\boldsymbol{r}^{\alpha}\cdot\boldsymbol{A}_{,\alpha})\\&=(\nabla_{\pi}\boldsymbol{A})\cdot\boldsymbol{n}-\boldsymbol{n}\nabla_{\pi}\cdot\boldsymbol{A}.\end{aligned} \tag{A.68}$$

The second term comes from the tangent divergence of $\boldsymbol{A}$, while the first term must be related to the normal component of $\boldsymbol{A}$; but even if $A_n=0$, the surface curvature may cause $\nabla_{\pi}\boldsymbol{A}$ to have normal components. In fact, we can further split the first term of (A.68) to

$$(\nabla_{\pi}\boldsymbol{A})\cdot\boldsymbol{n}=\nabla_{\pi}(\boldsymbol{A}\cdot\boldsymbol{n})-\boldsymbol{A}\cdot\nabla_{\pi}\boldsymbol{n}=\nabla_{\pi}A_n+\boldsymbol{A}\cdot\mathbf{K},$$

where $\mathbf{K}$ has only tangent components. Thus, it follows that

$$(\boldsymbol{n}\times\nabla)\times\boldsymbol{A}=\nabla_{\pi}A_n+\boldsymbol{A}_{\pi}\cdot\mathbf{K}-\boldsymbol{n}(\nabla_{\pi}\cdot\boldsymbol{A}). \tag{A.69}$$

In all the above examples $\boldsymbol{r}^{\alpha}$ are merely a temporary scaffold for the convenience of operation. However, if the final result is to be written in terms of components, then the derivatives of $\boldsymbol{r}^{\alpha}$ become inevitable. For example, in (A.69) and (A.68) we have

$$\nabla_{\pi}\cdot\boldsymbol{A}=\frac{1}{\sqrt{g}}(\sqrt{g}A^{\alpha})_{,\alpha},\quad \boldsymbol{n}\cdot(\nabla_{\pi}\times\boldsymbol{B})=\frac{1}{\sqrt{g}}(B_{2,1}-B_{1,2}), \tag{A.70a,b}$$

of which the proof requires the knowledge of $\Gamma^{\lambda}_{\alpha\beta}$ that is beyond our present concern.

**Orthonormal Surface Frame**

If in the above surface-moving frame the covariant tangent basis vectors $\boldsymbol{r}_1$ and $\boldsymbol{r}_2$ are already orthogonal, then by (A.50) there is $\boldsymbol{r}^\alpha = \boldsymbol{r}_\alpha/\sqrt{g}$, implying that there is no need to distinguish covariant and contravariant tangent basis vectors. Thus, like Cartesian tensors, it suffices to use one pair of tangent basis vectors and denote the components by subscripts only.

The orthogonality of basis vector implies that

$$g_{ii} = h_i^2 \delta_{ii} \quad \text{(no summation with respect to } i\text{)},$$

where

$$h_i = \sqrt{g_{ii}} = \sqrt{\boldsymbol{r}_i \cdot \boldsymbol{r}_i} \quad \text{(no summation with respect to } i\text{)} \tag{A.71}$$

is the length of $\boldsymbol{r}_i$, called *scale coefficients* or *Lamé coefficients*. They are still functions of the moving point $\boldsymbol{x}$. Nevertheless, we can now introduce a set of orthonormal basis vectors

$$\boldsymbol{e}_\alpha = \frac{\boldsymbol{r}_\alpha}{h_\alpha} \quad \text{(no summation with respect to } \alpha\text{)}, \quad \boldsymbol{e}_3 = \boldsymbol{n}, \tag{A.72}$$

which form an *orthonormal surface frame*. For a given curved surface $S$, $h_\alpha$ depends on its intrinsic geometric feature as well as the orientation of $\boldsymbol{r}_\alpha$, the latter can be arbitrarily chosen, not restricted by the Dupin theorem as long as the frame is only defined on a single surface $S$.

With the $\boldsymbol{e}_i$ frame and using the notation

$$\partial_i = \frac{1}{h_i}\frac{\partial}{\partial x_i}, \quad i = 1, 2, 3, \tag{A.73}$$

the Gauss formulas (A.60) and Weingarten formulas (A.61) can be cast to

$$\left.\begin{aligned}
\partial_1 \boldsymbol{e}_1 &= -\frac{h_{1,2}}{h_1 h_2}\boldsymbol{e}_2 + b_{11}\boldsymbol{e}_3 \\
\partial_1 \boldsymbol{e}_2 &= \frac{h_{1,2}}{h_1 h_2}\boldsymbol{e}_1 + b_{12}\boldsymbol{e}_3 \\
\partial_1 \boldsymbol{e}_3 &= -b_{11}\boldsymbol{e}_1 - b_{12}\boldsymbol{e}_2 \\
\partial_2 \boldsymbol{e}_1 &= \frac{h_{2,1}}{h_1 h_2}\boldsymbol{e}_2 + b_{12}\boldsymbol{e}_3 \\
\partial_2 \boldsymbol{e}_2 &= -\frac{h_{2,1}}{h_1 h_2}\boldsymbol{e}_1 + b_{22}\boldsymbol{e}_3 \\
\partial_2 \boldsymbol{e}_3 &= -b_{12}\boldsymbol{e}_1 - b_{22}\boldsymbol{e}_2
\end{aligned}\right\}, \tag{A.74}$$

and, of course,

$$\partial_i \boldsymbol{e}_3 = 0, \quad i = 1, 2, 3.$$

Here, $b_{\alpha\beta} = b_{\beta\alpha}$ $(\alpha, \beta = 1, 2)$ are redefined by

$$b_{\alpha\beta} = \boldsymbol{e}_\alpha \cdot \mathbf{K} \cdot \boldsymbol{e}_\beta \quad or \quad \mathbf{K} = b_{\alpha\beta} \boldsymbol{e}_\alpha \boldsymbol{e}_\beta \tag{A.75}$$

instead of (A.62). From $b_{\alpha\beta}$ one can construct two intrinsic scalar curvatures which describe the wall geometry and are independent of the choice of $\boldsymbol{e}_1$ and $\boldsymbol{e}_2$. One is

$$b_{11} + b_{22} = \kappa_B = -\nabla_\pi \cdot \boldsymbol{n}, \tag{A.76}$$

twice of the *mean curvature* as already seen in (A.63); the other is

$$b_{11} b_{22} - b_{12}^2 = \det\{b_{\alpha\beta}\} \equiv K, \tag{A.77}$$

the *total curvature*. Moreover, except some isolated points a curved surface has a pair of orthogonal *principal directions*. If $\boldsymbol{e}_1$ and $\boldsymbol{e}_2$ coincide with these directions then $b_{\alpha\beta} = 0$ for $\alpha \neq \beta$. In this case $b_{11} = K_1$ and $b_{22} = K_2$ are the *principal curvatures*, which are the greatest and least $b_{\alpha\beta}$ among all orientations of the tangent vectors. The total curvature is simply $K = K_1 K_2$. On a sphere any tangent direction is a principal direction.

It is convenient to express $b_{\alpha\beta}$ by principal curvatures since the latter are independent of the choice of $(\boldsymbol{e}_1, \boldsymbol{e}_2)$. Denote the unit tangent vectors along the principal directions by $\boldsymbol{p}_1$ and $\boldsymbol{p}_2$ (they define the curvature lines of the surface), then by (A.75) there is

$$\mathbf{K} = \boldsymbol{p}_1 \boldsymbol{p}_1 K_1 + \boldsymbol{p}_2 \boldsymbol{p}_2 K_2.$$

Thus, if $(\boldsymbol{p}_1, \boldsymbol{p}_2, \boldsymbol{e}_3)$ form a right-handed frame and $\beta$ is the angle by which the $(\boldsymbol{p}_1, \boldsymbol{p}_2)$ pair rotates to the $(\boldsymbol{e}_1, \boldsymbol{e}_2)$ pair in counterclockwise sense, there is

$$b_{11} = K_1 \cos^2\beta + K_2 \sin^2\beta, \tag{A.78a}$$

$$b_{12} = -\frac{1}{2}(K_1 - K_2)\sin 2\beta, \tag{A.78b}$$

$$b_{22} = K_1 \sin^2\beta + K_2 \cos^2\beta. \tag{A.78c}$$

Hence, for a given surface, $b_{\alpha\beta}$ depend solely on a single parameter $\beta$. Because reversing the direction of $(\boldsymbol{p}_1, \boldsymbol{p}_2)$ does not affect $\mathbf{K}$, without loss of generality we set $\beta \in [0, \pi/2]$.

On the other hand

$$\kappa_1 = (\partial_1 \boldsymbol{e}_1) \cdot \boldsymbol{e}_2 = -(\partial_1 \boldsymbol{e}_2) \cdot \boldsymbol{e}_1 = -\frac{h_{1,2}}{h_1 h_2}, \tag{A.79a}$$

$$\kappa_2 = (\partial_2 \boldsymbol{e}_2) \cdot \boldsymbol{e}_1 = -(\partial_2 \boldsymbol{e}_1) \cdot \boldsymbol{e}_2 = -\frac{h_{2,1}}{h_1 h_2} \tag{A.79b}$$

define a pair of *on-surface curvatures of coordinate lines* $x_1$ and $x_2$, respectively (they are the geometric curvatures of these lines if $\mathbf{K} = \mathbf{0}$). Therefore,

(A.74) can be written in a geometrically clearer form:

$$\left.\begin{aligned}
\partial_1 \boldsymbol{e}_1 &= \kappa_1 \boldsymbol{e}_2 + b_{11}\boldsymbol{e}_3 \\
\partial_1 \boldsymbol{e}_2 &= -\kappa_1 \boldsymbol{e}_1 + b_{12}\boldsymbol{e}_3 \\
\partial_1 \boldsymbol{e}_3 &= -b_{11}\boldsymbol{e}_1 - b_{12}\boldsymbol{e}_2 \\
\partial_2 \boldsymbol{e}_1 &= -\kappa_2 \boldsymbol{e}_2 + b_{12}\boldsymbol{e}_3 \\
\partial_2 \boldsymbol{e}_2 &= \kappa_2 \boldsymbol{e}_1 + b_{22}\boldsymbol{e}_3 \\
\partial_2 \boldsymbol{e}_3 &= -b_{12}\boldsymbol{e}_1 - b_{22}\boldsymbol{e}_2
\end{aligned}\right\} \tag{A.80}$$

Note that since in (A.71) $h_\alpha$ ($\alpha = 1, 2$) are functions of $x_1$ and $x_2$, operators $\partial_\alpha$ and $\partial_\beta$ for $\alpha \neq \beta$ are not commutative. Instead, there is

$$(\partial_1 - \kappa_2)\partial_2 = (\partial_2 - \kappa_1)\partial_1 \quad \text{or} \quad \partial_1\partial_2 - \partial_2\partial_1 = \kappa_1\partial_1 - \kappa_2\partial_2, \tag{A.81}$$

but we still have $\partial_\alpha \partial_3 = \partial_3 \partial_\alpha$.

The orthogonality of $x_1$-lines and $x_2$-lines implies that the variation of $\kappa_1$ and $\kappa_2$ are not independent. In fact, by (A.81) and using (A.80), there is

$$\begin{aligned}
\partial_2\kappa_1 &= \partial_2[(\partial_1 \boldsymbol{e}_1)\cdot \boldsymbol{e}_2] \\
&= (\partial_1\partial_2 \boldsymbol{e}_1)\cdot \boldsymbol{e}_2 + (\partial_1 \boldsymbol{e}_1)\cdot(\partial_2 \boldsymbol{e}_2) + \kappa_1^2 + \kappa_2^2 \\
&= -\partial_1\kappa_2 + b_{11}b_{22} - b_{12}^2 + \kappa_1^2 + \kappa_2^2,
\end{aligned}$$

from which it follows a *differential identity*

$$\partial_2\kappa_1 + \partial_1\kappa_2 = \kappa_1^2 + \kappa_2^2 + K. \tag{A.82}$$

Finally, by using (A.80), the components of the gradient of any vector $\boldsymbol{f} = \boldsymbol{e}_i f_i$ in the $(x_1, x_2, x_3)$-frame read

$$(\partial_i \boldsymbol{f})\cdot \boldsymbol{e}_j = \begin{pmatrix} c_{11} & c_{12} & c_{13} \\ c_{21} & c_{22} & c_{23} \\ \partial_3 f_1 & \partial_3 f_2 & \partial_3 f_3 \end{pmatrix}, \tag{A.83a}$$

where

$$\left.\begin{aligned}
c_{11} &= \partial_1 f_1 - \kappa_1 f_2 - b_{11} f_3 \\
c_{12} &= \partial_1 f_2 + \kappa_1 f_1 - b_{12} f_3 \\
c_{13} &= \partial_1 f_3 + b_{11} f_1 + b_{12} f_2 \\
c_{21} &= \partial_2 f_1 + \kappa_2 f_2 - b_{12} f_3 \\
c_{22} &= \partial_2 f_2 - \kappa_2 f_1 - b_{22} f_3 \\
c_{23} &= \partial_2 f_3 + b_{12} f_1 + b_{22} f_2
\end{aligned}\right\}. \tag{A.83b}$$

Thus, $b_{\alpha\beta}$ and $\kappa_\alpha$ appear in all tangent derivatives.

## A.4 Applications in Lagrangian Description

Tensor analysis is necessary in studying the transformation of physical quantities and equations between the physical space and the reference space (in Lagrangian description). In this section, we present some materials which are directly cited in the main text.

### A.4.1 Deformation Gradient Tensor and its Inverse

Consider the *deformation gradient tensor* and associated Jacobian in the reference space, defined by (2.3) and (2.4)

$$\mathbf{F} = \nabla_X \boldsymbol{x} \quad \text{or} \quad F_{\alpha i} = x_{i,\alpha}, \tag{A.84}$$

$$J = \frac{\partial(x_1, x_2, x_3)}{\partial(X_1, X_2, X_3)} = \det\mathbf{F}. \tag{A.85}$$

First, $J$ has a few explicit forms exactly the same as the determinant of a matrix

$$J = \epsilon_{\alpha\beta\gamma} x_{1,\alpha} x_{2,\beta} x_{3,\gamma}, \tag{A.86a}$$

$$\epsilon_{ijk} J = \epsilon_{\alpha\beta\gamma} x_{i,\alpha} x_{j,\beta} x_{k,\gamma}. \tag{A.86b}$$

Next, keeping the labels of particles, any variation of $J$ can only be caused by that of $\boldsymbol{x}$. Using (A.86), an infinitesimal change of $J$ is then given by

$$\begin{aligned}
\delta J &= \epsilon_{\alpha\beta\gamma}(\delta x_{1,\alpha} x_{2,\beta} x_{3,\gamma} + x_{1,\alpha}\delta x_{2,\beta} x_{3,\gamma} + x_{1,\alpha} x_{2,\beta}\delta x_{3,\gamma}) \\
&= \epsilon_{\alpha\beta\gamma} x_{1,\alpha} x_{2,\beta} x_{3,\gamma}(\delta x_{1,1} x_{2,2} x_{3,3} + x_{1,1}\delta x_{2,2} x_{3,3} + x_{1,1} x_{2,2}\delta x_{3,3}) \\
&= J\delta x_{l,l}.
\end{aligned}$$

Namely,

$$\delta J = J\nabla \cdot \delta\boldsymbol{x}. \tag{A.87}$$

Then, owing to (2.8), (2.3) is invertible, and hence $\mathbf{F}$ has inverse tensor defined in the physical space

$$\mathbf{F}^{-1} = \nabla \boldsymbol{X}, \quad \text{or} \quad F^{-1}_{i\alpha} = X_{\alpha,i}, \tag{A.88}$$

which satisfies $\mathbf{F}\cdot\mathbf{F}^{-1} = \mathbf{F}^{-1}\cdot\mathbf{F} = \mathbf{I}$, i.e.,

$$x_{i,\alpha} X_{\beta,i} = \delta_{\alpha\beta}, \quad X_{\alpha,i} x_{j,\alpha} = \delta_{ij}. \tag{A.89}$$

The Jacobian of $\mathbf{F}^{-1}$ is

$$J^{-1} = \det\mathbf{F}^{-1} = \frac{\partial(X_1, X_2, X_3)}{\partial(x_1, x_2, x_3)} = \frac{1}{J}, \tag{A.90}$$

which has expressions symmetrical to (A.86a,b). For example, we have

$$\epsilon_{ijk}J^{-1} = \epsilon_{\alpha\beta\gamma}X_{\alpha,i}X_{\beta,j}X_{\gamma,k}. \tag{A.91}$$

Similar to (A.87), there is

$$\delta J^{-1} = J^{-1}\delta X_{\alpha,\alpha} = J^{-1}\delta X_{\alpha,i}x_{i,\alpha} = J^{-1}\nabla_X \cdot \delta \boldsymbol{X}. \tag{A.92}$$

The deformation tensor $\mathbf{F}$ and its inverse $\mathbf{F}^{-1}$ have one index in physical space and one in the reference space. This property can be used to transform a physical-space vector to its *dual* or *image* in the reference space, or vise versa.

### A.4.2 Images of Physical Vectors in Reference Space

We are particularly interested in seeking the image of vorticity $\boldsymbol{\omega}$ in the $\boldsymbol{X}$-space. To this end consider a general vector $\boldsymbol{f}$ first. Multiply both sides of (A.86b) by $f_{k,j}/J$ and notice that

$$f_{k,j}x_{j,\beta} = f_{k,\beta}, \quad \epsilon_{\alpha\beta\gamma}x_{k,\beta\gamma} = 0.$$

It follows that:

$$\epsilon_{ijk}f_{k,j} = \frac{1}{J}\epsilon_{\alpha\beta\gamma}x_{i,\alpha}x_{k,\gamma}f_{k,\beta} = \frac{1}{J}\epsilon_{\alpha\beta\gamma}(x_{k,\gamma}f_k)_{,\beta}x_{i,\alpha},$$

of which the vector form is

$$\nabla \times \boldsymbol{f} = \frac{1}{J}[\nabla_X \times (\mathbf{F} \cdot \boldsymbol{f})] \cdot \mathbf{F}. \tag{A.93}$$

Taking inner product of this result with $\mathbf{F}^{-1}$, the inverse of (A.93) reads

$$\nabla_X \times (\mathbf{F} \cdot \boldsymbol{f}) = J(\nabla \times \boldsymbol{f}) \cdot \mathbf{F}^{-1}. \tag{A.94}$$

The mapping between $\nabla \times \boldsymbol{f}$ and $\nabla_X \times (\mathbf{F} \cdot \boldsymbol{f})$ is one-to-one, and has three features: (1) they are identical at $t = \tau = 0$; (2) if one vanishes, so must the other; and (3) they are divergenceless in their respective spaces. We therefore identify the latter as the image of the former in $\boldsymbol{X}$-space. Besides, for two-dimensional vector field $\boldsymbol{f} = (f_1, f_2, 0)$ it can be shown that (A.94) is simplified to

$$\nabla_X \times (\mathbf{F} \cdot \boldsymbol{f}) = J\nabla \times \boldsymbol{f}. \tag{A.95}$$

Note that the above identification naturally leads us to define the image of $\boldsymbol{f}$ itself in the $\boldsymbol{X}$-space as $\mathbf{F} \cdot \boldsymbol{f}$.

Now let $\boldsymbol{f} = \boldsymbol{u} = \partial \boldsymbol{x}/\partial\tau$ be the velocity field. Its image in $\boldsymbol{X}$-space is

$$U_\alpha = x_{i,\alpha}u_i \quad \text{or} \quad U = \mathbf{F} \cdot \boldsymbol{u}. \tag{A.96}$$

Then by (A.94), the image of $\boldsymbol{\omega}$ is

$$\boldsymbol{\Omega} \equiv \nabla_X \times \boldsymbol{U}, \tag{A.97}$$

which we call the *Lagrangian vorticity*. By using (A.89) and mass conservation (2.40), the transformation between $\boldsymbol{\omega}$ and $\boldsymbol{\Omega}$ is given by

$$\boldsymbol{\Omega} = J\boldsymbol{\omega} \cdot \mathbf{F}^{-1} = \boldsymbol{\omega}\frac{\rho_0}{\rho} \cdot \mathbf{F}^{-1}, \tag{A.98a}$$

$$\boldsymbol{\omega} = \frac{1}{J}\boldsymbol{\Omega} \cdot \mathbf{F} = \frac{\rho}{\rho_0}\boldsymbol{\Omega} \cdot \mathbf{F}. \tag{A.98b}$$

For two-dimensional flow there is

$$\Omega = J\omega = \frac{\rho_0}{\rho}\omega \tag{A.99}$$

and, if in addition the flow is incompressible we simply have $\Omega = \omega$.

Note that the images of $\boldsymbol{u}$ and $\boldsymbol{\omega}$ have opposite structures. In the former $\mathbf{F}$ is used but in the latter, in addition to the factor $J$, it is $\mathbf{F}^{-1}$. This is related to the fact that $\boldsymbol{u}$ is a true vector (polar vector) but $\boldsymbol{\omega}$ is a pseudo-vector (axial vector). One might switch the use of $\mathbf{F}$ and $\mathbf{F}^{-1}$ for true and pseudo vectors; which however does not lead to useful result unless $\boldsymbol{U}$ is to be written as the curl of another vector, which will be used once below.

Once we introduced the Lagrangian vorticity, we may study vorticity kinematics in physical space by that of $\boldsymbol{\Omega}$ in reference space. First, since

$$\frac{\partial}{\partial\tau}(x_{k,\gamma}u_k) = x_{k,\gamma}a_k + \frac{1}{2}q^2_{,\gamma},$$

where

$$A_\alpha \equiv x_{i,\alpha}a_i = A_\alpha \quad \text{or} \quad bF \cdot \boldsymbol{a} = \boldsymbol{A} \tag{A.100}$$

is the $\boldsymbol{X}$*-space image of acceleration*, there is

$$\frac{\partial \boldsymbol{U}}{\partial\tau} = \boldsymbol{A} + \nabla_X\left(\frac{1}{2}q^2\right). \tag{A.101}$$

This is *the* $\boldsymbol{X}$*-space image of* $\boldsymbol{a} = \mathrm{D}\boldsymbol{u}/\mathrm{D}t$. Its curl gives an elegant equation at once

$$\frac{\partial \boldsymbol{\Omega}}{\partial\tau} = \nabla_X \times \boldsymbol{A}, \tag{A.102a}$$

where by A.94,

$$\nabla_X \times \boldsymbol{A} = J(\nabla \times \boldsymbol{a}) \cdot \mathbf{F}^{-1} \tag{A.102b}$$

is the image of $\nabla \times \boldsymbol{a}$. Therefore, *the rate of change of the image of the curl of velocity (Lagrangian vorticity) equals the image of the curl of acceleration.* We stress that this result is not true for Lagrangian velocity $\boldsymbol{U}$ and acceleration

$\boldsymbol{A}$: in (A.101) there is an extra gradient term. The implication of this difference has been made clear in Sect. 3.6.

As an application of utilizing the vector images in reference space, we extend the content of Sect. 3.6.2 by showing that the circulation preserving is sufficient but not necessary for having a Bernoulli integral. Rewrite (A.101) as

$$\frac{\partial \boldsymbol{U}}{\partial \tau} = \boldsymbol{A}' + \nabla_X \Psi, \tag{A.103}$$

where $\Psi$ is defined in (3.152) and $\boldsymbol{A}'$ is the rotational part of $\boldsymbol{A}$. Similar to the approach leading to (3.148), assume there exists a family of material surfaces defined by two parameters, say $\xi_1(\boldsymbol{X})$ and $\xi_2(\boldsymbol{X})$, such that the normal $\nabla_X \xi_1 \times \nabla_X \xi_2$ is along $\boldsymbol{A}'$

$$\boldsymbol{A}' \times (\nabla_X \xi_1 \times \nabla_X \xi_2) = 0. \tag{A.104}$$

Then a Bernoulli integral like (3.155a) along these surfaces can be obtained. An important example is inviscid baroclinic flow without shock waves, for which $\mathrm{D}s/\mathrm{D}t = 0$ or $s = s(\boldsymbol{X})$ in the $\boldsymbol{X}$-space. Hence, any material surfaces are *isotropic*. Note that the existence of these surfaces is ensured by the Crocco–Vazsonyi equation (2.163), in which the rotational term $T\nabla s$ is a complex-lamellar vector field according to the definition in Sect. 3.3.1. Then, by using (A.96) there is

$$\boldsymbol{A}'(\boldsymbol{X}, \tau) = \mathbf{F} \cdot T\nabla s,$$

which is normal to isentropic surfaces. Therefore, on these surfaces we have Bernoulli integral (3.155). Correspondingly, those conservation theorems involves material integrals can survive along these surfaces. For example, instead of volume integrals (3.132) and (3.134) we may have a similar surface integrals; and the Kelvin circulation theorem (3.130c) will hold if the loop $\mathcal{C}$ is on one of such surfaces.

# References


Abramowitz M., Stegun A. (1972) *Handbook of Mathematical Functions.* Dover, Mineola New York.

Acarlar M.S., Smith C.R. (1987a) A study of hairpin vortices in a laminar boundary layer. Part.1, Hairpin vortices generated by a hemisphere protuberance. *J. Fluid Mech.* **175**: 1–41.

Acarlar M.S., Smith C.R. (1987b) A study of hairpin vortices in a laminar boundary layer. Part.2, Hairpin vortices generated by fluid injection. *J. Fluid Mech.* **175**: 43–83.

Adem J. (1956) A series solution for the barotropic vorticity equation and its application in the study of atmospheric vortices. *Tellus*, **8**: 364–372.

Adrian, R.J., Meinhart, C.D., Tomkins, C.D. (2000) Vortex organization in the outer region of the turbulent boundary layer. *J. Fluid Mech.* **422**: 1–54.

Ahlborn B., Lefrancois M., King D.H. (1998) The clockwork of vortex shedding. *Phys. Essays*, **11**: 144–154.

Ahlborn B., Seto M.L., Noack B.R. (2002) On drag, Strouhal number and vortex-street structure. *Fluid Dyn. Res.* **30**: 379–399.

Althaus W., Brucker C., Weimer M. (1995) Breakdown of slender vortices. In: Green S.I. (ed.) *Fluid Vortices*, Chap. IX, Kluwer, Dordrecht Netherlands 317–372.

Anderson C.R., Reider M.B. (1996) A high order explicit method for the computation of flow about a circular cylinder. *J. Comp. Phys.* **125**: 207–224.

Anderson J.D. Jr. (1991) *Fundamentals of Aerodynamics.* McGraw-Hill, New York.

Antkowiak A., Brancher P. (2004) Transient energy growth for the lamb-oseen vortex. *Phys. Fluids*, **16**(1): L1–L4.

Aref H. (1980) Vortex dynamics of the two-dimensional turbulent shear layer. *J. Fluid Mech.* **100**: 705.

Aref H. (1983) Integrable, chaotic and turbulent vortex motion in two-dimensional flows. *Ann. Rev. Fluid Mech.* **15**: 345–389.

Aref H., Flinchem E.P. (1984) Dynamics of a vortex filament in a shear flow. *J. Fluid Mech.* **148**: 477–497.

Aref H., Pomphrey N. (1982) Integratable and chaotic motions of four vortices. *Phys. Lett.* **78**A(4): 297–300.

Aref H., Zawadzki I. (1990) Comment of vortex ring reconnections. In: Moffatt H.K., Trinsber A. (eds.) *Topological Fluid Mechnics*, Proc. IUTAM Symp. Combridge, Cambridge University Press Cambridge, 535–539.

Aref H., Zawadzki I. (1991) Linking of vortex rings. *Nature*, **354**: 50–53.

Aris R. (1962) *Vectors, Tensors and the Basic Equations of Fluid Mechanics*. Dover, Mineala New York.

Arnold V.I. (1965a) Sur la totologie des écoulments stationaires des fluid parfaits. *C. R. Acad. Paries* A**261**: 17–20.

Arnold V.I. (1965b) Conditions for nonlinear stability of stationary plane curvilinear flows of an ideal fluid, *Dokl Akad. Nauk SSSR*, **162**: 975–978. (*Soviet Math.* **6**: 773–777.)

Arnold V.I. (1965c) Variational principle for three-dimensional steady-state flows of an ideal fluid. *Prikl Mat. Mekh.* **29**: 846–851.

Arnold V.I. (1969) On an apriori estimate in the theory of hydrodynamical stability. *Amer. Math. Soc. Transl.* **19**: 267–269.

Arnold V.I. (1989) *Mathematical Methods in Classical Mechanics*. Springer-Verlag, Berlin Heidelberg New York.

Arrese J.C., Fernandez-Feria R. (1996) Nuerical solution for the boundary layer induced by a conical vortex. *Proceedings of the CFD96*, Ottawa, Ontario, June 2–6, 1996.

Asai M., Nishioka M. (1995) Boundary-layer transition triggered by hairpin eddies at subcritical Reynolds numbers. *J. Fluid Mech.* **297**: 101–122.

Asai M., Nishioka M. (1997) Development of wall turbulence structure in transitional flows. In: Tatsumi T., Watanabe E., Kambe T. (eds.) *Theoretical and Applied Mechanics*, 19th IUTAM Congress, 1996, Elsevier Kyoto, Japan, 121–138.

Asai M., Sawada K., Nishioka M. (1996) Development of turbulent patch in a subcritical boundary-layer transition. *Fluid Dyn. Res.* **18**: 151–164.

Ash R.L., Khorrami M.R. (1995) Vortex stability. In: Green S.I. (ed.) *Fluid Vortices*, Chap. VIII, Kluwer, Dordrecht Netherlands 317–372.

Ashley H., Landahl M. (1965) *Aerodynamics of Wings and Bodies*, Dover Mineola New York.

Ashurst W.T., Meiburg E. (1988) Three-dimensional shear layer via vortex dynamics. *J. Fluid Mech.* **189**: 87–111.

Baggett J.S., Trefethen L.N. (1997) Low-dimensional models of subcritical transition to turbulence. *Phys. Fluids*, **9**(4): 1043–1053.

Baker G.R., Meiron D.I., Orszag S.A. (1982) Generalized vortex methods for free-surface flow problems. *J. Fluid Mech.* **123**: 477–501.

Baker S.J., Crow S.C. (1977) The motion of two-dimensional vortex pairs in a ground effect. *J. Fluid Mech.* **82**: 659–671.

Bakker P.G. (1991) *Bifurcations in flow patterns*. Kluwer, Dordrecht Netherlands.

Barkley D., Henderson B.D. (1996) Three-dimensional floquet stability analysis of the wake of circular cylinder. *J. Fluid Mech.* **322**: 215–241.

Baron A., Quadrio M. (1996) Turbulent drag reduction by spanwise wall oscillations. *Appl. Sci. Res.* **55**: 311–326.

Basdevant C., Philipovich T. (1994) On the validity of the "Weiss criterion" in two-dimensional turbulence. *Physica* D, **73**: 17–30.

Batchelor G.K. (1956a) Unsteady laminar flow with closed streamlines at large Reynolds number. *J. Fluid Mech.* **1**: 177–190.

Batchelor G.K. (1956b) A proposal concerning laminar wakes behind bluff bodies at large Reynolds number. *J. Fluid Mech.* **1**: 388–398.

Batchelor G.K. (1964) Axial flow in trailing line vortices. *J. Fluid Mech.* **20**: 645–658.

Batchelor G.K. (1967) *An Introduction to Fluid Mechanics*. Cambridge University Press, Cambridge, UK.

Batchelor G.K. (1969) Computation of the energy spectrum in homogeneous two-dimensional turbulence. *Phys. Fluids Suppl.* II **12**: 233–239.

Bayly B.J. (1986) Three-dimensional instability of strained vortices in a viscous fluid. *Phys. Rev. Lett.* **57(17)**: 2160–2163.

Beale J.T., Greengard C. (1992) Convergence of Euler-Stokes splitting of the Navier-Stokes equations. Research Report RC 18072, IBM.

Beale J.T., Kato T., Majda A. (1984) Remarks on the breakdown of smooth solution for the 3-D Euler equations. *Comm. Math. Phys.* **94**: 61–66.

Beckers M., Vlercx H.J.H., van Heijst G.J.F., Verzicco R. (2003) Evolution and instability of monopolar vortices in a stratified fluid. *Phys. Fluids*, **15**: 1033–1045.

Bellamy-Knights P.G. (1970) An unsteady two-celled vortex solution of the Navier-Stokes equations. *J. Fluid Mech.* **41**: 673–687.

Bengtsson L., Lighthill J. (eds.) (1982) *Intense Atmospheric Vortices*, Springer-Verlag, Berlin Heidelberg New York.

Benjamin T.B. (1962) Theory of the vortex breakdown phenomenon. *J. Fluid Mech.* **14**: 593–629.

Beran P.S., Culick F.E.C. (1992) The role of nonuniqueness in the development of vortex breakdown in tubes. *J. Fluid Mech.* **242**: 491–527.

Berestov A.L. (1979) Solitary rossby waves. *Izv. Acad. Sci. USSR Atmos. Oceanic Phys.* **15**: 443–447.

Bernal L.P., Roshko A. (1986) Streamwise vortex structure in plane mixing layers, *J. Fluid Mech.* **170**: 499–525.

Bernard P.S., Thomas J.M., Handler R.A. (1993) Vortex dynamics and the production of Reynolds stress. *J.Fluid Mech.* **253**: 385–419.

Bers A. (1975) Linear waves and instabilities. In: DeWitt C., Peyraud J. (eds.) *Physique des Plasmas*, Gordon & Breach, New York, 117–215.

Bers A. (1983) Space-time evolution of plasma instabilities - absolute and convective. In: Rosenbluth M.N., Sagdeev R.Z. (eds.) *Handbook of Plasma Physics*, North-Holland, Amsterdam, **1**: 451–517.

Bertozzi A.L. (1988) Heteroclinic orbits and chaotic dynamics in planer fluid flows. *SIAM J. Math. Anal.* **19**: 1271–1294.

Betchov R. (1965) On the curvature and torsion of an isolated vortex filament. *J. Fluid Mech.* **51**: 477.

Betz A. (1950) Wie entsteht ein Wirbel in einer wenig žahen Flussigkeit. *Naturwiss*, **37**: 193–196.

Bilanin A.J., Widnall S.E. (1973) *AIAA* 73–107.

Bippes H., Turk M. (1983) Oil flow patterns of separated flow on a hemisphere cylinder at incidence. *DFVLR-FB* 84–20.

Birkhoff G. (1960) *Hydrodynamics: A Study in Logic, Fact, and Simulitude.* Princeton University Press, Princeton, NJ 4.

Birkhoff G., Zarantonello E.H. (1957) *Jets, Wakes, and Cavities*, Academic Press, San Diego.

Bisplinghoff R.L., Ashley H., Halfman R.L. (1955) *Aeroelasticity*, Addison-Wesley, Milano Italy.

Bjerknes V. (1898) Über die Bildung von Circulationsbewegung und Wirbeln in reibungslosen Flüssigkeiten. *Videnskabsselskapets Skrifter. I Math. Naturv. Klasse*, **5**: 1–29.

Bjerknes V. (1902) Zirkulation relativ zu der Erde. *Met. Z.* **19**: 97–108.

Blackwelder R.F. (1979) Boundary-layer transition. *Phys. Fluids*, **22**: 583–584.

Blackwelder R.F. (1983) Analopgies between transitional and turbulent boundary layers. *Phys. Fluids*, **26**: 2807–2815.

Blackwelder R.F., Eckelmann H. (1978) The spanwise structure of the bursting phenomenon. In: Fiedler H. (ed.) *Structure and Mechanisms of Turbulence*, **1**: 190, Springer, Berlin Heidelberg New York.

Blackwelder R.F., Haritonidis J.H. (1983) Scaling of the bursting frequency in turbulent boundary layers. *J. Fluid Mech.* **132**: 87–103.

Blasius H. (1908) Grenzschichten in Flüssigkeiten mit kleiner Reibung. *Z. Math. u. Phys.* **56**: 1–37.

Bödewadt U.T. (1940) Die Drehströmung über festem Grunde. *Z Angew Math. Mech.* **20**: 241–245.

Boratav O.W., Peltz R.B., Zakusky N.J. (1992) Reconnection in orthogonally interacting vortex tubes: direct numerical simulations and quantifications. *Phys. Fluids*, A. **4**: 581–605.

Bouard R., Coutaneau M. (1980) The early stage of development of the wake behind an impulsively started cylinder for $40 < Re < 10^4$. *J. Fluid Mech.* **101**: 583–607.

Boulmezaoud T.Z., Amari T. (2000) Approximation of linear force-free fields in bounded 3-D domains. *Math. Comput. Modell.*, **31**: 109–129.

Bowles R.I. (2000) Transition to turbulent flow in aerodynamics. *Phil. Trans. R. Soc.* A **358**: 245–260.

Bradshaw P. (1971) *An introduction to Turbulence and its Measurement*. Pergamon Press, London.

Bradshaw P., Ferriss D.H., Atwell N.P. (1967) Calculation of boundary layer development using the turbulent energy equation. *J. Fluid Mech.* **28**: 593–616.

Bragg S.L., Hawthorne W.R. (1950) Some exact solutions of the flow through annular cascade actuator discs. *J. Aero. Sci.* **17**: 243.

Brechet M.E., Meneguzzi M., Politano H., Sulem P.L. (1988) The dynamics of freely decaying two-dimensional turbulence. *J. Fluid Mech.* **194**: 333–349.

Bretherton F.P. (1970) A note on hamilton's principle for perfect fluids. *J. Fluid Mech.* **44**: 19–31.

Briggs R.J. (1964) *Electron-Stream Interaction with Plasmas*. MIT Press, Cambridge, Mass.

Brooke J.W., Hanratty T.J. (1992) Origin of turbulence-producing eddies in a channel flow, *Phys. Fluids*, A**5**(4): 1011–1022.

Browand F.K. (1986) The structure of the turbulent mixing layer. *Physica D*, **18**: 135–148.

Browand F.K., Ho C.M. (1983) The mixing layer: An example of quasi two-dimensional turbulence. *Journal de Mecanique Theorique et Appliquee*, Numero special, 99–120.

Brown G.L., Lopez J.M. (1990) Axisymmetric vortex breakdown. Part I. Physical mechanism. *J. Fluid Mech.* **228**: 153–576.

Brown G.L., Roshko A. (1974) On density effects and large structure in turbulent mixing layers. *J. Fluid Mech.* **64**: 775–816.

Brown G.L., Thomas A.S.W. (1977) Large structure in a turbulent boundary layer. *Phys. Fluids*, **20**: 5243.

Buntine J.D., Saffman O.G. (1995) Inviscid swirling flows and vortex breakdown. *Proc. R. Soc. London*, A**449**: 139–353.

Bunyakin A.V., Chernyshenko S.I., Stepanov G.Y. (1996) Inviscid Batchelor-model flow past an airfoil with a vortex trapped in a cavity. *J. Fluid Mech.* **323**: 367–376.

Bunyakin A.V., Chernyshenko S.I., Stepanov G.Y. (1998) High-Reynolds-number Batchelor-model asymptotics of a flow past an aerofiol with a vortex trapped in a cavity. *J. Fluid Mech.* **358**: 283–297.

Burgers J.M. (1948) A mathematical model illustrating the theory of turbulence. *Adv. Appl. Mech.* **1**: 171–199.

Bushnell D.M., McGinley C.B. (1989) Turbulence control in wall flows. *Ann. Rev. Fluid Mech.* **21**: 1–20.

Butler K.M., Farrel B.F. (1992) Three-dimensional optimal perturbations in viscous shear flow. *Phys. Fluids*, A**4**: 1637–1650.

Caflisch R.E. (1989) Mathematical analysis of vortex dynamics. In: Caflisch R.E. (ed.) *Mathematical Aspects of Vortex Dynamics*, SIAM, Philadelphia, 1–24.

Cai J.S., Liu F., Luo S.J. (2003) Stability of symmetric vortices in two dimensions and over three-dimensional slender conical bodies. *J. Fluid Mech.* **480**: 65–94.

Cai J.S., Luo S.J., Liu F. (2004) Stability of symmetric and asymmetric vortex pairs over slender conical wings and bodies. *Phys. Fluids*, **16**: 424–432.

Callegari A.J., Ting L. (1978) Motion of a curved cortex filament with decaying vortical core and axial velocity. *SIAM J. Appl. Math.* **35**: 148–175.

Cantwell B.J., Coles D.E., Dimotakis P.E. (1978) Structure and entrainment in the plane of symmetry of a turbulent spot. *J.Fluid Mech.* **87**: 641.

Carnevale G.F., Briscolini M., Kloosterziel R.C., Vallis G.K. (1997) Three-dimensionally perturbed vortex tubes in a rotating flow. *J. Fluid Mech.* **341**: 127–163.

Carnevale G.F., Cavazza P., Purini R., Orlandi P. (1991b) An explanation for anomalous vortex merger in rotating tank experiments. *Phys. Fluids*, **3**: 1411–1415.

Carnevale G.F., Kloosterziel R.C. (1994) Emergence and evolution of triangular vortices. *J. Fluid Mech.* **259**: 305–331.

Carnevale G.F., Kloosterziel R.C., van Heijst G.J.F. (1991a) Propagation of barotropic vortices over topography in a rotating tank. *J. Fluid Mech.* **233**: 119–139.

Carnevale G.F., Vallis G.K. (1990) Pseudo-advective relaxation to stable states of inviscid two-dimensional fluids. *J. Fluid Mech.* **213**: 549–571.

Carnevale G.F., Vallis G.K., Purini R., Briscolini M. (1988) Propagation of barotropic modons over topography. *Geophys. Astrophys. Fluid Dyn.* **41**: 45–101.

Carton X.J., McWilliams J.C. (1989) Barotropic and baroclinic instabilities of axisymmetric vortices in a quasi-geostrophic model. In: Nihopul J.C., Jamart B.M. (eds.) *Mesoscale/Synoptic Coherent Structures in Geophysical Tuebulence*, Elsevier, Amsterdam, 225–244.

Case K.M. (1960) Stability of inviscid plane Couette flow. *Phys. Fluids*, **3**: 143–148.

Casey J., Naghdi P.M. (1991) On the lagrangian description of vorticity. *Arch. Rational Mech. Anal.* **115**: 1–14.

Caswell B. (1967) Kinematics and stress on a surface of rest. *Arch. Rat. Mech. Anal.* **26**: 385–399.

Chan J.C.L. (2005) The physics of tropical cyclone motion. *Ann. Rev. Fluid Mech.* **37**: 99–128.

Chan J.C.L., Ko F.M.F., Lei Y.M. (2002) Relationship between potential vorticity tendency and tropical cyclone motion. *J. Atmos. Sci.* **59**: 1317–1336.

Chandrasekhar S., Kendal P.C. (1957) On force-free magnatic fields. *Astrophys. J.* **26**: 457–460.

Chang C.C., Lei S.Y. (1996a) On the sources of aerodynamic forces: steady flow around a cylinder or a sphere. *Proc. R. Soc. London*, A**452**: 2369–2395.

Chang C.C., Lei S.Y. (1996b) An analysis of aerodynamic forces on a delta wing. *J. Fluid Mech.* **316**: 173–196.

Chang C.C., Su J.Y., Lei S.Y. (1998) On aerodynamic forces for viscous compressible flow. *Theort. Comput. Fluid Dyn.*, **10**: 71–90.

Chen J.Y. (1975) On the motion of gas bubble, liquid drop, and solid sphere in viscous fluid. *Sci. China*, **4**: 376–398 (in Chinese).

Chen J.Y. (1983) Slow viscous flow past a circular cylinder. *Proc. 2nd Asian Congr. Fluid Mech.* 723–731.

Chen J.Y. (1989) The slow viscous flow past an elliptic cylinder and a flat plate. *Proc. 4th Asian Congr. Fluid Mech.* Hong Kong, **1**: C15–C18.

Chen M.Z. (1986) *Turbulence and the Related Engineering Calculations*. Beijing Aeronautical Institute Press. In Chinese.

Chen Q.N., Chen S.Y., Eyink G.L. (2003) The joint cascade of energy and helicity in three-dimensional turbulence. *Phys. Fluids*, **15**: 361–374.

Chen Q.N., Chen S.Y., Eyink G.L., Holm D.D. (2005) Resonant interactions in rotating homogeneous three-dimensional turbulence. Submitted to *J. Fluid Mech.*

Chen S.Y., Ecke R.E., Eyink G.L., Wang X., Xiao Z.L. (2003) Physical mechanism of the two-dimensional enstrophy cascade. *Phys. Rev. Lett.* **91**(21):214501-1–214501-4.

Chernyshenko S.I. (1984) *Isv. Akad. Nauk SSSR, Mekh. Zhidk. Gaza* 2:40–45; English translation: *Fluid Dyn.* **19**(2): 206–210.

Chernyshenko S.I. (1988) The asymptotic form of the stationary separated flow around a body at high Reynolds numbers. *Prikl. Mat. Mekh.* **52**(6):958–966. Engl. transl. *J. Appl. Math. Mech.* **52**(6):746–753.

Chernyshenko S.I. (1998) Asymptotic theory of global separation. *ASME Appl. Mech. Rev.* **51**: 523–536.

Chester W. (1962) On Oseen's approximation. *J. Fluid Mech.* **13**: 557–569.

Chester W., Breach D.R. (1969) On the flow past a sphere at low Reynolds number. *J. Fluid Mech.* **37**: 751–760.

Childress S. (1970) New solutions of the kinematic dynamo problem. *J. Math. Phys.* **11**: 3063–3076.

Choi H., Moin P., Kim J. (1994) Active turbulence control for drag reduction in wall-bounded flows. *J. Fluid Mech.* **262**: 75.

Choi K.S. (1989) Near-wall structure of turbulent boundary layer with riblets. *J. Fluid Mech.* **208**: 417–458.

Chomaz J.M. (2005) Global instabilities in spatially developing flows: non-normality and nonlinearity. *Annu. Rev. Fluid Mech.* **37**: 357–392.

Chong M.S., Perry A.E., Cantwell B.J. (1990) A general classification of three-dimensional flow field. *Phys. Fluids*, A**2**: 765–777.

Chorin A.J. (1973) Numerical study of slightly viscous flow. *J. Fluid Mech.* **57**: 785–796.

Chorin A.J. (1982) Evolution of a turbulent vortex. *Commun. Math. Phys.* **83**: 517–535.

Chorin A.J. (1994) *Vorticity and Turbulence*. Springer, Berlin Heidelberg New York.

Chorin A.J., Marsdon J.E. (1992) *A Mathematical Introduction to Fluid Mechanics*. Springer-Verlag Berlin Heidelberg New York.

Christensen K.T., Adrian R.J. (2002) Measurement of instantaneous Eulerian acceleration fields by particle-image velocimetry: method and accuracy. *Exp. Fluids*, **33**: 759–769.

Clark R.W. (1976) Non-conical flow past slender wings with leading-edge vortex sheets. *ARC RM* 3814.

Cohen J., Wygnanski I. (1987a) The evolution of instabilities in the axisymmetric jet, Part 1, The linear growth of disturbances near the nozzle. *J.Fluid Mech.* **176**: 191–219.

Cohen J., Wygnanski I. (1987b) The evolution of instabilities in the axisymmetric jet. Part 2, The flow resulting from the interaction between two waves. *J.Fluid Mech.* **176**: 221–235.

Constantin P. (1994) Geometric statistics in turbulence. *SIAM Rev.* **36**: 73–98.

Cottet G.H., Koumoutsakos P. (2000) *Vortex Methods: Theory and Practice*. Cambridge University Press, Cambridge.

Couder Y., Basdevant C. (1986) Experimental and numerical study of vortex couple in two-dimensional flows. *J. Fluid Mech.* **173**: 225–251.

Cowley S.J., Van Dommenlen L.L., Lam S.T. (1990) On the use of lagrangian variables in descriptions of unsteady boundary-layer separation. *Phil. Trans. R. Soc. London*, A**333**: 343–378.

Crabtree L.F., Küchemann D., Sowerby L. (1963) Three-dimensional boundary layers. In Rosenhead L. (ed.), *Laminar Boundary layers*, Dover, Mineale New York 409–491.

Craik A.D.D. (1971) Nonlinear resonant instability in boundary layers. *J. Fluid Mech.* **50**: 393–413.

Craik A.D.D. (1985) *Wave interactions and fluid flows.* Cambridge University Press, Cambridge.

Craik A.D.D., Criminale W.O. (1986) Evolution of wavelike disturbances in shear flows: a class of exact solutions of the Navier-Stokes equations. *Proc. R. Soc. London*, A **406**: 13–26.

Crow S.C. (1970a) Aerodynamic sound emission as a singular perturbation problem. *Studies Appl. Math.* **49**: 21–44.

Crow S.C. (1970b) Stability theory for a pair of trailing vortices. *AIAA J.* **8**: 2172–2179.

Cucitore R., Quadrio M., Baron A. (1999) On the effectiveness and limitations of local criteria for the identification of a vortex. *Eur. J. Mech.* B**18**: 261–282.

Dahm W.J.A., Scheil C.M., Tryggvason T. (1989) Dynamics of vortex interaction with a density interface. *J. Fluid Mech.* **205**: 1–43.

Dallmann U. (1983) Topological structures of three-dimensional flow separation. *AIAA* 83–1935.

Dallmann U. (1984) Structural stability of three-dimensional vortex flows. In: Jordan H.L., Oertel H., Robert K. (eds.) *Nonlinear Dynamics of Transitional Flows*, Springer-Verlag, Berlin Heidelberg New York, 81–102.

Dallmann U. (1988) Three-dimensional vortex structure and vorticity topology. In: Hasimoto H., Kambe T. (eds.) *Vortex Motion*, North-Holland, 138–189.

Dang K.Q. (1986) The effect of viscosity upon an unsteady vortex. *M.S. Thesis Univ. Tenn. Space Inst.*

Danielsen E.F. (1967) Transport and diffusion of stratospheric radioactivity based on synoptic hemispheric analyses of potential vorticity. Dept. Met. Penn. State University, Report NYO-3317-3.

Danielsen E.F. (1968) Stratospheric-tropospheric exchange based on radioactivity, ozone and potential vorticity. *J. Atmos. Sci.* **25**: 502–518.

Darbyshire A.G., Mullin T. (1995) Transition to turbulence in constent-mass-flux pipe flow. *J.Fluid Mech.* **289**: 83–114.

Darmofal D.L. (1993) The role of vorticity dynamics in vortex breakdown. *AIAA* 93–3036.

Davidson P.A. (2001) *An Introduction to Magnetohydrodynamics*. Cambridge University Press, Cambridge.

Dean W.R. (1928) Fluid motion in a curved channel. *Proc. R. Soc. London*, A**121**: 402–420.

Deem G.S., Zabusky N.J. (1978) Vortex waves: stationary "V states" interactions, recurrence and breaking. *Phys. Rev. Lett.* **40**: 859–862.

Delbende I., Chomaz J.M., Huerre P. (1998) Absolute/convective instabilities in the Batchlor vortex: a numerical study of the linear impulse response, *J. Fluid Mech.* **355**: 229–254.

Délery J. (2001) Robert legendre and Henri Werlé: Toward the elucidation of three-dimensional separation. *Annu. Rev. Fluid Mech.* **33**: 129–154.

Dennis S.D.R., Chang G.Z. (1970) Numerical solutions for steady flow past a circular cylinder at Reynolds numbers up to 100. *J. Fluid Mech.* **42**: 471–489.

Despard R.A., Miller J.A. (1971) Separation in oscillating laminar boundary-layer flows. *J. Fluid Mech.* **47**: 21–31.

Dhanak M.R., Si C. (1999) On reduction of turbulent wall friction through spanwise oscillations. *J. Fluid Mech.* **383**: 175–195.

Dickinson R.E. (1978) Rossby waves — Long-period oscillations of oceans and atmospheres. *Ann. Rev. Fluid. Mech.* **10**: 159–195.

Didden N., Ho C.M. (1985) Unsteady separation in a boundary layer produced by an impinging jet. *J. Fluid Mech.* **160**: 235–256.

DiPrima R.C., Habetler G.J. (1969) A completeness theorem for non-selfadjoint eigenvalue problems in hydrodynamic stability. *Arch. Rat. Mech. and Anal.* **34**: 218–227.

Doak P.E. (1998) Fluctuating total enthalpy as the basic generalized acoustic field. *Theor. Comput. Fluid Dyn.* **10**: 115–133.

Doering C.R., Gibbon J.D. (1995) *Applied Analysis of the Navier-Stokes Equations*, Cambridge University Press, Cambridge.

Doligalski T.L., Smith C.R., Walker J.D.A. (1994) Vortex interactions with walls. *Annu. Rev. Fluid Mech.* **26**: 573–616.

Dombre T., Frisch U., Greene J.M., Hénon M., Mohr A., Soward A.M. (1986) Chaotic streamlines in the ABC flows. *J. Fluid Mech.* **167**: 353–391.

Dommermuth D.G. (1993) The laminar interaction of a pair of vortex tubes with a free surface. *J. Fluid Mech.* **246**: 91–115.

Dommermuth D.G., Mui R.C.Y. (1995) The vortical structure of a near-breaking gravity-capillary wave. *J. Fluid Eng.* **117**: 355–361.

Douady S., Couder Y., Brachet M.E. (1991) Direct observation of the intermittency of intense vortex filaments in turbulence. *Phys. Rev. Lett.* **67**: 983–986.

Draad A.A., Kuiken G., Nieuwstadt F.T.M. (1998) Laminar-turbulent transition in pipe flow for Neutonian and non-Newtonian fluids. *J.Fluid Mech.* **377**: 267–312.

Drazin P.G. (2002) *Introduction to Hydrodynamic Stability.* Cambridge University Press,Cambridge.

Drazin P.G., Reid W.H. (1981) *Hydrodynamic Stability.* Cambridge University Press,Cambridge.

Dritschel D.G. (1989) Contour dynamics and contour surgery: numerical algorithms for extended high-resolution modelling of vortex dynamics in two-dimensional, inviscid, incompressible flows. *Comput. Phys. Rep.* **10**: 79–146.

Du Y., Karniadakis G.E. (2000) Suppressing wall turbulence by means of a transverse traveling wave. *Science*, **288**: 1230–1234.

Du Y., Symeonidis V., Karniadakis G.E. (2002) Drag reduction in wall-bounded turbulence via a transverse traveling wave. *J. Fluid Mech.* **457**: 1–34.

Dubief Y., Delcayre F. (2000) On coherent-vortex identification in turbulence. *J. Turbulence*, **1**: 1–22.

Duck P.W., Foster M.R. (1980) The inviscid stability of a trailing line vortex. *J. Appl. Math. Phys.* (ZAMP), **31**: 524–532.

Durand W.F. (ed.) (1934–35) *Aerodynamic Theory.* 6 volumes. Dover,Mineola New York.

Dyer D.E., Fiddes S.P., Smith J.H.B. (1982) Asymmetric vortex formation from cones at incidence - a simple inviscid model. *Aero. Q.* **33**: 293–312.

Eaton J.K., Johnston J.P. (1981) Review of research on subsonic turbulent flow reattachment. *AIAA J.* **19**: 1093–1100.

Ellington C.P., Van den Berg C., Willmott A.P., Thomas A.L.R. (1996) Leading edge vortices in insect flight. *Nature*, **384**: 626–630.

Elliott J.W., Smith F.T., Cowley S.J. (1983) Breakdown of boundary layers: (i) on moving surfaces; (ii) in semi-similar unsteady flows; (iii) in fully unsteady flow. *Geophys. Astrophys. Fluid Dyn.* **25**: 77–138.

Eloy C., Le Dizès S. (1999) Three-dimensional instability of Burgers and Lamb-Oseen vortices in s strain field, *J. Fluid Mech.* **378**: 145–166.

Eloy C., Le Dizès S. (2001) Stability of the Rankine vortex in a multipolar strain field. *Phys. Fluids*, **13**(3): 660–676.

Emanuel K.A. (1984) A note on the instability of columnar vortices. *J. Fluid Mech.* **145**: 235–238.

Eraslan A.H. et al. (1983) *Oak Ridge Natl. Lab.* [*Rep.*] ORNL/TM 8401.

Ericsson L.E. (1992) Sources of high alpha vortex asymmetry at zero sideslip. *J. Aircraft*, **29**: 1086–1090.

Ertel H. (1942) Ein neuer hydrodynamischer Wirbelsatz. *Meteorol Z.* **59**: 271–281.

Escudier M. (1988) Vortex breakdown: observation and explanations. *Prog. Aerospace Sci.* **25**: 180–229.

Eskinazi S., Erian F.F. (1969) Energy reversal in turbulent flows. *Phys. Fluids*, **12**: 1988.

Fabre D., Cossu C., Jacqiun L. (2000a) Spatio-temporal development of the long and short -wave vortex-pair instabilities, *Phys. Fluids*, **12**(5): 1247–12350.

Fabre D., Cossu, C., Jacqiun L. (2000b) Absolute/convective instabilities and spatial growth in a vortex pair. In: Maurel A., Petitjeans P. (eds.) *Dynamics and Structures of Vortices*, Springer-Verlag, Berlin Heidelberg New York 162–172.

Falco R.E. (1983) New results, a review and synthesis of the mechanism of turbulence production in boundary layers and its modification. *AIAA* 83–0377.

Farrell B.F., Ioannou P.J. (1996) Generalized stability theory. Part I: Autonomous operators; Part II: Nonautonomous operators. *J. Atmos. Sci.* **53**: 2025–2040; 2041–2053.

Fey U., König M., Eckelmann H. (1998) A new Strouhal-Reynolds number relationship for the circular cylinder in the range $47 < Re < 2 \times 10^5$. *Phys. Fluids*, **10**: 1547–1549.

Fiddes S.P. (1980) A theory of separated flow past a slender elliptic cone at incidence. *AGARD CP*-291. Paper 30.

Fiddes S.P., Smith J.H.B. (1982) Calculations of asymmetric separated flow past circular cones at large angles of incidence. *AGARD CP*-336, Paper 14.

Fiedler H.E. (1988) Coherent structures in turbulent flows. *Prog. Aerospace Sci.* **25**: 231–269.

Fiedler H.E., Fernholz H.H. (1990) On management and control of turbulent shear flows. *Prog. Aerospace Sci.* **27**: 305–387.

Fine K.S., Driscoll C.F., Malmberg J.H., Mitchell T.B. (1991) Measurements of symmetric vortex merger. *Phys. Rev. Lett.* **67**, 588–591.

Fish S. (1989) Ambient free surface wave modification by a submerged vortex pair. *Ph.D. Thesis Univ. Maryland.*

Fjørtoft R. (1950) Application on integral theorems in deriving criteria of stability for laminar flows and for the baroclinic vortex. *Geofys. Publ. Oslo* **17(6)**: 1–52.

Fjørtoft R. (1953) On the changes in the spectral distribution of kinetic energy for twodimensional, nondivergent flow. *Tellus* **5**: 225–230.

Flierl G.R. (1987) Isolated eddy models in geophysics. *Ann. Rev. Fluid Mech.* **19**: 493–530.

Flierl G.R. (1988) On the instability of geostrophic vortices. *J. Fluid Mech.* **197**: 349–388.

Flierl G.R., Larivich V.D., McWillianms J.C., Reznik G.M. (1980) The dynamics of boroclinic and barotropic solitary eddies. *Dyn. Atmos.Oceans*, **5**: 1–41.

Flierl G.R., Stern M.E., Whitehead J.A. Jr. (1983) The physical significance of modons: laboratory experiments and general physical constraints. *Dyn. Atmos. Oceans*, **7**: 233–263.

Flor J.B. , Van Heijst G.J.F. (1996) Stable and unstable monopolar vortices in a straitified fluid. *J. Fluid Mech.* **311**: 257–287.

Fohl T., Turner J.S. (1975) Colliding vortex rings. *Phys. Fluids*, **18**: 433–36.

Föppl A. (1897) *Die Geometrie der Wirbelfeder*. Leipzig.

Föppl L. (1913) Wirbelbewegung hinter einem kreiszylinder. *Sitzb. d. k. baeyr. Akad. d. Wiss., Math-Physi. Klasse, Müchen* **1**: 1–17.

Ford R., McIntyre M.E., Norton W.A. (2000) Balance and the slow quasimanifold: Some explicit results. *J. Atmos. Sci.* **57**: 1236–1254.

Fornberg B. (1980) A numerical study of steady viscous flow past a circular cylinder. *J. Fluid Mech.* **98**: 819–855.

Fornberg B. (1985) Steady viscous flow past a circular cylinder up to Reynolds number 600. *J. Comput. Phys.* **61**: 297–320.

Fraenkel L.E. (1970) On steady vortex rings with small cross-section in an ideal fluid. *Proc. Roy. Soc. London*, A**316**: 29–62.

Fraenkel L.E. (1972) Examples of steady vortex rings of small cross-section in an ideal fluid. *J. Fluid Mech.* **51**: 119–135.

Fraenkel L.E., Burgers M.S. (1974) A global theory of steady vortex rings in an ideal fluid. *Acta Math.* **132**: 13–51.

Frisch U. (1995) *Turbulence*. Cambridge University Press,Cambridge.

Fukumoto Y. (1987) On integral invariants for vortex motion under th localized induction approximation. *J. Phys. Soc. Jpn.* **56**: 4207–4209.

Fukumoto Y. (2002) Higher-order asymptotic theory for the velocity field induced by an inviscid vortex ring. *Fluid Dyn. Res.* **30**: 65–92.

Fukumoto Y., Miyazaki M. (1986) N-solitons on a curved vortex filament. *J. Phys. Soc. Jp.* **55**: 4152–4155.

Fukumoto Y., Miyazaki M. (1991) Three-dimensional distortions of a vortex filamernt with axial velocity. *J. Fluid Mech.* **222**: 369–416.

Gad-el-Hak M. (1996) Modern developments in flow control. *Appl. Mech. Rev.* **49**: 365–379.

Gad-el-Hak M. (2000) *Flow Control*. Cambridge University Press, Cambridge.

Gad-el-Hak M., Blackwelder R.F. (1985) The discrete vortices from a delta wing. *AIAA J.* **23**: 961–962.

Gad-el-Hak M., Blackwelder R.F. (1986) Control of the discrete vortices from a delta wing. *AIAA* 86–1915.

Galdi G.P., Padula M. (1990) A new approach to energy theory in the stability of fluid motion. *Arch. Rat. Mech. Anal.* **110**: 187–286.

Gallaire F., Chomaz J.M. (2003a) Instability mechanisms in swirling flows. *Phys. Fluids*, **15**(9): 2622–2639.

Gallaire F., Chomaz J.M. (2003b) Mode selection in swirling jet experiments: a linear stability analysis. *J. Fluid Mech.* **494**: 223–253.

Gallaire F., Chomaz J.M. (2004) The role of boundary conditions in a simple model of incipient vortex breakdown. *Phys. Fluids*, **16**(2): 274–286.

Garg A.K., Leibovich S. (1979) Spectral characteristics of vortex breakdown. *Phys. Fluids*, **22**(11): 2053–2064.

Gaster M., Kit E., Wygnanski I. (1985) Large-scale structures in a forced turbulent mixing layer. *J.Fluid Mech.* **150**: 23–39.

Gerrard J.H. (1966) The mechanics of the formation region of vortices behind bluff bodies. *J. Fluid Mech.* **25**: 401–413.

Ghosh S., Leonard A., Wiggins S. (1998) Diffusion of a passive scalar from a no-slip boundary into a two-dimensional chaotic advection field. *J. Fluid Mech.* **372**: 119–163.

Giacomelli R., Pistolesi E. (1934) Historical sketch. In Durand W.F. (ed.), *Aerodynamic Theory*, **I**, Dover, Mineola New York 305–394.

Gill A.E. (1982a) *Atmosphere-Ocean Dynamics*. Academic Press, Inc. San Diego.

Gill A.E. (1982b) Studies of moisture effects in simple atmospheric models: the stable case. *Geophys. Astrophys. Fluid Dyn.* **19**: 119–152.

Glauert H. (1947) *The Elements of Aerofoil and Airscrew Theory*, second edition, Cambridge University Press, Cambridge.

Görtler H. (1940) Ueber eine driedimensionale instabilitat laminarer grenzshichten an konkaven wanden. *Math. Phys.* K1–K2.

Goldshtik M.A. (1960) A paradoxial solution of the Navier-Stokes equations. *Prik. Mat. Mekh.* **24**: 610–621.

Goldshtik M., Hussain F. (1997) The nature of inviscid vortex breakdown. *Phys. Fluids*, **9**: 263–265.

Goldshtik M., Hussain F. (1998) Analysis of inviscid vortex breakdown in a semi-infinite pipe. *Fluid Dyn. Res.* **23**: 189–234.

Goldshtik M.A., Shtern V.N. (1988) Conical flows of fluid with variable viscosity. *Proc. Roy. Soc.* A**419**: 61–106.

Goldstein S. (1929) The steady flow of viscous fluid past a fixed spherical obstacle at small Reynolds numbers. *Proc. R. Soc. A*, **123**: 225–235.

Goldstein S. (1938) *Modern Developments in Fluid Mechanics*. Vols. 1 & 2. Oxford University Press (Dover 1965).

Goldstein S. (1948) On laminar boundary-layer flow near a position of separation. *Q.J. Mech. Appl. Math.* **1**: 43–69.

Goldstein M.E., Hultgren L.S. (1988) Nonlinear spatial evolution of an externally excited instability wave in a free shear layer. *J. Fluid Mech.* **197**: 295–330.

Goldstein M.E., Hultgren L.S. (1989) Boundary-layer receptivity to long-wave free-stream disturbances. *Ann. Rev. Fluid Mech.* **21**: 137–166.

Golub G.H., van Loan C.F. (1996) *Matrix Computations*. The John Hopkins University Press, Baltimore, MD.

Gong H., Liu J., Jiang X.Q., Zhou M.D., She Z.S. (2004) Hierarchical structures in a turbulent free shear flow. Under consideration for publication in *J. Fluid Mech.*

Green R.B., Gerrard J.H. (1993) Vorticity measurements in the near wake of a circular cylinder at low Reynolds numbers. *J. Fluid Mech.* **246**: 675–691.

Green S.I. (ed.) (1995) *Fluid Vortices*, Kluwer, Dordrecht Nethulands.

Griffiths R.W., Hopfinger E.J. (1986) Experiments with Baroclinic vortex pairs in a rotating fluid. *J. Fluid Mech.* **173**: 501–518.

Griffiths R.W., Hopfinger E.J. (1987) Coalescing of geostrophic vortices. *J. Fluid Mech.* **178**: 73–97.

Guckenheimer J., Holmes P.J. (1983) *Nonlinear Oscillations, Dynamic Systems and Bifurcations of Vector Fields*. Springer-Verlag, Berlin Heidelberg New York.

Guiraud J.P., Zeytounian R.K. (1977) A double-scale investigation of the myptotic structure of rolled-up vortex sheets. *J. Fluid Mech.* **79**: 93–112.

Gustafson K.E., Sethian J.A. (1991) *Vortex Methods and Vortex Motion*. SIAM, Philadelphia.

Gustavsson L.H. (1991) Energy growth of three-dimensional disturbances in plane Poiseuille flow. *J. Fluid Mech.* **224**: 242–260.

Gutmark E.J., Grinstein F.F. (1999) Flow control with non-circular jets. *Annu. Rev. Fluid Mech.* **31**: 239–272.

Haken H. (1984) Self-organization in physics. In: Jordan H.L., Oertel H., Robert K.(eds.) *Nonlinear Dynamics of Transitional Flows*, Springer-Verlag, Berlin Heidelberg New York 37–50.

Hale J., Koçak H. (1991) *Dynamics and Bifurcations*, Springer-Verlag, Berlin Heidelberg New York.

Hall M.G. (1961) A theory for the core of a leading-edge vortex. *J. Fluid Mech.* **11**: 209–228.

Hall M.G. (1966) The structure of concentrated vortex cores. *Prog. Aeronaut. Sci.* **I**: 53–110.

Hall M.G. (1972) Vortex breakdown. *Ann. Rev. Fluid Mech.* **4**: 195–218.

Haller G. (2004) Exact theory of unsteady separation for two-dimensional flows. *J. Fluid Mech.* **512**: 257–311.

Hamilton J.M., Kim J., Waleffe F. (1995) Regeneration mechanisms of near-wall turbulence structures. *J.Fluid Mech.* **287**: 317–348.

Han G., Tumin A., Wygnanski I. (2000) Laminar-turbulent transition in Poiseuille pipe flow subjected to periodic perturbation emanating from the wall. Part 2. Late stage of transition. *J.Fluid Mech.* **419**: 1–27.

Harvey J.K., Perry F.J. (1971) Flowfield produced by trailing vortices in the vicinity of the ground. *AIAA J.* **9**: 1659–1660.

Hasimoto H. (1972) A solition on a vortex filament. *J. Fluid Mech.* **51**: 477.

Hasimoto H. (1985) Several aspects of the motion of vortex filaments. In: Tatsumi T., Takami H. (eds.) *Recent Studies on Turbulent Phenomena*, North Holland.

Hayes W.D. (1957) The vorticity jump across a gasdynamic discontinuity. *J. Fluid Mech.* **2**: 595–600.

Haynes P.H., McIntyre M.E. (1987) On the evolution of vorticity and potential vorticity in the presence of diabatic heating and frictional or other forces. *J. Atmos. Sci.* **44**: 828–841.

He K.R., Yang D.H., Wu J.Z. (1988) The extension of minimum energy dissipation theorem and limitation of minimum entropy production principle in fluid flow. *J. Engng. Thermophys.* **9**: 10–12 (in Chinese).

Head M.R., Bandyopahyay P. (1981) New aspects of turbulent boundary layer structure. *J. Fluid Mech.* **107**: 297.

van Heijst G.J.F., Kloosterziel R.C., Williams C.W.M. (1991) Laboratory experiments on the tripolar vortex in a rotating fluid. *J. Fluid Mech.* **225**: 301–331.

Helfrich K.R., Send U. (1988) Finite-amplitude evolution of two-layer geostrophic vortices. *J. Fluid Mech.* **197**: 331–348.

Helmholtz H. (1858) Über Integrale der hydrodynamischen Gleichungen, welche den Wirbelbewegungen ensprechen. *J. Reine Angew. Math.* **55**: 25–55. English translation: On intergal of the hydrodynamical equations which express vortex motion. *Phil. Mag.* (1867), **34**: 15–24.

Helmholtz H. (1868) Uber discontinuirliche Flüssigkeitsbewegungen Monatsber. *Klönig Akad Wiss B*, 215–228.

Henderson B.D., Barkley D. (1996) Secondary instability in the wake of a circular cylinder. *Phys. Fluids*, **8**: 1683–1685.

Henningson D.S., Reddy S.C. (1994) Rn the role of linear mechanism in transition to turbulence. *Phys. Fluids*, **6**(3):1396–1398.

Herbert T. (1975) On finite amplitudes of periodic disturbances of the boundary layer along a flat plate. In: Richtmyer R.D. (ed.) *Lecture Notes in Physics.* **5**.

Hill M.J.M. (1894) On a spherical vortex. *Phil. Trans. Roy. Soc.* A**185**: 213–245.

Hinze J.O. (1970) Turbulent flow regions with shear stress and mean velocity gradient of opposite sign. *Appl. Sci. Res.* 163.

Hinze J.O. (1975) *Turbulence*. McGraw-Hill, New York.

Hirota R. (1973) Exact envelope-solition solutions of a nonlinear wave equation. *J. Math. Phys.* **14**: 805–809.

Hirsa A., Lopez J.M., Kim S. (2000) Evolution of an initial columnar vortex terminating normal to a non-slip wall. *Exp. in Fluids*, **29**: 309–321.

Hirsch M.W., Smale S. (1974) *Differential Equations, Dynamic Systems, and Linear Algebra*. Academic Press, San Diego.

Ho C.M. (1982) In: Cebeci T. (ed.) *Numerical and Physical Aspects of Aerodynamic Flows*. Springer-Verlag, Berlin Heidelberg New York.

Ho C.M., Huang L.S. (1982) Subharmonics and vortex merging in mixing layers. *J. Fluid Mech.* **119**: 443–473.

Ho C.M., Huerre P. (1984) Perturbed free shear layers. *Ann. Rev. Fluid Mech.* **16**: 365–424.

Hogg N.G., Stommel M.M. (1985) The heton, an elementary interaction between discrete baroclinic geostrophic vortices and its implications concerning eddy heat flow. *Proc. R. Soc. London Ser.* A.**397**: 1–20.

Holm D.D. (1986) Lyapunov stability of ideal compressible and incompressible fluid equilibria in three dimensions. *Séminaire de Mathématiques Supérieures*. C.P. 6128, succ. A, Les Presses de L'Université de Montréal.

Hopfinger E.J., Browand F.K., Gagne Y. (1982) Turbulence and waves in a rotating tank. *J.Fluid Mech.* **125**: 505–534.

Hopfinger E.J., van Heijst G.I.F. (1993) Vortices in rotating fluids. *Ann. Rev. Fluid Mech.* **25**: 241–289.

Hornung H. (1989) Vorticity generation and transport. *Aust. Fluid Mech. Conf.* 10th, Melbourne.

Hornung H. (1990) Vorticity generation and transport. *AMS-SIAM Summer Seminar on Vortex Dynamics and Vortex Methods*, Seattle.

Hoskins B.J., McIntyer M.E., Robertson A.W. (1985) On the use and significance of isentropic potential vorticity maps. *Q. J.R. Met. Soc.* **111**: 877–946.

Hough S.S. (1897) On the application of harmonic analysis to the dynamic theory of the tide. Part I. On Laplace's 'oscillations of the first species', and on the dynamics of ocean currents. *Phil. Trans. R. Soc. London*, A **189**: 201–257.

Howard L.N. (1957) Divergence formulas involving vorticity. *Arch. Rational Mech. Anal.* **1**: 113–123.

Howard L.N., Gupta A.S. (1962) On the hydrodynamic and hydromagnetic stability of swirling flows. *J. Fluid Mech.* **14**: 463–476.

Howe M.S. (1975) Contribution to the theory of aerodynamic sound with application to excess jet noise and the theory of the flute. *J. Fluid Mech.* **71**: 625–673.

Howe M.S. (1989) On unsteady surface forces, and sound produced by the normal chopping of a rectilinear vortex. *J. Fluid Mech.* **206**: 131–153.

Howe M.S. (1991) On the estimation of the sound produced by complex fluid-structure interactions, with application to a vortex interacting with a shrouded rotor in a duct. *Proc. R. Soc. London*, A**433**: 573–598.

Howe M.S. (1995) On the force and moment exerted on a body in an incompressible fluid, with application to rigid bodies and bubbles at high and low Reynolds numbers. *Q.J. Mech. Appl. Math.* **48**: 401–426.

Howe M.S. (1998) *Acoustics of Fluid-Structure Interactions*. Cambridge University Press, Cambridge.

Howe M.S. (2003) *Theory of Vortex Sound*. Cambridge University Press, Cambridge.

Huang L.S., Ho C.M. (1990) Small-scale transition in a plane mixing layer. *J.Fluid Mech.* **210**: 475–500.

Huang M.K., Chow C.Y. (1996) Stability of leading-edge vortex pair on a slender delta wing. *AIAA J.* **34**: 1182–1187.

Huerre P., Monkewitz P.A. (1990) Local and global instabilities in spatially developing flows. *Ann. Rev. Fluid Mech.* **22**: 473–537.

Huerre P., Rossi M. (1998) Hydrodynamic instabilities in open flows. In: Godrè che C., Manneville P. (eds.) *Hydrodynamic and Nonlinear Instabilities*. Cambridge University Press, Cambridge. 81–294.

Hunt J.C.R. (1987) Vorticity and vortex dynamics in complex turbulent flows, *Transactions, CSME*, 1.

Hunt J.C.R., Abell C.J., Peterka J.A., Woo H. (1978) Kinematic studies of the flows around free or surface-mounted obstacles applying topology to flow visualization. *J. Fluid Mech.* **86**: 179–200.

Hunt J.C.R., Vassilicos J.C. (eds) (2000) *Turbulence Structure and Vortex Dynamics*. Cambridge University Press, Cambridge.

Hunt J.C.R., Wray A.A., Moin P. (1988) Eddies, stream, and convergence zones in turbulent flows. *Center for Turbulence Research Report* CTR-S88, 193.

Husain H.S., Hussain F. (1991) Elliptic jets. Part 2. Dynamics of coherent structures: pairing. *J. Fluid Mech.* **233**: 439–482.

Hussain A.K.M.F. (1983) Coherent structures - reality and myth. *Phys. Fluids*, **26**: 2816–2850.

Hussain F. (1992) Understanding turbulence via vortex dynamics. In: Gatski T.B., Sarkar S., Speziale C.G.(eds.) *Studies in Turbulence*. Springer-Verlag, Berlin Heidilberg New York, 157–178.

Hussain F. (2002) Vortex dynamics and coherent structures in turbulent flows. Fluid dynamics award lecture in 1st AIAA Flow Control Conference, St. Louis, Missouri, June 24–26.

Hussain F., Husain H.S. (1989) Elliptic jets. Part I. Characteristics of unexcited and excited jets. *J. Fluid Mech.* **208**: 257–320.

Itoh N. (1974) Spatial growth of finite wave disturbances in parallel and nonparallel flows. *Trans. Jpn. Soc. Aero. Space Sci.* **17**: 160–174.

Itoh N. (1980) Three-dimensional growth of finite wave disturbances in plane Poiseuille flow. *Trans Jpn Soc. Aero. Space Sci.* **23**: 91–103.

Jacobson S.A., Reynolds W.C. (1998) Active control of streamwise vortices and streaks in boundary layers. *J.Fluid Mech.* **360**: 179–211.

Jenson V.G. (1959) Viscous flow around a sphere at low Reynolds number (<40). *Proc. Roy. Soc. Lond.* A**249**: 346–366.

Jeong J., Hussain F. (1995) On the identification of a vortex. *J. Fluid Mech.* **285**: 69–94.

Jeong J., Hussain F., Schoppa W., Kim J. (1997) Coherent structures near the wall in a turbulent channel flow. *J.Fluid Mech.* **332**: 185–214.

Jiménez J. (1988) Linear stability of a non-stmmetric, inviscid Karman vortex street of small uniform vortices. *J. Fluid Mech.* **189**: 337–348.

Jiménez J., Moffatt H.K., Vasco C. (1996) The structure of the vorices in freely decaying two-dimensional turbulence. *J. Fluid Mech.* **313**: 209–222.

Jiménez J., Moin P. (1991) The minimal flow unit in near-wall turbulence. *J. Fluid Mech.* **225**: 213–240.

Jiménez J., Pinelli A. (1997) Wall turbulence: How it works and how to damp it. *AIAA* 97–2112.

Jiménez J., Pinelli A. (1999) The autonomous cycle of near-wall turbulence. *J. Fluid Mech.* **389**: 335.

Joseph D.D. (1976) *Stability of Fluid Motion*. Springer-Verlag, Berlin, Heidelberg New York.

Joukowski N.E. (1931) *Aérodynamique*. Gauthier-Villars, Paries.

Jung W.J., Mangiavacchi N., Akhavan R. (1992) Suppression of turbulence in wall-bounded flows by high frequency spanwise oscillations. *Phys. Fluids*, A**4**: 1605–1607.

Kachanov Y.S. (1994) Physical mechanisms of laminar-boundary-layer transition. *Annu. Rev. Fluid Mech.* **26**: 411–482.

Kachanov Y.S. (2002) On a universal essentially nonlinear mechanism of turbulence production in wall shear flows. *International Conference in Commemoration of Professor P.Y. Chou's 100th Anniversary*, Peking University, Beijing.

Kaden H. (1931) Aufwicklung einer unstabilen unstetigkeitsflache. *Ing. Arch.* **2**: 140–168.

Kambe T. (1984) Axisymmetric vortex solution of Navier-stokes equation. *J. Phys. Soc. Jpn.* **53**: 13–15.

Kambe T. (2003) Gauge principle and variational formulation for flows of an ideal fluid. *Acta Mech. Sinica*, **19**: 437–452.

Kambe T. (2004) *Geometrical Theory of Dynamical Systems and Fluid Flows*. World Scientific, Singapore.

Kambe, T., Minota, T., Takaoka, M. (1993) Oblique collision of two vortex rings and its acoustic emission. *Phys. Rev.* E **48**, 1866–1881.

Kaneda Y. (1990a) A representation of the motion of a vortex sheet in a three-dimensional flow. *Phys. Fluids*, A**2**: 458–461.

Kaneda Y. (1990b) On the three-dimensional motion of an infinitely thin vortex sheet in an ideal fluid. *Phys. Fluids*, A**2**: 1817–1826.

Kaplun S. (1957) Low Reynolds number flow past a circular cylinder. *J. Math. Mech.* **6**: 595–603.

Kármán Th. von. (1911,1912) Uber den mechanismus den Widrstands, den ein bewegter Korper in einer Flussigkeit erfahrt. *Göttingen Nachr. Math. Phys. Kl.* **12**: 509–546, **13**: 547–556.

Kármán Th. von. (1954) On the foundation of high speed aerodynamics. In: Sears W.R. (ed.), *General Theory of High Speed Aerodynamics*, Princeton University Press, Princeton, NJ.

Kármán Th. von., Burgers J.M. (1935) General aerodynamic theory - perfect fluids. In: Durand W.F. (ed.) *Aerodynamic Theory*, **II**, Dover, Mineola New York.

Karniadakis G.E., Choi K.S. (2003) Mechanisms on transverse motions in turbulent wall flows. *Ann. Rev. Fluid Mech.* **35**: 45–62.

Karniadakis G.E., Triantafyllou G.S. (1989) Frequency selection and asympototic states in laminar wakes. *J. Fluid Mech.* **199**: 441–469.

Katz Y., Nishri B., Wygnanski I. (1989) The delay of turbulent boundary layer separation by oscillatory active control. *AIAA* 89–1027.

Keller J.J. (1996) A pair of stream functions for three-dimensional vortex flows. *Z. Angew Math. Phys.* **47**: 821–836.

Keller J.J. (1998) Inverse Euler equations. *Z. Angew Math. Phys.* **49**: 363–383.

Keller J.J. (1999) Inverse equations. *Phys. Fluids.* **11**: 513–520.

Keller J.J., Egli W., Exley J. (1985) Force- and loss-free transitions between flow states. *Z. Angew. Math. Phys.* **36**: 864–889.

Kellogg O.D. (1929) *Foundations of potential Theory.* Dover, Mineola New York.

Kelvin Lord (1867) The traslatory velocity of a circular vortex ring. *Phil. Mag.* **33**: 511–512.

Kelvin Lord (1869) On vortex motion. *Trans. R. Soc. Edinb.* **25**: 217–260.

Kelvin Lord (1871) Hydrokinetic solutions and observations. *Phil. Mag.*, **42**(4): 362–377.

Kelvin Lord (1887) Stability of steady and of periodic fluid motion. *Phil. Mag.* **23**(5): 529–539.

Kerswell R.R. (2002) Elliptical Instability. *Annu. Rev. Fluid Mech.* **34**: 83–113.

Khorrami M.R. (1991) On the viscous modes of instability of a trailing line vortex. *J. Fluid Mech.* **225**: 197–212.

Kida S. (1981a) Motion of an elliptic vortex in a uniform shear flow. *J. Phys. Soc. Jpn.* **50**: 3517–3520.

Kida S. (1981b) A vortex filament moving without change of form. *J. Fluid Mech.* **112**: 394–409.

Kida S., Miura H. (1998) Identification and analysis of vortical structures. *Eur. J. Mech.* B**17**: 471–488.

Kida S., Takaoka M. (1991a) Vortex reconnection. *Kokyuroku RIMS Kyoto U.* **769**: 200–208 (in Japanese).

Kida S., Takaoka M. (1991b) Breakdown of frozen motion and vorticity reconnection. *J. Phys. Soc. Jpn.* **60**: 2184–2196.

Kida S., Takaoka M. (1994) Vortex reconnection. *Ann. Rev. Fluid Mech.* **26**: 169–189.

Kilic M.S., Haller G., Neishtadt A. (2005) Unsteady fluid separation by the method of averaging. *Phys. Fluids*, **17**, in press.

Kim G., Wang C.M., Wu J.C. (1996) Computation of flow over wings using integral-differential formulation. *AIAA* 96–1960.

Kim J. (1989) On the structure of pressure fluctuations in simulated turbulent channel flow. *J.Fluid Mech.* **205**: 421–451.

Kim J. (2003) Control of turbulent boundary layers. *Phys. Fluids*, **15**: 1093–1105.

Kim J., Lim J. (2000) A linear process in wall-bounded turbulent shear flows. *Phys. Fluids*, **12**(8): 1885–1888.

Kim J., Moin P., Moser R. (1987) Turbulence statistics in fully developed channel flow at low Reynolds number. *J.Fluid Mech.* **177**: 133.

Kirchhoff G. (1869) Zur Theorie freier-Flüssigkeitsstrahlen. *J. Reine Angrew Math. Bd.* **70**(H4): 289–298.

Klebanoff P.S., Tidstrom K.D., Sargent L.M. (1962) The three-dimensional nature of boundary-layer instability. *J. Fluid Mech.* **12**: 1–34.

Klein R., Knio O. (1995) Asymptotic vorticity structure and numerical simulation of slender vortex filaments. *J. Fluid Mech.* **284**: 275–321.

Klein R., Knio O., Ting L. (1996) Representation of core dynamics in slender vortex filament simulations. *Phys. Fluids*, **8**: 2415–2425.

Klein R., Majda A. (1991a) Self-stretching of a perturbed vortex filament. I. The asymptotic equations for deviations from a straight line. *Physica D*, **49**: 323–352.

Klein R., Majda A. (1991b) Self-stretching of perturbed vortex filaments. II. Structure of solutions. *Physica D*, **53**: 267–294.

Klein R., Majda A. (1993) An asymptotic theory for the nonlinear instability of anti-parallel pairs of vortex filaments. *Phys. Fluids*, A**5**: 369–387.

Klein R., Majda A., McLaughlin R.M. (1992) Asymptotic equations for the stretching of vortex filaments in a background flow field, *Phys. Fluids*, A**4**: 2271–2281.

Klein R., Ting L. (1992) Vortex filament with axial core structure variation. *Appl. Math. Lett.* **5**: 99–103.

Klein R., Ting L. (1995) Theoretical and experimental studies of slender vortex filaments. *Appl. Math. Lett.* **8**: 45–50.

Kleinschmidt E. (1950a) Über Aufbau und Entstehung von Zyklonen(1. Teil). *Met. Runds.* **3**: 1–6.

Kleinschmidt E. (1950b) Über Aufbau und Entstehung von Zyklonen(2. Teil). *Met. Runds.* **3**: 54–61.

Kleinschmidt E. (1951) Über Aufbau und Entstehung von Zyklonen(3. Teil). *Met. Runds.* **4**: 89–96.

Kleinschmidt E. (1955) Die Entstehung einer Höhenzyklone über Nordamerika. *Tellus*, **7**: 96–110.

Kleinschmidt E. (1957) In: Eliassen A., Kleinschmidt E. (eds.) *Dynamic meteorology Handbuck der Physik*, **48**: 112–129.

Kline S.J., Reynolds W.C., Schraub F.A., Runstadler P.W. (1967) The structure of turbulent boundary layers. *J. Fluid Mech.* **30**: 741–773.

Kline S.J., Robinson S.K. (1989) Turbulent boundary layer structure: Progress, status and challenges. *Proceedings of the 2nd IUTAM Symposium on Structure of Turbulence and Drag Reduction*, Zurich, Switzerland.

Kloosterziel R.C., Carnevale G.F. (1999) On the evolution and saturation of instabilities of two-dimensional isolated circular vortices. *J. Fluid Mech.* **388**: 217–257.

Kloosterziel R.C., Carnevale G.F. (2004) Formal stability of circular vortices.

Kloosterziel R.C., van Heijst G.J.F. (1991) An experimental study of unstable barotropic vortices in a rotating fluid. *J. Fluid Mech.* **223**: 1–24.

Kloosterziel R.C., van Heijst G.J.F. (1992) The evolution of stable barotropic vortices in a rotating free-surface fluid. *J. Fluid Mech.* **239**: 607–629.

Knio O., Ghoniem A. (1990) Numerical study of a three-dimensional vortex method. *J. Comput. Phys.* **86**: 75.

Koch W. (1985) Local instability characterestic and frequency determination of self-excited wake flows. *J. Sound Vib.* **99**: 53–83.

Kochin N.E., Kibel I.A., Roze N.V. (1964) *Theoretical Hydrodynamics*. Wiley, New York.

Kolár V. (2003) On the Lyman problem. *Central Euro. J. Phys.* **2**: 258–267.

Kolmogorov A.N. (1941) The local structure of turbulence in incompressible viacous fluid for very large Reynolds number. *C.R. Acad. Sci. URSS*, **30**: 301–305. (Reprinted in *Proc. R. Soc. London*, Ser. **A434**: 9–13.) (1991).

Kolmogorov A.N. (1962) A refinement of previous hypothesis concerning the local structure in a viscous incompressible fluid at high Reynolds number. *J. Fluid Mech.* **13**: 82–85.

Konrad H. (1976) Photo 176: Large-scale structure in a turbulent mixing layer. In: Van Dyke M. (ed.) *An Album of Fluid Motion*. 1982. Parabolic.

Korolev G.L. (1980) Numerical solution of the asymptotic problem of laminar boundary-layer separation from a smooth surface. *Uch. Zap. Tsagi*, **11**(2): 27–36.

Koromilas C.A., Telionis D.P. (1980) Unsteady laminar separation, an experimental study. *J. Fluid Mech.* **97**: 347–384.

Koshigoe S., Gutmark E., Schadow K. (1989) Initial development of noncircular jets leading to axis switching. *AIAA J.* **27**: 411.

Koumoutsakos P., Leonard A. (1995) High-resolution simulations of the flow around an impulsively started cylinder using vortex method. *J. Fluid Mech.* **296**: 1–38.

Koumoutsakos P., Leonard A., Pépin F. (1994) Boundary conditions for viscous vortex methods. *J. Comput. Phys.* **113**: 52–61.

Kraichnan R.H. (1967) Inertial ranges in two-dimensional turbulence, *Phys. Fluids*, **9**: 1937–1943.

Kraichnan R.H., Montgomery D. (1980) Two-dimensional turbulence. *Rep. Progr. Phys.* **43**: 547–619.

Krasny R. (1987) Computation of vortex sheet roll-up in the Trefftz plane. *J. Fluid Mech.* **184**: 123–155.

Kravchenko A.G., Choi H., Moin P. (1993) On the generation of near-wall streamwise vortices to wall skin friction in turbulent boundary layers. *Phys. Fluids*, A**5**: 3307–3309.

Kreplin H.P., Vollmers H., Meier H.U. (1980) Experimental determination of wall shear stress vectors on an inclined prolate spheroid. *DFVLR IB* 251 80 A 08.

Kroo I. (2001) Drag due to lift: Concepts for prediction and reduction. *Ann. Rev. Fluid Mech.* **33**: 587–617.

Küchemann D. (1965) Report on the IUTAM Symposium on concentrated vortex motion in fluids. *J. Fluid Mech.* **21**: 1.

Küchemann D. (1978) *Aircraft Aerodynamic Design*. Pergamon, New York.

Kurzweil Y., Livne E., Meerson B. (2002) Generation of vorticity and turbulent cooling of "hot channels" in gases. *Phys. Fluids*, **14**: 1030–1041.

La Porta A., Voth G.A., Crawford A.M., Alexander J., Bodenschatz E. (2001) Fluid particle accelerations in fully developed turbulence. *Nature*, **409**: 1017–1019.

Lagerstrom P.A. (1964) *Laminar Flow Theory*. Princeton University Press, Princeton, NJ.

Lagerstrom P.A. (1977) Solutions of the Navier-Stokes equation at large Reynolds number. In Rom J. (ed.) *Proc. Int. Symp. Modern Dev. Fluid Dyn.* SIAM.

Lamb G.L. (1980) *Elements of Soliton Theory*. Wiley, New York.

Lamb H. (1911) On the uniform motion of a sphere through a viscous fluid. *Philos. Mag.* **21**(6): 112–121.

Lamb H. (1932) *Hydrodynamics*. Cambridge University Press, Cambridge.

Lanczos C. (1970) *The Variational Principles of Mechanics*, Fourth edition, Dover, Mincola New York.

Landahl M.T. (1975) Wave breakdown and turbulence. SIAM *J. Appl. Math.* **28**: 735–756.

Landau L.D., Lifshitz E.M. (1944) *Mechanics of Continuous Media*. Gostekhizdat, Moscow. See also: Landau L.D., Lifshitz E.M. (1959) *Fluid Mechanics*. Pergamon, New York.

Landau L.D., Lifshitz E.M. (1976). *Mechanics*, Third edition. Pergamon, New York.

Landau L.D., Lifshitz E.M. (1987) *Fluid Mechanics* Second edition. Pergamon, New York.

Larichev V., Reznik G. (1976) Two-dimensional Rossby soliton, an exact solution. *Rep. U.S.S.R. Acad. Sci.* **231**: 1077–1079.

Lasheras J.C., Cho J.S., Maxworthy T. (1986) On the origin and scale of streamwise vortical structures in a plane, free shear layer. *J. Fluid Mech.* **172**: 231–258.

Lee C.B. (2000) Possible universal transitinal scenario in a transitional boundary layer. *Phys. Rev. E.* **62**: 3659–3670.

Lee C.B., Chen S.Y. (2006) Dynamics of transitional boundary layers. To be published in: Gad-el-Hak M.(ed.) *Transition and Tubulence Control*. World Scientific, 39–85.

Lee C.B., Fu S. (2001) On the formation of the chain of ring-like vortices in a transitional boundary layer. *Exp. Fluids*, **30**: 354–357.

Lee C.B., Lee R. (2001) On the dynamics in a transitional boundary layer. *Commun. Nonlinear Sci. Numer. Simul.* **6**: 111–171.

Legendre R. (1955) Décollement laminiare régulier. *C. R.* **241**: 732–734.

Legendre R. (1956) Séparation de l'écoulement laminaire tridimensionnel. *La Rech. Aéronaut.* **30**: 3–8.

Leibovich S. (1978) The structure of vortex breakdown. *Ann Rev. Fluid Mech.* **10**: 221–246.

Leibovich S. (1983) Vortex stability and breakdown: survey and extension. *AIAA J.* **22**(1): 1192–1206.

Leibovich S., Brown S.N., Patel Y. (1986) Bending waves on inviscid columnar vortices. *J. Fluid Mech.* **173**: 595–624.

Leibovich S., Kribus A. (1990) Large-amplitude wavetrains and solitary waves in vortices. *J. Fluid Mech.* **216**: 499–504.

Leibovich S., Ma H.Y. (1983) Solition propagation on vortex cores and Hasimoto solion. *Phys. Fluids*, **26**: 3173–3179.

Leibovich S., Randall J.D. (1972) Amplification and decay of long nonlinear waves. *J. Fluid Mech.* **53**: 481–493.

Leibovich S., Stewartson K. (1983) A sufficient condition for the instability of columnar vortices. *J. Fluid Mech.* **126**: 335–356.

Leith C.E. (1968) Diffusion approximation for two-dimensional turbulence. *Phys. Fluids*, **11**: 671–673.

Leonard A. (1985) Computing three-dimensional incompressible flow with vortex elements. *Ann. Rev. Fluid Mech.* **17**: 523–559.

Lesieur M. (1990) *Turbulence in Fluids*. Kluwer, Dordrecht Netherlands.

Lesieur M., Begou P., Briand E., Danet A., Delcayre F., Aider J.L. (2003) Coherent-vortex dynamics in large-eddy simulations of turbulence. *J. Turbulence*, **4**: 1–24.

Lesieur M., Comte P., Metais O. (2000) LES and vortex topology in shear and rotating flows. In: Hunt J.C.R., Vassilicos J.C.(eds.) *Turbulence Structure and Vortex Dynamics*. Cambridge University Press, Cambridge, 269–288.

Lesson M., Koh P.H. (1985) Instability and turbulent bursting in the boundary layer. In: Kozlov V.V. (ed.) *Laminar-Turbulent Transition*, Springer-Verlag, Berlin Heidelberg New York, 39–52.

Lessen M., Singh P.J., Paillet F. (1974) The stability of a trailing line vortex. Part I. inviscid theory. *J. Fluid Mech.* **63**: 753–763.

Leweke T., Williamson C.H.K. (1998) Cooprerative elliptic instability of a vortex pair. *J. Fluid Mech.* **360**: 85–119.

Leweke T., Williamson C.H.K. (2000) Three-dimensional instabilities of a counterrotating vortex pair. In: Maurei A., Petitjeans P.(eds.) *Dynamics and Structure of Vortices*, Springe-Verlg, Berlin Heidelberg New York, 221–230.

Lewellen W.S. (1993) Tornado vortex theory. In: C. Church et al. (eds.) *The tornado: Its structure, Dynamics, Prediction, and Hazards*, Amer. Geophys. Union, 19–40.

Lewellen W.S., Lewellen D.C. (1997) Large-eddy simulation of tornado's interaction with the surface. *J. Atmos. Sci.* **54**: 581–605.

Li Q.S., Guo M. (2005) The diagnosis and design of a low-speed compressor based on local dynamics. *Adv. Nat. Sci.* **15**: 221–228 (in Chinese).

Liao S.J. (1997) A kind of approaximate solution technique which does not depend upon small parameter: an application in fluid mechanics. *Int. J. Non-linear Mech.* **32**: 815–824.

Liao S.J. (1999a) An explicit, totally analytic approximate solution for Blasius' viscous flow problems. *Int. J. Non-linear Mech.* **34**: 759–778.

Liao S.J. (1999b) An uniformly valid analytic solution of 2D viscous flow past a semi-infinite flat plate. *J. Fluid Mech.* **385**: 101–128.

Liao S.J. (2002) An analytical approximation of the drag coefficient for the viscous flow past a sphere. *Int. J. Non-linear Mech.* **37**: 1–18.

Liepmann H.W., Roshko A. (1957) *Elements of Gas Dynamics*. Wiley, New York.

Lighthill M.J. (1956) *Nature*. **178**: 343.

Lighthill M.J. (1957) Dynamics of a dissociating gas. Part I: equilibrium flow. *J. Fluid Mech.* **2**: 1–32.

Lighthill M.J. (1963) Introduction of boundary layer theory. In: Rosenhead L.(ed.) *Laminar Boundary Layers*, Oxford University Press, New York. 46–113.

Lighthill M.J. (1986a) Fundamentals concerning wave loading on offshore structures. *J. Fluid Mech.* **173**: 667–681.

Lighthill M.J. (1986b) *An Informal Introduction to Theoretical Fluid Mechanics*. Clarendon Press, Oxford.

Lilley G.M. (1983) Vortices and turbulence. *Aeronautical J.* **87**: 371–393.

Lim T.T., Nickels T.B. (1995) Vortex rings. In: Green S.I. (ed.), *Fluid Vortices*, Kluwer, Derdrecht Netherlands.

Lin C.C. (1957) Motion in the boundary layer with a rapidly oscillating external flow. *Proc. 9th Int. Congr. Appl. Mech.* Brussels, 4, 155–167.

Lin J.C., Rockwell D. (1995) Evolution of a quasi-steady breaking wave. *J. Fluid Mech.* **302**: 29–43.

Lin S.J., Corcos G.M. (1984) The mixing layer: deterministic models of a turbulent flow. Part 3, the effect of plain strain on the dynamics of streamwise vortices. *J. Fluid Mech.* **141**: 139–178.

Liu C.S., Lee C.H. (1982) On the solution of the Prandtl boundary layer equations containing the point of zero skin friction. *Arch. Rat. Mech. Anal.* **79**: 291–304.

Liu C.S., Wan Y.H. (1985) A simple exact solution of the Prandtl boundary layer equations containing a point of separation. *Arch. Rat. Mech. Anal.* **89**: 177–185.

Liu X., Katz J. (2004) Measurements of pressure distribution in a cavity flow by integrating the meterial acceleration. HT-FED2004–56373, 2004 SAME Heat Transfer/Fluids Engineering Summer Conference, NC, USA, July 11–15, 2004.

Loiseleux T., Chomaz J.M., Huerre P. (1998) The effects of swirl on jets and wakes: linear instability of Rankine vortex with axial flow. *Phys. Fluids*, **10**(5): 1120–1134.

Long R.R. (1958) Vortex motion in a viscous fluid. *J. Meteorol.* **15**(1): 108–112.

Long R.R. (1961) A vortex in an infinite viscous fluid. *J. Fluid Mech.* **11**: 611.

Longuet-Higgins M.S. (1953) Mass transport in water waves. *Philos. Trans. R. Soc. London.* A**245**: 535–581.

Longuet-Higgins M.S. (1998) Vorticity and curvature at free surface. *J. Fluid Mech.* **356**: 149–153.

Lu S.S., Willmarth W.W. (1973) Measurements of the structure of the Reynolds stress in a turbulent boundary layer. *J. Fluid Mech.* **60**: 481–511.

Lu X.Y. (2002) Numerical study of the flow behind a rotary oscillating circular cylinder. *Int. J. Comput. Fluid Dyn.* **16**: 65–82.

Lucca-Negro O., Doherty T.O. (2001) Vortex breakdown: a review. *Prog. Energy Combustion Science*, **27**: 431–481.

Ludwieg H. (1960) Stabilitat der Stroemung in einen zylindrischen ringraum. *Z. Flugwiss.* **8**: 135–140.

Ludwieg H. (1962) Zur erklarung der instalitat der uber angestallen delta-flugeln auftretenden freien wirbelkerne. *Z. Flugwiss.* **10**: 242–249.

Ludwieg H. (1965) Erklarung des wirbelaufplatzens mit Hilfe der Stabilitat-sthoric fur stromungenmit schranbenlinienformigen Stromlinien. *Z. Flugwiss.* **13**: 437–442.

Lugt H.J. (1979) The dilemma of defining a vortex. In: Müller U., Roesner K.G., Schmidt B. (eds.) *Recent Developments in Theoretical and Experimental Fluid Mechanics*, Springer-Verlag, Berlin Heidelberg New York 309–321.

Lugt H.J. (1983) *Vortex Flow in Nature and Technology.* Wiley-Interscience.

Lugt H.J. (1996) *Introduction to Vortex Theory.* Vortex Flow Press, Potomac, Maryland.

Lugt H.J., Ohring S. (1992) The oblique ascent of a viscous vortex pair toward a free surface. *J. Fluid Mech.* **36**: 461–476.

Lundgren T.S. (1982) Strained spiral vortex model for turbulent fine structure. *Phys. Fluids*, **25**: 2193–2203.

Lundgren T.S. (1989) A free vortex method with weak viscous effects. In: Caflisch R.E. (ed.), *Mathematic Aspects of Vortex Dynamics*, SIAM, Philadelphia, 68–79.

Lundgren T.S., Koumoutsakos P. (1999) On the generation of vorticity at a free surface. *J. Fluid Mech.* **382**: 351–366.

Luo Y.B. (2004) Boundary vorticity dynamics, derivative moment theory, and their applications in flow diaguosis and control. M.S. thesis, Peking University, Beijing, China (in Chinese).

Luo Z.X., Chen L.S. (1995) Effect of orography of Taiwan Island on typhoon tracks. *Chinese J. Atmos. Sci.* **19**: 390–396.

Ma H.Y. (1984) Spatial stability analysis of swirling flows. *Applied Math. and Mech.*, **5**(2): 239–249. (In Chinese)

Ma H.Y., Jin X. (1991) The roll-up of leading-edge detached vortex and trailing-edge vortex and their interaction. *Acta Aerodyn.* **9**(3): 294–299. (in Chinese).

MacKay R.S., Meiss J.D. (1987) *Hamiltonian Dynamical Systems*, Adam Hilgar, Bristol.

Maekawa H., Mansour N., Buell J. (1992) Instability mode interactions in a spatially developing plane wake. *J. Fluid Mech.* **235**: 223–254.

Majda A.J. (1986) Vorticity and the mathematical theory of incompressible fluid flow. *Comm. Pure Appl. Math.* **39**: 187–220.

Majda A.J., Bertozzi A.L. (2002) *Vorticity and Incompressible Flow.* Cambridge University Press, Cambridge.

Makihara T., Kida S., Miura H. (2002) *J. Phys. Soc. Jpn.* **71**: 1622–1625.

Marchioro C., Pulivirenti M. (1984) Vortex methods in two-dimensional fluid dynamics. *Lecture Notes Phys.* **203**.

Maxworthy T. (1965) Accurate measurements of sphere drag at low Reynolds numbers. *J. Fluid Mech.* **23**: 369–372.

Maxworthy T. (1972) The structure and stability of vortex rings. *J. Fluid Mech.* **64**: 227–259.

Maxworthy T. (1977) Some experimental studies of vortex rings. *J. Fluid Mech.* **81**: 465–495.

Maxiworthy T. (1982) The laboratory modelling of atmospheric vortices: a critical review. In Bengtsson L., Lighthill J. (eds.) *Intense Atmospheric Vortices*, Springer-Verlag, Berlin Heidelberg New York 229–246.

Maxworthy T., Hopfinger E.J., Redekopp L.G. (1985) Wave motion on vortex cores. *J. Fluid Mech.* **151**: 141–165.

Maxworthy T., Mory M., Hopfinger E.J. (1983) Waves on vortex cores and thire relation to vortex breakdown. *AGARD*, CP-342.

Mayer E.W., Powell K.G. (1992) Viscous and inciscid instabilities of a trailing vortex. *J. Fluid Mech.* **245**: 91–114.

McIntyre M.E., Norton W.A. (1990) Dissipative wave-mean interactions and the transport of vorticity or potential vorticity. *J. Fluid Mech.* **212**: 403–435.

McIntyre M.E., Norton W.A. (2000) Potential vorticity inversion on a hemisphere. *J. Atmos. Sci.* **57**: 1236–1254.

McWilliams J.C. (1984) The emergence of isolated coherent vortices in turbulent flow. *J. Fluid Mech.* **146**: 21–43.

McWilliams J.C. (2005) *Fondamentals of Geophysical Fluid Dynamics*, Cambridge University Press, Cambridge.

McWilliams J.C., Flierl G.R. (1979) On the evolution of isolated, nonlinear vortices. *J. Phys. Oceanogr.* **9**: 1155–1182.

McWilliams J.C., Gent P.R. (1980) Intermediate models of planetary circulations in the atmosphere and ocean. *J. Atmos. Sci.* **37**: 1657–1678.

Meiron D.I., Saffamn P.G., Schatzman J.C. (1984) The linear two-dimensional stability of inviscid vortex streets of finite-cored vortices. *J. Fluid Mech.* **147**: 187–212.

Melander M.V., Hussain F. (1993a) Polarized vorticity dynamics on a vortex column. *Phys. Fluids*, A**5**(8): 1992–2003.

Melander M.V., Hussain F. (1993b) Coupling between a coherent structure and fine- scale turbulence. *Phys. Rev.* E, **48**(4): 2669–2689.

Melander M.V., Hussain F. (1994) Core dynamics on a vortex column. *Fluid Dyn. Res.*, **13**: 1–37.

Melander M.V., Hussain F., Basu A. (1991) Breakdown of a circular jet into turbulence. In: *Proceedings of the 8th Symposium on Turbulent Shear Flows*, Munich. 15.5.1–15.5.6.

Melander M.V., McWilliams J.C., Zabusky N.J. (1987) Axisymmetrization and vorticity gradient intensification of an isolated two-dimensional vortex through filamentation. *J. Fluid Mech.* **178**: 137–159.

Melander M.V., Zabusky N.J., McWilliams J.C. (1988) Symmetric vortex merger in two dimensions: causes and conditions. *J. Fluid Mech.* **195**: 303–340.

Meleshko V.V., van Heijst G.J.F. (1994) On Chaplykin's investigations of two-dimensional vortex structures in an inviscid fluid. *J. Fluid Mech.* **272**: 157–182.

Mezić I., Haller G. (1998) Reduction of three-dimensional, volume-preserving flows with symmetry. *Nonlinearity*, **11** 319–339.

Mied R.P., Lindemann G.J. (1979) The propagation and evolution of cyclonic Gulf Stream rings. *J. Phys. Oceanogr.* **9**: 1183–1206.

Milne-Thomson L.M. (1968) *Theoretical Hydrodynamics*, Dover, Mineola New York.

Mitchell A.M., Délery J. (2001) Research into vortex breakdown control. *Prog. Aerospace Sci.* **37**: 385–418.

Miyazaki T., Hunt J.C.R. (2000) Linear and nonlinear interactions between a columnar vortex and external turbulence. *J. Fluid Mech.* **402**: 349.

Moffatt H.K. (1969) The degree of knottedness of tangled vortex lines. *J. Fluid Mech.* **35**: 117–129.

Moffatt H.K., Kida S., Ohkitani K. (1994) Stretched vortices - the sinews of turbulence; large-Reynolds-number asymptotics. *J. Fluid Mech.* **259**: 241–264.

Möhring W. (1978) On vortex sound at low Mach numbers. *J. Fluid Mech.* **85**: 685–691.

Monkewitz P.A. (1988a) The absolute and convective nature of instability in two-dimensopnal wakes at low Reynolds numbers. *Phys. Fluids*, **31**: 999–1006.

Monkewitz P.A. (1988b) A note on vortex shedding from axisymmetric bluff bodies. *J. Fluid Mech.* **192**: 561–575.

Monkewitz P.A., Huerre P. (1982) The influence of velocity ratio on the spatial instability of mixing layers. *Phys. Fluids*, **25**: 1137.

Monkewitz P.A., Nguyen L.N. (1987) Absolute instability in the near wake of two-dimensiolnal bluff bodies. *J. Fluid Struct.* **1**: 165–184.

Moore D.W., Saffman P.G. (1971) Structure of a line vortex in an imposed strain. In: Olsen J.H., Goldburg A., Rogers M. (eds.) *Aircraft Wake Turbulence and its Detection*, Plenum, 339–354.

Moore D.W., Saffman P.G. (1972) The motion of a vortex filament with axial flow. *Phil. Trans. Roy. Soc.*, A**272**: 403–429.

Moore D.W., Saffman P.G. (1973) Axial flow in laminar trailing vortices. *Proc. R. Soc. London*, **A333**: 491–508.

Moore D.W., Saffman P.G. (1975) The instability of a straight vortex filament in a strained field. *Proc. R. Soc. London*, A**346**: 413–425.

Moore D.W., Saffman P.G., Tanveer S. (1988) The calculation of some Batchelor flows: The Sadovskii vortex and rotational corner flow. *Phys. Fluids*, **31**: 978–990.

Moore F.K. (1958) On the separation of the unsteady laminar boundary layer. In: Gortler H. (ed.) *Boundary Layer Research*, Springer-Verlag, Berlin Heidelberg New York 296–310.

Morkovin M.V. (1993) Bypass-transition research: issues and philosophy, In: Ashpis D.E., Gatski T.B., Hirsh R. (eds.) *Instabilities and Turbulence in Engineering Flows*, Kluwer, Derdrecht Netherlands 3–30.

Morkovin M.V., Reshotko E. (1990) Dialogue on progress and issues in stability and transition research. In: Arnal D., Michel R.(eds.) *Laminar-Turbulent Transition*, IUTAM Symposium, 1989 Toulouse, Springer, France, 3–29.

Morris P.J., Giridharan M.G., Lilley G.M. (1990) On the turbulent mixing of compressible free shear layers. *Proc. R. Soc. London*, A**431**: 219–243.

Morse P.M., Feshbach H. (1953) *Methods of Theoretical Physics*. McGrall-Hill New York.

Moses H.E. (1971) Eigenfunctions of the curl operator, rotationally invariant Helmholtz theorem, and application to electrodynamic theory and fluid mechanics. *SIAM J. Appl. Math.* **21**: 114–144.

Mu M. (2000) Nonlinear singular vectors and nonlinear singular values. *Sci. China*, **43**(4):375–385.

Müller E.A., Obermeier F. (1988) Vortex sound. In: Hasomoto H., Kambe T. (eds.) *Vortex Motion*, North-Holland, 43–51.

Nakagawa H., Nezu I. (1981) Structure of space-time correlations of bursting phenomena in an open-channel flow. *J. Fluid Mech.* **104**: 1–43.

Neiland V.Y. (1969) Theory of boundary-layer separation in supersonic flow. *Mekh. Zhid. Gaza*, **3**: 19–25. English translation: *Fluid Dyn.* **6**(3): 378–384.

Neu J.C. (1984a) The dynamics of a columnar vortex in an imposed strain. *Phys. Fluids*, **27**: 2397–2402.

Neu J.C. (1984b) The dynamics of stretched vortices. *J. Fluid Mech.* **143**, 253–276.

Neufville A.D. (1957) The decaying vortex. *Proc. 5th Northwestern Conf. Fluid Mech.* The University of Michigan Press, 365–375.

Newell A.C. (1985) Solitons in Mathematics and Physics. *CBMS-NSF Reg. Conf. Ser. in Appl. Math.* **48**. Society for Industrial and Applied Math., Philadelphia.

Newton P.K. (2001) *The N-Vortex Problem*. Springer-Verlag, Berlin Heidelberg New York.

Nielsen J.N. (1960) *Missile Aerodynamics*. McGraw-Hill, Inc, New York.

Nishioka M., Asai M. (1985) Some observations of the subcritical transition in plane Poiseuille flow. *J. Fluid Mech.* **150**: 441–450.

Nitsche M., Krasny R. (1994) A numerical study of vortex ring formation at the edge of a circular tube. *J. Fluid Mech.* **276**: 139–161.

Noack B.R. (1999) On the flow around a circular cylinder. Part I: laminar and transitional regime; Part II: turbulent regime. *Z. Angew. Math. Mech.* **79**: S223–S226; S227–S230.

Noble B., Daniel J.W. (1988) *Applied Linear Algebra*. Prentice Hall, NJ.

Noca F., Shields D., Jeon D. (1999) A comparison of methods for evaluating time-dependent fluid dynamic forces on bodies, using only velocity fields and their derivatives. *J. Fluids Structures*, **13**: 551–578.

Nolan D.S., Farrell B.F. (1999a) Generalized stability analyses of asymmetric disturbances in one- and two-celled vortices maintained by radial inflow. *J. Atoms. Sci.* **56**: 1282–1307.

Nolan D.S., Farrell B.F. (1999b) The structure and dynamics of tornado-like vortices. *J. Atmos. Sci.* **56**: 2908–2936.

Nolan D.S., Farrell B.F. (1999c) The intensification of two-dimensional swirling flows by stochastic asymmetric forcing. *J. Atmos. Sci.* **56**: 3937–3962.

Nolan D.S., Montgomery M.T. (2000) The algebraic growth of wavenumber one disturbances in hurricane-like vortices. *J. Atmos. Sci.* **57**: 3514.

Norberg C. (1994) An experimental investigation of the flow around a circular cylinder: influence of aspect ratio. *J. Fluid Mech.* **258**: 287–316.

Norbury J. (1973) A family of steady vortex rings. *J. Fluid Mech.* **57**: 417–431.

Novikov E.A. (1975) Dynamics and statistics of a system of vortices. *Soviet Phys.* JETP. **41**(5): 937–943.

Nuijten J., Velasco Fuentes O.U. (1994) Merging of cyclonic vortices in a rotating fluid. In: van Heijst G.J.F. (ed.) *Modelling of Oceanic Vortices*, North-Holland, 187–195.

Obukhov A.M. (1964) Adiabatic invariants of atmosphere processes. *Meteorogiya i gidrologiya*, **2**: 3–9.

Ohkitani K. (1990) Nonlocality in a forced two-dimensional turbulence. *Phys. Fluids*, A**2**: 1529–1531.

Ohring S., Lugt H.J. (1991) Interaction of a viscous vortex pair with a free surface. *J. Fluid Mech.* **227**: 47–70.

Oleddraru C., Sellier A. (2002) Viscous effects in the absolute-convective instability of the Batchelor vortex. *J. Fluid Mech.* **459**: 371–396.

Olendraru C., Sellior A., Rossi M., Huerre P. (1999) Inviscid instability of the Batchelor vortex: absolute-convective transition and spatial branches. *Phys. Fluids* **11(7)**: 1805–1820.

Olendraru C., Sellier A., Rossi M., Huerre P. (1996) Absolute/convective instability of the Batchelor vortex. *C. R. Acad. Sci. Paris*, **IIb**: 153–159.

Olsen J.H. (1971) Results of trailing vortex studies in lowing tank. In: Olsen J.H., Goldburg A., Rogers M. (eds.) *Aircraft Wake Turbulence and Its Detection*, Prenum, New York.

Orlandi P. (1990) Vortex dipole rebound fom a wall. *Phys. Fluids*, **A2**: 1429–36.

Orlandi P., Jiménez J. (1994) On the generation of wall friction. *Phys. Fluids*, **6**: 634–641.

Orszag S.A., Patera A.T. (1983) Secondary instability of wall-bounded shear flows. *J. Fluid Mech.* **128**: 347–385.

Oseen C.W. (1910) Ueber die Stokes'sche Formel, und ber eine verwandte Aufgabe in der Hydrodynamik. *Ark. Math. Astronom. Fys.* **6**: 29.

Oseen C.W. (1912) *Hydromechanik*. Ark. F. Math. Astrom. Och. Fys. **7**: 82.

Oshima Y., Asaka S. (1977) Interaction of two vortex rings along parallel axes in air. *J. Phys. Soc. Jpn*, **42**: 708–713.

Oshima Y., Izutsu N. (1988) Cross-linking of two vortex rings. *Phys. Fluids*, **31**: 2401.

Oster D., Wygnanski I. (1982) The forced mixing layer between parallel streams. *J. Fluid Mech.* **123**: 91.

Oswatitsch K. (1957) Die Ablösungsbedingung von Grenzschichten. *IUTAM Symposium on Boundary Layer Research*. Freiburg.

Oswatitsch K. (1959) Physikalishe Grundlagen der Strömungslehre. In: Flügge S. (ed.) *Handbuch der Physik*, **VIII/1**, Springer-Verlag, Berlin Heidelberg New York 1–124.

Overman E.A., Zabusky N.J. (1982) Evolution and merger of isolated vortex structures. *Phys. Fluids*, **25**: 1297–1305.

Padhye N., Morrison P.J. (1996) Fluid element relabeling symmetry. *Phys. Lett.* A**219**: 287–292.

Padula M. (1988) Energy instability methods: An application to Burgers equation. In: Galdi G.P., Straughan B. (eds.) *Proceeding of Meeting Energy Stability and Convection*, Pitman Research Notes in Mathematics, **168**.

Pagan D., Solignac J.L. (1986) Etude expérimentale deléclatement dun tourbillon engendré par une aile delta, *La Recherche Aérospatiale* (196–3),197–219. (French and English editions).

Panton R.L. (1968) The transient for Stokes' oscillating plate: a solution in terms of tabulated function. *J. Fluid Mech.* **31**: 819–825.

Panton R.L. (1984) *Incompressible Flow*. Wiley, New York.

Peace A.J., Riley N. (1983) A viscous vortex pair in ground effect. *J. Fluid Mech.* **129**: 409–426.

Peckham D.H., Atkison S.A. (1957) Preliminary results of low speed wind tunnel test on a gothic wing of aspect ratio 1.0. *ARC*, CP 508.

Pedlosky J. (1985) Instability of heton clouds. *J. Atmos. Sci.* 42:1477–1486.

Pedlosky J. (1987) *Geophysical Fluid Dynamics*. Springer-Verlag, Berlin Heidelber New York.

Peridier V.J., Smith F.T., Walker J.D.A. (1991) Vortex-induced boundary-layer separation. Part I. The limit problem Re $\rightarrow \infty$. *J. Fluid Mech.* **232**: 99–131.

Perry A.E., Chong M.S. (1986) A series expansion study of the Navier-Stokes equations with applications to three-dimensional separation patterns. *J. Fluid Mech.* **173** 207–223.

Perry A.E., Chong M.S., Lim T.T. (1982) The vortex-shedding process behind two-dimensional bluff bodies. *J. Fluid Mech.* **116**: 77–90.

Phillips H.B. (1933) *Vector Analysis*, Wiley, New York.

Picone J.M., Boris J.P. (1983) Vorticity generation by asymmetric energy deposition in a gaseous medium. *Phys. Fluids*, **26**: 365–382.

Picone J.M., Boris J.P., Greig J.R., Raleigh M.R., Fernsler R.F. (1981) Convective cooling of lightning channels. *J. Atmos. Sci.* **38**: 2056–2062.

Pierrehumbert R.T., Widnall S.E. (1981) Thestructure of organized vortices in a free shear layer. *J. Fluid Mech.* **102**: 301–313.

Plaschko P. (1979) Helical instability of slowly divergent jets. *J.Fluid Mech.* **92**: 209.

Platzman G.W. (1968) The Rossby wave. *Q.J. R. Meteorol. Sci.* **94**: 225–246.

Poincaré H. (1882) Les points singuliers des équations différentielles. *C.R. Acad. Sci. Paries*, **94**: 416–418.

Powell A. (1961) *Vortex Sound* (Rept. No. 61–70), Department of Engineering, University of California, Los Angeles.

Powell A. (1964) Theory of vortex sound. *J. Acoust. Soc. Am.* **36**: 177–195.

Powell A. (1994) Vortex sound theory: direct proof of the equivalence of "vortex force" and "vorticity-alone" formulations. *J. Acoust. Soc. Am.* **97**: 1534–1537.

Powell, A. (1995) Why do vortices generate sound? *J. Fluid Eng.* **117**: 252–260.

Pozrikidis C. (2000) Theoretical and computational aspects of the self-induced motion of three-dimensional vortex sheets. *J. Fluid Mech.* **425**: 335–366.

Pradeep D., Hussain F. (2000) Core dynamics of a coherent structure: a prototypical physical-space cascade mechanism. In: Hunt J.C.R., Vassilicos J.C. (eds.) *Turbulence Structure and Vortex Dynamics*. Cambridge University Press, Cambridge, 51–82.

Prandtl L. (1904) Über Flüssigkeitsbewegung bei sehr kleiner Reibung. *Proc. III Int. Math. Congr.* Heidelberg.

Prandtl L. (1905) Über Flüssigkeitsbewegung beu sehr kleiner Reibung. Vehr dIII Intern Math-Kongr, Heidelberg, 1904, Leipzig, Teubner, 484–491.

Prandtl L., Tietjens O.G. (1934) *Applied Hydro- and Aeromechanics*. Springer-Verlag, Berlin Heidelberg New York.

Praturi A.K., Brodkey R.S. (1978) A stereoscopic visual study of coherent structures in turbulent shear flow. *J.Fluid Mech.* **89**: 251–272.

Pridmore-Brown D.C. (1958) Sound propagation in a fluid flowing through an attenuating duct. *J. Fluid Mech.* **4**: 393–406.

Prigogine I. (1980) *From being to becoming*, Freeman, San fransixo, CA.

Prochazka A., Pullin D.I. (1998) Structure and stability of non-symmetric Burgers vortices. *J. Fluid Mech.* **363**: 199–228.

Proudman J. (1916) On the motion of solids in a liquid possessing vorticity, *Proc. R. Soc.* A**92**: 408–423.

Proudman I., Pearson J.R.A. (1957) Expansions at small Reynolds numbers for the flow past a sphere and a circular cylinder. *J. Fluid Mech.* **2**: 237–262.

Pruppacher H.R., Steinberger E.H. (1968) An experimental determination of the drag on a sphere at low Reynolds numbers. *J. Appl. Phys.* **39**: 4129–4132.

Pullin D.I. (1992) Contour dynamics methods. *Annu. Rev. Fluid Mech.* **24**: 89–115.

Quartapelle L., Napolitano M. (1983) Force and moment in incompressible flows. *AIAA J.* **21**: 911–913.

Randall J.D., Leibovich S. (1973) The critical state: a trapped wave model of vortex breakdown. *J. Fluid Mech.* **53**: 495–515.

Rayleigh L. (1880) On the stability or instability of certain fluid motions. *Proc. London Math. Soc.* **11**: 57–70.

Rayleigh L. (1916) On the dynamics of revoling fluids. *Prod. R. Soc. London*, A**93**: 148–154. 1

Reddy S.C., Schmid P.J., Henningson D.S. (1993) Pseudospectra of the orr-sommerfeld operator. *SIAM J. Appl. Math.* **53**(1):15–47.

Reed R.J., Sanders F. (1953) An investigation of the development of a mid-tropospheric frontal zone and its associated vorticity field. *J. Met.* **10**: 338–349.

Reshotko E. (1994) Boundary layer instability, transition and control. *AIAA* 94–0001.

Reuter J., Rempfer D. (1999) A hybrid spectral/finite-difference scheme for the simulastion of pipe-flow transition. In: Fasel H., Saric W. (eds.) *Laminar-Trubulent Transition*, IUTAM Symposium, 1999 Sedona, Springer, Berlin Heidelberg New York.

Reznik G.M. (1992) Dynamics of singular vortices on the beta-plane. *J. Fluid Mech.* **240**: 405–432.

Rhines P.B. (1979) Geostrophic turbulence. *Ann. Rev. Fluid Mech.* **11**: 401–441.

Ricca R.L. (1992) Physical interpretation of certain invariants for vortex filament motion under LIA. *Phys. Fluids*, A**4**: 938–944.

Ricca R.L., Berger M.A. (1996) Topological ideas and fluid mechanics. *Phys. Today* **49**(12) 28–34.

Richardson L.F. (1922) *Weather Prediction by Numerical Process*, Cambridge University Press, Cambridge.

Riley J.J., Metcalfe R.W. (1980) Direct numerical simulation of a perturbed turbulent mixing layer. *AIAA* 80–0274.

Rist U., Fasel H. (1995) Direct numerical simulation of controlled transition in a flat-plate boundary layer. *J.Fluid Mech.* **298**: 211–248.

Rist U., Kachanov Y.S. (1995) Numerical and experimental investigation of the K-regime of boundary-layer transition. In: Koboyashi R. (ed.) *Laminar-Turbulent Transition*, IUTAM Symposium, 1994 Sendai, Springer, Japan.

Rivera M.K., Vorobieff P., Ecke R.E. (1998) *Phys. Rev. Lett.* **81**: 1417.

Robinson S.K. (1991a) The kinematics of turbulent boundary layer structure. *NASA Tech. Mem.* 103859.

Robinson S.K. (1991b) Coherent motions in the turbulent boundary layer. *Annu. Rev. Fluid Mech.* **23**: 601–639.

Rockwell D. (1998) Vortex-body interactions. *Annu Rev. Fluid Mech.* **30**: 199–229.

Rosenhead L. (1931) The formation of vortices from a surface of discontinuity. *Proc. R. Soc.* A**134**: 170–192.

Rosenhead L. (1963) *Laminar Boundary Layer*. Dover, Mineole, New York.

Roshko A. (1954a) On the development of turbulent wakes from vortex streets. *NACA TN* 1191.

Roshko A. (1954b) On the drag and shedding frequency of two-dimensional bluff bodies. *NACA TN* 3169.

Roshko A. (1955) On the wake and drag of bluff bodies. *J. Aeronaut. Sci.* **22**: 124.

Roshko A. (1961) Experiments on the flow past a circular cylinder at very high Reynolds numbers. *J. Fluid Mech.* **10**: 345–356.

Roshko A. (1993) Perspectives on bluff body aerodynamics. *J. Wind Ind. Aerodyn.* **49**: 70–100.

Roshko A. (2000) On the problem of turbulence. *Curr. Sci.*. **79**(6):834–839.

Rossby C.G. (1936) Dynamics of steady ocean currents in the light of experimental fluid mechanics. *MIT & Woods Hole Oceanogr. Inst. Papers in Phys. Oceanogr. Met.* **5**(1): 1–43.

Rossby C.G. (1940) Planetary flow patterns in the atmosphere. *Q.J. R. Meteorol. Soc.* **66**, Suppl. 68–97.

Rossby C.G. (1948) On displacements and intensity changes of atmospheric vortices. *J. Mar. Res.* **7**: 175–187.

Rossi, M. (2000) Of vortices and vortical layers: An overview. In: Maurel A., Petitjeans P. (eds.) *Dynamics and Structure of Vortices*, Springer-Verlag, Berlin Heidelberg New York 40–123.

Rott N. (1956) Unsteady viscous flow in the vicinity of a stagnation point. *Q. Appl. Math.* **13**: 444–451.

Rott N. (1958) On the viscous core of a line vortex. *ZAMP* **9**: 543–553.

Rouchon P. (1991) On the Arnold stability criterion for steady-state flows of an ideal fluid. *Eur. J. Mech.* B/Fluids, **10**(6): 651–661.

Ruith M.R., Chen P., Meiburg E., Maxworth T. (2003) Three-diemnsional vortex breakdown in swirling jets and wakes: direct numerical simulation. *J. Fluid Mech.* **486**: 331–378.

Rusak Z., Wang S., Whiting C.H. (1998) The evolution of a vortex in a pipe to axisymmetric vortex breakdown. *J. Fluid Mech.* **366**: 211–237.

Sadovskii V.S. (1971) Vortex regions in a potential stream with a jump of Bernoulli constant at the boundary. *Prikl. Matem. Mekh.* **35**: 773–779; English translation: *Appl. Math. Mech.* **35**: 729–735.

Sadun L., Vishik M. (1993) The spectrum of the second variation of the energy for an ideal incompressible fluid. *Phys. Lett.* A**182**: 394–398.

Saffman P.G. (1970) The velocity of viscous vortex rings. *Stud. Appl. Math.* **49**: 371–380.

Saffman P.G. (1972) The motion of a vortex pair in a stratified atmosphere. *Stud. Appl. Math.* **51**: 107–119.

Saffman P.G. (1979) The approach of a vortex pair to a plane surface in invicid fluid. *J. Fluid Mech.* **92**: 497–503

Saffman P.G. (1981) Dynamics of vorticity. *J. Fluid Mech.* **106**: 49–58.

Saffman P.G. (1991) Approach of a vortex pair to a rigid free surface in viscous fluid. *Phys. Fluids*, A**3**(5): 984–985.

Saffman P.G. (1992) *Vortex Dynamics*. Canbridge University Press, Cambridge.

Saffman P.G., Baker G.R. (1979) Vortex interactions. *Ann. Rev. Fluid Mech.* **11**: 95–122.

Saffman P.G., Szeto R. (1981) Structure of a linear array of uniform vortices. *Stud. App. Math.* **65**: 223–248.

Saffman P.G., Tanveer S. (1984) Prandtl-Batchelor flow past a flat plate with a forward-facing flap. *J. Fluid Mech.* **143**: 351–365.

Sakajo T. (2001) Numerical computation of a three-dimensional vortex sheet in a swirl flow. *Fluid Dyn. Res.* **28**: 423–448.

Salmon R. (1988) Hamiltonian fluid mechanics. *Ann. Rev. Fluid Mech.* **20**: 225–256.

Salmon R. (1998) *Lecture on Geophysical Fluid Dynamics*. Oxford University Press, New York.

Saric W.S. (1994) Görtler vortices. *Annu. Rev. Fluid Mech.* **26**: 379–409.

Saric W.S., Benmalek A. (1991) Görtler vortices with periodic curvature. In: *Boundary Layer Stability and Transition to Turbulence*, ASME-FED **114**: 37–42.

Saric W.S., Nayfeh A.H. (1975) Nonparallel stability of boundary layer flows. *Phys. Fluids* **18**: 945–950.

Saric W.S., Thomas A.S.W. (1983) Experiments on the subharmonic route to turbulence in boundarys. In: *Proc. IUTAM Symp. on Turbulence and Chaotic Phenomena in Fluids*, Kyoto, Japan.

Sarpkaya T. (1971) On stationary and travelling vortex breakdown. *J. Fluid Mech.* **45**: 545–559.

Sarpkaya T. (1983) Trailing vortices in homogeneous and density stratified media. *J. Fluid Mech.* **136**: 85–109.

Sarpkaya T. (1992) Brief reviews of some time-dependent flows. *J. Fluid Eng.* **114**: 283–298.

Sarpkaya T. (1995) Turbulent vortex breakdown. *Phys. Fluids*, **7**: 2301–2303.

Sarpkaya T. (1996) Vorticity, free-surface, and surfactant. *Annu. Rev. Fluid Mech.* **28**: 83–128.

Sarpkaya T., Suthon P. (1991) Interaction of a vortex couple with a free surface. *Exp. Fluids* **11**: 205–217.

Schatzle P.R. (1987) An experimental study of fusion of vortex rings. *PhD. Thesis. Calif. Inst. Technol.*

Schewe G. (1983) On the force fluctuations acting on a circular cylinder in crossflow from subcritical up to transcritical Reynolds numbers. *J. Fluid Mech.* **133**: 265–285.

Schlichting H. (1978) *Boundary Layer Theory.* McGraw-Hill, New York.

Schmid P.J., Henningson D.S. (2001) *Stability and Transition in Shear Flows.* Springer-Verlag, Berlin Heidelberg New York.

Schmid P.J., Henningson D.S., Khorranmi M.R., Malik M.R. (1993) A study of eigenvalue sensitivity for hydrodynamic stability operators. *Theor. Comput. Fluid Dyn.* **4**: 227–240.

Schoppa W., Hussain F. (2002) Coherent structure generation in near-wall turbulence. *J. Fluid Mech.* **453**: 57–108.

Sears W.R. (1956) Some recent development in airfoil theory. *J. Aero. Sci.* **23**: 490–499.

Sears W.R., Telionis D.P. (1975) Boundary-layer separation in unsteady flow. *SIAM J. Appl. Math.* **28**: 215–235.

Seifert A., Bachar T., Koss D., Shepshelovich M., Wygnanski I. (1993) Oscillatory blowing: A tool to delay boundary-layer separation, *AIAA J.* **31**: 2052–2060.

Seifert A., Pack L.G. (1999) Oscillatory excitation of unsteady compressible flows over airfoils at high Reynolds number. *AIAA* 99–0925.

Serrin J. (1959) Mathematical principles of classic fluid dynamics. In: Flügge S. (ed.) *Handbuch der Physik* **VIII/1**, Springer-Verlag, Berlin Heidelberg New York 125–263.

Serrin J. (1972) The swirling vortex. *Phil. Trans. Roy. Soc.* A**271**: 325.

Serrin J. (ed.) (1986) *New Prospective in Thermodynamics.* Springer-Verlag, Berlin Heidelberg New York.

Shankar P.N. (1971) On acoustic refraction by duct shear layers. *J. Fluid Mech.* **47**: 81–91.

Shariff K., Leonard A. (1992) Vortex rings. *Annu. Rev. Fluid Mech.* **24**: 235–279.

She Z.S. (1997) Hierarchical structures and scaling in turbulence. In: Boratav O., Eden A., Erzan A. (eds.) *Turbulence Modeling and Votex Dynamics.* Lecture Notes in Physics, **491**: 28–51. Springer, Berlin Heidelberg New York.

She Z.S. (1998) Universal laws of cascade of turbulent fluctuations. *Prog. Theor. Phys. Supp.* **130**: 87–102.

She Z.S., Jackson E., Orszag S.A. (1990) Intermittent vortex structures in homogeneous isotropic turbulence. *Nature*, **344**: 226–228.

She Z.S., Leveque E. (1994) Universal scaling laws in fully developed turbulence. *Phys. Rev. Lett.* **72**: 336–339.

Shell M.J., Meiron D.I., Orszag S.A. (1993) Dynamical aspects of vortex reconnection of perturbed anti-parallel vortex tubes. *J. Fluid Mech.* **246**: 613–652.

Shen S.F. (1978) Unsteady separation according to boundary-layer equation. *Adv. Appl. Mech.* **18**: 177–220.

Shercliff J.A. (1965) *A Textbook of Magnetohydrodynamics.* Pergamon, New York.

Shi Z., Wu J.M., Wu J.Z. (1991) Symmetric and asymmetric jets in a uniform crossflow. *AIAA* 91–0722.

Shur M., Spalart P.R., Strelets M., Travin A. (1998) Detached-eddy simulation of an airfoil at high angle of attack. In: *4th Int. Symp. Engineering Turbulence Modeling and Measurements*, Corsica, France, May 24–26.

Siggia E.D. (1985) Collapse and amplification of a vortex filament. *Phys. Fluids*, **28**: 794–805.

Sipp D., Jacquin L. (1998) Elliptic instability in two-dimensional flatted Taylor-Green vortices. *Phys. Fluids*, **10**(4): 839–849.

Slezkin N.A. (1934) On the motion of viscous fluid between two cones. *Res. Rep.* Moscow State University, USSR, **2**: 89–90. (In Russian).

Smith A.C. (1973) On the stability of Föppl vortices. *J. Appl. Mech.* **40**: 610–612.

Smith C.R. (1984) A synthesized model of the near-wall behavior in turbulent boundary layers. *Proc. Symp. Turbul.* 8th, Rolla, Mo.

Smith F.T. (1977) The laminar separation of an incompressible fluid streaming past a smooth surface. *Proc. Roy. Soc. London*, A**356**: 443–463.

Smith F.T. (1978) Three-dimensional viscous and inviscid separation of a vortex sheet from a smooth non-slender body. *RAE TR* 78095.

Smith F.T. (1982) On high Reynolds theory of laminar flows. *IMA J. Appl. Math.* **131**: 207–281.

Smith J.H.B. (1968) Improved calculation of leading-edge separation from slender, thin delta wings. *Proc. R. Soc. London*, A**306**: 67–90.

Smith J.H.B. (1978) Inviscid fluid models, based on rolled-up vortex sheets, for three-dimensional separation at high Reynolds number. *AGARD LS*-94, Paper 9.

Smith J.H.B. (1984) Theoretical modelling of three-dimensional vortex flows in aerodynamics. *Aeronaut. J.* **88**: 101–116.

Smith R.A., Rosenbluth M.N. (1990) Algebraic instability of hollow electron columns and cylindrical vortices. *Phys. Rev. Lett.* **64**: 649.

Song M., Bernal L.P., Tryggvason G. (1992) Head-on collision of a large vortex ring with a free surface. *Phys. Fluids*, A**4**(7): 1457–1466.

Sozou C., Wilkinson L.C., Shtern V.A. (1994) On conical swirling flows in an infinite fluid. *J. Fluid Mech.* **276**: 261–271.

Spalart P.R. (1986) Numerical study of sink-flow boundary-layers, *J. Fluid Mech.* **172**: 306.

Spalart P.R., Allmaras S.R. (1992) A one-equation turbulence model for aerodynamic flows. *AIAA* 92–0439.

Sposito G. (1997) On steady flows with Lamb surfaces. *Int. J. Engng Sci.* **35**: 197–209.

Squire H.B. (1933) On the stability for three-dimensional disturbances of viscous fluid between parallel walls. *Proc. R. Soc. London*, A**142**: 621–628.

Squire H.B. (1956) Note on the motion inside a region of recirculation (cavity flow). *J.R. Aeron. Soc.* **60**: 203.

Srygley R.B., Thomas A.L.R. (2002) Unconventional lift-generating mechanisms in free-flying butterflies. *Nature*, **420**: 660–664.

Staley D.O., Gall R.L. (1984) Hydrodynamic instability of small eddies in a tornado vortex. *J. Atmos. Sci.* **41**: 422–429.

Starr V.P., Neiburger M. (1940) Potential vorticity as a conservative property. *J. Marine Res.* **3**: 202–210.

Stern M.F. (1975) Minimal properties of planetary eddies. *J. Mar. Res.* **33**: 1–13.

Stewartson K., Hall M.G. (1962) The inner viscous solution for the core of a leading-edge vortex. *J. Fluid Mech.* **15**: 306–318.

Stewartson K., Williams P.G. (1969) Self-induced separation. *Proc. Roy. Soc. London*, A**312**: 181–206.

Stoker J.J. (1958) *Water Waves: The Mathematical Theory with Applications*, Wiley, New York.

Stokes G.G. (1851) On the effect of internal friction of fluids on the motion of pendulums. *Trans. Camb. Phil. Soc.* **9**: Part II, 8–106.

Strouhal V. (1878) Uber eine besondere Art der Tonerregung. *Ann. Phys. Chem.(Liepzig)*, Neue Folge Bd. **5**(10): 216.

Stuart J.T. (1963) Unsteady boundary layer. In: Rosenhead L. (ed.) *Laminar Boundary Layers*. Oxford Clarendon Press, Oxford. 349–408.

Stuart J.T. (1967) On finite amplitude oscillations in laminar mixing layers. *J. Fluid Mech.* **29**: 417–440.

Stuart J.T. (1984) Instability of laminar flows, nonlinear growth of fluctuations and transition to turbulence. In: Tatsumi T.(ed.) *Turbulence and Chaotic Phenomena in fluids*, North-Holland Amsterdam, 17–26.

Stuart J.T. (1987) A critical review of vortex breakdown theory. Vortex control and breakdown behaviour, *Second International Colloquim on Vortex Flows*, Baden, Swotzerland, April 6–7, 1987.

Su W.D., Zhao H., Cai Q.D., Xiong A.K., Wu J.Z. (2002) A diagnosis of linear eddy-viscosity in turbulence modeling. *Phys. Fluids*, **14**: 1284–1287.

Sugavanam A. (1979) Numerical study of separated turbulent flow over airfoils. *Ph.D. thesis, Georgia Institute of Technology*, Atlanta.

Sullivan R.D. (1959) A two-cell solution of the Navier-Stokes equations. *J. Aero. Space Sci.* **26**: 767.

Sun M., Wu J.H. (2004) Large aerodynamic force generation by a sweeping wing at low Reynolds numbers. *Acta Mech. Sinica*, **20**: 24–31.

Surana A., Grunberg O., Haller G. (2005a) Exact theory of three-dimensional flow separation. Part I: steady separation. Submitted to *J. Fluid Mech.*

Surana A., Grunberg O., Haller G. (2005b) Exact theory of three-dimensional flow separation. Part II: Fixed unsteady separation. Preprint.

Surana A., Jacobs G., Haller G. (2005c) Exact separation patterns in cavity and backward-facing step flows. Preprint.

Sutyrin G.G. (1988) Motion of an intense vortex on a rotating globe. *Fluid Dyn.* **23**(4): 215–233.

Sutyrin G.G., Flierl G.R. (1994) Intense vortex motion on the beta plane: development of the beta gyres. *J. Atmos. Sci.* **51**: 773–790.

Swearingen J.D., Blackwelder R.F. (1987) The growth and breakdown of streamwise vortices in the presence of a wall. *J.Fluid Mech.* **182**: 255–290.

Sychev V.V. (1972) Laminar separation. *Mekh. Zhid. Gaza*, (3), 47–59. English translation: *Fluid Dyn.* **7**(3): 407–417.

Sychev V.V., Rubin A.I., Sychev Vic.V., Korolev G.L. (1998) *Asymptotic Theory of Separated Flows*, Cambridge University Press, Cambridge.

Synge J.L. (1933) The stability of heterogeneous liquids. *Trans. Roy. Soc. Can.* **3**: 1–18.

Ta Phuoc Loc., Bouard R. (1985) Numerical solution of the early stage of the unsteady viscous flow around a circular cylinder: a comparison with experimental visualization and measurement. *J. Fluid Mech.* **160**: 93–117.

Tabor M. (1989) *Chaos and Integrability in Nonlinear Dynamics*, Willey, New York.

Taneda S. (1956) Studies on wake vortices (III). Experimental investigation of the wake behind a sphere at low Reynolds numbers. *Rep. Res. Inst. Appl. Mech.* Kyushu Univ., **4**: 99–105.

Taneda S. (1985) Flow field visualization. In: Niordson F.I., Olhoff N. (eds.) *Theoretical and Applied Mechanics*. Elsevier Sci. 399–410.

Tani I. (1969) Boundary layer transition. *Ann. Rev. Fluid Mech.* **1**: 169–196.

Taylor G.I. (1918) On the dissipation of eddies. *Rep. Memo. Advis. Comm. Aeronaut.* no. 598.

Taylor G.I. (1923) Experiments on the motion of solid bodies in rotating fluids. *Proc. R. Soc.* A**104**: 213–218.

Telionis D.P. (1981) *Unsteady Viscous Flows*. Springer-Verlag, Berlin Heidelberg New York.

Teng Y.G., Liu T.S., Zhou M.D. (1987) An Experimental Study on the Vortex Control on a Delta Wing. In: Procedings of The First Chinese Symposium on Unsteady Flow and Vortex Control, Beijing.

Tennekes H., Lumley J.L. (1972) *A First Course in Turbulence*, MIT Press, Cambridge.

Theoderson T. (1952) *Mechanism of Turbulence*, Proc. 2nd. Midwestern Conf. In Fluid Mechanics.

Thomson, J.J. (1883) *A Treatise on the Motion of Vortex Rings*. London.
Thorpe A.J. (1985) Diagosis of balanced vortex structure using potential vorticity. *J. Atmos. Sci.* **42**: 397–406.
Ting L. (1971) Studies in the motion and decay of vortices. In: Olsen J.H., Goldburg A., Rogers M. (eds.) *Aircraft Wake Turbulence*, Plenum, New York. 11–39.
Ting, L. (1983) On the application of the integral invariants and decay laws of vorticity distributions. *J. Fluid Mech.* **127**: 497–506.
Ting L., Klein R. (1991) *Viscous Vortex Flows*. Spinger-Verlag, Berlin Heidelberg New York.
Ting L., Tung C. (1965) Motion and decay of a vortex in a nonuniform stream. *Phys. Fluids*, **8**: 1039–1051.
Tobak M., Peake D.J. (1982) Topology of three-dimensional separated flows. *Annu. Rev. Fluid Mech.* **14**: 61–85.
Tollmien W. (1935) General instability criterion of laminar velocity distributions. *NACA TM* 792.
Tong B.G., Cui R.J., Zhang B.X. (1993) *Unsteady Flow and Vortex Motion*. Defense Industrial Press (in Chinese).
Tong B.G., Yin X.Y., Zhu K.Q. (1994) *Theory of Vortex Motion*. University of Science and Technology of China Press (in Chinese).
Tong Y., Lombeyda S., Hirani A.N., Desbrun M. (2003) Discrete multiscale vector field decomposition. *Proc. SIGGRAPH 2003*, ACM, San Diego, July 27–31.
Townsend A.A. (1976) *The structure of turbulent shear flow*. Second edition, Cambridge University Press, Cambridge.
Trefethen L.N. (1991) Pseudospectra of matrices. In: Griffiths D.F., Watson G.A. (eds), *Numerical Analysis*, Longman, 234–266.
Trefethen L.N. (1993) Non-normal operators and pseudospectra(summary).
Trefethen L.N. (1997) Pseudospectral of linear operators. *SIAM Rev.* **39**(3): 383–406.
Trefethen L.N., Trefethen A.E., Reddy S.C., Driscoll T.A. (1993) Hydrodynamic stability without eigenvalues. *Science*, **261**: 578–584.
Triantafyllou G.S., Karniadakis G.E. (1990) Computational reducibility of unsteady viscous flow. *Phys. Fluids*, A**2**: 653–656.
Triantafyllou G.S., Triantafyllou M.S. (1986) On the formation of vortex streets behind stationary cylinders. *J. Fluid Mech.* **170**: 461–477.
Truesdell C. (1953) Two measures of vorticity. *J. Rat. Mech. Anal.* **2**: 173–217.
Truesdell C. (1954) *The Kinematics of Vorticity.* Indiana University Press, Bloomington, IN.
Truesdell C., Toupin R. (1960) The classic field theories. In: Flügge S. (ed.) *Handbuch der Physik* **III/1**, Springer-Verlag, Berlin Heidelberg New York 223–793.
Tryggvason G. (1988) Numerical simulation of the Rayleigh-Taylor instability. *J. Comput. Phys.* **75**: 253–282.

Tryggvason G. (1989) Vortex dynamics of stratified flows. In: Caflish R.E. (ed.) *Mathematical aspects of vortex dynamics*. SIAM, Philadelphia, 160–170.

Tryggvason G., Abdollahi-Alibreik J., Willmarth W.W., Hirsa A. (1992) Collision of a vortex pair with a contaminated free surface. *Phys. Fluids*, A**4**: 1215–1229.

Tsai C.Y., Widnall S.E. (1976) The stability of short waves on a straight filament in a weak externally imposed strain field. *J. Fluid Mech.* **73**: 721–733.

Tung C., Ting L. (1966) Motion and decay of a vortex ring. *Phys. Fluids*, **10**: 901–910.

Van Dommenlen L.L., Cowley S.J. (1990) On the Lagrangian description of unsteady boundary-layer separation. Part 1. General theory. *J. Fluid Mech.* **210**: 593–626.

Van Dommenlen L.L., Shen S.F. (1982) The genesis of separation. In: Cebici T. (ed.) *Numerical and Physical Aspects of Aerodynamic Flows*, Springer, Berlin Heidelberg New York 293–311.

Van Dyke M. (1970) Extension of Goldstein's series for the Oseen drag of a sphere. *J. Fluid Mech.* **44**: 365–372.

Van Dyke M. (1975) *Perturbation Methods in Fluid Mechanics*, Academic Press, San Diego.

Van Dyke M. (1982) *An Album of Fluid Motion*. The Parabolic stanford.

Varty R.L., Currie I.G. (1984) Measurements near a laminar separation point. *J. Fluid Mech.* **138**: 1–19.

Virk D., Hussain F. (1993) Influence of initial conditions on compressible vorticity dynamics. *Theor. Comput. Fluid Dyn.* **5**: 309–334.

Vladimirov V.A., Ilin K.I. (1988) Nonlinear stability of fluid flows: from Kelvin to Arnold. In: Tang Y.A., Zhao D.G. (eds.) *Proceedings of the Third International Conference on Fluid Mechanics*, Beijing, 1988, Beijing Institute of Technology Press.

Voropayev S.I., Afanasyev Y.D. (1994) *Vortex Structures in a Stratified Fluid*, Chapman and Hall.

Waleffe F. (1990) On the three-dimensional instability of strained vortices. *Phys. Fluids.* A**2**: 76–80.

Waleffe F. (1992) The nature of triad interactions in homogeneous turbulence. *Phys. Fluids.* A**4**: 350–363.

Waleffe F. (1993) Inertial transfers in the helical decomposition. *Phys. Fluids.* A**5**: 677–685.

Waleffe F. (1995a) Hydrodynamic stability and turbulence: Beyond transients to a self-sustaining process. *Studies Appl. Math.* **55**: 317–343.

Waleffe F. (1995b) Transition in shear flows. Nonlinear normality versus non-normal linearity. *Phys. Fluids.* **7**: 3060–3066.

Waleffe F. (1997) On a self-sustaining process in shear flows. *Phys. Fluids.* **9**(4): 883–900.

Walsh M.J. (1990) Riblets. In: Bushnell D., Hefner J., Reston V.A. (eds.) *Viscous Drag Reduction in Boundary Layers*, Progress in Astronautics and Aeronautics, *AIAA*, 123.

Wang C.M., Wu J.C. (1986) Numerical solution of Navier-Stokes problems using integral representation with series expansion. *AIAA J.* **24**: 1305–1312.

Wang C.Y. (1989) Exact solutions of the unsteady Navier-Stokes equations. *Appl. Mech. Rev.* **42**: S269-S282.

Wang C.Y. (1990) Exact solutions of the Navier-Stokes equations - the generalized Beltrami flows, review and extension. *Acta Mech.* **81**: 69–74.

Wang C.Y. (1991) Exact solutions of the steady Navier-Stokes equations. *Annu. Rev. Fluid Mech.* **23**: 159–177.

Wang K.C. (1970) Three-dimensional boundary layer near the plane of symmetry of a spheroid at incidence. *J. Fluid Mech.* **43**: 187–209.

Wang K.C. (1982) New developments in open separation. In: Fernholz H.H., Krause E. (eds.) *Three-dimensional Turbulent Boundary Layers*, Proceedings, IUTAM Symposium, Springer-Verlag, Berlin Heidelberg New York. 94–105.

Wang K.C. (1997) Features of three-dimensional separation and separated flow structure. In: Schmitt H. (ed.) *Flow at Large Reynolds Numbers*, Comput. Mech. Publications, 1–33.

Wang K.C., Zhou H.C., Hu C.H., Harrington S. (1990) Three-dimensional separated flow structure over prolate spheroids. *Proc. R. Soc. London*, A**421**: 73–90.

Wang S.X., Rusak Z. (1996a) On the stability of an axisymmetric rotating flow in a pipe. *Phys. Fluids*, **8**(4): 1007–1016.

Wang S.X., Rusak Z. (1996b) On the stability of non-columnar swirling flows. *Phys. Fluids*, **8**(4): 1017–1023.

Wang S.X., Rusak Z. (1997a) The dynamics of a swirling flow in a pipe and transition to axisymmetric vortex breakdown. *J. Fluid Mech.* **340**: 177–223.

Wang S.X., Rusak Z. (1997b) The effect of slight viscosity on a near-critical swirling flow in a pipe. *Phys. Fluids*, **9**(7): 1914–1927.

Wang Y.-X., Lu X.-Y., Zhuang L.-X. (2004) Numerical analysis of the rotating viscous flow approaching a solid sphere. *Int. J. Numer. Meth. Fluids* **44**: 905–925.

Weatherburn C.E. (1961) *Differential Geometry of Three Dimensions*. Cambridge University Press, Cambridge.

Wehausen J.V., Laitone E.V. (1960) Surface wave. In: Flügge S. (ed.) *Hundbuch der Physik*, **IX-III**, Springer-Verlag, Berlin Heidelberg New York 446–778.

Weidemann M.S. (1996) The weak wall-jet, Mater thesis, Department of Aerospace and Mechanical Engineering, the University of Arizona.

Weisbrot I., Wygnanski I. (1988) On coherent structures in a highly excited turbulent mixing layer. *J. Fluid Mech.* **195**: 137–159.

Weiss J. (1981) The dynamics of enstrophy transfer in two-dimensional hydrodynamics. LJI-TN-81–121, La Jolla Inst. La Jolla, California. Published in *Physica* D, **48**: 273–297.

Whitham G.B. (1963) The Navier-Stokes equations of motion. In: Rosenhead L. (ed.) *Laminar Boundary Layers*, Oxford University Press, New York 114–162.

Widnall S.E., Bliss D.B. (1971) Slender-body analysis of the motion and stability of a vortex filament containing an axial flow. *J. Fluid Mech.* **50**: 335–353.

Williamson C.H.K. (1989) Oblique and parallel modes of vortex shedding in the wake of a circular cylinder at low Reynolds numbers. *J. Fluid Mech.* **206**: 579–627.

Willaimson C.H.K. (1996) Vortex dynamics in the cylinder wake. *Annu. Rev. Fluid Mech.* **28**: 477–539.

Wiltse J.M., Glezer A. (1993) Manipulation of free shear flows using piezoelectric actuators. *J. Fluid Mech.* **249**: 261–285.

Wiltse J.M., Glezer A. (1998) Direct excitation of small-scale motions in free shear flows. *Phys. Fluids*, **10**: 2026–2046.

Winant C.D., Browand F.K. (1974) Vortex pairing - the mechanism of turbulent mixing layer growth at moderate Reynolds number. *J.Fluid Mech.* **63**: 237–255.

Wu J.C. (1976) Numerical boundary conditions for viscous flow problems. *AIAA J.* **14**: 1042–1049.

Wu J.C. (1981) Theory for aerodynamic force and moment in viscous flows. *AIAA J.* **19**: 432–441.

Wu J.C. (1982) Problems of general viscous flow. In: Benerjee P.K. (ed.) *Developments in Boundary Element Method*, **2**.

Wu J.C. (1984) Fundamental solutions and numerical methods for flow problems. *Int. J. Numer. Methods Fluids*, **4**: 185–201.

Wu J.C. (2005) *Elements of Vorticity Aerodynamics*, Tsinghua University Press, Tsinghua.

Wu J.C., Gulcat U. (1981) Separate treatment of attached and detached flow regions in general viscous flows. *AIAA J.* **19**: 20–27.

Wu J.C., Thomson J.F. (1973) Numerical solutions of time-dependent incompressible Navier-Stokes equations using an integral-differential formulation. *Computer & Fluids*, **1**: 197–215.

Wu J.C., Wang C.M., McAlister K.W. (2002) Wake-integral determination of aerodynamic drag, lift, and moment in three-dimensional flows. *AIAA* 2002–0555.

Wu J.M., Ondrusek B., Wu J.Z. (1996) Exact force and moment diagnostics of vehicle based on wake-plane data. *AIAA* 96–0559.

Wu J.M., Wu J.Z. (1992) Vortex lift at a very high angle of attack with massively separated unsteady flow. In: Kuwamura R., Aihara Y. (eds.) *Fluid Dynamics of High Angles of Attack*, Springer-Verlag, Berlin Heidelberg New York 35–63.

Wu J.Z. (1985) Asymptotic theory of flow separation. *Adv. Appl. Mech.* **15**: 31–48; 162–178. (in Chinese).

Wu J.Z. (1986a) Generation and absorption of vorticity at arbitrary three-dimensional body surfaces and its dissipation. *Acta Aerodyn.* **4**: 168 (in Chinese).

Wu J.Z. (1986b) Conical turbulent swirling vortex with variable eddy viscosity. *Proc. Roy. Soc.* A**403**: 235–268.

Wu J.Z. (1987) The force on moving bodies by vorticity field. *Acta Aerodyn.* **5**: 22–30 (in Chinese).

Wu J.Z. (1995) A theory of three-dimensional interfacial vorticity dynamics. *Phys. Fluids*, **7**: 2375–2395.

Wu J.Z., Gu J.W., Wu J.M. (1988a) Steady three-dimensional flow separation from arbitrary smooth surface and formation of free vortex layers. *Zeit Flugwiss. Weltraum.* **12**: 89–98.

Wu J.Z., Lu X.Y., Denny A.G., Fan M., Wu J.M. (1998) Post-stall flow control on an airfoil by local unsteady forcing. *J. Fluid Mech.* **371**: 21.

Wu J.Z., Lu X.Y., Zhuang L.X. (2005a) A unified derivative moment theory for aerodynamic force and moment. In: Yu H.R. (ed.) *Proc. Workshop on Modern Aerodynamics*, China Astronautics, China 243–262.

Wu J.Z., Ma H.Y., Wu J.M. (1994a) Viscous sound-vortex interaction in a duct shear flow. *J. Sound Vib.* **172**: 103–126.

Wu J.Z., Ma H.Y., Zhou M.D. (1993) *Introduction to Vorticity and Vortex Dynamics*, High Education Publications (in Chinese).

Wu, J.Z., Pan, Z.L., Lu, X.Y. (2005d) Unsteady fluid-dynamic force solely in terms of control-surface integral. *Phys. Fluids* **17**: 098102.

Wu J.Z., Roach R.L., Lo C.F., Zhu F.L., Dowgwillo R.M., Jiang L.B., Tramel R.W. (1999c) Aerodynamic diagnostics based on boundary vorticity dynamics. *AIAA* 99–3103.

Wu J.Z., Tramel R.W., Zhu F.L., Yin X.Y. (2000) A vorticity dynamic theory of three-dimensional flow separation. *Phys. Fluids*, **12**: 1932–1954.

Wu J.Z., Wu J.M. (1989) Vortical sourses of aerodynamic force and moment. SAE 89–2346.

Wu J.Z., Wu J.M. (1993) Interactions between a solid surface and a viscous compressible flow field. *J. Fluid Mech.* **254**: 183–211.

Wu J.Z., Wu J.M. (1996) Vorticity dynamics on boundaries. *Adv. Appl. Mech.* **32**: 19–275.

Wu J.Z., Wu J.M. (1998) Boundary vorticity dynamics since Lighthill's 1963 article. *Theor. Comput. Fluid Dyn.* **10**: 459–474.

Wu J.Z., Wu J.M., Wu C.J. (1988b) A viscous compressible theory on the interaction between moving bodies and flow field in the $(\omega, \vartheta)$ framework. *Fluid Dyn. Res.* **3**: 202–208.

Wu J.Z., Wu X.H., Ma H.Y., Wu J.M. (1994b) Dynamic vorticity condition: Theoretical analysis and numerical implementation. *Int. J. Numer. Method Fluids* **19**: 905–938.

Wu J.Z., Xiong A.K., Yang Y.T. (2005b) Axial stretching and vortex definition. *Phys. Fluids*, **17**: 038108.

Wu J.Z., Yang Y.T., Luo Y.B., Pozrikidis C. (2005c) Fluid kinematics on a deformable surface. *J. Fluid Mech.* **541**: 371–381.

Wu J.Z., Zhou Y., Fan M. (1999a) A note on kinetic energy, dissipation, and enstrophy. *Phys. Fluids*, **11**: 503–505.

Wu J.Z., Zhou Y., Lu X.Y., Fan M. (1999b) Turbulence as a diffusive field with vortical source. *Phys. Fluids*, **11**: 627–635.

Wu L.G., Wang B. (2000) A potential vorticity tendency diagnositic approach for tropical cyclone motion. *Mon. Weather Rev.* **128**: 1899–1991.

Wu T.Y. (2002) On theoretical modeling of aquatic and aerial animal locomotion. *Adv. Appl. Mech.* **38**: 291–353.

Wu X.H. (1994) On vorticity-based numerical methods for incompressible viscous flows. Ph. D. dissertation, University of Tennessee, Knoxville.

Wu X.H., Wu J.Z., Wu J.M. (1995) Effective vorticity-velocity formulations for three-dimensional incompressible viscous flows. *J. Comput. Phys.* **122**: 68–82.

Wygnanski I.J. (1997) Boundary layer and flow control by periodic addition of momentum. *AIAA* 97–2117.

Wygnanski I.J., Peterson R.A. (1987) Coherent motion in excited free shear flows. *AIAA J.* **25**(2): 201–213.

Xia X.J., Deng X.Y.(1991) *Engineering Separated Flow Dynamics*. Beijing University of Aeronautical and Astronautical Press. (in Chinese).

Xiong A.K. (2002) Mechanism of direct cascade of two-dimensional turbulence. *Proc. 9th Asian Congr. Fluid Mech.* May 27–31, Isfahan, Iran.

Xiong A.K., Wei Q.D. (1999) A study of analytical solutions for axisymmetric swirling flow. *Mech. Pract.* **21**(5): 15–16.

Xu H., Zhou M.D., Wygnanski I. (2000) Spatial correlation function as a tool to detect streamwise vortices. *Bull. Amer. Phys. Soc.* 45.

Yan Z.Y. (2002) *Theory of Low Reynolds-number Flows*. Peking University Press, Beijing. (in Chinese).

Yang Y.T. (2004) The effect of wave pattern of flexible wall on the drag reduction in turbulent channel flow. BS thesis, Peking University, Beijing. (in Chinese).

Yates J.E., Donaldson C. duP. (1986) A fundamental study of drag and an assessment of conventional drag-due-to-lift reduction devices. *NASA CP-4004*.

Yeung P.K., Brasseur J.G., Wang Q. (1995) Dynamics of direct large-small scale couplings in coherently forced turbulence: Concurrent physical- and Fourier-space views. *J. Fluid Mech.* **283**: 43.

Yih C.S., Wu F., Leibovich S., (1982) Conical vortices: a class of exact solutions of the Navier-Stokes equations. *Phys. Fluids*, **25**: 2147.

Yin X.Y., Sun D.J. (2003) *Vortex Stability*. National Defence Industry Press, Beijing (in Chinese).

Yin X.Y., Sun D.J., Wei M.J., Wu J.Z. (2000) Absolute and convective instabilities of viscous swirling vortices. *Phys. Fluids* **12**(5): 1062–1072.

Yin X.Y., Xia N. (1991) The investigation of spatial instability of swirling flow. In: Chien W.Z. (ed.) *Avance in Applied Mathematics and Mechanics in China*, **3**, International Academic Publishers, Twnhout Belgium.

Ying L.A. (1992) Optimal error estimates for a viscous splitting formula. In: Ying L.A., Guo B. (eds.) *Proceedings of 2nd Conference in Numerical Methods for Partial Differential Equations*, World Scientific, 139–147.

Yoshida Z., Giga Y. (1990) Remarks on spectra of operator rot. *Math. Z.* **204**: 235–245.

Yu D., Tryggvason G. (1990) The free-surface signature of unsteady, two-dimensional vortex flows. *J. Fluid Mech.* **218**: 547–572.

Zabusky N.J., Boratav O.W., Pelz P.B., Gao M., Silver D., Cooper S.P. (1991) Emergence of coherent patterns of vortex stretching during reconnection: a scattering paradigm. *Phys. Rev. Lett.* **67**: 2469–2472.

Zabusky N.J., Hughes M.H., Roberts K.V. (1979) Contour dynamics for the Euler equations in two dimensions. *J. Comput. Phys.* **30**: 96–106.

Zaman K.B.M.Q. (1996) Axis switching and spreading of an asymmetric jet: the role of coherent structure dynamics, *J. Fluid Mech.* **316**: 1–27.

Zdravkovich M.M. (1997) *Flow Around Circular Cylinders. Vol. 1: Fundamentals.* Oxford University Press, New York.

Zdravkovich M.M. (2002) *Flow Around Circular Cylinders. Vol. 2: Applications.* Oxford University Press, New York.

Zhang H.X. (1985a) The separation criteria and flow behavior for three-dimensional steady separated flow. *Acta Aerodyn.* **1**(1):1 (in Chinese).

Zhang H.X. (1985b) The behavior of separation line for three-dimensional steady viscous flow — based on boundary layer equation. *Acta Aerodyn.* **1**(4):1 (in Chinese).

Zhao H., Wu J.Z., Luo J.S. (2004) Turbulent drag reduction by traveling wave of flexible wall. *Fluid Dyn. Res.* **34**: 175–198.

Zhou H. (1982) On the nonlinear theory of stability of plane Poiseuille flow in the subcritical range. *Proc. Roy. Soc. A.* **381**: 407–418.

Zhou H., Zhao G.F. (2004) *Hydrodynamic Stability.* National Defence Industry Press, Beijing. (in Chinese).

Zhou Hong (1997) On the motion of slender vortex filaments. *Phys. Fluids* **9**(4): 978–981.

Zhou M.D. (1992) Separation, shear layer instability and their control. In Short Course Series "High Angle of Attack/Unsteady Flow Phenomena". University of Tennessee Space Institute, Tullahoma.

Zhou M.D., Fernholz H.H., Ma H.Y., Wu J.Z., Wu J.M. (1993) Vortex capture by two dimensional airfoil with small oscillating leading edge flap. *AIAA* 93–3266.

Zhou M.D., Wygnanski I. (1993) Parameters governing the turbulent wall jet in an external stream, *AIAA J.* **31**(5): 848–853.

Zhou M.D., Wygnanski I. (2001) The response of a mixing layer formed between parallel streams to a concomitant excitation at two frequencies. *J.Fluid Mech.* **441**: 139–168.

Zhou M.D., Wygnanski I. (2002) An experimental checking of MGL model, unpublished.

Zhu F.L. (2000) Applications of boundary vorticity dynamics to flow simulation, airfoil design, and flow control. Ph. D. Dissertation, University of Tennessee, Knoxville.

Zhu F.L., Yin X.Y., Wu J.Z. (1999) Short-wave instability of strained swirling vortex. *AIAA* 99–0139.

# Index

http://www.springer.com/978-3-540-29027-8

Vorticity and Vortex Dynamics

Wu, J.-Z.; Ma, H.-Y.; Zhou, M.-D.

2006, XIV, 776 p., 291 illus., Hardcover
ISBN: 978-3-540-29027-8

Jie-Zhi Wu
Hui-Yang Ma
Ming-De Zhou

# Vorticity and Vortex Dynamics

ISBN-13: 978-3-540-29027-8 © Springer-Verlag Berlin Heidelberg 2007

# Erratum

## Notations

Ch. x — Chapter x
p.y — page number y
Pg z — Paragraph number z
L u — Line number u
LB v — Line number v from bottom
$\Longrightarrow$ — changed to
[·] — contents to be changed is within square brackets

---

## Ch. 2:

P. 19, Equation (2.19b):

$$[\text{with} \quad \epsilon_{ijk}\Omega_{jk} = \omega_i] \Longrightarrow [\text{with} \quad -\epsilon_{ijk}\Omega_{jk} = \omega_i]$$

## Ch. 3:

P. 90, Equation (3.67):

$$[\boldsymbol{\omega} \times \boldsymbol{u} = \omega\nabla\psi = f(\psi, t)\nabla\psi = \ldots] \Longrightarrow [\boldsymbol{\omega} \times \boldsymbol{u} = f(\psi, t)\nabla_{\varphi} = \ldots]$$

## Ch. 4:

P. 141, the third term in the right-hand side of (4.26a):

$$[\boldsymbol{a}_p] \Longrightarrow [\boldsymbol{\sigma}_p]$$

P. 193, LB 6: [a commonly used formathrmis] $\Longrightarrow$ [a commonly used form is]

P. 209, The 3rd equation from bottom, left-hand side:

$$[\nu(\partial_3^3\omega_3)_B \ldots] \Longrightarrow [\nu(\partial_3^2\omega_3)_B \ldots]$$

## Ch. 6:

P. 258, Equation (6.12b):

$$\left[\boldsymbol{u}\cdot\left(\frac{\omega_\theta}{r}\right)=\ldots\right] \Longrightarrow \left[\boldsymbol{u}\cdot\nabla\left(\frac{\omega_\theta}{r}\right)=\ldots\right]$$

P. 262, L9: [The behavior of (6.25) for $r \gg 4\nu t$ approaches $\ldots$ ] $\Longrightarrow$ [The behavior of (6.25) for $r \gg \sqrt{4\nu t}$ approaches $\ldots$].

P. 273, Legend of Fig. 6.4: By the vector parallel to the $z$-direction, add velocity component $w$.

## Ch. 8:

P. 419, Equation (8.103):

$$\left[\frac{d}{dt}z_m(t)=\ldots\right] \Longrightarrow \left[\frac{d}{dt}\overline{z}_m(t)=\ldots\right]$$

## Ch. 9:

P. 510, Figure 9.31: the legend of the solid line, [(present throry)] $\Longrightarrow$ [(present theory)]

## Ch. 10:

P. 544, Caption of Fig. 10.22: [From Lee and Chen (2006)] $\Longrightarrow$ [From Lee and Chen (2005)]

## Ch. 11:

P. 609, Equation (11.46):

$$\left[\boldsymbol{F}_{\text{line}}=\frac{1}{2}\oint_{\partial S}\boldsymbol{x}\times(p d\boldsymbol{x}+2\mu\boldsymbol{\omega}\times d\boldsymbol{x})+\ldots\right] \Longrightarrow$$

$$\left[\boldsymbol{F}_{\text{line}}=\frac{1}{2}\oint_{\partial S}\boldsymbol{x}\times(p d\boldsymbol{x}+2\mu\boldsymbol{\omega}\times d\boldsymbol{x})+\ldots\right]$$

P. 629, Equation (11.79a,b):

$$\left[L = -\rho \int_V l_x dV = \ldots\right] \Longrightarrow \left[L = -\rho \int_V l_z dV = \ldots\right]$$

$$\left[D_{\text{in}} = -\rho \int_V l_y dV = \ldots\right] \Longrightarrow \left[D_{\text{in}} = -\rho \int_V l_x dV = \ldots\right]$$

## Appendix:

P. 694, L8: [Scalars and vectors are ...] $\Longrightarrow$ [Vectors and tensors are ...]

P. 696, Equation (A.6c):

$$\left[\Omega_{ij} \equiv \frac{1}{2}(u_{j,i} - u_{i,j}) = -\Omega_{ij}\right] \Longrightarrow \left[\Omega_{ij} \equiv \frac{1}{2}(u_{j,i} - u_{i,j}) = -\Omega_{ji}\right]$$

P. 706, Equation (A.42): the second term of the right-hand side,

$$\left[\boldsymbol{b}\frac{\partial \boldsymbol{t}}{\partial b}\right] \Longrightarrow \left[\boldsymbol{b} \cdot \frac{\partial \boldsymbol{t}}{\partial b}\right]$$

P. 707, the first line below equation (A.45),

$$[\xi 0] \Longrightarrow [\xi \neq 0]$$

## References:

P. 742, LB 5: [Lee C.B. Chen S.Y. (2006)] $\Longrightarrow$ [Lee C.B. Chen S.Y. (2005)]